UNIVERSIDADE TÉCNICA DE LISBOA

INSTITUTO SUPERIOR TÉCNICO

REFINED THREE-DIMENSIONAL SEISMIC ANALYSIS OF REINFORCED CONCRETE STRUCTURES

Luís André Marcos Mendes
(Mestre)

Orientador: Doutora Ema Paula de Montenegro Ferreira Coelho
Co-orientador: Doutor Luís Manuel Soares dos Santos Castro

Tese elaborada no Laboratório Nacional de Engenharia Civil para obtenção do Grau de Doutor em Engenharia Civil pela Universidade Técnica de Lisboa no âmbito do protocolo de cooperação entre o IST e o LNEC

Júri

Presidente: Presidente do Conselho Científico do IST
Vogais: Doutor António José Coelho Dias Arêde
Doutora Rita Maria do Pranto Nogueira Leite Pereira Bento
Doutor Luís Manuel Soares dos Santos Castro
Doutor Alfredo Peres de Noronha Campos Costa
Doutora Ema Paula de Montenegro Ferreira Coelho
Doutor Jorge Manuel Vinagre Alfaiate

Setembro de 2011

À Ana pela força,

ao André pela motivação,

ao João pelo exemplo.

Abstract

This thesis focuses on the development of advanced numerical models for the simulation of reinforced concrete structures under earthquake loading.

The main motivation for this work is the necessity felt to have a complementary, reliable and practical numerical tool to predict, follow and extend the experimental research developed in large-scale seismic testing facilities.

To contribute to this challenging goal, the methodology adopted is based on using refined three-dimensional meshes, the conventional Finite Element Method and a suitable time-integration scheme. The research presents three main axes: Firstly, to combine adequate constitutive relations to model the reinforced concrete response, which led to using continuum damage models for the concrete and global behaviour models for the reinforcing steel. Secondly, the concrete-steel interfaces were simulated by using zero-thickness interface elements and an original semi-analytical model defined at the reinforcement scale. Finally, the computational performance is enhanced by taking advantage of concurrent computations, using advanced substructuring techniques and reducing the problem size by using an innovative proposal of hybrid discretization.

The results obtained demonstrate that the proposed models are robust, accurate and present many advantages when compared to other approaches like static nonlinear analyses and modelling with fiber and phenomenological models.

Keywords:

Reinforced Concrete

Seismic Response Simulation

Incremental Dynamic Analyses

Inelastic Behaviour

Concrete-Steel Bond

Substructuring

Resumo

Esta tese centra-se no desenvolvimento de modelos avançados para a simulação de estruturas de betão armado sujeitas a acções sísmicas.

A principal motivação para este trabalho proveio da necessidade de existir uma ferramenta fiável e prática para prever, acompanhar e dar continuidade à investigação experimental desenvolvida em instalações de ensaios sísmicos.

A metodologia adoptada baseia-se na utilização da formulação convencional do método dos elementos finitos e de malhas refinadas. A investigação realizou-se segundo três eixos principais: i) Na combinação de modelos constitutivos adequados à simulação do betão armado, que conduziram à utilização da formulação da mecânica do dano contínuo para o betão, e de modelos de comportamento global para o aço em armaduras; ii) Na simulação da aderência aço-betão com elementos de interface de espessura nula e com base numa relação constitutiva semi-analítica original para a aderência; iii) Na melhoria da eficiência computacional tirando partido da computação paralela, de técnicas avançadas de análise estrutural e da redução da dimensão do problema usando uma proposta inovadora de discretização híbrida.

Os resultados obtidos demonstraram que os modelos propostos são robustos e precisos e que apresentam muitas vantagens quando comparados com outras metodologias, como as análises estáticas não lineares, e a modelação com recurso a fibras e a modelos fenomenológicos.

Palavras-chave:

Betão Armado

Simulação da Resposta Sísmica

Análise Dinâmica Incremental

Resposta Inelástica

Aderência Aço-Betão

Sub-estruturação

Agradecimentos & Acknowledgments

Em primeiro lugar gostaria de expressar toda a minha gratidão e reconhecimento à minha família, em particular aos meus Pais, que foram seguramente a principal razão pela qual consegui chegar a este nível científico bem como profissional. Estou seguro que o exemplo de trabalho e honestidade, foi e será um dos pilares mais fortes da minha vida e da minha carreira.

Este trabalho é dedicado a três pessoas que muito marcam a minha existência. À Ana, pela força, perseverança e amor que demonstrou nestes doze anos que estamos juntos, em particular, nos últimos cinco anos, que foram especialmente difíceis. Ao André, pela motivação que me deu e por ter mudado radicalmente a minha vida, enchendo-a de alegria e orgulho. Ao João, que desde tenra idade foi uma grande referência para mim.

Queria agradecer à Engenheira Ema Coelho, orientadora desta tese, pelo entusiasmo que demonstrou por este trabalho e por todo o apoio dado nestes últimos anos, em particular no início deste projecto, o qual considero ter sido muito importante para o desenvolvimento desta tese.

Queria expressar o meu sentido agradecimento ao Professor Luís Castro, co-orientador desta tese, pela confiança que demonstrou ter em mim nestes últimos dez anos, durante os quais tive o privilégio de trabalhar em conjunto. Queria manifestar a minha gratidão pelas sugestões que fez durante os trabalhos e pela incansável ajuda que me deu na melhoria da dissertação.

Queria também expressar o meu reconhecimento ao LNEC, na pessoa do Engenheiro João Almeida Fernandes, Director do Departamento de Estruturas, pelo apoio dado no processo de candidatura à bolsa de Doutoramento FCT, por ter proporcionado a minha participação em cursos no estrangeiro e pelo apoio logístico na execução das teses.

I would like to express my gratitude to the Researcher Pierre Pegon from the *Joint Research Center* (IPSC-ELSA) for all the support and suggestions made during the development of this thesis. In addition, also to Professor Sergio Proença from the *University of São Paulo* and to Professor Claudia Comi from the *University of Technology (Politecnico) of Milan,* for having the time to discuss some issues and for the suggestions made.

Gostaria de agradecer à Professora Rita Bento e ao Professor Jorge Alfaiate por terem aceitado fazer parte da *Comissão de Acompanhamento de Tese* e pelas sugestões que tiveram oportunidade de formular.

Não posso esquecer a contribuição dada pelos professores António Arêde e Nélson Vila Pouca no início deste trabalho, ajudando-me a definir alguns objectivos e algumas das abordagens que acabei por seguir.

Gostaria de agradecer à Conceição Melo pela ajuda administrativa que me deu nestes últimos meses e pelo profissionalismo e dedicação que testemunhei desde os meus tempos de aluno de mestrado.

Ao Engenheiro Júlio Pragana, agradeço as sugestões que deu relativamente a alguns aspectos relacionados com a escrita da tese na língua Inglesa.

Pese embora não tenha tido um relacionamento directo com a presente dissertação, não posso deixar passar esta oportunidade sem vincar a minha grande consideração profissional e estima pessoal pelo Engenheiro Alfredo Campos Costa.

Queria agradecer à *Fundação para a Ciência e a Tecnologia* pela atribuição da bolsa de Doutoramento com referência SFRH/BD/21491/2005/J03122797V2, entre 2006/10/01 e 2010/09/30.

Por último, agradeço a amizade da Rafaela e do Carlos, e dos meus primeiros colegas de gabinete o Mário e o Filipe. In addition, I cannot forget the fun moments I passed with Cường Tiến Phạm, and more recently, with Владимир Иванников.

À Clotilde, agradeço a amizade demonstrada e todo o apoio e carinho que tem dado à minha família nestes tempos de ausência forçada pela elaboração desta tese.

Se me esqueci de alguém que me ajudou neste trabalho, apresento as minhas sentidas desculpas e um grande Obrigado!

Obrigado a todos!

Thank you! Merci! Grazie! Cảm ơn! Спасибо!

Table of Contents

List of Figures

List of Tables

List of Algorithms

List of Symbols

Mathematical

$\mathbf{0}$	zero matrix
$\mathbf{I}$	identity matrix
$\mathbb{1}$	Boolean vector
$\varnothing$	null set
δ	Kronecker's delta
$\mathbf{A}^t$	transpose of matrix **A**
$\mathbf{A}^{-1}$	inverse of matrix **A**
$\mathbf{A}^+$	pseudoinverse of matrix **A**

Latin - Lower-case

a	acceleration; crack length
$\mathbf{a}$	acceleration vector
$\tilde{\mathbf{a}}$	virtual acceleration vector
$\mathbf{a}_G$	acceleration vector in modal or generalized coordinates
b	body force; width
$\mathbf{b}$	body force vector
c	viscous damping coefficient
c_c	critical damping
d	scalar damage variable; distance
d_+	tension damage
d_-	compression damage
d_a	maximum aggregate size
$\mathbf{d}_k$	kinematic equation *rhs* vector
e	specific internal energy by unit mass
e_r	relative error
f	loading function; dissipation potential
f_c	concrete compressive strength
f_{ct}	concrete tension strength
f_{ck}	5% characteristic concrete compressive strength
$f_{ctk,0.05}$	5% characteristic concrete tensile strength
f_c^d	dynamic concrete strength
f_c^s	static concrete strength
f_r	bond index
f_{sy}	steel yield strength
f_{su}	steel ultimate strength
$\mathbf{f}$	generalized Hooke's law (flexibility format); loading function; dissipation potential
g	gravity acceleration; fracture energy density
g_*	plastic potential function
g_f^{I}	mode I fracture energy density
$\mathbf{g}$	unbalanced forces vector
h	height; mesh size

h_r^m	mean rib height
k^*	nonlinear stiffness
k_0	initial peak stress secant stiffness
k_{pb}	perfect bond stiffness
k_s	secant constitutive matrix
k_{ul}	unloading stiffness
$\mathbf{k}$	generalized Hooke's law (stiffness format)
m	mass
n_{it}	number of iterations
n_{it}^{div}	maximum number of divergent iterations
$n_{it}^{\max}$	maximum number of iterations
$\mathbf{n}$	normal vector
$\mathbf{n}_*$	outward normal to the yield function vector
$\mathbf{p}$	modal participation factor vector
q	displacement
$\overline{q}$	displacement amplitude
q'	behaviour factor
q_{imp}	imposed/prescribed displacement
q_γ	displacement at the kinematic boundary
q_t	top displacement
q_t^*	top displacement of the equivalent *sdof* system
$\mathbf{q}$	displacement vector; heat flux by unit area vector
$\tilde{\mathbf{q}}$	virtual displacement vector
$\mathbf{q}_G$	displacement vector in modal or generalized coordinates
$\mathbf{q}^{rel}$	relative displacement vector
$\mathbf{q}_{ine}^{rel}$	inelastic displacement vector
r	ratio; radius; radius of gyration; radial relative displacement
$\mathbf{r}$	residual vector
s	slip; Line-Search slope
s_0	peak stress slip
s_f	severity factor
s_{ine}	equivalent inelastic slip
$s_{\max}$	maximum slip reached in both directions
s_{pb}	perfect bond slip limit
s_{pk}	peak stress slip
s_r	rib spacing
s_{res}	slip at the beginning of the loading residual stress plateau
s_{rld}	reload slip
s_s	lateral support spacing (bar buckling)
s^*	normalized accumulated slip
t	time; thickness
t_γ	boundary forces vector
t_c	computing time
t_c^p	computing time for the parallelized code

t_c^s	computing time for the sequential code
v	velocity
$\mathbf{v}$	velocity vector
$\tilde{\mathbf{v}}$	virtual velocity vector
$\mathbf{v}_G$	velocity vector in modal or generalized coordinates
w	width
w_c	crack width
w_{gp}	Gauss point weight
w_{gp}^{nl}	Gauss point weight for the nonlocal model
x	global Cartesian coordinates
$\tilde{\mathbf{x}}$	geometry approximation vector
y	local Cartesian coordinates
z	distance between the critical zone and the inflexion point (plastic hinge length)

Latin - Upper-case

A_{cr}	crack area
A_{cs}	cross-section area
A_r	area of the transversal ribs projected into the transversal direction
A_s	steel reinforcement cross-section area
A_s^{eff}	effective steel reinforcement cross-section area
$\mathbf{A}$	element to global domain assembler matrix; amplification matrix
$\mathbf{B}$	strain matrix
$\mathbf{C}$	damping matrix
$\mathbf{C}^C$	condensed damping matrix
D	dimension/size
D_f	dynamic factor
E	elasticity modulus; efficiency
E^*	damaged elasticity modulus
E_c	concrete elasticity modulus
E_d	dissipated energy
E_s	steel elasticity modulus
E_{sh}	steel hardening tangent modulus
G	distortion modulus
G_{cr}	critical strain energy release rate
G_f	fracture energy
G_f^{I}	mode I fracture energy
G_f^{II}	mode II fracture energy
G_f^{III}	mode III fracture energy
$\mathbf{G}$	rigid body mode matrix
H	enthalpy; subdomain size
J	Jacobian
$\mathbf{J}$	Jacobian matrix
K	stress intensity factor
K_{I}	fracture toughness

$\mathbf{K}$	stiffness matrix
$\hat{\mathbf{K}}$	effective stiffness matrix
$\mathbf{K}_s$	secant stiffness matrix
$\mathbf{K}_t$	tangent stiffness matrix
$\mathbf{K}^C$	condensed stiffness matrix
L	length;
L_a	anchorage length
L_b	interaction radius for computing the radial stress
L_c	characteristic length
L_e	element length
L_{FPZ}	fracture process zone length
L_{nl}	nonlocal length
L_p	plastic hinge length
L_r	rib length
L_{ref}	refined mesh length
L_t	transfer length
$\mathbf{L}$	compatibility differential operator; load operator
$\mathbf{L}^*$	equilibrium differential operator
M	mass; bending moment
M_p	plastic bending moment
$\mathbf{M}$	mass matrix; Story mass matrix
$\mathbf{M}^*$	mass of the equivalent *sdof* system
$\mathbf{M}^{-1}$	preconditioner matrix
$\mathbf{M}^C$	condensed mass matrix
$\mathbf{M}_{BDD}^{-1}$	Balancing Domain Decomposition preconditioner matrix
$\mathbf{M}_D^{-1}$	Dirichlet preconditioner matrix
$\mathbf{M}_L^{-1}$	Lumped preconditioner matrix
$\mathbf{M}_{NN}^{-1}$	Neumann-Neumann preconditioner matrix
N	normal force
N_c	Number of cycles
$\mathbf{N}$	outward normal matrix
P_c	contact perimeter
$\mathbf{P}$	penalty matrix; projection matrix; earthquake excitation factors
Q	force; heat
Q_r	radial force
Q_s	bond force
$\hat{\mathbf{Q}}$	effective forces vector
$\mathbf{Q}_b$	body forces vector
$\mathbf{Q}_i$	internal forces vector
$\mathbf{Q}_e$	external forces vector
$\overline{\mathbf{Q}}_e$	time-independent external force vector (load pattern)
$\mathbf{Q}_K$	kinematic constraint forces vector
$\mathbf{Q}_N$	nodal force vector
$\mathbf{Q}_\gamma$	static boundary force vector

$\mathbf{Q}_e^C$	condensed external forces vector
R	strength reduction factor; interaction radius; curvature radius (GMP model)
R_μ	reduction factor due to ductility
R	nullspace matrix
S	total area; Speed-up; entropy;
S_a	spectral acceleration
S_{ae}	elastic spectral acceleration
S_d	spectral displacement
S_{de}	elastic spectral displacement
S^{eff}	effective area
T	time function
T	period; temperature
T^*	equivalent period
T_c	characteristic period
T_e	effective fundamental period
T	transformation matrix
$\mathbf{T}_f$	tuning factor
$\mathbf{T}_{LK}$	kinematic transformation matrix
$\mathbf{T}_{xX}$	transformation matrix between global to structure coordinates
U	internal energy
V	shear force
V_b	base shear force
V_b^*	base shear force of the equivalent *sdof* system
W	work; Gauss point weight for the nonlocal model
W_d	work done by damping forces
W_i	work done by internal forces
W_{in}	work done by inertial forces
W_e	work done by external forces
X	global Cartesian coordinates (structure)
Y	thermodynamic forces; strain energy density release rate
Z	rigid body mode matrix

Greek - Lower-Case

α	α-Method coefficient; penalty number
α_d	mass matrix factor (proportional damping)
α	rigid body modes combination vector
β	plastic modulus ratio
β_d	stiffness matrix factor (proportional damping)
β_r	rib inclination with the longitudinal axis of the bar
β_{LS}	Line-Search method tolerance
β_q	displacement convergence tolerance
β_Q	force convergence tolerance
χ	Curvature; Gibbs free energy
δ	infinitesimal increment
γ	distortion; Newmark's coefficient; rate of entropy change per unit mass; speed-up correction fact.

γ^*	corrected speed-up correction factor
γ_b	cyclic strength degradation factor
γ_f	fatigue factor
ε	strain
$\tilde{\varepsilon}$	comparison strain
$\overline{\varepsilon}$	equivalent strain
ε_*	plastic multiplier
ε_{ap}	plastic strain amplitude
ε_s	steel axial strain
ε_{sh}	steel axial strain at the beginning of the strain hardening branch
ε_{sy}	steel axial strain at the yield stress
ε_{su}	steel axial strain at peak stress
ε^{eff}	effective strain
ε_s^*	normalized steel axial strain (GMP model)
ε_{sa}^*	normalized steel axial strain at the inversion point (GMP model)
ε_{sp}^{ac}	accumulated plastic strain
$\tilde{\varepsilon}_{sp}^{ac}$	corrected accumulated plastic strain
$\boldsymbol{\varepsilon}$	strain vector
$\underline{\boldsymbol{\varepsilon}}$	strain tensor
κ	condition number
κ_Q	Arc-Length coefficient
μ	friction coefficient; ductility factor; arithmetic mean
η	damping coefficient; Line-Search step length; entropy density per unit mass
$\eta_{\max}$	maximum time step increment
η_{rst}	time step reducing factor
$\eta_m^{\pm}$	strength scaling factor
λ	eigenvalue; size ratio; bar slenderness; model-prototype geometric scale; Lagrange multiplier
λ_c	nonlocal characteristic length
$\boldsymbol{\lambda}$	Lagrange multiplier vector
θ	rotation; Wilson-θ method coefficient
ϕ_*	yield function
ϕ_b	bond envelope function
ϕ_s	reinforcing bar diameter
ν	Poisson's coefficient; Newmark's method coefficient; normalized axial load
ν^*	apparent Poisson's ratio
ρ	specific mass; spectral radius; cross-modal coefficient
τ	tangential stress; relative time
τ_b	bond stress
σ	stress; standard deviation; local truncation error
$\tilde{\sigma}$	comparison stress
σ_{cr}	critical stress
σ_N	nominal stress
σ_{rad}	radial stress
σ_s	steel axial stress

σ_{su}	steel ultimate stress
σ_{sy}	steel yield stress
σ^{eff}	effective stress
σ_s^*	normalized steel axial stress (GMP model)
σ_{sa}^*	normalized steel axial stress at the inversion point (GMP model)
$\boldsymbol{\sigma}$	stress vector
$\underline{\boldsymbol{\sigma}}$	stress tensor
ψ	shape function; Helmholtz free energy
ω	angular frequency
ω_d	damped angular frequency
ξ	damping ratio; internal variable
$\overline{\xi}$	numerical damping ratio
$\overline{\xi}_r$	numerical frequency damping ratio
ζ	absolute value of the last plastic deformation (GMP model)

Greek - Upper-Case

Δ	finite increment
Π	potential energy
Π_i	internal force potential
Π_e	external force potential
Ω	domain; reduced angular frequency
Ω_c	critical reduced angular frequency
$\overline{\Omega}_r$	numerical resonant angular frequency
$\boldsymbol{\Omega}$	diagonal matrix holding the squared angular frequencies
Γ	boundary; Transformation factor between mdof and sdof systems
Γ_q	kinematic boundary
Γ_σ	static boundary
ρ	mass density
$\boldsymbol{\rho}$	mass density matrix
$\boldsymbol{\Psi}$	shape function matrix
$\boldsymbol{\Psi}'$	shape function derivative matrix
$\boldsymbol{\Psi}^*$	geometry approximation function matrix
$\boldsymbol{\Phi}$	mode shape matrix; displacement shape vector

Other Fonts

$\hat{\mathcal{A}}$	element to subdomain assembler matrix – unsigned Boolean operator (primal)
$\mathcal{A}$	subdomain to domain assembler matrix – unsigned Boolean operator (primal)
$\mathcal{B}$	signed Boolean operator (dual)
$\mathcal{C}$	Cauchy number
$\mathcal{C}_K$	kinematic constraint matrix
$\mathcal{C}_{LK}$	Local kinematic constraint matrix
$\mathcal{C}_{GK}$	Global kinematic constraint matrix
$\mathcal{D}$	Damping matrix in modal or generalized coordinates
$\mathcal{F}$	Froude number
$\mathcal{S}$	condensed stiffness matrix – Schur Complement

$\mathcal{Q}$	condensed force vector – Schur Complement *rhs*

Superscript

C	condensed
d	dynamic
e	elastic
eff	effective
el	element
i	iteration
MN	master node
nl	nonlocal
p	plastic; predictor
rel	relative
s	static
sd	subdomain
SN	slave node
t	total

Subscript

0	initial value
b	boundary; boundary local/subdomain
B	boundary global
c	concrete; cycle; condensed *dof*, local/subdomain corner node *dof*
C	global/domain corner node *dof*
d	damping
e	external
gp	Gauss point
G	global, modal or generalized coordinates
GK	global kinematic constraint
i	internal; internal local/subdomain
in	inertia
imp	imposed/prescribed
j	time step
LK	local kinematic constraint
m	master subdomain; mean
M	model; master global/domain
P	prototype
r	retained *dof*; remaining *dof*
s	slave; slave local/subdomain
S	slave global/domain
u	ultimate

List of Abbreviations

a.k.a.	Also known as
ADRS	Acceleration-Displacement Response Spectra
AL	Arc-Length
B2S	Beam2Solid
BDD	Balancing Domain Decomposition
BDDC	Balancing Domain Decomposition with Constraints
CC	Cylindrical crack
CDM	Continuum Damage Mechanics
CG	Conjugate Gradient
CPU	Central Processing Unit
CR	Clock Rate
CS	Capacity Spectrum
CSI	Concrete-Steel Interfaces
DD	Domain Decomposition
DIF	Dynamic Increase Factor
DM	Damage Mechanics
dof(s)	degree(s)-of-freedom
EBB	Euler-Bernoulli Beam
FE	Finite Element
FEM	Finite Element Method
FETI-1	One-level Finite Element Tearing and Interconnecting
FETI-2	Two-level Finite Element Tearing and Interconnecting
FETI-T	FETI with coarse problem designed for time-dependent problems
FLOPS	Floating point operations per second (Flop/s)
FM	Fracture mechanics; Fibre Model
FPZ	Fracture Process Zone
GE	Gaussian Elimination
GKC	Global Kinematic Constraints
GMP	Guiffrè-Menegotto-Pinto model
GR	Guyan Reduction
GSA	Global Structural Analysis
H20	20-noded hexahedron
H8	8-noded hexahedron
HD	Hybrid Discretizations
HPC	High Performance Computing
IDA	Incremental Dynamic Analyses
IPC	Instructions per cycle
IST	Instituto Superior Técnico
KC	Kinematic constraint(s)
L2	2-noded linear geometry element
LATIN	Large Time Increment
LEFM	Linear Elastic Fracture Mechanics
lhs	left-hand side
LKC	Local Kinematic Constraints
LM	Lagrange Multipliers
LNEC	Laboratório Nacional de Engenharia Civil
LS	Line-Search
mdof	multi degree-of-freedom
MIMD	Multiple Instructions - Multiple Data Streams
MISD	Multiple Instructions - Single Data Stream
MN	Master Node
mNR	Modified Newton-Raphson
MP	Message Passing

MPI	Message Passing Interface
MPU	Master Processing Unit
MSE	Master-Slave Elimination
NEFM	Nonlinear Elastic Fracture Mechanics
NL-IDA	Nonlinear Incremental Dynamic Analysis
NL-SA	Nonlinear Static Analysis
NN	Neumann-Neumann
NR	Newton-Raphson
NS	Number of samples
OS	Operator-splitting method; Operating System
ParaNoiD	Parallel Non-Linear Dynamic code
PB	Perfect Bond
PC	Personal Computer
PCG	Preconditioned Conjugate Gradient
PGA	Peak Ground Acceleration
PS	Primal Substructuring
PsD	Pseudo-dynamic
PU	Processing Unit
PVM	Parallel Virtual Machine
Q4	4-noded quadrilateral
RAM	Random-Access Memory
RB	Ribbed Bar
RBM	Rigid Body Modes
RC	Reinforced Concrete
REBAP	Regulamento de Estruturas de Betão de Armado e Pré-Esforçado
rhs	right-hand side
RP	Reduced Problem
RS	Response Spectrum
RSA	Regulamento de Segurança e Acções para Estruturas de Edifícios e Pontes
RSD	Relative Standard Deviation
SB	Smooth Bar
SC	Splitting Crack; Schur Complement
sdof	single degree-of-freedom
SIMD	Single Instruction - Multiple Data Streams
SISD	Single Instruction - Single Data Stream
SN	Slave Node; Secant Newton
SPU	Subdomain Processing Unit
SSA	Substructured Structural Analysis
SVD	Singular Value Decomposition
TE	Transformation Equations
TI	Time Integration
X-FEM	Extended Finite Element Method

Latin expressions

e.g.	*exempli gratia*, free as an example/for example
et al.	*et alii*, and others
etc.	*et cetera*, and other things/and so on
i.e.	*id est*, it is/that is
quasi	almost/as it were
vice versa	the other way around
vs.	*versus*, turned against

Chapter I

Introduction

1 Initial considerations

The inhabitants of *Planet Earth* are subjected to several natural hazards that can originate from geological, hydrological, climatic or from other sources. Some of those hazards, like earthquakes, are inevitable and unpredictable with our current knowledge level. Historical data shows that earthquakes had important social and cultural consequences, not only due to the large number of victims (*e.g.* about 830,000 for an earthquake in China during the 16th century), but also due to the cultural impact on society (*e.g.* the intellectual debate raised after the Lisbon earthquake in 1755 during the *Age of Enlightenment*).

Earthquake engineering has been able to respond with adequate solutions to mitigate the safety-related problem (life-preservation), and nowadays seismic vulnerability for modern structures is more related to incorrect design, deficient construction or inadequate materials than to insufficient knowledge to create anti-seismic constructions. Consequently, the highest vulnerability and the most serious safety problems are often found in less economically and technically developed societies, which experience deadly and devastating earthquakes, *e.g.* countries in Asia, the Middle-East and South and Central America. This problem is still very real, as earthquakes are still causing a large number of deaths. It should be emphasized that in the 21st century more than 520,000 fatalities occurred following three large earthquakes, precisely in those regions (the Sumatra, Haiti and

Sichuan-China earthquakes) [550].

On the other hand, in the most developed regions, it has been possible to observe the trend of the seismic events resulting in a relatively "small" number of deaths, in spite of having high ground shake intensities. Most of the times, this trend was combined with heavy economic losses that also caused a large impact on the societies, fortunately in a less devastating manner. This was the case of the *Northridge* earthquake in USA and of the *Kobe* and *Niigata-Chūetsu* earthquakes in Japan.

Earthquake economic impacts can be classified as direct, if they result directly from the seismic activity, like the costs associated with repair or to replace the building stock, but also from indirect sources, related to the impact of the earthquake on the economy, for example reductions in demand and supply shortages [70]. All together, these impacts represent a very significant handicap and introduce serious constraints on the economic health of the countries affected. Their consequences should not be ignored or underestimated.

Further information regarding earthquake consequences can be retrieved by analysing the global trend in terms of the number of deaths (ND) and the economic losses (EL). Figure I.1 presents the number of deaths and the economic losses worldwide during the 20th century. It is possible to observe that the total number of deaths presents a large dispersion that is related to the influence of particularly deadly events that significantly change the baseline tendency (*e.g.* two large earthquakes in the twenties and seventies) [419]. Nevertheless, the global evolution reveals a decreasing trend in terms of the number of deaths per decade, even though the world population has increased about 368% during this century. It should be noted that the first decade of the 21st century has been particularly deadly, mainly due to the three earthquakes already mentioned. Moreover, during the same period the estimated economic losses showed an undeniable growth propensity, which appears to be increasing at an exponential rate. This trend represents very significant information about the evolution of the consequences of earthquakes, which must be interpreted as an indication

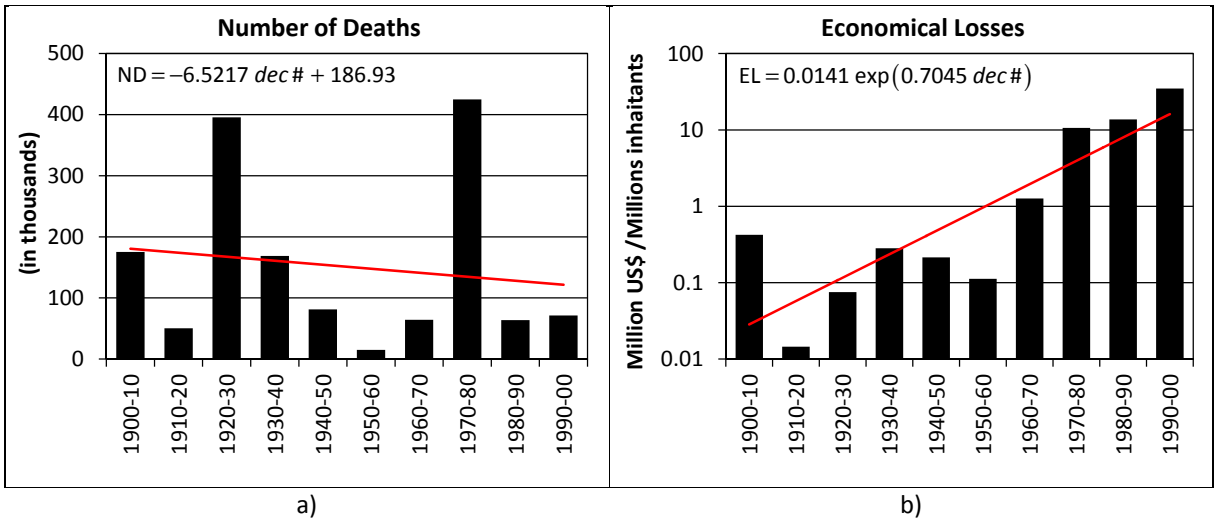

Figure I.1: Earthquake consequences for each decade of the 20th century, adapted from [419]:
a) Total number of deaths; b) Global economic losses.

for the future of earthquake engineering. From the author's point of view, earthquake engineering will gradually focus on reducing the damage caused by seismic events, and consequently the economic losses, rather than focus only on the safety problem (life preservation). Prescribing higher performance level for the structures is a desirable trend and a sign of technological advance and maturity.

To achieve higher seismic performance levels, the advisable design approach is currently more associated with controlling the displacements of the structure rather than controlling the forces. This concept is often called *displacement-based design*, in which the structure is designed using global or local displacement-related quantities in order to assess if the structure follows the desired performance level. This contrasts with the traditional *force-based design* that is roughly based on stiffness, yield strength and ductility, and is adopted in the majority of seismic codes (*e.g.* Eurocode 8 [92]), mainly because this approach is more suitable for the design for other load types, *e.g.* gravity, snow and wind induced forces.

Furthermore, the displacement-based design is considered to be more appropriate to control the level of structural and non-structural damage, because damage under intense nonlinear response is more sensitive to displacement than to force changes [215], as illustrated in Figure I.2 for the case of a slender reinforced concrete (RC) shear wall. According to FIB [215], structural damage starts at an early stage of loading (*e.g.* concrete cracking). On the other hand, extended damage on structural and non-structural elements requires large deformations that are more easily controlled by assessing the displacement rather than the forces.

Increasing the desired performance level for seismic loads must be accompanied by increased knowledge regarding the structural behaviour at intense inelastic stages. Experimental research plays an important role to achieve this and monotonic, cyclic and especially dynamic tests are a major source of technological developments. Dynamic testing of full structures is commonly made using the dynamic shaking tables or using the pseudo-dynamic testing procedure (see Chapter II-§4.3.3 and Figure II.12). These techniques allow testing large-scale RC models representing cast *in-situ* or precast RC structures. Common motivations for this type of research are the seismic vulnerability

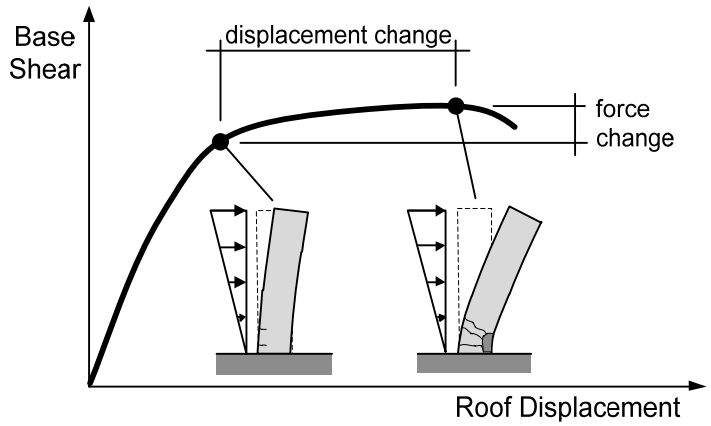

Figure I.2: The relation between damage and force and displacement changes, adapted from [215].

assessment of typical or models of existing structures, efficiency studies for reinforcing solutions, protection systems and dissipation devices, *etc.* Possible examples are the SPEAR [118] and PRECAST [392-394] projects, funded by the *European Commission*, for studying the seismic behaviour of torsionally unbalanced structures representative of southern Europe RC construction previous to specific seismic regulation and for studying a precast solution for buildings, respectively (see Figure I.3).

The dynamic shaking table tests are often made using reduced scales for large structures, because of the testing equipment limitations (*e.g.* shaking table payload, dimensions in plan, maximum acceleration, *etc*.), which introduce similitude law distortions and material dissimilar behaviour. On the other hand, pseudo-dynamic testing is commonly made with full-scale specimens that avoid this sort of problem. However, the dynamic response of the materials is not simulated and inertia forces are lumped in a discrete set of points. Nevertheless, both testing techniques are able to produce good quality results concerning the global and local structural behaviour. The major disadvantages of the experimental approach are related to the requirement of extremely specialized personnel and equipment, which present large access and operation costs. Moreover, the specimens are expensive to construct and reutilization is minimal due to the destructive nature of these tests. Furthermore, establishing conclusions about the structural reliability is difficult on the basis of one or a few tests, due to the statistical nature of this type of evaluation.

All these disadvantages accentuate the necessity of having reliable and practical complementary tools for the experimental approach. Clearly, this points to the numerical simulation technique that could be used for pre-test prediction, following and comparing with results from on-going tests and for extending the research programme in terms of quantity and diversity after post-test calibration.

Undeniably, the interconnection of experimental and numerical simulations is extremely convenient due to the complementary nature of both approaches. The experimental activity produces results that are strongly connected to the effective structural response. However this method is expensive

a)

b)

Figure I.3: Examples of experimental studies with RC structures performed at LNEC:
a) SPEAR Project [118]; b) Precast Project [392-394].

and lacks flexibility and the generalization to other situations is limited. On the other hand, numerical simulations can be used to overcome these drawbacks. Nevertheless, without an experimental calibration of the model parameters or confirmation of the global structural behaviour, these simulations can move far away from reality and lead to meaningless data.

Using numerical simulation tools to complement the large-scale dynamic experiments is still a challenging task because there are still many limitations for the numerical modelling of structures subjected to earthquake loading, in particular for RC structures. This type of simulation must be performed using nonlinear dynamic analyses to adequately represent the dynamic nature of the structural behaviour. This type of analysis is recognized as having a degree of complexity above other methods, like nonlinear static analyses, *a.k.a. pushovers*. Some of the additional sources of complexity associated with nonlinear dynamic analyses are:

i. They are often performed using time integration procedures to solve the motion equation using an incremental approach;
ii. They require time-based inputs (*e.g.* earthquake time histories) and output large amounts of time-based results (*e.g.* displacements, velocities, acceleration, strains, stresses, state variables, *etc*.);
iii. They require defining mass distributions and damping models that do not have a simple or ideal solution;
iv. They require considering the cyclic response in the constitutive relations for the materials, which significantly increases the modelling difficulty when compared with analyses based on the monotonic response. The introduction of rate-dependent constitutive relations is also not easy to implement efficiently.

Furthermore, when the objective is to simulate complex phenomena like three-dimensional strain and stress states in the concrete or imperfect concrete-steel bond, it is necessary to adopt refined three-dimensional meshes that invariably result in very large problem sizes. This leads to significant challenges, both in terms of the computation requirements (hardware) and in terms of the analysis codes (software).

In conclusion, performing refined three-dimensional seismic analyses of reinforced concrete structures presents significant difficulties in terms of the global formulation, the amount of input and output data, the complexity of the constitutive relations and meshes, and significant computational and implementation challenges. These are very significant drawbacks and the path seems to be a very arduous and laborious. This scenario has inhibited research and new developments in models using this approach. Researchers and earthquake engineers have asked the inevitable questions: Is it worth it? What is the cost-benefit scenario? Can we use a simplified approach?

From the author's point of view, the answers to these questions are not simple. Undoubtedly, using refined three-dimensional seismic analyses for common design tasks, or even, for seismic vulnerability assessment of ordinary structures, is currently not advisable or feasible. On the other hand, when the objective is to simulate the effective dynamic response or to have a complementary numerical tool for the experimental seismic tests, then this seems to be the best approach.

2 Scope and motivation

This thesis was developed following about nine years of activity of the author in the *Earthquake Engineering and Structural Dynamics division*, part of *Laboratório Nacional de Engenharia Civil* (LNEC). This research group has the opportunity to develop experimental activity in one of Europe's large testing facilities, which makes use of two shaking tables (see Figure I.4). Further details about the facility can be found in the work of Bairrão [24].

Within the framework of this activity, the research team to which the author belongs, always strived to take the most advantage possible of the enormous source of information provided by a shaking table test. As mentioned before, both the operation of the facility and the tests are quite expensive. Therefore, it is vital to exploit the results obtained as much as possible, and if possible, extend them to other cases. From the author's point of view, having an adequate numerical simulation tool is vital for the efficiency of the experimental research performed at LNEC.

A numerical simulation tool that could be a feasible partner for the experimental research being developed at LNEC must follow the approach described in the previous section. It is an irrefutable fact that there is still a long way to go in order to have a feasible and practical tool that could act as a complement and an extension to the experimental research performed at this type of facility.

Other sources of motivation for this work were the increasing availability of advanced computing tools and the recent advances made with substructuring techniques. Nowadays, most research facilities have access to some form of high performance computing system, either multi-processor workstations (*e.g.* 16-processor *Civil10* workstation installed at the Civil Engineering Department of *Instituto Superior Técnico* - IST) or to clusters (*e.g.* the 276-processor *Medusa* cluster installed at LNEC). Moreover, significant advances have been made with Mesh Partitioning techniques and Domain Decomposition methods. These issues are discussed in more detail in Chapter V.

Furthermore, developing numerical models that could complement the experimental seismic tests would be particularly beneficial from the financial point of view, because this would enhance the

a) b)

Figure I.4: Large-scale seismic testing facility at LNEC: a) Uniaxial shaking table; b) Triaxial shaking table.

research results and would contribute to reduce the necessity for experimental testing.

This work was developed with a strong conviction that the adopted approach represents the correct path to be followed and can be seen as an investment in a research direction that will play a significant role in the future of earthquake engineering.

3 Objectives

The etymology of the word *thesis* comes from the Greek θέσις, which means position and refers to an intellectual proposition [573]. Taking this into consideration, the position defended by this thesis is that *Nonlinear Incremental Dynamic Analyses* (NL-IDA) combined with refined meshes and advanced constitutive models, should be used to accurately simulate the seismic behaviour of RC structures.

As discussed before, it seems undeniable that using this approach results in complex models, large problem sizes and significant modelling challenges that must be overcome. Nevertheless, this was identified as a viable and fertile research direction. Therefore, the main objective of this thesis is to contribute to mitigate these difficulties and make this approach more feasible and attractive for research studies.

At this stage, the work done in the framework of a *Doctoral Thesis* must be objective and pragmatic. Consequently, the objectives for this work start from using NL-IDA and introducing the following contributions:

i. To develop an adequate combination of 3D-based elements and meshes to extend the simulation capacity of current numerical models as much as possible;
ii. To implement an adequate combination of material constitutive relations to be used in dynamic analyses. Those should be appropriate for general loading cases, and in particular, for earthquake loading;
iii. To potentiate the additional capacities of this approach by modelling the effect of bond failure and other phenomena that are difficult to include using other simulation techniques;
iv. To improve computational performance by taking advantage of modern computational hardware and advanced structural analysis techniques.

4 Methodology

The objectives formulated in the previous section represent a significant challenge and require an appropriate strategy to be accomplished. The first option taken to maximize the probability of success, was to circumscribe the modelling issues to be addressed. This made it possible to focus on specific problems, one at a time, instead of going directly to the final model with multiple features implemented. As a result, the thesis is separated in parts, addressing topics like RC modelling, concrete-steel bond simulation and computational performance improvements.

The details of the methodology that will be used to develop the numerical models can be summarized in the following list:

i. The traditional displacement-based formulation of the *Finite Element Method* (FEM) was chosen to solve the boundary-value problem by introducing a space-discretization using finite elements. This option was selected taking into consideration the flexibility of this approach and because of the advanced development stage reached by this formulation, although other formulations could have been used, like non-conventional Finite Element formulations *e.g.* [16, 510, 511];
ii. The dynamic equilibrium equations will be solved by adding a time-discretization using a suitable time integration procedure;
iii. The discretization of the structure will be made using three-dimensional finite element meshes and elements. The concrete will be modelled using solid elements (*e.g.* 8-noded hexahedra), the reinforcing steel bars using beam-column elements (*e.g.* 2-noded line elements) and zero-thickness interface elements will be used for the concrete-steel interfaces;
iv. The constitutive relations will take into consideration the dynamic nonlinear response of the materials. The adopted approach was to use damage mechanics models for the concrete elements, a global behaviour model for the steel reinforcements and a semi-analytical model for the concrete-steel interface elements;
v. The computational performance will be improved adopting three main strategies: i) take advantage of concurrent computations; ii) use advanced substructuring techniques; and iii) reduce the problem size using efficient discretization techniques.

5 Text presentation

This document is written in British English and the detail level adopted in the text was chosen after considering the following common approaches: Firstly, some authors prefer to leave the non-essential or non-innovative issues as references to other published works, resulting in a *narrow-band* text style. In opposition, others are inclined to produce an extensive, self-sufficient document that in some case comes closer to a textbook, rather than a thesis. This difference can result from a personal choice or from group, university or even national considerations and is always a subjective and controversial issue. Recent agreements regarding university-level academic degrees move towards the harmonization of the procedures, and in general, result in what seems to be a simplification. From this point of view, the tendency would be to follow a more concise approach for the text layout. This thesis attempts to find a compromise between these two approaches, trying to be as self-contained as possible for the most relevant issues and referencing other work for the non-vital aspects.

The basic structure of the chapters with innovative contributions includes an introduction followed by a summarized *state of the art* on the subjects addressed. The following sections focus on the original contributions and the chapter closes with a selected set of validation examples for the models and techniques proposed.

The outline of this thesis is composed of six chapters and two annexes. After this introductory chapter, the text organization is the following:

i. Chapter II is dedicated to a general overview about the subjects addressed in this thesis that are not discussed in a dedicated chapter. The main objective is to present the problems, make a summarized *state of the art*, present the main quantities and equations that govern the problems and introduce the notation used. This chapter spans all the areas related to the work presented in this thesis, except for the issues related to the reinforced concrete, to the concrete-steel interfaces and to the computational performance improvement, which are discussed in specific chapters;
ii. Chapter III is dedicated to reinforced concrete (RC). It starts by presenting a summarized state of the art regarding the most used constitutive models and the mechanical behaviour of the concrete, reinforcing steel and RC elements. Afterwards, the adopted models are presented for the simulation of the concrete and of the reinforcing steel. This chapter ends with a chosen set of validation examples;
iii. Chapter IV addresses the problem of the imperfect bond between the concrete and the reinforcing steel bar under general load situations. An initial *state of the art* is presented addressing the mechanical characterization, the most prominent experimental programmes and modelling strategies. Afterwards, a section is dedicated to developing the bond model, followed by the mathematical definition of the interface element adopted. At the end, a series of validation examples are presented;
iv. Chapter V focus on improving the computational performance of the proposed numerical models. This chapter addresses issues strongly related to the computational and applied mathematics fields, moving the furthest away from traditional earthquake engineering. The chapter includes a state of the art on hardware and software-related performance issues and a review of static and dynamic condensations, linear solvers, storage schemes and kinematic constraints. This section ends with a general overview of domain decomposition methods. The following sections address the hybrid discretization technique and issues related to the implementation of the parallelized algorithms, of the substructuring techniques and of the hybrid discretization. The chapter ends with a series of validation examples;
v. Chapter VI is dedicated to the closure of this thesis, including a summary of original contributions, the main conclusions and some indication about the future research that seems pertinent as a continuation of this work;
vi. Annex A presents some supporting mathematical relations and concepts that can help the reader to follow this document;
vii. Annex B is dedicated to compile the elastic constitutive relations used throughout this thesis;
viii. The bibliographic references are presented at the end of the document.

This organization resulted in a group of chapters that separates the topics addressed reasonably well. Nevertheless, a few issues are transversal to all chapters. This is the case of the computer implementation, which is mainly presented in Chapter V. Nevertheless, some aspects are relevant and discussed in previous chapters (*e.g.* Chapter III).

6 Notation

Before ending this introductory chapter, a few considerations about the notation are presented because they may be fruitful for the reader. The first aspect that should be mentioned is that the main criterion adopted for selecting the notation was the intention of producing easy to read and concise equations. Two main options seemed viable to cope with this objective. Using the so-called *indicial notation* can produce extremely compact expressions. However, readability can become more difficult for readers not used to this style. The second hypothesis considered was to use the *matrix notation*. This approach is able to produce reasonably compact expressions and readability is widespread. Taking into consideration that this work is considered to span more than one scientific domain (*e.g.* earthquake engineering and computational mechanics) the choice moved towards the latter possibility, because this style is more disseminated.

A possible summary of the rules adopted for the notation are:

i. *Matrix notation* was chosen as the basis for the equations in this thesis, *e.g.* $\mathbf{K}\mathbf{q}=\mathbf{Q}$;
ii. Scalar (vector and matrix) quantities are represented by italic (bold-italic) Latin or Greek letters *e.g.* c $\mathbf{A}\mathbf{v}$;
iii. Scalar and vector (matrix) related quantities are represented by lowercase (uppercase) symbols, although this was not considered an absolute rule, because sometimes priority was given to preserving the usual historical and bibliographic symbols;
iv. Tensors are represented by underlined bold-italic Latin or Greek letters, *e.g.* $\underline{\boldsymbol{\sigma}}$;
v. The *range convention* was adopted, hence by default the indexes range $\{1,2,3\}$, *e.g.* b_k;
vi. The *comma convention* was not adopted, thus, after a comma, a subscript index does not imply partial differentiation, *e.g.* $\mathcal{C}^{sd}_{LK,sm}$;
vii. When substructuring techniques are used, lowercase (uppercase) subscripts are associated with subdomain (global domain) related quantities, *e.g.* $\mathcal{A}^{sd}_{cC}$;
viii. When the same quantity was defined for positive and negative domains (*e.g.* envelope surfaces) and the resulting expression presented suitable formats, condensed expressions were used with the symbols $\pm$ and $\mp$, *e.g.* $\phi^{\pm}_{*}=\pm\sigma_{su}\mp\beta^{\pm}E_s\varepsilon_{su}+\beta^{\pm}E_s\varepsilon_s$. These expressions should be split in two, by substituting the symbol $\pm$ by $+$ for the first equation and by $-$ for the second equation. The symbol $\mp$ should be substituted the other way around.

The *indicial notation* and the *comma convention* were used in rare exceptional cases for historical or practical reasons, which are clearly identified and commented on in the text.

These guidelines regarding the notation are complemented by the *List of Symbols* presented before the main text. In this list, it is possible to identify some patterns about the subscript and superscript usage that could be useful to the reader. Moreover, a group of abbreviations are used to make the text more readable. The abbreviations used are also compiled in a list before the main text.

Chapter II

General Overview

1 Introduction

The main objective of this chapter is to present the problem formulation and the background of this work with regard to the subjects addressed in this thesis. This chapter presents the fundamental governing relations and introduces the notation that will be used throughout this document. It can be seen as a *State of the Art* on all pertinent subjects to this work, except for the issues related to reinforced concrete, to the concrete-steel interfaces and to the improvement of the computational performance, which are discussed in specific chapters. Consequently, no original contributions are included in this chapter. Moreover, all the formulations are presented using the most general format possible and the particularization to specific cases is only made in the subsequent chapters.

The outline of the text includes a section dedicated to the basic relations that govern dynamic mechanical problems, followed by a section devoted to presenting the general formulation of the traditional finite element method, which also includes some implementation issues. The following section is dedicated to making an overview of the most common structural analysis methods, namely for modal, static and dynamic analyses. The latter is discussed in more detail because they are vital for the objectives of this work. Afterwards, a review is presented of the most common solution procedures for nonlinear problems, namely, the incremental formulation is introduced and the techniques adopted in the predictor-corrector solving algorithm are presented. Finally, a section is

dedicated to making an overview of the most used seismic analysis methods. The framework and applicability of each of these methods are compared and discussed at the end of the chapter.

2 Basic relations

The most widespread approach for solving mechanical boundary-value problems is the *Finite Element Method* (FEM), which was initially introduced by Turner *et al.* [549], although the basic concept was published in 1943 by Courant [147]. The traditional formulation of FEM was adopted in this work. This formulation is based on the approximation of the displacement fields and the basic formulation is presented in section 3. The following base hypotheses were adopted in this thesis:

i. The materials can present nonlinear behaviour - *material nonlinearity*;
ii. The displacements and strains are considered to be small and negligible when compared to the dimension of the elements, hence the deformed and the initial configurations are similar - *geometric linearity*;
iii. The material nonlinearity is not influenced by time and temperature-related effects.

The main quantities involved in mechanical problems are the *external* and *internal forces* (stresses), which characterize the *static* fields, and the *strains* and *displacements* that are associated with the *kinematic* fields. These quantities can be related using *equilibrium*, *constitutive* and *compatibility* relations, as indicated in Figure II.1. The general formulation of these relations is presented in the following sub-sections.

2.1 Equilibrium relations

Considerer the generic element represented in Figure II.2. This element is defined in a Cartesian system (x_1, x_2, x_3) by the *domain* Ω and delimited by the *boundary* Γ, which includes parts where the displacements are prescribed (*kinematic boundary* Γ_q) and parts where the applied forces are known (*static boundary* Γ_σ).

The domain can be subjected to a set of *body forces b*, defined per unit volume, and to *boundary*

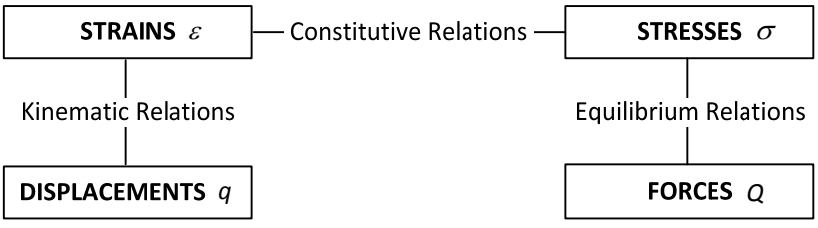

Figure II.1: Methodology used for the problem formulation.

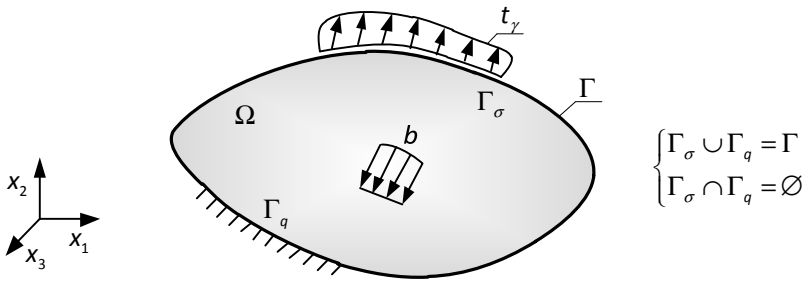

Figure II.2: Basic notation.

forces t_γ, which can be defined using their Cartesian components grouped into the following vectors:

$$\mathbf{b}^t = \begin{bmatrix} b_1 & b_2 & b_3 \end{bmatrix}, \tag{II.1}$$

$$\mathbf{t}_\gamma^t = \begin{bmatrix} t_1 & t_2 & t_3 \end{bmatrix}. \tag{II.2}$$

The equilibrium equations relate the stresses to the external forces applied to the element. The stress state in a point can be represented using a second-order Cartesian tensor, the *stress tensor*:

$$\underline{\boldsymbol{\sigma}} = \begin{bmatrix} \sigma_{11} & \sigma_{12} & \sigma_{13} \\ \sigma_{21} & \sigma_{22} & \sigma_{23} \\ \sigma_{31} & \sigma_{32} & \sigma_{33} \end{bmatrix}, \tag{II.3}$$

where the component σ_{ij} represents the stress applied along the direction *j*, in a face perpendicular to the direction i (see Figure II.3-a).

Taking into consideration the base hypotheses adopted in this work, this tensor becomes symmetric, which makes it possible to define the stress state at a point of the domain using a vector that only includes the independent components of the tensor:

$$\boldsymbol{\sigma}^t = \begin{bmatrix} \sigma_{11} & \sigma_{22} & \sigma_{33} & \sigma_{12} & \sigma_{13} & \sigma_{23} \end{bmatrix}. \tag{II.4}$$

The dynamic equilibrium of the infinitesimal volume presented in Figure II.3-b along direction x_1 leads to the following equation [340]:

$$\begin{aligned} \sum Q_1 = m a_1 = &\left(\sigma_{11} + d\sigma_{11}\right) dx_2\, dx_3 - \sigma_{11}\, dx_2\, dx_3 + \left(\sigma_{21} + d\sigma_{21}\right) dx_1\, dx_3 - \sigma_{21}\, dx_1\, dx_3 + \\ &\left(\sigma_{31} + d\sigma_{31}\right) dx_1\, dx_2 - \sigma_{31}\, dx_1\, dx_2 + b_1 = \rho a_1\, dx_1\, dx_2\, dx_3 \Leftrightarrow \\ \Leftrightarrow\ & d\sigma_{11}\, dx_2\, dx_3 + d\sigma_{21} dx_1\, dx_3 + d\sigma_{31} dx_1\, dx_2 + b_1 = \rho a_1\, dx_1\, dx_2\, dx_3 \end{aligned} \quad . \tag{II.5}$$

where ρ is the *specific mass* and a_1 is the acceleration along the x_1 direction.

Knowing that:

$$d\sigma_{11} = \frac{\partial \sigma_{11}}{\partial x_1} dx_1, \quad d\sigma_{21} = \frac{\partial \sigma_{21}}{\partial x_2} dx_2, \quad d\sigma_{31} = \frac{\partial \sigma_{31}}{\partial x_3} dx_3, \tag{II.6}$$

the previous expression can be simplified into:

$$\frac{\partial \sigma_{11}}{\partial x_1} + \frac{\partial \sigma_{21}}{\partial x_2} + \frac{\partial \sigma_{31}}{\partial x_3} + b_1 = \rho a_1, \tag{II.7}$$

and similar equations may be written for the other directions by adopting an analogous procedure.

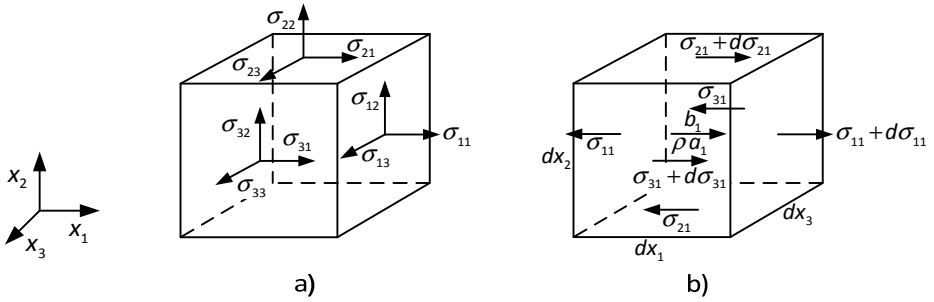

Figure II.3: Equilibrium of an infinitesimal volume: a) stresses acting on positive surfaces; b) equilibrium along direction x_1.

These domain equilibrium equations can be grouped and written as [12, 539][i]:

$$\sigma_{ij,i} + b_j = \rho a_j, \text{ in } \Omega. \tag{II.8}$$

or using the matrix format:

$$\mathbf{L}^* \boldsymbol{\sigma} + \mathbf{b} = \rho \mathbf{a}, \text{ in } \Omega, \tag{II.9}$$

where $\mathbf{L}^*$ represents the *equilibrium differential operator*, defined by:

$$\mathbf{L}^* = \begin{bmatrix} \partial/\partial x_1 & 0 & 0 & \partial/\partial x_2 & \partial/\partial x_3 & 0 \\ 0 & \partial/\partial x_2 & 0 & \partial/\partial x_1 & 0 & \partial/\partial x_3 \\ 0 & 0 & \partial/\partial x_3 & 0 & \partial/\partial x_1 & \partial/\partial x_2 \end{bmatrix}. \tag{II.10}$$

The *static boundary condition*, *a.k.a. natural* or *Neumann condition*, enforces the equilibrium between the internal stress field and the exterior forces applied to the element. Using Cauchy's formula, it is possible to define [12, 539]:

$$\sigma_{ij} n_i = t_{\gamma i}, \text{ on } \Gamma_\sigma, \tag{II.11}$$

where n_i represents the vector that groups the components of the unitary outward normal to the boundary along direction *i*. Using matrix format, the latter equation can be rewritten as:

$$\mathbf{N}\boldsymbol{\sigma} = \mathbf{t}_\gamma, \text{ on } \Gamma_\sigma, \tag{II.12}$$

where **N** represents the matrix that groups the components of the unitary outward normal to the static boundary, defined by:

$$\mathbf{N} = \begin{bmatrix} n_1 & 0 & 0 & n_2 & n_3 & 0 \\ 0 & n_2 & 0 & n_1 & 0 & n_3 \\ 0 & 0 & n_3 & 0 & n_1 & n_2 \end{bmatrix}. \tag{II.13}$$

[i] Expressions (II.8) and (II.20) are some of the few cases where the *comma convention* was adopted, hence partial differentiation is implied for the subscript indexes after the comma.

2.2 Compatibility relations

The displacements, velocities and accelerations at each point of the domain can be defined by vectors holding the corresponding Cartesian components:

$$\mathbf{q}^t = \begin{bmatrix} q_1 & q_2 & q_3 \end{bmatrix}, \tag{II.14}$$

$$\mathbf{v}^t = \begin{bmatrix} v_1 & v_2 & v_3 \end{bmatrix}, \tag{II.15}$$

$$\mathbf{a}^t = \begin{bmatrix} a_1 & a_2 & a_3 \end{bmatrix}. \tag{II.16}$$

The local strains can be characterized by a symmetric second-order Cartesian tensor, designated as the *strain tensor*:

$$\underline{\boldsymbol{\varepsilon}} = \begin{bmatrix} \varepsilon_{11} & \varepsilon_{12} & \varepsilon_{13} \\ \varepsilon_{21} & \varepsilon_{22} & \varepsilon_{23} \\ \varepsilon_{31} & \varepsilon_{32} & \varepsilon_{33} \end{bmatrix}, \tag{II.17}$$

where the components ε_{ii} represent the extension of an infinitesimal fibre that before the deformation was parallel to the axis *i*, and the other components represent half of the variation of the angle between two infinitesimal fibres, initially aligned with the directions *i* and *j*. The total value for this variation is usually called *distortion* and is defined by the equality:

$$\gamma_{ij} = 2\,\varepsilon_{ij}, \quad \text{for } i \neq j. \tag{II.18}$$

The independent components of the strain tensor can be grouped into:

$$\boldsymbol{\varepsilon}^t = \begin{bmatrix} \varepsilon_{11} & \varepsilon_{22} & \varepsilon_{33} & \gamma_{12} & \gamma_{13} & \gamma_{23} \end{bmatrix}. \tag{II.19}$$

Under the linear geometric hypothesis, the domain *compatibility conditions* can be expressed using the following set of equations, written using the comma convention [539]:

$$\varepsilon_{ij} = \frac{1}{2}\left(q_{i,j} + q_{j,i}\right), \text{ in } \Omega. \tag{II.20}$$

The *kinematic boundary* condition, *a.k.a. essential* or *Dirichlet condition*, produces the following compatibility condition:

$$q_i = q_{\gamma i}, \text{ on } \Gamma_q, \tag{II.21}$$

where the index *i* represents the direction considered.

These last two relations can be rewritten using matrix notation as:

$$\boldsymbol{\varepsilon} = \mathbf{L}\,\mathbf{q}, \text{ in } \Omega, \tag{II.22}$$

$$\mathbf{q} = \mathbf{q}_\gamma, \text{ on } \Gamma_q, \tag{II.23}$$

where **L** represents the *compatibility differential operator*.

Under the geometric linearity hypothesis adopted in this work, the compatibility and equilibrium differential operators are linear and adjoint, making (II.22) and (II.9) conjugated transformations [84]. For the case of odd or even differentiation orders, the following equalities are respectively verified:

$$\mathbf{L}^* = \mathbf{L}^t; \quad \mathbf{L}^* = -\mathbf{L}^t. \tag{II.24}$$

2.3 Constitutive relations

In the elastic phase, the material constitutive relations are linear and can be computed using the generalized Hooke's law in the flexibility format (II.25) or in the stiffness format (II.26) for isotropic materials [539]:

$$\boldsymbol{\varepsilon}^{e} = \mathbf{f}\,\boldsymbol{\sigma} + \boldsymbol{\varepsilon}_0\,, \tag{II.25}$$

$$\boldsymbol{\sigma}^{e} = \mathbf{k}\,\boldsymbol{\varepsilon} + \boldsymbol{\sigma}_0\,. \tag{II.26}$$

In the previous equations, $\boldsymbol{\varepsilon}_0$ and $\boldsymbol{\sigma}_0$ represent the initial strains and stresses. These terms can be used to model thermal-induced strains and residual stresses.

The matrices **f** and **k** group the elastic parameters of the material. Under the hypotheses adopted in this work, these matrices are symmetric and positive-definite and can be written using the matrix format as [98, 493, 539]:

$$\mathbf{f} = \frac{1}{E}\begin{bmatrix} 1 & -\nu & -\nu & 0 & 0 & 0 \\ -\nu & 1 & -\nu & 0 & 0 & 0 \\ -\nu & -\nu & 1 & 0 & 0 & 0 \\ 0 & 0 & 0 & 2(1+\nu) & 0 & 0 \\ 0 & 0 & 0 & 0 & 2(1+\nu) & 0 \\ 0 & 0 & 0 & 0 & 0 & 2(1+\nu) \end{bmatrix}, \tag{II.27}$$

$$\mathbf{k} = \frac{E}{(1+\nu)(1-2\nu)}\begin{bmatrix} (1-\nu) & \nu & \nu & 0 & 0 & 0 \\ \nu & (1-\nu) & \nu & 0 & 0 & 0 \\ \nu & \nu & (1-\nu) & 0 & 0 & 0 \\ 0 & 0 & 0 & \frac{(1-2\nu)}{2} & 0 & 0 \\ 0 & 0 & 0 & 0 & \frac{(1-2\nu)}{2} & 0 \\ 0 & 0 & 0 & 0 & 0 & \frac{(1-2\nu)}{2} \end{bmatrix}, \tag{II.28}$$

where *E* represents the *elasticity* or *Young's modulus* and ν *Poisson's ratio*.

The *distortion modulus* relates the tangential components of the stress tensor to the associated distortion components, and under the hypotheses adopted , it is defined by:

$$G = \frac{E}{2(1+\nu)}\,. \tag{II.29}$$

Alternatively, the constitutive relations can be written using indicial notation, as:

$$\varepsilon_{ij} = \frac{1+\nu}{E}\sigma_{ij} - \frac{\nu}{E}\sigma_{kk}\,\delta_{ij} + \varepsilon_{ij}^{0}\,, \tag{II.30}$$

$$\sigma_{ij} = \frac{E}{1+\nu}\varepsilon_{ij} + \frac{E\,\nu}{(1+\nu)(1-2\nu)}\varepsilon_{kk}\,\delta_{ij} + \sigma_{ij}^{0}\,. \tag{II.31}$$

Annex B presents additional information regarding elastic constitutive relations. The material nonlinearity is addressed in the following chapters.

3 Formulation and implementation of the Finite Element Method

3.1 Formulation of the Finite Element Method for dynamic problems

The unitary volume of a continuous material $d\Omega$ is subjected to a set of forces in the domain, on the boundaries and to a set of concentrated forces $\mathbf{Q}_N$. Considering an arbitrary pattern of kinematic admissible displacements $\delta\tilde{\mathbf{q}}$, the *virtual work principle* states that the work done by external forces must be equal to the work done by inertia, viscous damping and internal forces [141]:

$$W_{in}+W_d+W_i=W_e \Leftrightarrow \int \delta\tilde{\mathbf{q}}^t \rho\, \tilde{\mathbf{a}}\, d\Omega+\int \delta\tilde{\mathbf{q}}^t\, c\, \tilde{\mathbf{v}}\, d\Omega+\int \delta\tilde{\boldsymbol{\varepsilon}}^t \boldsymbol{\sigma}\, d\Omega=\int \delta\tilde{\mathbf{q}}^t\, \mathbf{b}\, d\Omega+\int \delta\tilde{\mathbf{q}}^t\, \mathbf{t}_\gamma\, \Gamma_\sigma+\sum_{k=1}^{n}\delta\tilde{\mathbf{q}}^t\, \mathbf{Q}_N^k\,, \quad \text{(II.32)}$$

where *c* is the viscous damping coefficient.

Applying the standard finite element space discretization [588]:

$$\tilde{\mathbf{q}}(x,y,z,t)=\boldsymbol{\Psi}(x,y,z)\,\mathbf{q}(t)\,, \quad \text{(II.33)}$$

$$\tilde{\mathbf{v}}(x,y,z,t)=\boldsymbol{\Psi}(x,y,z)\,\mathbf{v}(t)\,, \quad \text{(II.34)}$$

$$\tilde{\mathbf{a}}(x,y,z,t)=\boldsymbol{\Psi}(x,y,z)\,\mathbf{a}(t)\,, \quad \text{(II.35)}$$

where **q**, **v** and **a** are the nodal displacements, velocities and accelerations respectively, and $\boldsymbol{\Psi}$ is the matrix that groups the shape functions.

Putting the virtual displacements in evidence, introducing the approximations (II.33) to (II.35) and the compatibility relation (II.22) into equation (II.32), the following equation can be obtained:

$$\delta\tilde{\mathbf{q}}\left\{\int \boldsymbol{\Psi}^t\,\mathbf{b}\; d\Omega+\int \boldsymbol{\Psi}^t\,\mathbf{t}_\gamma\; d\Gamma_\sigma+\sum_{k=1}^{n}\boldsymbol{\Psi}^t\,\mathbf{Q}_N^k-\int \boldsymbol{\Psi}^t\,\rho\,\boldsymbol{\Psi}\,\mathbf{a}\; d\Omega-\int \boldsymbol{\Psi}^t\, c\,\boldsymbol{\Psi}\,\mathbf{v}\; d\Omega-\int (\mathbf{L}\,\boldsymbol{\Psi})^t\,\boldsymbol{\sigma}\; d\Omega\right\}=\mathbf{0}\,. \quad \text{(II.36)}$$

The last relation must be valid for any set of virtual displacements, so to satisfy (II.36) the second term must vanish:

$$\int \boldsymbol{\Psi}^t\,\mathbf{b}\; d\Omega+\int \boldsymbol{\Psi}^t\,\mathbf{t}_\gamma\; d\Gamma_\sigma+\sum_{k=1}^{n}\boldsymbol{\Psi}^t\,\mathbf{Q}_N^k-\int \boldsymbol{\Psi}^t\,\rho\,\boldsymbol{\Psi}\,\mathbf{a}\; d\Omega-\int \boldsymbol{\Psi}^t\, c\,\boldsymbol{\Psi}\,\mathbf{v}\; d\Omega-\int \mathbf{B}^t\,\boldsymbol{\sigma}\, d\Omega=\mathbf{0}\,, \quad \text{(II.37)}$$

where, **B** is the *strain matrix*, defined by:

$$\mathbf{B}=\mathbf{L}\,\boldsymbol{\Psi}\,. \quad \text{(II.38)}$$

This operator groups the shape functions derivatives and it can be used to express the compatibility relation for the discrete system, using:

$$\boldsymbol{\varepsilon}=\mathbf{B}\,\mathbf{q}\,. \quad \text{(II.39)}$$

The dynamic equilibrium relation (II.37) can be simplified into:

$$\mathbf{M}\,\mathbf{a}+\mathbf{C}\,\mathbf{v}+\mathbf{Q}_i=\mathbf{Q}_e\,, \quad \text{(II.40)}$$

where $\mathbf{M}$ is the *mass matrix*, $\mathbf{C}$ is the *damping matrix*, $\mathbf{Q}_i$ is the *internal* and $\mathbf{Q}_e$ is the *external forces vectors*. These discrete quantities can be defined by:

$$\mathbf{M}=\int \boldsymbol{\Psi}^t\,\rho\,\boldsymbol{\Psi}\; d\Omega\,, \quad \text{(II.41)}$$

$$\mathbf{C} = \int \boldsymbol{\Psi}^t \, c \, \boldsymbol{\Psi} \, d\Omega \,, \tag{II.42}$$

$$\mathbf{Q}_i = \int \mathbf{B}^t \, \boldsymbol{\sigma} \, d\Omega \,, \tag{II.43}$$

$$\mathbf{Q}_e = \mathbf{Q}_b + \mathbf{Q}_\gamma + \mathbf{Q}_N \,, \tag{II.44}$$

where $\mathbf{Q}_b$ are the *body forces*, $\mathbf{Q}_\gamma$ are the *boundary forces* and $\mathbf{Q}_N$ are the nodal forces. The first two vectors can be computed from:

$$\mathbf{Q}_b = \int \boldsymbol{\Psi}^t \, \mathbf{b} \, d\Omega \,, \tag{II.45}$$

$$\mathbf{Q}_\gamma = \int \boldsymbol{\Psi}^t \, \mathbf{t}_\gamma \, d\Gamma_\sigma \,. \tag{II.46}$$

Considering a linear elastic material, the internal forces vector $\mathbf{Q}_i$ can be computed by introducing (II.26), (II.33) and (II.22) into the definition of the internal forces vector (II.43). Neglecting the term associated with the initial strains and stresses, the following expression is obtained:

$$\mathbf{Q}_i = \mathbf{K}\,\mathbf{q} \,, \tag{II.47}$$

where $\mathbf{K}$ is the *stiffness matrix* that can be computed from:

$$\mathbf{K} = \int \mathbf{B}^t \, \mathbf{k} \, \mathbf{B} \, d\Omega \,. \tag{II.48}$$

Under these assumptions, the global equilibrium equation (II.40) can be rewritten as:

$$\mathbf{M}\mathbf{a} + \mathbf{C}\mathbf{v} + \mathbf{K}\mathbf{q} = \mathbf{Q}_e \,. \tag{II.49}$$

The matrix entries $M_{ij}\left(C_{ij}; K_{ij}\right)$ represents the inertia (damping; restoring) force mobilized along the direction *i* by a unitary acceleration (velocity; displacement) at the degree of freedom *j*.

Equation (II.40) represents a coupled, second-order, ordinary differential equations in time and is often called a finite element semi-discretization, because only a space discretization was applied and the time space is still continuous. *Time Integration* methods (see section 4.3.3) add the time discretization to solve the equations as a sequence of algebraic equations [141].

3.2 Implementation of the Finite Element Method

This sub-section is devoted to the implementation of the FEM described previously into a computer algorithm, in particular, the issues related to the approximations, to the coordinate transformations and to the numeric integration used to compute the element's structural operators.

- Approximations

In the framework of the FEM, at least two approximations are usually required. The first is used for the main unknowns of the problem, the kinematic fields (displacements, velocities and accelerations) as defined in (II.33), (II.34) and (II.35). These quantities can be defined as:

$$\tilde{\mathbf{q}} = \left[\begin{array}{ccc|c|ccc} \psi_1 & 0 & 0 & \cdots & \psi_n & 0 & 0 \\ 0 & \psi_1 & 0 & \cdots & 0 & \psi_n & 0 \\ 0 & 0 & \psi_1 & \cdots & 0 & 0 & \psi_n \end{array}\right] \left[\begin{array}{ccc|c|ccc} q_{x1}^1 & q_{x2}^1 & q_{x3}^1 & \cdots & q_{x1}^n & q_{x2}^n & q_{x3}^n \end{array}\right]^t, \tag{II.50}$$

and analogously for the velocity and accelerations fields. In this definition, it is implicit that the degrees of freedom (*dofs*) are grouped by joining first the *dofs* associated with each node.

The second approximation is related to the element's geometry, the so-called *element mapping*. For convenience in the computations and for ensuring the geometrical conformability of the elements, the element's geometry is defined from the nodal coordinates and using a group of functions $\boldsymbol{\Psi}^*$ defined in a local coordinate system y_k, *a.k.a. natural coordinates,* using the expression:

$$\tilde{\mathbf{x}}(x_k) = \boldsymbol{\Psi}^*(y_k)\ \mathbf{x}_N\,, \tag{II.51}$$

where $\tilde{\mathbf{x}}$ represents the approximation of the geometry in global coordinates, $\boldsymbol{\Psi}^*$ is the matrix that groups the shape approximation functions, and $\mathbf{x}_N$ is the vector that holds the global node coordinates. The element formulation is called *isoparametric* when the functions used for the element mapping and for the kinematic field approximations are the same, $\boldsymbol{\Psi}^* = \boldsymbol{\Psi}$ [141, 588].

For an isoparametric element, the element mapping equations (II.51) can be defined by:

$$\tilde{x} = \begin{bmatrix} \psi_1 & 0 & 0 & \cdots & \psi_n & 0 & 0 \\ 0 & \psi_1 & 0 & \cdots & 0 & \psi_n & 0 \\ 0 & 0 & \psi_1 & \cdots & 0 & 0 & \psi_n \end{bmatrix} \begin{bmatrix} x_{N,1}^{[1]} & x_{N,2}^{[1]} & x_{N,3}^{[1]} & \cdots & x_{N,1}^{[n]} & x_{N,2}^{[n]} & x_{N,3}^{[n]} \end{bmatrix}^t . \tag{II.52}$$

- Coordinate transformations

In the scope of this thesis, two coordinate transformations were used to compute the global structural operators. The first coordinate transformation relates the global coordinate system x_k and the local coordinate system y_k.

A *master element* is usually adopted to compute the element operators using a numerical integration scheme (see section 3.3). In this work, the *Gauss-Legendre quadrature* was used (see Annex A), so it is convenient to define the master element between [-1;1] in all directions (see Figure II.4).

It is also important for the finite element implementation to define the relation between infinitesimal variations of the global and local coordinates. This can be done by considering the following equations:

$$dx_i = \frac{\partial x_i}{\partial y_j} dy_j\,, \tag{II.53}$$

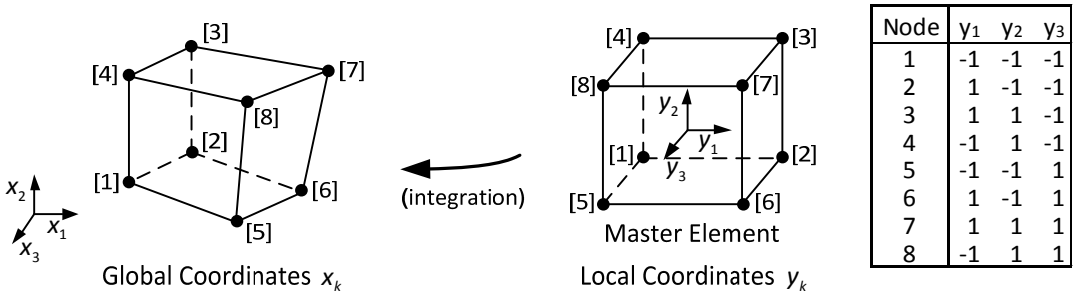

Node	y1	y2	y3
1	-1	-1	-1
2	1	-1	-1
3	1	1	-1
4	-1	1	-1
5	-1	-1	1
6	1	-1	1
7	1	1	1
8	-1	1	1

Figure II.4: Using a master element to compute the element's structural operators.

or in matrix notation:

$$\begin{bmatrix} dx_1 \\ dx_2 \\ dx_3 \end{bmatrix} = \begin{bmatrix} \frac{\partial x_1}{\partial y_1} & \frac{\partial x_1}{\partial y_2} & \frac{\partial x_1}{\partial y_3} \\ \frac{\partial x_2}{\partial y_1} & \frac{\partial x_2}{\partial y_2} & \frac{\partial x_2}{\partial y_3} \\ \frac{\partial x_3}{\partial y_1} & \frac{\partial x_3}{\partial y_2} & \frac{\partial x_3}{\partial y_3} \end{bmatrix} \begin{bmatrix} dy_1 \\ dy_2 \\ dy_3 \end{bmatrix} = \mathbf{J} \begin{bmatrix} dy_1 \\ dy_2 \\ dy_3 \end{bmatrix}, \tag{II.54}$$

where **J** is called the *Jacobian matrix* and its determinant the *Jacobian*. When the inverse coordinate transformation exists, it can be found computing:

$$\mathbf{J}^{-1} = \begin{bmatrix} \frac{\partial y_1}{\partial x_1} & \frac{\partial y_1}{\partial x_2} & \frac{\partial y_1}{\partial x_3} \\ \frac{\partial y_2}{\partial x_1} & \frac{\partial y_2}{\partial x_2} & \frac{\partial y_2}{\partial x_3} \\ \frac{\partial y_3}{\partial x_1} & \frac{\partial y_3}{\partial x_2} & \frac{\partial y_3}{\partial x_3} \end{bmatrix} = \frac{1}{det\,\mathbf{J}} \begin{bmatrix} J_{22}\,J_{33} - J_{23}\,J_{32} & J_{13}\,J_{32} - J_{12}\,J_{33} & J_{12}\,J_{23} - J_{13}\,J_{22} \\ J_{23}\,J_{31} - J_{21}\,J_{33} & J_{11}\,J_{33} - J_{13}\,J_{31} & J_{13}\,J_{21} - J_{11}\,J_{23} \\ J_{21}\,J_{32} - J_{22}\,J_{31} & J_{12}\,J_{31} - J_{11}\,J_{32} & J_{11}\,J_{22} - J_{12}\,J_{21} \end{bmatrix}. \tag{II.55}$$

It is necessary to take into consideration the differences between both spaces in order to make the integrations required for computing the element's operators presented in the following section 3.3. According to Zienkiewicz *et al.* [588], it can be proven that the following relation relates the global and local spaces:

$$dx_1\,dx_2\,dx_3 = det\,\mathbf{J}\;dy_1\,dy_2\,dy_3, \tag{II.56}$$

and that the integration of a volume-based operator can be made, using:

$$\int\int\int f(x_1,x_2,x_3)\,dx_1\,dx_2\,dx_3 = \int_{-1}^{1}\int_{-1}^{1}\int_{-1}^{1} f(y_1,y_2,y_3)\,det\,\mathbf{J}(y_1,y_2,y_3)\,dy_1\,dy_2\,dy_3\,. \tag{II.57}$$

For boundary-related operators similar to the element boundary forces defined in equation (II.46), the local space operator is defined along a boundary with fixed values at one of the local coordinates (say y_3). It is possible to define $d\Gamma$ as a vector oriented into the normal direction to the surface using the following vector product [588]:

$$d\Gamma = \begin{bmatrix} \frac{\partial x_1}{\partial y_1} & \frac{\partial x_2}{\partial y_1} & \frac{\partial x_3}{\partial y_1} \end{bmatrix}^t \times \begin{bmatrix} \frac{\partial x_1}{\partial y_2} & \frac{\partial x_2}{\partial y_2} & \frac{\partial x_3}{\partial y_2} \end{bmatrix}^t dy_1\,dy_2\,. \tag{II.58}$$

The surface integral can be computed by changing the limits of the integration into [-1;1].

The second coordinate transformation is required when the coordinate system in which the element is defined x_k, is not coincident with the structure's coordinate system X_k (see Figure II.5). The following expression can be used to relate the displacements defined in both coordinate systems:

$$\mathbf{q}(x_k) = \mathbf{T}_{xX}\,\mathbf{q}(X_k), \tag{II.59}$$

where $\mathbf{T}_{xX}$ is the *transformation matrix* between element and structure coordinates. This operator has a total number of rows and columns equal to the number of local and global *dofs* (6 *dofs* per node) present in the element. For a generic element with N nodes and 6 *dofs* per node (*e.g.* three-

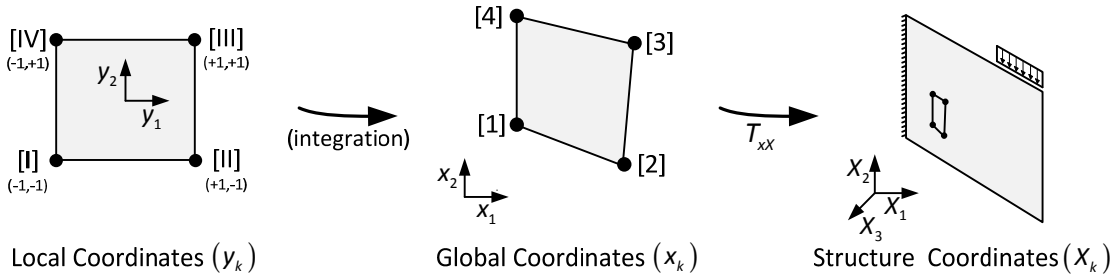

Figure II.5: Coordinate transformations.

dimensional beam-column element) this matrix will have the following format:

$$\mathbf{T}_{xX} = \begin{array}{c} \\ x_k^1 \\ \theta_k^1 \\ x_k^2 \\ \theta_k^2 \\ \vdots \\ x_k^N \\ \theta_k^N \end{array} \begin{array}{c} \begin{array}{cccccc} X_k^1 & \Theta_k^1 & X_k^2 & \Theta_k^2 & \cdots & X_k^N & \Theta_k^N \end{array} \\ \left[\begin{array}{cccccc} \mathbf{T}_{xX}^* & \mathbf{0} & \mathbf{0} & \mathbf{0} & \cdots & \mathbf{0} & \mathbf{0} \\ \mathbf{0} & \mathbf{T}_{xX}^* & \mathbf{0} & \mathbf{0} & \cdots & \mathbf{0} & \mathbf{0} \\ \mathbf{0} & \mathbf{0} & \mathbf{T}_{xX}^* & \mathbf{0} & \cdots & \mathbf{0} & \mathbf{0} \\ \mathbf{0} & \mathbf{0} & \mathbf{0} & \mathbf{T}_{xX}^* & \cdots & \mathbf{0} & \mathbf{0} \\ \vdots & \vdots & \vdots & \vdots & \ddots & \vdots & \vdots \\ \mathbf{0} & \mathbf{0} & \mathbf{0} & \mathbf{0} & \cdots & \mathbf{T}_{xX}^* & \mathbf{0} \\ \mathbf{0} & \mathbf{0} & \mathbf{0} & \mathbf{0} & \cdots & \mathbf{0} & \mathbf{T}_{xX}^* \end{array}\right] \end{array}, \tag{II.60}$$

where the size of the sub-matrices $\mathbf{T}_{xX}^*$ is 3x3 and the entries are defined by the *direction cosines* between both coordinate systems:

$$T_{xX,mn}^* = cos\left(x_m, X_n\right), \tag{II.61}$$

or in matrix format:

$$\mathbf{T}_{xX}^* = \begin{bmatrix} cos\left(x_1, X_1\right) & cos\left(x_1, X_2\right) & cos\left(x_1, X_3\right) \\ cos\left(x_2, X_1\right) & cos\left(x_2, X_2\right) & cos\left(x_2, X_3\right) \\ cos\left(x_3, X_1\right) & cos\left(x_3, X_2\right) & cos\left(x_3, X_3\right) \end{bmatrix}. \tag{II.62}$$

The sub-matrices $\mathbf{T}_{xX}^*$ can be seen as rotation matrices and the columns represent an orthogonal basis (see Annex A), therefore, the inverse coordinate transformation can be found, using:

$$\mathbf{q}\left(X_k\right) = \mathbf{T}_{xX}^t \, \mathbf{q}\left(x_k\right), \tag{II.63}$$

The number of rows of $\mathbf{T}_{xX}$ can be reduced when the element is not defined using all possible 6 *dofs* in each node. For example, this is the case of the solid elements that do not include the rotational *dofs* or of the truss element that has only one local *dof* per node.

According to Zienkiewicz *et al.* [587], this coordinate transformation can be introduced into the computation of the operators by imposing that the forces defined in both referentials produce the same amount of work:

$$\mathbf{Q}\left(x_k\right)^t \, \mathbf{q}\left(x_k\right) = \mathbf{Q}\left(X_k\right)^t \, \mathbf{q}\left(X_k\right). \tag{II.64}$$

Inserting expression (II.59) into the last expression leads to:

$$\mathbf{Q}(x_k)^t \ \mathbf{T}_{xX} \ \mathbf{q}(X_k) = \mathbf{Q}(X_k)^t \ \mathbf{q}(X_k), \tag{II.65}$$

which can be simplified into:

$$\mathbf{Q}(X_k) = \mathbf{T}_{xX}^t \ \mathbf{Q}(x_k). \tag{II.66}$$

Computing matrix-based operators, *e.g.* stiffness matrices, can be made recalling the equilibrium equation, written in local coordinates:

$$\mathbf{K}(x_k) \ \mathbf{q}(x_k) = \mathbf{Q}(x_k), \tag{II.67}$$

and inserting equation (II.59) and pre-multiplying by $\mathbf{T}_{xX}^t$, leading to:

$$\mathbf{T}_{xX}^t \ \mathbf{K}(x_k) \ \mathbf{T}_{xX} \ \mathbf{q}(X_k) = \mathbf{T}_{xX}^t \ \mathbf{Q}(x_k), \tag{II.68}$$

which can be simplified into:

$$\mathbf{K}(X_k) \ \mathbf{q}(X_k) = \mathbf{Q}(X_k), \tag{II.69}$$

where:

$$\mathbf{K}(X_k) = \mathbf{T}_{xX}^t \ \mathbf{K}(x_k) \ \mathbf{T}_{xX}. \tag{II.70}$$

Second order Cartesian tensors are also bounded to a similar coordinate transformation. For example, the stress tensor components can be expressed in a different reference system, using:

$$\underline{\boldsymbol{\sigma}}(X_k) = \mathbf{T}_{xX}^t \ \underline{\boldsymbol{\sigma}}(x_k) \ \mathbf{T}_{xX}. \tag{II.71}$$

- Relation between derivatives defined in the global and local coordinate systems

Some structural operators require the evaluation of the derivatives defined in the global coordinate system (*e.g.* the *equilibrium differential operator* $\mathbf{L}^*$). Consequently, it is necessary to define the global derivatives using local coordinates y_k in order to compute the element's operators at the master element level.

The following relations can be obtained using the chain rule [588]:

$$\frac{\partial()}{\partial x_i} = \frac{\partial()}{\partial y_j}\frac{\partial y_j}{\partial x_i} = \frac{\partial()}{\partial y_1}\frac{\partial y_1}{\partial x_1} + \frac{\partial()}{\partial y_2}\frac{\partial y_2}{\partial x_1} + \frac{\partial()}{\partial y_3}\frac{\partial y_3}{\partial x_1}. \tag{II.72}$$

This last expression specifies that the derivative with respect to the global coordinate x_i can be found by a weighted sum of derivatives with respect to the local coordinate system y_i. The ratios between the partial derivatives of both coordinate systems present in equation (II.72) can be found in the columns of the inverse Jacobian matrix (II.55), already defined within the scope of the element mapping transformation.

- Numerical Integration

Performing the analytical integration of the element operators can become extremely difficult for general situations, *e.g.* complex element geometries. Consequently, numerical integration techniques, *a.k.a. numerical quadrature rules*, are commonly used in general-purpose FE codes. Some of the most used are the *Newton-Cotes*, *Gauss-Legendre* and *Gauss-Lobatto* rules [588].

The *Newton-Cotes quadrature* uses a given set of sampling points to integrate the function, usually defined at equal intervals. It requires *n* points to integrate polynomials of degree $n-1$ with an error of order $O\left(h^n\right)$, where *h* is the element size [588]. The general formula to be used is the following:

$$\int_{-1}^{1} p(y)\, dy = \sum_{k=1}^{np} p(y_k)\, w_k \,, \tag{II.73}$$

where w_k is the weight of the function at point y_k. For $n=2$ the formula reproduces the *trapezoidal rule* and for $n=3$ the *Simpson rule*.

Moreover, using the *Gauss-Legendre quadrature* the position of the integration points is predefined to improve accuracy. The points are located at the roots of the *Legendre polynomials* and using *n* points to integrate a polynomial of degree $2n-1$ leads to an accuracy order of $O\left(h^{2n}\right)$. The *Gauss-Legendre quadrature* adopts the general expression:

$$\int_{-1}^{1} p(y)\, dy = \sum_{gp=1}^{ngp} p\left(y_{gp}\right) w_{gp} \,, \tag{II.74}$$

where y_{gp} represents the position of the integration points and w_{gp} the corresponding weight. If the integration is made for a non-polynomial function then the accuracy of the results is reduced. However, the accuracy can be improved by increasing the number of points [141]. The position and weights of the Gauss points are given in Annex A.

The *Gauss-Lobatto quadrature* works the same way as the Gauss-Legendre quadrature but it requires *n* points to integrate a $2n-3$ polynomial with similar accuracy. On the other hand, this technique has the advantage of using points at the edges (boundaries) of the domain being integrated, which can be convenient for nonlinear analyses because the stresses and the state variables would be controlled at the boundaries, where extreme values are often reached. For post-processing data visualization, having the results defined at the boundaries can also be more convenient. The position and weights of the integration points for this quadrature are presented in Annex A.

3.3 Computing the element operators

3.3.1 Stiffness matrix

The stiffness matrix defined at equation (II.48) can be defined at the master element level, using:

$$\mathbf{K}^{el} = \int_{-1}^{1}\int_{-1}^{1}\int_{-1}^{1} \mathbf{B}^t\left(y_1,y_2,y_3\right)\, \mathbf{k}\, \mathbf{B}\left(y_1,y_2,y_3\right) \det\mathbf{J}\left(y_1,y_2,y_3\right)\, dy_1 dy_2 dy_3 \,, \tag{II.75}$$

and computed using the *Gauss-Legendre* numerical quadrature, through:

$$\mathbf{K}^{el} = \sum_{gp=1}^{ngp} \mathbf{B}^t\left(y_1,y_2,y_3\right)_{gp}\, \mathbf{k}\, \mathbf{B}\left(y_1,y_2,y_3\right)_{gp} \det\mathbf{J}\left(y_1,y_2,y_3\right)_{gp}\, w_{gp} \,. \tag{II.76}$$

where *ngp* represents the total number of Gauss points and w_{gp} is the weight associated with each Gauss point, considering all the coordinates participating in the integration.

The *strain matrix* $\mathbf{B}$ is composed of different blocks $\mathbf{B}^{[N]}$ associated with each node *N* in the element:

$$\mathbf{B} = \left[\mathbf{B}^{[1]} \mid \mathbf{B}^{[2]} \mid \cdots \mid \mathbf{B}^{[nnod]} \right], \tag{II.77}$$

Taking the relationship (II.72) into consideration, each block $\mathbf{B}^{[N]}$ can be defined by:

$$\mathbf{B}^{[N]} = \begin{bmatrix} \frac{\partial()}{\partial y_1}\frac{\partial y_1}{\partial x_1} + \frac{\partial()}{\partial y_2}\frac{\partial y_2}{\partial x_1} + \frac{\partial()}{\partial y_3}\frac{\partial y_3}{\partial x_1} & 0 & 0 \\ 0 & \frac{\partial()}{\partial y_1}\frac{\partial y_1}{\partial x_2} + \frac{\partial()}{\partial y_2}\frac{\partial y_2}{\partial x_2} + \frac{\partial()}{\partial y_3}\frac{\partial y_3}{\partial x_2} & 0 \\ 0 & 0 & \frac{\partial()}{\partial y_1}\frac{\partial y_1}{\partial x_3} + \frac{\partial()}{\partial y_2}\frac{\partial y_2}{\partial x_3} + \frac{\partial()}{\partial y_3}\frac{\partial y_3}{\partial x_3} \\ \frac{\partial()}{\partial y_1}\frac{\partial y_1}{\partial x_2} + \frac{\partial()}{\partial y_2}\frac{\partial y_2}{\partial x_2} + \frac{\partial()}{\partial y_3}\frac{\partial y_3}{\partial x_2} & \frac{\partial()}{\partial y_1}\frac{\partial y_1}{\partial x_1} + \frac{\partial()}{\partial y_2}\frac{\partial y_2}{\partial x_1} + \frac{\partial()}{\partial y_3}\frac{\partial y_3}{\partial x_1} & 0 \\ \frac{\partial()}{\partial y_1}\frac{\partial y_1}{\partial x_3} + \frac{\partial()}{\partial y_2}\frac{\partial y_2}{\partial x_3} + \frac{\partial()}{\partial y_3}\frac{\partial y_3}{\partial x_3} & 0 & \frac{\partial()}{\partial y_1}\frac{\partial y_1}{\partial x_1} + \frac{\partial()}{\partial y_2}\frac{\partial y_2}{\partial x_1} + \frac{\partial()}{\partial y_3}\frac{\partial y_3}{\partial x_1} \\ 0 & \frac{\partial()}{\partial y_1}\frac{\partial y_1}{\partial x_3} + \frac{\partial()}{\partial y_2}\frac{\partial y_2}{\partial x_3} + \frac{\partial()}{\partial y_3}\frac{\partial y_3}{\partial x_3} & \frac{\partial()}{\partial y_1}\frac{\partial y_1}{\partial x_2} + \frac{\partial()}{\partial y_2}\frac{\partial y_2}{\partial x_2} + \frac{\partial()}{\partial y_3}\frac{\partial y_3}{\partial x_2} \end{bmatrix} \psi_N . \tag{II.78}$$

The non-null terms of this matrix block can be written using the auxiliary variable b_i^N:

$$\mathbf{B}^{[N]} = \begin{bmatrix} b_1^{[N]} & 0 & 0 \\ 0 & b_2^{[N]} & 0 \\ 0 & 0 & b_3^{[N]} \\ b_2^{[N]} & b_1^{[N]} & 0 \\ b_3^{[N]} & 0 & b_1^{[N]} \\ 0 & b_3^{[N]} & b_2^{[N]} \end{bmatrix}, \tag{II.79}$$

which is defined by the following expression:

$$b_i^N = \frac{\partial \psi_N}{\partial y_j}\frac{\partial y_j}{\partial x_i} = \psi'_{Nj}\ J_{ji}^{-1}, \tag{II.80}$$

where the terms ψ' can be grouped in the matrix $\mathbf{\Psi}'$ that holds the shape functions derivatives:

$$\mathbf{\Psi}' = \frac{\partial \psi_N}{\partial y_j} = \begin{bmatrix} \frac{\partial \psi_1}{\partial y_1} & \frac{\partial \psi_1}{\partial y_2} & \frac{\partial \psi_1}{\partial y_3} \\ \vdots & \vdots & \vdots \\ \frac{\partial \psi_{nnod}}{\partial y_1} & \frac{\partial \psi_{nnod}}{\partial y_2} & \frac{\partial \psi_{nnod}}{\partial y_3} \end{bmatrix}. \tag{II.81}$$

3.3.2 Mass matrix

The mass matrix can be computed using different approaches. The definition obtained for the FE formulation (II.41) is the so-called *consistent mass matrix*, because it results from the same approximation functions used to compute the stiffness matrix. This matrix can be defined in the local

coordinate system, using:

$$\mathbf{M}^{el} = \int_{-1}^{1}\int_{-1}^{1}\int_{-1}^{1} \mathbf{\Psi}^{t}\left(y_1, y_2, y_3\right) \boldsymbol{\rho}\, \mathbf{\Psi}\left(y_1, y_2, y_3\right) \det\mathbf{J}\left(y_1, y_2, y_3\right)\, dy_1 dy_2 dy_3 \,, \tag{II.82}$$

and computed using the Gauss-Legendre numerical integration procedure, through:

$$\mathbf{M}^{el} = \sum_{gp=1}^{ngp} \mathbf{\Psi}^{t}\left(y_1, y_2, y_3\right)_{gp} \boldsymbol{\rho}\, \mathbf{\Psi}\left(y_1, y_2, y_3\right)_{gp} \det\mathbf{J}\left(y_1, y_2, y_3\right)_{gp}\, w_{gp} \,. \tag{II.83}$$

When different mass densities are used, these can be considered using the following *mass density matrix*:

$$\boldsymbol{\rho} = \begin{bmatrix} \rho_1 & 0 & 0 \\ 0 & \rho_2 & 0 \\ 0 & 0 & \rho_3 \end{bmatrix}. \tag{II.84}$$

Another hypothesis is using the *lumped mass matrix*. This matrix results by considering that the mass associated with a given *dof* only produces inertia forces on that *dof*, consequently, no cross terms are considered. The result is a diagonal matrix that has some advantages for FE computations. Several schemes can be used to compute the lumped version of the mass matrix. The *HRZ Lumping Scheme* [273] is frequently used for the translation mass *dofs* and it can be described by the steps presented in Algorithm II.1. This technique preserves the global element mass and the mass matrix becomes positive-definite. More information can be found in the bibliography, *e.g.* Cook *et al.* [141].

3.3.3 Damping matrix

Damping is frequently approximated by a viscous phenomenon as expressed in equation (II.40). This hypothesis is used in fluid mechanics and is usually adopted in structural mechanics because it presents some advantages for defining the movement equations.

Recalling the expression (II.42) obtained for the FE formulation, the element contribution for the

Algorithm II.1: Steps of the *HRZ Lumping scheme*.

1. Compute the consistent mass matrix.
2. Compute the sum of all the matrix entries:
   $S = \sum_{i=1}^{n}\sum_{j=1}^{n} M_{ij}^{el}$.
3. Compute the sum of all diagonal matrix terms:
   $D = \sum_{i=1}^{n} M_{ii}^{el}$.
4. Assemble the lumped mass matrix, using:
   $$M_{ij}^{el,lump} = \begin{cases} \dfrac{S}{D} M_{ij}^{el,}, & i = j \\ 0, & i \neq j \end{cases}.$$

damping matrix can be defined in the local coordinate system, using:

$$\mathbf{C}^{el} = \int_{-1}^{1}\int_{-1}^{1}\int_{-1}^{1} \mathbf{\Psi}^{t}\left(y_1, y_2, y_3\right)\, c\, \mathbf{\Psi}\left(y_1, y_2, y_3\right) \det\mathbf{J}\left(y_1, y_2, y_3\right)\, dy_1 dy_2 dy_3 \,, \tag{II.85}$$

and computed using the Gauss-Legendre quadrature, through:

$$\mathbf{C}^{el} = \sum_{gp=1}^{ngp} \mathbf{\Psi}^{t}\left(y_1, y_2, y_3\right)_{gp}\, c\, \mathbf{\Psi}\left(y_1, y_2, y_3\right)_{gp} \det\mathbf{J}\left(y_1, y_2, y_3\right)_{gp}\, w_{gp} \,. \tag{II.86}$$

This definition for the damping matrix is usually not implemented in the FE codes. Instead, the so-called *proportional damping matrix* is commonly used. This formulation is presented and discussed in some detail in section 4.3.1.

3.3.4 Internal forces vector

The element contribution to the discrete internal forces vector defined in equation (II.43) can be computed at the master element using the following expression:

$$\mathbf{Q}_i^{el}\left(x_1, x_2, x_3\right) = \int_{-1}^{1}\int_{-1}^{1}\int_{-1}^{1} \mathbf{B}^{t}\left(y_1, y_2, y_3\right)\, \boldsymbol{\sigma}\left(y_1, y_2, y_3\right)\, det\,\mathbf{J}\left(y_1, y_2, y_3\right)\, dy_1\, dy_2\, dy_3 \,. \tag{II.87}$$

Adopting the Gauss-Legendre quadrature to compute this operator leads to:

$$\mathbf{Q}_i^{el}\left(x_1, x_2, x_3\right) = \sum_{gp=1}^{ngp} \left\{ \mathbf{B}^{t}\left(y_1, y_2, y_3\right)\, \boldsymbol{\sigma}\left(y_1, y_2, y_3\right)\, det\,\mathbf{J}\left(y_1, y_2, y_3\right)\, w \right\}_{gp} \,. \tag{II.88}$$

Note that there are cases where a geometric parameter should be introduced to obtain the correct value for the internal forces. A possible example is a truss element, in which the integral can be evaluated only along one dimension, consequently, the stress should be multiplied by the cross-section area A_{cs}.

3.3.5 Body forces vector

Analogously, the body forces vector defined in equation (II.45) can be evaluated at the master element, using:

$$\mathbf{Q}_b^{el}\left(x_1, x_2, x_3\right) = \int_{-1}^{1}\int_{-1}^{1}\int_{-1}^{1} \mathbf{\Psi}^{t}\left(y_1, y_2, y_3\right)\, \mathbf{b}\, det\,\mathbf{J}\left(y_1, y_2, y_3\right)\, dy_1\, dy_2\, dy_3 \,, \tag{II.89}$$

and computed using a Gauss-Legendre numeric integration procedure by:

$$\mathbf{Q}_b^{el}\left(x_1, x_2, x_3\right) = \sum_{gp=1}^{ngp} \left\{ \mathbf{\Psi}^{t}\left(y_1, y_2, y_3\right)\, \mathbf{b}\left(y_1, y_2, y_3\right)\, det\,\mathbf{J}\left(y_1, y_2, y_3\right)\, w \right\}_{gp} \,. \tag{II.90}$$

The components of **b** are directly associated with the global directions:

$$\mathbf{b}^{t} = \begin{bmatrix} b_{x1} & b_{x2} & b_{x3} \end{bmatrix}.$$

3.3.6 Boundary forces vector

The boundary forces vector defined in equation (II.46) can also be computed at the master element level, using:

$$\mathbf{Q}_{\gamma}^{el}\left(x_1,x_2,x_3\right)=\int_{-1}^{1}\int_{-1}^{1}\boldsymbol{\Psi}^{t}\left(y_1,y_2\right)t_{\gamma}\;det\,\mathbf{J}\left(y_1,y_2\right)\;dy_1dy_2\;. \tag{II.91}$$

The definition presented in equation (II.58) can be used to compute this operator.

3.4 State determination and unbalanced forces

Commonly, the element's state determination starts by computing the strains using equation (II.39):

$$\boldsymbol{\varepsilon}=\mathbf{B}\,\mathbf{q}\,.$$

The compatibility operator **B** is commonly defined at the Gauss points for computing the structural operators using the Gauss-Legendre quadrature, as demonstrated in equation (II.76). Consequently, the strains will also be known at the Gauss points. In addition, the global discrete displacements are written for the structure coordinate system and should be transformed into the element's coordinates x_k, using expression (II.59). This can be done using the following expression:

$$\boldsymbol{\varepsilon}_{gp}^{el}=\mathbf{B}_{gp}^{el}\,\mathbf{T}_{xX}^{el}\,\mathbf{q}_{X}^{el}\,. \tag{II.92}$$

The following step consists of computing any nonlocal variable required for the element's state determination. As an example, an *comparison strain* $\tilde{\varepsilon}$ is used in the scope of the *continuum damage mechanics*, which is computed from a weighted average on a set of chosen Gauss points:

$$\tilde{\varepsilon}_{gp}^{nl}=\sum_{gp=1}^{ngp}\tilde{\varepsilon}_{gp}\,w_{gp}^{nl}\,, \tag{II.93}$$

where w_{gp}^{nl} represents the weight associated with each Gauss point in the nonlocal model. This topic will be addressed in more detail in Chapter III-§2.1.6.

The stress at each Gauss point can be computed using the model's constitutive relation, *e.g.* an uniaxial model experiencing damage and plastic strains, the equation to be used would be similar to (see Chapter II-§2.1):

$$\sigma_{gp}^{el}=\left\{1-d_{gp}\left(\hat{\varepsilon}_{gp}^{nl}\right)\right\}E\left(\varepsilon_{gp}-\varepsilon_{gp}^{p}\right). \tag{II.94}$$

The stress field is usually evaluated at the Gauss points for two reasons. First, having the strains at the gauss points, computing the stresses at these points is straightforward. Moreover, it can be proved that the stress field accuracy is optimal at these locations. Finally, the results obtained from this last expression can be directly used to compute the internal forces vector, using expression (II.88). On the other hand, the visualization is also more complex with the stresses defined at the Gauss points. However, most visualization codes are prepared to handle this issue (*e.g.* GiD [240]).

The final step consists in computing the internal forces vector using equation (II.88).

3.5 Assembling the global operators

In the context of the FEM, the assemblage operation can be defined as the process of joining the contributions from the elements to the global operators. Several techniques can be used to achieve this. A simple method consists in using mapping operators that relate the element and the structure spaces. These operators are represented by unsigned Boolean matrices. The following expression can be adopted to make this relation:

$$\mathbf{q}^{el}(X_k) = \mathbf{A}^{el}\,\mathbf{q}(X_k)\,, \tag{II.95}$$

where $\mathbf{A}^{el}$ is a matrix with a number of rows (columns) equal to the number of *dofs* in the element (structure). All entries of the matrix are zero, except when the element *dof* (row) corresponds to the global *dof* (column), where a unitary value is found.

This formula is similar to the one presented in equation (II.59) and the same type of procedures can be used to map the element operator into the domain. Consequently, the following expressions can be used for matrix-based operators:

$$\mathbf{K}(X_k) = \sum_{el=1}^{nel} \mathbf{A}^{el,t}\;\mathbf{K}^{el}(X_k)\;\mathbf{A}^{el}\,, \tag{II.96}$$

$$\mathbf{M}(X_k) = \sum_{el=1}^{nel} \mathbf{A}^{el,t}\;\mathbf{M}^{el}(X_k)\;\mathbf{A}^{el}\,, \tag{II.97}$$

$$\mathbf{C}(X_k) = \sum_{el=1}^{nel} \mathbf{A}^{el,t}\;\mathbf{C}^{el}(X_k)\;\mathbf{A}^{el}\,, \tag{II.98}$$

and for vector-based operators:

$$\mathbf{Q}_i(X_k) = \sum_{el=1}^{nel} \mathbf{A}^{el,t}\,\mathbf{Q}_i^{el}(X_k)\,, \tag{II.99}$$

$$\mathbf{Q}_e(X_k) = \sum_{el=1}^{nel} \mathbf{A}^{el,t}\,\mathbf{Q}_e^{el}(X_k)\,. \tag{II.100}$$

Using this approach to assemble the global operators is easy to implement because it only requires matrix multiplications. Nevertheless, this methodology can present poor computational performance if sparse arrays and sparse routines are not used, due to the high sparsity levels of the matrix $\mathbf{A}^{el}$.

Within the scope of this thesis, these matrices were not stored as sparse matrices, instead, only the indexes associated with non-null entries were saved. It should be noted that this technique may not be the most efficient, however in the *Matlab* developing language [376] used in the implementation, the matrix-based operations are extremely optimized when compared with regular interpreted code, which presents the overhead associated with this high-level programming language. The efficiency of this technique was confirmed in tests made using different assembling techniques, therefore, it was adopted in this work.

The definition for the assembler operator is extended in Chapter V for the substructured structural analyses implemented to enhance the computational performance.

4 Structural analysis methods

This section presents a general overview of the methods used for structural analysis. The basic formulation associated with modal, static and dynamic analyses is addressed. Most of the attention will be given to this last topic because it is vital to the objectives of this work.

4.1 Modal analysis

Modal analyses are used to compute the natural frequencies and mode shapes of a structure. The theoretical basis of this analysis type is that an undamped oscillator undergoing free vibration, *i.e.* with no external loads applied, will present a harmonic response with all the *dofs* moving in phase [141]. Consequently, the movement can be expressed for the vibration mode *n*, using:

$$q_n = \overline{q}_n \, sin\left(\omega_n t\right), \tag{II.101}$$

$$a_n = -\omega_n^2 \, \overline{q}_n \, sin\left(\omega_n t\right), \tag{II.102}$$

where $\overline{q}_n$ represents the mode amplitude and ω the mode angular frequency.

Introducing these relations into the dynamic equilibrium equation (II.49) without damping and considering $\lambda_n = \omega_n^2$, the following generalized eigenvalue problem is retrieved:

$$\left(\mathbf{K} - \lambda_n \mathbf{M}\right) \mathbf{\Phi}_n = \mathbf{0}. \tag{II.103}$$

The non-trivial solutions $\left(\mathbf{\Phi}_n \neq \mathbf{0}\right)$ can be found by computing the eigenvalues using:

$$det\left(\mathbf{K} - \lambda_n \mathbf{M}\right) = 0, \tag{II.104}$$

and the eigenvectors can be computed from (II.103). These eigenvectors represent the *mode shapes* of the structural system and the vibration frequencies can be retrieved from $\lambda_k = \omega_k^2$.

The number of modes is limited by the number of dynamic degrees of freedom present in the system. If both the stiffness and mass matrices are positive-definite then all the frequencies have positive values. Zero frequencies are usually associated with rigid body modes, as a consequence of positive semi-definite stiffness matrices $\left(x^t \mathbf{K} x \geq 0\right)$. According to Cook *et al.* [141], when diagonal mass matrices are used (*e.g.* lumped mass matrices), zero or negative entries in the mass matrix can lead to infinite or negative eigenvalues, which can result in infinite or imaginary frequencies.

One important characteristic of the mode shapes is that they present convenient orthogonal properties regarding the mass and stiffness matrices. If the mode shapes are normalized with respect to the mass matrix, the following expressions hold [279]:

$$\mathbf{\Phi}^t \, \mathbf{M} \, \mathbf{\Phi} = \mathbf{I}, \tag{II.105}$$

$$\mathbf{\Phi}^t \, \mathbf{K} \, \mathbf{\Phi} = \mathbf{\Omega}^2, \tag{II.106}$$

where $\mathbf{I}$ is the identity matrix and $\mathbf{\Omega}^2$ is a diagonal matrix with the entries equal to ω_n^2.

For small problems, the eigenvalue problem can be solved by a direct solver, although, most of the times the higher modes present very small structural contributions and are mostly related to the

numerical discretization rather than to effective structural behaviour [279]. Consequently, only a few lower frequency modes are of interest in practice. This is quite convenient because direct eigenproblem solvers are demanding in terms of the computational and memory requirements. Consequently, iterative solvers (*e.g.* the *Lanczos* method) are often used to compute the first modes of vibration [279, 492]. This subject is discussed in more detail in Chapter V.

Massless *dofs* are frequent in common numerical simulations and this can be used to reduce the size of the eigenvalue problem to be solved. Recalling equation (II.103), assuming that the mass matrix is diagonal (*e.g.* lumped) and grouping first the *dofs* with mass (subscript *m*) and the massless *dofs* last (subscript *c*), it is possible to obtain:

$$\left(\begin{bmatrix} \mathbf{K}_{mm} & \mathbf{K}_{mc} \\ \mathbf{K}_{cm} & \mathbf{K}_{cc} \end{bmatrix} - \lambda_n \begin{bmatrix} \mathbf{M}_{mm} & \mathbf{0} \\ \mathbf{0} & \mathbf{0} \end{bmatrix} \right) \begin{bmatrix} \boldsymbol{\Phi}_m \\ \boldsymbol{\Phi}_c \end{bmatrix}_n = \begin{bmatrix} \mathbf{0} \\ \mathbf{0} \end{bmatrix}. \tag{II.107}$$

This problem can be solved after condensing the massless *dofs*, using:

$$\left(\mathbf{K}^C_{mm} - \lambda_n \mathbf{M}_{mm} \right) \boldsymbol{\Phi}_{m,n} = \mathbf{0}, \tag{II.108}$$

where:

$$\mathbf{K}^C_{mm} = \mathbf{K}_{mm} - \mathbf{K}_{mc} \mathbf{K}_{cc}^{-1} \mathbf{K}_{cm}. \tag{II.109}$$

After solving the reduced problem, the modal coefficients associated with the condensed *dofs* can be recovered from:

$$\boldsymbol{\Phi}_c = -\mathbf{K}_{cc}^{-1} \left(\mathbf{K}_{cm} \boldsymbol{\Phi}_m \right). \tag{II.110}$$

This technique does not introduce any approximation and apart from numerical accuracy losses, the result would be the same as if the *massless dofs* were not condensed. Nevertheless, the condensed operators are generally denser and with larger bandwidth, which may lead to a significant overhead. Condensation procedures will also be discussed in more detail in Chapter V.

4.2 Static analysis

A static analysis for a set of external forces can be executed by solving the governing system expressed in (II.49), after removing the damping and inertia contributions:

$$\mathbf{K}\mathbf{q} = \mathbf{Q}_e. \tag{II.111}$$

where **K** is most of the time symmetric and positive-definite.

The displacements can be calculated by inverting the stiffness matrix:

$$\mathbf{q} = \mathbf{K}^{-1} \mathbf{Q}_e. \tag{II.112}$$

This approach is generally not used because matrix inversion is computationally more expensive and less accurate than the procedure adopted in traditional direct solvers based on Gaussian elimination and other factorization-based algorithms. Iterative methods are also often used for solving the system of equations (II.111), in particular for very large problems. Chapter V presents a summary of the most used linear solvers and storage schemes.

4.3 Dynamic analysis

According to Cook *et al.* [141], dynamic problems can be classified as:

i. *Wave propagation problems*, where loading is often an impact or an explosive blast, hence, the excitation and consequently the structural response is rich in high frequencies. Interest usually lies in the effects of shear wave propagation, consequently, the time duration of the analysis is short and typically of the order of a wave transversal time across a structure;
ii. *Structural dynamics*, where the inertia forces are important and the frequency of excitation is usually of the order of the structure's lowest natural frequency of vibration. The work presented in this thesis focus on this problem type.

For structural dynamic problems, the analysis is made in the large majority of cases using either the *Mode Superposition* method or *Time Integration* (TI) algorithms. Mode Superposition takes advantage of the mode shapes' orthogonal properties in order to solve the problem as a sum of uncoupled second-order differential equations. This method is very often used for seismic analyses although the application is, in principle, limited to linear elastic analyses. Alternatively, TI methods solve the problem by a direct time integration of the motion equations, adding a time discretization to the simulation. This discretization leads to the use of incremental procedures, therefore this method is often called *Incremental Dynamic Analysis* (IDA) and will be used throughout this thesis. Other methods can be adopted to perform dynamic analyses, like *frequency domain* methods and stochastic-based approaches, like *power spectrum density* analyses.

After a short discussion regarding the simulation of damping, the *Mode Superposition* and the *Time Integration* methods will be addressed in some detail.

4.3.1 Damping

- Proportional damping

Damping is usually not simulated using the operator resulting from expression (II.42). Instead, the so-called *proportional damping*, *a.k.a. Rayleigh damping*, is often used. This type of damping results from the linear combination of the mass and stiffness matrices:

$$\mathbf{C} = \alpha_d \mathbf{M} + \beta_d \mathbf{K}, \tag{II.113}$$

where α_d and β_d are the mass and stiffness proportional coefficients, respectively.

Using this approach, the global damping operator will inherit the advantages resulting from the orthogonal properties of the stiffness and mass matrices, and consequently, the governing equation can be diagonalized leading to uncoupled modal equations. This issue is very relevant when the response is computed using the mode superposition method, but loses its main interest when direct time integration is used to compute the response.

The damping levels can be set independently for each mode when the motion equations are written in modal coordinates and proportional damping is adopted (see section 4.3.2). On the other hand,

when time integration methods are used, it is only possible to define specific levels of damping for two frequencies because of the two variables (α_d, β_d) present in the damping definition (II.113). This can be done by remembering that the damping ratio is defined as $\xi = c/c_c$, where c_c is the *critical damping* defined as the amount of damping that limits a vibratory response. For a single degree-of-freedom (*sdof*) system it is possible to obtain [116]:

$$\begin{cases} \xi = c/c_c \\ c_c = 2M\omega \end{cases} \Rightarrow \xi_i = \frac{1}{2}\left(\frac{\alpha_d}{\omega_i} + \beta_d \omega_i\right). \tag{II.114}$$

After solving the simultaneous algebraic equations defined after imposing the relation expressed in (II.114) for two damping levels (ξ_1, ξ_2) and two frequency values (ω_1, ω_2), the following relations are obtained [116]:

$$\alpha_d = 2\omega_1\omega_2 \frac{\xi_1\omega_2 - \xi_2\omega_1}{\omega_2^2 - \omega_1^2}, \tag{II.115}$$

$$\beta_d = 2\frac{\xi_2\omega_2 - \xi_1\omega_1}{\omega_2^2 - \omega_1^2}. \tag{II.116}$$

Analysing the expression (II.114) and observing Figure II.6, it is possible to conclude that increasing the parameter α_d associated with the mass matrix creates decreasing damping for increasing frequencies. The opposite occurs with the influence of the stiffness matrix through increasing values of the parameter β_d, which tends to increase damping for higher frequencies.

Using proportional viscous damping formulations produces satisfactory results as long as the material stays in the linear range or with minor inelasticity (*e.g.* micro-hysteresis at low amplitude) and becomes far from reality for intense nonlinear phenomena due to material hysteresis, RC bond failure, frictional phenomena concentrated at the plastic hinges and for concentrated non-viscous damping sources.

This damping formulation presents at least the following drawbacks: Firstly, using TI methods, damping is only accurately set for two frequency values. In addition, when damping is associated with the initial stiffness, it does not take into consideration the fact that the stiffness can change

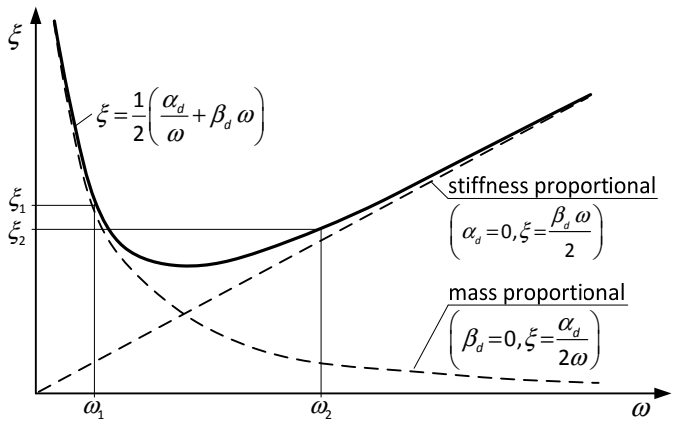

Figure II.6: Proportional damping, adapted from Cook *et al.* [141].

significantly throughout the nonlinear analysis, *e.g.* often to one third [388]. On the other hand, if the damping matrix is recomputed during the incremental analysis then the damping levels would tend to decrease following the stiffness. This is not consistent with the increasing damping levels observed in structures experiencing high damage levels, *e.g.* resulting from friction. In addition, the mass-related damping can also introduce some problems because this term introduces dissipation for rigid body motions [32]. For some problem types, this can become a serious problem and it is convenient to exclude the damping proportional to the mass, by setting $\alpha_d = 0$ and using [123]:

$$\beta_d = \frac{2\xi}{\omega_1}. \tag{II.117}$$

Nevertheless, this approach results in damping that is linearly proportional to the frequency and tends to over-damp and filter the higher frequency contributions [388].

In conclusion, it is possible to stress that the use of proportional damping is mainly due to numerical reasons associated with the simplicity of the formulation and to the preservation of the orthogonal properties in the global viscous damping matrix. According to Mazars *et al.* [388], this approach has no specific physical meaning and can present a significant distortion from reality for intense inelastic phenomena.

- Alternative ways to simulate damping

Damping can also be modelled as a friction phenomenon, similar to one occurring within concrete cracks and at the concrete-steel interfaces. In the case of dry friction, this leads to the global force displacement curve represented in Figure II.7-a [105] with an elastic stiffness system in parallel, which can be mathematically modelled using the expression [123]:

$$Q_d = -\mu\, N_0 \langle v \rangle. \tag{II.118}$$

where μ is a *friction coefficient* that only depends on the velocity sign. The vibrations do not decrease exponentially as in viscous damping models. Instead, they decrease linearly (see Figure II.7-a).

Moreover, according to Chopra [105], the dynamic hysteresis associated with viscous damping results in a rotated ellipsis when combined with an elastic stiffness system (see Figure II.7-b). In addition, rate-independent damping can be simulated in the frequency domain assuming a damping force proportional to the stiffness and inversely proportional to the frequency [105]:

$$Q_d = \frac{\eta k}{\omega} v, \tag{II.119}$$

where η is a *damping coefficient*. According to Chopra [105], the transformation back to the time domain can present some difficulties.

Rate-independent local material hysteresis can also be simulated through the shape of the unloading-reloading cycles. This option was adopted by Mazars *et al.* [388] by introducing a sliding strain in a continuum damage model. The resulting constitutive relation enables modelling energy dissipation through hysteresis loops as presented in Figure II.7-c.

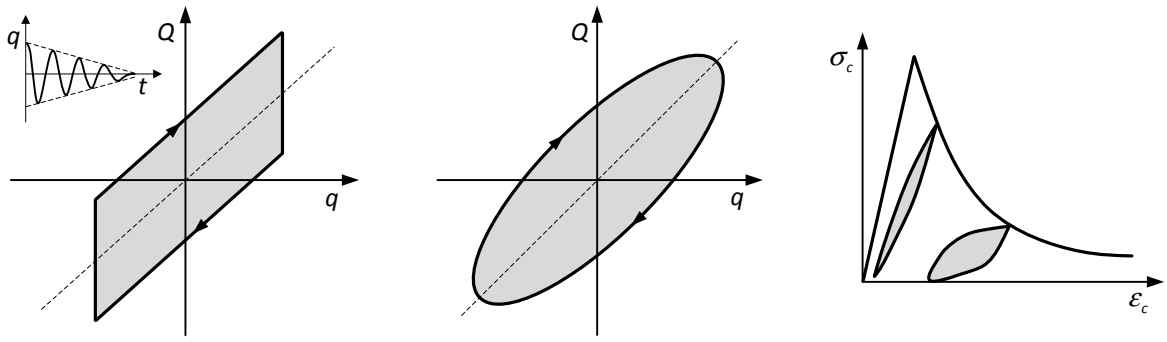

a) Dry friction damping b) Dynamic Hysteresis c) Material Hysteresis

Figure II.7: Alternative types of damping: a) dry friction, adapted from Chopra [105];
b) dynamic hysteresis, adapted from Chopra [105]; c) material hysteresis, adapted from Mazars *et al.* [388].

4.3.2 Mode Superposition method

In the *Mode Superposition* method, the dynamic equilibrium equation (II.49):

$$\mathbf{M}\,\mathbf{a}(t)+\mathbf{C}\,\mathbf{v}(t)+\mathbf{K}\,\mathbf{q}(t)=\mathbf{Q}_e(t),$$

is computed assuming that the solution can be written as [574]:

$$\mathbf{q}(t)=\boldsymbol{\Phi}\,\mathbf{q}_G(t), \tag{II.120}$$

$$\mathbf{v}(t)=\boldsymbol{\Phi}\,\mathbf{v}_G(t), \tag{II.121}$$

$$\mathbf{a}(t)=\boldsymbol{\Phi}\,\mathbf{a}_G(t), \tag{II.122}$$

where $\boldsymbol{\Phi}$ is the matrix that holds the relevant mode shapes[i] and $\mathbf{q}_G$, $\mathbf{v}_G$ and $\mathbf{a}_G$ are the coefficients (weights), *a.k.a. modal or generalized coordinates*, associated with each mode shape for defining the solution in terms of the displacements, velocities and accelerations, respectively. The procedure to compute the structural response from individual modal components is often called the *modal synthesis* method [141].

Introducing equations (II.120) to (II.122) in the dynamic equilibrium equation (II.49) and pre-multiplying each term by $\boldsymbol{\Phi}^t$, it is possible to obtain:

$$\mathbf{I}\,\mathbf{a}_G(t)+\mathcal{D}\,\mathbf{v}_G(t)+\boldsymbol{\Omega}^2\mathbf{q}_G(t)=\boldsymbol{\Phi}^t\,\mathbf{Q}_e(t). \tag{II.123}$$

If the external forces are written as a sum for all loads:

$$\mathbf{Q}_e(t)=\sum_{j=1}^{nl}\bar{\mathbf{Q}}_{e,j}\;\mathrm{T}_j(t), \tag{II.124}$$

where $\bar{\mathbf{Q}}_{e,j}$ is a time-independent vector (load pattern) and $\mathrm{T}_j(t)$ is a *time function* associated with the load, then the equilibrium equation can be written as [574]:

[i] Note that matrix $\boldsymbol{\Phi}$ is orthogonal, consequently: $\boldsymbol{\Phi}^{-1}=\boldsymbol{\Phi}^t$.

$$\mathbf{I}\,\mathbf{a}_G(t)+\mathcal{D}\,\mathbf{v}_G(t)+\mathbf{\Omega}^2\mathbf{q}_G(t)=\sum_{j=1}^{nl}\mathbf{p}_j\,\mathrm{T}_j(t)\,, \tag{II.125}$$

where $\mathbf{p}_k$ are the *modal participation factors* associated with load *j*, defined by:

$$\mathbf{p}_j=\mathbf{\Phi}^t\,\bar{\mathbf{Q}}_{e,j}\,. \tag{II.126}$$

Using proportional damping, the damping-related matrix $\mathcal{D}$ will inherit the orthogonal properties of the mass and stiffness matrices and under the previous hypothesis, it will become a diagonal matrix whose entries can be written as [116]:

$$\mathcal{D}_{nn}=2\xi_n\,\omega_n\,, \tag{1.127}$$

where ξ_n is the percentage of critical damping for mode *n*.

The system of equations presents a very convenient property related to the fact that the equations are uncoupled because only diagonal operators are present in (II.125). Consequently, it is possible to solve all the equations independently for each vibration mode, using [574]:

$$a_{G,n}(t)+2\xi_n\,\omega_n\,v_{G,n}(t)+\omega_n^2\,q_{G,n}(t)=\sum_{j=1}^{nl}p_{j,n}\,\mathrm{T}_j(t)\,. \tag{II.128}$$

This type of analysis is very attractive due to the small computational cost required for finding the solution and is used many times in earthquake engineering for elastic analyses using *response spectra* (RS) to define the seismic input (see section 6.1.2).

After computing the solution in time for each generalized coordinate, the solution back in the normal Cartesian coordinate system can be computed using equations (II.120) to (II.122).

4.3.3 Time Integration methods

The *Time Integration* (TI) methods, *a.k.a. Step-by-Step* methods, are used to solve the dynamic equations of motion using a finite difference approximation [141]. Most of the times, an equally spaced time discretization is used (proportional to the time step, Δt), although other time discretization schemes can be used. Several TI methods have been developed and they differ mostly in terms of the stability, accuracy and numerical damping introduced. These methods are often classified as e*xplicit*, *implicit* or *mixed*. In the explicit methods, the solution for the current time step is computed only from data from the previous time steps [141]:

$$\mathbf{q}_{j+1}=f\left(\mathbf{q}_j,\mathbf{v}_j,\mathbf{a}_j,\mathbf{q}_{j-1},\mathbf{v}_{j-1},\mathbf{a}_{j-1},\ldots\right). \tag{II.129}$$

On the other hand, implicit methods require knowing the derivatives of the displacements at the end of the current time step:

$$\mathbf{q}_{j+1}=f\left(\mathbf{v}_{j+1},\mathbf{a}_{j+1},\mathbf{q}_j,\mathbf{v}_j,\mathbf{a}_j,\ldots\right). \tag{II.130}$$

Mixed methods combine the advantages of the explicit and implicit methodologies and they are normally used when the structure to be analysed is heterogeneous, *e.g.* in the context of multi-physics problems, analyses with substructuring and using the pseudo-dynamic testing method [49,

59, 60, 126, 280-282, 411, 412].

Explicit methods are often conditionally stable regarding the time step, thus this parameter must be small. On the other hand, larger time steps are often used with implicit methods, which can be conditionally or unconditionally stable [141]. Explicit methods are common in wave propagation and high velocity impact problems, and implicit methods are often associated with low frequency systems, like structural dynamic problems [155]. It should be noted that although the implicit methods require, in principle, the use of an iterative procedure due to their dependency on the variables resulting from the time step itself, an assumption is usually made regarding these unknowns in order to avoid using an iterative algorithm [116].

Another source of distinction between these methods is related to the number of past steps required for the computation. The TI method is called a *single-step method* when only information from the previous step is required. On the contrary, *multi-step* methods require information from the last two or more steps. Consequently, multi-step methods may require some attention during the starting phase in order to produce accurate results [141].

Table II.1 presents a list of the most used time integration methods, together with the characteristics in terms of formulation type, stability, accuracy and dissipative properties. For historical reasons, the multi-step methods proposed by Houbolt [276] and Park [430] are also mentioned.

- Characteristics of the TI methods

It is of vital importance to assess the stability, accuracy, dissipative and dispersive characteristics of each TI method. The procedures to achieve this are well described in the work of *Hilber* [265] or in other bibliography, *e.g.* [266, 267, 279, 441]. Most of these techniques are based on writing the TI algorithm using a first-order recursive form, either for free vibration:

$$\mathbf{X}_{j+1} = \mathbf{A}\,\mathbf{X}_j\,, \tag{II.131}$$

Table II.1: Characteristics of the most used time integration methods.

Method	Type	Stability	Accuracy	Num. Damping
Piecewise Exact	Analytical	Stable	Exact*	No
Forward-Euler	Explicit	Unstable	-	No
Backward-Euler	Implicit	Stable	-	Yes
Mixed-Euler	Implicit	Stable	-	No
Exp. Artificially Damped Newmark	Explicit	Conditionally stable	$O(\Delta t)$	Yes
Central-differences	Explicit	Conditionally stable	$O(\Delta t^2)$	No
Average Acceleration	Implicit	Stable	$O(\Delta t^2)$	No
Linear Acceleration	Implicit	Conditionally stable	$O(\Delta t^2)$	No
Imp. Artificially Damped Newmark	Implicit	Stable	$O(\Delta t)$	Yes
Wilson-θ	Implicit	Stable**	$O(\Delta t^2)$	Yes
α-Method* **	Implicit	Stable	$O(\Delta t^2)$	Yes

* for piecewise loading; ** for $\theta \geq 1.3(6)$, *** for $\alpha =]0,-1/3]$ and (γ,β) according to (II.199).

Note: the Central-differences is a multi-step method, all the others are single-step methods.

or for forced vibration:

$$\mathbf{X}_{j+1} = \mathbf{A}\,\mathbf{X}_j + \mathbf{L}\,\mathbf{F}_{j+1}, \tag{II.132}$$

where $\mathbf{A}$ is the *amplification matrix* and $\mathbf{L}$ is the *load operator,* defined by:

$$\mathbf{X}_j = \left[\mathbf{q}_j \quad \Delta t\,\mathbf{v}_j \quad \Delta t^2\,\mathbf{a}_j\right]^t, \tag{II.133}$$

$$\mathbf{F}_j = \left[\mathbf{Q}_{e,j} \quad \mathbf{Q}_{e,j+1}\right]^t. \tag{II.134}$$

To introduce the basic variables, the response in time for the simple case of an undamped *sdof* oscillator undertaking free vibration is given by [105]:

$$q(t) = q_0 \cos(\omega t) + \frac{v_0}{\omega}\sin(\omega t), \tag{II.135}$$

and the recursive form (II.131), would be written with the amplification matrix [265]:

$$\mathbf{A} = \begin{bmatrix} \cos(\Omega) & \sin(\Omega)/\Omega \\ -\Omega\sin(\Omega) & \cos(\Omega) \end{bmatrix}, \tag{II.136}$$

where the third row and column of $\mathbf{A}$ is removed because the motion equation does not depend explicitly on the acceleration. The variable Ω is called the *reduced angular frequency*:

$$\Omega = \omega\Delta t. \tag{II.137}$$

The amplification matrix is used to analyse several properties of the TI algorithms. An example is the stability assessment, which is related to avoiding having uncontrolled increasing amplitudes in the solution. This is usually evaluated by the spectral analysis of this matrix. This can be done by writing the cubic characteristic equation in terms of the invariants [266]:

$$\det(\mathbf{A} - \lambda\mathbf{I}) = -\lambda^3 + A_1\lambda^2 - A_2\lambda + A_3 = 0, \tag{II.138}$$

where A_k are the three matrix invariants (see Annex A) and the roots of this equation are the eigenvalues λ_k. A parameter commonly used is the *spectral radius* $\rho = \max\{|\lambda_1|, |\lambda_2|, |\lambda_3|\}$. According to Hilber *et al.* [266], the TI method is said to be stable if $\rho \le 1$ and if the eigenvalues of multiplicity greater than one satisfy $|\lambda| < 1$.

Truncation errors are present in all numerical methods that adopt a finite discretization to model a continuum variable and TI methods are no exception. A TI method is said to have an order of accuracy of $k-1$, if the *local truncation error* σ in a single step for $k > 0$, follows:

$$\sigma = f\left(\Delta t^k\right) + O\left(\Delta t^{k-1}\right). \tag{II.139}$$

The effect of distortion is usually assessed measuring the tendency to overshoot, *i.e.* peak amplitude errors, from the amplification matrix spectral properties. The norm or other energy-related norm forms are commonly used for this purpose [266]. Additionally, the frequency content distortion is commonly measured using the *relative period error*:

$$e_r^T = \left(\overline{T} - T\right)/T, \tag{II.140}$$

where $T=2\pi/\omega$, $\bar{T}=2\pi/\bar{\omega}$, with $\bar{\omega}=\bar{\Omega}/\Delta t$ and $\bar{\Omega}$ is the limit value for Ω, in which there are two complex conjugate roots, λ_1 and λ_2 named the *principal roots*, and the so-called *spurious root* λ_3. More information can be obtained in the bibliography, *e.g.* [265, 266].

Other parameters can be used to evaluate the performance of the TI methods. As an example, Pegon [441] proposes the use of a *numerical resonant angular frequency* $\bar{\Omega}_r$ and the *numerical frequency damping ratio* $\bar{\xi}_r$ to assess the effect on the position and intensity of the resonant frequencies by using TI methods for *multi degree-of-freedom* (*mdof*) elastic systems subjected to harmonic loading.

To assess the numerical dissipation introduced by the TI methods, the recursive equation is often written for the free vibration case (II.131) considering an undamped *sdof* system. At this point, it is clear that if $\rho\leq 1$ the algorithm is dissipative. The *numerical damping ratio* $\bar{\xi}$ is often used to quantify the amount of damping introduced (see Figure II.11-c). For under-damped systems, the eigenvalues of **A** are complex conjugate $\left(\rho=a\pm bi\right)$ and this variable can be computed from [441]:

$$\bar{\xi}=-\ln\left(\sqrt{a^2+b^2}\right)\Big/2\bar{\Omega}\,. \tag{II.141}$$

In the following part of this section, a summarized description of the formulation associated with the most used TI methods and their most relevant characteristics are presented.

- Piecewise Exact method

The *Piecewise Exact method* is based on the exact solution of a linear *sdof* subjected to a series of linear varying loading steps. Under general loading, this method is only approximated. However, the accuracy can be improved by decreasing the time step in order to better define the loading history [116]. The loading is assumed to change linearly in each time step (see Figure II.8-a):

$$Q_e\left(\tau\right)=Q_e^0+\alpha\tau\,, \tag{II.142}$$

where Q_e^0 is the loading force at beginning of the time step, α is the loading slope and τ is the elapsed time relative to the beginning of the time step.

The equation of motion for each time step, can written as:

$$m\,a+c\,v+k\,q=Q_e^0+\alpha\tau\,, \tag{II.143}$$

for which the solution can be computed by adding the free vibration contribution (homogeneous component) due to the initial movement conditions to the forced vibration solution (particular component), which leads to [116]:

$$q\left(\tau\right)=A_0+A_1\tau+A_2e^{-\xi\omega t}\cos\left(\omega_d\tau\right)+A_3e^{-\xi\omega t}\sin\left(\omega_d\tau\right), \tag{II.144}$$

where:

$$A_0=\frac{Q_e^0}{\omega^2}-\frac{2\xi\alpha}{\omega^3},\quad A_1=\frac{\alpha}{\omega^2},\quad A_2=q_j-A_0,\quad A_3=\frac{1}{\omega_d}\left(v_j+\xi\omega A_2-\frac{\alpha}{\omega^2}\right), \tag{II.145}$$

and the solution in terms of the velocity is given by:

$$v\left(\tau\right)=A_1+\left(\omega_dA_3-\xi\omega A_2\right)e^{-\xi\omega t}\cos\left(\omega_d\tau\right)-\left(\omega_dA_2-\xi\omega A_3\right)e^{-\xi\omega t}\sin\left(\omega_d\tau\right). \tag{II.146}$$

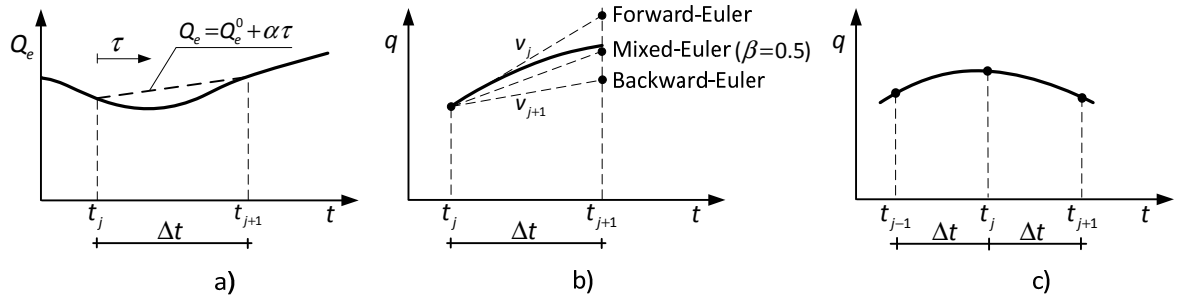

Figure II.8: Time integration methods: a) Piecewise Exact method; b) Euler methods; c) Central-difference method.

- Euler algorithms

In this family of algorithms, the displacements at the end of the time step can be computed from the velocities: i) at the beginning of the time step in the *Forward-Euler* method (II.147); ii) at the end of the time step in the *Backward-Euler* method (II.148); or iii) by a combination of these values in the *Mixed-Euler* method (II.149) (see Figure II.8-b) [123, 154]:

$$\mathbf{q}_{j+1} = \mathbf{q}_j + \Delta t\ \mathbf{v}_j\,, \tag{II.147}$$

$$\mathbf{q}_{j+1} = \mathbf{q}_j + \Delta t\ \mathbf{v}_{j+1}\,, \tag{II.148}$$

$$\mathbf{q}_{j+1} = \mathbf{q}_j + \Delta t\left(\beta\ \mathbf{v}_j + \left(1-\beta\right)\mathbf{v}_{j+1}\right). \tag{II.149}$$

According to Combescure [123], it can be proved that the *Forward-Euler* method is unstable, that the Backward-Euler method is stable but dissipative and that the Mixed-Euler method $\left(\beta = 0.5\right)$ is stable and conservative.

- Central-Difference method

In the *Central-Differences method* [105, 116], the equilibrium is established at the end of the time step:

$$\mathbf{M}\ \mathbf{a}_{j+1} + \mathbf{C}\ \mathbf{v}_{j+1} + \mathbf{K}\ \mathbf{q}_{j+1} = \mathbf{Q}_{e,j+1}\,. \tag{II.150}$$

The displacement time derivatives (velocity and acceleration) are approximated using finite differences. A Taylor series decomposition truncated to the second term followed by some algebraic manipulations is used to express the displacements at the instant t_j. Assuming a time increment of Δt and $-\Delta t$ around this point, it is possible to obtain the following expressions for the displacements (see Figure II.8-c):

$$\mathbf{q}_{j+1} = \mathbf{q}_j + \mathbf{v}_j\,\Delta t + \frac{\mathbf{a}_j\,\Delta t^2}{2}, \tag{II.151}$$

$$\mathbf{q}_{j-1} = \mathbf{q}_j - \mathbf{v}_j\,\Delta t + \frac{\mathbf{a}_j\,\Delta t^2}{2}. \tag{II.152}$$

It is possible to remove the acceleration or the velocity terms by subtracting or adding these two equations, resulting in:

$$\mathbf{v}_j = \frac{\mathbf{q}_{j+1} - \mathbf{q}_{j-1}}{2\Delta t}, \tag{II.153}$$

$$\mathbf{a}_j = \frac{\mathbf{q}_{j+1} + \mathbf{q}_{j-1} - 2\mathbf{q}_j}{\Delta t^2}. \tag{II.154}$$

Introducing (II.153) and (II.154) in (II.49) and grouping the terms for each time step, leads to:

$$\hat{\mathbf{K}}\,\mathbf{q}_{j+1} = \hat{\mathbf{Q}}_j, \tag{II.155}$$

where:

$$\hat{\mathbf{K}} = \frac{\mathbf{M}}{\Delta t^2} + \frac{\mathbf{C}}{2\Delta t}, \tag{II.156}$$

$$\hat{\mathbf{Q}}_j = \mathbf{Q}_{e,j} + \frac{\mathbf{M}}{\Delta t^2}\left(2\mathbf{q}_j - \mathbf{q}_{j-1}\right) + \frac{\mathbf{C}}{2\Delta t}\left(\mathbf{q}_{j-1}\right) - \mathbf{K}\mathbf{q}_j. \tag{II.157}$$

For starting the algorithm, it is necessary to define the value of $\mathbf{q}_{j-1}$ that can be computed from equation (II.152), using the initial condition of the problem $\boldsymbol{q}_0$, $\mathbf{v}_0$ and $\mathbf{a}_0$ obtained from (II.49) defined at $t = 0$:

$$\mathbf{a}_0 = \mathbf{M}^{-1}\left\{\mathbf{Q}_{e,0} - \mathbf{C}\mathbf{v}_0 - \mathbf{K}\mathbf{q}_0\right\}. \tag{II.158}$$

When using diagonal mass and damping matrices, the governing system becomes uncoupled and this method gains competitiveness with respect to the implicit methods [141].

- Average Acceleration method

The *Average Acceleration* method, *a.k.a. Trapezoidal Rule*, is an implicit method that assumes that the accelerations are constant and equal to the average of the values at the beginning and at the end of the time step (see Figure II.9-a):

$$\mathbf{a}(\tau) = \frac{\mathbf{a}_j + \mathbf{a}_{j+1}}{2}. \tag{II.159}$$

It is possible to obtain the following expressions for computing the velocities and displacements at the end of the time step by integrating the last equation:

$$\mathbf{v}_{j+1} = \mathbf{v}_j + \Delta t\,\frac{\mathbf{a}_j + \mathbf{a}_{j+1}}{2}, \tag{II.160}$$

$$\mathbf{q}_{j+1} = \mathbf{q}_j + \Delta t\,\mathbf{v}_j + \frac{\Delta t^2}{4}\left(\mathbf{a}_j + \mathbf{a}_{j+1}\right). \tag{II.161}$$

Inserting (II.160) into (II.161), the following relation is obtained:

$$\mathbf{q}_{j+1} = \mathbf{q}_j + \Delta t\,\frac{\mathbf{v}_j + \mathbf{v}_{j+1}}{2}. \tag{II.162}$$

Equations (II.160) and (II.162) can be used to define the accelerations and velocities at the end of the time step, respectively by [105]:

$$\mathbf{a}_{j+1} = \frac{2}{\Delta t}\left(\mathbf{v}_{j+1} - \mathbf{v}_j\right) - \mathbf{a}_j, \tag{II.163}$$

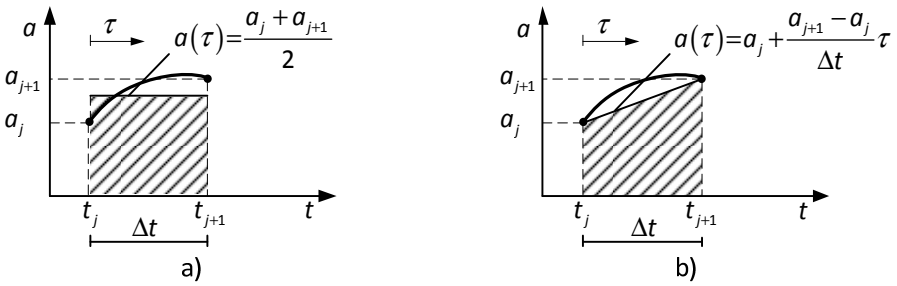

Figure II.9: Time integration methods: a) Average Acceleration; b) Linear Acceleration.

$$\boldsymbol{v}_{j+1}=\frac{2}{\Delta t}\left(\boldsymbol{q}_{j+1}-\boldsymbol{q}_j\right)-\boldsymbol{v}_j\,. \tag{II.164}$$

Introducing (II.164) into (II.163) to eliminate the term $\boldsymbol{v}_{j+1}$, leads to:

$$\mathbf{a}_{j+1}=\frac{4}{\Delta t^2}\left(\mathbf{q}_{j+1}-\mathbf{q}_j\right)-\frac{4}{\Delta t}\mathbf{v}_j-\mathbf{a}_j\,. \tag{II.165}$$

Introducing (II.164) and (II.165) into the dynamic equilibrium equation (II.49) defined at instant $j+1$, it is possible to obtain:

$$\mathbf{M}\left(\frac{4}{\Delta t^2}\left(\mathbf{q}_{j+1}-\mathbf{q}_j\right)-\frac{4}{\Delta t}\mathbf{v}_j-\mathbf{a}_j\right)+\mathbf{C}\left(\frac{2}{\Delta t}\left(\mathbf{q}_{j+1}-\mathbf{q}_j\right)-\mathbf{v}_j\right)+\mathbf{K}\mathbf{q}_{j+1}=\mathbf{Q}_{j+1}\,. \tag{II.166}$$

Separating the terms associated with the displacements at the end of the time step, this last equation can be rewritten in the condensed format:

$$\hat{\mathbf{K}}\,\mathbf{q}_{j+1}=\hat{\mathbf{Q}}_{j+1}\,, \tag{II.167}$$

with:

$$\hat{\mathbf{K}}=\frac{4}{\Delta t^2}\mathbf{M}+\frac{2}{\Delta t}\mathbf{C}+\mathbf{K}\,, \tag{II.168}$$

$$\hat{\mathbf{Q}}_{j+1}=\mathbf{Q}_{e,j+1}+\left(\frac{4}{\Delta t^2}\mathbf{q}_j+\frac{4}{\Delta t}\mathbf{v}_j+\mathbf{a}_j\right)\mathbf{M}+\left(\frac{2}{\Delta t}\mathbf{q}_j+\mathbf{v}_j\right)\mathbf{C}\,, \tag{II.169}$$

where $\hat{\mathbf{K}}$ and $\hat{\mathbf{Q}}$ are often called the *effective stiffness* and the *effective forces*, respectively.

Starting the algorithm can be done by specifying the initial conditions $(\mathbf{q}_0,\mathbf{v}_0)$ and by computing $\mathbf{a}_0$ using equation (II.158). The system of equations is always coupled, even if the mass and damping matrices are diagonal [141], which presents a disadvantage with respect to the *Central-Differences* method.

- Linear Acceleration method

The *Linear Acceleration* method assumes that the accelerations change linearly between the values at the beginning and at the end of the time step (see Figure II.9-b):

$$\mathbf{a}(\tau)=\mathbf{a}_j+\frac{\mathbf{a}_{j+1}-\mathbf{a}_j}{\Delta t}\tau\,. \tag{II.170}$$

Integrating this equation, it is possible to retrieve the following expressions for the velocities and displacements [105]:

$$\mathbf{v}_{j+1} = \mathbf{v}_j + \Delta t \, \frac{\mathbf{a}_j + \mathbf{a}_{j+1}}{2}, \tag{II.171}$$

$$\mathbf{q}_{j+1} = \mathbf{q}_j + \Delta t \, \mathbf{v}_j + \frac{\Delta t^2}{3} \mathbf{a}_j + \frac{\Delta t^2}{6} \mathbf{a}_{j+1}. \tag{II.172}$$

Using a similar procedure to the one used for the Average Acceleration method, it is possible to write the condensed dynamic equilibrium equation using the same expression adopted in (II.167). In this case, the *effective stiffness matrix* and the *effective forces vector* are given by:

$$\hat{\mathbf{K}} = \frac{6}{\Delta t^2}\mathbf{M} + \frac{3}{\Delta t}\mathbf{C} + \mathbf{K}, \tag{II.173}$$

$$\hat{\mathbf{Q}}_{j+1} = \mathbf{Q}_{e,j+1} + \left(\frac{6}{\Delta t^2}\mathbf{q}_j + \frac{6}{\Delta t}\mathbf{v}_j + 2\mathbf{a}_j \right) M + \left(\frac{3}{\Delta t}\mathbf{q}_j + 2\mathbf{v}_j + \frac{\Delta t}{2}\mathbf{a}_j \right) \mathbf{C}. \tag{II.174}$$

The algorithm can be started using the same procedure reported for the Average Acceleration method.

- Newmark methods

This family of time integration methods [415] adopts the following general expression for the acceleration variation in the time step (see Figure II.10-a).

$$\mathbf{a} = \left\{ (1-\gamma)\mathbf{a}_j + \gamma \mathbf{a}_{j+1} \right\} \Delta t \ . \tag{II.175}$$

Adopting a similar procedure to the one used in the previous methods, it is possible to express the displacements and velocities at the end of the time step, using [415]:

$$\mathbf{v}_{j+1} = \mathbf{v}_j + \left\{ (1-\gamma)\mathbf{a}_j + \gamma \mathbf{a}_{j+1} \right\} \Delta t, \tag{II.176}$$

$$\mathbf{q}_{j+1} = \mathbf{q}_j + \Delta t \, \mathbf{v}_j + \frac{\Delta t^2}{2} \left\{ (1-2\beta)\mathbf{a}_j + 2\beta \, \mathbf{a}_{j+1} \right\}. \tag{II.177}$$

The following expression can be obtained by rearranging the terms present in equation (II.177):

$$\mathbf{a}_{j+1} = \frac{1}{\beta \Delta t^2} \left\{ \mathbf{q}_{j+1} - \mathbf{q}_j - \Delta t \, \mathbf{v}_j - \left(\frac{1}{2} - \beta \right) \Delta t^2 \, \mathbf{a}_j \right\}. \tag{II.178}$$

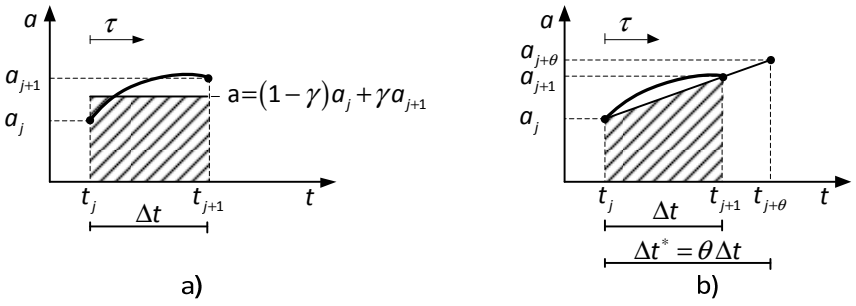

Figure II.10: Time integration methods: a) Newmark family of methods; b) Wilson-θ method.

The velocities at the end of the time step are obtained by introducing the previous expression into equation (II.176):

$$\mathbf{v}_{j+1}=\frac{\gamma}{\beta\Delta t}\left(\mathbf{q}_{j+1}-\mathbf{q}_j\right)+\left(1-\frac{\gamma}{\beta}\right)\mathbf{v}_j+\left\{\left(1-\gamma\right)-\frac{\gamma}{\beta}\left(\frac{1}{2}-\beta\right)\right\}\Delta t\ \mathbf{a}_j\,. \tag{II.179}$$

Inserting (II.178) and (II.179) into the standard dynamic equilibrium equation (II.49) defined at the time step $j+1$ and by rearranging the terms, it is possible to obtain once again equation (II.167). For this method, the *effective stiffness* and *effective forces* are given by:

$$\hat{\mathbf{K}}=\frac{1}{\beta\Delta t^2}\mathbf{M}+\frac{\gamma}{\beta\Delta t}\mathbf{C}+\mathbf{K}\,, \tag{II.180}$$

$$\begin{aligned}\hat{\mathbf{Q}}_{j+1}=\mathbf{Q}_{e,j+1}+&\left\{-\mathbf{v}_j-\left(1-\gamma\right)\Delta t\,\mathbf{a}_j+\frac{\gamma}{\beta\Delta t}\mathbf{q}_j+\frac{\gamma}{\beta}\mathbf{v}_j+\frac{\gamma}{\beta}\left(\frac{1}{2}-\beta\right)\Delta t\,\mathbf{a}_j\right\}\mathbf{C}+\\&\frac{1}{\beta\Delta t^2}\left\{\mathbf{q}_j+\Delta t\,\mathbf{v}_j+\left(\frac{1}{2}-\beta\right)\Delta t^2\,\mathbf{a}_j\right\}\mathbf{M}\end{aligned}\,. \tag{II.181}$$

The governing system (II.167) can be solved for the displacements at the end of the time step and the accelerations and velocities can be computed from (II.178) and (II.179), respectively.

According to Hilber [265], the amplification matrix for the Newmark family of methods can be found by considering a damped *sdof* oscillator. This matrix can be written as:

$$\mathbf{A}=\begin{bmatrix}1+\beta A_1 & 1+\beta A_2 & 1/2+\beta\left(A_3-1\right)\\ \gamma A_1 & 1+\gamma A_2 & 1+\gamma\left(A_3-1\right)\\ A_1 & A_2 & A_3\end{bmatrix}, \tag{II.182}$$

where:

$$A_1=-\Omega^2/B\,, \tag{II.183}$$

$$A_2=-\left(2\xi\Omega+\Omega^2\right)/B\,, \tag{II.184}$$

$$A_3=1-\left(1+2\xi\Omega+\Omega^2/2\right)/B\,, \tag{II.185}$$

$$B=1+2\gamma\xi\Omega+\beta\Omega^2\,. \tag{II.186}$$

Regarding stability, it can be proved from (II.182) that the resulting TI method is unconditionally stable if the following relation is respected [141]:

$$2\beta\geq\gamma\geq 1/2\,, \tag{II.187}$$

and conditionally stable when,

$$\gamma\geq 1/2\,,\beta<1/2\,, \tag{II.188}$$

requiring for stability that [265]:

$$\Omega_c=\Delta t\,\omega_{\max}\leq\frac{\xi\left(\gamma-1/2\right)+\sqrt{\gamma/2-\beta+\xi^2\left(\gamma-1/2\right)^2}}{\left(\gamma/2-\beta\right)}\,, \tag{II.189}$$

Table II.2: Parameters for the Newmark family of TI methods and for the α-Method.

Method	Type	$(\alpha;\gamma;\beta)$	Num. Damping	Ω_c	Accuracy
Exp. Artificially Damped Newmark	Explicit	$(0;>1/2;0)$	Yes	(II.189)	$O(\Delta t)$
Central-Differences	Explicit	$(0;1/2;0)$	No	2	$O(\Delta t^2)$
Average Acceleration	Implicit	$(0;1/2;1/4)$	No	∞	$O(\Delta t^2)$
Linear Acceleration	Implicit	$(0;1/2;1/6)$	No	$2\sqrt{3}$	$O(\Delta t^2)$
Imp. Artificially Damped Newmark	Implicit	$(0;>1/2;>\gamma/2)$	Yes	∞	$O(\Delta t)$
α-Method	Implicit	$(-0.100;0.600;0.3025)$	Yes (Low)	∞	$O(\Delta t^2)$
		$(-0.200;0.700;0.3600)$	Yes (Medium)	∞	$O(\Delta t^2)$
		$(-0.333;0.833;0.4444)$	Yes (High)	∞	$O(\Delta t^2)$

and unstable if $\gamma<1/2$. The parameter $\omega_{\max}$ represents the maximum frequency in the system comprising the structure and the loading.

In terms of accuracy, it can be proven by performing a local truncation error analysis that this method presents second-order accuracy if $\gamma=1/2$. The use of $\gamma>1/2$ introduces numerical damping but the accuracy is reduced to first-order [141, 265].

The central differences, average acceleration and linear acceleration methods belong to the Newmark family of TI algorithms. Table II.2 presents the combination of parameters that allows these integrations schemes to be retrieved.

- Wilson-θ method

The *Wilson*-θ method [575] is a modification of the conditionally stable *Linear Acceleration* method in order to achieve unconditional stability. This method performs the motion equation verification outside the time step interval, hence it is also known as a *collocation method*. This algorithm uses an extended time step $\Delta t^* = \theta \Delta t$, where $\theta \geq 1.0$ (see Figure II.10-b) is called the *collocation point*. In order to be unconditionally stable, the colocation point should follow the rule $\theta \geq 1.3(6)$. Adopting $\theta = 1.42$ leads to optimal accuracy [105]. However, according to Bathe [32], $\theta = 1.4$ is used most of the time. This method considers the same expressions of the *Linear Acceleration* method to integrate the velocities (II.171) and the displacements (II.172) in the time step, but in this case considering an extended time step Δt^* (see Figure II.10-b).

Using similar algebraic manipulations to the ones presented for the previous methods and assuming that the external forces change linearly in the extended time step, it is possible to obtain [32, 105]:

$$\hat{\mathbf{K}}^* \mathbf{q}_{j+1}^* = \hat{\mathbf{Q}}_{j+1}^* , \tag{II.190}$$

where:

$$\hat{\mathbf{K}}^* = \frac{6}{\left(\Delta t^*\right)^2}\mathbf{M} + \frac{3}{\Delta t^*}\mathbf{C} + \mathbf{K} , \tag{II.191}$$

$$\hat{\mathbf{Q}}_{j+1}^{*}=\mathbf{Q}_{e,j+1}+\left(\frac{6}{\left(\Delta t^{*}\right)^{2}}\mathbf{q}_{j}+\frac{6}{\Delta t^{*}}\mathbf{v}_{j}+2\mathbf{a}_{j}\right)M+\left(\frac{3}{\Delta t^{*}}\mathbf{q}_{j}+2\mathbf{v}_{j}+\frac{\Delta t^{*}}{2}\mathbf{a}_{j}\right)\mathbf{C}. \tag{II.192}$$

Equation (II.190) is used to compute $\mathbf{q}_{j+1}^{*}$, and for $\mathbf{a}_{j+1}^{*}$ the following expression can be used:

$$\mathbf{a}_{j+1}^{*}=\frac{6}{\left(\Delta t^{*}\right)^{2}}\boldsymbol{q}_{j+1}^{*}-\frac{6}{\Delta t^{*}}\boldsymbol{v}_{j}^{*}-3\mathbf{a}_{j+1}^{*}. \tag{II.193}$$

The accelerations at the end of the normal time step can be computed using:

$$\mathbf{a}_{j+1}=\frac{1}{\theta}\mathbf{a}_{j}^{*}, \tag{II.194}$$

and the displacements and velocities using equations (II.172) and (II.171), respectively.

The Wilson-θ method is an unconditionally stable, second-order accurate algorithm that can simulate numerical damping through the θ parameter. Nevertheless, according to Hilber [266] this method presents an overshoot tendency when large time steps are adopted.

- α-Method

The α-Method, *a.k.a.* the *Hilber-Hughes-Taylor* method [267], presents the same definition of Newmark's family of methods for the finite differences (II.176) and (II.177). However, this method defines the dynamic equilibrium, using [279]:

$$\mathbf{M}\mathbf{a}_{j+1}+(1+\alpha)\mathbf{C}\mathbf{v}_{j+1}-\alpha\mathbf{C}\mathbf{v}_{j}+(1+\alpha)\mathbf{K}\mathbf{q}_{j+1}-\alpha\mathbf{K}\mathbf{q}_{j}=(1+\alpha)\mathbf{Q}_{e,j+1}-\alpha\mathbf{Q}_{e,j}, \tag{II.195}$$

where the dynamic equilibrium is verified at:

$$t_{j+\alpha}=(1+\alpha)t_{j+1}-\alpha t_{j}=t_{j+1}+\alpha\Delta t. \tag{II.196}$$

Introducing (II.178) and (II.179) into the dynamic equilibrium equation (II.195) and rearranging the terms, it is possible to obtain the same format as presented in (II.167). In this case, the effective terms are computed with the following expressions [155]:

$$\hat{\mathbf{K}}=(1+\alpha)\left(\mathbf{K}+\frac{\gamma}{\beta\Delta t}\mathbf{C}\right)+\frac{1}{\beta\Delta t^{2}}\mathbf{M}, \tag{II.197}$$

$$\begin{aligned}\hat{\mathbf{Q}}_{j+1}=&(1+\alpha)\mathbf{Q}_{e,j+1}-\alpha\mathbf{Q}_{e,j}+\alpha\mathbf{K}\mathbf{q}_{j}+\mathbf{M}\left\{\frac{1}{\beta\Delta t^{2}}\mathbf{q}_{j}+\frac{1}{\beta\Delta t}\mathbf{v}_{j}+\frac{1-2\beta}{2\beta}\mathbf{a}_{j}\right\}+\\&(1+\alpha)\,\mathbf{C}\left\{\frac{\gamma}{\beta\Delta t}\mathbf{q}_{j}-\left(1-\frac{\gamma}{\beta}\right)\mathbf{v}_{j}+\Delta t\frac{\gamma(1-2\beta)}{2\beta}\mathbf{a}_{j}-\Delta t(1-\gamma)\mathbf{a}_{j}\right\}+\alpha\mathbf{C}\mathbf{v}_{j}\end{aligned}. \tag{II.198}$$

The parameter α can be used to introduce numerical damping into the solutions without degrading the second-order accuracy of some Newmark methods [279]. If $\alpha=0$, no artificial damping is introduced and the Average Acceleration method is recovered using $\gamma=1/2$ and $\beta=1/4$. Decreasing the numerical value of α, increases the amount of numerical damping until $\alpha=-1/3$, where stability problems arise. According to Hughes [279], the method is implicit, unconditional stable and second-order accurate if the following combination of the parameters is met:

$$-1/3\le\alpha\le 0;\quad \gamma=(1-2\alpha)/2;\quad \beta=(1-\alpha)^{2}/4. \tag{II.199}$$

The α-Method presents a series of advantages that were already emphasized by several authors, *e.g.* Hilber *et al.* [266]. Apart from being unconditionally stable, second-order accurate and self-starting, the most attractive feature of the α-Method is the capacity to add a controlled level of numerical dissipation to damp out high frequency spurious modes, which are unrealistic and at the same time do not significantly change the response for the frequency band relevant for typical civil engineering structures.

Figure II.11 presents some relevant data about the numerical response of selected TI methods. The evolution of the *spectral radius* ρ with the ratio between the time step and the period of the *sdof* oscillator is presented in Figure II.11-a. It can be seen that all the methods present $\rho<1$, so stability is achievable. For higher time steps, the spectral radius tends to decrease smoothly except for the Wilson-θ method that exhibits an undesired regain. For this method using $\theta=1.3(6)$ is the minimum value that ensures that $\rho<1$ and achieves unconditional stability.

In addition, if the time step is similar to the period of the oscillator, Figure II.11-b shows that there is a relevant period error in the response. To mitigate this effect the time step should be at least one order of magnitude smaller than the oscillator period.

Furthermore, Figure II.11-c presents the numerical damping ratio introduced by the algorithms. It is possible to confirm that both the Wilson-θ and the α-Method present good dissipation properties for high frequencies. However, the Wilson-θ dissipation is more intense and appears sooner than the α-Method, which is more gradual.

These results show that both the Wilson-θ and the α-Method are good candidates to be used as the chosen TI method in the FE code. The choice moved towards the α-Method because it is easy to implement, it has the possibility of recreating several algorithms from the Newmark family and the dissipative intensity is easier to be adjusted for different problem types.

- Mixed methods

For the completeness of this overview, mixed (implicit-explicit) TI methods should be mentioned. These methods combine the advantages of the explicit and implicit methodologies and are often used when the structure to be analysed is heterogeneous. An example is fluid-structure interaction problems, where both domains present a very different time scale [49] and can be integrated more efficiently using implicit methods for the structure and explicit methods for the fluid [141].

The development of the so-called *Operator-splitting* procedure [282, 456] should also be mentioned. In this method the contribution of the nonlinear material is divided into time-dependent and time-independent terms that are integrated explicitly and implicitly, respectively [141]. This methodology led the way to significant developments for pseudo-dynamic (PsD) testing [411, 412].

The PsD technique is a hybrid testing methodology, where the inertial and viscous damping forces are computer modelled and physically simulated using electro-hydraulic actuators. In addition, the nonlinear restoring forces are measured experimentally, making it possible to simulate the structural response under dynamic loading in a *quasi*-static test (see Figure II.12-a). The PsD technique uses the numerical time integration of the motion equations condensed in a suitable set of *dofs*.

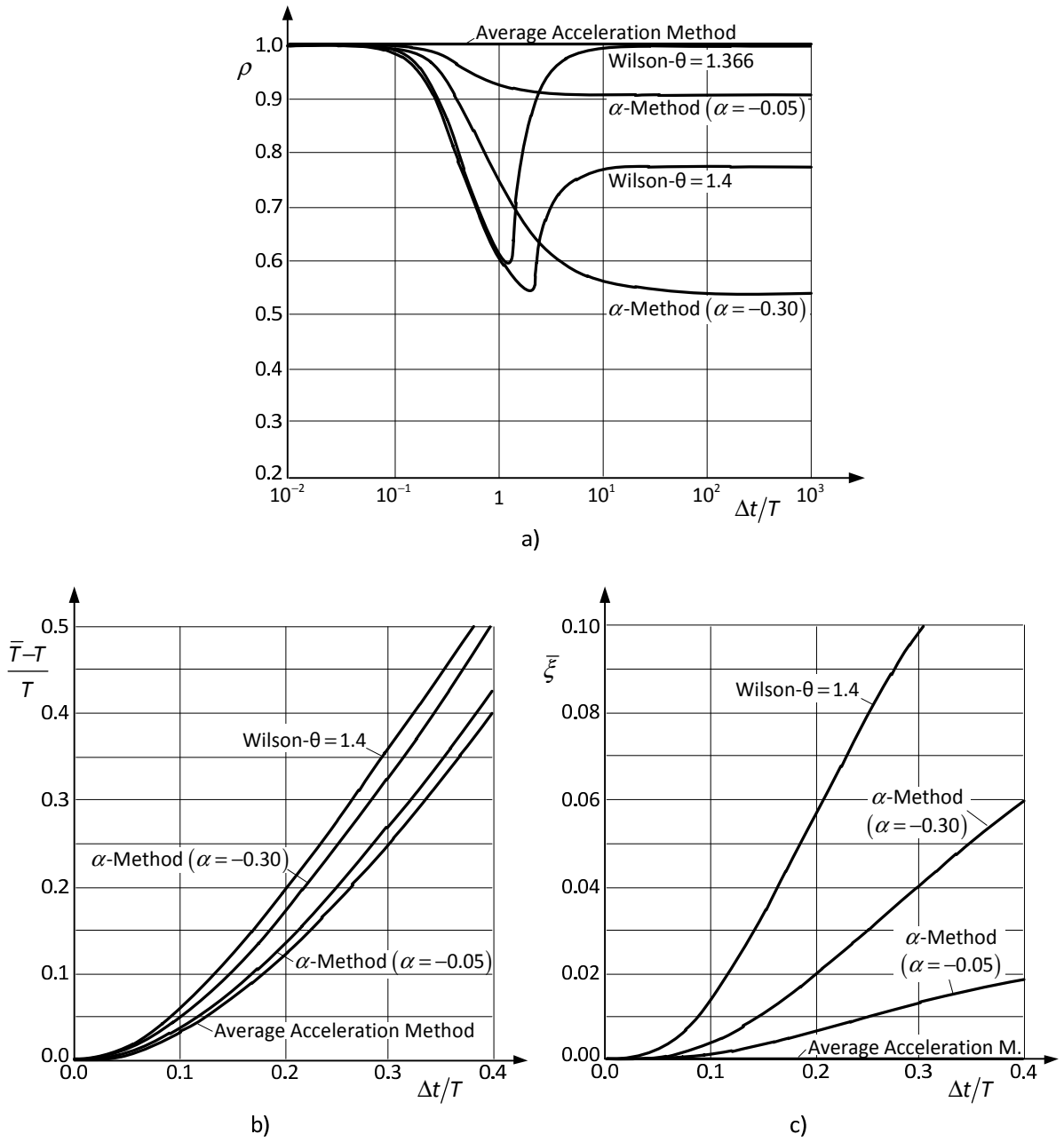

Figure II.11: Response characteristics of some TI methods, adapted from Hilber *et al.* [266]:
a) Spectral radius; b) Relative period error; c) Numerical damping ratio.

It should be noted that the operators in the motion equation associated with the experimental part have a reduced accuracy. In addition, the measurements are also subjected to random and systematic errors [126]. Taking this into consideration, using explicit TI methods is attractive, because it requires only knowing the movement characteristics at the beginning of the time step. However, the time step must be relatively small due to stability reasons. On the other hand, iterative and non-iterative implicit procedures are also attractive due to the possibility of achieving unconditional stability, and consequently, not having such strong constraints for the time step size.

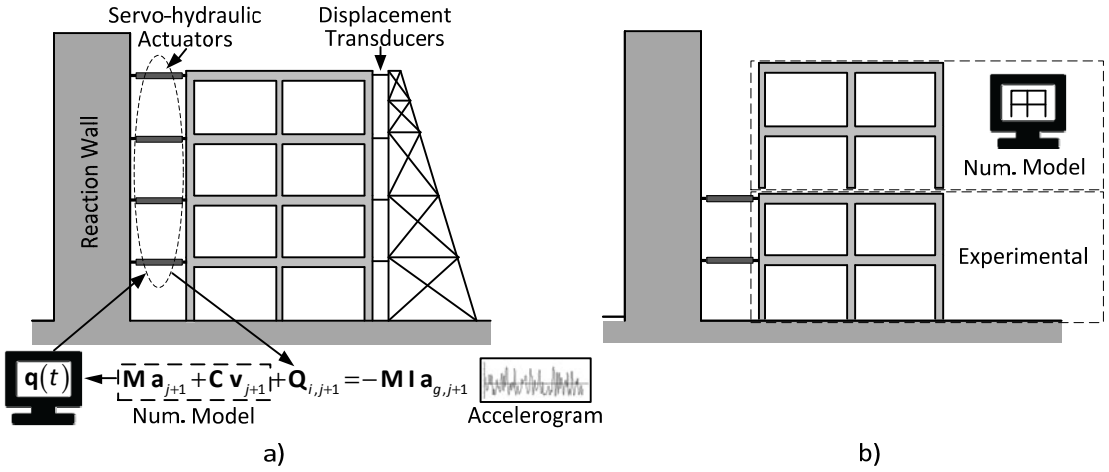

Figure II.12:Pseudo-Dynamic testing method: a) dynamic response simulation scheme [59]; b) Substructuring [442]

The *Operator-splitting* method has been used as an integrator to avoid using an iterative scheme [124, 411], while maintaining the unconditional stability. Using this procedure, the TI method becomes explicit for the nonlinear part of the structure and implicit for the elastic part, although not requiring an iterative procedure [450]. The internal forces at the end of the step can be approximated by [126]:

$$\mathbf{Q}_{i,j+1}\left(\mathbf{q}_{j+1}\right)\approx\mathbf{K}^{*}\mathbf{q}_{j+1}+\left(\mathbf{Q}^{p}_{i,j+1}\left(\mathbf{q}^{p}_{j+1}\right)-\mathbf{K}^{*}_{i,j+1}\mathbf{q}^{p}_{j+1}\right). \tag{II.200}$$

where $\mathbf{K}^{*}$ is an approximated stiffness matrix, usually taken as close as possible to the elastic stiffness and $\mathbf{q}^{p}_{j+1}$ are trial displacements computed from a predictor step calculated by neglecting $\mathbf{a}_{j+1}$ in expression (II.177).

The *Operator-splitting* procedure has been associated with numerical dissipation algorithms like the α-Method, resulting in the so-called *α-OS* algorithm [124, 126]. This integrator is used to damp out the undesired spurious high frequencies oscillations, which are more prone to appear due to the uncontrolled phenomena associated with the hybrid testing methodology. More information about this procedure can be found in the references [124, 126].

Another source of motivation for using these types of integrators is the recent development of hybrid substructuring techniques for dynamic problems. In this methodology, part of the structure is simulated experimentally (subdomain A) and the other part is simulated numerically (subdomain B). Both subdomains present clearly different time scales regarding the TI method, because the subdomain B can be computed with a larger time step and associated with an implicit scheme (*e.g. Average Acceleration* method). On the other hand, subdomain A is often associated with a conditional stable explicit method (*e.g.* Central-Difference method), and consequently, computed with a smaller time step [442]. More information about this technique can be found in the references [59, 60, 442].

5 Solution procedures

This section is devoted to making an overview of the most used solution procedures for nonlinear analyses within the framework of the FE method. After addressing some basic energy concepts, the incremental algorithm is introduced, and afterwards, the predictor-corrector solving procedure is described. At the end of this section, some issues related to the solver implementation are presented. The published works from Crisfield [154, 155] were particularly useful for writing this section and they are considered the main bibliographic references.

5.1 Basic concepts

Let us start by defining the *internal* and *external force potentials* for a group of concentrated forces:

$$\Pi_i = \int \underline{\boldsymbol{\sigma}} : \underline{\boldsymbol{\varepsilon}} \, d\Omega = \int \boldsymbol{\varepsilon}^t \boldsymbol{\sigma} \, d\Omega \,, \tag{II.201}$$

$$\Pi_e = -\mathbf{Q}_e^t \, \mathbf{q} \,. \tag{II.202}$$

For a mechanical system defined in the domain Ω, subjected to a group of external forces $\mathbf{Q}_e$ and subjected to a displacement field $\mathbf{q}$, the *total potential energy* Π is defined by:

$$\Pi = \Pi_i + \Pi_e = \int \boldsymbol{\varepsilon}^t \boldsymbol{\sigma} \, d\Omega - \mathbf{Q}_e^t \, \mathbf{q} \,. \tag{II.203}$$

After inserting the equation (II.39), the derivative of the total potential energy is given by [154]:

$$\frac{\partial \Pi}{\partial \mathbf{q}} = \frac{\partial \left(\int \boldsymbol{\varepsilon}^t \boldsymbol{\sigma} \, d\Omega - \mathbf{Q}_e^t \, \mathbf{q} \right)}{\partial \mathbf{q}} = \int \mathbf{B}^t \boldsymbol{\sigma} \, d\Omega - \mathbf{Q}_e = \mathbf{Q}_i - \mathbf{Q}_e = \mathbf{g} \,, \tag{II.204}$$

where $\mathbf{g}$ is often called the *unbalanced forces vector* and the symbol is commonly chosen because it represents the gradient of the total potential energy.

The second derivative of the total potential energy can be computed using [154]:

$$\frac{\partial^2 \Pi}{\partial \mathbf{q}^2} = \frac{\partial \mathbf{g}}{\partial \mathbf{q}} = \frac{\partial \left(\int \mathbf{B}^t \boldsymbol{\sigma} \, d\Omega - \mathbf{Q}_e \right)}{\partial \mathbf{q}} = \mathbf{K}_t \,, \tag{II.205}$$

where $\mathbf{K}_t$ is called the *tangent stiffness matrix*, defined by:

$$\mathbf{K}_t = \frac{\partial \mathbf{Q}_i}{\partial \mathbf{q}} = \int \mathbf{B}^t \frac{\partial \boldsymbol{\sigma}}{\partial \mathbf{q}} \, d\Omega \,. \tag{II.206}$$

The stress derivative can be computed using the chain rule and the following relation can be defined by introducing the equation (II.39):

$$\frac{\partial \boldsymbol{\sigma}}{\partial \mathbf{q}} = \frac{\partial \boldsymbol{\sigma}}{\partial \boldsymbol{\varepsilon}} \frac{\partial \boldsymbol{\varepsilon}}{\partial \mathbf{q}} = \mathbf{k}^* \left(\boldsymbol{\varepsilon}, t \right) \mathbf{B} \,. \tag{II.207}$$

where $\mathbf{k}^*$ is the tangent constitutive operator that depends on the strain history.

The tangent stiffness matrix definition (II.206) can be rewritten using:

$$\mathbf{K}_t = \int \mathbf{B}^t \; \mathbf{k}^* \left(\boldsymbol{\varepsilon}, t \right) \mathbf{B} \; d\Omega \,, \tag{II.208}$$

and for an elastic material (II.26), this relations simplifies into:

$$\mathbf{K}_t = \int \mathbf{B}^t \, \mathbf{k} \, \mathbf{B} \; d\Omega \,. \tag{II.209}$$

The *Principle of Stationary Total Potential Energy* states that between two configurations in equilibrium that respects the compatibility conditions, the change in the energy should be zero [154]. In other words, between all kinematic admissible displacement fields (boundary conditions and domain continuity) the ones that correspond to an equilibrium configuration make the total potential energy stationary. For elastic linear materials, this degenerates into the minimization of the total potential energy. Mathematically this can be expressed by:

$$\Pi(\mathbf{q}+\delta\mathbf{q}) - \Pi(\mathbf{q}) = 0 \,, \tag{II.210}$$

being $\delta\mathbf{q}$ an infinitesimal variation in the displacement field. This is equivalent to writing:

$$\frac{\partial \Pi}{\partial \mathbf{q}} = \mathbf{g} = \mathbf{0} \,. \tag{II.211}$$

The variation of the total potential energy can be expressed using a Taylor Series expansion:

$$\Pi(\mathbf{q}+\delta\mathbf{q}) = \Pi(\mathbf{q}) + \frac{\partial \Pi}{\partial \mathbf{q}} \delta\mathbf{q} + \frac{1}{2} \delta\mathbf{q}^t \frac{\partial^2 \Pi}{\partial \mathbf{q}^2} \delta\mathbf{q} + \ldots \,, \tag{II.212}$$

and for this equilibrium to be stable the solution should be a local minimum [154]:

$$\delta\mathbf{q}^t \frac{\partial^2 \Pi}{\partial \mathbf{q}^2} \delta\mathbf{q} = \delta\mathbf{q}^t \, \mathbf{K}_t \, \delta\mathbf{q} > 0 \,. \tag{II.213}$$

This last equation implies that for a stable equilibrium, $\mathbf{K}_t$ should be positive-definite (see Annex A) at the equilibrium point.

In conclusion, it is possible to state that solving a linear or nonlinear problem is the same as finding solutions that minimizes the total potential energy [154], or in other words, to find a solution that cancels out the unbalanced forces $\mathbf{g}$, if a kinematic admissible displacement field is considered.

5.2 Incremental formulation

This work is focused on the development of nonlinear dynamic analyses using time integration methods and three-dimensional FE meshes. To cope with these objectives, it is necessary to make some adaptations to the problem formulation presented in the previous sections. The first adaption is related to the internal or restoring forces term from the dynamic equilibrium equation (II.49). Until now, these were considered as the product of the stiffness and the displacements. For a nonlinear material, this relation ceases to be valid for the global analysis, as a result of the stiffness changes throughout the analysis. Instead, a general *internal forces vector* $\mathbf{Q}_i$ should be used to represent the restoring forces in the equilibrium equation (II.49):

$$\mathbf{M}\mathbf{a}_{j+1} + \mathbf{C}\mathbf{v}_{j+1} + \mathbf{Q}_{i,j+1} = \mathbf{Q}_{e,j+1} \,, \tag{II.214}$$

Another necessary change is to write the formulation using an incremental procedure. The incremental formulation is necessary, mainly for three reasons. Firstly, some constitutive relations

are path-dependent, either due to accuracy reasons related to the integration of the constitutive relations or to convergence reasons related to the element's state determination. Secondly, as discussed in section 4.3.3, it is necessary to apply a time domain discretization to integrate the equation of motion. Finally, in most cases the analyst wants to follow the structural response at a set of time steps, in order to assess the global response of the structure.

Consequently, the kinematic fields (displacements, velocities and accelerations) are written in the incremental format, using:

$$\mathbf{q}_{j+1} = \mathbf{q}_j + \Delta\mathbf{q}\,, \tag{II.215}$$

$$\mathbf{v}_{j+1} = \mathbf{v}_j + \Delta\mathbf{v}\,, \tag{II.216}$$

$$\mathbf{a}_{j+1} = \mathbf{a}_j + \Delta\mathbf{a}\,, \tag{II.217}$$

and similarly, for the internal forces and the external forces:

$$\mathbf{Q}_{i,j+1} = \mathbf{Q}_{i,j} + \Delta\mathbf{Q}_i\,, \tag{II.218}$$

$$\mathbf{Q}_{e,j+1} = \mathbf{Q}_{e,j} + \Delta\mathbf{Q}_e\,. \tag{II.219}$$

Introducing these definitions into the nonlinear dynamic equilibrium equation, written at the end of the time step (II.214), leads to the following expression:

$$\mathbf{M}\left(\mathbf{a}_j + \Delta\mathbf{a}\right) + \mathbf{C}\left(\mathbf{v}_j + \Delta\mathbf{v}\right) + \mathbf{Q}_{i,j} + \Delta\mathbf{Q}_i = \mathbf{Q}_{e,j} + \Delta\mathbf{Q}_e\,, \tag{II.220}$$

and the finite difference expressions for the velocities and accelerations can be rewritten as:

$$\mathbf{a}_{j+1} = \mathbf{a}_j + \Delta\mathbf{a} = \frac{1}{\beta\Delta t^2}\left\{\Delta\mathbf{q} - \Delta t\ \mathbf{v}_j - \left(\frac{1}{2} - \beta\right)\Delta t^2\ \mathbf{a}_j\right\}, \tag{II.221}$$

$$\mathbf{v}_{j+1} = \mathbf{v}_j + \Delta\mathbf{v} = \frac{\gamma}{\beta\Delta t}\Delta\mathbf{q} + \left(1 - \frac{\gamma}{\beta}\right)\mathbf{v}_j + \left\{(1-\gamma) - \frac{\gamma}{\beta}\left(\frac{1}{2} - \beta\right)\right\}\Delta t\ \mathbf{a}_j\,. \tag{II.222}$$

For the general case, the internal forces increment is nonlinear and depends on the displacement field. This nonlinearity can be approximated using a *Taylor Series* truncated after the first term (see Annex A) for the finite evolution of the internal forces written at the beginning of the time step:

$$\mathbf{Q}_{i,j+1}\left(\mathbf{q}_j + \Delta\mathbf{q}\right) = \mathbf{Q}_{i,j}\left(\mathbf{q}_j\right) + \frac{\partial\mathbf{Q}_i}{\partial\mathbf{q}}\Delta\mathbf{q} + O\left(\Delta\mathbf{q}^2\right) = \mathbf{Q}_{i,j}\left(\mathbf{q}_j\right) + \mathbf{K}_t\,\Delta\mathbf{q} + O\left(\Delta\mathbf{q}^2\right), \tag{II.223}$$

where the last term expresses the truncation error, which will be quadratic when the other terms are exact.

Introducing the relations (II.221), (II.222) and (II.223) into the motion equation (II.220), it is possible to write after some simplifications:

$$\hat{\mathbf{K}}\,\Delta\mathbf{q} = \Delta\hat{\mathbf{Q}}\,, \tag{II.224}$$

where the *effective stiffness* matrix and *effective forces* vector can be computed for the α-Method, using [155]:

$$\hat{\mathbf{K}} = \frac{1}{\beta\Delta t^2}\mathbf{M} + (1+\alpha)\left(\frac{\gamma}{\beta\Delta t}\mathbf{C} + \mathbf{K}\right), \tag{II.225}$$

$$\Delta\hat{\mathbf{Q}}_e = (1+\alpha)\left(\mathbf{Q}_{e,j} + \Delta\mathbf{Q}_e - \mathbf{Q}_{i,j}\right) - \alpha\left(\mathbf{Q}_{e,j} - \mathbf{Q}_{i,j}\right) + \frac{1}{\beta\Delta t}\mathbf{M}\mathbf{v}_j + \frac{1-2\beta}{2\beta}\mathbf{M}\mathbf{a}_j + (1+\alpha)\frac{\gamma-\beta}{\beta}\mathbf{C}\mathbf{v}_j + (1+\alpha)\left(\frac{\gamma-2\beta}{2\beta}\right)\Delta t\,\mathbf{C}\mathbf{a}_j \quad . \tag{II.226}$$

After solving (II.224) for the displacement increment $\Delta\mathbf{q}$, the displacements at the end of the time step can be computed using equation (II.215). When the material has a nonlinear response, an iterative procedure is required to compute the solution, leading to the predictor-corrector scheme that is described in the following section.

5.3 Predictor-corrector procedure

As expressed by the designation itself, the *Predictor-Corrector* procedure comprises two steps. The *predictor step* consists in making an initial guess on the evolution of the problem, based on the previous structural behaviour. Then, the *corrector step* consists in rectifying the trial solution in order to produce a solution that respects the basic governing equations.

5.3.1 Predictor

The predictor step is used to obtain an approximated solution with a small amount of computational effort and reducing the analysis time. The predictor step is not mandatory. It may be used only when it is convenient to adopt such a procedure and skipped otherwise.

The displacements increments obtained in the predictor step $\Delta\mathbf{q}^p$ can be obtained using several procedures. The most used approaches are the following [154, 211]:

$$\Delta\mathbf{q}^p = \hat{\mathbf{K}}^{-1}\,\Delta\hat{\mathbf{Q}}^p\,, \tag{II.227}$$

$$\Delta\mathbf{q}^p = \Delta\mathbf{q}_j\,, \tag{II.228}$$

$$\Delta\mathbf{q}^p = \Delta t\,\mathbf{v}_j + \frac{\Delta t^2}{2}(1-2\beta)\mathbf{a}_j\,, \tag{II.229}$$

$$\Delta\mathbf{q}^p = \Delta t\,\mathbf{v}_j + \frac{\Delta t^2}{2}\mathbf{a}_j\,, \tag{II.230}$$

$$\Delta\mathbf{q}^p = \mathbf{0}\,. \tag{II.231}$$

The predictor mathematically expressed in equation (II.227) requires solving the governing system, which is a significant drawback. Nevertheless, this technique has the advantage of not requiring recalculating the element's state and the unbalanced forces vector, because only the updated load increments are required. On the other hand, the predictor expressed in equation (II.228) adopts the displacement increments from the previous time step for the current increment. The trial increment can be scaled to take into account changes in the time step size. This approach is easy to implement and can be efficient to produce good solutions, or even, a solution that respects the global equilibrium dismissing the corrector step, *e.g.* under linear behaviour. Some of the advantages of this approach are related to the fact that the solution of the previous step can be a very good

approximation for the current step, or even, avoid solving the governing system, which is time consuming.

The third and fourth options, expressed in equations (II.229) and (II.230), are only used for dynamic analyses. In these cases, the predictor can be computed from expression (II.177), by considering the acceleration vector at the end of the time step null or equal to the one from the previous step, respectively.

The last option presented for the predictor (II.231) is the same as not considering the predictor step. In this work, only equation (II.228) or (II.231) were adopted to define the predictor, depending on the analysis characteristics.

5.3.2 Corrector

As stressed before, the corrector is generally a multi-step procedure used to obtain a solution that respects the governing equations of the problem, *i.e.* the global equilibrium. With this objective in mind, it is convenient to rewrite the dynamic equilibrium equation associated with the α-Method (II.195) in terms of the unbalanced forces, as follows:

$$\mathbf{g}_{j+1}^{i+1} = (1+\alpha)\left(\mathbf{Q}_{i,j+1}^{i+1} - \mathbf{Q}_{e,j+1}^{i+1} + \mathbf{C}\mathbf{v}_{j+1}^{i+1}\right) - \alpha\left(\mathbf{Q}_{i,j}^{i+1} - \mathbf{Q}_{e,j}^{i+1} + \mathbf{C}\mathbf{v}_{j}^{i+1}\right) + \mathbf{M}\mathbf{a}_{j+1}^{i+1}, \tag{II.232}$$

where the superscript $j+1$ states that the expression is defined at the end of the time step, after *i* corrector iterations. The subscript $j+1$ is implicit and will be omitted for simplicity in the equations associated with the iterative procedure.

Using this formulation, it becomes evident that the objective of the corrector is to eliminate, or reduce to an acceptable amount, the unbalanced forces, *i.e.* to obtain an acceptable solution in terms of equilibrium.

For the general case, the evolution of the unbalanced forces vector is nonlinear and it is not possible to define an analytical expression for the evolution. Usually, this problem is overcome by writing an approximated expression for the evolution of the internal forces vector using a truncated Taylor series. If the truncation is made after the first linear term, as in equation (II.223), this approach is often called a linearized method:

$$\mathbf{g}^{i+1} = \mathbf{g}^{i} + \frac{\partial \mathbf{g}^{i}}{\partial \mathbf{q}} \Delta \mathbf{q}. \tag{II.233}$$

Taking into consideration the definition (II.232), the derivative of the unbalanced forces with respect to the displacements vector is only associated with the internal forces vector, because the other terms are not dependent on this variable. Due to the approximated nature of this approach, an acceptable solution is generally not obtained after the first attempt. Acceptable results require a series of iterations and displacement increments, in order to eliminate the unbalanced forces, or to reduce them to an acceptable amount.

From equation (II.233), the following expression can be used to compute the displacement

increments:

$$\mathbf{g}^{i+1} = \mathbf{0} \Rightarrow \frac{\partial \mathbf{g}^{i}}{\partial \mathbf{q}} \Delta \mathbf{q} = -\mathbf{g}^{i} \,. \tag{II.234}$$

and the new solution for the displacement vector at the end of the time step can be computed from:

$$\mathbf{q}^{i+1} = \mathbf{q}^{i} + \Delta \mathbf{q} \,. \tag{II.235}$$

After convergence, the solution results from adding the following terms:

$$\mathbf{q}_{j+1} = \mathbf{q}_{j} + \Delta \mathbf{q}^{p} + \sum_{i=1}^{nit} \Delta \mathbf{q}^{i} \,, \tag{II.236}$$

where *nit* represents the number of iterations required for convergence and $\Delta \mathbf{q}^{i}$ is the displacement increment for each iteration.

There are many alternatives to compute the corrector step using the linearized method expressed in equation (II.234). Most of the choices differ in terms of the type of derivative used. A non-exhaustive list of these methods is the following [154]:

i. Newton-Raphson (NR) method;
ii. Modified Newton-Raphson (mNR) method;
iii. Secant-Newton (SN) method;
iv. Line Search (LS) method;
v. Arc-Length (AL) method.

The formulation of these methods is briefly presented and discussed in the following paragraphs.

- Newton-Raphson method

The Newton-Raphson (NR) method adopts the exact first derivative for the variations of the unbalanced forces (see Figure II.13-a), which is the tangent stiffness matrix $\mathbf{K}_{t}$ defined in equation (II.206). Due to the exactness of the linear term, the residue has a quadratic reduction rate for subsequent iterations and the method is said to have quadratic convergence. This can be demonstrated by introducing equation (II.234), expressed in order of $\Delta \mathbf{q}$, into the Taylor series approximation of the unbalanced forces at the beginning of the time step (II.233) [154]:

$$\mathbf{g}^{i+1} = \mathbf{g}^{i} - \frac{\partial \mathbf{g}^{i}}{\partial \mathbf{q}} \left\{ \left(\frac{\partial \mathbf{g}^{i}}{\partial \mathbf{q}} \right)^{-1} \mathbf{g}^{i} \right\} + O\left(\Delta \mathbf{q}^{2} \right) \Rightarrow \mathbf{g}^{i+1} = O\left(\Delta \mathbf{q}^{2} \right), \tag{II.237}$$

leading to the conclusion that the remaining terms are quadratic proportional.

It should be noted that the tangent stiffness matrix, defined in an arbitrary iteration, is not the genuine matrix due to the lack of the equilibrium during the iterative process. In addition, the tangent stiffness matrix is positive-definite only if computed at an equilibrium state, meaning that during an iterative algorithm there is no guarantee that $\mathbf{K}_{t}$ is positive-definite. Instead, it can be zero-definite or negative-definite, singular or indefinite [154] (see Figure II.13-f).

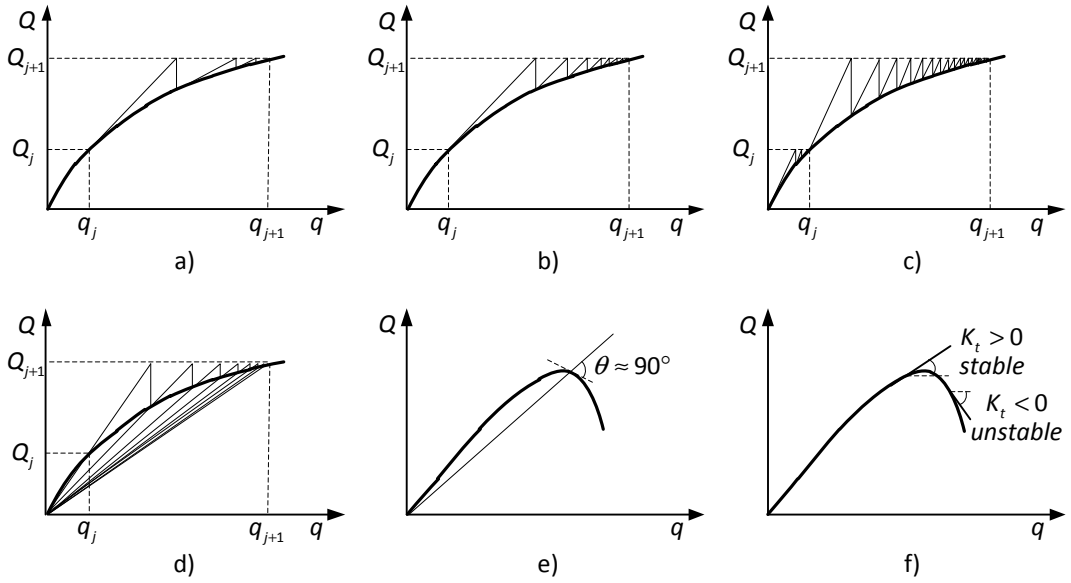

Figure II.13: Newton methods: a) Newton-Raphson method; b) and c) Modified Newton-Raphson; d) and e) Secant-Newton method; f) Stiffness types [154].

- Modified Newton-Raphson method

The *modified-Newton-Raphson* (mNR) method tries to avoid the computation of the tangent stiffness matrix in each iteration, by adopting a previous stiffness matrix definition. The following two types of stiffness matrices are commonly used:

i. The stiffness matrix at the beginning of the time step, $\mathbf{K}_{j+1}^{1}$ (Figure II.13-b);
ii. The stiffness matrix at the beginning of the analysis, $\mathbf{K}_{0}^{1}$ (Figure II.13-c).

These definitions for the mNR method have the advantage of always using genuine tangent stiffness matrices, because they are defined at equilibrium points. On the other hand, the quadratic convergence is lost because the linear term in (II.233) becomes inexact.

- Secant-Newton method

In the *Secant-Newton* (SN) method, instead of computing the stiffness matrix using the exact stress derivative, as in equation (II.206), the secant matrix is adopted by neglecting the strain dependence of the constitutive operator:

$$\int \mathbf{B}^t \frac{\partial \boldsymbol{\sigma}}{\partial \mathbf{q}} d\Omega = \int \mathbf{B}^t \frac{\partial \left(\mathbf{k}(\boldsymbol{\varepsilon})\, \boldsymbol{\varepsilon} \right)}{\partial \boldsymbol{\varepsilon}} \frac{\partial \boldsymbol{\varepsilon}}{\partial \mathbf{q}} d\Omega \approx \int \mathbf{B}^t \, \mathbf{k}_s \, \mathbf{B} \, d\Omega = \mathbf{K}_s \,, \tag{II.238}$$

where $\mathbf{k}_s$ is the secant constitutive matrix and $\mathbf{K}_s$ is called the *secant stiffness matrix*.

Using this method, the corrector iterations will have a secant slope as illustrated in Figure II.13-d. This approach has the advantage of not making it necessary to compute the tangent stiffness matrix that is usually more complicated to compute, and sometimes, an analytical expression is extremely complex to define. Nevertheless, the simplicity of the formulation and of the implementation can be

largely overcome by the poor convergence rate (generally not quadratic), therefore requiring many more iterations for the same convergence criterion. The lower convergence rate is particularly significant for materials with softening branches, where the secant approximation is nearly orthogonal to the force-displacement curve (see Figure II.13-e).

- Line Search method

The first aspect that should be stressed is that the *Line Search* (LS) method is not a solving algorithm, but instead, it is a convergence enhancer. The idea is to scale the iterative solution $\Delta\mathbf{q}$ by a factor η, called the *step length*, which is the only variable of the method, in order to obtain a solution closer to equilibrium:

$$\mathbf{q}^{i+1}(\eta) = \mathbf{q}^{i} + \eta\ \Delta\mathbf{q}\,. \tag{II.239}$$

This method is based on the *principle of stationary total potential energy* (see section 5.1) for finding an equilibrated solution. For the total potential energy to be stationary, it is required that:

$$s(\eta) = \frac{\partial\Pi(\eta)}{\partial\eta} = 0\,, \tag{II.240}$$

where $s(\eta)$ is the slope of the total potential energy for a given value of η. Please note that the total potential energy is not a function of the displacements, because for the *LS* method these are fixed and only the *step length* changes.

Using the chain rule and considering the relation (II.239), it is possible to obtain:

$$s(\eta) = \frac{\partial\Pi(\eta)}{\partial\eta} = \frac{\partial\Pi}{\partial\mathbf{q}(\eta)}\frac{\partial\mathbf{q}(\eta)}{\partial\eta} = \mathbf{g}^{t}(\eta)\ \Delta\mathbf{q}\,. \tag{II.241}$$

The value with at $\eta = 0$ is an important value. Introducing the relation (II.234) it is possible to obtain:

$$s_0 = s(\eta = 0) = \mathbf{g}^{t}(\eta = 0)\ \Delta\mathbf{q} = -\Delta\mathbf{q}^{t}\ \mathbf{K}_{t}\ \Delta\mathbf{q}\,, \tag{II.242}$$

hence, if $\mathbf{K}_t$ is positive-definite (see Annex A) then the last expression always returns a negative slope $s(\eta = 0) < 0$ (see Figure II.14-a). However, using $\mathbf{K}_t$ defined in an arbitrary iteration that is not in equilibrium, it is not guaranteed that this matrix is positive-definite. If $s(\eta = 0) \geq 0$ the total potential energy will not decrease for the displacement increments defined with the pattern $\Delta\mathbf{q}$, so the LS method cannot be applied and should be skipped for this particular iteration.

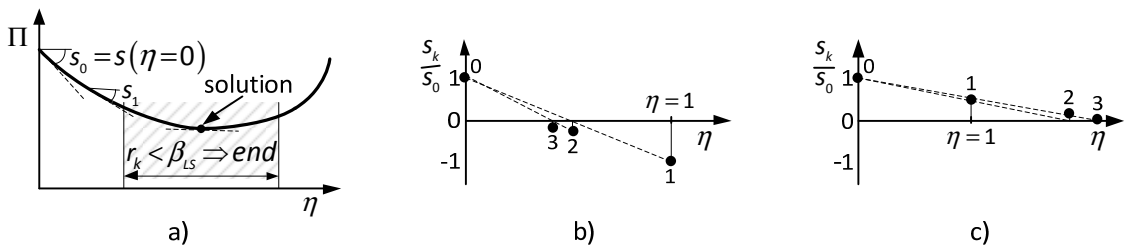

Figure II.14: Line Search method: a) initial slope; b) interpolation and c) extrapolation, adapted from Crisfield [154].

For the general case, using the slope defined in equation (II.242) to find a solution closer to the one that satisfies the global equilibrium will require iterations because of at least two reasons: i) the *total potential energy* Π does not change linearly (see Figure II.14-a), so the linear search procedure will probably not find the correct value for the step length; ii) the displacement increment pattern $\Delta\mathbf{q}$ is generally not able to find the exact solution by scaling it. The LS iterations are referenced with the superscript *k* to avoid confusion with the main iteration procedure adopted in the corrector algorithm.

To be more efficient, the LS method is often implemented by accepting a solution in which the ratio between slopes is below a certain threshold (see Figure II.14-a):

$$r_k = \left| \frac{s_k(\eta_k)}{s_0} \right| < \beta_{LS} . \tag{II.243}$$

As a reference, the author Crisfield [154] advises on using $\beta_{LS} = 0.8$.

The LS method uses a linear interpolation or extrapolation to find η that approximates $s_k(\eta_k) = 0$ (see Figure II.14-b/c). This can be done by using the expression:

$$\eta_{k+1} = \eta_k \left(\frac{-s_0}{s_k(\eta_k) - s_0} \right). \tag{II.244}$$

To avoid dangerous extrapolations (see Figure II.14-c) that are highly prone to errors (*e.g.* round-off errors) the step length should be limited to a maximum value. Similarly, a minimum value can also be used. In this work, the step length was constrained as follows:

$$\eta_{\min} = 0.1 \le \eta_k \le \eta_{\max} = 10.0 . \tag{II.245}$$

The LS algorithm can be summarized as presented in Algorithm II.2.

Algorithm II.2: Line Search.

1. Store the vectors $\mathbf{q}^i$ and $\mathbf{g}^i$.
2. Compute the corrector iteration using one of the methods presented before (*e.g.* NR, etc.).
3. Set $\eta_k = 1$ and $\eta_0 = 1$.
4. Compute: $s_0 = -\Delta\mathbf{q}^t \, \mathbf{K}_t \, \Delta\mathbf{q}$.
5. If $s_0 \ge 0$, update $\mathbf{q}^{i+1}(\eta) = \mathbf{q}^i + \Delta\mathbf{q}$ and EXIT.
6. Compute: $s_k(\eta_k) = \mathbf{g}^t(\eta_k) \, \Delta\mathbf{q}$.
7. Compute: $r_k = \left| \frac{s_k(\eta_k)}{s_0} \right|$.
8. If $r_k < \beta_{LS}$, EXIT.
9. Compute: $\eta_{k+1} = \eta_k \left(\frac{-s_0}{s_k(\eta_k) - s_0} \right)$.
10. Update : $\mathbf{q}^{i+1}(\eta) = \mathbf{q}^i + \eta_k \, \Delta\mathbf{q}$.
11. Recompute: $\mathbf{g}(\eta_k)$.
12. Return to step 6.

- Arc-Length method

The *Arc-Length* (AL) method was originally developed by *Riks* and *Wempner* [481, 482, 562] and later modified by *Crisfield* [152, 153] and others. The objective is to follow the load/displacement path after limit points (points 1 and 2 in Figure II.15-a/b) and avoid jumping to other possible equilibrium configurations (point 3 in Figure II.15-a/b) due to instabilities in the analysis. Possible examples are the *snap-through* instability, which is unstable under load control, and the *snap-back* instability, which is unstable using displacement control (see Figure II.15). Under dynamic analyses passing from points 1 directly to points 3 on Figure II.15, would be accompanied by vibrations in the response.

The Arc-Length method consists in limiting a combination of the displacement and load increments to a fixed norm. This Arc-Length constraint can be mathematically defined by:

$$\Delta L = \sqrt{\Delta \mathbf{q}^t \Delta \mathbf{q} + \kappa_Q{}^2 \Delta \mathbf{Q}_e^t \, \Delta \mathbf{Q}_e} \,, \tag{II.246}$$

where κ_Q is a coefficient to weight the load increment and ΔL is the length adopted for the arc. If $\kappa_Q = 1$ then the AL method is called *spherical* (see Figure II.16-a) and if $\kappa_Q = 0$ then it is called *cylindrical*.

To cope with the AL constraint the time step is changed using:

$$\Delta t^{i+1} = \Delta t^i + \delta t \,. \tag{II.247}$$

Controlling the load increment (force or prescribed displacement) is made through the *time functions* $\mathrm{T}(t)$, using the following expressions:

$$\mathbf{Q}_e(t) = \bar{\mathbf{Q}}_e \; \mathrm{T}(t) \,, \tag{II.248}$$

$$\mathbf{q}_{imp}(t) = \bar{\mathbf{q}}_{imp} \; \mathrm{T}(t) \,, \tag{II.249}$$

where $\bar{\mathbf{Q}}_e$ and $\bar{\mathbf{q}}_{imp}$ are the time-independent external force and prescribed displacement magnitudes (load pattern).

The first step for implementing the AL algorithm is to establish an expression for the variation of the *unbalanced forces vector* **g**. This must be done taking into consideration that not only the displacements increments are variable, but also the time step size. Consequently, the *internal forces vector* $\mathbf{Q}_i$ is dependent of the prescribed displacements and of the time variable itself, through equation (II.249).

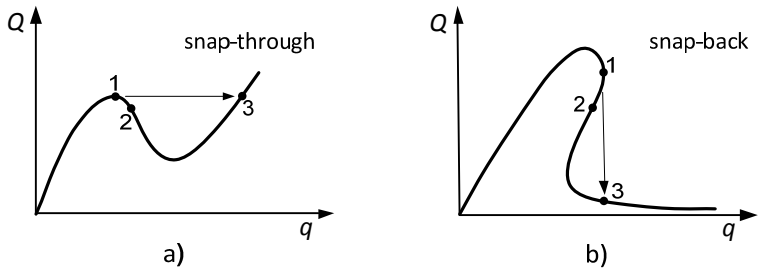

Figure II.15: Possible instabilities for Newton solvers: a) Load control; b) Displacement control.

The equation to compute the unbalanced forces vector (II.232) can be reduced to the static case for simplicity, without losing generality:

$$\mathbf{g}^{i+1} = \mathbf{Q}_i\left(\mathbf{q}^{i+1}, t^{i+1}\right) - \mathbf{Q}_e\left(t^{i+1}\right). \tag{II.250}$$

The evolution of the *unbalanced forces vector* in iteration $i+1$ can be approximated using the following Taylor series truncated after the first derivative:

$$\mathbf{g}^{i+1} = \mathbf{Q}_i^i + \frac{\partial \mathbf{Q}_i}{\partial \mathbf{q}}\delta\mathbf{q} + \frac{\partial \mathbf{Q}_i}{\partial t}\delta t - \mathbf{Q}_e^i - \frac{\partial \mathbf{Q}_e}{\partial t}\delta t, \tag{II.251}$$

which can be expanded introducing the relations (II.248) and (II.206):

$$\mathbf{g}^{i+1} = \mathbf{Q}_i^i + \mathbf{K}_t\,\delta\mathbf{q} + \int \mathbf{B}^t \frac{\partial \boldsymbol{\sigma}}{\partial t}\, d\Omega\, \delta t - \overline{\mathbf{Q}}_e\,\mathrm{T}\left(t^i\right) - \overline{\mathbf{Q}}_e \frac{\partial \mathrm{T}\left(t^i\right)}{\partial t}\delta t\,. \tag{II.252}$$

The term $\partial\boldsymbol{\sigma}/\partial t$ requires some attention. Knowing that only the terms associated with the prescribed displacements are a function of time (II.249), the following expression can be established:

$$\frac{\partial \boldsymbol{\sigma}}{\partial t} = \mathbf{k}\mathbf{B}\,\overline{\mathbf{q}}_{imp}\frac{\partial \mathrm{T}\left(t^i\right)}{\partial t}. \tag{II.253}$$

Introducing this last expression into equation (II.252) leads to:

$$\mathbf{g}^{i+1} = \mathbf{g}^i + \mathbf{K}_t\,\delta\mathbf{q} + \left\{\mathbf{K}_t\,\overline{\mathbf{q}}_{imp}\frac{\partial \mathrm{T}\left(t^i\right)}{\partial t} - \overline{\mathbf{Q}}_e\frac{\partial \mathrm{T}\left(t^i\right)}{\partial t}\right\}\delta t\,. \tag{II.254}$$

To implement the AL method, the following separation of the iterative time increments should be made [154]:

$$\delta\mathbf{q} = \delta\mathbf{q}_c + \delta\mathbf{q}_t\,\delta t\,, \tag{II.255}$$

with:

$$\delta\mathbf{q}_c = -\mathbf{K}_t^{-1}\,\mathbf{g}_i\,, \tag{II.256}$$

$$\delta\mathbf{q}_t = \mathbf{K}_t^{-1}\left\{\overline{\mathbf{Q}}_e\frac{\partial \mathrm{T}\left(t^i\right)}{\partial t} - \mathbf{K}_t\,\overline{\mathbf{q}}_{imp}\frac{\partial \mathrm{T}\left(t^i\right)}{\partial t}\right\}. \tag{II.257}$$

Defining the displacement increment $\Delta\mathbf{q}^i$ as follows:

$$\Delta\mathbf{q}^i = \mathbf{q}^i - \mathbf{q}_j\,, \tag{II.258}$$

the new time step increment is given by:

$$\Delta\mathbf{q}^{i+1} = \Delta\mathbf{q}^i + \delta\mathbf{q}_c + \delta\mathbf{q}_t\,\delta t\,. \tag{II.259}$$

The only variable from this equation is the variable δt, which will be computed from the AL constraint (II.246), after inserting equation (II.259) [154]:

$$\begin{aligned}&\left(\Delta\mathbf{q}^i + \delta\mathbf{q}_c + \delta\mathbf{q}_t\,\delta t\right)^t\left(\Delta\mathbf{q}^i + \delta\mathbf{q}_c + \delta\mathbf{q}_t\,\delta t\right) + \\ &\quad \kappa_Q^{\,2}\left(\mathbf{Q}_e^i + \overline{\mathbf{Q}}_e\frac{\partial \mathrm{T}\left(t^i\right)}{\partial t}\delta t\right)^t\left(\mathbf{Q}_e^i + \overline{\mathbf{Q}}_e\frac{\partial \mathrm{T}\left(t^i\right)}{\partial t}\delta t\right) - \Delta L^2 = 0.\end{aligned} \tag{II.260}$$

Expanding this last expression and grouping the terms, it is possible to obtain [154]:

$$a_1 \delta t^2 + a_2 \delta t + a_3 = 0 , \tag{II.261}$$

where:

$$a_1 = \delta \mathbf{q}_t^t \delta \mathbf{q}_t + \kappa_Q^{\,2} \left(\frac{\partial \mathrm{T}\left(t^i\right)}{\partial t} \overline{\mathbf{Q}}_e \right)^t \left(\frac{\partial \mathrm{T}\left(t^i\right)}{\partial t} \overline{\mathbf{Q}}_e \right), \tag{II.262}$$

$$a_2 = 2 \delta \mathbf{q}_t \left(\Delta \mathbf{q}^i + \delta \mathbf{q}_c \right) + 2 \kappa_Q^{\,2} \left(\mathbf{Q}_e^i \right)^t \left(\frac{\partial \mathrm{T}\left(t^i\right)}{\partial t} \overline{\mathbf{Q}}_e \right), \tag{II.263}$$

$$a_3 = \left(\Delta \mathbf{q}^i + \delta \mathbf{q}_c \right)^t \left(\Delta \mathbf{q}^i + \delta \mathbf{q}_c \right) + \kappa_Q^{\,2} \left(\mathbf{Q}_e^i \right)^t \left(\mathbf{Q}_e^i \right) - \Delta L^2 . \tag{II.264}$$

Note that only the first terms of the last expressions are non-null for the *cylindrical* AL.

Equation (II.261) can have two roots, resulting in two solutions for the displacement increments (II.259). The next step consists in deciding which root to use. According to Crisfield [154], for the *cylindrical AL* a possible choosing method is to select the root which is more close to the last iteration increment, hence, avoiding that the algorithm selects the root associated with going back in time. This can be done by minimizing the angle θ, or maximizing its cosine, defined by [154]:

$$cos\left(\theta_k\right) = \frac{\left(\Delta q^i\right)^t \left(\Delta \mathbf{q}^i + \delta \mathbf{q}_c + \delta \mathbf{q}_t \delta t \right)}{\Delta L^2} = \frac{a_4 + a_5 \delta t_k}{\Delta L^2}, \; k = \{1,2\}, \tag{II.265}$$

with:

$$a_4 = \left(\Delta q^i\right)^t \left(\Delta \mathbf{q}^i + \delta \mathbf{q}_c \right), \tag{II.266}$$

$$a_5 = \left(\Delta q^i\right)^t \delta \mathbf{q}_t . \tag{II.267}$$

In situations of sharp snap-backs, the author Crisfield [155] defends that this methodology can lead to choosing an incorrect root, because in this cases it is desirable that the algorithm chooses the root that apparently corresponds to going back in the analysis. The same author advises on finding the *unbalanced forces vector* associated to both solutions and choosing the one with lower norm [155].

There are also linearized forms for the AL method. These algorithms have the advantage of avoiding choosing between roots of quadratic formulas. However, these methods do not constrain the increment within the time step to a specific value, hence the solution is more prone to miss the desired branch.

Consider the following linearized version of the arc constraint equation (II.246):

$$\left(\Delta \mathbf{q}^i \right)^t \delta \mathbf{q} + \kappa_Q^{\,2} \left(\Delta \mathbf{Q}_e^i \right)^t \delta \mathbf{Q}_e = -a_i / 2 , \tag{II.268}$$

with:

$$\delta \mathbf{q} \; = \delta \mathbf{q}_c + \delta \mathbf{q}_t \, \delta t , \tag{II.269}$$

$$\delta \mathbf{Q}_e = \overline{\mathbf{Q}}_e \frac{\partial \mathrm{T}\left(t^i\right)}{\partial t} \delta t . \tag{II.270}$$

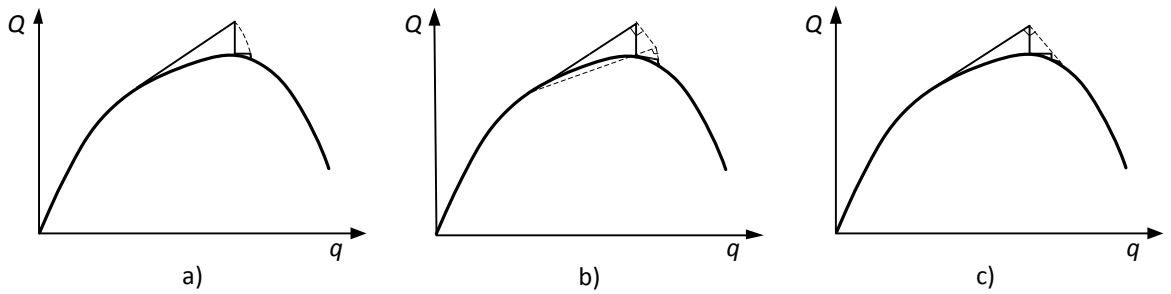

Figure II.16: Arc-Length methods: a) *Spherical*; b) *Ramm's* method; c) *Riks-Wempner* method [154].

Introducing these last definitions into equation (II.268), it is possible to obtain:

$$\delta t = \frac{-a_i/2 - \left(\Delta\mathbf{q}^i\right)^t \delta\mathbf{q}_c}{\left(\Delta\mathbf{q}^i\right)^t \delta\mathbf{q}_t + \kappa_Q{}^2 \left(\Delta\mathbf{Q}_e^i\right)^t \left(\overline{\mathbf{Q}}_e \frac{\partial \mathrm{T}\left(t^i\right)}{\partial t}\right)}. \tag{II.271}$$

If $a_i = 0$, the last expression establishes that the iterative change is orthogonal to the secant change [154], *a.k.a. Ramm's* method, see Figure II.16-b. This is similar to the original proposal of Riks and Wempner, where the iterative change is orthogonal to the predictor solution [154], also with $a_i = 0$, see Figure II.16-c. More details can be found in the work of Crisfield [154, 155].

5.4 Implementation issues

- Convergence criteria

To implement the solver for nonlinear analyses, it is necessary to define an adequate convergence criterion. In this work, the following expression was adopted:

$$\left\|\mathbf{g}\right\| = \sqrt{\mathbf{g}^t \mathbf{g}} < \beta_Q \ \wedge \ \left\|\mathbf{q}_{imp}^{err}\right\| = \sqrt{\left(\mathbf{q}_{imp}^{err}\right)^t \mathbf{q}_{imp}^{err}} < \beta_q, \tag{II.272}$$

where β_Q and β_q are the force and displacement convergence tolerances and $\mathbf{q}_{imp}^{err}$ represents the absolute error between the target and the current values for the *dofs* with imposed displacements. Typical values adopted for the tolerances were $\beta_Q = 1.0\text{e-}04$ and $\beta_q = 1.0\text{e-}06$. Other convergence criteria could be used, like energy-related criteria adopted in several authors, *e.g.* in the work of Crisfield [154].

- Automatic time step length

Another feature useful for optimizing the computational time for nonlinear analyses is to adjust the time step automatically. This can be done using the *tuning factor* T_F:

$$\Delta t_{j+1} = \Delta t_j \ T_F. \tag{II.273}$$

In this work, when this feature was enabled the tuning factor was linked to the convergence effort

for the previous corrector step, using the following expression [154]:

$$T_F = \left(\frac{I_d}{n_{it}} \right)^n , \tag{II.274}$$

where n_{it} is the *number of iterations* required to satisfy the convergence criteria at the previous step, I_d is the *desired number of iterations* and the exponent *n* is a non-negative number used to adjust the tuning pattern evolution (see Figure II.17). Although this feature was not used in the examples presented in this thesis, typical values for these parameters are: $I_d = \{3,4,5\}$ and $n = 0.50$.

The time step value is constrained to a maximum value to avoid an uncontrolled increase in this quantity:

$$\Delta t_{j+1} \le \Delta t_{\max} = \Delta t_0 \ \eta_{\max} . \tag{II.275}$$

If divergence is detected, an automatic time step cut is implemented. Divergence can be identified if one of the following conditions is met:

i. The number of iterations exceeded $n_{it}^{\max}$ without satisfying the convergence criteria;
ii. The number of iterations that satisfies $\|\mathbf{g}\|^{i+1} > \|\mathbf{g}\|^{i} \ \vee \ \left\|\mathbf{q}_{imp}^{err}\right\|^{i+1} > \left\|\mathbf{q}_{imp}^{err}\right\|^{i}$ exceeded n_{it}^{div} .

In those cases, the time step is cut and the analysis is reset to the state at the beginning of the time increment and restarted with a new time step, defined by:

$$\Delta t_{j+1} = \Delta t_j \ \eta_{rst} , \tag{II.276}$$

where η_{rst} is the *time step reducing factor*, typically set to 2.

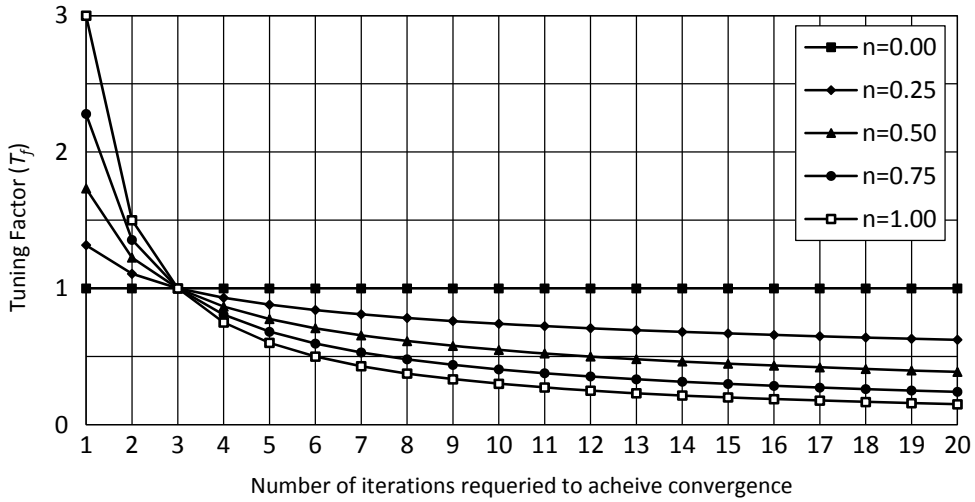

Figure II.17: Influence of the exponent for defining the time step tuning factor $(I_d = 3)$.

6 Seismic analysis methods

This section presents an overview of the methods used for design, assessment and simulation of structures under seismic loads. A summarized description of each method is presented, together with the discussion of their main advantages and drawbacks. At the end of the section, a comparison and some conclusions are presented about the framework and applicability of each method.

6.1 Linear analyses

Linear analyses have been used since the beginning of earthquake engineering and are still the most common way to evaluate the effect of seismic loading. These methods combine linear elastic analyses with simplified methods to take into consideration the nonlinear structural behaviour. Among those techniques, the *q-factors*, *a.k.a. behaviour factors*, are the most common way to achieve this.

The *behaviour factors* (q') are a particular type of *strength reduction factors* (R), which are defined for ideal elastoplastic systems as the ratio between the forces obtained from a linear analysis and the ones that would have been obtained considering the nonlinear behaviour (see Figure II.18-a). The behaviour factor takes this concept one step further, to the non-perfect response of common structures. According to Eurocode 8 [92], these factors are used for design purposes to reduce the forces obtained from linear analyses, in order to take into consideration the nonlinear response of the structure, associated with the material, the structural system and the design procedures.

Consequently, the behaviour factors can be defined as the ratio between the forces obtained from a linear analysis and the ones used for design (see Figure II.18-b). These factors are adopted in modern seismic codes (*e.g.* REBAP [471] and Eurocode 8 [92]) and are strongly connected to the properties of the materials, to the type of structure and to the ductility characteristics of the structural members.

Ductility is another important concept for seismic performance. It is often defined as the capacity of the material, structural element or the entire structure to sustain inelastic deformation after initial yielding without significantly losing the yield strength. Mathematically, the *ductility factor* (μ) is commonly defined as the ratio between the maximum displacement and the yield displacement of an ideal elastoplastic material (see Figure II.18-a).

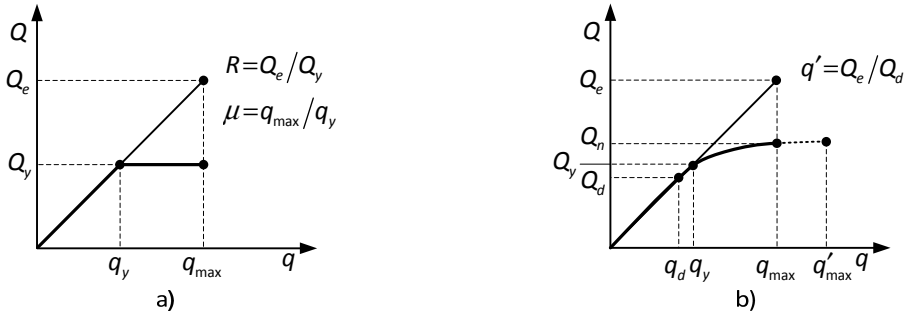

Figure II.18: Basic parameters for seismic design: a) ideal elastoplastic system; b) design system, adapted from Pinto [450].

6.1.1 Lateral force method

The *lateral force method* was adopted in the initial seismic codes, *e.g.* the Portuguese code RSCCS [489] published in 1958. In order to separate the analysis in the two main horizontal directions, these methods are restrained to regular structures. In addition, this method should be only applied to structures with a large contribution from the first modes of vibration, because in this case the adopted distributions for vertical forces (*e.g.* triangular distribution) are a likely configuration for the effective inertia forces. The lateral forces values are usually calculated through the *base shear force* V_b, which commonly depends on the fundamental period of the direction being analysed, structural characteristics and on the local earthquake scenarios using a simplified procedure. Afterwards, the forces are often distributed at the storey levels proportionally to the storey height and to the first mode shape coefficients [92, 471] (see Figure II.19-a). Torsional effects can also be taken into consideration using simplified methods.

After the analysis is complete and if the nonlinear behaviour is not considered directly in the definition of the base shear force (*e.g.* RSA [488]), then the generalized stresses used for design are defined from the elastic values affected by behaviour factors, in order to take the nonlinear response into consideration.

6.1.2 Modal methods

In recent decades, modal methods have significantly increased the accuracy of structural simulations made with earthquake loads. These methods are based on the *mode superposition method* discussed in section 4.3.2, and consequently, their application is, in principle, restrained to linear analyses. Using this approach, a modal analysis is often performed using a three-dimensional model of the structure and the modal configurations can be used to transform the dynamic equilibrium equation into *modal* or *generalized coordinates*, leading to an uncoupled system of equations, which can be solved for each *dof* independently. Afterwards, the contribution of each mode can be joined to compute the global response using the concept of *modal synthesis* expressed in equations (II.120) to (II.122). When compared to the lateral force method, the major advantage of this approach is that it

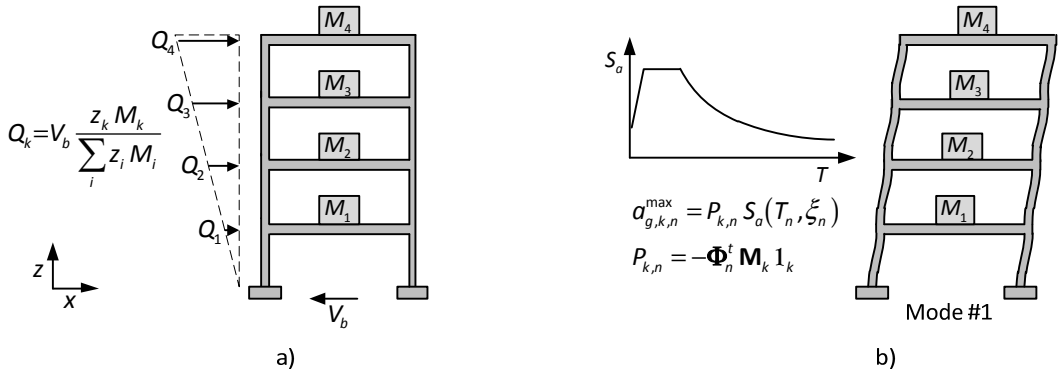

Figure II.19: Linear seismic analysis methods: a) Lateral Force method; Modal Response Spectrum Analysis method.

is possibly to consider directly the contribution of higher modes, of plan or elevation irregularities and the coupling between horizontal directions.

For an earthquake loading, the motion equation written for a mode *n* using modal coordinates (II.123), becomes [574]:

$$a_{G,n}(t)+2\xi_n\omega_n v_{G,n}(t)+\omega_n^2 q_{G,n}(t)=P_{1,n}a_{g,1}(t)+P_{2,n}a_{g,2}(t)+P_{3,n}a_{g,3}(t)\,, \tag{II.277}$$

where $p_{k,n}$ are the *earthquake excitation factors*, defined by:

$$P_{k,n}=-\boldsymbol{\Phi}_n^t\,\mathbf{M}\,1_k\,, \tag{II.278}$$

in which, **M** holds the mass associated with each storey and 1_k is a Boolean vector that has unit values for the *dofs* associated with the direction x_k.

For design purposes, the response in time is not required, just the maximum values are critical for designing the elements. In the case of linear behaviour, the maximum response can be computed using *response spectra* (RS) and the method is often called the *Modal Response Spectrum Analysis* method (see Figure II.19-b). The elastic response spectra is by definition the frequency domain representation of the maximum response of a series of *sdof* systems for a given damping level, when subjected to a series of base displacements associated with an earthquake loading. Consequently, the maximum response for each mode can be found for a linear system directly from the RS ordinate associated with the abscissa for the period of the mode *n*, along direction x_k, using:

$$a_{g,k,n}^{\max}=P_{k,n}\,S_a(\omega_n,\xi_n),\quad v_{g,k,n}^{\max}=P_{k,n}\,S_v(\omega_n,\xi_n),\quad q_{g,k,n}^{\max}=P_{k,n}\,S_q(\omega_n,\xi_n)\,. \tag{II.279}$$

After solving equation (II.277) for each mode with the *rhs* terms defined by maximum values computed using *response spectra* (II.279), the next step consists in combining the modal responses in order to obtain a feasible result for the structural response, because it is highly unlikely that the maximum responses of each mode are simultaneous. Several modal combination techniques have been developed for this purpose. Among them, the most prominent are the *Square Root of the Sum of the Squares*, which for a displacement would be given by [574]:

$$q^{\max}\approx\sqrt{\sum_{n=1}^{nmod}\left(q_n^{\max}\right)^2}\,, \tag{II.280}$$

which considers that the maximum modal values are statistically independent, or by using the *Complete Quadratic Combination* when the modes frequencies are close [576]:

$$q^{\max}\approx\sqrt{\sum_{i=1}^{nmod}\sum_{j=1}^{nmod}\rho_{ij}\,q_i^{\max}\,q_j^{\max}}\,, \tag{II.281}$$

where the *cross-modal coefficients* ρ_{ij} take into consideration the proximity of the mode frequencies and can be computed from:

$$\rho_{ij}=\frac{8\xi^2(1+r)r^{3/2}}{\left(1+r^2\right)^2+4\xi^2 r(1+r)^2},\quad r=\frac{\omega_i}{\omega_j}\le 1.0\,. \tag{II.282}$$

6.2 Nonlinear analyses

This section is devoted to nonlinear methods for seismic analysis. Nowadays, linear analyses are considered insufficient to fully evaluate seismic structural behaviour and reveal important structural vulnerabilities. The nonlinear analysis methods are often divided into static and dynamic analyses, when the earthquake loading and the structural response are simulated as a *quasi*-static or a fully dynamic event.

6.2.1 Nonlinear static analyses

Nonlinear Static Analyses (NL-SA) are used in the scope of earthquake engineering to simulate the structural response for seismic loads, using a static analysis that tries to emulate the dynamic response of the structure. The most widespread methods are the so-called *pushover analyses*. In this type of approach, the *mdof* structure is modelled considering the nonlinear response of the structural elements and the dynamic earthquake loading is simulated by patterns of monotonically increasing lateral loads, associated with the inertia forces that would be experienced by the structure when subjected to the ground shaking.

The results of these analyses are most of the time represented in terms of a force *vs*. displacement diagram, usually base shear *vs.* the displacement of a control node, which is commonly considered as the top or roof node (see Figure II.20). The so-called *capacity curve* of the structure is a measure of the structure's capacity to resist the seismic demand and depends on the strength and deformation capacity of the individual structural components.

The nonlinear response of the structural members is frequently simulated by beam-column elements with concentrated plasticity at the extremities using calibrated M-θ relations. Another common approach is to use fibre models along cross-sections distributed in the element span (see Chapter III-§2.5.6).

One important question arises when performing a pushover analysis, which is, what vertical distributions of lateral loads should be used to simulate the inertia forces. The answer to this question is not trivial and there is not a single solution. Uniform, triangular, modal [104] or even

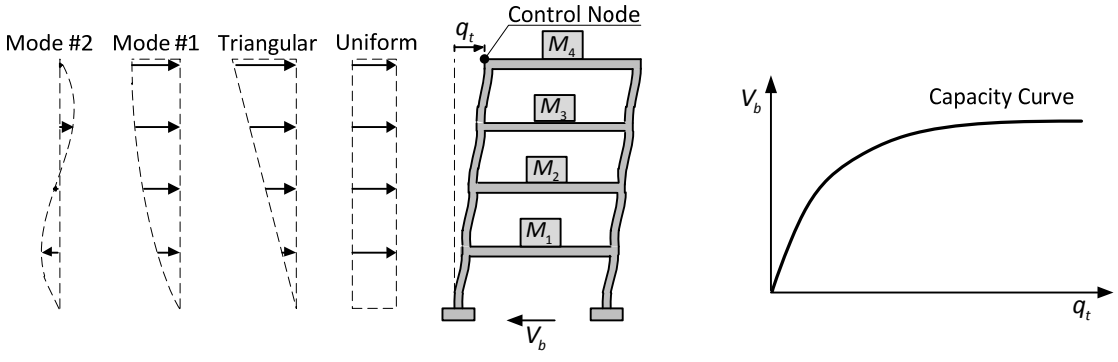

Figure II.20: Typical pushover analysis.

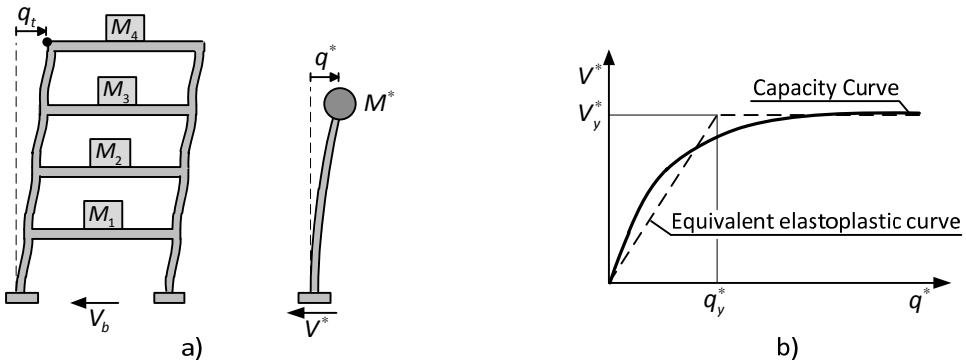

Figure II.21: Equivalent *sdof* system, adapted from Fajfar [196]: a) Transformation between *mdof* and *sdof* systems; b) simplified elastoplastic model.

adaptive [11] configurations were tested by several authors (see Figure II.20).

The pushover analyses are often used in the context of *Seismic Performance Evaluation Methods*, which combine information from the capacity of the structure with the seismic demand to assess the performance of the structure. Some of the most known methods are the following:

i. *Displacement Coefficient* method, proposed in FEMA-273/356 [19, 20];
ii. *Capacity Spectrum* (CS) method, firstly developed by Freeman [226] and adopted in ATC-40 [18];
iii. *N2 Method*, proposed by Fajfar and co-workers [196-201] and adopted in Eurocode 8 [92];

The basic characteristics of these three methodologies are briefly addressed later in this section. To improve the completeness of this review the work of Chopra and co-workers [106-109], Kalkan *et al.* [302] and Casarotti *et al.*[82] should be referenced.

These methods present some key concepts or idealizations that should be discussed prior to presenting the basics of each formulation. This is the case of using the equivalent *sdof* to perform the seismic analysis. According to *Fajfar* [197], this concept was first introduced by *Saiidi* and *Sozen* [495] and is adopted in the N2 Method. The basic idea is transform the *mdof* nonlinear structure being analysed, into an equivalent *sdof* that is used to assess the performance of the original structure (see Figure II.21). Another important concept is the *target displacement* that is used in the framework of the displacement-based design to evaluate the seismic demand of the structure under nonlinear behaviour. The *equal displacement rule* states that the displacement demand for an inelastic system is equal to that of the corresponding elastic system with the same period.

- Displacement coefficient method

The *Displacement Coefficient* method was proposed in FEMA-273 [19] within the scope of the rehabilitation of buildings. This method proposes performing a NL-SA using monotonically increasing lateral forces or displacements until the target displacement q_t is reached at the control node or the structure collapses [19]. In this method, the control node is considered the centre of mass at the roof of the building. The target displacement represents the maximum displacement likely to be experienced by the structure when subjected to the design earthquake loading. For buildings with

rigid diaphragms at each floor level this parameter can be estimated from [19]:

$$q_t = C_0 C_1 C_2 C_3 S_a \frac{T_e^2}{4\pi^2} = C_0 C_1 C_2 C_3 S_d \,, \tag{II.283}$$

where: C_0 is a modification factor that relates the spectral displacement and the likely building roof displacement; C_1 is a modification factor that relates the expected maximum inelastic displacements to the displacements computed from the linear elastic response; C_2 is a modification factor used to represent the effect of the hysteresis shape on the maximum displacement response; C_3 is a modification factor to represent the effect of dynamic P-Δ effects; $S_a(S_d)$ is the linear elastic spectral acceleration (displacement) for the fundamental period and damping ratio of the building; and finally, T_e is the effective fundamental period of the building in the direction under consideration, computed using a secant value of stiffness given by the base shear *vs*. displacement curve at 60% of the yielding strength.

The lateral force distribution is set to simulate the inertia forces that develop during an earthquake. The FEMA-273 [19] considers that at least two distributions must be used: Firstly, the *uniform pattern* in which the lateral forces are proportional to the storey mass. Secondly, the so-called modal pattern defined by: i) a formula that returns a triangular distribution for uniform storey weights at uniform heights, when at least 75% of the total mass participates in the fundamental mode for the direction considered; ii) a pattern proportional to the storey inertia forces consistent with the storey shear distribution from the combination of modal responses using a RS analysis with an appropriate ground motion spectrum, for modes with a participating mass of at least 90% of the total mass.

- Capacity Spectrum Method

The *Capacity Spectrum* (CS) method was introduced by Freeman [226] and later adopted in the ATC-40 [18]. This method is based on the computation of a capacity curve using pushover analyses, similar to the ones described before, and express this curve using spectral coordinates. In the CS method, the force *vs*. top displacement curve is converted into spectral coordinates using the following relations:

$$S_a = \frac{V_b}{\alpha_1 W} \,, \tag{II.284}$$

$$S_q = \frac{q_t}{P_1 \Phi_{t,1}} \,, \tag{II.285}$$

where V_b is the base force, q_t is the top displacement, W is the total weight of the building (dead weight and live loads); $\Phi_{t,1}$ is the roof level amplitude for the first mode, and α_1 and P_1 are the *modal mass coefficient* and *modal participation factor* for the first mode, which are given by [18]:

$$\alpha_1 = \frac{\left(\sum_{k=1}^{ndof} M_k \Phi_{1,k}\right)^2}{\left(\sum_{k=1}^{ndof} M_k\right)\left(\sum_{k=1}^{ndof} M_k \Phi_{1,k}^2\right)} \,, \qquad P_1 = \frac{\sum_{k=1}^{ndof} M_k \Phi_{1,k}}{\sum_{k=1}^{ndof} M_k \Phi_{1,k}^2} \,, \tag{II.286}$$

with M_k and $\Phi_{1,k}$ representing the mass and the first mode amplitude at level *k*.

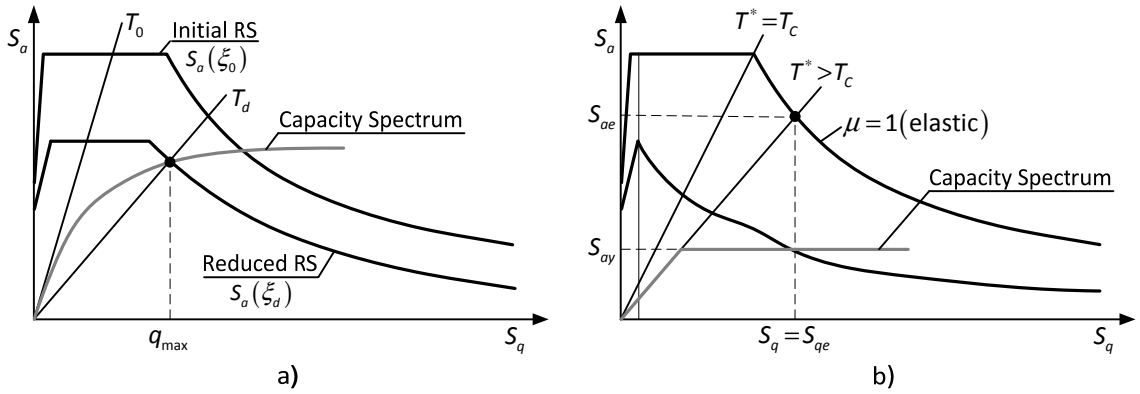

Figure II.22: Simplified seismic performance evaluation methods: a) Capacity Spectrum method [18]; b) N2 method [196].

Once again, the seismic demand is introduced as a displacement demand representative of the earthquake ground motion. The elastic RS is written in the *Acceleration-Displacement Response Spectra* (ADRS) format considering the following relation for an elastic *sdof*:

$$S_{qe} = \frac{T^2}{4\pi^2} S_{ae}\,, \tag{II.287}$$

defining the demand spectrum [18]. Afterwards, this elastic RS is reduced in order to take into consideration the nonlinear demand using an *effective damping*. This parameter represents the value of the equivalent viscous damping corresponding to the energy dissipated by the building, or element, during a response cycle.

The *performance point* is defined by the intersection of the capacity and the reduced elastic demand spectrum, when they are written for the same damping value, hence, an iterative method is often required (see Figure II.22-a).

The FEMA-440 [21] report proposed some improvements to the original CS method, *e.g.* in the estimation of damping and in the spectral scaling, and this method has been extended to plan-asymmetrical buildings by several authors, *e.g.* [51, 55, 449].

- N2 Method

This method is commonly related to the work of Fajfar and co-workers [196-201] and has been increasing its significance in Europe to the point of being included in the draft version of Eurocode 8 [92]. In this method, the seismic demand is expressed in ADRS format. For an inelastic *sdof* system with bilinear force-displacement response the following relation can be applied [196, 557]:

$$S_a = \frac{S_{ae}}{R_\mu}\,, \tag{II.288}$$

$$S_q = \frac{\mu}{R_\mu} S_{qe}\,, \tag{II.289}$$

where μ is the *ductility factor*, defined as the ratio between the maximum displacement and the yield displacement, and R_μ is the *reduction factor* due to ductility, *i.e.* due to the hysteretic energy

dissipation. In the N2 Method proposed by Fajfar, the following expression is adopted [196, 398]:

$$\begin{cases} R_\mu = (\mu - 1)\dfrac{T}{T_C} + 1, & \text{if } T < T_C \\ R_\mu = \mu, & \text{if } T \geq T_C \end{cases}, \tag{II.290}$$

where T_C is the *characteristic period of the ground motion* usually defined by the transition between constant acceleration and constant velocity branches. In the second term, it is implicit that the equal displacement rule is adopted. From the point of view of the seismic demand, the N2 Method considers an *inelastic demand spectrum*, which adopts a different approach when compared to the CS method, which uses the elastic RS reduced by an equivalent damping.

The next step is to define the capacity in the same ADRS format. This is achieved by performing a *pushover* analysis to define the *capacity curve* of the structure (*mdof*), in terms of the relation between the base shear force and the control node displacement. The vertical distribution of lateral loads is made after assuming a displacement shape $\boldsymbol{\Phi}$, using:

$$\mathbf{Q}_L = p\mathbf{M}\boldsymbol{\Phi}, \tag{II.291}$$

where *p* is a scalar that controls the magnitude of the lateral forces.

The force-displacement response of the *mdof* system is transformed into the equivalent *sdof* system with bilinear response (see Figure II.21). This is done by computing the equivalent mass, top displacement and base forces, as follows [196]:

$$M^* = p\sum_k M_k \Phi_k, \quad q_t^* = \frac{q_t}{\Gamma}, \quad V_b^* = \frac{V_b}{\Gamma}, \tag{II.292}$$

where Γ is the factor that makes the transformation between *mdof* and *sdof* systems, which can be seen as a *modal participation ratio* [196], and is defined by [196]:

$$\Gamma = \frac{M^*}{\sum_k M_k \Phi_k^2}. \tag{II.293}$$

The *equivalent period* of the *sdof* system is computed from an approximated elastoplastic force-displacement relationship, using (see Figure II.21-b) [196]:

$$T^* = 2\pi\sqrt{\frac{M^* q_y^*}{V_y^*}}, \tag{II.294}$$

and finally, the capacity curve is converted into ADRS format using [196]:

$$S_a = \frac{V_b^*}{M^*}. \tag{II.295}$$

The next step is to define the *reduction factor* R_μ, using the following relation [196]:

$$R_\mu = \frac{S_{ae}(T^*)}{S_{ay}}, \tag{II.296}$$

where $S_{ae}(T^*)$ is defined by the intersection of the radial line corresponding to the elastic period

with the one from the elastic demand spectrum. If the elastic period T^* is larger or equal to T_C, then $S_q = S_{qe}$ and $\mu = R_\mu$. Otherwise, the *ductility demand* can be computed from [196]:

$$\mu = \left(R_\mu - 1\right)\frac{T_C}{T^*} + 1 . \tag{II.297}$$

Afterwards, the top displacement for the *mdof* system associated with the seismic demand can be computed from (II.292) and other parameters (*e.g.* inter-storey drifts and joint rotations) can be assessed by performing a pushover analysis until the top displacement is reached. At the end, damage indices can also be computed using the *Park & Ang Damage Model* [433, 434].

Recently, the N2 Method has been improved to take into account plan asymmetries [203, 312] and higher mode effects in elevation [313], leading to the so-called *Extended N2 Method*.

6.2.2 Nonlinear dynamic analyses

The nonlinear dynamic analyses, abbreviated by NL-IDA or simply IDA in this thesis, are known to have most potential to accurately simulate the seismic behaviour. This is because both the load and the structural response are considered as dynamic events. This methodology is associated with direct time integration algorithms, as presented in section 4.3.3, and with incremental procedures, as described in section 5.2, leading to an equilibrium equation similar to expression (II.220). The basic formulation of these methods has already been presented in this chapter and this approach has been adopted in this thesis.

6.3 Comparison between seismic analysis methods

Table II.3 presents a possible comparison between the different seismic analysis methods described before. This table tries to relate the type of application, the framework of the analyses and the most adequate analysis methods.

The type of application was divided into three categories: i) *design*, either for new structures or for rehabilitation (strengthening) of existing structures; ii) *assessment*, which concerns studies to evaluate the seismic vulnerability of existing structures or the simplified assessment of groups or typologies of structures for seismic risk studies; iii) *simulation*, in which the analyst wishes to simulate the real response of a structure using the best and most accurate procedures available (*e.g.* prediction, comparison, and extrapolation of dynamic shaking table tests).

Linear analyses are still very much used for design purposes together with corrector factors to take into consideration the nonlinear effects. Nevertheless, currently these methods are not considered to be the best option for design in intense seismic regions, because they can conceal important structural vulnerabilities, and they do not provide information about effective structural strength, ductility and energy dissipation [197]. Within the scope of seismic vulnerability assessment studies and detailed simulations, linear analyses are considered inappropriate as the main analysis tool, because they are not able to simulate with sufficient accuracy the real structural behaviour.

Table II.3: Applicability and framework of different seismic analyses methods.

Application		Framework	Analysis Methods
Design	Design of new structure	Design Offices	Linear, NL-SA
	Rehabilitation of an existing structure	Design/Rehabilitation Offices	Linear, NL-SA
Assessment	Seismic vulnerability of individual structures	Specialized Offices Laboratories/Universities R&D Corporations	NL-SA, NL-IDA
	Seismic vulnerability of existing groups of structures (*e.g.* Seismic Risk Analyses)	Laboratories/Universities R&D Corporations	NL-SA
Simulation	Laboratory models, Industrial prototypes	Laboratories/Universities R&D Corporations	NL-IDA

Nonlinear Static Analysis (NL-SA), based on pushover procedures, presents a significant step forward for design when compared to elastic methods combined with correction factors, mainly due to the following factors:

i. The nonlinear behaviour of the structure is considered directly in the structural model;
ii. It is possible to follow the development of structural nonlinear phenomena and reveal important weaknesses (critical zones), although, it detects only the first mode of collapse;
iii. The global seismic capacity of the structure can be accurately estimated for certain types of structures and information about ductility can be extracted;
iv. The seismic performance can be assessed for difference performance levels, *e.g.* VISION-2000 [501].

All these factors combined with the simplification and standardization of the methodologies led to the increase of use observed in common practice. This is an undeniable trend that already justified the incorporation of these procedures in the most modern seismic codes and guideline reports, *e.g.* Eurocode 8 [92] and FEMA-273 [19].

According to Fajfar [196], the most significant limitation of the N2 method, which can be generalized to other NL-SA methods, is related to the approximation made for the pushover analysis and to the way the seismic demand is considered (*e.g.* inelastic RS).

The accuracy of the pushover simulation depends on the characteristics of the structure being analysed. For example, these methods have a significant difficulty to model the effect of higher vibration modes, because they associate the global response with the one obtained with simplified systems. Moreover, these methods present important drawbacks for simulating buildings with significant asymmetric behaviour in plan and in height, which leads to coupling between horizontal directions, soft-storey situations and global response with torsion. Consequently, the target structures for these methods are uniform structures, in which the structural behaviour is strongly related to the first modes (*e.g.* small symmetric structures). Nevertheless, a significant effort has been made to extend these methods to asymmetric buildings, *e.g.* [51, 55, 202, 449].

According to Krawinkler *et al.* [311], pushover analyses are used under the assumption that the displacement shape, and consequently, the lateral force pattern is time-independent. This procedure is not suitable for considering the contribution of higher modes and the evolution of damage within

the analysis. This limitation can be mitigated by considering two or more displacement shapes, or even, modal [104] or adaptive [11] configurations, and afterwards, considering the envelope of the results. Furthermore, for structures with coupling between horizontal directions, most guidelines, *e.g.* FEMA-273 [19], stress that the pushover analyses should be considered in both planar directions and that multidirectional excitation must be considered, *e.g.* using the 100%-30% rule. In addition, most codes impose the use of at least two lateral load patterns. Consequently, the number of pushover analyses can easily reach eight or more. In addition, as stressed by Elnashai [194], the transformation of the capacity curve from the force *vs.* displacement space into the spectral domain is not trivial and is subject to errors, for example using adaptive procedures.

Regarding the seismic demand, using the equivalent damping or the ductility-based reduction factors to compute reduced or inelastic RS is always an approximated methodology prone to inaccuracies, *e.g.* in situations where the hysteretic behaviour, model damping and post-yield stiffness have non-standard characteristics. Moreover, the target displacement used to define the performance point, can be incorrectly estimated, because this parameter is very sensible to variations in the yield strength, stiffness degradation, strength deterioration, *P-delta* effects, torsional effects, semi-rigid diaphragms [311]. Furthermore, questions regarding the correct combination of the target displacements for multidirectional analyses can arise.

In addition, even if the use of traditional behaviour factors is avoided, these methods introduce other parameters that are to some degree subjective or difficult to quantify for non-expert analysts. Possible examples are the coefficients in equation (II.283) for the *Displacement Coefficient* method in the case of non-regular structures, the *equivalent damping* for the *Capacity Spectrum method* or the *reduction factor* (II.290) for the *N2 Method*.

Regarding seismic assessment studies, the NL-SA are becoming preponderant for both individual structures and for groups of structures (*e.g.* seismic risk studies), because these methods can estimate the seismic capacity of the structure and assess the structural performance. Nevertheless, the *Nonlinear Incremental Dynamic Analyses* are still used for special structures, like important buildings and bridges.

Nonlinear Incremental Dynamic Analyses (NL-IDA) are recognized, even by researchers most connected to NL-SA, as the most accurate approach and is considered to be the correct, natural, and perhaps, inevitable method to be used for seismic analyses [197, 311]. Nevertheless, these methods are currently considered inappropriate for design purposes and there are still challenges to be solved in order to use this approach more frequently within the scope of research studies. Some of the most common difficulties pointed out, are:

i. The complexity of the formulation, *e.g.* time integration algorithms;
ii. The high computational effort required for the analyses. High performance computers and advanced structural analysis codes must be used to enhance the performance and make the analyses feasible for large problem sizes;
iii. Complex material constitutive relations must be adopted (*e.g.* reversed cyclic response);
iv. The requirement for additional input data, *e.g.* earthquake records, mass distributions, *etc.*

NL-IDA is rarely used for design purposes, except for very particular or important structures, due to the complexity of the formulation and to the computational requirements. Nevertheless, modern seismic codes consider this possibility. For example, Eurocode 8 [92], contemplates the possibility of using a series of earthquake records to design buildings for earthquake loading.

From the opposite point of view, the NL-IDA presents important advantages when compared to the other analysis methods. A possible compilation of these advantages is presented in the following list:

i. The capacity to simulate accurately the earthquake loading, as a time-variable imposed displacement at the base of the structure, which can also be space-variable. The capacity to simulate the vertical component of the earthquake movements;
ii. The capacity to simulate with enhanced accuracy the three-dimensional structural response (*e.g.* torsion effects and the contribution of higher vibration modes);
iii. The capacity to represent several sources of damping directly in the model, *e.g.* viscous damping through global operators or hysteretic damping on the constitutive relations [388];
iv. The capacity to represent the rate-dependent material behaviour directly in the model;
v. The capacity to provide a large amount of information about the structural response.

A particular interest for NL-IDA is the capacity of acting as a complement to laboratory-based dynamic experiments (*e.g.* shaking table tests). If the most important drawbacks of this methodology are overcome, it will be possible to predict, follow, compare and extend the results from this type of tests. This approach presents an undeniable interest for research, and working as a complement to experimental testing may potentiate research results and reduce the overall costs.

Table II.4: Comparison between nonlinear seismic analysis methods.

Characteristics		NL-SA	NL-IDA
Model	Mesh Discretization	Detailed	Detailed
	Material Constitutive Relations	Medium (Monotonic)	Complex (Cyclic)
Loading	Type	Approximated (Static)	Detailed (Time-history)
	Time variable	No	Yes
	Spatial variable	No	Yes
	Vertical component	No	Yes
	Simplified for design	Yes	No
Response	Viscous Damping	Yes (Response Spectrum)	Yes (Motion Equations)
	Hysteretic Damping	Approx. (Inelastic RS)	Yes (Material C. Rel.)
	3D coupled response	Limited	Yes
	Simulation of higher modes	Limited	Yes
	Rate-dependent response	No	Yes
Analysis	Complexity	Medium	High
	Hardware Requirements	Normal	Advanced
	Software Requirements	Normal (NL Code)	High (Adv. NL Code)
Results	Type	Global/local parameters	Detailed, Time-based
	Accuracy	Medium-Good (depends)	Potentially V. Good
Applicability	Design	Yes	Limited
	Assessment	Yes	Yes
	Simulation	No	Yes

As a conclusion, it is possible to stress that linear methods are practically limited to design applications and nonlinear procedures must be adopted for assessment studies and detailed simulations. Among these, the NL-SA are predominant in assessment studies, although NL-IDA are also used. The NL-SA method has an important role within the scope of earthquake engineering and is expected to have increasing influence over the next few years. It is a fact that some drawbacks have been delaying the dissemination of the NL-IDA approach, *e.g.* the computational demand, the complexity of the formulation and of the constitutive relations. However, overcoming these difficulties is vital for successful dynamic detailed simulations, where the NL-IDA are unmatched in potential and in simulation capacity.

Table II.4 presents a possible, and yet subjective, comparison between the most relevant features of the two nonlinear seismic analysis methods discussed in this work.

Chapter III

Reinforced Concrete

1 Introduction

Reinforced concrete (RC) represents a very significant structural solution for buildings, bridges and other types of structures. To have an idea of the importance of this solution, according to *Sousa* [520], the survey made in the *Census 2001* revealed that 30.3% (about 909 thousand) of the buildings in Portugal have a RC structure. This typology is only overcome by low-rise masonry buildings (1 or 2 storeys) and is the most used for buildings with three or more storeys. This structural solution is also commonly adopted for vital services such as hospitals and perilous structures like cooling towers for nuclear power stations, which clearly demonstrates the significance of this structural solution for society.

This chapter is dedicated to studying possible approaches for RC modelling. The mechanical behaviour of this composite material results from the interaction of concrete, steel reinforcements and what will be called the *concrete-steel interfaces* (CSI) and the *concrete-concrete interfaces*. The structural response is unquestionably complex mainly because the RC experiences severe inelastic behaviour for intense loading, *e.g.* concrete cracking, steel yielding and bond failure.

The methodology that will be used in this chapter is to make a separate analysis for the concrete and for the steel reinforcements. Nevertheless, the adopted solutions for each of these materials are

chosen taking into consideration that they will be combined at the end for RC modelling. Chapter IV is dedicated to the CSI, hence, this subject will only by briefly referenced in this part of the text.

The outline of the chapter is the following: at the beginning, a summarized state of the art regarding the main characteristics of the RC response will be presented. This section includes a succinct description of the basic aspects regarding the most used constitutive models and sections dedicated to the behaviour of the concrete, reinforcing steel, interfaces and RC elements in general. Afterwards, the proposed models for concrete and for the reinforcing steel bars will be presented. The chapter ends with a series of validation tests made to assess the efficiency and representativeness of the adopted solutions.

2 State of the art

2.1 Constitutive models

This sub-section will start with a small introduction to some thermodynamic basic principles. Most formulations can be deduced only from mechanical considerations and all the models considered in this work are considered to be thermal-independent, so, the reader may question why this scientific domain is introduced. The reason for including some thermodynamic concepts is related to the fact that this science presents a robust theoretical background for any material model, with special interest for developing constitutive models associated with irreversible processes. For example, plasticity and damage mechanics models can be based on the thermodynamics of irreversible processes with internal variables [257, 329].

In the remaining part of this section, a summarized description of the most relevant theories for developing constitutive models will be presented, namely: the plasticity theory, fracture and damage mechanics, and some aspects concerning size effect and the localization phenomenon.

2.1.1 Thermodynamic framework

Thermodynamics is the science that studies energy transfer and conservation involving heat and other forms of energy, like mechanical energy. Historically, this science was initially developed in the *steam engine era* (19^{th} century), with important contributions from *Carnot*, *Kelvin*, *Thompson*, *Clausius*, *Maxwell*, *Boltzmann*, *Gibbs*, to name a few [572].

Basic notions of thermodynamics are the concepts of *system*, *surroundings* and *boundaries*. A *thermodynamic system* is a collection of matter separated by boundaries, which has its macroscopic properties described by a set of macroscopic physical and chemical *state variables*. The surroundings can be defined as the external matter that can interact with the system [5, 572]. In a *closed system*, the mass remains the same and only heat and work can be exchanged across the boundaries. Furthermore, in an *isolated system* both mass and energy remains constant, hence it does not interact with the surroundings in any way [229].

Furthermore, there are several types of thermodynamic processes. The most common types the so-called *isobaric*, *isochoric* and *isothermal* processes occur when the pressure, volume, or temperature remains constant, respectively. In addition, in an *adiabatic* process the net heat transfer is zero [5, 407].

Another basic notion is the concept of *thermodynamic free energy* that consists of the amount of work that the system can perform. This quantity can be represented by the *internal energy* (*U*) of a system minus the amount of energy unavailable to perform work, which can be computed from the entropy (*S*) multiplied by the temperature of the system [571].

The *state variables* completely define the material at any time. They can be classified as *observable* and *internal variables* (ξ_k) depending on whether they can or not be measured directly. Table III.1 presents the most common state variables associated with thermo-elasticity, plasticity and damage mechanical problems according to Lemaitre [329].

- Equations of state and thermodynamic state potentials

The state variables can be related under some conditions through *equations of state*. These consist in thermodynamic equations that represent constitutive relations that relate the state variables describing the matter, *e.g.* temperature, internal energy, or for thermo-mechanical problems, strain, and stress.

Within the framework of mechanical problems, the equations of state are commonly derived from *thermodynamic state potentials* [329]. These are represented by continuous scalar functions that are used to define the stored energy in a system. The most common thermodynamic state potentials are the *internal energy* (*U*), *enthalpy* (*H*), the *Helmholtz free energy* (ψ) and the *Gibbs free energy* (χ).

These potentials are formulated adopting different quantitative measures. Nevertheless, they are equivalent and may be interrelated. For example, the Helmholtz and Gibbs free energies are associated with the available energy in a system when temperature and volume or the temperature and pressure are constant, respectively. Consequently, the *Helmholtz free energy* may be written in terms of the strain tensor, which is associated with volume changes, and the Gibbs free energy in terms of the stress tensor, which is associated with the pressure applied, and to a set of *m* general

Table III.1: Thermodynamic variables for thermo-elasticity, plasticity and damage problems, adap.from [329].

State Variables	**Associated Variables**
T (absolute temperature)*	s (entropy density)
ε (total strain)*	σ (Cauchy stress)
ε^e (elastic strain)	σ
ε^p (plastic strain)	$-\sigma$
r (plastic strain damage)	R (strain hardening)
d (damage)	Y (energy density release)
α (back strain)	X_D (back stress)

Note: * Observable state variable.

internal variables $\xi_k \left(1 \le k \le m\right)$, which for simplicity are considered to be scalar quantities:

$$\psi = \psi\left(\underline{\boldsymbol{\varepsilon}}, T, \xi_k\right), \tag{III.1}$$

$$\chi = \chi\left(\underline{\boldsymbol{\sigma}}, T, \xi_k\right), \tag{III.2}$$

where *T* represents the *absolute temperature*.

- Laws of thermodynamics

Thermodynamics is governed by three universal laws [407, 452, 519], plus the so-called *zeroth law*, that is implied in the other three laws. The *first law of thermodynamics* states that the internal energy gained by a system must be equal to the heat absorbed by the system plus the work done on the system. Mathematically, this can be written as:

$$dU = Q + W, \tag{III.3}$$

where dU is a variation of the internal energy, Q and W are the amounts of heat supplied to the system and the work done on the system respectively [i]. This law can be interpreted as an application of the *conservation of energy principle*, *i.e.* the energy can be transformed, but not created or destroyed.

For an *adiabatic process*, *i.e.* the system does not experience any heat transfer with the surroundings, the change of the internal energy must be equal to the work done:

$$dU = W. \tag{III.4}$$

Moreover, in an *isothermal process*, *i.e.* the system undergoes a change in state but does not experience a change in temperature, the internal energy remains constant:

$$Q + W = 0. \tag{III.5}$$

At this stage, the concepts of *reversible* and *irreversible processes* should be introduced. In thermodynamics, if a system that changes state by means of a reversible process returns to the original state then the energy balance will be null. On the other hand, for an irreversible process, if the original state is achievable there will be permanent energy transfer, *e.g.* the environment cannot restore its initial conditions because the irreversible process increased the *entropy* of the system, *a.k.a. reduced heat*. The *entropy* of the system can be seen as a measure of the disorder or of the amount of energy unavailable to do useful work [5].

This leads to the *second law of thermodynamics* that states that the total entropy *S* of any system can only decrease by increasing the entropy of some other system. Consequently, for an isolated system the entropy cannot decrease:

$$dS \ge 0. \tag{III.6}$$

Finally, the *third law of thermodynamics* states that the entropy of a perfect crystal approaches zero as the absolute temperature reaches zero [5].

[i] a minus sign would be introduced in the work term if the work done by the system is considered, instead of the work done on the system.

- Thermomechanics

The next step consists in applying the thermodynamics concepts and laws to continuum mechanics. This complex task requires specific knowledge that is outside the scope of this thesis. The following summarized description follows the work of Asaro *et al.* [17] and Han *et al.* [257]. More details can be found in the references [120, 167, 227, 329, 332, 344, 417, 585].

The energy balance in the first law of thermodynamics (III.3) can be written as follows [17, 167, 257]:

$$\frac{d}{dt}\left(\int \rho e \, d\Omega\right)+\frac{d}{dt}\left(\frac{1}{2}\int \rho \left|\mathbf{v}\right|^2 \, d\Omega\right)=-\int \mathbf{q}\cdot\mathbf{n} \, d\Gamma+\int \rho r \, d\Omega+\int \mathbf{b}\cdot\mathbf{v} \, d\Omega+\int \mathbf{t}_\gamma \cdot \mathbf{v} \, d\Gamma_\sigma \,, \tag{III.7}$$

where *e* represents the *specific internal energy by unit mass*, ρ the *specific mass*, **v** the *velocity vector*, **q** the *heat flux by unit area* (the minus sign means that the body losses energy if **n** points outwards), *r* the *rate of heat input per unit mass*, **b** the *body forces* and $\mathbf{t}_\gamma$ the stresses applied at the static boundary. The first term in the *left-hand side* (lhs) of equation (III.7) represents the kinematic energy and the second the internal energy assumed to be distributed in the domain.

The last relation must be valid for the whole body or for any part of it. Therefore, after some algebraic manipulations and introducing the divergence theorem, it is possible to redefine (III.7) as:

$$\rho \delta e = \underline{\boldsymbol{\sigma}} : \delta \underline{\boldsymbol{\varepsilon}} - \mathrm{div}\left(\mathbf{q}\right)+\rho r \,. \tag{III.8}$$

Before introducing the second law of thermodynamics, let us recall that Clausius proposed the following equation for computing the change in entropy of a system undergoing a reversible process:

$$dS=\frac{\delta Q}{T} \,, \tag{III.9}$$

where δQ represents an infinitesimal heat supplied to the system performed at the equilibrium temperature *T*. This equation implies that supplying heat to the system at lower temperatures causes more disorder and a higher entropy change than at higher temperatures.

The entropy of a system can change by heat transfer with the surroundings or by irreversible changes in the matter. Consequently, the following equation can be written for the rate of entropy change:

$$\frac{dS}{dt}=\frac{d}{dt}\left(\int \rho \eta \, d\Omega\right)=-\int \frac{\mathbf{q}\cdot\mathbf{n}}{T} \, d\Gamma+\int \frac{\rho r}{T} \, d\Omega+\int \rho \gamma \, d\Omega \,, \tag{III.10}$$

where γ represents the *rate of entropy change per unit mass* caused by irreversible changes in the matter and η represents the *entropy density per unit mass*.

Recalling the second law of thermodynamics expressed in (III.6), it is possible to conclude that the entropy change per unit mass caused by irreversible changes must be non-negative:

$$\gamma \geq 0 \,. \tag{III.11}$$

The equation (III.10) maybe rewritten for each point leading to the *Clausius-Duhem inequality* [17]:

$$\frac{d\eta}{dt} \geq -\frac{\mathrm{div}\left(\mathbf{q}\right)}{\rho T}+\frac{r}{T} \,. \tag{III.12}$$

The equality holds for reversible processes and the inequality holds for irreversible processes.

- State equations for irreversible thermodynamics processes

Within the scope of irreversible thermodynamics processes, internal variables ξ_k are used to describe the phenomena occurring in the matter. According to Asaro *et al.* [17], the inelasticity develops in constrained equilibrium states created by constraining the internal variables using *thermodynamic forces* Y_k, which are defined such that the power dissipation can be expressed as:

$$T\,\gamma = Y_k\,\delta\xi_k \geq 0\,, \tag{III.13}$$

which must be non-negative due to equation (III.11).

The energy dissipated in the irreversible process generates entropy that must be removed from the free energy available to perform work. Joining the equations (III.8) and (III.12), results in:

$$\delta e = \frac{1}{\rho}\underline{\boldsymbol{\sigma}} : \delta\underline{\boldsymbol{\varepsilon}} + T\,\delta\eta - Y_k\,\delta\xi_k\,, \tag{III.14}$$

hence, the internal energy is the thermodynamic potential for computing $\underline{\boldsymbol{\sigma}}$, T and Y_k, when $\underline{\boldsymbol{\varepsilon}}$, η and ξ_k are considered independent state variables [17]:

$$e = e\left(\underline{\boldsymbol{\varepsilon}}, \eta, \xi_k\right), \tag{III.15}$$

hence, by partial differentiation:

$$\underline{\boldsymbol{\sigma}} = \rho\frac{\partial e}{\partial \underline{\boldsymbol{\varepsilon}}}, \quad T = \frac{\partial e}{\partial \eta}, \quad Y_k = -\frac{\partial e}{\partial \xi_k}. \tag{III.16}$$

Recalling that the *Helmholtz free energy* that represents the amount of internal energy available for doing work at constant temperature [257]:

$$\psi = \psi\left(\underline{\boldsymbol{\varepsilon}}, \eta, \xi_k\right) = e\left(\underline{\boldsymbol{\varepsilon}}, \eta, \xi_k\right) - \eta T\,. \tag{III.17}$$

The rate change of the *Helmholtz free energy* can be defined as [17]:

$$\delta\psi = \frac{1}{\rho}\underline{\boldsymbol{\sigma}} : \delta\underline{\boldsymbol{\varepsilon}} + \eta\,\delta T - Y_k\,\delta\xi_k\,, \tag{III.18}$$

which represents the thermodynamic potential for computing $\underline{\boldsymbol{\sigma}}$, η and Y_k, when $\underline{\boldsymbol{\varepsilon}}$, T and ξ_k are considered independent state variables [17]. Once again, by partial differentiation:

$$\underline{\boldsymbol{\sigma}} = \rho\frac{\partial \psi}{\partial \underline{\boldsymbol{\varepsilon}}}, \quad \eta = \frac{\partial \psi}{\partial T}, \quad Y_k = -\frac{\partial \psi}{\partial \xi_k}. \tag{III.19}$$

Introducing the *Gibbs energy* defined as:

$$\chi = \chi\left(\underline{\boldsymbol{\sigma}}, T, \xi_k\right) = \frac{1}{\rho}\underline{\boldsymbol{\sigma}} : \underline{\boldsymbol{\varepsilon}} - \psi\left(\underline{\boldsymbol{\sigma}}, T, \xi_k\right), \tag{III.20}$$

which represents the thermodynamic potential for computing $\underline{\boldsymbol{\varepsilon}}$, T and Y_k, when $\underline{\boldsymbol{\sigma}}$, η and ξ_k are considered independent state variables. Using the same procedure as before, leads to [17]:

$$\delta\chi = \frac{1}{\rho}\underline{\boldsymbol{\sigma}} : \delta\underline{\boldsymbol{\varepsilon}} + \eta\,\delta T - Y_k\,\delta\xi_k\,, \tag{III.21}$$

$$\underline{\boldsymbol{\varepsilon}} = \rho\frac{\partial \chi}{\partial \underline{\boldsymbol{\sigma}}}, \quad \eta = \frac{\partial \chi}{\partial T}, \quad Y_k = -\frac{\partial \chi}{\partial \xi_k}. \tag{III.22}$$

2.1.2 Plasticity theory

Plasticity-based theories were one of the first attempts to explain the material nonlinear behaviour using a consistent mathematical formulation. Modern plasticity theory originates from the end of the 19th century, in particular from the works of Tresca [545], Saint Venant [554] and Levy [335], and at the beginning of the 20th century, from the work of von Mises [559] and Prandtl [459]. To complete this non-exhaustive list, the contributions from Drucker and Prager [183, 184, 458] should also be referenced.

Starting by considering a material with elastoplastic behaviour and under the premise that the thermodynamic process is isothermal and rate-independent, the variations of the *Gibbs free energy* can be defined by [344]:

$$\delta\chi = \frac{\partial\chi}{\partial\underline{\boldsymbol{\sigma}}} : \delta\underline{\boldsymbol{\sigma}} + \frac{\partial\chi}{\partial\xi_k}\delta\xi_k \,. \tag{III.23}$$

It can be proved only by thermodynamic considerations that the total strain tensor can be decomposed into the elastic and plastic addends [344]:

$$\underline{\boldsymbol{\varepsilon}} = \underline{\boldsymbol{\varepsilon}}^e\left(\underline{\boldsymbol{\sigma}}\right) + \underline{\boldsymbol{\varepsilon}}^p\left(\xi\right), \tag{III.24}$$

and that the Helmholtz and the Gibbs free energies can also be decomposed into the elastic and plastic components [257]:

$$\psi\left(\underline{\boldsymbol{\varepsilon}}, \xi_k\right) = \psi^e\left(\underline{\boldsymbol{\varepsilon}}^e\right) + \psi^p\left(\xi\right), \tag{III.25}$$

$$\chi\left(\underline{\boldsymbol{\sigma}}, \xi_k\right) = \chi^e\left(\underline{\boldsymbol{\sigma}}\right) + \chi^p\left(\xi\right). \tag{III.26}$$

The additive decomposition of the total strain into the elastic and reversible component, and into plastic irreversible deformations is a basic assumption adopted in most plasticity formulations.

Inserting the relations (III.22) into equation (III.23) and considering the strain decomposition expressed in equation (III.24), it is possible to write:

$$\frac{\partial\chi}{\partial\underline{\boldsymbol{\sigma}}} = \frac{1}{\rho}\underline{\boldsymbol{\varepsilon}}^e; \quad \frac{\partial\chi}{\partial\xi_k} = -Y_k \,. \tag{III.27}$$

The mathematical model adopted to simulate the elastoplastic response is usually defined using: i) a *yield criterion*, ii) a *hardening law*; iii) a *flow rule*; iv) a *consistency rule*; and v) *complementarity conditions*. The yield criterion is often defined by the scalar *yield function* ϕ_*, dependent on a *comparison stress* $\tilde{\sigma}$, and is used to define the state of the material:

$$\phi_*\left(\tilde{\sigma}, \xi\right) = S\left(\tilde{\sigma}\right) - Y\left(\xi\right) \leq 0 \,. \tag{III.28}$$

where $S\left(\tilde{\sigma}\right)$ is a function dependent on the comparison stress and $Y\left(\xi\right)$ is related to the material history through the definition of the internal variable ξ.

If $\phi_* < 0$ the material behaves elastically and if $\phi_* = 0$ it is in a plastic state and plastic deformations can occur. The region defined by $\phi_* > 0$ is inaccessible to the material (see Figure III.1-a).

The most well-known yield criteria are the Tresca [545] and the von Mises [559] criteria and for

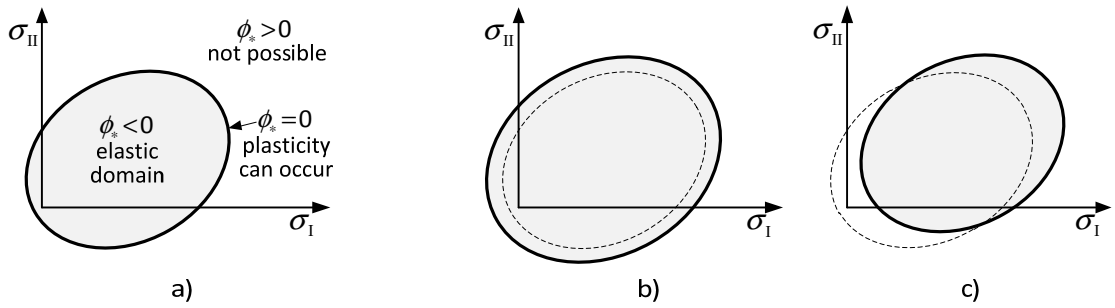

Figure III.1: Plasticity theory : a) Yield criterion; b) Isotropic hardening; c) Kinematic hardening.

materials sensitive to the hydrostatic pressure, like concrete, the *Mohr-Coulomb* [146] and the *Drucker-Prager* [184] criteria. More detailed information can be found in the following references [171, 257, 301, 580].

Changes in the yield function position in the stress space are introduced by the *hardening law*. Within the scope of this thesis, the term hardening, *a.k.a. strain hardening*, is used in a generalized sense as it can also be associated with a decrease in size of the elastic region, and hence, with softening-like behaviour. The most common hardening laws can be classified as (see Figure III.1-b/c): i) *isotropic*, if the yield surface evolves uniformly along all stress space directions; ii) *kinematic*, if the yield surface only moves in the stress space and does not change size; and iii) *mixed*, when it combines the previous definitions. Hardening can be introduced in the formulation using the term $Y(\xi)$ in the yield criterion resulting in a non-stationary yield surface.

The flow rules can be classified into the following two types: i) *associated flow* and ii) *non-associated flow*. The latter uses the *yield criterion function* (ϕ_*) to define the elastic limit and a *plastic potential function* (g_*) to determine the plastic strain increments. This approach can introduce additional complexity in the formulation, like non-unique limit loads and unstable structural behaviour [556], thus most of the time it is not adopted. Nevertheless, the internal friction present in some materials (*e.g.* soils, concrete and rock) exhibits the so-called *dilatancy phenomenon* [477], which can be defined as the change in volume associated with shear distortion. The volume increase for these materials is related to the granular nature of the meso-structure, as presented in Figure III.2. Using an *associated flow* rule, the volume increase is over-estimated during yielding [160], therefore, it is necessary to use *non-associated* flow to adequately simulate the response.

The constitutive relation can be defined by the traditional *elasticity modulus* and by *Poisson's ratio* to

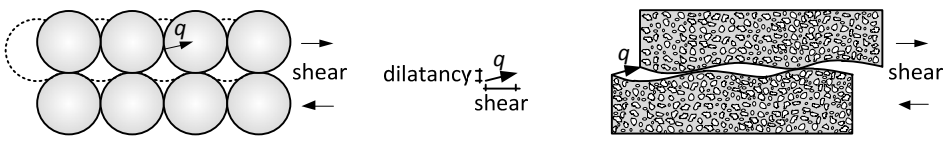

Figure III.2: Dilatancy phenomenon for granular materials, adapted from Vermeer *et al.* [556].

define the stiffness characteristics. To define the strength, the cohesion (c) and *friction angle* (ϕ) are often used. For a dilatant material, the *dilatancy angle* (ψ) should be added. This parameter was introduced by Hansen [258] and represents the ratio between the plastic volume change and the plastic shear strain. According to Vermeer and de Borst [556], the internal friction angle is usually between 15° and 45° for soils, and between 30° and 35° for concrete, and the dilatancy angle usually ranges between 5° an 15°. This difference is considerable and justifies using a non-associated flow rule for this type of materials.

Drucker [183] introduced the so-called *Drucker's postulate*, *a.k.a.* the *material stability criterion*, which states that a material is stable, if the work done by the plastic deformation in a closed stress cycle is always non-negative [103]:

$$\delta\underline{\boldsymbol{\sigma}} : \delta\underline{\boldsymbol{\varepsilon}}^{p} \geq 0 . \tag{III.29}$$

This implies that a material with hardening or perfectly plastic post-yield behaviour is stable and a material with softening is unstable. Combining Drucker's postulate and the *associated flow* rule makes it possible to associate the stress and plastic strain spaces and demonstrate that for a stable material the surface defined in the stress space by the yield criterion must be convex and the plastic strain increment must be normal to this surface [580], leading to the so-called *normality rule.* Under these hypotheses, the plastic strain increment during yielding can be written as:

$$\delta\underline{\boldsymbol{\varepsilon}}^{p} = \delta\varepsilon_{*} \frac{\partial\phi_{*}}{\partial\underline{\boldsymbol{\sigma}}} = \delta\varepsilon_{*}\ \mathbf{n}_{*} , \tag{III.30}$$

where $\mathbf{n}_{*}$ is the outward normal to the yield surface and ε_{*} is often known as the *plastic multiplier*, which is always non-negative, in order to have a positive work resulting from (III.29), leading to the *plastic flow condition*:

$$\delta\varepsilon_{*} \geq 0 . \tag{III.31}$$

The plastic multiplier increment is defined by the *consistency condition* [458]. Knowing that plastic strains can only be developed for a plastic state $(\phi_{*} = 0)$, this condition enforces that loading must lead to another plastic state after the infinitesimal variations of stress and other internal variables [580]. Mathematically, this can be expressed as:

$$d\phi_{*} = \frac{\partial\phi_{*}}{\partial\tilde{\sigma}} \frac{\partial\tilde{\sigma}}{\partial\underline{\boldsymbol{\sigma}}} d\underline{\boldsymbol{\sigma}} + \frac{\partial\phi_{*}}{\partial\xi} d\xi = 0 . \tag{III.32}$$

If the second term of (III.32) is neglected this is known as *neutral loading*, which means that the stress moves around the yield surface that remains unchanged in the stress space. Otherwise, the second term reflects the changes of the yield surface due to hardening.

For completeness, the formulation requires introducing the *loading/unloading conditions*, *a.k.a. complementarity* or *Kuhn-Tucker conditions*:

$$\phi_{*}\ \delta\varepsilon_{*} = 0 , \tag{III.33}$$

$$\delta\phi_{*}\ \delta\varepsilon_{*} = 0 , \tag{III.34}$$

where the first equation enforces that for having a plastic strain increment the material must be in a

plastic state $(\phi_* = 0)$ and the second equation imposes that for an unloading situation $(d\phi_* < 0)$ the plastic strain increment must be null. These equations are usually not introduced directly in the governing system. Instead, they are introduced as conditions in the implementation.

The constitutive model is completely defined by combining the yield criterion and the hardening law (III.28), the flow rule (III.30), the plastic flow condition (III.31), the consistency rule (III.32) and the complementarity conditions (III.33) and (III.34).

Before concluding this section, it should be emphasized that the constitutive model is defined in a rate format. Consequently, it is necessary to integrate the expressions to perform an incremental analysis. This integration raises difficulties for compliance with the normality rule (III.30), where for the general case it is not possible to define an expression for the evolutions of the yield surface normal. A *Backward-Euler* method, *a.k.a. return-mapping* algorithm, similar to the one presented in Chapter II-§4.3.3 is often implemented to overcome this problem:

$$\Delta\boldsymbol{\varepsilon}^p = \Delta\varepsilon_* \, \mathbf{n}_{*,j+1} \,, \tag{III.35}$$

where $\Delta\varepsilon_*$ represents the increment of the plastic multiplier and $\mathbf{n}_{*,j+1}$ represents the normal to the yield surface at the end of the time step.

It can be proved that the *Backward-Euler* method is stable. However, the formulation is implicit because it requires knowing $\mathbf{n}_*$ at the end of the time step. Consequently, an iterative procedure must be implemented to compute (III.35).

More information about plasticity theory can be obtained in [103, 171, 257, 301, 427, 580, 584].

2.1.3 Fracture mechanics

Fracture Mechanics (FM) is a field of mechanics that studies the propagation of cracks in materials. Clearly, this scientific area presents concepts and formulations that are useful to describe the behaviour of materials with discontinuities, such as concrete. Historically, modern FM is often considered to have originated from the pioneer work of Griffith [253] with brittle materials, such as glass. Griffith realized that after introducing a weakening in the material (small crack) the problem could be treated as an energy balance problem, which resulted in the well-known relation for the critical stress σ_{cr}, and the response is characterized by catastrophic crack propagation [487]:

$$\sigma_{cr} = \sqrt{\frac{E\,G_{cr}}{\pi a}} \,, \tag{III.36}$$

where *E* is the *elasticity modulus*, *a* is the *crack length* and G_{cr} is the critical *strain energy release rate* measured in $\mathrm{J/m^2}$ or $\mathrm{N/m}$. The latter is often considered as a material property and can be seen as the rate at which the energy is released by crack growth, or in other words, as the amount of energy dissipated in the formation and growth of a crack of unit area. Other relevant developments were introduced by Irwin [287] by extending the Griffith theory to arbitrary cracks and by showing that the stress field near the crack tip can be determined by the *stress intensity factor K*, which can be associated with the strain energy release rate for mode I fracture using:

$$G = G_f^{\mathrm{I}} = \begin{cases} \dfrac{K_{\mathrm{I}}^2}{E}, & \text{plane stress} \\ \dfrac{(1-\nu^2)\,K_{\mathrm{I}}^2}{E}, & \text{plane stress} \end{cases} . \qquad \text{(III.37)}$$

The mode I fracture mode, *a.k.a. opening mode*, presents the tensile stress normal to the plane of the crack and is one of the three basic forms to apply a force and propagate a crack (see Figure III.3). The other two modes are the in-plane shear (Mode II), in which a shear stress acts parallel to the plane of the crack and perpendicular to the crack front, and the out-of-plane shear (Mode III), where the crack grows by the action of a shear stress acting parallel to the plane of the crack and parallel to the crack front.

The author Rice [478] also contributed significantly to the development of FM by introducing a new parameter that is often used as a crack growth criterion for metals. This parameter is the so-called *J-integral* that is independent of the integration path considered around the crack tip.

A breakthrough in FM was introduced by considering cohesive forces near the crack tip, which extended the traditional linear elastic formulation. According to Ceriolo and Tommaso [94], the first step in this direction was taken by Banreblatt [30] and Dugdale [190], although the major advance was achieved by Hillerborg [270] by considering a tension softening process zone between the crack tip and the real crack (fully open), which avoids the stress concentrations at the crack tip.

This methodology considers the concrete behaviour sub-divided into three stages: i) *crack initiation*, related to the development of micro-cracking; ii) evolution to a macro-crack; iii) fully open crack with opening-closing and sliding movements. Geometrically, these phases are associated with the specific regions as presented in Figure III.4-a, namely: i) the *virgin material* region, where there are no discontinuities other than initial imperfections; ii) the *fracture process zone* (FPZ), where the stored energy is being dissipated; and iii) the fully open crack, which is a traction-free zone.

In the scope of this work, the fully open crack region is treated as a *concrete-concrete interface*, which can be subjected to aggregate interlocking and to debounding forces, as presented in section 2.4.1.

These two crack conceptions are associated with two of the most well-known theories used in FM (see Figure III.5). In *Linear Elastic Fracture Mechanics* (LEFM), it is assumed that energy dissipation

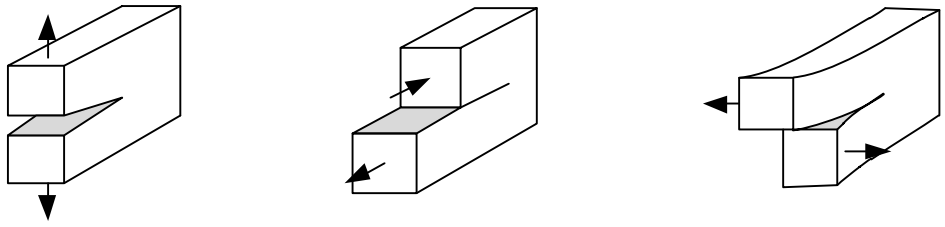

a) Mode I – Tension (Opening) b) Mode II – Sliding (In-Plane Shear) c) Mode III - Tearing (Out-Of-Plane Shear)

Figure III.3: Crack separation modes.

occurs at the crack tip and that the fracture energy can be associated with the separation energy required to propagate the crack [296]. This formulation leads to the unrealistic stress concentrations at the crack tip already discussed. On the other hand, in *Nonlinear Elastic Fracture Mechanics* (NEFM), *a.k.a. Elastic-Plastic Fracture*, it is considered that the energy dissipation occurs at a finite length of material (fracture process zone), similarly to what is observed in real materials. This length can be related to a material property and the inelastic response in this region tends to smooth the stress distributions.

Using experimental data, it is possible to determine a stress *vs*. crack opening graph $(\sigma - w_c)$ that presents a curve similar to the one presented in Figure III.4-b for concrete. The mode I fracture energy can be computed from the area shadowed in Figure III.4-b. Mathematically this can be defined as:

$$G_f^{\mathrm{I}} = \int_0^{\infty} \sigma \, dw_c \, . \tag{III.38}$$

This quantity can be related to the *fracture toughness* K_{I} using the relations (III.37) and this is usually considered a material property, although there is no absolute consensus in this matter. This is related to the dependency, in some extent, that this parameter presents, on the size of the specimen. This phenomenon is the well-known *size effect* associated with fracture, which is addressed in the following section.

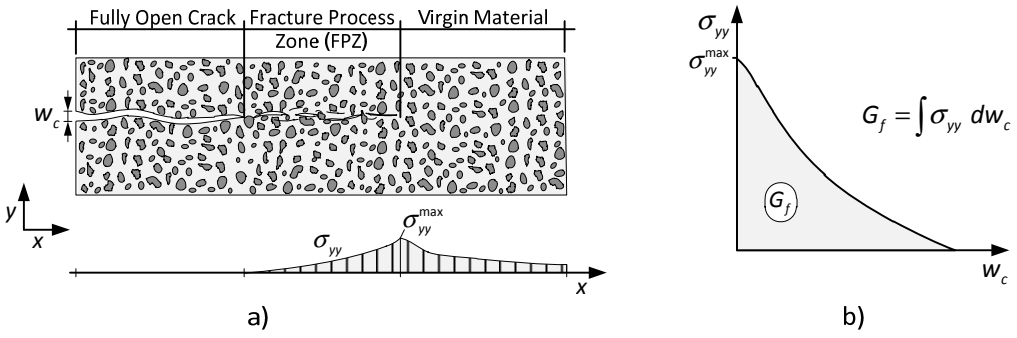

Figure III.4: Fracturing process in concrete, adapted from Carpinteri *et al.* [80].

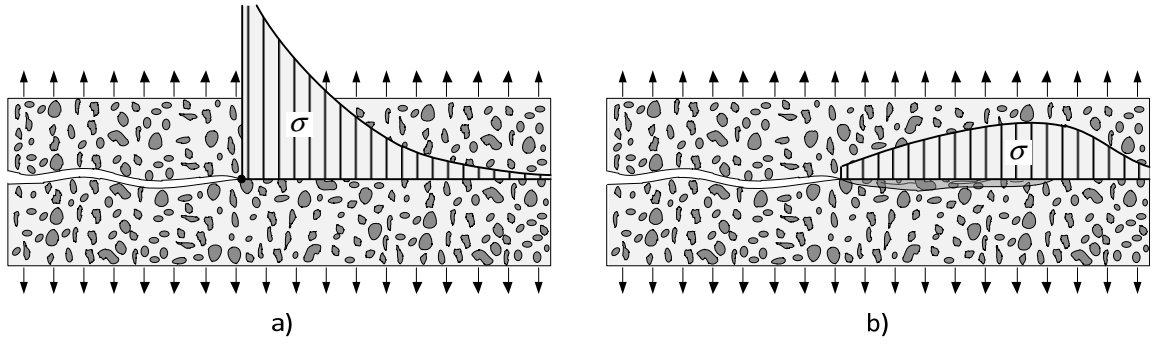

Figure III.5: Different theories used in FM: a) Linear Elastic Fracture Mechanics; b) Nonlinear Elastic Fracture Mechanics.

2.1.4 Size effect

The size effect is a phenomenon that can be defined as the dependence between the global response of a structural system and its size. In other words, a size effect phenomenon is present whenever a homothetic scaling made to a structural system does not result in a nominal strength[i] proportional to that scaling. This effect is often neglected in common analyses, despite the fact that it is capable of changing the structural response.

Experimental studies confirm that the mechanical characteristics of same materials change with the size of the tested specimen for geometrical identical systems subjected to the same type of loading. A possible example is reported in the work of L'Hermite [315] that showed that the nominal tensile strength of concrete in three-point bending tests decreased with the increase of the specimen volume. Another example is described in the work of Bažant and co-workers with notched specimens made of concrete, rocks and ceramics, which showed a size dependence on the fracture energy and on the effective process zone length, see Bažant *et al.* [42].

This issue has been addressed in several studies and the comprehension of this phenomenon is reasonably good. Nevertheless, the level of implementation in numerical and experimental structural simulations is still quite low. It is possible to relate this to the fact that structural systems with predominant ductile elastoplastic response are less susceptible to this problem, contrary to *quasi*-brittle materials, which experience post-peak softening that are very prone to this effect (*e.g.* concrete, rocks, ceramics, *etc.*).

There can be different types and sources for the size effect. The most common are related to the non-homogeneity of the material properties and to the fracture dependency on material properties. Nonetheless, there are many other sources of size effects, *e.g.* the size of a RC member that can influence the concrete hydration inside and consequently the heterogeneity of the material. The first two size effect types will be addressed separately in the following paragraphs.

- Size effect related to fracture

The fracture process in *quasi*-brittle materials with softening post-peak response is an important source of size effect. This phenomenon is related to the fact that a homothetic scaling of the structure will not be followed by the same scaling of the zone where fracture is developed, the *fracture process zone* (FPZ). As a result, the fracture process zone occupies a smaller relative zone in a larger structure, creating a size effect source. The authors Sener *et al.* [502] emphasize this idea by stressing that the FPZ can be considered as approximately independent of the structure size. Furthermore, it is known that in real structures cracking develops not only at the crack tip, as considered in *Linear Elastic Fracture Mechanics* (LEFM). Instead, it occurs in a finite region that is proportional to the aggregate size, among others, as considered in *Nonlinear Elastic Fracture Mechanics* (NEFM).

[i] the nominal term is used in the sense of effective strength.

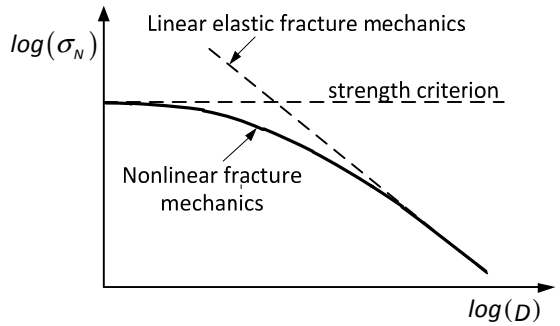

Figure III.6: Size effect law for concrete structures proposed by Bažant [34].

According to Bažant [34], experimental results show that the nominal stress at failure decreases with the increase of the size for structures that present the same geometrical and cracking patterns. The author also proposed the well-known size effect law presented in Figure III.6, which relates the nominal stress at failure σ_N, to the parameter *D* that is related to the size of the structure.

Drawn as a horizontal line in Figure III.6 is the strength criterion that represents the situation where the nominal stress equals a maximum admissible stress characteristic of the material, *e.g.* the tensile strength of the concrete $\sigma_N = f_{ct}$. For small specimens the FPZ occupies a significant portion of the domain and the strength criterion is representative and adequate to estimate the nominal stress at collapse.

On the other hand, when considering that cracking develops only at the crack tip, as in the LEFM formulation, a homothetic scaling results in the increase of the volume that is not followed by a proportional increase of the cracking area, because the fracture process zone is a surface. Consequently, the nominal stress at failure varies inversely with the square root of the dimension parameter and thus when these two parameters are plotted on logarithmic scales, like in Figure III.6, the LEFM solution will be a line with slope $-1/2$, as pointed out by Carpinteri [78]. This solution also represents a good estimation of the experimental results for large enough structures.

For intermediate cases, Bažant [34] proposes considering the nominal stress at failure proportional to:

$$\sigma_N \approx \frac{1}{\sqrt{1+\lambda/\lambda_0}}, \tag{III.39}$$

where parameter λ is related to the ratio between the size of the structure and the maximum size of the aggregate and λ_0 is a constant related to the size of the fracture process zone. This will result in a smooth transition from the strength criterion to the LEFM solution, as shown in Figure III.6.

It is worth noting that in the continuum damage mechanics framework, the nonlocal regularization technique is capable of simulating this type of size effect as concluded by Le Bellégo *et al.* [323]. This is done by using material-dependent fracture parameters for structures with different sizes, such as the nonlocal length.

- Size effect related to the material heterogeneity

This type of size effect is related to the fact that there is a higher probability of having a weaker material zone conditioning the overall response in a larger structural element. Therefore, this effect is more important for materials that present a large dispersion in the mechanical characteristics. This is particular significant for concrete, because this material presents a large scattering for some mechanical parameters, such as the tensile strength.

This type of size effect is also more significant when the dimension of the critical zone increases. For example, in a concrete tie (see Figure III.7-a) all length is subjected to similar axial stress due to equilibrium. Therefore, the region that conditions the collapse is larger, and thus, it is more likely to have a weaker zone. On the other hand, a concrete beam subjected to a three-point bending test (see Figure III.7-b) is less prone to this effect because the critical zone is a limited zone at mid-span. Consequently, the loading type also plays an important role for this type of size effect.

This source of size effect can be seen as having a probabilistic nature as stated by Mazars *et al.* [387], as a result of being related to the distribution of defects in the material. In sections 2.2.6 and 2.3.6, the issues related to the implementation of probabilistic distributions are addressed for some mechanical properties used in the constitutive relations adopted for concrete and for the steel reinforcements.

- Conclusions

As a conclusion, the size effect should be taken into consideration to correct the global results when failure is conditioned by quasi-brittle materials with softening post-peak response, at least for the following situations:

i. When the analyst wants to evaluate the structural response of a given prototype system, based on information collected from models that present a significant size difference when compared to the target structure [34];
ii. When the structural systems presents large critical zones and the materials have high strength dispersion;

The first situation is very common in experimental studies with scaled models that are often used together with similitude laws to recreate the response of larger prototypes (*e.g.* shaking table tests) and in numerical simulations calibrated with data from small laboratory tests, in which the numerical formulation is not able to include the size effect.

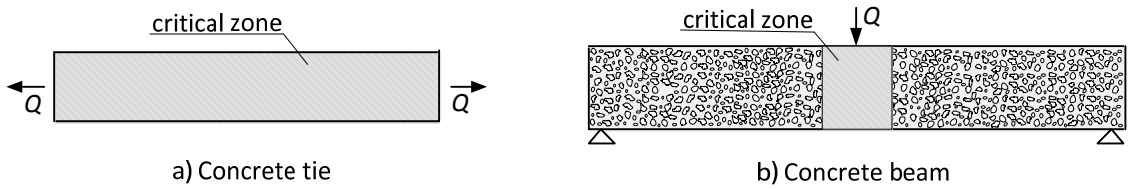

Figure III.7: Critical zone for two types of structural systems.

2.1.5 Damage mechanics

Historically, the starting steps of Damage Mechanics (DM) are often credited to Kachanov [299, 300] with the introduction of the damage concept within the framework of creep rupture. Later on, Rabotnov [466] introduced the effective stress notion and the material stiffness correction by factors depending on damage variables, also within the same framework. The work of Lemaitre and co-workers [96, 328-332] should also be emphasized because they developed the formulation using thermodynamic principles giving it a consistent theoretical background.

- Basic Concepts

Damage is the process of deterioration of the material due to loadings or other mechanisms. Damage results in material zones that are not able to resist the loads, which changes the global material properties, like stiffness or resistance. Damage is commonly simulated using damage variables or other internal variables within the framework of the thermodynamics of irreversible processes. These internal variables are often considered as non-observable state variables, because they are not easy to measure and are usually evaluated indirectly by their effects on the response.

It is possible to associate damage with a given direction using the outwards direction defined by the vector $\vec{n}$ (see Figure III.8-a). This way the local damage variable can be defined as:

$$d = \frac{S - S^{eff}}{S}, \tag{III.40}$$

where S^{eff} is the *effective area* to receive loads and S is the *total area* (see Figure III.8-b). Consequently, the damage variable assumes values between zero (virgin material) and one (completely damaged material).

In the previous definition, the damage variable depends on the direction considered, hence for the same point the material can be completely damaged in one direction and intact in another direction. In this type of model, the damage is said to be *anisotropic*, which is the most general case. However, most applications considerer a simpler type of damage that does not depend on the direction considered, which is known as *isotropic damage*.

Another important concept of DM is the *effective stress*, usually attributed to Rabotnov [466]. This concept states that for a damaged material, the stress associated with an applied external force cannot be computed from the total area, as in the *Cauchy stress* definition (σ). Instead, it is necessary to use the *effective area* (see Figure III.8-b):

$$\sigma^{eff} = \frac{N}{S^{eff}}. \tag{III.41}$$

Considering the damage variable defined in equation (III.40), it is possible to obtain:

$$\sigma^{eff} = \frac{N}{S(1-d)} = \frac{\sigma}{1-d}. \tag{III.42}$$

From the last equation, it can be concluded that for a virgin material $(d=0)$ the effective stress equals the Cauchy stress: $\sigma = \sigma^{eff}$.

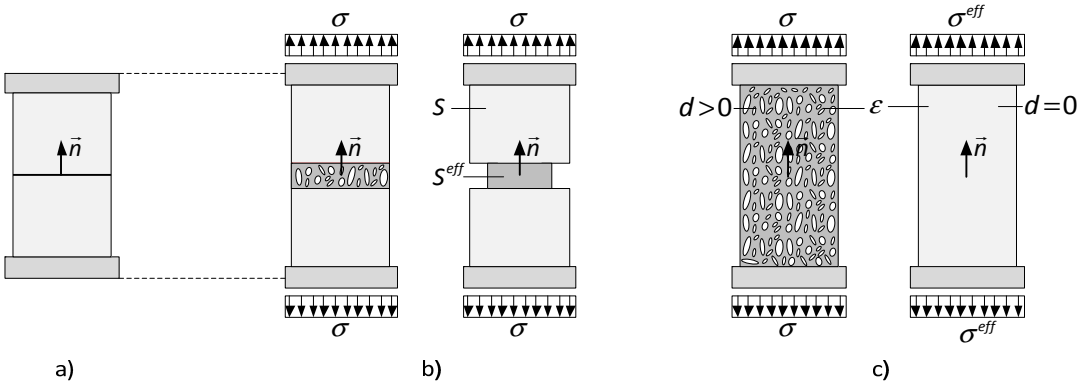

Figure III.8: Basic concepts of damage mechanics: a) damage direction; b) effective area; c) strain equivalence.

The *strain equivalence principle* [466] is also a hypothesis often adopted in the context of DM. This concept can be described for the uniaxial problem presented in Figure III.8-c, without losing generality. In this example, all the fibres are defined by the same constitutive relation, *e.g.* elasticity modulus *E*, but present slightly different resistances. Moreover, all fibres are subjected to the same increasing static load through a rigid plate. After the rupture of the first fibres, the effective area that receives loading decreases and the stresses in the working fibres increase to compensate, although all fibres are subject to the same strain. Using this approach, the model is said to adopt a kinematic definition of damage and the formulation is said to be strain-driven. The deformation is equivalent in all fibres, so it is possible to establish what is called the *strain equivalence principle* [466]. This principle states that is possible to use any strain constitutive relation for the material, both for intact and damaged material, as long as the stress takes into account the damage in the material (see Figure III.8-c).

Mathematically this relation can be defined has:

$$\varepsilon = \frac{\sigma}{E\left(1-d\right)}. \tag{III.43}$$

This last expression leads to the following stress-strain relation:

$$\sigma = E^{*}\,\varepsilon\,, \tag{III.44}$$

where is called the *damaged elasticity modulus* or *secant modulus* and is defined by:

$$E^{*} = \left(1-d\right)E\,. \tag{III.45}$$

Considering the relation (III.42), it is possible to define the effective stress using:

$$\sigma^{eff} = E\,\varepsilon\,. \tag{III.46}$$

Other types of formulations are possible, like the *stress equivalence* or *energy equivalence*. In these cases, the formulation will result in an *equivalent strain* $\varepsilon^{eff} = \left(1-d\right)\varepsilon$ and in equivalent stress and strain simultaneously, respectively. More information about these formulation can be obtained in the following references [180, 461]. These DM principles are adopted in the so-called *Continuum Damage Mechanics* (CDM). This approach considers the fracture as a damage accumulation process

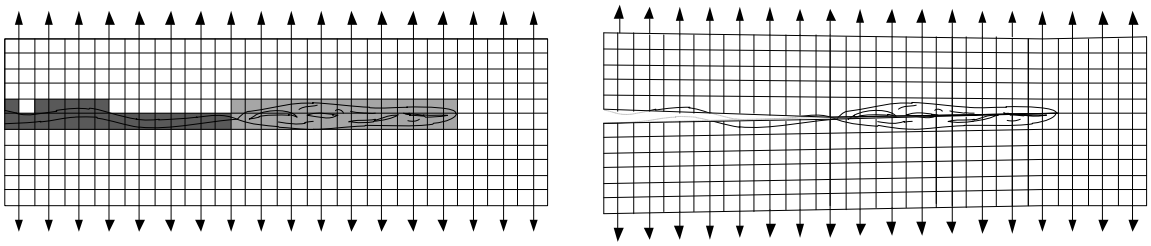

Figure III.9: Smeared *vs.* discrete crack models.

distributed in a finite zone of the domain [283, 309, 389] (see Figure III.9-a). This type of formulation is also called *smeared crack modelling* and seems to be an obvious solution to simulate the dispersed development of concrete micro-cracking. This formulation has been also used for modelling other materials, such as metals, rock, *etc*. (see Desmorat [166] for a list of models).

This approach contrasts with modelling fracture as a discontinuity introduced at the element interfaces (see Figure III.9-b), in which the amplitude and propagation are controlled by a rupture criteria [112, 162, 454, 455, 525]. The so-called *discrete crack modelling* lies outside the scope of the damage mechanics addressed in this section and presents the best modelling approach to the physical problem after localization, because the crack is directly simulated as a discontinuity. Nevertheless, the traditional approach requires following the crack propagation and making sequential adaptations to the mesh [58, 75, 581], although this can be avoided using enriched elements with embedded cracks, *e.g.* within the framework of the extended FEM (see section 2.2.7).

- Damage variables

The large majority of the damage models are based on scalar damage variables. In this formulation, damage is represented as an averaged damage density, which is not associated with any direction (isotropic damage) [95, 128, 136, 381, 387]. This can be acceptable to model micro-cracking that has to some extent a diffuse nature, although clearly direction oriented, but is not a representative way to simulate macro-cracking, which has very significant anisotropy. Despite this limitation, the directional tension-compression response of the concrete can be simulated to some extent by using two independent variables, *tension damage* d_+ and *compression damage* d_-. Despite these drawbacks, isotropic damage models present significant advantages related to the simplicity and efficiency of this solution.

Other types of damage variable were used to extend the concept of isotropic to anisotropic damage [142, 310, 463, 470], like the use of high-order tensor damage variables [423, 551] and coupling with plasticity models [2, 41, 327, 343, 345, 462].

Table III.2 presents a non-exhaustive list of damage variables proposed in the bibliography, ordered by the type of damage variable adopted.

Table III.2: Damage model classification in terms of the damage variable.

Damage Variable Types		Examples
Scalar	1 variable	Kachanov [299], Yazdani [583], Comi *et al.* [140]
	2 dependent variables	Mazars [381, 382], Oliver *et al.* [421]
	2 independent variables	Lemaitre *et al.* [330], Ortiz [423], La Borderie [316], Faria [211], Comi *et al*. [128, 137]
Vector	1 variable	Davison [161]
Tensor	2^{nd} Order	Murakami *et al.* [410], Dragon *et al*. [179], Ramtani [469]
	4^{th} order	Ju [297], Lemaitre *et al*. [331]

- Thermodynamic framework

The damage formulation can be based on the thermodynamics of irreversible processes to ensure that the damage evolution process is thermodynamically consistent and with a correct dissipation of the available internal energy [211]. The basic assumption used in the majority of damage models is that the material characteristics are temperature independent and the process is isothermal, thus removing the temperature from the thermodynamic state potentials and equations.

According to what is presented in section 2.1.1, the first step is to identify the *state variables* of the process that define the material state at any time. The thermodynamic *potential* is written as a function of the state variables, usually using the *Helmholtz free energy* or the *Gibbs free energy*.

Considering the *Helmholtz free energy* defined in terms of the strain tensor and of a single scalar damage variable *d* for simplicity:

$$\psi = \psi\left(\underline{\boldsymbol{\varepsilon}}, d\right). \tag{III.47}$$

According to the equations (III.19), the stress tensor and the thermodynamic force associated with the damage variable are given by:

$$\underline{\boldsymbol{\sigma}} = \rho \frac{\partial \psi}{\partial \underline{\boldsymbol{\varepsilon}}}, \tag{III.48}$$

$$Y = -\frac{\partial \psi}{\partial d}, \tag{III.49}$$

where Y is known as the *strain energy density release rate* that can be interpreted as the thermodynamic force released by a unit growth of the damage variable. From equation (III.13), it is also possible to conclude that the development of damage is irreversible $\delta d \geq 0$.

- Constitutive model

The constitutive model requires defining: i) a *dissipation potential,* ii) the *loading/unloading conditions* to define when damage can occur; ii) an *evolution law*, to define how much damage is generated; and iii) the *constitutive relation*, to relate deformation and stress fields.

The *dissipation potential* defines when damage can occur using the *loading function f*. The most common definition for this function is to use negative values for the elastic domain, a null value

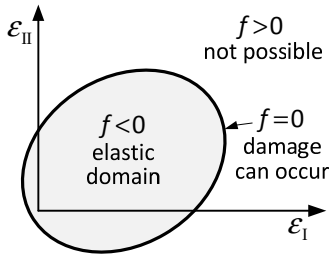

Figure III.10: Dissipation potential.

when the material can dissipate energy by developing damage and positive values are not admissible (see Figure III.10). Commonly, the *dissipation potential* is defined in terms of the strain field using an *comparison strain* $(\tilde{\varepsilon})$:

$$f = \tilde{\varepsilon} - \tilde{\varepsilon}^e(t) \leq 0\,, \tag{III.50}$$

where $\tilde{\varepsilon}^e$ represents the current kinematic limit for the elastic behaviour, defined by:

$$\tilde{\varepsilon}^e(t) = \max\left\{\tilde{\varepsilon}_0^e, \max_{\forall \tau \leq t}\left(\tilde{\varepsilon}(\tau)\right)\right\}, \tag{III.51}$$

leading to a non-decreasing parameter.

The non-decrease restriction for $\tilde{\varepsilon}^e$ is not mandatory because a material can develop inelasticity at a lower level of the dissipation potential (*e.g.* the *Bauschinger effect*). However, it will be shown ahead that the evolution of the damage variable is indirectly related to this function, hence, a decrease of $\tilde{\varepsilon}^e$ will result in a decrease of damage, which is not acceptable thermodynamically.

The dissipation potential is very similar to the yield function adopted in most plasticity models (see Figure III.1-a). The major difference is related to the fact that the dissipation potential is usually defined in the strain space instead of the stress space.

The *loading/unloading conditions* identify when damage can occur. This can be achieved using the following equations:

$$f \leq 0\,, \tag{III.52}$$

$$\delta d \geq 0\,, \tag{III.53}$$

$$f\ \delta d = 0\,. \tag{III.54}$$

The first two relations give the domain of validity of each variable, *i.e.* the dissipation potential must be non-positive and the damage increments cannot be negative. The third expression relates both variables imposing that in order to have damage increments the dissipation potential must be null.

The *evolution law* defines how much damage is generated using the function *g*. Similarly to the dissipation potential, this law is defined as a function of an *comparison strain* $\tilde{\varepsilon}$ and of memory variables $\tilde{\varepsilon}^e$:

$$g = g\left\{\tilde{\varepsilon}\ , \tilde{\varepsilon}^e(t)\right\}. \tag{III.55}$$

Different rules can be chosen for this function. However, they must result in non-negative energy

dissipation. A simple way to define this function is to use the same procedure adopted in the associative plasticity models, which is to use the same function used to define the dissipation potential (yield function) and the damage evolution law (plastic strain evolution law):

$$g = f = \tilde{\varepsilon} - \tilde{\varepsilon}^{e}(t)\,. \tag{III.56}$$

For a continuous and convex dissipation function, it is possible to define the damage increments as normal to the dissipation potential with regard to the strain energy density release rate, similarly to what is done in plasticity (III.30):

$$\delta d = \delta d_{*}\frac{\partial f}{\partial Y}\,. \tag{III.57}$$

The constitutive relation can be computed from (III.48). Assuming for a moment that the thermodynamic potential is defined by:

$$\rho\psi = \frac{1}{2}(1-d)\,\underline{\boldsymbol{\varepsilon}} : \underline{\mathbf{k}} : \underline{\boldsymbol{\varepsilon}}\,, \tag{III.58}$$

where d is a scalar damage variable and $\mathbf{k}$ and $\boldsymbol{\varepsilon}$ are the elastic stiffness and the strain tensors, respectively. Then, using equation (III.48), it is possible to retrieve:

$$\underline{\boldsymbol{\sigma}} = \rho\frac{\partial\psi}{\partial\underline{\boldsymbol{\varepsilon}}} = (1-d)\,\mathbf{k}\,\boldsymbol{\varepsilon} = \mathbf{k}^{*}\,\boldsymbol{\varepsilon}\,. \tag{III.59}$$

This last equation is usually called the *secant constitutive relation* and results in a generalized form of the expression obtained in (III.44) using a physical approach.

The strain energy density release rate can be computed from (III.49):

$$Y = -\frac{\partial\psi}{\partial d} = \frac{1}{2}\,\boldsymbol{\varepsilon}\,\mathbf{k}\,\boldsymbol{\varepsilon}\,, \tag{III.60}$$

which returns the elastic energy.

This last result can be used to justify the restriction made to the increase of the damage variable in equation (III.53). Going back to the definition (III.13):

$$Y\,\delta d \geq 0\,, \tag{III.61}$$

it is possible to confirm that $\delta d \geq 0$ because the elastic energy defined in equation (III.60) results from a quadratic form that is always positive.

Most models used in the framework of CDM are defined using one of the following strategies:

i. Adopt an expression both for the dissipation potential and for the evolution law and compute the damage evolution through the evolution law, *e.g.* Mazars' model [381] (see section 2.2.7);
ii. Adopt an expression for the dissipation potential and compute the damage evolution equating $f = 0$, *e.g.* Comi-Perego 2DV model [128, 137];
iii. Adopt an associative model $f = g$ to define the constitutive model, *e.g.* Comi-Perego 1DV [140] model (see section 2.2.7).

2.1.6 Localization and regularization

Localization, *a.k.a. strain localization*, is a real physical phenomenon that occurs in materials with softening behaviour, in which the deformations tend to concentrate in a single and reduced region. This phenomenon is evident in *quasi*-brittle materials, such as concrete, where the inelastic behaviour starts with a more or less distributed micro-cracking that concentrates into a macro-crack.

The size of the region exhibiting localization is finite and can be related to a material property because it depends on the meso-structure of the material, *e.g.* dimension of the aggregates. In the scope of this thesis, the *nonlocal length* will be referred to by the symbol L_{nl} and common values for concrete are discussed in section 2.2.4.

To illustrate this phenomenon, Figure III.11 presents the simple case of a tie made of a material that presents a linear behaviour up to the peak stress $(\varepsilon_0, \sigma_0)$, and afterwards a linear softening branch up to ε_u. The response of the tie can be divided into three main stages (see Figure III.11): i) firstly, the deformation is uniform and proportional to the total length *L*; ii) afterwards, there will be a region made of a slightly weaker material, *e.g.* in the middle of the element, where the deformation tends to localize and the rest of the bar unloads elastically; iii) when the tie fails, all strain is concentrated (localized) near the weaker part of the material and the global displacement is proportional to this length.

A similar phenomenon occurs when materials exhibiting softening are simulated numerically. In this case, local models have no knowledge about the finite dimension of a localized region representative of the material. The results from numerical simulation using local models show that the deformation tends to concentrate in the smallest possible structural unit, which in the case of the FEM is a finite element. As a result, the boundary value problem becomes ill-posed and the solution becomes mesh-

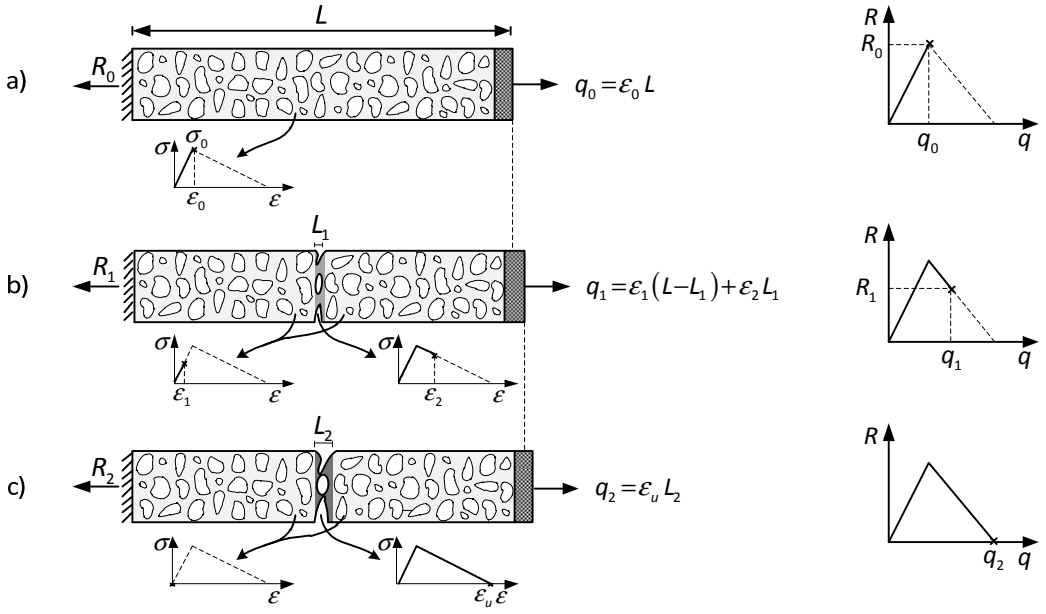

Figure III.11: Strain localization phenomenon.

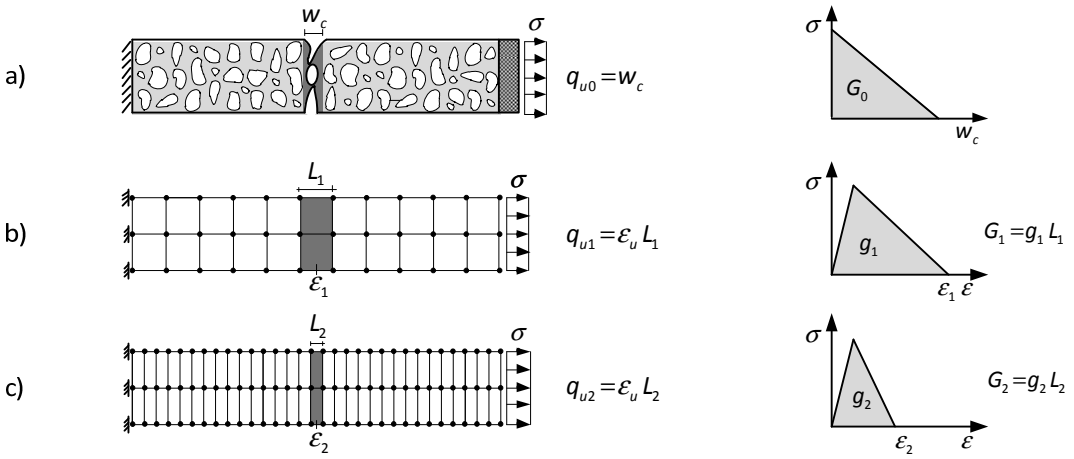

Figure III.12: Mesh dependency of local continuum damage models.

dependent and therefore losses objectivity [296]. Translated into mathematical language, this is called the loss of ellipticity of the governing differential equations. At a limit case, decreasing the element size will result in null energy dissipation when cracking develops, which is not physically acceptable. This situation is illustrated in Figure III.12, where the mesh dependency is evident and the energy dissipated tends to be null when the width of the element approximates zero.

The main concept of smeared cracking is also represented in Figure III.12. In this type of approach the width of a crack w_c is simulated on average by an *equivalent strain* $\bar{\varepsilon}$ that in this case depends on the *element length* L_e:

$$w_c = \bar{\varepsilon}\, L_e \,. \tag{III.62}$$

Several techniques were proposed to avoid the loss of objectivity within the framework of the CDM. The most used are based on the *fracture energy* [44, 211, 420], on *nonlocal variables* [35, 39, 40, 45, 46, 61, 138-140, 292, 295, 448] and on the *gradient formulation* [127, 129, 428] explicit [135, 181, 182] inspired on plasticity models [195, 409] and implicit [436-439], which can be interpreted as nonlocal integral models [440].

Table III.3 presents a non-exhaustive compilation of the regularization techniques with some examples of the most relevant works.

Table III.3: Most common regularization techniques used with the framework of CDM.

Regularization Type		**Examples**
Energy-Based		Bažant *et al.* [44, 47]; Oliver [420], Faria [211]
Nonlocal	**Integral Nonlocal**	Bažant *et al.* [35, 39-41, 45, 46], Borino *et al.* [61], Comi *et al.* [138-140], Jirásek [291, 292, 294, 295], Pijaudier-Cabot *et al.* [448]
	Gradient	Comi *et al*. [127, 129], Driemeier *et al.* [181, 182] Engelen *et al.* [195], Frémond *et al.* [228], Mühlhaus *et al.* [409] Pamin [428], Peerlings *et al.* [436-439]

- Energy-based regularization

Energy-based regularization [44, 47, 420] enforces that the evolution of a crack dissipates a specific amount of energy, which is considered a characteristic of the material. It is important to notice that this methodology does not regularize the problem, *i.e.* mesh dependency is not avoided and mathematically the boundary value problem is still ill-posed. Instead, this approach only ensures that the global energy dissipated in the fracture by the model is similar to that experienced by the simulated material.

Generally, this approach starts from estimating the fracture energy (*e.g.* mode I) by experimental testing and assumes that this can be considered a material property, thus neglecting the size effect related to fracture. The definition of this parameter is given by (III.38):

$$G_f^{\mathrm{I}} = \int_0^{\infty} \sigma \, dw_c \, .$$

In practice, this quantity is computed from global measures, *e.g.* from three-point bending or tension tests. This issue will be discussed in more detail in section 2.2.4 for concrete.

In CDM the equivalent quantity is the energy dissipated in the continuum-based fracture (see Figure III.13):

$$g_f^{\mathrm{I}} = \int_0^{\infty} \sigma \, d\bar{\varepsilon} \, , \tag{III.63}$$

where g_f represents the fracture energy distributed in the element and is often known as the *fracture energy density*.

For local models, the averaged fictitious equivalent strain $\bar{\varepsilon}$ develops in a single finite element band. Consequently, the dissipated energy is dependent on the finite element size. This parameter is often called the *characteristic length* of the finite element L_c (see Figure III.13).

Enforcing that both approaches dissipate the same amount of energy results in:

$$G_f^{\mathrm{I}} = g_f^{\mathrm{I}} L_c \;\Rightarrow\; g_f^{\mathrm{I}} = \frac{G_f^{\mathrm{I}}}{L_c} \, . \tag{III.64}$$

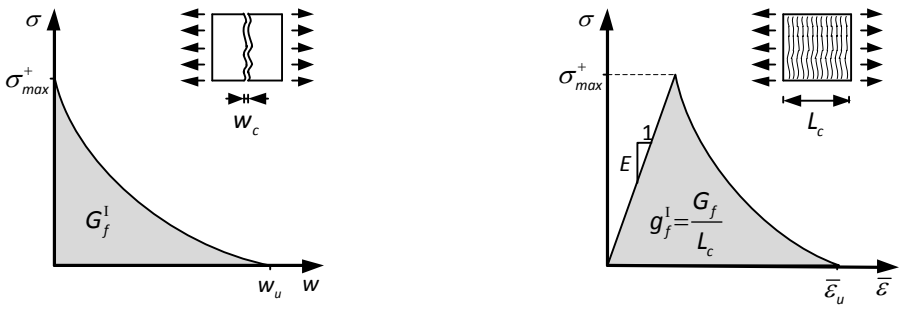

a) discrete cracking b) smeared cracking

Figure III.13: Energy-based regularization, adapted from Faria [211].

This last equation presents two options to equate the fracture energy. This first approach is to change the element size, and thus the characteristic length and leave the constitutive relation unchanged. This method has a large impact on the discretization and can have an impact on the problem size and on the accuracy of the results.

The second option is to adjust the fracture energy density through the softening branch of the constitutive model. This approach is very convenient because it has a very small impact on the discretization. Nevertheless, for large elements, *e.g.* the ones used to model large structures such as dams, the regularization can lead to the undesirable situation of having very sharp softening branches, or even, of going back in the stress-strain curve [211].

By adjusting the softening branch of the constitutive model, the ultimate strain becomes dependent on the characteristic length. However, the displacement ceases to depend on the element size:

$$\begin{cases} q_u = \varepsilon_u \; L_c \\ \varepsilon_u = f\left(g_f = \dfrac{G_f}{L_c} \right) \end{cases} \Rightarrow \quad q_u = f\left(G_f\right). \tag{III.65}$$

The characteristic length can become not so obvious for general two-dimensional or three-dimensional cases. Most applications use an approximated averaged value for this parameter. Oliver [420] proposed a generalized and consistent way to compute the characteristic length even for complex cases. A simple estimative can be computed from [211]:

$$L_c = \sqrt[nd]{\Omega}\,, \tag{III.66}$$

where *nd* represents the number of dimensions of the element and Ω represents the length/area/volume of the domain associated with the Gauss point.

- Nonlocal regularization

The second group of regularization models are the so-called *nonlocal regularizations models*. This approach includes the *integral nonlocal methods* and the *gradient methods*. The *gradient method* was not adopted in this work. Additional information about this method can be obtained in the following references [127, 129, 228, 428, 509].

The nonlocal approach consists in replacing a local-based variable with its nonlocal counterpart obtained by combining the values in the spatial vicinity of the point under consideration [294]. In particular, the *integral nonlocal method* computes the nonlocal variable $\overline{a}$ using the following general expression [139]:

$$\overline{a}\left(\mathbf{x}\right) = \int_V W\left(\mathbf{x},\mathbf{s}\right) a\left(\mathbf{s}\right) d\mathbf{s}\,, \tag{III.67}$$

where *a* is the local variable, $W\left(\mathbf{x},\mathbf{s}\right)$ is the *nonlocal weight function*, ***s*** are the coordinates of the local variable (*reference point)* and ***x*** are the coordinates of the neighbouring point (*source point*) being considered to the nonlocal definition of the variable *a*.

Commonly, the weights depend on the distance between the reference and source points that can be computed from $r = \left\| \mathbf{x} - \mathbf{s} \right\|$.

The *nonlocal weight functions* are often considered as the *Gaussian function* [294]:

$$W_0(d) = exp\left(-\frac{r^2}{2L_{nl}^2}\right), \tag{III.68}$$

or the *bell-shaped function* [294]:

$$W_0(d) = \begin{cases} \left(1-\frac{r^2}{R^2}\right)^2, & \text{if } 0 \le r \le \text{R} \\ 0, & \text{otherwise} \end{cases}, \tag{III.69}$$

where L_{nl} represents the nonlocal length, *a.k.a. internal length*, that controls the opening of the weight function and R is a parameter related to L_{nl} that can be seen as an *interaction radius*.

Figure III.14 presents both functions defined in terms of the parameter r and it is possible to conclude that the shapes are similar. However, there is a significant difference between both formulations related to the fact that the Gaussian function is unbounded, *i.e.* the interaction ratio is theoretically infinity [294].

At the end, the weights should be rescaled to avoid changes in the absolute values of the original local variables. This can be achieved for each weight by using:

$$W(\mathbf{x},\mathbf{s}) = \frac{W_0(\mathbf{x},\mathbf{s})}{\int_V W_0(\mathbf{x},\mathbf{s})\, d\mathbf{s}}. \tag{III.70}$$

It is common to define a cut-off distance for the Gaussian function to avoid compromising the efficiency of the models by considering source points associated with very small weights, which contribute very little to the nonlocal variable. For example, points located at a distance to the reference point larger than $3L_{nl}$ will be associated with a weight less than $W_0 < exp(-4.5) \approx 1.111\%$ and this value would decrease even more after scaling the weights using expression (III.70).

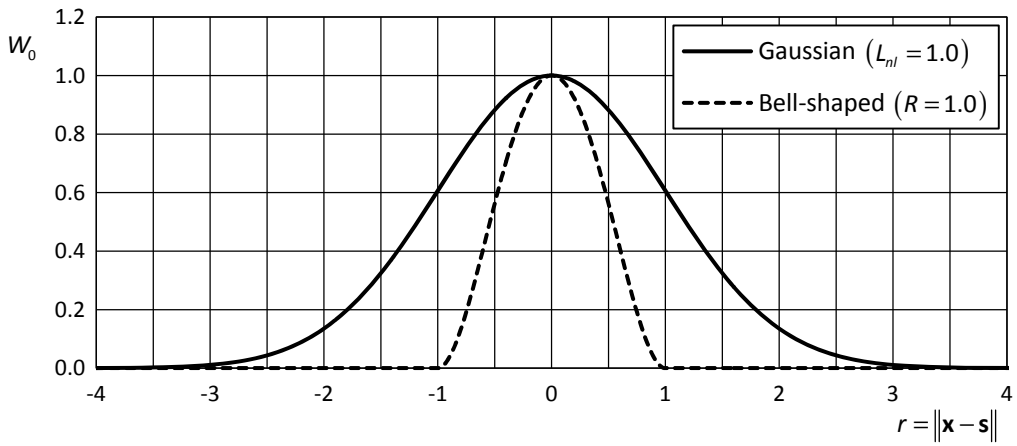

Figure III.14: Nonlocal weight functions.

2.2 Concrete

Concrete presents a complex behaviour at the micro, meso and macro scales. At the macro scale, concrete presents very different responses under compression and tension loads. It is strongly affected by multi-axial stress states and presents intense cyclic degradation. The response is governed by the development of dispersed and localized cracking, and inelastic deformations. In addition, it is sensitive to strain-rate and presents a significant size effect and strength dispersion. This section presents a summarized description of the main mechanical characteristics of concrete.

2.2.1 Material description

- Composition

Concrete is a composite material that is made from mixing: i) *cement* (commonly Portland cement); ii) *aggregates*, generally a coarse aggregate such as gravel limestone or granite, plus a fine aggregate such as sand; iii) *water* and iv) *admixtures*, such as fly ash or silica fume. The admixtures are used to improve or change specific concrete characteristics, like for example: strength improvement; drying acceleration or retardation; shrinkage reduction; flowability improvement; corrosion protection; mix water reduction; alkali-silica reactivity inhibition; air entrainment and colouring. Concrete solidifies and hardens after mixing due to a chemical process known as *hydration*. The amounts of each component in the mixture and the cure process determine the strength and other mechanical characteristics (see Figure III.15-a).

Concrete can be seen as composed by the following components: i) *cement paste*; ii) *aggregates*; iii) the *transition zone* between the cement paste and the aggregates (see Figure III.15-b). Although most of the fragility is concentrated in the transition zone, cracks can occur through the aggregates, *e.g.* Figure III.16-c. The aggregates also develop chemical interaction with the cement paste.

- Deterioration mechanisms

Concrete can be a durable material if preserved from some well-known degradation mechanisms, such as: i) *freeze-thaw cycles*, which result in expansion upon freezing of the water inside the pores, leading to cracking. Air entrainment admixtures are used to produce uniformly spaced air bubbles for stress relief; ii) *alkali-silica reaction*, which is a chemical reaction between the alkalis contained in the cement paste and certain reactive forms of silica within the aggregates. This reaction creates a gel that swells and causes cracking (see Figure III.16-a); iii) *sulphate attack* is a widespread form of chemical attack, in which the mono-sulphate phases, present in groundwater, soil, and seawater, are converted into ettringite phases, leading to large volume increases, which generate internal stresses and cause cracking (see Figure III.16-b); iv) *carbonation* occurs because the calcium bearing phases are attacked by the carbon dioxide in the air and converted to calcium carbonate, resulting in pH decrease from 12-13 to around 7-9, enabling corrosion that can lead to cracking and delamination; v) *chloride penetration* in the concrete from contact with environments containing chlorides, such as seawater or de-icing agents. The consequences are similar to carbonation.

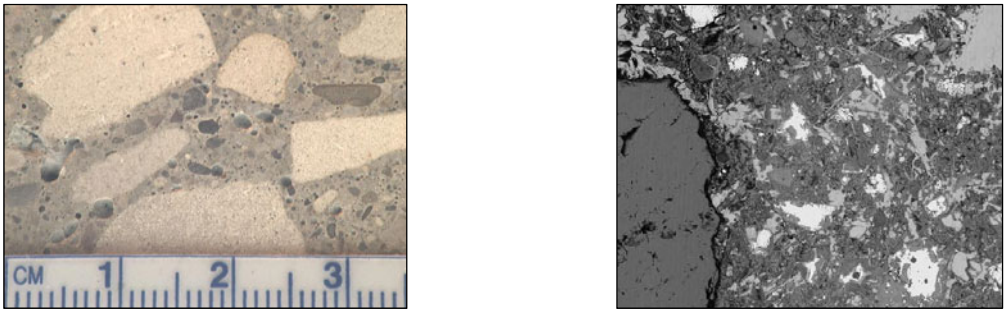

a) b)

Figure III.15: Concrete samples [529]: a) common concrete; b) paste/aggregate interface at 28 days (magnified by 750).

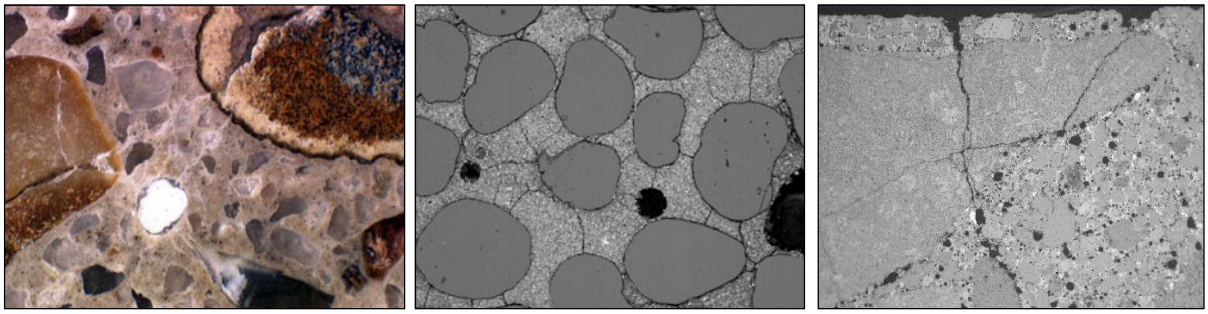

a) b) c)

Figure III.16: Concrete pathologies [529]: a) gel produced by an alkali-silica reaction;
b) cracks resulting from cement paste expansion; c) cracks through cement paste and aggregates.

2.2.2 Response to uniaxial loading

- Compression

The *compressive strength* f_c is normally given by tests for 28 days old cylinder or cube samples made while casting the concrete. The concrete strength tends to increase with time but that increase is very small after the 28 days and is often neglected to determine the strength to be used for the analysis and design of structures. Compressive strength tests are usually performed by hydraulic jacks compressing cylindrical or cubic samples up to failure (see Figure III.17-a).

When stressed with compression forces up to the *maximum resistance* f_c, a typical concrete specimen presents at least three distinct responses (see Figure III.18-a):

i. Under low intensity stresses $\sigma < 0.3 f_c$, the deformation is mainly due to reversible atom motions resulting in a nearly elastic behaviour;
ii. Increasing the stress to $0.3 f_c < \sigma < 0.7 f_c$, micro-cracking starts to develop, generating a clear nonlinear behaviour, stiffness degradation and permanent deformations;
iii. When the stress reaches the maximum resistance $\sigma \approx f_c$, some macro-cracks start to appear, spreading into a global discontinuity surface throughout the specimen;
iv. After reaching maximum resistance $\varepsilon_c > \varepsilon_c(f_c)$, a softening branch characterizes the response to prescribed displacements.

a) b) c)

Figure III.17: Concrete tests: a) and b) Compression test of a cylinder sample [563];
c) Brazilian splitting tensile test [259].

When subjected to high stresses, concrete develops irreversible internal damage until a brittle collapse occurs (see Figure III.17-b). Figure III.18-b presents typical experimental stress-strain curves for concrete with different resistance levels. It is possible to observe that the strain at peak stress presents small changes for all concrete grades (≈2-2.5‰). On the other hand, high resistance concrete presents less deformation capacity and is more fragile.

- Tension

The *tensile strength* f_{ct} is a difficult parameter to evaluate experimentally. Normally, three types of tests can be used [339]: i) *direct pull test*, where a tension force is directly applied to the specimen using gripping devices on the edges. This type of test presents some difficulties related to the eccentricity and additional stresses resulting from the gripping devices, that can lead to premature collapses. ii) *modules of rupture* test, in this indirect method a concrete beams is subjected to centre-point or two-point symmetric loading and the tensile strength is calculated assuming a linear stress distribution in the section. Usually this results in higher values when compared with the ones from the other tests; iii) the *Brazilian splitting test* was proposed by Carneiro *et al*. [76] and is also an indirect test for measuring the tensile strength that is very popular due to its simplicity. In this test, a cylindric concrete specimen is subjected to a compression force perpendicular to the cylinder axis by top and bottom plates (see Figure III.17-b). The cylinder will probably split in two halves and based on the load at which the cylinder splits, it is possible to compute an estimation of the tensile strength. More information can be found in the work of Lin and Wood [339].

The stress-strain relations are roughly linear until about 80% of f_{ct}. The tensile strength presents a large dispersion and is much lower than the one for compression loads: often $f_{ct} < 20\% f_c$. When the maximum value is reached, a large crack opens and the resistance decreases significantly following a sharp softening branch. The energy dissipated in this inelastic procedure, *a.k.a. fracture energy* (see section 2.1.3), and the softening branch depend on the composite structure of the material. It is essentially governed by the mechanical interaction of the aggregates with the cement-based matrix.

Near to failure, an inelastic volume increase occurs, *a.k.a. dilatancy* (see section 2.1.2), as presented in Figure III.20-a. Moreover, this phenomenon increases Poisson's ratio from values of about 0.20 to values up to 0.30-0.35, as presented in Figure III.20-b.

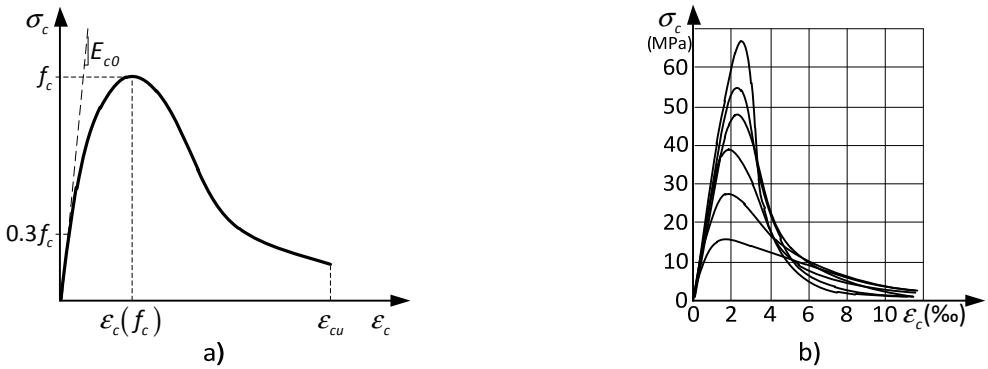

Figure III.18: Concrete under monotonic compression: a) typical response; b) experimental results, adapted from [577].

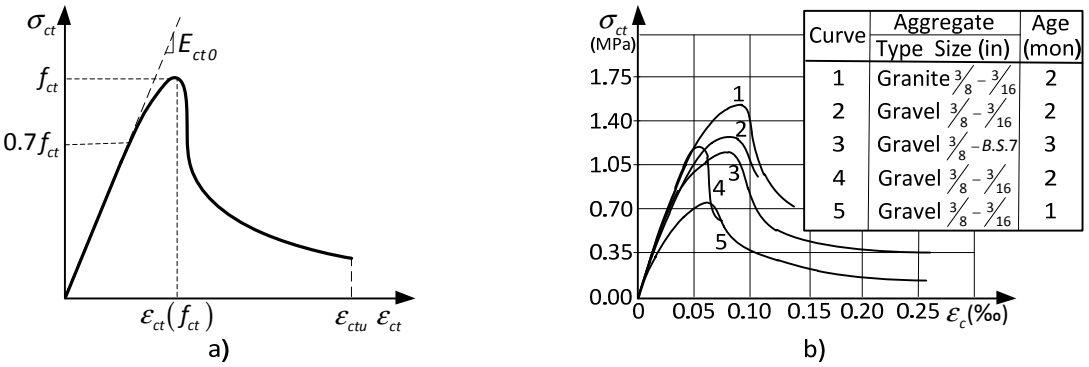

Figure III.19: Concrete under monotonic tension: a) typical response; b) experimental results, adapted from [278].

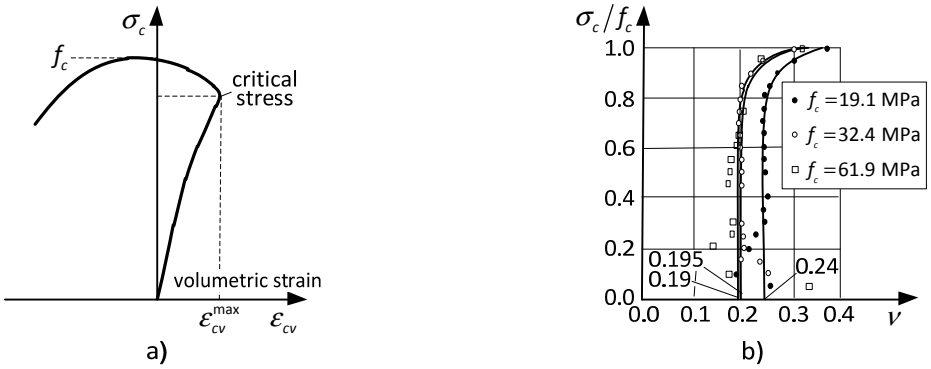

Figure III.20: Concrete deformation under compressive loads, adapted from Chen [102]:
a) volumetric strain; b) lateral deformation.

- Cyclic and alternating loading

The typical concrete response to compressive and tensile cyclic loads is presented in Figure III.21-a and Figure III.22-a. It can be observed that the cycles are enveloped by the monotonic curve [83, 387, 515] and the unloading and loading paths tend to cross at levels with a regular pattern.

Moreover, under compressive loads the successive cycles are followed by stiffness degradation mainly due to the spread of micro-cracks. Irreversible deformations are also present caused by concrete crushing. Furthermore, for tensile loading the stiffness degradation is also present and permanent deformations occur due to locking and slip phenomena between surfaces avoiding the complete closure of the cracks [211]. The experimental data presented in Figure III.21-b and in Figure III.22-b exemplifies and confirms this behaviour.

Under alternating loads, when passing from compression to tension and *vice-versa,* the concrete presents what is called the *stiffness recuperation effect, a.k.a.* the *unilateral effect* (see Figure III.23), which results from the directional properties of the micro-cracks [211, 582].

2.2.3 Response to multi-axial loading

In practical situations, concrete is under multi-axial stress states. Concrete is particularly sensitive to combined stresses that can significantly increase or decrease the resistance.

Figure III.24 presents a selection of experimental results performed with different combinations of biaxial stresses. It can be seen that for biaxial compression (see Figure III.24-a/d) the resistance can increase more than 20%. It is also possible to identify a slight ductility increase.

On the other hand, when tensile forces are combined with compression, the resistance and the ductility tend to decrease substantially as presented in Figure III.24-b. From the data presented in Figure III.24-c, it is possible to observe that the combination of biaxial tensile forces seems to produce a less significant effect on the resistance and ductility.

Biaxial stress states can result from the confinement effect resulting from the passive constraining forces created by the reinforcements when the concrete expands due to Poisson's effect. Confinement can significantly change the response of concrete, not only in terms of resistance but also of ductility. This topic is covered in the work of Richart *et al.* [480] and section 2.5.3 presents more details about this subject.

The presence of shear forces may significantly reduce the compressive and tensile concrete resistance. This effect is demonstrated in the experiments performed by Bresler *et al.* [67] that are presented in the Figure III.25.

Under triaxial compressive stress states, the increase of compressive resistance can be very remarkable. This can be observed in the results obtained by Coutinho *et al.* [148] (see Figure III.26-a) and by Balmer [27] (see Figure III.26-b). Furthermore, when tensile longitudinal stresses are combined with biaxial compressive forces, a considerable strength decrease can be observed (see Figure III.26-a).

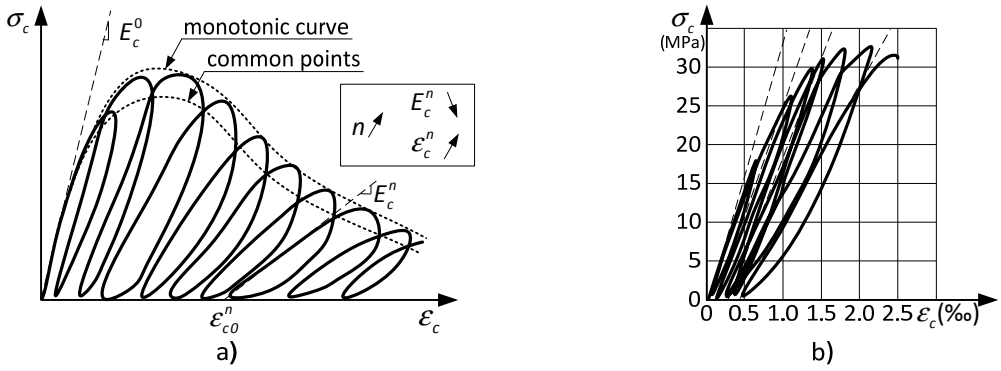

Figure III.21: Concrete under cyclic compression: a) typical response, adapted from [303]; b) experimental results, adapted from [383].

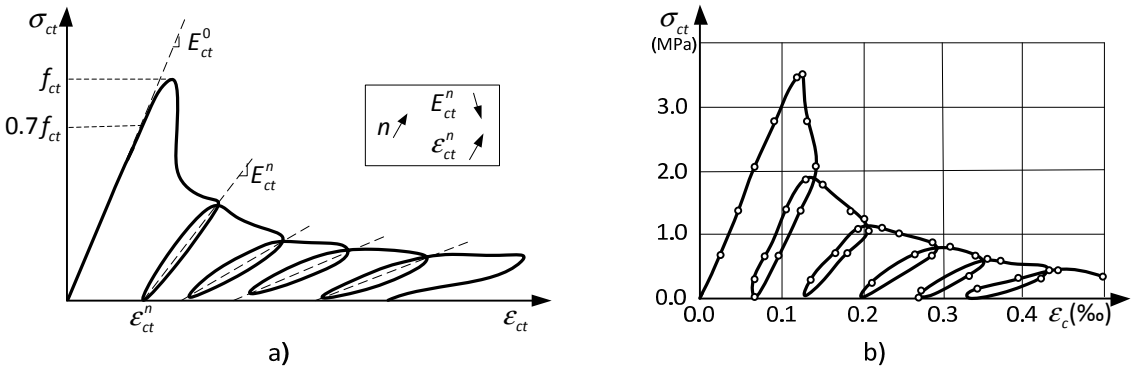

Figure III.22: Concrete under cyclic tension: a) typical response; b) experimental results, adapted from [249].

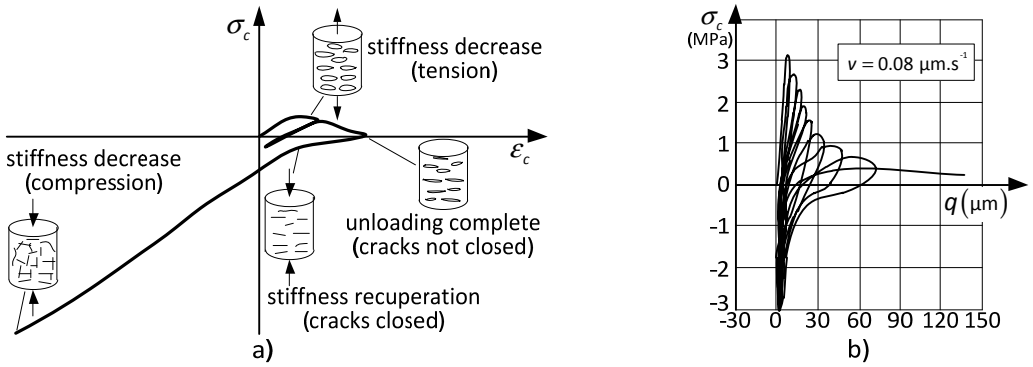

Figure III.23: Stiffness recuperation effect under alternating loads: a) typical response, adapted from [469]; b) experimental results, adapted from [475].

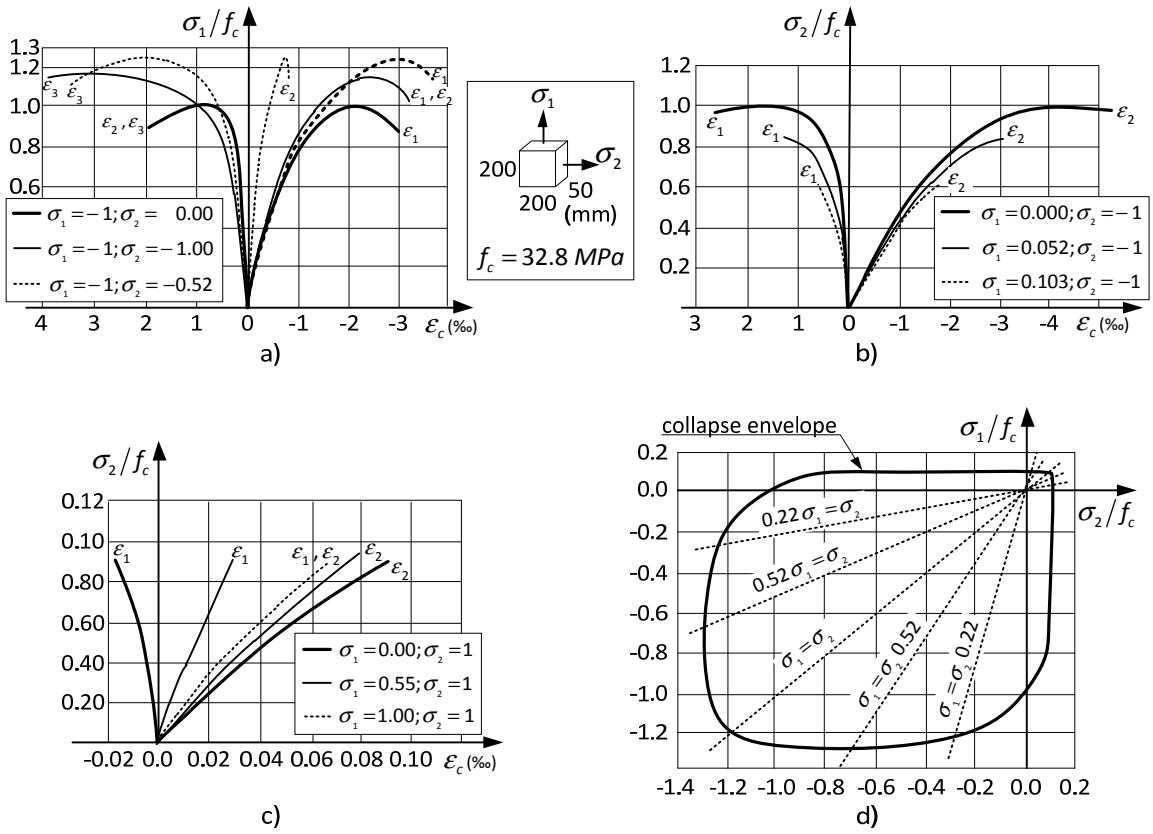

Figure III.24: Concrete under biaxial loads, adapted from [236, 272, 314]: a) compression-compression; b) tension-compression; c) tension-tension; d) effect on resistance.

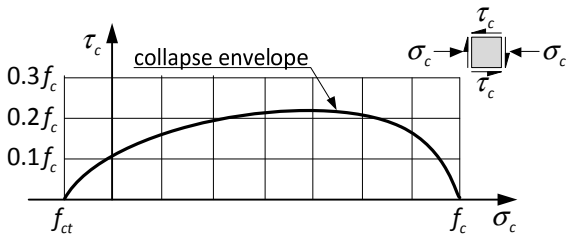

Figure III.25: Effect on the tensile and compressive strength of shear stresses, adap.from [67].

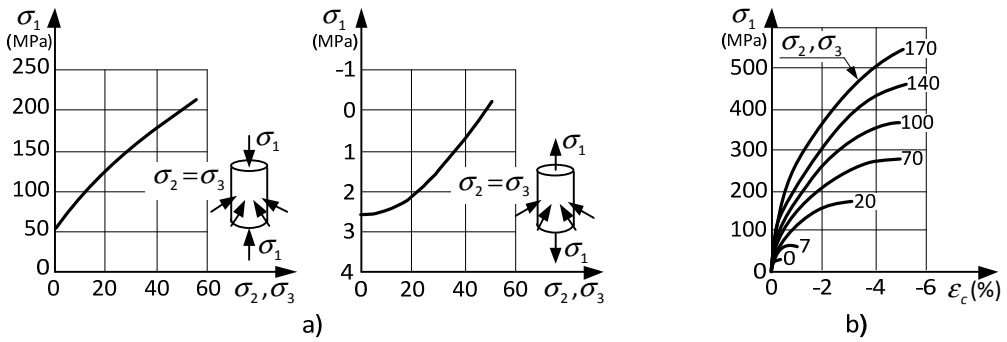

Figure III.26: Concrete under triaxial loads: a) experimental results, adapted from [148]; b) experimental results, adapted from [27].

2.2.4 Fracture behaviour

There has been some heterogeneity in the nomenclature used to describe the concrete fracture. To avoid any misunderstanding, it is advisable to clarify the meaning of some crack-related quantities, namely: for nonlocal length or average width of the *fracture process zone* (FPZ), the symbols w_c or L_{nl} are used (see section 2.1.6) and for the length of the FPZ the symbol L_{FPZ} is used (see Figure III.27-a). In addition, $G_f^{\mathrm{I}}, G_f^{\mathrm{II}}, G_f^{\mathrm{III}}$ will be used to describe the mode I, II and III fracture energy, respectively.

The authors Bažant and coworkers [34, 44] defend that the width of the FPZ is constant and should be treated as a material property. This quantity can be seen as the relation between the energy dissipated per unit area $\left(\mathrm{J/m^2}\right)$ and the energy dissipated per unit volume $\left(\mathrm{J/m^3}\right)$ [46]. Data from numerous experimental data show that L_{nl} is roughly constant and that for stable direct tensile tests the following expression can be used:

$$w_c = L_{nl} = n d_a ,$$

where d_a is the *maximum aggregate size* and n is an empirical constant, which can be taken as around $n = 3.0$ for concrete. Using strain measurements with *Fiber Bragg Gratings*, Denarié *et al.* [163] confirmed the expression proposed by Bažant et al., in this case with $n = 3.75$.

Concerning the length of the FPZ, following the work of Irwin [288], Hillerborg [270] proposed the following expression for this material-related parameter:

$$L_{FPZ} = \frac{G_f^{\mathrm{I}} E}{f_{ctm}^2}, \tag{III.71}$$

where G_f^{I} is the mode I fracture energy, E is the elasticity modulus and f_{ctm} is the mean tensile strength.

As described before, the fracture energy is strongly related to the post-peak resistance of the concrete and this is influenced by the size and shape of the aggregates. This relation is well demonstrated in Figure III.19. Nevertheless, some other concrete parameters influence the fracture energy, and as before, this parameter is influenced by the size of the specimen.

There are several ways to determine the fracture energy for cementitious materials, *e.g.* see Gdoutos [234]. As presented in Figure III.27-b, the fracture energy can be computed from the global force-

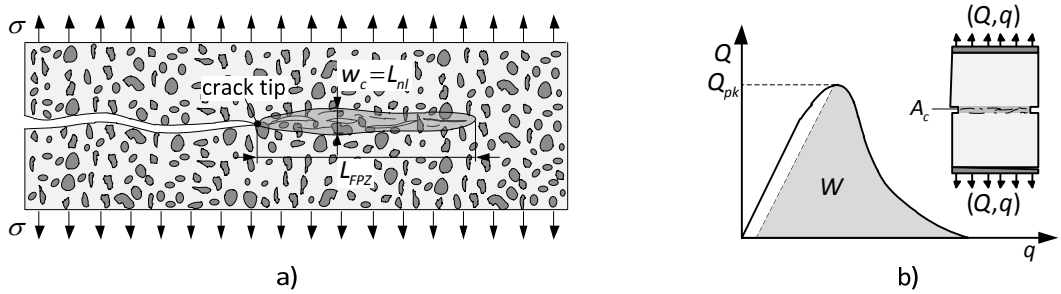

Figure III.27: Concrete fracture: a) crack-related quantities; b) computing mode I fracture energy from tension tests.

displacement curve that characterizes the post-peak response of the specimen under tensile loading. This can be done by computing the area *W* below this curve and removing the work developed at the pre-peak phase, because this work is not associated with the fracture process. The author Petersson [445] defends that the pre-peak work should be defined by an unloading branch parallel to the initial stiffness (see Figure III.27-b), although some other authors adopt a secant to the origin. This energy should be divided by the *crack area* A_{cr}, leading to:

$$G_f^{\mathrm{I}} = \frac{W}{A_{cr}} . \tag{III.72}$$

The results from tension or bending tests with different specimen sizes and different notch geometries may result in significant differences in the results. This led to the need of having a standard test to compute the force-displacement curve. In 1985, RILEM [483] presented a recommendation regarding the determination of the fracture energy for mortar and concrete using a standardized three-point bending test using notched beams (see Figure III.28), which was strongly influenced by the work of Hillerborg [269]. In this test, the size of the specimen is related to the *maximum aggregate size* $\left(d_{\max}\right)$ and the notch depth should be half the height of the beam and the width less than 10 mm. The fracture energy is computed from the expression:

$$G = \frac{W_0 + M\,g\,q_0}{A_{lig}} . \tag{III.73}$$

where W_0 is the shadowed area below the force-load curve, *M* is the total mass of the specimen between the supports plus the supported loading equipment, g is the gravity acceleration, q_0 is the displacement at failure and A_{lig} is the area of the ligament, which is defined as the projection of the fracture zone on a plane perpendicular to the beam axis. The theoretical basis of this test is presented in the work of Hillerborg for RILEM [269]. The Japanese Concrete Institute also published a standard for computing the concrete fracture energy, which is also based in three-point bending tests and in a similar procedure [289].

In the work of Wittmann and co-workers [277, 546, 578], a series of specimens to evaluate the mode I fracture energy G_f^{I} for different types of concrete was tested. The results are expressed in terms of the maximum aggregate size in Figure III.29. It can be observed that the lowest fracture energy is measured on pure hardened cement paste, in which $d_a = 0.01$ mm, which corresponds to the

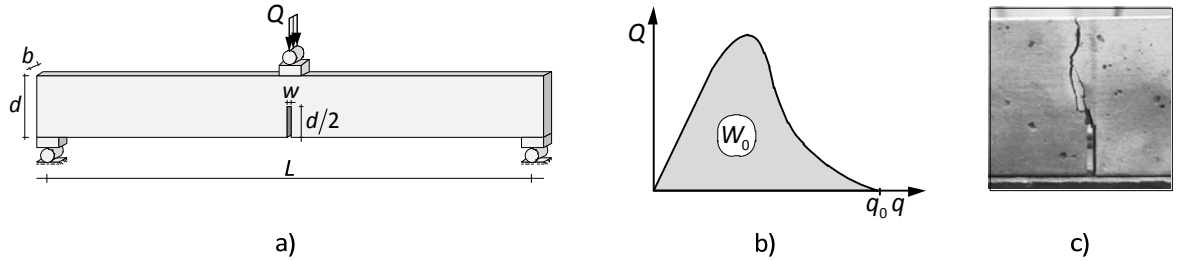

Figure III.28: RILEM's recommendation for computing the fracture energy for mortar and concrete elements:
a) test apparatus [483]; b) global force-displacement curve [483]; c) Example of a specimen tested, taken from [543].

dimensions of the remaining unhydrated clinker particles [578]. The maximum values were obtained for concrete typically used in dams with aggregate sizes up to 120 mm.

The authors Trunk and Wittmann [546] suggested the following expression to determine the fracture energy as a function of the maximum aggregate size based on the experimental data presented in Figure III.29-a:

$$G_f^{\mathrm{I}}\left(\mathrm{J/m^2}\right)=80.6\left\{d_a(\mathrm{mm})\right\}^{0.32}. \tag{III.74}$$

A chosen set of numerical values obtained using this expression are also presented in Table III.4-a. It can be seen that fracture energy values around 125 to 200 $\mathrm{J/m^2}$ are expected for a micro-concrete, 200-250 $\mathrm{J/m^2}$ for a normal concrete and up to 380 $\mathrm{J/m^2}$ for the concrete used in dams.

In the work published by Hillerborg [268], the results of 197 beams tested by six laboratories according to the draft RILEM recommendations [483] are presented. The data collected is summarized and presented graphically in Figure III.29-b. It can be seen that this values are similar to ones presented in Figure III.29-a, although slightly inferior.

Hilsdorf *et al.* [271] proposed the following expression to estimate G_f^{I} in the absence of experimental data:

$$G_f^{\mathrm{I}}\left(\mathrm{J/m^2}\right)=a_d\left\{f_{cm}\left(\mathrm{MPa}\right)\right\}^{0.7}, \tag{III.75}$$

where f_{cm} is the mean concrete compressive strength that can be taken as $f_{cm}=f_{ck}+8$, and a_d is a coefficient depending on the maximum aggregate size d_a defined for three values: $a_d=4$ for $d_a=8$ mm; $a_d=6$ for $d_a=16$ mm and $a_d=10$ for $d_a=32$ mm. The same authors presented an expression for the FPZ length that is derived from (III.75) and (III.71):

$$L_{FPZ}=600\left\{f_{cm}\left(\mathrm{MPa}\right)\right\}^{-0.3}. \tag{III.76}$$

The experimental results that led to the expressions (III.75) and (III.76) are presented in Figure III.30 and compared with the results provided by these equations. The work of Hilsdorf *et al.* [271] was adopted in the Model Code 90 [390] for estimating the fracture energy of concrete. For common concrete classes the resulting fracture energy is presented in Table III.5.

As a conclusion regarding the mode I fracture energy, it is possible to stress that this parameter presents some dispersion and is affected by phenomena other than material-related parameters, such as the size effect. Nevertheless, for micro concrete the fracture energy should take values around 50-100 $\mathrm{J/m^2}$ and for common concrete around 100-150. Greater values can be achieved for dam concrete, which uses aggregates with large dimensions. Moreover, the results from Wittmann and co-workers that led to the expression (III.74) were considered above the typical results. This could be related to the procedures adopted in the tests or for computing the fracture energy.

Much higher values are associated with mode II and III fracture energy. As an example, Neto *et al.* [414] reported $G_f^{\mathrm{II}}=1500$ $\mathrm{J/m^2}$ for concrete strengthened with CFRP resulting in a ratio of $G_f^{\mathrm{II}}/G_f^{\mathrm{I}}=15$ considering $G_f^{\mathrm{I}}=100$ $\mathrm{J/m^2}$ for ordinary concrete. Moreover, Reinhardt *et al.* [476] defends a ratio $G_f^{\mathrm{II}}/G_f^{\mathrm{I}}=20$ to 25 for a concrete with $f_c^{cube}=39.5$ MPa.

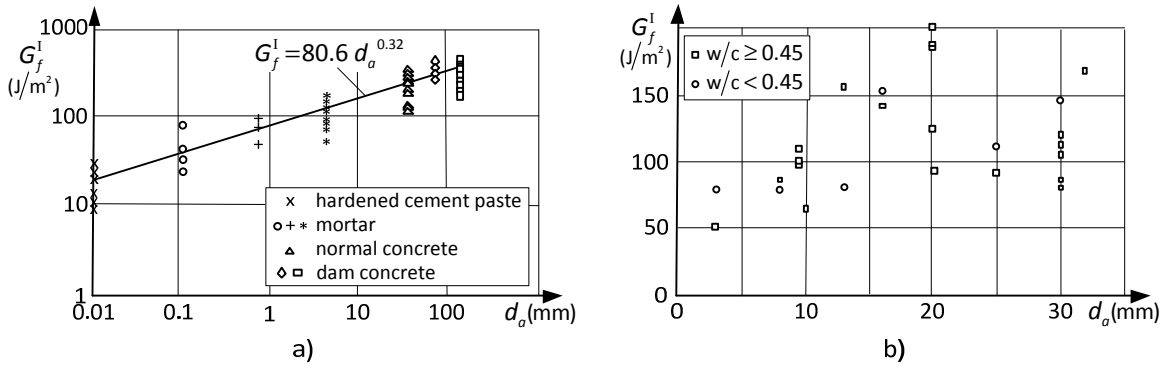

Figure III.29: Concrete mode I fracture energy: a) obtained by Wittmann and co-workers [277, 546, 578]; b) obtained by 197 tests in 6 laboratories according to RILEM's recommendations, adapted from [268].

Table III.4: Concrete mode I fracture energy obtained by the formula proposed by Trunk and Wittmann [546].

d_a (mm)	**5**	**10**	**15**	**20**	**25**	**30**	**50**	**75**	**100**	**125**
G_f^I (J/m²)	135	168	192	210	226	239	282	321	352	378

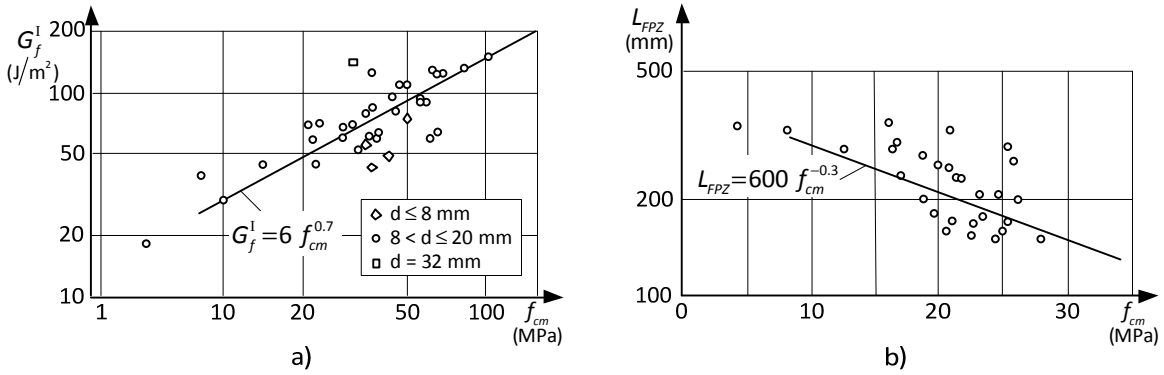

Figure III.30: Concrete mode I fracture energy and FPZ extension after Hilsdorf *et al.* [271].

Table III.5: Concrete mode I fracture energy (J/m²) adopted by Model Code 90 [390].

d_a (mm)	**C12**	**C20**	**C30**	**C40**	**C50**	**C60**	**C70**	**C80**
8	40	50	65	70	85	95	105	115
16	50	60	75	90	105	115	125	135
32	60	80	95	115	130	145	160	175

Note: Model Code 90 [390] adopts concrete grades associated with characteristic strength for cylindrical specimens and the following expression can be used to compute the mean compressive strength: $f_{cm} = f_{ck} + 8$.

2.2.5 Strain-rate effect

Another important phenomenon with great relevance for the seismic behaviour of RC structures is the *strain-rate effect*. It is generally accepted that for high velocity loading, *e.g.* resulting from impact, explosions or strong earthquakes, the concrete may present a significant over-strength, both for compressive and tensile loading. This effect is commonly related to the decrease of micro-cracking with increasing strain-rates, and also, due to inertia effects on crack propagation [552]. Figure III.31 presents the expected levels of strain-rate for different loading cases proposed by Bischoff [56]. The author Chappuis [100] extends this definition by defending that a typical earthquake can produce stain-rates from 10^{-6} to 10^{-1} s^{-1}.

The experimental tests performed to measure the strain-rate effect usually range between $10^{-7} s^{-1}$ to $10^{-3} s^{-1}$ for *quasi*-static testing, and up to $10^{2} s^{-1}$ for assessing the dynamic effect. For the highest loading rates, the experiments are commonly performed using the *Split Hopkinson Bar* technique [275]. The principle underlying this method consists in generating a one-dimensional stress wave that travels across the bar and specimen, making it possible to span a large range of loading rates. More details about this technique can be found in the work of Solomos *et al.* [517].

The most common parameter extracted is the *dynamic factor* D_f, *a.k.a. dynamic increase factor* (DIF), given by the ratio of the dynamic *vs.* static strength f_c^d / f_c^s. In some cases, it is possible to measure the stress *vs.* strain relationship, although some difficulties may arise, especially in the softening branch.

The authors Solomos *et al.* [517] presented the experimental results for 100 mm concrete cubes subjected to compressive loading. Two concrete grades were considered (C25/30 and C50/60) with a maximum aggregate size of 16 mm. The stress *vs.* strain curves for concrete grade C25/30 are presented in Figure III.32-a, where there were some difficulties to record the softening phase for the specimens tested with the intermediate loading rate. The dynamic increase factors for both concrete grades are presented in Figure III.32-b. A strength increase above 50% can be seen for strain-rates greater or equal to $10^{-3} s^{-1}$.

Under tensile loading, the authors Kormeling *et al.* [308] studied the influence of strain-rate and low temperature on the mechanical characteristics of plain and steel fibre reinforced concrete. The plain concrete specimens presented 43.7 MPa cube compressive strength and were tested using a servo-hydraulic testing machine at strain rates between $1.25 \times 10^{-6} s^{-1}$ and $2.50 \times 10^{-3} s^{-1}$. The split Hopkinson bar techniques was used for the strain velocities of $1.5 - 20\ s^{-1}$. The stress *vs.* strain curves for the lowest and highest velocities are presented in Figure III.33-a and the dynamic increase factors for the three velocities in Figure III.33-b.

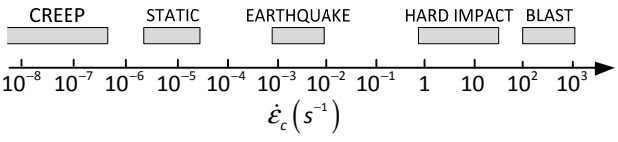

Figure III.31: Expected strain rates for different loading cases, adapted from Bischoff *et al.* [56].

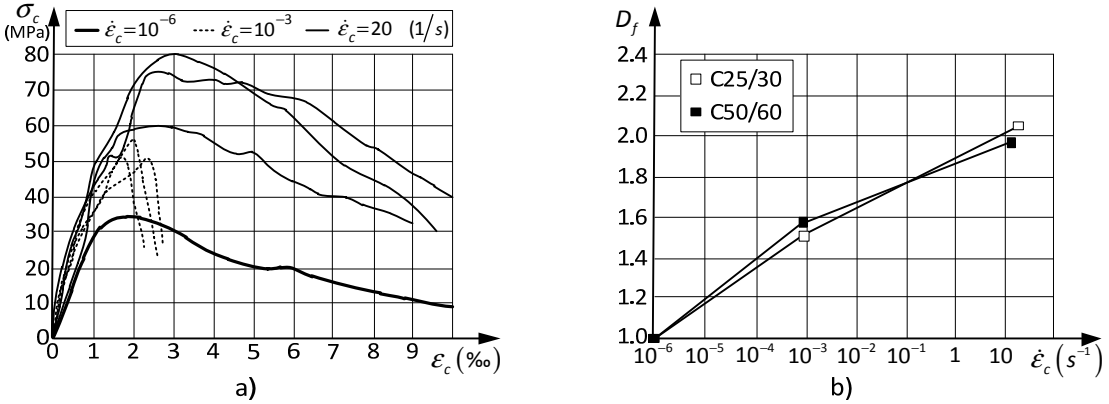

Figure III.32: Concrete strain-rate effect under compressive loads, adapted from Solomos *et al.* [517]: a)stress vs. strain for grade C25/30 specimens; b) dynamic factors for the compressive strength.

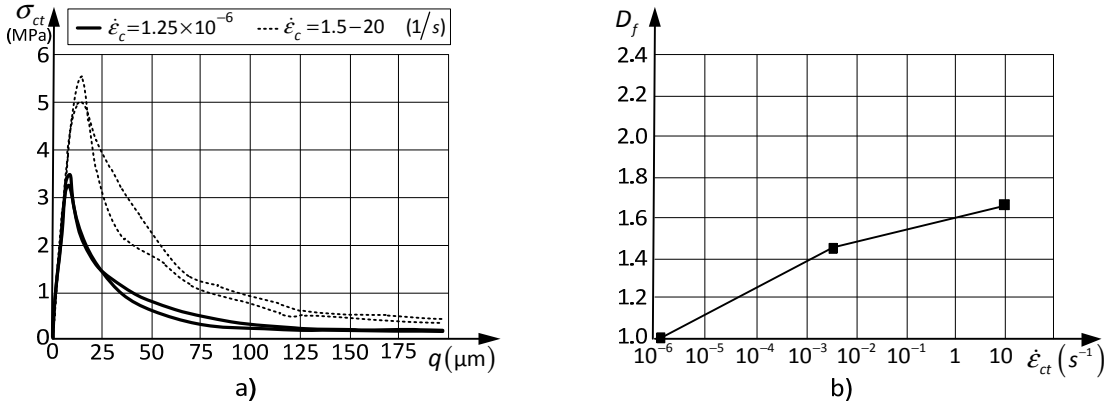

Figure III.33: Concrete strain-rate effect under tension loads, adapted from Kormeling *et al.* [308]: a) stress vs. strain curve; b) dynamic factors for the tensile strength.

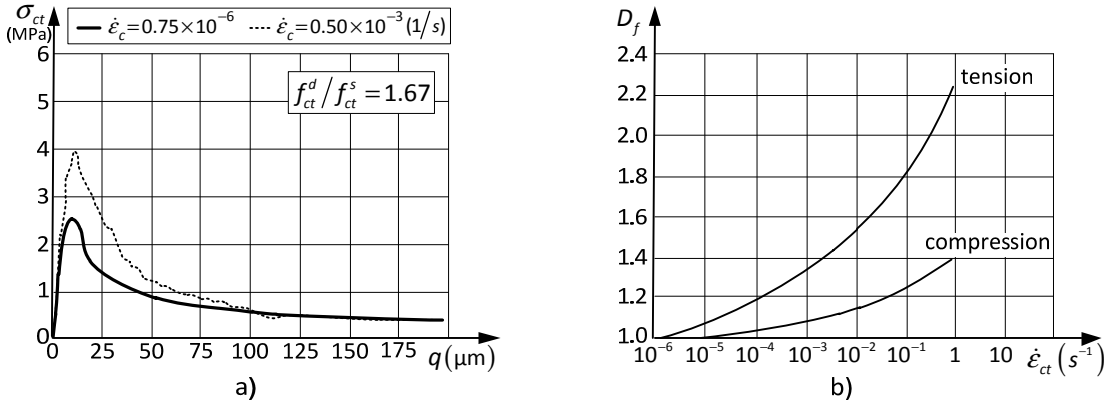

Figure III.34: Concrete strain-rate effect: a) stress *vs.* strain curve, adapted from van Doormaal *et al.* [552]: b) dynamic factors for the compressive and tensile strength obtained by Suaris *et al.* [531, 532].

Also for tensile loading, the authors van Doormaal *et al.* [552] tested notched and unnotched prismatic specimens using the *Split Hopkinson Bar* technique. The concrete had a maximum aggregate size of 8 mm. The cylindrical specimens were 74 mm in diameter and 100 mm long. For the case of 4 mm notch depth, the loading rate was 0.03 and 19.7 MPa/s for the quasi-static and dynamic load cases, respectively. Considering an elasticity modulus of 40 GPa for the concrete this leads to strain rates of $0.75\times10^{-6}\,s^{-1}$ and $0.50\times10^{-3}\,s^{-1}$, respectively. The stress *vs.* strain curves are presented in Figure III.34-a. A dynamic factor of 1.67 is obtained by comparing the peak stress values of both curves.

The results obtained by Suaris *et al.* [530] presented in Figure III.34-b confirm the general trend of the strain-rate effect on resistance. However, in this case the dynamic increase under compressive loads seems to be lower than the results obtained by Solomos *et al.* [517]. This difference can be related to the testing equipment used for the highest velocities, which in this case was a drop-weight impact testing machine instead of the *Split Hopkinson Bar* technique.

There have been some attempts to extend this analysis to the fracture energy, which is related to the area underneath the stress-displacement diagram and is also influenced by this phenomenon. However, there is still some discussion about this issue because this effect is considered a combination of a material property, but also, a structural effect caused by inertia forces [552].

Figure III.35 presents the variation of the *apparent Poisson's ratio* ν^* with the strain-rate measured by Suaris *et al.* [531]. The numerical values of Poisson's ratio for the dynamic tests were measured at the strain corresponding to peak stress under *quasi*-static loading. It is possible to observe in this figure that this parameter increases (decreases) with the increasing strain-rates under tensile (compressive) loading. The authors indicate that these variations are related to the decrease of micro-cracking along the principal tensile strain directions when the strain-rate increases.

Once again, it should be emphasized that standard strain-rate tests have some problems to separate the part of the response that is related to the material from the part that is related to a structural response, like the development of inertia forces.

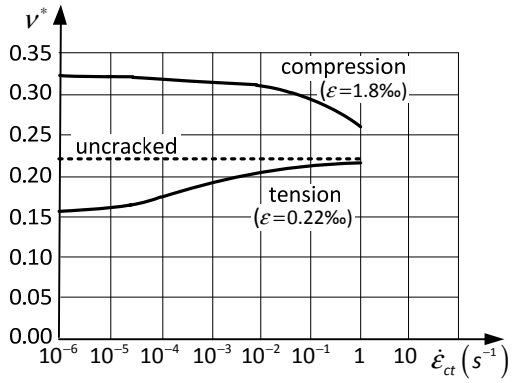

Figure III.35: Concrete strain-rate effect: Effect on the apparent Poisson's ratio, adap.from Suaris *et al.* [531].

2.2.6 Variable mechanical properties

Reinforced concrete is a composite material that is far from being homogeneous. Accordingly, it is necessary to consider the variability of the mechanical properties to simulate the real response. In this way, it is possible to introduce the possibility of having defects, fragilities and over-resistances.

One of the simplest ways to achieve this is by introducing probability distributions for some mechanical material properties calibrated from statistical analyses of experimental data. A question arises about what material properties should be selected to introduce the material heterogeneity. A material defect can lead to strength and stiffness variations. Hence, directly scaling the peak stress value will result in the desired effect. Although, the peak stress deformation will not change.

The *normal or Gaussian distribution* seems to be adequate to simulate strength distributions that tend to cluster around the mean value and present a decrease of probability moving away from this value. Two parameters are required to define this distribution: the arithmetic mean μ_X and the standard deviation σ_X of the random variable *X*. As mentioned before, these statistical parameters should be defined from experimental results obtained with representative samples of the material.

- Using the statistical distributions associated with the concrete classes in Eurocode 2

An estimation of the concrete strength dispersion can be made from the experimental data used to define the concrete classes in Eurocode 2 [91]. The major disadvantage of using this procedure is associated with not having direct access to experimental data. Therefore, the information presented in EC2 could have been treated conservatively, because of being targeted for design purposes. Nevertheless, assuming these limitations it is possible to have a feasible estimation of the concrete strength dispersion.

The Eurocode 2 [91] defines the concrete strength using a series of classes that groups the mechanical characteristics determined from concrete sample tested after 28 days from casting. For compressive (tensile) strength the Eurocode 2 gives information about the mean value $f_{cm}\left(f_{ctm}\right)$ and the characteristic 5% cylinder strength $f_{ck}\left(f_{ctk,0.05}\right)$, which corresponds to the resistance value that has the probability of 95% to be exceeded. This document adopts the following expressions for these parameters:

$$f_{ck} = f_{cm} - 8 \text{ (MPa)}, \tag{III.77}$$

$$f_{ctk,0.05} = 0.7\ f_{ctm}\ . \tag{III.78}$$

Assuming a *Gaussian* distribution, it is possible to compute the *standard deviation* and the *relative standard deviation* (RSD), *a.k.a. coefficient of variation*, using:

$$\sigma_X = \frac{f_{c,0.05} - \mu_X}{z_a}, \tag{III.79}$$

$$RSD_X = \frac{\sigma_X}{\mu_X}\ . \tag{III.80}$$

where $f_{c,0.05}$ should be substituted by f_{ck} or by $f_{ctk,0.05}$ for compressive or tensile strength. For this

case, $z_a = F^{-1}(5\%) = -1.64485$ and F^{-1} is the inverse function of the *Gaussian cumulative distribution*.

Table III.6 presents the results obtained using this procedure. Owing to expressions (III.77) and (III.78), the standard deviation for the compressive (tensile) resistance is constant (variable) and the relative standard deviation is variable (constant). Figure III.36 presents the histogram obtained with a set of 1000 pseudorandom numbers generated with the statistical properties of concrete class C25/30. It is possible to verify that the data follows the Gaussian distribution represented by a red line in the same figure.

It should be noted that the statistical distributions presented in Table III.6 are associated with a specific specimen size, *e.g.* cylinders 150 mm in diameter and 300 mm long or 150 mm cubes [390]. The statistical parameters should be corrected for the size effect to take into consideration the size of the structure being analysed and the approach used to simulate this effect in the numerical model, *e.g.* if the dispersion is implemented at the Gauss points or in the element's constitutive operator.

Table III.6: Some concrete classes adopted in Eurocode 2 [91] and their statistical properties assuming a Gaussian distribution.

Class	f_{cm}	f_{ck}	$\sigma(f_c)$	RSD	f_{ctm}	$f_{ctk,0.05}$	$\sigma(f_{ct})$	RSD
C15/20	24	16	4.864	20.3%	1.9	1.3	0.347	18.2%
C20/25	28	20	4.864	17.4%	2.2	1.5	0.401	18.2%
C25/30	33	25	4.864	14.7%	2.6	1.8	0.474	18.2%
C30/37	38	30	4.864	12.8%	2.9	2.0	0.529	18.2%
C35/45	43	35	4.864	11.3%	3.2	2.2	0.584	18.2%
C40/50	48	40	4.864	10.1%	3.5	2.5	0.638	18.2%
C45/55	53	45	4.864	9.2%	3.8	2.7	0.693	18.2%
C50/60	58	50	4.864	8.4%	4.1	2.9	0.748	18.2%
C55/67	63	55	4.864	7.7%	4.2	2.9	0.766	18.2%
C60/75	68	60	4.864	7.2%	4.4	3.1	0.803	18.2%

(Note: All values in MPa except RSD)

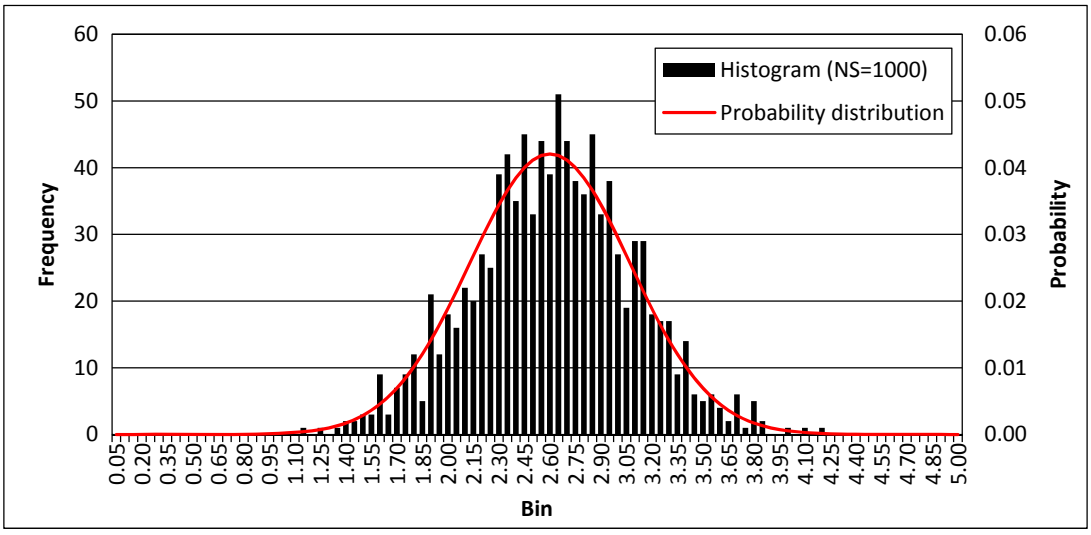

Figure III.36: Tensile strength distribution for a C25/30 class concrete $(\mu = 2.60;\ \sigma = 0.474;\ \text{RSD} = 18.2\%)$.

2.2.7 Models for concrete

Modelling concrete for general loading cases is still a challenging task. Numerous models have been proposed to simulate this material but a consensus regarding what is the best strategy to adopt is still very far from being established. Before cracking, the concrete is often modelled by considering an isotropic continuum domain and this hypothesis usually leads to good results, despite the initial heterogeneities present in the concrete matrix. After cracking, two approaches are commonly used to simulate the fracture-like phenomena that characterise the response [37, 79, 291, 293, 386]. The *discrete cracking* approach (see Figure III.37-a) simulates the development of cracking through physical discontinuities introduced at the element interfaces, in which the amplitude and propagation are controlled by rupture criteria [112, 162, 454, 455, 525]. Alternatively, the *continuum* approach, *a.k.a. smeared models* (Figure III.37-b), considers the fracture as a damage accumulation process distributed in a finite zone of the continuum domain, *i.e.* without introducing a physical discontinuity [283, 309, 389].

The *discrete crack models* present the best modelling approach to the physical problem because the crack is directly simulated as a discontinuity in the domain. On the other hand, this approach requires following the crack propagation and consequently making sequential adaptations to the mesh [58, 75, 581] because the crack path is not known when the mesh is generated. On the other hand, the *smeared crack* approach seems to be an obvious solution to simulate the development of micro-cracking because of the distributed nature of this phenomenon. Moreover, this leads to a stiffness decrease distributed in a finite region so that the *continuum damage mechanics* (CDM) approach is often used (see section 2.1.5). Nevertheless, it should be emphasized that modelling open cracks or multiple interacting cracks with this approach can become a rough estimation and produce unrealistic results for advanced inelastic states.

Recent theoretical developments have improved the possibility of using finite elements with *embedded cracks* (Figure III.37-c) by locally enriching the displacement field approximation. These new element formulations are based on the so-called "*Extended*" [15, 133, 159, 252, 368, 401, 402] and "*Generalized*" [31, 186, 244, 514, 527, 528] extensions of the finite element method (FEM)

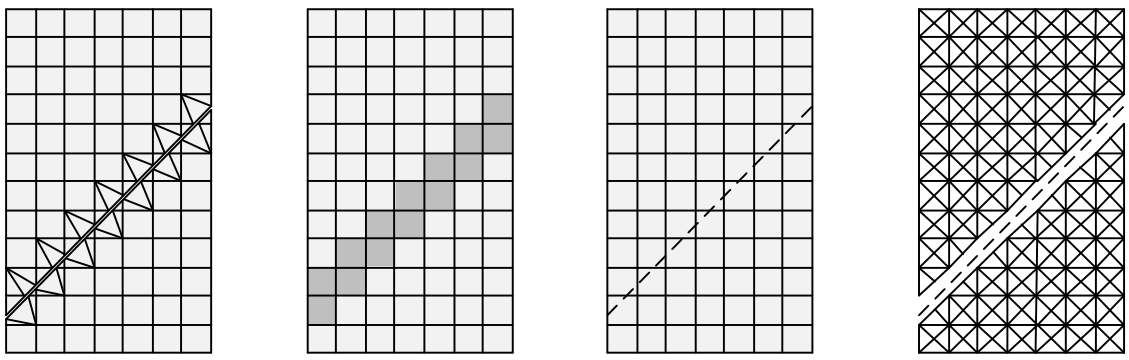

Figure III.37: Possible modelling strategies for concrete cracking, adapted from [496]

within the framework of the *Partition of Unity Method* [187, 513, 555]. This approach is still far from reaching a mature stage of development and extensive research is still needed. Nevertheless, the new possibilities introduced by these formulations and some preliminary results have contributed to rise expectations regarding this approach.

Furthermore, in the last decade several works presented proposals to couple both the continuum damage approach for the early micro-cracking generation and the discrete fracture for the propagation of macro-cracking [130, 422, 561]. This is achieved by setting limit values for the damage parameter and implementing discrete cohesive constitutive relation calibrated by energy criteria [131, 132, 512]. For example, the authors Comi *et al*. [130, 131, 134] proposed making the transition to mode I discrete cohesive crack models when a critical level of damage is exceeded, which depends on the local mesh size and on an analytical estimate for the current bandwidth by means of a perturbation analysis. Moreover, the cohesive law of the crack is defined through an energy balance criterion, in terms of the energy left to dissipate in the damage bands.

Finally, the *Lattice* approach (Figure III.37-d) uses one-dimensional elements that are removed to simulate the development of the crack. This formulation can present problems under general loading cases and becomes prohibitive for large problem sizes. These models are mostly used for smaller scales than the one targeted in this work.

The smeared crack approach and continuum damage models were adopted in this work to simulate the concrete fracture. Developing and testing a new damage model is a complex and laborious task, which was considered to be outside the scope of this thesis. Accordingly, it was necessary to choose a model from the ones published in the literature. The selection criteria adopted was to select an isotropic damage model from those that could be used for modelling RC elements. The following models were considered in this work:

i. *Comi-Perego 1DV* model [140];
ii. *Mazars'* model [381];
iii. *Comi-Perego 2DV* model [128, 137];
iv. *La Borderie's* model [316];
v. *Mazars-Ragueneau-Pijaudier-Cabot* model [388];
vi. *Faria-Oliver-Cervera* model [211-213].

Models with two damage mechanisms are more suitable to simulate the concrete response because of the differences and some independency in the response to tension and compression. The *Comi-Perego 1DV* model [140] does not distinguish between tensile and compressive stresses. Nevertheless, this model was used for testing the global model with simple tensile experiments of small concrete specimens. In addition, this model turned out to be very useful to test the nonlocal model implementation, because the authors proposed expressions to estimate the localization band (see Example RC1).

Mazars' model [381] was considered as the main damage model in this work. In fact, this model can represent well the concrete response. Nevertheless, some problems were revealed by the tests made and some proposals are made in section 3 to improve the representativeness and the

robustness of the original model.

The *Comi-Perego 2DV* model [128, 137] was also implemented in the FE package developed in this thesis. This model presents an interesting and elegant formulation and works well for monotonic problems. Nonetheless, after load reversal, some problems were experienced in computing the state determination and this model was abandoned.

The *La Borderie's* model [316], the *Mazars-Ragueneau-Pijaudier-Cabot* model [388] and *Faria-Oliver-Cervera* model [211-213] were also considered but were not fully implemented in the FE code. Different reasons led to this decision. In the first case, the model is formulated in a flexibility format and some difficulties were experienced in finding an explicit stiffness-based constitutive relation for three-dimensional problems. The second model was relatively recent at the beginning of this work. Few implementations are known with this model and it presents some innovative features, such as the sliding mechanism to simulate hysteretic damping, which are not fully tested yet. Finally, the *Faria-Oliver-Cervera* model [211-213] also presents an interesting formulation and features, such as considering plastic deformations, but the convergence difficulties reported by Faria [211] led to some reluctance in adopting it for refined three-dimensional models of RC structures.

In the following part of this sub-section, a summarized description of the formulation of the *Comi-Perego 1DV* and *Mazars'* models will be presented, which will be used in this and in subsequent chapters.

- Comi-Perego 1DV Model

The *Comi-Perego 1DV* model [140] is an isotropic damage model that adopts the following definition for the Helmholtz free energy:

$$\rho\psi\left(\underline{\boldsymbol{\varepsilon}},d,\xi\right)=\frac{1}{2}\left(1-d\right)\underline{\boldsymbol{\varepsilon}}:\underline{\mathbf{k}}:\underline{\boldsymbol{\varepsilon}}+\psi^{ine}\left(\xi\right), \tag{III.81}$$

where ξ is a scalar kinematic internal variable and ψ^{ine} is a convex inelastic potential used to model the evolution of the elastic domain during the analysis defined by [140]:

$$\psi^{ine}\left(\xi\right)=k\left[\sum_{i=0}^{n-1}\frac{n!}{i!}ln^{i}\left(c\right)+\left(1-\xi\right)ln^{n}\left(c\right)-\left(1-\xi\right)\sum_{i=0}^{n}\frac{n!}{i!}ln^{i}\left(\frac{c}{1-\xi}\right)\right],\ c\geq1, \tag{III.82}$$

where *k*, *c* and *n* are material parameters.

The following state equations can be obtained [140]:

$$\underline{\boldsymbol{\sigma}}=\rho\frac{\partial\psi}{\partial\underline{\boldsymbol{\varepsilon}}}=\left(1-d\right)\mathbf{k}\,\boldsymbol{\varepsilon}, \tag{III.83}$$

$$Y=-\frac{\partial\psi}{\partial d}=\frac{1}{2}\,\boldsymbol{\varepsilon}\,\mathbf{k}\,\boldsymbol{\varepsilon}, \tag{III.84}$$

$$\chi=\frac{\partial\psi}{\partial\xi}=k\,ln^{n}\left(\frac{c}{1-\xi}\right)-k\,ln^{n}c, \tag{III.85}$$

The model parameter *n* is related to the softening branch and can be used to adjust the fracture

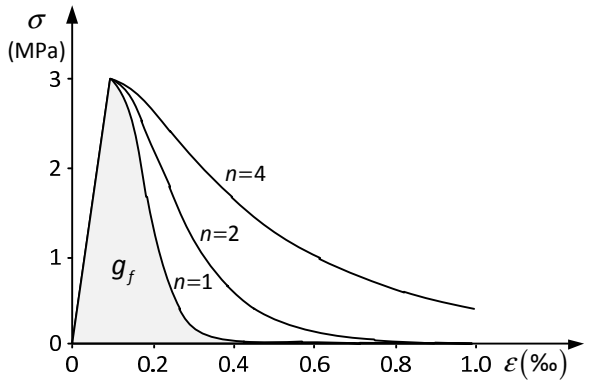

Figure III.38: Schematic representation of the *Comi-Perego 1DV model*, adapted from [140].

energy density g_f^1 (see Figure III.38). The parameter *k* is related to the initial limit for the elastic response and the parameter *c,* which must be greater than unity, is related to the slope of the hardening/softening branch: hardening for $c < e^{n/2}$, horizontal slope with $c = e^{n/2}$ and softening for $c > e^{n/2}$.

The dissipation potential is defined by:

$$f = Y - Y_0 - \chi = \frac{1}{2}\,\boldsymbol{\varepsilon}\,\mathbf{k}\,\boldsymbol{\varepsilon} - k\,ln^n\left(\frac{c}{1-\xi}\right), \tag{III.86}$$

with $Y_0 = k\,ln^n c$.

The following evolutions for the internal variables are adopted by the authors [140]:

$$\delta d = \frac{\partial f}{\partial Y}\delta\gamma, \tag{III.87}$$

$$\delta\xi = -\frac{\partial f}{\partial \chi}\delta\gamma, \tag{III.88}$$

where γ is a non-negative scalar.

Taking equation (III.86) into consideration, it is possible to conclude that:

$$\delta d = \delta\xi = \delta\gamma. \tag{III.89}$$

Considering this last equation, updating the damage variable can be performed by imposing $f = 0$:

$$f = 0 \Rightarrow \frac{1}{2}\,\boldsymbol{\varepsilon}\,\mathbf{k}\,\boldsymbol{\varepsilon} = k\,ln^n\left(\frac{c}{1-\xi}\right), \tag{III.90}$$

$$d = \xi = 1 - c\;exp\left\{-\left(\frac{\boldsymbol{\varepsilon}\,\mathbf{k}\,\boldsymbol{\varepsilon}}{2k}\right)^{\frac{1}{n}}\right\}. \tag{III.91}$$

The loading/unloading conditions (III.52)-(III.54) can be adopted for this model and extended to the other internal variables due to the relation (III.89).

The secant constitutive relation is defined by equation (III.83). The authors advise on using the *strain energy density release rate Y* as a nonlocal variable for nonlocal versions of the model.

- Mazars' model

The model proposed by Mazars in 1984 [381] considers two dependent isotropic scalar damage variables and can be used for situations of radial loading or increasing proportional loading [453]. Damage is considered isotropic, which means that all constitutive tensor components are affected by damage. Permanent inelastic strains are not considered.

The dissipation potential is defined by:

$$f = \tilde{\varepsilon} - \tilde{\varepsilon}_0^*(t) \leq 0 \,, \tag{III.92}$$

where the *comparison strain* $\tilde{\varepsilon}$ and the elastic limit are given by[i]:

$$\tilde{\varepsilon} = \sqrt{\sum_i \langle \varepsilon_i \rangle_+^2} = \sqrt{\left(\varepsilon_{\mathrm{I}}^+\right)^2 + \left(\varepsilon_{\mathrm{II}}^+\right)^2 + \left(\varepsilon_{\mathrm{III}}^+\right)^2} \,, \tag{III.93}$$

$$\tilde{\varepsilon}_0^*(t) = \max\left\{\tilde{\varepsilon}_0 \,, \max_{\forall \tau \leq t}\left(\tilde{\varepsilon}(\tau)\right)\right\} . \tag{III.94}$$

This definition of the *comparison strain* implies that only positive strains cause damage.

In order to capture the different behaviour in tension and compression, typical of concrete and other materials, this model defines 2 auxiliary damage variables d_+ and d_-, so two different damage evolution laws are defined:

$$\delta d_\pm = F_\pm\left(\tilde{\varepsilon}\right) \left\langle \delta\tilde{\varepsilon} \right\rangle_+ \,, \tag{III.95}$$

with:

$$F_\pm\left(\tilde{\varepsilon}\right) = \frac{\tilde{\varepsilon}_0^*\left(1 - A_\pm\right)}{\tilde{\varepsilon}^2} - \frac{A_\pm B_\pm}{exp\left(B_\pm\left(\tilde{\varepsilon} - \tilde{\varepsilon}_0^*\right)\right)} \,, \tag{III.96}$$

where the parameters $A_\pm$ and $B_\pm$ are used to describe the tension and compression response and can be calibrated using data from uniaxial tests.

These last expressions are written in terms of infinitesimal increments. It is required to integrate these expressions to compute damage variables increments. Considering equation (III.95):

$$\Delta d_\pm = \int \delta d_\pm \; dt = \int \delta d_\pm \; \frac{dt}{d\tilde{\varepsilon}} \, d\tilde{\varepsilon} = \int F_\pm \left\langle \frac{d\tilde{\varepsilon}}{dt} \right\rangle_+ \frac{dt}{d\tilde{\varepsilon}} \, d\tilde{\varepsilon} \,. \tag{III.97}$$

Under the basic assumptions of the model, namely, the loads are radial or proportionally increasing, the last expression can be integrated, using:

$$d_\pm = c + \int F_i \; d\tilde{\varepsilon} \,. \tag{III.98}$$

Computing (III.98) by taking into account that: $d_\pm\left(\tilde{\varepsilon} = \tilde{\varepsilon}_0^*\right) = 0$, leads to:

$$d_\pm = 1 - \frac{\tilde{\varepsilon}_0^*\left(1 - A_\pm\right)}{\tilde{\varepsilon}} - \frac{A_\pm}{exp\left(B_\pm\left(\tilde{\varepsilon} - \tilde{\varepsilon}_0^*\right)\right)} \,. \tag{III.99}$$

[i] $\langle . \rangle_\pm = \frac{1}{2}\left(. \pm |.|\right)$. The symbol $\pm$ implies 2 equations: one for tension $(+)$ and the other for compression $(-)$.

The auxiliary damage variables $d_{\pm}$ are combined to define a unique damage variable *d*, using the following expression:

$$d = \alpha_{+} d_{+} + \alpha_{-} d_{-}, \tag{III.100}$$

where:

$$0 < \alpha_{\pm} < 1; \quad \alpha_{+} + \alpha_{-} = 1. \tag{III.101}$$

Algorithm III.1 presents the steps to be used for computing $\alpha_{\pm}$. The equation (III.100) assumes that the parameters $\alpha_{\pm}$ are constant within the time step, which is an additional approximation.

The secant form of the constitutive relation is then defined by:

$$\boldsymbol{\sigma} = (1-d)\,\mathbf{k}\,\boldsymbol{\varepsilon}, \tag{III.102}$$

and the loading/unloading conditions can be written as:

$$\begin{cases} \delta d_{\pm} \geq 0, & \text{if } f = 0 \ \wedge \ \delta f = 0 \\ \delta d_{\pm} = 0, & \text{otherwise} \end{cases}. \tag{III.103}$$

The Mazars' damage model has been improved to enhance the capacity for simulating concrete under multi-axial load conditions. For the case of biaxial loading, the resistance curve presents a reasonable agreement with the experimental data. Nevertheless, some differences can be found for $\sigma_{\mathrm{I}} = \sigma_{\mathrm{II}} < 0$ (see Figure III.39).

To improve this issue, some authors have proposed correcting the *comparison strain* using a scaling factor as follows [23]:

$$\tilde{\varepsilon}_{cor} = \tilde{\varepsilon}\ \gamma(\sigma_i), \tag{III.104}$$

with:

$$\gamma(\sigma_i) = \frac{\sqrt{\sum_i \langle \sigma_i \rangle_{-}^{2}}}{\left| \sum_i \sigma_i \right|} \leq 1, \tag{III.105}$$

when:

$$\sum_i \sigma_i < 0. \tag{III.106}$$

Figure III.39 presents a comparison between the resistance envelope of the original *Mazars' model* and the same model with this improvement. All the values are normalized by f_c and compared with the experimental results obtained by Kupfer *et al.* [314]. From the analysis of this figure, it is possible to conclude that this correction considerably improved the simulation under biaxial compression. However, there are still some deviations when the magnitude of the compressions is very different in both principal stress directions.

Algorithm III.1: Mazars' model - Computing the damage combination factors $\alpha_{\pm}$.

1. From the strain tensor, compute the principal strains ε_i.
2. Compute a fictitious principal stress σ_i, using the elastic constitutive relation:

$$\sigma_i = \frac{E}{1+\nu}\varepsilon_i + \frac{E\nu}{(1+\nu)(1-2\nu)}\sum_k \varepsilon_k .$$

3. Separate the tension from the compression components of σ_i, using:

$$\langle \sigma_i \rangle_{\pm} = \frac{1}{2}\left(\sigma_i \pm |\sigma_i|\right).$$

4. Compute the equivalent strain to $\langle \sigma_i \rangle_{+}$ and $\langle \sigma_i \rangle_{-}$, using:

$$(\varepsilon_i)_{\pm} = \frac{1+\nu}{E}\langle \sigma_i \rangle_{\pm} - \frac{\nu}{E}\sum_k \langle \sigma_k \rangle_{\pm} .$$

5. Compute $\alpha_{\pm}$ using one of the following expressions:

$$\alpha_{\pm} = \sum_i H_i \frac{(\varepsilon_i)_{\pm}\left(\varepsilon_{i,+} + \varepsilon_{i,-}\right)}{\hat{\varepsilon}^2},$$

where:

$$H_i = \begin{cases} 1, \text{ if } \varepsilon_i = \varepsilon_{i,+} + \varepsilon_{i,-} > 0 \\ 0, \text{ otherwise} \end{cases}.$$

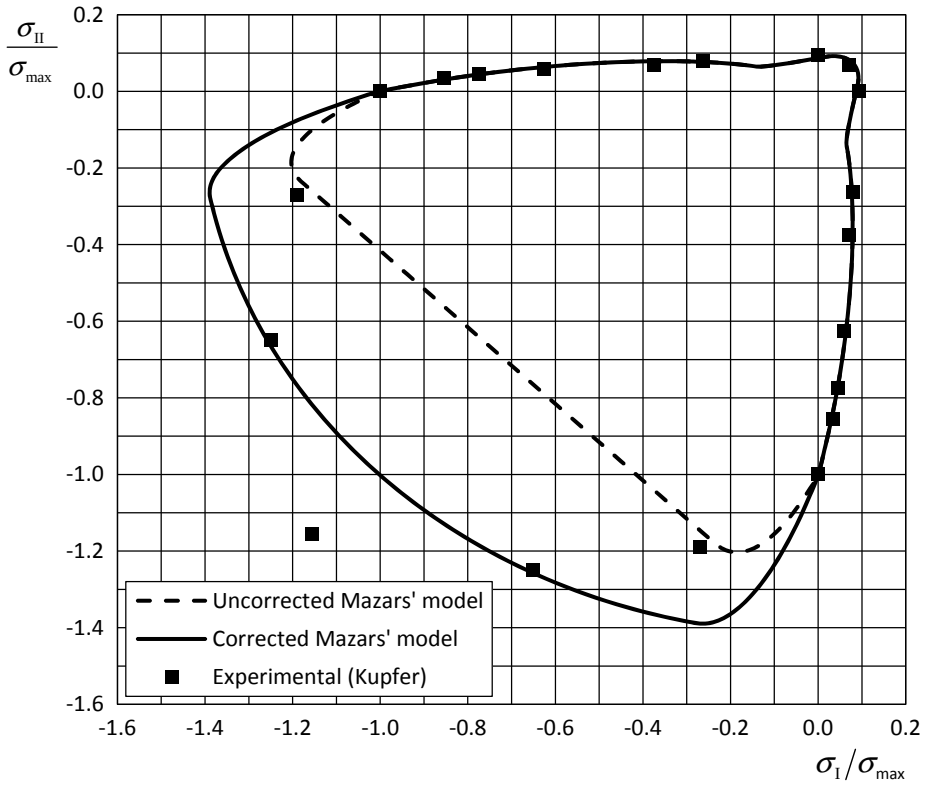

Figure III.39: Mazars' model – Comparison between resistance envelope curves.

2.3 Reinforcing steel

The steel reinforcements commonly used in RC structures are ferrous alloys usually known as *carbon steel*, which are composed of iron and a small amount of carbon (<2.1% per mass). Another steel type used for reinforcements is the well-known *stainless steel*, *a.k.a. inox steel*, which is made of an alloy of iron and about 11%-12% chromium. The chromium reacts with oxygen and creates a protective layer that improves the resistance to corrosion, which can enhance the durability of the RC structure. The chemical composition and the manufacturing process of the reinforcing bars are well documented and lie outside the scope of this thesis, *e.g.* see the references [74, 372].

According to the Eurocode 2 [91], the steel used in reinforcements can be classified into two classes: *hot rolled* and *cold worked*. The latter type is often obtained by temperature, mechanical and chemical treatments (*e.g.* tempering, rolling) made to strengthen the steel.

The response of steel reinforcements is well known both for monotonic and for reversed cyclic loading. It is characterized by yielding, by strain hardening, by the Bauschinger effect and by cyclic hardening. In addition, it is also sensitive to low-cycle fatigue, buckling and to strain-rate. In the following sections, a summarized description of the most relevant characteristics of the response of ordinary steel reinforcements used in RC structures is presented.

2.3.1 Monotonic loading

When subjected to monotonic increasing tensile loading, the reinforcing steel presents stress-strain relationships similar to the ones presented in Figure III.40, both for hot rolled and cold worked steel. The former type presents a well defined yield plateau after the elastic branch. Afterwards, the steel starts to harden with increasing plastic deformation until reaching the peak resistance. Subsequently, a softening branch characterizes the response that is associated with strain localization in a small length of the bar and unloading in the remaining.

The cold worked steel does not present a clearly defined yield stress and yield plateau. Consequently, the 0.2% proof stress is commonly used to define the yield. Most of the time, this type of steel reinforcement offers a higher strength that is achieved at the cost of reducing the available ductility.

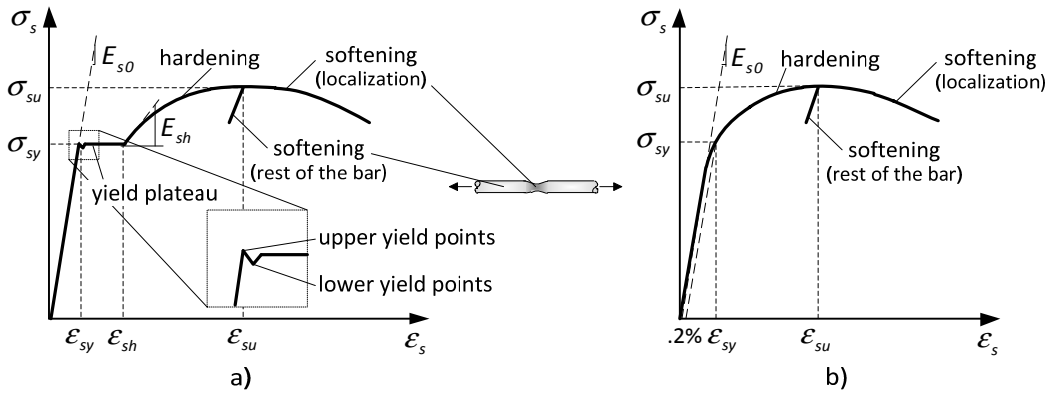

Figure III.40: Typical response of reinforcing steel bars on tension tests: a) hot rolled; b) cold worked.

The *elasticity modulus* can be considered between 200 and 210 GPa and *Poisson's ratio* between 0.25 and 0.30. Current values for the yield strength of ordinary reinforcements range between 250-600 MPa and values up to 2000 MPa are common for prestressing steel. Most of the steel mechanical parameters are subjected to normalization. Nevertheless, the effective values present some dispersion that should be considered in the analysis.

When buckling effects are restrained, the response under compressive and tensile loading is similar and it is usual practice to neglect the differences (see Figure III.41).

2.3.2 Cyclic and alternating loading

Under cyclic and alternating loads, the unloading and reloading branches are characterized by stiffness similar to that for the first loading E_s (see Figure III.41). Moreover, the response is characterized by two additional phenomena. At first, after experiencing plastic deformation the stress-strain response after reversal presents the so-called *Bauschinger effect,* which is associated with the anticipation of the departure from the elastic stiffness after reversal (see Figure III.41-c). Secondly, the response experiences *isotropic cyclic hardening* that consists in the increase of resistance for the reversed direction due to strain hardening. Both phenomena are clearly observed in the experimental results obtained by Ma *et al.* and represented in Figure III.41-d.

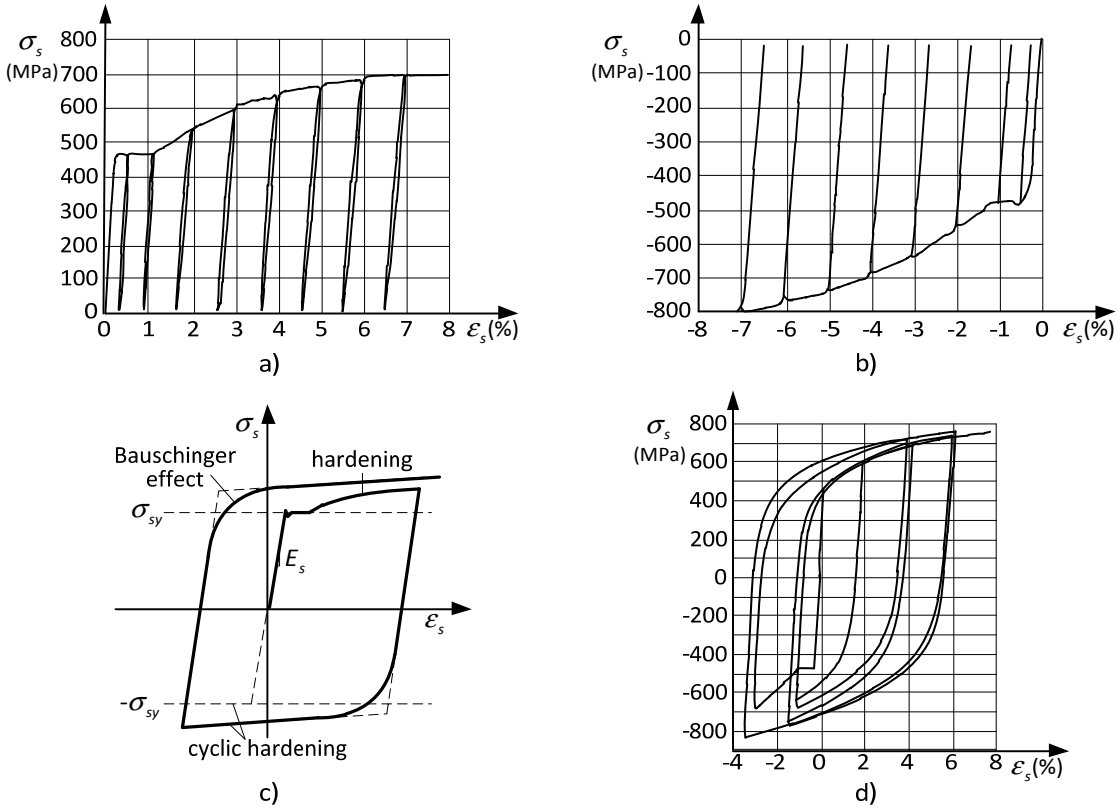

Figure III.41: Response of the reinforcements: a) cyclic tension tests [68]; b) cyclic compression tests [68]; c) typical response under cyclic and alternating loading; d) test results under cyclic and alternating loading [348].

2.3.3 Low-cycle fatigue

Fatigue can be seen as the process that leads to damage or to failure of a structural member due to repeated loading. In particular, *low-cycle fatigue* develops when this phenomenon occurs with a relative small number of cycles. In contrast, *medium-cycle* and *high-cycle fatigue* occurs for a larger number of cycles, generally between 10^3 to 10^8 cycles, and is mostly associated with service loading.

The fatigue-life curve of a material can be defined as the number of cycles required to produce a fatigue failure for a given stress or strain amplitude. According to Brown and Kunnath [72], for an engineering alloy (*e.g.* steel) this curve takes the form represented in Figure III.42. When the loading amplitude is large, but below the ultimate strength for a single load application, there will be plastic deformation and failure occurs after a reduced number of cycles, typically under 1000 (*low-cycle fatigue*).

On the other hand, elastic deformation will occur when the loading amplitude is small and the number of cycles required to produce fatigue failure is very large, often in the order of millions (*high-cycle fatigue*). For very small loading amplitudes, fatigue will not occur or the number of cycles to induce failure is so large that this phenomenon is neglected.

Fatigue develops by the damage generated and by the creation and propagation of fatigue cracks due to the effect of repeated loading. Ultimately, this will lead to failure when the specimen does not have sufficient resistance to withstand the prescribed loading. During this process, cyclic degradation of strength and stiffness can be observed in the response of reinforcing steel bars.

One question arises regarding what would be the number of cycles expected to occur under a seismic event. According to Panthaki [429], an earthquake load can result in large tension and compression strains in the reinforcements and between 2 to 10 full cycles for common structures and up to 30 cycles for structures with high natural frequencies. Considering this information, it is possible to conclude that this phenomenon is likely to result in cyclic degradation, or even in anticipated collapse of the reinforcements. Consequently, this effect should be included as a relevant phenomenon in the models used to simulate the response of the reinforcements.

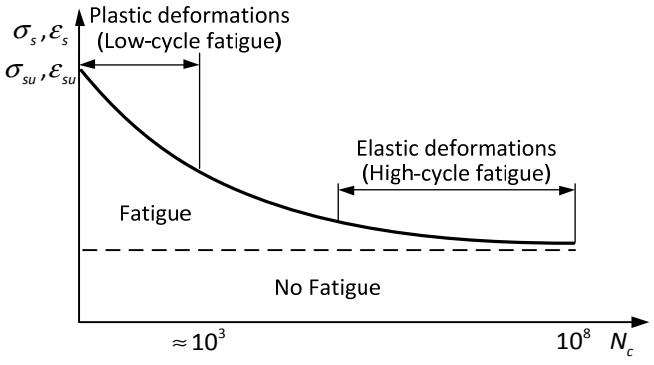

Figure III.42: Typical fatigue-life curve for an engineering alloy, taken from Brown *et al.* [72].

In the work of Mander and co-workers [364, 429], a series of fatigue tests performed with $5/8$ in. $(15.9\ \text{mm})$ reinforcing bars (grade 40) and high strength prestressing thread bars is presented. The reinforcing bars were also tested under monotonic tension and the following results were obtained: $E_s = 215$ GPa; $\sigma_{sy} = 331$ MPa; $\sigma_{su} = 565$ MPa; $\varepsilon_{su} = 17\%$. Figure III.43 shows the results obtained with reinforcing bar R11 subjected to a strain amplitude of $\varepsilon_a = \pm 1.75\%$. The results are presented in terms of stress vs. strain curves (Figure III.43-a) and of the normalized stress at reversal for each cycle number (Figure III.43-b). The latter was obtained from the ratio between the stress at reversal of the current σ_s^c and of the first cycle σ_s^0. Moreover, Table III.7 compiles the relevant information of all tests made with reinforcing bars with constant amplitude cycles. In this data, the *plastic strain amplitude* is computed from:

$$\varepsilon_{ap} = \frac{\Delta\varepsilon_p}{2}, \tag{III.107}$$

where $\Delta\varepsilon_p$ is the *plastic strain range* (see Figure III.45). In addition, the same table presents the cycle number in which the failure condition was met $\left(N_c^f\right)$, the *total dissipated energy* until failure $\left(E_d^t\right)$, which was obtained from the area enclosed within the hysteresis loops and the *dissipated energy per cycle* until failure, computed from:

$$E_d^c = \frac{E_d^t}{N_c^f}. \tag{III.108}$$

The failure criterion adopted by the authors included a combination of two conditions [364]. For small amplitude cycles $\varepsilon_a < \pm 2\%$, the failure was recognized by monitoring the σ_s^c / σ_s^0 curves (*e.g.* Figure III.43-b) and by identifying when this ratio starts to drop. For larger amplitude cycles, the stress at reversal decreased continuously, so, it is not possible to identify a well-defined saturation level. Consequently, the failure was identified by visual observation of fatigue crack initialization.

Several models were proposed to simulate the fatigue-life of a material. The *Coffin-Manson* model [119, 366] relates the *plastic strain amplitude* and the number of reversals until failure $\left(2N_c^f\right)$ using a power function:

$$\varepsilon_{ap} = c\left(2\,N_c^f\right)^n, \tag{III.109}$$

and the *Koh-Stephens* model uses the *strain amplitude* instead [307]:

$$\varepsilon_a = c\left(2\,N_c^f\right)^n. \tag{III.110}$$

The authors *Mander-Panthaki-Kasalanati* [364] suggested the following energy-based models:

$$E_d = c\left(\varepsilon_{ap}\right)^n, \tag{III.111}$$

$$E_d = c\left(\varepsilon_a\right)^n. \tag{III.112}$$

Other models have been proposed, *e.g.* models that account for the effects of the mean stress, *a.k.a. SWT* model, proposed by Smith *et al.* [516]. More information is available in the references [364, 429]. Table III.8 presents the parameters of these models that resulted from fitting the experimental data using a linearized least-squares regression analysis.

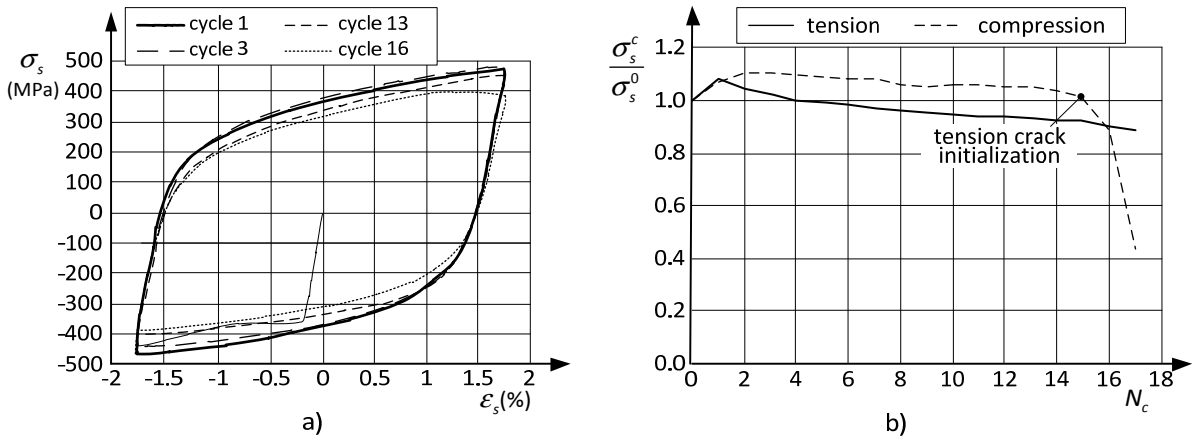

Figure III.43: Low-cycle fatigue tests of reinforcing steel bars performed by Mander *et al*. [364, 429] – Specimen R11: a) Stress-strain curves; b) normalized stress at reversal.

Table III.7: Results of low-cycle fatigue tests performed by Mander *et al*. [364, 429].

Specimen	ε_a (%)	ε_{ap} (%)	N_c^f	Failure Criteria	E_d^t (MPa)	E_d^c (MPa)
R8	±0.80	0.65	148	normalized tensile stress starts dropping	1227	8.3
R4	±1.00	0.83	49		542	11.0
R10	±1.25	1.10	23		350	15.2
R21	±1.34	1.17	25		423	16.3
R7	±1.50	1.30	21		403	19.2
R11	±1.75	1.60	13		301	23.1
R5	±2.00	1.80	9.2	tension crack initialization	252	27.4
R9	±2.50	2.20	5.6		199	35.8
R1	±3.00	2.70	4.1		175	44.6

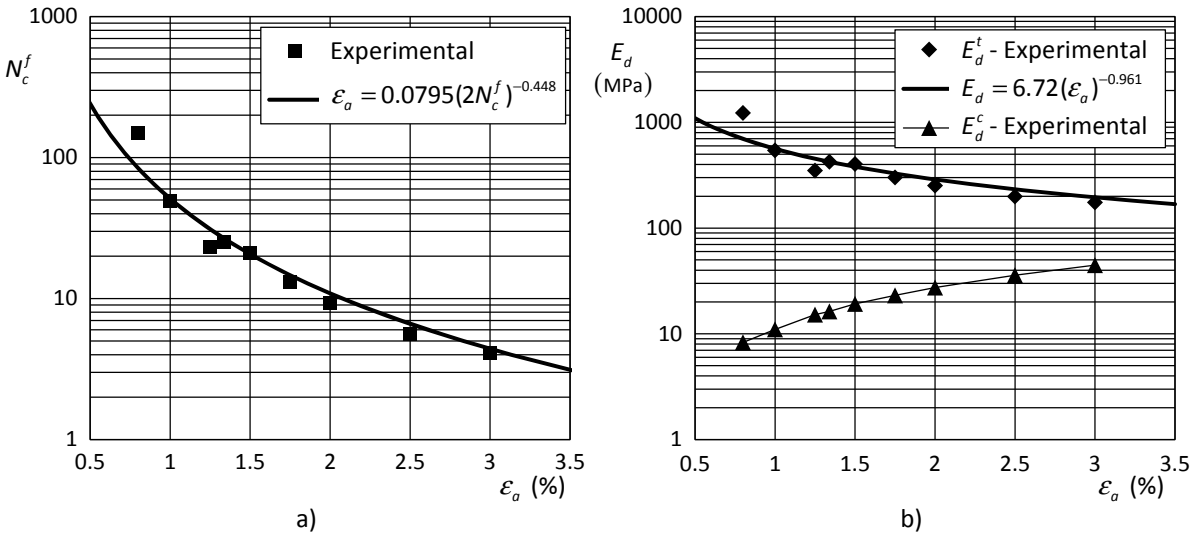

Figure III.44: Fatigue-life models for the tests performed by Mander *et al*. [364, 429] with constant amplitude levels: a) Koh-Stephens model; b) Mander-Panthaki-Kasalanati model.

Table III.8: Fatigue-life models for the tests performed by Mander *et al*. [364, 429].

Model	Equation	Parameter *c*	Parameter *n*	R^2
Coffin-Mason	$\varepsilon_{ap} = c(2N_c^f)^n$ (III.109)	0.0777	-0.486	0.984
Koh-Stephens	$\varepsilon_a = c(2N_c^f)^n$ (III.110)	0.0795	-0.448	0.985
Mander-Panthaki-Kasalanati #1	$E_d = c(\varepsilon_{ap})^n$ (III.111)	8.00	-0.884	0.911
Mander-Panthaki-Kasalanati #2	$E_d = c(\varepsilon_a)^n$ (III.112)	6.72	-0.961	0.914

Figure III.44-a presents the experimental data obtained by Mander *et al.* [364, 429] in the format ε_a *vs.* N_c^f, plotted together with the Koh-Stephens fatigue-life model and in Figure III.44-b the Mander-Panthaki-Kasalanati model relating E_d and ε_a. It can be observed that the fatigue-life models fit the experimental data well and it can be concluded that they can be used to predict the low-cycle fatigue response. Figure III.44-b also presents the plot of the mean energy dissipated in each cycle until failure. It can be observed that the energy dissipated per cycle increases with the amplitude of the cycles, as expected. Nevertheless, due to a higher degradation for the cycles with larger amplitude the total energy dissipated is less and tends to decreases with the amplitude of the cycles.

The work of Brown and Kunnath [71, 72] presents the results of 34 low-cycle fatigue tests with constant amplitude. The tested reinforcements were #6, #7 and #8 bars, which correspond to diameters of 19.1, 22.2 and 25.4 mm, respectively. The steel was Grade 60 with the following characteristics: $\sigma_{sy} = 420$ MPa; $\sigma_{su} = 620$ MPa; $\varepsilon_{su} = 8\%$-9%. Figure III.45 presents typical stress-strain curves of two of the specimens tested and Table III.9 presents chosen data collected from the tests performed. In order to compare with the results obtained by Mander *et al.*, it is necessary to take into consideration that in this work the reported data for N_c^f is associated with the number of half cycles, instead of the number of full cycles. Consequently, the data from this test was corrected to be comparable with the previous results. In addition, the failure criterion adopted was the effective failure of the specimen, instead of the first fatigue crack identification as in the work of Mander *et al.* The number of cycles when the first crack was identified is also presented in Table III.9.

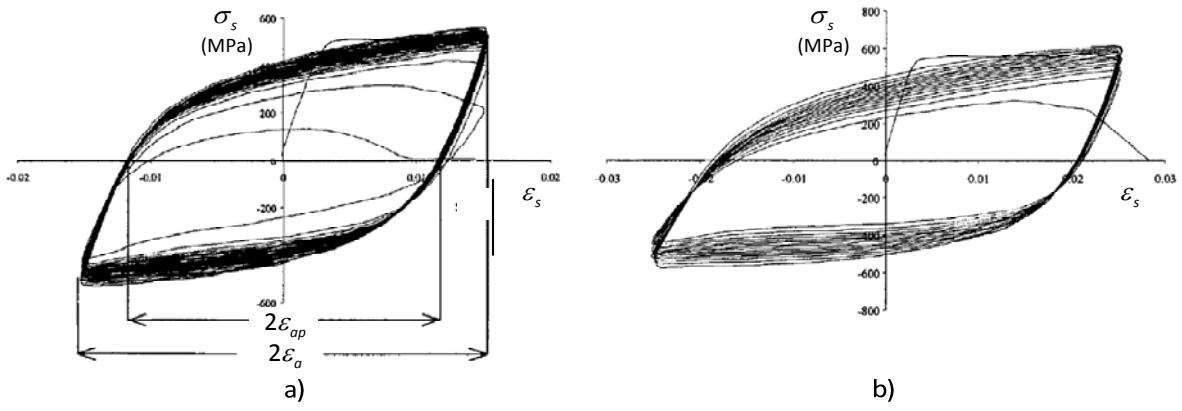

Figure III.45: Stress-strain curves obtained from low-cycle fatigue tests performed by Brown *et al*. [72]: a) Specimen #32 (ϕ22 mm) ; b) Specimen #24 (ϕ19 mm) .

Moreover, the dissipated energy is associated with the failure criteria that is different from that adopted in the work of Mander *et al.* [364, 429], so both results are not directly comparable.

According to Brown and Kunnath [72], the presence of a single or even multiple fatigue cracks does not result in immediate failure. Instead, based on experimental results they defend that 40% to 50% of the fatigue-life is after the first crack formation.

Table III.9: Results of low-cycle fatigue test performed by Brown *et al*. [72].

Specimen	ϕ (mm)	ε_a (%)	ε_{ap} (%)	N_c^f (1st crack)	N_c^f (failure)	E_d^t (MPa)
#21	19	±1.50	1.10	28	43.5	725.5
#22		±1.75	1.35	15.5	30.5	600.1
#23		±2.00	1.55	15.5	24.5	-
#26		±2.25	1.80	12.5	22	642.1
#24		±2.50	1.98	8.5	15	478.9
#25		±3.00	2.30	4.5	11	385.8
#33	22	±1.25	0.94	43.5	77	1123.0
#32		±1.50	1.10	21.5	46	831.3
#28		±1.75	1.35	16.5	30.5	608.0
#34		±1.75	1.35	17.5	47.5	1011.2
#27		±2.00	1.55	11.5	23	570.3
#29		±2.25	1.80	10.5	21	601.7
#30		±2.50	1.98	10.5	19	655.7
#35		±2.50	1.98	11	19	633.8
#31		±2.75	2.29	7.5	11	428.2
#36		±3.00	2.30	5	12	518.8
#43	25	±1.50	1.10	22.5	55.5	962.7
#46		±1.75	1.35	10.5	39	884.4
#44		±2.00	1.55	16.5	30.5	767.6
#47		±2.25	1.80	7.5	22	672.5
#45		±2.50	1.98	10.5	14	454.9

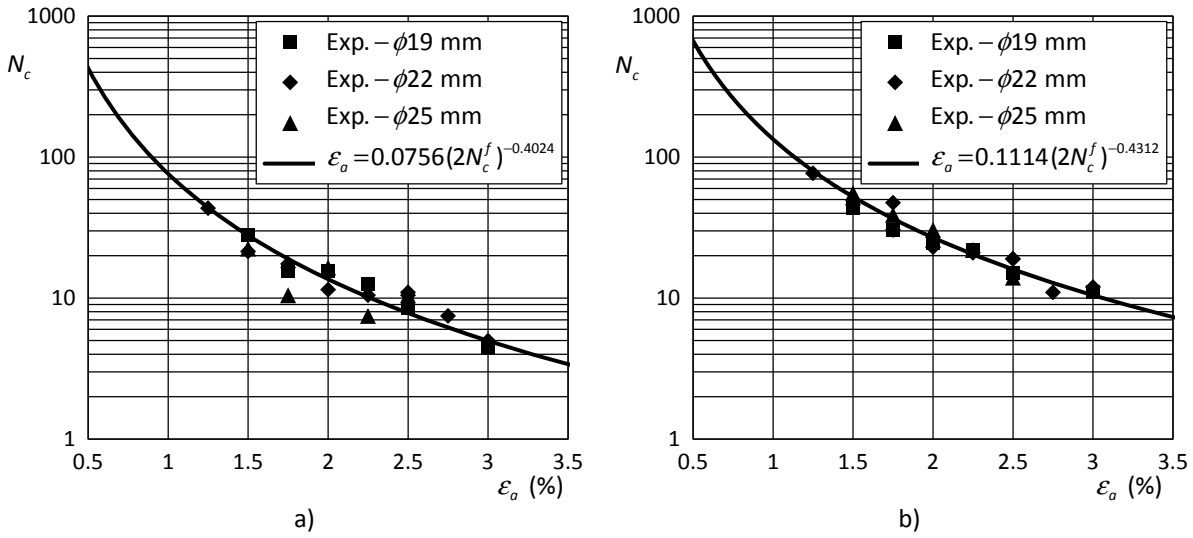

Figure III.46: Koh-Stephens fatigue-life model for the tests performed by Brown *et al*. [72]: a) 1st crack initialization; b) Failure of the specimen.

Table III.10: Fatigue-life models for the tests performed by Brown *et al*. [72].

Model	Equation	Parameter *c*	Parameter *n*	R^2
Coffin-Mason (1st crack)	$\varepsilon_{ap}=c(2N_c^f)^n$ (III.109)	0.0622	-0.4191	0.811
Koh-Stephens (1st crack)	$\varepsilon_a=c(2N_c^f)^n$ (III.110)	0.0756	-0.4024	0.843
Coffin-Mason (failure)	$\varepsilon_{ap}=c(2N_c^f)^n$ (III.109)	0.0980	-0.4628	0.942
Koh-Stephens (failure)	$\varepsilon_a=c(2N_c^f)^n$ (III.110)	0.1114	-0.4312	0.939
Mander-Panthaki-Kasalanati #1	$E_d=c(\varepsilon_{ap})^n$ (III.111)	2.062	-0.7488	0.683
Mander-Panthaki-Kasalanati #2	$E_d=c(\varepsilon_a)^n$ (III.112)	1.936	-0.7003	0.687

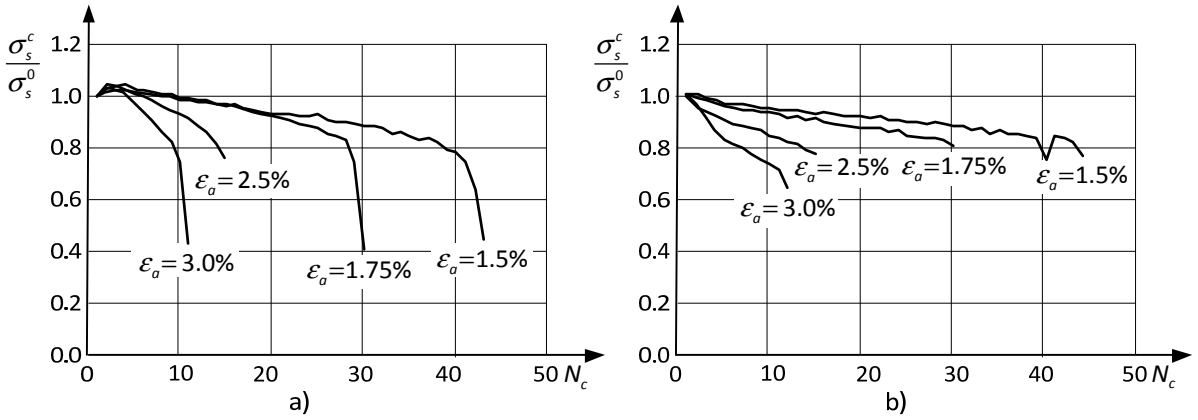

Figure III.47: Normalized stress at reversal obtained by Brown *et al*. [72] for the ϕ19 mm bar: a) tension; b) compression.

Table III.10 presents the parameters of the fatigue-life models that fit the experimental results best. This data was recomputed in order to take into consideration N_c^f as the number of full cycles to failure, instead of the number of half cycles and are compared with the experimental data in Figure III.46. The data of the Coffin-Mason and of the Koh-Stephens fatigue-life models can be compared with the results from Mander and co-workers. These results show a good agreement between the two tests. On the other hand, the energy-based fatigue models are not analogous because the results presented in Table III.10 refer to the energy dissipated until failure, instead of the energy dissipated until the first crack was identified, as presented in Table III.8. In both cases, the energy-based fatigue-life models presented inferior correlation with the experimental data, as demonstrated by the value of the square correlation coefficient R^2. The Coffin-Mason and the Koh-Stephens fatigue-life models presented inferior correlation with the data obtained by Brown *et al.* than that published by Mander *et al.* This can be related to the fact that the tests of Brown *et al.* included different bar diameters, which increases the variance of the results.

Figure III.47 presents the normalized stress at reversal of the tension and compression cycles for the tests with the ϕ19 mm bar performed by Brown *et al.* [72]. The authors concluded that independently of the strain amplitude, the degradation is gradual and not too intense until a value of around $\sigma_s^c/\sigma_s^0 \approx 0.75$ [72]. Afterwards, the degradation is very intense and failure is imminent.

The authors Brown and Kunnath [72] adopted the so-called *Rainflow Cycle Counting* method, proposed by Suidan *et al.* [533], to compute an equivalent strain amplitude from random strain histories, like the ones resulting from a seismic event.

2.3.4 Buckling

Experimental tests show that after concrete cover detachment, the longitudinal compressed reinforcing steel bars may buckle and present a significant loss of strength and energy dissipation capacity. This subject has been addressed by several authors, *e.g.* [247, 362, 380, 405]. Two main questions arise when addressing this topic. The first is the prediction of when buckling is likely to occur and the second is related to the post-buckling response. The first question does not have a simple answer. First, the concrete cover inhibits the buckling of the reinforcements. Therefore, this phenomenon may only occur after concrete spalling. Afterwards, the main factor that influences buckling is the ratio between the *lateral support spacing* s_s and the *bar diameter* ϕ_s. Regarding this issue, the compression tests of isolated reinforcements performed by Monti *et al.* [405] with different bar diameters show that buckling only occurs for $s_s > 5\phi_s$ (see Figure III.48-a). In addition, Monti and Nuti concluded that the post-buckling softening branches tend to an asymptotic value:

$$\sigma_{\infty} = \frac{6\sigma_{sy}}{s_s/\phi_s}. \tag{III.113}$$

Furthermore, the same type of tests performed by Mander *et al.* [362] with ϕ16 mm bars confirm this trend (see Figure III.48-b). In this case, the tests with $s_s \leq 6.5\phi_s$ showed only a small reduction in the ultimate strength. On the other hand, significant buckling occurred for $s_s \geq 10\phi_s$ and the specimens were unable to sustain the yield stress.

An initial estimation of the critical stress characterising buckling can be developed by using the elastic buckling theory. This leads to:

$$\sigma_{cr} = \frac{\pi^2 E_s}{\lambda^2}, \tag{III.114}$$

where λ is the *bar slenderness* given by:

$$\lambda = \frac{L_e}{r}, \tag{III.115}$$

where L_e is the *effective length* and *r* is the *radius of gyration* given by the square root of the ratio

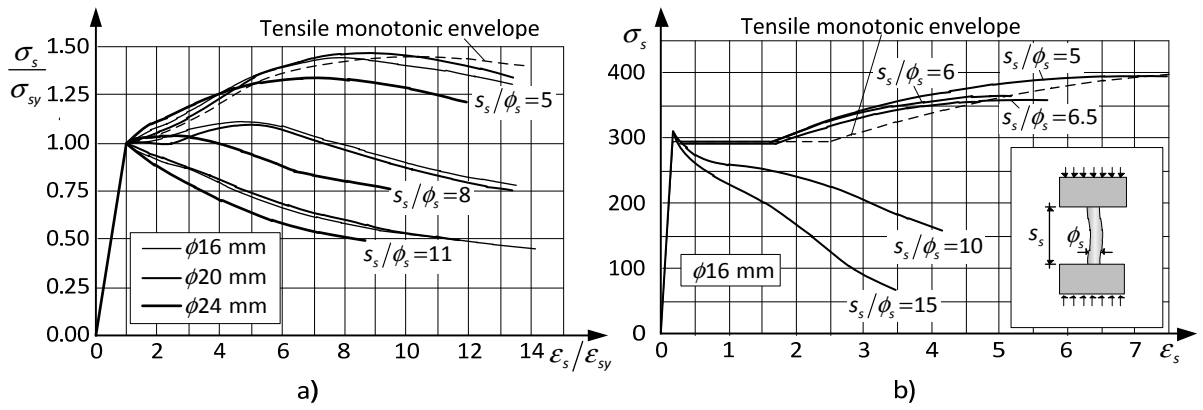

Figure III.48: Compression tests with reinforcing steel bars: a) performed by Monti *et al.* [405]; b) performed by Mander *et al.* [362].

between the moment of inertia and the area of the cross-section. For a circular section the *radius of gyration* equals $\phi_s/4$. However, Mander *et al.* [362] proposed scaling this value by 0.955 to take into consideration the geometrical deviations measured in common ribbed bars.

Considering that the reinforcing bar is clamped at both ends, the *effective length* is twice the lateral support spacing, thus the critical spacing between lateral reinforcing can be computed from:

$$s_{cr} = \frac{\pi \phi_s}{2} \sqrt{\frac{E_s}{\sigma_{cr}}} \,. \tag{III.116}$$

This approach gives a rough overestimation of the critical load and spacing level. For example, using directly the equation (III.116) and equating σ_{cr} to σ_{sy} , the following critical lateral support spacing is obtained for the $\phi 16$ mm bar tested by Mander *et al.* [362] (see Figure III.48-b):

$$s_{cr} = \frac{\pi \phi_s}{2} \sqrt{\frac{200 \times 10^3}{300}} = 40.6 \phi_s \,. \tag{III.117}$$

It should be noted that the previous formulation is defined for ideal bars, with no geometrical imperfections and considering full fixity at both bar ends.

Alternatively, inelastic buckling may be used to compute more realistic critical stress values. The authors Mander *et al.* [362] show that using different post-yield moduli produces more accurate results. For example, considering that buckling occurs only in the strain hardening range, using $E_s = E_{sh} \approx 3500$ MPa in equation (III.116) would lead to $s_{cr} = 5.3\phi_s$, which is below the expected value. Moreover, it is also demonstrated that values of the critical spacing between $6\phi_s$ and $9\phi_s$ are obtained using a reduced modulus, resulting from specific combinations of the elastic modulus E_s and of the strain hardening modulus E_{sh} . More information can be obtained in the work of Mander *et al.* [362].

The second question is related to the stress-strain evolution after buckling. Under tensile loading, the experimental results show that the stress-strain curve is not significantly affected by buckling in the previous compression cycles and a usual practice is to neglect this phenomenon for the tensile part of the response. Moreover, under compression the experiments show that the post-buckling stress-strain curve follows a softening branch. Several models have been proposed to simulate this phenomenon. For example, the authors Mau *et al.* [380] proposed a new finite element for steel reinforcements that includes inelastic buckling. However, according to Monti *et al.* [405], it requires costly numerical integrations over the cross-section and over the length of the element.

The authors Monti *et al.* [405] proposed a model that includes the post-buckling response of reinforcing steel bars under compression. This model considers four hardening rules: kinematic, isotropic, memory, and saturation. If buckling is identified, the hardening rules are used to simulate the post-buckling softening branch. The authors adopted the stress-strain law of the *Guiffrè-Menegotto-Pinto* model [396] (see section 2.3.7) but other constitutive relations may be used.

Another model that should be mentioned is the one proposed by Gomes and Appleton [247]. As presented in Figure III.49-a, this proposal considers a plastic mechanism for the longitudinal bar between two consecutive lateral reinforcements.

From the equilibrium of the buckled reinforcing bar and making some approximations regarding the kinematics of the problem, such as assuming that the bar is subjected to an average strain $\varepsilon_s = q/s_s$, the following hyperbolic stress-strain relation is obtained [247]:

$$\sigma_s = \frac{2\sqrt{2}\,M_p}{A_s\,s_s}\frac{1}{\sqrt{\varepsilon_s}}, \tag{III.118}$$

where M_p is the *plastic moment*, which for a circular cross-sections can be defined by:

$$M_p = Z_p\,\sigma_{sy} = 0.053\,\pi\,\phi_s^3\,\sigma_{sy}. \tag{III.119}$$

This last equation does not take into account the interaction between the axial force and the bending moment. The authors proposed another expression that considers this effect, but they concluded that the difference between the two formulations is not too significant and the first option was preferred due to its simplicity.

To include the stress-strain expression (III.118) in a global stress-strain model, the equation should be translated to the zero-stress point. This can be done introducing the following variable substitution [247]:

$$\varepsilon_{sr} = \varepsilon_s - \varepsilon_{sQ}. \tag{III.120}$$

Figure III.48-b presents a schematic representation of this model implemented in a general stress-strain law for steel reinforcements, *e.g.* the *Guiffrè-Menegotto-Pinto* model. It can be observed that the transition point P is defined by the intersection of the loading path AB with the buckling curve CD. Moreover, an iterative process is required to compute the stress-strain coordinates of the point B after the load reversal, in order to obtain the reload path that contains point D (branch BF) [247].

Gomes and Appleton propose to activate the buckling mode when the bar is subjected to compression and only after the rupture of the concrete cover. This can be assessed in a finite element code by monitoring the damage state of the neighbouring concrete elements. In addition, this model should only be used for large transversal reinforcement spacing, *e.g.* $s_s > 5\phi_s$.

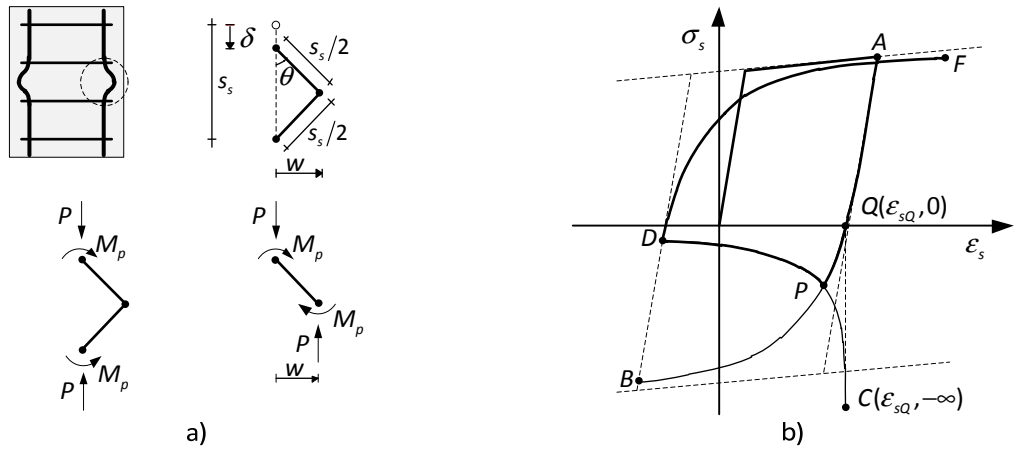

Figure III.49: Inelastic buckling model for reinforcing steel bars proposed by Gomes *et al.* [247].

2.3.5 Stain-rate effect

The experimental results for common reinforcing steel bars tested at increasing strain rates show that the reinforcements present a consistent increase of yield and ultimate strength. Several works addressing this topic have been published and most of those are supported by experimental results. Two main difficulties arise when performing this type of tests. At first, the traditional testing equipment (electro-hydraulic servo-controlled test systems) is generally not prepared for high speed testing and the results can be inaccurate. Secondly, the separation between what is a material response and what is related to inertia forces is once again difficult to evaluate. Nevertheless, the next paragraphs will present some information available in the bibliography about this effect.

One of the first works addressing this topic was published by Mahin *et al.* [350] in 1972, in which three reinforcing bars (ϕ19 mm) were tested with increasing strain rates. The bars present the following mean characteristics: $E_s = 208$ GPa, $\sigma_{sy} = 318$ MPa, $\sigma_{su} = 567$ MPa and $\varepsilon_{su} = 21\%$. The results obtained are summarized in Figure III.50. The first specimen was tested under monotonic tension at a strain rate $\dot{\varepsilon} = 5\times10^{-5}$ and was used to establish the *quasi*-static stress-strain envelope. The other two were tested cyclically without stress reversal with strain rates of 5×10^{-3} and 5×10^{-2} until the beginning of the strain hardening response, as presented in Figure III.50-a. Afterwards, these last two specimens were subjected to several load cycles in the strain hardening phase with high and low strain rates with reversal. The specimen #2 was tested with strain rates of 5×10^{-5} and 5×10^{-3} and the specimen #3 with strain rates of 5×10^{-5} and 5×10^{-1} (see Figure III.50-b). The authors concluded that the effect on the initial elastic stiffness is negligible and that the yield strength increased by 14% and 22% for specimens tested at 5×10^{-3} and 5×10^{-1}, respectively. Moreover, the authors found that the strength increase is less significant in the strain hardening range.

Figure III.51 presents the experimental data collected by several authors for different types of steel regarding the strain-rate effect on yield strength and these results show a steady and significant increase of yield strength. In addition, the increases seem to be less significant for more resistant steels (see Figure III.51).

Moreover, Malvar *et al.* [354] conducted a literature review regarding the dynamic characteristics of reinforcing steel bars and concluded that this effect is more significant for the yield stress than for the ultimate stress. The same authors proposed the following expression to estimate the *dynamic factor* $D_f = f_d / f_s$, *a.k.a. dynamic increase factor* (DIF), for the yield and ultimate strength of common reinforcing steel used in the USA [354]:

$$D_f = \left(\frac{\dot{\varepsilon}}{10^{-4}} \right)^{\alpha}, \tag{III.121}$$

where:

$$\alpha = \begin{cases} 0.074 - 0.040 \dfrac{\sigma_{sy}(\text{MPa})}{414}, & \text{for the yield stress} \\ 0.019 - 0.009 \dfrac{\sigma_{sy}(\text{MPa})}{414}, & \text{for the ultimate stress} \end{cases}. \tag{III.122}$$

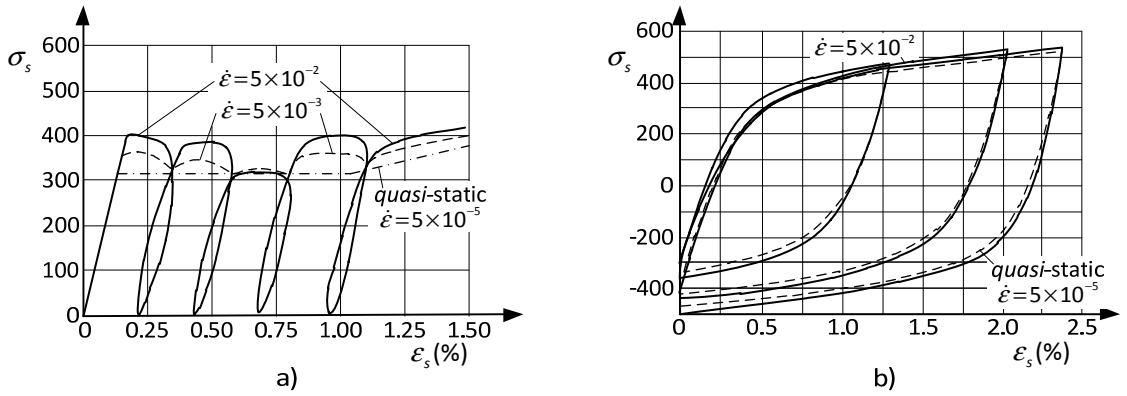

Figure III.50: Strain rate effect of reinforcing bars under cyclic and alternating loading, adapted from Mahin *et al.* [350].

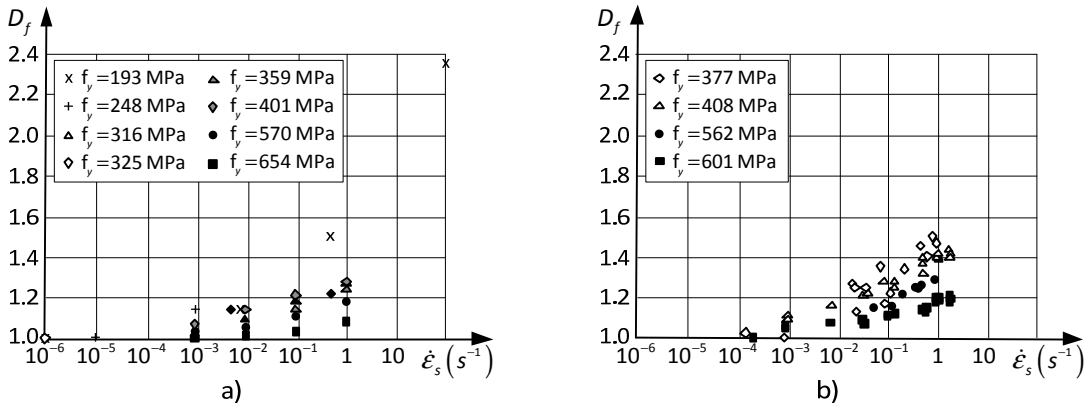

Figure III.51: Strain rate effect on the yield strength of reinforcing steel bars:
a) taken from Lowes [342], after [99, 149, 350, 365]; b) taken from Malvar *et al.* [354], after [149, 500, 579].

This formula was considered by the authors to be valid for reinforcing bars with yield stress between 290 and 350 MPa and for strain rates between $10^{-4}\ s^{-1}$ and 225 s^{-1}. In addition, the author Otani [424] defends that no significant effect is observed in the ductility and in the global energy dissipation capacity.

The ACI Committee 439 published some data regarding the effect of strain rate on the lower yield strength of reinforcing steel bars. This data is presented in Table III.11 and graphically illustrated in Figure III.52. These results show an increase of strength of about 10%-30% for normal steel $\sigma_{sy} \approx 350$ MPa and a less visible effect for high resistant steels. The authors Mander *et. al* [362, 363] proposed the following expressions after making a regression analysis on this data:

$$D_f = \begin{cases} 0.953\left(1+\sqrt[6]{\left|\frac{\dot{\varepsilon}}{700}\right|}\right), \text{ for the lower strength steel (Curve A)} \\ 0.949\left(1+\sqrt[10]{\left|\frac{\dot{\varepsilon}}{50\times10^{6}}\right|}\right), \text{ for the higher strength steel (Curve B)} \end{cases} . \quad \text{(III.123)}$$

These functions are plotted in Figure III.52 together with the experimental results.

Table III.11: Strain rate effect on the lower yield strength of reinforcing steel bars, data taken from [363] after [1].

$\dot{\varepsilon}_s(s^{-1})$	$\sigma_{sy}=310$ MPa	$\sigma_{sy}=352$ MPa	$\sigma_{sy}=393$ MPa	$\sigma_{sy}=558$ MPa
10^{-3}	1.05	1.07	1.02	1.03
10^{-2}	1.11	1.14	1.07	1.05
10^{-1}	1.19	1.21	1.16	1.08
1	1.28	1.28	1.25	1.10

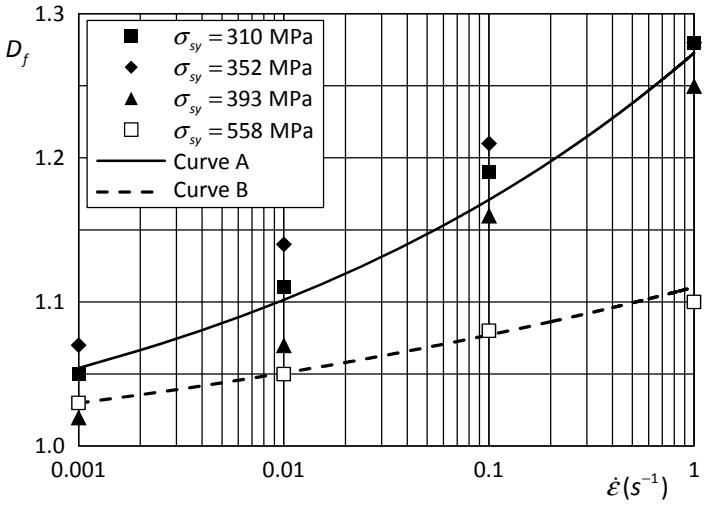

Figure III.52: Strain rate effect on the lower yield strength of reinforcing steel bars, data taken from [363] after [1].

Furthermore, the authors Mander *et al.* [362, 363] tested at different strain rates $\phi 16$ mm high yield steel bars (DH16) and mild steel bars used in bridge piers with diameters raging between 16 mm and 28 mm (D16, D20, D24 and D28). The first steel type presented a yield stress of 360 MPa and the second type an average value of 284 MPa. The experimental programme included *quasi*-static tension and compression tests and two sets of experiments with high strain-rate compressive loading. The stress-strain data obtained for the specimen DH16 is presented in Figure III.53-a and Figure III.53-b to Figure III.53-d present the *dynamic factors* D_f of all tested specimens for the elasticity modulus, lower yield and ultimate stresses, respectively. The results show a steady increase of the yield and ultimate strength. Contrary to the previous tests, the authors identified an increase of the same magnitude in the elasticity modulus. Although the results are consistent, the authors stress that some dispersion can be related to the stroke control mode [362].

Furthermore, Mander *et al* [362, 363] proposed the following expression for the *dynamic factors*:

$$D_s = 0.966\left(1+\sqrt[6]{\left|\frac{\dot{\varepsilon}}{5000}\right|}\right), \text{ (Curve C)}. \tag{III.124}$$

This new equation is similar to expression (III.123) and is plotted in Figure III.53 together with the experimental data.

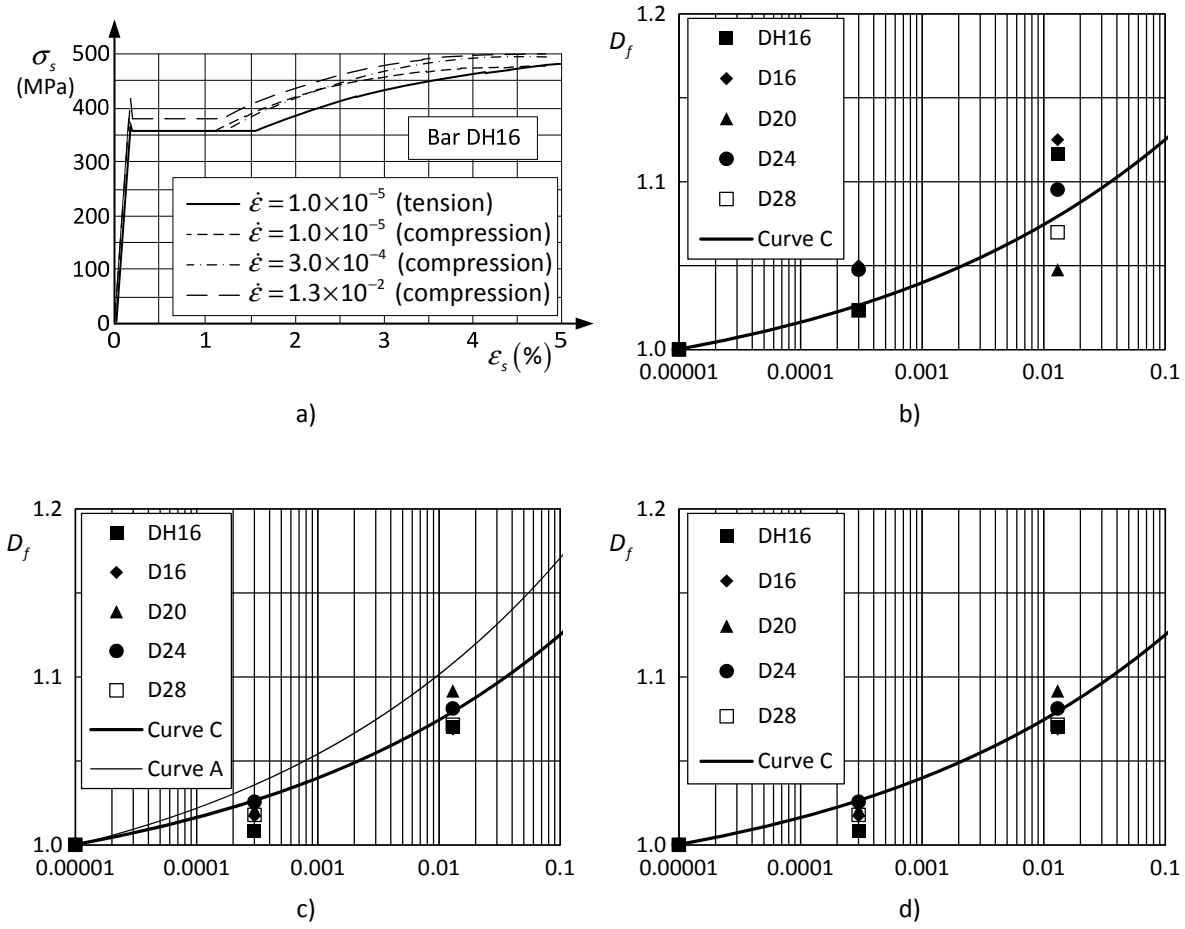

Figure III.53: Strain-rate effect obtained in the tests performed by Mander *et al.* [362, 363]: a) typical stress-strain curve; b) effect on initial elasticity modulus c) effect on lower yield stress; d) effect on ultimate stress.

Figure III.53-c also presents the curve fit obtained for the lower yield stress with the data published by the ACI Committee 439 for lower strength steel (III.123). Comparing both curves it is possible to conclude that although a similar qualitative pattern was obtained, the results from the tests performed by Mander and co-workers revealed a lower strain rate effect.

From the results presented in this section, it is possible to conclude that increasing strain rates in reinforcing bars results in a gradual increase of the yield and ultimate strength. Nevertheless, an accurate definition of this increase is still difficult to extract from the data collected in the bibliography. There is still some dispersion in the results obtained by different authors and by different methods.

Another aspect that appears to be not conclusive is whether the strain-rate also affects the elasticity modulus, both for the first loading and for subsequent unloading and reloading branches. Some authors defend that this effect is not significant and others defend that it is similar to the one for strength. Furthermore, the works presented in this section are consistent in defending that the increase is more significant for lower resistant steel and for the yield strength, rather than for the ultimate strength.

2.3.6 Variable mechanical properties

Similarly to what was presented in section 2.2.6 for concrete, it is relevant to have an order of magnitude regarding the variability of the mechanical properties of the steel used in reinforcements. One possible way to achieve this is to assume a Gaussian distribution for the mechanical parameter *X*, which can be defined using the arithmetic mean μ_X and the standard deviation σ_X. Moreover, the *relative standard deviation* (RSD), *a.k.a. coefficient of variation*, can also be used to represent the variability of each parameter, as defined in (III.80).

The author Pipa [451] published this data for the B400 *Tempcore* (B400T) and B500 *Tempcore* (B500T) steel classes, which led to the A400 and A500 classes largely used in Europe. In addition, Almunia [6] published similar data for the reinforcements used in the construction of bridges in Spain, which included data from reinforcing steel bars from several origins and collected by several authors. These results are reproduced in Table III.12 and include the statistical data regarding the most used mechanical parameters, and also, some geometrical data like the ratio between the effective and nominal cross-section area A_s^{eff}/A_s.

Observing the data presented in Table III.12-a, it can be concluded that the manufacturing procedure used to produce the *Tempcore* reinforcements resulted in small dispersions of the mechanical properties, about 4%-5%. On the other hand, the results reported in Table III.12-b show a higher dispersion of about 7%-8% for strength-related parameters, probably due to considering different sampling sets or manufactures.

Table III.12: Statistical characteristics of the mechanical properties of common reinforcing steel:
a) obtained by Pipa [451] for *Tempcore* steel; b) obtained by Almunia [6] for steel used in bridge reinforcements.

a)

Parameter		B400T	B500T
σ_{sy}	μ [MPa]	496	585
	σ [MPa]	23.3	30.3
	RSD [%]	4.7	5.2
σ_{su}	μ [MPa]	598	680
	σ [MPa]	19.8	28.5
	RSD [%]	3.3	4.2
ε_{su}	μ [%]	11.8	9.4
	σ [%]	1.69	1.40
	RSD [%]	14.3	14.9
E_{sh}	μ [MPa]	3005	3510
	σ [MPa]	657	534
	RSD [%]	22	15
ε_{sh}	μ [%]	2.2	1.4
	σ [%]	0.45	0.44
	RSD [%]	20	31

b)

Parameter		Bridges in Spain
σ_{sy}	μ [MPa]	601.8
	σ [MPa]	48.7
	RSD [%]	8.1
σ_{su}	μ [MPa]	689.9
	σ [MPa]	53.7
	RSD [%]	7.8
$\frac{\sigma_{su}}{\sigma_{sy}}$	μ	1.147
	σ	0.045
	RSD [%]	4.0
ε_{su}	μ [%]	23.28
	σ [%]	2.95
	RSD [%]	12.7
$\frac{A_s^{eff}}{A_s}$	μ	1.005
	σ	0.021
	RSD [%]	2.1

Table III.13: Statistical characteristics of the mechanical properties of reinforcing steel from several origins, taken from [263] after [6].

Origin	σ_{syk}	σ_{sy}	RSD(σ_{sy})
Denmark (see ref. in Almunia [6])	370-420 MPa	-	4%-5% (a) 10% (b)
Sweden (see ref. in Almunia [6])	-	-	8% (b)
EUA, Canada, West Europe [399]	280 MPa 410 MPa	337 MPa 490 MPa	10.7% (b) 9.3% (b)
France [85]	-	-	4% (a) 10% (b)
Spain [6]	500 MPa	602 MPa	8.1 (b)
Europe [451]	400 MPa 500 MPa	496 MPa 585 MPa	4.7% (a) 5.2% (b)
Note: (a) single sample set or single manufacturer; (b) several manufacturers			

Table III.13 reproduces the compilation of results presented by Henriques [263] with data from bars used in western Europe and in North America. These results include tests made with samples from a single set or a single manufacturer and for samples originating from several producers.

According to Henriques [263], the results in Table III.13 permits the conclusion that the dispersion associated with the mechanical parameters increased from around 4%-5% to 8%-10%, when samples from several manufactures are tested, even for the same steel grades. These results confirm the conclusions made for the data presented in Table III.12.

Furthermore, the authors Mirza and MacGregor [399] tested steel reinforcements used in western Europe, in the USA and Canada, and found that the elasticity modulus presented an average value of 201 GPa and a dispersion of 3.3 %. In addition, the ratio between the effective and nominal area of the bar A_s^{eff}/A_s was also tested and revealed mean values between 0.96 to 1.20 and a dispersion of 0.2% to 9.0% [263].

2.3.7 Models for reinforcing steel

Several models have been proposed to simulate the response of the reinforcing steel used in reinforced concrete structures. They can be classified according to several criteria and the most common are the following:

i. Type of stress-strain curves, *e.g.* bilinear, multi-linear, nonlinear;
ii. Applicability to different types of steel [373], *e.g.* to smooth steel or to high strength steel without a significant yield plateau;
iii. Type of formulation [217], *e.g.* explicit algebraic equation for stress $\sigma = f(\varepsilon)$, explicit algebraic equation for strain $\varepsilon = f(\sigma)$ or based on a differential equation.

In the following paragraphs, a summarized review of the most widespread models for reinforcing steel will be presented. The complete mathematical formulation lies outside the scope of this thesis. Instead, only the main characteristics of the models and their main advantages and drawbacks will be addressed.

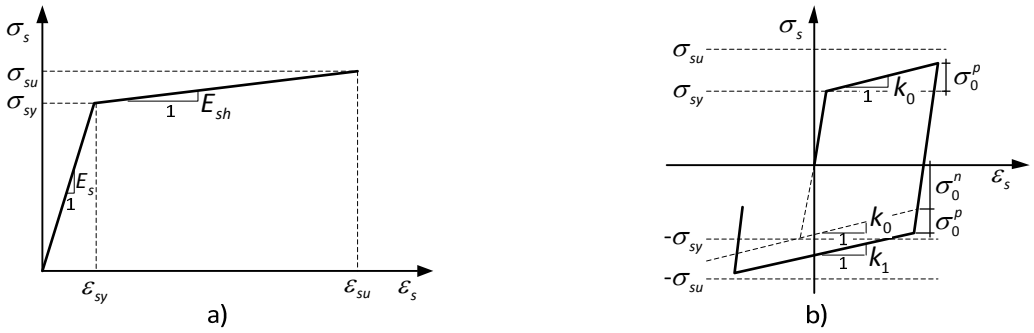

Figure III.54: Reinforcing steel models: a) bilinear; b) Aktan-Karlsson multi-linear model, adapted from [4].

- Bilinear and Multi-linear models

This type of models ranges from the traditional bilinear model for monotonic loading, with and without strain hardening (see Figure III.54-a), to multi-linear models for cyclic and alternating loading. A possible example of the latter type is the model proposed by Aktan and Karlsson [4] which is represented in Figure III.54-b. In this model, an elastoplastic curve is followed during the first loading. After reversal, the position of the envelope and of the strain-hardening slope is variable and depends on the plastic strain attained before the loading reversal.

As illustrated in Figure III.54-b, the current envelope is computed from the initial envelope defined by σ_{i-1}^{n} and is further incremented in tension or compression by the stress associated with the plastic phase in the last half-cycle σ_{i-1}^{p}. Moreover, the slope of the new envelope is defined by [4]:

$$k_i = k_{i-1}\frac{\pm\sigma_{su} - \left(\sigma_{i-1}^{n} + \sigma_{i-1}^{p}\right)}{\pm\sigma_{su} - \sigma_{i-1}^{n}}. \tag{III.125}$$

- Ramberg-Osgood model

The *Ramberg-Osgood* model [468] was proposed in 1943 to describe the stress-strain curves with smooth elastic-plastic transition and using only three parameters. The original expression proposed by the authors is the following [468]:

$$\varepsilon_s = \frac{\sigma}{E_s} + K\left(\frac{\sigma}{E_s}\right)^{n}. \tag{III.126}$$

This equation can be divided into two additive components. The first term is related to the elastic part and the second to the plastic part. The parameters *K* and *n* are material constants defining the hardening response. This definition of the constitutive equation implies that there is always an elastic and a plastic component. At the beginning, the plastic component is very small and negligible and afterwards it becomes dominant.

Equation (III.126) can be rewritten by inserting the relation $\alpha = K\left(\sigma_0/E_s\right)^{n-1}$ [570]:

$$\varepsilon_s = \frac{\sigma}{E_s} + \alpha\frac{\sigma_{sy}}{E_s}\left(\frac{\sigma}{\sigma_{sy}}\right)^{n}. \tag{III.127}$$

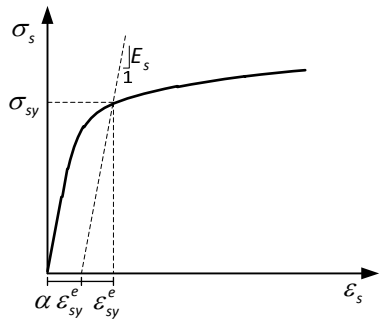

Figure III.55: The Ramberg-Osgood model.

The first term in equation (III.127) can be interpreted as the elastic strain at yield:

$$\varepsilon_{sy}^e = \frac{\sigma_{sy}}{E_s}, \tag{III.128}$$

and the second term the plastic strain at yield, which can be seen as a yield offset (see Figure III.55):

$$\varepsilon_{sy}^p = \alpha \frac{\sigma_{sy}}{E_s} = \alpha\, \varepsilon_{sy}^e . \tag{III.129}$$

Regarding the material parameters, both α and *n* can be obtained to match the experimental data. Common values for the parameter *n* are usually greater or equal to 5 and α can be set as the 0.2% proof stress ($\varepsilon_{sy}^p = 0.2\%$) for cold worked steel. In the work of Martino *et al.* [373], the selection of this and other parameters related to the *Ramberg-Osgood* model is discussed.

The Ramberg-Osgood model is considered to be adequate for modelling the response of cold worked steel [373]. Nevertheless, the difficulty associated with finding an explicit expression for stress in terms of strain, makes this model less used for stiffness-based formulations.

- Mander's model

This model was proposed by Mander and co-workers [362, 363] within the framework of the seismic design of bridge piers. The monotonic skeleton curve is defined by (see Figure III.56-a):

$$\sigma_s = \begin{cases} E_s \varepsilon_s, & \text{if } \varepsilon_s \le \varepsilon_{sy} \\ \sigma_{sy}, & \text{if } \varepsilon_{sy} < \varepsilon_s \le \varepsilon_{sh} \\ \sigma_{su} + \left(\sigma_{sy} - \sigma_{su}\right)\left(\dfrac{\sigma_{su} - \sigma_s}{\sigma_{su} - \sigma_{sh}}\right)^p, & \text{if } \varepsilon_{sh} < \varepsilon_s \le \varepsilon_{su} \end{cases}, \tag{III.130}$$

where the power *p* is defined by the ratio between the strain-hardening modulus and the secant modulus, obtained between the initial and final coordinates of the strain-hardened curve [363]:

$$p = E_{sh}\left(\frac{\varepsilon_{su} - \varepsilon_{sh}}{\sigma_{su} - \sigma_y}\right). \tag{III.131}$$

Under cyclic and alternating loading, the unloading curve is defined by a softening branch to take into consideration the well-known *Bauschinger effect*. This softened branch is shifted in the strain

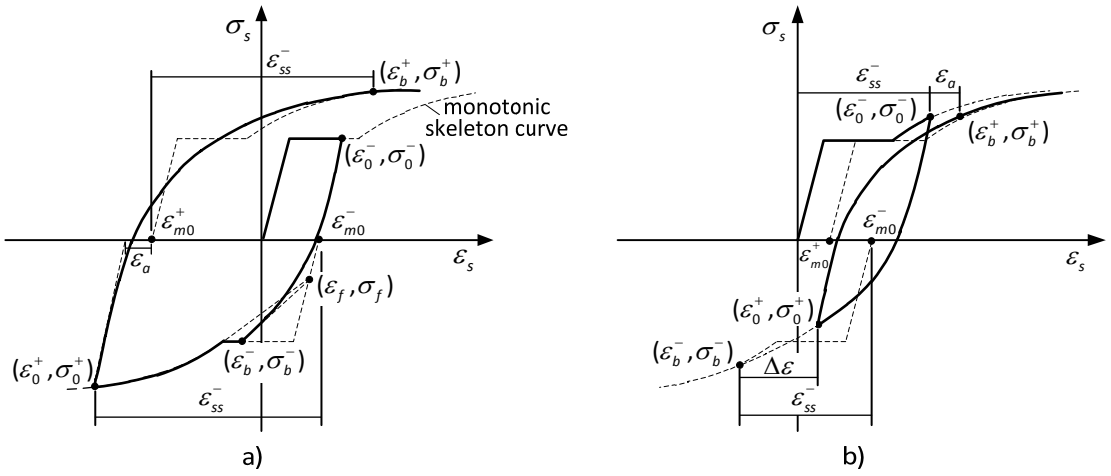

Figure III.56: Mander's model for reinforcing steel, adapted from Mander [363]:
a) reversal from the skeleton curve; b) reversal from a softened branch.

axes to take into consideration the cyclic loading history [363]. Two situations are considered: i) when the reversal starts from the skeleton branch (see Figure III.56-a) and ii) when the reversal starts from the softened branch (see Figure III.56-b).

In the first case, the new skeleton curve for the reversed direction is shifted by ε_{m0}, given by:

$$\varepsilon_{m0} = \varepsilon_0 - \frac{\sigma_0}{E_s} + \varepsilon_a \,, \tag{III.132}$$

in which, $(\varepsilon_0, \sigma_0)$ are the stress-strain coordinates at reversal and ε_a is given by:

$$\varepsilon_a = \begin{cases} 0, & \text{if } |\varepsilon_s| \le \varepsilon_{sh} \\ \dfrac{\varepsilon_{ss}^2}{\varepsilon_{su}} + 2\dfrac{\sigma_{sy}}{E_s}, & \text{if } |\varepsilon_s| > \varepsilon_{sh} \end{cases}, \tag{III.133}$$

where ε_{ss} is the skeleton strain in the previous cycle, as illustrated in Figure III.56-a. The unloading develops until crossing this new skeleton curve, which is followed afterwards.

In the second case, the reversal occurs before reaching the skeleton curve and there will be a strain gap between the reversal strain and the skeleton curve strain, as demonstrated in Figure III.56-b. The following relation is verified:

$$\varepsilon_b = \varepsilon_{\max} + \varepsilon_a \,, \tag{III.134}$$

$$\sigma_b = \sigma_{\max} \,, \tag{III.135}$$

where $(\varepsilon_{\max}, \sigma_{\max})$ correspond to the maximum strain and stress attained in the previous cycle and ε_a is given by:

$$\varepsilon_a = \begin{cases} \varepsilon_{su}\ \varepsilon_b, & \text{if } |\varepsilon_{\max}| \le |\varepsilon_{sh}| \\ \varepsilon_{su}\ \varepsilon_b - 0.5\dfrac{\sigma_{sy}}{E_s}, & \text{if } |\varepsilon_{\max}| > |\varepsilon_{sh}| \end{cases}, \tag{III.136}$$

The softened branch is defined by a modified form of the Guiffrè-Menegotto-Pinto equation. More information about this model can be retrieved from the references [362, 363, 451].

- *Guiffrè-Menegotto-Pinto* model

The *Guiffrè-Menegotto-Pinto* (GMP) model originated from the work of Guiffrè and Pinto [241] and was implemented and used by Menegotto and Pinto [396]. This model is widely used and can accurately reproduce experimental results with similar amplitude cycles. The formulation is based on the definition of a series of monotonic stress-strain curves that represent a transition from the elastic stiffness to an asymptote representing a hardening stage. Mathematically, the constitutive relation is defined by the equation [396]:

$$\sigma_s^* = \beta \varepsilon_s^* + (1-\beta)\frac{\varepsilon_s^*}{\left(1+\left(\varepsilon_s^*\right)^R\right)^{1/R}}, \tag{III.137}$$

where $\left(\sigma_s^*, \varepsilon_s^*\right)$ represent a coordinate transformation, defined in the first loading by:

$$\begin{cases} \varepsilon_s^* = \dfrac{\varepsilon_s}{\varepsilon_{sy}} \\ \sigma_s^* = \dfrac{\sigma_s}{\sigma_{sy}} \end{cases}, \tag{III.138}$$

and afterwards, by:

$$\begin{cases} \varepsilon_s^* = \dfrac{\varepsilon_s - \varepsilon_{sa}}{2\varepsilon_{sy}} \\ \sigma_s^* = \dfrac{\sigma_s - \sigma_{sa}}{2\sigma_{sy}} \end{cases}, \tag{III.139}$$

where $\left(\varepsilon_{sa}, \sigma_{sa}\right)$ represent the strain and stress at the inversion point preceding each branch and β represents the ratio between the elastic and hardening slopes (see Figure III.57-a).

The parameter *R* is similar to a curvature radius for the transition between the unloading/reloading and the hardening slope and is used to take into consideration the *Bauschinger effect.* The following expression was proposed by Menegotto and Pinto for this parameter [396]:

$$R_k = R_0 - \frac{a_1 \zeta_k}{a_2 + \zeta_k}, \tag{III.140}$$

where R_0, a_1 and a_2 are material parameters to be identified and ζ_k is a parameter associated with the absolute value of the last plastic deformation (see Figure III.57-b).

Two improvements were made to the original formulation by Filippou, Popov and Bertero [217]. The first improvement consists of a new definition for the variable transformation in order to improve the accuracy of the model [246]:

$$\begin{cases} \varepsilon_s^* = \dfrac{\varepsilon_s - \varepsilon_{sa}}{\varepsilon_{s0} - \varepsilon_{sa}} \\ \sigma_s^* = \dfrac{\sigma_s - \sigma_{sa}}{\sigma_{s0} - \sigma_{sa}} \end{cases}, \tag{III.141}$$

where $\left(\varepsilon_{s0}, \sigma_{s0}\right)$ represents the strain and stress at the intersection between the elastic and

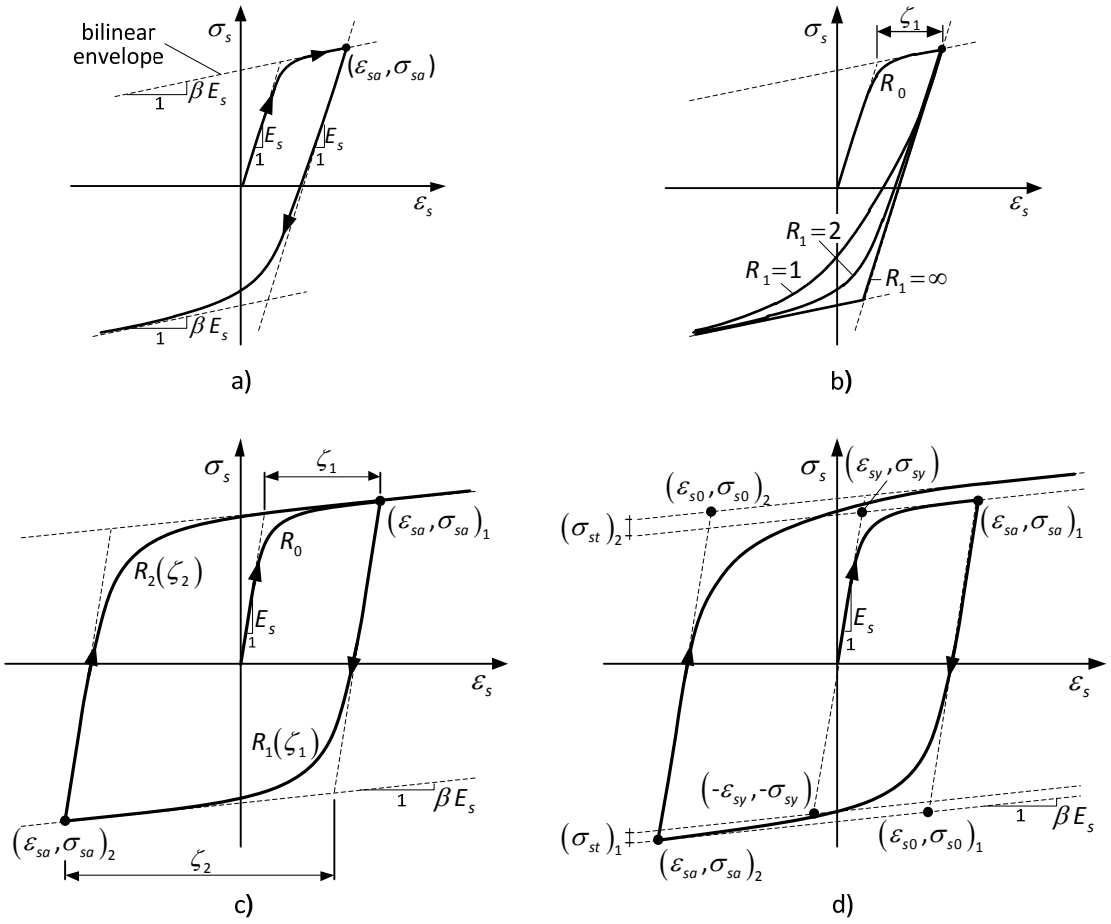

Figure III.57: Guiffrè-Menegotto-Pinto model: a) definition of the softened curve; b) the effect of the parameter *R*; c) initial version [396]; d) improvements proposed by Filippou *et al* [217].

hardening slopes (see Figure III.57-c).

The second improvement corresponds to the inclusion of a stress evolution to model the cyclic hardening. This latter phenomenon could not be simulated with the early version of the GMP model. This is made by shifting the yield stress by σ_{st}, using the expression (see Figure III.57-d):

$$\left(\sigma_{st}\right)_k = \sigma_{sy}\ a_3\left(\frac{\left(\varepsilon_s^{\max}\right)_k}{\varepsilon_{sy}} - a_4\right), \tag{III.142}$$

where $\varepsilon_s^{\max}$ is the absolute maximum strain at the instant of strain reversal and a_3, a_4 are material parameters to be identified.

As a general appreciation, the original GMP model has proven to be adequate for simulating the response of reinforcing steel subjected to cycles with similar amplitude and is less accurate for incomplete cycles. The mathematical equation for the softened curve is adequate for simulating the *Bauschinger effect* and the model presents a convenient format for stiffness-based FE formulations. The improvements introduced by Filippou *et al.* made it possible to use this model for more general loading situations and enhanced the accuracy, in particular for asymmetric cycles.

2.4 Interfaces

2.4.1 Concrete-concrete interfaces

Discontinuities are present in the concrete matrix for low intensity loading stages, or even, before loading, *e.g.* cracks and concrete cast joints. These discontinuities are rather common in concrete and their consequences should not be underestimated [87]. Within the scope of this thesis, these discontinuities are called *concrete-concrete interfaces*. Normal loadings to these interfaces generate the complex mechanism of crack opening and closure. With regard to tangential loads, the main load transmitting mechanisms are the following: i) *aggregate interlock*; ii) *dowel action*; and iii) *debounding forces* (see Figure 13).The aggregate interlock is related to the micro-roughness between macro-cracks. High shear forces can be obtained, if there is enough normal force to mobilize friction (see Figure III.58-a). The most influencing parameters are the size and shape of the aggregates and the tensile concrete resistance. More information can be retrieved from the references [69, 290].

Part of the shear forces can also be transmitted by shear and bending of the reinforcements, *a.k.a. dowel action*. This is mainly a structure-based phenomenon because the main parameters are the amount and distribution of reinforcement, the shape of the section and some material parameters like the concrete's compression and tension resistance (see Figure III.58-b). Another mechanism, usually not considered, are the forces of debounding that are responsible for the softening branch of concrete under tension, which generates low but important forces (see Figure III.58-c).

CEB's report [87] presents a summary of the available models to describe these mechanisms.

2.4.2 Concrete-steel interfaces

The *concrete-steel interfaces* (CSI) play the important role of transmitting forces between the reinforcements and the concrete. These interfaces can be very significant to the response of the RC elements because they include the well-known *bond mechanism*, which in case of failure accelerates the stiffness and strength degradation, potentiates intense pinching, and leads to the decrease of the energy dissipation by hysteresis. Chapter IV is entirely dedicated to this significant phenomenon.

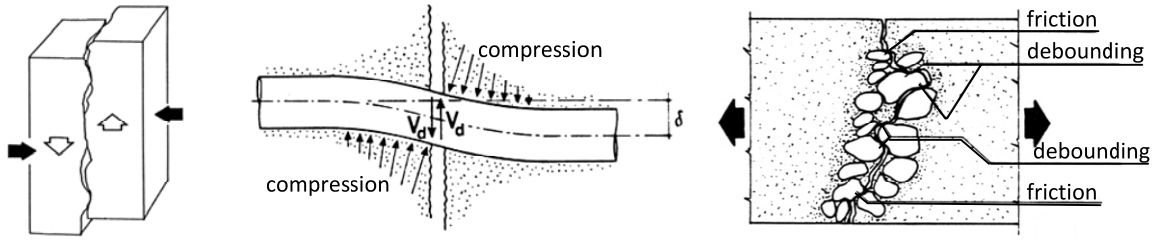

Figure III.58: Load transmission in concrete-concrete interfaces, adapted from [87]:
a) aggregate interlock; b) dowel action; c) debounding forces.

2.5 RC elements

This section presents a summarized description of the most relevant characteristics of the response of RC elements. The presentation is made in terms of the response under simple or combined loading types and is followed by some particular effects that change the global response of the elements, *e.g.* confinement. More information about the response of RC elements can be obtained in the following references [86-89, 117, 403, 424, 432].

2.5.1 Response to bending with and without axial loading

- Monotonic loads

When properly designed, the response of RC elements subjected to bending is controlled by the steel reinforcements, which concentrates most of the inelastic behaviour. The qualitative response is illustrated in Figure III.59-a and can be summarized as follows. At an early stage, the tensioned concrete cracks and stiffness decreases. This phenomenon can be delayed due to the influence of compressive stresses associated with the axial forces, as in the experimental results presented in Figure III.59-b. Afterwards, the RC element behaves like a cracked RC element until the reinforcement yields. This phase is followed by a large increase in the global displacements and by some strength increase due to steel hardening until rupture of the reinforcements. Failure controlled by compressed concrete may occur if the strength of the tensioned reinforcements is very high, leading to an undesirable fragile collapse.

The presence of compressive axial loads increases the flexure resistance of a RC element until the collapse is caused by concrete crushing $\left(\nu = N/bd\,f_c \approx 0.40 \text{ to } 0.50\right)$. After this value, resistance is decreased by early concrete crushing (see Figure III.60). In terms of ductility, axial forces reduce the maximum curvature of the element and create a more brittle collapse due to earlier concrete crushing [117].

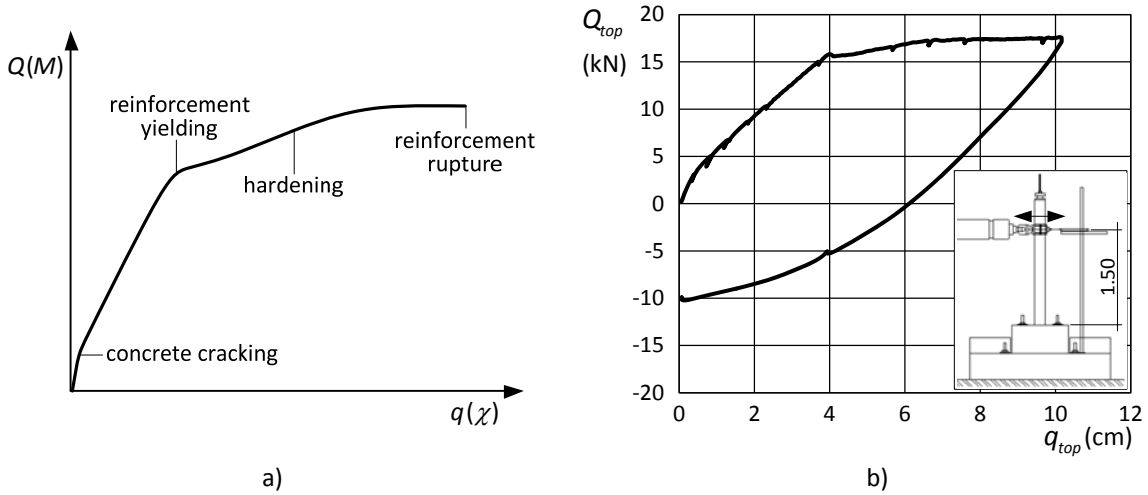

Figure III.59: RC elements subjected to bending: a) typical response; b) experimental data, adap. from Mendes *et al.* [394].

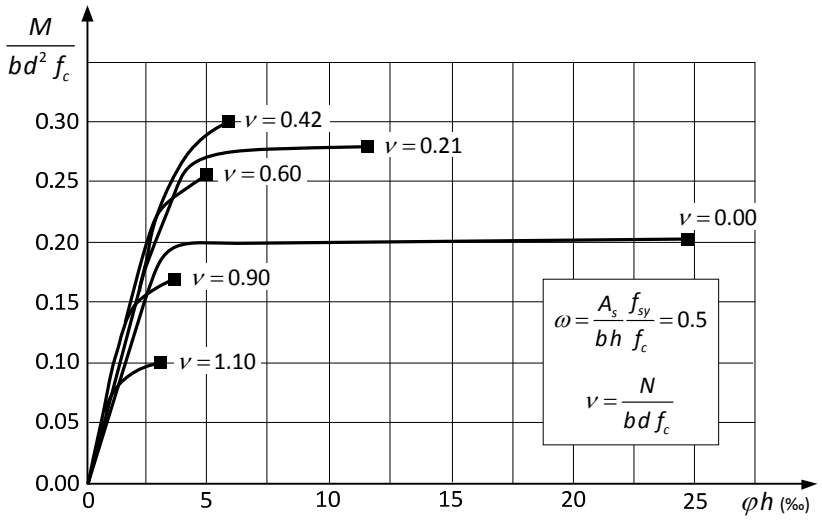

Figure III.60: Effect of axial forces on the resistance and ductility of RC elements, adap. from Monteiro *et al.* [403].

- Cyclic and alternating loads

The response of RC elements subjected to cyclic and alternating loading is summarized in Figure III.61. This figure represents the results of cyclic tests with symmetrically reinforced RC elements without axial loading performed by Ma *et al.* [348]. The response is characterized by:

i. Stiffness degradation on reloading after plastic excursions – *Bauschinger effect*;
ii. Sudden increase of stiffness on reloading due to crack closure – *pinching effect*;
iii. Resistance degradation due to accumulated concrete damage and bond failure;
iv. Collapse of the RC element by failure of tensioned reinforcements or by concrete crushing.

On asymmetrically reinforced elements, the cycles can be characterized by the absence of *pinching* in one direction due to insufficient forces to close the cracks on the side with smaller area of reinforcements. In the opposite direction, when the smaller reinforcement area is compressed, the stronger tensioned reinforcements present a stiffer response, even elastic, and can mobilize more strength. The combination of higher stiffness and resistance in tensioned reinforcements leads to sudden crack closure and to a very clear *pinching* effect (see Figure III.62-b).

Moreover, when reversed bending is coupled with compressive axial loads, the crack closure is improved by the presence of axial forces and *pinching* is less significant.

The absence or the reduction of the *pinching effect* contributes to wider hysteretic cycles, and consequently, to higher energy dissipation. In addition, the *pinching effect* is generally associated with intensified degradation due to higher damage in the concrete-concrete interfaces, *e.g.* concrete crushing.

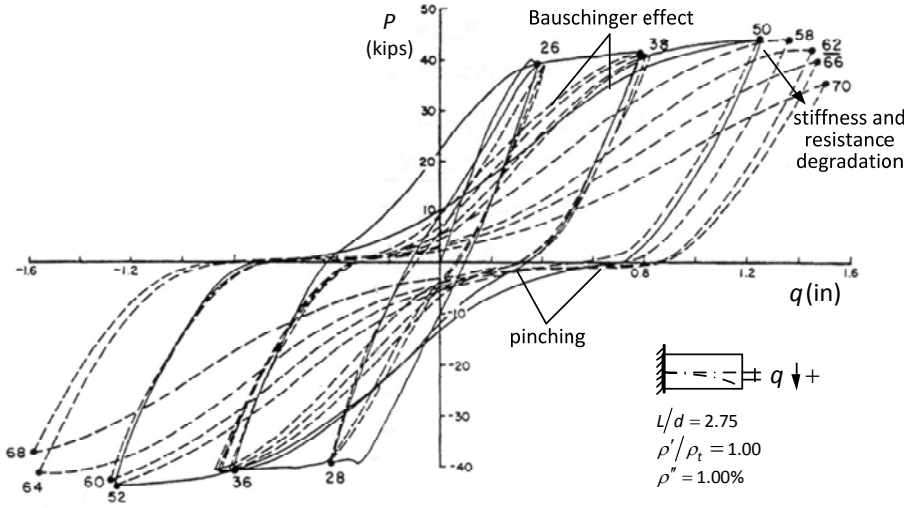

Figure III.61: Force-displacement diagram of RC elements under bending, low shear forces and without axial forces, adapted from Ma *et al.* [348].

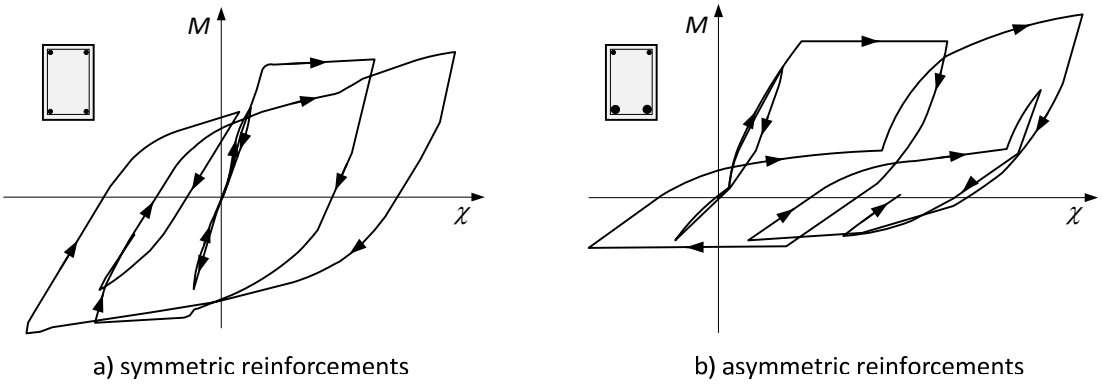

Figure III.62: Bending moment vs. curvature diagrams of RC elements, adapted from Park *et al.* [431].

2.5.2 Effect of shear forces

The presence of high shear forces leads to stiffness and strength decrease and to the reduction of energy dissipation capacity of RC elements subjected to cyclic and alternating loading [117]. This is the case of short columns and beams or shear walls. This happens mainly because shear deteriorates the contact surfaces of the concrete-steel and concrete-concrete interfaces, leading to early bond failure and to degradation of the aggregate interlock and dowel action mechanisms.

The experimental data regarding the concrete response under intense shear stress states is not as extensive as that for the other basic deformation modes (axial and bending forces). Nevertheless, the experimental results obtained by Bertero *et al.* [54] and Çelebi *et al.* [90], presented in Figure III.63 and in Figure III.64 respectively, show that the specimens with smaller span/depth ratio present higher degradation and significant *pinching effects*, and consequently, narrow hysteretic cycles and lower energy dissipation.

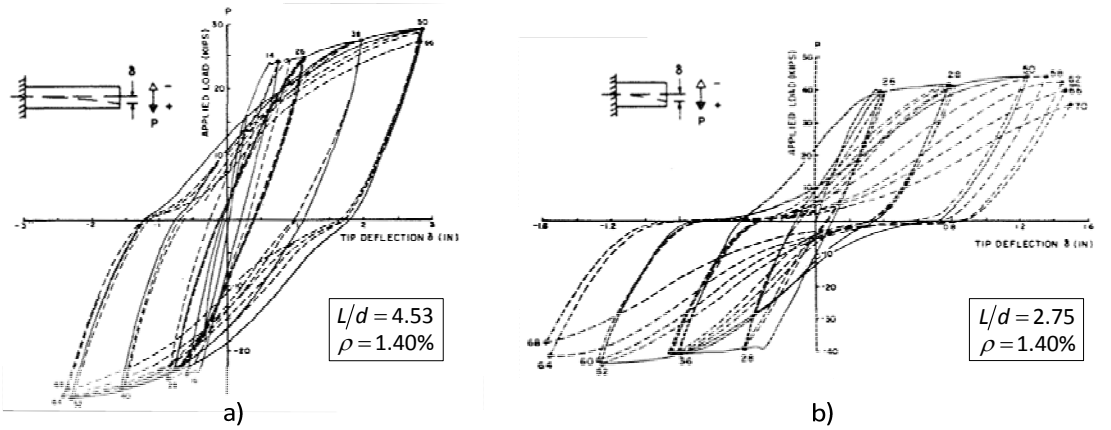

a) b)

Figure III.63: Effect of shear forces on the response of RC elements, adapted from Bertero *et al.* [54].

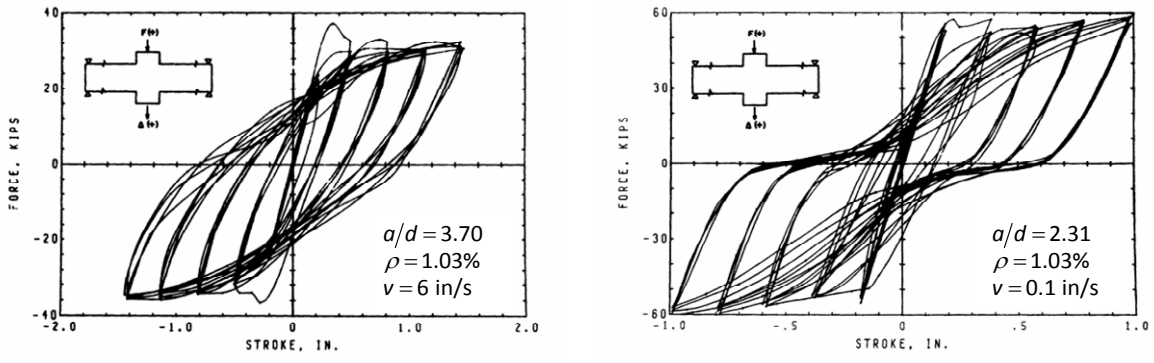

a) b)

Figure III.64: Effect of shear forces on the response of RC elements, adapted from [424], after the original [90].

2.5.3 Passive confinement

When a RC member is axially compressed, the transverse reinforcements create the so-called *passive confinement effect*, by restraining the expansive lateral deformations associated with Poisson's effect. The main quantities that influence passive confinement are the lateral deformation induced in the concrete and the amount, spacing and stiffness of the transverse reinforcements. When the compressive forces are low, the transverse reinforcements are only lightly stressed and the passive confinement is also low. On the other hand, when the compressive forces are high this effect becomes more significant.

The effect of the type and spacing of transverse reinforcements is illustrated in Figure III.65 by grey colouring of the zones where the confinement effect is more effective. Other factors influencing the passive confinement are the areas of the transverse and longitudinal reinforcements that influence the stiffness of the bars enclosing the concrete core.

Concerning the effect of the type and spacing of the transverse reinforcements, spiral transverse reinforcements tend to produce a higher confinement effect than rectangular hoops. As illustrated in

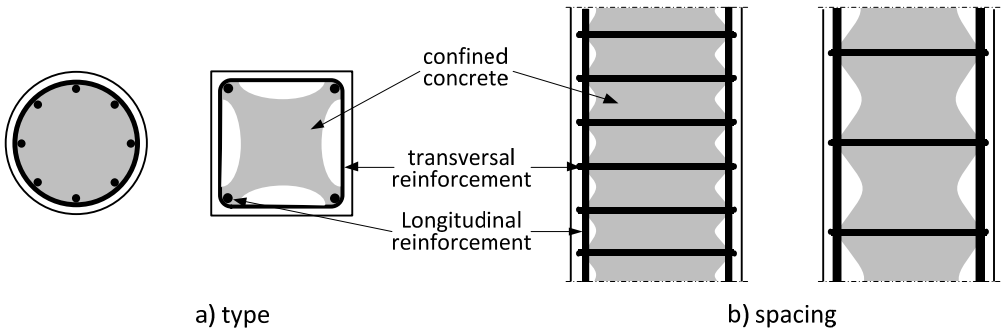

Figure III.65: Effect of spacing and reinforcement type on the effectiveness of the passive confinement effect, adap.[432].

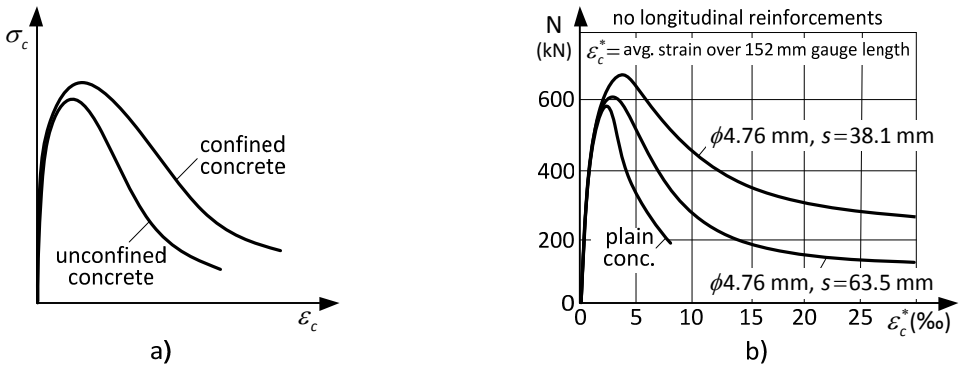

Figure III.66: Passive confinement effect: a) typical response; b) experimental results, adap from [432] after [53].

Figure III.65-a, spiral reinforcements are more effective mainly because they are tensioned for expanding concrete deformations, which presents a high stiffness that leads to high confinement levels. Conversely, the rectangular hoops are less effective in between the bends near the longitudinal reinforcements, because in these regions they are mainly subjected to lateral deformation (bending) that is much less effective. Transversal reinforcement spacing is also very important in order to ensure a relatively homogenous confinement distribution along the RC member axis (see Figure III.65-b).

Figure III.66-a presents the typical stress-strain curve for compressed concrete with and without passive confinement by the reinforcements. It can be seen that the ascending branch of the stress-stress relation is not significantly affected by the passive confinement, because the lateral deformation induced by the compressive forces is low.

For very high levels of compression, concrete crushing may occur and cover spalling is likely to occur. Confinement can compensate for the decrease of lever due to cover spalling by increasing the core concrete compressive strength and ductility and significantly change the post-peak branch (see Figure III.66-a). Figure III.66-b presents the axial load-strain curves obtained by Bertero and Felippa with square concrete prisms with various contents of square ties, which confirm the general observations made before and demonstrate the importance of this phenomenon.

Additional information about this subject can be found in the following references [363, 432].

2.5.4 Ductility

After resistance, ductility is one of the most important parameters governing the response of RC elements. Ductility is known as the capacity of a RC element to deform beyond the elastic domain without significant changes in resistance. Ductility is very important for ensuring stable hysteretic cycles in which high quantities of energy can be dissipated without developing high internal forces [403]. A common parameter used to measure the ductility of a RC member is the so-called *ductility factor* (μ) that was already introduced in Chapter II-§6.1 (see Figure II.18-a). Energy dissipation capacity depends on the ductility of the elements but also on other structural parameters, such as redundancy.

Figure III.67-a presents a situation of a car park collapse after large inelastic deformation in the columns, demonstrating the high level of ductility in RC elements. On the contrary, Figure III.67-b illustrates a case of lack of ductility in a column subjected to large displacements due to torsional effects in a plane-asymmetric building, which resulted in a shear failure due to insufficient transversal reinforcements.

2.5.5 Plastic hinge length

The *plastic hinge length* (L_p) represents the length over which the inelasticity phenomena develops in RC linear elements, *e.g.* columns and beams. Theoretically, this length extends to the entire bar length [432] but the most significant inelastic response concentrates in a finite region that is referred to as the plastic hinge length. Figure III.67-a and Figure III.67-c show two situations that led to very different plastic hinge lengths, which seems to be also related to the collapse type of the structure.

The plastic hinge length has been associated with many factors. Some of those are material-related quantities, such as the steel yield and ultimate strength and the concrete properties. Others are structurally related, such as the geometric dimensions of the member and the bending moments, the shear and the axial forces installed in the RC element. In addition, other factors can be seen as materially and structurally dependent, *e.g.* the cracking pattern and propagation.

Several proposals have been made to estimate the plastic hinge length. Most of them are based on

a) b) c)

Figure III.67: RC ruptures following earthquakes [52, 498]: a) Collapse of car park structure in Northridge 1994; b) shear failure in a plan-asymmetric building in Guatemala 1976; c) Hinging at the ends of *soft storey* columns in Managua 1972.

experimental studies that result in empirical formulas.

The author Bento [50] presents a compilation of the most used expressions for estimating the plastic hinge length, which is summarized in the following paragraphs.

Mattock [379] proposed the following expression following the work of Corley [143]:

$$L_p = 0.5d + 0.05z\,, \tag{III.143}$$

where is *d* is the *effective depth* and *z* is the distance between the critical zone and the inflexion point.

Moreover, Tassios in a study for the initial developing phase of Eurocode 8 [92] proposed the following expression for columns in buildings:

$$L_p = h + 0.50L\,, \tag{III.144}$$

where *h* represents the section height and *L* the length of the RC element. In addition, the same author suggested the following expression for a conservative estimate:

$$L_p = 0.1L\,. \tag{III.145}$$

After a series of experiments with bridge piers, Priestley *et al.* [460] proposed using the expression:

$$L_p = 0.08L + 6\phi_s\,, \tag{III.146}$$

where ϕ_s the diameter of the longitudinal bars.

The same authors proposed also for bridge piers a formula that defines the *plastic hinge length* as dependent only on the cross-section height:

$$L_p = 0.50h\,. \tag{III.147}$$

Following this work, Pauley and Priestley [435] suggested introducing the yield strength of steel reinforcing bar in equation (III.146):

$$L_p = 0.08L + 0.022 f_{sy}\,\phi_s\,, \tag{III.148}$$

where f_{sy} is expressed in MPa.

A similar formula is proposed in Part 2 of Eurocode 8 [93], which addresses bridge structures:

$$L_p = 0.10z + 0.015 f_{sy}\,\phi_s\,, \tag{III.149}$$

where *z* is the distance from the plastic hinge to the section of zero moment.

More recently, Coleman *et al.* [121] proposed an expression mainly dependent on the concrete characteristics, such as the compressive strength and the fracture energy in compression, see *Scott et al.* for further details [499].

These proposals for estimating the *plastic hinge length* show a lack of consensus and consistency in the parameters chosen to describe this quantity.

The plastic hinge concept is a very useful to define the length of the refined mesh within the scope of the hybrid discretization proposed in this thesis and presented in Chapter V-§3.

2.5.6 Modelling strategies

This subsection reviews the most prominent modelling strategies for simulating the nonlinear response of RC elements subjected to seismic loading. It presents a summarized description of each approach and their main advantages and drawbacks. Further information regarding this issue can be retrieved from the state of the art presented in the following references [117, 537].

- Nonlinear formulations

Different strategies have been used to simulate the nonlinear response of RC elements. The authors Miramontes *et al.* [397] proposed a classification with regard to the formulation of the inelastic model, which seems to result in a consistent classification. This proposal can be summarized as follows (see Figure III.68):

i. *Global Models, a.k.a. Hysteretic* or *Phenomenological Models,* are formulated in terms of hysteretic rules defined using generalized variables, *e.g.* (N,ε) or (M,χ). They usually adopt a simplified kinematic hypothesis, *e.g.* Navier-Bernoulli, and take directly into consideration the combined response of the concrete, steel and their bond;
ii. *Semi-local Models* present some level of discretization to simulate the inelastic phenomena, usually at the cross-section level, but some part of the element is still considered using a global approach, *e.g.* along the bar length;
iii. *Local Models, a.k.a. Microscopic* or *Refined Finite Element Models*, try to simulate the structural elements and the materials locally as a continuous media using constitutive relations defined by material-related properties, such as stiffness, resistance, *etc*.

Global Models (GM) have been used since the beginning of nonlinear computational modelling of RC structures subjected to seismic loading. This approach can be very efficient from the computational point of view because combining hysteretic rules with simplified element formulations, such as classical beam theory, results most of the time in relatively small problem sizes and in constitutive

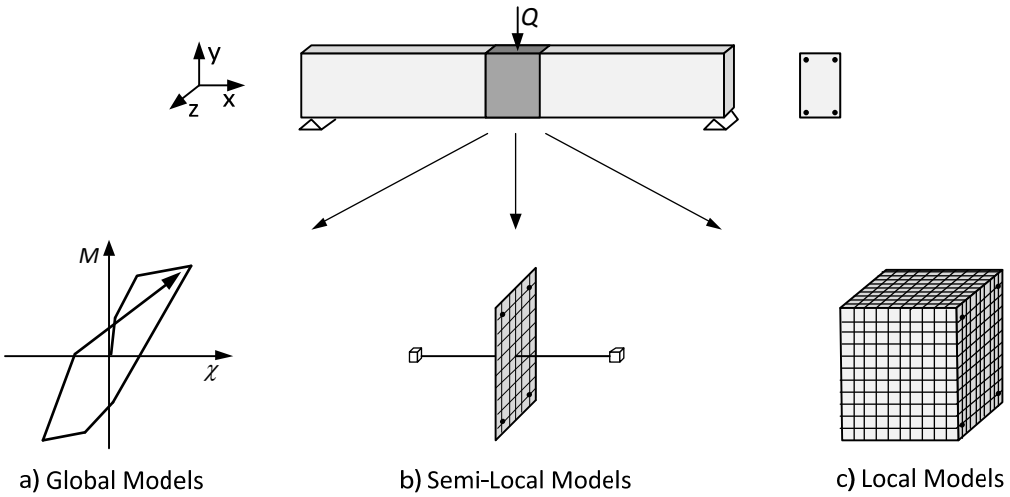

Figure III.68: Different nonlinear modelling formulations

relations which are easy to evaluate. The former is true for modelling RC elements subjected essentially to axial load and uniaxial bending (*e.g.* beams and columns in two-dimensional analyses). However, it becomes extremely difficult to model the effect of biaxial bending with axial loads, because the hysteretic rules are extremely difficult to define, especially under cyclic and alternating loading, although, some proposals have been made, *e.g.* Bousias *et al.* [62].

Some examples of global models are the classical bilinear, with or without hardening, and multi-linear models. Among those, are the contributions of Clough *et al.* [115], Giberson [239], Takeda *et al.* [535], Anagnostopoulos [9], Saiidi *et al.* [494], or more recently, the models proposed in the following references [62, 125, 145, 216, 397], to name just a few.

Global models have been used by several authors in the context of seismic performance assessment, *e.g.* [14, 50, 117]. However, the use of this approach has been decreasing. The main reason for this is related to the development of alternative techniques, in particular, formulations based on semi-local modelling, in particular the so-called *Fibre Models* (FM), *a.k.a. Multi-layered* or *Multi-fibre models* (see Figure III.69).

Currently, *Fibre Models* are being intensively used for nonlinear modelling of RC structures and have been applied to a great variety of structures, such as buildings [51, 122, 384, 385, 449] and bridges [82, 254, 553]. When compared to the *Global Models*, the main advantages of this technique are the innate ability for considering biaxial bending and the increased flexibility of the approach for extending the application to different materials, geometries, *etc.*, still with an acceptable computational efficiency.

In the original version, the FM approach was formulated in the traditional finite element displacement approximation, *e.g.* [36, 262, 298, 367]. The basic steps of this approach consist of using classic beam theory assuming that plane sections remain plane after deformation and computing the bar stiffness operator, using:

$$\mathbf{K}_b = \int_0^L \mathbf{B}_b^t \mathbf{k}_s \mathbf{B}_b \, dx \,, \tag{III.150}$$

where $\mathbf{k}_s$ represents the cross-section stiffness, which relates the generalized stresses and displacements of the cross-sections, and $\mathbf{B}_b$ holds the derivatives of the bar's interpolation functions, which in this case are the well-known *Hermite cubic polynomials*.

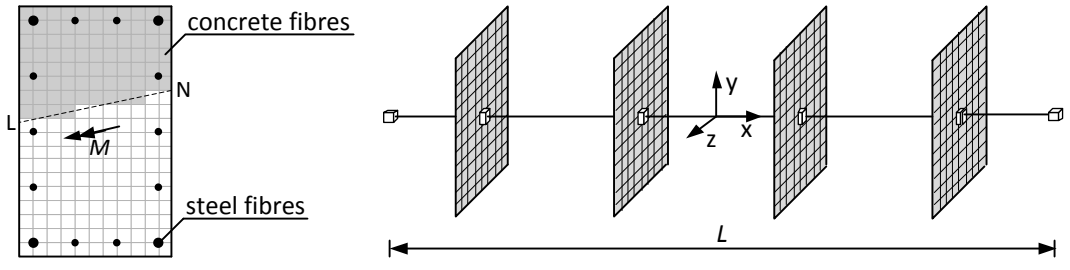

Figure III.69: Fibre Models – Schematic representation.

The cross-section stiffness can be found by adding the contribution of all fibres, using:

$$\mathbf{k}_s = \int \mathbf{B}_s^t \mathbf{k}_f \mathbf{B}_s \, d\Omega \,, \tag{III.151}$$

where $\mathbf{k}_f$ holds the stiffness of each fibre and $\mathbf{B}_s$ holds the cross-section deformation modes.

According to *Taucer et al.* [537], the stiffness-based elements present some drawbacks near the ultimate resistance and in the softening phase. Moreover, the linear curvature distribution along the element, implicit in using the cubic Hermitian interpolation, is not representative of the effective distribution after intense inelastic phenomena, which become strongly nonlinear. These and other drawbacks led to the introduction of flexibility-based approximation functions, still in displacement-based FE implementations [349]. These functions can be updated throughout the analysis in order to follow the evolution of the inelasticity in the bar [537]. FM have also been defined in flexibility-based formulations that can be more accurate in modelling the effective force distribution in the bar element. In this case, the bar flexibility matrix can be obtained from:

$$\mathbf{F}_b = \int_0^L \mathbf{S}_b^t \mathbf{f}_s \mathbf{S}_b \, dx \,, \tag{III.152}$$

where $\mathbf{f}_s$ represents the cross-section flexibility that can be obtained by inverting the cross-section stiffness defined in equation (III.151). The operator $\mathbf{S}_b$ represents the interpolations functions for the generalized forces, which often considers linear distributions for the bending moments in the bar [537]. On the other hand, when flexibility-based formulations are implemented in stiffness-based FE codes, the state determination is more complex, although some proposals to address this issue have been made [13, 14, 65, 110, 521].

Nevertheless, common fibre models are formulated at the cross-section level (see Figure III.69), thus it is difficult to directly simulate the effect of shear forces, the effect of concrete-steel bond failure and the deformability of joints. Consequently, fibre models are more accurate for elements with a predominant flexure-related response and should not be used for elements under high shear, *e.g.* short columns and RC walls. Some fibre models include in parallel a strut-tie model to simulate the response for shear loading, *e.g.* Guedes [254].

Local Models are rarely adopted as the modelling solution for RC structures subjected to seismic loading, except for a few exceptions [523]. The reason for this is strongly related to some disadvantages associated with the increased complexity of the formulation and the high computational cost. Most of the applications refer to the study of local behaviour of structures, *e.g.* isolated elements and connections. However, this formulation may be extremely general and able to simulate most phenomena, *e.g.* the behaviour of the interfaces, shear forces effect, warping of sections and joint behaviour. The disadvantages of these models are becoming less significant due to recent developments in constitutive relations and high performance computational tools. Under these circumstances, new advances in these models are expected in the near future and their use will probably spread. This is the approach adopted in this work and the advantages *vs.* disadvantages analysis is made throughout the thesis.

- Nonlinear element formulations

Another possible classification is with respect to the zone where the inelastic behaviour is considered. The following classification is common [117]:

i. The *Concentrated Plasticity models, a.k.a. Lumped models,* consider the inelastic phenomena concentrated in a finite region of the element, usually associated with the *plastic hinge*[i] *length* and located at the element extremities;
ii. The *Distributed Plasticity models* consider the inelasticity distributed along the length of the bar.

Figure III.70 presents some examples of nonlinear models used for the simulation of RC elements subjected to seismic loading. Figure III.70-a represents the well-known *Clough-Benuska* model [114], which considers two sub-elements in parallel: a fixed elastic contribution and an elastoplastic component that becomes hinged after steel yielding. In addition, Figure III.70-b represents the *Giberson model*, in which nonlinear rotational springs are located at the bar ends, where the highest stresses are expected. These springs can be associated with an hysteretic model in terms of bending moment *vs.* relative rotation (M,θ). These two models can be classified as *Concentrated Plasticity models.* Other proposals using this approach can be found in the references [9, 145, 216, 494, 499].

Figure III.70-c presents an example of a *Distributed Plasticity model.* It is represented the proposal made by Takayanagi-Schnobrich [534] that consists in dividing the element into a finite number of sub-elements that are associated with nonlinear rotational springs, which become less stiff near the bar ends. Other examples of *Distributed Plasticity models* are when fibre discretizations are used in cross-sections distributed over the element's length and the *Refined Finite Element Models* that are adopted in this thesis.

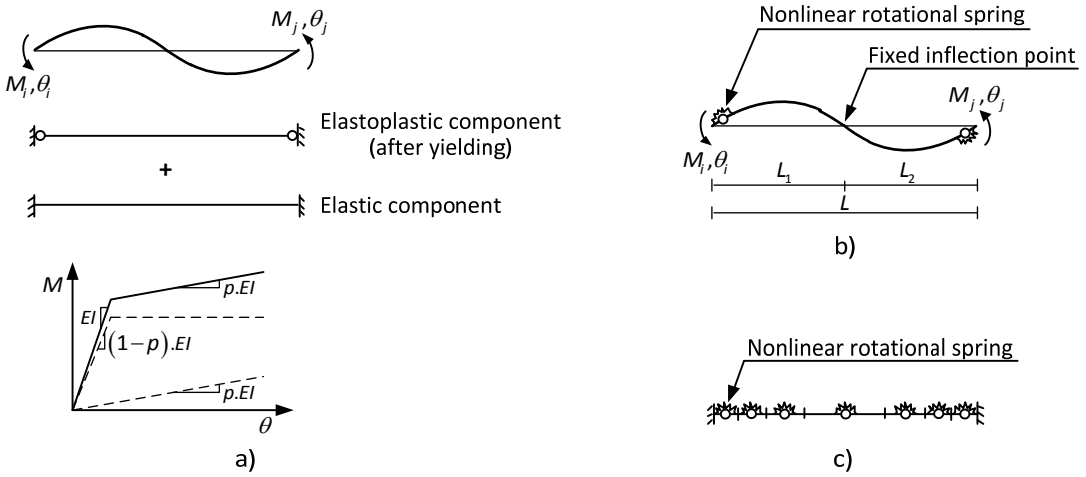

Figure III.70: Examples of nonlinear element formulations, adapted from Taucer *et al.* [537]:
a) *Clough-Benuska model* [114]; b) *Giberson model* [239]; c) *Takayanagi-Schnobrich model* [534].

[i] the term *plastic hinge* is used as in section 2.5.5 because it is widespread in the scientific community. Nevertheless, the phenomena in question are not only governed by steel yielding, so the term *inelastic* seems more appropriate.

3 Models for concrete

3.1 Introduction

As presented in Chapter I, one of the objectives of this thesis is to combine adequate material constitutive relations for simulating RC structures subjected to general loading. The methodology adopted for concrete is to use damage mechanics models to simulate the fracture phenomena that develop in the concrete. This was considered a fixed choice in this thesis and the objective was to test the representativeness and robustness of these models for the intended numerical simulations.

This thesis is not only dedicated to concrete modelling. It addresses other issues like modelling the reinforcing steel bars, the concrete-steel interfaces and improving the computational efficiency of the models. Accordingly, it was not feasible to propose a new damage model. This would have required an extensive development effort, followed by equally demanding validation work. Instead, it was decided to perform an extensive bibliographic research and implement the most suitable damage models to simulate the RC elements under seismic loading.

Three damage models were implemented and used to compute the validation examples presented in this thesis. The first model is referred to ahead as *SConcrete*, abbreviated designation for *Simplified Concrete* model*.* This model was developed and implemented to test the FE code developed and specific issues regarding the use of the damage mechanics approach, in particular, in situations with softening and localization.

Secondly, the *Comi-Perego 1DV* model [140], already presented in section 2.2.7, was used to test the nonlocal model implementation with the validation example RC1 and make further tests on the global model using simple tensile tests (*Hassanzadeh test*) by comparing the results obtained with experimental and other numerical results.

Furthermore, the Mazars' model [381] was used to simulate concrete in the most general situations considered in this work. This model was already presented and discussed in section 2.2.7 and this section addresses only the enhancements proposed in this thesis.

3.2 Simplified Concrete model (*SConcrete*)

The *Simplified Concrete* model will only be adopted for one-dimensional test cases. This model adopts the following definition for the Helmholtz free energy:

$$\rho\psi\left(\varepsilon,d\right)=\frac{1}{2}\left(1-d\right)E\,\varepsilon^2\,. \tag{III.153}$$

The state equations and the associated variables can be obtained from (III.48) and (III.49), leading to:

$$\sigma=\rho\frac{\partial\psi}{\partial\varepsilon}=\left(1-d\right)E\,\varepsilon\,, \tag{III.154}$$

$$Y=-\frac{\partial\psi}{\partial d}=\frac{1}{2}E\,\varepsilon^2\,. \tag{III.155}$$

For this simplified one-dimension case, the dissipation potential is defined by:

$$f = \varepsilon - \varepsilon^*(t) \leq 0, \tag{III.156}$$

with the elastic limit strain ε^* defined by:

$$\varepsilon^*(t) = \max\left\{\varepsilon_0, \max_{\forall \tau \leq t}\left(\varepsilon(\tau)\right)\right\}. \tag{III.157}$$

The evolution law for the damage variable is computed by equating the secant equation (III.154) with the softening branch equation presented in Figure III.71:

$$d(\varepsilon) = \frac{\varepsilon_0}{\varepsilon}\left(\frac{\varepsilon - \varepsilon_0}{\varepsilon_u - \varepsilon_0} - 1\right) + 1. \tag{III.158}$$

The damage variable presents the following variation with strain:

$$\begin{cases} d = 0, & \varepsilon \in \left]-\infty, \varepsilon_0\right] \\ d = \dfrac{\varepsilon_0}{\tilde{\varepsilon}}\left(\dfrac{\varepsilon - \varepsilon_0}{\varepsilon_u - \varepsilon_0} - 1\right) + 1, & \varepsilon \in \left]\varepsilon_0, \varepsilon_u\right] \\ d = 1, & \varepsilon \in \left]\varepsilon_u, +\infty\right] \end{cases}. \tag{III.159}$$

In the softening branch, damage does not relate linearly to the strain because there are two terms in equation (III.154) that are strain dependent (ε, d), leading to a quadratic relation.

The stress derivative required to compute the tangent matrix (II.206) is given by:

$$\frac{\partial \sigma}{\partial q} = \frac{\partial \sigma}{\partial \varepsilon}\frac{\partial \varepsilon}{\partial q} = \frac{\partial\left\{\left(1 - d(\varepsilon)\right)E\,\varepsilon\right\}}{\partial \varepsilon}\frac{\partial \varepsilon}{\partial q} = \left\{\left(1 - d\right)E - \frac{\partial d(\varepsilon)}{\partial \varepsilon}E\,\varepsilon\right\}\frac{\partial \varepsilon}{\partial q}, \tag{III.160}$$

where:

$$\frac{\partial d}{\partial \varepsilon} = \frac{\varepsilon_0^2 + \varepsilon_0\left(\varepsilon_u - \varepsilon_0\right)}{\varepsilon_{11}^2\left(\varepsilon_u - \varepsilon_0\right)}. \tag{III.161}$$

Introducing the strain matrix definition (II.38), the tangent matrix can be computed from:

$$\mathbf{K}_t = \sum_{gp=1}^{ngp}\left\{\left(\mathbf{B}^t(1-d)E\,\mathbf{B} - \mathbf{B}^t\frac{\partial d}{\partial \varepsilon}E\,\varepsilon\mathbf{B}\right)\det\mathbf{J}\,w\right\}_{gp}. \tag{III.162}$$

Table III.14 presents the parameters that define this model.

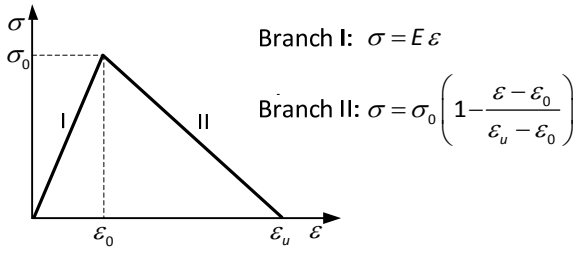

Figure III.71: *SConcrete model*: Definition of the stress-strain curve.

Table III.14: *SConcrete model* parameters.

Param.	Unit	Definition	Domain
E_s	Pa	elastic modulus	$[0,\infty]$
ν	-	Poisson's ratio	$[0,0.5]$
ε_0	-	strain at peak stress	$[0,\varepsilon_u]$
ε_u	-	strain at ultimate stress	$[\varepsilon_0,\infty]$
L_{nl}	m	nonlocal length	$[0,\infty]$

3.3 Modified Mazars' model (*MMazars*)

In this chapter, the Mazars' model was subjected to some modifications to improve the representativeness and the efficiency of the model. This variant will be designated as *Modified Mazars'* model, or simply by *MMazars,* and the original version simply by *Mazars'* model. The modifications consist of changing the stress-strain relation for tensile loading and introducing the non-deterministic strength into the model. These changes are discussed in detail in the following sub-sections.

- Response under tensile loading

The reason for making this proposal is related to some difficulties experienced using the original model in order to increase the mode I fracture energy without requiring the use of large values for L_{nl}. The original Mazars' model tended to create a brittle material response under tension and it was necessary to increase the mode I fracture energy to avoid unrealistic collapses.

The proposed material response under tensile loading is illustrated in Figure III.72. After the elastic range, a linear softening branch is adopted until the *comparison strain* $\tilde{\varepsilon}$ reaches $\tilde{\varepsilon}_u$. The material presents an adjustable residual resistance, controlled by the parameter R_p.

This residual resistance was used for two main reasons. Firstly, to avoid undesirable collapses associated with the isotropic nature of the damage considered (*e.g.* unrealistic shear failures). Secondly, it was used to avoid numerical problems by always having some stiffness level in the elements when the secant stiffness is adopted.

The damage evolution law can be defined by equating the secant constitutive law (III.102) with the desired stress-strain curve presented in Figure III.71, considering a one-dimensional stress state. This leads to:

$$\begin{cases} d_+ = 0, & \tilde{\varepsilon} \in \left]0, \tilde{\varepsilon}_0\right] \\ d_+ = 1 + \dfrac{\tilde{\varepsilon}_0}{\tilde{\varepsilon}}\left\{\left(1 - R_p\right)\dfrac{\tilde{\varepsilon} - \tilde{\varepsilon}_0}{\tilde{\varepsilon}_u - \tilde{\varepsilon}_0} - 1\right\}, & \tilde{\varepsilon} \in \left]\tilde{\varepsilon}_0, \tilde{\varepsilon}_u\right] \\ d_+ = 1 - \dfrac{\tilde{\varepsilon}_0}{\tilde{\varepsilon}} R_p, & \tilde{\varepsilon} \in \left]\tilde{\varepsilon}_u, +\infty\right] \end{cases} . \tag{III.163}$$

Figure III.76 presents the resistance envelope curve for biaxial loading. It is possible to observe that this modification in the model does not introduce significant changes in the overall response.

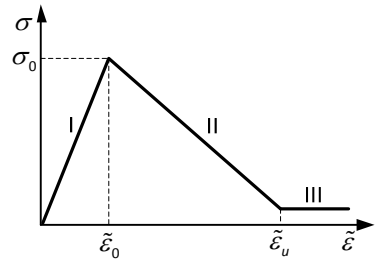

Branch **I:** $\sigma = E\tilde{\varepsilon}$

Branch II: $\sigma = \sigma_0\left\{1 + \left(R_p - 1\right)\dfrac{\tilde{\varepsilon} - \tilde{\varepsilon}_0}{\tilde{\varepsilon}_u - \tilde{\varepsilon}_0}\right\}$

Branch II: $\sigma = \sigma_0 R_p$

Figure III.72: *Modified Mazars' model* – Definition of the stress-strain curve for tensile loading.

- Variable mechanical properties

To implement a probabilistic distribution for strength it is necessary to generate random numbers which will be used to create a material scaling factor that simulates weaker and stronger materials. This can be achieved using a pseudorandom number generator it is possible to create a set of numbers that follow the Gaussian distribution with the desired arithmetic mean and standard deviation. It should be taken into consideration that pseudorandom number generators use deterministic algorithms, thus, if the internal state of the algorithm is influenced by some action, like restarting, the generated numbers cease to be random, in the sense that the same numbers will be always outputted. To overcome this problem it is necessary to ensure that the seeds used by the algorithm are not recurrent. One of the most used and simplest way to do this is by resetting the internal state of the algorithm with data from a source with very low probability to be repeated. In most situations, the computer internal clock can be used as a data source, taking advantage of the high accuracy used to specify the seconds.

Concrete is a material for which the strength dispersion is particularly high and this can have a significant effect on the fracture-related phenomena, which are conditioned by the weakest part of the material. Concrete also has a particular characteristic of having very different responses in tension and in compression, leading to different statistical characteristics.

The following general expression was used to compute the material strength in tension or in compression[i]:

$$f_{0,\eta}^{\pm} = f_0^{\pm}\ \eta_m^{\pm}, \tag{III.164}$$

where $f_0^{\pm}$ represents the mean strength $\left(f_{cm}, f_{ctm}\right)$ and $\eta_m^{\pm}$ the *strength scaling factor* defined to simulate variable material properties.

The material scaling factor is therefore defined by:

$$\eta_m^{\pm} = \frac{\hat{f}^{\pm}}{f_0^{\pm}}. \tag{III.165}$$

where $\hat{f}^{\pm}$ refers to the local strength values generated with the desired statistical properties.

To introduce the strength deviation in most constitutive relations it is simply necessary to scale one or just a few model parameters. For the Mazars' model changing the ε_{d0} parameter alone will only produce the desired results for some relations of model parameters. The desired effect can be introduced by scaling simultaneously the following model parameters:

$$\varepsilon_{d0}^{\eta} = \varepsilon_{d0}\ \eta_m. \tag{III.166}$$

$$B_{\pm}^{\eta} = \frac{B_{\pm}}{\eta_m}. \tag{III.167}$$

[i] the following expression results in two equations by considering all $\pm$ signs equal to $+$ or to $-$.

Using these expressions implies that the same dispersion is considered for compressive and tensile loading, which is not true as presented in Table III.6 and involves an approximation. If this effect is significant, it is always possible to use two scaling factors, one for tension and one for compression, or associate both, using the ratio between the two relative standard deviations, $\alpha = f_{RSD}^{-} / f_{RSD}^{+}$:

$$\eta_m^- = 1 + \left(1 - \eta_m^+\right)\alpha \ . \tag{III.168}$$

Figure III.73 and Figure III.74 present an illustrative example of changing these model parameters

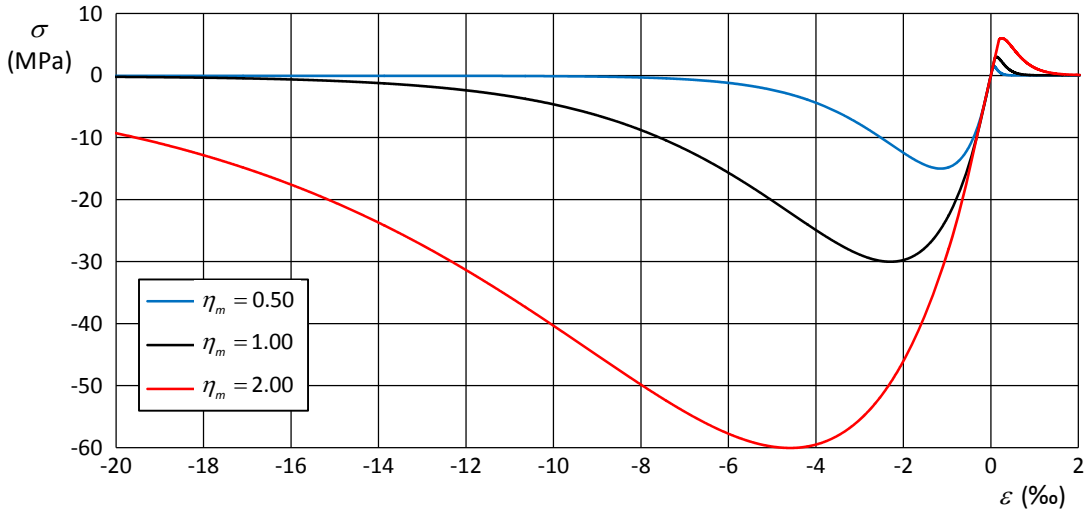

Figure III.73: *Mazars' model*: Stress-strain curves for a material subjected to uniaxial loading and considering variable strength.

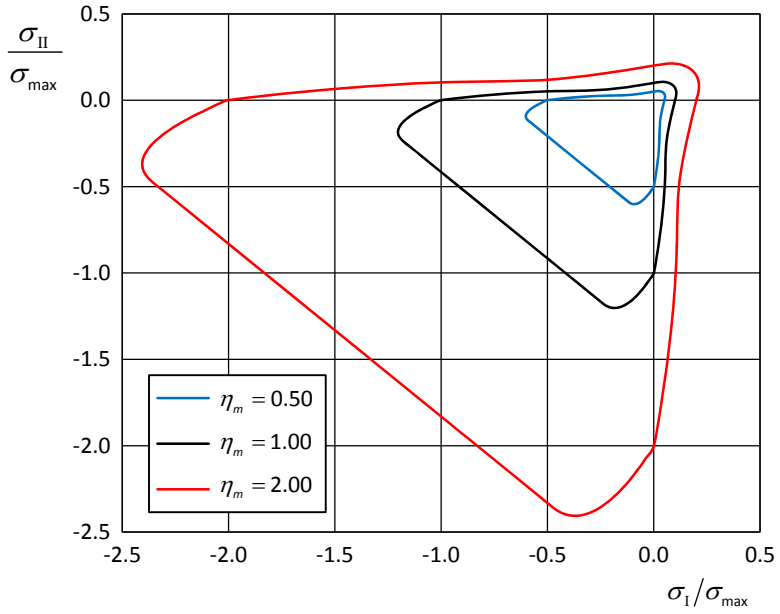

Figure III.74: *Mazars' model*: Resistance envelopes for a material subjected to biaxial loading and considering variable strength, $\sigma_{III} = 0$.

using equations (III.166) and (III.167) for a material defined with the following parameters: $E = 31$ GPa, $\nu = 0.20$, $\varepsilon_{d0} = 9.333\text{E-}05$, $A_{+} = 0.99$, $B_{+} = 8000$, $A_{-} = 0.99$ and $B_{-} = 1540$.

Only the model parameters ε_{d0} and B_{-} must be scaled for the *Modified Mazars' model* to produce the desired effects. Figure III.75 and Figure III.76 presents an illustrative example of changing these model parameters using equations (III.166) and (III.167) for a material defined with the following parameters: $E = 31$ GPa, $\nu = 0.20$, $\varepsilon_{0} = 9.333\text{E-}05$, $\varepsilon_{u} = 0.004$, $R_{p} = 0.03$, $A_{-} = 0.99$ and $B_{-} = 1540$.

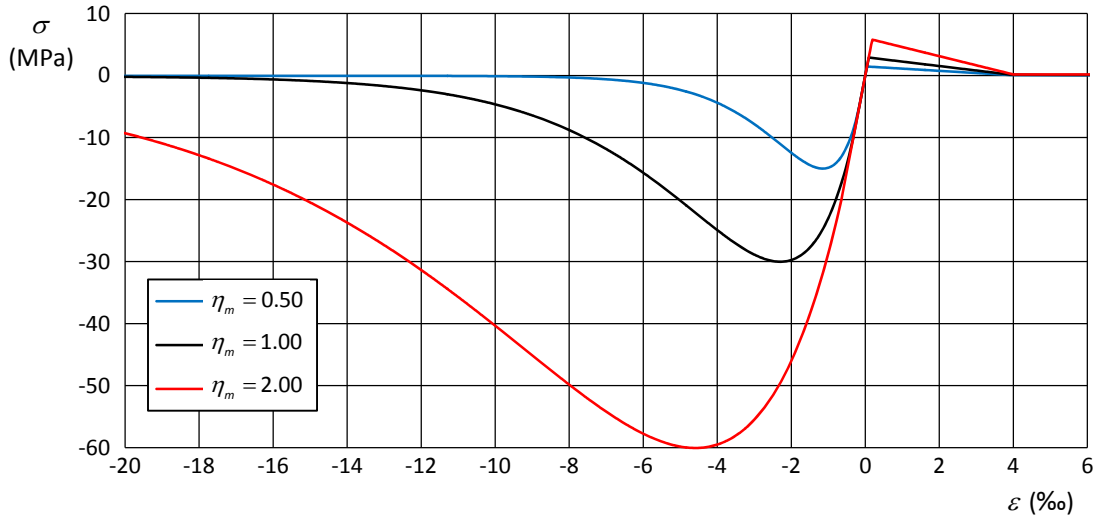

Figure III.75 *Modified Mazars' model*: Stress-strain curves for a material subjected to uniaxial loading and considering variable strength.

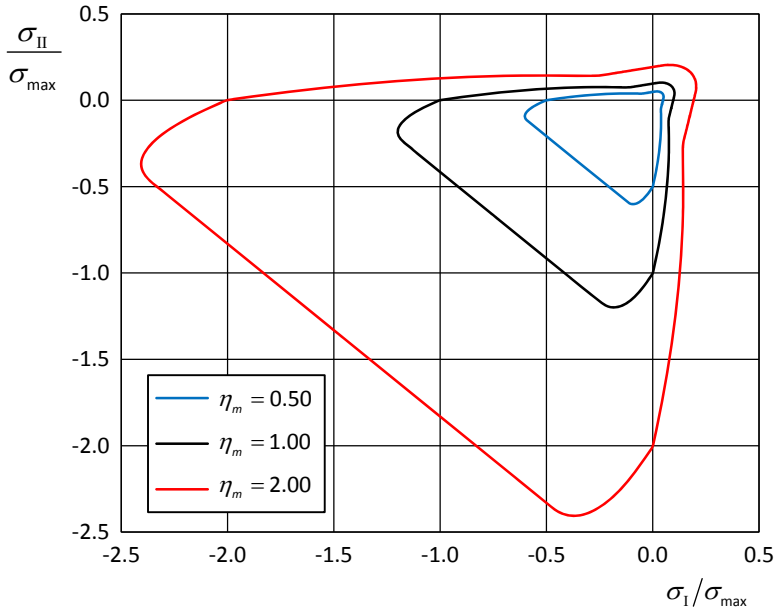

Figure III.76: *Modified Mazars' model*: Resistance envelopes for a material subjected to biaxial loading and considering variable strength, $\sigma_{III} = 0$.

A final question arises regarding where to implement the strength variation. Two possibilities seem feasible and rational: at the Gauss points or at the element level. Implementing at Gauss point level implies that the constitutive operator **k** will not be constant in the element's domain. In fact, it will have a random distribution, leading to accuracy lost in the numeric integration scheme. Nevertheless, this already happens in the CDM models where the damage changes at each Gauss point without any predefined pattern and no specific integration problem was identified. On the other hand, if the strength variation is implemented at the element level the constitutive tensor will not change in the element domain due to the implementation of this effect. These options lead to some difference in the brittleness of the resulting elements, as discussed in the Example CSI3 in Chapter IV.

Table III.15 summarizes the parameters required for the Modified Mazars' model.

Table III.15: *Modified Mazars' model* parameters.

Parameter	Unit	Definition	Domain
E_c	Pa	elastic modulus	$[0,\infty]$
ν	-	Poisson's ratio	$[0,0.5]$
$\tilde{\varepsilon}_0$	-	comparison strain at peak tensile stress	$[0,\tilde{\varepsilon}_u]$
$\tilde{\varepsilon}_u$	-	comparison strain at the beginning of the residual tensile stress branch	$[\tilde{\varepsilon}_0,\infty]$
R_p	-	residual tensile stress factor	$[0,1]$
A_-	-	original compression-related factor	-
B_-	-	original compression-related factor	-
L_{nl}	m	nonlocal length	$[0,\infty]$
f_{RSD}	-	relative standard deviation for yielding and peak stress	$[0,\infty]$

4 Models for reinforcing steel

4.1 Introduction

It is generally accepted that the reinforcements have a predominant effect on the hysteretic response of properly designed RC members. Consequently, the correct simulation of their response is vital for the overall accuracy of the numerical model. The monotonic response is reasonably easy to be simulated with accuracy. On the other hand, the response under cyclic and alternating loading is more challenging, due to the complexity associated with several simultaneous effects.

After taking into consideration the response characteristics of the steel reinforcements presented in section 2.3, it is possible to conclude that for monotonic loading, it is necessary to include the initial elastic response, the yielding plateau when present, and the strain-hardening branch. Furthermore, for reversed loading the *Bauschinger effect* should also be considered because it is a significant effect and the same for the cyclic hardening.

According to the results presented in section 2.3.3, low-cycle fatigue can result in significant steel resistance degradation, or even, in the early collapse of the reinforcing bar. Consequently, this phenomenon should also be included. Furthermore, the variability of the mechanical parameters should also be implemented to produce results that are more representative. According to the data presented in section 2.3.6, the yield and ultimate strength of the reinforcing steel presents a relative standard deviation of about 4-10%, which is not as large as in the concrete but is not negligible. Consequently, this effect should also be included in the proposed models.

The buckling of compressed steel reinforcements is also relevant as presented in section 2.3.4. This effect will not be included because it would introduce some additional complexity into the formulation, such as the dependency on other elements, because this phenomenon can only occur after concrete cover spalling. In addition, buckling would have to be identified using an average transversal reinforcement spacing that would also introduce another source of approximation. The same option was taken for the strain-rate effect, also because of the additional complexity brought into the formulation, in particular, for the definition of the tangent stiffness that would be dependent on the structural response.

The proposed models were validated against experimental results of common reinforcing bars tested under cyclic and alternating loading. Asymmetric cycles were used because after concrete cracking the steel reinforcements are more stressed for tensile loading because the concrete ceases to have the predominant contribution.

Two models are proposed in this work. The first is basically a simplified elastoplastic model with probabilistic resistance, which can simulate reasonably well the global response, but it can be inaccurate in capturing some of the effects identified. The second model is more complex and tries to simulate the selected effects identified in the previous paragraphs. It adopts the well-known *Guiffrè-Menegotto-Pinto's* softened curve and includes new contributions for the yield surface evolution, for the curvature of the curves, a low-cycle fatigue sub-model and probabilistic-based resistance.

4.2 Simplified Reinforcing Steel model (*SSteel*)

The *SSteel* model can be classified as a multi-linear model and is one of the simplest approaches to simulate with some realism the response of the steel reinforcements under cyclic and alternating loading. This constitutive relation includes elastic loading and unloading branches, and also, a kinematic hardening and a softening branch. Figure III.77 presents a schematic representation of the model. The formulation defines positive and negative yielding surfaces $\phi_*^{\pm}$ that work as envelope functions for the stress-strain curves. In addition, the dispersion associated with the yielding and the ultimate stress can be simulated using a simplified approach.

This model is defined by the eight parameters presented in Table III.16 and the constitutive equation is defined by:

$$\sigma = E_s\left(\varepsilon_s - \varepsilon_s^p\right). \tag{III.169}$$

The positive and the negative yielding surfaces are defined by:

$$\phi_*^+ = \begin{cases} \sigma_{sy}\left(1-\beta_1\right) + \beta_1 E_s\,\varepsilon_s, & \text{if } \varepsilon_s \le \varepsilon_{su} \\ \sigma_{sy}\left(1-\beta_1\right) + \beta_1 E_s\,\varepsilon_{su} + \beta_2 E_s\left(\varepsilon_s - \varepsilon_{su}\right), & \text{if } \varepsilon_s > \varepsilon_{su} \end{cases}, \tag{III.170}$$

$$\phi_*^- = \begin{cases} -\sigma_{sy}\left(1-\beta_1\right) - \beta_1 E_s\,\varepsilon_{su} + \beta_2 E_s\left(\varepsilon_s + \varepsilon_{su}\right), & \text{if } \varepsilon_s < -\varepsilon_{su} \\ -\sigma_{sy}\left(1-\beta_1\right) + \beta_1 E_s\,\varepsilon_s, & \text{if } \varepsilon_s \ge -\varepsilon_{su} \end{cases}. \tag{III.171}$$

The dispersion of the yield and ultimate strength can be simulated by scaling the mean value of the yield strength, using:

$$\sigma_{sy} = \eta_y\, E_s\, \varepsilon_{sy}, \tag{III.172}$$

where η_y is the scaling factor. This parameter can be computed using a pseudorandom number generator associated with a Gaussian distribution with the parameters $\mu = 1.0, \sigma = f_{RSD}$, where f_{RSD}, represents the r*elative standard deviation* for these parameters (see section 2.3.6).

The state determination algorithm is based on conditional statements that are summarized in Algorithm III.2. Moreover, the constitutive operator defined in (II.208) can be defined for each

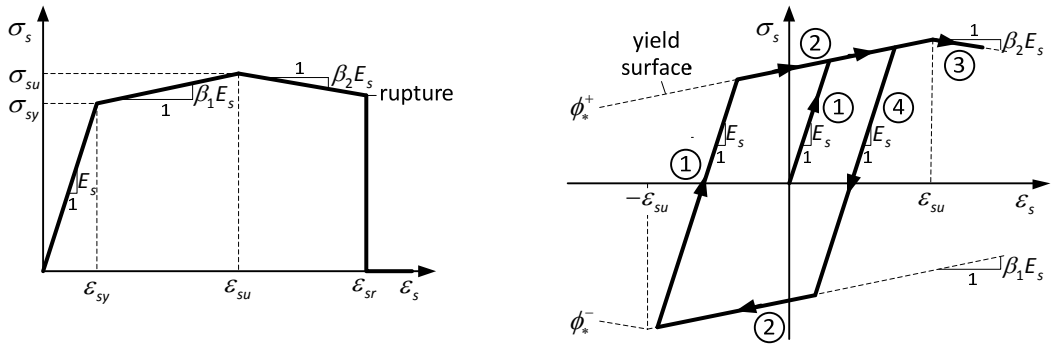

a) Monotonic b) Cyclic and Alternating

Figure III.77: Schematic representation of the *SSteel model*.

branch represented in Figure III.77-b, using:

$$k^* = \begin{cases} E_s, & \text{case 1} \\ \beta_1 E_s, & \text{case 2} \\ \beta_2 E_s, & \text{case 3} \\ E_s, & \text{case 4} \end{cases}. \tag{III.173}$$

It should be noted that this model presents a softening branch and consequently the strain localization phenomenon presented in section 2.1.6 can occur. Without an appropriate regularization technique, the finite element model will tend to concentrate the strains into the weakest steel bar element and unload in the remaining elements. It is necessary to adjust the model's softening branch definition or the size of the bar elements to enforce a specific amount of dissipated energy when the bar enters the softening phase. Nevertheless, the softening branch can be switched off by setting $\varepsilon_{sr} = \varepsilon_{su}$.

Table III.16: *SSteel model* parameters.

Parameter	Unit	Definition	Domain
E_s	Pa	elastic stiffness	$[0,\infty]$
σ_{sy}	Pa	yield stress	$[0,\infty]$
ε_{su}	m/m	strain at peak stress	$[\varepsilon_{sy},\varepsilon_{sr}]$
β_1	-	hardening stiffness factor	$[-\infty,\infty]$
β_2	-	softening stiffness factor	$[-\infty,\infty]$
ε_{sr}	m/m	strain at rupture	$[\varepsilon_{sr},\infty]$
f_{RSD}	-	relative standard deviation for yielding and peak stress	$[0,\infty]$

Algorithm III.2: *SSteel model*.

1. At the initialization of the element, compute η_y using a pseudorandom number generator associated with a Gaussian distribution.
2. Compute the current yield stress using equation (III.172).
3. Compute the positive and negative envelope curves using equations (III.170) and (III.171).
4. Compute the trial stress using the current plastic strain:
   $\sigma^{trial} = E\left(\varepsilon_s - \varepsilon_s^p\right)$.
5. If $|\varepsilon_s| > \varepsilon_{su}$ (rupture), set:
   $\varepsilon_s^p = \varepsilon_s$.
6. If $\sigma^{trial} > \sigma_y^+$ (positive envelope violated), set:
   $\varepsilon_s^p = \varepsilon_s - \sigma_y^+ / E_s$.
7. If $\sigma^{trial} < \sigma_y^+$ (negative envelope violated), set:
   $\varepsilon_s^p = \varepsilon_s - \sigma_y^- / E_s$.
8. Recompute the corrected stress using equation (III.169).

Figure III.78 presents several experimental results of steel reinforcement bars tested under cyclic and alternating loading. These results are compared with the data obtained by inputting the same strain history into the *SSteel* model. Table III.17 presents the model parameters used for each case.

From these results, it can be seen that, even if this model can capture the basic characteristics of the response, it is possible to observe some difficulties for simulating the stress evolution at reversal, which is associated with the strain hardening and with the cyclic degradation. Moreover, the fact of using linear loading and unloading branches between the yield envelopes generates significant differences when compared to the experimental results, which can also lead to the differences observed for the stress levels at reversal.

In conclusion, the *SSteel* model presents some advantages related to the simplicity of the formulation and to the computational efficiency. It is possible to obtain reasonable simulations for the response of the steel reinforcements under general loading cases. Nevertheless, the model is not fully able to simulate the relevant phenomena associated with the response of the reinforcements and significant inaccuracies can be identified. It can be concluded that the *SSteel* model can be used for large structures, where the particularities of the response of each reinforcement is not determinant for the global response, or when it is not necessary to have detailed information about the response of the steel reinforcements to simulate with accuracy the structural response. In other cases, a more advanced model should be used.

Table III.17: *SSteel* model parameters used for computing the stress-strain curves presented in Figure III.78.

Parameter	**a) Kent and Park [304]**	**b) Leslie and Park [333]**	**c) d) Aktan *et al.* [4]**		**e) f) Ma *et al.* [348]**	
Steel Type	New Zealand Mild Steel (Gr. 275)	New Zealand High Strength S. (Gr. 380)	USA High Strength Steel (Grade 60 KSI)		USA High Strength Steel (Grade 60 KSI)	
Test	Spec. 17, after [363]	Spec. A, after [363]	Test 5, #9	Test 8, #6	Spec. 3	Spec. 2
E_s (GPa)	180	210	210	200	200	200
σ_{sy} (MPa)	325	380	540	520	460	450
ε_{su} (%)	18.0	12.0	14.0	14.0	12.0	12.0
β_1 (%)	0.60	1.90	2.80	280	2.40	2.00
ε_{sr} (%)	20.0	15.0	18.0	18.0	15.0	15.0
β_2 (%)	0.00	0.00	0.00	0.00	0.00	0.00
f_{RSD}	0.00	0.00	0.00	0.00	0.00	0.00

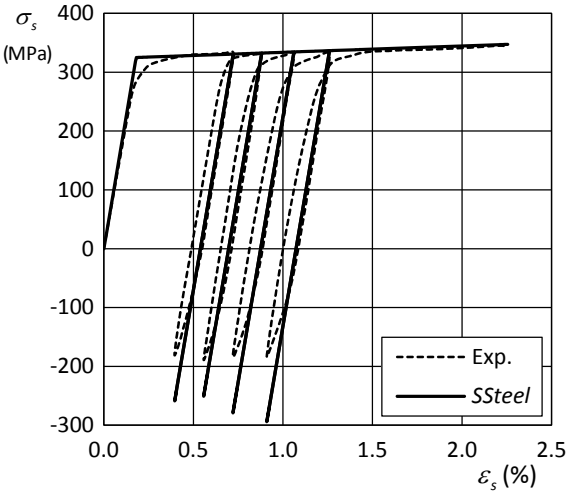

a) Tests by Kent and Park [304], Spec. 17, after [363]

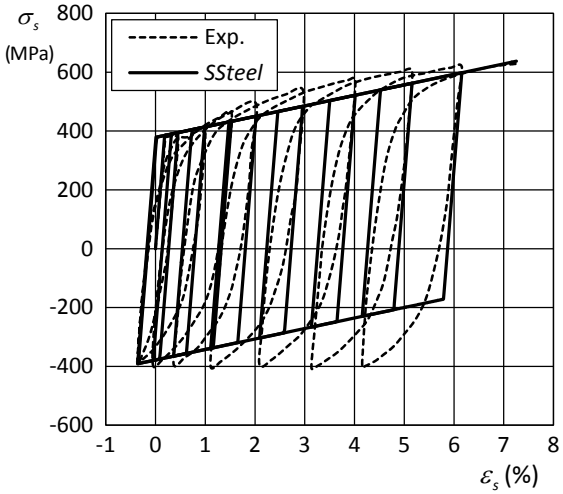

b) Tests by Leslie and Park [333], Spec. A, after [363]

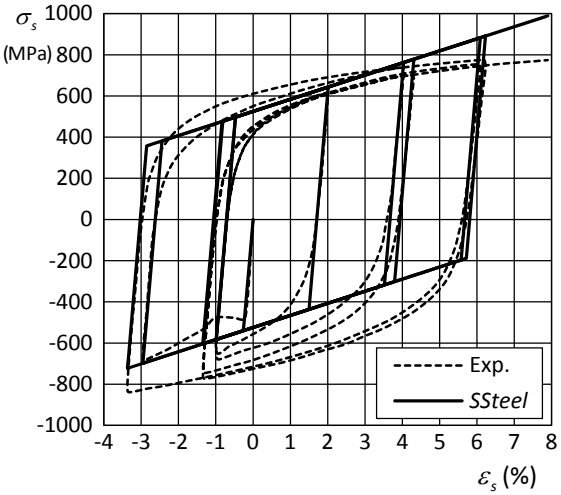

c) Tests by Aktan *et al.* [4], Test 5, #9 bar

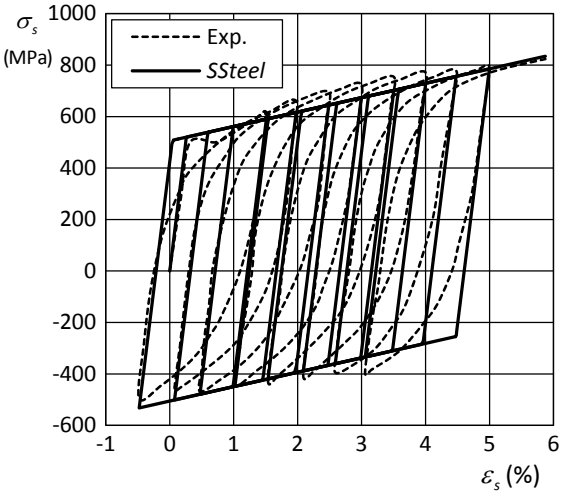

d) Tests by Aktan *et al.* [4], Test 8, #6 bar

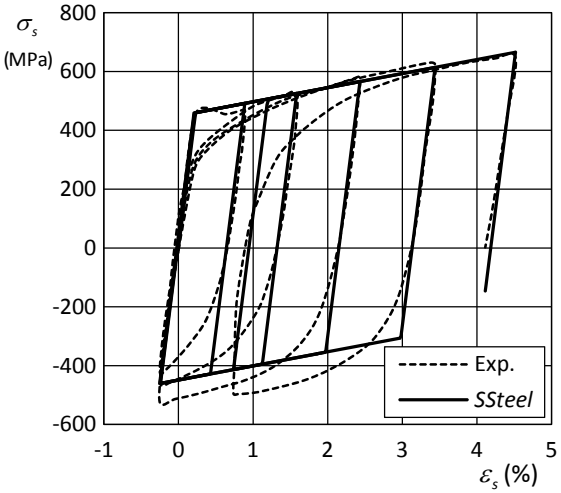

e) Tests by Ma *et al.* [348], Specimen 3

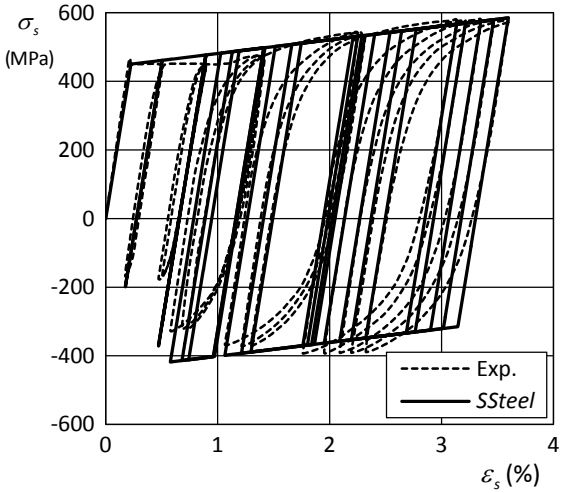

f) Tests by Ma *et al.* [348], Specimen 2

Figure III.78: *SSteel model* – Comparison with experimental results.

4.3 Refined Reinforcing Steel model (*RSteel*)

The refined reinforcing steel model consists of a base model and two additional sub-models. The base model adopts initially a bilinear relation until the first load reversal, which is followed by a softened branch to simulate the *Bauschinger effect*. The equation of the softened branch is the well-known *Guiffrè-Menegotto-Pinto* (GMP) equation improved by Filippou *et al.* (see section 2.3.7). Nevertheless, a new expression is proposed for the evolution of a curvature-related parameter. In addition, the base model includes a new formulation for considering the isotropic cyclic hardening observed in the reinforcements. The *RSteel* model is complemented with two sub-models that can be used to simulate the low-cycle fatigue and for defining a probabilistic-based strength.

- Base model

The general equation of the *RSteel* model is the following:

$$\sigma_s = E_s\left(\varepsilon_s - \varepsilon_s^p\right), \tag{III.174}$$

where ε_s^p is the plastic strain that for the softened curve can be computed by subtracting the elastic strain from the total strain, using:

$$\varepsilon_s^p = \varepsilon_s - \frac{\sigma_s}{E_s}. \tag{III.175}$$

The yield and ultimate strength are computed from:

$$\sigma_{sy} = E_s\,\varepsilon_{sy}, \tag{III.176}$$

$$\sigma_{su} = \sigma_{sy} + \left(\varepsilon_{su} - \varepsilon_{sy}\right)E_s\,\beta_0, \tag{III.177}$$

where β_0 represents the *initial plastic modulus ratio* (see Figure III.79-a).

The majority of the models proposed for steel reinforcements consider a constant plastic modulus throughout the analysis, which leads to the combination of monotonic strain hardening with

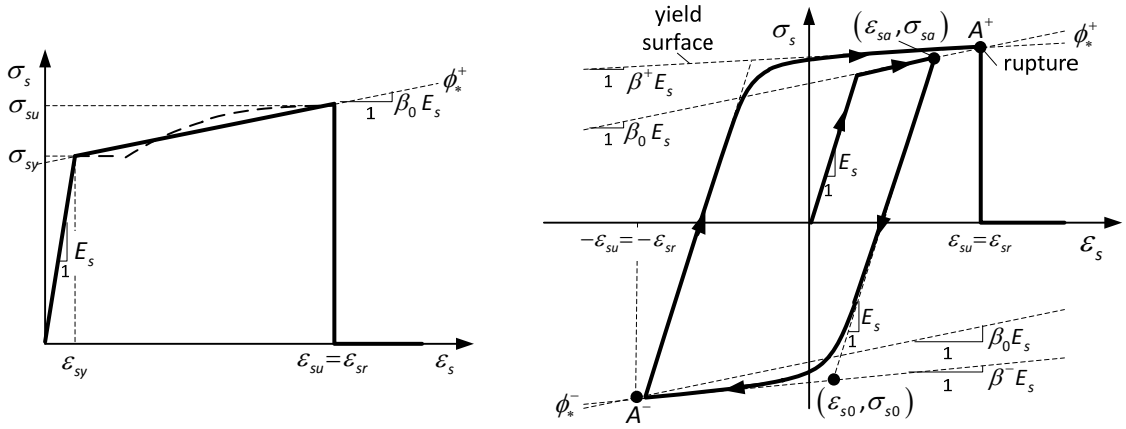

a) Monotonic b) Cyclic and Alternating

Figure III.79: Schematic representation of the *RSteel* model.

kinematic cyclic hardening. This is the case of the *SSteel* model presented in section 4.2. In the *RSteel* model, the plastic modulus changes throughout the analysis, as follows[i]:

$$\beta^{\pm}\left(\varepsilon_{\max}\right)=\begin{cases}\beta_0, & \text{if } \varepsilon_{\max}\le\varepsilon_{sy}\\ \beta_0\left(1-\dfrac{\varepsilon_{\max}-\varepsilon_{sy}}{\varepsilon_{su}-\varepsilon_{sy}}\right), & \text{if } \varepsilon_{sy}<\varepsilon_{\max}\le\varepsilon_{su},\\ 0, & \text{otherwise}\end{cases} \tag{III.178}$$

where $\varepsilon_{\max}$ stores the maximum absolute value of the strain reached previously. This definition implies that $\beta^{\pm}$ changes linearly between β_0 and zero at $\varepsilon_{\max}=\varepsilon_{su}$, as represented in Figure III.80-a. It should be emphasized that β^{+} and β^{-} are only updated after a negative and positive load reversal, respectively.

The present model adopts the following definition for the yielding surface[ii]:

$$\phi_{*}^{\pm}=\pm\sigma_{su}\mp\beta^{\pm}E_s\,\varepsilon_{su}+\beta^{\pm}E_s\,\varepsilon_s\,. \tag{III.179}$$

This definition implies that the positive and negative yielding surfaces rotate about the points A^{+} or A^{-}, respectively (see Figure III.79-b). This definition allows simulating isotropic cyclic hardening because the rotation leads to a homothetic expansion of the yield surface in both loading directions.

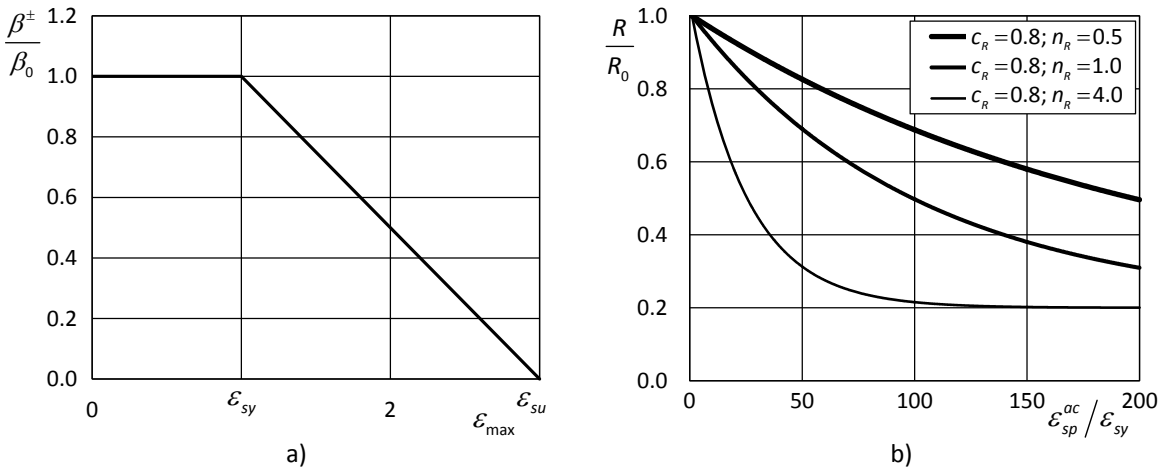

Figure III.80: *RSteel* model: a) Evolution of the parameter $\beta^{\pm}$; b) Evolution of the parameter R with c_R and n_R.

[i] The symbol $\pm$ should be substituted by $+$ or $-$, resulting in the plastic modulus associated with the positive ϕ_{*}^{+} and negative ϕ_{*}^{-} yield surface.

[ii] As before, equation (III.179) condenses two equations for the positive ϕ_{*}^{+} and negative ϕ_{*}^{-} yielding surfaces, which are defined by replacing the symbol $\pm$ by $+$ for the first equation and by $-$ for the second equation and for $\mp$ the other way around (see Chapter I-§6).

The adopted equation for the softened branch is the well-known *Guiffrè-Menegotto-Pinto* expression, already presented in section 2.3.7 (III.137):

$$\sigma_s^* = \beta^{\pm}\,\varepsilon_s^* + (1-\beta^{\pm})\frac{\varepsilon_s^*}{\left(1+\left(\varepsilon_s^*\right)^R\right)^{1/R}},$$

and the enhanced coordinate transformation proposed by Filippou, Popov and Bertero [217] is assumed (III.141):

$$\begin{cases}\varepsilon_s^* = \dfrac{\varepsilon_s - \varepsilon_{sa}}{\varepsilon_{s0} - \varepsilon_{sa}} \\ \sigma_s^* = \dfrac{\sigma_s - \sigma_{sa}}{\sigma_{s0} - \sigma_{sa}}\end{cases},$$

where $(\varepsilon_{sa}, \sigma_{sa})$ represents the strain and stress at the inversion point preceding each branch and $(\varepsilon_{s0}, \sigma_{s0})$ represents the strain and stress at the intersection between the elastic and hardening slopes (see Figure III.79-b).

The coordinates $(\varepsilon_{s0}, \sigma_{s0})$ of each softened branch can be computed by equating the envelope curve with the equation of a line with slope E_s passing through $(\varepsilon_{sa}, \sigma_{sa})$:

$$\phi_*^{\pm} = \sigma_{sa} - E_s\,\varepsilon_{sa} + E_s\,\varepsilon_s, \tag{III.180}$$

leading to:

$$\varepsilon_{s0}^{\pm} = \frac{-\sigma_{sa} + E_s\,\varepsilon_{sa} \mp \beta^{\pm} E_s\,\varepsilon_{su} \pm \sigma_{su}}{\left(1-\beta^{\pm}\right)E_s}, \tag{III.181}$$

$$\sigma_{s0}^{\pm} = \pm\sigma_{su} \mp \beta^{\pm} E_s\,\varepsilon_{su} + \beta^{\pm} E_s\,\varepsilon_{s0}. \tag{III.182}$$

As discussed before, the parameter *R* in equation (III.137) is related to the curvature of the transition between the elastic and the hardening branches. The present model adopts the following alternative definition for the evolution of this parameter:

$$R\left(\varepsilon_{sp}^{ac}\right)\begin{cases} R_0, & \text{if } \varepsilon_{sp}^{ac} \le \varepsilon_{sy} \\ R_0\left(1 - c_R\left(1 - \left(\dfrac{\exp\left(-\varepsilon_{sp}^{ac}/\varepsilon_{sy}\right)}{\exp(-1)}\right)^{\frac{n_R}{100}}\right)\right), & \text{if } \varepsilon_{sp}^{ac} > \varepsilon_{sy}\end{cases}, \tag{III.183}$$

where R_0, c_R, n_R are material parameters to be identified and ε_{sp}^{ac} represents the accumulated plastic strain until the previous load reversal. This variable can be computed in the adopted incremental formulation, using:

$$\varepsilon_{sp}^{ac} = \sum_{j=1}^{ns}\left|\Delta\varepsilon_{sp,j}\right|, \tag{III.184}$$

where $\Delta\varepsilon_{sp,j}$ represents the plastic strain increment *j*, which can be easily computed using the values returned by equation (III.175). Figure III.80-b presents the evolution of the parameter R with c_R and n_R.

- Low-cycle fatigue sub-model

The information compiled in section 2.3.3 showed that the low-cycle fatigue could lead to a significant decrease of strength or even to failure of the reinforcing bars under earthquake loading. Consequently, this phenomenon should be included in the simulation of the steel reinforcements.

The most obvious parameter that can feed the model with information about the fatigue induced in the material is the number and the amplitude of the cycles the bar is subjected. However, under general loading cases, the stress-strain history is not repetitive as in a fatigue test. As a result, alternative parameters must be used for this purpose. The *accumulated plastic strain* experienced by the bar throughout the loading history ε_{sp}^{ac} (III.184) is a natural choice.

Figure III.81 presents the values of ε_{sp}^{ac} for the tests made by Brown *et al*. [72] already presented in section 2.3.3. In this case, the expression (III.184) can be simplified using the following expression, which was used to compute the values presented in Table III.9:

$$\varepsilon_{sp}^{ac} = 4\,\varepsilon_{ap}\,N_c\,, \tag{III.185}$$

where ε_{ap} is the *plastic amplitude of the cycles* and N_c is the *number of cycles* at the identification of the first crack or at failure. This figure shows that this quantity presents some variance and that it is possible to identify what seems to be a linear dependency between ε_{sp}^{ac} and the plastic amplitude of the cycles. This effect can be seen as a *severity factor* related to the extension of the plastic deformation for each cycle. For the same level of the accumulated plastic strain, larger plastic amplitudes induce higher fatigue-type damage than smaller plastic amplitudes. This effect represents a loading-related response that is not a material property, and therefore, should be avoided. To achieve this, the following linear *severity factor* was introduced:

$$s_f = \frac{\Delta\varepsilon_{sp}^{*}}{\varepsilon_{sy}}\,, \tag{III.186}$$

where $\Delta\varepsilon_{sp}^{*}$ represents the *amplitude of the plastic deformation* between load reversals and ε_{sy} the monotonic yield stress. Introducing the *severity factor* into equation (III.184), it is possible to obtain the definition of the *corrected accumulated plastic strain*:

$$\tilde{\varepsilon}_{sp}^{ac} = \sum_{cyc=1}^{ncyc} \left|\Delta\varepsilon_{sp}^{*}\right| s_f = \frac{\left(\Delta\varepsilon_{sp}^{*}\right)^2}{\varepsilon_{sy}}\,. \tag{III.187}$$

It is implied in the last equation that the variable $\tilde{\varepsilon}_{sp}^{ac}$ is only computed when a load reversal is identified. Moreover, the possibility of partial unloading should be taken into consideration and an effective reversal should only be considered when the stress changes from tension to compression or *vice versa* (see Figure III.84-a).

Figure III.82 presents the same data used for Figure III.81 after correcting the accumulated plastic strain using equation (III.187). This expression can be simplified for this case:

$$\tilde{\varepsilon}_{sp}^{ac} = \sum_{cyc=1}^{ncyc} \frac{8\,\varepsilon_{ap}^2\,N_c}{\varepsilon_{sy}}\,. \tag{III.188}$$

From Figure III.82 it is possible to observe that the introduction of the *severity factor* significantly reduces the dependency of the amplitude of the cycles observed previously. This can be seen by noting the nearly constant regression after the identification of the first crack and for the failure of the bar. Nevertheless, the same level of dispersion in the results is still observed because this mainly originates from dispersion in the original test results.

The procedure adopted to remove the load amplitude dependency observed in Figure III.81 is based on the observation of the linear dependency identifiable in this figure. There is not a physical foundation for this option, other than it is intuitive that larger amplitude plastic strains tend to be more penalizing for the reinforcement than smaller amplitude strains. This approach was adopted due to its simplicity, the ease of the application in a common FE code, and because the results obtained showed that the load dependency was removed or significantly reduced for the examples considered. Nevertheless, it should be clearly stressed that there is not a well-established physical framework to support this option. This approach should also be tested with other data sources.

Accordingly, the results obtained by Mander *et al*. [72] were also used for assessing the efficiency of the correction procedure and the results obtained are presented in Figure III.83. It can be observed that after removing one value that was clearly out of the general trend of the results, a similar improvement for the load dependency can be observed. This gives a good indication about the generality of the approach adopted. Nevertheless, some questions about the accuracy for small amplitude cycles may arise from the experimental result rejected in the analysis.

The introduction of the proposed low-cyclic fatigue sub-model into the *RSteel* model is made by multiplying the yielding surfaces (III.179) by a *fatigue factor* defined by:

$$\gamma_f = 1.0 - c_f \left(\frac{\tilde{\varepsilon}_{sp}^{ac}}{\varepsilon_f} \right)^{n_f}, \tag{III.189}$$

where ε_f is a load independent material property that specifies the values of the corrected accumulated plastic strain $\tilde{\varepsilon}_{sp}^{ac}$ at bar failure. The parameters c_f and n_f control the fatigue evolution. In particular, the parameter c_f defines the amount of degradation before failure. According to the results obtained by Brown *et al*. [72], this value should be about 0.20-0.30, as reported in section 2.3.3 (see Figure III.47), plus the component associated with the isotropic cyclic hardening. On the other hand, the parameter n_f can be used to change the evolution of the degradation with the corrected accumulated plastic strain. Figure III.84-b presents the effect of changing this parameter in the fatigue factor.

Moreover, the steel reinforcement bar is considered to have achieved rupture and γ_f is set to zero, if the following condition is met:

$$\tilde{\varepsilon}_{sp}^{ac} > \varepsilon_f \ \wedge \ \sigma_s > 0 . \tag{III.190}$$

The last equation in (III.190) enforces that the rupture of the steel reinforcement bar can only happen under tensile loading.

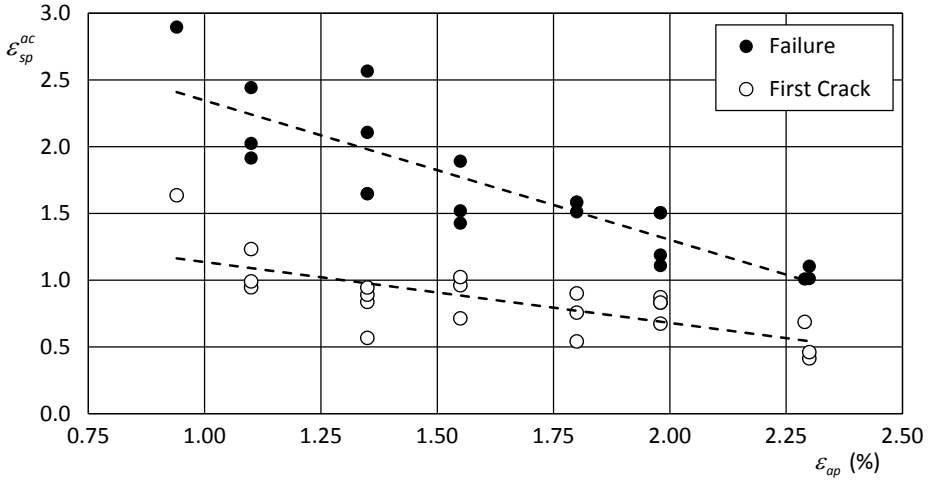

Figure III.81: Values of the accumulated plastic strain until the identification of the first crack or to the failure of the bar for the tests made by Brown *et al.* [72].

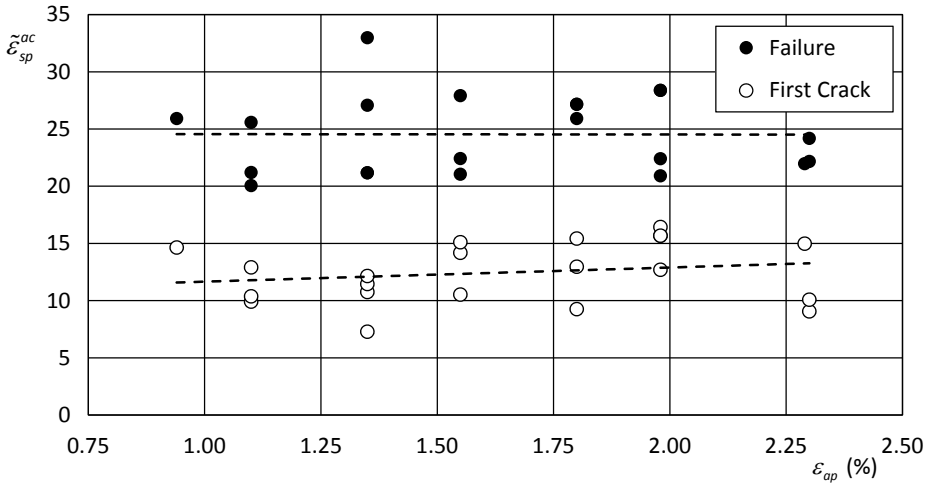

Figure III.82: Corrected values of the accumulated plastic strain for the tests made by Brown *et al*. [72]:

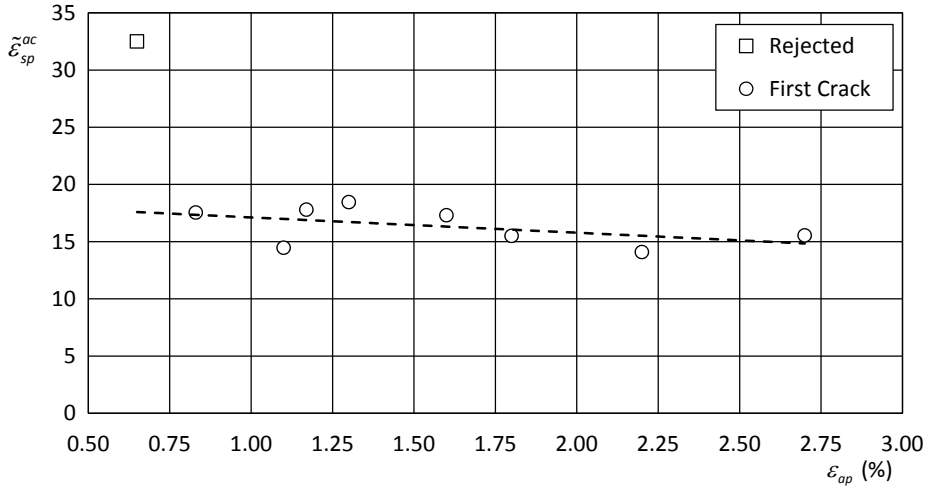

Figure III.83: Corrected values of the accumulated plastic strain for the tests made by Mander *et al*. [72]:

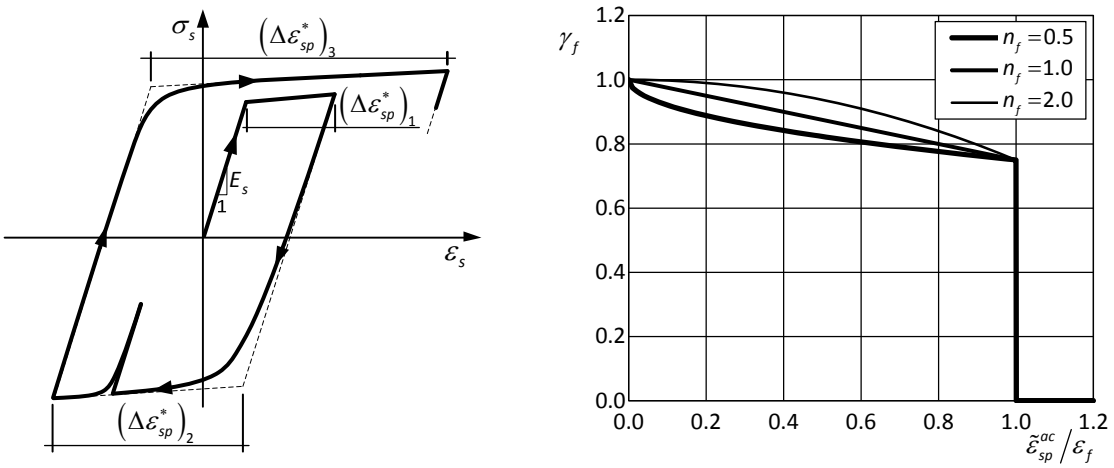

Figure III.84: Fatigue sub-model incorporated in the *RSteel* model: a) definition of the accumulated plastic strain; b) evolution of the fatigue factor with the parameter n_f ($c_f = 0.25$) .

Figure III.85 presents a comparison between the results of the fatigue tests performed by Brown *et al*. [72] with ϕ19 mm bars and the results obtained using the *RSteel* model.

Figure III.85-a to Figure III.85-e present the results obtained for cycles with amplitudes of 1.50%, 1.75%, 2.50%, 3.00%, respectively. All the results were obtained with the following model parameters: $E_s = 215$ GPa; $\beta_1 = 0.5\%$; $\sigma_{sy} = 540$ MPa; $\varepsilon_{su} = 8.5\%$; and $R_0 = 3.0$; $c_R = 0.5$; $n_R = 0.5$ for the evolution of the softened curve curvature; and $e_f = 21$; $c_f = 0.25$; $n_f = 1.0$ for the fatigue sub-model. In addition, f_{RSD} was set to zero to switch off the probabilistic strength distribution.

For the case of the test with strain amplitude of 2.50%, the stress-strain curve is available in the published work by Brown *et al*. [72] and was already presented in Figure III.45-b. This result is compared side-by-side with the results obtained using the *RSteel* model in Figure III.85-c and Figure III.85-d, respectively. A good match can be observed between both data sets. The results could even be more similar, but the goal of using the same parameters for all tests limited the adjusting range for the parameters. Furthermore, the experimental results under compression and tension showed some asymmetry and this effect could not be simulated with this model.

Using the definition for bar rupture expressed in equation (III.190) means that the rupture of the bar can happen anywhere under tensile loading. This is visible in the ruptures presented in Figure III.85.

Figure III.85-f presents the normalized stress at reversal under tension forces obtained for all the tests considered. This data is compared to the experimental results published by Brown *et al*. [72] and already presented in Figure III.47-a. The results show that the *RSteel* model and in particular the low-cycle fatigue sub-model was able to simulate all the tests results with sufficient accuracy and using the same set of parameters. This demonstrates that the sub-model is reproducing well the fatigue-induced failure.

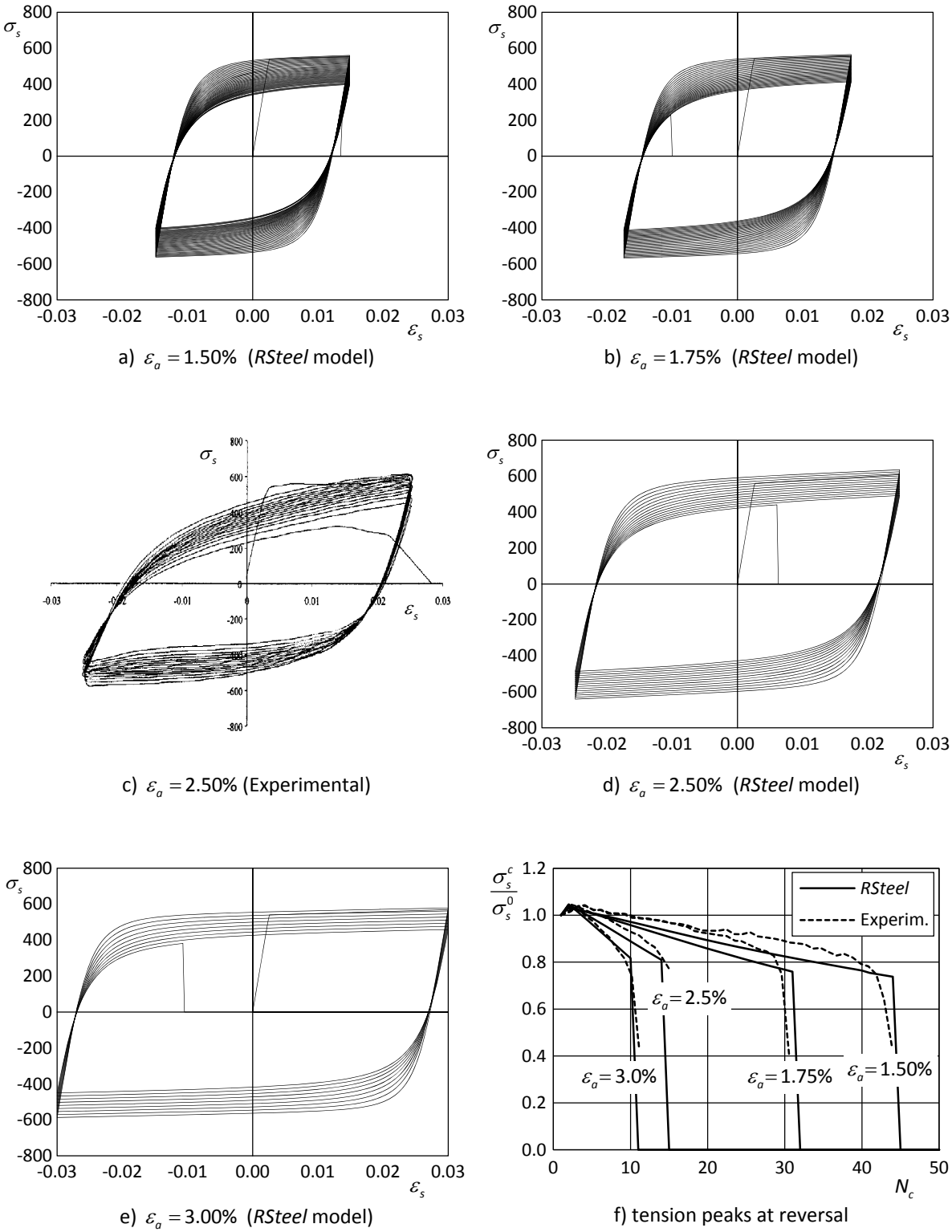

Figure III.85: Comparison of the low-cycle fatigue tests performed by Brown *et al*. [72] (ϕ19 mm) with the results obtained using the *RSteel* model.

Param.: E_s =215 GPa; β_0 =0.5%; σ_{sy} =540 MPa; ε_{su} =8.5%; R_0 =3.0; c_R =0.5; n_R =0.5; e_f =21; c_f =0.25; n_f =1.0; f_{RSD} =0.0

- Probabilistic strength

The probabilistic yield and ultimate strength is implemented by computing:

$$\sigma_{sy}^{*} = \eta_y \, \sigma_{sy} \,, \tag{III.191}$$

where η_y is a scaling factor used to simulate the dispersion of the yield and ultimate stress. As before, this parameter can be defined using a pseudorandom number generator associated with a Gaussian distribution and using the parameters $\mu = 1.0, \sigma = f_{RSD}$, where f_{RSD}, represents the adopted *relative standard deviation* for the material yielding and ultimate stress.

- Tangent stiffness matrix

Using the tangent stiffness matrix presents important advantages in terms of the convergence rate although at the expense of additional complexity and inferior robustness. The constitutive operator defined in (II.208) can be computed from:

$$k^{*}\left(\varepsilon_s\right) = \frac{\partial \sigma_s}{\partial \varepsilon_s} \,. \tag{III.192}$$

Applying the chain rule:

$$k^{*}\left(\varepsilon_s\right) = \frac{\partial \sigma_s}{\partial \varepsilon_s} = \frac{\partial \sigma_s}{\partial \sigma_s^{*}} \frac{\partial \sigma_s^{*}}{\partial \varepsilon_s^{*}} \frac{\partial \varepsilon_s^{*}}{\partial \varepsilon_s} \,, \tag{III.193}$$

and taking into consideration the relations presented in equation (III.141), it is possible to obtain:

$$\frac{\partial \sigma_s}{\partial \sigma_s^{*}} = \sigma_{s0} - \sigma_{sa} \,, \tag{III.194}$$

$$\frac{\partial \varepsilon_s^{*}}{\partial \varepsilon_s} = \frac{1}{\varepsilon_{s0} - \varepsilon_{sa}} \,, \tag{III.195}$$

and the remaining term, considering equation (III.137):

$$\frac{\partial \sigma_s^{*}}{\partial \varepsilon_s^{*}} = \beta^{\pm} - \frac{\beta^{\pm} - 1}{\left(1 + \left(\varepsilon_s^{*}\right)^{R}\right)^{1+1/R}} \,. \tag{III.196}$$

It should be noted that the parameters $\beta^{\pm}$ and R do not depend on ε_s^{*} because they are only updated after reversal. Moreover, the constitutive operator defined in (II.208) can be defined for each branch represented in Figure III.86-b, using:

$$k^{*} = \begin{cases} E_s \,, & \text{case 1} \\ \beta_0 E_s \,, & \text{case 2} \\ \dfrac{\sigma_{s0} - \sigma_{sa}}{\varepsilon_{s0} - \varepsilon_{sa}} \left[\beta^{\pm} - \dfrac{\beta^{\pm} - 1}{\left(1 + \left(\varepsilon_s^{*}\right)^{R}\right)^{1+1/R}} \right], & \text{case 3} \\ \approx 0, & \text{case 4} \end{cases} \,. \tag{III.197}$$

Table III.18 presents the pertinent information regarding the *RSteel* model parameters.

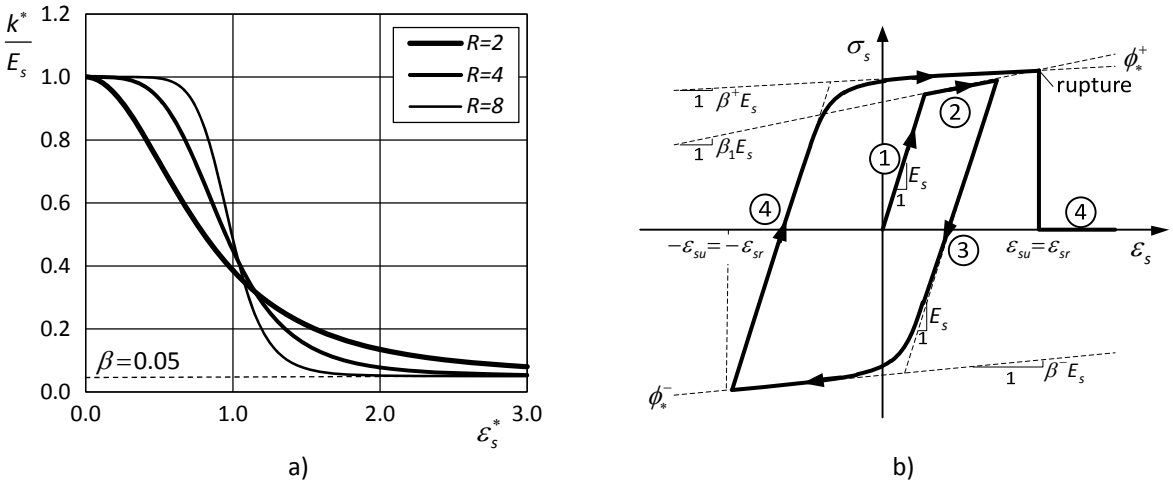

Figure III.86: *RSteel model*: a) influence of the parameter *R* on the softened branch slope; b) stress-strain branches.

Table III.18: *RSteel* model parameters.

Parameter	Unit	Definition	Domain
E_s	Pa	elastic stiffness	$[0,\infty]$
σ_{sy}	Pa	yield stress	$[0,\infty]$
β_0	-	Initial hardening stiffness factor	$[0,\infty]$
ε_{su}	m/m	strain at peak stress	$[\sigma_{sy}/E_s,\infty]$
R_0	-	initial value of *R*	$[0,\infty]$
c_R	m/m	reduction factor of *R*	$[0,1]$
n_R	-	exponent used to control the evolution of *R*	$[0,\infty]$
e_f	-	value of $\tilde{\varepsilon}_{sp}^{ac}$ at failure	$[0,\infty]$
c_f	-	reduction factor of γ_f	$[0,1]$
n_f	-	exponent used to control the evolution of γ_f	$[0,\infty]$
f_{RSD}	-	relative standard deviation for yielding and peak stress	$[0,\infty]$

Figure III.87 presents the same data from multiple reversed cyclic tests of reinforcing bars presented in Figure III.78, this time compared with the results obtained by feeding the strain history into the *RSteel* model. The model parameters used in each case are presented in Table III.19.

This comparison reveals that is possible to obtain a very good match with the experimental results using the *RSteel* model. This demonstrates the flexibility of the proposed model and the adjustment to the effective behaviour of the steel reinforcing bars. Nevertheless, it is possible to observe minor differences in some cases for the stress at reversal and for curvature. In addition, some asymmetries can be observed between the tensile and compressive response of the reinforcements. This type of behaviour is not too significant and cannot be simulated with the *RSteel* model proposed, or in fact, with the large majority of the models available for steel reinforcing bars.

Comparing the results in Figure III.87 (*RSteel*) to Figure III.78 (*SSteel*), it is possible to observe a clear improvement in the quality of the simulation by using the *RSteel* model.

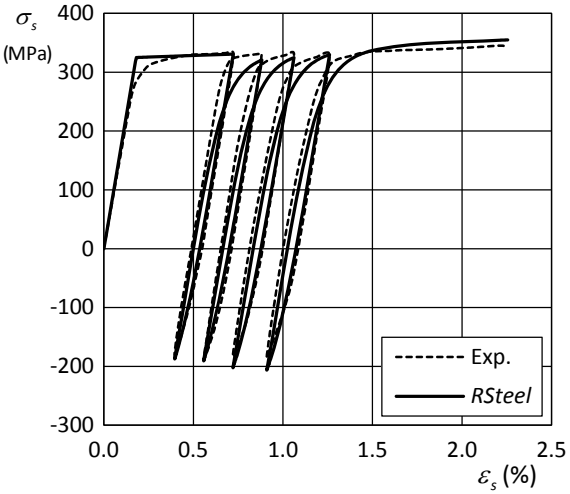

a) Tests by Kent and Park [304], Spec. 17, after [363]

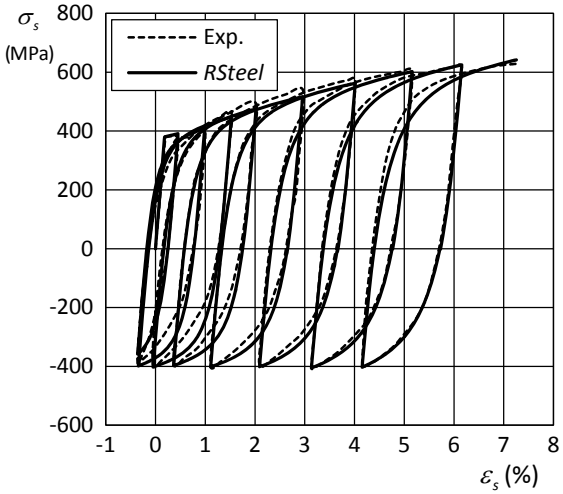

b) Tests by Leslie and Park [333], Spec. A, after [363]

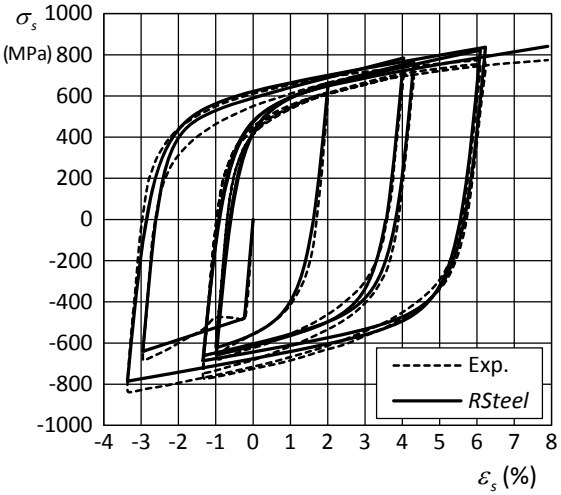

c) Tests by Aktan *et al.* [4], Test 5, #9 bar

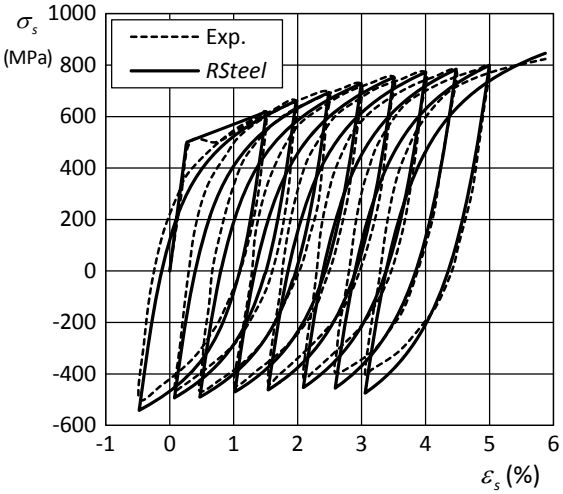

d) Tests by Aktan *et al.* [4], Test 8, #6 bar

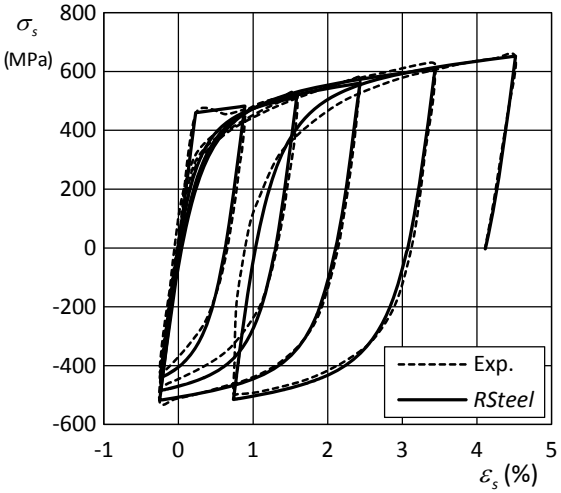

e) Tests by Ma *et al.* [348], Specimen 3

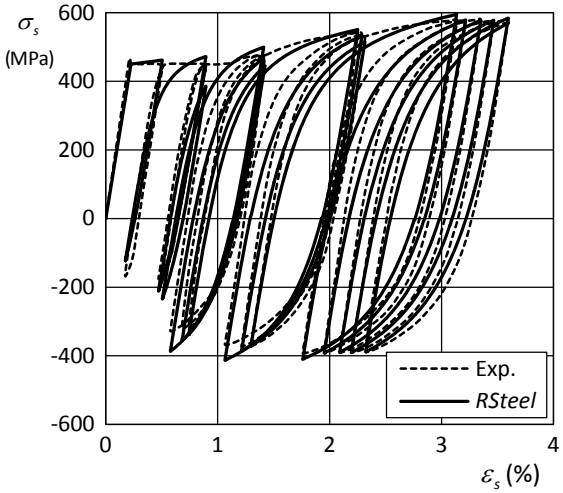

f) Tests by Ma *et al.* [348], Specimen 2

Figure III.87: *RSteel model* – Comparison with experimental results.

Table III.19: Model parameters used for computing the stress-strain curves presented in Figure III.87.

Parameter	**a) Kent and Park [304]**	**b) Leslie and Park [333]**	**c) d) Aktan *et al.* [4]**		**e) f) Ma *et al.* [348]**	
Steel Type	New Zealand Mild Steel (Gr. 275)	New Zealand High Strength S. (Gr. 380)	USA High Strength Steel (Grade 60 KSI)		USA High Strength Steel (Grade 60 KSI)	
Test	Spec. 17, after [363]	Spec. A, after [363]	Test 5, #9	Test 8, #6	Spec. 3	Spec. 2
E_s (GPa)	180	210	210	190	200	200
σ_{sy} (MPa)	325	380	480	500	460	450
ε_{su} (%)	18.0	12.0	14.0	8.0	12.0	12.0
β_0 (%)	0.60	1.90	2.80	5.00	1.70	2.10
R_0	4.00	2.50	2.50	1.80	2.50	2.80
c_R	0.60	0.60	0.20	0.20	0.25	0.40
n_R	0.80	0.80	4.00	3.00	4.00	6.00
e_f	24.50	24.50	24.5	24.50	24.50	24.50
c_f	0.40	0.40	0.30	0.45	0.30	0.35
n_f	0.60	0.60	0.40	0.38	1.00	1.00
f_{RSD}	0.00	0.00	0.00	0.00	0.00	0.00

5 Validation examples

This section presents a series of examples developed to test the combination of models adopted to simulate RC elements. The problems are chosen in order to be simple and trying to isolate as much as possible each feature being analysed and with gradual complexity. The first example is related to the use of local and nonlocal damage models to analyse a bar under tension. Although this example is very simple, it includes several important phenomena that should be carefully tested, such as snap-back instabilities and localization. The following example addresses a benchmark test used by several authors (*Hassanzadeh test*) and the goal is to compare the performance of the nonlocal damage model with experimental and other numerical results. The third example consists in simulating a RC beam subjected to a mid-span vertical monotonic load (*Burns-Seiss test*). Finally, the fourth example concerns the monotonic, cyclic and seismic behaviour of a precast column-foundation connection (*Mendes-Coelho-Costa test*).

5.1 Example RC1 – Tensioned truss

This example is used mainly to test the implementation of the damage model and to identify the main differences between the use of local and nonlocal models for materials with softening, thus exhibiting the strain localization phenomena. The simple case of a tensioned truss is chosen to make this assessment (see Figure III.88).

Two uniform meshes were used in the FE discretization. Mesh #1 divides the bar length in 3 truss elements and Mesh #2 in 60 truss elements (see Figure III.88). Two static analyses were performed and Table III.20 presents their characteristics and the model parameters used in each case. In this example all elements are subjected to the same stress level due to equilibrium conditions.

- Analysis RC1.1 – Local damage model

In this case, mesh #1 with 3 elements is used and all materials adopt the same constitutive relation parameters, except for the elements 1 and 3 that are slightly more resistant, $\sigma_0^{el1} = \sigma_0^{el3} > \sigma_0^{el2}$ .This difference is large enough to concentrate all nonlinear phenomena in element 2.

The global response is composed by piecewise linear segments because this mechanical system is composed by three elements working in series with a constitutive relation with linear branches and the model's branch switching occurs in between time steps. Furthermore, the response is expected to be linear and uniform until the strain reaches $0.10‰$, resulting in a prescribed displacement of $0.10‰ \times 0.60\ \text{m} = 60\ \mu\text{m}$. After entering the softening branch of the weaker element (element 2),

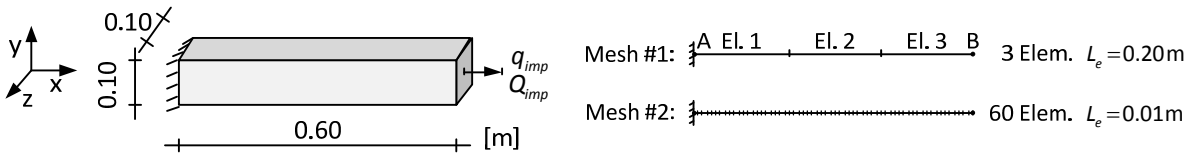

Figure III.88: Example RC1 – Definition of the problem and of the characteristics of the meshes adopted.

Table III.20: Example RC1 – Characteristics of the analyses and model parameters used.

ID	Analysis Type	Mesh	Model	Parameters
RC1.1	Static	Mesh #1	SConcrete	E=30 GPa, ε_0=0.10‰, ε_u=0.25‰, L_{nl}=0.00 m
RC1.2	Static	Mesh #2	Comi-Perego 1DV	E=30 GPa, n=2, k=0.150 kPa, c=2.72, L_{nl}=0.06 m (Gaussian function)

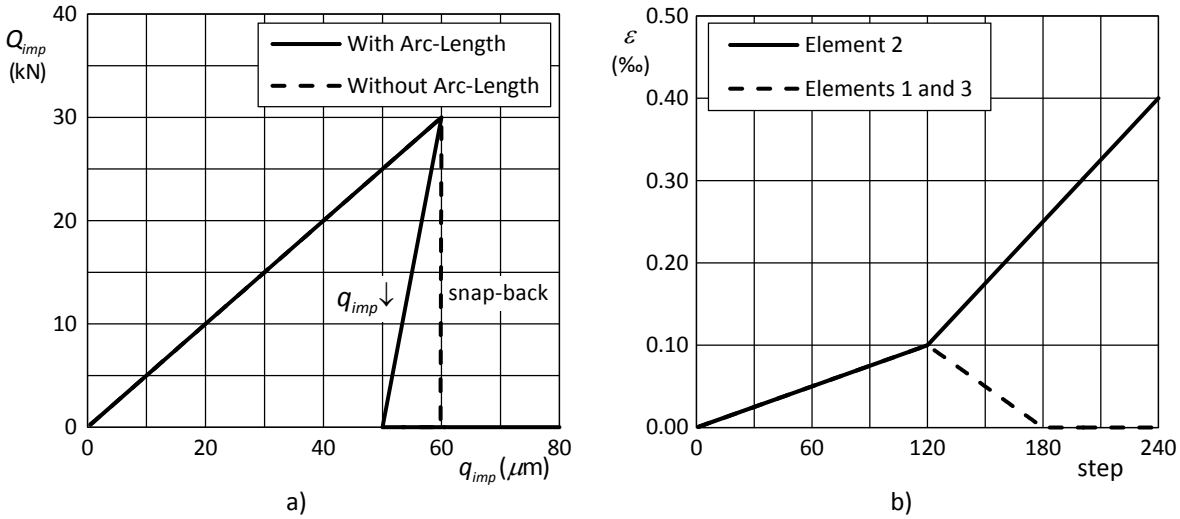

Figure III.89: Example RC1: a) Global response; b) Evolution of the axial strain.

the strains will localize in this element and the other elements will unload elastically. Subsequently, the weaker element will reach a fully damaged state and it is unable to resist further loading. This is expected to occur when the concentrated strain in the element reaches $0.25‰$, thus at a prescribed displacement of $0.25‰ \times 0.20\ \text{m} = 50\ \mu\text{m}$.

This case will result in a *snap-back* instability after the peak stress (see Figure II.15) because the imposed displacement at failure ($50\ \mu$m) is inferior to the one at peak stress ($60\ \mu$m). Consequently, using a Newton method with displacement control results in the global response curve represented in Figure III.89-a with a dashed line.

The *Arc-Length* (AL) method (see Chapter II-§5.3.2) can be used in the softening phase to avoid this phenomenon and follow the entire force-displacement curve. The resulting global force *vs.* displacement curve is represented by the continuous line in Figure III.89-a. From the analysis of this figure, it is possible to conclude that using the AL algorithm resulted in decreasing the prescribed displacement after the peak stress, in order to follow the force-displacement curve. This reduction pattern is unique.

Figure III.89-b presents the evolution of the axial strain in the elements. The initial prescribed displacement increment was set to $\Delta q_{imp}^0 = 0.5\ \mu\text{m}$, therefore, the peak stress will be obtained at step #120 ($0.10‰ = 120 \times 0.5\ \mu\text{m}/0.60\text{m}$). After the peak stress, the strain concentrates (localizes) in element 2, as expected.

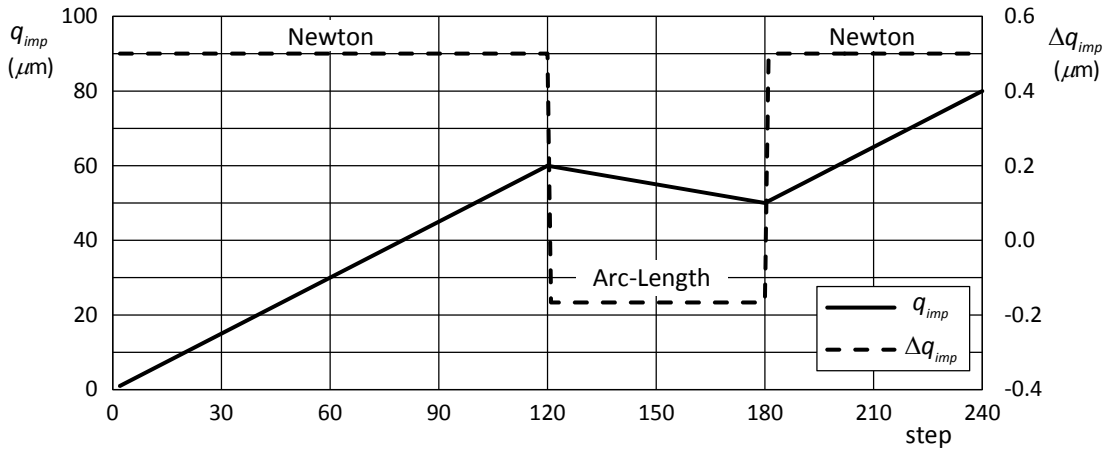

Figure III.90: Example RC1: Evolution of the prescribed displacements.

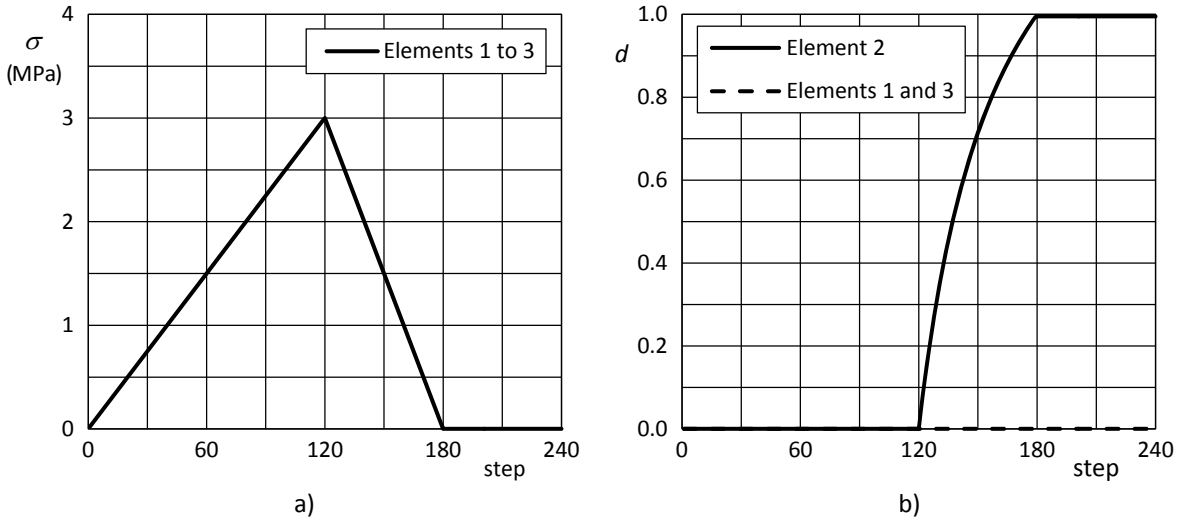

Figure III.91: Example RC1: a) Evolution of the stress in the elements; b) Evolution of the damage in the elements.

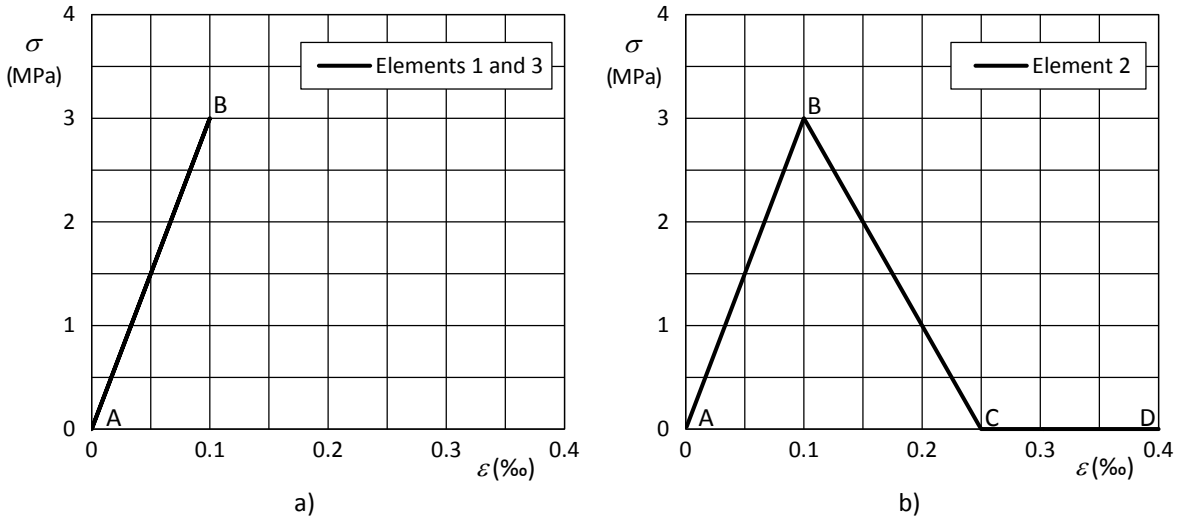

Figure III.92: Example RC1: Stress *vs.* strain evolution in the elements.

Figure III.90 presents the evolution of the prescribed displacement values and of the prescribed displacement increments throughout the analysis. It can be confirmed that the imposed displacement decreases between the steps #120 and #180. This information is complemented by knowing that the initial displacement increments $\Delta q_{imp} = 0.5\ \mu$m are automatically adjusted by the AL algorithm to $\Delta q_{imp} = -0.1(6)\ \mu$m, in order to respect the constraint for the cylindrical AL method.

Figure III.91-a presents the stress evolution in the elements that is uniform in all elements as expected. Furthermore, Figure III.91-b presents the damage evolution and it can be seen that that damage concentrates in the weaker element (#2), while the other elements remain undamaged in the analysis. In addition, the stress *vs.* strain curves for the three elements are plotted in Figure III.92. It can be confirmed that the stress has exactly the same evolution on all elements. Nevertheless, after reaching the peak resistance, the stress in the elements #1 and #3 decreases elastically (from B to A in Figure III.92-a) and in the element #2 it decreases following the softening branch due to damage (from B to C in Figure III.92-b).

Moreover, quadratic convergence was achieved in the Newton iterations.

- Analysis RC1.2 – Nonlocal damage model

The second analysis was performed to validate the nonlocal model implementation. In this case, mesh #2 was considered, in which 60 uniform truss elements are used to discretize the domain. The *Comi-Perego 1DV model* was considered (see section 2.2.7) with the parameters reported in Table III.20 that results in the stress-strain relation presented in Figure III.93-a. To induce damage at the middle of the truss, a slightly weaker material was defined in the two elements near the middle of the bar for maintaining symmetry. This was achieved by changing the parameter *k* to 0.149 kPa.

The nonlocal model uses the *Integral Nonlocal* regularization method described in section 2.1.6 and the *strain energy density release* (*Y*) was used as the nonlocal variable. The Gaussian function defined in equation (III.68) was used as weight function adopting $L_{nl} = 0.06$ m. Figure III.93-b presents the global response of the model. It can be seen that for the adopted geometry and model parameters, there is no snap-back instability in the global response.

Furthermore, Figure III.94 presents the damage evolution in the analysis for the entire truss length. It can be seen that, initially the damage is distributed uniformly in the bar, and gradually it tends to concentrate around the centre of the truss and stop increasing at the edges. The damage concentration occurs not only in the weaker elements, as in a local model, but instead, in a finite length that should be mesh-independent in order to preserve the objectivity of the problem.

The authors Comi and Perego [140] deduced the following relation between the *nonlocal characteristic length* λ_c and the damage variable *d* for the *Comi-Perego 1DV model*:

$$\lambda_c = \sqrt{2}\,\pi L_{nl}\left[-\ln\left(\frac{n}{2\ln\left(\frac{c}{1-d}\right)}\right)\right]^{-0.5} . \qquad \text{(III.198)}$$

This relation was obtained analytically by making a wave propagation analysis for a one-dimensional homogeneous domain. More details can be found in the reference [140].

Computing equation (III.198) for the adopted model parameters results in $\lambda_c \approx 0.20$ m. On the other hand, it is possible to compute the residual damage outside the nonlocal characteristic length by changing the damage variable *d*. Using the same expression, this results in $\lambda_c \approx L = 0.60\,m$ for $d \approx 0.195$, which represent the residual damage near the edges of the truss. These two values are consistent with the results presented in Figure III.94. Consequently, it is possible to conclude that the *Integral Nonlocal* regularization method is working as expected.

The fracture energy can by computed from the dissipated energy obtained from the global response curve presented in Figure III.93-b or from the sum of the dissipated energy density in all elements, obtained from the stress-strain curves multiplied by the length of the elements (III.64). In either case, the computation results in $G_f^{\mathrm{I}} \approx 167$ J/m^2 for $q_{imp} = 150$ μm.

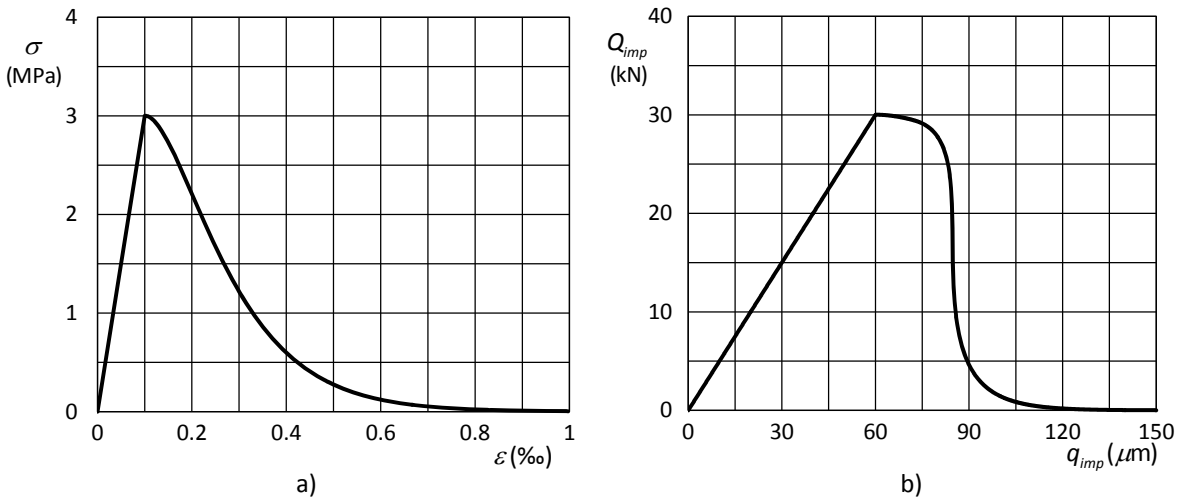

Figure III.93: Example RC1: a) Constitutive relation; b) Global response.

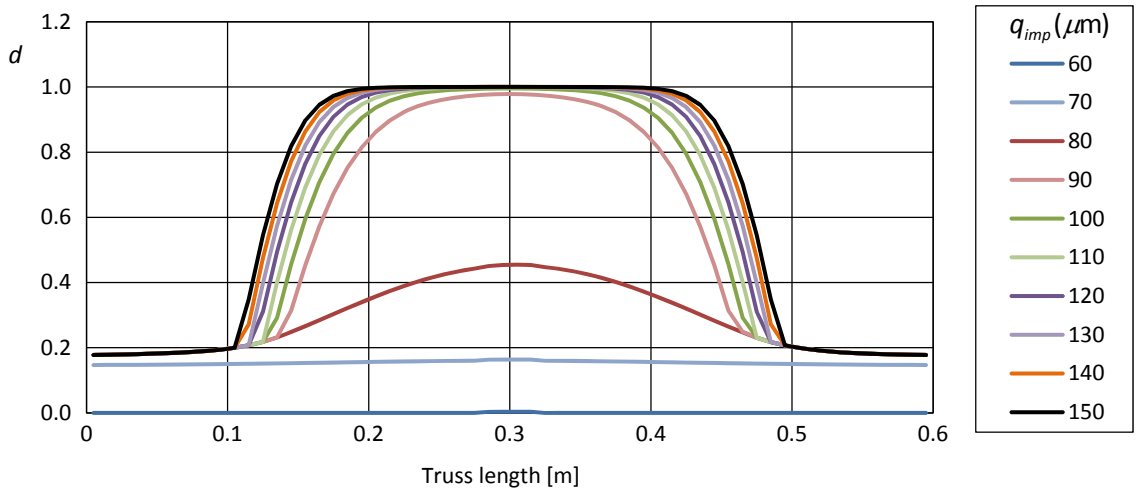

Figure III.94: Example RC1: Damage evolution in the truss length for different levels of prescribed displacement.

5.2 Example RC2 – Hassanzadeh test

The second validation example consists in testing the nonlocal damage model using experimental results obtained by Hassanzadeh [260] with a plain concrete specimen. The so-called *Hassanzadeh test*, consists of a direct tension test on a four edge notched specimen performed under monotonic prescribed displacements at the top surface (see Figure III.95-a). Similarly to other published works [128, 168, 508], the numerical model is simplified adopting a two-dimensional idealization of the problem and a plane strain hypothesis is considered (see Figure III.95-b).

It was reported by Hassanzadeh [260] that the concrete presents a compression resistance of $f_{cm} = 50$ MPa , therefore according to the classification proposed in Eurocode 2 [91], the concrete will be considered to belong to grade C40/50 or C45/55. Moreover, the fracture energy obtained from the experimental force-displacement curve presented in Figure III.97 leads to $G_f^{\mathrm{I}} = 73.35\ \mathrm{J/m^2}$.

A mesh with 528 Q4 elements was used resulting in 1128 *dofs* (see Figure III.95-c). Moreover, the *Comi-Perego 1DV* [140] damage model presented in section 2.2.7 was chosen due to its simplicity and to the fact that this is predominantly a tension fracture test. The model parameters adopted to simulate the reported concrete characteristics are listed in Table III.21 and the resulting stress-strain curve is presented in Figure III.96-a.

As suggested by Comi and Perego [128], the forces associated with the prescribed displacements at the top surface obtained with this two-dimensional model have to be corrected to take into consideration the three-dimensional effect of the problem (see Figure III.96-b). Consequently, the forces obtained were multiplied by a factor computed from the relation of the areas between the three-dimensional and two-dimensional problems.

Figure III.97 presents the global response of the specimen by plotting the total force applied *vs.* the prescribed displacement at the top surface. The results are plotted together with the experimental results obtained by Hassanzadeh [260] and with the results presented by Comi and Perego [138], using the same damage model and the traditional displacement-based finite element method. Accordingly, the results are directly comparable and should be similar, despite the differences in the adopted meshes and elements (constant strain triangles *vs.* bilinear quadrilaterals).

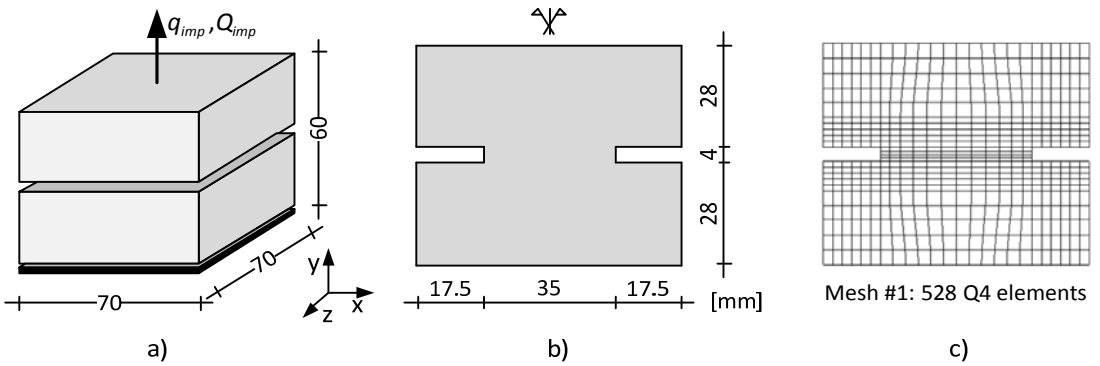

Figure III.95: Example RC2 – Definition of the problem and of the mesh adopted in the FE discretization.

Table III.21: Example RC2 – Characteristics of the analyses and model parameters used.

ID	Analysis Type	Mesh	Model	Parameters
RC2.1	static	mesh #1	Comi-Perego 1DV	E=36 GPa, n=12, k=5.8×10^{-11}kPa, c=405, L_{nl}=1.6 mm (Gaussian function)

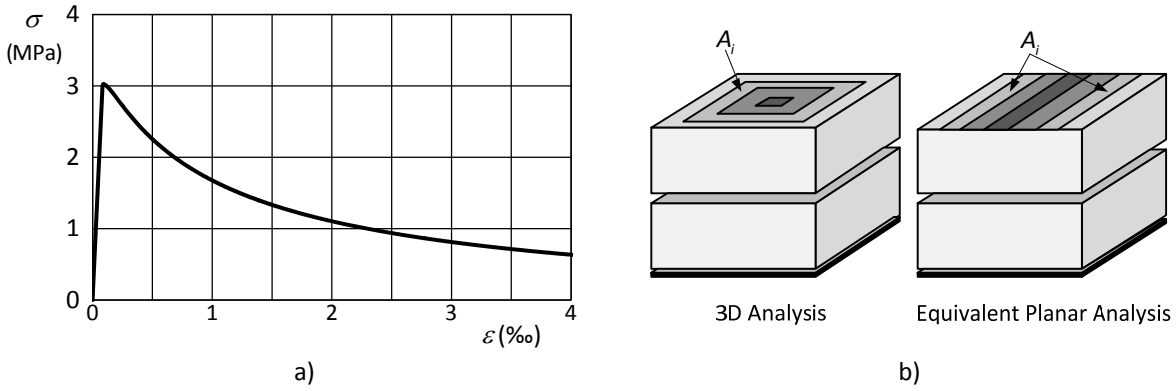

Figure III.96: Example RC2: a) Constitutive relation; b) 3D-effect correction, adapted from Comi *et al.* [128].

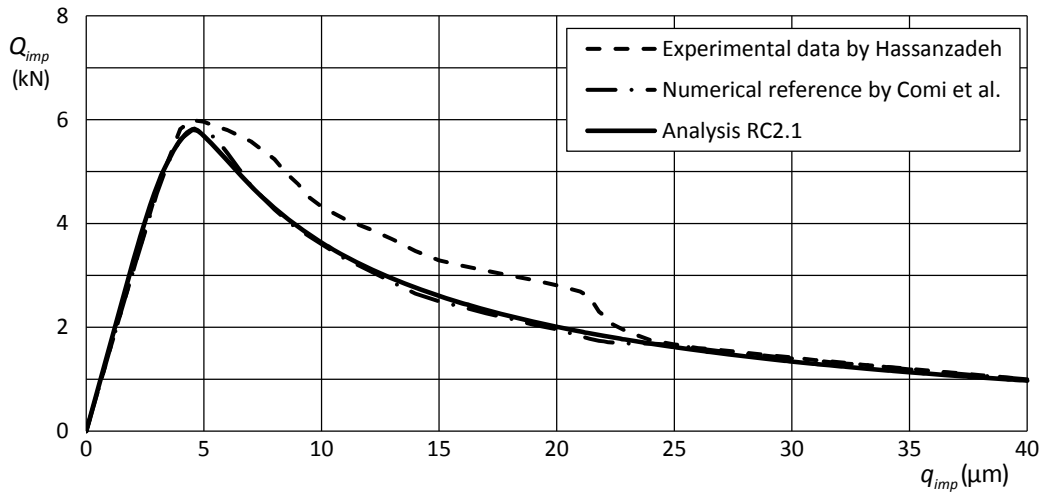

Figure III.97: Example RC2 – Global force-displacement curves.

From the analysis of Figure III.97, it is possible to observe that both numerical models resulted in very similar results and the differences can be perfectly justified by the differences in the mesh and finite elements used. When compared to the experimental curve, it is possible to observe that until reaching the maximum stress the curve is very well simulated. However, a higher strength can be observed in the experimental data. Nevertheless, the experimental and numerical curves tend to converge for higher values of the prescribed displacement.

These results are complemented in Figure III.98 by presenting the evolution of the displacements, of the principal strains and stresses and of the damage variable. It is clear in Figure III.98-d that the damage concentrates in a finite length, apparently independent of the mesh. As a result, the strain-localization phenomenon seems to be regularized.

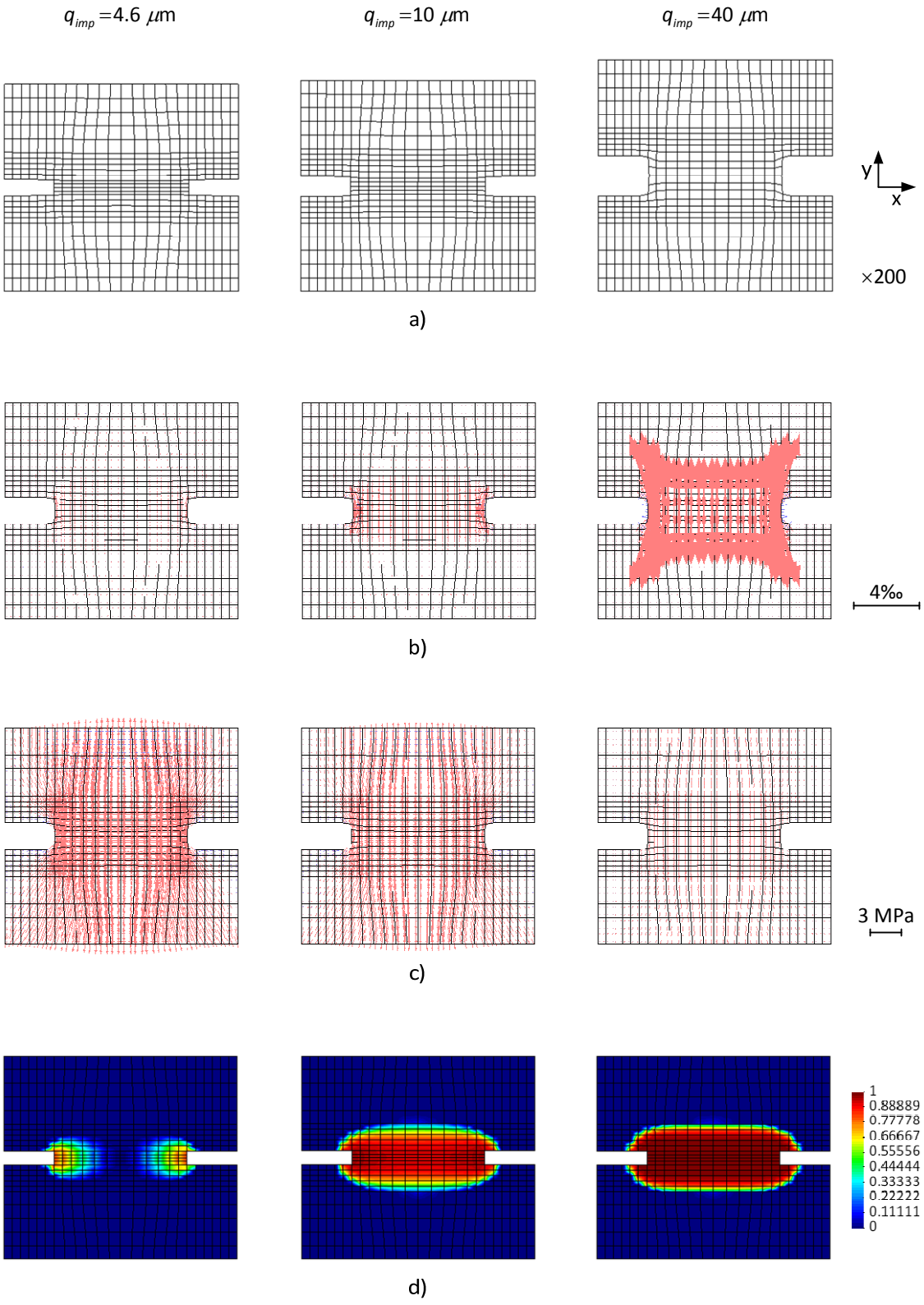

Figure III.98: Example RC2 – Evolution of the main structural quantities at selected time steps: a) displacements; b) principal strains; c) principal stresses; d) damage variable.

5.3 Example RC3 – RC beam test by Burns and Seiss

The authors Burns and Seiss [73] performed static tests on 21 RC beams with different heights, compression reinforcement ratios, loading sequence and direction. This example considers the specimen J-4, in which the beam does not have top longitudinal reinforcements and only two #8 bars $\left(\phi = 1 \text{ in.} = 25.4 \text{ mm}\right)$ at the bottom. The stirrups are #3 bars $\left(\phi = 3/8 \text{ in.} = 9.52 \text{ mm}\right)$ with 6 in. of spacing. A series of displacements is prescribed at the top face of the central top salience of the beam, which corresponds to point A in the model (see Figure III.99). Moreover, the vertical displacement is measured at the bottom face of the central bottom salience of the beam, which corresponds to point B in the model. Figure III.100 presents a general view of the test layout and of the cracking and crushing pattern for specimen J-10, which present the same reinforcements and geometry of specimen J-4, except for the beam height that was reduced to 16 in.

The authors reported for specimen J-4 a concrete cylinder strength of 4.82 ksi (33.2 MPa) and a steel yield stress of 44.9 ksi (309.6 MPa). More information about the material properties can be found in the report published by the authors [73].

The concrete elasticity modulus was estimated using the formula adopted by Burns and Seiss:

$$E_c = \frac{30000}{6 + 10/f_c}, \tag{III.199}$$

with E_{cm} and f_{cm} in ksi, which leads to $E_c = 3715$ ksi. Nevertheless, a value slightly smaller was adopted $E_c = 3500$ ksi, similarly to what other authors have done [342]. Information regarding the concrete mode I fracture energy is not reported by the authors. Lowes [342] adopted $G_f^{\text{I}} = 1.50 \text{ lb/in.} \left(262.7 \text{ N/m}\right)$ to perform an energy-based regularization using a local damage model. This value seems excessive. After some tests, $g_f^{\text{I}} = 1.05 \text{ lb/in}^2 \left(183.9 \text{ N/m}^2\right)$ and $L_{nl} = 1.0$ in. were adopted and the *bell-shaped function* defined in equation (III.69) was chosen to define the nonlocal model. The constitutive relations are presented in Figure III.101.

Figure III.102 presents the finite element mesh adopted in the analyses. A total of 3264 square Q4 elements were considered for modelling the concrete ($b = h = 1$ in.) and the *Modified Mazars* (*MMazars*) model and a plane strain hypothesis was adopted. The longitudinal reinforcements were modelled with 156 bar elements adopting the *Simplified Reinforcing Steel* (*SSteel*) model and the stirrups were simulated by 26 elastic trusses. This discretization led to 7060 *dofs* plus one equation for imposing the displacement at point A using the Lagrange Multipliers technique (see Chap. V-§2.4.3). Table III.22 lists the model parameters adopted for simulating the materials.

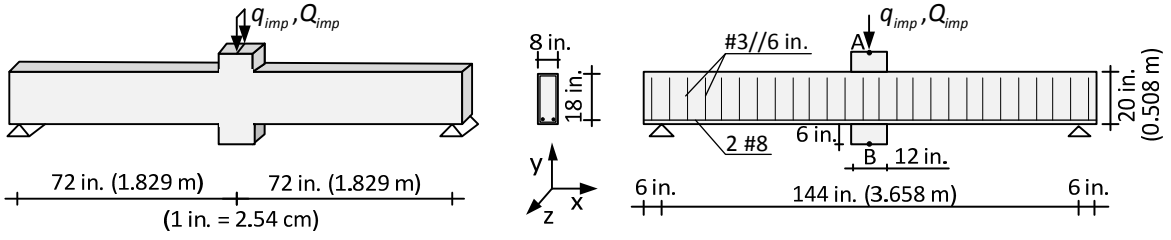

Figure III.99: Example RC3 – Definition of the problem.

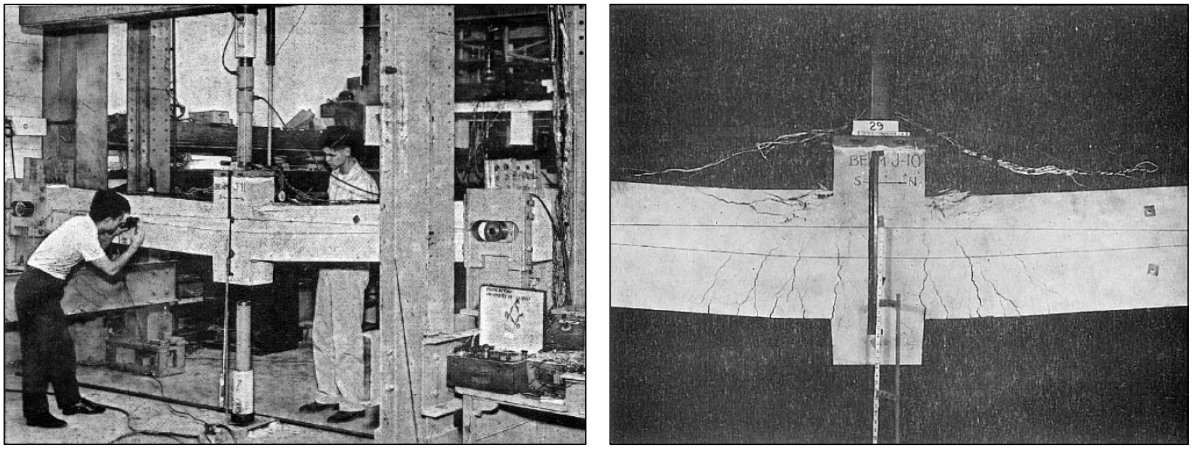

a) b)

Figure III.100: Example RC3 - Taken from Burns *et al.* [73]: a) Test layout; b) Concrete cracking and crushing for beam J-10.

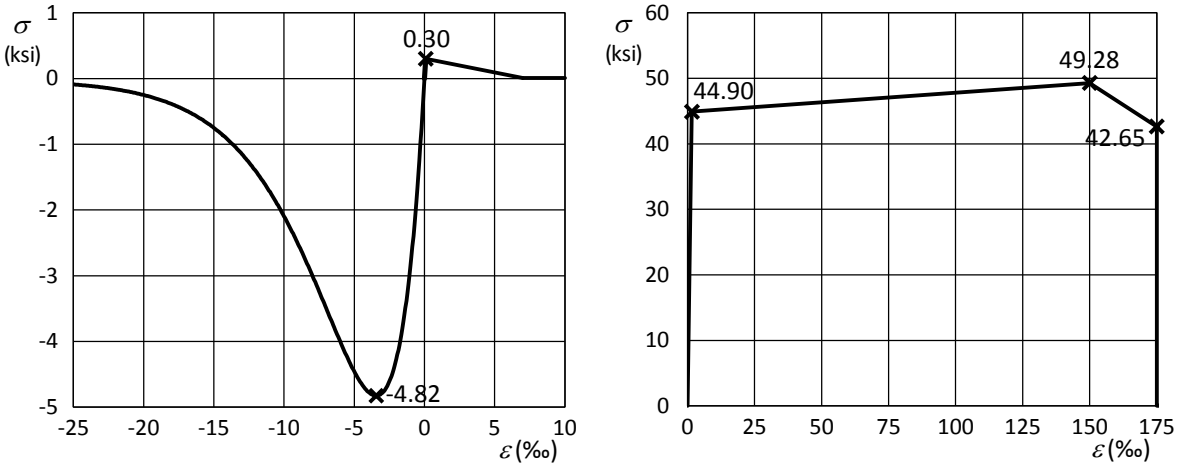

a) b)

Figure III.101: Example RC3 – Constitutive relations: a) Concrete; b) Steel.

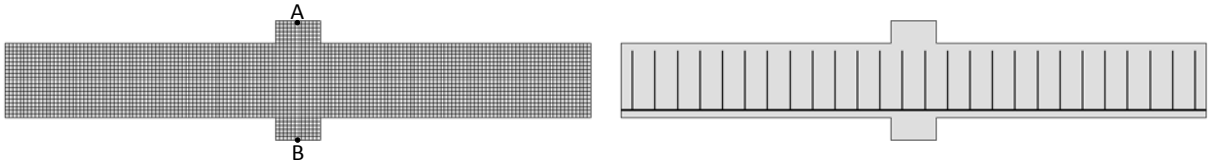

a) Concrete: 3264 Q4 elements (Plane stress) b) Longitudinal reinf. + Stirrups: 156 + 26 L2 elements

Figure III.102: Example RC3 – Finite element mesh adopted.

Three static analyses were performed and Table III.23 compiles their characteristics. The main difference consists in not considering the resistance dispersion in the concrete for analysis RC3.1. In the other two examples, a relative standard deviation of 18% was adopted for the tensile and compressive concrete resistance.

Table III.22: Example RC3 – Model parameters.

Model	Type	Parameters
1	*MMazars*	E_c =3500 ksi, ν=0.175, $\tilde{\varepsilon}_0$ =0.086‰, $\tilde{\varepsilon}_u$ =7.0‰, R_p =0.03, A_- =0.98, B_- =1067, L_{nl} =1.0 in. (bell-shaped function), f_{RSD} =0.00
2	*MMazars*	E_c =3500 ksi, ν=0.175, $\tilde{\varepsilon}_0$ =0.086‰, $\tilde{\varepsilon}_u$ =7.0‰, R_p =0.03, A_- =0.98, B_- =1067, L_{nl} =1.0 in. (bell-shaped function), f_{RSD} =0.18
3	*Elastic*	$E = 35000$ ksi, $\nu = 0.175$
4	*SSteel*	E_s =29500 ksi, σ_{sy} =44.9 ksi, β_1 =0.001, β_2 =−0.009, ε_{sr} =0.175, f_{RSD} =0.00
5	*SSteel*	E_s =29500 ksi, σ_{sy} =44.9 ksi, β_1 =0.001, β_2 =−0.009, ε_{sr} =0.175, f_{RSD} =0.05
6	*Elastic*	$E = 29500$ ksi, $\nu = 0.30$

Table III.23: Example RC3 – Characteristics of the analyses.

ID	Analysis Type	Concrete	Long. Reinforcements	Stirrups
RC3.1	static, Δq_{imp}=0.0025 in.	model #1, model #3*	model #4	model #6
RC3.2	static, Δq_{imp}=0.0025 in.	model #2, model #3*	model #5	model #6
RC3.3	static, Δq_{imp}=0.0025 in.	model #2, model #3*	model #5	model #6

* on the two top finite element row near point A (where the displacements are prescribed).

Table III.24: Example RC3 – Summary of the concrete characteristics.

ID	Model	Concrete Properties
Case #1 (Figure III.103)	Mazars	f_{ct} =0.386 ksi; f_{ct} =− 4.80 ksi; g_f^{I} =0.27 lbs/in.*; L_{nl} =1.0 in.
Case #2 (Figure III.103)	Mazars	f_{ct} =0.350 ksi; f_{ct} =− 4.80 ksi; g_f^{I} =0.41 lbs/in.*; L_{nl} =1.0 in.
Case #3 (Figure III.103)	Modified Mazars	f_{ct} =0.350 ksi; f_{ct} =− 5.33 ksi; g_f^{I} =1.08 lbs/in.*; L_{nl} =1.0 in.
Case #4 (Figure III.103)	Modified Mazars	f_{ct} =0.350 ksi; f_{ct} =− 5.33 ksi; g_f^{I} =0.75 lbs/in.*; L_{nl} =1.0 in.
Case #5 (Figure III.103)	Modified Mazars	f_{ct} =0.280 ksi; f_{ct} =− 5.52 ksi; g_f^{I} =0.71 lbs/in.*; L_{nl} =1.0 in.
RC3.1 to RC3.3	Modified Mazars	f_{ct} =0.300 ksi; f_{ct} =− 5.52 ksi; g_f^{I} =1.07 lbs/in.*; L_{nl} =1.0 in.

* fracture energy computed with the stress-strain curves truncated at $\varepsilon_c = 1\%$.

The three analyses presented in this section (RC3.1 to RC3.3) were preceded by a series of trial computations that will be described to justify some of the choices made. Five of these analyses were selected (Cases #1-5) and they differed from the analyses RC3.1 to RC3.3, mainly in terms of the concrete characteristics, which are summarized in Table III.24, and by the absence of stirrups.

Chronologically, the first two cases (#1 and #2) simulated the concrete using the original *Mazars' model*. As stressed before, trying to match the tensile and compressive concrete resistance with realistic strains at peak stresses tends to result in fragile materials, as it can be observed in the mode I fracture density energy represented in Table III.24 $\left(g_f^{\mathrm{I}} < 0.5 \text{ lbs/in.}\right)$. In the numerical simulations, these beams reached a nearly collapsed state at an early and unrealistic stage. These observation can be confirmed in the global force-displacement curves presented in Figure III.104 or in the deformed shaped configurations and damage distributions presented in Figure III.103.

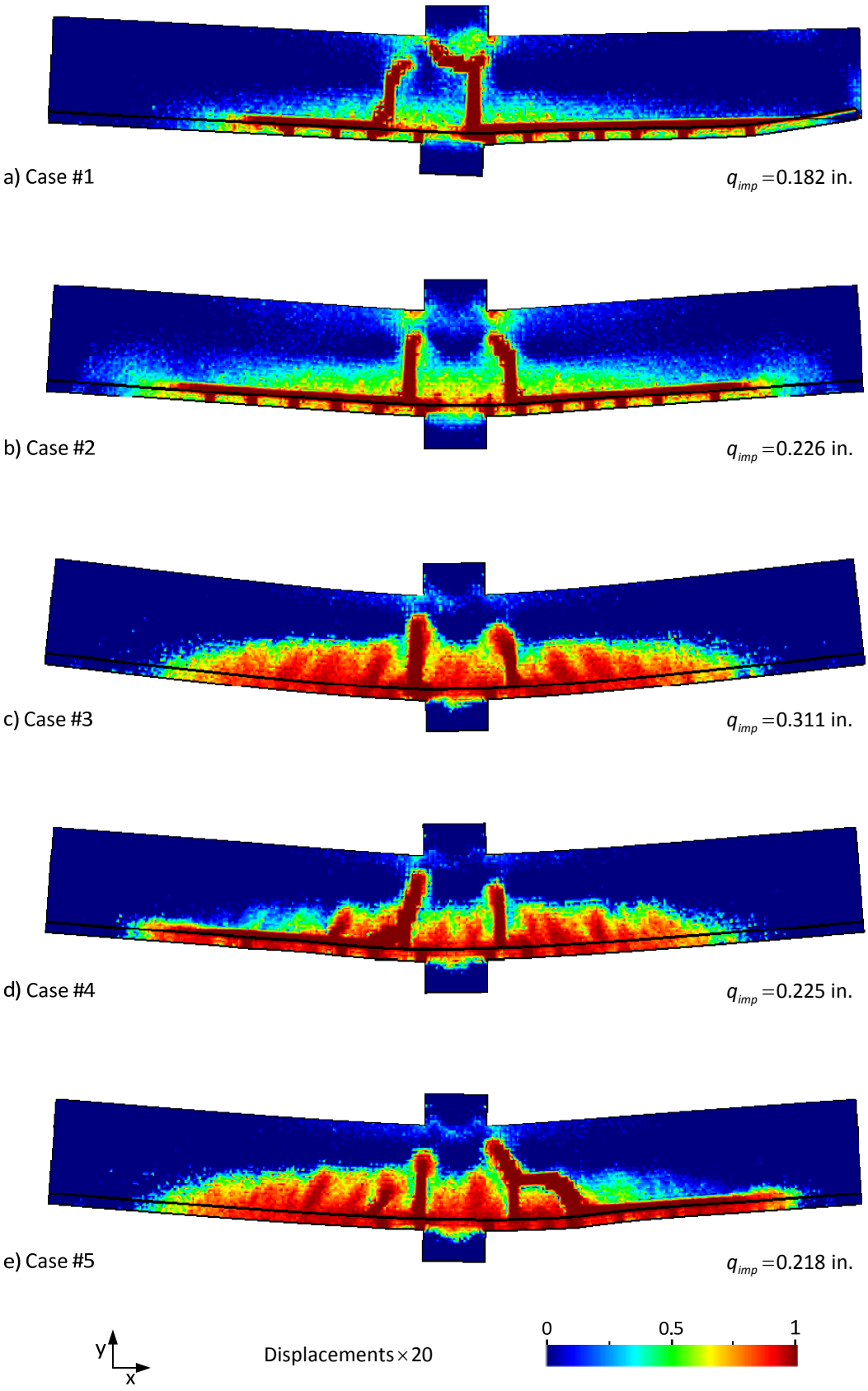

Figure III.103: Example RC3 – Deformed shape and damage distribution at selected time steps for analyses with premature collapses.

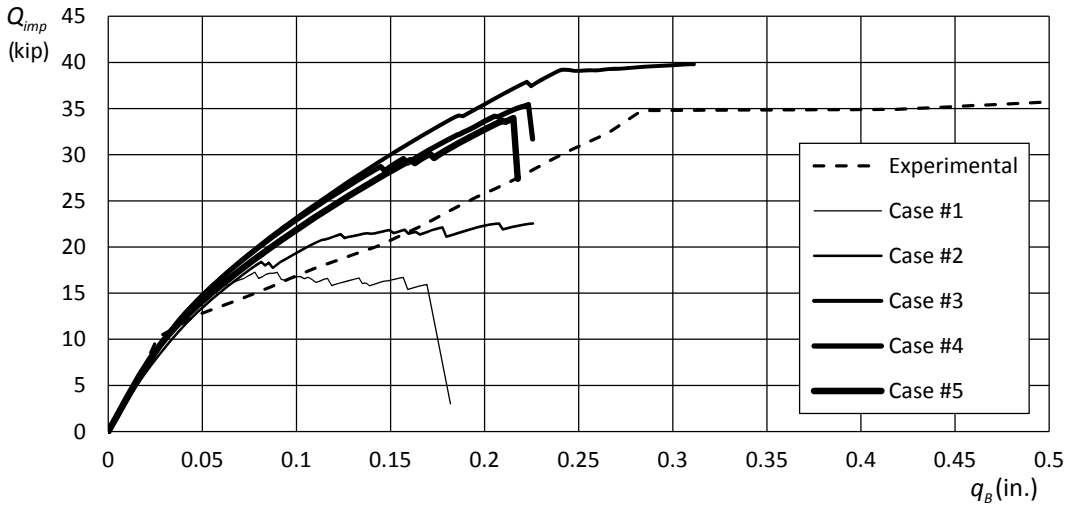

Figure III.104: Example RC3 – Global force-displacement curves for the analyses with premature collapses.

For the following cases, the *Modified Mazars' model* was used (see section 3.3) and the fracture energy density was increased to values about $0.7-1.1$ lbs/in. (see Table III.24). As it can be seen in Figure III.104, this change improved the results and these simulations were conducted until yielding of the reinforcements, or nearby. Nevertheless, these results were not satisfactory.

The next step consisted in adding the beam stirrups to the simulation. This way, all the steel reinforcements are included in the analysis. This decision was made after observing the shear-like collapses in the last two analyses (Case #4 and Case #5). This change and some minor adjustments in the material properties lead to the main results obtained in this example, which will be described in the following paragraphs.

The static analyses RC3.1 to RC3.3 were performed by imposing monotonic displacements at point A and the deformed shapes and damage distributions at several phases of the analyses are presented in Figure III.105 to Figure III.107. These three analyses present a very clear difference. For the analysis RC3.1, the strength dispersion in the materials was not considered (see Table III.22 and Table III.23). This can be seen in the tendency of the response to follow the symmetry of the beam, loading and boundary conditions. In the absence of softening, the response should present a perfect symmetric pattern. Nonetheless, the concrete presents softening branches that lead to localization, which is very sensitive to numerical accuracy variations and tend to destroy the symmetry by localization in one of the beam sides. This means that the response will tend to be very similar up to a certain point. Afterwards, the damage will tend to concentrate in the most damaged zones, which consists in a limitation for the analyses because damage will tend to occur in similar positions.

On the other hand, for the analyses RC3.2 and RC3.3, the response is asymmetric and much more variable because strength dispersion is implemented at the Gauss points level (see sections 2.2.6 and 3.3). This randomness in the response can be clearly observed in Figure III.106 and Figure III.107 by noting the differences in the damage distributions and in the macro-cracks position.

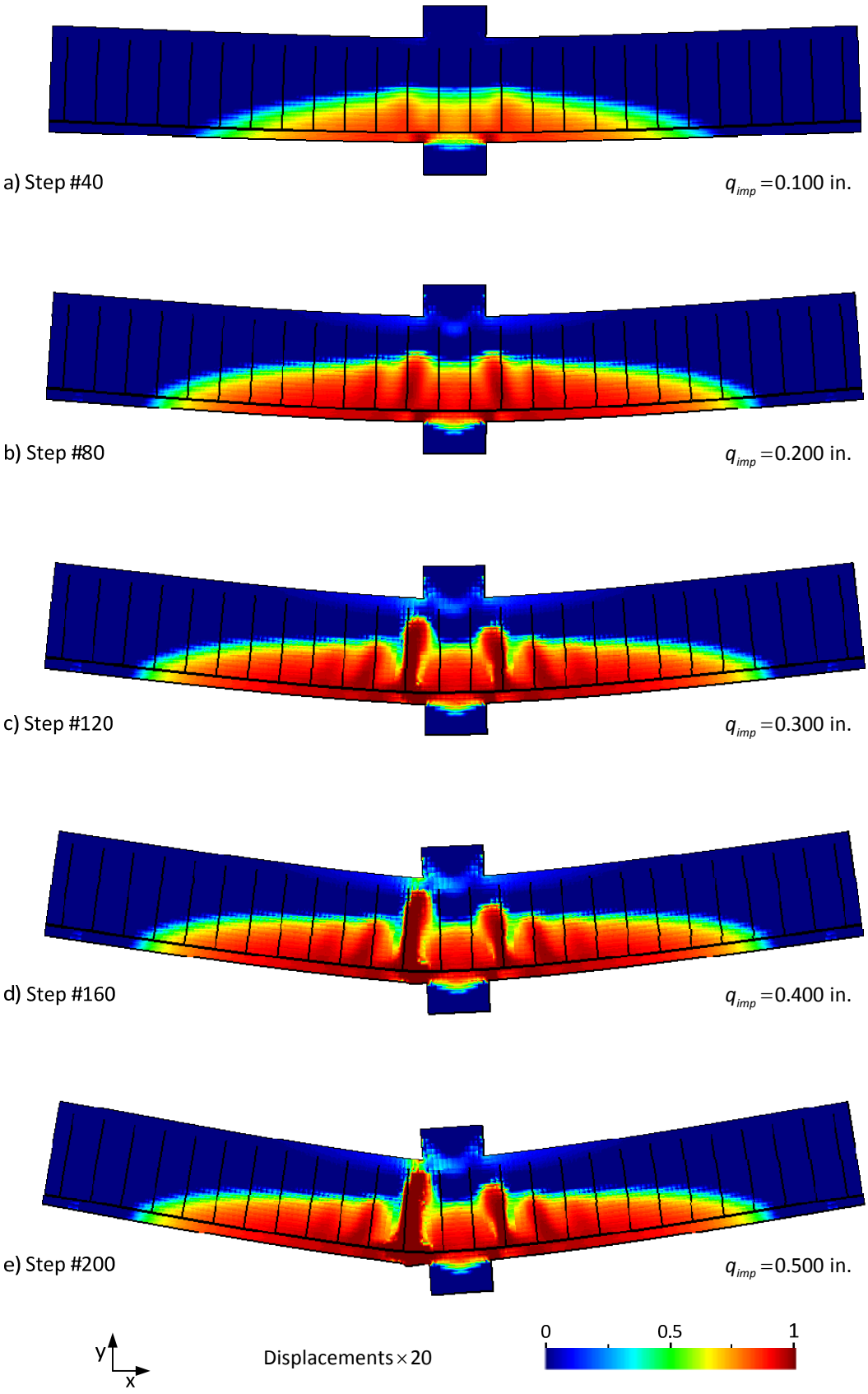

Figure III.105: Analysis RC3.1 – Deformed shape and damage distribution at selected time steps.

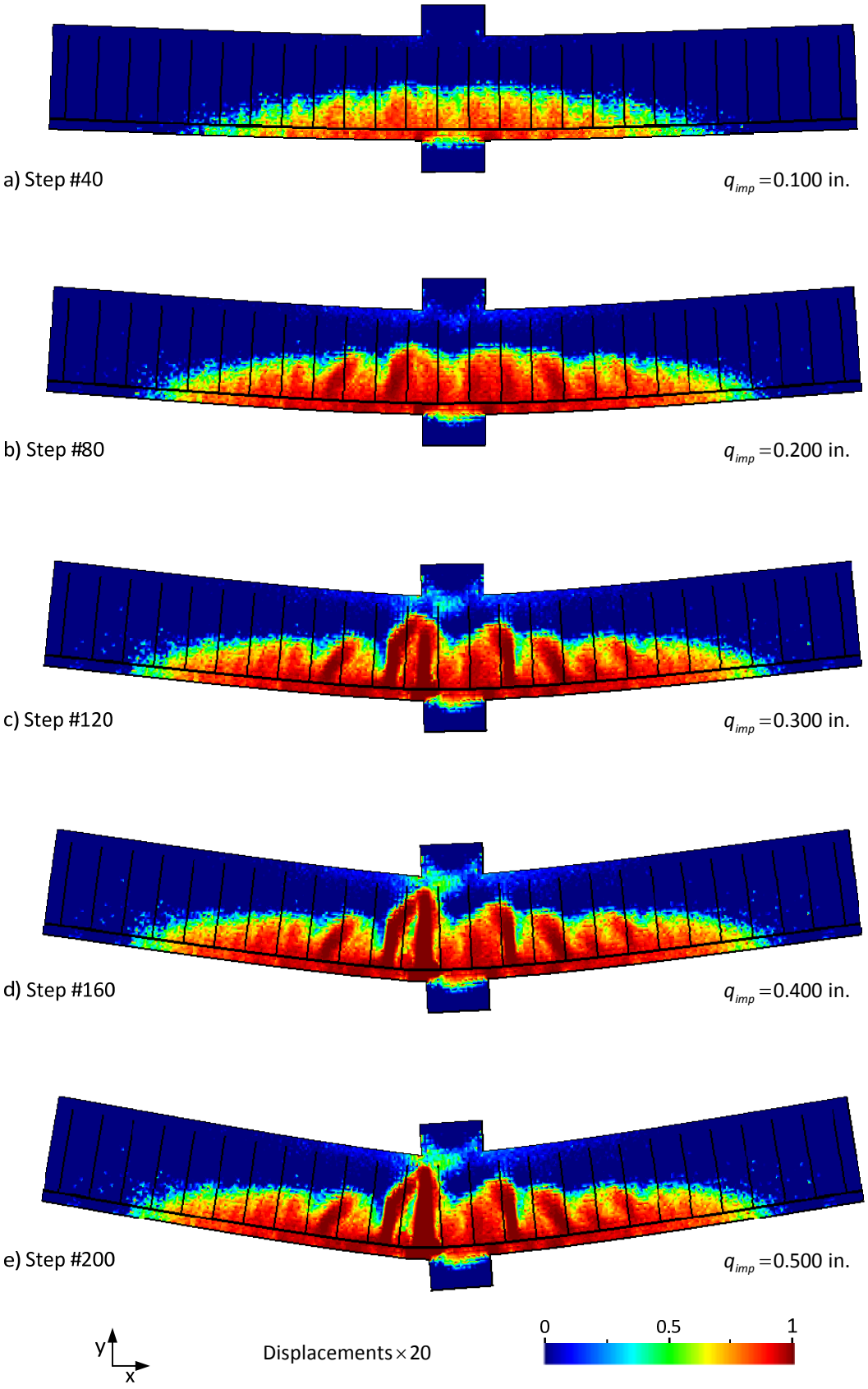

Figure III.106: Analysis RC3.2 – Deformed shape and damage distribution at selected time steps.

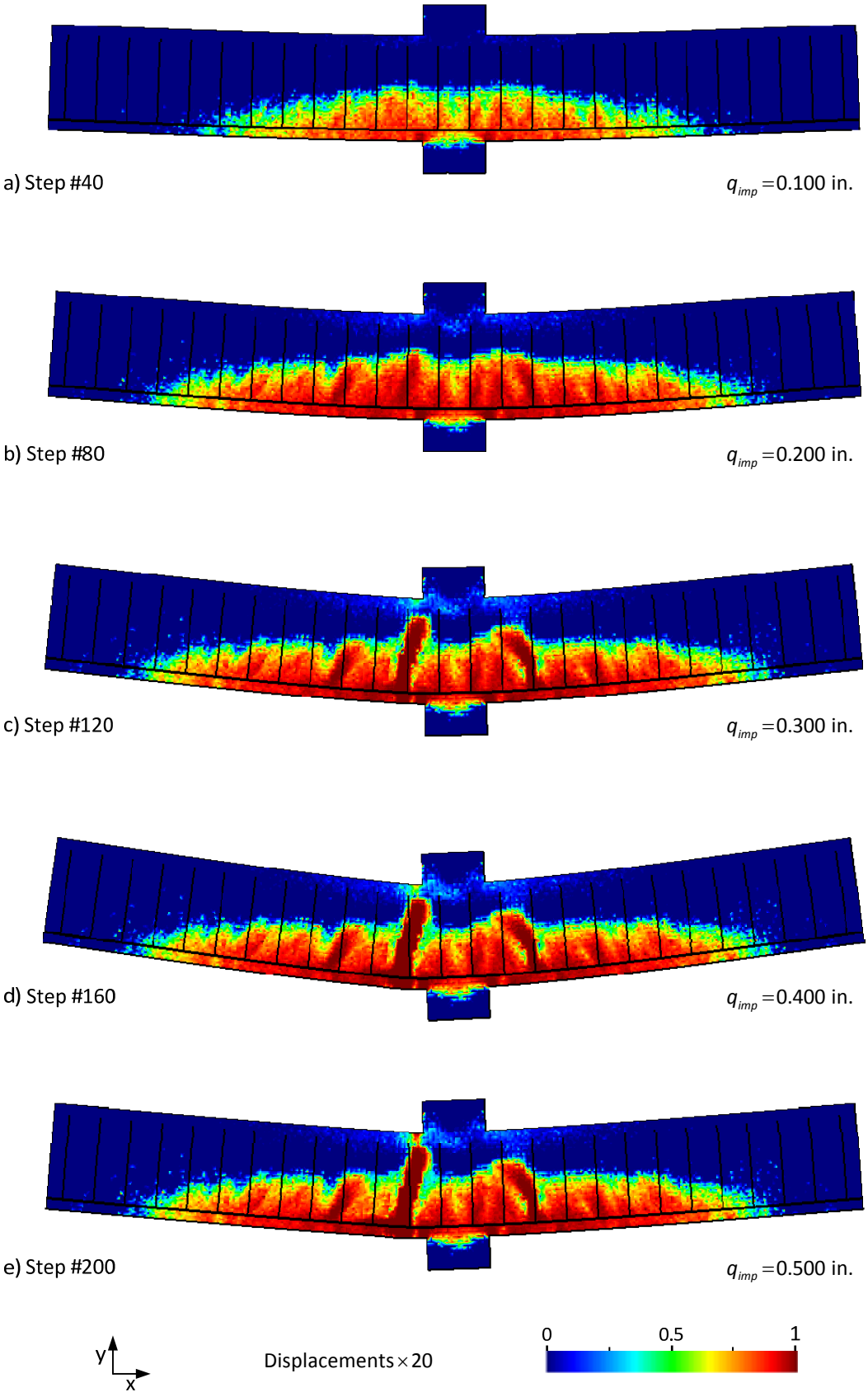

Figure III.107: Analysis RC3.3 – Deformed shape and damage distribution at selected time steps.

This means that running different analyses will produce different results in terms of the crack position and orientation. This is a clear improvement for simulating the effective concrete response. In terms of the numerical model, considering this effect does not present any relevant additional complexity and it was not possible to identify any decrease of efficiency or robustness.

Furthermore, Figure III.108 presents a general view of specimens J-13 and J-6, after being tested and just before complete failure. Both beams are similar to the specimen J-4 considered in this example, except for having also two compression longitudinal reinforcing bars (#8 bars). In addition, Beam J-13 has 14 in. of height. Comparing these photographs with the damage pattern in Figure III.106 and in Figure III.107, or even in Figure III.105, it is possible to observe a good match between the crack position and orientation. Nevertheless, it should be taken into consideration that the photographs were taken after the beams reached a much higher inelastic state (about $q_B = 15$ in.) and the differences in the smeared crack approach for representing an opened macro-crack.

Figure III.109 presents the principal strains in the concrete and in the longitudinal reinforcing steel bars obtained at selected steps in the analysis RC3.2. The crack initiation can be identified at an early stage in the analysis (see step #80 in Figure III.109-b) and for the following step represented in Figure III.109 (step #120) it is already possible to identify five macro-cracks being created. Afterwards, the strains tend to concentrate in one macro-crack and the rest of the structure unloads. At the end, the longitudinal steel bars yields and the crack opening increases substantially. These results are considered to match reasonably well the expected structural response of the RC beam.

Furthermore, Figure III.110 presents the principal stresses obtained for the same analysis and in the same steps considered for the principal strains. In this case, only the concrete stresses are displayed because the higher levels of stress in the reinforcement would make the data visualizations very difficult. Initially, it can be seen that tensile stresses concentrate at the lower part of the beam and compressive at the upper part. With the development of cracking, the concrete stresses tend to reduce due to micro-cracking. At the end, the tensile stresses are mostly transmitted by the reinforcements and the stresses in the concrete are nearly zero in the region of the macro-cracks.

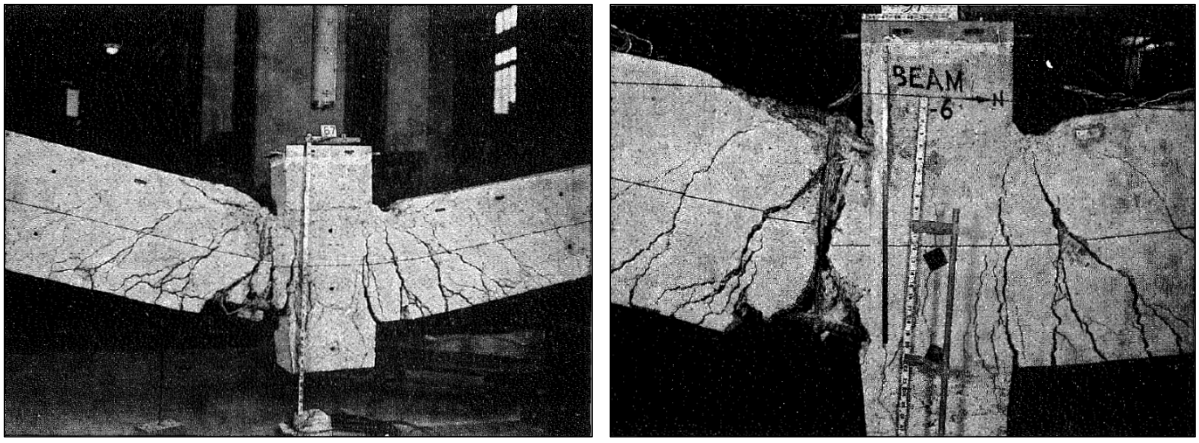

a) b)

Figure III.108: Example RC3 – Taken from Burns *et al.* [73]: a) Beam J-13 after failure ; b) Beam J-6 after failure.

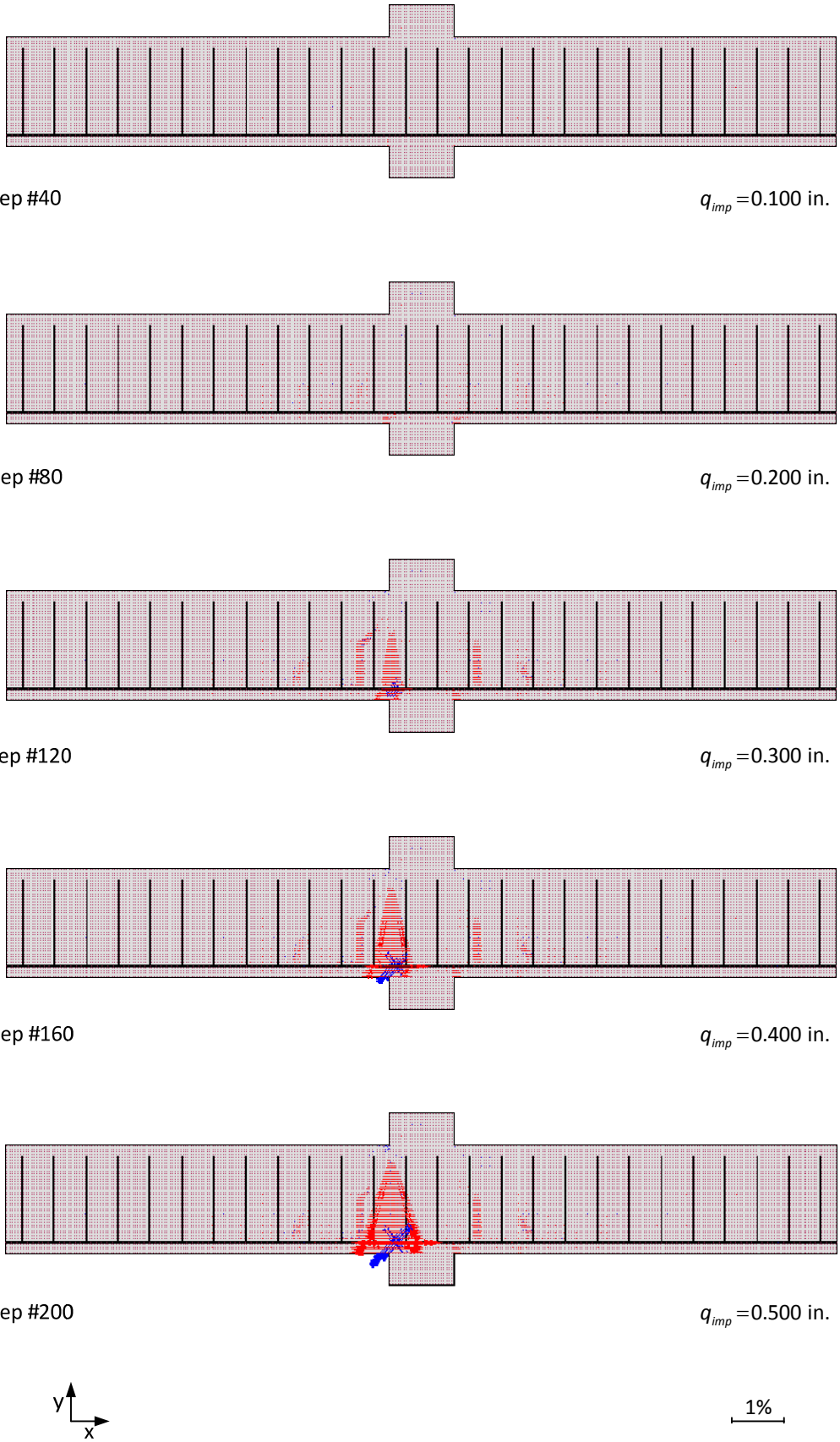

Figure III.109: Analysis RC3.2 – Principal strains in the concrete and longitudinal reinforcing bar at selected time steps.

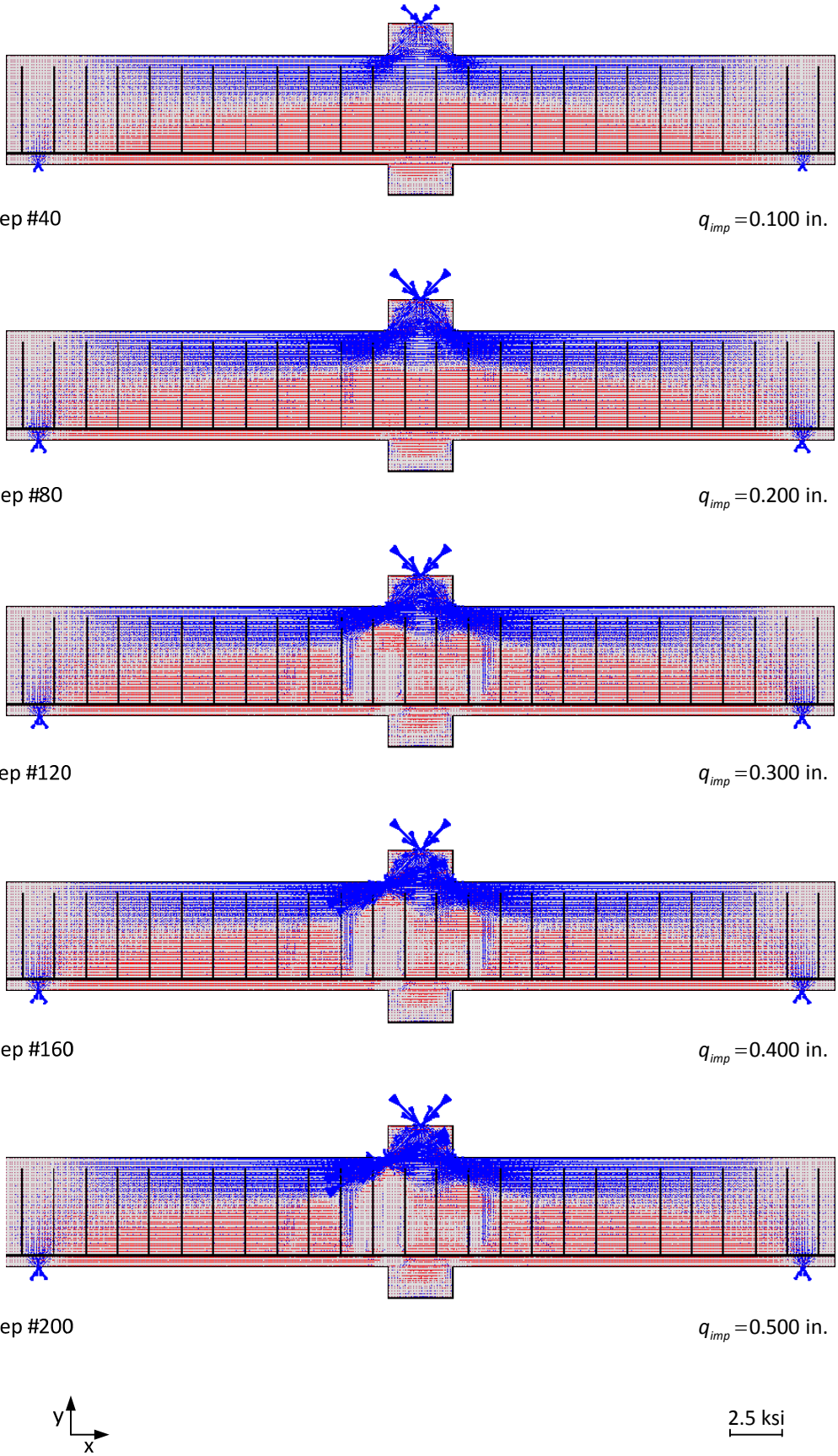

Figure III.110: Analysis RC3.2 – Principal stresses in the concrete at selected time steps.

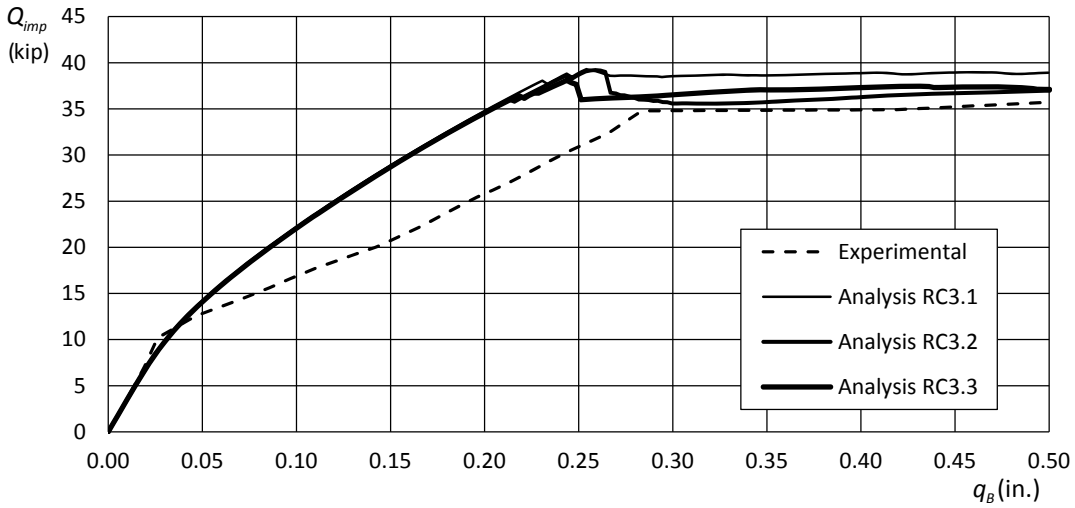

Figure III.111: Example RC3 – Global force-displacement curves.

Figure III.111 presents the global force-displacement curves obtained in the three analyses, which are plotted against the experimental data obtained by Burns *et al.* [73]. It can be seen that the experimental and numerical curves are very close before the development of micro-cracking. On the other hand, the numerical curves are significantly above the experimental after cracking and up to yielding of the reinforcements. For instance, for $q_B = 0.20$ in. the average of the numerical curves is 34% above the experimental result. This difference is mainly due to three reasons. Firstly, the fracture energy of the concrete was increased in order to avoid the unrealistic shear collapses caused by considering an isotropic damage model, which penalizes the shear strength. Secondly, a residual concrete tensile strength of 3% was adopted (see Table III.22) to avoid having elements with no strength or stiffness (when the secant stiffness is adopted), in order to improve the numerical stability of the model. Finally, the experimental curve presents an unusual positive curvature between the cracking and yielding zones, which is associated with stiffness increase. This seems difficult to explain because the steel bars did not reach the strain-hardening plateau, not even yielding. In addition, the concrete tends to crack and decrease stiffness. Perhaps, the tests presented some additional source of flexibility that shifted to some extend the experimental curve. Nevertheless, a stiffer concrete response in the numerical model is expected due to options taken to simulate the concrete.

Moreover, the analysis RC3.1 without strength variability is associated with the most resistant response, as expected. On the other hand, the stiffness is similar in all the analyses. This is expected because the strength dispersion implemented does not change the initial stiffness (see Figure III.75).

In what concerns the numerical efficiency of the model, it was possible to observe a poor convergence rate in the iterations. To support this statement, Figure III.112 to Figure III.114 present the number of iterations required by each time step to achieve convergence when a tolerance of $\beta_Q = 0.001$ in equation (II.272) is adopted. It can be seen that the number of iterations is high and with an average around 85-100 iterations and with peaks when cracks are developing.

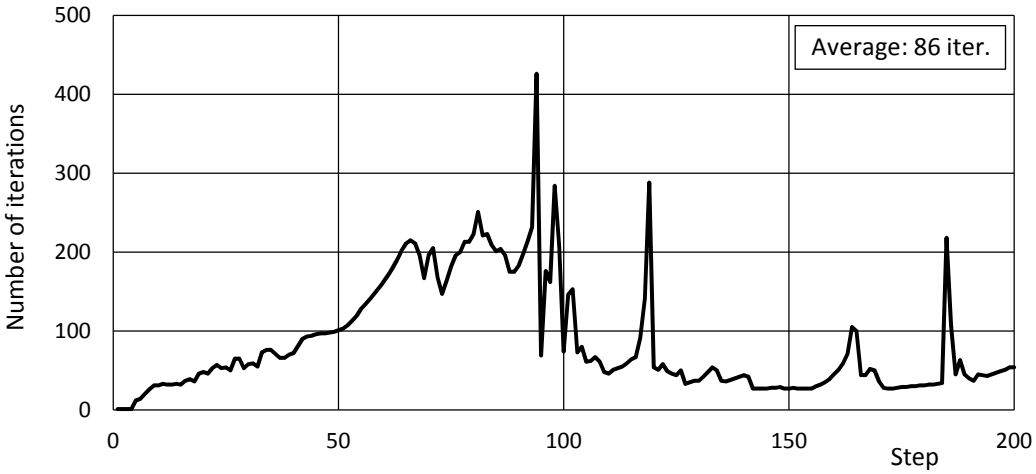

Figure III.112: Analysis RC3-1 – Number of iterations required to achieve convergence.

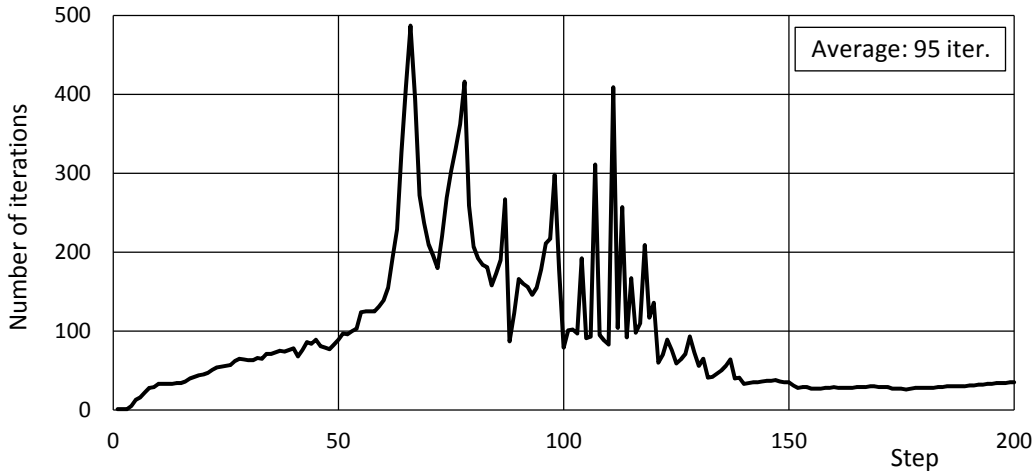

Figure III.113: Analysis RC3-2 – Number of iterations required to achieve convergence.

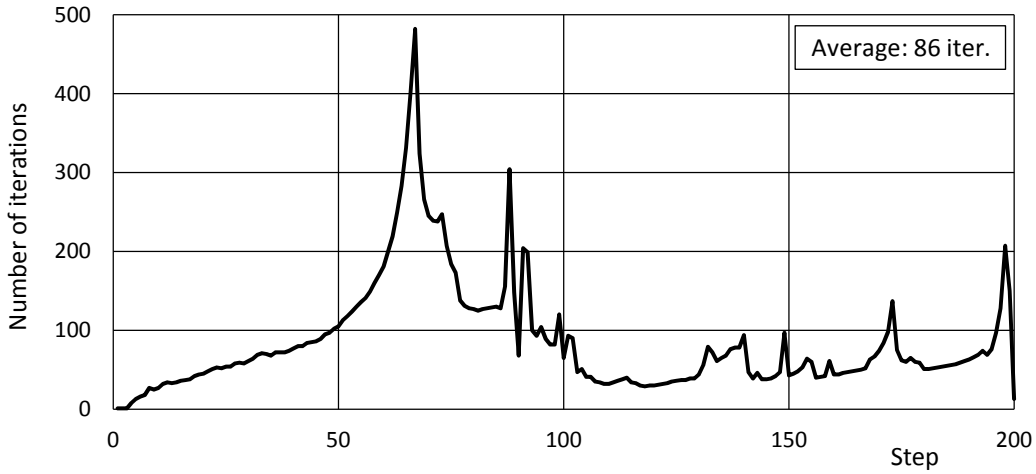

Figure III.114: Analysis RC3-3 – Number of iterations required to achieve convergence.

This behaviour is caused by the model used for simulating concrete because for most of the analysis the steel response is elastic. As discussed in Chapter II-§5.3.2, using the secant stiffness as in (III.59) or (III.102) leads to poor convergence rates as this modulus can be very inefficient to find equilibrium. Other authors experienced similar convergence rates when working with continuum damage models for simulating concrete, *e.g.* Faria [211]. Nevertheless, this comparison must take into consideration the convergence tolerance, the type of analysis and the time step adopted.

In addition, the model presented monotonic convergence for the majority of the iterations, except when the most significant inelastic phenomena develops, *e.g.* opening of macro-cracks.

As a global appreciation, it can be concluded that the adopted models for simulating the reinforced concrete element can simulate reasonably well the inelastic response. This seems clear at the early inelastic stages where micro-cracking is well simulated. The main problems arise for intense nonlinear response involving opening of macro-cracks. In those situations, the convergence is very slow and unrealistic collapses can occur due to the approximations adopted in the models, in particular, the isotropic damage formulation. The adopted solution to mitigate this problem was to increase the mode I tensile fracture energy and to add residual strength levels to the concrete. This resulted in higher stiffness and resistance. Nevertheless, the development of macro-cracks was possible to be simulated with an interesting accuracy, considering the implicit approximation in the smeared crack approach for modelling the concrete fracture.

5.4 Example RC4 – RC precast column test by Mendes, Coelho and Costa

This example illustrates the use of the proposed numerical model in the analysis of a three-dimensional problem. For this purpose, the RC precast column shown in Figure III.115-a was chosen, which was tested at LNEC by Mendes, Coelho and Costa [392-394]. These tests were carried out in the scope of the European Project "*PRECAST - Seismic Behaviour of Precast Concrete Structures With Respect to Eurocode 8*" and financed by the European Commission. The experimental activity was divided in two phases. At first, a two-storey structure was tested using the triaxial shaking table (see Figure I.3-b). Afterwards, the structural response of the precast column-foundation and beam-column connections were characterized using *quasi*-static monotonic and cyclic tests.

This example concentrates on the monotonic and cyclic tests executed on the socket-type column-foundation connections presented in Figure III.115-a. The footing and the column are precast and joined together *in-situ* by inserting the column into a pre-existing hole in the footing and by sealing them using a micro-mortar, as illustrated in Figure III.115-a. According to the authors, the precast connection performed very well in the tests and no significant damage was identified in this part of the specimens. In fact, almost all the visible damage was distributed in the span of the columns and the response was typical of a regular cast *in-situ* RC member.

It should be noted that the connection tests were executed also using reduced scale specimens. The authors defend that this way it is possible to better characterize the response of the connection in the two-storey building tested in the shaking table, thus avoiding differences related to the similitude law adopted and to the size effect. The dimensions of the specimens are presented in Figure III.115-b and the detailing of the reinforcements in Figure III.115-c.

The test layout was unusual for this type of experiment (see Figure III.116). LNEC's uniaxial shaking table was used to impose a series of displacements at the top of the column using a large truss and a guiding system. A load cell can be found at the end of the truss to measure the load applied to the

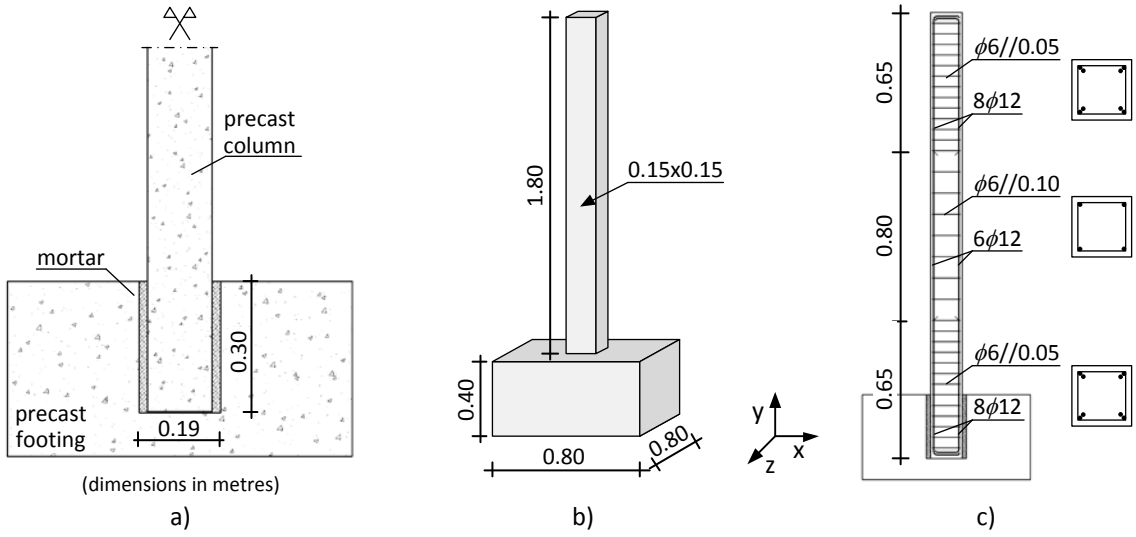

Figure III.115: Example RC4– Definition of the problem.

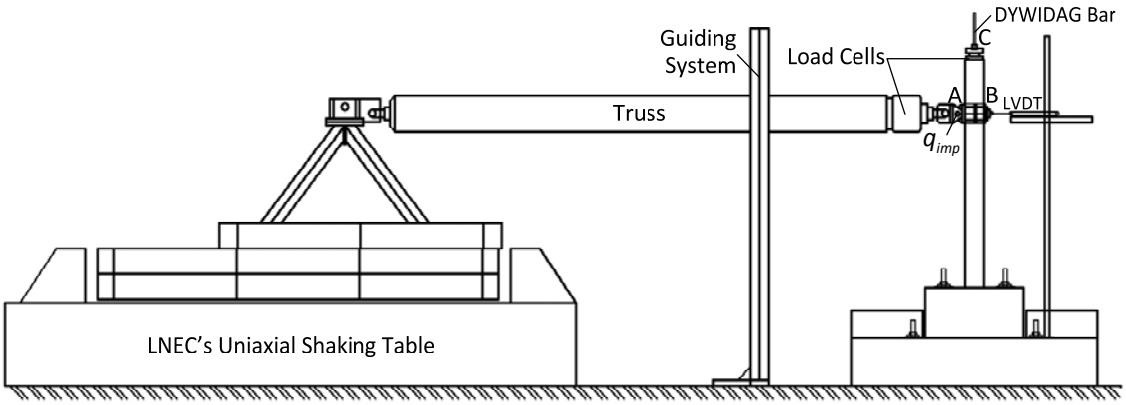

Figure III.116: Example RC4 – Test layout.

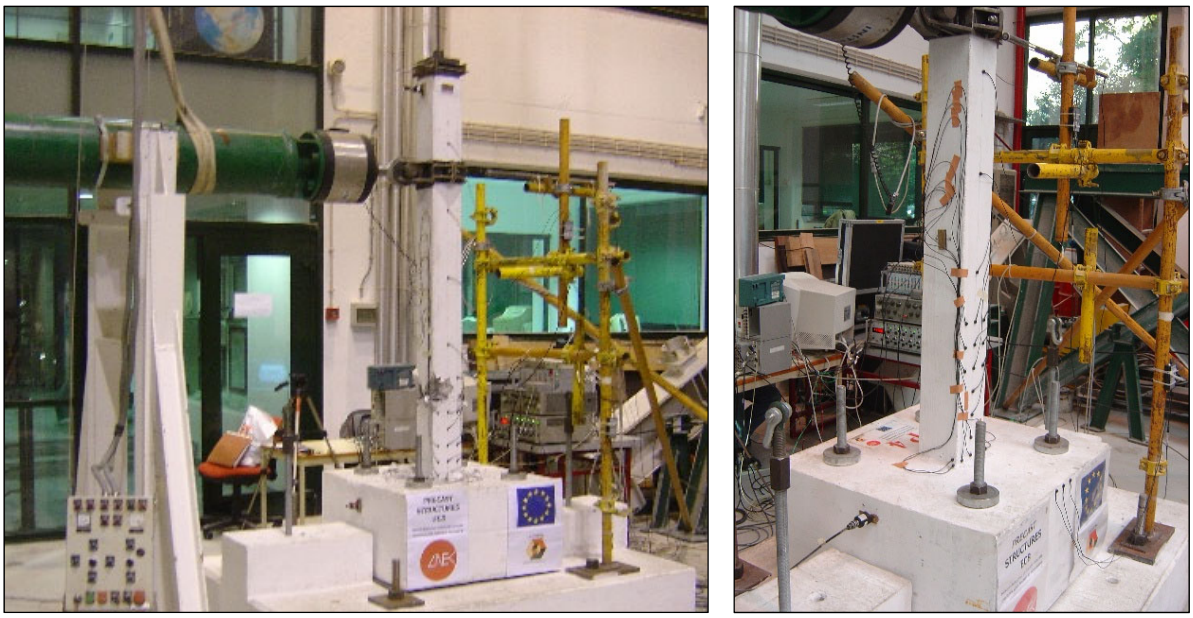

a) b)

Figure III.117: Example RC4 – General views of the test layout and instrumentation: a) Specimen P1; b) Specimen P4.

specimen (near point A in Figure III.116). The prescribed displacements were controlled using an external PID loop and the LVDT installed near point B in Figure III.116, in order to avoid errors due to the flexibility of this relatively large load application system. Furthermore, a *Dywidag* bar (ϕ15 mm) placed in a hole inside the column was used to simulate typical levels of axial load and the load installed was measured during the tests using a load cell (near point C in Figure III.116). Figure III.117 presents general views of the test layout and of the sensors used in the tests, which were mainly load cell, LVDTs and 3D optical displacement transducers.

Table III.25 presents the characteristics of the four analyses that will be presented and discussed ahead. These include two static analyses that will be compared with the monotonic (specimen P1) and cyclic (Specimen P4) tests executed by Mendes *et al*. [394]. In addition, two dynamic analyses

Table III.25: Example RC4 - Characteristics of the analyses.

Analysis	Type	Mesh	Time Integration	Mass/Damping	Loads & Time History
RC4.1	Static (Monotonic)	Mesh #1	-	-	#1 ($Q_V = 74$ kN); #2 (Δq_{imp}=0.5 mm)
RC4.2	Static (Cyclic)	Mesh #2	-	-	#1 ($Q_V = 135$ kN); #3 (TF #1 x 1.00, $\Delta q_{imp} \approx 0.12$ mm)
RC4.3	IDA	Mesh #2	Newmark γ=0.50;ν=0.25 $\Delta t = 0.02$ s	M_x=M_y=2.0 ton Proportional D. α_d =5.3330E-1 β_d =3.8818E-3	#1 ($Q_V = 74$ kN) #4 (TF #2 x 0.07); #5 (TF #3 x 0.08)
RC4.4	IDA	Mesh #2			#1 ($Q_V = 74$ kN) #4 (TF #2 x 0.21); #5 (TF #3 x 0.14)

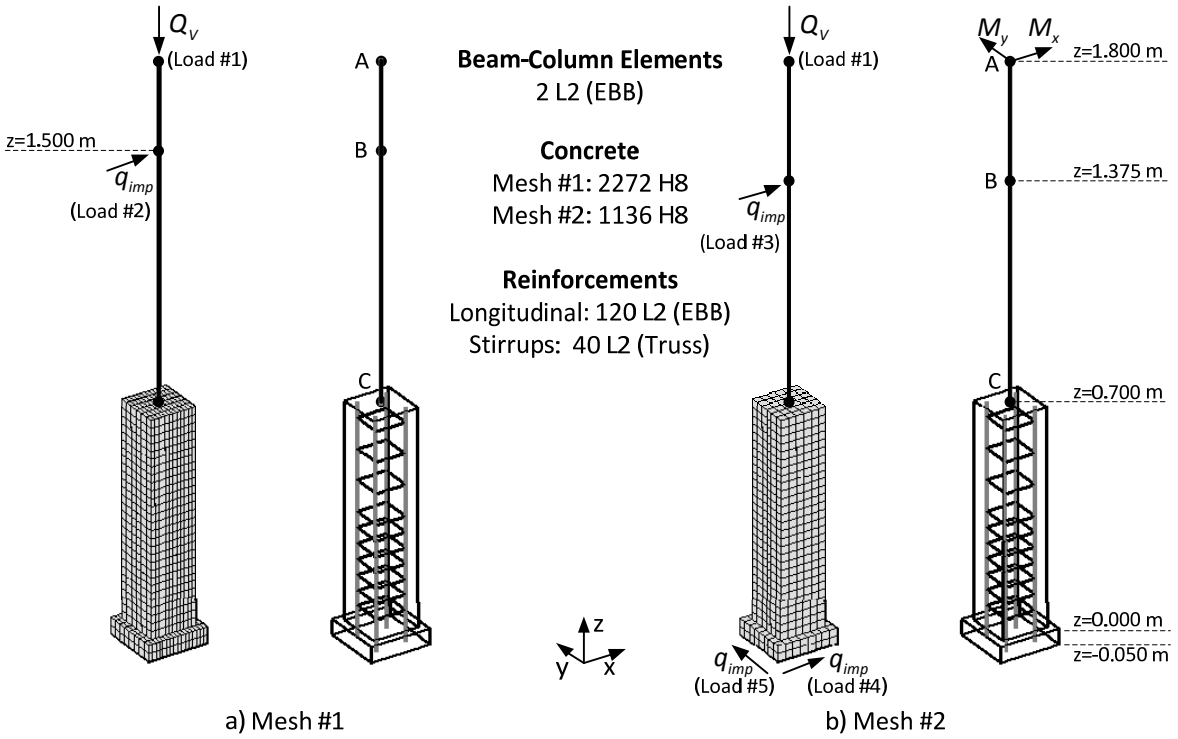

Figure III.118: Example RC4 – Finite element meshes adopted.

were computed to assess the response of the models for simulating seismic events.

The two meshes presented in Figure III.118 were used in the analyses. Mesh #2 uses 1136 cubic hexahedrons with 2.5 cm edge and 160 bar elements 2.5 cm long for the longitudinal reinforcements and 10.0 cm for the stirrups. Mesh #1 was used for the monotonic test simulation because this experiment reached higher inelasticity levels, which required a more refined mesh. This mesh is similar to Mesh #2 and the only difference is in the hexahedron-size along direction *x* that is reduced to 1.25 cm, thus doubling the number of elements used to simulate the concrete.

Both meshes adopt what is called a *Hybrid Discretization* in the scope of this thesis (see Chapter V-§3). This technique was used to decrease the number of unknowns in the simulation by using a

simplified mesh in the zones expected to remain elastic or with minor nonlinear effects. This is the case of the top of the column where only minor micro-cracking is expected to occur. As a result, elastic Euler-Bernoulli beam-column elements are used to simulate the column top. The same elasticity modulus used for the concrete hexahedrons were used and the elastic cross section geometric parameters were adopted to define the relevant bar properties, *e.g.* area, moment of inertia, *etc*. Only the inertia moments were reduced by half to take micro-cracking into consideration.

The transition between the refined and simplified parts of the mesh is made using kinematic constraints. This is achieved by enforcing the *Beam2Solid* constraint presented in Chapter V-§3 and using the *Lagrange Multipliers* technique discussed in Chapter V-§2.4.3.

All the analysis included a vertical load used to simulate the axial load installed in the column during the experiments. As reported in Table III.25, this load was considered constant during the computations, which involves an approximation because Mendes *et al.* [394] report changes in the axial load value during the test due to the lateral displacements and to crack imperfect closure in between cycles. The other loads considered were an prescribed displacement along direction *x* at point B in Figure III.118 for the analyses #1 and #2, and base displacements along direction *x* and *y* for the analyses #3 and #4.

Table III.26 presents the description of the constitutive models used in the analyses. The concrete was simulated with the nonlocal *Modified Mazars' model* (*MMazars*) described in section 3.3 and the longitudinal reinforcements with Euler-Bernoulli beam-column elements defined by *Refined Steel* (*RSteel*) model for the axial component. The stirrups were considered elastic during the analyses. The Euler-Bernoulli beam-column formulation was used to simulate the longitudinal reinforcements in order to add lateral resistance to the RC member and to reduce the risk of unrealistic shear failures associated with the isotropic damage model used for concrete.

The reinforcement detailing presented in Figure III.115-c was followed to create the mesh. Accordingly, the stirrup spacing changes were considered in the mesh and the reduction of the number of longitudinal reinforcements was taken into consideration by changing the area of beam-column elements. This last transition was introduced at coordinates z=0.30 m, instead of z=0.35 m, to take into consideration that the stress transfer between the concrete and the steel bars is gradual.

In what concerns the concrete, a Eurocode 2 [91] C35/45 concrete class was adopted because Mendes *et al.* [394] report that the concrete presented an excellent quality and response and it is probable that the precast company used a higher class concrete than the one specified in the technical drawings, which is C25/30. The adopted uniaxial stress-strain relation is presented in Figure III.119-a and the tensile strength dispersion was considered by adopting 18% of *relative standard deviation* and 2/3 of this value (12%) for the compressive strength. These values are consistent with the ones presented in Table III.6.

Regarding the reinforcing steel, the A500NR steel class was adopted as specified in the technical drawings. This steel specification is very common in Portugal and the mean values for the mechanical parameters were considered as the ones listed in Table III.12 for the B500 *Tempcore* steel, which

presents similar mechanical characteristics. The adopted monotonic stress-strain relationship is presented in Figure III.119-b.

During the test, the authors observed that the base of the specimen presented some deformability and moved concomitantly with the prescribed displacements. This undesirable deformability seems to be associated with the uncommon test layout used to perform the tests. If this effect is not taken into consideration, some differences in the global response curves in terms of deformability may appear. This problem was avoided by simulating the base movements measured by the optical displacement transducers spread in the column and in the base (see Figure III.117). This way, the base translational movement along the *x* direction and the rotation about the axis *y* were simulated using the measured time histories and enforced using kinematic constraints and the Lagrange Multipliers technique. This simulation can be easily observed in the results presented in Figure III.120-b/c.

Table III.26: Example RC4 – Model parameters.

Model	Type	Use	Parameters
1	*MMazars*	Concrete hexahedrons	E_c =34 GPa, ν=0.18, $\tilde{\varepsilon}_0$ =0.0945‰, $\tilde{\varepsilon}_u$ =7.0‰, R_p =0.03, A_- =0.90, B_- =1185, L_{nl} =2.0 cm (bell-shaped function), f_{RSD} =0.18
2	*RSteel*	Longitudinal reinforcements	E_s =200 GPa, σ_{sy} =585 MPa, ε_{su} =9.4%, β_0 =0.51%, R_0 =1.5, c_R =0.2, n_R =2.0, e_f =24.5, c_f =0.3, n_f =1.0, f_{RSD} =0.05
3	*Elastic*	Stirrups	E = 200 GPa, ν = 0.30
4	*Elastic*	Concrete EBB	E_c =34 GPa, ν=0.18, $\left(A_s,\ I_t,\ 0.5\,I_{x2},\ 0.5\,I_{x3}\right)$

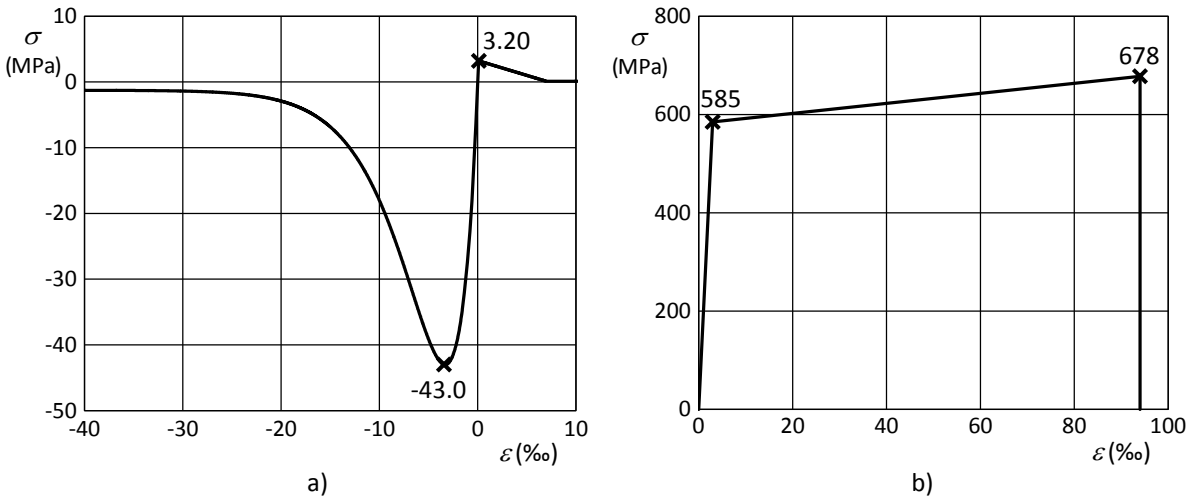

Figure III.119: Example RC4 – Constitutive relations: a) Concrete; b) Steel.

- Analysis RC4.1 – Monotonic test

The first analysis was performed by imposing a monotonic *quasi*-static lateral displacement at point B (*z*=1.50 m, see Figure III.118). This test layout follows the experiment performed by Mendes *et al.* [394] with the specimen P1. Mesh #1 was used because the nonlinearity level is very high. This can be concluded by noting that at the end of the numerical simulation the drift between the base and loading point was $0.058/1.500 = 3.86\%$.

The numerical simulation included 9417 *dofs* and 747 kinematic constraints used to enforce the *Beam2Solid* constraint, the base translation and rotation and the displacements prescribed at the column top.

Figure III.120 present the most relevant results to characterize the concrete response throughout the analysis. Figure III.120-a presents the Mazars' combined damage variable distribution on the deformed configuration. It can be seen that initially the damage concentrates mainly in the tensioned part of the column, making it possible to simulate distributed micro-cracking along the member. Afterwards, the damage starts to concentrate between *z*=0.30 m and *z*=0.35 m, precisely in the same position where half of the reinforcements are removed. Subsequently, the most damaged zone spreads to a wider region and the column deformations tend to concentrate into the macro-crack and the rest of the bar presents reduced deformations. Furthermore, a clear tendency of the macro-crack to become diagonal along the *x* direction can be identified.

The same response can be observed in Figure III.120-b that presents the principal strains on the deformed configuration. The strains are originally dispersed and start to concentrate at the most damaged zone. In addition, strain concentrations can be identified in the upper part of the column and along the tensioned longitudinal reinforcements.

Figure III.120-c presents the principal stresses in the concrete. It can be noted that initially the tensile and compressive stresses are nearly equally divided on each side of the column. Afterwards, the neutral axis starts to move into the compressed zone and the most damaged zones are nearly unstressed, as expected.

Figure III.121 complements this information with the most significant data from the response of the longitudinal and transversal reinforcements. Figure III.121-a represents the axial strain in the longitudinal bars and confirms that the two bars in the rightmost side of the figure are compressed and the other are tensioned. Moreover, for last time steps and in the region with fewer longitudinal bars, it can be seen that the tensioned bars are subjected to much higher strain levels reaching up to 2%. It can be concluded that these bars achieved yielding during the simulation.

This conclusion is confirmed by the axial stresses presented in Figure III.121-b. It can be observed that in the same region the reinforcements present values of stress of about 600 MPa, hence working already in the strain-hardening branch. It can be verified that the remaining longitudinal bars are working elastically, with higher stresses for the tensioned bars and lower stresses for the compressed bars, which are assisted by the concrete.

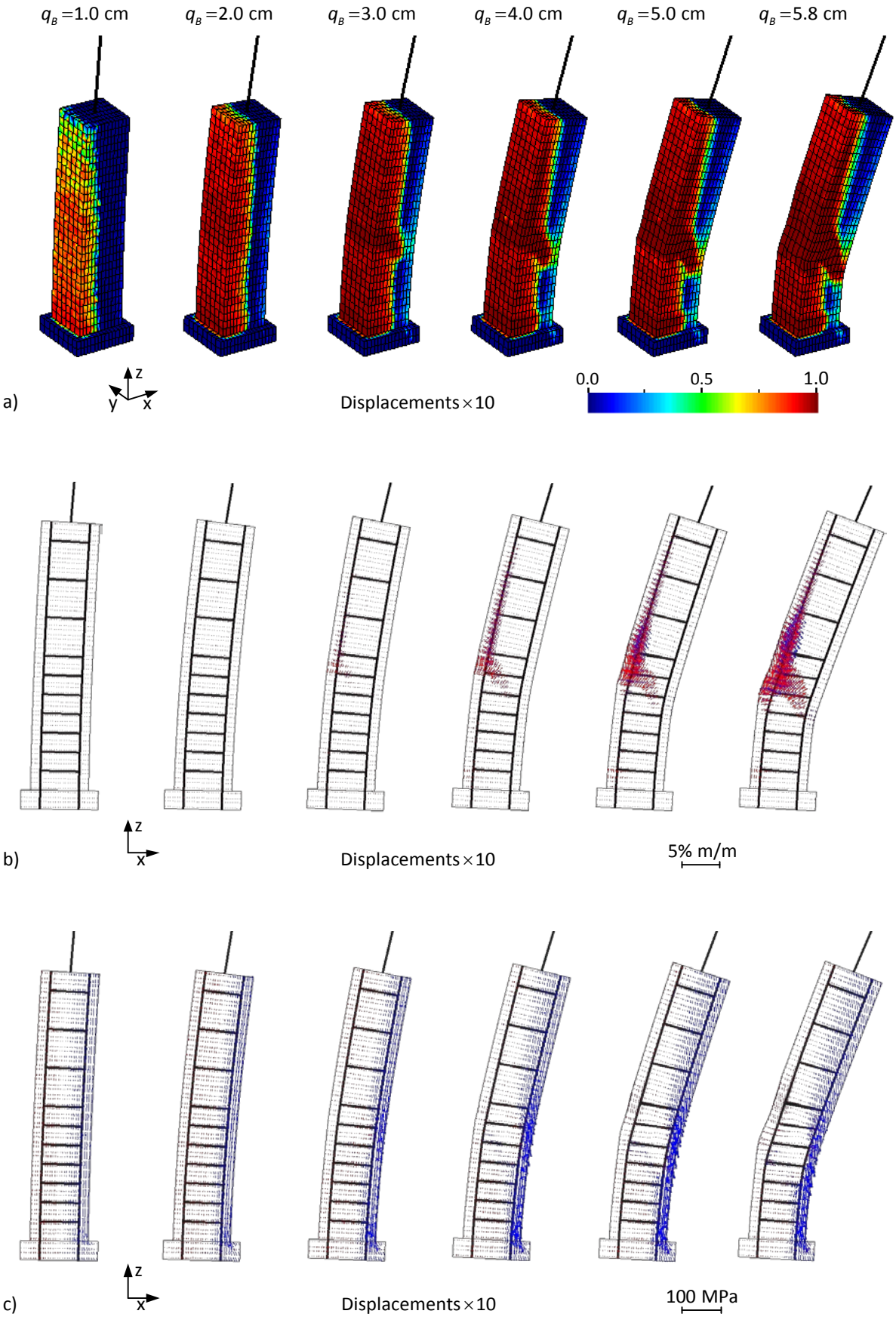

Figure III.120: Analysis RC4.1 – Structural response of the concrete at selected time steps:
a) Damage distributions; b) Principal strains; c) Principal stresses.

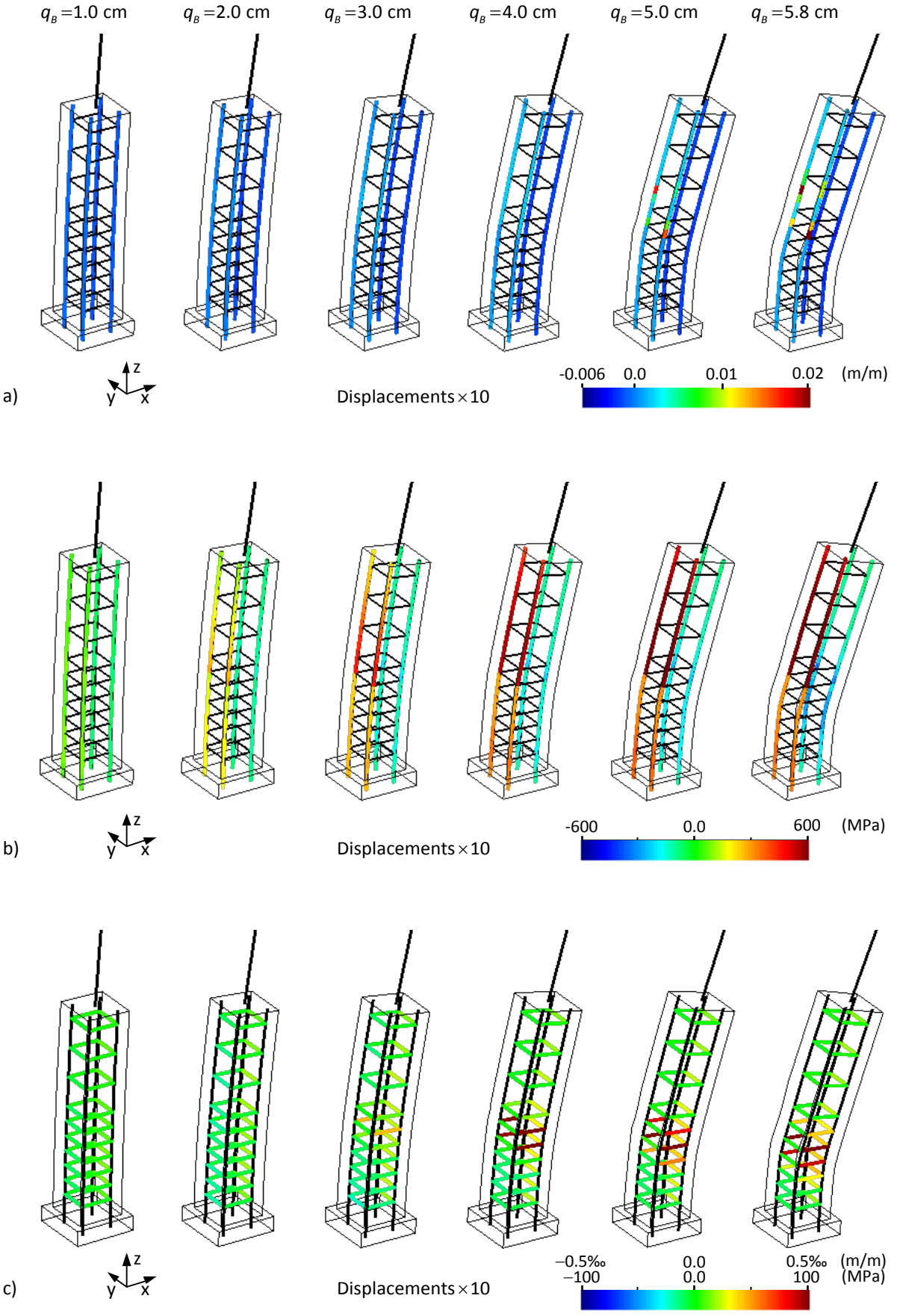

Figure III.121: Analysis RC4.1 – Structural response of the reinforcements at selected time steps: a) Axial strains in the longitudinal reinforcing bars; b) Axial stresses in the longitudinal reinforcing bars; c) Axial strains and stresses in the stirrups.

Furthermore, Figure III.121-c presents the strain and stress distributions in the stirrups, which were simulated with an elastic constitutive relation. It can be seen that for all time steps represented the stresses are always below ±100 MPa, hence considering an elastic constitutive relation proved to be adequate. In addition, all stirrups seem to be lightly stressed, except for the stirrups near the macro-crack zone where the bars are mainly under tensile stresses. This is most visible in the stirrups along the *x* direction near the macro-crack, giving the indication that these bars are contributing to keep the macro-cracking from opening. This effect can be augmented by the use of the smeared crack approach that results in larger and unrealistic cracking lengths, thus potentiating the mobilization of the stirrups, which for a localized macro-crack would be more difficult to be achieved. In conclusion, this stirrups contribution is amplified by the fracture approach adopted for the concrete simulation.

Figure III.122 presents the force *vs.* prescribed displacement curve plotted against the experimental curve obtained by Mendes *et al.* [394]. The first aspect that is visible in this figure is that the numerical model using this discretization was not able to follow the entire experimental curve, although yielding of the reinforcements can be clearly identified. This is certainly related to the high inelasticity level concentrated in the macro-crack, for which the CDM approach becomes unrealistic and presents convergence problems. This can be seen in Figure III.123 that presents the number of iterations required to achieve convergence for the adopted tolerance, which in this case was set to $\beta_Q = 0.005$ as defined in equation (II.272). The average number of iteration was relatively high and it can be seen that some steps required up to 160 iterations to converge, which demonstrates the model inefficiency for high inelasticity levels.

The global force-displacement curve presented in Figure III.122 has some similarities with the one obtained in the previous example (see Figure III.111). Namely, the initial stiffness is simulated with a good accuracy level using typical material parameters for defining the constitutive models. Furthermore, after concrete cracking and up to steel yielding the global response curve is stiffer than the experimental one. Once again, this can be related to the use of high mode I fracture energy density in the concrete model $\left(g_f^{\mathrm{I}} = 11286\ \mathrm{N/m^2},\ L_{nl} = 2.0\ \mathrm{cm}\right)$. As before, this is done to avoid premature and unrealistic shear-type collapses caused mainly by the isotropic damage formulations adopted. In this case the difference was smaller than the one observed in the previous example, *e.g.* 18% at $q_B = 2.0$ cm against the 34% reported before. As before, after steel yielding the numerical and experimental curves converge and remain very close in most of the post-yielding branch, until the model stops converging.

Figure III.124-a presents a general view of the experiments in progress where it can be easily seen that the deformation tends to concentrate at about 0.35 m from the foundation top, as reported by Mendes *et al.* [394]. Moreover, Figure III.124-b presents a detail of the P1 specimen after the test and after removing the cover concrete to identify the effective position of the reinforcements. The authors found that the macro-crack opened exactly in the region where half of the reinforcements are interrupted, as can be seen in Figure III.124-b.

Furthermore, Figure III.125 presents a detail of the macro-crack zone during the test, which illustrates the cracking pattern in the column. Bending cracks in the tensioned side of the column can

be easily observed. In addition, it can be identified that a macro-crack is clearly opened on the tensioned side of the column and that the concrete starts to be crushed in the compressed face. Another interesting aspect to be noticed is that the same diagonal crack observed in the numerical model (see Figure III.120-a/b) can be also detected in the images from the experiments. The tendency to generate this diagonal crack can be associated with perturbations in the stress fields in the transition zone between four and eight longitudinal reinforcements.

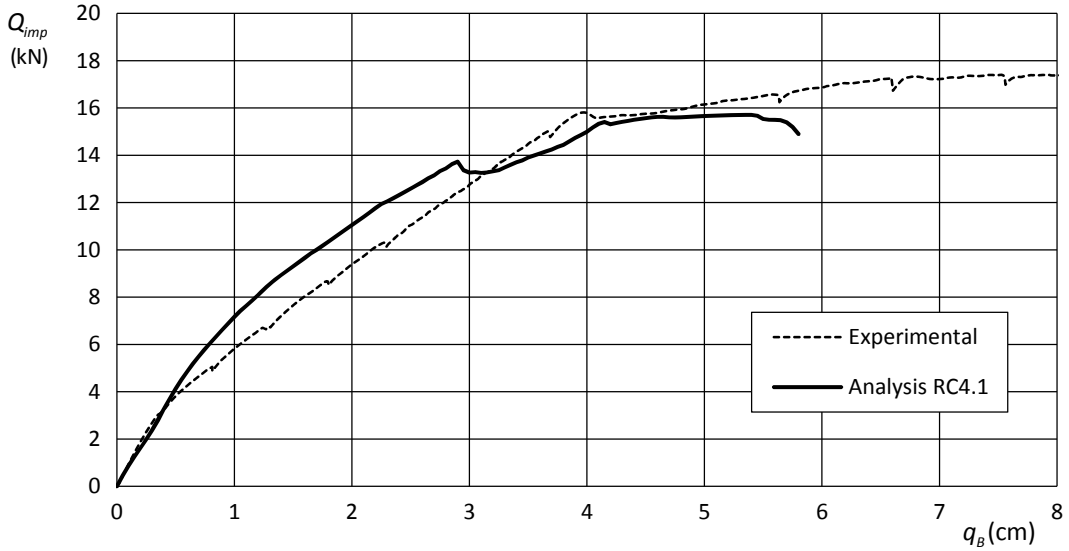

Figure III.122: Analysis RC4.1 – Global force-displacement curves.

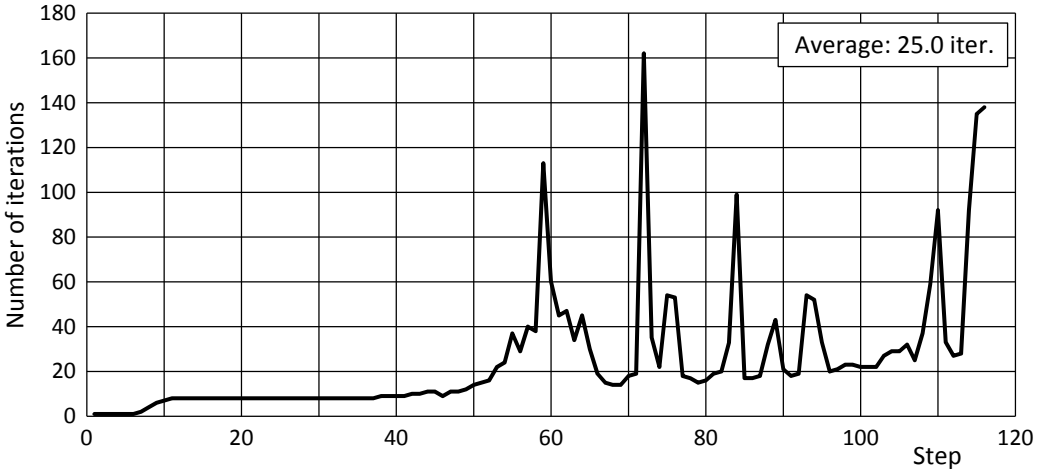

Figure III.123: Analysis RC4.1 – Number of iterations required to achieve convergence.

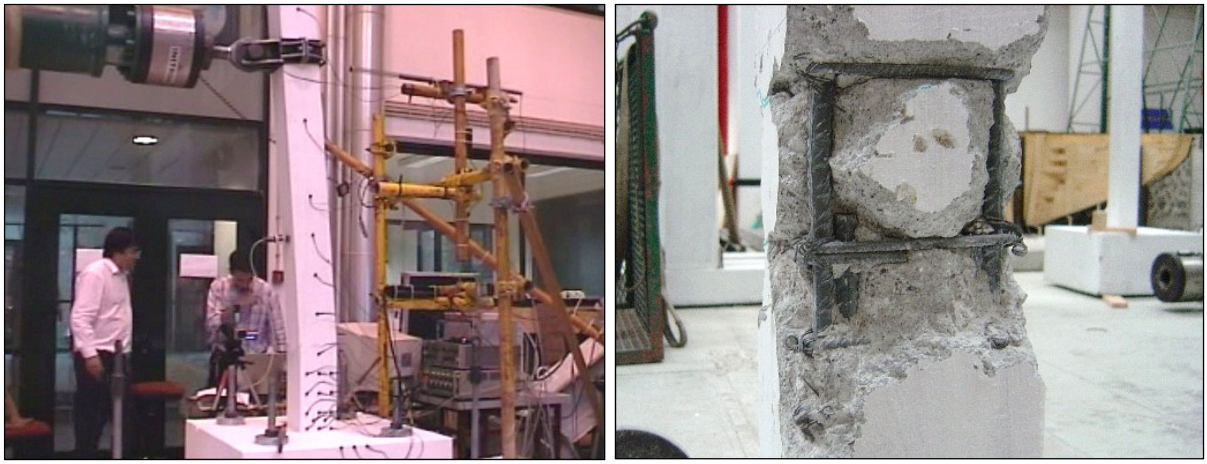

a) b)

Figure III.124: Monotonic test with specimen P1 performed by Mendes *et al.* [394]:
a) test under execution; b) Inspection made to the reinforcements after the test.

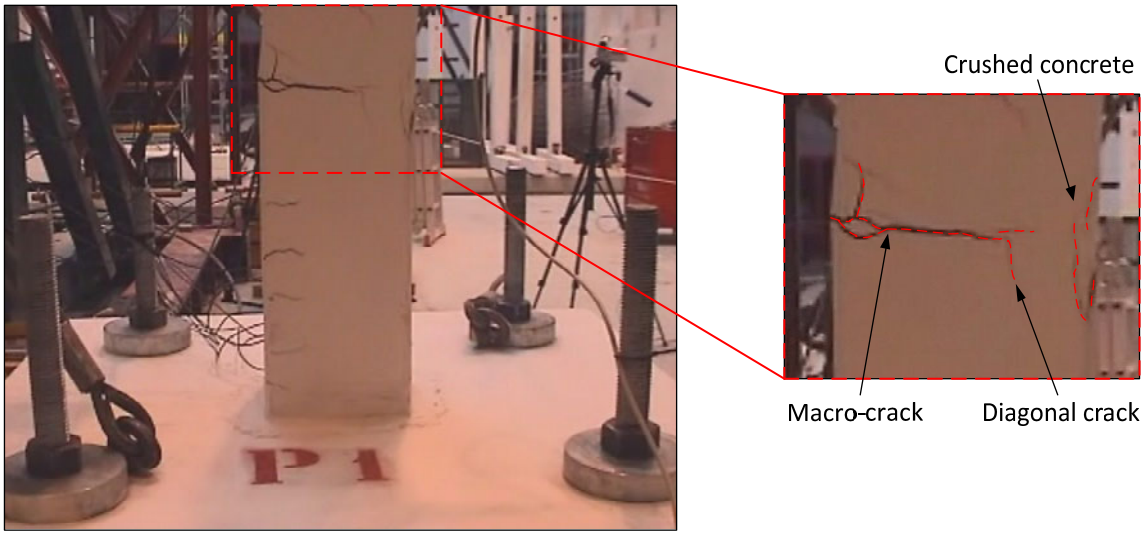

Figure III.125: Monotonic test with specimen P1 performed by Mendes *et al.* [394] – Cracking pattern.

- Analysis RC4.2 – Cyclic test

This analysis was performed to test the models under cyclic and alternating loading. The cyclic test with specimen P4 executed in the scope of the same testing programme was used as the reference for this computation. It should be emphasized that the loading point was repositioned at coordinate z=1.375 m instead of z=1.500 m to optimize the shaking table stroke, in order to prescribe higher displacements at the column top (see Figure III.118). In addition, the uniform mesh (mesh #2) was used in this analysis and the numerical model included 5241 *dofs* and 405 kinematic constraints.

Figure III.126 presents the loading time history used in the numerical simulation, which corresponds to the one adopted in the experiments, except for some neutral loading steps that were removed to

decrease the number of time steps computed during the numerical simulation.

The experimental programme included a series of cycles with higher displacement amplitudes (up to ±7.0 cm, see Mendes *et al.* [394]). However, these amplitudes revealed to be difficult to simulate with the numerical models adopted, in particular, using the CDM approach to simulate concrete fracture. Consequently, the numerical simulation included only the cycles with amplitudes up to ±3.2 cm. The monotonic test showed that this amplitude level is close to, or even beyond, the yielding point of the reinforcements.

Figure III.127 presents the distributions of the damage-related variables in the concrete. In particular, Figure III.127-a presents the combined Mazars' damage variable (III.100), which shows that the distribution of this variable is strongly affected depending on whether the concrete is mainly under tension or compression. This effect is introduced by the parameters $\alpha_{\pm}$ that are represented in Figure III.127-d $\left(\alpha_{-}=1-\alpha_{+}\right)$. It can be seen that this parameter takes the expected values considering the deformation of the column. Observing Figure III.127-a, the damage distributions apparently decrease throughout the analysis, which seems to violate the basic thermodynamic principles mentioned at the beginning of the chapter (see section 2.1). Nevertheless, this damage reduction is not due to an actual reduction of damage, but instead to the combination of damage in tension and in compression as expressed by equation (III.100). Moreover, it can be seen in Figure III.127-b and in Figure III.127-c that the damage in tension and in compression do not decrease in the analysis, thus respecting the thermodynamic restrictions (III.53).

Going back to Figure III.127-a, it can be seen that the *Mazars'* combined damage variable starts to concentrate in the transition zone of the longitudinal reinforcements for the cycles with wider amplitudes. The damage distribution seems to indicate that a macro-crack is generated in this region on both sides of the element.

Figure III.128 gathers the most relevant information of the reinforcements. The strains and stresses installed in the longitudinal reinforcements are presented in Figure III.128-a and in Figure III.128-b, respectively. Moreover, the same quantities installed in the stirrups are shown in Figure III.128-c.

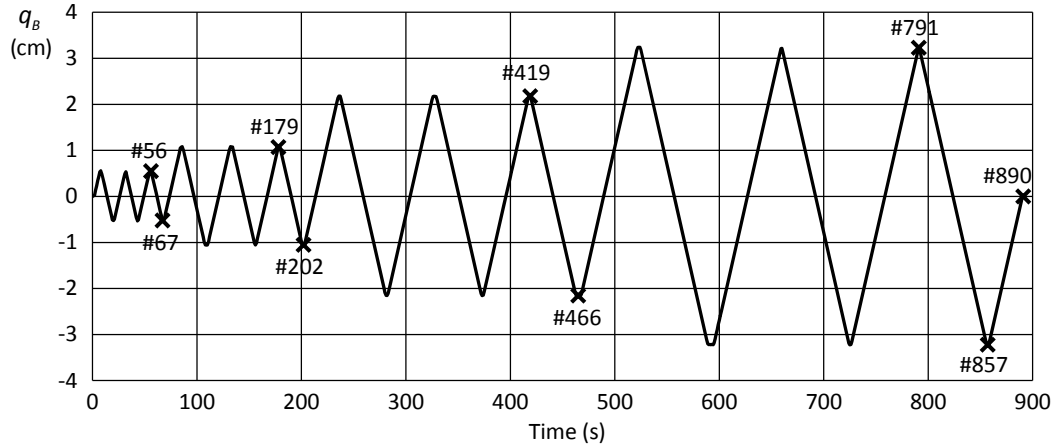

Figure III.126: Analysis RC4.2 – Time History #1.

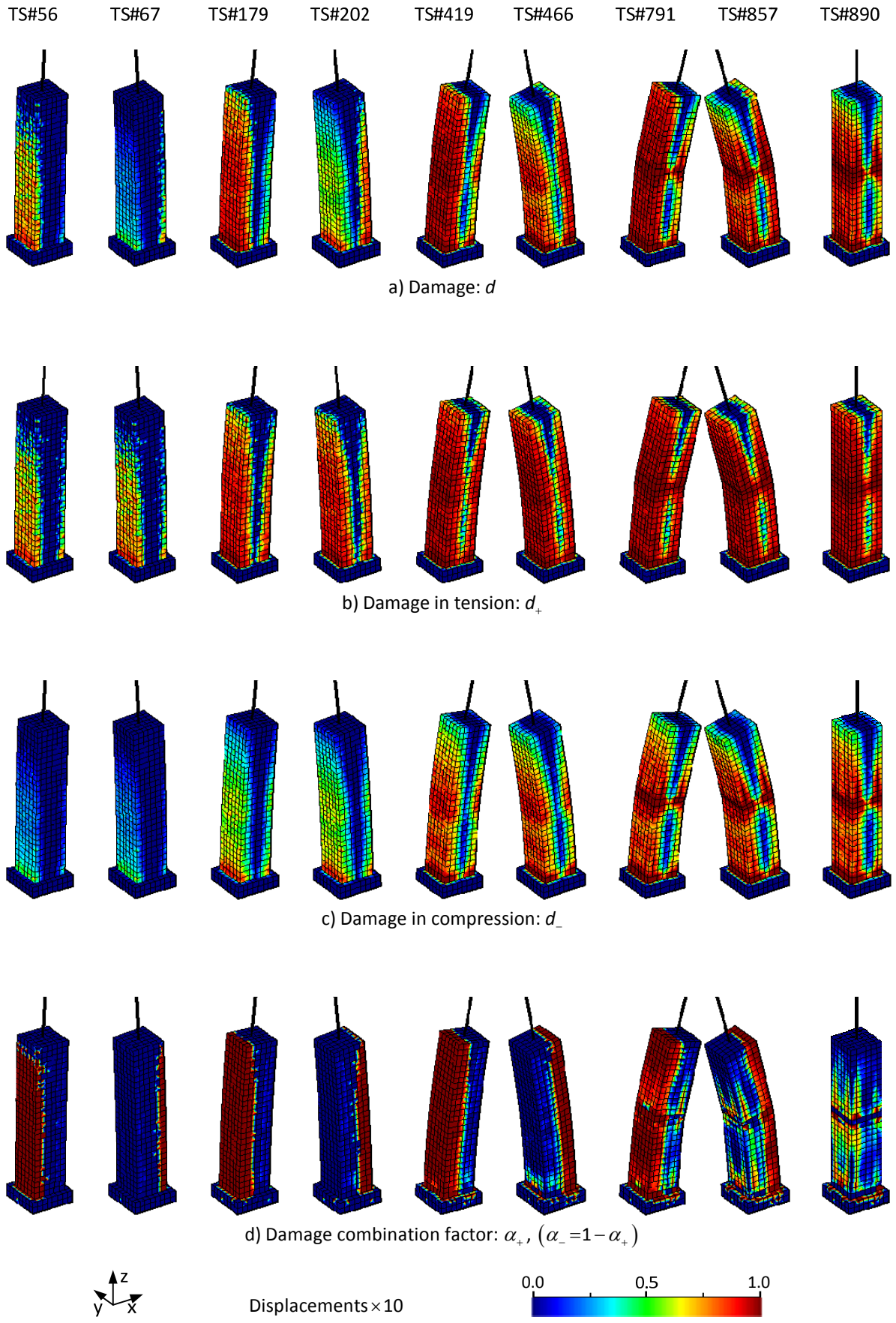

Figure III.127: Analysis RC4.2 – Evolution of the *Modified Mazars'* damage model variables.

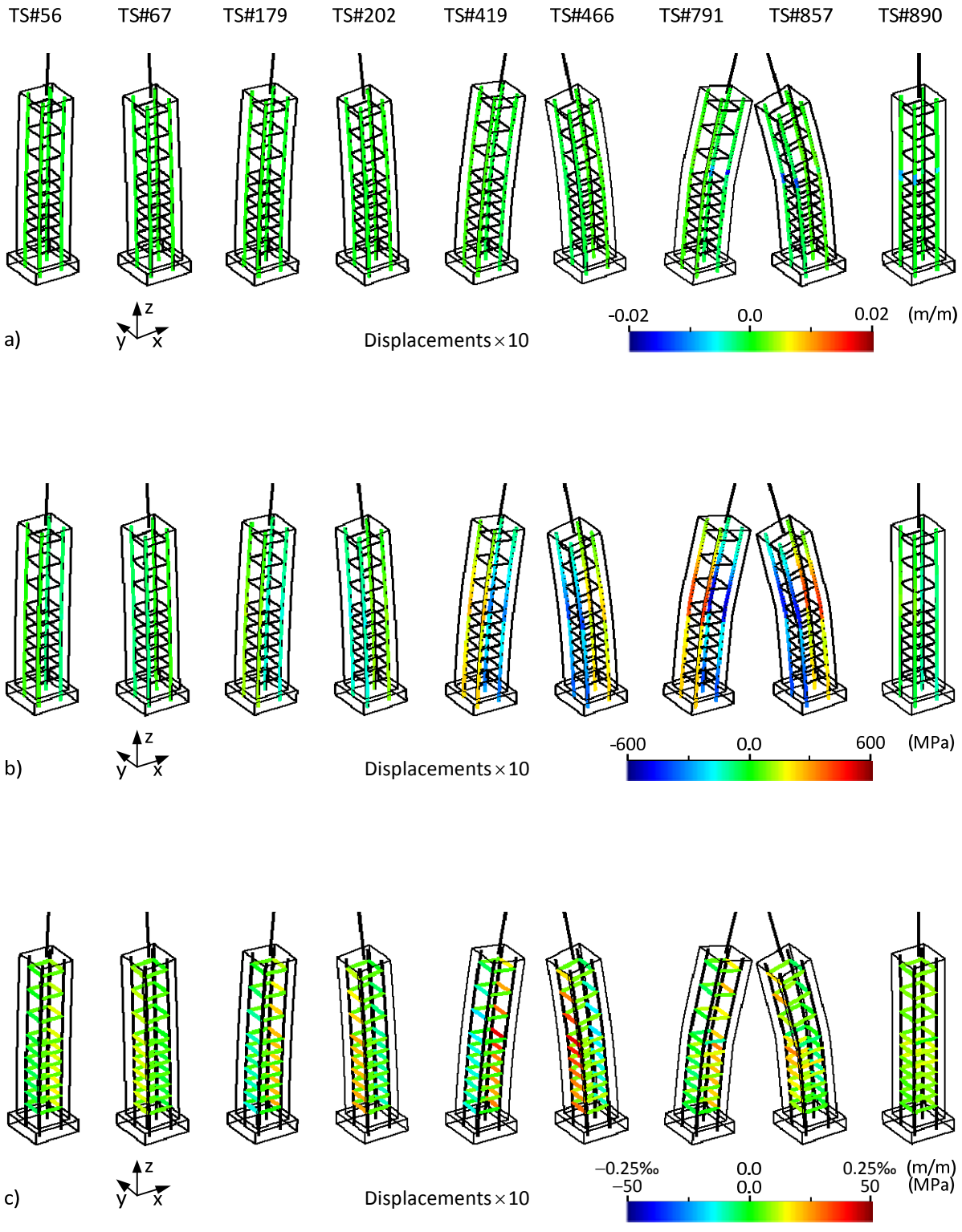

Figure III.128: Analysis RC4.2 – Structural response of the reinforcements at selected time steps: a) Axial strains in the longitudinal reinforcing bars; b) Axial stresses in the longitudinal reinforcing bars; c) Axial strains and stresses in the stirrups.

The strain distributions in the longitudinal reinforcements presented in Figure III.128-a, show that the strain concentrates in the compressed bars near the detailing transition and leading to the conclusion that the reinforcements yield under compressive loading. This was initially surprising because yielding was expected to occur under tension like in the Analysis RC4.1. However, several factors can explain this response. Firstly, the axial load is much higher in this case (135 kN instead of 74 kN), and secondly, the concrete area under compression is relatively small due to the effect of the bending forces and concrete cracking. Consequently, the concentration of compressive forces enables the reinforcement yielding in compression. Nevertheless, this response may not be realistic because reinforcement buckling could occur after concrete cover spalling, in particular, because the stirrups spacing increases in that region to 10 cm $\left(s_s/\phi_s = 8.3\right)$. This effect is not simulated in the numerical model due to reasons presented in section 4. The previous observation can be confirmed by the stress distribution presented in Figure III.128-b. In addition, it can be seen that in spite of the high axial compressive forces, the tensioned reinforcements are nearly at yielding.

In what concerns the strains and stresses installed in the stirrups, it can be observed that the generality of the stirrups are lightly stressed, except for the stirrups near the most compressed concrete, in which the stirrups present higher tension levels because they are restraining the concrete lateral deformation caused by Poisson's effect.

Figure III.129 presents the force *vs.* prescribed displacement curve plotted against the experimental results obtained by Mendes *et al.* [394]. It can be seen that the experimental cycles are reasonably followed by the numerical model. Nonetheless, it can be observed that the numerical curve presents a higher stiffness in the first series of cycles with amplitude ±0.54 cm. This can also be observed in the hysteretic loops presented in Figure III.130-a, only for the cycles with this amplitude. Furthermore, the same behaviour can be observed in Figure III.129 and in Figure III.130-b for the following series of cycles (±1.07 cm). The only difference besides the higher stiffness is that the experimental cycles are slightly more open. The cycles with amplitude ±2.16 cm are the most similar with the experimental results. In addition, the experimental loops seems to present a slight offset into positive values of q_B. Finally, for the largest amplitude cycles (±3.23 cm), the numerical results reveal a higher strength degradation and the differences become more significant. This can be related to the fact that for this load level the response is already significantly inelastic. Hence, the CDM approach adopted to simulate the concrete becomes less realistic.

Figure III.131 presents the number of iterations required to achieve convergence for the same tolerance adopted for the previous analysis. It can be concluded that the average number of iterations decreased significantly by comparing these results with the ones from the previous analysis. This can be related to the fact that the branches associated with unloading or reloading until a previous load level tend to not generate new damage in the element. Therefore, the convergence is easier and faster. Nevertheless, four peaks can be identified in this chart around the time steps #232, #276, #517 and #580, which coincide with the first cycle peaks in each direction of the two cycle series with larger amplitude (see Figure III.126). The reason for this increase is probably related to the fact that these steps are related to higher load levels never experienced before. Therefore, damage is already large and increasing significantly, thus the convergence rate deteriorates.

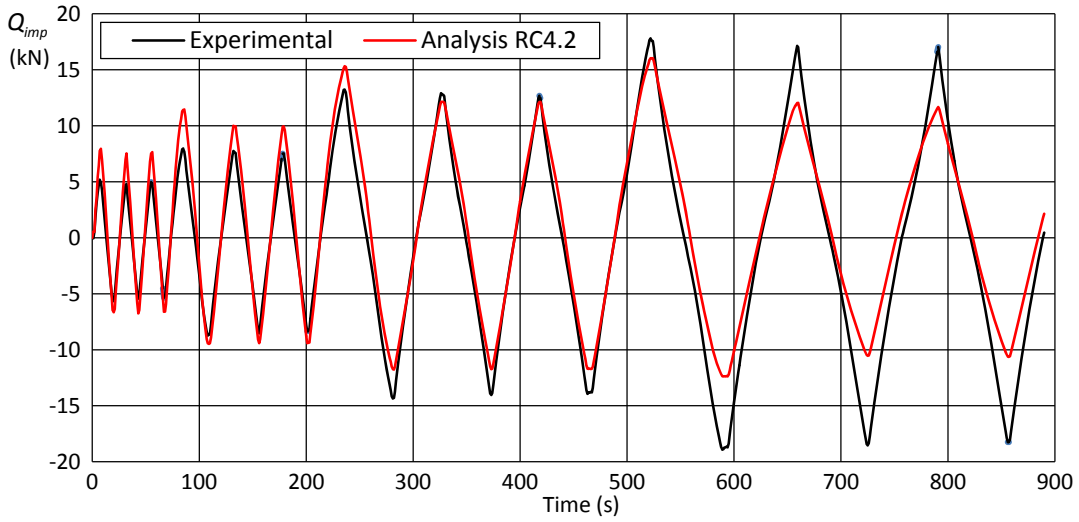

Figure III.129: Analysis RC4.2 – Evolution in time of the force associated with the prescribed displacement.

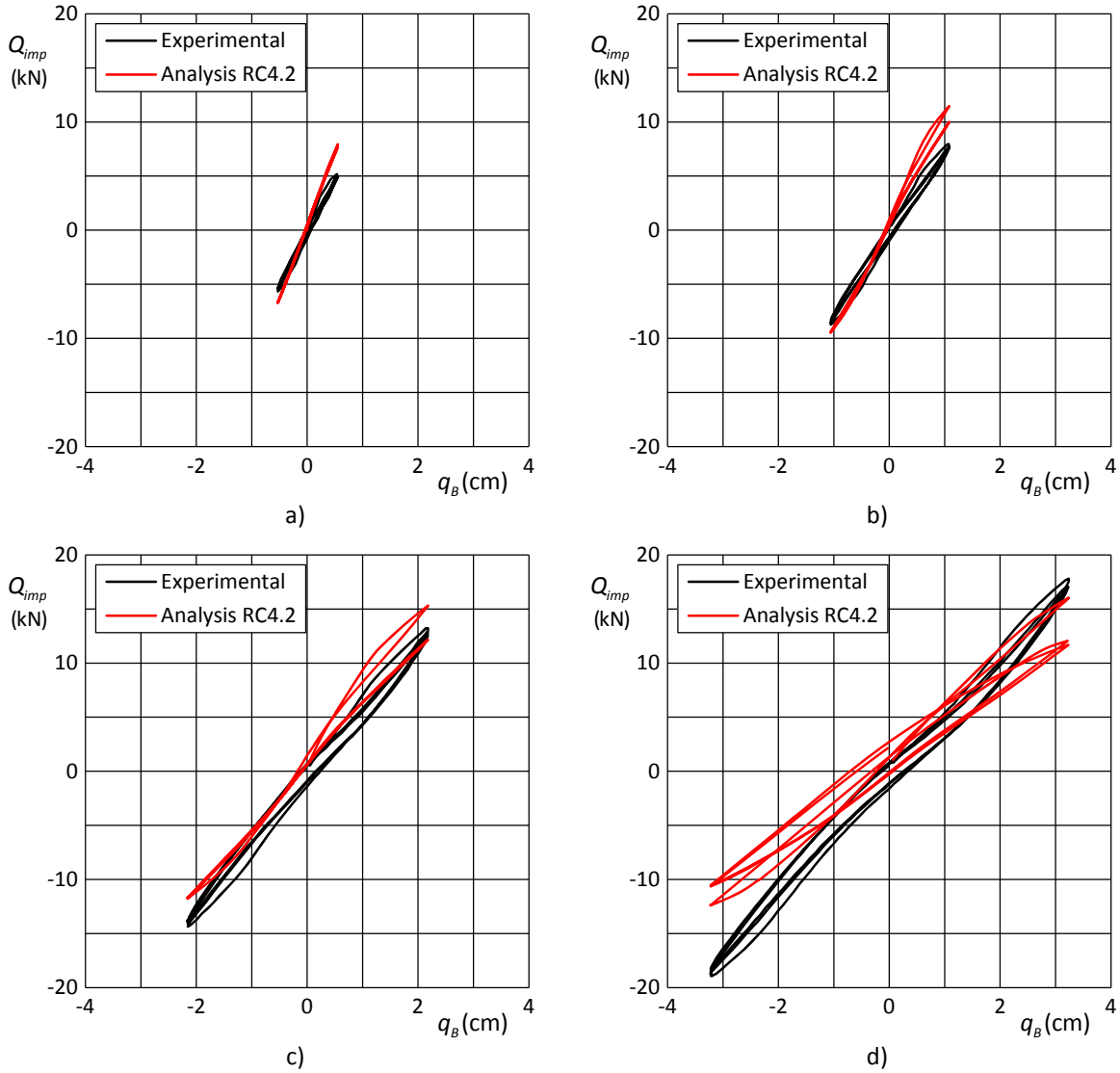

Figure III.130: Analysis RC4.2–Hysteretic loops for cycles with amplitude: a) ±0.54 cm; b) ±1.07 cm; a) ±2.16 cm; b) ±3.23 cm.

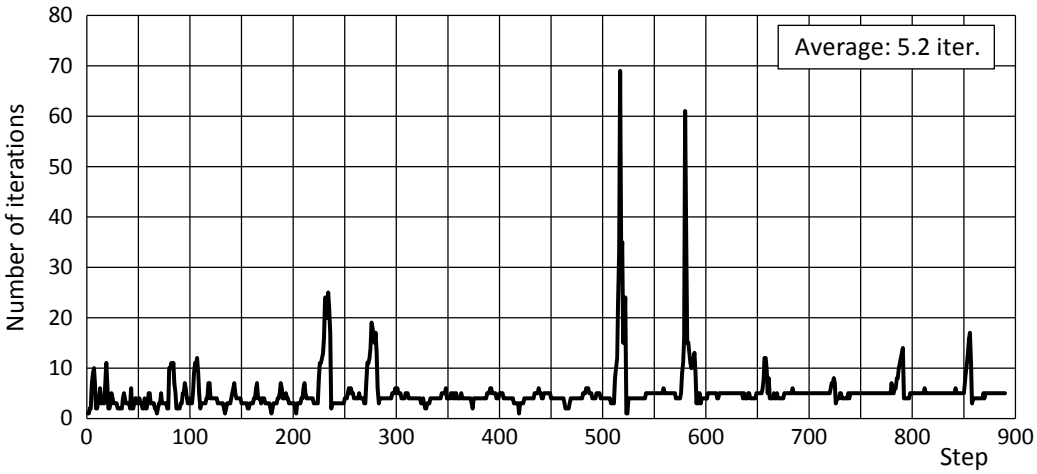

Figure III.131: Analysis RC4.2 – Number of iterations required to achieve convergence.

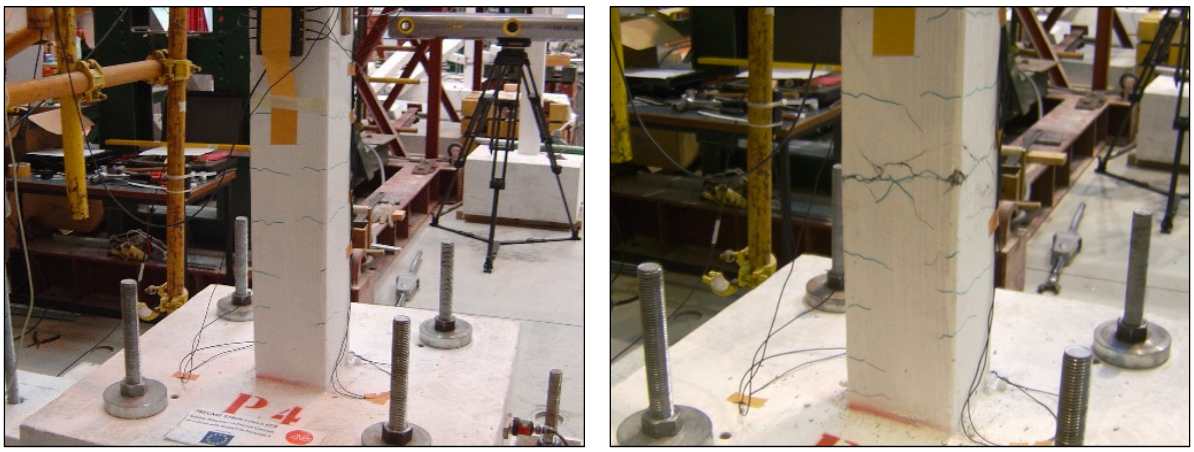

a) b)

Figure III.132: Example RC4 – Cracking evolution observed in the test made with specimen P4.

a) b)

Figure III.133: Example RC4 – Specimens after the testing: a) Specimen P4 after inspection;
b) General view of the four column-foundation specimens.

Figure III.132 presents the cracking evolution observed in the tests made with specimen P4. The first cracking phase is illustrated in Figure III.132-a, which shows well distributed bending cracks along the first 60 cm of the column counting from the base. In addition, Figure III.132-b shows that the crack opening remains roughly the same except for the crack in the detailing transition zone, which develops and presents larger openings. As before, diagonal cracks are visible in this zone, this time on both directions due to the reversed load applied. This cracking pattern follows the expected response. The only aspect that was not anticipated is the excellent response at the column base.

Figure III.133-a presents a detail of this specimen after testing and after making an inspection to the reinforcements. It can be seen that the reinforcement ruptured probably due to low-cycle fatigue because the rupture strain expected for this steel type (about 9.4%) is very large, and probably was not achieved. In addition, it can be seen that after cover spalling the compressed bars tend to buckle, which contributes to an intensified resistance degradation and fatigue damage.

It can be concluded from Figure III.133-b that the same collapse mode was experienced by the four specimens tested, one under monotonic loading (specimen P1) and the rest under cyclic loading (specimens P2 to P4).

- Analysis RC4.3 and RC4.4 – Seismic test

These last two analyses were performed to assess the performance of the numerical model under dynamic load cases. There is no experimental data available for this loading type in the tests made with the column-foundation specimens. In the scope of this experimental programme, dynamic loading was considered only for the three-dimensional structure tested in the shaking table [392, 393]. Consequently, it was decided to use this data as much as possible to calibrate the model used in the analyses RC4.3 and RC4.4.

The model idealization took into consideration the characteristics of LNEC's triaxial shaking table. In particular, the plan dimensions of the platform (4.60 x 5.60 m^2) and the payload capacity (40 ton). To cope with these limitations, a 1/3 geometric scale was adopted, as indicated in equation (III.200). Adopting this geometric scale made it possible to use the prototype materials in the scaled specimen (III.201) and still not exceeding the 40 ton payload capacity:

$$L_P / L_M = \lambda = 3\,, \tag{III.200}$$

$$E_P / E_M = 1\,. \tag{III.201}$$

According to Carvalho [81], it is usual to adopt the Cauchy similitude and the Froude similitude simultaneously for dynamic testing. The *Cauchy number* represents the ratio between the inertia and restoring forces and the *Froude number* the ratio between inertia and gravity forces [81], respectively defined by:

$$\mathcal{C} = \frac{\rho v^2}{E}\,, \tag{III.202}$$

$$\mathcal{F} = \frac{v^2}{Lg}\,. \tag{III.203}$$

Enforcing that the prototype and model are similar in terms of the Cauchy and Froude numbers, leads to the additional relationships:

$$\left(\frac{\rho v^2}{E}\right)_P = \left(\frac{\rho v^2}{E}\right)_M , \tag{III.204}$$

$$\left(\frac{v^2}{Lg}\right)_P = \left(\frac{v^2}{Lg}\right)_M . \tag{III.205}$$

Using the relationships (III.200), (III.201), (III.204) and (III.205), it is possible to define all the relevant similitude scale factors [81], which can be found particularized for this experimental programme in the references [392-394].

The main consequences of using this similitude law are the time "compression" during the test:

$$t_P / t_M = \sqrt{\lambda} = 1.732 , \tag{III.206}$$

and the necessity of adding additional masses due to the relationship:

$$\rho_P / \rho_M = \lambda^{-1} = 0.33(3) . \tag{III.207}$$

On the other hand, the accelerations are equivalent on the model and on the reference prototype:

$$a_P / a_M = 1 . \tag{III.208}$$

These analyses required defining an adequate earthquake input to simulate the seismic event. It was decided to adopt the same records used in the shaking table tests. Accordingly, the horizontal components of the semi-artificial records obtained from the *Tolmezzo station* record (*Diga Ambiesta*) of the *Friuli earthquake* in Italy (6/5/1976) were used. The records scaled to 1 g (9.81 m/s^2) are presented in Figure III.134 and Figure III.135 by joining the original earthquake record and the resulting semi-artificial record obtained to match the design response spectra specified in an older version of the Eurocode 8 (soil B). This fit is evident when plotting the elastic response spectra of the original and final records against the Eurocode 8 design envelope, as presented in Figure III.137 and Figure III.138. It should be emphasized that this signal processing task was not made be the author, only the transformation into displacement records was executed in the scope of this thesis (see Figure III.136), which was done using the LNEC-SPA [395] software.

The original records have 15 s of duration but due to the similitude law the time should be compressed according to (III.206) and the acceleration values should remain unchanged. Accordingly, it is only necessary to scale time by a factor of $3^{-1/2}$, leading to a final duration of 8.66 s.

In addition, it was necessary to define the intensity of the earthquake motions for the analyses. This was done by considering the PGA values from the shaking table test stages reported by Mendes *et al.* [392, 393], which are compiled in Table III.27. It can be seen that the shaking table test included five stages that simulated extremely severe earthquakes. Considering the information collected in this chapter, some problems of representativeness and convergence are expected for the most intense stages using the models adopted in this thesis. Consequently, only the first two stages were included in the analyses, which were computed using the PGA values for the transversal (*x*) and longitudinal (*y*) directions reported in Table III.27 for Stage 00 (Analysis RC4-3) and for Stage 01 (Analysis RC4-4).

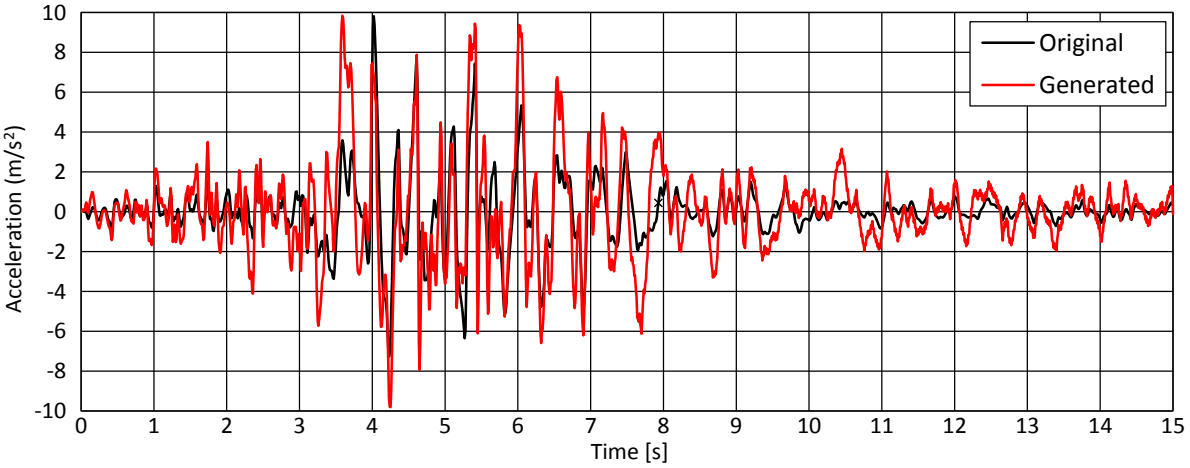

Figure III.134: Example RC4 – Friuli Earthquake (1976): Ground acceleration at station Tolmezzo (Diga Ambiesta, N-S).

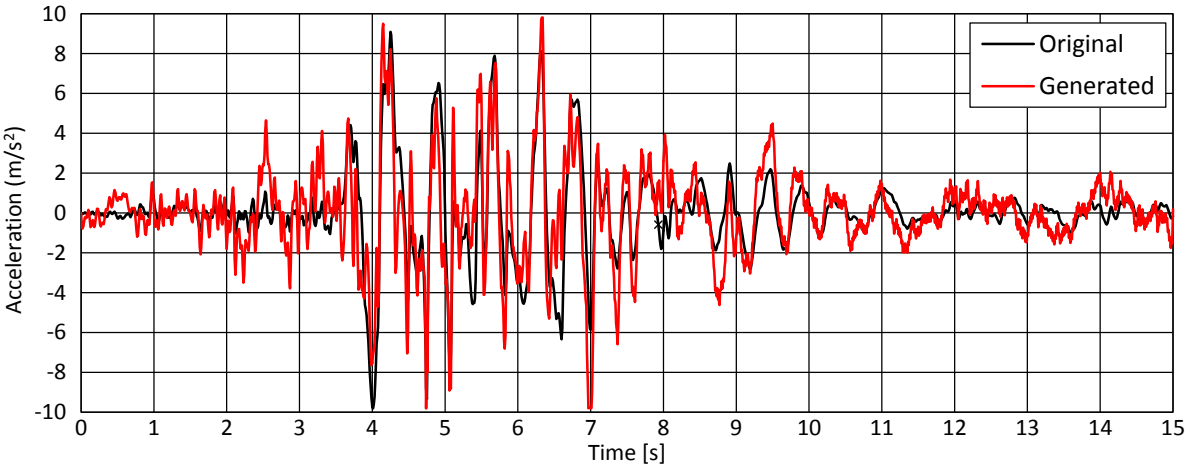

Figure III.135: Example RC4 – Friuli Earthquake (1976): Ground acceleration at station Tolmezzo (Diga Ambiesta, E-W).

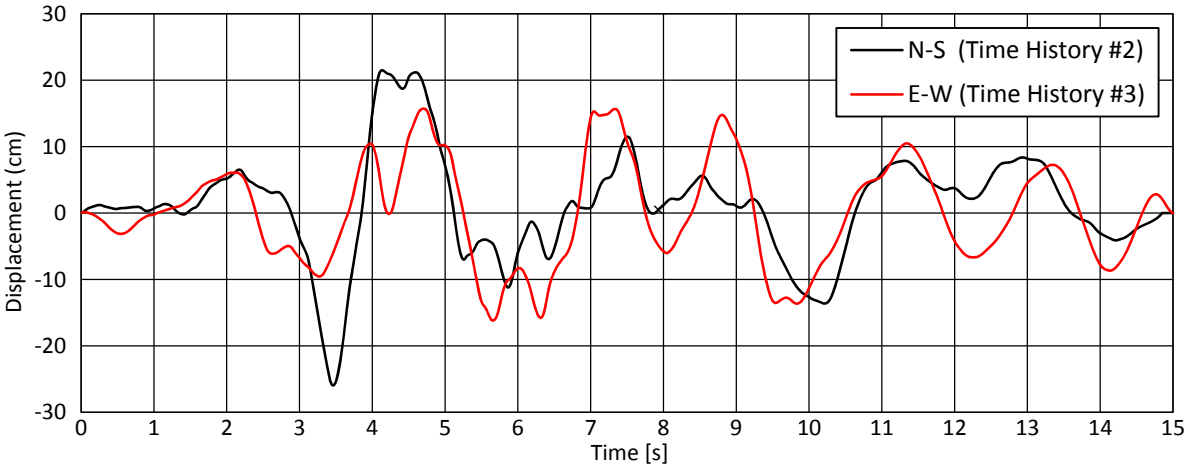

Figure III.136: Example RC4 – Friuli Earthquake (1976): Computed displacements for station Tolmezzo (Diga Ambiesta).

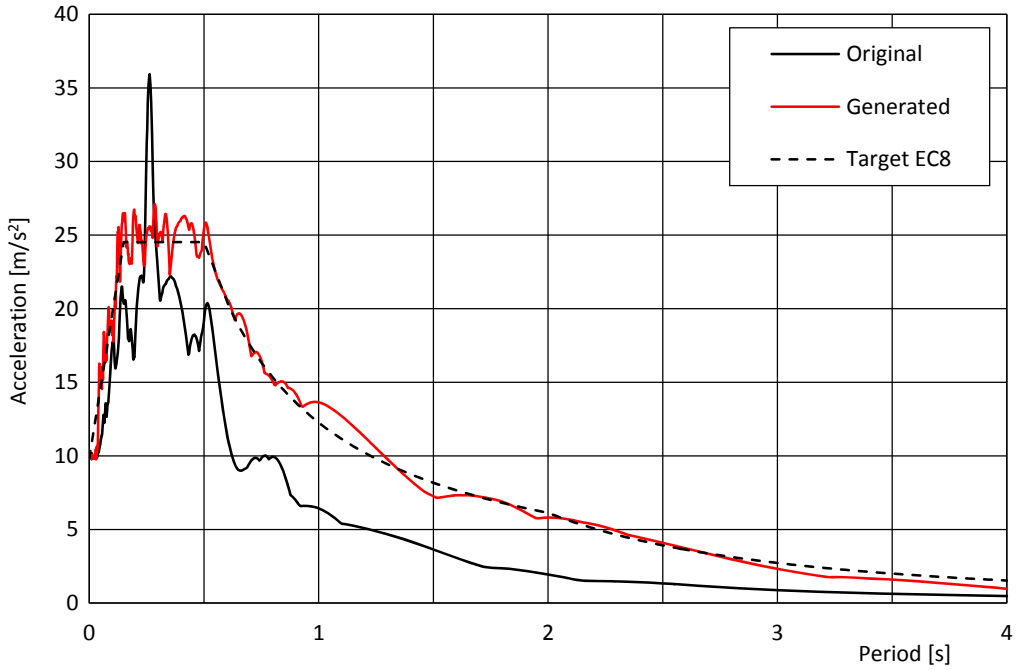

Figure III.137: Example RC4 – Friuli Earthquake (1976), Tolmezzo (Diga Ambiesta, N-S): Elastic response spectra $(\xi = 5\%)$.

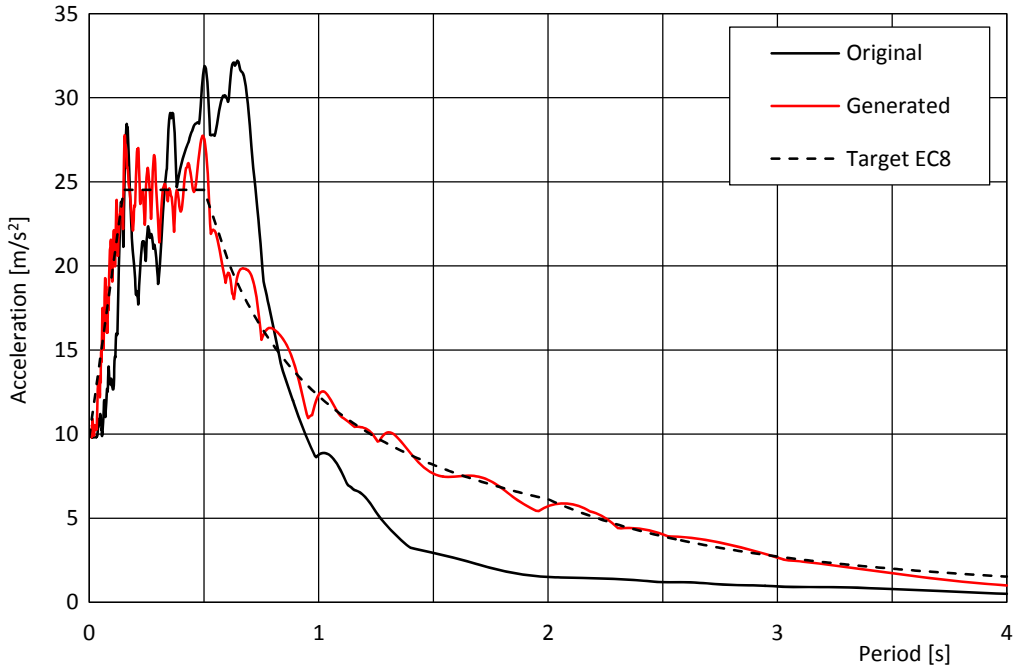

Figure III.138: Example RC4 – Friuli Earthquake (1976), Tolmezzo (Diga Ambiesta, E-W): Elastic response spectra $(\xi = 5\%)$.

Table III.27: PGA values measured in the tests, taken from Mendes *et al.* [392, 393].

Series	PGA Transversal Dir. (g)	PGA Longitudinal Dir. (g)
Stage 00	0.07	0.08
Stage 01	0.21	0.14
Stage 02	0.32	0.23
Stage 03	0.67	0.48
Stage 04	0.95	0.72

In addition, it was necessary to define the mass and damping of the structure to compute the dynamic analyses. Different approaches could have been followed because the analyses will not be compared with experimental tests. It was decided to use the results obtained from the structure tested in the shaking table test.

In what concerns the mass, the authors Mendes *et al.* [392, 393] performed a modal identification to the structure that revealed a first mode frequency in the transversal direction of 2.9 Hz and 1.2 Hz, before and after the test. Consequently, after making a simple modal analysis to the adopted model, it was found that adding a 2.0 ton mass at the top of the column (point A in Figure III.118) would result in a first mode frequency of about 2.9 Hz. Accordingly, the analyses were executed considering a 2.0 ton mass at point A for both horizontal directions. As reported in Table III.25, damping was considered as proportional to the stiffness and mass matrices and the coefficients were computed by setting 5% of damping at the initial and final first mode frequencies reported before.

The results from the analyses are difficult to be illustrated with a reduced number of time steps. Nevertheless, the distributions of the damage-related variables are presented in Figure III.139 and in Figure III.140 for a uniform distribution of time steps. It can be seen in Figure III.139 that in the analysis RC4.3 (Stage 00) the seismic event is not intense and the column only accumulates a moderate amount of damage in tension, which represents the micro-cracking that would occur for this intensity level. In addition, it can be observed that damage in compression is less and that the distribution of the combinations factors $\alpha_{\pm}$ is very variable due to the loading randomness. On the other hand, the simulation of Stage 01 made in the Analysis RC4.4 revealed that the damage becomes much higher and starts to show signs of localization in the detailing transition zone and at the column base.

This information is complemented by Figure III.141 to Figure III.152. These charts present the comparison between displacements records at the base and at the top node, the comparison between the relative displacement between the top and base nodes and the base shear, and the hysteretic cycles expressed by the previous quantities. Generally, for analysis RC4.3 (Stage 00), the top displacement is slightly larger than the base movements and the first mode frequency is clearly present in the response (see Figure III.141 and Figure III.144). In what concerns the top-bottom relative displacements and the base shear, it can be observed that these quantities present a similar evolution, which leads to the conclusion that inelasticity is still minor in the response (see Figure III.142 and Figure III.145). This can be confirmed by observing the narrow hysteretic loops presented in Figure III.143 and Figure III.146.

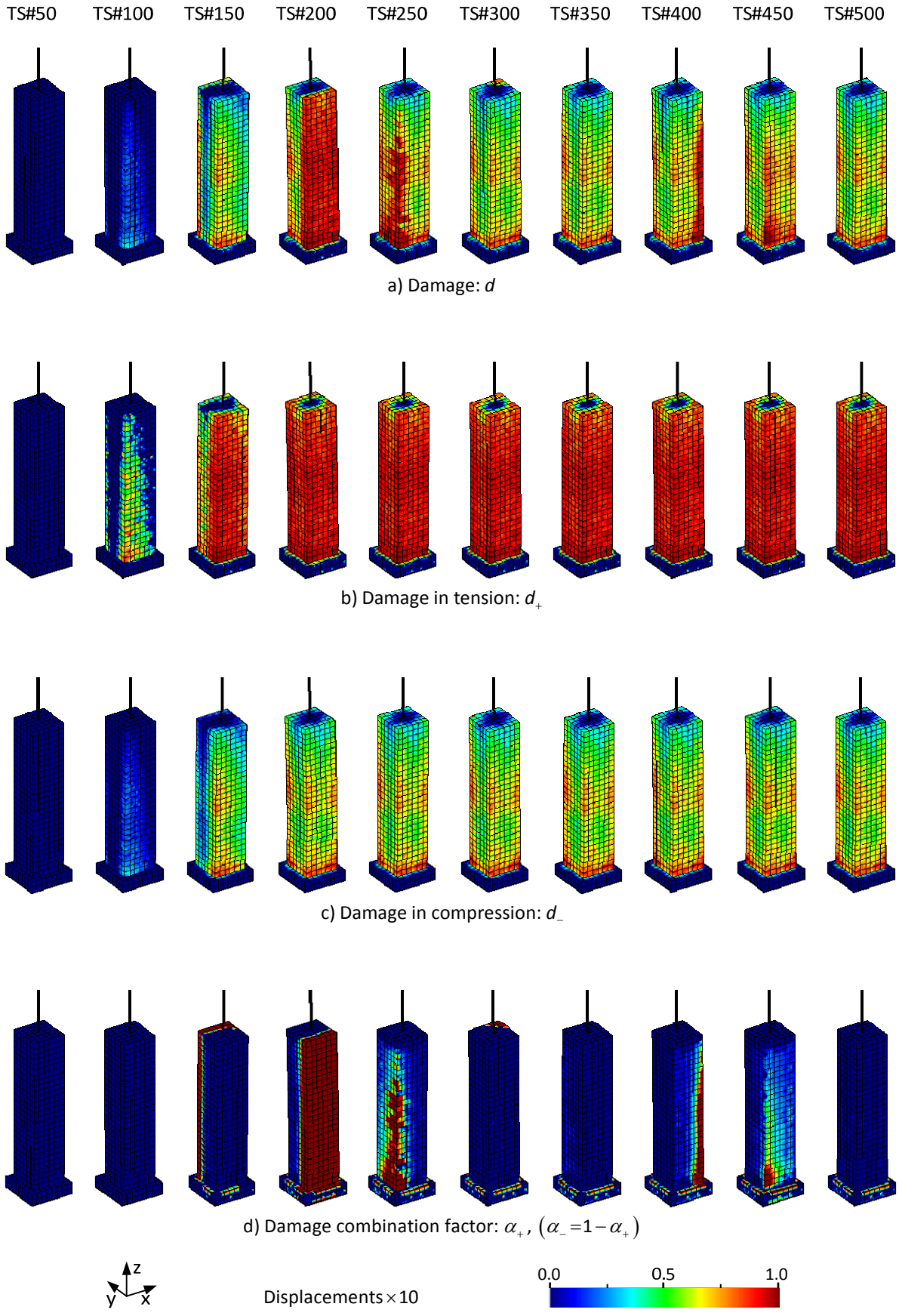

Figure III.139: Analysis RC4.3 – Evolution of the *Modified Mazars*' damage model variables (Stage 00).

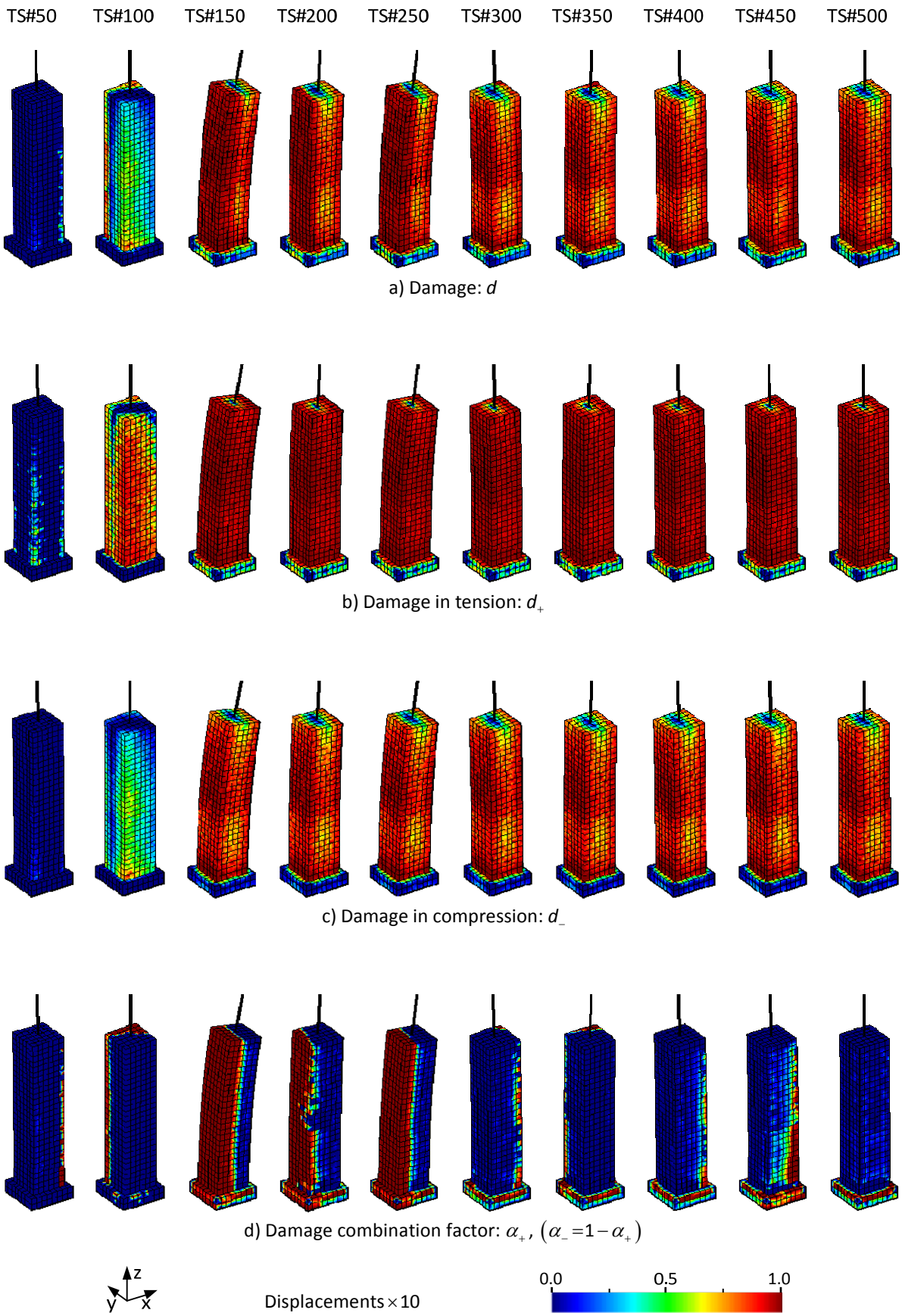

Figure III.140: Analysis RC4.4 – Evolution of the *Modified Mazars*' damage model variables (Stage 01).

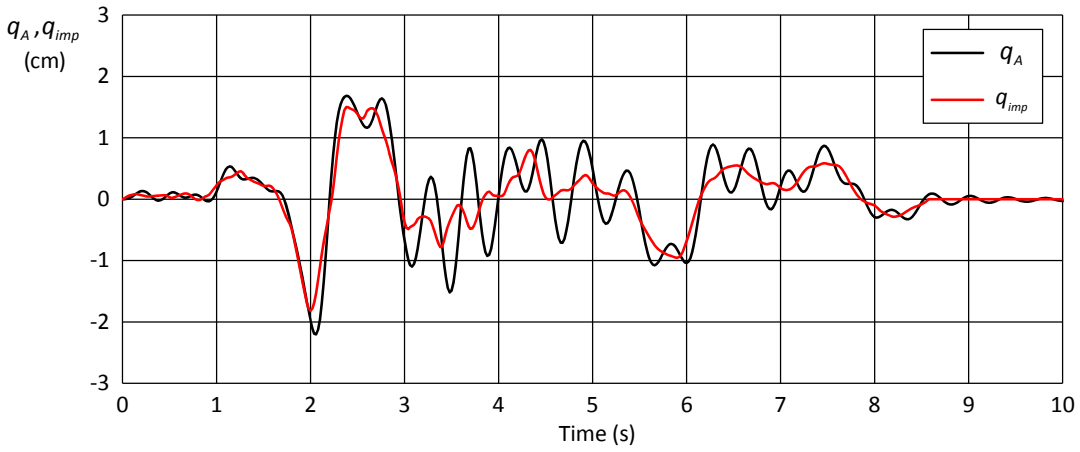

Figure III.141: Analysis RC4.3 (Stage 00) – Top and base displacements (*x* dir.).

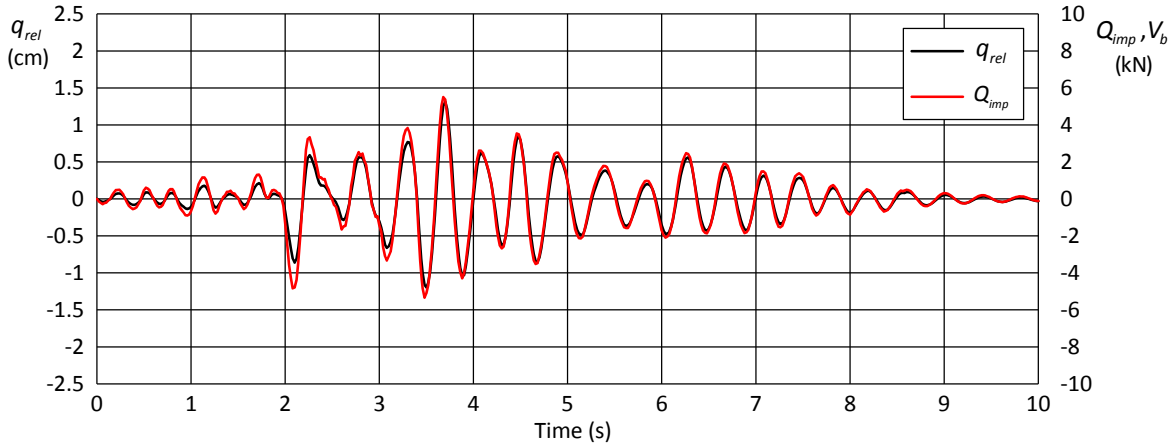

Figure III.142: Analysis RC4.3 (Stage 00) – Relative displacement between the top and base nodes and base shear (*x* dir.).

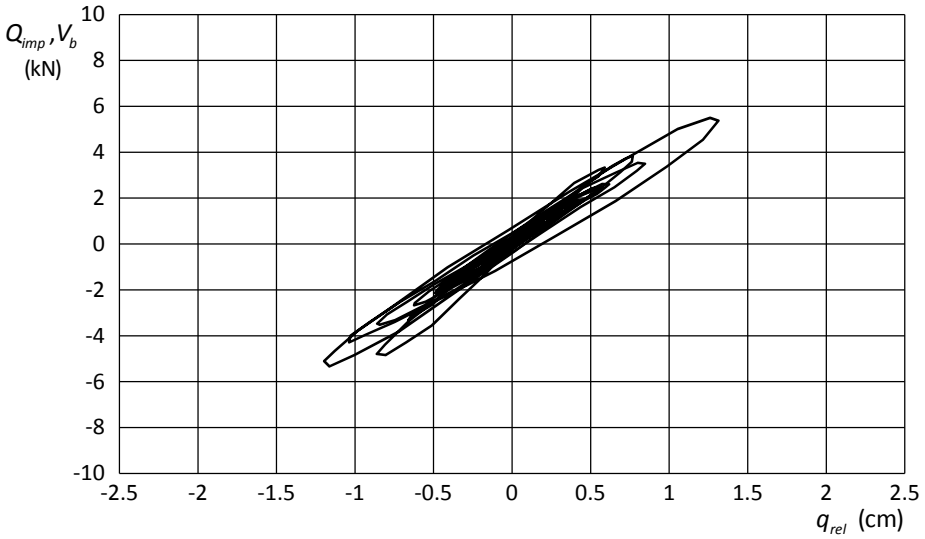

Figure III.143: Analysis RC4.3 (Stage 00) – Base shear *vs.* relative displacement between the top and base nodes (X dir.).

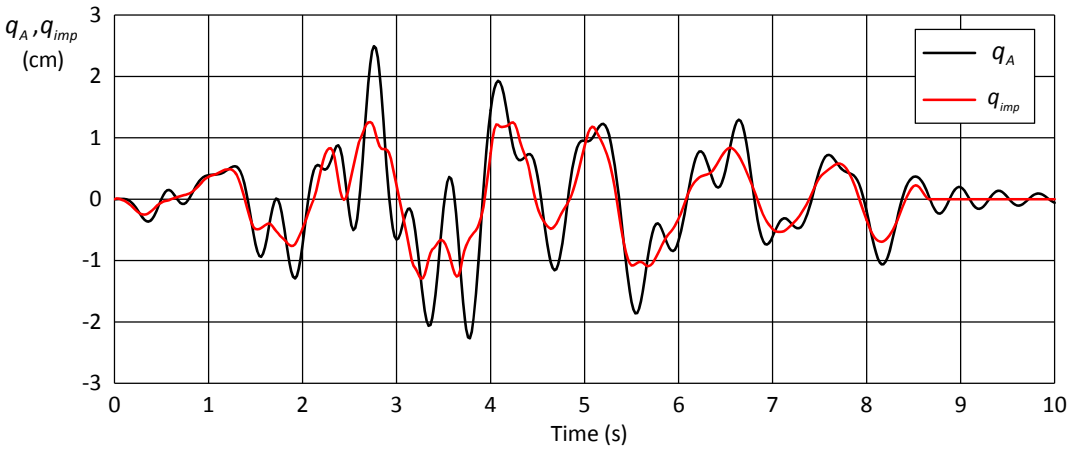

Figure III.144: Analysis RC4.3 (Stage 00) – Top and base displacements (Y dir.).

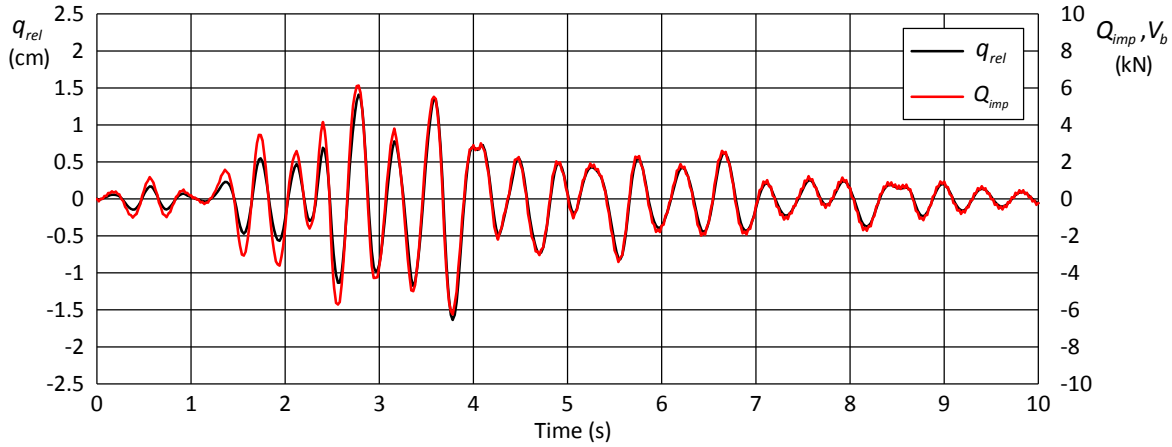

Figure III.145: Analysis RC4.3 (Stage 00) – Relative displacement between the top and base nodes and base shear (*y* dir.).

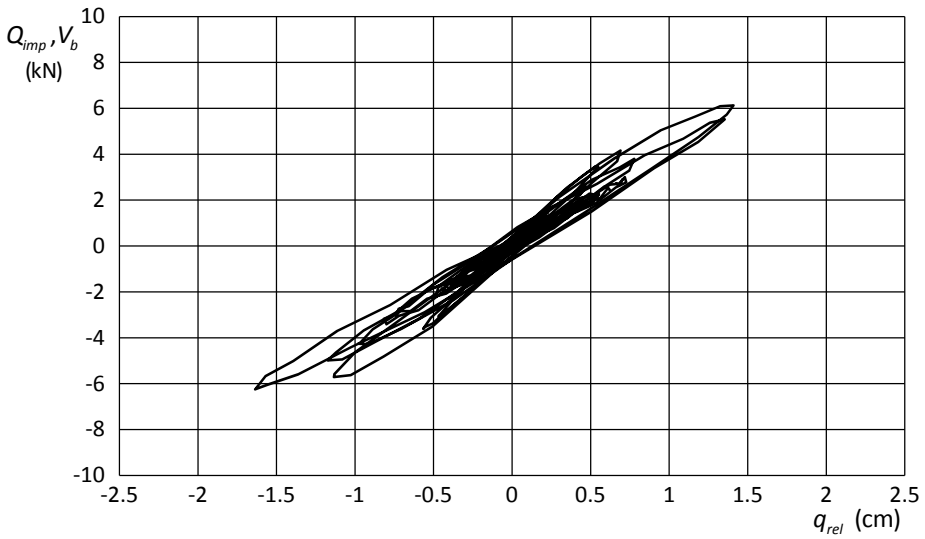

Figure III.146: Analysis RC4.3 (Stage 00) – Base shear *vs.* relative displacement between the top and base nodes (Y dir.).

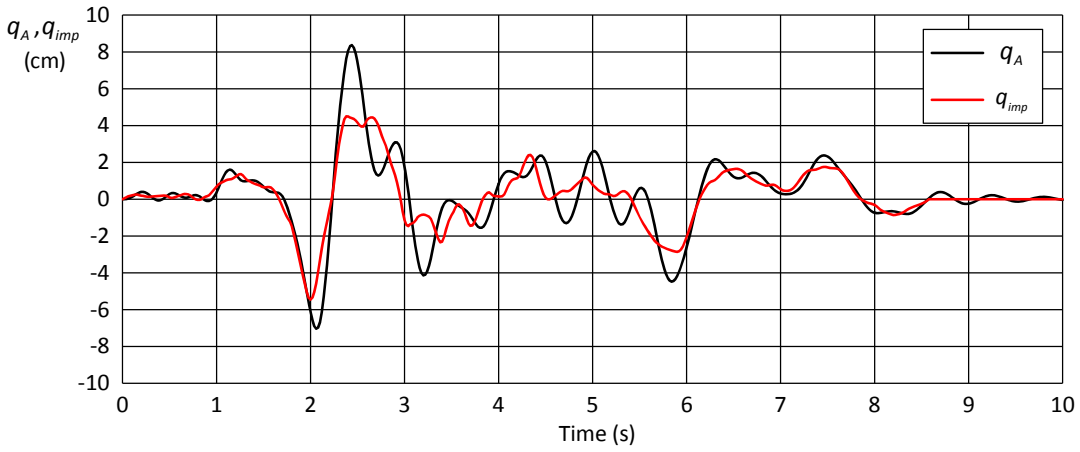

Figure III.147: Analysis RC4.4 (Stage 01) – Top and base displacements (X dir.).

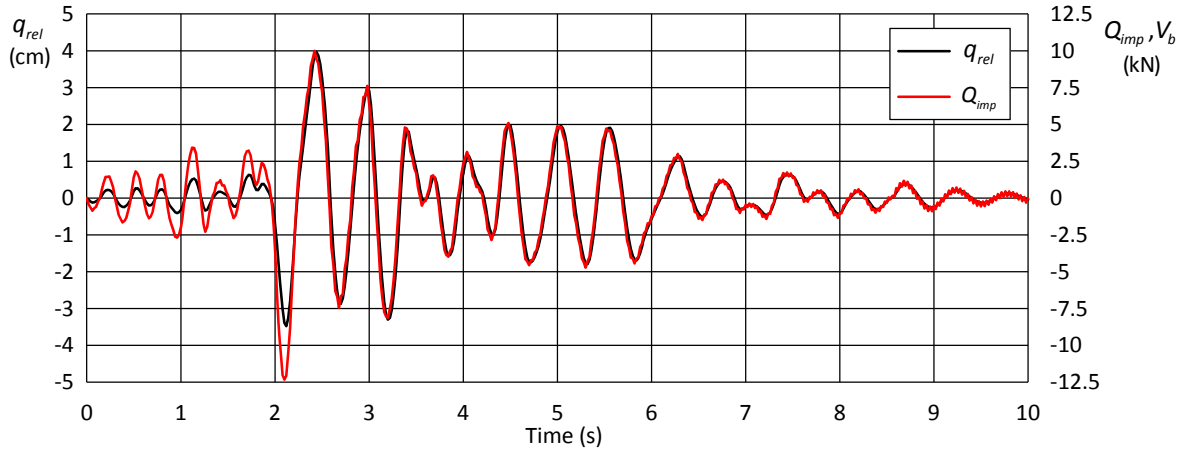

Figure III.148: Analysis RC4.4 (Stage 01) – Relative displacement between the top and base nodes and base shear (*x* dir.).

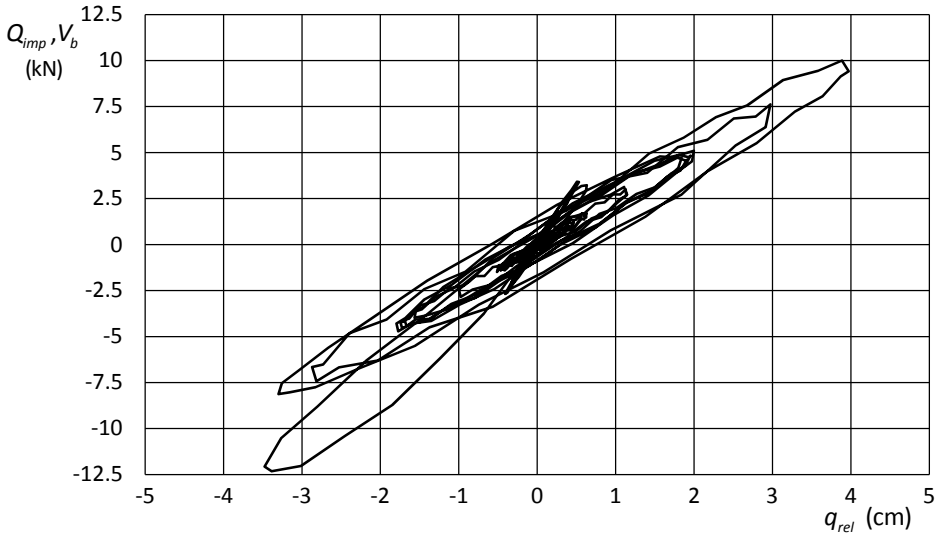

Figure III.149: Analysis RC4.4 (Stage 01) – Base shear *vs.* relative displacement between the top and base nodes (X dir.).

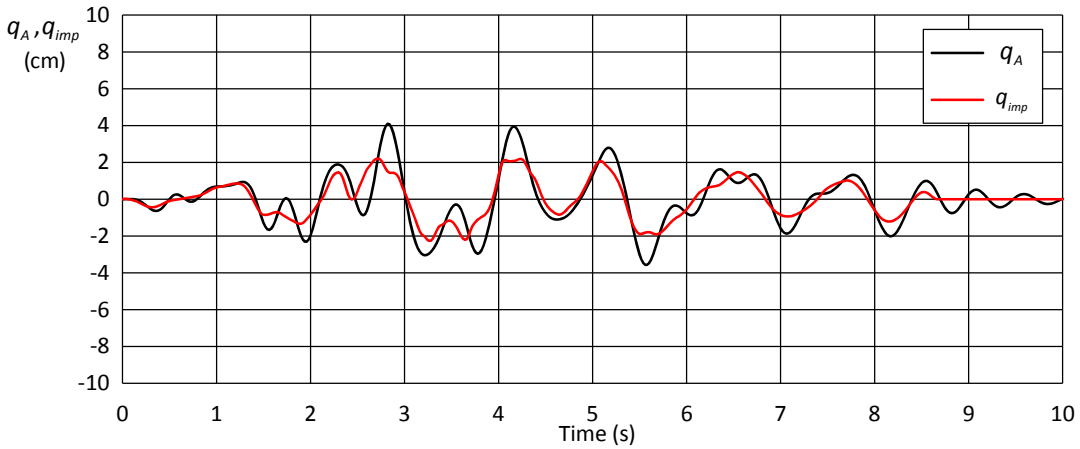

Figure III.150: Analysis RC4.4 (Stage 01) – Top and base displacements (Y dir.).

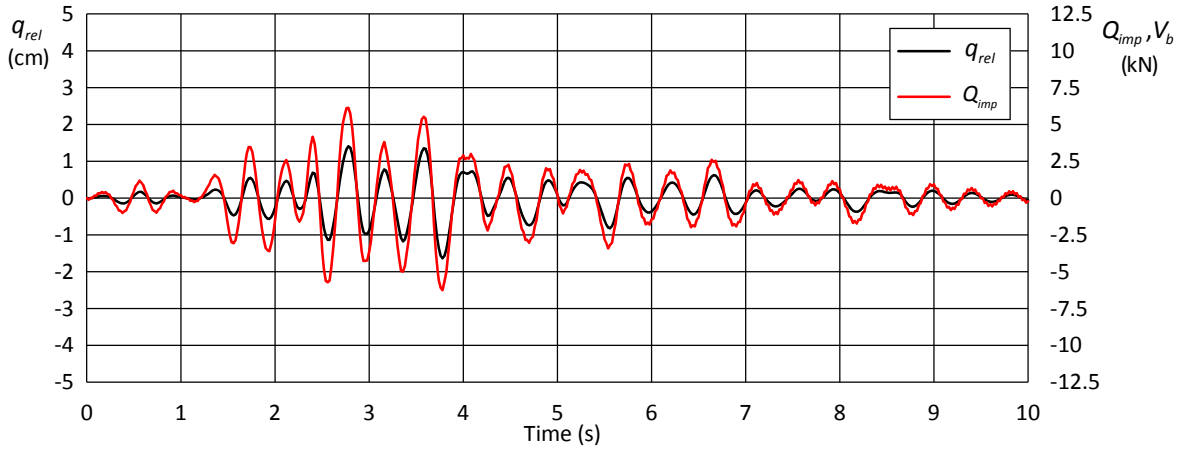

Figure III.151: Analysis RC4.4 (Stage 01) – Relative displacement between the top and base nodes and base shear (*y* dir.).

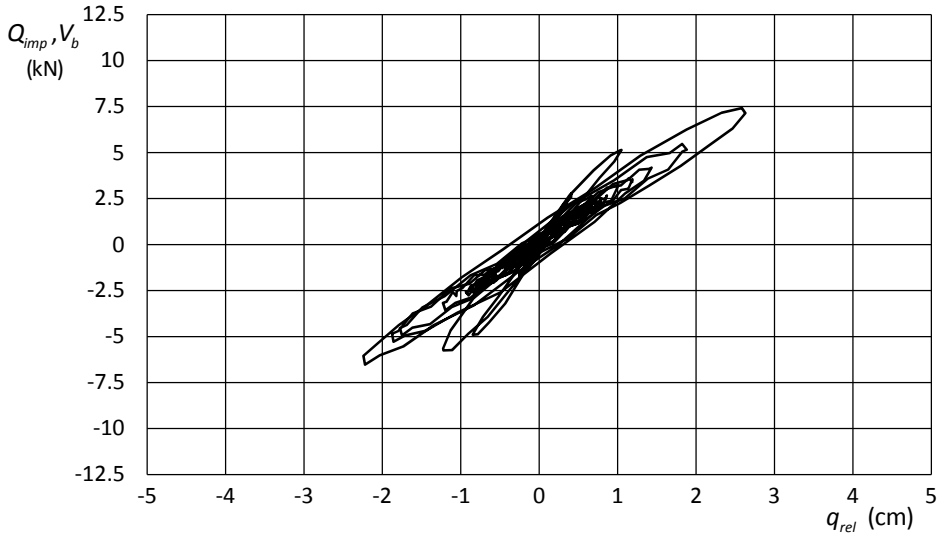

Figure III.152: Analysis RC4.4 (Stage 01) – Base shear *vs.* relative displacement between the top and base nodes (Y dir.).

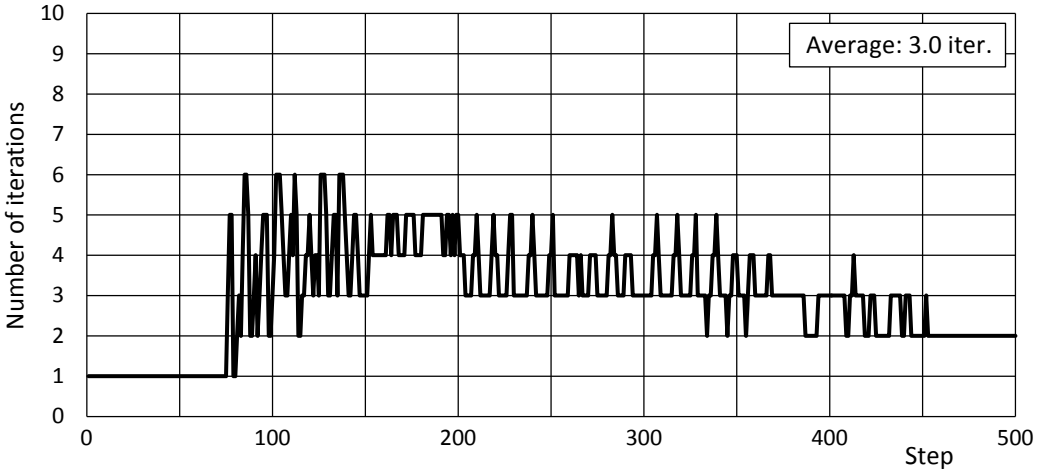

Figure III.153: Analysis RC4.3 – Number of iterations required to achieve convergence.

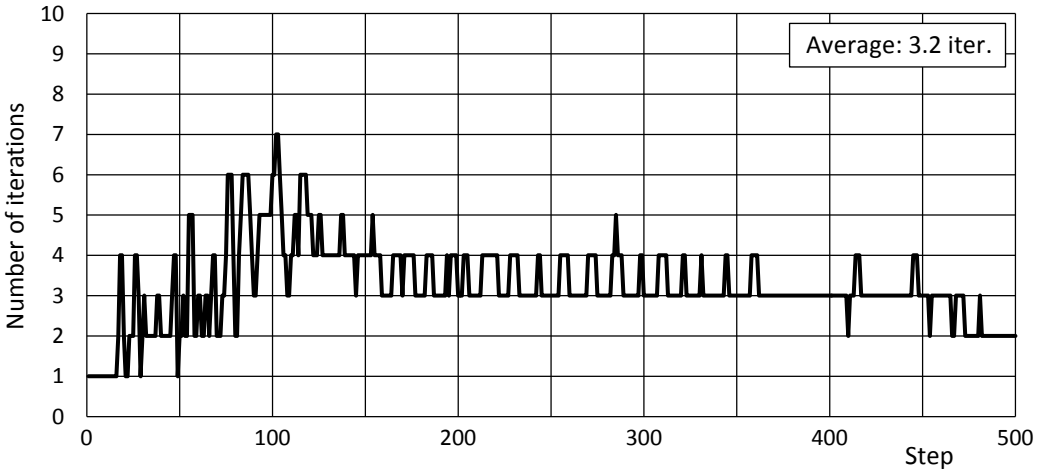

Figure III.154: Analysis RC3.4 – Number of iterations required to achieve convergence.

On the other hand, in the analysis RC4.4 (Stage 01) the evolution of the top-bottom relative displacements and of the base shear show a clear reduction tendency due to damage. In particular, for the *x* direction that experiences a more intense seismic action (see Figure III.148 and Figure III.151). Once again, this can be confirmed by the analysis of the hysteretic loops presented in Figure III.149 and in Figure III.152, which are wider and show a stiffness reduction that can be observed in the inclination of the cycles.

Figure III.148 and Figure III.151 presents an interesting aspect of the numerical response. It can be identified a small high-frequency fluctuation in the response in terms of base shear. This is not due to an actual physical response of the structure, but instead, it is related to the numerical issues caused by the development of inelasticity. In this case, the amplitude is not large enough to contaminate the solution. Nevertheless, for higher levels of inelasticity this may happen. Some possible ways to mitigate this problem correspond to the use of time integration methods with numerical damping to

damp out the high-frequencies in the response (see Chapter II-§4.3.3) and to the change of the time step increment used in the analysis.

To complete the information extracted from the seismic analyses, Figure III.153 and Figure III.154 present the number of iterations required for converge. It can be seen that this number is relatively low when compared to the one registered in the monotonic test (see Figure III.123). This can be related to the fact that damage is not very high and that several time steps are associated with unloading or reloading, which tend to not create additional damage in the structure. In addition, the presence of inertia and damping forces can also contribute to improve the convergence characteristics.

One last aspect should be mentioned. It was endeavoured to compute a simulation for Stage 02. The convergence was achieved but proved to be more difficult. Nevertheless, the results showed that the columns and the footing were heavily damaged and the results are not representative of the effective structural response. Therefore, they were not included in this example. This confirms that the adopted CDM approach is feasible for moderate levels of inelasticity and becomes inefficient and unreliable for intense loading.

Chapter IV

Concrete-Steel Interfaces

1 Introduction

For economic reasons, common reinforced concrete (RC) structures are designed in such way that they dissipate energy with large inelastic deformations when subjected to severe earthquakes or other intense load sources. In those situations, RC elements are exposed to high loading demands that can lead to a strong nonlinear response. A particular vulnerable component is the connection between the reinforcing bars and the concrete that in the scope of this thesis will be called the *concrete-steel interfaces* (CSI). These interfaces play the important role of transmitting forces between the reinforcements and the concrete. The CSI incorporate the well-known and complex longitudinal stress transfer mechanism, commonly called the *bond mechanism*, but also the radial stress transfer that develops at these interfaces. Although the radial stresses and deformations can play a significant role in the response, they will be considered only indirectly and the focus will be drawn to the bond mechanism.

When the forces to be transmitted are too high, the perfect connection between the materials is lost and relative displacements will occur. This can influence the amount, size and distribution of cracks, potentiate higher stiffness and resistance degradation, intense stress redistributions and result in significant changes in the response.

Most numerical simulations consider only the flexural and shear deformation modes for the transversal flexibility of a RC element (see Figure IV.1), and most of the times, the stiffness is over-estimated by not considering the influence of bond failure. This problem is easily understood by considering the case of flexural cracking. Initially, these cracks are well distributed and with a small opening. When the bond starts to fail, the stress transfer to the concrete is greatly compromised near the cracks. In those situations, the reinforcement is heavily stressed and must ensure almost all stress transfer in that region. This response potentiates highly localized deformations that result in large increases in crack opening and in the element's flexibility (see Figure IV.1-c).

Bond failure also influences the dynamic response of a RC structure. When the bond fails, the opening of cracks is superior and therefore the hysteretic response is characterized by long branches with reduced stiffness and pinching effects, which contributes decisively to narrower cycles, and consequently, to lower hysteric energy dissipation.

As an example to emphasize the importance of this phenomenon, Figure IV.2 presents the moment *vs.* rotation relationship obtained by Bertero and Popov [54] by testing half-scale subassemblages of

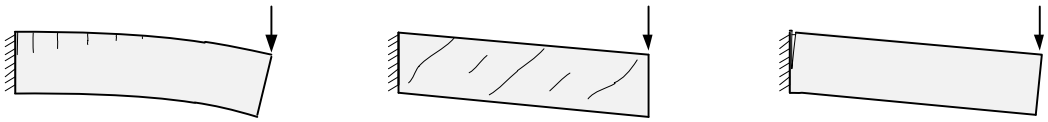

a) flexural b) shear c) bond failure

Figure IV.1: Deformation types in a RC member.

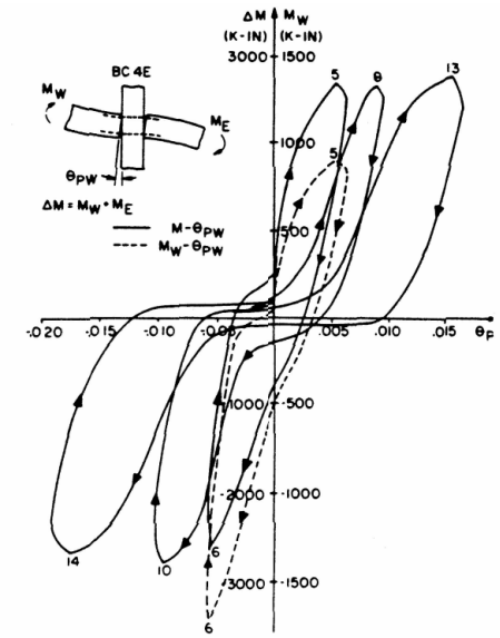

Figure IV.2: Moment *vs.* rotation relationship obtained from scaled subassemblages of interior joints from moment-resisting frames, from the original work of Bertero *et al.* [54].

interior joints from a 20-storey moment-resisting frame. The response showed an intense stiffness and resistance degradation, which reduced the ductility ratio by 5 in the monotonic test and about 2.5 for the specimen tested under repeated reversals with increasing deformation (see Figure IV.2). According to the authors, the resistance degradation and the severe pinching on the hysteresis loops are mainly caused by bond failure of the beam reinforcements [54]. This example demonstrates the significance of considering the bond mechanism for the accurate simulation of RC elements under general loading cases (*e.g.* earthquake loading).

The methodology used to address this problem starts by trying to understand the physical behaviour of the interfaces. This is achieved by making a wide-ranging bibliographic research regarding the information collected from the extensive experimental programmes carried out to characterize the bond mechanism. This bibliographic research is also extended to the most prominent modelling techniques adopted to simulate this phenomenon. All this information is combined to develop a new model for the bond that can be used to simulate the response of the concrete-steel interfaces under general loading (*e.g.* earthquake loading). It was decided that the most feasible way to achieve this is to adopt a semi-analytical bond model implemented at the reinforcement scale. The bond model is inserted into an interface element and a simplified constitutive relation is adopted for the radial components. This element connects the elements used to model the steel reinforcements and the concrete and allows considering relative displacements between both materials. Afterwards, the proposed solution is tested in the framework of the *Finite Element Method* (FEM) by a group of validation examples. These validation examples were developed with increasing complexity and trying to isolate, as much as possible, each relevant aspect of the response. In most occasions, the results are compared with data from experimental results, with other numerical tools or with both, when possible.

The terminology used in most of the bibliography that addresses the behaviour of the concrete-steel interfaces is also used in this thesis. Nevertheless, there is some heterogeneity in the terms used for some quantities. As an example, the term *smooth bar* is preferred to the term *plain bar* for reinforcing steel bars with smooth surfaces. Similarly, the term *ribbed bar* is used instead of *deformed bar* to designate the reinforcing bars with ribs to enhance the bond. Moreover, the term *rib* is chosen to address the prominences on the bar surface, instead of the term *lug* that is also used.

Regarding the outline of the chapter, at the beginning a non-exhaustive but objective *state of the art* is presented about the behaviour of concrete-steel interfaces. This section will start with the problem formulation, followed by the most relevant aspects about the mechanical response and by a summary of the most relevant experimental programmes and numerical tools available in the bibliography. The subsequent section is dedicated to present the proposed bond model, followed by the issues related to the implementation on the interface element. The chapter ends with the validation examples that are complemented with some comments about the performance of the solution proposed.

2 State of the art

2.1 Problem formulation

Let us consider the small domain of the RC element represented in Figure IV.3-a. This domain includes the reinforcing bar, with diameter ϕ_s, and the surrounding concrete. For the sake of simplicity, this domain will be considered as two-dimensional without compromising the generality of the formulation that can always be expanded to the general three-dimensional case, in a straightforward manner.

This domain has been subjected to a set of loads that induced relative displacements between the reinforcement and the concrete, as shown in Figure IV.3-b. The relative displacements along the axis of the reinforcement bar $q_1^{rel}(x_1)$ are commonly called *slips* $s(x_1)$, and the relative displacements perpendicular to the axis of the bar $q_2^{rel}(x_1)$ will be called *radial relative displacements* in this thesis $r_2(x_1)$ or simply *opening/closing* displacements.

According to Figure IV.3, for each point along the axis of the reinforcement bar, these relative displacements can be defined as follows:

$$q_1^{rel}(x_1) = s(x_1) = q_1^A - q_1^B = q_1^A - q_1^C, \tag{IV.1}$$

and,

$$q_2^{rel}(x_1) = r_2(x_1) = \left(q_2^B - q_2^A\right) - \left(q_2^C - q_2^A\right) = q_2^B - q_2^C. \tag{IV.2}$$

Please note that for the general three-dimensional case, there will be also another radial relative displacement along the perpendicular direction to the plane defined by x_1 and x_2.

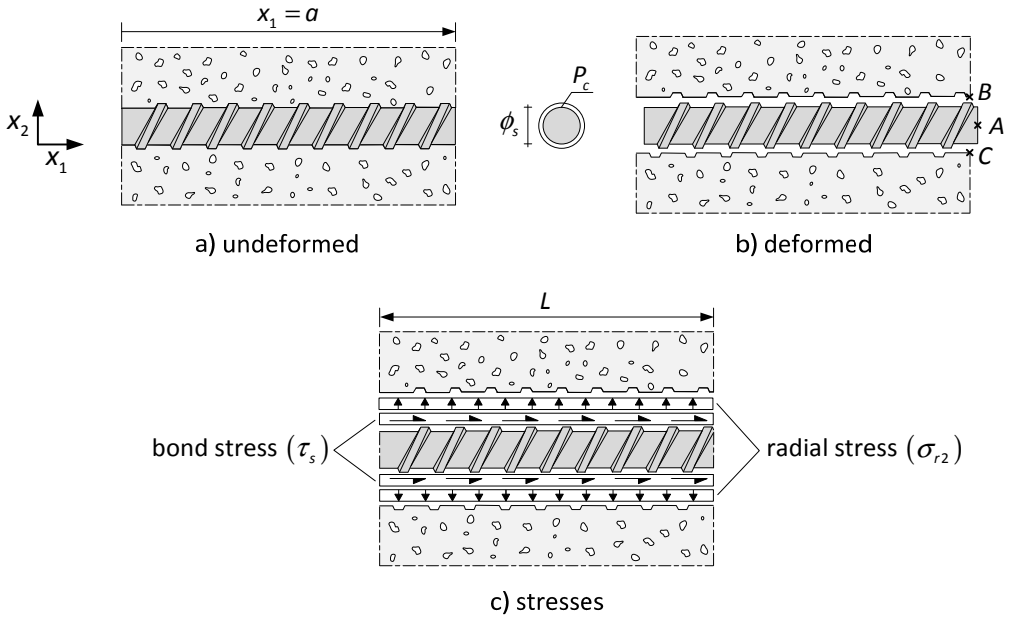

Figure IV.3: Denomination of the basic CSI quantities.

Adopting equations (IV.1) and (IV.2) implies the following sign convention: positive slips correspond to protruding reinforcements in the edge with higher x_1 coordinate and positive radial displacements implies opening movements.

As represented in Figure IV.3-c, associated with the slips and radial displacements are the *bond stress* τ_s and the *radial stress* σ_{r2}. The equivalent global forces for the domain represented in Figure IV.3 can be computed from:

$$Q_s = \int_0^L \tau_b P_c \, dx_1 \,, \tag{IV.3}$$

$$Q_{r2} = \int_0^L \sigma_{r2} \, dx_1 \,, \tag{IV.4}$$

where P_c is the *contact perimeter* by unit length defined by the perimeter of a circle with diameter ϕ_s, and thus, neglecting the contribution of the ribs. These expressions imply that τ_b and σ_{r2} only vary along x_1 and that the bond stress is defined by perimeter unit, contrary to the radial stress.

2.2 Mechanical characterization of the bond mechanism

A brief summary of the mechanical response associated with the bond mechanism will be presented in this section. Further information can be found in the *state of the art* report published by FIB in 2000 [214] or in other bibliography addressing this topic, *e.g.* [172, 342]. As mentioned before, most of the attention will be drawn to the bond mechanism and the mechanical response associated with the radial components will be considered only by their effect on the bond.

2.2.1 Response in basic bond tests

The bond mechanism is usually characterized with data from experimental tests. Figure IV.4 presents a summary of the most common experimental tests used for this purpose. The majority of these tests are made with static monotonic loads. Among these, the pull-out tests are predominant.

- Pull-out tests

The pull-out tests are made by imposing a series of monotonic increasing displacements on protruding reinforcing steel bars anchored inside concrete blocks, as presented in Figure IV.4-a. The push-in configuration is also used and the differences in the test apparatus are mainly the direction of the prescribed displacements and the supported concrete edge (see Figure IV.4-b). Moreover, the combined pull-out and push-in tests represented in Figure IV.4-c present the advantage of avoiding loading-related asymmetries for tests with reversed loading. In addition, in this way it is possible to generate a more uniform stress and strain distribution for monotonic tests, due to having two loading points. Most of the time, the connection between the reinforcing bar and the concrete is eliminated near the concrete edges by isolators to avoid stress concentrations that could distort the results.

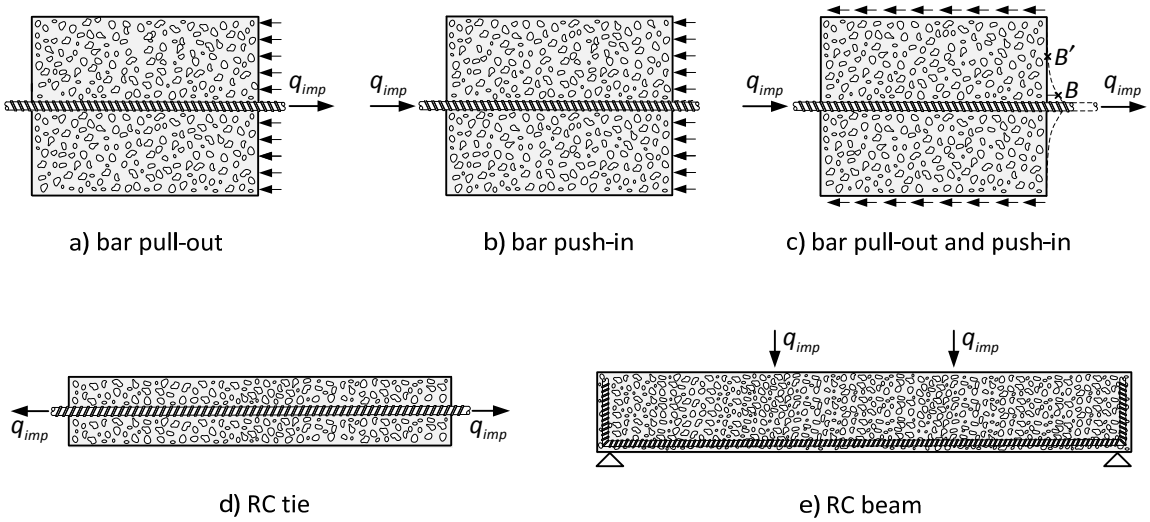

Figure IV.4: Most common types of tests made to characterize the bond mechanism.

One important characteristic of these tests is the *anchorage length* L_a. The specimens can be classified as having long or short anchorage lengths. In the former case, the slip and stress distribution will change along the bar and will depend on the stiffness and strength of all components. On the other hand, for specimens with small anchorage lengths, the slip and stress distribution will tend to be uniform and it is considerable easier to analyse the results and characterize the bond mechanism. The distinction between both cases in terms of anchorage length is difficult to determine explicitly, as it strongly depends on the stiffness of the interface. However, many authors have used values of $L_a \approx 5\phi_s$ and the results showed that the response was very close to being uniform, as will be seen in the examples developed in this chapter.

Another aspect that differentiates the usual test layouts is related to the position of the concrete support, either at the face near the prescribed displacement of the bar (see Figure IV.4-a) or at the lateral edges (see Figure IV.4-c). This issue must be taken into consideration because it can change the strain and stress distributions, especially for specimens with long anchorage lengths. For lateral supported specimens, it must be taken into consideration if the concrete displacement used to compute the slips with relation (IV.1) is measured near the reinforcement (point *B* in Figure IV.4-c) or in undisturbed concrete (point B' in Figure IV.4-c). The latter case will include not only the relative displacements between the concrete and the reinforcing steel, but additionally, the concrete shear deformation. This will result in a slip shift proportional to the bond stress if a linear response is assumed for the concrete. Obviously, the results in terms of the overall strength will not be affected.

The specimens can also be classified as short or long. The distinction is made when there is sufficient anchorage length to stabilize the force transfer mechanism, and thus, reaching a state where the concrete and steel strains are equalized and, therefore, not developing bond stresses. This behaviour is presented in Figure IV.5 both for pull-out and push-in tests. For the first case, it is possible to observe the tension stresses created by pulling the reinforcing bar decreases by moving inside the specimen, due to the stress transfer into the concrete. For short specimens, the steel and concrete

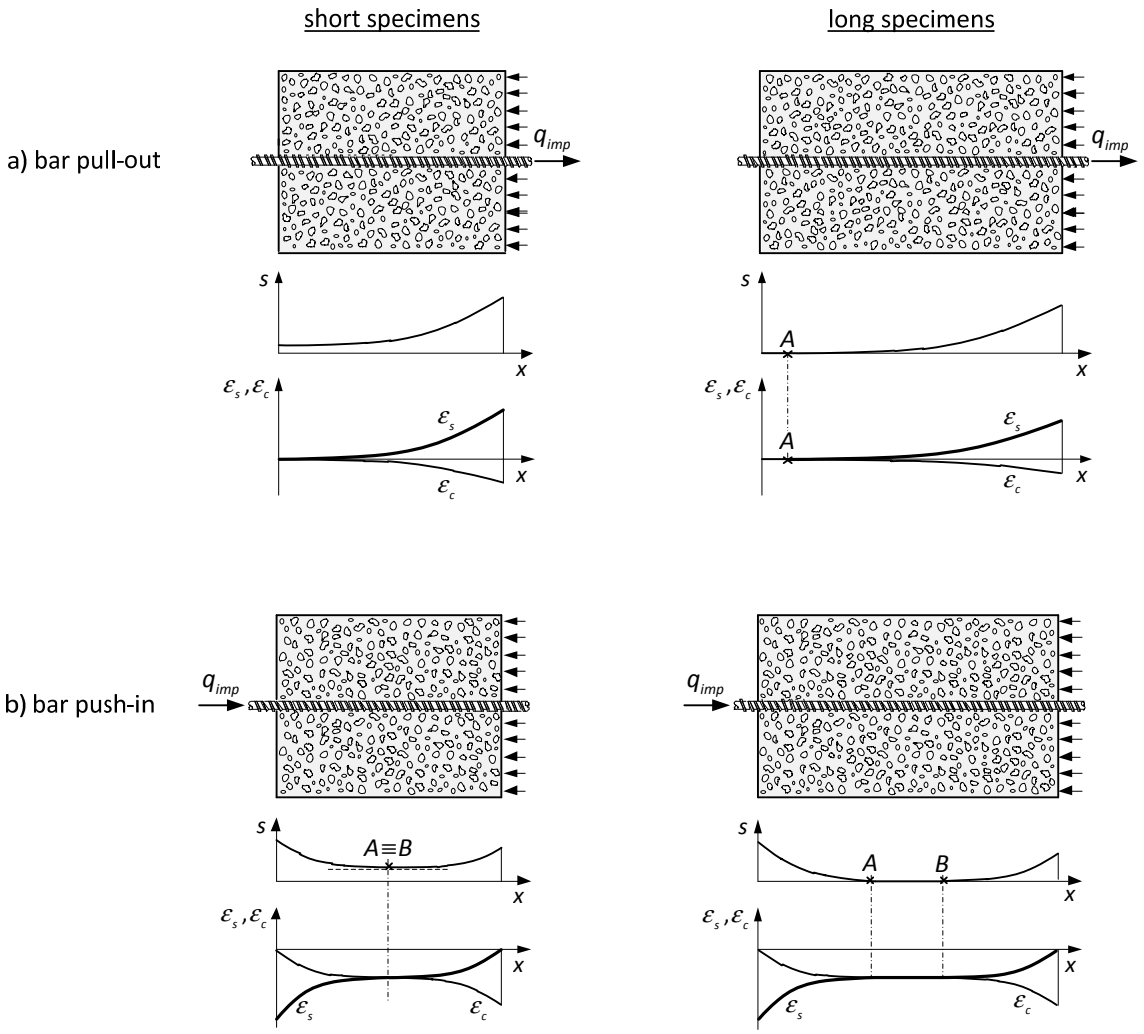

Figure IV.5: Typical slip and strain distributions in pull-out and push-in tests, adapted from [214, 490].

strains are null near the unrestrained concrete edge due to boundary conditions and not as a result of having completed the stress transfer, so that bond forces exist throughout the anchorage length as shown by the non-null slip near that edge (see the leftmost part of Figure IV.5-a). For long specimens, the anchorage length is sufficient to stabilize the stress transfer, and between point A and the unloaded edge there is no slip and the deformation is equal in the concrete and steel (see the rightmost part of Figure IV.5-a).

- Push-in tests

The response is similar in the push-in tests (see Figure IV.5-b). For short specimens, stress transfer and slips occurs throughout the entire anchorage length. For long specimens, a zone without slips and differential strain is created between point *A* and *B* in the rightmost part of Figure IV.5-b, meaning that all stress transfer is achieved.

The slip and strain distributions presented in Figure IV.5 are only valid for specimens with linear response of the materials and interfaces. If the response enters the nonlinear range, *e.g.* due to bond

failure, concrete cracking or steel bar yielding, stress and strain redistributions will occur and these can completely change the response of the element. This can be easily understood by analysing the qualitative results of RC ties presented in the following paragraph.

- RC ties

The bond tests with RC ties are performed by tensioning a reinforcing bar that is embedded inside a concrete block, as represented in Figure IV.6. This test type includes many of the characteristics of the response of RC members. Figure IV.6-a/b presents the typical stress and strain distribution of uncracked RC ties, both for short and long specimens. Most of the observations made for pull-out and push-in tests are also applicable here. For example, for the case of long specimens, a zone without stress transfer occurs in the interior of the tie between points *A* and *B* (see Figure IV.6-b). Furthermore, the response is also characterized by symmetry or anti-symmetry properties before cracking, owing to the symmetry in the loading conditions.

The response becomes strongly nonlinear when the stress level increases. For short specimens cracking tends to occur at mid-span because this is the location of the highest concrete strains (see Figure IV.6-c). Afterwards, the initial tie of length *L* is divided into two new units with similar lengths, loading and boundary conditions. The process restarts independently for these two new units. For non-ideal materials, like concrete, the dispersion of the mechanical properties will induce some level of randomness in the crack location.

The *transfer length* L_t plays an important role after the transformation of the initial bond unit into two or more sub-units. This concept was first introduced by Somayaji and Shah [518] and refers to the length necessary for the bond mechanism to transfer enough stresses from the reinforcement to the concrete to enable the development of new cracks. For homogenous materials, this parameter is independent of the specimen size and is related only to the stiffness and strength relations. Recalling the cracked short specimen in Figure IV.6-c, cracking will occur again independently in both new units if the length of each unit is greater than $2L_t$. If this condition is not met, cracking stops and the cracking process is said to be stabilized. Before the first crack, the response of long specimens is characterized by a mid-span zone where the steel and concrete strains and stresses tend to be equalized, resulting in no bond stresses. In this region the concrete reaches the maximum strains (see Figure IV.6-b). Cracking will be likely to occur in the weakest part of this zone, in a location difficult to predict. Subsequent cracks will occur until stabilization is reached. Figure IV.6-d tries to illustrate these characteristics of the response.

This behaviour is clearly affected by the size effect. The load level associated with the first crack is strongly affected by the size of the concrete region with maximum concrete strains. Larger RC elements will have larger probability of having a weaker zone, which induces the size effect. This issue is addressed in more detail in the section dedicated to the *size effect* in Chapter III-§2.1.4.

One can be led to think that the results from RC ties are associated with a particular situation of loading and boundary conditions and are not representative of general RC members. This point of

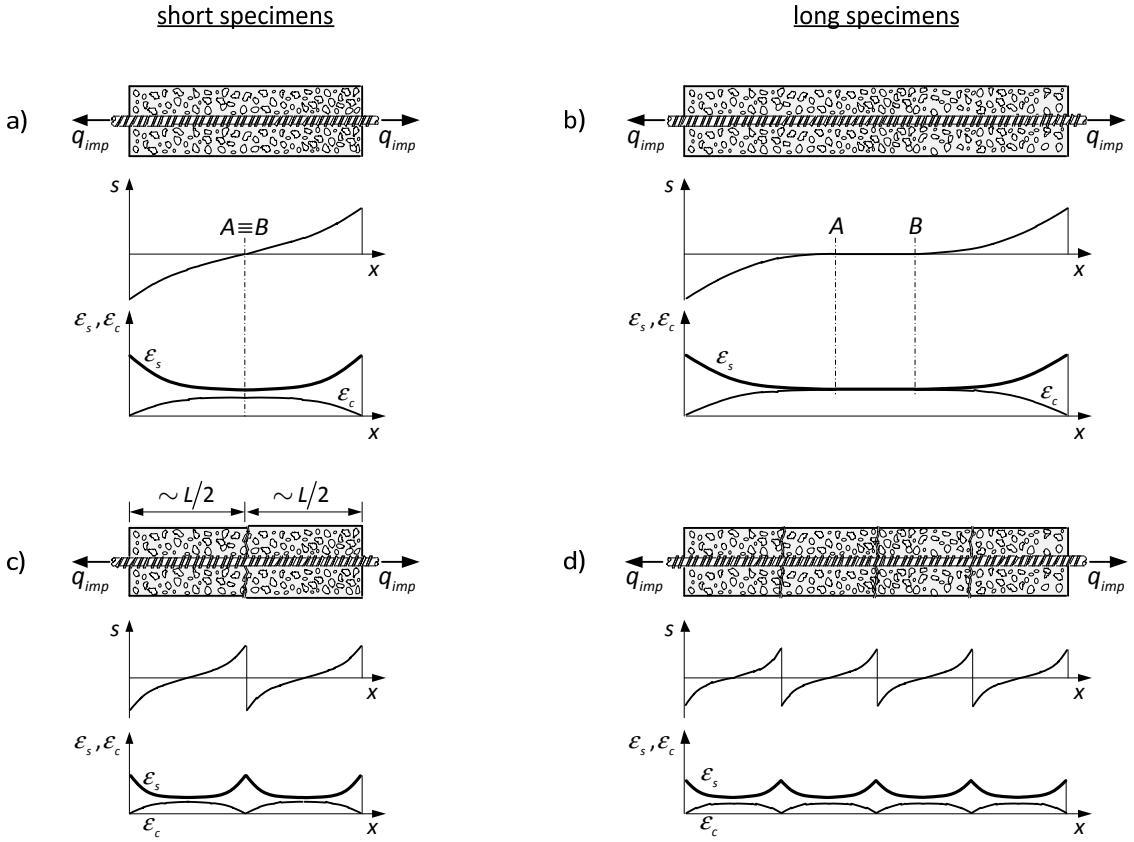

Figure IV.6:.Typical slip and strain distributions in tests with RC ties, adapted from [214, 490]:
a) and b) before cracking; c) and d) after crack stabilization.

view is not correct because similar structural situations are frequent in common RC members. For example, the concrete near the bottom reinforcement of a beam subjected to a sagging bending moment will tend to crack just like a tie. The major difference is related to the fact that the longitudinal stresses are not uniform in the cross-section like in a tensioned member.

The common response of RC elements subjected to tension is represented in Figure IV.7. This behaviour is characterized by at least four stages. The first stage occurs when the concrete is still mainly uncracked (until point A is reached) and is followed by a cracking stage that lasts until cracking stabilization is achieved (from point A to D). No additional macro-cracks are created during the following stage because there is not enough stress transfer to the concrete to create new cracks. This response is maintained until yielding of the reinforcements is reached (point E), which generates large deformations and increases the opening of the nearby crack (see Figure IV.7).

The stiffness associated with the generation of macro-cracks (*e.g.* slope between point A and B) depends on the energy dissipated in the crack formation. Some experimental results indicate that this phenomenon does not occur abruptly and that a significant amount of inelastic deformation is necessary to completely open the macro-crack. The results obtained by Clément [113] and Daoud [158] are perfect examples of this behaviour (see section 2.3.2). The order of appearance of each

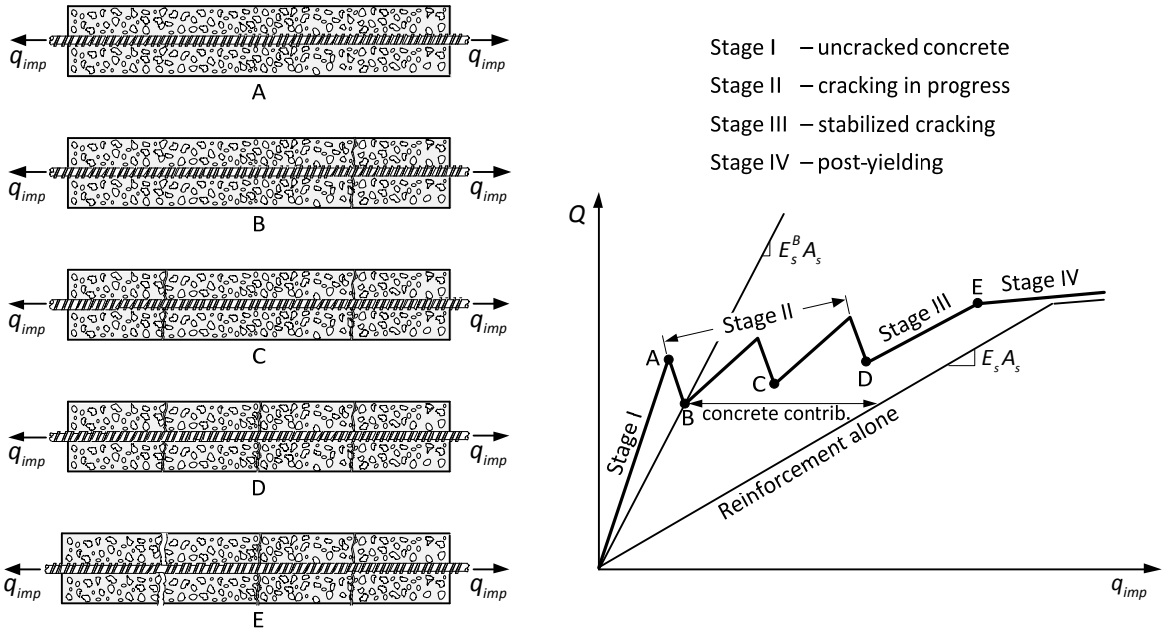

Figure IV.7: Typical response of a RC tie.

macro-crack has some degree of randomness and depends on factors like the length of the specimen, the bond characteristics and on the spatial distribution of the concrete heterogeneities. Therefore, the sequence presented in Figure IV.7 is arbitrary and subjective.

The force-displacement curve considering only the reinforcement is also represented in Figure IV.7. This curve presents a slope equal to the steel elasticity modulus times the area of the reinforcement $\left(E_s A_s\right)$. This allows identification of the additional contribution of the concrete between cracks and demonstrates a phenomenon commonly called the *tension-stiffening effect*, introduced by Giuriani [242]. This effect results from the stress transfer to the concrete in between cracks and this concrete contribution can be considered for the global response as an increase in stiffness in the reinforcing bars. For example, the equivalent secant stiffness $\left(E_s^B A_s\right)$ should be considered for the level of cracking at point B in Figure IV.7. This value decreases with the spreading of cracking in the element because of the consequent reduction of the concrete contribution.

- Other tests

Tests with RC beams are also used to assess the bond performance. Frequently the loading system is chosen to create a pure bending stress distribution by removing, in theory, the influence of shear stresses. This can be done with the four-point bending test configuration presented in Figure IV.4-e.

In these tests, the analysis of the bond mechanism is more complex. Hence they represent a minority when compared to pull-out and tie tests. Nevertheless, the bibliography presents some experimental programmes with RC beams with the specific purpose of assessing the bond performance. An example is the tests from Türk *et al.* [547], which are presented in section 2.3.3.

- Failure modes

One of the following four failures is likely to occur in pull-out tests:

i. *Splitting crack failure* (see Figure IV.8-a), in which the relative displacements of the ribs create radial forces that, if not balanced by confinement forces, will end up by creating a longitudinal crack along the bar that reduces the resistance to a friction-related value leading to the premature bar pull-out (see Figure IV.9-d);
ii. C*ylindrical crack failure* (see Figure IV.8-b), in which the bar pull-out occurs with the creation of cylindrical cracks along the bar and this mode is associated with the highest level of bond stress;
iii. *Concrete cone failure* (see Figure IV.8-c) occurs when the dimensions of the element or the passive reinforcements are not sufficient to avoid a brittle concrete failure around the protruding bar;
iv. *Reinforcing steel yield* (see Figure IV.8-d), in which the global strength of the bond mechanism and of the concrete are greater than the yielding strength of the reinforcing steel bar. This usually happens only in specimens with long anchorages.

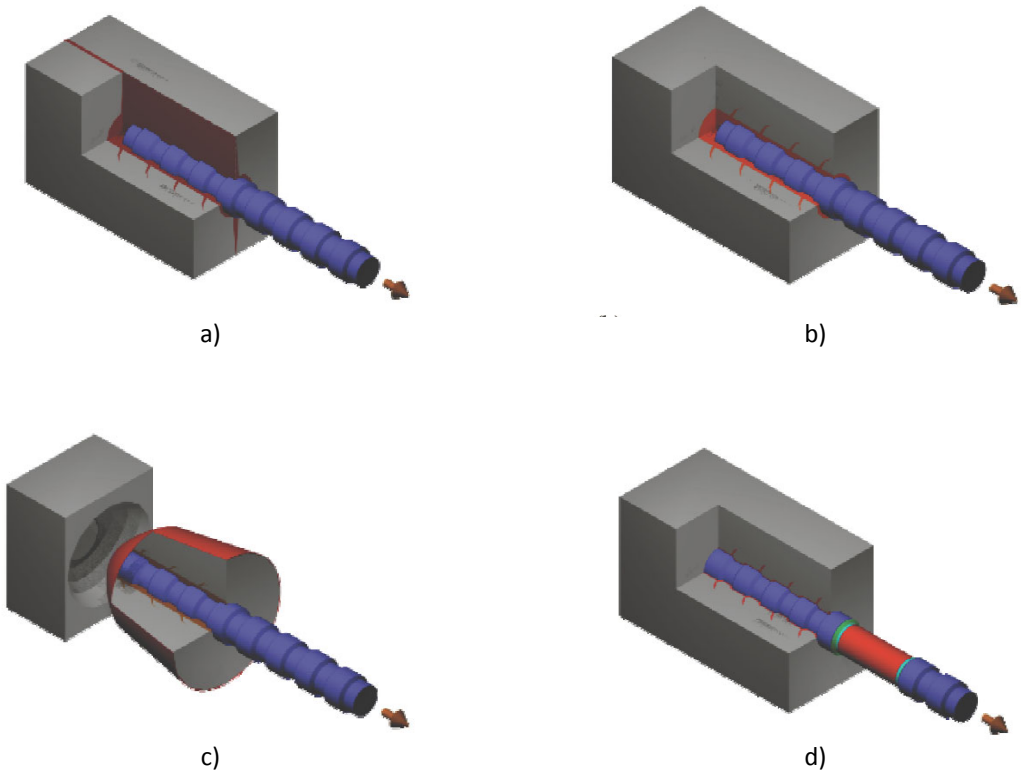

Figure IV.8: Typical failure modes in pull-out tests, adapted from Dominguez [172]:
a) Splitting crack; b) cylindrical crack; c) concrete cone failure; d) reinforcing steel yield.

2.2.2 Response under monotonic loading

Most of the authors producing work in this field agree that the bond between steel and concrete results from the combined effect of: i) the *chemical adhesion* between cement paste and steel; ii) the *friction* between surfaces; and iii) the *mechanical resistance* associated with the ribs. As a consequence, for *ribbed bars* (RB), the bond strength results from the combined strength of these 3 effects, generally much higher than the strength for *smooth bars* (SB), where only adhesion and friction contributes to the resistance. The mechanical resistance associated with the ribs includes the shear resistance of the concrete between ribs and the resistance associated with the compression struts generated by splitting forces (see Figure IV.9-c).

A recurrent way of studying the bond mechanism is by the analysis of the results from *pull-out* tests in terms of bond stress *vs.* slip. If the anchorage length is small, the global response of the specimen can be representative of the local response. The following paragraphs present a summary of the characteristics reported in the bibliography for the response under monotonic loading [390]:

i. Under low values of bond stress $\tau_b = 0.2$ to $0.8\, f_{ct}$, the resistance is mainly achieved by chemical adhesion and micromechanical interlock between the concrete and steel surfaces. In this phase, virtually no slip occurs and the concrete is mainly uncracked. However, stress concentrations start to build-up close to the rib tips. This phase ranges from point *O* to *B* in Figure IV.9-a For smooth bars the peak stress coincides with the *perfect bond* (PB) limit $\tau_1^{SB} \equiv \tau_0^{PB}$ and is achieved

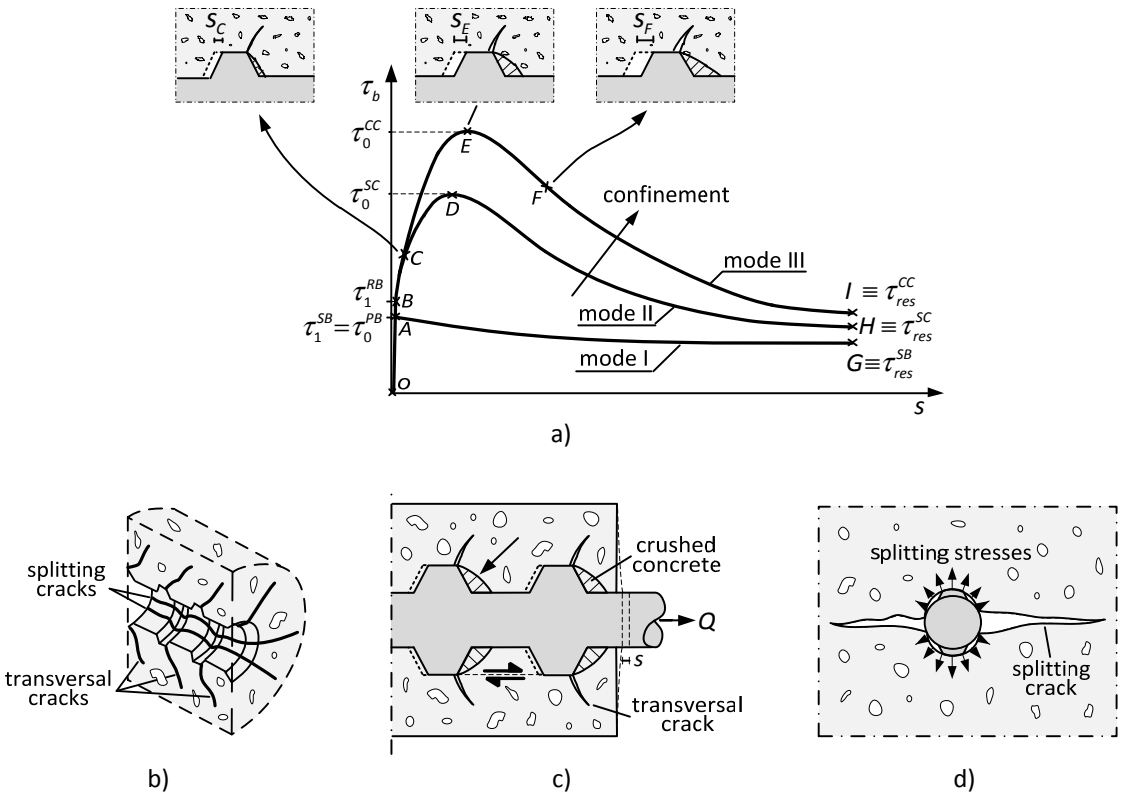

Figure IV.9: Typical monotonic response in pull-out tests, adapted from [214].

at point *A*. Afterwards, the response is characterized by a softening branch until reaching the sliding friction stress for this type of bars (point G), which is highly affected by confinement (failure mode I represented in Figure IV.9-a). For ribbed bars, the perfect bond limit τ_1^{RB} is achieved at a higher stress level due to the additional contribution of the ribs (point B).

ii. For ribbed bars, when the perfect bond stress level is exceeded $\left(\tau_b > \tau_1^{RB}\right)$, the stresses near the rib tips increases and will lead to transversal cracking (see Figure IV.9-b-c). When the specimen presents a low level of confinement (passive or active) at the radial directions, increasing the bond stress levels to values about $\tau_b = 1.0$ to $3.0\, f_{ct}$ will generate *splitting cracks* (SC) created by the splitting forces caused by rib displacements (see Figure IV.9-b/d). The peak stress is reached at stress equal to τ_0^{SC} (point D). At this phase, the openings of the transversal cracks increases and the ribs crush most of the surrounding concrete. The subsequent response is characterized by softening until reaching a nearly constant sliding friction plateau and the complete pull-out failure (failure mode II).

iii. On the other hand, if the confinement forces are enough to prevent the splitting cracks from opening, the behaviour is considerable better in terms of resistance. The response follows points C-E-I in Figure IV.9-a, together with increasing transversal cracking and concrete crushing. The peak stress is reached at point τ_0^{CC} (point E). and failure is reached after shearing-off completely the concrete between adjacent ribs and forming *cylindrical cracks* (CC) (failure mode III).

Table IV.1 presents the ranges proposed by Eligehausen *et al.* [193] for the strength of each bond mechanism for ribbed bars embedded in common concrete.

2.2.3 Response under cyclic or alternated loading

The bond performance under cyclic and alternated loading presents additional stiffness and strength degradation caused by progressive micro-cracking and concrete crushing. According to FIB [214], the most important factors influencing this degradation are the type of ribs and the maximum slip reached in both directions s_{max}. Other relevant parameters are the concrete resistance, the confinement forces and the number of load cycles.

On smooth bars, the inexistence of ribs causes the response to be of poor quality since the peak stress is easily surpassed and a friction-like response quickly emerges. On the other hand, on ribbed

Table IV.1: Typical values of the bond-related stresses under monotonic tests [193].

Parameter	Typical values
Chemical adhesion	0.5 to 1.0 MPa
Perfect bond limit τ_1^{RB}	2.0 to 3.0 MPa
Peak resistance (with splitting cracks) τ_0^{SC}	2.0 to 7.0 MPa
Peak resistance (without splitting cracks) τ_0^{CC}	10.0 to 15.0 MPa
Sliding friction plateau τ_{res}^{RB}	0.4 to 10.0 MPa

Note: For commercial ribbed bars and common concrete $\left(f_c \approx 30\ \text{MPa}\right)$

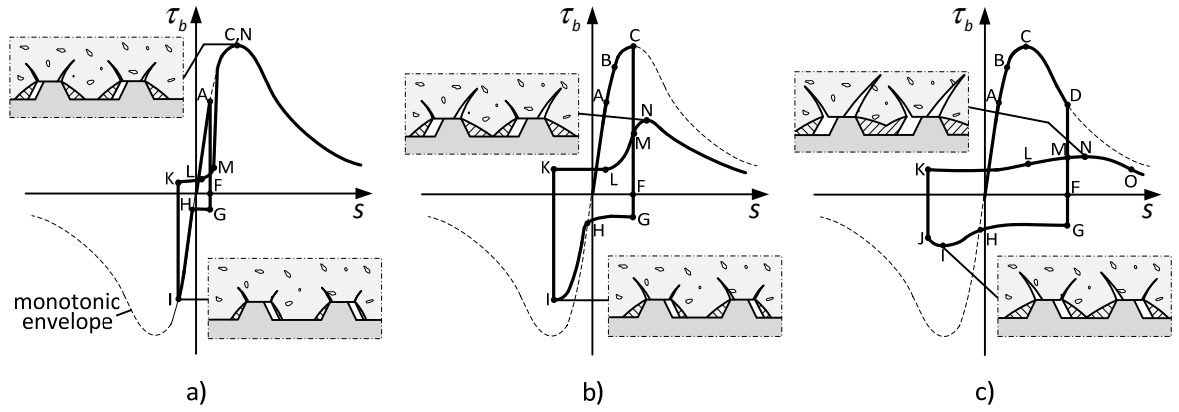

Figure IV.10: Typical response of the bond mechanism under cyclic and reversed loading, adapted from [214].

bars the response is of better quality and more complex. The following paragraphs try to summarize the most relevant characteristics of the bond mechanism of ribbed bars under cyclic and alternating loading, as reported by Eligehausen *et al.* [193]:

i. When loaded for the first time the response follows the curve from monotonic tests. For the following cycles, the stiffness and strength characteristics are strongly influenced by the presence of cracks and concrete crushing;
ii. The first case (see Figure IV.10-a) represents the situation where unloading occurs before significant damage at the interface (point A). Unloading is very stiff (AF) because degradation is very small. The reloading branch along the other direction, reaches a low stiffness zone (friction) until the inelastic slip reached before is nulled (GH). Then a sudden increase in stiffness occurs and the monotonic curve is nearly followed (HI). Reloading along the initial direction is similar to the first loading branch but with one relevant difference, the regain of stiffness only starts after reaching the inelastic slip achieved in the first loading branch and is gradual (LM);
iii. In the second case (see Figure IV.10-b), the first unload occurs already with the presence of significant cracking and crushing (point C). A higher bond stress (G) is needed to reach the friction zone (GH) and the accumulated damage justifies a less stiff and resistant reloading (HI). Unloading and reloading in the initial direction (LMN) show even more intense stiffness and strength degradation and it can also be seen that the slip at peak stress increases (C *vs*. N);
iv. In the third case (see Figure IV.10-c), the first unloading occurs after reaching the peak bond stress (point D). The bond mechanism becomes heavily compromised because almost all the concrete between ribs is damaged leading to a reverse reload branch with low stiffness and resistance. Reloading in the initial direction (KLMN) shows that the degradation intensifies with practically only the contribution of friction between surfaces, and again, the slip at peak stress increases (C *vs*. N).

Part or all transversal crack opening can be closed when the slip direction changes. However, cracking in adjacent rib tips can generate cone-shaped cracks that can cross each other, creating looser concrete blocks and worse bond performance.

2.2.4 Other aspects influencing the bond mechanism

The previous sections emphasized the importance of the *type of reinforcement surface* (smooth or ribbed) and of the *loading history*. Nonetheless, many other factors can influence the bond performance. A short summary of the main factors influencing the bond is presented in this section.

- Geometric characteristics of the ribs (bar roughness)

It is generally accepted that the geometric characteristics of the ribs plays a determinant role in bond resistance. Over the years, different geometrical configurations have been used. Nowadays, this issue is subjected to regulation in order to harmonize and ensure adequate bond levels, *e.g.* LNEC [341]. Best bond characteristics are obtained by particular combinations of the *rib height* h_r, *rib spacing* s_r and the *bar diameter* ϕ_s. The *relative area* f_r of the ribs or *bond index* is one of the most common parameters to measure the transversal rib efficiency. The FIB's state of the art report [214] defines this parameter as:

$$f_r = \frac{A_r}{\pi \phi_s s_r}, \tag{IV.5}$$

where A_r is the area of the transversal ribs projected in the transversal direction. For common rib patterns, this parameter can be computed from: $A_r = 2 h_r^m L_r \sin\beta_r$, where h_r^m is the *mean rib height*, L_r is *rib length* and β_r is the *rib inclination* with the longitudinal axis (see Figure IV.11). According to FIB [214], experimental studies show that similar bond properties are obtained for reinforcing bars with the same relative area and optimal values for this parameter are between 0.05 and 0.10. The author Fleury [219] associates the increases in the relative area with increases in the bond stiffness and strength before the peak stress. Additionally, the parameter s_r is associated with the beginning of the softening and friction branches.

- Steel bar diameter

The diameter of the steel reinforcing bar is known to influence the bond strength. However, a well-established quantitative relation is difficult to extract from the bibliography. It is commonly accepted that the bond strength decreases with the increase in the bar nominal diameter. This can be seen as resulting from the size effect, *i.e.* the zone of influence of the bond mechanism does not scale as the increase in the bar diameter. The author Lowes [342], reporting on the work of Viwathanatepa *et al.* [558] and Eligehausen *et al.* [193], presents variations of bond strength ranging from 10% to 20% for common commercial bar diameters.

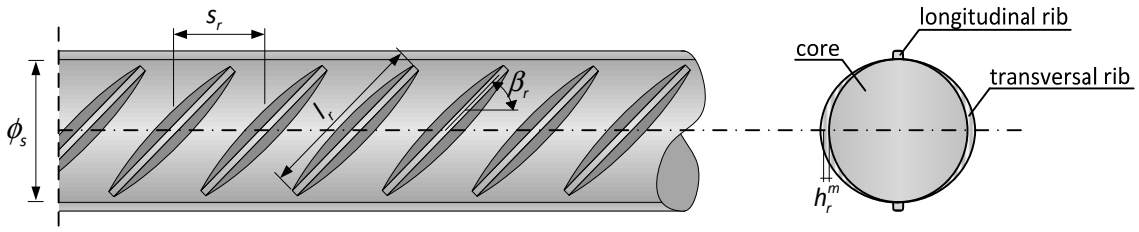

Figure IV.11: Geometric characteristics of the ribs, adapted from Fleury [219].

- Concrete characteristics

The concrete is of great importance in the overall response of the concrete-steel interface because most inelastic response occurs in the concrete surrounding the reinforcing bar. On ribbed bars, the concrete close to the ribs is subjected to intense solicitations and a typical failure mechanism occurs after severe concrete cracking and crushing. Generally, it is possible to say that better concrete quality leads to better bond response. In the work of Dominguez [172], the tensile concrete strength is considered to be strongly related to the perfect bond limit of the concrete-steel interface. In addition, the authors Eligehausen *et al.* [193] conclude that there is an inverse proportional relation between the compressive concrete strength and the slips, and consequently, also the bond stiffness. The same work also identifies a direct proportional relation between the bond strength and the compressive concrete strength and proposes the following expression:

$$\tau_b^{\max} \propto \left(f_c\right)^{\beta}, \quad \text{with } \frac{1}{3} \leq \beta \leq \frac{1}{2}. \tag{IV.6}$$

Other aspects that can significantly influence the bond mechanism are the concrete casting and curing conditions. Weaker interfaces may be caused by an incorrect concrete cast, which leads to an increase of the number and size of voids. An incorrect concrete cure may result in a more brittle response. The concrete casting direction can also influence significantly the bond strength if preferential contact zones are established. Self-compacting concrete tends to be less influenced by this aspect as a result of better filling capacity.

- Effect of radial stress

The adopted definition for radial stress includes all forces from external sources that are applied perpendicularly to the reinforcement axis. Radial stresses can be classified as being *passive* or *active*. Passive radial stresses, *a.k.a. passive confinement*, result mainly from the reactive action of transversal reinforcements and *active radial stresses* result from imposed lateral forces, either by external forces or by interaction with other structural elements.

Regarding the bond performance, the major effects of radial stresses are the inhibition of splitting cracks and the increase in the friction component. Nonetheless, some differences between the effect of passive and active forms of radial stresses must be established. It is commonly accepted that passive confinement forces are only mobilized in the presence of expanding movements, either caused by Poisson's effect in compressed elements (*e.g.* columns) or by the action of the splitting movements. Consequently, in elements with low levels of compression (*e.g.* beams) the effect of the passive confinement on the bond is mostly caused by splitting movements. Nevertheless, there is a *consensus* regarding the fact that the lateral confinement forces play an important role for the global bond response. For example, in the work of Eligehausen *et al.* [193], it was estimated that the existence of code prescribed amounts of passive reinforcements in RC elements, increases the bond strength by 33%, when compared with the same specimen without lateral confinement.

The effect of active radial stresses can be manifested in all bond phases because, contrary to passive radial stresses, they do not have a reactive nature. This was observed in the work of Malvar [352]

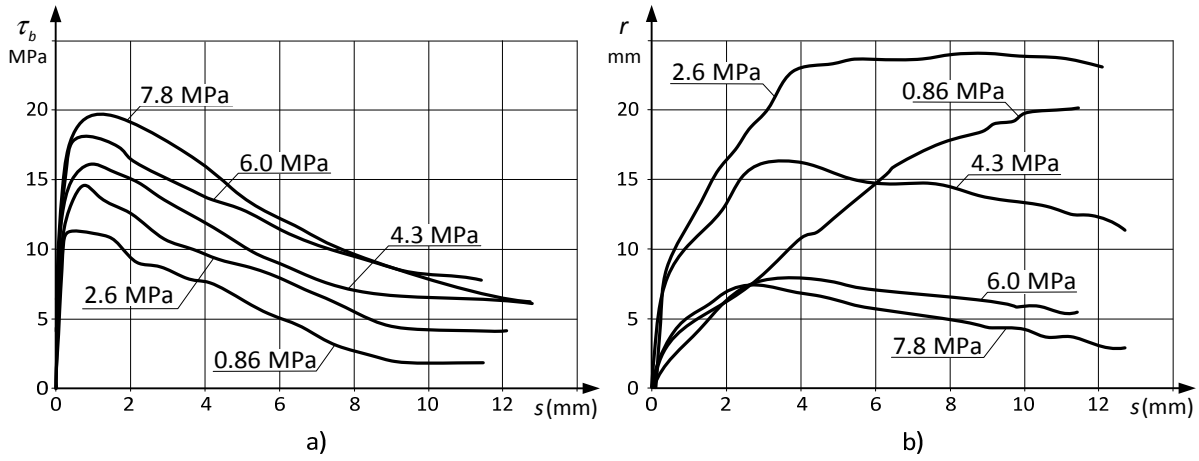

Figure IV.12: Effect of active confinement forces: a) on the bond strength; b) on the radial deformation, adapted from [352].

that is represented in Figure IV.12. It is possible to observe that, although the initial stiffness seems not to be affected by active radial stresses, the bond strength, the softening and the final residual strength branches denote a clear correlation with the active radial stress levels. The radial deformation evolution is presented in Figure IV.12-b. These results show a tendency of the maximum radial deformation to be anticipated for larger levels of active confinement.

- Size effect

The data presented in the previous section showed that both for monotonic and cyclic and reversed loading the concrete-steel interface experiences a softening phase after reaching the peak stress. This response is mainly associated with fracture-like phenomena that occur in the concrete near the interface.

As presented in Chapter III-§2.1.4, the fracture process in *quasi*-brittle materials like concrete results into a significant size effect source that should not be neglected, especially for comparing experimental results obtained with structures of different sizes or when the mechanical properties are extracted from small experiments and are used to calibrate models for larger structures.

Figure IV.13 presents a possible experimental test series used to study the size effect with pull-out tests. It is possible to observe that by doing a homothetic scaling to the specimens, the *fracture process zone* (FPZ), displayed with a darker grey, does not scale in the same way as the rest of the specimen, even though the size of the ribs may justify a larger width. This is because the FPZ is mainly influenced by intrinsic material properties, like the aggregate dimension that do not change with this geometric scaling.

Several studies were made to bond-related size effect by series of pull-out tests. More information can be obtained from the work of Bažant *et al.* [38, 43], Coronelli *et al.* [144] and Bamonte *et al.* [28].

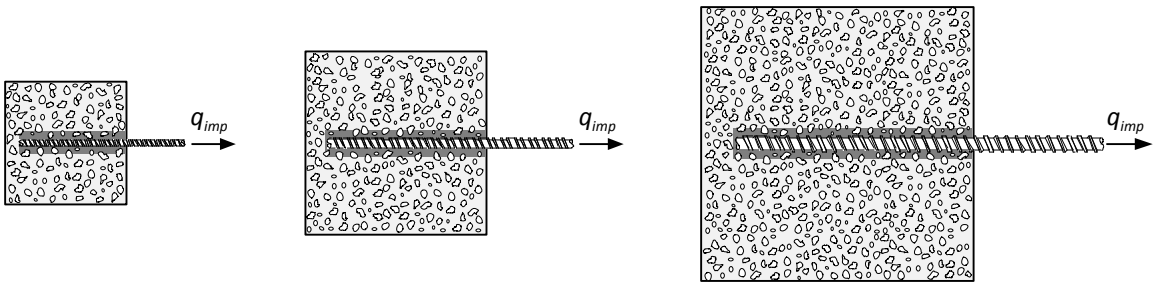

Figure IV.13: Size effect on pull-out tests.

- Effect of steel bar corrosion

Steel corrosion is known to be one of the most important causes of deterioration of RC structures and has the potential of affecting the service conditions and their durability. Steel corrosion is initially limited by the alkaline environment created by the surrounding concrete that generates a protective layer around the steel bar. This protecting layer can be broken by several mechanisms, like the well-known *carbonation* or *chloride penetration*, among others (see Chapter III-§2.2.1). If this happens, steel corrosion may develop and reduce the nominal section of the steel bars and intensify the concrete degradation. This last effect is caused mainly by the corrosion products that generate a large increase in volume when compared to the originating components. This will create expanding stresses that will lead to concrete cracking and possibly to concrete cover spalling, which will tend to intensify even more the corrosion mechanism by increasing the access to oxygen.

Regarding the effect of steel bar corrosion on the bond mechanism, it is possible to stress that the consequences are globally negative. It is true that the radial stresses, created by the corrosion products at early stages, can improve the frictional contribution and improve the bond strength as reported by Almusallam *et al.* [7]. However, soon afterwards, it can induce longitudinal cracking and reduce significantly the bond resistance. Moreover, the corrosion products are composed of granular materials that will contribute to a weak and ineffective source of bond strength. According to FIB [214], corrosion can lead to a significant reduction of the steel bar cross-section, in particular, in the height of the ribs, and consequently can contribute to their loss of efficiency by disengagement from the concrete.

More information can be found in the state of the art report published by FIB [214] that presents a chapter dedicated to this issue. In addition, it is also presented information regarding experimental tests performed by Almusallam [7] and concerning numerical analyses made by Richard *et al.* [479].

- Effect of steel bar yielding

Experimental testing demonstrates that bond strength decreases when the bar yields in tension and increases when the bar yields in compression. According to Lowes [342], this behaviour can be attributed to Poisson's effect. When a bar yields in tension, the transversal diameter of the bar decreases in the yield segment, thus reducing the bond strength by disengagement from the

concrete keys. Similarly, when yielding occurs in compression, the bar expands and creates a sort of confining force that enhances the bond characteristics. The experimental data collected by Shima *et al.* [506] corroborates this response by showing a clear loss of bond strength in the post-yield range (see section 2.3.1).

- Effect of the loading rate

The availability of experimental and numerical studies regarding the loading rate effect on bond is quite sparse, even nowadays. Most experimental work done in this field is made under *quasi*-static loading or impact loading, and therefore, conclusions regarding this effect on earthquake loaded structures is difficult to extract.

In 1976, Hjorth [274] published the results of pull-out tests using impact loading for smooth and ribbed bars. The diameter of the reinforcement was chosen to be 16 mm and the anchorage length varied from ϕ_s to $10\phi_s$. The author observed that smooth bars are practically insensitive to the loading rate. On the other hand, ribbed bars present a significant dependence upon this parameter, in particular, it was observed that the bond strength increases by decreasing loading time.

The work of Vos and Reinhardt [560] presents a series of results accomplished with impact testing using the *Split Hopkinson Bar* technique [275]. The principle of this technique is based on the generation of a one-dimensional stress wave that travels across the bar, making it possible to achieve a large range of loading rates. The variables adopted in this work were the concrete compressive strength $f_c = \{22, 45, 55\}$ MPa, the type of reinforcement steel (smooth or ribbed reinforcing bars and pre-stressing strands) and the loading rate. The authors were able to conclude that for smooth bars, neither the maximum bond strength nor the stiffness were significantly influenced by the loading rate, and consequently, that adhesion and friction load bearing mechanisms are almost loading rate-independent (see Figure IV.14). For ribbed bars, the results showed strong dependence on loading rate and higher bond strength and resistance were achieved with higher loading rates. This influence was more evident for less resistant concrete and for smaller bar displacements. The authors also concluded that the pattern of the loading dependence is similar to that of plain concrete, both under tension and compression.

Figure IV.15 combines the results obtained by Eligehausen *et al.* [193] with the ones obtained by Hjorth [274] and Tassios [536]. It can be observed that all these works are consistent by showing that the bond strength increases at higher slip rates. Lowes [342] estimates that the maximum slip rate in a bridge structure is about 0.08 mm/s and concludes that taking into consideration the results presented in Figure IV.15, the increments of bond strength for an earthquake loading are expected to be less than 5% over the static response. Considering the dispersion of the bond strength, Lowes concluded that this effect may be disregarded.

- Other effects

The spacing between reinforcements is also a factor that can influence the bond strength. The work of Eligehausen *et al.* [193] showed that this effect is significant if the spacing is less than four times the bar diameter and nearly insignificant for larger values.

Concrete creep also influences the bond stress *vs*. slip relation by decreasing the slope of the increasing part of the curve. The *Model Code 90* [390] proposes a model to cope with this effect.

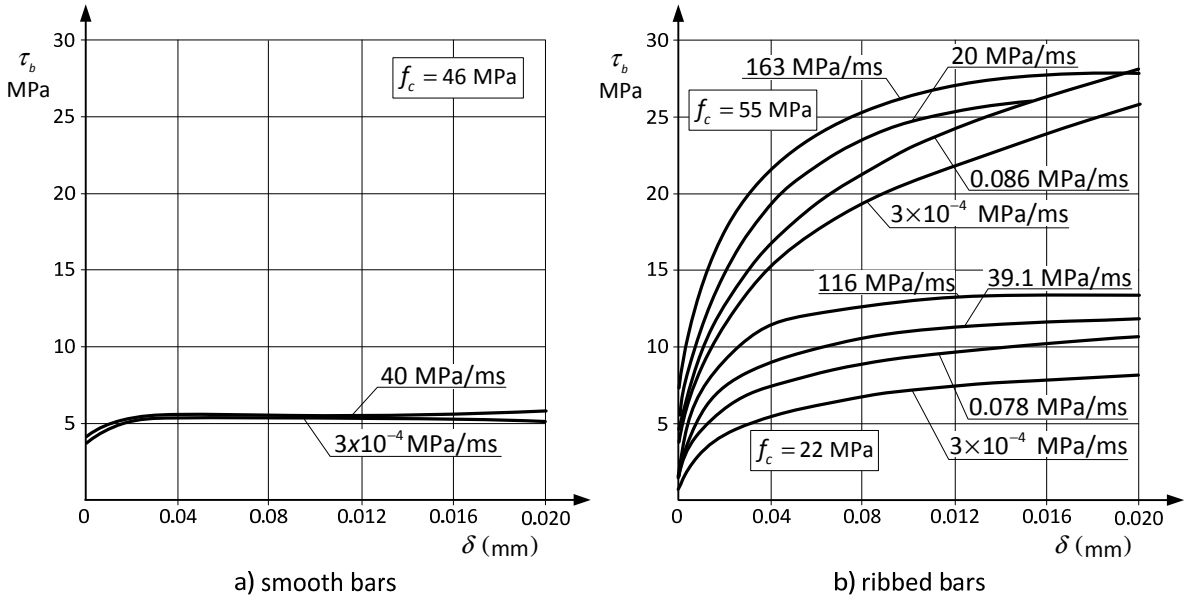

Figure IV.14: Effect of the loading rate on the bond, adapted from Vos et al.[560]: a) smooth bars; b) ribbed bars.

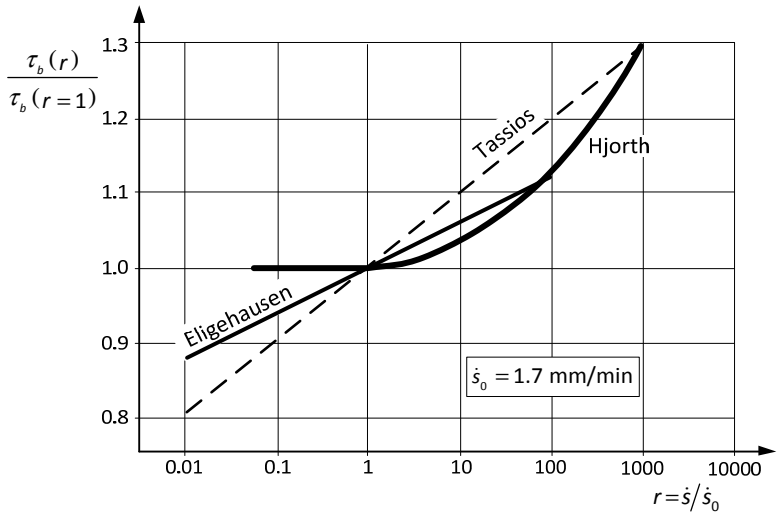

Figure IV.15: Effect of the loading rate on bond strength for deformed bars, adapted from Eligehausen *et al.* [193].

2.3 Experimental programmes

This section presents a review of the most relevant experimental programmes addressing the bond characteristics of the concrete-steel interfaces. This topic was included to give an overview of the most relevant characteristics and results of the experimental programmes available in the bibliography, and also, to justify some of the choices made in the development of the interface model. Nevertheless, taking into consideration the scope of this work, it is only feasible to make a summarized review.

As mentioned before, the majority of the tests made to characterize the bond performance were made under *quasi*-static conditions. Data available with dynamic loading is still rare and limited to simple test layouts, mainly due to technical difficulties with these tests. The data available for RC structural elements is even more limited or inexistent. This increases the difficulty in validating the models for general loading situations.

The classification presented in Figure IV.4 seems to be a convenient and representative way to classify the experimental programmes and an additional group named *other tests* was included to contain the tests with specific characteristics that do not fit the first types. This classification includes the analysis of geometric, loading and boundary conditions of the specimens. The classification adopted in this work is very similar to the one used by Dominguez [172]:

i. Pull-out and/or push-in tests;
ii. Tests with RC ties;
iii. Tests with RC beams;
iv. Other tests.

The works of Lowes [342] and Dominguez [172] present an updated review of the experimental programmes on the bond mechanism. These documents provided most of the information presented in this section and should be consulted for further details.

2.3.1 Pull-out and/or push-in tests

- Pull-out and push-in tests by Viwathanatepa, Popov and V. Bertero

In 1979, Viwathanatepa *et al.* [558] published a very complete and pioneer experimental work regarding the response of ribbed bars anchored in concrete blocks. The test layout is represented in Figure IV.16-a and consists of concrete specimens fixed to a reaction wall, with 25 inches of width, 48 inches of height and 10 inches of thickness. The complete experimental activity consisted of 17 specimens with different bar diameters, anchorage lengths, longitudinal and transverse reinforcement amounts, loading and slip histories.

A typical test setup included a ribbed reinforcing steel bar (Grade 60) with 1 inch (25.4 mm) of nominal diameter, which is anchored over all the width of the concrete specimen $\left(L_a = 25 \text{ in.}\right)$. The longitudinal and transversal reinforcements presented ratios to the concrete volume of 2% and 0.8% respectively, and loading is applied at both ends of the protruding bar.

Although this experimental programme was considered a bar pull-out and push-in test, the geometry and boundary conditions are uncommon for these test types. Bending deformations were observed during the tests and these can induce non-uniform radial stress fields along the anchorage length, in particular, tensile stresses near the pull-out edge and compression stresses near the push-in edge, as reported by Lowes [342]. This issue is very significant and can completely change the bond properties. Thus, all the analysis made with these results must take this issue into consideration.

Most of the tests are characterized by having what is considered a long anchorage length. As a result, non-uniform bond stress distributions were observed by the authors along the anchorage (see Figure IV.16-b), even though the loading is applied at both bar ends. The length of the anchorage made the steel bar yielding possible and this must be taken into consideration in the analysis of the results presented in Figure IV.16-b. Another effect that probably had a large influence on the bond response is the radial stress variations, caused by the already mentioned flexural deformability of the specimen.

The monotonic response presented in Figure IV.16-c shows a very stiff initial response followed by intense and gradual stiffness degradation until the peak stress is reached. The global degradation is amplified by the yielding of the reinforcement bar. Afterwards, a softening branch occurs until a sliding friction plateau is reached.

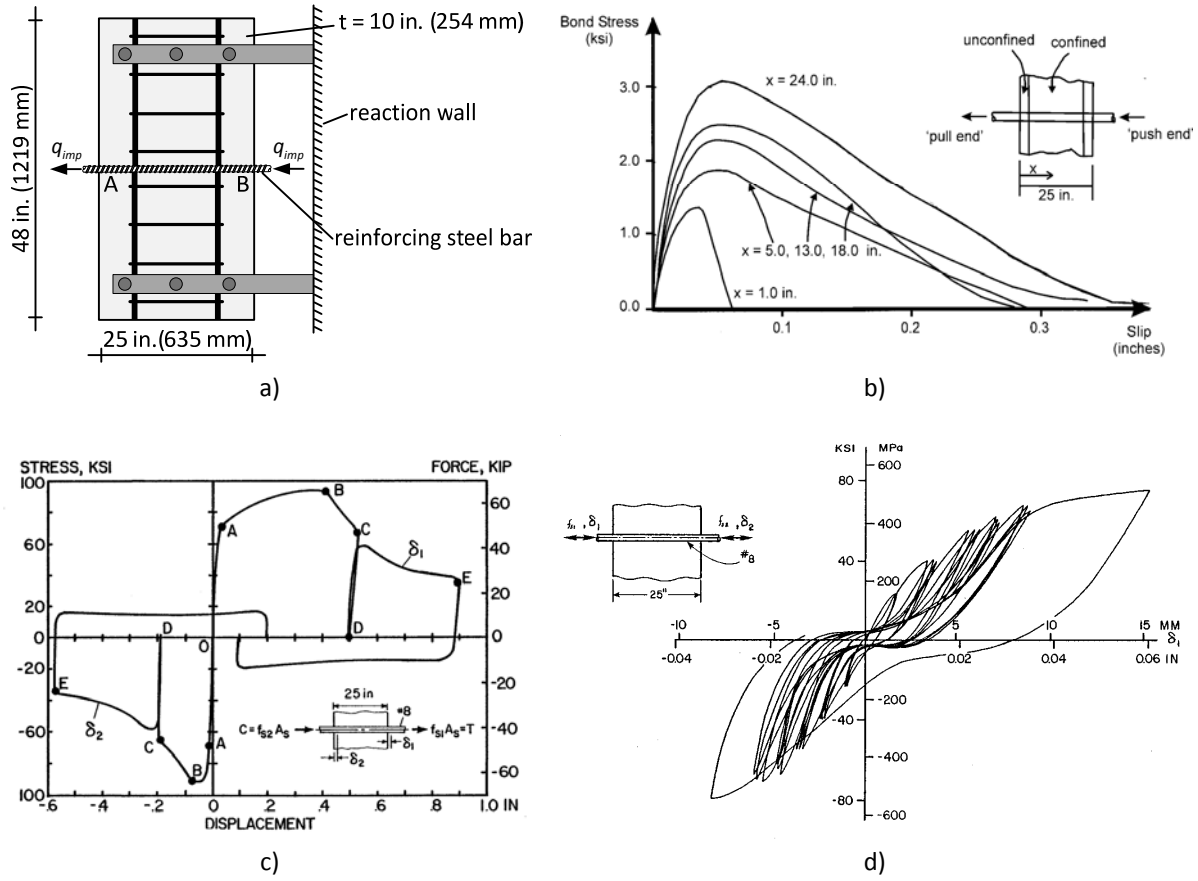

Figure IV.16: Tests performed by Viwathanatepa *et al.* [558]: a) test layout; b) bond stress and slip distribution; c) bar stress *vs.* slip under monotonic loading; d) bar stress *vs.* slip under reversed cyclic loading.

The post-yielding cyclic response presented in Figure IV.16-d shows than upon load reversal the global response is characterised by low stiffness branches, followed by sudden stiffness regains. When compared to the monotonic response, cyclic degradation is also visible by observing the relative continuous decrease of the peak stress values.

This programme also tested the influence of the bar size on the bond properties by using different reinforcement diameters, ranging from nominal bar sizes #6 to #10 (0.75-1.25 inches, 19-31 mm). According to Lowes [342], the results indicate that increasing the bar diameter slightly decreased the bond resistance (about 15% decrease between bar #10 relatively to bar #6), both under monotonic and reversed cyclic loading.

Although this work resulted in a major breakthrough in the understanding of the bond mechanism, three test characteristics made it difficult to analyse the results and use them to feed numerical tools, namely:

i. the long anchorage, which makes the analysis of the local bond properties more complex and dependent on other parameters;
ii. the radial stress variations, which can completely change the response of the concrete-steel interface;
iii. the steel bar yielding, which introduces an additional level of complexity.

- Bar pull-out tests by Eligehausen, Bertero and Popov

Probably the most famous and complete experimental programme made on bond performance was presented by Eligehausen *et al.* [193]. Sharing two authors with the work of Viwathanatepa *et al.* [558], this can be seen as having some level of continuity with that work. As a matter of a fact, all three issues that placed difficulties for the analysis and usage of the first results, were not adopted in this test programme (long anchorage length, deformability of the specimen, yielding of the reinforcements). This work resulted in valuable and reliable data that has been used in several subsequent works.

The vast experimental programme included 125 specimens tested in a pull-out configuration. Figure IV.17-a presents the test layout that consists of a concrete specimen of 15x12x7 inches (381x305x178 mm) with a compressive resistance of about 30 MPa. An embedded ribbed reinforcing bar, with 1 inch of diameter, crosses the entire specimen. The bar is disconnected from the concrete near both edges to avoid stress concentrations and perturbations that could lead to erroneous results (see Figure IV.17-a). The resulting anchorage length is 5 inches $\left(5\phi_s\right)$, which is considered to be small and should result in nearly uniform slip and stress distributions. Probably, there is not enough anchorage length to force the reinforcements into yielding. Loading is imposed using controlled displacements at one edge of the protruding bar (point A in Figure IV.17-a), even under reversed cyclic loading, and the displacements are measured at the opposite edge of the bar (point B in Figure IV.17-a). The amount of longitudinal and transversal steel reinforcements was set to 0.8% of the concrete volume, whenever these parameters were not subjected to a particular study.

The experiments included a series of tests to characterize the response under monotonic loading

(see Figure IV.17-b). These tests showed an initial very stiff phase that decreases gradually until the peak stress is reached. After that point, the resistance decreases until reaching a friction plateau, which commences approximately at a slip level equal to the clear distance between ribs.

The authors concluded from this study that the bond strength is proportional to the square root of concrete compressive strength and found that the deformability of the interface is inversely proportional to the same parameter [193].

The authors also concluded that splitting cracks induce the premature failure of the connection and that passive transversal reinforcements are an efficient way to avoid this premature failure mode. In the results presented in Figure IV.17-c it can be seen that a relatively small amount of transversal reinforcement is enough to avoid this failure mode. However, increasing the amount of transversal reinforcements will not lead to a peak resistance increase for the pull-out failure mode.

The effect of active confining forces was also analysed in this work. It was possible to conclude that compressive pressure leads to a significant increase in the bond strength. The results presented in Figure IV.17-d show that a lateral compressive pressure of only $0.17 f_c$ results in a peak stress increase of about 15%. Nevertheless, increasing this value by 2.5 times to $0.44 f_c$ will only result in a gain of 22%, revealing that after some level of active confinement the gains are much less significant.

Regarding the response under reversed cyclic loading, the experimental results showed stiff unloading branches that are followed by sliding friction zones that occur until the stiffness is recovered in the opposite direction. This work also concluded that for ribbed bars the most important parameter for the characterization of the cyclic degradation is the load history, in particular, the maximum slip reached in the previous cycles. They also identified a significant influence due to the number of cycles and the difference between peak slips in alternating directions. The authors concluded that for cycles with amplitude up to 80% of the peak stress slip, the degradation is only moderated in terms of resistance. This is clearly visible in Figure IV.17-e. For cycles with slip amplitude that exceeds the peak stress slip, the strength and stiffness of the interface is substantially affected in each cycle (see Figure IV.17-f). This work also presents the results under reversed cyclic loading for up to 10 cycles with gradual variations in the cycle amplitude. These results were used to simulate the cyclic resistance degradation and are presented in more detail in section 3.3.1.

The authors stressed that an increase of bond strength around 20% is expected when the reinforcement spacing passes from one to four bar diameters and that after this value no further gain is observed. In addition, it was possible to observe with a specific series of tests that the bond strength tends to increase at higher loading rates.

This programme also tested the influence of the bar size on the bond properties by using different steel bar diameters, ranging from nominal bar sizes #6 to #10 (0.75-1.25 inches, 19-31 mm). As emphasized by Lowes [342], this work reports that the bar #10 achieved a peak stress 10% inferior to the bar #8, which also showed a strength 10% inferior to the bar #6, both under monotonic and reversed cyclic loading.

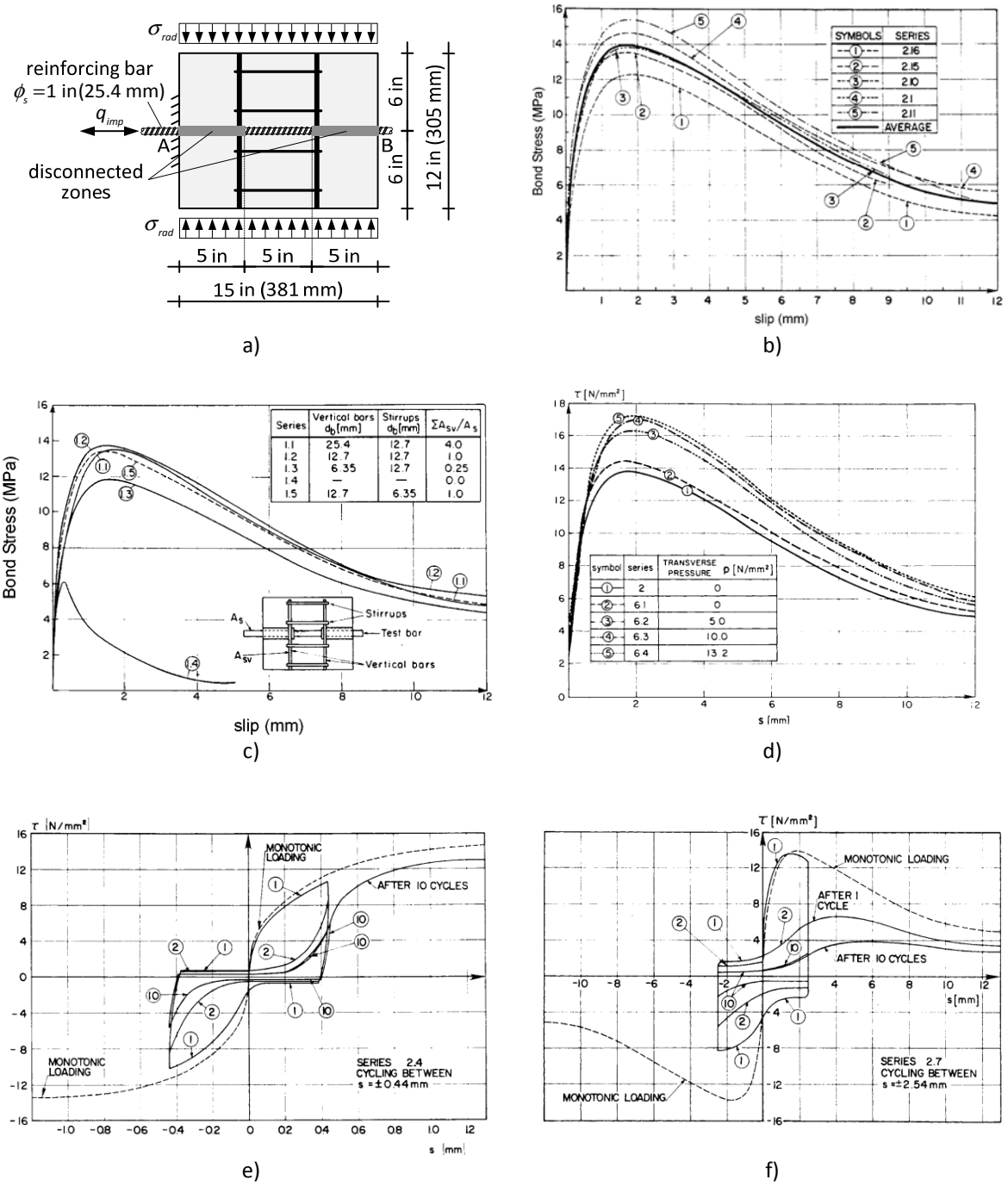

Figure IV.17: Tests by Eligehausen *et al.* [193]: a) test layout; b) response under monotonic loading; c) effect of the transversal reinforcement area; d) effect of active confining pressure; e) response under reversed slips with amplitudes of 0.44 mm; f) response under reversed slips with amplitudes of 2.54 mm.

- Bar pull-out tests by La Borderie and Pijaudier-Cabot

The work of La Borderie *et al.* [317] consists of a series of pull-out tests made with 80 mm concrete cubes (see Figure IV.18-a), which presented a compressive strength of 14.5 MPa at the time of the test $\left(E_c = 15.5 \text{ GPa}, \nu_c = 0.17\right)$. Embedded in the concrete cube is a protruding ribbed steel

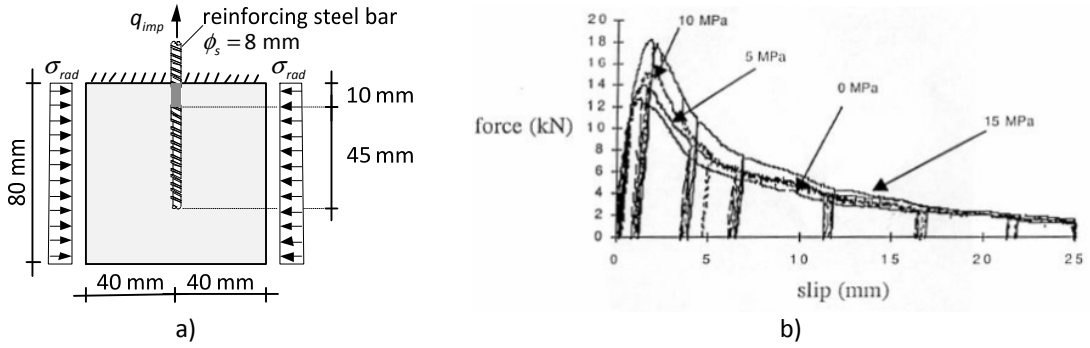

Figure IV.18: Tests performed by La Borderie [317]: a) test layout; b) effect of the active confining pressure.

reinforcement with an anchorage length of 45 mm. To avoid misleading results caused by stress concentrations, the bar is disconnected from the concrete on the 10 mm near the bar's insertion point. The main objective of this study was to assess the effect of the stress state on the bond performance. Therefore, the tests were performed with four levels of confinement: 0, 5, 10 and 15 MPa.

The results from this experimental programme confirmed that the presence of confining forces inhibits the development of splitting cracks that weakens the strength of the interface. Moreover, when compared to the case without compressive pressure the test showed an increase of the bond peak stress of about $\{11\%, 20\%, 45\%\}$ for $\{5, 10, 15\}$ MPa of confining pressure.

- Bar pull-out tests by Malvar

The work presented by Malvar [352, 353] comprises twelve specimens tested in a pull-out layout. This test programme is focused on the effects of active confining forces on the bond mechanism. The test layout is presented in Figure IV.19-a and consists of concrete cylinders with 3 in. in diameter and 4 in. long with an embedded #6 nominal bar size and with different rib patterns (inclined and perpendicular to the bar axis). The anchorage length is limited to five ribs by silicone rubber spacers (see Figure IV.19-a).

For tests #1 to #5, the concrete presented a mean compressive resistance of 5830 psi (40.2 MPa), the ribs are inclined and form an 68° angle with the longitudinal axis, the measured rib spacing is 0.481 in. (12.2 mm) and the clear rib spacing is 0.36 in. (9.2 mm). With the objective of obtaining data independent of the amount of concrete, the author decided to preload all the specimens until reaching splitting crack formation, unload the specimens, apply the confinement pressure and reload the specimen until failure. In the first loading phase, it was not possible to establish a clear relation between the confining pressure and the bond strength before the development of the splitting cracks. On the other hand, in the post-cracking range, the increases in the confining pressure resulted in a clear increase in bond strength. This is clearly demonstrated in the bond stress *vs*. slip diagrams presented in Figure IV.19-b.

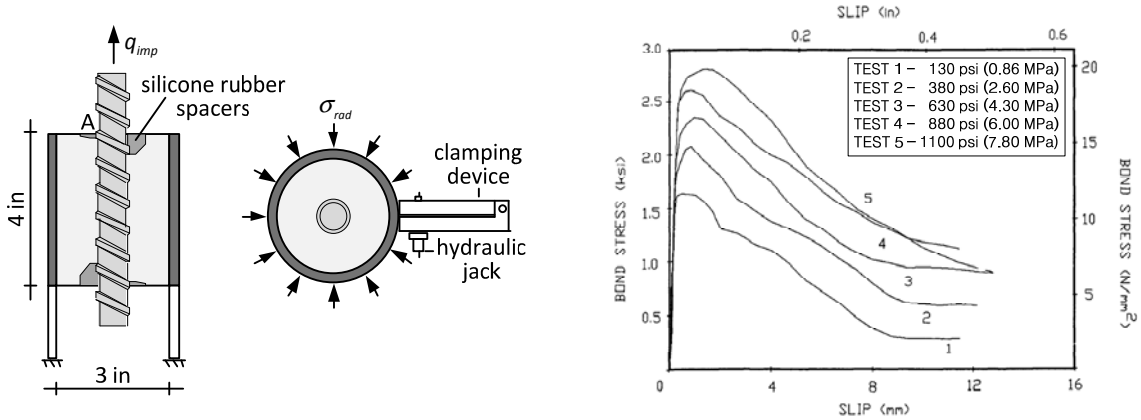

Figure IV.19: Tests performed by Malvar [352]: a) test layout; b) effect of the active confining pressure.

- Bar pull-out tests by Shima-Chou-Okamura

The work of Shima *et al.* [506, 507] is also very relevant because it is one of the few experimental programmes that is focused on the characteristics of bond performance in the post-yield range. A series of pull-out tests was made on large-diameter (50 cm) concrete cylinders, with the purpose of avoiding splitting cracks and harmonizing the stress state in the concrete (see Figure IV.20-a). A reinforcing bar with 19 mm in diameter is embedded and centred inside the concrete specimen and crosses the entire concrete cylinder length $(60\phi_s)$. A long anchorage $(50\phi_s)$ was used in order to enable steel yielding. The reinforcement is disconnected from the concrete over a length of $10\phi_s$, near the loaded concrete edge (see Figure IV.20-a).

A screw-shaped deformed bar is used instead of the traditional ribbed bars in order to facilitate the attachment of a set of strain gauges. These gauges are placed at a distance from the loading edge of $2.5\phi_s$ and $5.0\phi_s$, and at the transition to the disconnected bar length (see Figure IV.20-a). A series of specimens with steel bars with different yield strength was tested. The bar strength is labelled SD30, SD50 and SD70, which presents a yield strength of 350, 610, 820 MPa, respectively. Figure IV.20-b shows the stress *vs*. strain diagrams of these bars.

After a set of algebraic computations to estimate the yielding position with the information of the strain gauges, the authors achieved the bond stress *vs*. slip diagrams presented by the markers in Figure IV.20-c. In these diagrams a sudden and significant loss of strength can be clearly seen after yielding.

According to Shima *et al.* [506], the bond stress *vs*. slip relation is dependent on the steel stress-strain relationship, in particular, on the yield strength, strain from which strain hardening starts and the stiffness at the strain hardening range. To cope with this, the authors proposed a relation between bond stress, slip and steel strain to be applicable to the post-yield range. The results from this model are represented by the continuous line in Figure IV.20-c and show a good agreement with the experimental results.

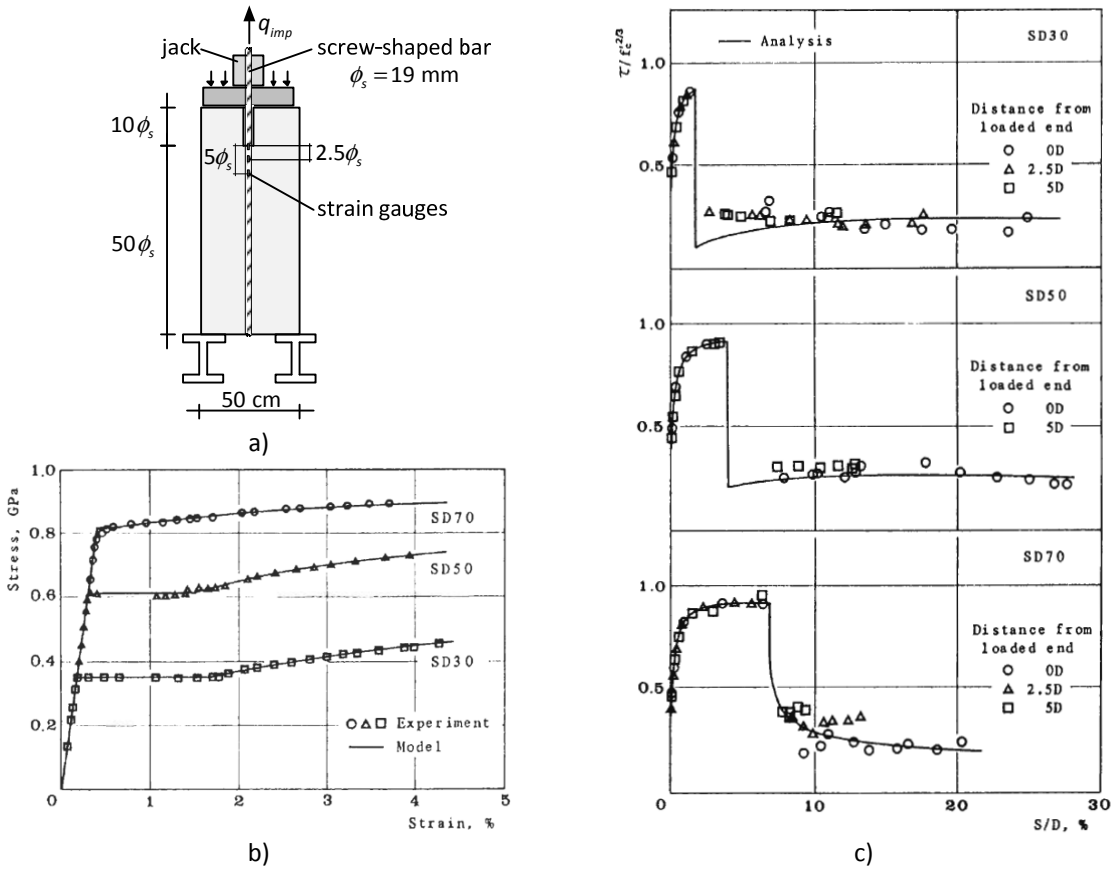

Figure IV.20: Tests performed by Shima *et al.* [506]: a) test layout; b) steel bar stress-strain curves; c) computed bond stress-slip curves for specimens with reinforcing steel bars SD30, SD 50 and SD 70.

- Bar pull-out and push-in tests by Gambarova and co-workers

Gambarova and co-workers published several works based on experimental campaigns addressing the bond mechnism. One of these works addressed the effect of splitting crack on the bond [230, 231]. This is achieved by a series of pull-out tests made with short anchorage and concrete specimens with preformed splitting cracks (see Figure IV.21-a). The experiments were made by controlling the opening of the pre-existing crack or by applying a constant compression force, creating a similar effect to passive or active confining forces. The authors concluded that the opening of splitting cracks has a negative effect on the bond performance and that the bond strength and the active confinement stress have a linear dependency.

Another topic addressed by Gambarova and co-workers is the influence of the size effect on the bond performance, see Coronelli *et al.* [144] and Bamonte *et al.* [28]. A series of pull-out and push-in tests were made with smooth and ribbed reinforcements and cylindrical ordinary and high strength concrete specimens. Splitting cracks were controlled by surrounding the concrete with a steel sleeve (see Figure IV.21-b). The specimens are characterized by having different relations between the bar diameter and the concrete specimen size, which influences the anchorage length. The authors concluded that the size effect has a different nature for smooth and ribbed bars. For smooth bars,

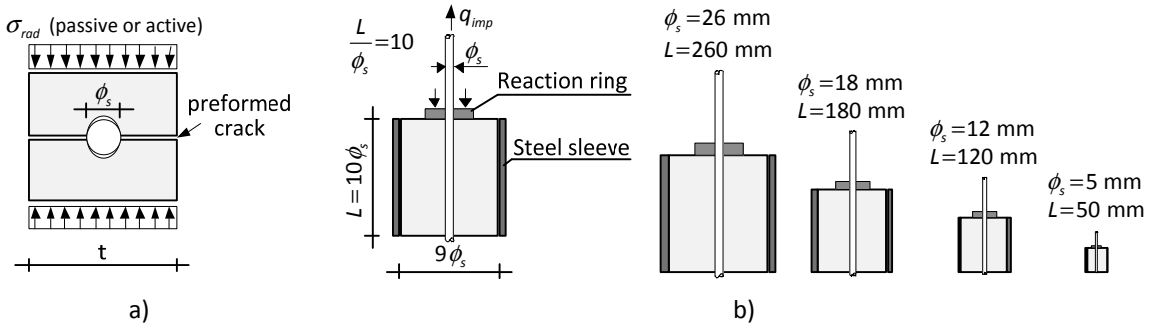

Figure IV.21: Tests by Gambarova *et al.* [231]: a) tests on the effect of splitting cracks b) tests on the size effect with smooth bars, taken from [172].

the size effect is mainly due to bar debonding, which is strongly correlated to the anchorage length. For ribbed bars, the size effect is more associated with the concrete inelastic behaviour near the ribs. According to Bamonte *et al.* [29], the observed size effect can be described by Bažant's general-purpose size effect law and is more significant for the specimens made with high strength concrete, as a consequence of inferior deformation capacity.

- Other tests

For historical reasons, the pioneer work of Rehm [473, 474] and Lutz *et al.* [346, 347] should be mentioned. The former work is recognized as the first monotonic pull-out tests addressing the subject of the bond for smooth reinforcing bars and the latter included a rebar with a single rib. See Dominguez [172] for more details.

2.3.2 Tests with RC ties

- RC tie tests by Clément

In 1987, Clément [113] presented an experimental programme with RC ties as part of his doctoral thesis that involved testing seven prismatic specimens with a square cross-section of 10 cm and 68 cm long (see Figure IV.22-a). A micro-concrete was used due to the small dimensions of the specimens. The concrete used is characterised by a compressive strength of $f_c = 32$ MPa and a tensile strength of $f_{ct} = 2.8$ MPa. Embedded and centred in the concrete can be found a high bond reinforcing steel bar with 10 mm of diameter. The test was made imposing a series of monotonic *quasi*-static displacements on both reinforcing bar edges.

The results obtained in this experimental programme are represented in the force *vs.* displacement diagram presented in Figure IV.22-b. The curves for the three tests made show that the response is initially very stiff and almost linear. Afterwards, the curve shows a strong stiffness decrease, probably related to bond failure and to concrete micro-cracking. The formation of the transversal macro-crack is clearly visible in the sudden loss of force in the diagram. Clément reported that the first macro-crack appeared between 21 cm and 31.5 cm of the closest longitudinal edge. The tests were stopped

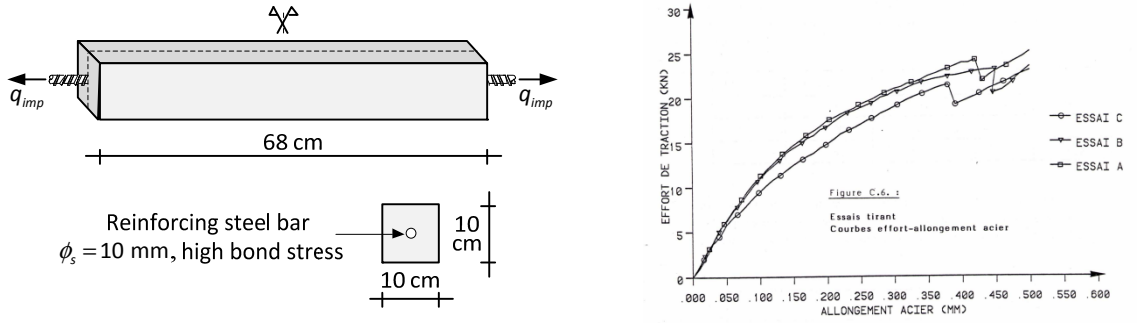

a) b)

Figure IV.22: Tests performed by Clément [113]: a) test layout; b) force-displacement curves for the three specimens tested.

soon after the crack formation.

The concrete was instrumented with eight strain gauges and the reinforcing bar with seven gauges. The results obtained by the strain gauges are also available. However, it is difficult to use this data because it represents a sparse discrete measurement of local quantities.

Similarly to what is defended by Dominguez [172], the main disadvantage of this experimental programme is considered to be the fact that the tests were stopped soon after the creation of the first macro crack. It would be interesting to analyse the behaviour after the creation of the two new bond units.

- RC tie tests by Dauod

The test with RC ties performed by Daoud [158] also used a prismatic square cross-section of 10 cm, similar to the tests performed by Clément, although in this case the length of the tie is 100 cm (see Figure IV.23-a). For common bond characteristics, a specimen with this length is considered to be a long tie (see section 2.2.1), and consequently, if the test in not stopped prematurely, it is expected to observe several cracks with a spacing pattern clearly defined and practically constant. This is the case of the tested specimens presented in Figure IV.23-b.

These tests included specimens made with ordinary vibrated concrete and self-compacting concrete, with a compressive strength of 45 MPa and 42 MPa, respectively. The reinforcing bar presented a diameter ranging from 12, 16 and 20 mm and smooth and ribbed reinforcements were included in the study.

The typical force-displacement curves for the tests with ordinary vibrated concrete and self-compacting concrete are presented in Figure IV.23-c, by the symbol BV/BO and BAP, respectively. These curves show an initial very stiff response, much larger than the response of the reinforcement alone, which is also represented in the figure. With the developments of transversal cracks, the stiffness of the element tends to decrease and approximates that of the isolated reinforcement bar. Even after the stabilization of the cracking process, the additional stiffness associated with the concrete between cracks, or in other words, the well-known tension stiffening effect can be seen.

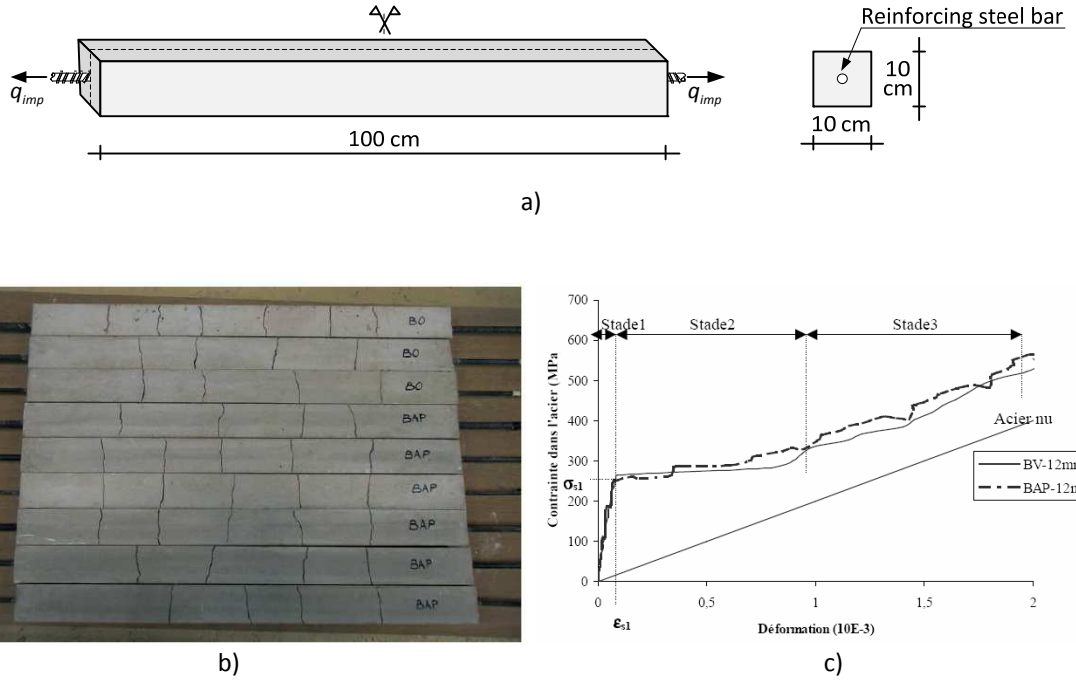

Figure IV.23: Tests performed by Daoud [158]: a) test layout; b) some of the specimens after testing; c) typical force-displacement curves for ordinary vibrated concrete and self-compacting concrete specimens.

- Other tests

Another important experimental programme involving RC ties was developed by Goto [251]. This test series focused on the understanding of the load transfer between the steel bar and the concrete. With that purpose, an ink injection system was included in the specimens to put ink under pressure near the concrete-steel interface. This ink filled the cracks and voids created throughout the test. At the end of the test, it was possible to inspect their shape and distribution by cutting the specimen longitudinally. Nevertheless, the effect of having embedded an ink injection system and of the ink itself is likely to have changed the results from the tests. Nevertheless, the objective of observing the bond mechanism qualitatively was fully achieved.

2.3.3 Tests with RC beams

- RC Beam tests by Türk, Benli and Calayir

Türk and co-workers published two works addressing the bond performance of tension lap-splices, see Türk *et al.* [547, 548]. This last work consisted of an experimental campaign with twelve rectangular full-scale beams with 2000x300x300 mm. The tests were made in a typical four-point bending configuration (see Figure IV.24-a), creating a shear-free constant moment zone. All the specimens presented a 310 mm lap splice in the constant moment zone. This length was selected so that bars would fail by splitting the concrete cover before reaching the yield point. Four groups of

three specimens were created by combinations of different diameters of the bottom reinforcements (16 or 20 mm) and different concrete types (normal NC, or self-compacting SCC). The self-compacting concrete is expected to deliver superior bond strength when compared to normal concrete with the same compressive strength, due to the contribution of the enhanced workability that allows a better concrete filling near the reinforcements.

After comparing the specimens with the same bottom reinforcements and with different concrete types, the authors concluded that the specimens made with SCC mixes presented about 4% more strength than the specimens made with common concrete.

According to Türk *et al.* [547], a considerable size effect was found in the experimental results, *i.e.*, as the diameter of the steel bar increased from 16 to 20 mm the bond strength decreased, regardless of the concrete type.

Figure IV.24-b presents the global force-displacement curve. An initial stiffer branch can be seen until cracking, which occurred at approximately 65 kN for the SCC specimens and 56 kN for the NC specimens. Afterwards, cracking develops by creating bending vertical cracks and some inclined cracks for higher loads. The cracking pattern is presented in Figure IV.24-c and Figure IV.24-d. Failure occurs by splitting the concrete cover near the lap-splice.

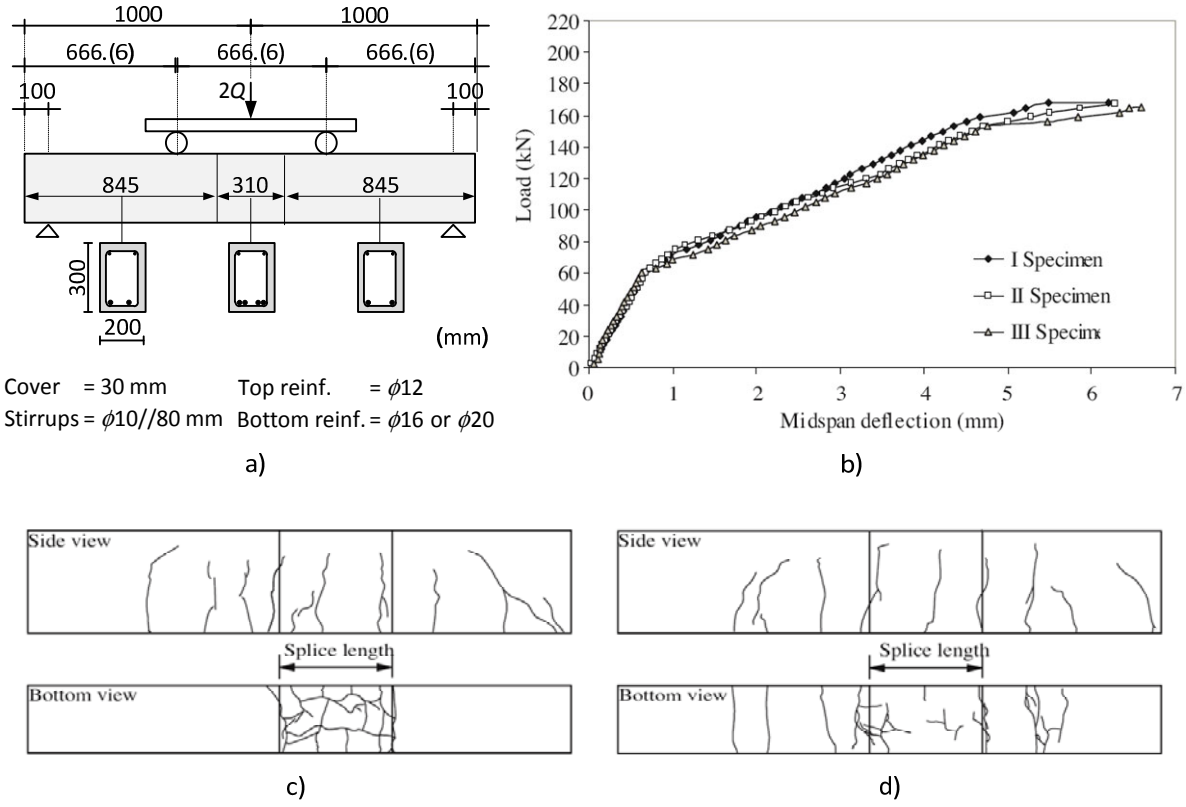

Figure IV.24: Tests performed by Türk *et al.* [547]: a) test layout; b) global force-displacement curve for the specimen B.SCC.16; c) crack pattern for the specimen B.NC.16; d) crack pattern for the specimen B.SCC.16.

- Other tests

Many experimental programmes made with RC beams could be included in this section (*e.g.* experimental programmes by Burns and Seiss [73] and Ma *et al.* [348]). However, the criterion adopted was to include only tests made with the specific intention of studying the bond performance and not to study the response of RC beams or other members.

2.3.4 Other tests

- Corrosion tests by Ouglova and co-workers

A series of five specimens were tested in a special configuration developed by Ouglova *et al.* [425, 426] to study the effect of the steel bar corrosion on bond performance. Three reinforcing bars embedded in the concrete were submitted to accelerated corrosion using an external current source, resulting in a steel bar corrosion level that varied from 0% to 0.76% of weight loss (see Figure IV.25-a). The experiments were made by imposing a series of relative displacements to the reinforcing bars. As a result of the particular geometry of the specimens, it was possible to acquire 1024x1024 pixel images using a CCD camera (see Figure IV.25-b), which allows the analysis of the bond mechanism using a different perspective than the one used in other experimental programmes.

In the bond stress *vs.* displacement chart represented in Figure IV.25-c, it is possible to observe that the bond strength increases for corrosion levels of less than 0.4% of weight loss. For higher corrosion levels these curves presents a clear bond strength decrease. These results are consistent with the analysis presented in section 2.2.4, namely the corrosion can be beneficial up to some level because the corrosion product represents a large increase in volume, which results in radial stresses that improve the bond strength. Afterwards, the strength is reduced mainly because corrosion induces cracking, reduces the effective cross-section area of the steel bar and the corrosion products can reduce the frictional component of the bond mechanism.

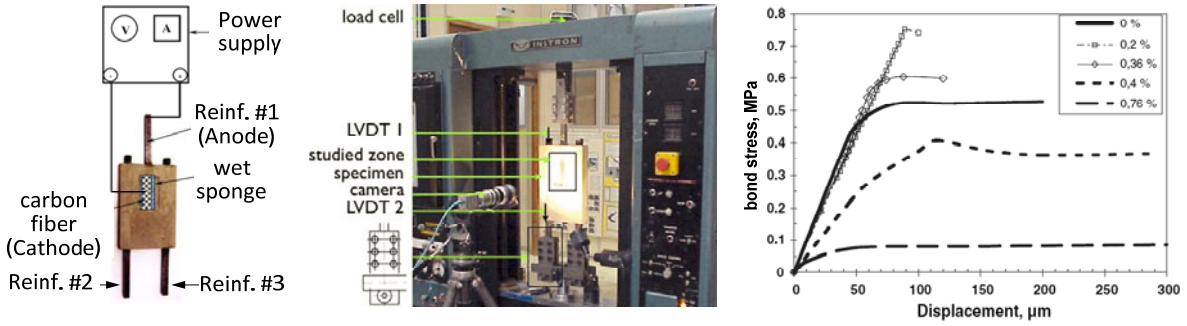

Figure IV.25: Tests performed by Ouglova *et al.* [426]: a) corrosion acceleration method; b) test layout; c) effect of corrosion on the bond stress.

2.4 Modelling the bond mechanism

2.4.1 Modelling scale

The first issue to be taken into consideration is what scale should be used to represent the bond mechanism. This is a fundamental aspect since all subsequent modelling techniques will be influenced by this choice. The classification regarding this issue adopted by Lowes [342] seems to be appropriate and will be followed in the review presented in the following paragraphs.

One possible way to include the bond mechanism in a numeric simulation is to represent it using a global response constitutive relation. This can be called modelling the concrete-steel bond on an *element scale* (see Figure IV.26-a). This type of approach has the advantage of being extremely effective from the computational point of view, because all the inelastic response, including bond and other inelastic sources, is included in a single force *vs*. displacement or moment *vs*. curvature relation. Consequently, this modelling approach is commonly used with one-dimensional elements like beams and columns. The main drawbacks of this methodology are related to not considering the inelastic response distributed along the element. Instead it is usually concentrated on critical sections (see Chapter III-§2.5.6). Moreover, merging all the inelastic sources into a single relation will end up not being flexible enough and adaptable to other cases, and commonly, each relation is deemed to be used on a specific geometry combination, type and position of reinforcements, *etc*.

On the other side of the spectrum is the *rib scale* representation of the concrete-steel bond (see Figure IV.26-c). In this technique, all bond-related elements are geometrically incorporated in the model, including the ribs of the reinforcements and the concrete keys between ribs. This methodology has the advantage of being extremely general and potentially very accurate. However, it is necessary to adopt very complex models to achieve this level of accuracy, since the constitutive relations must be able to adequately reproduce all inelastic phenomena (*e.g.* concrete cracking and crushing). Another consequence will be the size of the model that taking into consideration the capacity of current computers, will make this type of approach only feasible for local simulations, *e.g.* to calibrate constitutive relations to be used on global simulations.

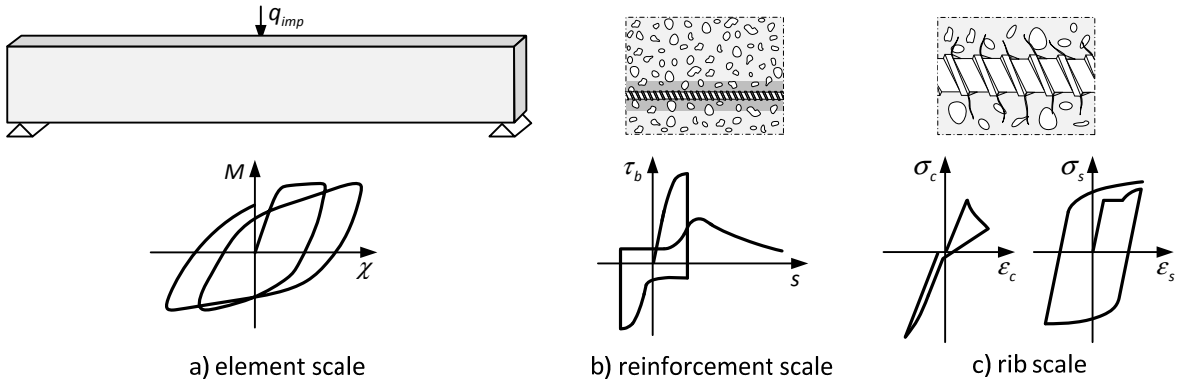

Figure IV.26: Some possible modelling scales for the bond mechanism simulation.

A possible compromise solution would be to model the concrete-steel bond at the *reinforcement scale* (see Figure IV.26-b). This approach uses a single constitutive relation, commonly defined in terms of bond stress *vs*. slip, to simulate all inelastic phenomena associated with the combined response of the reinforcement surface and of the surrounding concrete, *e.g.* concrete cracking and crushing. This constitutive relation is usually introduced in interface elements that include the reinforcement surface and the surrounding concrete. The fact of combining the bond response into a single model will mean that different bond characteristics (*e.g.* different rib types, different levels of corrosion or different concrete casting conditions) will require different bond constitutive relations.

2.4.2 Implementation in the framework of the finite element method

A discontinuity in the displacement field is created when the bond between reinforcement and concrete starts to fail. This discontinuity consists in relative displacements between adjacent points in the domain. In the scope of the finite element method, these displacement discontinuities can be simulated in several ways. It is possible to classify them as: i) *element-based*, when the discontinuity is embedded inside the element and no mesh modification is required; and ii) *mesh-based*, when the discontinuity simulation requires adding nodes and/or special interface elements. For now, the focus will be placed on the mesh-based discontinuity simulation. The following paragraphs present some of the possible techniques that can be used to implement this approach.

- Meshing

The first decision to be made is related to the approach used to incorporate the interface elements in the mesh. It is possible to use *interface elements in series* with the main domain as presented in Figure IV.27-a. This solution has the advantage of inserting the interface element into the global domain, and thus, the stress state is reflected on the interface elements, which is attractive for constitutive relations that depend on the stress state (*e.g.* radial stress effect on the bond mechanism). The implementation in two-dimensional or three-dimensional meshes is simple when the interface elements are associated with surface geometries (*e.g.* contraction joints in dams and soil-structure interfaces, etc.). However, when the discontinuity is associated with linear geometries (*e.g.* bond mechanism) the mesh discretization is extremely difficult to conceive and implement.

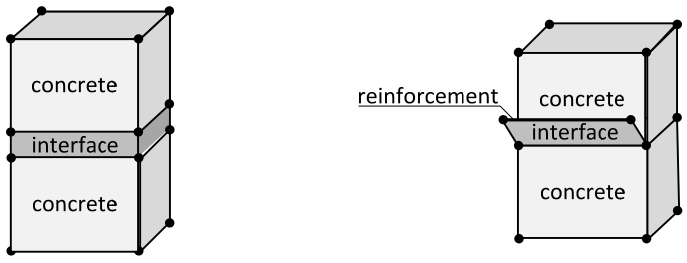

a) interface elements in series b) interface elements in parallel

Figure IV.27: Possible meshing techniques for mesh-based discontinuity simulations.

For those situations, using *interface elements in parallel* with the main domain (see Figure IV.27-b) presents some advantages. The mesh is simple to be generated even for three-dimensional analyses because the concrete sub-domain is unaffected and continuous. The interface elements enforce the connection with the linear-geometry elements used to simulate the reinforcements, as presented in Figure IV.27-b. The main disadvantage of this technique is that the interface element is insensitive to the stress state of the concrete domain, and consequently, when this information is needed it must be extracted from the concrete neighbouring elements.

- Type of interface element

A second option arises for the choice of type of interface element adopted. The simplest option would be using *discrete springs* (see Figure IV.28-a) together with linear or more advanced nonlinear constitutive relations. The main advantage of this technique is related to its simplicity. Nevertheless, the nodal-based definition is often considered as an important and limiting drawback.

Another possible approach would be modelling the interfaces as *zero-thickness elements* (see Figure IV.28-b).These elements were originally developed by Goodman *et al.* [248], however, it was only in the eighties that Beer [48] and Carol and Alonso [77] presented an isoparametric zero-thickness element to be used for interfaces. The element works as one-dimensional due to considering the mechanical formulation in the mid-plane of the interface. Their main advantages are related to the formulation and implementation simplicity and the fact of being able to produce accurate results.

Finally, the *thin-layer elements* can also be used (see Figure IV.28-c). These interface elements were introduced by Desai *et al.* [164], although there were previous works with similar techniques made by Zienkiewicz *et al.* [586] and Ghaboussi *et al.* [237]. It is considered that the interface mechanism occurs in a narrow finite zone and models the interfaces as thin continuum elements, *i.e.* with one dimension much smaller than the others. Consequently, this element behaves as a standard continuum element with the only peculiarity of being "*thin*" in one or more direction. The formulation of the thin-layer elements can be found in the work of Sharma and Desai [504]. In this work, the authors conclude that the thin-layer formulation can include the zero-thickness approach as a special case when $t \to 0$. In addition, a parametric study is presented and an empirical criterion is proposed for choosing the element thickness. This type of approach can simulate a wide range of practical situations involving interfaces with good accuracy. However, setting the correct thickness

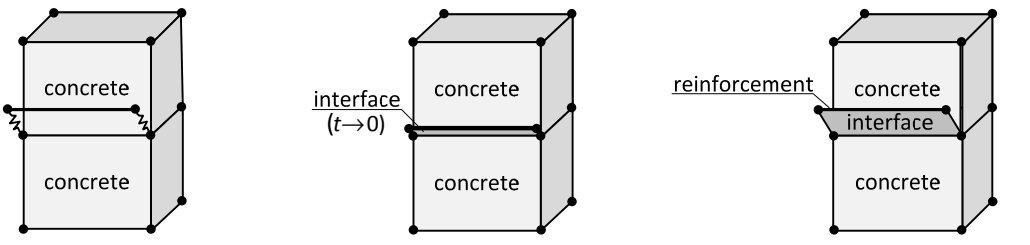

a) nodal springs b) zero-thickness elements c) thin-layer elements

Figure IV.28: Types of interface elements for bond mechanism simulation.

for each problem with an objective procedure is sometimes not easy to accomplish. Numerical problems have been reported for some types of these elements with very small thickness, *e.g.* degenerated standard continuum elements [172].

2.4.3 Review of the most important bond models

Models for simulating the bond mechanism have been developed since the sixties of the last century, resulting in a large number of proposals. These can be classified in several ways, for example simply chronologically, based on what type of hypothesis they adopt (*e.g.* uncracked concrete, elastic reinforcements, *etc*.) or in terms of the fundamental principles used to define the model. This last approach seems to be the one that produces a more clear distinction between the capacities and drawbacks of the models and was already adopted by other authors, *e.g.* Dominguez [172]. Adopting this approach, the models can be classified as *empirical,* if the basis is simply to simulate the global response of the phenomenon, without any attempt to model any of the participating phenomena. On the opposite side are the *analytical* models, which are not based on experimental results to simulate the bond response. They attempt to achieve this by modelling the intrinsic material behaviour in a framework of a theoretical material theory. In addition, *semi-analytical* or *semi-empirical* are those which combine the analytical and empirical approach.

The following paragraphs present a non-exhaustive list of the most relevant models that can be found in the bibliography. More details can be found in the state of the art reports [87, 88, 214] and in the individual references made.

- Empirical models

The first models to appear were purely empirical and used simple expressions to cope with experimental results. This is the case of expressions proposed by Rehm [474], Nilson [418], Mirza and Houde [400], Martin [371], Tepfers [538] and Shima *et al.* [507]. These models resulted in good simulations only for a particular number of cases and their lack of flexibility led to the decrease of usage. More details can be found in the bibliography [25, 214].

- Semi-analytical/semi-empirical models

The semi-analytical models appeared together with the first attempts to simulate the reversed cyclic response of bond. One of the first models to include this phenomenon was presented by Morita and Kaku [408], by assuming that after load reversal, the monotonic envelope was reached with increasing slips. However, according to Li *et al.* [336], the cyclic deterioration of the friction component was not adequately taken into consideration.

The model introduced by Tassios [536] was based on equilibrium and compatibility conditions of the reinforcing steel bar embedded in semi-infinite concrete domain. After some geometrical deductions, the following expression was proposed:

$$\tau_b + \frac{E_s \phi_s}{4} \frac{\partial^2 s}{\partial x^2} - \frac{E_s \phi_s}{4} \frac{\partial \varepsilon_c}{\partial x} - \frac{\nu_s \phi_s}{2} \frac{\partial \sigma_r}{\partial x} = 0 , \qquad \text{(IV.7)}$$

where E_s, ν_s and ϕ_s are the elasticity modulus, Poisson's coefficient and the diameter of the steel bar, respectively; σ_r and ε_c are the radial stress and the axial strain in the concrete; *s* is the slip between the steel bar and the surrounding concrete and *x* is the coordinate along the reinforcement axis. The local bond stress-slip constitutive relation is obtained after solving the differential equation (IV.7). Based on this expression, Tassios proposed a local constitutive relation with softening and residual stress branches. According to FIB [214], the major breakthrough of this model was to include cyclic deterioration for slips smaller or equal to the previous cycle peak slip.

In 1981, Ciampi *et al.* [111] proposed for monotonic loading the well-known expression for the ascending part of the curve:

$$\tau_b = \tau_1 \left(\frac{s}{s_1} \right)^{\alpha}, \quad 0 \le s \le s_1, \tag{IV.8}$$

which is followed by constant, softening and friction linear branches as represented in Figure IV.29-a.

A milestone version of this model that includes the hysteretic response was proposed by Eligehausen *et al.* [193], which was improved latter by Filippou *et al.* [218]. This model considers that the cyclic deterioration is simulated by multiplying the monotonic bond stress by damage variables. The expressions for these damage variables are defined by adjusting the dissipated energy obtained from experimental results as presented in Figure IV.30. For the reloading branch and for the reduced envelope (#4 and #5 in Figure IV.29-b), the expression to be used is:

$$d = 1 - \exp\left\{ -1.2 \left(\frac{E}{E_0} \right)^{1.1} \right\}, \tag{IV.9}$$

alternatively, for the friction branch (#3 in Figure IV.29-b), one should consider:

$$d_f = 1 - \exp\left\{ -1.2 \left(\frac{E_f}{E_{0f}} \right)^{0.67} \right\}. \tag{IV.10}$$

where E, E_0, E_f and E_{0f} are computed as presented in Figure IV.30.

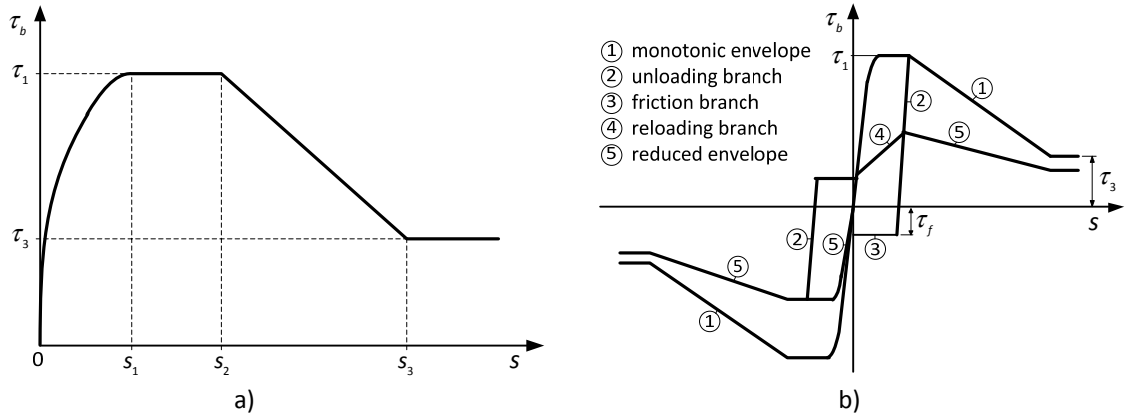

Figure IV.29: a) Bond mechanism model for monotonic loading proposed by Ciampi *et al.* [111];
b) Bond mechanism model for cyclic and alternating loading proposed by Filippou *et al.* [218].

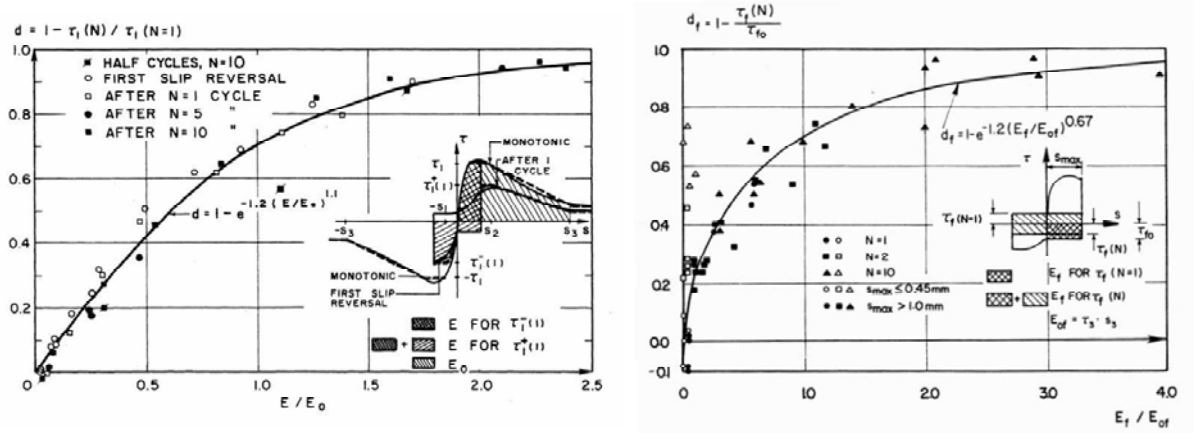

a) b)

Figure IV.30: Damage variable proposed by Eligehausen *et al.*, taken from [193]: a) general damage; b) friction damage.

Table IV.2: Bond model parameters for smooth bars adopted in the Model Code 90 [390].

Model Parameter	Unconfined concrete		Confined concrete	
	Good bond conditions	All other bond conditions	Good bond conditions	All other bond conditions
$s_1 = s_2 = s_3$	0.01 mm	0.01 mm	0.1 mm	0.1 mm
α	0.5	0.5	0.5	0.5
$\tau_1 = \tau_3$	$0.1\sqrt{f_{ck}}$	$0.05\sqrt{f_{ck}}$	$0.3\sqrt{f_{ck}}$	$0.15\sqrt{f_{ck}}$

Table IV.3: Bond model parameters for ribbed bars adopted in the Model Code 90 [390].

Model Parameter	Unconfined concrete		Confined concrete	
	Good bond conditions	All other bond conditions	Good bond conditions	All other bond conditions
s_1	0.6 mm	0.6 mm	1.0 mm	0.6 mm
s_2	0.6 mm	0.6 mm	3.0 mm	0.6 mm
s_3	1.0 mm	2.5 mm	clear rib spacing	
α	0.4	0.4	0.4	0.4
τ_1	$2.0\sqrt{f_{ck}}$	$1.0\sqrt{f_{ck}}$	$2.5\sqrt{f_{ck}}$	$1.25\sqrt{f_{ck}}$
τ_3	$0.15\tau_1$	$0.15\tau_1$	$0.40\tau_1$	$0.40\tau_1$

The *Model Code 90* [390] also addresses the bond mechanism. Basically, this design-oriented code adopts the monotonic relation propped by Ciampi, Eligehausen and co-workers (see Figure IV.29-a) together with a proposal of numerical values for the model parameter, both for smooth bars (Table IV.2) and ribbed bars (Table IV.3).

More recently, it should be mentioned the work carried out by Lowes [342] that addresses the mechanical behaviour of RC beam-column connections from bridges, using two-dimensional finite element analyses with the bond mechanism simulated within zero-thickness interface elements. The bond model starts with a simplification of the model proposed by Eligehausen *et al.* [193] and adds nonlocal state variables in order to consider the stress, strain and damage states of the concrete and steel in the vicinity of the concrete-steel interface.

The model proposed by Monti *et al.* [404] adopts a flexibility formulation to simulate the hysteresis response of RC elements, by formulating a frame element that includes the effect of bond failure. In the work of D'Ambrisi *et al.* [157], the frame element is also defined in a flexibility format, although in this case by considering the combination of several sub-elements, namely; an elastic sub-element, a spread plasticity sub-element, an interface bond-slip sub-element and a shear sub-element.

The semi-analytical modelling approach is still considered to be the most balanced and feasible formulation for the general loading case (*e.g.* cyclic and alternated loading). This formulation is the most used and has resulted in numerous proposals, *e.g.* Stanton *et al.* [524], Viwathanatepa *et al.* [558], Hawkins *et al.* [261], Pochanart and Harmon [457] and Balázs [26].

- Analytical models

As mentioned before, the analytical models are considered as those attempting to model the intrinsic material phenomena that govern the response, in the framework of a material theory. The main material models are based on linear or nonlinear elastic constitutive relations, on fracture and damage mechanics or on the plasticity theory.

One of the simplest formulations results from considering a linear elastic behaviour for all materials. The work of Russo *et al.* [491] presents the system of differential equations to be solved for computing the analytical solutions for any type of constitutive relation for the bond, considering uncracked concrete and a bilinear steel model. In addition, the expressions that govern the bond mechanism when the bond stress *vs.* slip relation is given by exponential, monomial or linear functions are also presented (see FIB [214] for details).

Developing a model based in the *plasticity theory* seems to be a feasible starting point because the bond mechanism is characterized by large inelastic deformations, together with stiff loading, unloading and reloading branches. Cox and Herrmann [150, 151] presented a non-associative plasticity model for modelling the concrete-steel bond between ribbed bars and concrete that allows considering the damage state at a finite-thickness region in the vicinity of the reinforcing bar. This region is defined with a width related to a characteristic length associated with the geometrical characteristics of the ribs. The plasticity model components (*e.g.* yielding surfaces, hardening and flow rules) are formulated considering a complete set of experimental results from pull-out tests. The

main disadvantage of this model is related to the resulting complexity even under monotonic loading, which makes the generalization to other loading cases very difficult to achieve.

Romdhane and co-workers proposed a set of models for modelling the bond mechanism, see Désir *et al.* [165] and Romdhane and Ulm [485]. These models adopt a classical continuous isotropic plasticity behaviour that is extended to account for bond deterioration and are implemented in a one-dimensional truss element with additional slip-related *dofs*. The same disadvantage stressed for the model proposed by Cox and Herrmann can also be associated with this formulation.

Some models were developed in the framework of the *damage mechanics*. This is the case of the model proposed by Clément [113] that is based on the adaptation of Mazars' model for concrete [381]. According to Dominguez [172], this model works well for small slips, despite the differences between the damage mechanics concept and the real response of the concrete-steel interfaces. For larger displacements, the typical problems of these formulations arise (*e.g. localization*), although nonlocal approaches were used to mitigate this problem, *e.g.* Pijaudier-Cabot [447]. According to Dominguez [172], the work presented by Daoud [158] also introduced an adaptation of Mazars' model to interface elements with better results in terms of the concrete fracture energy simulation.

More recently, the works presented by Dominguez [172] and Ragueneau *et al.* [467] propose using an inelastic constitutive model for the bond mechanism that decouples the normal and tangential bond response. This model is implemented in a thermodynamic framework and in the scope of the *continuum damage mechanics* (CDM). It allows simulating a large number of effects that influence the concrete-steel bond (*e.g.* cracking, inelastic strains, hysteretic behaviour, *etc*.). The constitutive model definition requires performing an explicit-implicit numerical integration for the tangential direction and an explicit integration for the normal direction. As emphasized in Dominguez [172], the authors reported some convergence difficulties in the constitutive model. The bond model is implemented in a zero-thickness interface element, based on a 2D-degenerated four-node quadrilateral element and was used in several two-dimensional analyses. The work of Dominguez [172], also presents the formulation of an enriched finite element defined within the framework of the *extended finite element method* (X-FEM). This seems to be an interesting step towards the definition of a reinforced concrete element, which includes the concrete, the reinforcing steel and their connection. Other analytical formulations that should be mentioned in this non-exhaustive review are the work of Gastebled and May [233], which is defined within the framework of rupture mechanics, and the work of Ghandehari *et al.* [238] also defined within the same framework together with a cohesive crack model. Finally, the work of Maker *et al.* [351] that adopts contact mechanics concepts should also be mentioned. A summary of these models with a brief appreciation is presented in Dominguez [172].

As a conclusion, it is possible to stress that the majority of analytical bond models are based on strong theoretical material formulations with a very attractive mathematical definition, although sometimes extremely complex. When compared to semi-analytical models, these models still present significant drawbacks related to the inferior numerical efficiency and to difficulties for the extension to general loading situations (*e.g.* cyclic and earthquake loading).

3 Development of the bond model

3.1 Introduction

This section is dedicated to the development of a new bond model defined at the reinforcement scale (see section 2.4.1). Using this approach it is possible to include the main mechanical characteristics of the bond mechanism without creating a prohibitive model size. The bond model is defined along the reinforcement axis and relates the bond stress to the relative displacements between the steel bar and the concrete. The bond model is uncoupled from the model for the radial directions discussed later on in section 4. Nevertheless, the effect of radial-related phenomena (*e.g.* radial stress) can still be included in the bond model. The bond mechanism is influenced by a large number of heterogeneities and other local random factors, so the formulation presented here should be interpreted as an averaged mechanical model for the concrete-steel interaction.

The objectives and priorities should be defined before starting the development of the bond model. At first, the model is designed to be used under general loading situations, such as earthquake loading. Therefore, it is mandatory that the model is prepared for dealing with reversed cyclic loading. In addition, this model is designed to be used in large three-dimensional simulations that require that all constituent parts to be as efficient as possible. Taking into consideration these requirements and the analysis carried out in section 2.4.3, it is possible to conclude that the most feasible approach is to develop a semi-analytical model implemented at the reinforcement scale.

The choice of the phenomena to be incorporated in the model is also of great importance. A strict criterion should be set to differentiate which effects are to be incorporated and which should not be considered, always by balancing the quality of the simulation against the additional complexity and computational cost to be paid. The summarized review presented in section 2.2 is a valuable source for defining the chosen effects. As a result, the model should be able to simulate:

i. the response in the perfect bond domain;
ii. the premature collapse for smooth bars (failure mode I in Figure IV.9-a);
iii. the stiffness decreases for ribbed bars until the peak stress is reached;
iv. the effect of splitting cracks on the peak stress (failure mode II or III in Figure IV.9-a);
v. the softening and friction branches after the peak stress under monotonic loading;
vi. the unloading and friction branches upon loading reversal;
vii. the stiffness regain on reloading;
viii. the cyclic degradation;
ix. the evolution of the slip at peak stress;
x. the evolution of the reload slip;
xi. the radial stress effect.

The effect of the steel bar corrosion cannot be explicitly simulated in the model by a specific parameter (*e.g.* corrosion level). Nonetheless, it is possible to adjust the model parameters to simulate this effect for reinforcing bars that are known to present corrosion.

The effect of the loading rate is not included in the model. Taking into consideration the results presented in section 2.2.4, this effect was considered to be not so important when compared to the levels of dispersion of the experimental results.

The bond-related size effect presented in section 2.2.4 can be simulated to some extent by using concrete models that are capable of simulating the softening behaviour of concrete. The continuum damage modelling technique together with a nonlocal regularization technique to control the localization phenomenon is a possible example.

It was considered preferable to have a simpler model formulation, even if sometimes the local accuracy would be compromised, than a complex mathematical definition. This option is supported by the assumption that for real situations the global response of a RC structural element is much more influenced by spatial bond failure variations than by complex local model definitions. As a result, linear branches were used to connect most of the key points used to define the model.

The model will be developed in several phases to separate as much as possible each feature and to develop a hierarchal-based solution. At first, the basic model will be presented that will act as the skeleton, and afterwards, it will be enriched with sub-models with the purpose of simulating specific bond-related phenomena. At the end, the complete mathematical description of the proposed model will be presented.

3.2 Base model

Figure IV.31 presents a schematic plot of the base model under monotonic and reversed cyclic loading. This model is characterized by:

i. Under monotonic loading (see Figure IV.31-a), the response starts with a stiffer linear loading branch with slope k_{pb}, until the slip value s_{pb} is reached. Afterwards, another linear loading branch connects the point at coordinates $\left(s_{pb}, \tau_0 = k_{pb} s_{pb}\right)$ to the peak stress at $\left(s_0, k_0 s_0\right)$. The peak stress is followed by a softening branch to $\left(s_{res}, f_1 \tau_0\right)$ and by a residual sliding friction plateau at stress level $f_1 \tau_0$;
ii. Under cyclic loading (see Figure IV.31-b), to cope with the stiff unloading branches observed in the experimental programs, a slope of k_{ul} is adopted for the unloading branches. Under reversed loading, an unloading sliding friction stress is reached at stress level $f_2 \tau_0$, after the bond stress changes sign. Reloading occurs in order to connect the friction stress at null slip to the peak stress τ_0 again at s_0. It should be noted that the stiffer loading branches with slope k_{pb} only occur for the first complete loading cycle.

Figure IV.32 compares the results obtained with this model with the average monotonic and cyclic responses reported by Eligehausen *et al.* [193] and represented in Figure IV.17-b and Figure IV.17-f, respectively. It can be easily observed that the monotonic response can be very well simulated with the base model. On the other hand, under reversed loading, there is a clear difference between the experimental and numerical results. The main differences are related to the incorrect peak stress simulation after the first loading, the incorrect simulation of the slip where reloading occurs and the

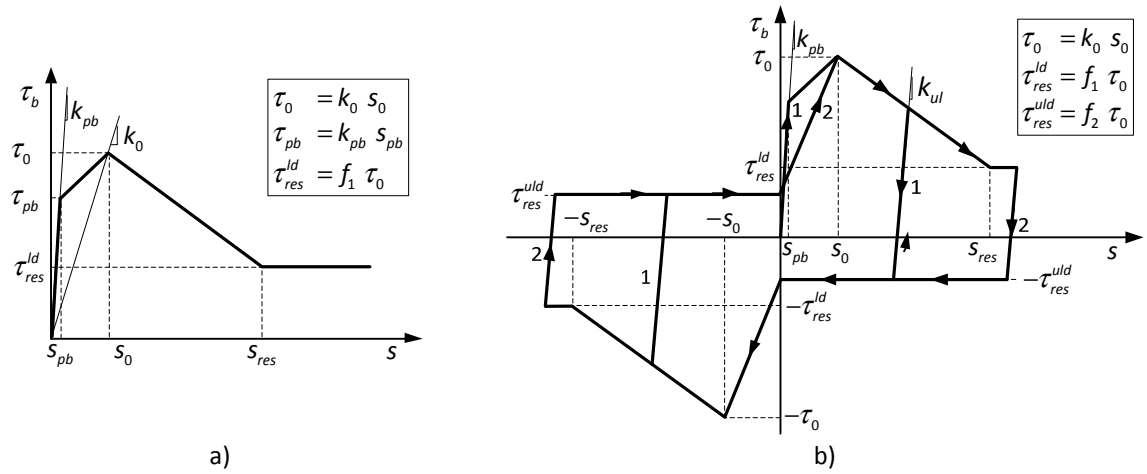

Figure IV.31: Schematic representation of the base model: a) monotonic loading; b) reversed cyclic loading.

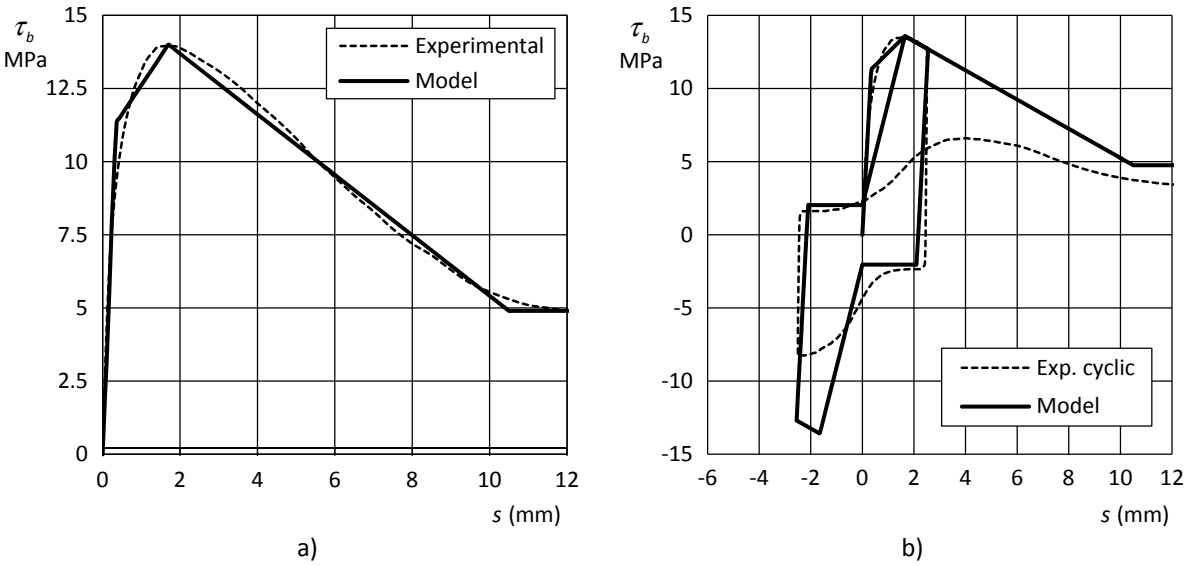

Figure IV.32: Base model - Comparison with experimental data [193]:
a) monotonic loading; b) reversed cyclic loading.

Model Parameters: $k_{pb} = k_{ul} = 32.94$ GPa/m, $k_0 = 8.235$ GPa/m, $s_{pb} = 0.343$ mm, $s_0 = 1.70$ mm, $s_{res} = 10.50$ mm, $f_1 = 0.35$, $f_2 = 0.15$.

incorrect simulation of the peak stress slip after the first loading.

In order to overcome these difficulties, the base model was enriched with a series of sub-models for considering: i) the *cyclic resistance degradation*, ii) the *peak stress slip evolution* and iii) the *reload slip evolution*. Subsequently, the base model will also be improved to take into consideration the effect of the radial stress using nonlocal information from the structural analysis. This phenomenon is especially important for introducing the effect of confinement.

The shape of the softening branch can be defined as nonlinear by changing the value of the parameter c_{soft}. This parameter can be set to zero resulting in a linear branch, or to values greater than zero that will result in increasing smother transitions to the residual loading plateau. Figure IV.33 illustrates the effect of this parameter for the same cases considered in Figure IV.32.

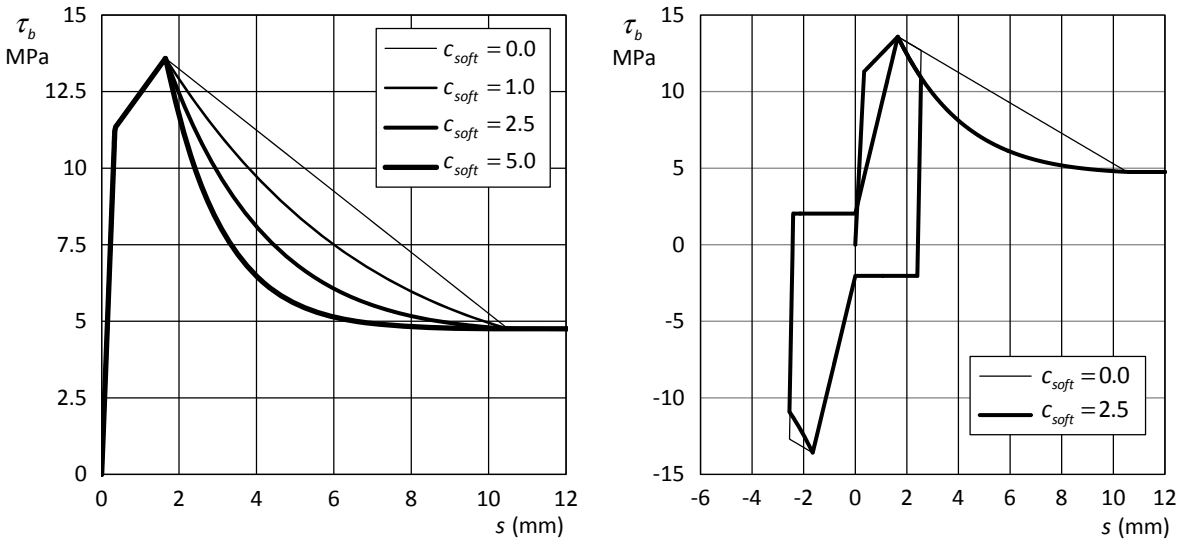

Figure IV.33: Effect of the parameter c_{soft} : a) monotonic loading; b) reversed cyclic loading.

3.3 Sub-models

3.3.1 Sub-model for the cyclic resistance degradation

The experimental data represented in Figure IV.34 was obtained by Eligehausen *et al.* [193] by performing a series of pull-out tests under reversed loading with RC specimens constructed with common reinforcing bars and concrete. The data presents the ratio between the stress before unloading at cycle *n* and the one for the first cycle. This quantity gives information related with the cyclic resistance degradation and is considered to be strongly related to the *cyclic peak stress ratio* defined by:

$$\gamma_b = \frac{\tau_0^{cyc}}{\tau_0^1}. \tag{IV.11}$$

Two distinct factors are presented together in Figure IV.34, namely the cycle amplitude and the number of cycles. These two factors can be combined into an equivalent value by introducing the non-negative parameter:

$$s^* = \frac{1}{s_0}\sum_{cyc}\tilde{s}_k, \tag{IV.12}$$

where $\tilde{s}_k$ represents the absolute value of the loading slip reached in each cycle and the sum is normalized by the initial peak stress slip. As an example, in the cases presented in Figure IV.34 the cycles have equal amplitude. Therefore the following expression may be used to compute s^*:

$$s^*(n) = (2n+1)\frac{s_{\max}}{s_0}. \tag{IV.13}$$

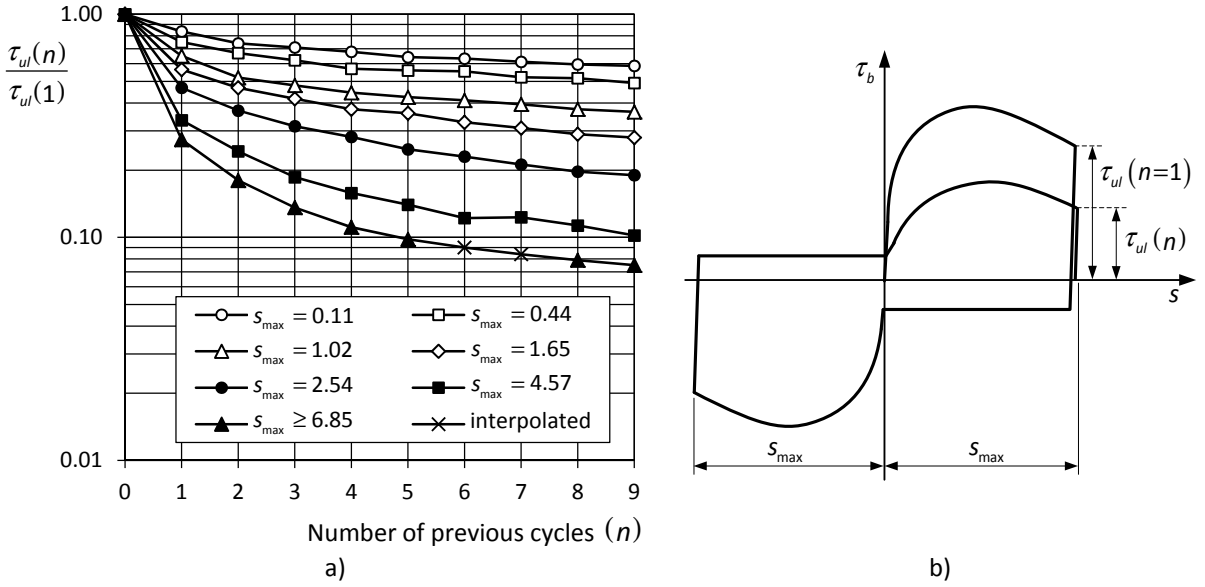

Figure IV.34: Bond strength deterioration with the number and amplitude of the cycles, adap. from Eligehausen *et al.* [193].

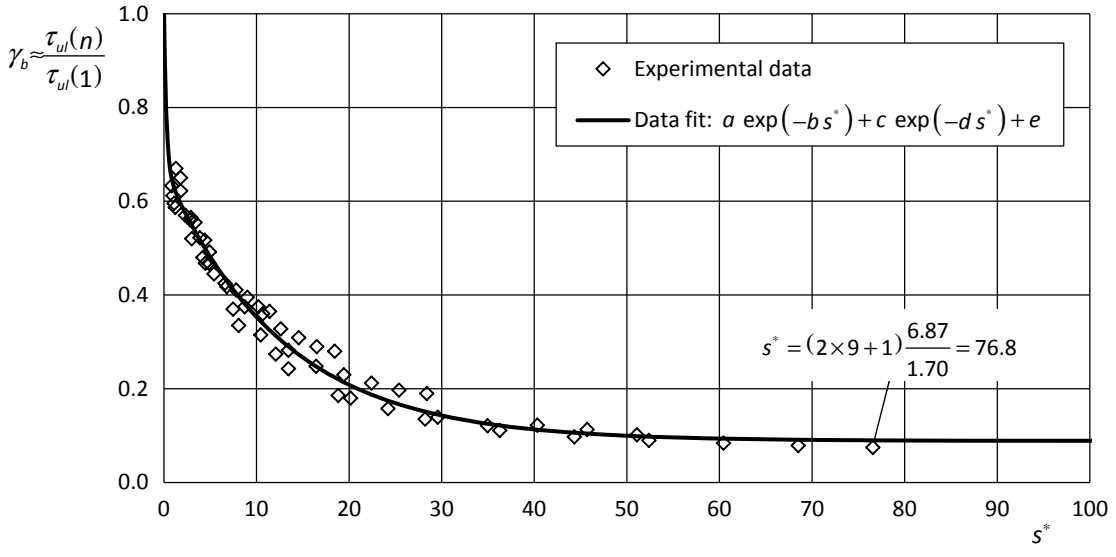

Figure IV.35: Relation between the cyclic peak stress ratio and the parameter s^*.

The same data represented in Figure IV.34 is re-plotted in Figure IV.35, showing a clear trend and correlation with the proposed parameter s^*. This data can be approximated with the following expression:

$$\gamma_b(s^*) = a\ \exp\left(-b\, s^*\right) + c\ \exp\left(-d\, s^*\right) + e\,. \tag{IV.14}$$

The unknown coefficients were computed by a nonlinear fit using the *Levenberg-Marquardt* algorithm [334, 369] resulting in *a*=0.5838; *b*=0.0792; *c*=0.3456; *d*=3.8290 and *e*=0.0887. The resulting fit is also presented in Figure IV.35 and it is possible to observe the good quality of the fit and relatively small data dispersion.

The adopted exponential relation (IV.14) returns $\gamma_b(0) \approx 1.0$ and converges asymptotically to the value at $\gamma_b(\infty)$. For $s^* = 100$ this approximation returns a value already very close $(<0.24\%)$ to the value for very large values of γ_b, thus for simplicity, this function is truncated at $s^* = 100$.

Although the expression presented in (IV.14) is closely associated with this specific experimental data, it can be redesigned to be more general and adaptable to other situations. With that purpose, two new parameters were inserted: i) γ_{res} that represents the *residual cyclic resistance ratio* after an infinite number of cycles and γ_n that can be used to change the shape of the curve and gives more flexibility and generalization to the sub-model.

The enhanced expression is given by:

$$\gamma_b\left(s^*\right) = \frac{\left(1-\gamma_{res}\right)}{1-e}\left\{a\ \exp\left(-b\ \gamma_n\, s^*\right) + c\ \exp\left(-d\ \gamma_n\, s^*\right)\right\} + \gamma_{res}\,. \tag{IV.15}$$

Changing the parameter γ_{res} changes the final value of the cyclic peak stress ratio without changing the shape of the curve (see Figure IV.36-a). On the contrary, changing γ_n has the opposite effect (see Figure IV.36-b).

The implementation of this sub-model in the bond model can be done simply by scaling the peak stress value, previously $\tau_0 = k_0\, s_0$, with the factor $1-\gamma_b\left(s^*\right)$, where s^* is defined for the previous completed semi-cyclic using (IV.12). The new value for the peak stress can be defined by:

$$\tau_0^*\left(s^*\right) = \left\{1-\gamma_b\left(s^*\right)\right\}\tau_0\,. \tag{IV.16}$$

Consequently, the loading and unloading residual stress plateau, which are related to the peak stress, are now defined respectively by $f_1\,\tau_0^*$ and $f_2\,\tau_0^*$. Figure IV.37-a presents a qualitative example of the implementation of this sub-model.

The same analysis case considered to compute the data represented in Figure IV.32-b can be re-used to compute the data represented in Figure IV.37-b, this time considering the resistance degradation. Comparing both figures, it is possible to conclude that this enhancement in the bond model has a large impact in the quality of the simulation, although it is possible to verify that there are some differences in terms of the location of the peak stress and of the reloading slip. The next two sub-models address precisely these two quantities.

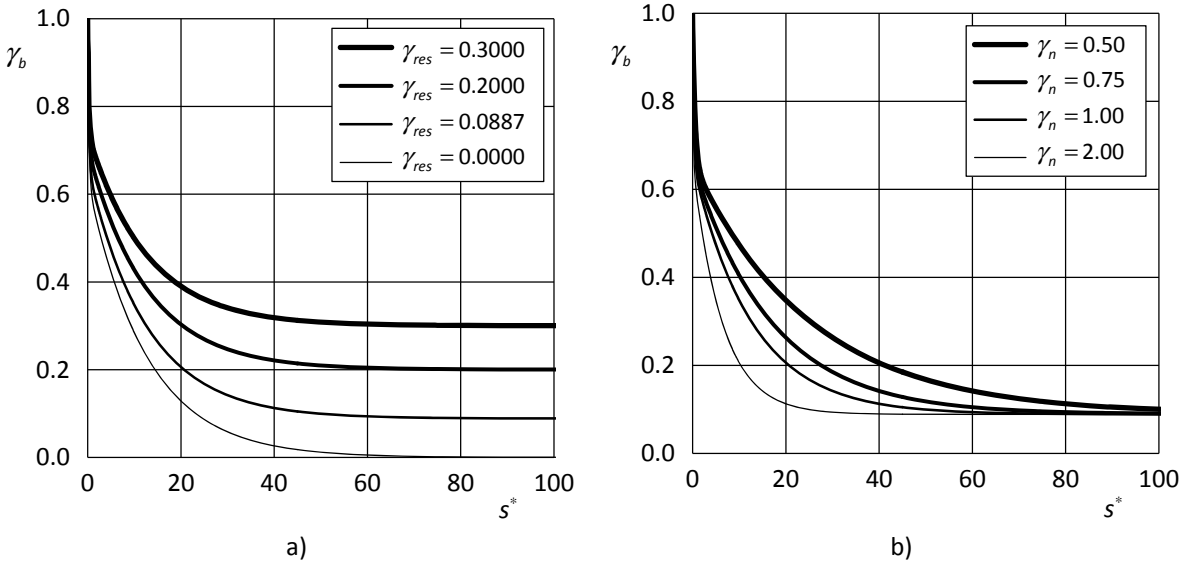

Figure IV.36: Sub-model for the cyclic resistance degradation: a) effect of the parameter γ_{res} $(\gamma_n = 1.00)$; b) effect of the parameter γ_n $(\gamma_{res} = 0.0887)$.

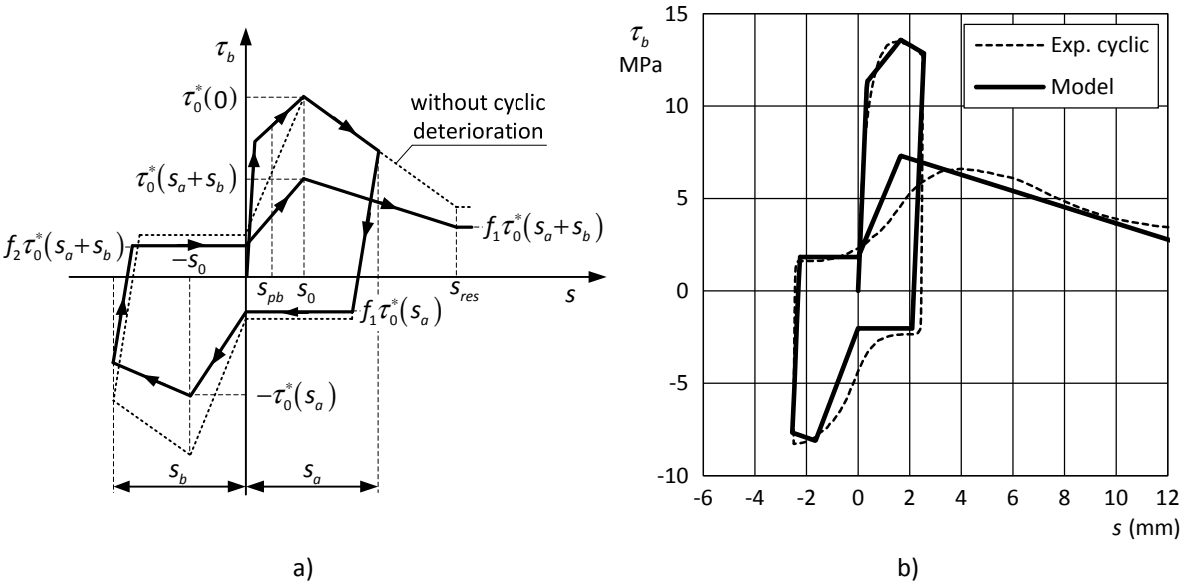

Figure IV.37: Cyclic resistance degradation: a) Schematic representation; b) comparison with experimental data [193]. Model parameters in b) are the same as Figure IV.32-b and additionally: $\gamma_{res} = 0.0887$; $\gamma_n = 1.00$.

3.3.2 Sub-model for the peak stress slip evolution

The data collected in experimental results shows that the slip value in which the peak stress is reached is not constant for all the phases characterizing the bond mechanism. In fact, this data shows an increasing tendency that can be related to fact that a higher relative displacement is necessary to mobilize all available strength after concrete cracking and crushing. This is clearly visible in the results obtained by Eligehausen *et al.* [193], as shown in Figure IV.17-f. This behaviour is considered an important aspect of the bond mechanism. Hence, to improve the quality of the simulation, a sub-model will be added to the base model.

This sub-model adopts the following assumptions for the slip in which the peak stress is reached:

i. this value increases with the development of inelastic phenomena at the interface;
ii. this value varies between s_0, which characterizes the response for the virgin state, and the value for the beginning sliding friction plateau s_{res}, which is considered to be constant.

The adoption of a constant value for the sliding friction plateau seems to be consistent with most experimental results and in the cases where some variation can be observed their amplitude is not significant in the overall interface response.

The following expression is adopted to simulate this phenomenon:

$$s_{pk}(s^*) = s_0 + (s_{res} - s_0)\left(\frac{s^*}{100}\right)^{n_{pk}} \leq s_{res}, \tag{IV.17}$$

where s_{pk} is the slip value in which the peak stress is reached; n_{pk} is a non-negative parameter used to change the profile of the evolution, as showed in Figure IV.38-a, and s^* is the same parameter used in the sub-model for the cyclic resistance degradation (IV.12). Figure IV.38-b presents a qualitative representation of the effect of this sub-model in the bond model.

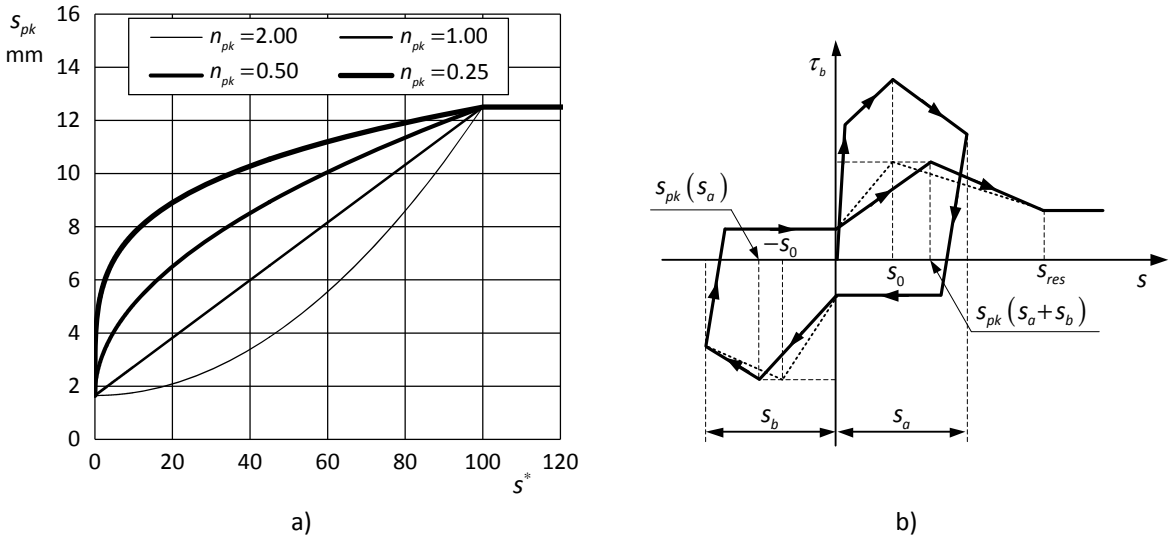

Figure IV.38: Sub-model for the peak stress slip evolution: a) effect of the parameter n_{pk} $(s_0 = 1.65 \text{ mm}, s_{res} = 12.5 \text{ mm})$; b) schematic representation.

3.3.3 Sub-model for the reload slip evolution

For the reloading branches, the experimental results also show that the slip in which the stiffness increases changes throughout the tests. This can be clearly observed in the results obtained by Eligehausen *et al.* [193] presented in Figure IV.17-f.

For this factor, a clear pattern cannot be observed for the evolution. It seems indubitable that this slip value has the tendency to move into the loading sliding friction plateau. However, the starting and ending slip values, and also, the evolution pattern are not clearly recognizable from the available data. Consequently, the sub-model must be more flexible in order to adapt to different situations.

The following expression is adopted to simulate the reload slip evolution:

$$s_{rld}\left(s^*\right)=s_{rld}^0+\left(s_{rld}^\infty-s_{rld}^0\right)\left(\frac{s^*}{100}\right)^{n_{rld}}\le s_{rld}^\infty, \tag{IV.18}$$

where s_{rld} represents the slip value in which the reloading branch begins; s^* is the same parameter used in the previous sub-models; s_{rld}^0 represents the initial value at $s^*=0$; s_{rld}^∞ is the final value at $s^*=100$, and as before, n_{rld} allows changing the shape of the evolution (see Figure IV.39-a).

Note that the sign of both s_{rld}^0 and s_{rld}^∞ is not associated with the absolute slip values, instead it is a relative slip in which the negative values are associated with anticipating the reload branch, and thus, positive values mean delaying the reload branch. It should be taken into consideration that if the cycle amplitude is not enough to exceed s_{rld}^0, the reload offset must be truncated to this value. Figure IV.39-b presents a qualitative representation of the sub-model effect in the bond model.

Figure IV.40 presents a comparison with the same experimental data considered previously.

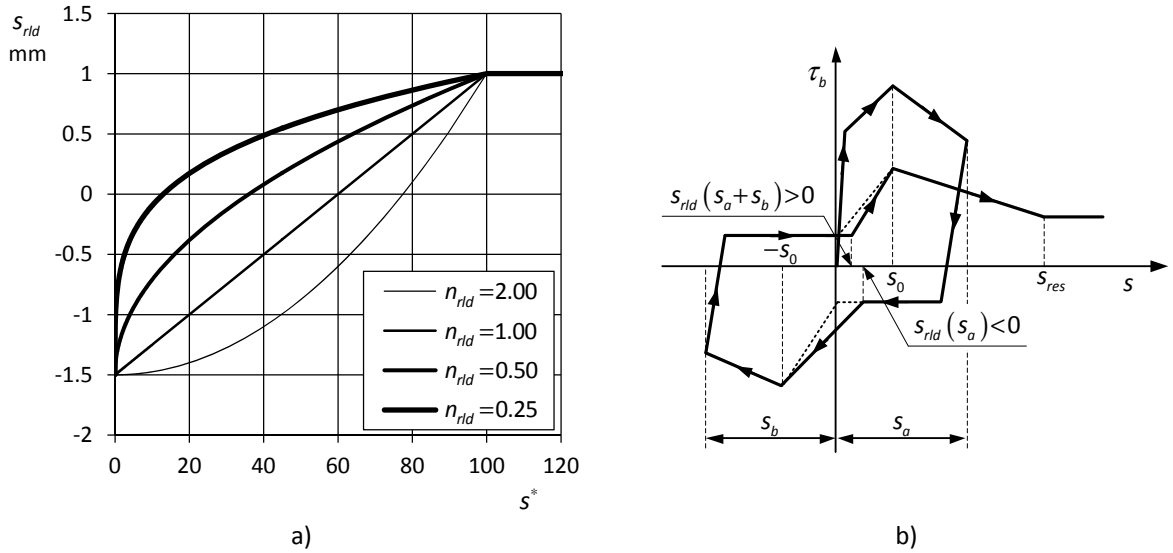

Figure IV.39: Sub-model for the peak stress slip evolution: a) effect of the parameter n_{rld} $\left(s_{rld}^0=-1.5\text{ mm}, s_{rld}^\infty=1.0\text{ mm}\right)$; b) schematic representation.

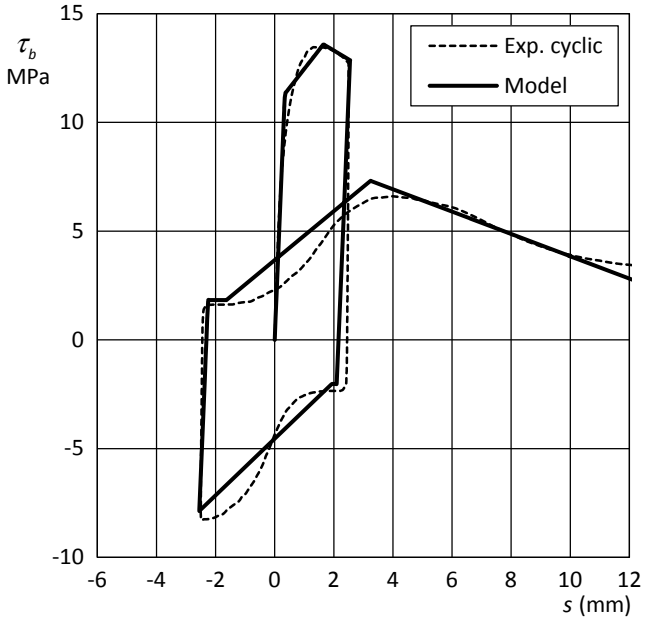

Figure IV.40: Proposed bond model considering the peak slip and the reload slip evolution. Comparison with exp. data [193] Model parameters: The same used in Figure IV.37 and $n_{pk} = 0.57$; $s_{rld}^{0} = -3.0$ mm; $s_{rld}^{\infty} = 9.0$ mm; $n_{rld} = 0.55$.

Observing Figure IV.40, It is possible to observe that adding the sub-models for the cyclic resistance degradation, for the peak stress slip evolution and for the reload slip evolution, has improved the quality of the simulation significantly.

3.3.4 Sub-model for the radial stress effect

It is necessary to have information about the stress in the surrounding concrete for introducing the radial stress effect into the bond model. A difficulty emerges because the concrete stress is not reflected in the zero-thickness concrete-steel interface element that will be presented in section 4. A possible solution is to extend the state determination of the interface element with information from other elements. This will be done by adopting a similar procedure to one used for the nonlocal regularization technique (see Chapter III-2.1.6).

The first step is to compute the perpendicular direction to the interface axis in the direction towards the reference Gauss point. This can be done by following the procedure that will be presented below.

Let us consider the two Gauss points drawn in black in Figure IV.41. The Gauss point labelled GP_{ref} belongs to the interface element and the one labelled GP_k is part of the surrounding concrete. It is possible to define the unit vector $\mathbf{v}_1$ with the direction connecting the position of these points, using:

$$\mathbf{v}_1 = \frac{\mathbf{X}^{GP_k} - \mathbf{X}^{GP_{ref}}}{\left\| \mathbf{X}^{GP_k} - \mathbf{X}^{GP_{ref}} \right\|}. \tag{IV.19}$$

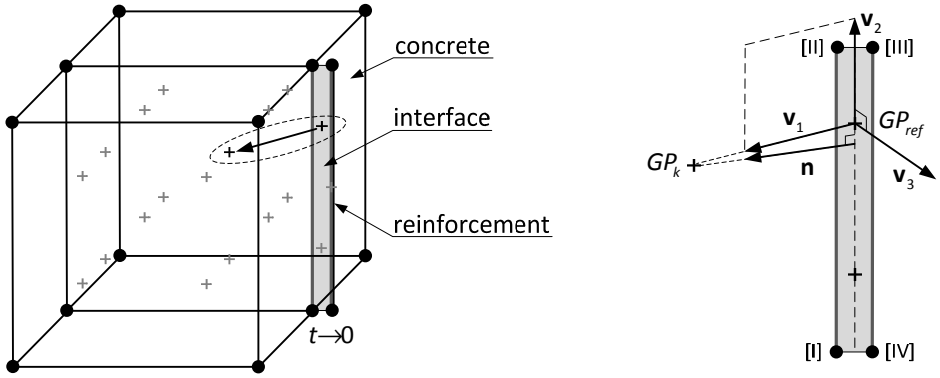

Figure IV.41: Radial stress effect – Computing the stress acting on the interface.

Another unit vector can be defined with the direction of the central axis of the interface element. Considering that a zero-thickness interface element with linear geometry will be used in this work, this direction can be computed using the expression:

$$\mathbf{v}_2 = \frac{\mathbf{X}^{II} - \mathbf{X}^{I}}{\left\| \mathbf{X}^{II} - \mathbf{X}^{I} \right\|}, \tag{IV.20}$$

where $\mathbf{X}^k$ is the global coordinate of the local node *k*.

Note that $\mathbf{v}_1$ and $\mathbf{v}_2$ are not necessarily perpendicular to each other. To correct this, the following equation can be applied:

$$\mathbf{v}_3 = \mathbf{v}_1 \times \mathbf{v}_2, \tag{IV.21}$$

and finally, the unit vector **n** that is perpendicular to $\mathbf{v}_2$ and points towards GP_k can be obtained:

$$\mathbf{n} = \mathbf{v}_3 \times \mathbf{v}_1. \tag{IV.22}$$

The Cauchy stress formula (II.11) can be used to compute the stress vector **t** acting in the direction defined by **n**:

$$\sigma_{ij}\, n_i = t_i,$$

and the component in the direction perpendicular to the interface by applying the internal product:

$$\sigma_{rad} = \sigma_{ij}\, n_i\, n_j, \tag{IV.23}$$

or in matrix format:

$$\sigma_{rad} = \mathbf{n}^t\, \boldsymbol{\sigma}\, \mathbf{n}. \tag{IV.24}$$

A weighted average value for the radial stress is used to improve the quality and representativeness of the stress value in the surrounding concrete. This can be done using the following formula:

$$\bar{\sigma}_{rad} = \sum_{gp} \left(\sigma_{rad}\, W \right)_{gp}, \tag{IV.25}$$

where *W* is the weight associated with each Gauss point selected.

The selection of the eligible Gauss points and the computation of the weights can be made using a similar approach to the one used in nonlocal constitutive relations (see Chapter III-2.1.6). The same weighting functions used before can be used to compute $\bar{\sigma}_{rad}$., namely the *Gaussian function* (III.68) and the *bell-shaped function* (III.69). A new parameter called the *bond length* L_b is introduced to characterize the width in which the bond mechanism develops. This way, the weights of each Gauss point can be computed from:

$$W_{gp} = \frac{1}{W_{tot}} f\left(L_b, X_{gpref}, X_{gp}\right), \tag{IV.26}$$

where X_{gpref} and X_{gp} are the coordinates of the reference and of the selected Gauss point. To enforce that the sum of the weights is unitary, the parameter W_{tot} should be computed from:

$$W_{tot} = \sum_{gp} W_{gp} \ . \tag{IV.27}$$

The final step consists in defining the sub-model for the radial stress effect and introducing it into the basic model. This is done using the parameter η :

$$\eta\left(\bar{\sigma}_{rad}\right) = \begin{cases} \eta_0 + \left(\eta_- - \eta_0\right)\left(\dfrac{\left|\bar{\sigma}_{rad}\right|}{f_c}\right)^{n_{\eta-}} \le \eta_-, & \text{if } \sigma_{rad} < 0 \\ \eta_0, & \text{if } \sigma_{rad} = 0, \\ \eta_0 + \left(\eta_+ - \eta_0\right)\left(\dfrac{\bar{\sigma}_{rad}}{0.10 f_c}\right)^{n_{\eta+}} \ge 0, & \text{if } \sigma_{rad} > 0 \end{cases} \tag{IV.28}$$

where η_0 is the value of the function in the absence of radial stress, η_- and η_+ are the values for $\bar{\sigma}_{rad} = -f_c$ [i] and for $\bar{\sigma}_{rad} = 0.10\, f_c$, respectively, and $n_{\eta-}$ and $n_{\eta+}$ are exponents used to define the shape of the function for negative and positive values of the radial stress. Figure IV.42 presents an example of this function. The reference value of $0.10\, f_c$ was adopted for the positive branch to estimate the tension peak resistance of common concrete and to avoid defining another parameter explicitly.

One possible way to introduce this effect into the bond model is to scale the envelopes. However, that would result in unwanted slope changes that are not observed in experimental results, for example the initial ascending branch seems to be barely influenced by radial stress, as it can be seen in Figure IV.17-d, Figure IV.18-b and Figure IV.19-b.

Another possible way is to scale the reference slips s_{pb} and s_0 , using the following expressions:

$$s_{adh}\left(\eta\right) = s_{adh}\left(\eta_0\right)\eta, \tag{IV.29}$$

$$s_0\left(\eta\right) = s_0\left(\eta_0\right)\eta, \tag{IV.30}$$

this would result in the desired uniform change of the peak stresses and of the corresponding slip values. However, it does not change the slopes of most branches, even when the radial stress changes throughout the analysis.

[i] the concrete resistance under compression f_c is considered a positive value, although the stress is negative.

The changes made to the model imply that the beginning slip for the residual friction stress level s_{res} is considered to be unchanged by the radial stress. This option is supported by observations made in experimental results (see Figure IV.17-d, Figure IV.18-b and Figure IV.19-b). The symbol η_{pk} refers to the value of η when the peak stress is reached. This value will be used to define the slope of the softening branch, so that these values must be stored until the end of each cycle.

Figure IV.43 schematically represents the effect of constant and variable radial stresses for monotonic loading. In addition, Figure IV.44 presents an example of the constitutive relation with and without the radial stress effect for reversed cyclic loading.

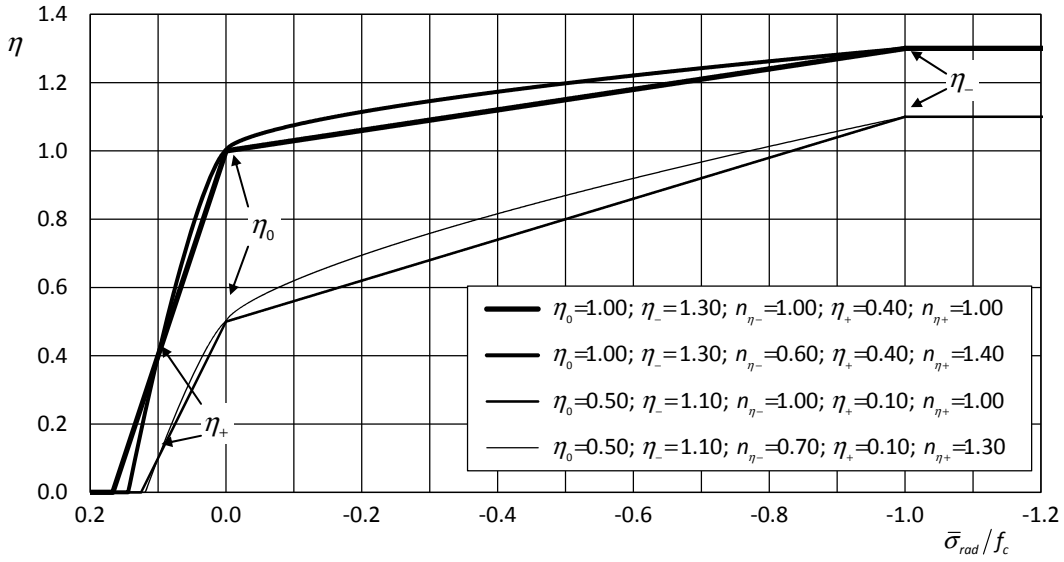

Figure IV.42: Radial stress effect: Influence of the parameters on the shape of the function η.

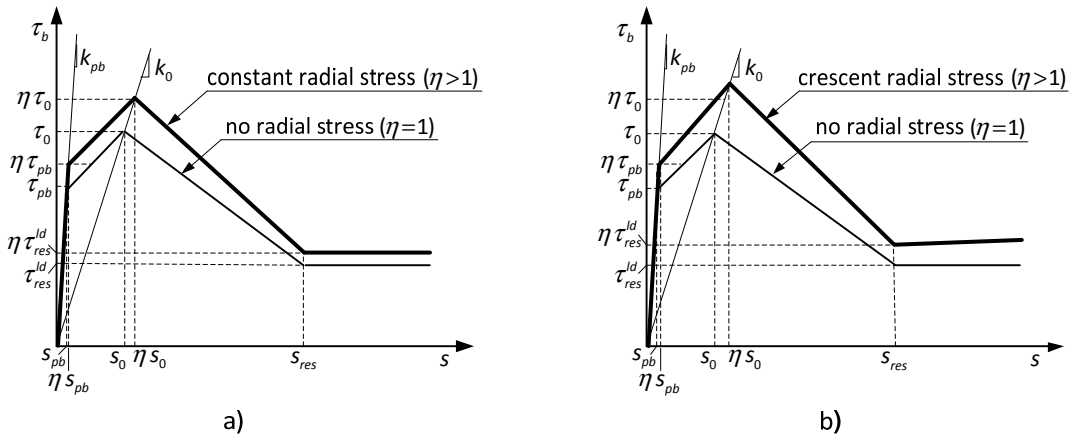

Figure IV.43: Schematic representation of the radial stress effect for monotonic loading:
a) constant radial stress; b) increasing radial stress.

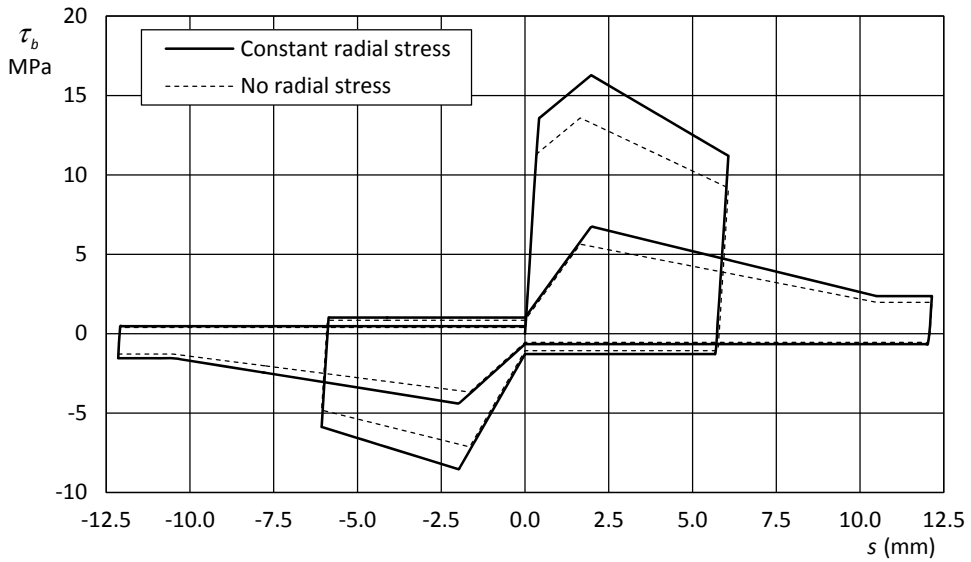

Figure IV.44: Radial stress effect for reversed cyclic loading $\left(\sigma_{cf}/f_c = 0.50\right)$.

Model parameters: The same of Figure IV.37 and $\sigma_{cf}/f_c = 0.50$; η_0=1.00; η_-=1.30; $n_{\eta-}$=0.60; η_+=0.40; $n_{\eta+}$=1.40 .

3.4 Mathematical formulation

3.4.1 State determination algorithm

The bond model is defined by the parameters presented in Table IV.4 and the constitutive relation adopts the following expression:

$$\tau_b = k_{ul}\left(s - s_{ine}\right), \tag{IV.31}$$

where k_{ul} is the *unloading stiffness* and s_{ine} is the equivalent *inelastic slip*.

A *bond envelope function* $\phi_b^{\pm}$ is defined for the positive and for the negative limit of the bond stress. Taking advantage of the fact that these two functions are odd, it is possible to write a condensed expression that can be used for either the positive and negative envelops[i]:

$$\phi_b^{\pm} = \begin{cases} \pm f_2\,\tau_0^*\,\eta, & \text{if } \pm s \le s_{rld} \\ \pm f_2\,\tau_0^*\,\eta_{pk} \pm \dfrac{\tau_0^*\,\eta_{pk}\left(1-f_2\right)}{s_{pk}\,\eta_{pk} - s_{rld}}\left(\pm s - s_{rld}\right), & \text{if } s_{rld} < \pm s \le s_{pk} \\ \pm\lambda\left\{\tau_0^*\left(\eta_{pk} - f_1\tau_0^*\right) + \dfrac{\tau_0^*\left(f_1\,\eta - \eta_{pk}\right)}{s_{res} - s_{pk}\,\eta_{pk}}\left(\pm s - s_{pk}\,\eta_{pk}\right)\right\} \pm f_1\,\tau_0^*\,\eta, & \text{if } s_{pk} < \pm s \le s_{res} \\ \pm f_1\,\tau_0^*\,\eta, & \text{if } s_{res} < \pm s \end{cases}, \tag{IV.32}$$

with:

$$\tau_0^* = \left(1-\gamma\right)k_0\,s_0, \tag{IV.33}$$

$$\lambda = \exp\left(-c_{soft}\,\frac{\pm s - s_{pk}\,\eta_{pk}}{s_{res} - s_{pk}\,\eta_{pk}}\right). \tag{IV.34}$$

During the first load, the envelope function is changed to:

$$\phi_b^{\pm} = \begin{cases} k_{pb}\,s, & \text{if } |s| \le s_{pb}\,\eta_{pk} \\ \pm k_{pb}\,s_{pb}\,\eta_{pk} + \dfrac{k_0\,s_0 - k_{pb}\,s_{pb}}{s_{pk} - s_{pb}}\left(s - s_{pb}\,\eta_{pk}\right), & \text{if } s_{pb}\,\eta_{pk} < |s| \le s_{pk} \end{cases}. \tag{IV.35}$$

As in plasticity theory[ii], the admissible values for the envelope function are defined by $\phi_b \le 0$. This condition must be satisfied during the state determination procedure. With that objective, the following procedure may be adopted:

At a general load step a trial bond stress τ_b^{trial} can be computed for the current slip value from the expression (IV.31). If the trial bond stress violates the envelope curve this means that the inelastic slip must be corrected.

---

[i] The symbol $\pm$ should be substituted with a $+$ or a $-$ sign, resulting in the positive and negative limit of ϕ_b.

[ii] the *bond envelope function* can be seen as similar to the *yield function* used in plasticity. Nonetheless, this terminology is avoided because the inelastic phenomena are more related to fracture than to yield.

This can be done by computing:

$$s_{ine} = s - \phi_b^{\pm} / k_{ul} \ . \tag{IV.36}$$

The last expression can be seen as the *consistency relation* of the traditional plasticity theory. Nonetheless, in this case, the formulation is not incremental and no iteration is required.

3.4.2 Stiffness matrix

The total derivative of the bond stress must be calculated in order to compute the tangential components of the interface element stiffness matrix. As seen before, the bond stress is a function of the slip and a set of state parameters that only changes between cycles, with the exception of radial stress that can change without any constraint. Therefore, the total derivative can be expressed as:

$$d\tau_b = \frac{\partial \tau_b}{\partial s} ds + \frac{\partial \tau_b}{\partial \eta} d\eta \ . \tag{IV.37}$$

The term $\partial \tau_b / \partial \eta$ is not possible to compute within the element scope, as a consequence of the parameter η being dependent on $\bar{\sigma}_{rad}$, which is defined by the averaged information from the surrounding concrete elements.

To mitigate this problem, the model was developed in such way that the branches #1, #2 and #6 represented in Figure IV.45 are not affected by the changes of $\bar{\sigma}_{rad}$. In these cases, quadratic convergence is achieved even if the radial stress changes. On the other hand, for the other branches the quadratic convergence is lost. Nonetheless, even in those situations the convergence is revealed to be extremely efficient and fast, as a consequence of the changes of slope being relatively small.

The term $\partial \tau_b / \partial s$ in (IV.37) can be computed for each branch represented in Figure IV.45, from:

$$\frac{\partial \tau_b}{\partial s} = \begin{cases} k_{pb}, & \text{case \#1} \\ \dfrac{k_0 s_0 - k_{pb} s_{pb}}{s_{pk} - s_{pb}}, & \text{case \#2} \\ \dfrac{\tau_0^* (f_2 - 1) \eta_{pk}}{s_{pk} \eta_{pk} - s_{rld}}, & \text{case \#3} \\ \dfrac{\tau_0^* (f_1 \eta - \eta_{pk})}{s_{res} - s_{pk} \eta_{pk}}, & \text{case \#4 } (\text{if } c_{soft} = 0) \\ 0, & \text{case \#5} \\ k_{ul}, & \text{case \#6} \\ 0, & \text{case \#7} \end{cases} . \tag{IV.38}$$

For the case with $c_{soft} > 0$, case #4 turns into:

$$\frac{\partial \tau_b}{\partial s} = \frac{c_{soft} \left\{ \tau_0^* (f_1 \eta - \eta_{pk}) - \dfrac{\tau_0^* (s - \eta_{pk} s_{pk})(f_1 \eta - \eta_{pk})}{s_{res} - s_{pk} \eta_{pk}} \right\}}{\exp\left(\dfrac{c_{soft} (s - s_{pk} \eta_{pk})}{s_{res} - s_{pk} \eta_{pk}} \right) (s_{res} - s_{pk} \eta_{pk})} + \frac{\tau_0^* (f_1 \eta - \eta_{pk})}{\exp\left(\dfrac{c_{soft} (s - s_{pk} \eta_{pk})}{s_{res} - s_{pk} \eta_{pk}} \right) (s_{res} - s_{pk} \eta_{pk})} . \tag{IV.39}$$

Table IV.4: Bond model parameters.

Parameter	Unit	Definition	Domain
k_{pb}	Pa/m	initial tangent stiffness (perfect bond)	$[0,\infty]$
k_0	Pa/m	initial secant stiffness to peak stress	$[0,\infty]$
k_{ul}	Pa/m	unloading stiffness	$[0,\infty]$
s_{pb}	m	initial perfect bond slip limit	$[0,s_0]$
s_0	m	initial slip at peak stress	$[s_{pb},s_{res}]$
s_{res}	m	slip at the beginning of the loading residual stress plateau	$[s_0,\infty]$
f_1	-	loading residual stress ratio	$[0,1]$
f_2	-	unloading residual stress ratio	$[0,1]$
c_{soft}	-	parameter controlling the shape of the softening branch	$[0,\infty]$
γ_{res}	-	γ at $s^*=100$	$[0,1]$
γ_n	-	parameter controlling the evolution of the resistance degradation	$[0,\infty]$
n_{pk}	-	parameter controlling the evolution of the peak slip	$[0,\infty]$
s_{rld}^0	m	initial reload slip $(s^*=0)$	$[-s_{res},s_{rld}^\infty]$
s_{rld}^∞	m	final reload slip $(s^*=100)$	$[-s_{rld}^0,s_{res}]$
n_{rld}	-	parameter controlling the evolution of the reload slip	$[0,\infty]$
L_b	m	bond length	$[0,\infty]$
f_c	Pa	concrete resistance under compression	$[0,\infty]$
η_0	-	η factor for $\bar{\sigma}_{rad}=0$	$[0,\infty]$
η_-	-	η factor for $\bar{\sigma}_{rad}=-f_c$	$[0,\infty]$
η_+	-	η factor for $\bar{\sigma}_{rad}=0.10\,f_c$	$[0,\infty]$
$n_{\eta-}$	-	parameter controlling the evolution of η (negative $\bar{\sigma}_{rad}$)	$[0,\infty]$
$n_{\eta+}$	-	parameter controlling the evolution of η (positive $\bar{\sigma}_{rad}$)	$[0,\infty]$

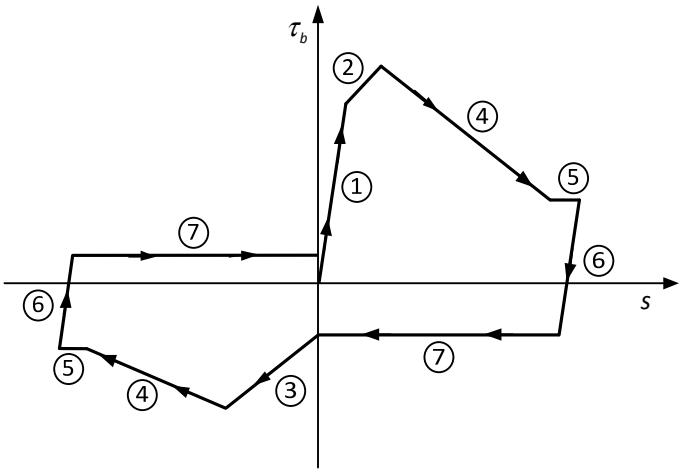

Figure IV.45: Bond model branch numbering.

4 Development of the interface element

The interface element combines the bond model presented in the previous section and an additional model for the radial direction. In this work, an elastic relation was adopted for the radial direction with large numerical values for the stiffness. The objective is to impose near null radial relative displacements between the steel and concrete elements adopting a procedure similar to a *penalty method*. Using this approach implies that nonlinear movements (*e.g.* opening and closure of cracks) cannot be simulated. As a result, no direct information to evaluate the state of splitting cracks is extractable from the model. This can only be assessed by knowing the passive confinement level and by evaluating the active confinement level with data from the radial stress computed in the analysis.

Taking into consideration the information collected in section 2.4.2, the *zero-thickness* interface elements will be used due to their easier implementation in three-dimensional meshes. The isoparametric formulation presented by Beer [48] is adopted.

The kinematics of the interface element includes the *longitudinal relative displacement* (*slips*) and the *radial relative displacements* (*opening* and *closure* movements), which in a three-dimensional simulation will have two orthogonal components perpendicular to the reinforcement longitudinal axis. These kinematics variables can be joined together in the following vector:

$$\mathbf{q}^{rel} = \begin{bmatrix} s & r_2 & r_3 \end{bmatrix}^t, \tag{IV.40}$$

where s is the slip between concrete and reinforcement and r_i is the radial relative displacement (opening/closure) along the local direction i.

The associated static variables can be grouped in the following stress vector:

$$\boldsymbol{\sigma} = \begin{bmatrix} \tau_b & \sigma_{r2} & \sigma_{r3} \end{bmatrix}^t, \tag{IV.41}$$

where τ_b represents the *tangential stress* (*bond stress*) created by the slips and σ_{ri} are the *radial stresses* associated with the radial displacement along the local direction i.

According to the isoparametric formulation presented by Beer [48], the following expressions are adopted for the element mapping:

$$\tilde{x}_k^{bot} = \psi_1 \, y_k^{[I]} + \psi_2 \, y_k^{[II]}, \tag{IV.42}$$

$$\tilde{x}_k^{top} = \psi_2 \, y_k^{[III]} + \psi_1 \, y_k^{[IV]}, \tag{IV.43}$$

and for the relative displacement approximations:

$$\tilde{q}_k^{bot} = \psi_1 \, q_k^{[I]} + \psi_2 \, q_k^{[II]}, \tag{IV.44}$$

$$\tilde{q}_k^{top} = \psi_2 \, q_k^{[III]} + \psi_1 \, q_k^{[IV]}, \tag{IV.45}$$

where the *shape functions* ψ_k are defined as first order polynomials (see Figure IV.46).

According to Beer [48], the relative displacement approximations can be computed from the top and bottom edge displacements (see Figure IV.46), using:

$$q_k^{rel} = q_k^{top} - q_k^{bot} = \psi_2 \, q_k^{[III]} + \psi_1 \, q_k^{[IV]} - \psi_1 \, q_k^{[I]} - \psi_2 \, q_k^{[II]}. \tag{IV.46}$$

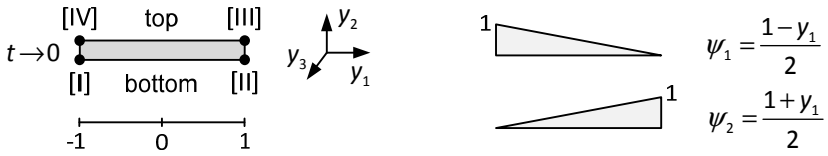

Figure IV.46: Zero thickness 4-noded isoparametric interface element: Geometric definitions and approximation functions.

Note that for the dynamic analyses the velocity and acceleration approximations can be computed from similar expressions to those used for the displacements (IV.44), (IV.45) and (IV.46).

This formulation results in a model that directly relates the stresses with the relative displacements. Hence, the compatibility equations are not similar to the ones used in the continuum mechanics framework, which involves derivatives. Instead, they are simply defined by differences between displacements.

The compatibility relations can be computed from:

$$\mathbf{q}^{rel} = \mathbf{B}\ \mathbf{q}\,, \tag{IV.47}$$

with:

$$\mathbf{B} = \left[\begin{array}{ccc|ccc|ccc|ccc} -\psi_1 & 0 & 0 & -\psi_2 & 0 & 0 & \psi_2 & 0 & 0 & \psi_1 & 0 & 0 \\ 0 & -\psi_1 & 0 & 0 & -\psi_2 & 0 & 0 & \psi_2 & 0 & 0 & \psi_1 & 0 \\ 0 & 0 & -\psi_1 & 0 & 0 & -\psi_2 & 0 & 0 & \psi_2 & 0 & 0 & \psi_1 \end{array}\right]. \tag{IV.48}$$

- Elastic interface element

As a first approach, the following elastic constitutive relation is considered:

$$\boldsymbol{\sigma} = \mathbf{k}\ \mathbf{q}^{rel}\,, \tag{IV.49}$$

with:

$$\mathbf{k} = \begin{bmatrix} k_s & 0 & 0 \\ 0 & k_{r2} & 0 \\ 0 & 0 & k_{r3} \end{bmatrix}, \tag{IV.50}$$

where k_s, k_{r2} and k_{r3} are the stiffness components for each displacement component. However in this case their units are not a force by unit area, but instead a force by unit volume, due to the kinematics being defined in terms of relative displacements instead of the traditional dimensionless strain.

Using a similar approach to the one used for equation (II.32), the work done by internal forces in the interface element is given by:

$$W_i = \int \delta\left(\tilde{\mathbf{q}}^{rel}\right)^t \boldsymbol{\sigma}\, d\Omega\,. \tag{IV.51}$$

Developing this last expression and taking into consideration the compatibility relation (IV.47) and the elastic constitutive relation (IV.49), the expression for computing the stiffness matrix results in:

$$\mathbf{K} = \int_{-1}^{1} \mathbf{B}^t(y_1)\ \mathbf{k}\ \mathbf{B}(y_1)\ \det\mathbf{J}\ dy_1\ . \tag{IV.52}$$

For the elastic case, the integration can be made analytically and the following symmetric stiffness matrix is obtained:

$$\mathbf{K} = \frac{L}{6}\left[\begin{array}{ccc|ccc|ccc|ccc} 2k_s & 0 & 0 & k_s & 0 & 0 & -k_s & 0 & 0 & -2k_s & 0 & 0 \\ & 2k_{r2} & 0 & 0 & k_{r2} & 0 & 0 & -k_{r2} & 0 & 0 & -2k_{r2} & 0 \\ & & 2k_{r3} & 0 & 0 & k_{r3} & 0 & 0 & -k_{r3} & 0 & 0 & -2k_{r3} \\ \hline & & & 2k_s & 0 & 0 & -2k_s & 0 & 0 & -k_s & 0 & 0 \\ & & & & 2k_{r2} & 0 & 0 & -2k_{r2} & 0 & 0 & -k_{r2} & 0 \\ & & & & & 2k_{r3} & 0 & 0 & -2k_{r3} & 0 & 0 & -k_{r3} \\ \hline & & & & & & 2k_s & 0 & 0 & k_s & 0 & 0 \\ & & & & & & & 2k_{r2} & 0 & 0 & k_{r2} & 0 \\ & & & & & & & & 2k_{r3} & 0 & 0 & k_{r3} \\ \hline & & & & & & & & & 2k_s & 0 & 0 \\ & sym & & & & & & & & & 2k_{r2} & 0 \\ & & & & & & & & & & & 2k_{r3} \end{array}\right], \tag{IV.53}$$

where *L* represents the length of the interface element in the global coordinate system.

- Interface element adopting the proposed bond model for the longitudinal direction

The following constitutive relation is adopted to include the bond model developed in the previous sections to simulate the longitudinal response of the interface element.

$$\boldsymbol{\sigma} = \mathbf{k}^* \left(\mathbf{q}^{rel} - \mathbf{q}_{ine}^{rel}\right), \tag{IV.54}$$

where $\mathbf{k}^*$ is the constitutive tensor and $\mathbf{q}_{ine}^{rel}$ is the *inelastic displacement vector*, non-null only for the slip component. These operators are defined by:

$$\mathbf{k}^* = \begin{bmatrix} k_s^* & 0 & 0 \\ 0 & k_{r2} & 0 \\ 0 & 0 & k_{r3} \end{bmatrix}, \tag{IV.55}$$

$$\mathbf{q}_{ine}^{rel} = \begin{bmatrix} s_{ine} & 0 & 0 \end{bmatrix}^t. \tag{IV.56}$$

where the secant modulus can be defined by $k_s^* = \tau_s / s$.

The secant stiffness matrix can be computed using the *Gauss-Legendre* numerical quadrature using two Gauss points:

$$\mathbf{K}_s = \sum_{gp=1}^{2} \mathbf{B}^t(y_1, y_2, y_3)_{gp}\ \mathbf{k}_{gp}^*\ \mathbf{B}(y_1, y_2, y_3)_{gp}\ \det\mathbf{J}(y_1, y_2, y_3)_{gp}\ w_{gp}\ , \tag{IV.57}$$

where **J** is the *Jacobian matrix* and *w* is the quadrature weight associated with each Gauss point (see Chapter II-§3.2).

On the other hand, using the *tangent stiffness matrix* can enhance the computational efficiency of the numerical model by increasing the convergence rate to the solution in each time step. This matrix can be defined by recalling the expression (II.206):

$$\mathbf{K}_t = \frac{\partial \mathbf{Q}_i}{\partial \mathbf{q}} = \int \mathbf{B}^t \frac{\partial \boldsymbol{\sigma}}{\partial \mathbf{q}} \, d\Omega \, .$$

Considering the relation (IV.47), the stress derivative term can be computed from:

$$\frac{\partial \boldsymbol{\sigma}}{\partial \mathbf{q}} = \frac{\partial \boldsymbol{\sigma}}{\partial \mathbf{q}^{rel}} \frac{\partial \mathbf{q}^{rel}}{\partial \mathbf{q}} = \frac{\partial \boldsymbol{\sigma}}{\partial \mathbf{q}^{rel}} \mathbf{B} \, . \tag{IV.58}$$

For the radial components, the $\partial \boldsymbol{\sigma} / \partial \mathbf{q}^{rel}$ terms are simply the radial stiffness along each radial direction k_{ri} as in equation (IV.55). On the other hand, the bond-related component is given by $\partial \tau_b / \partial s$ defined in (IV.38) and (IV.39).

The stiffness matrix can be computed using the expression (II.76) adapted to this case:

$$\mathbf{K}^{el} = \sum_{gp=1}^{2} \mathbf{B}^t \left(y_1, y_2, y_3 \right)_{gp} \left(\frac{\partial \boldsymbol{\sigma}}{\partial \mathbf{q}^{rel}} \right)_{gp} \mathbf{B} \left(y_1, y_2, y_3 \right)_{gp} \det \mathbf{J} \left(y_1, y_2, y_3 \right)_{gp} w_{gp} \, , \tag{IV.59}$$

with:

$$\frac{\partial \boldsymbol{\sigma}}{\partial \mathbf{q}^{rel}} = \begin{bmatrix} \frac{\partial \tau_b}{\partial s} P_c & 0 & 0 \\ 0 & k_{r2} & 0 \\ 0 & 0 & k_{r3} \end{bmatrix} , \tag{IV.60}$$

where P_c is the *contact perimeter* defined in section 2.1.

The interface element was implemented and tested in a finite element package "*ParaNoiD - Parallel Nonlinear Dynamic"* developed in the scope of this thesis. More details about this implementation are presented in Chapter V-§4.

5 Validation examples

The concrete-steel interface element will be assessed in this section by means of a group of examples developed for testing and validation purposes. The examples were chosen for assessing individual aspects of the model and isolating them as much as possible from other phenomena. The examples present an increasing degree of complexity, and most of the time, the results are compared with experimental data or other numerical results in order to assess the quality and efficiency of the proposed formulation.

5.1 Example CSI1 – Pull-out tests by Eligehausen, Bertero and Popov

The objective of this example is to simulate the response of the pull-out tests performed by Eligehausen *et al.* [193]. These tests were considered as an ideal case for a first validation test, because there is an extensive amount of data available and a short anchorage was used $\left(5d_b = 127 \text{ mm}\right)$, which creates a nearly uniform response throughout the anchorage.

Figure IV.47 presents the main geometric and mechanical characteristics of the tests, which can be complemented with the information already presented in section 2.3.1. A plane model was used to simulate the experiment and the concrete was modelled with isoparametric 4-noded elements (Q4), adopting an elastic constitutive relation and a plane stress hypothesis. The steel bar was simulated

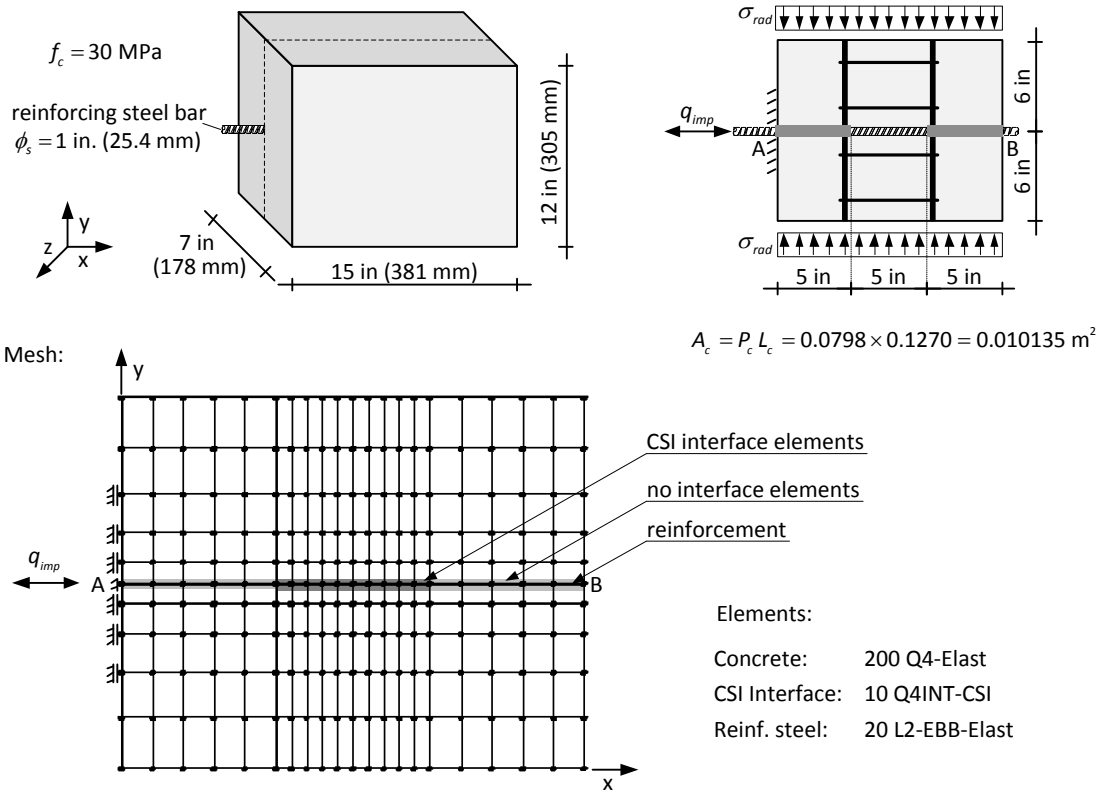

Figure IV.47: Example CSI1 – Geometric and mechanical characteristics and mesh used in the numerical analyses.

Table IV.5: Example CSI1 – Model parameters.

Model	Type	Parameters
1	Elastic	$E = 30.5$ GPa, $\nu = 0.20$, $t = 0.178$ m (plane stress)
2	EBB-Elastic	$E = 200.0$ GPa, $\nu = 0.30$, $A_s = 5.067$ cm^2, $I_z = 2.043$ cm^4
3	CSI	$k_{pb} = 32.94$ GPa/m, $k_0 = 8.235$ GPa/m, $k_{ul} = 90.0$ GPa/m, $k_{o2} = k_{o3} = 1000$ GPa/m ; $s_{pb} = 0.343$ mm, $s_0 = 1.70$ mm, $s_{res} = 10.50$ mm, $c_{soft} = 0.00$, $f_1 = 0.35$, $f_2 = 0.00$; $\gamma_{res} = 1.00$, $\gamma_n = 1.00$, $n_{pk} = 1.00$, $s^0_{rld} = 0.00$ mm, $s^\infty_{rld} = 0.00$ mm, $n_{rld} = 1.00$; $l_\eta = 0.00$ m, $f_c = 0.0$ MPa, $\eta_0 = 1.0$, $\eta_- = 1.0$, $\eta_+ = 1.0$, $n_{\eta_-} = 1.0$, $n_{\eta_+} = 1.0$.
4	CSI	$k_{pb} = 9.50$ GPa/m, $k_0 = 8.235$ GPa/m, $k_{ul} = 90.0$ GPa/m, $k_{o2} = k_{o3} = 1000$ GPa/m ; $s_{pb} = 0.343$ mm, $s_0 = 1.45$ mm, $s_{res} = 12.00$ mm, $c_{soft} = 0.00$, $f_1 = 0.47$, $f_2 = 0.25$; $\gamma_{res} = 0.45$, $\gamma_n = 3.50$, $n_{pk} = 0.57$, $s^0_{rld} = -3.00$ mm, $s^\infty_{rld} = 9.00$ mm, $n_{rld} = 0.55$; $l_\eta = 0.00$ m, $f_c = 0.0$ MPa, $\eta_0 = 1.0$, $\eta_- = 1.0$, $\eta_+ = 1.0$, $n_{\eta_-} = 1.0$, $n_{\eta_+} = 1.0$.
5	CSI	$k_{pb} = 8.35$ GPa/m, $k_0 = 8.235$ GPa/m, $k_{ul} = 90.0$ GPa/m, $k_{o2} = k_{o3} = 1000$ GPa/m ; $s_{pb} = 0.360$ mm, $s_0 = 1.70$ mm, $s_{res} = 11.00$ mm, $c_{soft} = 0.00$, $f_1 = 0.36$, $f_2 = 0.00$; $\gamma_{res} = 1.00$, $\gamma_n = 1.00$, $n_{pk} = 1.00$, $s^0_{rld} = 0.00$ mm, $s^\infty_{rld} = 0.00$ mm, $n_{rld} = 1.00$; $L_b = 0.02$ m, $f_c = 30.0$ MPa, $\eta_0 = 1.0$, $\eta_- = 1.293$, $\eta_+ = 1.0$, $n_{\eta_-} = 0.347$, $n_{\eta_+} = 1.0$

Table IV.6: Example CSI1 – Characteristics of the analyses.

ID	Analysis Type	Models	Loads
CSI1.1	Static	Concrete #1, Reinforcements: #2, Interface #3	q_{imp} (monotonic), $\sigma_{rad} = 0.0$ MPa
CSI1.2	Static	Concrete #1, Reinforcements: #2, Interface #4	q_{imp} (0,2.7,-2.7,13) mm, $\sigma_{rad} = 0.0$ MPa
CSI1.3	Static	Concrete #1, Reinforcements: #2, Interface #5	q_{imp} (monotonic), $\sigma_{rad} = \{0.0, -5.0, -10.0, -13.2\}$ MPa

with elastic Euler-Bernoulli beam/column elements. The interface elements are modelled using the proposed CSI element. All the parameters of the models are presented in Table IV.5.

As mentioned in section 2.3.1, this test was executed by prescribing a set of *quasi*-static displacements and measuring the equivalent force on one side of the protruding steel reinforcement bar (point A on Figure IV.47) and by measuring the displacement on the other side of the bar (point B on Figure IV.47). A set of boundary conditions were implemented at the concrete nodes near point A, as presented in Figure IV.47.

Three static analyses were performed (see Table IV.6). The first analysis is characterized by imposing a monotonic displacement and not having any active confinement (radial stress). The second test simulates the reversed cyclic response of the interface, again with no imposed radial stress. This effect is studied in detail in the third analysis case by considering four levels of radial stress.

- CSI1.1 – Monotonic loading with no radial stress

Figure IV.48 presents the results of the analysis made with monotonic loading and no radial stress. The results are obtained in terms of constraint force at point A (Q_c) *vs.* displacement measured at point B (q_B). These values are compared with the average value of the group of monotonic tests carried out by Eligehausen *et al.* [193] expressed in terms of bond stress *vs*. slip (see Figure IV.17-b).

As one will see further on, the structural response reveals that the behaviour of the interface is not uniform. However, the variations are minimum, and consequently, it can be assumed that the following relation represents a good approximation: $\tau_b \approx Q_c / A_c$, where A_c is the *contact area* given by the *contact perimeter* P_c times the *contact length* L_c. This relation considers that the force associated with the prescribed displacement can be transformed into the equivalent bond stress assuming a uniform stress throughout the anchorage length. The bond stresses obtained through this relation will be represented by τ_b^{eq} and denoted by the *equivalent bond stress* to avoid confusions. Figure IV.48 was drawn using two vertical axes that were scaled using this formula in order for results to be comparable. For simplicity, this hypothesis will be adopted throughout this example.

The results presented in Figure IV.48 show a very good match between the experimental response obtained by Eligehausen *et al.* [193] and the numeric data obtained with the numerical model. The model was capable of reproducing all the phases of the monotonic response, namely: i) the initial stiffer loading branch; ii) the stiffness decrease until peak stress is reached; iii) the peak stress value; iv) the softening branch and v) the sliding friction residual stress.

Figure IV.49 presents a series of numeric results obtained at the Gauss points of the interface elements at peak force. Figure IV.49-a represents the slip variation and these results confirm that the slips are not uniform. As expected, the slips are larger near the loaded edge and smaller at the other end. This figure also shows the plot of the bond stress along the interface. It is possible to confirm that the stress is not uniform, although the variations are relatively small.

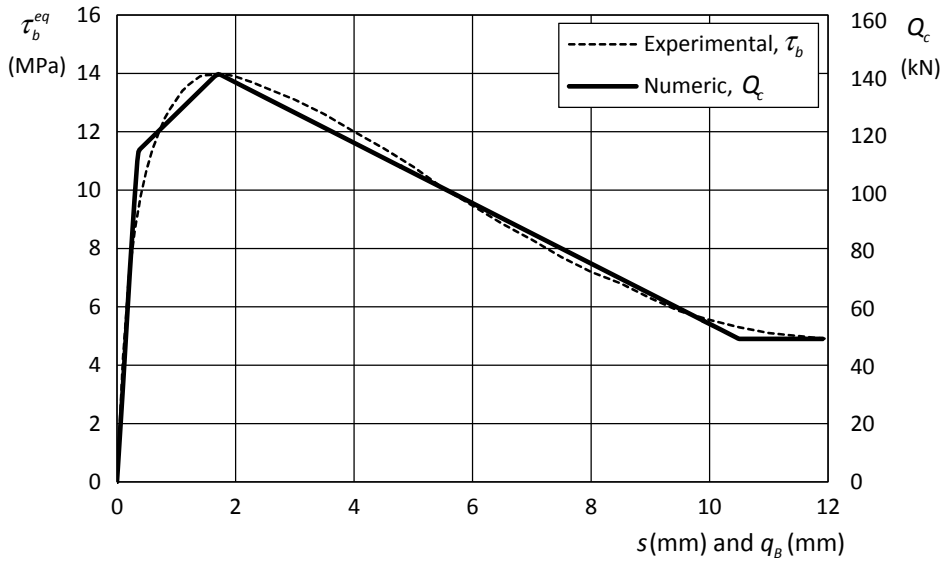

Figure IV.48: Example CSI1.1 – Response under monotonic loading, experimental data from Eligehausen *et al.* [193].

a)

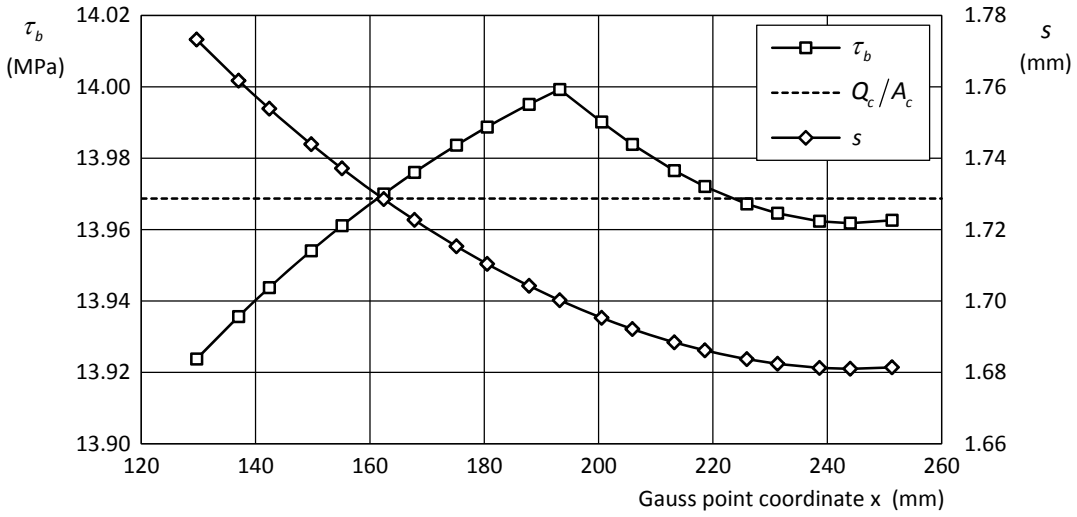

b)

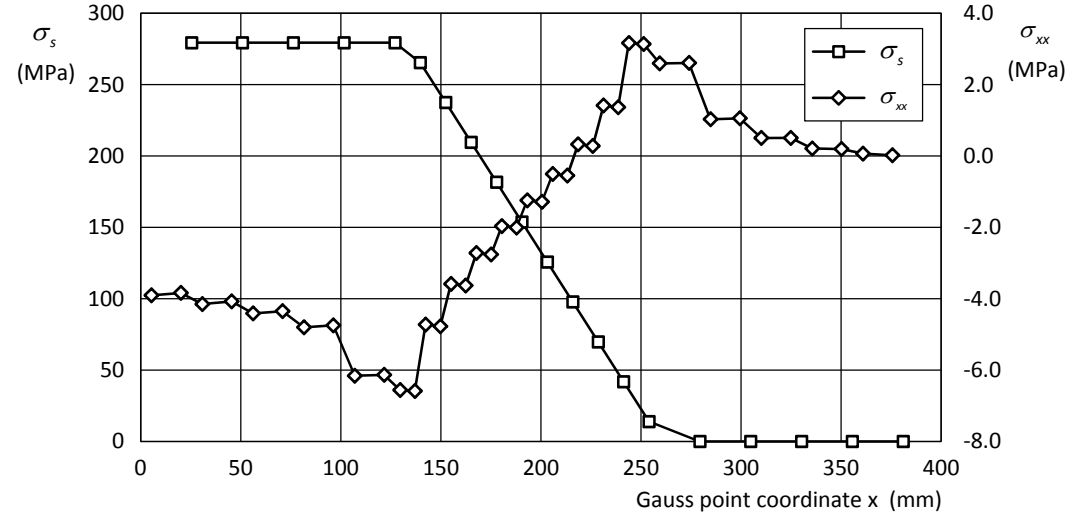

c)

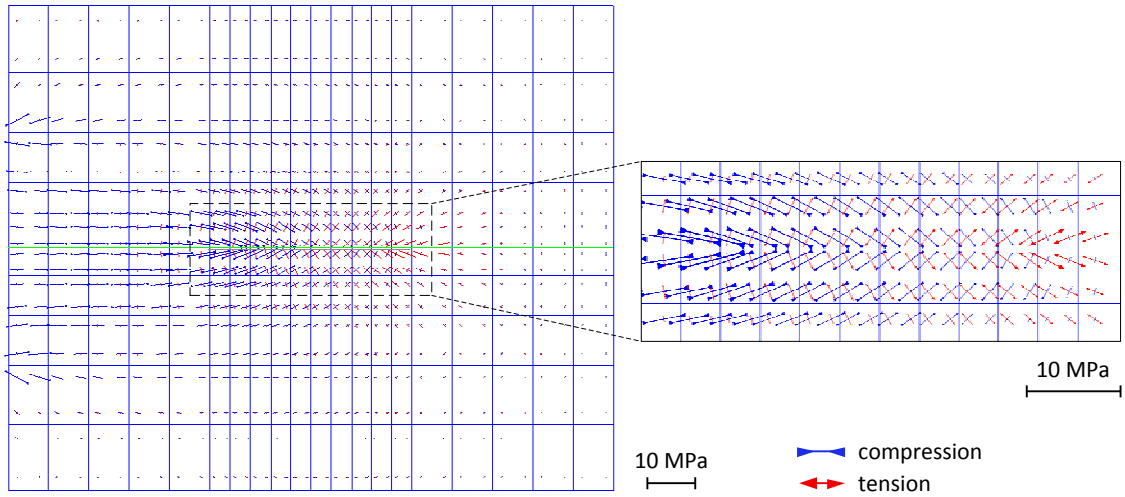

Figure IV.49: Example CSI1.1 – Values at peak force $\left(q_{imp} = \text{-}1.975 \text{ mm, step \#79}\right)$: a) Bond stress and slip variation along the interface; b) steel axial stress and surrounding concrete stress; c) principal stress vectors in the concrete.

It can be seen in Figure IV.49-a that the interface zone on the right of the figure ($x \geq 200$ mm) is still loading, which is easily identifiable by the shape similar to the slip distribution. On the other hand, the zone on the left, closer to the loading end, is already in the softening branch. The *equivalent bond stress* that is obtained by assuming a uniform slip distribution is also presented in this figure using a dotted line. It is possible to conclude that this approximation is feasible and can be used for the analysis of the results with a minor loss of accuracy.

Figure IV.49-b presents the distribution of axial stress along the reinforcement bar. As expected, it can be seen that the stress is approximately uniform along the first and last third of the bar length. This is because the reinforcing steel bar is not connected to the concrete by interface elements in those regions (see Figure IV.47). Inside the specimen, the stress gradually reduces to zero due to the loading and boundary conditions.

The concrete stress σ_{xx} is also plotted in Figure IV.49-b for the Gauss points closer to the interface. The results show compression stresses near the loading edge, tensile stresses near the free edge and a transition zone in the middle of the specimen. In addition, the results present variations that are considered as acceptable taking into consideration the formulation, the type of finite elements used for concrete and the mesh density.

Figure IV.49-c presents the principal stress vectors in the concrete elements at peak force. On the left edge, near the loading end, the concrete is mainly compressed and the principal stress directions are clearly influenced by the boundary conditions. The concrete is mainly tensioned at the opposite edge of the interface. Along the bond length, the transition from a predominant compression to tensile states is clearly identifiable, and is accompanied by rotation of the principal stress directions, creating radial stresses (see detail in Figure IV.49-c).

- CSI1.2 – Reversed cyclic loading with no radial stress

This analysis has the objective of testing the model for simulating pull-out tests with reversed loading. The model parameters are presented in Table IV.5 and are identical to the ones adopted for the monotonic loading case, with the inclusion of calibrated parameters for simulating the cyclic resistance degradation, the peak stress slip evolution and the reload slip evolution.

The parameters related to the radial stress effect were left neutral, *i.e.* with no effect on the simulation. The loading history for this analysis is indicated in Table IV.6

The equivalent bond stress *vs.* slip diagram is presented in Figure IV.50 and is plotted against the experimental data obtained by Eligehausen *et al.* [193]. It is possible to observe a good match between both curves and conclude that the experimental response was simulated with a good level of accuracy.

Figure IV.51 displays the bond stress distribution along the interface at the three local peak stress points indicated in Figure IV.50. Similarly to what occurred under monotonic loading, the stress distributions showed small variations along the bond length.

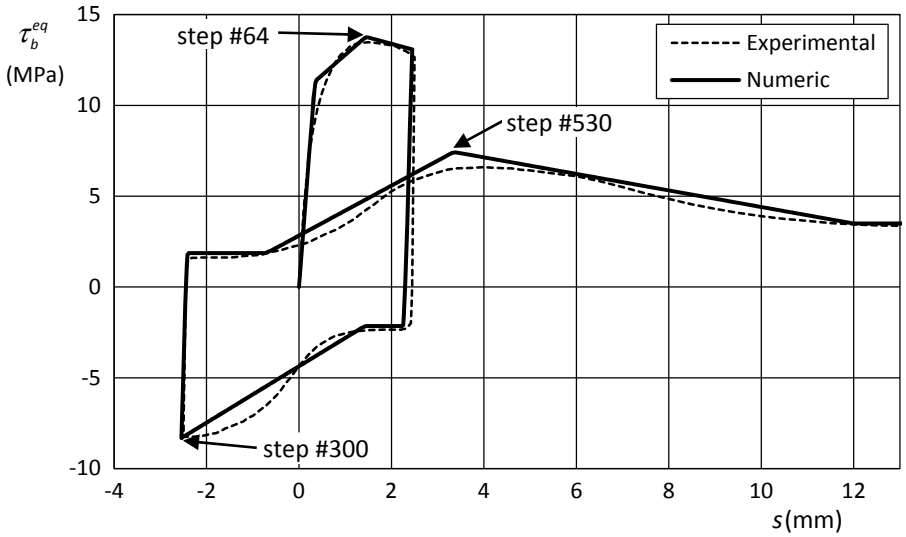

Figure IV.50: Example CSI1.2 – Equivalent bond stress *vs*. slip, experimental data from Eligehausen *et al.* [193].

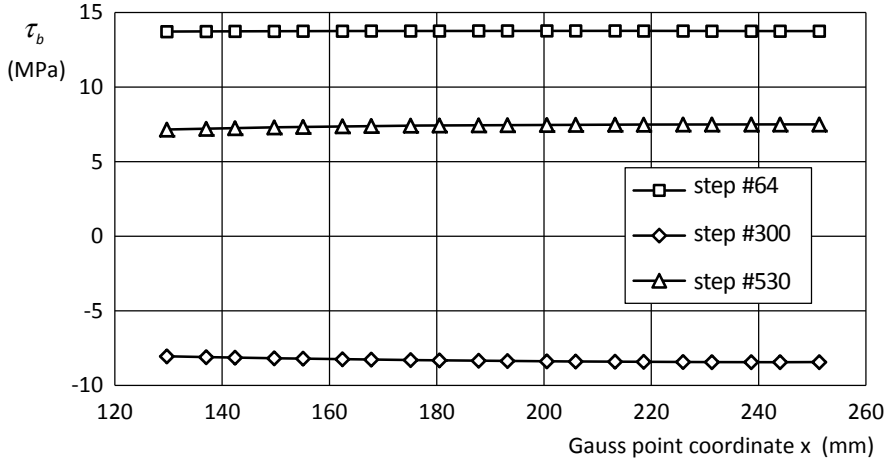

Figure IV.51: Example CSI1.2 – Bond stress distribution along the interface at chosen points.

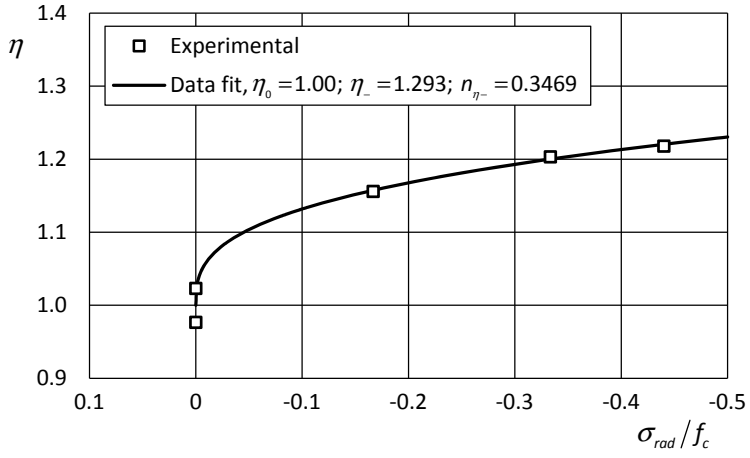

Figure IV.52: Example CSI1.3 – Calibration of the radial stress sub-model, experimental data from Eligehausen *et al.* [193].

- CSI1.3 – Monotonic loading with variable levels of radial stress

The objective of this analysis case is to assess the capacity of the proposed numerical model to simulate the effect of active radial stresses.

The starting point of this analysis is to calibrate the sub-model for the radial stress effect (see section 3.3.4) with the pre-existing data from the tests. This was done by fitting this data using the *Levenberg-Marquardt* algorithm [334, 369], in order to find the best values for the parameters η_- and n_{η_-} associated with compressive radial stresses (IV.28). The resulting sub-model curve is presented in Figure IV.52 and reveals a very good match with the experimental data, showing that the sub-model is flexible enough to reproduce this data.

No information is available for characterizing the effect of tensile radial stresses so that no data fit was made for the sub-model parameters associated with the tensile domain, which were left neutral, *i.e.* with no effect on the simulation $\left(\eta_+ = 1.0,\ n_{\eta_+} = 1.0\right)$. This effect is only relevant for the case where no radial stress is applied to the specimen, because radial tensile stresses can occur in the interface. In all other cases, the compression stresses are more than enough to eliminate this possibility.

For this simple two-dimensional model it is possible to present a schematic representation of how the nonlocal radial stress is computed. In Figure IV.53 it can be seen that for each interface Gauss point, a group of concrete Gauss points are chosen using a criterion related to the adopted *bond length* L_b. The *bell-shaped function* (III.69) is used to compute the weights of the Gauss points. The weights are represented in Figure IV.53 by the shade level of each Gauss point, using blacker shades for larger weights and lighter shades for smaller weights.

A series of four analyses were performed for the four levels of imposed radial stress $\sigma_{rad} = \{0.0, -5.0, -10.0, -13.2\}$ MPa, which were applied in the first loading step and maintained constant throughout the analysis. The *equivalent bond stress vs*. *slip* diagrams are presented in Figure IV.54. The results show a very good match between the numerical and experimental results, not only

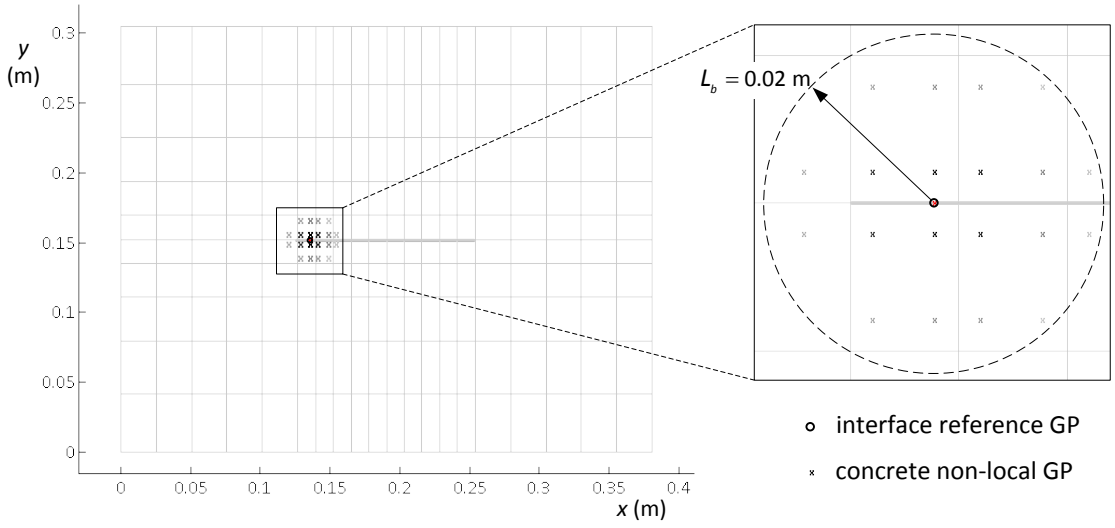

Figure IV.53: Example CSI1.3 – Schematic representation of the nonlocal radial stress computation.

in terms of the calibrated peak stress, but also in terms of the shape of the loading, softening and sliding friction plateau.

Figure IV.55 presents the computed nonlocal radial stresses along the interface elements. As mentioned before, the pull-out forces generate additional compression and tension stresses at the interface (see Figure IV.49-b), so as expected, the radial stress distribution is not uniform along the anchorage length. This interpretation is consistent with the fact that higher radial stress variations occur when the pull-out force is larger (peak stress, $q_{imp} = -2.375$ mm) and smaller variations occur when the pull-out force is smaller.

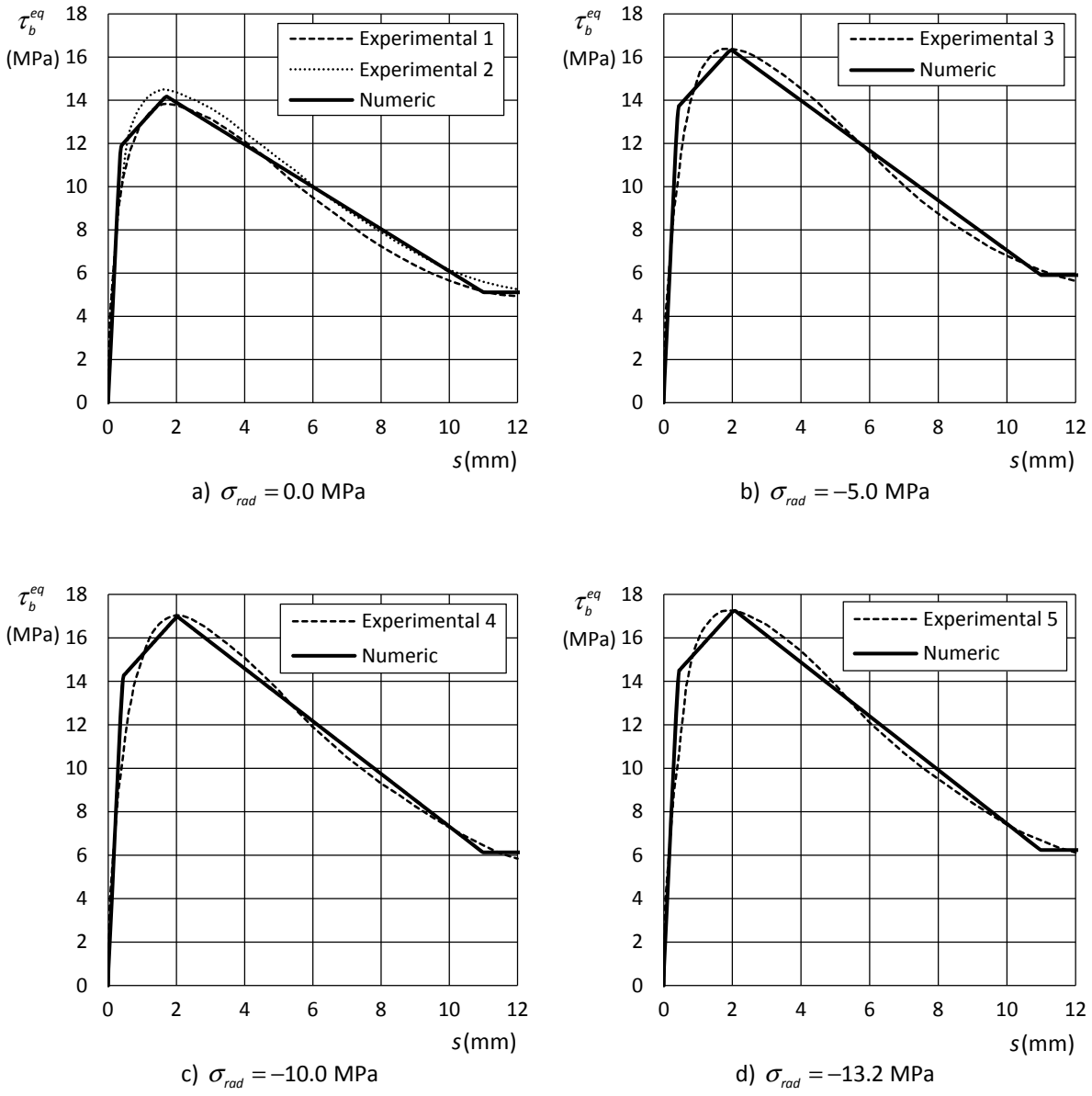

Figure IV.54: Example CSI1.3 – The effect of the radial stress, experimental data from Eligehausen *et al.* [193].

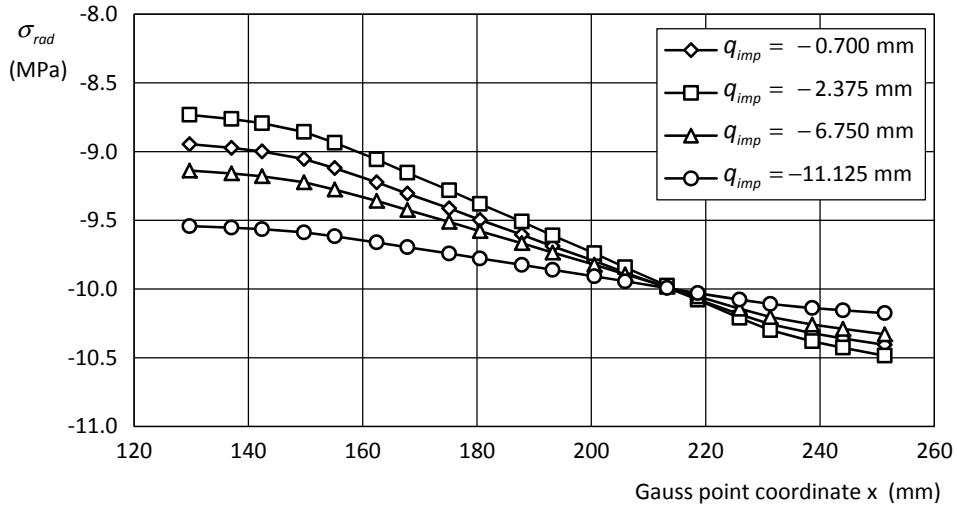

Figure IV.55: Example CSI1.3 –Computed nonlocal radial stresses along the anchorage $(\sigma_{rad} = -10.0 \text{ MPa})$.

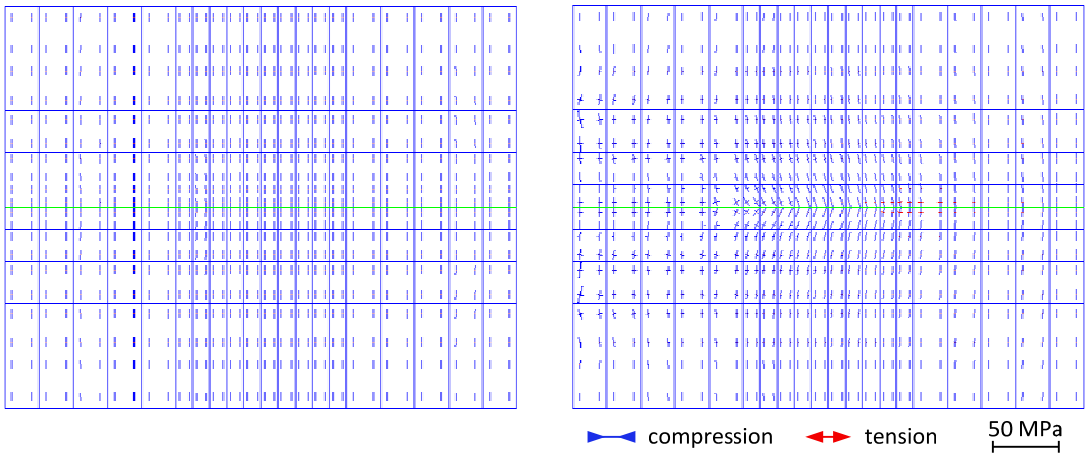

a) $q_{imp} = -0.025$ mm b) $q_{imp} = -2.375$ mm

Figure IV.56: Example CSI1.3 – Principal stress vectors at chosen steps of the analysis $(\sigma_{rad} = -10.0 \text{ MPa})$.

The principal stresses in the concrete are plotted in Figure IV.56 for the case $\sigma_{rad} = -10.0$ MPa. The principal stresses show a nearly uniform compression state at the first time step $(q_{imp} = -0.025 \text{ mm})$. On the other hand, the influence of the bond forces on the radial stress are clearly visible when the peak bond stress is reached $(q_{imp} = -2.375 \text{ mm})$. Nevertheless, this effect is not important for the global results of the numeric simulation.

- Conclusions

Considering the results from the three analyses, it is possible to conclude that the proposed concrete-steel interface model was able to reproduce with a good level of accuracy, the experimental results obtained under monotonic, with and without active radial stresses, and under reversed cyclic loading.

5.2 Example CSI2 – Pull-out tests by La Borderie and Pijaudier-Cabot

The pull-out tests performed by La Borderie and Pijaudier-Cabot [317], already presented in section 2.3.1, were used to validate the model in a three-dimensional analysis case. The geometric and mechanical characteristics of this experimental programme, together with the mesh and boundary conditions adopted are summarized in Figure IV.57. The anchorage length was 45 mm, approximately $5.6\phi_s$, which is considered to be a small anchorage, hence, it is expected that the strain and stress fields will be nearly uniform. The concrete was modelled using elastic three-dimensional isoparametric 8-noded hexahedral elements (H8), the reinforcements were modelled with one-dimensional elastic truss elements (L2) and the concrete-steel interface is simulated using the model proposed in this chapter. Table IV.7 presents the details of all models used.

Four analyses were computed by changing the radial stress in both horizontal directions to $\sigma_{rad} = \{0.0, -5.0, -10.0, -15.0\}$ MPa.The load was imposed as a monotonic *quasi-static* displacement at the protruding steel bar. As before, the parameters for simulating the radial stress effect were computed by fitting the experimental data, using the *Levenberg-Marquardt* algorithm [334, 369], by finding the best values for the parameters η_- and $n_{\eta-}$ for the compression domain of the radial stress equation (IV.28). The experimental data and the radial stress effect sub-model curve resulting from the data fit are represented in Figure IV.58.

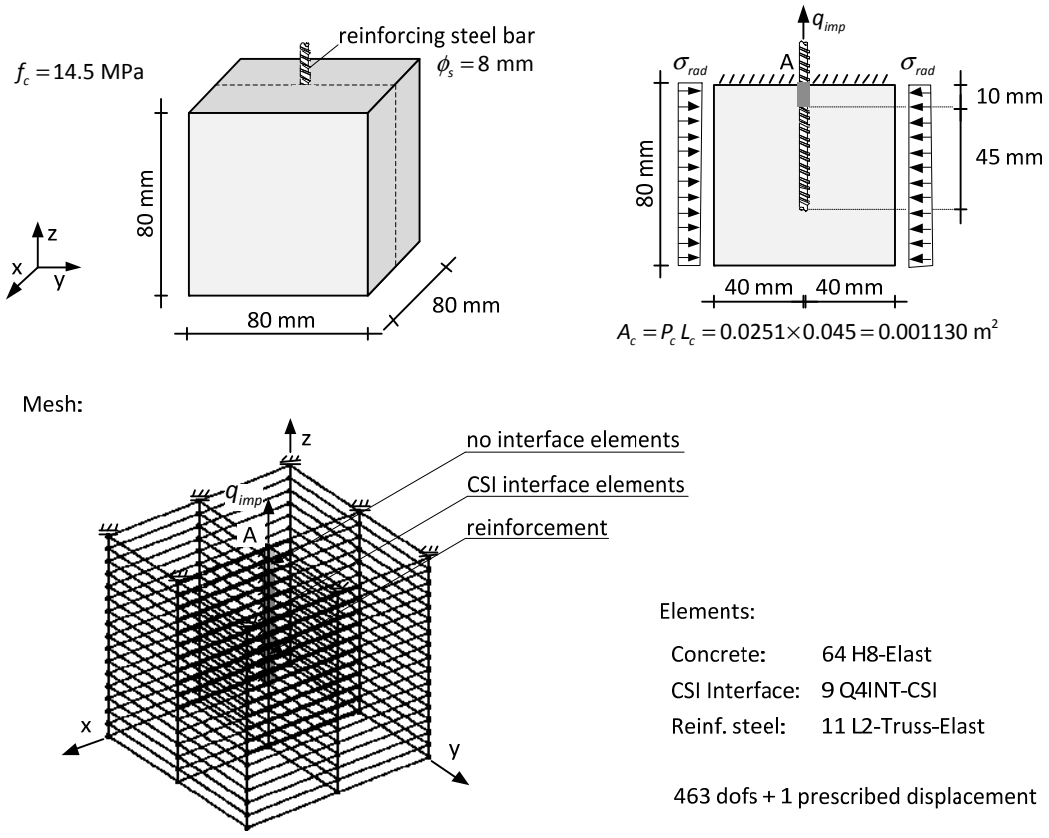

Figure IV.57: Example CSI2 – Geometric and mechanical characteristics and mesh used in the numerical analyses.

Table IV.7: Example CSI2 – Model parameters.

Model	Type	Parameters
1	Elastic	$E = 15.5$ GPa, $\nu = 0.17$
2	EBB-Elastic	$E = 200.0$ GPa, $\nu = 0.30$, $A_s = 0.5026$ cm^2
3	CSI	$k_{pb} = 14.4$ GPa/m, $k_0 = 9.72$ GPa/m, $k_{ul} = 90.0$ GPa/m, $k_{r2} = k_{r3} = 1000$ GPa/m ; $s_{pb} = 0.68$ mm, $s_0 = 1.15$ mm, $s_{res} = 25.00$ mm, $c_{soft} = 2.80$, $f_1 = 0.09$, $f_2 = 0.00$; $\gamma_{res} = 1.00$, $\gamma_n = 1.00$, $n_{pk} = 1.00$, $s^0_{rld} = 0.00$ mm, $s^\infty_{rld} = 0.00$ mm, $n_{rld} = 1.00$; $L_b = 0.015$ m, $f_c = 14.5$ MPa, $\eta_0 = 1.0$, $\eta_- = 1.418$, $\eta_+ = 1.0$, $n_{\eta_-} = 1.562$, $n_{\eta_+} = 1.0$.

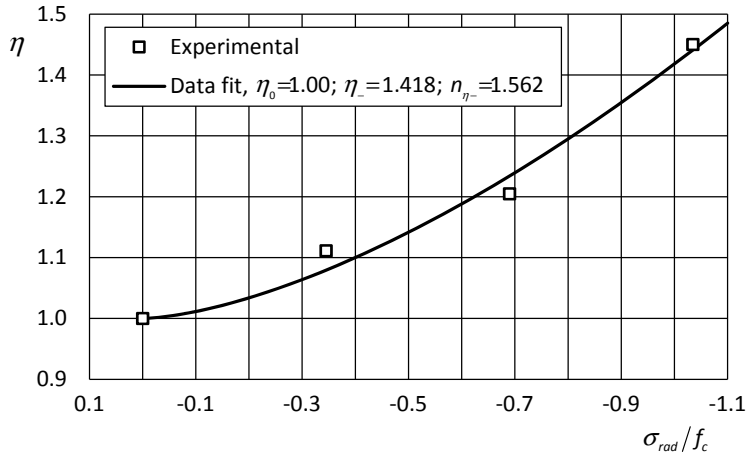

Figure IV.58: Example CSI2 – Calibration of the radial stress sub-model, experimental data from La Borderie *et al.* [317].

Figure IV.59 shows the computed radial stress in the interface elements at the chosen steps, for the analysis with $\sigma_{rad} = -10.0$ MPa . As before, these results show that the bond stress transfer introduces a small variation in the radial stress that is proportional to the pull-out forces.

For the analysis with no radial stress, Figure IV.60-a presents a graphical representation created from the σ_{zz} values at the Gauss points. This figure shows a feasible stress distribution, with stress concentrations near the extremity of the bar embedded in the concrete and near the protruding bar zone. The tensile stress concentration inside the specimen could result in cracking and the elastic model used for simulation the concrete response was not able to capture this effect. Nevertheless, this effect is only local and would not significantly influence the pull-out test results.

The axial stress distribution along the reinforcing bar is presented in Figure IV.60-b. These results confirm the gradual stress transfer between the steel bar and the concrete.

In Figure IV.61, the applied force *vs*. the prescribed displacement at point A is plotted for the four cases of radial stress. Also plotted is the data from the tests obtained by La Borderie and Pijaudier-Cabot [317]. From the analysis of this figure it is possible to observe a good match between the experimental and numerical results. Moreover, it is possible to conclude that, after being calibrated, the model was able to simulate accurately the behaviour observed in all the tests.

Figure IV.62 presents the slip and the equivalent bond stress distribution $\left(\tau_b^{eq} = Q_c / A_c\right)$ along the interface and the axial stress along the steel reinforcing bar for the analysis without radial stress. This data confirms that the slips and the bond stress are almost constant along the concrete-steel interface. In addition, the stress distribution in the steel reinforcement reveals a smooth transmission of forces into the concrete, confirming what was observed in Figure IV.60-b.

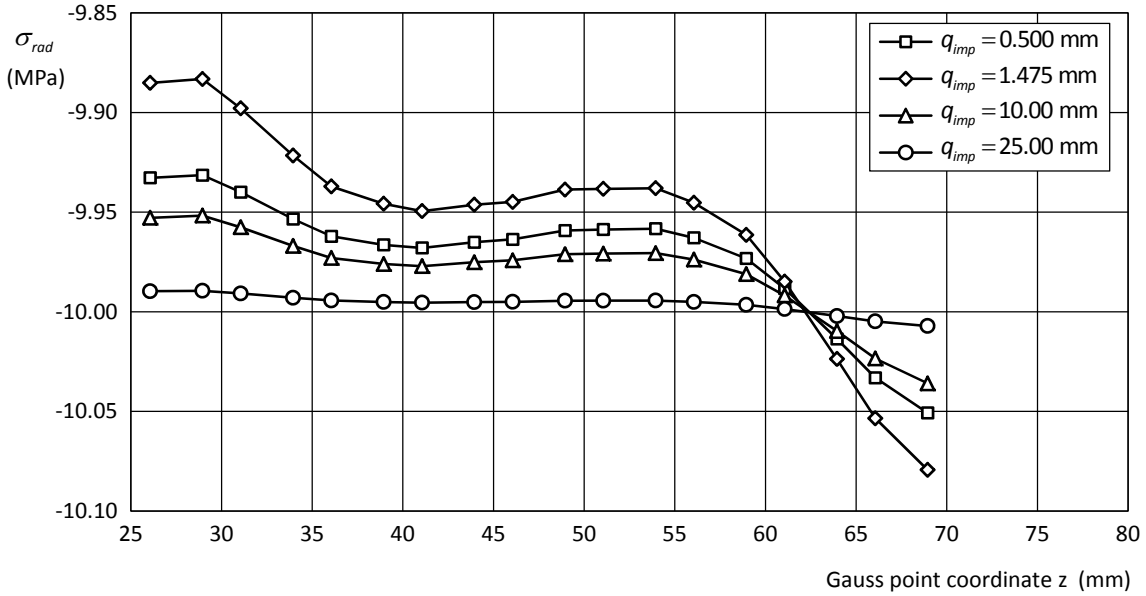

Figure IV.59: Example CSI2 – Distribution of the radial stress along the interface at chosen steps, $\sigma_{rad} = -10.0$ MPa .
Note: see Figure IV.61 to identify the chosen time steps.

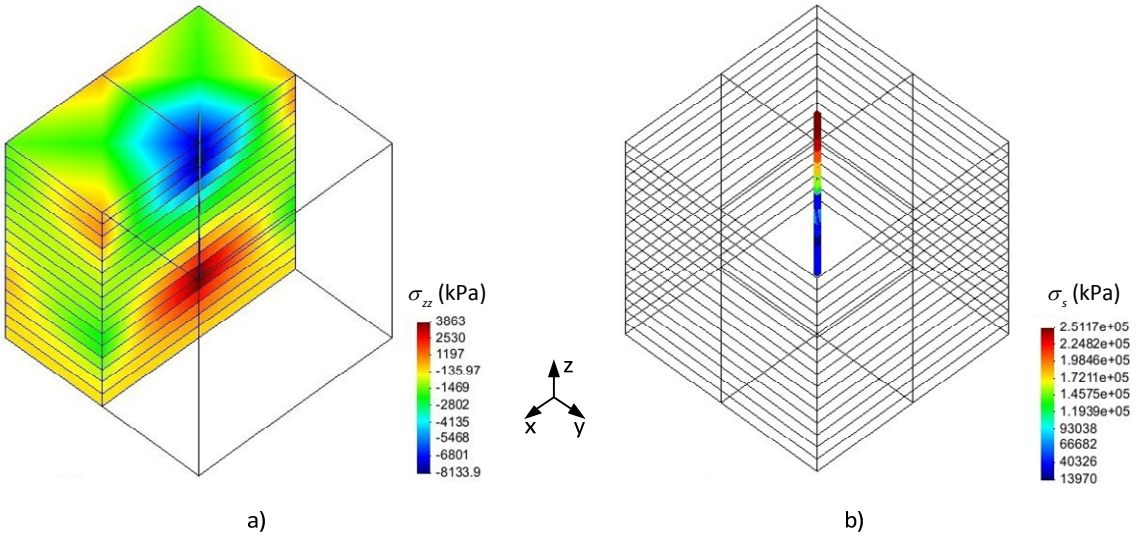

Figure IV.60: Example CSI2 – Analysis without external radial stress $\sigma_{rad} = 0.0$ MPa , values for $q_{imp} = 1.20$ mm :
a) stress field σ_{zz} in the concrete elements; b) axial stress distribution in the reinforcing steel bar.

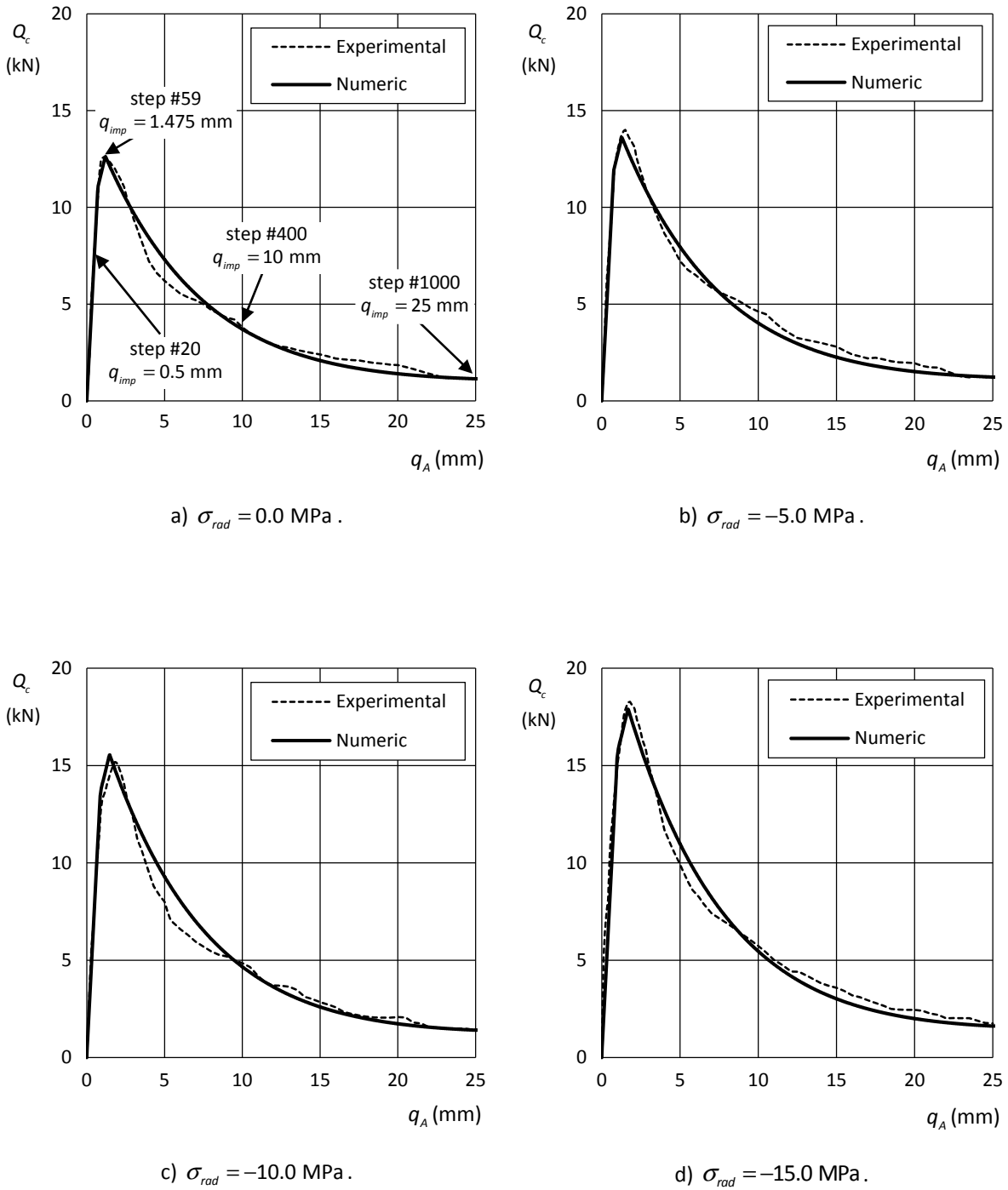

a) $\sigma_{rad} = 0.0$ MPa .

b) $\sigma_{rad} = -5.0$ MPa .

c) $\sigma_{rad} = -10.0$ MPa .

d) $\sigma_{rad} = -15.0$ MPa .

Figure IV.61: Example CSI2 – The effect of the radial stress on the monotonic response: Experimental data from La Borderie *et al.* [317].

a)

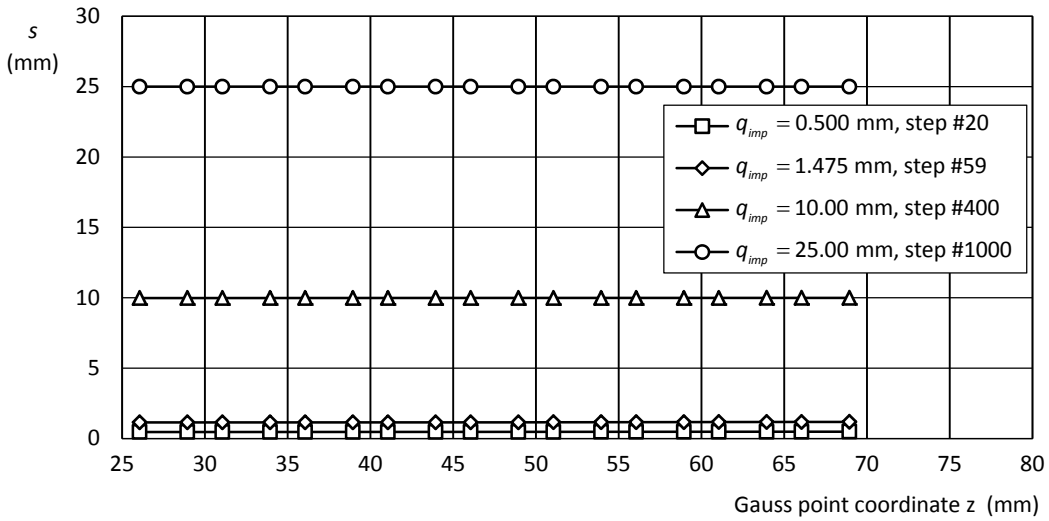

b)

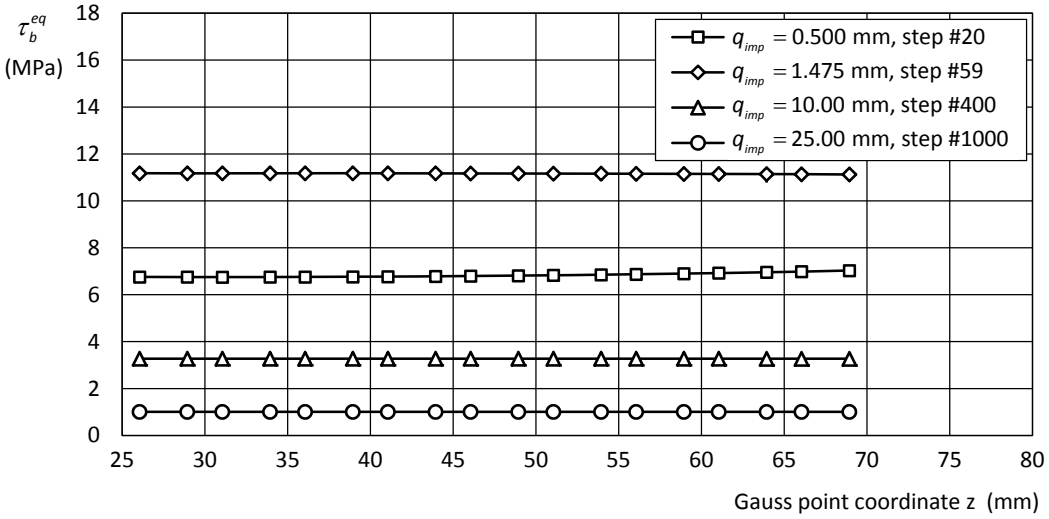

c)

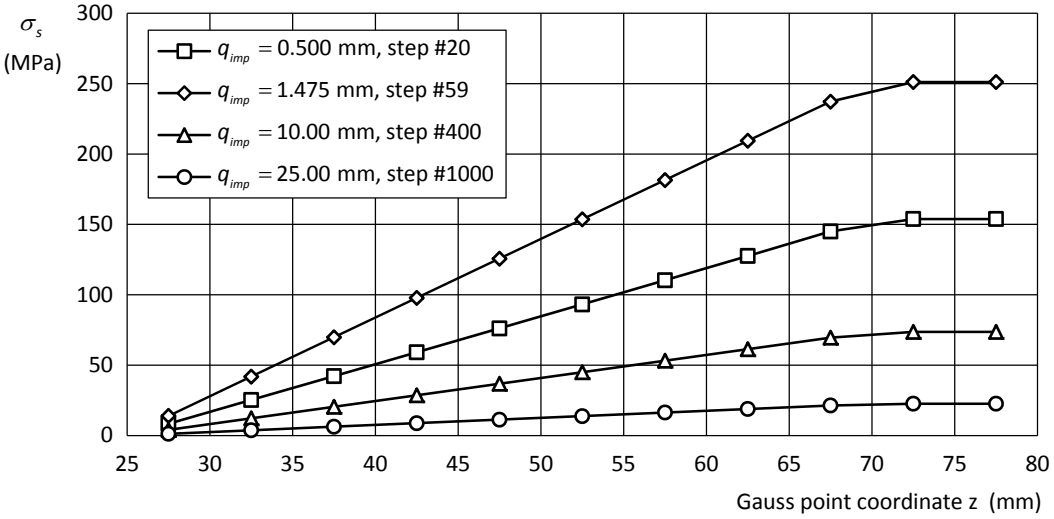

Figure IV.62: Example CSI2 – Analysis with σ_{rad} = 0.0 MPa , values at chosen steps: a) slip distribution along the interface; b) bond stress distribution along the interface; c) axial stress distribution in the steel reinforcing bar.

5.3 Example CSI3 – RC tie tests by Clément

This example concerns the simulation of the experimental tests performed by Clément [113] with tensioned RC elements (see section 2.3.2). The main objective is to test the concrete-steel interface model in a more general situation that includes long anchorages and the inelastic response of the concrete not only in the vicinity of the steel reinforcing bar.

This example may seem a particular case of loading and boundary conditions that are not representative of real RC structures. However, as discussed before, it should be taken into consideration that this test includes many of the phenomena that characterizes the typical response of RC elements and is representative of many situations in these elements, *e.g.* in a beam subjected to bending forces.

The tested specimen consists of a concrete element with a square section of 10 cm and 68 cm long, as represented in Figure IV.63. Centred inside the concrete element is a ribbed reinforcing steel bar with 10 mm diameter. A series of symmetrical displacements are prescribed on both protruding edges of the bar and the total displacement can be computed from:

$$q_{imp} = -q_A + q_B \,. \tag{1.61}$$

The numerical simulation was made using a two-dimensional mesh that includes 760 4-noded isoparametric quadrilaterals (Q4) for simulating the concrete, 76 truss elements (L2) for the reinforcing bars and 76 concrete-steel interface elements. A total of 1771 *dofs* were considered in the analysis and a plane stress constitutive relation was adopted for the concrete elements.

This example comprises six static analyses that are described in Table IV.9. The model parameters adopted are compiled in Table IV.8. The choice of these parameters was the first difficulty to be overcome. Regarding the concrete, there is information regarding the tensile and compressive strength and this data was sufficient. An elastic constitutive relation was adopted for the steel used in the reinforcing bars and common mechanical parameters were adopted. Regarding the concrete-

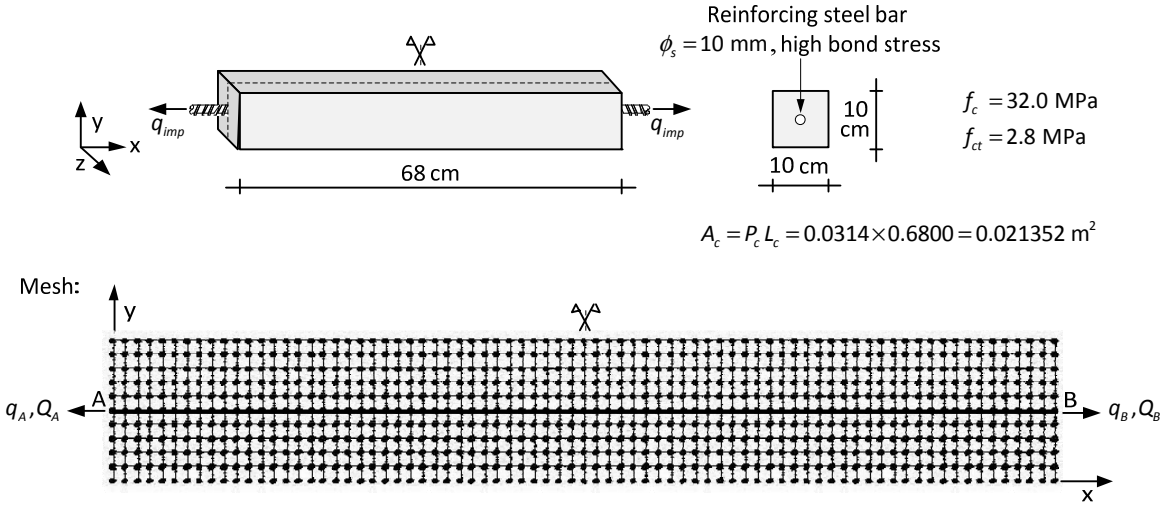

Figure IV.63: Example CSI3 – Geometric, mechanical data and mesh used in the numerical analyses.

Table IV.8: Example CSI3 – Model parameters.

Model	Type	Parameters
1	1D-Elastic	$E = 210$ GPa, $\nu = 0.30$
2	2D-Elastic	$E = 31$ GPa, $\nu = 0.20$, $t = 0.10$ m, plane stress
3	CSI-Elastic	$k_s = \{0; 7.5; 15; 30; 60; 120; 240\}$ GPa/m, $k_{r2} = k_{r3} = 1000$ GPa/m
4	2D-Mazars	$E = 31$ GPa, $\nu = 0.20$, $\varepsilon_{d0} = 9.33$E-05, $A_+ = 0.80$, $B_+ = 18000$, $A_- = 0.90$, $B_- = 1300$ $L_{nl} = 5$ mm (bell-shaped function), $t = 0.10$ m, plane stress
5	CSI-Bond Model	$k_{pb} = 180.0$ GPa/m, $k_0 = 5.6$ GPa/m, $k_{ul} = 60.0$ GPa/m, $k_{r2} = k_{r3} = 1000$ GPa/m ; $s_{pb} = 0.01667$ mm, $s_0 = 2.50$ mm, $s_{res} = 10.8$ mm, $c_{soft} = 0.00$, $f_1 = 0.35$, $f_2 = 0.35$; $\gamma_{res} = 1.00$, $\gamma_n = 1.00$, $n_{pk} = 1.00$, $s_{rld}^0 = 0.00$ mm, $s_{rld}^\infty = 0.00$ mm, $n_{rld} = 1.00$; $L_b = 0.00$ m, $f_c = 32.0$ MPa, $\eta_0 = 1.0$, $\eta_- = 1.0$, $\eta_+ = 1.0$, $n_{\eta_-} = 1.0$, $n_{\eta_+} = 1.0$.
6	CSI-Elastic	$k_s = 10000$ GPa/m, $k_{r2} = k_{r3} = 1000$ GPa/m

Table IV.9: Example CSI3 – Characteristics of the analyses.

ID	Analysis Type	Reinforcements	Concrete	Interface
CSI3.1	Static, Δq_{imp}=0.01 mm	Model #1	Model #2	Model #3
CSI3.2	Static, Δq_{imp}=0.01 mm	Model #1	Model #2	Model #5
CSI3.3	Static, Δq_{imp}=0.01 mm	Model #1	Model #4	Model #5
CSI3.4.1 to CSI3.4.6	Static, Δq_{imp}=0.01 mm	Model #1	Model #4 with strength dispersion implemented at the Gauss points	Model #5
CSI3.5.1 to CSI3.5.6	Static, Δq_{imp}=0.01 mm	Model #1	Model #4 with strength dispersion implemented at the elements	Model #5
CSI3.6	Static, Δq_{imp}=0.01 mm	Model #1	Model #4 with strength dispersion implemented at the Gauss points	Model #6

steel interfaces, there is no information available to estimate bond model parameters. These were chosen using a series of trial analyses made to match the global force-displacement curve that is available from the tests (see Figure IV.22-b).

This procedure started by performing a group of analyses (CSI3.1 in Table IV.9) considering an elastic constitutive relation for the concrete, steel and for the concrete-steel interface (models #1 to #3 in Table IV.8). To calibrate the parameter k_{pb} of the nonlinear bond model proposed, it was used the parameter k_s for the elastic interface element model (IV.49). The results obtained in these analyses are presented and compared with the experimental curve in Figure IV.64. From this comparison, it is possible to conclude that a very stiff initial branch (between 120-240 GPa/m) is required to match the experimental results.

The *contour fill* representation in Figure IV.65 refers to the stress component σ_{xx} for $q_{imp} = 0.25$ mm. It is possible to observe that stress distributions are realistic and are strongly influenced by the parameter k_s, which conditions the load transfer mechanism.

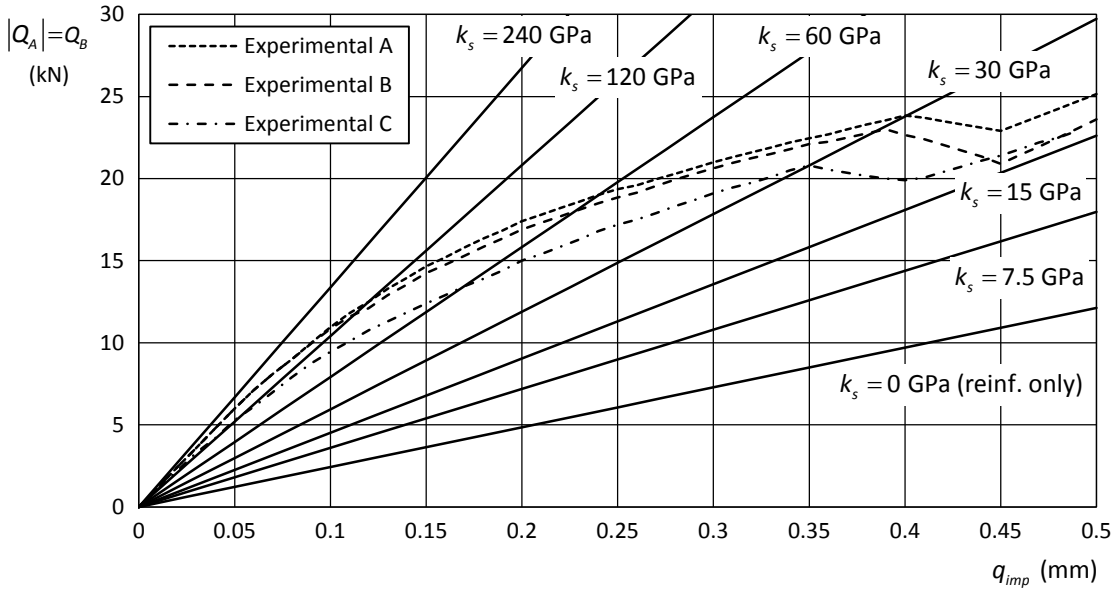

Figure IV.64: Example CSI3.1 – Force-displacement curves for different values of the parameter k_s.

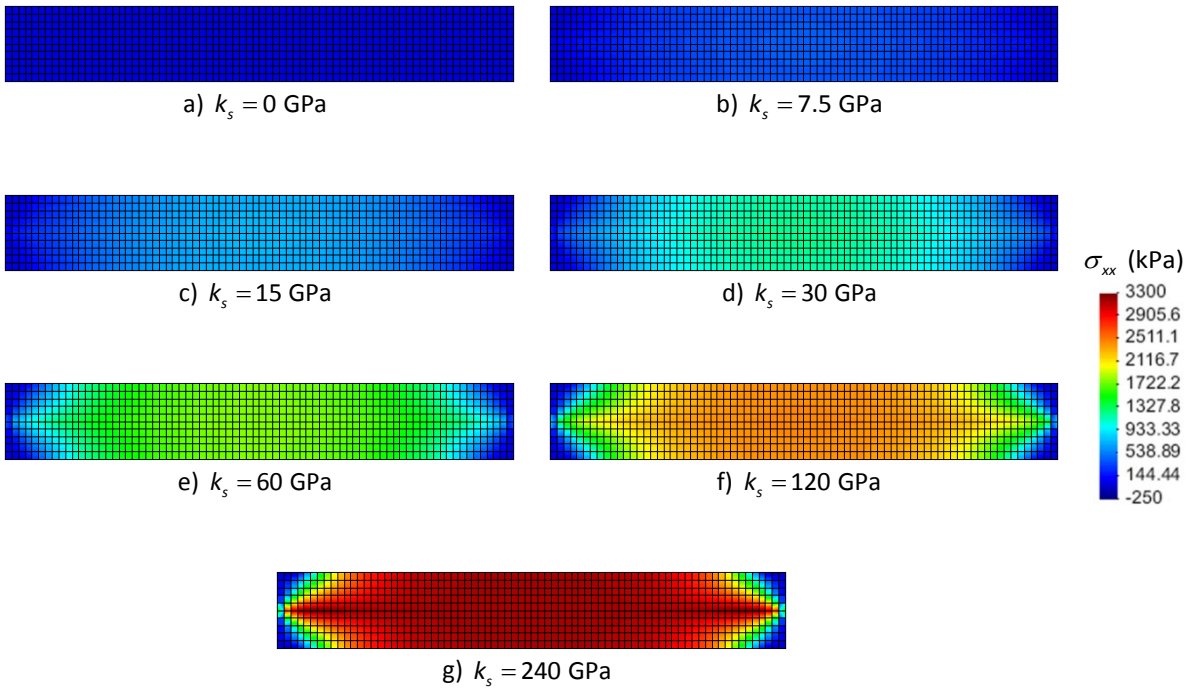

Figure IV.65: Example CSI3.1 – Concrete stresses σ_{xx} for $q_{imp} = 0.25$ mm using different values of the parameter k_s.

Another observation that can be made regarding these results is to analyse if they follow what is expected for an uncracked RC tie, and thus, assess the quality of the data obtained with the elastic interface element. The expected response is described in section 2.2.1 and the typical slip and strain distribution in a RC tie before cracking is presented in Figure IV.6-a/b. Comparing this figure with the data obtained from the numerical model, namely the reinforcing steel stress (Figure IV.66), the bond stress and slip distribution (Figure IV.67) and the stress in the concrete surrounding the bar (Figure IV.68), it is possible to conclude that the same qualitative response is recovered by the numerical model.

Another aspect that can be evaluated is if the tie tested by Clément can be considered a short or a long specimen. From what is presented in section 2.2, long specimens are those where the length of the element and the bond stiffness are able to equalize the strains in the steel and in the concrete, and thus, create a zone where no bond stresses are mobilized. Both the reinforcing steel stress (Figure IV.66) and the stress of the concrete surrounding the bar (Figure IV.68) are consistent in showing that in the middle of the tie this uniform concrete and steel strain is nearly achieved for the highest values of the stiffness k_s. Consequently, the tested tie was considered to be in the transition from a short to a long specimen for the numerical values of k_s compatible with the global experimental results.

After performing the calibration of the stiffness associated with the perfect bond branch, it was necessary to continue the estimation of the rest of the bond parameters. The second step consisted in the evaluation of the second branch between the perfect bond limit and the maximum strength (branch #2 in Figure IV.45). Three parameters must be set for defining this branch, namely: s_{pb}, s_0 and k_0. This branch will influence the way the stiffness of the global curve decreases after the perfect bond limit is overcome, starting from the edges and moving inside the tie.

As a consequence of the lack of information regarding the bond parameters, the adopted procedure was to iterate the parameters manually in order to match the global experimental curve. The resulting model parameters define the monotonic constitutive relation presented in Figure IV.69-a and they were used in the analysis CSI3.2, whose results are presented in Figure IV.71 with the reference to the analysis #2. It was possible to obtain a good match with the experimental results. The differences are acceptable taking into consideration the differences observed in the three tests made.

The concrete constitutive relation must be changed in order to simulate the first macro-crack reported by Clément [113] and evinced in the global force-displacement curve. The model chosen is a nonlocal implementation of the Mazars' continuum damage model (see Chapter III-2.2.7).

The chosen parameters are presented in Table IV.8 (model #4). These parameters were defined to match the reported tensile and compression strength. No information was available for the mode I fracture energy, so, a common softening curve and nonlocal length were adopted. The nonlocal length was chosen taking into consideration that a micro-concrete was used and the value of 5 mm was selected after some tests.

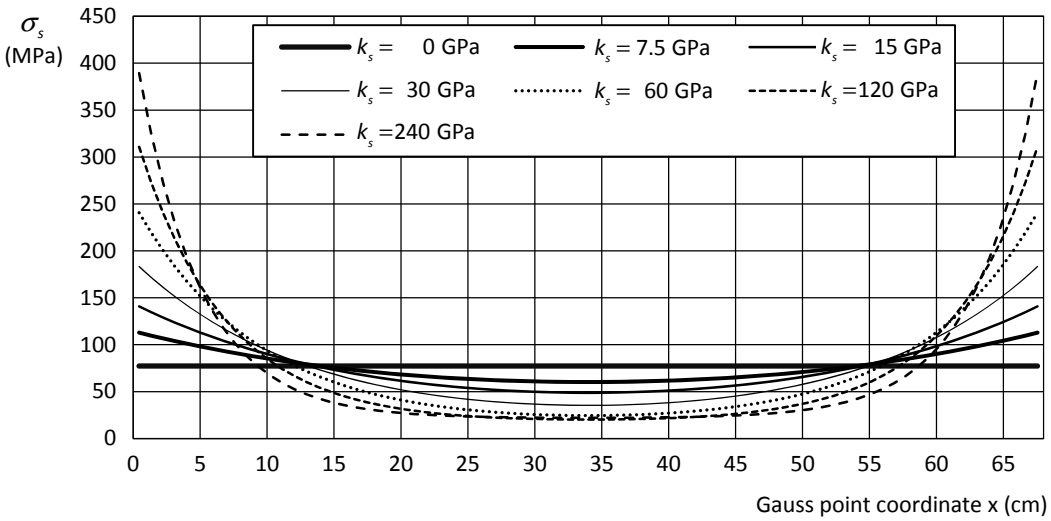

Figure IV.66: Example CSI3.1 – Steel axial stress for $q_{imp} = 0.25$ mm .

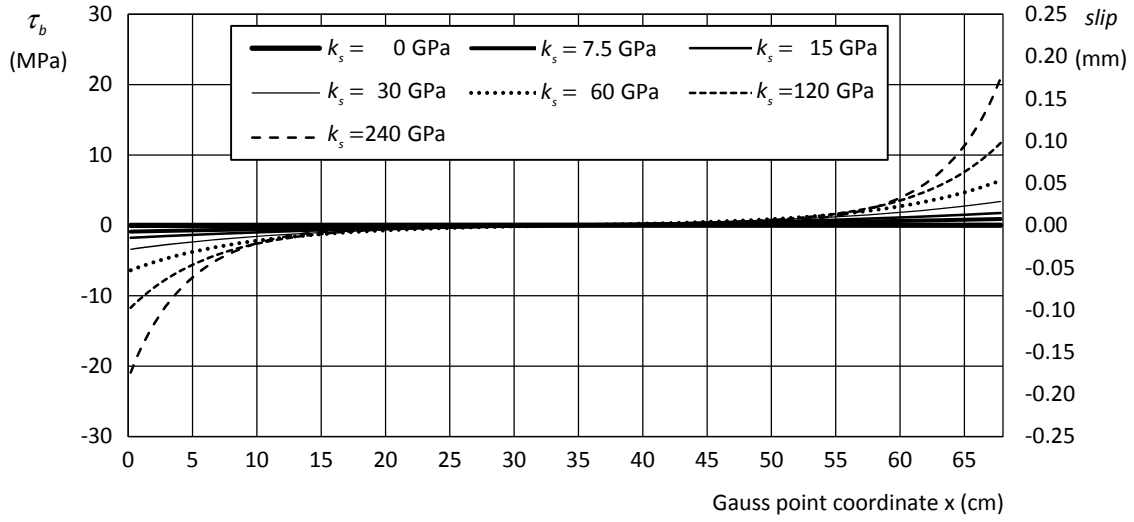

Figure IV.67: Example CSI3.1 – Interface bond stress and slip for $q_{imp} = 0.25$ mm .

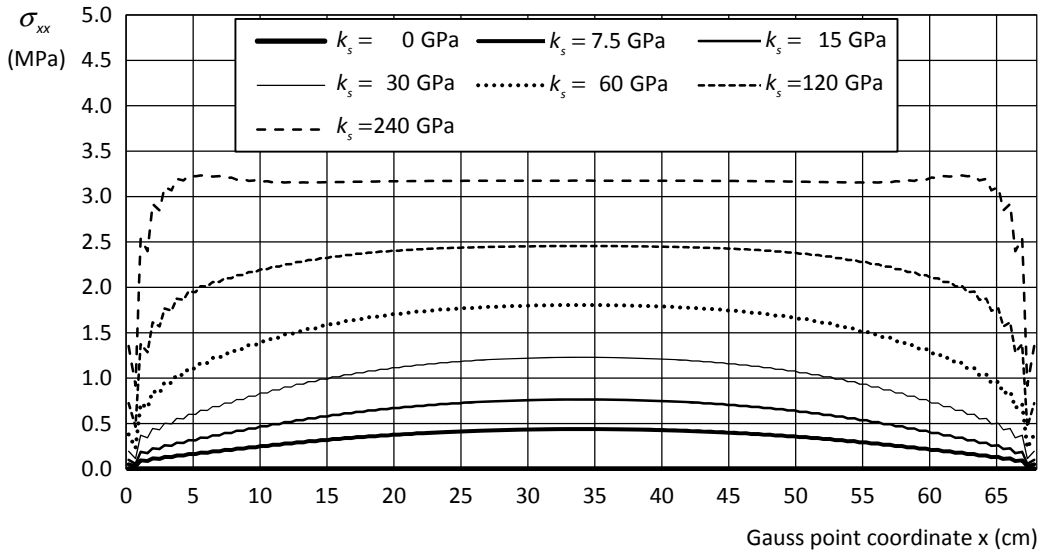

Figure IV.68: Example CSI3.1 – Concrete stress σ_{xx} for $q_{imp} = 0.25$ mm .

Figure IV.71 presents the results from the analysis CSI3.3 (marked as #3) that were computed with this model for the concrete. An immediate conclusion is that the simulation overestimates the cracking loading level. Another indication of how the model is performing is given in Figure IV.73-a that presents the deformed mesh and the damage distribution at step #60 $\left(q_{imp}=0.60 \text{ mm}\right)$. These results show that the damage is concentrated in the mid-section of the tie and the solution is symmetric.

Taking into consideration that Clément reported that the first macro-crack appeared between 21 cm and 31.5 cm of the closest longitudinal edge, it is possible to conclude that the dispersion of the concrete resistance is missing and should be added. This can have a large impact on the results, especially for this case, because long ties create nearly constant normal stress distributions in the interior of the specimen, and thus, all that region can be influenced by a weaker zone that can trigger an earlier fracture. The macro-crack will appear at lower load levels, for larger constant normal stress regions, because there will be a higher probability of having a weaker concrete segment.

The implementation of the concrete resistance variability in the Mazars' model was made using the procedure presented in Chapter III-§3.3. The concrete was considered to belong to a C25/30 class taking into consideration the reported concrete strength $\left(f_c=32.0 \text{ MPa}; f_{ct}=2.8 \text{ MPa}\right)$. Consequently, the tensile strength was implemented with a standard deviation of $\sigma=0.474$ $(\text{RSD}=18.2\%)$ considering the results in Table III.6. For illustrative purposes, Figure IV.69-b presents the resulting constitutive relation under pure tension defined in terms of the strength factor (III.165):

$$\eta_m^+=\frac{\hat{f}^+}{f_0^+}.$$

One question arises regarding where to implement the dispersion. Two options are feasible: i) at the Gauss points, which will result in a constitutive tensor that changes inside the element, similar to what is done within the framework of continuum damage mechanics; or ii) at the elements, which tend to create weaker or stronger elements, and possibly, avoiding having numerical problems in the integration of the structural operators, due to having a constant constitutive tensor inside the element. These two options were implemented in order to assess their numerical behaviour. The series of analyses #4.1 to #4.6 were made by implementing the strength dispersion at the Gauss points and the analyses #5.1 to #5.6 at the elements. The global results are presented in Figure IV.71 and in Figure IV.72, respectively.

Figure IV.70 presents the tensile strength factor histogram and the spatial distribution for the analysis CSI3.5.1, in which the strength dispersion was implemented at the elements. This analysis was selected because when the strength dispersion is implemented at Gauss points, the contour fill representation uses data extrapolations to make the graphical representation in the rest of domain, and consequently, the graph is more difficult to read. The represented data respects quite well the statistical properties $\left(\mu=1.024; \sigma=0.19307; RSD=18.85\%\right)$, although in this case some differences to the theoretical distribution are observable, mainly due to having a relatively small number of samples (NS=760).

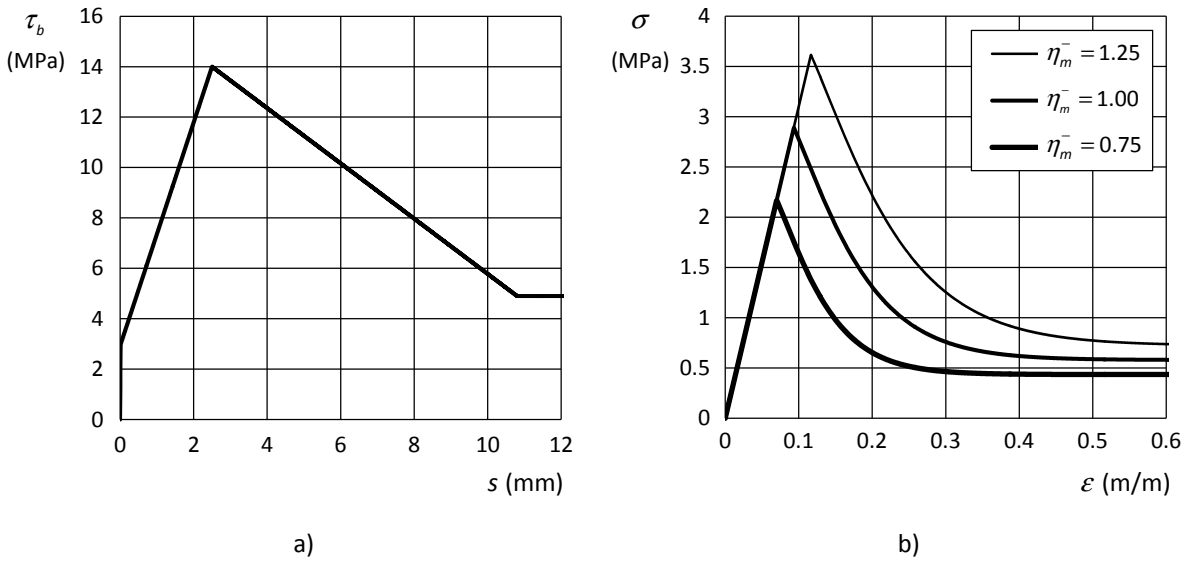

Figure IV.69: Constitutive relations: a) concrete-steel interface; b) concrete.

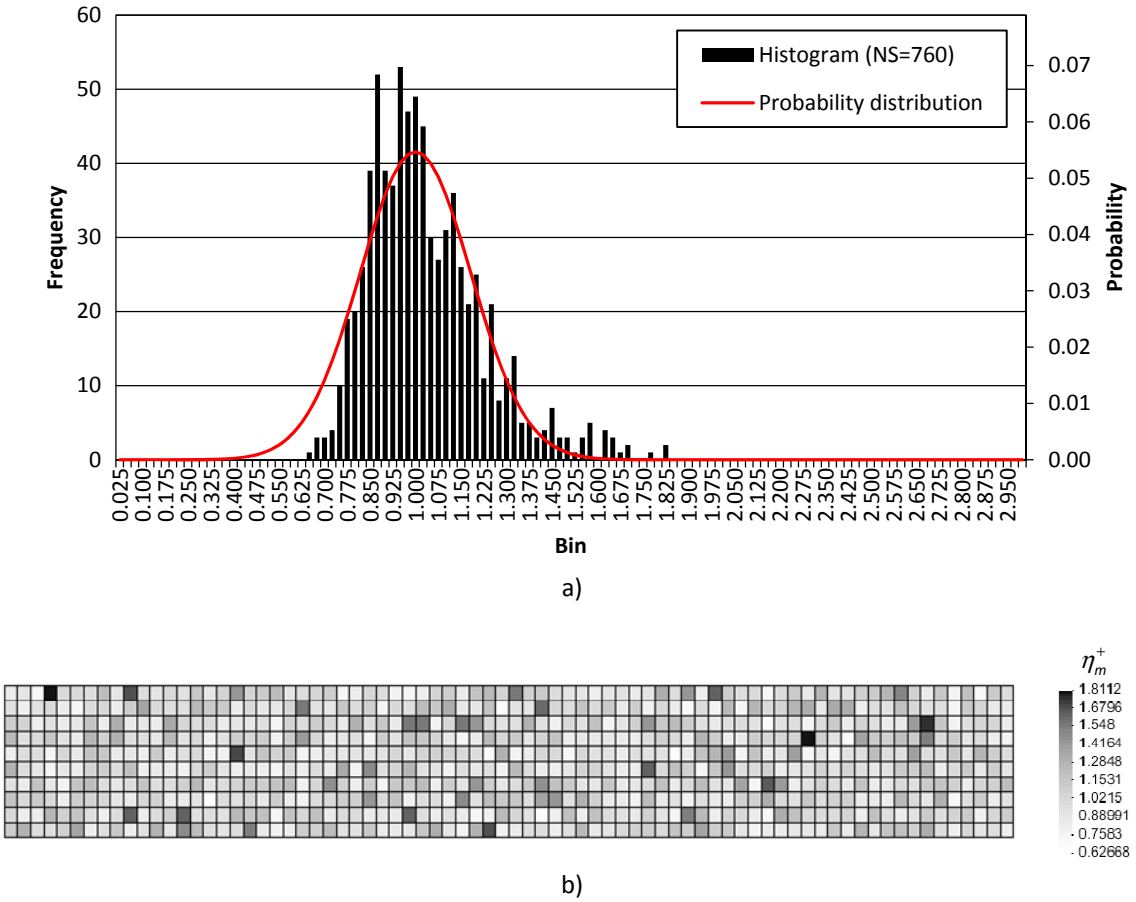

Figure IV.70: Example CSI3.5.1 – Concrete tensile strength factor: a) histogram; b) spatial distribution.

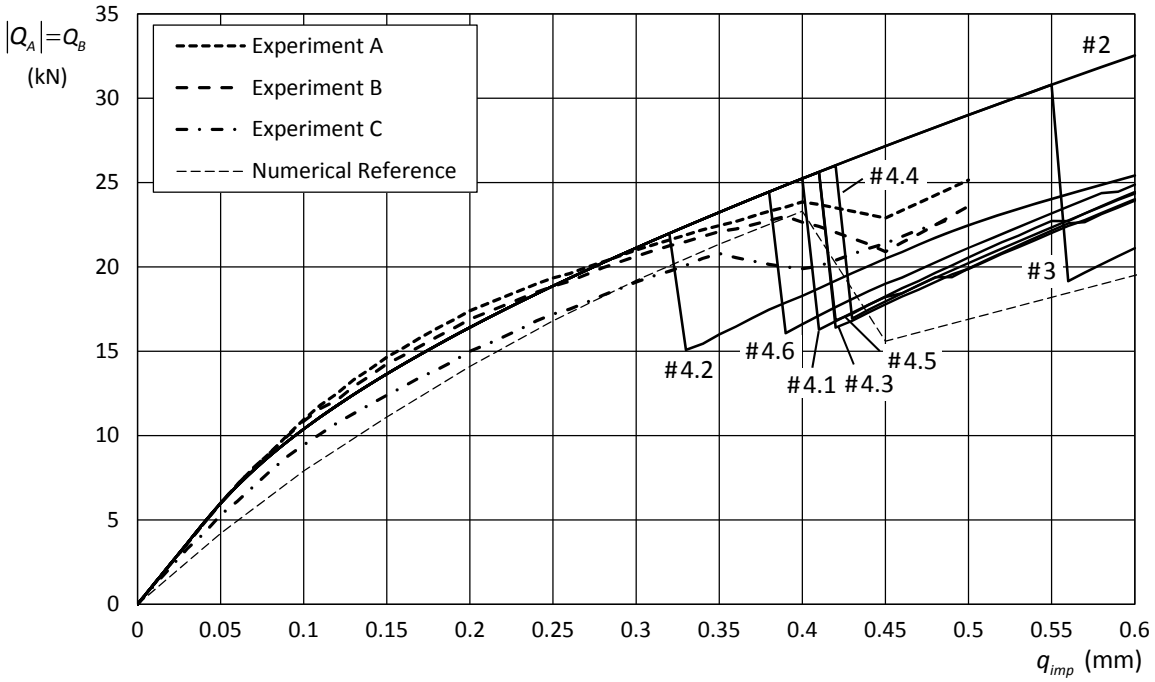

Figure IV.71: Example CSI3 – Force displacement curves for the analyses with the strength variation implemented at the Gauss points, experimental data from Clément [113] and numerical reference data from Dominguez [172].

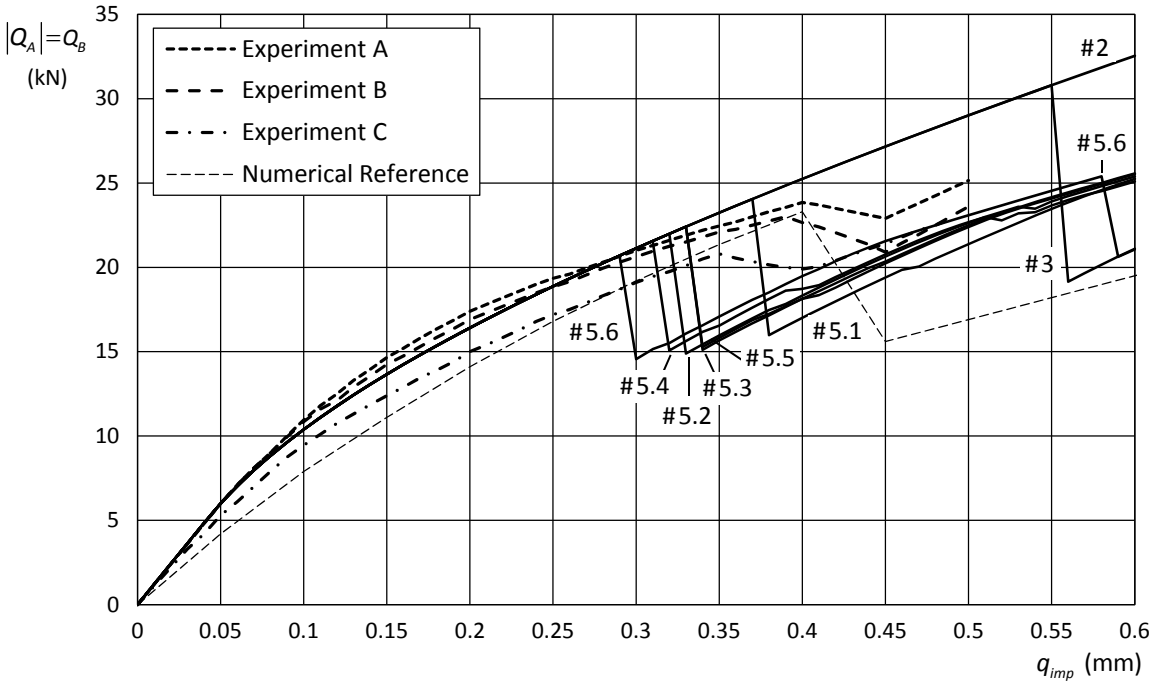

Figure IV.72: Example CSI3 – Force displacement curves for the analyses with the strength variation implemented at the elements, experimental data from Clément [113] and numerical reference data from Dominguez [172].

The results presented in Figure IV.71, with the strength variation implemented at the Gauss points, show a good simulation of the response shape until the macro-crack develops. The cracking load level is also reasonably simulated and the dispersion of the results is compatible with the experimental data. Only analysis #4.2 presented an earlier macro-crack due to a weaker concrete zone that conditioned the results. The number of numerical analyses doubles the number of available experimental tests and thus there is no guarantee that for the same number of experimental tests a weaker specimen would not be found.

The major difference between the numerical and experimental results in Figure IV.71 is the more intense and sudden strength decrease. The macro-crack appeared in a single analysis step and this is related to the type of numerical model used to simulate the concrete. In addition, the shape of the softening branch and the nonlocal length that coped best with the experimental results create a more brittle fracture without dissipating as much energy as observed in the experimental data. After the generation of the macro-crack, the numerical force-displacement curve followed the experimental curve although with the reported force offset. It is not possible to continue this comparison because the experimental tests were stopped just after the development of the first macro-crack.

The same observation made before can be made for the results presented in Figure IV.72, for the case of having the strength variation implemented at the elements. The only noteworthy difference is related to the lower cracking load level. This is expected because cracking is influenced by the weaker concrete zone and by having the variation defined for the entire element domain there will be a larger probability of having a weaker concrete zone that anticipates cracking.

From the analysis of these results, both methods implemented for the concrete strength variation seem to be qualitatively similar. However, when the implementation of the strength variation is based on a larger domain the RC tie results have the tendency of being less resistant and more brittle. This can be observed in Table IV.10 that reports that the average cracking load level for the Gauss point implementation is $q_{imp} = 0.400$ mm versus $q_{imp} = 0.335$ mm for the element-based implementation.

The results presented by Dominguez [172] are also represented in Figure IV.71 and in Figure IV.72. The results are similar and the major difference is that a larger force decrease occurs during the opening of the macro-crack. This is probably related to the fact that the model presented by Dominguez uses a local implementation of Mazars' model that leads to a more brittle response.

The experimental and numerical results can also be compared with respect to the crack location. As mentioned before, the author reported distances between 21 cm and 31.5 cm of the closest longitudinal edge. The results presented in Table IV.10 show an average value of 30.3 cm for the analyses with the strength variation at the Gauss points and 29.6 cm at the elements. As a consequence of not having any information regarding the distribution of the three tests (only the maximum and minimum values), it is not possible to extend the analysis and conclude if the simulation presented realistic or unrealistic results. Nonetheless, the numerical results are within the interval reported, although close to the maximum value.

Table IV.10: Example CSI3 – Cracking load level and distance to closest longitudinal edge.

	q_{imp} (mm)	d_{cr} (cm)
CSI3.4.1	0.41	29
CSI3.4.2	0.33	31
CSI3.4.3	0.42	31-32
CSI3.4.4	0.43	31
CSI3.4.5	0.42	30
CSI3.4.6	0.39	29-30
Average	**0.400**	**30.3**

	q_{imp} (mm)	d_{cr} (cm)
CSI3.5.1	0.38	33
CSI3.5.2	0.33	29
CSI3.5.3	0.34	31
CSI3.5.4	0.32	33-34
CSI3.5.5	0.34	23-27
CSI3.5.6	0.30	25
Average	**0.335**	**29.6**

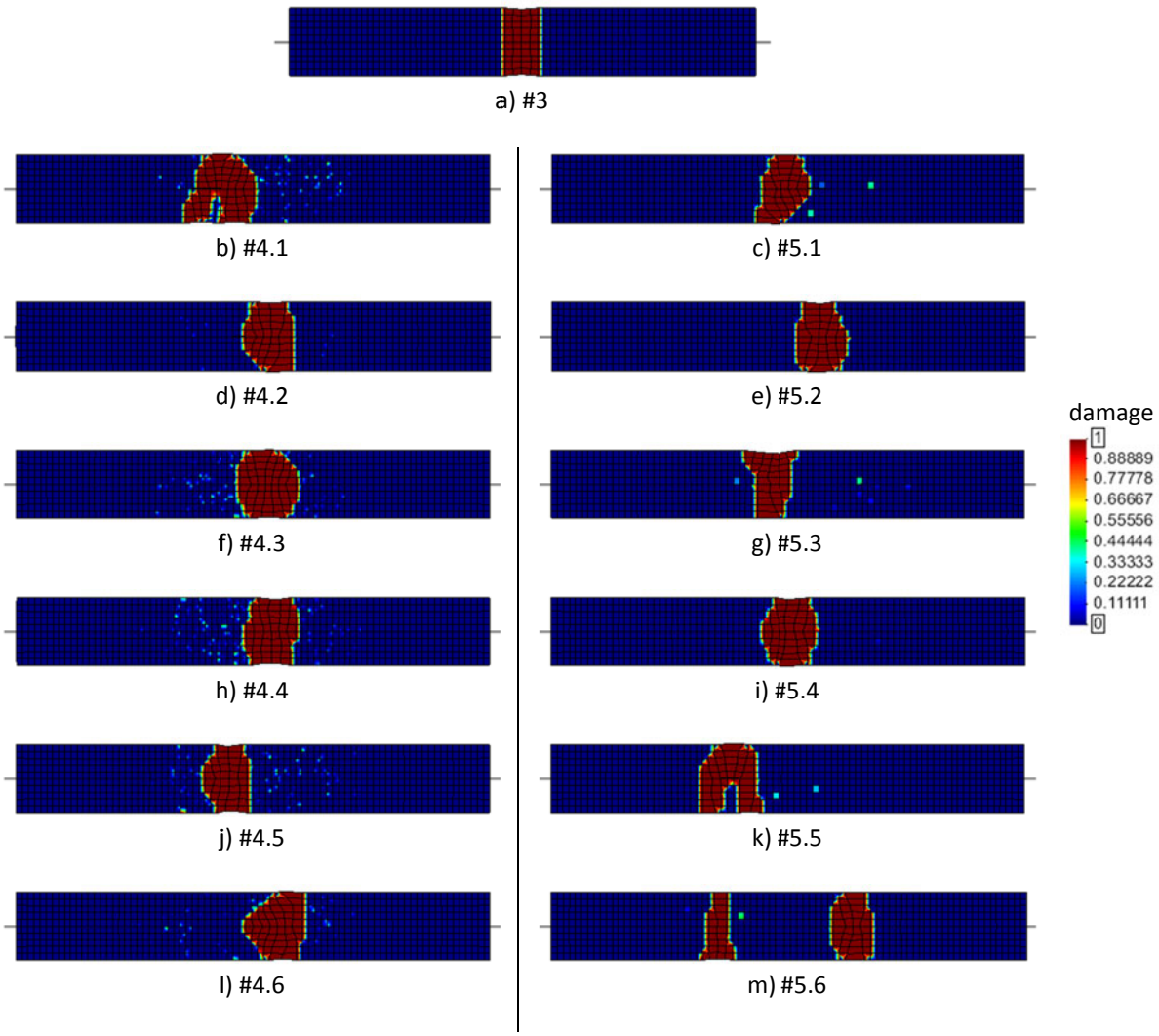

Figure IV.73: Example CSI3 – Deformed mesh (magnified by 100) and concrete damage distribution at $q_{imp} = 0.60$ mm .

Figure IV.73 presents the deformed configuration and the damage distribution at the end of the analyses $\left(q_{imp} = 0.60 \text{ mm}\right)$. The expected changes of the crack position caused by the concrete strength variation can be clearly seen. There was one case where more than one crack was created simultaneously. These figures show clearly that the element-based strength variation tends to concentrate the damage more than the implementation at the Gauss points.

Figure IV.74 and the following present the most important structural quantities that can be used to characterize the deformations and stresses of the steel bar, of the surrounding concrete and of the interface. The analysis #4.1 was chosen to illustrate the response with no particular reason. The other analyses could also have been selected and would have presented similar results.

Figure IV.74 presents the axial stress in the reinforcing steel bar. In the earlier stages, the stress transfer to the concrete is quite clear. Figure IV.75 represents the stress component of the surrounding concrete and confirms the load transfer into the concrete. Nonetheless, in the later analysis steps, a significant stress loss for *x* coordinates between 26 and 34 cm can be seen. This stress decrease is related to the generation of the macro-crack that developed in this region (see Figure IV.73-b). Consequently, the axial stress in the reinforcing steel bar increased after cracking to receive the load that the concrete is not able to sustain anymore (see Figure IV.74). Figure IV.76 presents the damage variable of Mazars' model (III.100). From the analysis of this figure, it is possible to identify the macro-crack position and other concrete damage locations, which are related to the concrete strength variation that results in some randomness in the damage distributions near the most stressed locations (see also Figure IV.73-b). One of the major differences between the numeric and experimental responses is related to the size of the localization band. In a real RC tie the macro-crack is a phenomenon much more concentrated than the equivalent smeared approximation used in the numeric model (see Figure III.9).

Figure IV.75 presents some fluctuations in the concrete stresses that are considered normal, taking into consideration that the static fields resulting from the traditional finite element method have inferior quality. Nonetheless, these variations are small and do not compromise the global results of the analysis.

Figure IV.77 shows the distribution of the slips along the concrete-steel interface. In the first steps the response is already similar to that of the elastic analysis #1 (see Figure IV.67). After the development of the equivalent smeared representation of the macro-crack, the slips in the crack region show a large jump and a sign inversion. This response clearly demonstrates that after cracking, the RC tie with 68 cm of length turns into two new RC ties with around half of the initial length. The bond response of these two new sub-members is similar to the initial RC tie for the early stages.

The analysis of Figure IV.77 also demonstrates that the crack in the concrete creates slip inversions that also requires defining the parameters of the constitutive model for dealing with load reversals, even though the loading is monotonic. For example, the parameters k_{ul} and f_2 were clearly necessary to compute the results presented.

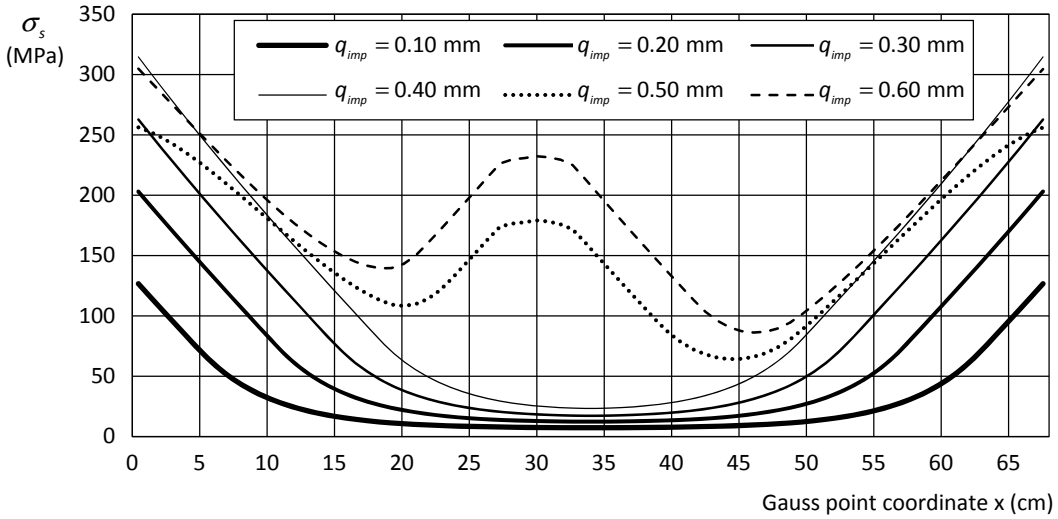

Figure IV.74: Example CSI4.1 – Reinforcing bar axial stress at selected steps.

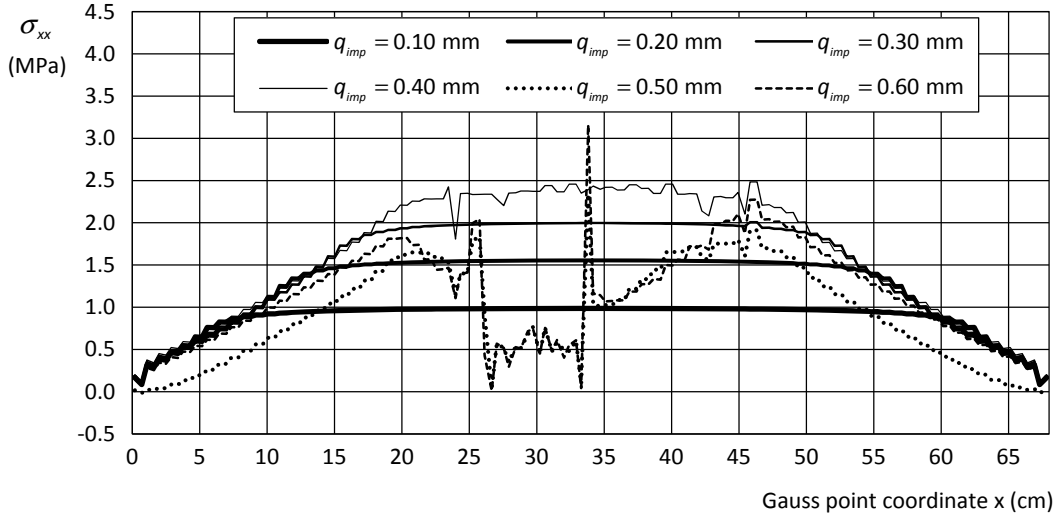

Figure IV.75: Example CSI4.1 – Concrete stress σ_{xx} at selected steps.

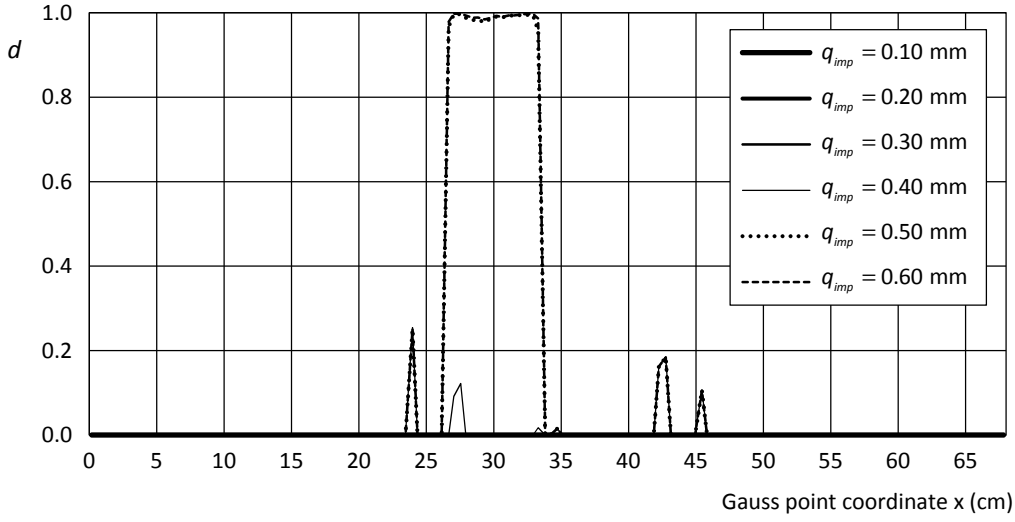

Figure IV.76: Example CSI4.1 – Concrete damage variable at selected steps.

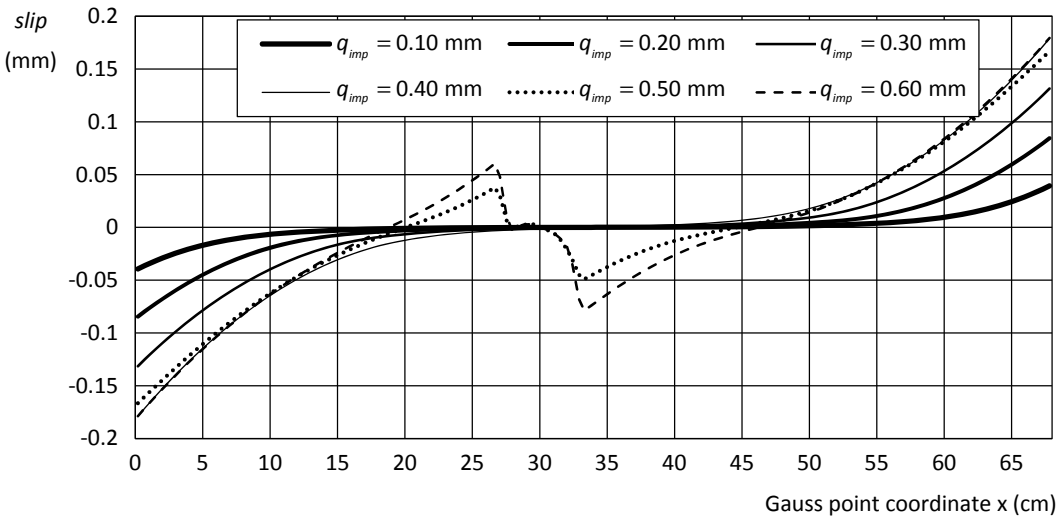

Figure IV.77: Example CSI4.1 – Slips in the concrete-steel interface at selected steps.

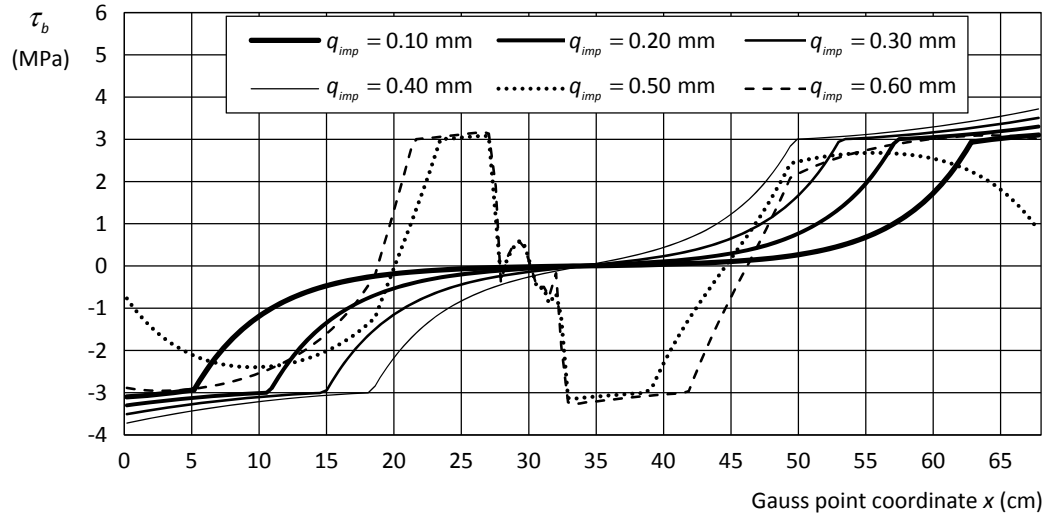

Figure IV.78: Example CSI4.1 – Bond stress in the concrete-steel interface at selected steps.

Figure IV.78 presents the distribution of the bond stress along the interface. The response starts to be similar to the elastic response (see Figure IV.67). However, even before cracking, the perfect bond is reached and passed. The bond model branch that connects the perfect bond limit to the peak stress (branch #2 in Figure IV.45) is clearly visible near the longitudinal edges of the tie.

The following characteristics of the bond response are identifiable after cracking: i) in the crack region, the bond stress is nearly zero because no stress is being transferred to the concrete; ii) in the vicinity of the crack, the unloading branch is visible (branch #6 in Figure IV.45), and also, the unloading residual stress (branch #7 in Figure IV.45); iii) near the longitudinal tie edges, unloading occurs followed by reloading after the transition to the two new bond units.

- Analysis CSI3.6 - Stiff elastic concrete-steel interface

The last analysis case (CSI3.6) was made with the objective of testing if the steel, concrete and interface models are capable of simulating the response of long RC ties with multiple cracks. It was not possible to find experimental data for this case. Hence, no comparison and validation can be made. Consequently, It was decided to use most of the characteristics of the RC tie tested by Clément [113] and change some parameters to simulate a long tie. This can be done in at least two ways. The first approach is to change the tie dimensions, in particular its length. This had the drawback of requiring remeshing. To avoid this, it was decided to follow the alternative approach of increasing the bond stiffness. This will augment the stress transfer to the concrete, and thus, create the desired strain equalization between the concrete and the steel bar, which characterizes a long RC tie (see section 2.2.1 and Figure IV.6). This methodology will enable the generation of multiple cracks and does not require any mesh changes, only changing the parameters of the bond constitutive relation. The analysis was made considering a very stiff elastic bond model for the interface element $\left(k_s = 10000 \text{ GPa/m}\right)$. The nonlocal Mazars' model with strength variation implemented at the Gauss points is once more used to simulate the concrete (see Table IV.5).

It was decided to adopt an elastic bond model instead of the proposed model. This choice was made to simplify the analysis and because increasing the initial stiffness by several orders of magnitude will result in a bond model with no physical meaning. Moreover, the other parameters would have to be chosen with no criteria, so this complexity was considered unnecessary for the objectives of the analysis.

The global force-displacement curve, presented in Figure IV.79, is characterized by an initial very stiff ascending branch that decreases with the damage in the concrete near the reinforcing bar. The representation of the concrete damage variable in Figure IV.80-a clearly shows this behaviour. This longitudinal damage is likely to be augmented by the use of the CDM approach to simulate the concrete response. Approximately, for $q_{imp} = 0.20$ mm the first transversal crack appears in the response (Figure IV.80-b), as expected near the longitudinal edges. This distance to the edge represents the *anchorage length* necessary to transfer enough stress to the concrete and creating a transversal crack. This length depends on the concrete and bond characteristics and tends to be constant when these properties are homogeneous. The next part of the analysis occurs in the same manner: longitudinal cracking near the reinforcement followed by transversal cracking. The global force *vs.* displacement curve presents a gradual stiffness decrease and a series of simultaneous jumps associated with transversal cracking. At the end of the analysis, the tie presents eight cracks with a regular spatial distribution and an average distance of 7.50 cm.

The solution for the tie without considering the concrete is also represented in Figure IV.79. This makes it possible to identify very clearly the *tension stiffening* effect (see Figure IV.7), related to the contribution of the concrete in between cracks to the global response. In this case, this leads to an increase of 43% in the secant stiffness when compared to the reinforcement alone.

All these observations are according to what is expected to be the response of a RC tie. It is possible to conclude that the proposed bond model was able to simulate the response of a long RC tie.

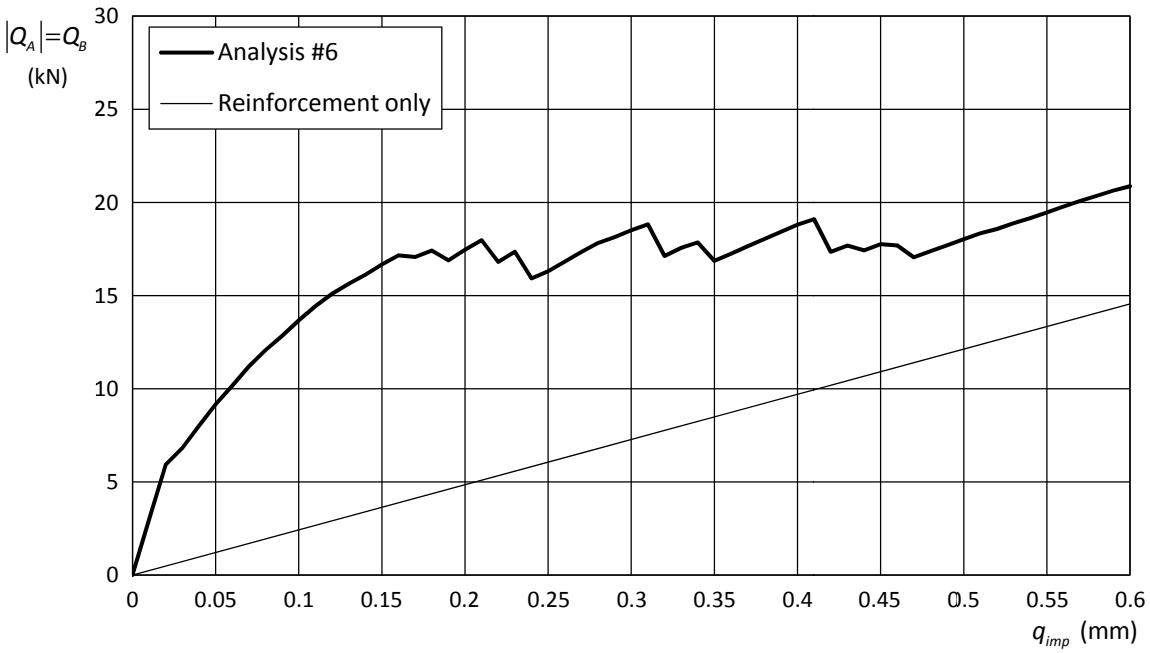

Figure IV.79: Example CSI3.6 – Force-displacement curves.

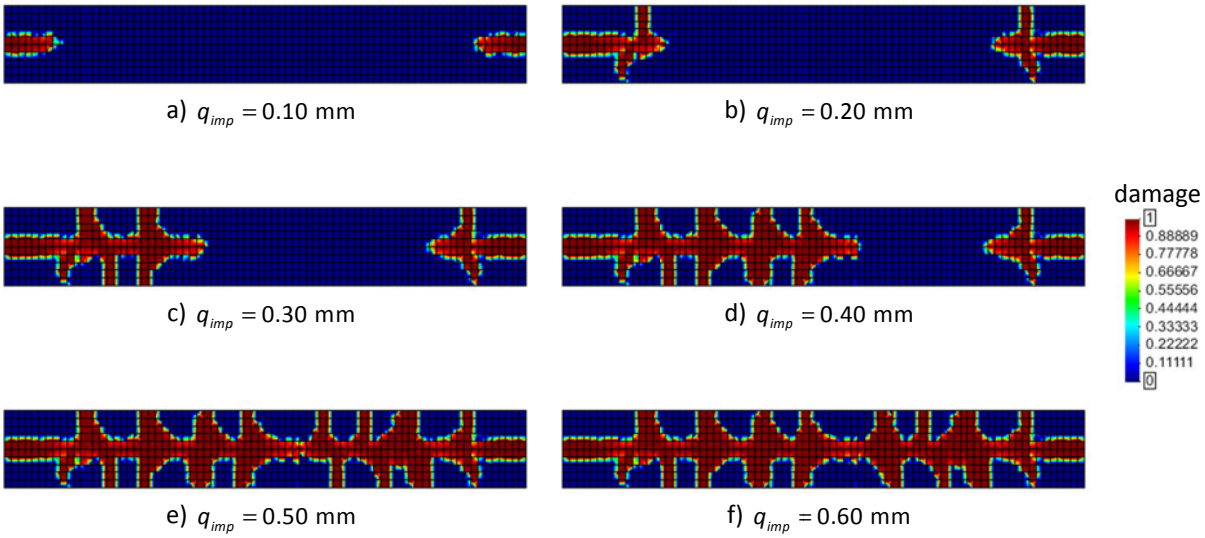

Figure IV.80: Example CSI3.6 – Concrete damage distribution at selected steps.

Chapter V

Computational Performance

1 Introduction

Within the framework of structural mechanics, the main objective of improving the computational performance of numerical simulations using high performance computers and specially designed solving algorithms, is to solve larger and more detailed simulations in order to better represent the structural behaviour, which otherwise would be unachievable or unfeasible. The *nonlinear incremental dynamic analyses* (NL-IDA) considered in this work are particularly demanding from the computational point of view, as a result of using meshes with a large number of *degrees of freedom* (*dofs*) and due to the large number of increments (time steps) required to produce accurate results. These difficulties represent a demanding challenge that requires using state of the art techniques and equipment to generate viable numeric simulations.

On the other hand, during the last decades it has been possible to observe great developments in the computational hardware and in the algorithms available for solving large scale problems. During this period, the evolution of computational hardware has been considerable and consistent. However, lately, the technological solutions adopted to improve the overall computational efficiency shifted from increasing the performance of each *processing unit* (PU) to increasing the number of PUs, by using multi-core processors and multi-processor computers. This has been an undeniable hardware trend in recent years, resulting in accessible products with up to 12 PUs in a single processor in 2010

(*e.g. AMD Opteron 6000 series*). Additionally, multi-core processors have spread to the majority of modern personal computers and laptops, and accessibility to high-performance computers has improved significantly in the last decade. Nowadays, most research laboratories and universities have some type of access to this equipment (*e.g.* the *Medusa* cluster installed at LNEC with 276 PUs and a peak performance of 2649 GFlop/s). This trend presents a very strong justification by itself for adopting concurrent computations. This step has proven to be difficult to take, and perhaps until recently unjustified, mainly because of the additional complexity in the algorithms and of the steady increase in speed of single PUs observed until the first half of the last decade. These issues created a large and justifiable inertia to take this step in the scientific and engineering communities, which most of the time choose to adopt sequential algorithms. Furthermore, concomitant to this hardware trend, it has been possible to observe significant activity and new developments in the substructuring methodologies that adopt the *divide and conquer* approach to solve large numerical problems. These algorithms, *a.k.a. Domain Decomposition* (DD) methods, had a strong contribution from computational mathematics research groups, often associated with high performance computational centres, and are perfectly suitable for parallelized implementations.

In conclusion, it is possible to provide well founded reasons for the necessity and pertinence of using concurrent algorithms to cope with the high computational demand resulting from the type of simulations adopted in this work. A medium-term goal for the proposed models and numerical techniques is to become a viable complement or alternative to large-scale testing, which most of the time is more expensive and requires a longer time for execution. This point of view clearly justifies a chapter in this thesis dedicated to the improvement of the computational performance for NL-IDA, resulting in a part of the work more related to mathematical and computer science issues, than to structural or earthquake engineering.

The methodology that will be used to achieve the goal of improving the computational performance is based on three main strategies: i) concurrent computations will be used to improve the performance of the algorithms; ii) advanced substructuring techniques will be used to adapt the code and potentiate the gains associated with the parallelization; and iii) the problem size will be reduced by using different discretization approaches and densities, leading to what will be called *hybrid discretization* in this thesis.

The terminology related to the subjects addressed in this chapter will be presented gradually throughout the text. However, there are some key or ambiguous expressions that should be clarified at this stage. In the context of computational hardware, the term *processing unit* (PU), or simply *processor*, will be used to refer to a unitary physical processing device instead of a *central processing unit* (CPU), which could cause some confusion about whether it refers to a single processing unit or to the chip that may unite several PUs. Moreover, the term *memory unit* will be used to refer to volatile data storage devices (*e.g.* RAM). On the other hand, a *data storage unit* refers to a persistent data storage device (*e.g.* hard disk and flash drives). A *computer node* refers to a computer unit that can incorporate several processing, memory and data storage units, and also, communication devices. Furthermore, regarding the structural analysis algorithm, the term *substructuring* will be used to mean that the global response of the structure is evaluated by combining simpler structural

units, which will be called *subdomains*. Moreover, the term *Domain Decomposition* (DD) method refers to the numeric formulation that can be used to implement substructuring.

The outline of this chapter is the following: At the beginning, a summarized state of the art is presented regarding the main issues related to the computational performance, condensation methods, matrix storage schemes, linear and modal solvers, kinematic constraints and transition elements. Afterwards, the issues related to hybrid discretization and to the implementation of substructured analyses using parallelized algorithms are addressed. The chapter closes with a set of validation examples, chosen to test the techniques and methodologies proposed in this chapter and to assess their performance.

2 State of the art

2.1 Computational hardware and algorithms

2.1.1 Introduction

A computer can be seen as an electric machine that presents the capacity of performing fast processing and communications, and holding large amounts of data. The most common computer hardware configurations can be classified into the following four groups:

i. A *Laptop* is a portable computer that due to constraints regarding size and energy consumption, usually possesses less performance than a personal computer;
ii. A *Personal Computer* (PC) is a local single machine that takes its name from being widespread and available for individual users. It is characterized by having its own local computational resources (processor, memory, *etc.*);
iii. A *Workstation* presents a similar configuration to a PC. What differentiates them is that a workstation is commonly used in professional environments to perform demanding computations that require improved hardware capacities (*e.g.* several multi-core CPUs, larger amount of RAM memory or better graphics capacities);
iv. A *Supercomputer* is a machine designed to deliver high performance computations. The most common type of supercomputer is a *cluster*. A cluster takes its name from the fact that it consists of a group of interconnected computers, working together closely so that in many respects they form a single computer. The processing capacity is most of the time achieved by increasing the number of PUs, rather than increasing the capacity of each PU. Therefore, using concurrent computations is vital for achieving the desired performance;
v. A *Virtual Supercomputer* is a high performance computing machine similar to a supercomputer but in this case the physical presence of each computer element is geographically spread over the territory. They can work as a single computer using appropriate software and network or internet communications. The concept and technology is closely related to *Grid* and *Cloud* computing (see section 2.1.6).

The main resources of a computer are the processing, memory, data storage and communications capacity. In the following sections, a resume of the main characteristics of these hardware-related components is presented, followed by an overall view of the most common instructions and algorithm types. At the end, some issues related to performance analysis are addressed.

2.1.2 Processing capacity

The processing capacity of a computer is commonly evaluated by the number of instructions it can execute per time unit. Most of the time, this is measured in *floating point operations per second* (Flop/s or FLOPS). The number of Flop/s a computer can execute can be a difficult number to measure. Different benchmarks have been proposed with this objective (*e.g. Linpack benchmark* [174]). The maximum theoretical (peak) value of floating point operations per second of a homogeneous system can be estimated using the following formula:

$$FLOPS = NPU \times CR \times IPC\,, \tag{V.1}$$

where NPU is the *number of processing units* (cores), CR is the processor's *clock rate* and IPC is the *number of instructions per cycle* of the processor. The NPU of a homogenous system may be computed by multiplying the number of nodes existing in a cluster, by the number of processors and by the number of cores per processor.

The clock rate is a technical specification of each processor which is quite easy to retrieve. However, recently, Intel's *Turbo Boost* technology has somewhat complicated this parameter, because this technology increases the base clock rate dynamically, if the processor is operating bellow a set of limits related to the temperature, power and current consumption [284]. The number of IPC is a figure which is quite more difficult to evaluate. This number represents the number of floating point operations each processing unit can perform simultaneously, or in other words, the parallelism within a single PU. This number is not constant for a given processor and even less so between different processor architectures. It depends on hardware-related factors and how the software being run interacts with the processor. Nevertheless, a constant value is frequently adopted to estimate the peak processing capacity. The IPC value is taken as four for most modern processor architectures.

The peak value of floating point operations per second for the most relevant supercomputers since 1950 is presented in Figure V.1, which confirms the consistent growth of the processing capacity [173]. One historical fact regarding the processing capacity should be mentioned. In 1965, the co-founder of Intel, Gordon Moore, published a paper describing that the number of transistors per unit area on an integrated circuited presents a doubling tendency for each year since the invention of the first integrated circuits in 1958 [406]. The same author predicted that this trend would continue for at least one decade. This prediction has proven to be very accurate although the doubling pace has decreased to about 18-24 months and it is expected to be followed at least until 2015. Figure V.2 presents a record of the evolution of the number of transistors in a CPU chip, which confirms a 2-year doubling rate basis [569].

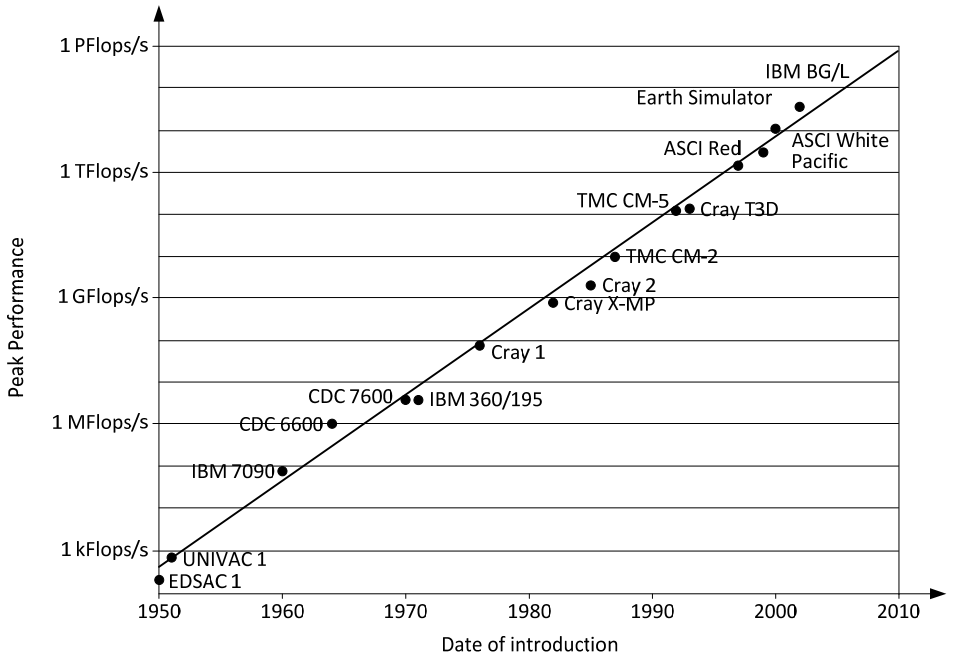

Figure V.1: Peak performance of supercomputers, adapted from [173].

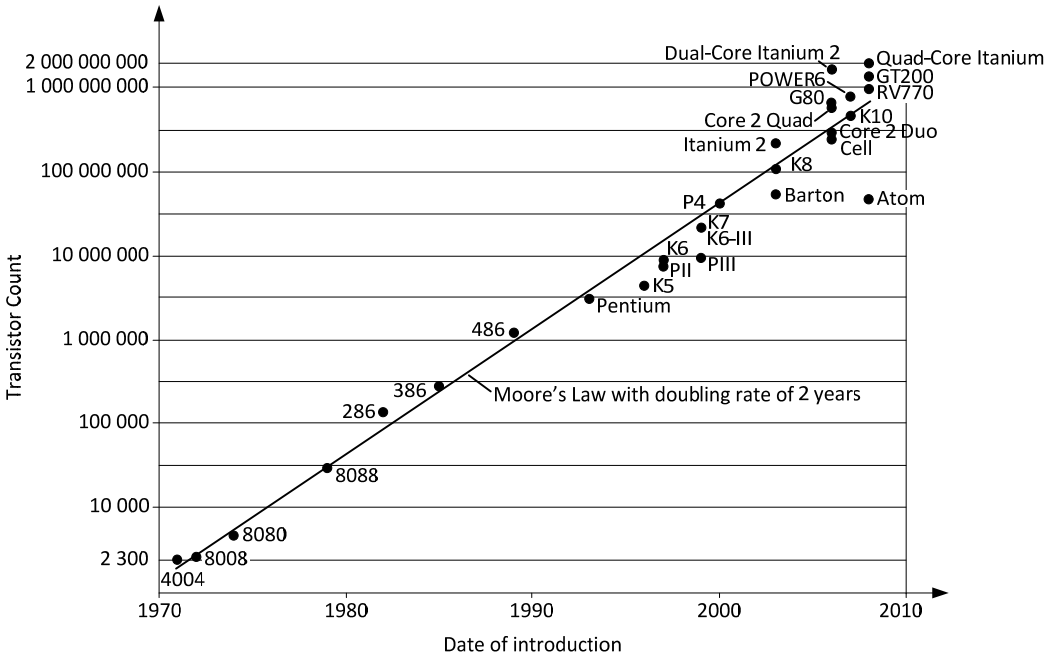

Figure V.2: Number of transistors in a CPU chip *vs.* Moore's Law, adapted from [569].

2.1.3 Memory-related capacities

This section addresses only volatile data storage devices. Persistent data storage devices (*e.g.* hard disk and flash drives) will be referenced in the following section. The *random-access memory* (RAM) is the most common and efficient method of data storage in common computer programs. This type of memory is classified as volatile because all the information stored in the integrated circuits is lost when the power is switched off.

The memory systems can be classified into the following three groups (see Figure V.3):

i. *Distributed* or *local* memory systems occur when each PU has its own dedicated memory that is not available directly to other PUs. Data transfer must be carried out by communication with the remote PUs, *e.g. message passing* (MP);
ii. In a *shared* memory system the data is stored in a memory that is accessible for all processors. Sometimes it is necessary to implement mechanisms to ensure the integrity of the data (*e.g.* semaphores);
iii. In *distributed-shared* or *combined* memory systems, the processing unit has access to its own local memory and to a global memory space available for all processing units. These systems occur mainly in clusters where each PU has access to its own local memory in addition to the node's shared memory.

Shared memory systems are easier to program, since all processing units have access to the same data. However, the communication between the processing units with the memory often becomes the bottleneck, meaning that this architecture does not scale very well. Distributed systems present better results in terms of scalability. However, there is an overhead caused by the need of *inter-processor communications*. Shared memory systems seems to be more adjusted for small high performance computers (*e.g.* workstations) and distributed memory systems are common and dominant in supercomputers (*e.g.* clusters).

In terms of terminology, it is usual to associate *parallel computing* with shared memory systems and *distributed computing* with distributed memory systems, although these definitions are not universal and there can be some variations in these concepts. In this work, the term *parallel computations* will be used to address concurrent computations, regardless of the memory architecture type.

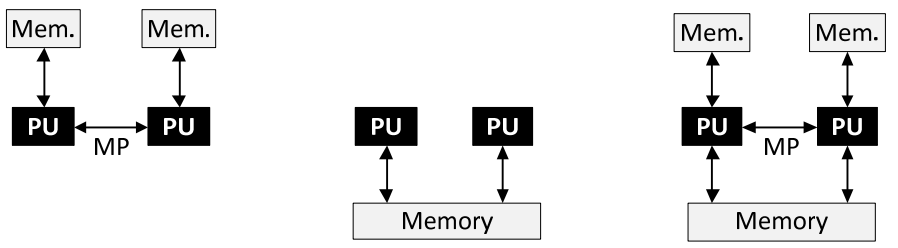

a) distributed b) shared c) distributed-shared

Figure V.3: Types of memory systems.

Two relevant characteristics related to RAM memory should be considered: the storage and data access capacity. Regarding the storage capacity, it should be mentioned that until the second part of the last decade the large majority of CPUs and operating systems (OS) used a single integer register system to address the data stored in memory. This leads to what is commonly called 32-bit systems, in which the maximum theoretical amount of RAM handled is $2^{32} = 4$ GB and this value is often reduced even further by the OS. This resulted in a real capacity limitation for current problem sizes. Fortunately, after the introduction and generalization of 64-bit compatible CPUs and OSs, this limit was reset to a maximum value of $2^{64} = 17.18 \times 10^9$ GB. Most computer systems work at an effective limit much lower than this value. Nevertheless, it is high above the current needs and physical possibilities.

Memory data access is also a determining issue regarding computational performance. Commonly, the PU has a small and faster *memory cache* associated with it (usually a few MB for a L3 cache), which holds the most frequently used data. However, most of the data comes from volatile memory (*e.g.* RAM). A question arises about the speed for memory access, and in particular, how can this factor influence the performance of the system. To search for an answer to this question, the following paragraphs will describe the typical layout of the hardware related to memory access, their functions and their influence on the overall performance.

The most common motherboard chipset layout is represented in Figure V.4. It includes the *Northbridge Memory Controller hub* or *integrated memory controller* that is connected directly to the PU and ensures the connection to the most speed-dependent components, such as RAM memory and graphic cards. Additionally, the *Southbridge* or *I/O controller hub* connects and controls data flow with slower components such as hard disks, USB ports, LAN, *etc*. The *Southbridge* is not connected directly to the PU and it requires the *Northbridge* to reach the PU. The data is transferred between components using data buses. The PU is connected by the *Front-side bus* to the Northbridge, which is connected to the memory by the memory bus (see Figure V.4). Typically, these two buses operate at the same frequency, although asynchronous systems are sometimes used.

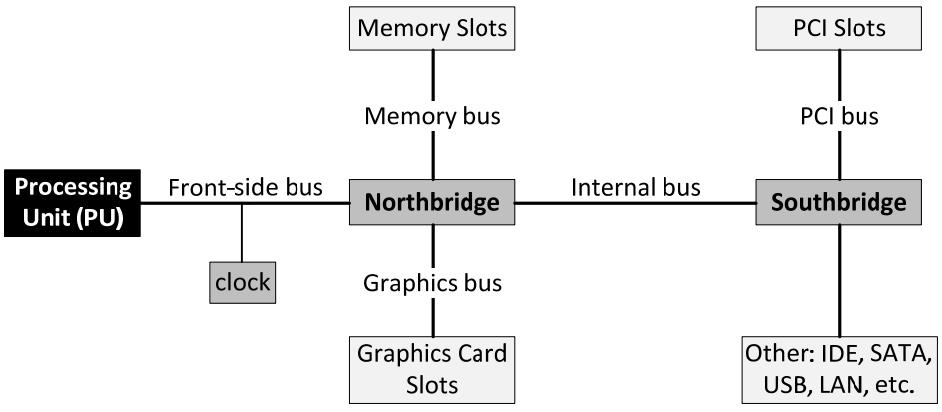

Figure V.4: A typical motherboard chipset layout.

The maximum theoretical (peak) *data transfer rate* can be computed using the following formula:

$$DT = MCR \times BCM \times DR\,, \tag{V.2}$$

where MCR stands for *memory clock rate,* BCM for *bus clock multiplier* and DR for *data rate.*

As an example, a common DDR3-1333 (third generation double data rate SDRAM) has $MCR = 133\ \text{MHz}$, $BCM = 4$ and double data rate. Using expression (V.2) the maximum data transfer rate is 1333 MT/s (million transfers per second). Taking into consideration that modern buses work with 64 bits data width, this means that every transfer consists of 8 bytes (64 bits / 8 bits per byte) or of double precision floating point numbers, and thus, the equivalent of 10666 MB/s.

Noting that a single core in PU can easily execute 8 GFlop/s (2 GHz x 4 IPC), the 1333 MT/s limit of double precision floating point data transfers can be far behind the peak demand level of the PU. In this theoretical case, a single core can compute numbers six times as fast as the memory can deliver. This may generate a serious bottleneck, especially for computations that require a large data flow (*e.g.* computing continuously with different data sets). In multiprocessor computers, this problem can be mitigated by having dedicated memory access buses to each processor. This can easily be identified by having motherboards with groups of CPUs, memory slots and Northbridge controllers.

2.1.4 Data storage capacity

In terms of persistent data storage capacity (*e.g.* hard disk drives), the age of Terabytes in a single disk unit has already arrived. This capacity is enough for most civil engineering tasks, but the access of data stored on hard disks presents a serious constraint in terms of speed, which is much inferior to the performance obtained in volatile data storage devices, such as RAM. The introduction and spread of solid-state drives will mitigate this problem, because these systems are potentially faster and do not require moving parts. Nevertheless, this solution has not reached a widespread and mature state yet.

2.1.5 Communication capacity

Most distributed computing systems are based on *inter-processor communication* with one or more Gigabit Ethernet devices per computer node. This communication standard allows a theoretical data rate of one Gigabit per second (around 120 MB/s). Nowadays, with the developments with regard to optics-based communication systems, 10 and 100 Gigabit Ethernet standards are being developed and introduced into the market. These solutions have the potential of improving the communication speed by several orders of magnitude. Another technology frequently used for high-performance computing is the *InfiniBand* system. This solution presents high data transfer rate, low latency and is designed to be scalable. The theoretical data transfer rates vary between 2.5 and 300 Gigabit/s. According to the internet site *top500* [540], 45.6% of the 500 faster supercomputers use Gigabit Ethernet devices and 42.6% use *InfiniBand* systems.

2.1.6 Grid and cloud computing

Grid computing takes its name from the electric power grid because the concept is to join geographically dispersed, heterogeneous, and loosely coupled processing units to reach a common computational goal. Grid computing can be seen as a way of creating a virtual computer cluster, but contrary to the approach followed in supercomputers, the hardware characteristics are often heterogeneous and usually they are interconnected with less powerful communications networks (private, public or internet-based), which penalizes the inter-processor data transfer. Consequently, this computing architecture is more focused on running independent and highly dissociated tasks. Grid computing is ideal for algorithms designed for *Event Parallelism* or *Task Farming* (see section 2.1.8). Nevertheless, applications to Civil Engineering are still not common.

Grid computing implementations have the advantage of presenting much better cost-benefit relationships than the traditional supercomputer approach, because they can be assembled with hardware belonging to different organizations with the aid of general-purpose grid software libraries, known as *middleware*. See Foster *et al.* [222] for more details.

Cloud computing is an internet-based computing approach that is based on the grid computing architecture. According to Dolenc [170], the term "cloud" is an abstraction for the complex infrastructure that allows the user to use it without knowledge, expertise or control over it. One of the differentiating aspects is that the provision of resources (processing time, network bandwidth or disk space) is made on demand contrary to grid computing where the resources can be pre-allocated. This results in an extremely flexible, available and cheap way of doing large computations or storing information.

2.1.7 Instruction and data stream architectures

The most common classification of instruction and data stream architectures is based on Flynn's taxonomy, proposed by Michael Flynn in 1966 [220], which proposes the following four classifications [568] (see Figure V.5):

i. *Single Instruction - Single Data Stream* (SISD), when a single instruction stream is executed on the data stored in a single memory unit. In this case, no parallelism exists in either the instruction or the data stream. An implementation of this architecture is a sequential computer;
ii. *Single Instruction - Multiple Data Streams* (SIMD), when a computer is able to perform the same instruction on multiple data simultaneously, usually using multiple processing units. This is also called *Data Parallelism*. A possible example is an array processor;
iii. *Multiple Instructions - Single Data Stream* (MISD), when different operations are made on the same data. This architecture is rare in real situations;
iv. *Multiple Instructions - Multiple Data Streams* (MIMD), when multiple autonomous processor units execute simultaneously different instructions on different data. This architecture is widespread and is used in most distributed computing systems.

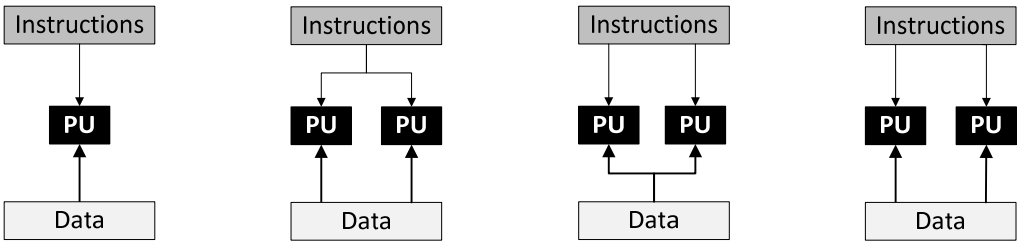

Figure V.5: Instructions and data streams architectures, adapted from [568].

Nowadays, the most used parallel architectures are the SIMD and the MIMD. The data parallelism in the SIMD approach can result in extremely efficient systems, particularly, when the problem to be solved is highly regular (*e.g.* image processing). For this architecture to be efficient the workload should be balanced or adjusted to the capacity of each processor. Otherwise, the computation would have to wait for the slowest and the performance would be compromised. The SIMD architecture can be subdivided into shared memory systems and distributed or local memory systems. In the former, the performance can be affected by queuing, when several processors want to access the same data.

The dominant computer architecture in modern *high performance computing* (HPC) systems is the MIMD, which can also be subdivided into shared memory systems and distributed or local memory systems. In the former, asynchronous threads may try to access or change the same data and this may result in unexpected results. Thus, most of the time locking mechanisms are required, *e.g.* semaphores. The MIMD architecture with distributed memory systems is much more common and can achieve better results in terms of scalability. In this case, each processing unit has its own local memory and data interaction is assured by *message passing* (MP). The MIMD architectures correspond to a wide range of supercomputers, high performance multi-processor computers and loosely coupled networks of workstations or PCs.

2.1.8 Algorithm classification

Closely related to the architectures and memory system types presented in section 2.1.7 and 2.1.3, the parallel algorithms can be classified as [541]:

i. *Geometric* or *Data Parallelism,* when each processing unit executes the same instructions on different data sets. Most of the time, the communication between processing units is possible through message passing. This represents a SIMD architecture implementation as presented in the previous section and a practical example would be a finite element code performing concurrent state determination on elements belonging to different subdomains;
ii. *Algorithmic Parallelism*, when different processing units perform different instructions on the data sets in sequence, similarly to an assembly line. This would represent a MISD or a MIMD

architecture;

iii. *Event Parallelism*, when each processing unit executes isolated instructions on local data sets and generally, communications are only permitted to the *Master* or *Root* processor. This type of algorithm is also called *Processor Farming, Independent Task* or *Task Farming* and is associated with distributed systems. Grid computing can be seen as an example when communications are centralized by the Root processor. Otherwise, it can be seen as any computation with distributed memory systems, such as cluster computing.

In order to produce good results and to avoid having PUs waiting idle, the assigned computational load must be balanced in all of these algorithm types. This can be achieved by controlling the amount of data or the number of instructions associated with the processing request.

2.1.9 Message passing

Message passing (MP) is the most common methodology to share data from different processing units, most of the time in MIMD architectures with distributed data. The most popular packages for the implementation of this methodology are the *Message Passing Interface* (MPI) [221], the *OpenMP* [97] and the *Parallel Virtual Machine* (PVM) [235], which consists of a set of libraries with routines that can be called from C/C++ and Fortran programs. OpenMP focuses on shared memory systems whereas MPI can work on either shared or distributed memory systems. Each of these packages has their own advantages and drawbacks.

2.1.10 Performance analysis

The objective of every parallelization algorithm is to achieve a greater speed and/or to solve larger problems by using a *divide and conquer* strategy. In theory, for the same amount of work, an algorithm using a *number of processing units* NPU should run NPU times faster when compared to the time used with a single PU. However, there are many sources of overheads and inefficiencies that make this performance level very difficult or even impossible to achieve. Some of those sources are related to load imbalance, data movement, and algorithm restructuring. The performance of a parallelized algorithm is therefore an important source of information concerning the reasonability of using a concurrent code instead of a sequential one.

- Speed-up and efficiency of homogeneous systems

One of the simplest parameters that can be computed to assess the performance of the parallelized algorithm is the *concurrent speed-up.* For a homogeneous system, this parameter is given by:

$$S = \frac{t_c^s}{t_c^p}, \tag{V.3}$$

where t_c^s is the computing time for the sequential code and t_c^p is the computing time of the concurrent version of the code using NPU processing units. It is important to emphasize that the sequential version of the code should be used to determine t_c^s, and not the parallelized version with

$\text{NPU}=1$. Considering that normally $t_c^s < t_c^p(1)$, owing to the overhead caused by the parallelization (*e.g.* algorithm restructuring), if $t_c^p(1)$ is used instead of t_c^s in equation (V.3) then the results may be misleading and not entirely correct.

The *concurrent efficiency* of a homogeneous system is defined as the concurrent speed-up per processor [223]:

$$E = \frac{S}{\text{NPU}}. \tag{V.4}$$

Linear speed-up or an efficiency of 100% occurs when the concurrent algorithm is NPU times faster using NPU processing units. When the computations to be executed do not change in the parallelized algorithm, linear speed-up values or efficiencies of 100% are considered to be excellent scalabilities. Typical efficiency levels are below 100%, but *super linear scalabilities* can be achieved, although this is rare. This situation may result from hardware-related efficiency gains, such as the well-known *cache effect*. This is a consequence of the overall increase of cache memory, resulting from using several processors, which improves the data transfer efficiency [566].

A central aspect of a parallel algorithm is the *scalability*. This property measures how well the performance of an algorithm is affected when the problem size and the computational resources increase. According to Gupta *et al.* [255], an algorithm is said to be scalable if the concurrent efficiency depends on the problem size and on the number of processing units only through their ratio, which can be seen as the problem size per processing unit.

- Efficiency of heterogeneous systems

A heterogeneous system occurs when the PUs are not capable to deliver the same performance level. This factor must be taken into consideration when computing the efficiency of the system, otherwise, if the sequential time of the slower (faster) PU is used, then this would overestimate (underestimate) the performance of the concurrent algorithm. A possible solution can be to weight the sequential time of each processor with the assigned computation load. This way the efficiency of the *k* processing unit would be defined by [541]:

$$E^k = \frac{f^k \left(t_c^s\right)^k}{t_c^p}, \tag{V.5}$$

where f^k is the *load weighting factor* defined by the ratio between the demand in the *k* processing unit and the overall demand. Adopting this definition, $\sum f^k = 1$ and for a homogeneous system f^k is constant and equal to $1/\text{NPU}$, and equation (V.5) returns the same value as the expression (V.4).

- Amdahl's law

An important notion regarding the computational performance is given by *Amdahl's law* [8], *a.k.a. Amdahl's argument*, which sets the basic rules used to estimate the maximum improvement of a system when only part can be improved. Later on, it was applied to the estimation of the maximum speed-up of a computer algorithm when parallel computing is used to improve part of the code, assuming that the problem size remains constant.

This law can be enunciated as follows: The maximum achievable speed-up of a computer algorithm where the proportion *P* of that computation can benefit from parallelization and presents a speed-up of S_p , is given by:

$$S^{\max} = \frac{1}{(1-P)+\frac{P}{S_p}}. \tag{V.6}$$

If the speed-up is proportional to the number of processing units (NPU) the previous formula can be rewritten as:

$$S^{\max} = \frac{1}{(1-P)+\frac{P}{NPU}}. \tag{V.7}$$

Figure V.6 presents the maximum expected speed-up in terms of the number of processing units (NPU) for different values of *P*. It can be observed that the maximum speed-up is limited, no matter how many processing units are used. This limit becomes obvious by noting that for equation (V.7), the following relation holds:

$$\lim_{\text{NPU}\to\infty} S = \frac{1}{1-P}. \tag{V.8}$$

As an example, for an algorithm where the part of the code associated with 5% of the total time cannot be parallelized, then the maximum speed-up is limited to 20, no matter how many PUs are used (see Figure V.51).

In conclusion, it is possible to stress that the parallelization is more efficient for algorithms where *P* is close to 1, *i.e.* when almost all code can be parallelized, and that the investment *vs.* benefit of adding processing units to a system tends to be less and less effective.

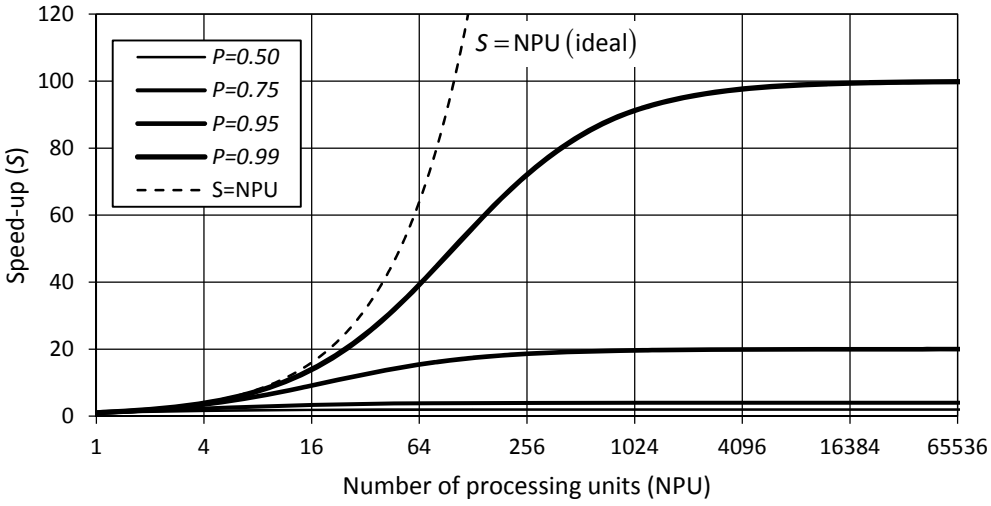

Figure V.6: Maximum expected speed-up according to Amdahl's law [8].

2.2 Condensation methods

2.2.1 Static condensation

Condensation is the technique of reducing the number of *dofs* in an element or structure using some sort of relation between the *retained* (*master*) *dofs* and the *condensed* (*slave) dofs*.

Starting from the symmetric system of equations describing the response of a static linear mechanical system and by reordering the *dofs*, putting the ones to be eliminated q_c at the end and the ones to be retained q_r at the beginning, the following system of equations would be obtained[i]:

$$\begin{bmatrix} \mathbf{K}_{rr} & \mathbf{K}_{rc} \\ \mathbf{K}_{cr} & \mathbf{K}_{cc} \end{bmatrix} \begin{bmatrix} \mathbf{q}_r \\ \mathbf{q}_c \end{bmatrix} = \begin{bmatrix} \mathbf{Q}_{e,r} \\ \mathbf{Q}_{e,c} \end{bmatrix}. \tag{V.9}$$

The following equation can be retrieved by manipulating the upper group of equations:

$$\mathbf{q}_c = \mathbf{K}_{cc}^{-1} \left\{ \mathbf{Q}_{e,c} - \mathbf{K}_{cr}\, \mathbf{q}_r \right\}, \tag{V.10}$$

which can be inserted into the lower group of equations, leading to:

$$\mathbf{K}^C\, \mathbf{q}_r = \mathbf{Q}_e^C, \tag{V.11}$$

where $\mathbf{K}^C$ is the *condensed stiffness matrix* and $\mathbf{Q}_e^C$ is the *condensed external force vector*, defined by:

$$\mathbf{K}^C = \mathbf{K}_{rr} - \mathbf{K}_{rc}\, \mathbf{K}_{cc}^{-1}\, \mathbf{K}_{cr}, \tag{V.12}$$

$$\mathbf{Q}_e^C = \mathbf{Q}_{e,r} - \mathbf{K}_{rc}\, \mathbf{K}_{cc}^{-1}\, \mathbf{Q}_{e,c}. \tag{V.13}$$

After solving the system (V.11) for the retained *dofs* $\mathbf{q}_r$, the *recovery* of the condensed *dofs* $\mathbf{q}_c$ can be made from equation (V.10).

The static condensation is strictly an algebraic manipulation and no approximation is made, because the relations used to eliminate the condensed dofs are already present in the governing system. Consequently, apart from possible losses of numeric accuracy in the computations, solving the linear system using the condensed (V.11) or the original (V.9) system results in the same solution.

- Static condensation as a coordinate transformation

It is possible to write the reordered displacement vector in terms of the retained *dofs*, as follows:

$$\mathbf{q} = \begin{bmatrix} \mathbf{q}_r \\ \mathbf{q}_c \end{bmatrix} = \mathbf{T}\, \mathbf{q}_r + \mathbf{q}_c^*, \tag{V.14}$$

with:

$$\mathbf{T} = \begin{bmatrix} \mathbf{I} \\ -\mathbf{K}_{cc}^{-1}\, \mathbf{K}_{cr} \end{bmatrix}, \tag{V.15}$$

[i] the subscript *c* stands for *condensed* and *r* for *retained dofs.*

$$\mathbf{q}_c^* = \begin{bmatrix} \mathbf{0} \\ \mathbf{K}_{cc}^{-1}\,\mathbf{Q}_{e,c} \end{bmatrix}. \tag{V.16}$$

where $\mathbf{I}$ and $\mathbf{0}$ are the identity and zero matrices, respectively.

This approach could be seen as a coordinate transformation, where $\mathbf{T}$ would be the transformation matrix. Inserting equation (V.14) into the initial governing system, leads to:

$$\mathbf{K}\left(\mathbf{T}\,\mathbf{q}_r + \mathbf{q}_c^*\right) = \mathbf{Q}_e\,, \tag{V.17}$$

and pre-multiplying both sides by $\mathbf{T}^t$, the following expression would be retrieved:

$$\mathbf{T}^t\,\mathbf{K}\,\mathbf{T}\;\mathbf{q}_r = \mathbf{T}^t\,\mathbf{Q}_e - \mathbf{T}^t\,\mathbf{K}\,\mathbf{q}_c^*\,, \tag{V.18}$$

Taking into consideration that $\mathbf{T}^t\,\mathbf{K}\,\mathbf{q}_c^* = \mathbf{0}$, the previous expression can be rewritten in the condensed format:

$$\mathbf{K}^C\,\mathbf{q}_r = \mathbf{Q}_e^C\,, \tag{V.19}$$

with:

$$\mathbf{K}^C = \mathbf{T}^t\,\mathbf{K}\,\mathbf{T}\,, \tag{V.20}$$

$$\mathbf{Q}_e^C = \mathbf{T}^t\,\mathbf{Q}_e\,. \tag{V.21}$$

After some basic algebraic manipulations, it is easy to see that expression (V.20) is the same as (V.12) and that equation (V.21) is equivalent to (V.13), hence proving that both formulations are equivalent.

2.2.2 Dynamic condensation

A significant difference between static and dynamic condensation is that in the latter case a structural assumption is usually required which leads to an approximation. Therefore, dynamic condensation is often called *reduction*.

One of the most known methods for dynamic condensation is the *Guyan Reduction* (GR) which was proposed by Guyan *et al.* [256]. Starting from the dynamic equilibrium of an undamped mechanical system:

$$\mathbf{M}\,\mathbf{a} + \mathbf{K}\,\mathbf{q} = \mathbf{Q}_e\,, \tag{V.22}$$

and by grouping first the *dofs* to be retained $\mathbf{q}_r$ and afterwards the ones to be condensed $\mathbf{q}_c$, it is possible to obtain:

$$\begin{bmatrix} \mathbf{M}_{rr} & \mathbf{M}_{rc} \\ \mathbf{M}_{cr} & \mathbf{M}_{cc} \end{bmatrix} \begin{bmatrix} \mathbf{a}_r \\ \mathbf{a}_c \end{bmatrix} + \begin{bmatrix} \mathbf{K}_{rr} & \mathbf{K}_{rc} \\ \mathbf{K}_{cr} & \mathbf{K}_{cc} \end{bmatrix} \begin{bmatrix} \mathbf{q}_r \\ \mathbf{q}_c \end{bmatrix} = \begin{bmatrix} \mathbf{Q}_{e,r} \\ \mathbf{Q}_{e,c} \end{bmatrix}. \tag{V.23}$$

Solving the lower group of equations in order of the condensed *dofs* leads to the following equation:

$$\mathbf{q}_c = \mathbf{K}_{cc}^{-1}\left(\mathbf{Q}_{e,c} - \mathbf{M}_{cc}\,\mathbf{a}_c - \mathbf{M}_{cr}\,\mathbf{a}_r - \mathbf{K}_{cr}\,\mathbf{q}_r\right). \tag{V.24}$$

The basic assumption of the Guyan Reduction is to neglect the contributions of the mass associated with the condensed *dofs*: $\mathbf{M}_{cc}$, $\mathbf{M}_{cr}$ and $\mathbf{M}_{rc}$. Consequently, the previous equation can be simplified into the same expression obtained for the static condensation (V.10):

$$\mathbf{q}_c = \mathbf{K}_{cc}^{-1}\left(\mathbf{Q}_{e,c} - \mathbf{K}_{cr}\,\mathbf{q}_r\right).$$

The concept of the coordinate transformation can also be extended to the GR, because the same expression is used to eliminate the displacements of the condensed *dofs*.

Inserting (V.10) into the lower group of equations in (V.23), results in:

$$\mathbf{M}^C\,\mathbf{a}_r + \mathbf{K}^C\,\mathbf{q}_r = \mathbf{Q}_e^C, \tag{V.25}$$

where the condensed mass matrix and the accelerations vector are defined by:

$$\mathbf{M}^C = \mathbf{M}_{rr} = \mathbf{T}^t\,\mathbf{M}\,\mathbf{T}, \tag{V.26}$$

$$\mathbf{a} = \mathbf{T}\,\mathbf{a}_r, \tag{V.27}$$

and $\mathbf{K}^C$ and $\mathbf{Q}_e^C$ are the same as in equations (V.12) and (V.13) or (V.20) and (V.21), respectively.

The use of the Guyan Reduction implies that only static equilibrium relates the condensed and retained *dofs*, or in other words, this corresponds to assuming that the inertia forces on the condensed *dofs* are not important when compared with the elastic forces between them.

- Computation of mode shapes and frequencies

Starting from an undamped mechanical system undergoing free vibration:

$$\mathbf{M}\mathbf{a} + \mathbf{K}\mathbf{q} = \mathbf{0}, \tag{V.28}$$

the eigenvalue equation can be written for the governing system with the *dofs* reordered:

$$\left(\begin{bmatrix}\mathbf{K}_{rr} & \mathbf{K}_{rc}\\ \mathbf{K}_{cr} & \mathbf{K}_{cc}\end{bmatrix} - \lambda\begin{bmatrix}\mathbf{M}_{rr} & \mathbf{M}_{rc}\\ \mathbf{M}_{cr} & \mathbf{M}_{cc}\end{bmatrix}\right)\begin{bmatrix}\boldsymbol{\Phi}_r\\ \boldsymbol{\Phi}_c\end{bmatrix} = \begin{bmatrix}\mathbf{0}\\ \mathbf{0}\end{bmatrix}. \tag{V.29}$$

Applying the Guyan reduction, the last equation results in:

$$\left(\mathbf{K}^C - \lambda\mathbf{M}^C\right)\boldsymbol{\Phi}_r = \mathbf{0}. \tag{V.30}$$

After solving for the mode shapes and frequencies, the mode shape coefficients of the condensed *dofs* can be computed using (V.10). According to Cook *et al.* [141], this information can be recovered with more accuracy from the lower group of equations in (V.29), because the neglected mass on the condensed *dofs* is reconsidered:

$$\boldsymbol{\Phi}_{c,i} = -\left(\mathbf{K}_{cc} - \lambda_i\,\mathbf{M}_{cc}\right)^{-1}\left\{\left(\mathbf{K}_{cr} - \lambda_i\,\mathbf{M}_{cr}\right)\boldsymbol{\Phi}_{r,i}\right\}. \tag{V.31}$$

To be efficient the reduced system must have considerable less *dofs* than the full system because the transformations necessary to compute $\mathbf{K}^C$ and $\mathbf{M}^C$ may turn these operators into full matrices, independently of being initially banded or diagonal.

In the general case, the Guyan Reduction produces only approximated results. However, if the mass matrix is diagonal, $\mathbf{M}_{cr} = \mathbf{M}_{rc} = \mathbf{0}$ (*e.g.* lumped mass matrix) and the condensed *dofs* do not have any mass, $\mathbf{M}_{cc} = \mathbf{0}$, the results with or without dynamic condensation would be the same [141], apart from the numerical precision losses.

For lumped mass systems, the total mass of the system can be conserved by scaling the part of the

mass belonging to the retained *dofs*. This can be done by implementing

$$\mathbf{M}_{rr}^{*} = \gamma_M \, \mathbf{M}_{rr} \,, \tag{V.32}$$

with:

$$\gamma_M = \frac{\sum_i (\mathbf{M})_{ii}}{\sum_j (\mathbf{M}_{rr})_{jj}} \,. \tag{V.33}$$

This approach can produce better results because the total mass is conserved. However, the distribution of the original mass is distorted and consequently the results will still be approximate.

- Dynamic equilibrium

The dynamic equilibrium equation of a system condensed using the Guyan Reduction can be written as:

$$\mathbf{M}^C \, \mathbf{a}_r + \mathbf{C}^C \, \mathbf{v}_r + \mathbf{K}^C \, \mathbf{q}_r = \mathbf{Q}_e^C \,, \tag{V.34}$$

where the *condensed damping matrix* and the *condensed velocity vector* are given by:

$$\mathbf{C}^C = \mathbf{T}^t \, \mathbf{C} \, \mathbf{T} \,, \tag{V.35}$$

$$\mathbf{v} = \mathbf{T} \, \mathbf{v}_r \,. \tag{V.36}$$

2.3 Matrix storage schemes, linear and eigenvalues solvers

2.3.1 Matrix storage schemes

The use of an efficient matrix storage scheme is vital for the performance of the computer implementation. The most common matrix storage schemes are listed below [10, 189, 492]:

i. *Full* or *conventional storage,* when all matrix elements are stored in a two dimensional array;
ii. *Packed storage* is used to store special matrices (*e.g.* symmetric, Hermitian or triangular) in a more efficient and compact way;
iii. *Band storage* is used when the matrix presents all the non-null elements within a finite index distance (bandwidth) from the main diagonal;
iv. *Sparse storage* is used when the matrix presents a large percentage of zeros. Usually, only the non-zero coefficients are stored using one vector with the numerical values and one or two integer arrays indicating the position of the coefficients in the matrix. Different formats can be used: *coordinate*, *compressed row*, *compressed column*, *compressed diagonal*, *jagged diagonal* and *skyline* are some examples.

The full storage scheme is very inefficient and easily prohibitive. This can be highlighted by taking into consideration that the stiffness matrix of a problem with 50k *dofs* would require 18.6 GB of memory for double precision storage. *Packed storage* can be inefficient for common coefficient matrices and the band storage efficiency is highly dependent on the bandwidth.

The sparse storage schemes are adequate for the majority of large civil engineering problems, because it is possible to take advantage of the high sparsity-level of typical structural operators. For example, the same matrix presented in the previous paragraph with 1% of non-zero coefficients could require only 186+95=281 MB to be stored. According to Saad [492], the most popular sparse matrix storage format is the compressed row. Sparse matrices should be combined with optimized computing algorithms in order to be efficient (*e.g.* matrix multiplication, linear solvers).

2.3.2 Linear solvers

Solving the linear systems $\mathbf{A}\mathbf{x}=\mathbf{b}$ is the same as finding the solution from $\mathbf{x}=\mathbf{A}^{-1}\mathbf{b}$. Solvers that avoid the explicit computation of the inverse of the coefficient matrix are commonly preferred because they can be more efficient and accurate.

The most used methods can be classified as follows:

i. Direct methods [188, 189] that usually try to find **x** by performing matrix operations with the coefficients in **A** and **b** (*e.g.* factorizations), in order to obtain a convenient format for the linear system that permits computing the unknowns. Direct methods are usually variants of the *Gaussian elimination* (GE) and the most common factorizations schemes are the LU, *Cholesky* and QR *factorizations* (see Annex A);
ii. *Iterative* methods or *Indirect* methods [101, 492] find a sequence of solutions $\mathbf{x}^{i+1}$ using the previous residual vector $\mathbf{r}^{i+1}=\mathbf{b}-\mathbf{A}\mathbf{x}^{i}$. After a finite number of iterations, a good approximation for the solution vector can be obtained under certain conditions. Iterative methods produce only an approximate solution after a finite number of steps and the coefficient matrix is sometimes only included through matrix-vector products. The classical *Jacobi*, *Gauss-Seidel* and *Successive Over-Relaxation* iterative methods should be mentioned. However, currently the most popular iterative methods are based on Krylov subspace methods, like the *Conjugate Gradient* method for symmetric positive-definite matrices and the G*eneralized Minimal Residual* method and the *Conjugate Residual* method for non-symmetric indefinite systems (see Annex A).

Direct methods are used in a large majority of finite element codes. They are more robust, more generally applicable than iterative methods and are faster and more reliable for most current Civil Engineering applications. The required computing time to solve the linear system can be predicted because the performance of direct methods is mainly dependent on the problem size and on the characteristics of the coefficient matrix. Direct methods are also very competitive and efficient for solving the system of equations for multiple *rhs* (*e.g.* using a LU decomposition). Nevertheless, the storage requirements of direct methods are potentially greater than the ones associated with the use of iterative methods, because *Gaussian Elimination* and decomposition techniques are based on matrix factorizations that require additional matrix storage. Alternatively, iterative methods can be based only on matrix-by-vector multiplications and on vector storage.

When compared to direct solvers, the lack of robustness and reliability are widely recognized weaknesses of iterative solvers [492]. Their performance depends on the problem physics,

differential order and discretization scheme, and the computing time is often difficult to predict [209]. However, since the second half of the previous century, a number of efficient iterative methods have been developed and the performance and stability of these methods have been improved. To be competitive in relation to direct solvers, the coefficient matrix should be very large and sparse (*e.g.* millions of unknowns) and the solution must be computed only approximately. Asking for accuracy similar to that delivered by direct solvers would be generally uncompetitive. In these cases, iterative methods can out-perform direct methods. These methods are usually implemented with a preconditioner to improve the accuracy and the convergence rate to the solution. The effect of the preconditioner is to reduce the condition number of the coefficient matrix, which influences the convergence rate.

Currently, most *Domain Decomposition* (DD) methods (see section 2.6) are based on iterative methods because of two main reasons: at first, these methods are prone to be used in very large problems where the iterative methods are competitive; secondly, most domain decomposition methods work with floating subdomains that present rigid body modes associated with the null space of the structural matrices. The iterative methods can handle this numerical problem with higher flexibility using techniques such as preconditioning and projections to avoid entering the null space of these matrices.

2.3.3 Eigenvalue problem solvers

Several techniques can be used to solve generalized eigenvalue problems. The most popular methods are listed below [245, 492]:

i. The *Direct eigenvalue method* computes all eigenvalues and eigenvectors. For large problem sizes, this can be extremely inefficient and also unviable in terms of storage space;
ii. The *QR method* is a very efficient procedure and particularly competitive when all the eigenvalues must be computed;
iii. *Jacobi's method* is an iterative algorithm that can be used with symmetric matrices. The formulation of this method is favourable to parallel implementations;
iv. *Subspace iteration method* is used for finding only the first eigenvalues;
v. *Lanczos' method* is used for large systems and when only the first eigenvalues are of interest.

According to Nguyen [416], *Lanczos' method* is preferable to the *Subspace iteration method* when the number of desired eigenvalues increases because the latter method becomes inefficient. Addressing the mathematical formulations of these algorithms lies outside the scope of this thesis. Further information can found in the bibliography, *e.g.* [33, 245, 446, 492].

In order to reduce the problem size, the massless *dofs* can be removed by condensation using the same procedure presented in section 2.2.2, resulting in the condensed eigenvalue problem represented in equation (V.30).

2.4 Kinematic constraints

Kinematic constraints (KC) can be used to impose a specific behaviour on the unknowns of the simulation. Within the scope of the traditional finite element method, the unknowns are the node displacements, and generally, the constraints are kinematic relations enforced between one or several *dofs*. Within the scope of this thesis, the kinematic constraints are linear because the analyses are also geometrically linear. However, in the case of nonlinear geometric analyses the KC would also result into nonlinear equations. In addition, the mathematical formulation for the KC presented are written under the assumption of small displacements, *e.g.* by adopting $\theta \approx \sin(\theta)$.

A typical use for the kinematic constraints is to impose a specific structural behaviour such as connecting different parts of the structure or enforcing certain types of rigid-body behaviour. In the following paragraphs, some of the most used kinematic constraints will be briefly presented.

- Common kinematic constraints

In the *rod constraint*, all constrained nodes move together as a straight rod that is rigid against axial deformation. This is the same as connecting both nodes with a rigid, pinned and massless bar. Mathematically, this can be expressed by:

$$q_i^{SN} = q_j^{MN} . \tag{V.37}$$

where q_i^{SN} represents the displacement of the *slave node* (SN) along the coordinate *i* and q_j^{MN} represents the displacement of the *master node* (MN) along the coordinate *j*.

The slave and master node terminology is used to harmonize the notation of this section, although in this case there is no hierarchical relation between the nodes. Different coordinate subscripts are used to emphasize that the rod constraint does not have to be applied in the same direction.

In the *diaphragm constraint,* all constrained nodes are enforced to move together in a rigid diaphragm plane. This is the same as connecting the nodes with a rigid bar for in-plane deformation and with no rigidity for out-of-plane movements. This implies the following equations when the constraint axis is the direction X_1, as represented in Figure V.7:

$$q_2^{SN} = q_2^{MN} - X_3\,\theta_1^{MN} , \tag{V.38}$$

$$q_3^{SN} = q_3^{MN} + X_2\,\theta_1^{MN} , \tag{V.39}$$

$$\theta_1^{SN} = \theta_1^{MN} . \tag{V.40}$$

where $\theta_1^{SN}\left(\theta_1^{MN}\right)$ represents the *slave* (*master*) node rotation about the axis X_1.

The *plate constraint* considers that all constrained nodes belong to a plane that is rigid for out-of-plane bending. For the same constraint axis used for the diaphragm constraint, the following relations are imposed.

$$q_1^{SN} = q_1^{MN} + X_3\,\theta_2^{MN} - X_2\,\theta_3^{MN} , \tag{V.41}$$

$$\theta_2^{SN} = \theta_2^{MN} , \tag{V.42}$$

$$\theta_3^{SN} = \theta_3^{MN} . \tag{V.43}$$

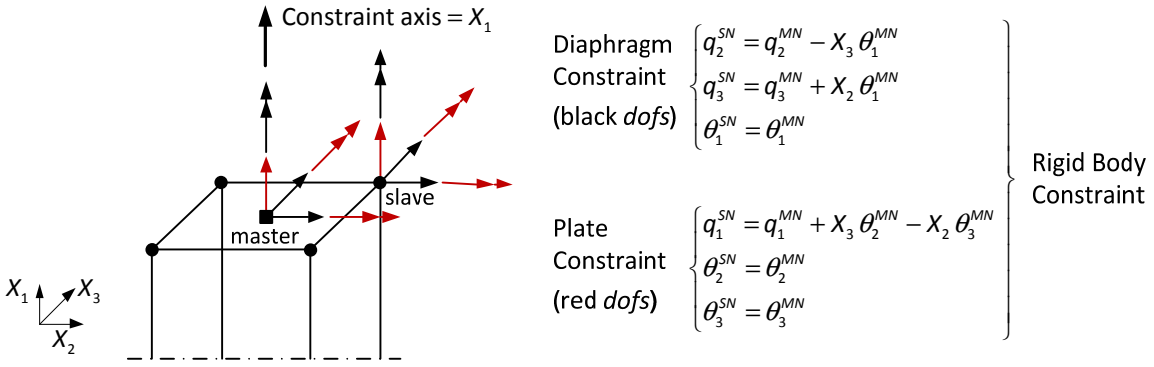

Figure V.7: Implementation of the diaphragm and plate kinematic constraints.

This constraint relates the *dofs* that are not affected by the diaphragm constraint, as illustrated in Figure V.7.

Finally, in the *rigid body constraint* all constrained nodes move together like a three-dimensional rigid body. This constraint can be defined as applying the diaphragm and the plate constraints simultaneously.

- Basic formulation

The kinematic constraint can be expressed in the matrix format:

$$\mathcal{C}_K\,\mathbf{q} = \mathbf{d}_K\,, \tag{V.44}$$

where $\mathcal{C}_K$ is the *kinematic constraint matrix, a.k.a. connectivity matrix*, which contains only constants and $\mathbf{d}_K$ is a constant vector. The matrix $\mathcal{C}_K$ has a number of rows equal to the number of kinematic constraint equations and a number of columns equal to the total number of *dofs*.

There are several methods to impose the kinematic constraints. Some of the most used are:

i. Master-Slave Elimination;
ii. Penalty Augmentation;
iii. Lagrange Multipliers.

A summarized explanation of their formulation is presented in the following sections. This subject has been described by several authors and further details can be found in the references [141, 340].

2.4.1 Master-slave elimination

The *Master-Slave Elimination* (MSE) method, also known as *Transformation Equations* (TE) in Cook *et al.* [141], consists of eliminating a group of *dofs* (*slave dofs*) using the equations that relate them to a set of special *dofs* (*master dofs*). This can be seen as a static condensation. However, in this case a set of custom kinematic relations are used instead of the relations already included in the governing system.

If the *dofs* are ordered leaving the slave node *dofs* at the end, it is possible to rewrite (V.44) as:

$$\begin{bmatrix} \mathcal{C}_{K,m} & \mathcal{C}_{K,s} \end{bmatrix} \begin{bmatrix} \mathbf{q}_m \\ \mathbf{q}_s \end{bmatrix} = \mathbf{d}_K \,. \tag{V.45}$$

where the subscript *m* represents the master (retained) *dofs* and the subscript *s* represents the slave (condensed) *dofs*.

After some simple algebraic manipulations to equation (V.45), the slave *dof* displacements can be defined in terms of the master *dof* displacements, using:

$$\mathbf{q}_s = \mathcal{C}_{K,sm}\, \mathbf{q}_m + \mathbf{d}_{K,s}\,, \tag{V.46}$$

with:

$$\mathcal{C}_{K,sm} = -\mathcal{C}_{K,s}^{-1}\, \mathcal{C}_{K,m}\,, \tag{V.47}$$

$$\mathbf{d}_{K,s} = \mathcal{C}_{K,s}^{-1}\, \mathbf{d}_K \,. \tag{V.48}$$

It is possible to rewrite equation (V.46) as:

$$\begin{bmatrix} \mathbf{q}_m \\ \mathbf{q}_s \end{bmatrix} = \mathbf{T}_K\, \mathbf{q}_m + \begin{bmatrix} \mathbf{0} \\ \mathbf{d}_{K,s} \end{bmatrix}, \tag{V.49}$$

where $\mathbf{T}_K$ can be seen as a transformation matrix similar to the one used in 2.2.1, which in this case is defined by:

$$\mathbf{T}_K = \begin{bmatrix} \mathbf{I} \\ \mathcal{C}_{K,sm} \end{bmatrix}. \tag{V.50}$$

Recalling the governing system of a mechanical linear system subjected to static forces (V.9), where the master *dofs* are ordered first and the slave *dofs* at last:

$$\begin{bmatrix} \mathbf{K}_{mm} & \mathbf{K}_{ms} \\ \mathbf{K}_{sm} & \mathbf{K}_{ss} \end{bmatrix} \begin{bmatrix} \mathbf{q}_m \\ \mathbf{q}_s \end{bmatrix} = \begin{bmatrix} \mathbf{Q}_{e,m} \\ \mathbf{Q}_{e,s} \end{bmatrix}, \tag{V.51}$$

after introducing equation (V.49), it is possible to write:

$$\begin{bmatrix} \mathbf{K}_{mm} & \mathbf{K}_{ms} \\ \mathbf{K}_{sm} & \mathbf{K}_{ss} \end{bmatrix} \mathbf{T}_K\, \mathbf{q}_m + \begin{bmatrix} \mathbf{K}_{mm} & \mathbf{K}_{ms} \\ \mathbf{K}_{sm} & \mathbf{K}_{ss} \end{bmatrix} \begin{bmatrix} \mathbf{0} \\ \mathbf{d}_{K,s} \end{bmatrix} = \begin{bmatrix} \mathbf{Q}_{e,m} \\ \mathbf{Q}_{e,s} \end{bmatrix}, \tag{V.52}$$

and pre-multiplying by $\mathbf{T}_K^t$:

$$\mathbf{T}_K^t \begin{bmatrix} \mathbf{K}_{mm} & \mathbf{K}_{ms} \\ \mathbf{K}_{sm} & \mathbf{K}_{ss} \end{bmatrix} \mathbf{T}_K\, \mathbf{q}_m + \mathbf{T}_K^t \begin{bmatrix} \mathbf{K}_{mm} & \mathbf{K}_{ms} \\ \mathbf{K}_{sm} & \mathbf{K}_{ss} \end{bmatrix} \begin{bmatrix} \mathbf{0} \\ \mathbf{d}_{K,s} \end{bmatrix} = \mathbf{T}_K^t \begin{bmatrix} \mathbf{Q}_{e,m} \\ \mathbf{Q}_{e,s} \end{bmatrix}, \tag{V.53}$$

then the system can be rewritten as:

$$\mathbf{K}^C\ \mathbf{q}_m = \mathbf{Q}_e^C - \mathbf{d}^C\,, \tag{V.54}$$

with:

$$\mathbf{K}^C = \mathbf{T}_K^t\, \mathbf{K}\, \mathbf{T}_K = \mathbf{K}_{mm} + \mathcal{C}_{K,sm}^t\, \mathbf{K}_{sm} + \mathbf{K}_{ms}\, \mathcal{C}_{K,sm} + \mathcal{C}_{K,sm}^t\, \mathbf{K}_{ss}\, \mathcal{C}_{K,sm}\,, \tag{V.55}$$

$$\mathbf{Q}_e^C = \mathbf{T}_K^t\, \mathbf{Q}_e = \mathbf{Q}_{e,m} + \mathcal{C}_{K,sm}^t\, \mathbf{Q}_{e,s}\,, \tag{V.56}$$

$$\mathbf{d}^C = \mathbf{T}_K^t \, \mathbf{K} \begin{bmatrix} \mathbf{0} \\ \mathbf{d}_{K,s} \end{bmatrix} = \left(\mathbf{K}_{ms} + \mathcal{C}_{K,sm}^t \, \mathbf{K}_{ss} \right) \mathbf{d}_{K,s} . \tag{V.57}$$

After solving (V.54) for the master displacements, the slave *dof* displacements can be computed from equation (V.46).

This method presents the advantage of eliminating the constrained *dofs* from the governing system, leading to a smaller number of equations to be solved. Nevertheless, this benefit can be largely outweighed by the necessary manipulations and by the need of solving the additional system of equations to recover $\mathbf{q}_s$. The major disadvantage of this method consists of the rearrangement of the governing system.

2.4.2 Penalty augmentation

This method is based on rewriting (V.44) as follows [340]:

$$\mathbf{t} = \mathcal{C}_K \, \mathbf{q} - \mathbf{d}_K . \tag{V.58}$$

If $\mathbf{t} = \mathbf{0}$, this means that the constraint equations have been satisfied.

The *total potential energy* functional presented in (II.203) can be augmented with a *penalty function* [141]:

$$p = \frac{1}{2} \mathbf{t}^t \, \boldsymbol{\alpha} \mathbf{t} , \tag{V.59}$$

where $\boldsymbol{\alpha}$ is a diagonal matrix with the *penalty numbers* α_k located along the diagonal.

The *total potential energy* functional becomes:

$$\Pi(\mathbf{q}) = \int \underline{\boldsymbol{\sigma}} : \underline{\boldsymbol{\varepsilon}}(\mathbf{q}) \, d\Omega - \mathbf{Q}_e^t \, \mathbf{q} + \frac{1}{2} \mathbf{t}^t \, \boldsymbol{\alpha} \mathbf{t} . \tag{V.60}$$

If the constraints are satisfied $(\mathbf{t} = \mathbf{0})$, no change has been introduced to the total potential energy. Otherwise the total potential energy increases with a rate defined by the penalty numbers.

Introducing (V.58) into (V.60) and imposing the stationary condition, the following expression can be obtained:

$$\frac{\partial \Pi}{\partial \mathbf{q}} = \mathbf{Q}_i - \mathbf{Q}_e + \mathbf{P} \, \mathbf{q} - \mathcal{C}_K^t \, \boldsymbol{\alpha} \mathbf{d}_K = \mathbf{0} , \tag{V.61}$$

where **P** is called the *penalty matrix* and is defined by:

$$\mathbf{P} = \mathcal{C}_K^t \, \boldsymbol{\alpha} \, \mathcal{C}_K . \tag{V.62}$$

In this case, the corrector used to eliminate the residues of the linearized system of equations is given by (II.205):

$$\frac{\partial^2 \Pi}{\partial \mathbf{q}^2} = \frac{\partial \mathbf{g}}{\partial \mathbf{q}} = \mathbf{K}_t + \mathbf{P} . \tag{V.63}$$

Each dimensionless penalty number α_k is related to a specific constraint equation. If the value of α_k

is small the accuracy in imposing the constraint is also small. On the other hand, if this value becomes larger, the penalty of violating the constraint also becomes larger and the model tends to respect the constraint. However, increasing the numerical value of the penalty numbers leads to more and more ill-conditioned governing systems with respect to inversion [370]. The choice of the penalty numbers is therefore not a trivial issue. The ideal situation is to select a balanced value that does not compromise the accuracy neither causes numerical problems. According to Liu *et al.* [340], choosing values for α_k between $\left[10^4, 10^6\right] \max\left(K_{kk}\right)$ gives good results for most cases, similarly for choosing values of $\left[10^5, 10^8\right] E$, where *E* is the elasticity modulus. On the other hand, the authors Zienkiewicz *et al.* [588] advise using the expression $\alpha_k = const\left(1+h\right)^{p+1}$, where *h* is the characteristic size of the elements and *p* is the order of the element.

In conclusion, it is possible to state that this method has the advantage of not changing the size of the governing system. However, the choice of the penalty numbers and the fact that the constraint equations can only be satisfied approximately represent clear disadvantages.

2.4.3 Lagrange multipliers

This method introduces new variables called *Lagrange multipliers* (LM) λ to the system of equations. The Lagrange multipliers can be grouped into the following vector:

$$\boldsymbol{\lambda}^t = \left[\lambda_1 \quad \lambda_2 \quad \cdots \quad \lambda_{nc}\right], \tag{V.64}$$

where *nc* is the *number of constraint equations*.

The Lagrange Multipliers are used to impose the constraint equations (V.44) directly on the variational problem, using:

$$\boldsymbol{\lambda}^t \left(\boldsymbol{\mathcal{C}}_K \mathbf{q} - \mathbf{d}_K\right) = 0\,, \tag{V.65}$$

This equation can be seen as the energy necessary to impose the constraints and can be added to the *total potential energy* functional represented in equation (II.203):

$$\Pi\left(\mathbf{q}, \boldsymbol{\lambda}\right) = \int \underline{\boldsymbol{\sigma}} : \underline{\boldsymbol{\varepsilon}}\left(\mathbf{q}\right) d\Omega - \mathbf{Q}_e^t \mathbf{q} + \boldsymbol{\lambda}^t \left(\boldsymbol{\mathcal{C}}_K \mathbf{q} - \mathbf{d}_K\right). \tag{V.66}$$

Considering the relation (II.39) and imposing the stationary condition, it is possible to obtain the following groups of equations:

$$\frac{\partial \Pi}{\partial \mathbf{q}} = \mathbf{Q}_i - \mathbf{Q}_e + \boldsymbol{\mathcal{C}}_K^t \boldsymbol{\lambda} = \mathbf{0}\,, \tag{V.67}$$

$$\frac{\partial \Pi}{\partial \boldsymbol{\lambda}} = \boldsymbol{\mathcal{C}}_K \mathbf{q} - \mathbf{d}_K = \mathbf{0}\,, \tag{V.68}$$

where the internal force vector is given by equation (II.43) or for a linear elastic material by (II.47).

Grouping these equations into an augmented governing system results in:

$$\begin{bmatrix} \mathbf{K} & \boldsymbol{\mathcal{C}}_K^t \\ \boldsymbol{\mathcal{C}}_K & \mathbf{0} \end{bmatrix} \begin{bmatrix} \mathbf{q} \\ \boldsymbol{\lambda} \end{bmatrix} = \begin{bmatrix} \mathbf{Q}_e \\ \mathbf{d}_K \end{bmatrix}. \tag{V.69}$$

From equation (V.69), it can be seen that $\mathcal{C}_K^t$ acts like an equilibrium operator, and therefore, the nodal forces $\mathbf{Q}_c$ that impose the constraints, can be computed from:

$$\mathbf{Q}_c = \mathcal{C}_K^t \boldsymbol{\lambda} . \tag{V.70}$$

As highlighted by Liu *et al.* [340], there are two main disadvantages associated with the use of this method: firstly, the number of equations increases, and secondly, the expanded stiffness matrix becomes indefinite due to the zeros in the diagonal terms. The latter reduces the efficiency in solving the system of equations and some solvers rely on positive definiteness. On the other hand, the advantages of this method are related to the fact that the constraint equations are satisfied exactly. In addition, it is not necessary to make any subjective decision for the inputs, such as choosing penalty weights, and it is not necessary to rearrange or to perform any additional operation to the system of equations. This last feature can compensate in many cases for the fact of having a larger number of equations to solve [370].

2.5 Transition elements

Transition elements are used when the nodal *dofs* between different types of elements are not compatible. This is the case between solid and beam elements, where the first type presents only translation displacements and the beam elements present also rotational *dofs*. This problem can be solved by using compatible transition elements, which have nodes with different types of *dofs* and are formulated to handle this incompatibility internally. Figure V.8 presents examples of transition elements for two-dimensional and three-dimensional cases. Detailed information about these elements can be obtained in the references [232, 243, 338, 589].

To illustrate how these elements work, let's consider the two-dimensional case presented in Figure V.8-c. The nodal displacements can be assembled in the following vector [472]:

$$\mathbf{q}_N = \left[q_1^{[I]} \quad q_2^{[I]} \quad \theta_3^{[I]} \quad q_1^{[II]} \quad q_2^{[II]} \quad q_1^{[III]} \quad q_2^{[III]} \right]^t . \tag{V.71}$$

The finite element approximation would be defined in matrix format by:

$$\mathbf{q} = \begin{bmatrix} \psi_1 & 0 & y_2 \dfrac{h}{2} \psi_1 & \psi_2 & 0 & \psi_3 & 0 \\ 0 & \psi_1 & 0 & 0 & \psi_2 & 0 & \psi_3 \end{bmatrix} \left[q_1^{[I]} \quad q_2^{[I]} \quad \theta_3^{[I]} \quad q_1^{[II]} \quad q_2^{[II]} \quad q_1^{[III]} \quad q_2^{[III]} \right]^t . \tag{V.72}$$

using local coordinates y_k and with the approximation functions defined by:

$$\psi_1 = \frac{1}{2}(1+y_1); \quad \psi_2 = \frac{1}{4}(1-y_1)(1+y_2); \quad \psi_3 = \frac{1}{4}(1-y_1)(1-y_2) .$$

The element operators can be defined using conventional finite element methodologies, see Chapter II or standard FEM bibliography [32, 472, 587].

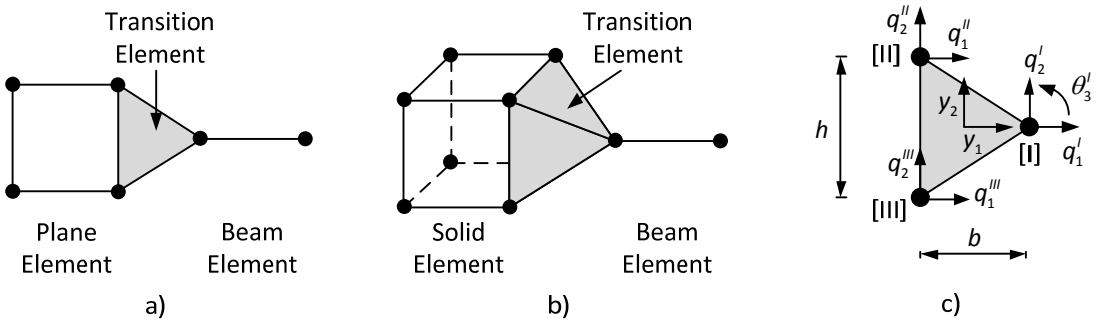

Figure V.8: Transition elements: a) two-dimensional case; b) three-dimensional case; c) nodal dofs for the two-dimensional case.

2.6 Domain Decomposition methods

2.6.1 Introduction

The starting point of this section will be the definition of some concepts and the terminology adopted, in order to set a common base for the addressed topics, since there is still some need of harmonization.

Within the scope of this thesis, a structural analysis can be made using two approaches:

i. *Global Structural Analysis* (GSA), when the analysis is performed by considering simultaneously all the domain of the structure in a single governing system (see Figure V.9-a);
ii. *Substructured Structural Analysis* (SSA)*, a.k.a. Substructuring*, when the analysis is performed using a multi-step procedure by combining information from simpler structural units (subdomains), in order to evaluate the global response of the structure (see Figure V.9-b).

The basic concept of substructuring applied to FEM problems is to solve the original problem in a two-level format: i) a *reduced* or *coarse* problem, commonly defined at the subdomain boundaries, which acts as a interconnecting and load balancing mechanism, and ii) an *internal* problem defined at the subdomain-level with all the condensed and boundary unknowns associated with each subdomain.

The concept of SSA can be taken one step further in *Hybrid Simulation*, where part of the structure is computationally modelled while the other part is physically tested, combining the economy and efficiency of the numerical simulation and the realism of physical testing (see Figure V.9-c).

One of the first steps to perform a SSA is to separate the original domain into several smaller and simpler subdomains forming a partition of the original domain. Each of those subdomains can be analysed separately as a smaller problem, together with boundary conditions that are used to enforce continuity or equilibrium. For complex problems, this task is usually done by *Mesh Partitioning* methods in order to generate optimized subdomain configurations, by minimizing the

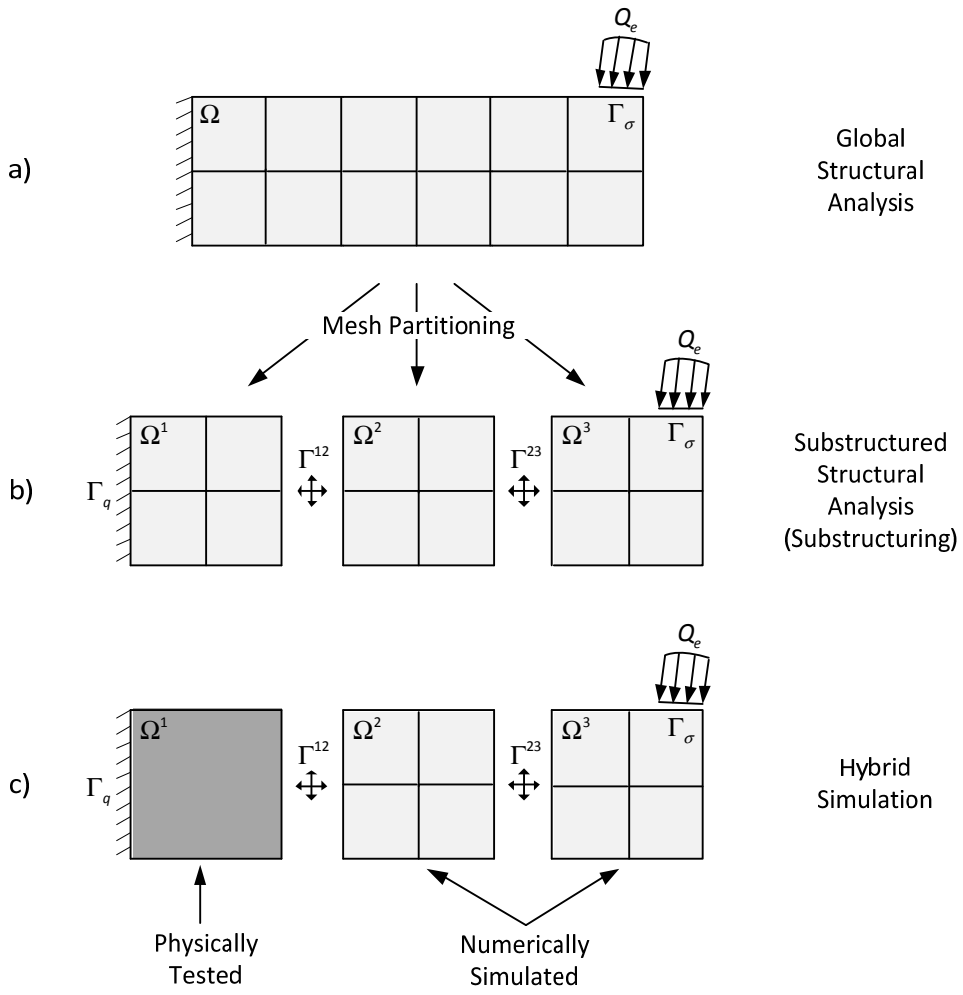

Figure V.9: Structural analysis techniques.

number of boundary nodes and by balancing the size or load associated with each subdomain.

The mesh partitions, or subdomains, can be classified as: i) *non-overlapping*, when the subdomains only share the common boundaries; or ii) *overlapping*, when the subdomains also share elements. The overlapping mesh partitions are commonly used together with the *Schwarz alternating method* and the *additive Schwarz method*. Further details on overlapping mesh partitions lie outside the scope of this thesis and more information can be found in the reference [542]. Most algorithms used for SSA using the FEM are based on non-overlapping subdomains and this will be the case of the methods presented in this section.

The following step consists of implementing a *Domain Decomposition* (DD) method, which can be described as the numerical method/algorithm used to solve the problem taking advantage of the partitioned domain. In recent years, these methods have been subjected to increasing interest from the scientific community that has led to significant developments. This interest cannot be dissociated from recent developments in high performance computing, such as the tendency of using multi-

processor computing architectures.

The DD methods applied to traditional FEM can be classified in terms of the variables used in the reduced problem [250]: i) *Primal* methods define the coarse problem in terms of the boundary displacements (primal variables); ii) *Dual* methods add static (dual) variables to the problem and these are commonly implemented as Lagrange multipliers; iii) *Dual-Primal* methods combine both primal and dual variables to define the reduced problem; and finally, iv) *Mixed methods* introduce the mechanical response of the interface into the problem, using unknowns defined by mixed boundary fields.

Table V.1 lists the DD methods that will be referred to in this work, together with the classification in terms of the variables used in the reduced problem. The selected DD methods were chosen using three criteria. At first, only methods designed for non-overlapping mesh partitions were considered. The possibility of being applicable to mechanical problems was another selection criterion, and finally, the most used methods were chosen. It should be mentioned that the objective of this state of the art is not to present the formulation underlying each method exhaustively, but to present a global view that could justify the choices made.

The DD methods that will be presented in this section are closely related to parallel computations, in which scalability plays an important role. Consequently, it is very important to assess the behaviour of the algorithms in terms of accuracy and performance with the size and number of subdomains. This will be achieved by analysing the concurrent speed-up, the condition number of the structural operators and the number of iterations required for convergence when iterative methods are used to solve the governing system.

In the following sections, a summarized description of the DD methods considered in this thesis will be presented. Before addressing the DD methods themselves, some common definitions and terminology will be established.

- Basic concepts and Boolean operators

As a common basis for all the methods that will be presented, let's consider that the original domain Ω is partitioned into non-overlapping subdomains Ω^{sd} with boundaries $\Gamma^{sd,sd}$, as presented in

Table V.1: Summary of some of the most used Domain Decomposition methods.

Domain Decomposition Methods	Acronym	Type
Primal Substructuring	PS	Primal
Neumann-Neumann	NN	Primal
Balancing Domain Decomposition	BDD	Primal
Balancing Domain Decomposition with constraints	BDDC	Primal
One-level Finite Element Tearing and Interconnecting	FETI-1	Dual
Two-level Finite Element Tearing and Interconnecting	FETI-2	Dual
FETI with coarse problem designed for time-dependent problems	FETI-T	Dual
Dual-Primal Finite Element Tearing and Interconnecting	FETI-DP	Dual-Primal
Large Time Increment	LATIN	Mixed

Figure V.9. In this case, the following relations are satisfied:

$$\begin{cases} \bigcup_{sd=1}^{nsd} \Omega^{sd} = \Omega \\ \bigcap_{sd=1}^{nsd} \Omega^{sd} = \varnothing \end{cases}, \tag{V.73}$$

where *nsd* refers to the number of subdomains.

Within the framework of DD methods, *Boolean operators* are often used to express *dof* selections/restrictions for subdomain variables and these matrices act as mapping or connective operators. Similarly to DD methods, the Boolean operators can be classified as *Primal* or *Dual*. The first type relates primal *dofs* (displacements) and the second type operates on dual variables (*e.g.* forces at the boundaries).

The *primal Boolean operators* are typically implemented in expressions analogous to:

$$\mathbf{q}_A^{sd} = \boldsymbol{\mathcal{A}}_{Aa}^{sd}\, \mathbf{q}_a , \tag{V.74}$$

where $\boldsymbol{\mathcal{A}}$ is an unsigned Boolean operator (0 or 1 entries). The subscripts in uppercase are associated with global/domain spaces and in lowercase to local/subdomain spaces.

These operators can be seen as permutation matrices (see Annex A), although they are generally not symmetric. The inverse operation may be computed from:

$$\mathbf{q}_a = \boldsymbol{\mathcal{A}}_{Aa}^{sd,t}\, \mathbf{q}_A^{sd} . \tag{V.75}$$

Regarding *dual Boolean operators*, they have a similar usage and definition but in this case they are signed operators (-1, 0 or 1 entries). The reason for having the negative entries is linked to the need of ensuring continuity and equilibrium between subdomains. As an example, using kinematic constraints similar to the ones defined in (V.44):

$$\boldsymbol{\mathcal{C}}_K\, \mathbf{q} = \mathbf{d}_K ,$$

continuity would require to set $\mathbf{d} = \mathbf{0}$. Therefore, it is the same as writing for a global *dof k*:

$$q_k^{sd1} = q_k^{sd2} \Leftrightarrow q_k^{sd1} - q_k^{sd2} = 0 , \tag{V.76}$$

hence, the minus sign associated with some *dofs*.

Another distinguishing issue of the dual Boolean operators is the need for defining a sign convention for the subdomain boundaries. This sign convention should define the positive side for the boundary and should be consistent for all subdomains. In this work, the symbol $\boldsymbol{\mathcal{B}}$ will be adopted for the dual Boolean operators in order to follow the most used nomenclature within the scope of DD methods.

It should be noted that, similarly to the assembler operators, the primal and dual Boolean operators are not stored in full or even in sparse matrix format. For example, only the linear integer indexes of the non-null matrix entries may be saved to define the primal operators. The possibility of having -1 entries in dual operators must also be considered in the storage format.

Further information on primal and dual Boolean operators can be found in the DD-related bibliography, *e.g.* [224, 250].

2.6.2 Primal substructuring method

This DD method is known with different names in different frameworks. In this thesis, the term *Primal Substructuring* (PS) method will be used, although in the mathematics community it is known as the *Schur Complement* (SC) method, after *Issai Schur* (1875-1941) and owing to his work in this subject.

This method is referenced in several works [374, 375, 416, 465, 542] and the formulation can be established by considering a static linear mechanical system subjected to external loads, in which the structural domain is divided into *nsd* non-overlapping subdomains Ω^{sd} with interconnecting boundaries $\Gamma^{sd,sd}$ (see Figure V.9). Ordering first the interior *dofs*, grouped by subdomain, and afterwards the *dofs* at the boundary, the following governing system would be obtained:

$$\left[\begin{array}{ccc|c} \mathbf{K}_{ii}^{1} & \mathbf{0} & \mathbf{0} & \mathbf{K}_{iB}^{1} \\ \mathbf{0} & \ddots & \mathbf{0} & \vdots \\ \mathbf{0} & \mathbf{0} & \mathbf{K}_{ii}^{nsd} & \mathbf{K}_{iB}^{nsd} \\ \hline \mathbf{K}_{Bi}^{1} & \cdots & \mathbf{K}_{Bi}^{nsd} & \mathbf{K}_{BB} \end{array}\right] \left[\begin{array}{c} \mathbf{q}_{i}^{1} \\ \vdots \\ \mathbf{q}_{i}^{nsd} \\ \hline \mathbf{q}_{B} \end{array}\right] = \left[\begin{array}{c} \mathbf{Q}_{i}^{1} \\ \vdots \\ \mathbf{Q}_{i}^{nsd} \\ \hline \mathbf{Q}_{B} \end{array}\right]. \tag{V.77}$$

where the stiffness sub-matrices associated with the boundary *dofs* are defined by:

$$\mathbf{K}_{Bi}^{sd} = \mathcal{A}_{bB}^{sd,t}\, \mathbf{K}_{bi}^{sd}, \tag{V.78}$$

$$\mathbf{K}_{iB}^{sd} = \mathbf{K}_{ib}^{sd}\, \mathcal{A}_{bB}^{sd}, \tag{V.79}$$

$$\mathbf{K}_{BB} = \sum_{s=1}^{ns} \mathcal{A}_{bB}^{sd,t}\, \mathbf{K}_{bb}^{sd}\, \mathcal{A}_{bB}^{sd}, \tag{V.80}$$

where the subscripts (*i, b* and *B)* represent the (internal, subdomain boundary and global boundary) degrees of freedom.

The matrices $\mathcal{A}$ are primal Boolean operators used to define mappings between global and local operators. The symbol was chosen to be consistent with the terminology used for the analyses without substructuring, because these matrices can be seen as assembler operators. Section 4.5.2 presents a more detailed definition for these operators.

The system of equations presented in (V.77) clearly shows the independence of the blocks $\mathbf{K}_{ii}^{sd}$, $\mathbf{K}_{iB}^{sd}$ and $\mathbf{K}_{Bi}^{sd}$, as these sub-matrices have contributions only from elements belonging to only one subdomain. Additionally, the sub-matrix $\mathbf{K}_{BB}$ can be computed from the sum of the independent subdomain contributions $\mathbf{K}_{bb}^{sd}$ (V.80).

Already at this stage, the computation and the assemblage of the governing system could be made more efficiently by taking advantage of parallelization. Nevertheless, the parallelization will be taken one-step further, using a multi-step approach to solve the linear system. To achieve this goal, a condensation method similar to the one described in section 2.2.1 will be adopted in order to eliminate the internal *dofs* of each subdomain.

Let's start by simplifying the notation by using the symbols $\mathcal{S}$ and $\mathcal{Q}$ for the *condensed stiffness matrix* and for the *condensed force vector*, where $\mathcal{S}$ is *a.k.a.* the *Schur Complement*.

These can be computed by assembling the contribution of each subdomain using:

$$\mathcal{S} = \sum_{sd=1}^{nsd} \mathcal{A}_{bB}^{sd,t} \; \mathcal{S}^{sd} \; \mathcal{A}_{bB}^{sd} \,, \tag{V.81}$$

$$\mathcal{Q} = \sum_{sd=1}^{nsd} \mathcal{A}_{bB}^{sd,t} \; \mathcal{Q}^{sd} \,, \tag{V.82}$$

where:

$$\mathcal{S}^{sd} = \mathbf{K}_{bb}^{sd} - \mathbf{K}_{bi}^{sd} \left(\mathbf{K}_{ii}^{sd} \right)^{-1} \mathbf{K}_{ib}^{sd} \,, \tag{V.83}$$

$$\mathcal{Q}^{sd} = \mathbf{Q}_{e,b}^{sd} - \mathbf{K}_{bi}^{sd} \; \mathbf{K}_{ii}^{sd,-1} \mathbf{Q}_{e,i}^{sd} \,. \tag{V.84}$$

The reduced governing system to be solved becomes:

$$\mathcal{S} \, \mathbf{q}_B = \mathcal{Q} \,. \tag{V.85}$$

After solving (V.85) for the global boundary displacements, the internal *dof* displacements can be recovered using:

$$\mathbf{q}_i^{sd} = \left(\mathbf{K}_{ii}^{sd} \right)^{-1} \left(\mathbf{Q}_{e,i}^{sd} - \mathbf{K}_{ib}^{sd} \, \mathbf{q}_b^{sd} \right), \tag{V.86}$$

with:

$$\mathbf{q}_b^{sd} = \mathcal{A}_{bB}^{sd} \, \mathbf{q}_B \,. \tag{V.87}$$

It should be emphasized that no approximation is made by solving (V.85) instead of (V.77), and consequently, the same results should be recovered, apart from numerically related accuracy losses. Furthermore, it should be noted that the size of the reduced system (V.85) is generally much smaller than the one without using substructuring (V.77).

The computations associated with expressions (V.83), (V.84) and (V.86) can also benefit from parallelization and be computed independently by different processing units. Assembling the reduced system using expressions (V.81) and (V.82), and afterwards solving the governing system, (V.85) must be centralized on one *root* or *master processing unit* (MPU). Nevertheless, the size of the reduced system is most of the time extremely small when compared to the global model.

One aspect that should be taken into consideration is that the condensed operators (V.83) are potentially full matrices and this represents a significant overhead, because for the same problem size more computations and data exchanges with the master processing unit are required.

The issues related to the implementation of the parallelized algorithm are discussed in detail in section 4.

2.6.3 Neumann-Neumann method

The governing system (V.85) can be solved using a direct method such as the *Gaussian Elimination*, or alternatively, it can be solved with an iterative procedure. Considering that the coefficient matrix of the system is most of the time symmetric and positive definite, the *Conjugate Gradient* method becomes a strong candidate (see Annex A). Frequently, this method is combined with the *Neumann-*

Neumann preconditioner [326, 484]:

$$\mathbf{M}_{NN}^{-1} = \sum_{sd=1}^{nsd} \mathcal{A}_{bB}^{sd,t} \, \mathcal{S}^{sd,-1} \, \mathcal{A}_{bB}^{sd} \,, \tag{V.88}$$

resulting in what will be called the *Neumann-Neumann* (NN) method within the scope of this thesis.

This preconditioner approximates the optimal preconditioner, which in this case would be the inverse of the global Schur Complement $\mathcal{S}$, by the assembled sum of the inverses of the local Schur Complements.

This method presents a significant disadvantage related to the fact that the local Schur Complements are singular matrices for floating subdomains, due to the lack of Dirichlet boundary conditions. This problem can be overcome by using a generalized inverse, such as the *Moore–Penrose pseudoinverse* [406, 443] briefly presented in Annex A. Nevertheless, this computation is considerably more expensive to compute and special attention must be drawn to avoid entering the null space of the singular matrices.

Two of the most important advantages of using iterative solvers are related to the fact that these can outperform the direct solvers for very large problem sizes, *e.g.* $ndofs = O\left(10^6\right)$, and requiring much less data storage capacity [492].

One additional advantage of this method is associated with the possibility of solving the governing system iteratively without assembling explicitly the global Schur Complement [156]. To illustrate this approach, Algorithm V.1 presents the procedure to be used for solving a static mechanical system using the NN method and the *Preconditioned Conjugate Gradient* (PCG) method.

It should be emphasized that the multiplications of matrix $\mathcal{S}$ by vector $\mathbf{p}$, appearing twice in the PCG loop (see Algorithm V.1), can be computed only once and by summing the subdomain contributions, as follows:

$$\mathcal{S}\,\mathbf{p} = \sum_{sd=1}^{nsd} \left(\mathcal{A}_{bB}^{sd,t} \; \mathcal{S}^{sd} \; \mathcal{A}_{bB}^{sd} \; \mathbf{p} \right). \tag{V.89}$$

Similarly, the preconditioning of the residue can be done by computing:

$$\mathbf{z} = \mathbf{M}_{NN}^{-1} \, \mathbf{r} = \sum_{sd=1}^{nsd} \left(\mathcal{A}_{bB}^{sd,t} \, \mathcal{S}^{sd,-1} \, \mathcal{A}_{bB}^{sd} \, \mathbf{r} \right). \tag{V.90}$$

This aspect results in an important advantage in terms of the computing time and storage capacity required for very large problem sizes. On the other hand, the major drawback associated with the Neumann-Neumann method is caused by the accentuated decrease in the convergence rate with the number of subdomains [156]. This phenomenon is reflected in the increase in the condition number of the structural operators and in the number of iterations required for convergence. This behaviour can be observed in the validation example HPC2, presented later in this chapter (see section 5.2).

Algorithm V.1: PCG iterative solver for the Neumann-Neumann method.

1. Compute: $\mathbf{r}^0 = \mathcal{Q} - \mathcal{S}\mathbf{q}_B^0$;
2. Compute: $\mathbf{z}^0 = \mathbf{M}_{NN}^{-1}\mathbf{r}^0$;
3. Compute: $\mathbf{p}^0 = \mathbf{z}^0$;
4. While $i \le niter_{\max}$:
   4.1 Compute: $\alpha^i = \dfrac{\left\langle \mathbf{r}^i, \mathbf{z}^i \right\rangle}{\left\langle \mathbf{p}^i, \mathcal{S}\mathbf{p}^i \right\rangle}$;
   4.2 Compute: $\mathbf{q}_B^{i+1} = \mathbf{q}_B^i + \alpha^i \mathbf{p}^i$;
   4.3 Compute: $\mathbf{r}^{i+1} = \mathbf{r}^i - \alpha^j \mathcal{S}\mathbf{p}^i$;
   4.4 If $\left\langle \mathbf{r}^{i+1}, \mathbf{r}^{i+1} \right\rangle < tol$ Exit;
   4.5 Compute: $\mathbf{z}^{i+1} = \mathbf{M}_{NN}^{-1}\mathbf{r}^{i+1}$;
   4.6 Compute: $\beta^i = \dfrac{\left\langle \mathbf{r}^{i+1}, \mathbf{z}^{i+1} \right\rangle}{\left\langle \mathbf{r}^i, \mathbf{z}^i \right\rangle}$;
   4.7 Compute: $\mathbf{p}^{i+1} = \mathbf{z}^{i+1} + \beta^i \mathbf{p}^i$;
   4.8 Increment *i*;
End While

2.6.4 Balancing Domain Decomposition method

To mitigate the dependency of the convergence rate on the number of subdomains observed using the NN method, the authors Mandel [355] and Le Tallec [324] introduced the *Balancing Domain Decomposition* (BDD) method, which includes a coarse problem that works as a balancing mechanism between the subdomains. This formulation uses only the original unknowns, and consequently, it can be classified as a primal method. In addition, it is often considered as belonging to the class of Neumann–Neumann methods, because the preconditioner involves the solution of Neumann problems for all subdomains.

In the following part of this section, a summarized description of the BDD algorithm will be presented. Further details can be obtained in the references presented throughout the text.

- Formulation as a preconditioner

The BDD method can be formulated in several ways. Mandel and co-workers [355, 356] expressed this method as a preconditioner for the PCG algorithm [156]:

$$\mathbf{M}_{BDD}^{-1} = \mathbf{P}\,\mathbf{M}_{NN}^{-1}, \tag{V.91}$$

with:

$$\mathbf{P} = \mathbf{I} - \mathbf{G}\left(\mathbf{G}^t \mathcal{S}\mathbf{G}\right)^{-1}\mathbf{G}\mathcal{S}, \tag{V.92}$$

$$\mathbf{G} = \left[\mathcal{A}^1\mathbf{Z}^1, \ldots, \mathcal{A}^{nsd}\mathbf{Z}^{nsd}\right], \tag{V.93}$$

where the matrix $\mathbf{Z}^{sd}$ groups the subdomain *rigid body modes* (RBM) and **P** can be seen as a matrix that represents a projection onto the complement of the subdomain rigid body mode space (see Annex A).

Special care must be taken with the initialization of the vector of unknowns, in order to avoid entering the null space of the local Schur Complements. This can be done using the following initialization:

$$\mathbf{q}_b^0 = \mathbf{A}_c \, \mathcal{Q}, \tag{V.94}$$

where:

$$\mathbf{A}_c = \mathbf{G}\left(\mathbf{G}^t \mathcal{S} \mathbf{G}\right)^{-1} \mathbf{G} = \left(\mathbf{I} - \mathbf{P}\right) \mathcal{S}^{-1}. \tag{V.95}$$

Alternatively, the solution can be found without initializing the displacement vector but in this case, the preconditioner should be redefined as [224]:

$$\mathbf{M}_{BDD}^{-1} = \mathbf{P}\, \mathbf{M}_{NN}^{-1}\, \mathbf{P} + \mathbf{A}_c. \tag{V.96}$$

- Formulation as a two-level method

Another possible approach to the formulation of the BDD method is to apply a standard two-level solution technique similar to what is done in the framework of the *Multigrid methods* [224]. Let's start by using an arbitrary matrix **C** to enforce equation (V.85) in a weak form:

$$\mathbf{C}^t \left(\mathcal{Q} - \mathcal{S} \mathbf{q}_B\right) = \mathbf{0}. \tag{V.97}$$

A possible way to satisfy this last equation and to preserve the symmetry of the original governing system is by introducing the following displacement split [224]:

$$\mathbf{q}_B = \hat{\mathbf{q}}_B + \mathbf{C}\, \mathbf{q}_C. \tag{V.98}$$

The following system of equation can be retrieved by inserting equation (V.98) into (V.85) and afterwards into (V.97):

$$\begin{bmatrix} \mathcal{S} & \mathbf{C}\mathcal{S} \\ \mathbf{C}^t \mathcal{S} & \mathbf{C}^t \mathcal{S} \mathbf{C} \end{bmatrix} \begin{bmatrix} \hat{\mathbf{q}}_B \\ \mathbf{q}_C \end{bmatrix} = \begin{bmatrix} \mathcal{Q} \\ \mathbf{C}^t \mathcal{Q} \end{bmatrix}. \tag{V.99}$$

Solving the lower group of equations in order to $\mathbf{q}_C$ leads to:

$$\mathbf{q}_C = \left(\mathbf{C}^t \mathcal{S} \mathbf{C}\right)^{-1} \mathbf{C}^t \left(\mathcal{Q} - \mathcal{S} \hat{\mathbf{q}}_B\right), \tag{V.100}$$

and inserting this last equation into the upper group of equations, results in:

$$\mathbf{P}_C^t \, \mathcal{S} \, \hat{\mathbf{q}}_B = \mathbf{P}_C^t \, \mathcal{Q}. \tag{V.101}$$

If the matrix **C** is set to be the restriction to the global boundary *dofs* of the *rigid body modes* (RBM), or in other words equal to matrix **G**, then the matrix $\mathbf{P}_C$ equals **P**, as defined in (V.92).

The system (V.101) can be solved using a conventional PCG algorithm with the Neumann-Neumann preconditioner to enhance the convergence rate. After solving the system for $\hat{\mathbf{q}}_B$, the displacements of the boundary *dofs* can be obtained by computing (V.100) and finally (V.98).

In the work of Klawonn and Widlund [306], it is demonstrated that the condition number of the BDD preconditioner as defined in (V.96), is approximated by:

$$\kappa\left(\mathbf{M}_{BDD}^{-1}\right)=o\left(1+\log\frac{H}{h}\right)^2, \tag{V.102}$$

where *H* is the subdomain size and *h* is the mesh size. This result proves that for the same problem and mesh size, increasing the number of subdomains by decreasing their size *H* then the condition number decreases and convergence rate improves. In addition, if the problem size is increased by augmenting the number of subdomains but leaving the element and subdomain size the same, then the condition number stays roughly constant. Finally, if the mesh is refined and the number or size of subdomains remains equal, then for the same problem size the condition number increases but only at a polylogarithmic rate [209]. These results clearly prove the scalability of the BDD method as a result of introducing the coarse problem that introduces a balancing mechanism between the subdomains.

2.6.5 FETI-1 method and other dual FETI methods

The original format of the *One-level Finite Element Tearing and Interconnecting* method, also known by the acronym FETI-1, was introduced by Farhat and Roux in 1991 [210] and consists of a DD method that uses Lagrange multipliers to enforce the continuity between non-overlapping subdomains (see Figure V.10). This formulation adopts a dual approach because it implements an additional set of unknowns (Lagrange Multipliers) that represent the subdomain interaction forces, which in nature are dual to the original primal unknowns (displacements).

Different combinations of Lagrange Multipliers can be defined when the boundary nodes are shared by more than two subdomains [224]. These combinations can represent non-redundant and redundant definitions of Lagrange Multipliers, as represented in Figure V.11. These configurations change the definition of the signed Boolean matrices $\mathcal{B}$ and can also change the convergence characteristics of the FETI algorithm. The analysis of the influence of this issue on the condition number can be found in the work of Klawonn *et al.* [306].

A summarized description of the formulation of this method is presented afterwards. Further details can be found in the references [204, 210].

Let's start by reformulating the *total potential energy* functional of an elastic solid body with a set of constraint equations imposed using Lagrange Multipliers, similarly to what was done in equation (V.66) of section 2.4.3:

$$\Pi\left(\mathbf{q},\boldsymbol{\lambda}\right)=\int\underline{\boldsymbol{\sigma}}:\underline{\boldsymbol{\varepsilon}}\left(\mathbf{q}\right)d\Omega-\mathbf{Q}_e^t\,\mathbf{q}+\boldsymbol{\lambda}^t\mathcal{B}\,\mathbf{q}\,. \tag{V.103}$$

In this case, the more general kinematic constraint matrix $\mathcal{C}_K$ is replaced by a dual Boolean operator $\mathcal{B}$ and the *rhs* vector **d** in equation (V.44) is set to zero to impose the continuity between subdomains.

Considering the domain partitioned into *nsd* non-overlapping subdomains, the total potential energy

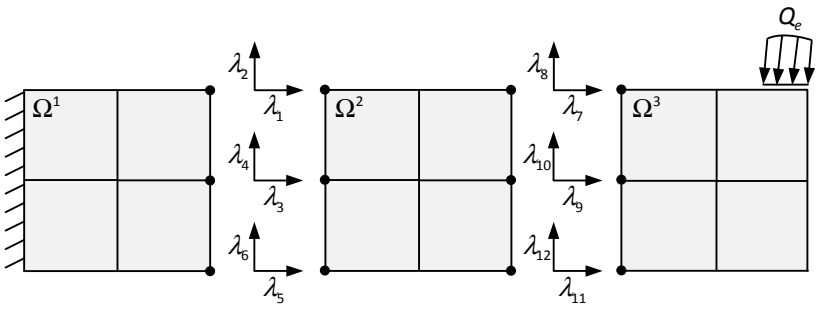

Figure V.10: Using Lagrange multipliers to impose the continuity between subdomains in the scope of the FETI-1 method.

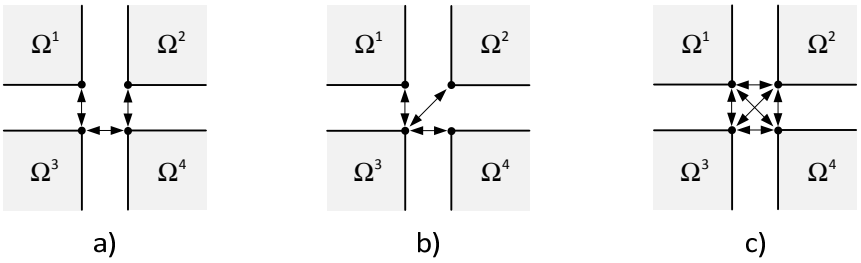

Figure V.11: Different definitions of Lagrange Multipliers: a) and b) non-redundant; c) redundant.

can be computed from the sum of the energy from all subdomains:

$$\Pi(\mathbf{q},\boldsymbol{\lambda}) = \sum_{sd=1}^{nsd} \left(\int \underline{\boldsymbol{\sigma}} : \underline{\boldsymbol{\varepsilon}}(\mathbf{q}) d\Omega - \mathbf{Q}_e^t \, \mathbf{q} + \boldsymbol{\lambda}^t \boldsymbol{\mathcal{B}} \mathbf{q} \right)^{sd} . \tag{V.104}$$

Considering for now an elastic material, it is possible to obtain without losing generality the following equations by imposing the stationary condition:

$$\frac{\partial \Pi}{\partial \mathbf{q}} = \sum_{sd=1}^{nsd} \left(\mathbf{K}^{sd} \, \mathbf{q}^{sd} - \mathbf{Q}_e^{sd} + \boldsymbol{\mathcal{B}}^{sd,t} \, \boldsymbol{\lambda} \right) = \mathbf{0} , \tag{V.105}$$

$$\frac{\partial \Pi}{\partial \boldsymbol{\lambda}} = \sum_{sd=1}^{nsd} \boldsymbol{\mathcal{B}}^{sd} \, \mathbf{q}^{sd} = \mathbf{0} . \tag{V.106}$$

Equation (V.105) represents the global equilibrium that must also be achieved for each subdomain separately, when the interface forces are included. The solution for the displacements can normally be found by computing:

$$\mathbf{q}^{sd} = \left(\mathbf{K}^{sd} \right)^{-1} \left(\mathbf{Q}_e^{sd} - \boldsymbol{\mathcal{B}}^{sd,t} \, \boldsymbol{\lambda} \right). \tag{V.107}$$

However, for floating subdomains, which do not have enough Dirichlet boundary conditions to avoid rigid body modes (*e.g.* subdomains 2 and 3 represented in Figure V.10), the stiffness matrix is singular and the inverse cannot be found.

As before, this problem can be avoided by using the generalized inverse of the subdomain stiffness matrix (see Annex A) [210]. This matrix only considers the useful columns and row spaces and

discards the null space of the rank-deficient stiffness matrices. For floating subdomains, equation (V.107) may be rewritten as:

$$\mathbf{q}^{sd} = \left(\mathbf{K}^{sd}\right)^{+}\left(\mathbf{Q}_e^{sd} - \boldsymbol{\mathcal{B}}^{sd,t}\,\boldsymbol{\lambda}\right) + \mathbf{R}^{sd}\boldsymbol{\alpha}, \tag{V.108}$$

where $\left(\mathbf{K}^{sd}\right)^{+}$ and $\mathbf{R}^{sd}$ represents the pseudoinverse and null space (rigid body modes) of the subdomain stiffness matrix, respectively, and $\boldsymbol{\alpha}$ specifies a linear combination of the columns of $\mathbf{R}^{sd}$. For each subdomain the number of RBM is limited to three in two-dimensional problems and to six in three-dimensional problems.

The coarse problem is defined by eliminating the subdomain displacements in the compatibility equation (V.106) using expression (V.107) or (V.108). This results in:

$$\sum_{sd=1}^{nsd}\left(\boldsymbol{\mathcal{B}}^{sd}\,\mathbf{K}^{sd,+}\,\mathbf{Q}_e^{sd} - \boldsymbol{\mathcal{B}}^{sd}\,\mathbf{K}^{sd,+}\,\boldsymbol{\mathcal{B}}^{sd,t}\,\boldsymbol{\lambda} + \boldsymbol{\mathcal{B}}^{sd}\,\mathbf{R}^{sd}\boldsymbol{\alpha}\right) = \mathbf{0}, \tag{V.109}$$

where for non-floating subdomains the pseudoinverse can be replaced by the traditional inverse and the last term between parentheses is null.

The coarse problem must be complemented with an equation that enforces that the term between parentheses in (V.107) or (V.108) has no component in the null space of the subdomain stiffness matrix. Physically, this means that the loads (external and interconnecting forces) do not excite the subdomain rigid body modes. Mathematically, this can be expressed by:

$$\left\langle \mathbf{R}^{sd},\, \mathbf{Q}_e^{sd} - \boldsymbol{\mathcal{B}}^{sd,t}\,\boldsymbol{\lambda} \right\rangle = \mathbf{0}. \tag{V.110}$$

Equation (V.109) and (V.110) can be combined together in the condensed system representing the coarse problem of the method:

$$\begin{bmatrix} \mathbf{F} & -\mathbf{G} \\ -\mathbf{G}^{t} & \mathbf{0} \end{bmatrix}\begin{bmatrix} \boldsymbol{\lambda} \\ \boldsymbol{\alpha} \end{bmatrix} = \begin{bmatrix} \mathbf{d} \\ -\mathbf{e} \end{bmatrix}, \tag{V.111}$$

with:

$$\mathbf{F} = \sum_{sd=1}^{nsd} \boldsymbol{\mathcal{B}}^{sd}\,\mathbf{K}^{sd,+}\,\boldsymbol{\mathcal{B}}^{sd,t}, \tag{V.112}$$

$$\mathbf{G} = \left[\boldsymbol{\mathcal{B}}^{1}\,\mathbf{R}^{1}, \ldots, \boldsymbol{\mathcal{B}}^{nsd}\,\mathbf{R}^{nsd}\right], \tag{V.113}$$

$$\mathbf{d} = \sum_{sd=1}^{nsd} \boldsymbol{\mathcal{B}}^{sd}\,\mathbf{K}^{sd,+}\,\mathbf{Q}_e^{sd}, \tag{V.114}$$

$$\mathbf{e} = \left[\mathbf{R}^{1,t}\,\mathbf{Q}_e^{1}, \ldots, \mathbf{R}^{nsd,t}\,\mathbf{Q}_e^{nsd}\right]. \tag{V.115}$$

It is possible to observe that the reduced problem is defined only in terms of the dual variables and RBM coefficients, and consequently, the primal unknowns (displacements) are missing from the coarse problem.

Solving equation (V.111) can be performed using a direct method (*e.g.* Gaussian Elimination) or an iterative procedure. Farhat and Roux [210] propose using a modified version of the PCG method that can also be seen as a two-step PCG. The procedure to be followed is presented in Algorithm V.2.

Algorithm V.2: FETI-1 method with the modified PCG procedure, adapted from [204].

1. Initialize: $\boldsymbol{\lambda}^0 = \mathbf{G}\left(\mathbf{G}^t\,\mathbf{G}\right)^{-1}\mathbf{e}$;
2. Compute: $\mathbf{P} = \mathbf{I} - \mathbf{G}\left(\mathbf{G}^t\,\mathbf{G}\right)^{-1}\mathbf{G}^t$;
3. Compute: $\mathbf{r}^0 = \mathbf{d} - \mathbf{F}\boldsymbol{\lambda}^0$;
4. While $i \le niter_{\max}$
   - 4.1 Compute: $\mathbf{w}^{i-1} = \mathbf{P}^t\mathbf{r}^{i-1}$;
   - 4.2 Compute: $\mathbf{z}^{i-1} = \mathbf{M}^{-1}\,\mathbf{w}^{i-1}$;
   - 4.3 Compute: $\mathbf{y}^{i-1} = \mathbf{P}\,\mathbf{z}^{i-1}$;
   - 4.4 Compute: $\beta^i = \dfrac{\left\langle \mathbf{y}^{i-1}, \mathbf{w}^{i-1} \right\rangle}{\left\langle \mathbf{y}^{i-2}, \mathbf{w}^{i-2} \right\rangle}$, $\left(\beta^1 = 0\right)$;
   - 4.5 Compute: $\mathbf{p}^i = \mathbf{y}^{i-1} + \beta^i\,\mathbf{p}^{i-1}$, $\left(\mathbf{p}^1 = \mathbf{y}^0\right)$;
   - 4.6 Compute: $\alpha^i = \dfrac{\left\langle \mathbf{y}^{i-1}, \mathbf{w}^{i-1} \right\rangle}{\left\langle \mathbf{p}^i, \mathbf{F}\,\mathbf{p}^i \right\rangle}$;
   - 4.7 Compute: $\boldsymbol{\lambda}^i = \boldsymbol{\lambda}^{i-1} + \alpha^i\mathbf{p}^i$;
   - 4.8 Compute: $\mathbf{r}^i = \mathbf{r}^{i-1} - \alpha^i\mathbf{F}\mathbf{p}^i$;
   - 4.9 If $\left\langle \mathbf{r}^i, \mathbf{r}^i \right\rangle < tol$, then Exit;
   - 4.10 Increment i;

End While

It should be emphasized that it is not necessary to assemble the matrix **F** because the matrix-by-vector multiplications $\left(\mathbf{F}\mathbf{p}\right)$, present twice in the modified PCG algorithm, can be computed by joining the contribution from all subdomains already in a vector format, similarly to what was presented for equation (V.89).

The initial value for $\boldsymbol{\lambda}$ must be chosen to also fulfil the relation (V.110), which is already present in the lower group of equations in (V.111). After some algebraic manipulations, this can be done by imposing [210]:

$$\boldsymbol{\lambda} = \mathbf{G}\left(\mathbf{G}^t\mathbf{G}\right)^{-1}\mathbf{e}. \tag{V.116}$$

Additionally, no components in the null space of the subdomains can be considered in the residue and in the search directions. This can be implemented using the projection matrix (see Annex A):

$$\mathbf{P} = \mathbf{I} - \mathbf{G}\left(\mathbf{G}^t\,\mathbf{G}\right)^{-1}\mathbf{G}^t. \tag{V.117}$$

In what concerns the preconditioner, most authors advice on using the *Dirichlet preconditioner*, defined as:

$$\mathbf{M}_D^{-1} = \sum_{sd=1}^{nsd} \mathcal{B}^{sd}\;\mathcal{A}_{bB}^{sd,t}\;\mathcal{S}^{sd}\;\mathcal{A}_{bB}^{sd}\;\mathcal{B}^{sd,t}, \tag{V.118}$$

or the *Lumped preconditioner*:

$$\mathbf{M}_L^{-1} = \sum_{sd=1}^{nsd} \mathcal{B}^{sd}\mathcal{A}_{bB}^{sd,t}\;\mathbf{K}_{bb}^{sd}\;\mathcal{A}_{bB}^{sd}\;\mathcal{B}^{sd,t}. \tag{V.119}$$

According to the references [209, 224, 305], the Dirichlet preconditioner gives a *quasi*-optimal condition number for the coefficient matrix, because it approximates the global inverse by the sum of the subdomain inverses. However, computing this preconditioner is more expensive than the Lumped preconditioner that lumps the Dirichlet operator on the substructure interfaces, which is easier to compute and often proved to be more efficient for solving second-order elasticity problems.

After computing the vector of Lagrange multipliers using the modified PCG algorithm, the vector $\boldsymbol{\alpha}$ can be computed from the upper group of equations in (V.111). Nevertheless, the matrix $\mathbf{G}$ is not square and consequently is not invertible, hence an optimized solution, in the least squares sense, can still be found by pre-multiplying by $\mathbf{G}^t$ (see Annex A), leading to:

$$\boldsymbol{\alpha} = \left(\mathbf{G}^t\mathbf{G}\right)^{-1}\left\{\mathbf{G}^t\left(\mathbf{F}\boldsymbol{\lambda} - \mathbf{d}\right)\right\}. \tag{V.120}$$

Either using a direct or an indirect method for solving the coarse system (V.111), after knowing $\boldsymbol{\lambda}$ and $\boldsymbol{\alpha}$, the displacements can be recovered using equation (V.107) for non-floating subdomains, or using (V.108), otherwise.

The convergence rate of the FETI-1 method is closely related to the condition number of the coarse problem. Farhat *et al.* [204] stress that the condition number of the Unpreconditioned Conjugate Gradient method for static problems is expressed by the following expression:

$$\kappa\left(\mathbf{F}\right) = O\left(\frac{H}{h}\right), \tag{V.121}$$

where *H* is the subdomain size and *h* is the mesh size. Furthermore, Mandel and Tezaur [360] proved that in two-dimensional and three-dimensional elasticity, using the *Dirichlet* preconditioner on the coarse problem leads to a condition number in some cases bounded by:

$$\kappa\left(\mathbf{M}_D^{-1}\mathbf{F}\right) = O\left(1 + \log\frac{H}{h}\right)^2. \tag{V.122}$$

Due to the similarity of this last relation with the one reported for the BDD preconditioner (V.102), the same qualitative analysis can be extended to the FETI-1, thus, implying the good scalability of the method.

The original FETI-1 was extended to contact problems by Dostál and co-workers [175-178].

- FETI-2 Method

For fourth-order problems (*e.g.* analyses with plates), the scalability of the FETI-1 method is destroyed by the appearance of singularities at the corners of substructures (corner nodes or cross points). The authors Farhat and Mandel [209] proposed to regularize this problem by enforcing the continuity of the transversal displacement field at these corners. This can be done by introducing a set of additional Lagrange multipliers at the subdomain corner nodes. The FETI method is enriched with an additional coarse problem defined in terms of the subdomain rigid body and corner modes [206]. This procedure restores the scalability of the FETI method and is also applicable to time-dependent and shell problems [205].

This methodology is often called the *two-level FETI method* (FETI-2) because this new coarse problem can be expressed as the projection on a subspace of the original FETI interface problem. Additional information regarding the formulation and the convergence characteristics of the method can be found in the references [205, 209, 326, 486].

- FETI-T Method

For time-dependent problems (*e.g.* heat transfer and dynamics), the presence of additional matrices change the coefficient matrix in such a way that the null space of the governing system becomes absent, and consequently, the FETI-1 algorithm cannot be applied. To illustrate this problem for incremental dynamic analyses (IDA), let's start by recalling that most of the time the following general expression is used to solve the problem (II.167):

$$\hat{\mathbf{K}}\mathbf{q} = \hat{\mathbf{Q}}, \tag{V.123}$$

where:

$$\hat{\mathbf{K}} = c_1\mathbf{M} + c_2\mathbf{C} + \mathbf{K}. \tag{V.124}$$

The mass matrix contribution in the definition of $\hat{\mathbf{K}}$ may remove the rigid body modes of the floating subdomains, which are necessary to define the FETI-1 algorithm.

To overcome this problem, Farhat and co-workers [204] proposed the so-called FETI-T method that changes the original coarse problem of the FETI-1 method, in order to propagate the error globally and restore the scalability of the procedure. According to Fragakis *et al.* [225], this procedure can be seen as a two-level solution technique similar to the one adopted in the BDD and FETI-2 methods, with the constrained matrix defined by the null space of the static stiffness matrix and using the Dirichlet or Lumped preconditioners. Further information can be found in the bibliography *e.g.* [204, 225].

2.6.6 FETI-DP method

The *Dual-Primal Finite Element Tearing and Interconnecting* method, also known by the acronym FETI-DP, is a dual-primal method that enforces the continuity in the subdomain boundary *dofs* by using dual Lagrange multipliers like in the traditional FETI-1 method, except for a chosen group of corner *dofs* where the continuity is enforced by primal variables (displacements). If the corner nodes are adequately chosen, the subdomain stiffness matrix associated with the rest of the *dofs* becomes non-singular, and consequently, the use of generalized inverses and RBM is avoided. The FETI-DP method was first introduced by Mandel and Tezaur [361] and later developed by Farhat and co-workers [206, 207]. In the following part of this section, the basic formulation of this method will be presented.

Let us start by reordering the subdomain *dofs*, as follows:

$$\mathbf{K}^{sd} = \begin{bmatrix} \mathbf{K}_{rr}^{sd} & \mathbf{K}_{rc}^{sd} \\ \mathbf{K}_{cr}^{sd} & \mathbf{K}_{cc}^{sd} \end{bmatrix}, \quad \mathbf{q}^{sd} = \begin{bmatrix} \mathbf{q}_{r}^{sd} \\ \mathbf{q}_{c}^{sd} \end{bmatrix}, \quad \mathbf{Q}^{sd} = \begin{bmatrix} \mathbf{Q}_{r}^{sd} \\ \mathbf{Q}_{c}^{sd} \end{bmatrix}, \tag{V.125}$$

where the subscript *c* and *r* are associated with the corner node *dofs* and with the remaining *dofs*.

The remaining *dofs* are subdivided into:

$$\mathbf{q}_r^{sd} = \begin{bmatrix} \mathbf{q}_i^{sd} \\ \mathbf{q}_b^{sd} \end{bmatrix}, \quad \mathbf{Q}_r^{sd} = \begin{bmatrix} \mathbf{Q}_i^{sd} \\ \mathbf{Q}_b^{sd} \end{bmatrix}, \tag{V.126}$$

where the subscript *i* represents the displacements associated with the interior *dofs* of the subdomain and *b* represents the displacements associated with the boundary *dofs*.

The displacements of the corner *dofs* are defined for the global domain using the vector $\mathbf{q}_C$, which has a number of rows equal to the global number of corner node *dofs* (*nc*).

$$\mathbf{q}_C = \begin{bmatrix} \mathbf{q}_C^1 & \cdots & \mathbf{q}_C^{nc} \end{bmatrix}^t. \tag{V.127}$$

A primal Boolean operator is used for mapping between the local and global corner *dof* displacements:

$$\mathbf{q}_c^{sd} = \mathcal{A}_{cC}^{sd}\, \mathbf{q}_C, \tag{V.128}$$

where $\mathcal{A}_{cC}^{sd}$ is an unsigned Boolean operator with a number of rows equal to the number of subdomain boundary corner *dofs* and a number of columns equal to the global number of corner *dofs*.

In addition, a dual Boolean operator is used for the selection of the *dofs* associated with the remaining boundary *dofs*:

$$\mathbf{q}_b^{sd} = \mathcal{B}_{br}^{sd}\, \mathbf{q}_r^{sd}, \tag{V.129}$$

where $\mathcal{B}_{br}^{sd}$ is a signed Boolean operator with a number of rows equal to the number of subdomain boundary remaining *dofs* and a number of columns equal to the subdomain internal and boundary remaining *dofs*. In this context, the boundary remaining *dofs* refer to all subdomain boundary *dofs* other than the ones associated with corner nodes.

Similarly to what was presented for the FETI-1 method (V.104), let's start by considering the domain partitioned into *nsd* non-overlapping subdomains and equating the total potential energy from the sum of the energy from all subdomains:

$$\Pi(\mathbf{q},\boldsymbol{\lambda}) = \sum_{sd=1}^{nsd} \left(\int \underline{\boldsymbol{\sigma}} : \underline{\boldsymbol{\varepsilon}}(\mathbf{q})\, d\Omega - \mathbf{Q}_e^t\, \mathbf{q} + \boldsymbol{\lambda}_b^t\, \mathcal{B}_{br}\, \mathbf{q}_r \right)^{sd}. \tag{V.130}$$

Considering an elastic material and imposing the stationary condition, one obtains:

$$\frac{\partial \Pi}{\partial \mathbf{q}} = \begin{cases} \dfrac{\partial \Pi}{\partial \mathbf{q}_r^{sd}} \dfrac{\partial \mathbf{q}_r^{sd}}{\partial \mathbf{q}} = \displaystyle\sum_{sd=1}^{nsd} \left(\mathbf{K}_{rr}^{sd}\, \mathbf{q}_r^{sd} + \mathbf{K}_{rc}^{sd}\, \mathcal{A}_{cC}^{sd} \mathbf{q}_C - \mathbf{Q}_r^{sd} + \mathcal{B}_{br}^{sd,t}\, \boldsymbol{\lambda}_b \right) = \mathbf{0} \\ \dfrac{\partial \Pi}{\partial \mathbf{q}_C^{sd}} \dfrac{\partial \mathbf{q}_C^{sd}}{\partial \mathbf{q}} = \displaystyle\sum_{sd=1}^{nsd} \left(\mathbf{K}_{cr}^{sd}\, \mathbf{q}_r^{sd} + \mathbf{K}_{cc}^{sd}\, \mathcal{A}_{cC}^{sd} \mathbf{q}_C - \mathbf{Q}_c^{sd} \right) = \mathbf{0} \end{cases}, \tag{V.131}$$

$$\frac{\partial \Pi}{\partial \boldsymbol{\lambda}_b} = \sum_{sd=1}^{nsd} \mathcal{B}_{br}^{sd}\, \mathbf{q}_r^{sd} = \mathbf{0}. \tag{V.132}$$

It is possible to notice the absence of the term associated with the Lagrange multipliers in the lower

group of equations in (V.131). This is due to the fact that there are no Lagrange Multipliers associated with the corner *dofs*. The interface continuity equation (V.132) is only necessary to be defined for the boundary remaining *dofs*.

The equilibrium condition represented in the upper group of equations in (V.131) must also be verified for each subdomain separately when the interconnecting forces represented by the Lagrange Multipliers are included. If the *dofs* associated with the corner nodes are chosen adequately, the upper group of equations in (V.131) can be solved for $\mathbf{q}_r^{sd}$ using:

$$\mathbf{q}_r^{sd} = \left(\mathbf{K}_{rr}^{sd}\right)^{-1}\left(\mathbf{Q}_r^{sd} - \mathbf{K}_{rc}^{sd}\,\mathcal{A}_{cC}^{sd}\,\mathbf{q}_C - \mathcal{B}_{br}^{sd,t}\,\boldsymbol{\lambda}_b\right), \tag{V.133}$$

Introducing (V.133) into (V.132), leads to:

$$\mathbf{F}_{bb}\,\boldsymbol{\lambda}_b + \mathbf{F}_{bC}\,\mathbf{q}_C = \mathbf{d}_b\,, \tag{V.134}$$

with:

$$\mathbf{F}_{bb} = \sum_{sd=1}^{nsd} \mathcal{B}_{br}^{sd}\left(\mathbf{K}_{rr}^{sd}\right)^{-1}\mathcal{B}_{br}^{sd,\,t}\,, \tag{V.135}$$

$$\mathbf{F}_{bC} = \sum_{sd=1}^{nsd} \mathcal{B}_{br}^{sd}\left(\mathbf{K}_{rr}^{sd}\right)^{-1}\mathbf{K}_{rc}^{sd}\,\mathcal{A}_{cC}^{sd}\,, \tag{V.136}$$

$$\mathbf{d}_b = \sum_{sd=1}^{nsd} \mathcal{B}_{br}^{sd}\left(\mathbf{K}_{rr}^{sd}\right)^{-1}\mathbf{Q}_r^{sd}\,. \tag{V.137}$$

Pre-multiplying the lower group of equation in (V.131) by $\mathcal{A}_{cC}^{sd,t}$, leads to the following expression:

$$\sum_{sd=1}^{nsd}\left(\mathcal{A}_{cC}^{sd,t}\mathbf{K}_{cr}^{sd}\,\mathbf{q}_r^{sd}\right) + \mathbf{K}_{CC}\,\mathbf{q}_C = \mathbf{Q}_C\,, \tag{V.138}$$

with:

$$\mathbf{K}_{CC} = \sum_{sd=1}^{nsd} \mathcal{A}_{cC}^{sd,t}\,\mathbf{K}_{cc}^{sd}\,\mathcal{A}_{cC}^{sd}\,, \tag{V.139}$$

$$\mathbf{Q}_C = \sum_{sd=1}^{nsd} \mathcal{A}_{cC}^{sd,t}\,\mathbf{Q}_c^{sd}\,. \tag{V.140}$$

Inserting (V.133) into (V.138):

$$\mathbf{F}_{Cb}\,\boldsymbol{\lambda}_b - \mathbf{K}_{CC}^{*}\,\mathbf{q}_C = -\mathbf{Q}_C^{*} \tag{V.141}$$

with:

$$\mathbf{F}_{Cb} = \mathbf{F}_{bC}^{t} = \sum_{sd=1}^{nsd} \mathcal{A}_{cC}^{sd,t}\,\mathbf{K}_{cr}^{sd}\,\mathbf{K}_{rr}^{sd,-1}\mathcal{B}_{br}^{sd,t}\,, \tag{V.142}$$

$$\mathbf{K}_{CC}^{*} = \mathbf{K}_{CC} - \sum_{sd=1}^{nsd} \mathcal{A}_{cC}^{sd,t}\,\mathbf{K}_{rc}^{sd,t}\,\mathbf{K}_{rr}^{sd,-1}\,\mathbf{K}_{rc}^{sd}\,\mathcal{A}_{cC}^{sd}\,, \tag{V.143}$$

$$\mathbf{Q}_C^{*} = \mathbf{Q}_C - \sum_{sd=1}^{nsd} \mathcal{A}_{cC}^{sd,t}\,\mathbf{K}_{rc}^{sd,t}\,\mathbf{K}_{rr}^{sd,-1}\mathbf{Q}_r^{sd}\,. \tag{V.144}$$

Equations (V.134) and (V.141) can be combined to form the following system of equations:

$$\begin{bmatrix} \mathbf{F}_{bb} & \mathbf{F}_{bC} \\ \mathbf{F}_{Cb} & -\mathbf{K}^{*}_{CC} \end{bmatrix} \begin{bmatrix} \boldsymbol{\lambda}_b \\ \mathbf{q}_C \end{bmatrix} = \begin{bmatrix} \mathbf{d}_b \\ -\mathbf{Q}^{*}_C \end{bmatrix}, \tag{V.145}$$

and this system can be further condensed by eliminating the corner node displacements $\mathbf{q}_C$, using:

$$\mathbf{q}_C = \mathbf{K}^{*,-1}_{CC} \left(\mathbf{Q}^{*}_C + \mathbf{F}_{Cb} \boldsymbol{\lambda}_b \right), \tag{V.146}$$

that leads to the system:

$$\mathbf{F}^{*}_{bb} \boldsymbol{\lambda}_b = \mathbf{d}^{*}_b, \tag{V.147}$$

with:

$$\mathbf{F}^{*}_{bb} = \mathbf{F}_{bb} + \mathbf{F}_{bC} \mathbf{K}^{*,-1}_{CC} \mathbf{F}_{Cb}, \tag{V.148}$$

$$\mathbf{d}^{*}_b = \mathbf{d}_b - \mathbf{F}_{bC} \mathbf{K}^{*,-1}_{CC} \mathbf{Q}^{*}_C. \tag{V.149}$$

After solving for $\boldsymbol{\lambda}_b$ and $\mathbf{q}_C$ the displacements of the remaining *dofs* can be computed from (V.133).

The FETI-DP governing system can be solved either using a direct or an iterative method. If an iterative method is adopted, the *Preconditioned Conjugate Gradient* (PCG) method is once again a natural choice taking into consideration the characteristics of the operators. The authors Farhat *et al.* in reference [207] presented an efficient strategy to solve the FETI-DP algorithm using the PCG algorithm. Regarding the choice of preconditioners, the same authors advise adapting the well-known Dirichlet (V.118) and Lumped (V.119) preconditioners to the governing system to be solved [207], namely taking into consideration the *dof* restrictions.

At this point, it is interesting to notice that if all boundary nodes are considered corner nodes the system (V.145) leads exactly to the PS method (see section 2.6.2) and equation (V.85) can be recovered. On the other hand, if the corner nodes are absent, then the FETI-1 governing system (V.111) is obtained and solved by adding the terms associated with the contribution of the RBM, adding the solvability condition (V.110) and by using the pseudoinverse for floating subdomains.

This method has been also extended by Farhat and co-workers to modal analyses [208].

2.6.7 Other Domain Decomposition methods

In this section, some other significant Domain Decomposition methods will be briefly presented. The Balancing Domain Decomposition (BDD) presented in section 2.6.4 performs well only for second-order problems, such as two-dimensional and three-dimensional elasticity. To improve the performance of the method for fourth-order problems (*e.g.* plate bending), Le Tallec *et al.* [325] added corner node constraints to the coarse space. This was the beginning of the *Balancing Domain Decomposition with Constraints* (BDDC), which was introduced by Dohrmann and co-workers [169, 357] and by other authors [156, 224] with similar formulations. This method shares many similarities with the FETI-DP method, such as adding corner primal constraints to the algorithm that can avoid solving singular systems. Nevertheless, it has an important difference regarding the fact that only

primary variables (displacements) are used in the iterative solver [169]. In addition, due to the fact that the original and coarse problem of the BDDC method have the same form, the BDDC algorithm can be applied recursively using multilevel approaches, as presented in reference [359].

Nowadays, the BDDC and the FETI-DP methods are the most advanced algorithms of each family of DD methods. It should be emphasized that, although the mathematical formulations are not equivalent, it was proved that the eigenvalues of the BDDC and FETI-DP methods are very similar [66, 337, 358], which leads to similar convergence characteristics.

Finally, the *Large Time Increment* (LATIN) method should be mentioned. This method was first introduced by Ladevèze [318, 319] and can also be used for non-overlapping subdomains. It was designed for nonlinear structural analysis and uses a different approach from the methods presented previously. Instead of considering the structural response concentrated in the elements and using the boundaries between subdomains only for enforcing connectivity, the LATIN method considers that these interfaces also participate in the structural response. Accordingly, the interfaces have their own set of unknowns, namely the generalized stresses and the displacements, making this a mixed approach [191]. Moreover, a non-incremental two stage iterative computational strategy is applied over the entire time interval being studied to obtain the solution of the problem. Convergence has only been proved under limited conditions. Nevertheless, it has been observed in a wider set of cases. Further information about the LATIN method can be obtained in the bibliography [191, 192, 318-322, 413].

2.6.8 Applicability to incremental dynamic analyses.

One of the goals of this work is to perform analyses with dynamic loading, in particular, using incremental time integration algorithms and earthquake loading. Therefore, some comments regarding the applicability of the different DD methods to this type of analyses are presented in this section.

It was mentioned in section 2.6.5 that for IDA, the dynamic problem is most of the time solved in the format (V.123), where $\hat{\mathbf{K}}$ results from a weighted sum of the mass, damping and stiffness matrices (V.124), which can remove the null space from the coefficient matrices associated with floating domains. Consequently, the methods that require these null spaces will not be applicable to time-dependent problems. This is the case of the FETI-1 and FETI-2 methods. On the other hand, the FETI-T method was adapted specifically to handle this problem and is therefore applicable.

As presented in section 2.6.4, the BDD method can be seen as a two-level method using the matrix **C** to impose a redundant constraint. This redundancy makes the rigid body modes of the equivalent static problem (null space of the original stiffness matrix) useable for transient dynamic problems [225]. Furthermore, the matrices used in the FETI-DP and BDDC methods are non-singular if the primal constraints are chosen correctly. Consequently, these methods are also applicable for IDA.

Table V.2 presents a summary regarding the scope of application of each DD method considered in this thesis.

Table V.2: Summary of the applicability of the Domain Decomposition methods considered in this thesis.

Domain Decomposition Methods	2nd Order P.	4th Order P.	Dynamic A.
Primal			
Primal Substructuring (PS)	✓	✓	✓
Neumann-Neumann (NN)	✓	✓	✓
Balancing Domain Decomposition (BDD)	✓	×	×
Balancing Domain Decomposition with constraints (BDDC)	✓	✓	✓
Dual			
One-level Finite Element Tearing and Interconnecting (FETI-1)	✓	×	×
Two-level Finite Element Tearing and Interconnecting (FETI-2)	✓	✓	×
FETI with coarse problem for time-dependent probs. (FETI-T)	✓	×	✓
Dual-Primal			
Dual-Primal Finite Element Tearing and Interconnecting (FETI-DP)	✓	✓	✓

3 Hybrid discretization

One of the most significant drawbacks of using three-dimensional meshes to perform dynamic analyses is related to the high number of unknowns associated with this type of discretization. To mitigate this problem and improve the efficiency of the simulations, the possibility of using what is called within the scope of this thesis *Hybrid Discretizations* (HD) was studied. The term hybrid was chosen to indicate that the resulting mesh combines two different natures of discretizations. Accordingly, a refined mesh is used in the zones expected to be the most stressed, and consequently, to develop a significant nonlinear response. In contrast, the zones anticipated to remain elastic or with minor nonlinear effects are modelled with a simplified mesh (see Figure V.12-a). For reinforced concrete structures using framing systems, the typical choice for the simplified mesh are linear-geometry elements, such as Euler or Timoshenko beams. Furthermore, In this work solid elements (hexahedra) were used for the refined part of the mesh and these were combined with truss or beam elements for simulating the steel reinforcements and zero-thickness interface elements for modelling the imperfect bond between both materials (see Chapter III and IV).

In general, the hybrid discretization proposed in this work is expected to introduce the following advantages:

i. Reduce the number of degrees of freedom and therefore make the analysis more efficient and feasible, without a significant impact on the accuracy of the numeric simulation.
ii. Create a natural and efficient partition between the subdomains to be used in the substructured analysis. This topic will be discussed in more detail in section 4 that addresses the issues related to the implementation of the substructured analysis.

Using this methodology, the analyst must be able to predict where most of the nonlinear phenomena will occur. This was not considered a significant problem because of two reasons. At first, the zones with stress concentrations can be reasonably well predicted for RC structures, by knowing the characteristics and the intensity of the loads acting on the structure. Secondly, the mesh can always be readjusted and the analysis rerun if the structural behaviour is different from what was predicted.

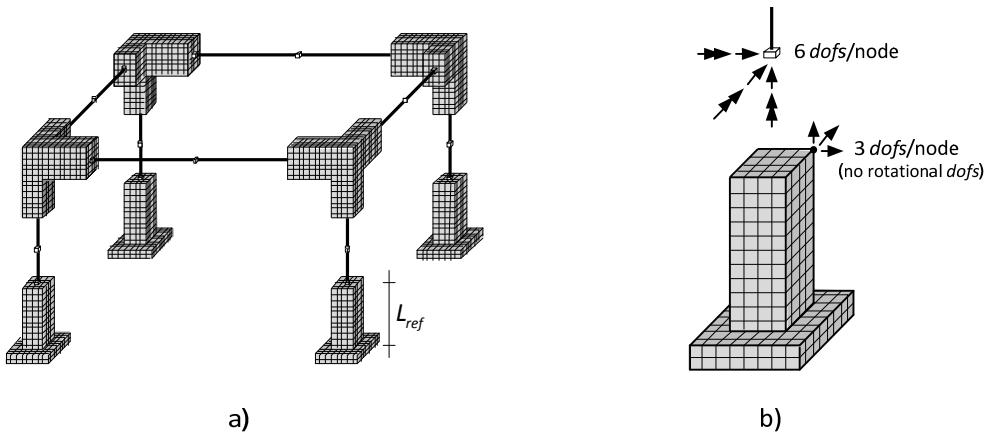

Figure V.12: Schematic representation of the hybrid discretization approach.

Figure V.12-a shows what would be a feasible hybrid discretization for the main structural elements of a common RC structure subjected to predominant horizontal loading. In this case, the refined mesh would be concentrated at the joints and at the extremities of the beams and columns. The interior spans of these members are supposed to develop, at most, only minor nonlinear effects, which is a reasonable hypothesis when subjected to earthquake loading. Intense permanent loads or earthquakes with intense vertical accelerations could change these assumptions. Normally, the first case would only result in stabilized cracking and stress redistribution that would have a minor impact on the global response of the structure. Moreover, considering that the permanent loading effects are present before the earthquake loading, their effect can be simulated by creating a segment of the beams (*e.g.* centred at mid-span) with reduced stiffness. Regarding the second case, it is always possible to use nonlinear beam elements or extend the refined mesh to the interior of the beam span.

In order to generate the mesh, it is necessary to estimate the size of the refined mesh segments. The basic parameter to be defined is the length of the refined mesh segments near the edges of the elements (L_{ref} in Figure V.12-a). This parameter is strongly related to the plastic hinge length (see Chapter III-§2.5.5). A first estimation for this parameter can be made assuming that it depends only on the cross-section dimensions:

$$L_{ref} = \lambda_h \max\left(w_{x2}, w_{x3}\right), \text{ with } \lambda_h = \left[2.0; 3.0\right], \tag{V.150}$$

where w_{x2} and w_{x3} represent the transversal widths in the local direction x_2 and x_3, respectively.

Regarding the connection between the beam and solid elements, the possibilities of using the linear kinematic constraints and transition elements presented in the state of the art were considered. The transition elements have some disadvantages when compared with the kinematic constraints, mainly because they introduce additional complexities to the model, related to the numerical behaviour of these elements. Moreover, the discretization would also present additional difficulties and the usage of transition elements increases the number of elements in the mesh. On the other hand, linear kinematic constraints present a predictable structural behaviour and represent a minor increase in

the complexity of the model. Furthermore, this approach does not increase the number of nodes or elements. Nevertheless, there will be an increase in unknowns if the constraints are enforced using Lagrange Multipliers. At the end, the choice tended clearly towards using kinematic constraints.

The kinematic constraints are used to impose the connection between beam and solid elements, which present 6 and 3 *dofs* per node for the general three-dimensional case, respectively (see Figure V.12-b). Within the scope of this thesis, this constraint is called *Beam2Solid* (B2C). This constraint consists of enforcing part of the equation of the *diaphragm* and *plate* constraints, already described in section 2.4. Only the equations associated with the translational *dofs* of the solid elements are enforced (see Figure V.13), hence reducing the number of constrained equations to one half.

Considering the case of the constraint axis located along the global direction X_1, the equations adopted by the *Beam2Solid constraint* are:

$$q_1^{SN} = q_1^{MN} + X_3\,\theta_2^{MN} - X_2\,\theta_3^{MN}, \tag{V.151}$$

$$q_2^{SN} = q_2^{MN} - X_3\,\theta_1^{MN}, \tag{V.152}$$

$$q_3^{SN} = q_3^{MN} + X_2\,\theta_1^{MN}, \tag{V.153}$$

where: $q_i^{SN}\left(q_i^{MN}\right)$ represents the displacement of the slave (master) node along the global coordinate X_i and $\theta_i^{SN}\left(\theta_i^{MN}\right)$ represents the rotation about the axis X_i of the slave (master) node. For other constraint axes, the equations can be defined using a direct cycle permutation of the direction indexes.

The *Beam2Solid* constraint will be implemented by the *Master-Slave Elimination* (MSE) method or using *Lagrange Multipliers* (LM), already discussed in section 2.4. Further details regarding the advantages and drawbacks of both methodologies in the scope of substructured structural analyses are presented in section 4.2.

The approach of using hybrid discretizations and *Beam2Solid* constraints to switch between different mesh types augments the possibilities regarding using different modelling strategies within a single simulation. To illustrate this, Figure V.14 presents a schematic representation of the mesh used to model a four storey building subjected to an earthquake loading. In this case, the lower storeys were

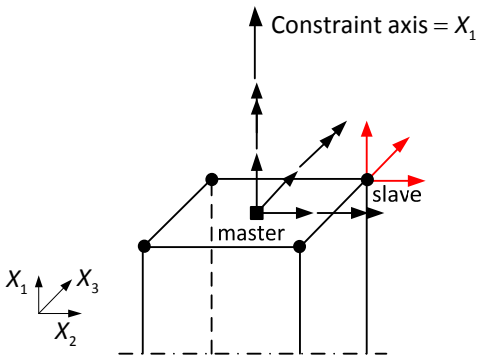

Figure V.13: Implementation of the *Beam2Solid* kinematic constraint for constraint axis X_1.

simulated using refined meshes and more complex constitutive models, because this is where most of the nonlinear phenomena are expected to occur. On the other hand, simplified meshes and models were adopted for the upper storeys, where the structure is expected to have a nearly elastic response.

Fibre models implemented in beam-column elements could be used for the simplified mesh when some nonlinear response may still be developed on the upper storeys. Otherwise, using linear constitutive relations would be the most adequate solution. Global response models with concentrated plasticity could also be considered. However, this formulation presents some disadvantages for three-dimensional models, in particular for columns subjected to bi-axial bending, due to the increased complexity for defining the force-displacement relations.

In conclusion, this approach makes it possible to adopt different modelling strategies. The basic concept is to use refined meshes and models where they are needed and to simplify the discretization elsewhere.

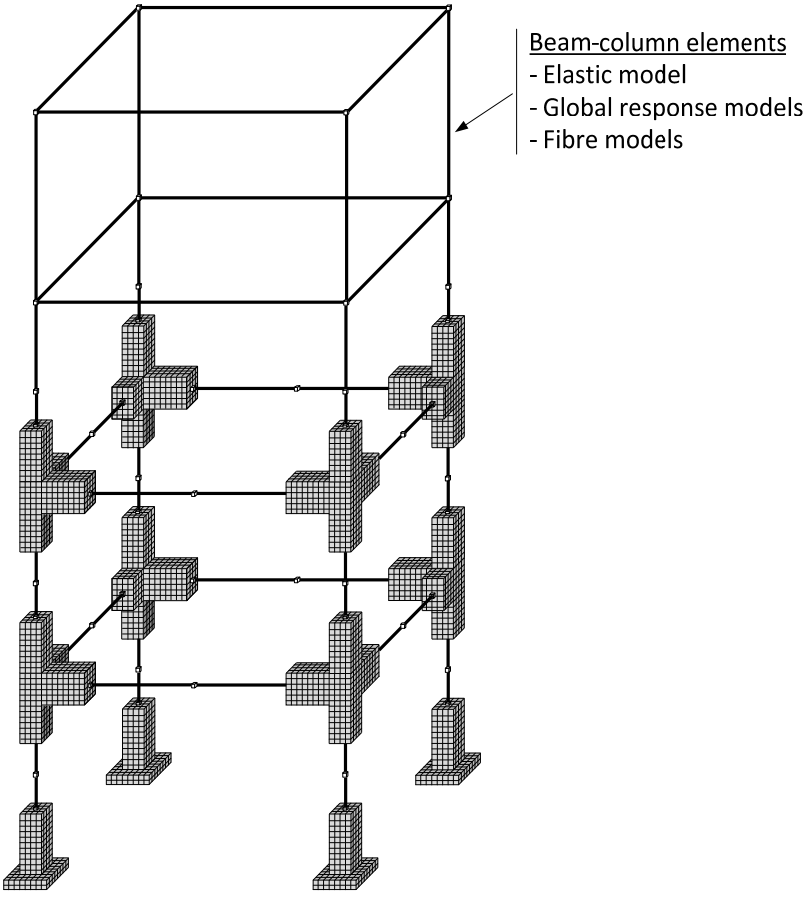

Figure V.14: Schematic representation of different possibilities arising from using hybrid discretizations and *Beam2Solid* constraints in the case of earthquake loading.

4 Implementation

4.1 Introduction

In what concerns the implementation in a computer-based algorithm, this chapter introduces three new key features that require particular attention: i) the parallelization of the computations; ii) the implementation of the domain decomposition methods to perform the structural analysis; and iii) the use of kinematic constraints to implement the hybrid discretizations.

After this introductory text, this section includes three subsections addressing in detail these three new features. Afterwards, a summarized description of the computing algorithms is presented, including the pre-processing, processing (modal and incremental analyses), and post-processing computing stages.

As mentioned before, the numerical models were implemented and tested in a program named "*ParaNoiD - Parallel Nonlinear Dynamic*", which was developed in *Matlab* [376] for the *Windows* OS. Figure V.15 presents a screen capture of the *Matlab* environment running the *ParaNoiD* code and the *graphical user interface* developed to assist the user in the different computation stages. This figure represents an analysis made with 24 subdomains. This can be observed in the number of *Matlab* processes reported by the *Task Manager* monitoring tool (see Figure V.15), namely, one process for the *Matlab* client session and 24 processes associated with the 24 subdomains.

Later on in this section, a summarized overview of the *Matlab* software is presented, in particular concerning the tools designed for parallel and distributed computing.

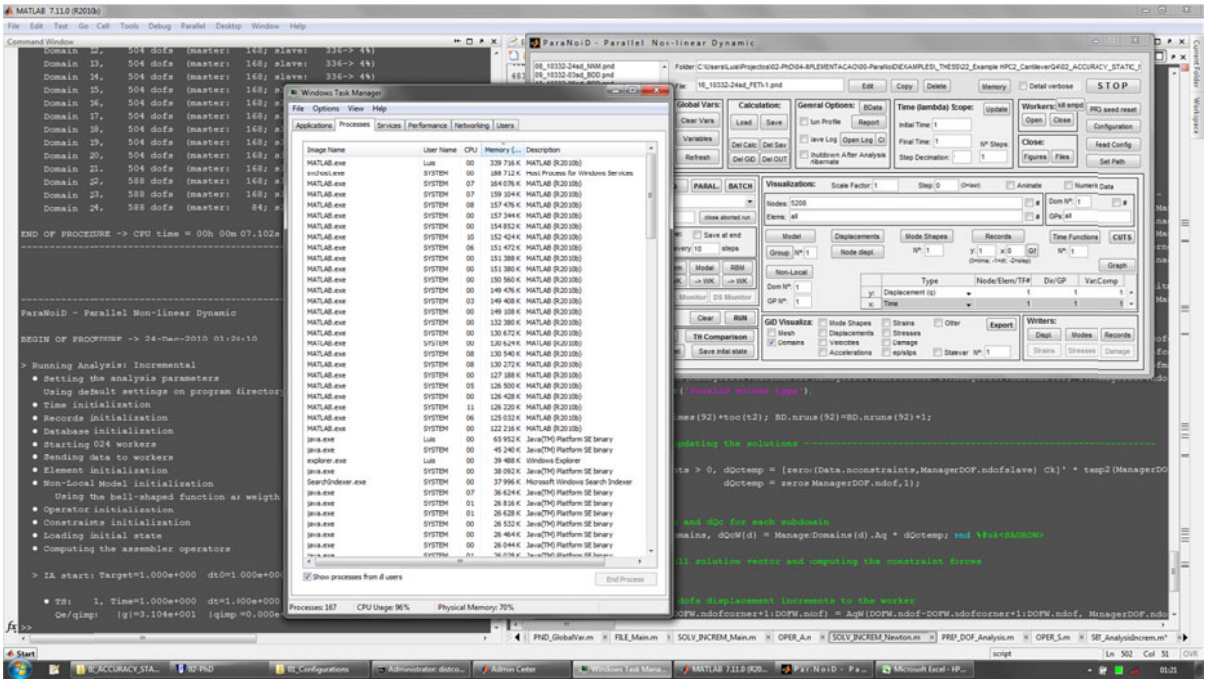

Figure V.15: ParaNoiD – *Matlab* developing environment and graphical user interface.

4.2 Parallelization

This subsection addresses the issues related to the implementation of the parallelized version of the code. The issues related to the implementation of the *substructured structural analysis* are presented in the following subsection.

A common finite element code can be divided into the *pre-processing*, *processing* and *post-processing* stages. The pre-processing stage mainly consists of reading the input data and preparing for the processing stage. This state was not parallelized although it presents some computations that are suitable to be parallelized and to achieve reasonable gains in performance using the *Data Parallelism* approach (*e.g.* element initialization and management of the subdomains and *dofs*). The processing stage includes the main computations of the analysis and the post-processing includes computing additional results and visualization. The computations of these two stages were parallelized, although most of the focus was drawn to the processing stage because it is the most time consuming step, in particular for IDA.

Nevertheless, a good performance using parallelized algorithms starts at the pre-processing stage by making an adequate load distribution, by taking into consideration the hardware characteristics of the computer. It is extremely important to minimize load unbalance by distributing as uniformly as possible the computing demand over the available *processing units* (PU). The ideal situation is to associate each subdomain with a dedicated PU and to distribute the number of *dofs* uniformly. On the other hand, the nonlinear phenomena may occur heterogeneously throughout the subdomains and lead to load unbalance (*e.g.* the lower storeys of the structure presented in Figure V.14 are likely to be more stressed than the upper floors). This problem could be mitigated by implementing a dynamic load balancing procedure. This technique often works by migrating elements from the most loaded subdomains to the neighbouring ones. This procedure can be very effective for the analysis of continuous domains but it would be extremely difficult to implement with the hybrid discretization proposed in this thesis, because the subdomain boundaries present an inflexible location.

Data transfer is another significant source of overhead, with increased importance for distributed systems, where the data transfer occurs through the network, although for local systems, the memory buses can also be overloaded for data demanding operations or if accessed by several PUs. To mitigate this problem the code should be written in order to avoid sending and receiving large amounts of data.

Figure V.16 and Figure V.17 illustrate some of the possible architectures used for parallelized computations. These figures were drawn under the hypothesis that eight PUs, distributed by four CPUs, are available for the subdomain computations. An additional *master processing unit* (MPU) is also considered, although this work could be done by any of the previous PUs, because most of the calculations done by this unit are interdependent on the subdomain computations, and therefore cannot be executed simultaneously. The master PU receives the information from all subdomains and solves the reduced problem. Afterwards, the trial solution is send to the subdomains to execute the element state determination and compute the global unbalanced forces that are once again combined at the master PU.

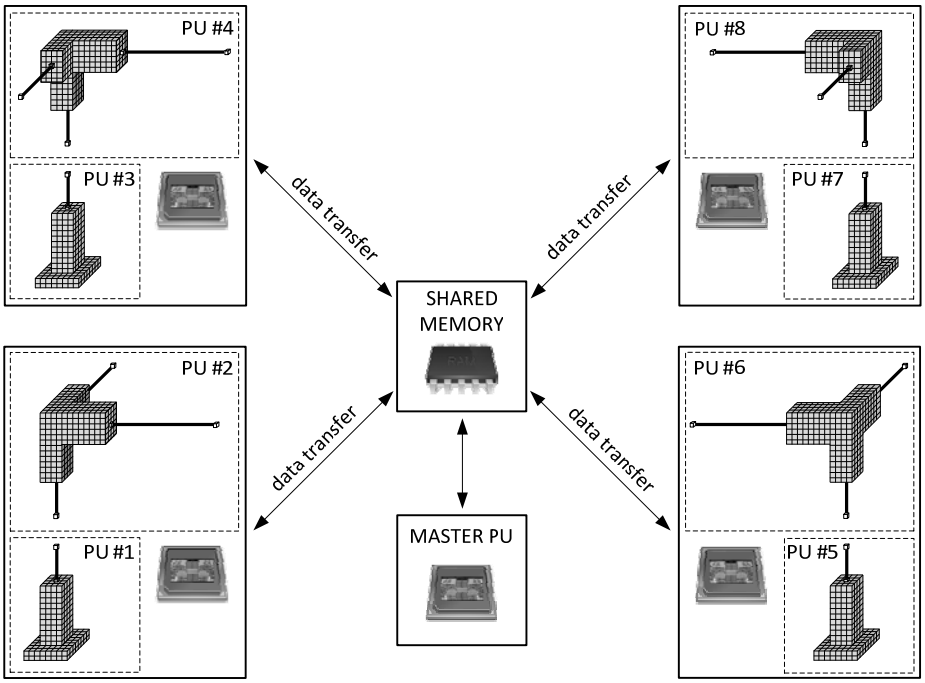

Figure V.16: Parallelization in a shared memory system.

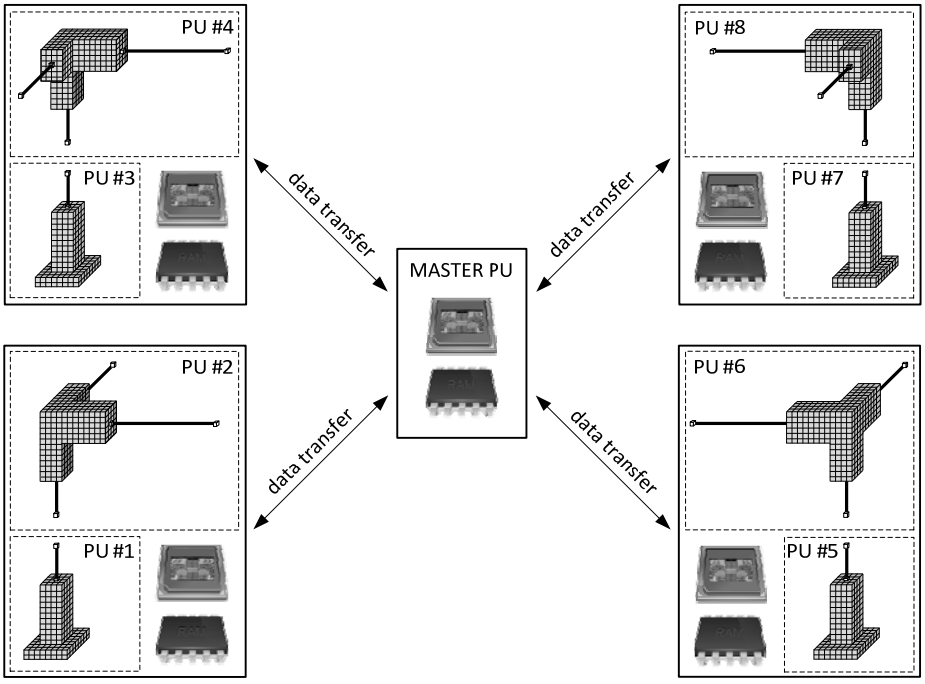

Figure V.17: Parallelization in a distributed or local memory system.

Figure V.16 represents what could be a single computer implementation (*e.g.* workstation), with each subdomain associated with a single PU. In this case, the memory is centralized and shared by all processes. This could allow an efficient data transfer rate, although the memory bus capacity can be easily exhausted by the data requirements of several PUs and create a significant bottleneck. On the other hand, Figure V.17 represents a typical multi-node computer (*e.g.* cluster). As before, each subdomain is associated with a single PU, however in this case each node has its own local memory system, thus avoiding accessing the centralized memory for subdomain-based computations. This architecture reduces the problem of exceeding the memory bus capacity. However the data transfer to the master PU is often made in network-based communication, which is much slower.

The main computing steps of the processing phase of a conventional FE code are: i) the element state determination; ii) the assembly of the structural operators; iii) the solution of the governing system, and iv) the global equilibrium evaluation. All these computations are made with the domain partitioned into several subdomains and can benefit from the inherent data parallelism that arises from the independency of most computations.

The remaining part of this section will present some of the tools available in *Matlab* to implement the parallelized version of the FE code.

- *Matlab* tools for non-sequential computing

The *Matlab* software [376] is an advanced high-level developing language that is interpreted during runtime to achieve better platform independence, programming flexibility and interactive debugging. These features result in an increased overhead and leads to a slower computational performance when compared to compiled languages, such as *C* and *Fortran*. Nevertheless, most core functions (*e.g.* basic linear algebra operations) are run with pre-compiled high performance routines, and therefore, their performance is comparable to compiled programming languages.

Multithreaded computations were implemented for basic linear algebra functions since the release of *Matlab* 7.4 (R2007a). When available, the software automatically takes advantage of several processing units to enhance the computing performance. This behaviour can be easily observed by monitoring the activity of the available processing units. Nowadays, this feature is implemented in a wide set of basic parallelizable functions such as matrix multiplication, matrix factorization and analysis, solution of linear systems, *etc*. (see *Matlab* documentation for more details). In the latter *Matlab* versions (*e.g.* version 7.11-R2010b), the multithread computations can be switch off by starting the application at command-line with the argument " `-singleCompThread`".

At this point, it is important to make a clear distinction between *processes* and *threads*. The first source of difference is hierarchy-related, because a process can consist of multiple threads and threads can be associated with a common process. Furthermore, different processes have different memory address spaces resulting in independent and secure computing. On the other hand, threads share the same address space of the hosting process, leading to unsecure computing, since a thread can modify the memory used by another thread, which may cause memory corruption problems. *Inter-thread communication* is relatively inexpensive as a result of sharing the same address space.

Conversely*, inter-process communication* is much more expensive because data cannot be shared directly.

During the second half of the last decade, the *Matlab* developers made a large effort to extent the *Matlab* language with tools and functions for parallel and distributed computing. This resulted in the *Parallel Computing Toolbox* [378] and in the *Distributed Computing Server* [377], which are designed for local and remote computations, respectively. These toolboxes offer a set of high level functions for non-sequential computations [378] (*e.g.* parallel for-loops, special array types, and parallelized numerical algorithms) that are implemented in *Matlab* sessions called *workers*, which can be defined as *Matlab* computational engines that run separately from the interactive *Matlab* session, *a.k.a. Matlab client session*. This approach uses process-based computations rather than the threaded-based approach described before. Each worker is then associated with an independent process, with its own memory allocated from the resources of the machine where the process is running.

The *Parallel Computing Toolbox* is designed to potentiate the available performance in multicore processors by implementing as many as eight *local workers* on the local machine. Alternatively, the *Distributed Computing Server* implements as many remote workers as licensing permits and therefore makes scaling possible using the resources from other computers. One advantage of using these toolboxes is that the same code can be used for local and for remote workers. Furthermore, using local machine computations simplifies the development process, although a performance difference can exist when switching to remote workers, resulting from the overhead associated with network-based data transfers.

In the framework of these toolboxes, a *job* is created for parallel or distributed computations. *Matlab* uses a *scheduler*, *a.k.a.* a *job manager*, for deploying and managing the execution of the jobs. For local computations a default and simplified scheduler is used. Figure V.18 presents the basic configuration for parallel computing used by *Matlab*.

As mentioned before, the *Parallel Computing Toolbox* and the *Distributed Computing Server* toolboxes offer a collection of functions and programming tools for parallelized computations. Among those, the programming language offers the so-called *single program multiple data* (*spmd*) blocks. These *spmd* statements make it possible to define a set of code statements that will be run

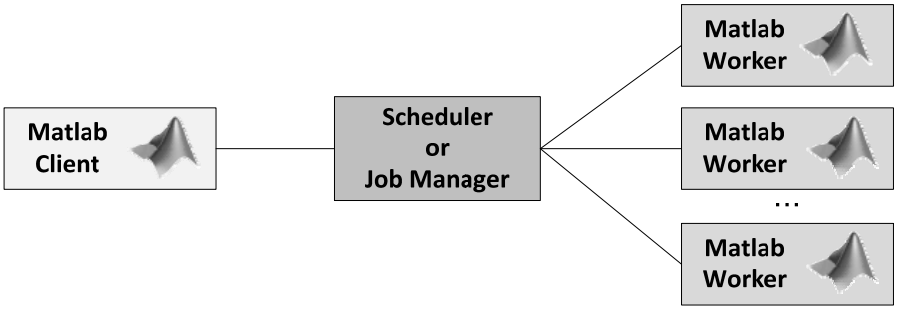

Figure V.18: Basic parallel computing configuration used by *Matlab*, adapted from [378].

simultaneously in each worker. Although different lines of code can be ran in different workers by using the *labindex* property, all workers receive the same set of code statements to process.

As a result of each worker having its own memory space, the *spmd* instructions will be executed on different data sets associated with each worker. The *spmd* blocks can be seen as an implementation of the *Geometric* or *Data Parallelism* (see section 2.1.8). Regarding the instruction and data stream architecture, it is similar to the *Single Instruction - Multiple Data streams* of Flynn's taxonomy (see section 2.1.7).

The *Matlab* client session is an ideal place to run the reduced problem of most domain decomposition methods, because it has direct and simplified access to the data stored in the workers. As mentioned before, situations where data parallelism can be exploited are frequent in FE codes. This is the case of computing the element state determination and assembling the subdomain contributions to the reduced problem. On the other part of the spectrum, would be the algorithm parallelization with built-in functions that have embedded parallelization schemes (*e.g. parfor* loops and *Scalapack* linear solvers) [503].

Algorithm V.3 presents a parallel code example written in the *Matlab* language that includes a *spmd* block to compute the subdomain contribution to the unbalanced forces vector and a computation executed at the *Matlab* client session for joining the contributions of all subdomains.

Algorithm V.3: Basic parallel code in *Matlab*.

```
matlabpool('open',nworkers);
...
%Computing the subdomain unbalanced forces (executed in the workers)
spmd
  gW =  + (1+alpha) * (QiW  -  QeW  + CW * vW  + QcW ) ...
        -    alpha  * (QijW -  QejW + CW * vjW + QcjW)  +  MW * aW;
end

%Computing the global unbalanced forces (executed in the client session)
g = zeros(ndofs,1);
for sd=1:nsd,
  g = g + Subdomains(sd).Aq' * gW{sd};
end
...
matlabpool close;
```

4.3 Substructuring

This subsection addresses the issues related to the implementation of the *Domain Decomposition* (DD) methods adopted in this work for structural analysis.

The previous section focused on parallelizing roughly the same computations that would be executed in the sequential version of the code. Conversely, in this section the computations to be executed are associated with the formulation of each *Domain Decomposition* method and may change significantly. All the DD methods whose formulation is presented in section 2.6 were implemented in the *ParaNoiD* software. Consequently, it was possible to test and compare the accuracy and the performance of these methods.

During this work, it was necessary to choose the most suitable DD method for the goals formulated and optimize the implementation. It is vital that the method is applicable to time-dependent problems, in particular to IDA. The three methods considered were the Primal Substructuring (PS) method, Balancing Domain Decomposition with constraints (BDDC) and Dual-Primal Finite Element Tearing and Interconnecting (FETI-DP). The last two methods become competitive when the number of unknowns is extremely large (millions of *dofs*), but require the use of a high performance computer (*e.g.* cluster) and an optimized implementation (*e.g.* using a compiled code language), which lies outside the scope for this thesis. The algorithms of the BDDC and FETI-DP methods are also more complex and less robust than the PS method associated with a direct solver. This last method presents the advantage of being applicable to static, modal and incremental dynamic analyses and for different types of structural elements (plates, solids, beams, shells, *etc.*). Consequently, the PS method was chosen as the main DD method and the implementation of this method was optimized for performance. Special attention will be drawn to this method in the rest of the chapter.

In the following part of this section, the most important steps in the implementation of each DD method are presented, separating the computations that are performed at the *master processing unit* (MPU) and the ones that are performed in parallel, at the *subdomain processing units* (SPUs) or *workers*.

- Primal Substructuring (PS) method

The PS method starts by computing the subdomain contributions to the global Schur Complements. This computation is executed in parallel at the SPUs, using (V.83):

$$\mathcal{S}^{sd} = \mathbf{K}_{bb}^{sd} - \mathbf{K}_{bi}^{sd}\,\mathbf{K}_{ii}^{sd,-1}\,\mathbf{K}_{ib}^{sd} .$$

The *rhs* vector associated with the reduced problem is similar to equation (V.84). However, in this case the external force vector is replaced by the unbalanced force vector, to adapt the formulation to non-linear incremental analyses:

$$\mathcal{Q}^{sd} = -\mathbf{g}_{b}^{sd} + \mathbf{K}_{bi}^{sd}\,\mathbf{K}_{ii}^{sd,-1}\,\mathbf{g}_{i}^{sd} . \qquad \text{(V.154)}$$

Afterwards the reduced problem is assembled at the MPU, using (V.81) and (V.82):

$$\mathcal{S} = \sum_{sd=1}^{nsd} \mathcal{A}_{bB}^{sd,t}\;\mathcal{S}^{sd}\;\mathcal{A}_{bB}^{sd} ,$$

$$\mathcal{Q} = \sum_{sd=1}^{nsd} \mathcal{A}_{bB}^{sd,t} \; \mathcal{Q}^{sd} \,,$$

and the governing system (V.85):

$$\mathcal{S}\, \delta \mathbf{q}_B = \mathcal{Q} \,,$$

is solved for the global boundary *dof* increments using a direct solver.

The last steps consist of sending the relevant boundary *dof* displacements increments to the SPUs and computing the internal unknowns, also at the SPUs. This is done using equations (V.87) and (V.86), respectively:

$$\delta \mathbf{q}_b^{sd} = \mathcal{A}_{bB}^{sd} \, \delta \mathbf{q}_B^{sd} \,,$$

$$\delta \mathbf{q}_i^{sd} = \mathbf{K}_{ii}^{sd,-1} \left(-\mathbf{g}_{,i}^{sd} - \mathbf{K}_{ib}^{sd} \, \delta \mathbf{q}_{ib}^{sd} \right). \tag{V.155}$$

Finally, it is necessary to update the displacement field:

$$\mathbf{q}^{sd} = \mathbf{q}^{sd} + \begin{bmatrix} \delta \mathbf{q}_i^{sd} \\ \delta \mathbf{q}_b^{sd} \end{bmatrix}. \tag{V.156}$$

- Neumann-Neumann (NN) method

The NN method also includes computing the subdomain Schur complements and *rhs* vectors, and additionally, the *Neumann-Neumann preconditioner*, using (V.88):

$$\mathbf{M}_{NN}^{-1} = \sum_{sd=1}^{nsd} \mathcal{A}_{bB}^{sd,t} \, \mathcal{S}^{sd,-1} \, \mathcal{A}_{bB}^{sd} \,.$$

This operation requires the computation of the Schur complement pseudoinverse for floating subdomains, which can be parallelized for all subdomains at the SPUs.

The same governing system of the PS method must be solved (V.85), but in this case the preconditioned conjugate gradient (PCG) method is used most of the time. Even if this last computation is performed at the MPU, the use of an iterative solver avoids the assembly of the Schur complement and of the preconditioned matrices, as presented in section 2.6.3. Only the resulting subdomain vector from the matrix-by-vector multiplications $\mathcal{S}\,\mathbf{p}$, $\mathbf{M}_{NN}^{-1}\,\mathbf{r}$ must be transferred to the MPU, which represents a significant computational advantage for large problem sizes.

- Balancing Domain Decomposition (BDD) method

The BDD method includes the main steps of the NN method, but in this case a coarse problem is introduced by an enhanced preconditioner, used to distribute the unbalanced forces throughout the subdomains (V.96):

$$\mathbf{M}_{BDD}^{-1} = \mathbf{P}\, \mathbf{M}_{NN}^{-1} \, \mathbf{P} + \mathbf{G} \left(\mathbf{G}^t \mathcal{S}\, \mathbf{G} \right)^{-1} \mathbf{G} \,.$$

In this case, the preconditioner includes computing not only the pseudoinverse of floating subdomain Schur complements, but also the null space in order to assemble the matrix $\mathbf{G}$. All these computations can be performed in parallel at the SPUs.

- One-level Finite Element Tearing and Interconnecting (FETI-1) method

The FETI-1 method also includes computing the pseudoinverse and the null space for floating subdomains at the SPUs. However, in this case the subdomains stiffness matrices are used instead of the Schur complements. This can introduce an important computation overhead because it requires computing a *singular value decomposition* (SVD), which may require a very large number of operations and memory space. This issue will be discussed in detail in the example HPC2, presented in section 5.2.

The dual governing system results from the contribution of the subdomains that can be computed in parallel at the SPUs, using:

$$\mathbf{F}^{sd} = \boldsymbol{\mathcal{B}}^{sd}\, \mathbf{K}^{sd,+}\, \boldsymbol{\mathcal{B}}^{sd,t}, \tag{V.157}$$

$$\mathbf{G}^{sd} = \boldsymbol{\mathcal{B}}^{sd}\, \mathbf{R}^{sd}, \tag{V.158}$$

$$\mathbf{d}^{sd} = -\boldsymbol{\mathcal{B}}^{sd}\, \mathbf{K}^{sd,+}\, \mathbf{g}^{sd}, \tag{V.159}$$

$$\mathbf{e}^{sd} = -\mathbf{R}^{sd,t}\, \mathbf{g}^{sd}. \tag{V.160}$$

Afterwards, the subdomain contributions are assembled at the MPU, using:

$$\mathbf{F} = \sum_{sd=1}^{nsd} \mathbf{F}^{sd}, \quad \mathbf{G} = \left[\, \mathbf{G}^{1}, ..., \mathbf{G}^{nsd} \,\right], \quad \mathbf{d} = \sum_{sd=1}^{nsd} \mathbf{d}^{sd}, \quad \mathbf{e} = \left[\, \mathbf{e}^{1}, ..., \mathbf{e}^{nsd} \,\right]. \tag{V.161}$$

The governing system is often solved for the Lagrange multipliers using the modified PCG method described in Algorithm V.2, with *Dirichlet* (V.118) or *Lumped* (V.119) preconditioners:

$$\mathbf{M}_{D}^{-1} = \sum_{sd=1}^{nsd} \boldsymbol{\mathcal{B}}^{sd}\, \boldsymbol{\mathcal{A}}_{bB}^{sd,t}\, \boldsymbol{\mathcal{S}}^{sd}\, \boldsymbol{\mathcal{A}}_{bB}^{sd}\, \boldsymbol{\mathcal{B}}^{sd,t}, \quad \mathbf{M}_{L}^{-1} = \sum_{sd=1}^{nsd} \boldsymbol{\mathcal{B}}^{sd} \boldsymbol{\mathcal{A}}_{bB}^{sd,t}\, \mathbf{K}_{bb}^{sd}\, \boldsymbol{\mathcal{A}}_{bB}^{sd}\, \boldsymbol{\mathcal{B}}^{sd,t},$$

which can also benefit from parallelization as in the previous methods. The modified PCG requires computing the projection matrix for the coarse problem, using (V.117):

$$\mathbf{P} = \mathbf{I} - \mathbf{G}\left(\mathbf{G}^{t}\, \mathbf{G}\right)^{-1} \mathbf{G}^{t}.$$

Once again, it should be emphasized that using this approach does not require computing the global matrix $\mathbf{F}$. Only matrix-by-vector multiplications $\left(\mathbf{F}\mathbf{p}\right)$ are required for the modified PCG method.

Special attention must be drawn to the initialization of the Lagrange multipliers at the MPU, which can be performed using equation (V.116):

$$\boldsymbol{\lambda} = \mathbf{G}\left(\mathbf{G}^{t}\mathbf{G}\right)^{-1} \mathbf{e}.$$

Afterwards, the vector $\boldsymbol{\alpha}$ associated with the *rigid body modes* can be computed at the MPU, using expression (V.120):

$$\boldsymbol{\alpha} = \left(\mathbf{G}^{t}\mathbf{G}\right)^{-1} \left\{\mathbf{G}^{t}\left(\mathbf{F}\boldsymbol{\lambda} - \mathbf{d}\right)\right\}.$$

The subdomain displacements can be computed in parallel at the SPUs, for the case of floating subdomains using:

$$\delta\mathbf{q}^{sd} = \mathbf{K}^{sd,+}\left(-\mathbf{g}^{sd} - \boldsymbol{\mathcal{B}}^{sd,t}\, \boldsymbol{\lambda}\right) + \mathbf{R}^{sd}\boldsymbol{\alpha}. \tag{V.162}$$

- Dual-Primal Finite Element Tearing and Interconnecting (FETI-DP) method

The FETI-DP algorithm starts by computing in parallel the subdomain contributions to the reduced problem, using:

$$\mathbf{F}_{bb}^{sd} = \mathcal{B}_{br}^{sd}\, \mathbf{K}_{rr}^{sd,-1}\, \mathcal{B}_{br}^{sd,t}\,, \tag{V.163}$$

$$\mathbf{F}_{bC}^{sd} = \mathcal{B}_{br}^{sd}\, \mathbf{K}_{rr}^{sd,-1}\, \mathbf{K}_{rc}^{sd}\, \mathcal{A}_{cC}^{sd}\,, \tag{V.164}$$

$$\mathbf{F}_{Cb}^{sd} = \mathcal{A}_{cC}^{sd,t}\, \mathbf{K}_{cr}^{sd}\, \mathbf{K}_{rr}^{sd,-1} \mathcal{B}_{br}^{sd,t}\,, \tag{V.165}$$

$$\mathbf{K}_{CC}^{*,sd} = \mathcal{A}_{cC}^{sd,t}\, \mathbf{K}_{cc}^{sd}\, \mathcal{A}_{cC}^{sd} - \mathcal{A}_{cC}^{sd,t}\, \mathbf{K}_{rc}^{sd,t}\, \mathbf{K}_{rr}^{sd,-1}\, \mathbf{K}_{rc}^{sd}\, \mathcal{A}_{cC}^{sd}\,, \tag{V.166}$$

and:

$$\mathbf{d}_{b}^{sd} = -\mathcal{B}_{br}^{sd}\, \mathbf{K}_{rr}^{sd,-1}\, \mathbf{g}_{r}^{sd}\,, \tag{V.167}$$

$$\mathbf{Q}_{C}^{*,sd} = -\mathcal{A}_{cC}^{sd,t}\, \mathbf{g}_{c}^{sd} + \mathcal{A}_{cC}^{sd,t}\, \mathbf{K}_{rc}^{sd,t}\, \mathbf{K}_{rr}^{sd,-1} \mathbf{g}_{r}^{sd}\,. \tag{V.168}$$

Afterwards, the subdomain contributions are joined together at the MPU, using:

$$\mathbf{F}_{bb} = \sum_{sd=1}^{nsd} \mathbf{F}_{bb}^{sd}\,,\quad \mathbf{F}_{bC} = \sum_{sd=1}^{nsd} \mathbf{F}_{bC}^{sd}\,,\quad \mathbf{F}_{Cb} = \sum_{sd=1}^{nsd} \mathbf{F}_{Cb}^{sd}\,,\quad \mathbf{K}_{CC}^{*} = \sum_{sd=1}^{nsd} \mathbf{K}_{CC}^{*,sd}\,,\quad \mathbf{d}_{b} = \sum_{sd=1}^{nsd} \mathbf{d}_{b}^{sd}\,,\quad \mathbf{Q}_{C}^{*} = \sum_{sd=1}^{nsd} \mathbf{Q}_{C}^{*,sd}\,. \tag{V.169}$$

The governing system (V.147):

$$\mathbf{F}_{bb}^{*}\, \boldsymbol{\lambda}_{b} = \mathbf{d}_{b}^{*}\,, \tag{V.170}$$

is solved at the MPU using the PCG method with the *Dirichlet* (V.118) or the *Lumped* (V.119) preconditioners, adapted to the FETI-DP *dof* split.

Subsequently, the corner *dof* displacement increments can be recovered at the MPU, using (V.146):

$$\delta\mathbf{q}_{C} = \mathbf{K}_{CC}^{*,-1} \left(\mathbf{Q}_{C}^{*} + \mathbf{F}_{Cb}\, \boldsymbol{\lambda}_{b} \right). \tag{V.171}$$

The final steps consist of sending the corner *dof* displacement increments to the SPUs, using:

$$\delta\mathbf{q}_{c}^{sd} = \mathcal{A}_{cC}^{sd}\, \delta\mathbf{q}_{C}\,, \tag{V.172}$$

and computing the remaining *dof* displacement increments:

$$\delta\mathbf{q}_{r}^{sd} = \mathbf{K}_{rr}^{sd,-1} \left(-\mathbf{g}_{r}^{sd} - \mathbf{K}_{rc}^{sd}\, \delta\mathbf{q}_{c}^{sd} - \mathcal{B}_{br}^{sd,t}\, \boldsymbol{\lambda}_{b} \right), \tag{V.173}$$

and finally, the trial displacements are updated by computing:

$$\mathbf{q}^{sd} = \mathbf{q}^{sd} + \begin{bmatrix} \delta\mathbf{q}_{r}^{sd} \\ \delta\mathbf{q}_{c}^{sd} \end{bmatrix}. \tag{V.174}$$

4.4 Kinematic constraints

Within the framework of this thesis, *kinematic constraints* (KC) were used for three different purposes: i) for imposing displacements (*e.g.* base displacement to simulate earthquakes); ii) for implementing the *Hybrid Discretization* (HD) technique; and iii) for enforcing a specific structural behaviour (*e.g.* rigid floor diaphragms).

The *Lagrange Multipliers* (LM) and the *Master-Slave Elimination* (MSE) method were used for enforcing the kinematic constraints in the simulations. These methods were used in different situations and presented different advantages and consequences for the numerical model. The *Lagrange Multipliers* method was used for imposing displacements and for enforcing constraints that are defined within the scope of more than one subdomain, *e.g.* rigid floor diaphragms. This method was implemented in the reduced problem and resulted in an augmented governing system with a new set of unknowns, the *Lagrange Multipliers*. Within the scope of this thesis, this technique will be referred to as *global kinematic constraints* (GKC).

Alternatively, the *Master-Slave Elimination* (MSE) method was used when no interaction with the other subdomains is necessary. This corresponds to the general case of enforcing the *Hybrid Discretization* technique. This methodology reduces the number of unknowns in the governing system by associating the *dofs* to be condensed with the ones retained in the model using a mathematical relation. To avoid being confused with the *dofs* split used in the D*omain Decomposition* method, from this point on the condensed (retained) *dofs* will be referred to as slave (master) and this enforcing technique will be called *local kinematic constraints* (LKC).

Figure V.19 presents an example of a possible distribution of *global kinematic constraints* enforced with Lagrange Multipliers (GKC-LM) and *local kinematic constraints* enforced by the Master-slave Elimination method (LKC-MSE). In this example, the former is used to impose absolute displacements at the base of the structure (*e.g.* earthquake loading) and to impose a rigid diaphragm constraint to simulate the rigid slab. In addition, LKC are used to enforce the *Beam2Solid* constraints used to implement the Hybrid Discretization technique.

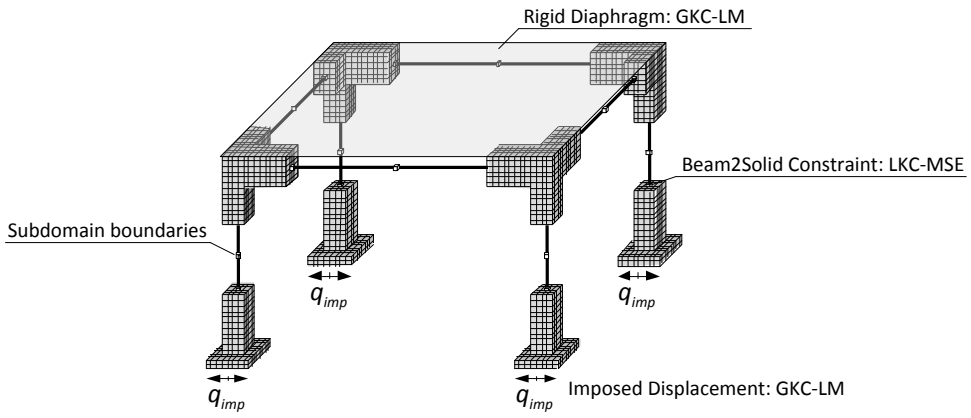

Figure V.19: Schematic representation of the use of different methods to enforce kinematic constraints.

- Local Kinematic Constraints

The following *dof* ordering is proposed for each subdomain:

$$\mathbf{q}^{sd} = \begin{bmatrix} \mathbf{q}_m^{sd} \\ \mathbf{q}_s^{sd} \\ \mathbf{q}_b^{sd} \end{bmatrix}, \tag{V.175}$$

where the subscripts *m* and *s* refer to master (retained) and slave (condensed) internal subdomain *dofs* and *b* refers to the subdomain boundary *dofs.*

Consequently, equation (V.49) should be rewritten as:

$$\begin{bmatrix} \mathbf{q}_m^{sd} \\ \mathbf{q}_s^{sd} \\ \mathbf{q}_b^{sd} \end{bmatrix} = \mathbf{T}_{LK}^{sd} \begin{bmatrix} \mathbf{q}_m^{sd} \\ \mathbf{q}_b^{sd} \end{bmatrix} + \begin{bmatrix} \mathbf{0} \\ \mathbf{d}_{LK,s}^{sd} \\ \mathbf{0} \end{bmatrix}, \tag{V.176}$$

where the new *kinematic transformation matrix* (V.50) is defined as:

$$\mathbf{T}_{LK}^{sd} = \begin{bmatrix} \mathbf{I}_{mm}^{sd} & \mathbf{0} \\ \mathcal{C}_{LK,sm}^{sd} & \mathcal{C}_{LK,sb}^{sd} \\ \mathbf{0} & \mathbf{I}_{bb}^{sd} \end{bmatrix}, \tag{V.177}$$

in which the subscript *LK* identifies *local kinematic constraints* and $\mathcal{C}_{LK,sm}^{sd}$ and $\mathcal{C}_{LK,sb}^{sd}$ are the extension to the subdomain scope and to the proposed *dof* reordering of the matrix $\mathcal{C}_{K,sm}$ defined in (V.47). The submatrices $\mathbf{I}_{mm}^{sd}$ and $\mathbf{I}_{bb}^{sd}$ are identity matrices of size equal to the number of master and boundary subdomain *dofs*, respectively. The remaining entries are zero matrices defined with consistent sizes.

The usage that will be given to the local constraints implies that $\mathbf{d}_{LK,sc}^{sd} = \mathbf{0}$, so that the last term in equation (V.176) becomes irrelevant and will be omitted from now on. It should be emphasized that the subdomain matrices $\mathbf{T}_{LK}^{sd}$ are highly sparse and very prone to be stored in matrix sparse format.

Under these assumptions, the subdomain structural operators become defined by:

$$\mathbf{K}^{C,sd} = \mathbf{T}_{LK}^{sd,t}\, \mathbf{K}^{sd}\, \mathbf{T}_{LK}^{sd}, \tag{V.178}$$

$$\mathbf{C}^{C,sd} = \mathbf{T}_{LK}^{sd,t}\, \mathbf{C}^{sd}\, \mathbf{T}_{LK}^{sd}, \tag{V.179}$$

$$\mathbf{M}^{C,sd} = \mathbf{T}_{LK}^{sd,t}\, \mathbf{M}^{sd}\, \mathbf{T}_{LK}^{sd}, \tag{V.180}$$

and the dynamic effective stiffness associated with the α-Method (II.197) is given by:

$$\hat{\mathbf{K}}^{C,sd} = (1+\alpha)\left(\mathbf{K}^{C,sd} + \frac{\gamma}{\beta\Delta t}\mathbf{C}^{C,sd}\right) + \frac{1}{\beta\Delta t^2}\mathbf{M}^{C,sd}. \tag{V.181}$$

After computing the subdomain boundary *dof* displacements in substructured analyses, the rest of the unknowns can be computed using equation (V.176).

The application of *local kinematic constraints* for modal analyses is straightforward, considering the definitions presented in equations (V.178) and (V.180).

- Global Kinematic Constraints

As mentioned before, the *global kinematic constraints* were imposed using the *Lagrange Multipliers* method. Using this approach, the incremental reduced problem used for *substructured structural analysis* (V.85) becomes augmented with the GKC operators:

$$\begin{bmatrix} \hat{\mathcal{S}} & \mathcal{C}_{GK}^{t} \\ \mathcal{C}_{GK} & \mathbf{0} \end{bmatrix} \begin{bmatrix} \delta \mathbf{q}_{B} \\ \boldsymbol{\lambda} \end{bmatrix} = \begin{bmatrix} -\hat{\mathcal{Q}} \\ \delta \mathbf{d}_{GK} \end{bmatrix}. \tag{V.182}$$

The matrix $\mathcal{C}_{GK}$ is the global constraint matrix of size $ngc \times ndof_{M}$, where *ngc* represents the number of global kinematic constraints and $ndof_{B}$ represents the number of boundary *dofs* in the global reduced problem. In addition, $\boldsymbol{\lambda}$ is a vector of size $ngc \times 1$ that holds the Lagrange Multipliers.

In this case, the rhs vector $\mathbf{d}_{GK}$ cannot be eliminated as before, because this vector will be used to enforce absolute values on the unknowns (*e.g.* imposed displacements) and can also be used to enforce relative displacements between *dofs* (*e.g.* opening/closure of discrete cracks).

The operators $\hat{\mathcal{S}}$ and $\hat{\mathcal{Q}}$ are the dynamic versions of the *Schur Complement* and *rhs* vector, respectively. Using *local kinematic constraints*, these operators must be redefined as follows:

$$\hat{\mathcal{S}}^{C,sd} = \hat{\mathbf{K}}_{bb}^{C,sd} - \hat{\mathbf{K}}_{bi}^{C,sd} \hat{\mathbf{K}}_{ii}^{C,sd,-1} \hat{\mathbf{K}}_{ib}^{C,sd}, \tag{V.183}$$

$$\hat{\mathcal{Q}}^{C,sd} = -\hat{\mathbf{g}}_{b}^{C,sd} + \hat{\mathbf{K}}_{bi}^{C,sd} \hat{\mathbf{K}}_{ii}^{C,sd,-1} \hat{\mathbf{g}}_{i}^{C,sd}. \tag{V.184}$$

where the superscript *C* indicates that these operators are defined after condensing the internal slave *dofs* using relation (V.176), as in equation (V.178).

The expressions (V.81) and (V.82) can be used for assembling the contribution of all subdomains, because these are defined for the global boundary *dofs* and do not change by eliminating the slave condensed *dofs*.

4.5 Computing algorithms

In this subsection, the most relevant steps of the computing algorithms for modal and incremental static or dynamic analyses are addressed. Only the PS method will be considered because this formulation was adopted in this thesis as the main DD technique. The algorithms for the other DD methods implemented can be recovered by making the changes reported in section 4.3. The *local kinematic constraints* (LKC) imposed by the *Master-Slave Elimination* method and the *global kinematic constraints* (GKC) imposed using *Lagrange Multipliers* are presented in the algorithms.

4.5.1 Pre-processing

The pre-processing step flowchart is presented in Figure V.20. This procedure starts by reading the data file that includes all the relevant information to the analysis: node coordinates, element types and nodes defining the element; subdomain and information regarding the DD method, constraint and restraint data, geometry definitions; material models; analysis characteristics; time functions and time history data; load and mass information, *etc*.

The second step consists of making the analysis of the KC data, in order to select the condensed degrees of freedom associated with the LKC and the ones associated with the GKC, which will be included in the global boundary *dofs*. In the following step, the subdomain information is collected and organized (*e.g.* mesh partition and element numbering). The final step consists of the classification and numbering of all *dofs*, both for the global domain and for the subdomain scope.

4.5.2 Processing - Incremental analyses

The flowchart of the processing stage for both static and dynamic incremental analyses is presented in Figure V.21. The algorithm starts by initializing the time-related variables and the files that will be used for storing the computation data. The next steps are related to the *Matlab workers*. These are independent processes that are initialized and populated with general data about the simulation and specific information related to the subdomain that is associated with the *worker*. After the workers are running, the elements, the nonlocal models, the general operators and the constraints are

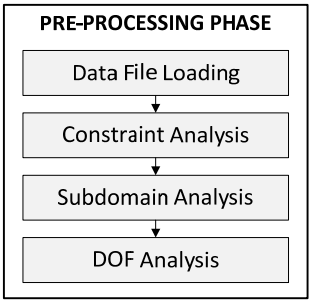

Figure V.20: Flowchart of the pre-processing phase implemented in the code *ParaNoiD*.

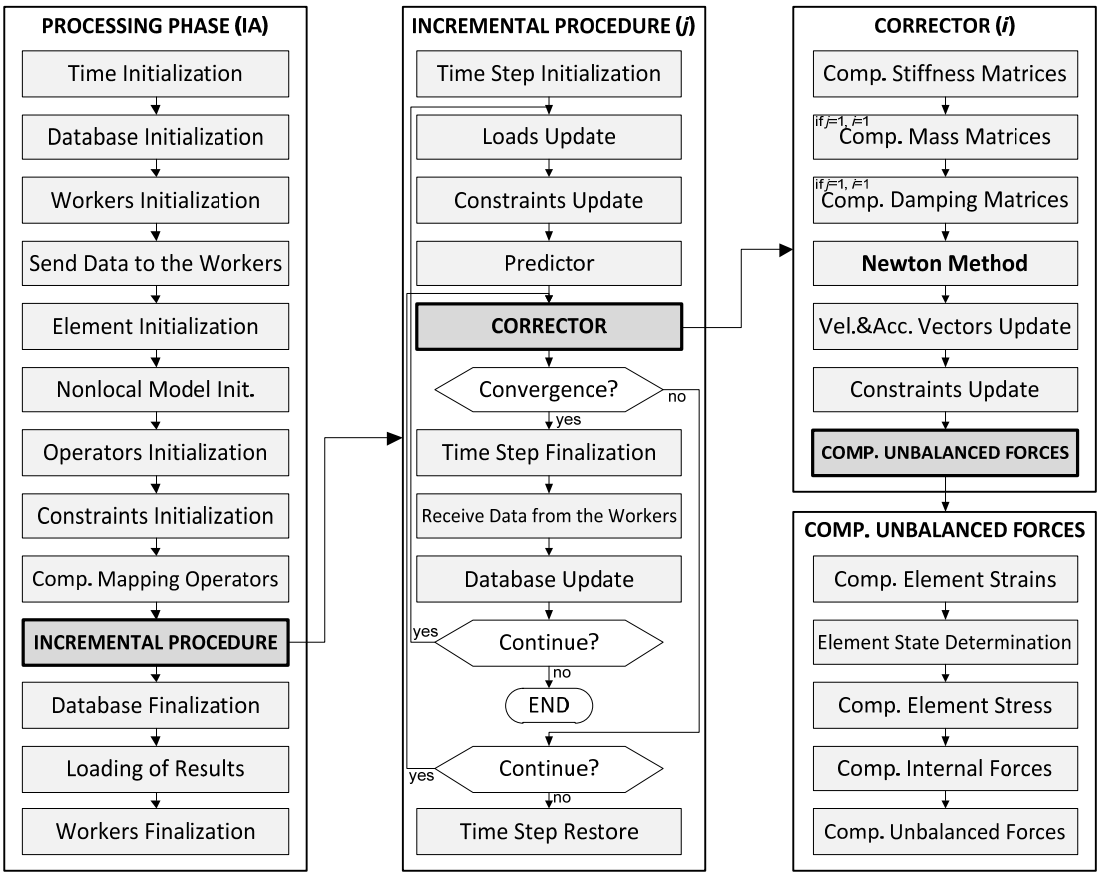

Figure V.21: Flowchart of the processing phase for incremental analyses implemented in the code *ParaNoiD*.

initialized both at the *Matlab client session* and at the *workers*. The next step consists of computing the mapping or assembler operators. In the following subsection, the formulation used for these operators is discussed in more detail.

- Mapping Operators

Let's start by defining a set of *Mapping Operators*, *a.k.a. Assembling Operators*, which consists of unsigned Boolean operators, used to relate the *dofs* between different spaces. In the previous chapters, element operators were directly assembled to the global domain using the mapping operator $\mathbf{A}^{el}$ (Chapter II-§3.5). At least three different spaces can be defined for the analyses with substructuring (see Figure V.22): i) the *element* or *local space*; ii) the *subdomain space*; and iii) the *global or domain space*. Consequently, two new assembling operators will be used for mapping the operators into these spaces.

The first mapping operator $\mathbb{A}$ is represented by a matrix of size $ndof^{el} \times ndof^{sd}$ and is used to relate the element and the subdomain *dofs*:

$$\mathbf{q}^{el}(X_k) = \mathbb{A}^{el,sd}\,\mathbf{q}^{sd}(X_k)\,. \tag{V.185}$$

where X_k are the structure coordinates as presented in Figure II.5.

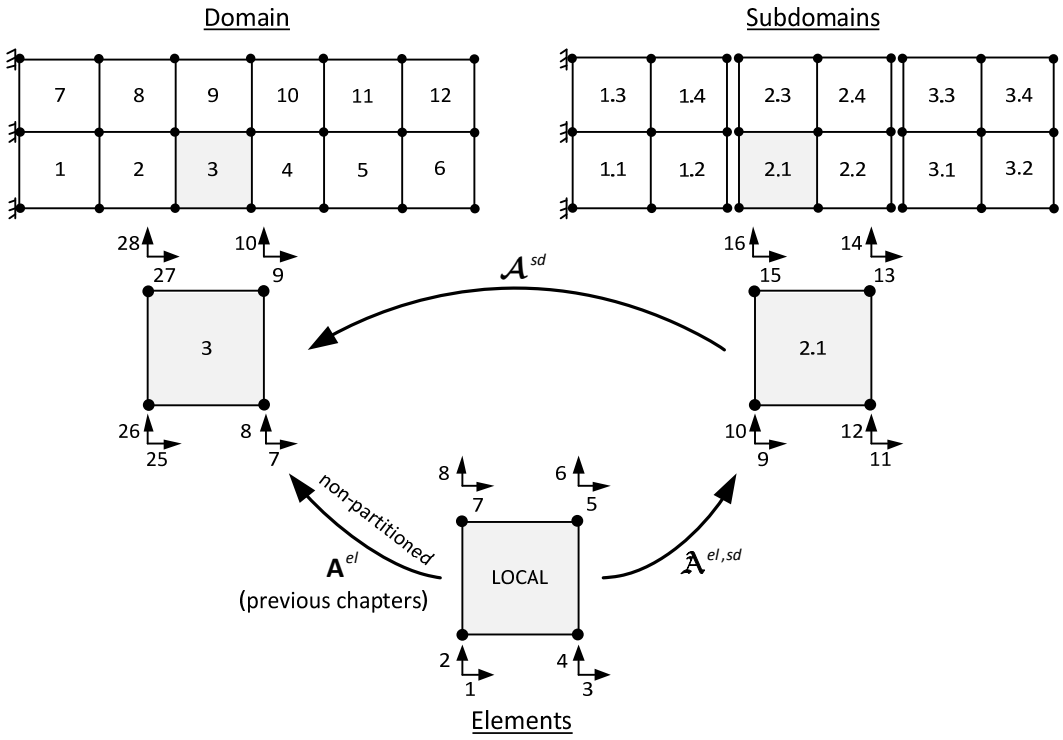

Figure V.22: Assembling the structural operators in substructured structural analyses.

A second mapping operator $\mathcal{A}$, with dimensions $ndof^{sd} \times ndof$, is used to assemble the subdomain contribution to the global domain:

$$\mathbf{q}^{sd}(X_k) = \mathcal{A}^{sd}\,\mathbf{q}(X_k)\,. \tag{V.186}$$

In the schematic representation presented in Figure V.22, it can be seen that the domain and the subdomains have their own element and *dof* numbering systems. Once again, it should be emphasized that the mapping operators are not stored in full or even in sparse format. Instead, they are stored using one or two integer indexes for each non-null entry.

The global operators for the analyses without substructuring can still be recovered using these two new mapping operators, both for matrices and vectors:

$$\mathbf{M}_G = \sum_{sd=1}^{nsd}\left\{\mathcal{A}^{sd,t}\sum_{el=1}^{nel}\left(\hat{\mathbf{A}}^{el,sd,t}\,\mathbf{M}^{el,sd}\,\hat{\mathbf{A}}^{el,sd}\right)\mathcal{A}^{sd}\right\}, \tag{V.187}$$

$$\mathbf{v}_G = \sum_{sd=1}^{nsd}\left(\mathcal{A}^{sd,t}\sum_{el=1}^{nel}\hat{\mathbf{A}}^{el,sd,t}\,\mathbf{v}^{el,sd}\right), \tag{V.188}$$

hence, the operator $\mathbf{A}^{el}$ becomes unnecessary (see Figure V.22).

Considering the *dof* reordering made in the context of the *local kinematic constraints* and of the PS method, the assembling operators can be defined as:

$$\begin{bmatrix}\mathbf{q}_m^{sd}\\ \mathbf{q}_s^{sd}\\ \mathbf{q}_b^{sd}\end{bmatrix} = \begin{bmatrix}\mathcal{A}_{mM}^{sd} & \mathcal{A}_{mM}^{sd} & \mathcal{A}_{mB}^{sd}\\ \mathcal{A}_{sM}^{sd} & \mathcal{A}_{sM}^{sd} & \mathcal{A}_{sB}^{sd}\\ \mathcal{A}_{bM}^{sd} & \mathcal{A}_{bM}^{sd} & \mathcal{A}_{bB}^{sd}\end{bmatrix}\begin{bmatrix}\mathbf{q}_M\\ \mathbf{q}_S\\ \mathbf{q}_B\end{bmatrix}, \tag{V.189}$$

where the subscript (m,M) refers to (subdomain, domain) master *dofs*, the subscript (s,S) refers to (subdomain, domain) slave *dofs*, and finally, the subscript (b,B) refers to (subdomain, domain) boundary *dofs*.

- Incremental procedure

Returning to the description of the processing stage algorithm, the following step is the incremental procedure itself, which is followed by closing the file databases, loading the results obtained into memory and closing the *Matlab workers*.

The incremental procedure starts by the initialization of the time steps and updating the external loads and the constraints for the new time step.

- External forces and prescribed displacements

The external forces are defined for *dof k* using:

$$Q_{e,k}(t) = \overline{Q}_{e,k}\ \mathrm{T}_k(t), \tag{V.190}$$

where $Q_{e,k}$ is the load magnitude and $\mathrm{T}_k(t)$ is the time function associated with the load.

The vector $\delta\mathbf{d}_{GK}$ in the incremental reduced problem (V.182) must be updated for each time step and iteration, when *global kinematic constraints* are used to impose displacements. This is because the iterations of the incremental procedure are defined in terms of the error between the current and target state. When forces are considered this leads to unbalanced forces and for imposed displacements to the error between the current displacement at *dof k* and the target value. Taking into consideration the definition adopted in (V.182), the following expression can be used for the prescribed displacement at *dof k*:

$$\delta d_{GK,k}(t) = \overline{q}_{imp,k}\ \mathrm{T}_k(t) - q_k(t), \tag{V.191}$$

where $\overline{q}_{imp,k}$ represents the base value for the prescribed displacement, $\mathrm{T}_k(t)$ the value of the associated time function and q_k the current displacement.

- Predictor

After setting the external loads and updating the constraints, a predictor step can be used to estimate the increments of the displacement vector, based on the results from the previous step. When adopted, the predictor was computed using the equation:

$$\mathbf{q}_{j+1}^{p} = \mathbf{q}_j + \Delta\mathbf{q}_j \frac{\Delta t_{j+1}}{\Delta t_j}, \tag{V.192}$$

where $\mathbf{q}_{j+1}^{p}$ represents the trial displacements at the end of the time step after applying the predictor, $\mathbf{q}_j$ is the displacements at the beginning of the time step and $\Delta\mathbf{q}_j$ represents the displacement increment from the previous time step. The term $\Delta t_{j+1}/\Delta t_j$ is used to take into consideration that the time step amplitudes can change in the analysis.

Moreover, when *global kinematic constraints* are used these should also be included in the predictor:

$$\mathbf{Q}^{p}_{K,j+1} = \mathbf{Q}_{K,j} + \Delta\mathbf{Q}_{K,j}\frac{\Delta t_{j+1}}{\Delta t_j}, \tag{V.193}$$

where $\mathbf{Q}^{p}_{K,j+1}$ represents the trial kinematic constraint forces at the end of the time step after applying the predictor, $\mathbf{Q}_{K,j}$ is the kinematic constraint forces at the beginning of the time step and $\Delta\mathbf{Q}_{K,j}$ represents the increment of the kinematic constraint forces in the previous time step.

- Corrector

The corrector is the most important step of the solving algorithm. It starts by computing the stiffness, mass and damping matrices for all subdomains. These last two operators are only computed once because within the scope of this thesis the mass and damping are considered to remain constant during the analysis.

The subdomain stiffness matrix can be computed at the workers, using:

$$\mathbf{K}^{sd}\left(X_i\right) = \sum_{el=1}^{nel} \hat{\mathbf{A}}^{el,sd,t}\left(\mathbf{T}^{t}_{xX}\ \mathbf{K}^{el}\left(x_i\right)\mathbf{T}_{xX}\right)\hat{\mathbf{A}}^{el,sd}, \tag{V.194}$$

where $\mathbf{T}_{xX}$ is the transformation operator between global to structure coordinates and $\hat{\mathbf{A}}$ is the local to subdomain mapping operator.

Similarly, the subdomain mass matrix is given by:

$$\mathbf{M}^{sd}\left(X_i\right) = \sum_{el=1}^{nel} \hat{\mathbf{A}}^{el,sd,t}\left(\mathbf{T}^{t}_{xX}\ \mathbf{M}^{el}\left(x_i\right)\mathbf{T}_{xX}\right)\hat{\mathbf{A}}^{el,sd}, \tag{V.195}$$

where $\mathbf{M}^{el}$ is computed according to the *lumped* or *consistent mass* definitions (see Chap. II-§3.3.2).

For nodal masses, the subdomain mass matrix entry associated with *dof k* $\left(M^{sd}_{kk}\right)$ should be augmented by the mass value.

The damping matrix is considered to be proportional to the initial stiffness and mass matrices:

$$\mathbf{C}^{sd} = \alpha\mathbf{M}^{sd} + \beta\mathbf{K}^{sd}, \tag{V.196}$$

where α and β are defined in Chapter II-§4.3.1.

- Newton Method

The first step of the Newton method is to compute the subdomains dynamic or effective stiffness associated with the α-Method (see Chapter II-§4.3.3). This computation is performed at the workers, using (V.181):

$$\hat{\mathbf{K}}^{C,sd} = \left(1+\alpha\right)\left(\mathbf{K}^{C,sd} + \frac{\gamma}{\beta\Delta t}\mathbf{C}^{C,sd}\right) + \frac{1}{\beta\Delta t^2}\mathbf{M}^{C,sd}.$$

It should be noted that the structural operators are already affected by the local kinematic constraints, enforced by the *Master-Slave Elimination* method (see section 4.4) using equations (V.178), (V.179) and (V.180).

The following step is associated with the *Domain Decomposition* method adopted. Considering that the *Primal Substructuring* (PS) method is chosen, this step would require computing the *Schur Complements* and the associated *rhs* vectors. This computation can be executed at the workers, using:

$$\hat{\mathcal{S}}^{sd} = \hat{\mathbf{K}}_{bb}^{sd} - \hat{\mathbf{K}}_{bi}^{sd}\, \mathbf{K}_{ii}^{sd,-1}\, \hat{\mathbf{K}}_{ib}^{sd}\,, \tag{V.197}$$

$$\hat{\mathcal{Q}}^{sd} = -\mathbf{g}_{b}^{sd} + \hat{\mathbf{K}}_{bi}^{sd}\, \hat{\mathbf{K}}_{ii}^{sd,-1}\, \mathbf{g}_{i}^{sd}\,. \tag{V.198}$$

The assemblage of the global operators is made at the *Master Processing Unit*, in this case the *Matlab client session*, using the following equations:

$$\hat{\mathcal{S}} = \sum_{sd=1}^{nsd} \mathcal{A}_{bB}^{sd,t}\; \hat{\mathcal{S}}^{sd}\; \mathcal{A}_{bB}^{sd}\,, \tag{V.199}$$

$$\hat{\mathcal{Q}} = \sum_{sd=1}^{nsd} \mathcal{A}_{bB}^{sd,t}\; \hat{\mathcal{Q}}^{sd}\,. \tag{V.200}$$

The basic theory of the PS method must be extended in order to include the global kinematic constraints enforced using *Lagrange Multipliers* (see section 4.4). This leads to the following augmented reduced problem, which must be solved for each iteration:

$$\begin{bmatrix} \hat{\mathcal{S}} & \mathcal{C}_{GK}^{t} \\ \mathcal{C}_{GK} & \mathbf{0} \end{bmatrix} \begin{bmatrix} \delta\mathbf{q}_{B} \\ \boldsymbol{\lambda} \end{bmatrix} = \begin{bmatrix} \hat{\mathcal{Q}} \\ \delta\mathbf{d}_{GK} \end{bmatrix}. \tag{V.201}$$

From the previous equation, it is possible to observe that the displacements are expressed in the form of increments. On the other hand, the *Lagrange Multipliers* can be seen as the forces necessary to impose the kinematic constraints and do not have an incremental nature.

- Updating the kinematic fields

The first step is to send the relevant boundary *dof* displacements increments to the workers, using the equation (V.87):

$$\delta\mathbf{q}_{b}^{sd} = \mathcal{A}_{bB}^{sd}\, \delta\mathbf{q}_{B}\,.$$

The recovery of the subdomain internal *dofs* can be made at the workers, using:

$$\delta\mathbf{q}_{i}^{sd} = \mathbf{K}_{ii}^{sd,-1} \left(-\mathbf{g}_{,i}^{sd} - \mathbf{K}_{ib}^{sd}\, \delta\mathbf{q}_{b}^{sd} \right). \tag{V.202}$$

It should be noted that the internal *dofs* computed in the previous expression do not include the slave *dofs* that are condensed by the *local kinematic constraints*. These can be recovered afterwards by adapting equation (V.176) to this purpose:

$$\mathbf{q}_{s}^{sd} = \mathcal{C}_{LK,sm}^{sd}\; \mathbf{q}_{m}^{sd}\,.$$

The final step consists of updating the trial displacements. This computation can be made at the worker, using:

$$\mathbf{q}^{sd} = \mathbf{q}^{sd} + \begin{bmatrix} \delta\mathbf{q}_{m}^{sd} & \delta\mathbf{q}_{s}^{sd} & \delta\mathbf{q}_{b}^{sd} \end{bmatrix}^{t}. \tag{V.203}$$

For dynamic analyses, the trial velocities and accelerations should also be updated, using:

$$\mathbf{v}^{sd} = \frac{\gamma}{\beta \Delta t}\left(\mathbf{q}^{sd} - \mathbf{q}_j^{sd}\right) + \left(1 - \frac{\gamma}{\beta}\right)\mathbf{v}_j^{sd} + \left\{(1-\gamma) - \frac{\gamma}{\beta}\left(\frac{1}{2} - \beta\right)\right\}\Delta t\ \mathbf{a}_j^{sd}\,, \tag{V.204}$$

$$\mathbf{a}^{sd} = \frac{1}{\beta \Delta t^2}\left[\mathbf{q}^{sd} - \mathbf{q}_j^{sd} - \Delta t\ \mathbf{v}_j^{sd} - \left(\frac{1}{2} - \beta\right)\Delta t^2\ \mathbf{a}_j^{sd}\right]. \tag{V.205}$$

where the subscript *j* represents the values at the beginning of the time step.

It is important to emphasize that the slave internal *dofs*, condensed by local kinematic constraints, are removed from the static variables, because they are implicitly defined in terms of the remaining *dofs*. Nevertheless, these unknowns must be recovered for the element state determination.

If another domain decomposition method is chosen for substructuring, then other computations would be required (see section 4.3). Nevertheless, apart from minor additional data definitions, all the changes to be made are circumscribed to the algorithm block called the *Newton method*.

- Computing the unbalanced forces

The unbalanced forces vector is computed after performing the basic element-based computations presented in Chapter II-§3.4, namely: the strains; the nonlocal variables (when included in the models), the element state determination; the stresses and the internal forces.

The unbalanced forces vector associated with the *α-Method* dynamic equilibrium equation (II.232) can be computed at the subdomain level, using:

$$\mathbf{g}^{sd} = (1+\alpha)\left(\mathbf{Q}_i^{sd} + \mathbf{Q}_K^{sd} - \mathbf{Q}_e^{sd} + \mathbf{C}\mathbf{v}^{sd}\right) - \alpha\left(\mathbf{Q}_{i,j}^{sd} + \mathbf{Q}_{K,j}^{sd} - \mathbf{Q}_{e,j}^{sd} + \mathbf{C}\mathbf{v}_j^{sd}\right) + \mathbf{M}\mathbf{a}^{sd}\,, \tag{V.206}$$

and assembled to the global domain, using:

$$\mathbf{g} = \sum_{sd=1}^{nsd} \mathcal{A}^{sd,t}\ \mathbf{g}^{sd}\ . \tag{V.207}$$

The subdomain internal forces vector can be computed at the workers, using:

$$\mathbf{Q}_i^{sd} = \sum_{el=1}^{nel} \hat{\mathbf{A}}^{el,sd,t}\ \mathbf{Q}_i^{el}\ . \tag{V.208}$$

The equation (V.206) includes two additional terms $\left(\mathbf{Q}_K^{sd}, \mathbf{Q}_{K,j}^{sd}\right)$ that represent the forces associated with the GKC, defined at the end of the current iteration and at the beginning of the time step, respectively.

After solving the governing system for the global boundary *dof* displacements and for the Lagrange Multipliers, the increments of the forces associated with the GKC can be computed from:

$$\delta\mathbf{Q}_K = \begin{bmatrix} \mathbf{0} \\ \mathbf{0} \\ \delta\mathbf{Q}_{K,B} \end{bmatrix} = \begin{bmatrix} \mathbf{0} \\ \mathbf{0} \\ \mathcal{C}_{GK} \end{bmatrix}\boldsymbol{\lambda}\,, \tag{V.209}$$

where $\mathbf{0}$ are zero matrices that should have a combined size of $ndofs_S \times ngc$ and the uppercase *B* represents the global boundary *dofs*.

Afterwards, the forces should be transformed to the subdomain level, using:

$$\delta \mathbf{Q}_K^{sd} = \boldsymbol{\mathcal{A}}^{sd} \; \delta \mathbf{Q}_K \,, \tag{V.210}$$

and finally, the trial constraint forces can be computed, from:

$$\mathbf{Q}_K^{sd,i+1} = \mathbf{Q}_K^{sd,i} + \delta \mathbf{Q}_K^{sd} \,. \tag{V.211}$$

4.5.3 Processing - Modal analyses

The flowchart for the processing phase associated with modal analyses is presented in Figure V.23. This algorithm includes basically the same computations made for the incremental analyses, except for the eigenvalue problem solver. When the substructuring technique adopted in this thesis is used, the characteristic equation includes the global and local kinematic constraints:

$$\det\left(\begin{bmatrix} \boldsymbol{\mathcal{S}}^C & \mathcal{C}_K^t \\ \mathcal{C}_K^t & \mathbf{0} \end{bmatrix} - \lambda_f \begin{bmatrix} \mathbf{M}^C & \mathbf{0} \\ \mathbf{0} & \mathbf{0} \end{bmatrix} \right) = 0 \,,$$

where:

$$\boldsymbol{\mathcal{S}}^C = \sum_{sd=1}^{nsd} \boldsymbol{\mathcal{A}}_{bB}^{sd,t} \; \boldsymbol{\mathcal{S}}^{C,sd} \; \boldsymbol{\mathcal{A}}_{bB}^{sd} \,, \tag{V.212}$$

$$\boldsymbol{\mathcal{S}}^{C,sd} = \mathbf{K}_{bb}^{C,sd} - \mathbf{K}_{bi}^{C,sd} \, \mathbf{K}_{ii}^{C,sd,-1} \, \mathbf{K}_{ib}^{C,sd} \,, \tag{V.213}$$

$$\mathbf{M}^C = \sum_{sd=1}^{nsd} \boldsymbol{\mathcal{A}}_{bB}^{sd,t} \; \mathbf{M}_{bb}^{sd} \; \boldsymbol{\mathcal{A}}_{bB}^{sd} \,, \tag{V.214}$$

and $\mathbf{K}^{C,sd}$ is defined in equation (V.178).

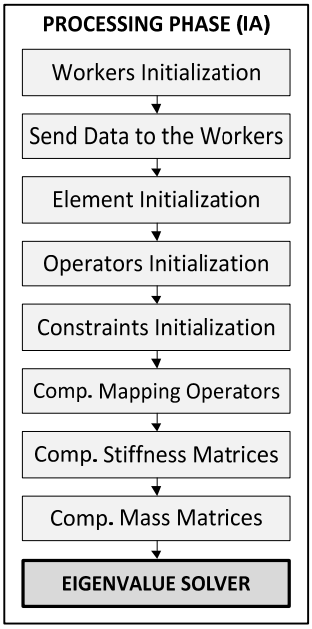

Figure V.23: Flowchart of the processing phase for modal analyses implemented in the code *ParaNoiD*.

Adopting the *Guyan Reduction* (GR) method [256], presented in section 2.2.2, the contribution of the mass associated with the slave or interior *dofs* $\left(\mathbf{M}_{ii}=\mathbf{M}_{ib}=\mathbf{M}_{bi}=\mathbf{0}\right)$ is neglected. In this case, the condensed stiffness and mass matrices are given by expression (V.12) and (V.26), respectively, which should be adapted to substructuring.

Afterwards, the modal coefficients associated with the interior *dofs* can be recovered, using:

$$\mathbf{\Phi}_{m}^{sd}=-\mathbf{K}_{mm}^{sd,-1}\left(\mathbf{K}_{mb}^{sd}\,\mathbf{\Phi}_{b}^{sd}\right). \tag{V.215}$$

Moreover, if interior condensed *dofs* exist, these can be recovered by once again using the general equation (V.176):

$$\mathbf{\Phi}_{s}^{sd}=\mathcal{C}_{LK,sm}^{sd}\;\mathbf{\Phi}_{m}^{sd}. \tag{V.216}$$

4.5.4 Post-processing

To complete the presentation of the computing algorithms used for the analyses with substructuring, the post-processing stage should also be addressed. The computing flowchart is presented in Figure V.24. Taking into consideration that the results from the analyses are already stored for the global domain, the post-processing stage is not affected by the use of substructuring. Consequently, the expressions presented in the previous chapters can be used.

Nevertheless, a code parallelization was implemented to speed up the computations. Consequently, the time step results are first sent to the *workers*, using:

$$\mathbf{q}^{sd}=\mathcal{A}^{sd}\,\mathbf{q},$$

and afterwards, the element displacements are transformed to the element coordinate system, using:

$$\mathbf{q}^{el}\left(x_i\right)=\mathbf{T}_{xX}\,\hat{\mathbf{A}}^{el,sd}\,\mathbf{q}^{sd}\left(X_i\right). \tag{V.217}$$

These displacements are used to compute the strains, stresses and internal forces using the expressions presented in Chapter II-§3.4. The final steps consist of sending the post-processing results back to the *Matlab Client Session*, to be written in a file or to be visualized.

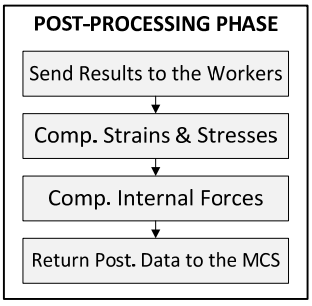

Figure V.24: Flowchart of the post-processing phase implemented in the code *ParaNoiD*.

5 Validation examples

This section presents a series of examples developed to test the behaviour of the strategies adopted to improve the computational performance of the numerical model. The problems were chosen in order to be simple and attempting to isolate, as much as possible, each feature that is being analysed.

The tests will start with a performance benchmark to assess the characteristics of the computational equipment used to run the examples. Afterwards, most of the domain decomposition methods addressed in this chapter will be tested for their accuracy and performance, using a plane elasticity problem. The third example was designed to be more general and to include most of the features proposed in this chapter, such as the *Hybrid Discretization* and *Global Kinematic Constraints*. The fourth example was created to test the efficiency between *Global* and *Local Kinematic Constraints*, and finally, the fifth example was designed to simulate a more general RC structure. The results are compared with the solutions obtained from other FE packages or with the data obtained using different solving techniques (*e.g.* without using substructuring).

5.1 Example HPC1 – Benchmarking

As mentioned before, this example was designed to characterize the computational equipment used in this work, using common linear algebra operations included in most FE algorithms. The analysis is made mainly for the hardware, although it is also extended to the assessment of some software-related issues. This characterization proved to be relevant and important due to three main reasons. Firstly, before trying to improve the performance of the computations, it is necessary to understand how the equipment and software work. It is also important to identify what are the most significant bottlenecks that can compromise the performance. In addition, it was necessary to perform the characterization of the dynamic overclocking procedure implemented in the CPU used (Intel's *Turbo Boost* technology, see section 2.1.2), in order to correctly evaluate the speed-up values achieved using substructuring. Finally, this example also tries to assess what are the performance consequences of using a Matlab-based implementation.

It must be clearly stressed that the performance of a computer is a complicated issue, which is dependent on many interrelated aspects associated with both hardware and software. Consequently, the results presented in this example should be considered as an estimate of the global computational performance, rather than a precise measurement of performance.

The first issue to take into consideration is that computing the speed-up and efficiency between sequential and parallelized codes, as defined in section 2.1.10, should be made using purely sequential computations, and therefore, the multithreaded computations implemented by default in *Matlab* will lead to erroneous results. To avoid this, the multithreaded computations were switched off for the computation made to assess the performance of the algorithms. This was done by starting the *Matlab* application at the command-line with the argument "`-singleCompThread`".

The relevant data regarding the processing and memory capacity of the computer used in this work

Table V.3: Processing capacity data of the computer used in this work.

NPU	CR (GHz)		IPC	Peak Speed (GFlop/s)		Measured Speed (GFlop/s)
4	1.6	2.8	4	25.6	44.8	22.5 (benchmark #1)

Table V.4: RAM memory data of the computer used in this work.

Total memory (GB)	Type of Memory	Memory Speed (MHz)	Data Rate (MT/s)
8	DDR3 (PC3-10700)	667	1333

Table V.5: Example HPC1 - Analyses characteristics.

ID	Analysis Type	Expression	Memory Req.	Number of Flop
HPC1.1	Vector dot Product	$\langle \mathbf{u},\mathbf{v} \rangle$	$3n$	$2n-1$
HPC1.2	Matrix-by-Matrix Multiplication	$\mathbf{MN}$	$3n^2$	$2n^3-n^2$
HPC1.3	Linear System Solving by GE	$\mathbf{Ax}=\mathbf{b}$	$2n^2+2n$	$2/3n^3-2n^2$

are presented in Table V.3 and in Table V.4, respectively. The characteristics of the three benchmark tests are presented in Table V.5. This information includes an estimate of the number of operations and of the memory requirements for the computations.

All benchmark tests were made with vector and square matrices with dimension *n*. The matrix entries were generated using uniformly distributed pseudorandom numbers in the open interval $]0,1[$, resulting in dense matrices and vectors. The results will be presented in terms of an estimate for *floating point operations per second* that were computed by considering the estimate for the total number of Flop (see Table V.5) of each operation and by the elapsed time required for the computation. The results shown correspond to the average result of three independent computations made for chosen sets of vector or matrix dimensions. Five results will be presented for each analysis. The first was computed in the Matlab client session and the others were run considering one to four local workers.

Some measures have been taken to mitigate, as much as possible, the possibility of other processes allocating significant computing time, which would change the results of the benchmark. This was achieved by ending non-vital processes and by stopping services that are not essential to the operating system. In order to avoid erroneous results caused by the initial conditions, warm up computations were implemented to set, as much as possible, the hardware in similar computing conditions, considering the dynamic overclock installed at the CPU used.

- Vector dot product

The first example corresponds to computing a dot product. The vectors were created in such a way that it was not required to transpose the arrays, which would introduce an additional overhead that could result in misleading values for the performance.

The results presented in Figure V.25 show that the number of *floating point operations per second* was relatively uniform for all the vector sizes considered. Speeds of around 0.8-1.4 GFlop/s were measured. These values are quite below the theoretical peak value for the computer used, which is about 25.6 GFlop/s, considering four cores running at 1.6 GHz (see Table V.3).

The reason for this underperformance is related to the memory access velocity. As presented in section 2.1.3, the peak data transfer rate for memory operations is estimated by formula (V.2), which for the type of memory installed in the computer is 1333 MT/s of double precision numbers (see Table V.4). Considering that for this calculation the demand from data stored in memory and the number of operations have the same order of magnitude ($3n$ *vs.* $2n-1$, see Table V.5), the performance is limited by the slower link, which in this case is clearly the speed for memory access operations.

The value 1333 MT/s is undoubtedly present in Figure V.25. The only exception is for the results obtained with only one worker that are slightly above this value. Nevertheless, these figures can only be seen as an estimate because memory operations involve a more complex mechanism than the one presented in this simplified analysis, and additionally, measurements are also subjected to errors.

Another aspect that must be mentioned is the tendency for the performance to decrease with increasing number of workers. This can be related to the amplification of data requests to the memory that cannot be fully satisfied and tend to deteriorate the overall performance.

- Matrix-by-matrix multiplication

The second benchmark is a matrix-by-matrix multiplication. In this case, the number of Flop is one order of magnitude superior to the number of memory operations. Therefore, the performance of the computations is not expected to be conditioned by the memory access capacity, but instead, by the processing capacity.

The results obtained are presented in Figure V.26 and show three clear performance phases. An initial phase with inferior performance is visible for small matrices. This can be related to the relative weight increase of the initialization and auxiliary computations. Therefore, it is possible to conclude that the size of the matrices is not enough to potentiate the maximum computational performance.

In the second phase, the number of operations tends to stabilize at an approximate constant value that is considered as the peak performance for the matrix-by-matrix multiplication. This value was about 22.4 GFlop/s for four workers and this result is considered very coherent with the theoretical peak performance of 25.6 GFlop/s (see Table V.3). This data confirms that the basic linear algebra operations are highly optimized in Matlab and is possible to achieve a very good performance.

Finally, in the last stage the rate of the operations decreases rapidly to values quite below the peak performance. This can be explained by the beginning of *paging*, or in other words, the use of secondary memory sources (normally, hard disk space) to store data, when the free physical random-access memory (RAM) is not enough to accommodate the storage demands.

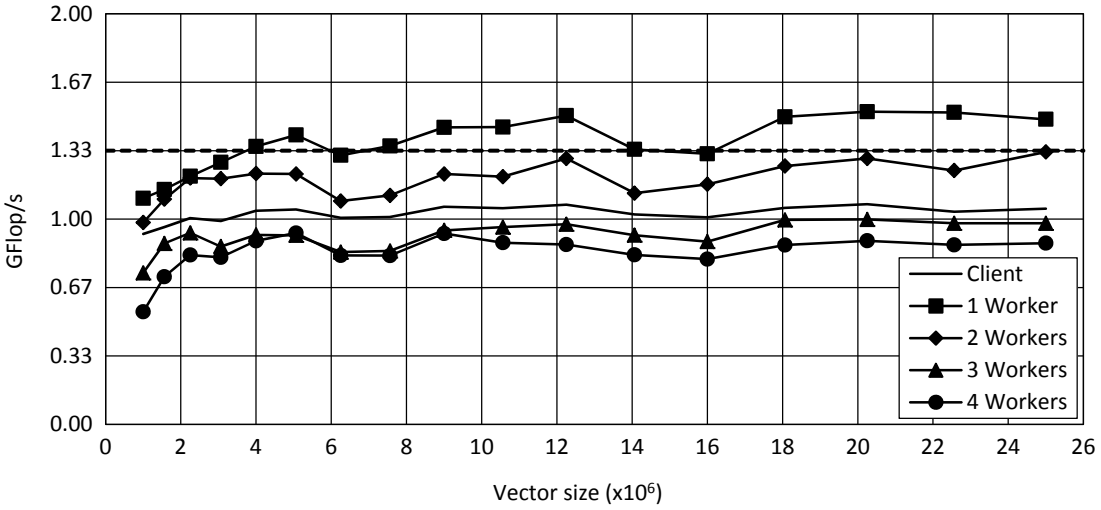

Figure V.25: Example HPC1.1 – Floating point operations per second for the vector dot product calculation.

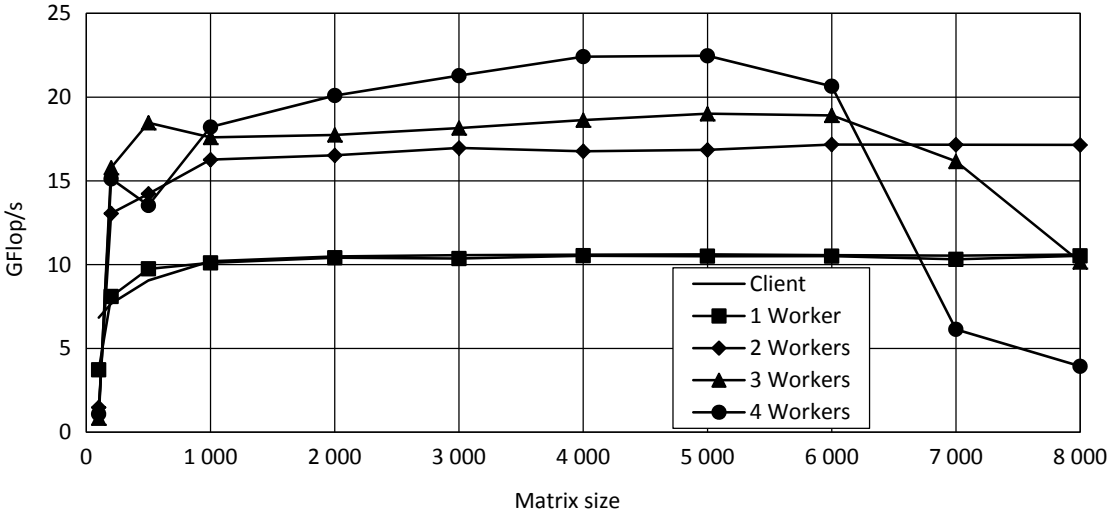

Figure V.26: Example HPC1.2 – Floating point operations per second for the matrix-by-matrix multiplication.

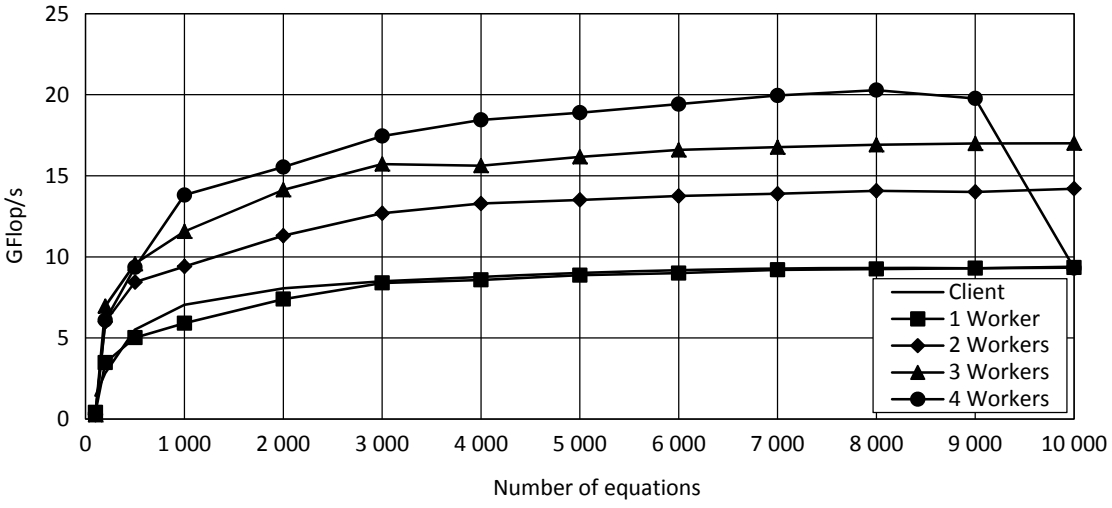

Figure V.27: Example HPC1.3 – Floating point operations per second for solving a linear system by Gaussian elimination.

Paging will start not just when the size of the data storage request is above the amount of free memory. Other factors must be taken into consideration, such as the requirement of storing the data in continuous memory blocks for some data types. As an example, for the analysis ran with 4 workers and with a matrix of size equal to 8000, a total free memory space of 5859 MB $\left(3\times8000^2\times8 \text{ bytes/double}\times4 \text{ workers}\right)$ would be required. It is possible to conclude that paging is very likely to occur by taking into consideration that 2 GB of the 8 GB installed on the computer are used by the operating system and by the loaded applications such as the Matlab client session and the run-time engines for the four workers. The consequences of paging were also physically observed by a large increase in terms of disk activity and a reduction in rotating speed of the fans used to cool down the CPU, revealing that the processing speed was below the maximum capacity.

One last consideration must be stressed about this analysis. The maximum value for the computation speed showed an undeniable tendency to increase with the number of workers. This corresponds to the expected behaviour, except for the fact that the increases do not scale directly with the number of workers. This issue will be addressed latter in this section.

- Linear system solving by Gaussian Elimination

The third and last benchmark is one of the most important linear algebra operations, which is solving linear systems using *Gaussian Elimination* (GE). This operation is considered so important that one of the most used performance benchmarks for supercomputers [540], the *Linpack benchmark* [174], is precisely the speed of the computations associated with solving a linear system using the LU decomposition, which is similar to Gaussian elimination (see Annex A). Although presenting some similarities with the *Linpack benchmark*, this test is different due to the fact that independent linear systems are solved in each worker, instead of solving one larger linear system using a parallelized algorithm. The adopted algorithm should present performances closer to the theoretical peak values because the interchange of data between workers is avoided. For this benchmark the number of operations is again one order of magnitude higher than the number of memory operations, so that the performance should be once again governed by the processing capacity.

The results are presented in Figure V.27. As before, an initial increase of performance for the smaller linear systems can be seen, which in this case is slower than for the matrix-by-matrix multiplications. Afterwards, a stabilization tendency at about 20 GFlop/s using four workers can be observed.

Similarly to what happened before, for the computation with the largest system of equations and four workers, a clear performance degradation due to paging can be seen. In this case, the amount of memory required is about $\left(2\times10000^2+2\times10000\right)\times8 \text{ bytes/double}\times4\text{workers}=6104 \text{ MB}$, which is likely to produce paging for the hardware characteristics of the computer.

When compared to the theoretical peak performance of 25.6 GFlop/s (see Table V.3), the value of 20 GFlop/s confirms the good performance of the direct linear solver implemented in Matlab.

One of the main reasons for developing this example was the assessment of the influence on the global performance of the dynamic overclocking procedure installed in the CPU used for the tests. Analysing the technical data published by the CPU manufacturer [285, 286], the *Turbo Boost*

technology installed in the Intel Core i7 720QM processor sets the processor clock rate (CR) to the base value of 1.6 GHz if all cores are being used (see Table V.3). On the other hand, if only one core is active, the operating frequency should be dynamically increased to a maximum value of 2.8 GHz. For intermediate core activity, the processor clock rate should also be working at intermediate values. The *Turbo Boost technology* increases and decreases the CR by steps of 133.33 or 266.66 MHz depending on the estimated current and power consumption and on the processor temperature. Taking into consideration that warm-up computations were used to make the initial state of the processor uniform and that the computing time was relatively long, it was considered that the CR was relatively constant during the computing time. Consequently, it is possible to compute an estimate for a correction factor γ, that takes into account the variation of the CPU's CR. The following expression was adopted:

$$\mathrm{F}^{*} = \gamma \, \mathrm{F}_{seq} \, n_w \,, \tag{V.218}$$

where n_w is the number of workers and F_{seq} is the number of floating point operations per second for the sequential code run in the Matlab client session. F^{*} represents the estimate of the *number of floating point operations per second* using parallel computations and taking the dynamic overclocking into consideration. The correction factors were computed assuming a constant clock rate for a specific number of workers running, which is related to the number of active cores. For the processor installed in the computer, the adopted CR distribution was $\{2.80;2.20;1.60;1.60\}$ GHz for $\{1;2;3;4\}$ workers or active cores, leading to the following correction factors $\{1.000;0.786;0.571;0.571\}$, respectively.

This procedure was tested for the data obtained by analysis HPC1.2 and HPC1.3. The results are presented in Table V.6 and Table V.7. The relative error turned out to be always below 8% and most of the time below 5%. These results were considered as very satisfactory taking into consideration the uncertainties associated with the measurements, additional processing in the OS, and associated with the real-time overclocking procedure implemented in the hardware. Consequently, these factors will be used to correct the speed-up values in the following examples.

Table V.6: Example HPC1.2 – Estimated Peak Flop/s for the parallelized computations using the correction factors γ.

	Client	**1 worker**	**2 workers**	**3 workers**	**4 workers**
Measured Peak FLOPS (GFlop/s)	10.56	10.45	16.78	18.38	22.44
Estimated Peak FLOPS (GFlop/s)	-	10.56	16.60	18.11	24.15
Relative Error	-	1.08%	-1.04%	-1.48%	7.61%

Table V.7: Example HPC1.3 – Estimated Peak Flop/s for the parallelized computations using the correction factors γ.

	Client	**1 worker**	**2 workers**	**3 workers**	**4 workers**
Measured Peak FLOPS (GFlop/s)	9.30	9.22	13.99	16.84	20.12
Estimated Peak FLOPS (GFlop/s)	-	9.30	14.61	15.94	21.26
Relative Error	-	0.81%	4.49%	-5.32%	5.66%

5.2 Example HPC2 – Plane elasticity

This example was developed to characterize the accuracy and the performance of the *Domain Decomposition* (DD) methods considered in this thesis, both for static and modal analyses. The plane elasticity problem presented in Figure V.28 was chosen because of its simplicity and due to the fact that under static analyses all DD methods considered in this thesis can be applied. The response of the cantilever was simulated using a two-dimensional mesh of isoparametric Q4 elements and a plane stress elastic constitutive relation was adopted. Structured uniform meshes were created by specifying different values of h_h and h_v, leading to the seven meshes presented in Table V.8. The chosen mesh densities were selected to create convenient values for the number of *dofs*.

Similarly, the *number of subdomains* (*nsd*) was defined by selecting values for the subdomain size H_h and by fixing $H_v = 1.00$ m (see Figure V.28). This procedure led to subdomains connected only by the edges located along the *Y* axis. This approach was chosen to avoid introducing additional phenomena into the simulation (*e.g.* nodes connecting more than two subdomains, *etc*.), which could raise difficulties for drawing conclusions.

The example will start by performing static analyses to assess the accuracy and efficiency of the different DD methods considered in this work. These tests were made to study the influence of the problem size and of the number of subdomains. Furthermore, a dedicated set of analyses were made to assess the computational performance of the *Primal Substructuring* method for different problem sizes. Afterwards, a modal analysis is performed to discuss the combination of the *Primal Substructuring* method with the *Guyan Reduction* presented in sections 2.2.2 and 4.5.3.

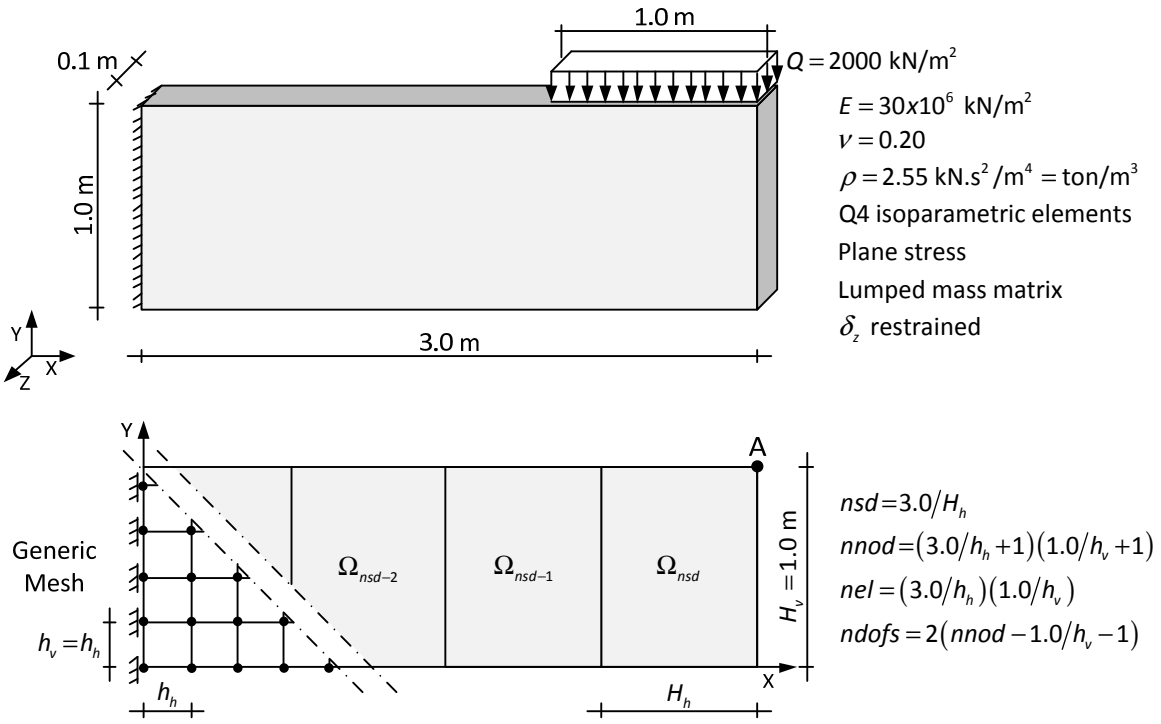

Figure V.28: Example HPC2 – Definition of the problem.

Table V.8: Example HPC2 – Mesh Characteristics.

Mesh	***nnod***	***nel***	h_h [m] (*ndofs*)		$ndiv_v = 1.0/h_h$
#1	21	12	0.500000000	(36)	2
#2	560	507	0.076923077	(1092)	13
#3	2640	2523	0.034482759	(5220)	29
#4	5208	5043	0.024390244	(10332)	41
#5	10325	10092	0.017241379	(20232)	58
#6	25208	24843	0.010989011	(50232)	91
#7	50440	49923	0.007751938	(100620)	129

- Static Analyses: Accuracy and efficiency for different problem sizes and number of subdomains

A series of static analyses were performed to test the influence of the problem size on the accuracy of the DD methods. As presented in Figure V.28 and in Table V.9, the structure was subjected to a distributed load applied at the top of the cantilever and six mesh densities with a number of *dofs* ranging from 36 to about 100000 were considered. Furthermore, the number of subdomains was fixed to three by setting $H_h = 1.00$ m (see Figure V.32-a).

The following *Domain Decomposition* (DD) methods were considered: the *Primal Substructuring* (PS) method, the *Neumann-Neumann* (NN) method, the *Balancing Domain Decomposition* (BDD) method, the *One-level Finite Element Tearing and Interconnecting* (FETI-1) method and the *Dual-Primal Finite Element Tearing and Interconnecting* (FETI-DP) method. For the DD methods using iterative solvers, the convergence tolerance was set to 1E-6 and the maximum number of iterations was defined as the minimum between the size of the governing system and 1000 iterations.

Table V.9 presents the results obtained from the analyses performed by changing the problem size and the DD method used. The results reported in Table V.9 include the vertical displacement of point A and the work done by the external forces in the discrete system. This data is compared with the data obtained using the commercial FE software *ADINA* [3], whose results are labelled as "*reference*" in this example.

The results clearly show that the solutions obtained match the reference results for all mesh densities and for all DD methods. For this example, it is possible to conclude that the DD methods did not introduce any visible approximation in the results and their accuracy was revealed to be insensitive to the problem size.

Figure V.29 shows the evolution of the vertical displacement and of the work done by the discrete forces for the different problem sizes considered. From the analysis of the results, it is possible to observe the expected asymptotic convergence to higher displacement and energy levels, when the mesh is homothetically refined.

The results for the analyses using the FETI-1 and meshes #6 and #7 are missing from Table V.9, because computing the null space and the pseudoinverse of the subdomain stiffness matrices (V.108) requires computing a full *singular value decomposition* (SVD), which is a demanding operation.

Table V.9: Example HPC2 – Characteristics and results of the analyses made for assessing the influence of the problem size.

Analysis	Mesh (*ndofs*)	H_h (m) (*nsd*)	DD Met.	$\delta_Y^A\ (e_{rel})$ [m]	$W_e = -U^e\ (e_{rel})$ [kN.m]
Reference	#1 (36)	3.0 (1)	-	-5.24732e-3	4.08800e-1
HPC2.01	#1 (36)	1.0 (3)	PS	-5.24732e-3 (0.00%)	4.08800e-1 (0.00%)
HPC2.02	#1 (36)	1.0 (3)	NN	-5.24732e-3 (0.00%)	4.08800e-1 (0.00%)
HPC2.03	#1 (36)	1.0 (3)	BDD	-5.24732e-3 (0.00%)	4.08800e-1 (0.00%)
HPC2.04	#1 (36)	1.0 (3)	FETI-1	-5.24732e-3 (0.00%)	4.08800e-1 (0.00%)
HPC2.05	#1 (36)	1.0 (3)	FETI-DP	-5.24732e-3 (0.00%)	4.08800e-1 (0.00%)
Reference	#2 (1092)	3.0 (1)	-	-5.9028e-3	4.61198e-1 (0.00%)
HPC2.06	#2 (1092)	1.0 (3)	PS	-5.9028e-3 (0.00%)	4.61199e-1 (0.00%)
HPC2.07	#2 (1092)	1.0 (3)	NN	-5.9028e-3 (0.00%)	4.61199e-1 (0.00%)
HPC2.08	#2 (1092)	1.0 (3)	BDD	-5.9028e-3 (0.00%)	4.61199e-1 (0.00%)
HPC2.09	#2 (1092)	1.0 (3)	FETI-1	-5.9028e-3 (0.00%)	4.61199e-1 (0.00%)
HPC2.10	#2 (1092)	1.0 (3)	FETI-DP	-5.9028e-3 (0.00%)	4.61199e-1 (0.00%)
Reference	#3 (5220)	3.0 (1)	-	-5.9192e-3	4.62533e-1
HPC2.11	#3 (5220)	1.0 (3)	PS	-5.9192e-3 (0.00%)	4.62533e-1 (0.00%)
HPC2.12	#3 (5220)	1.0 (3)	NN	-5.9192e-3 (0.00%)	4.62533e-1 (0.00%)
HPC2.13	#3 (5220)	1.0 (3)	BDD	-5.9192e-3 (0.00%)	4.62533e-1 (0.00%)
HPC2.14	#3 (5220)	1.0 (3)	FETI-1	-5.9192e-3 (0.00%)	4.62533e-1 (0.00%)
HPC2.15	#3 (5220)	1.0 (3)	FETI-DP	-5.9192e-3 (0.00%)	4.62533e-1 (0.00%)
Reference	#4 (10332)	3.0 (1)	-	-5.92142e-3	4.62714e-1
HPC2.16	#4 (10332)	1.0 (3)	PS	-5.92142e-3 (0.00%)	4.62714e-1 (0.00%)
HPC2.17	#4 (10332)	1.0 (3)	NN	-5.92142e-3 (0.00%)	4.62714e-1 (0.00%)
HPC2.18	#4 (10332)	1.0 (3)	BDD	-5.92142e-3 (0.00%)	4.62714e-1 (0.00%)
HPC2.19	#4 (10332)	1.0 (3)	FETI-1	-5.92142e-3 (0.00%)	4.62714e-1 (0.00%)
HPC2.20	#4 (10332)	1.0 (3)	FETI-DP	-5.92142e-3 (0.00%)	4.62714e-1 (0.00%)
Reference	#6 (50232)	3.0 (1)	-	-5.92331e-3	4.62869e-1
HPC2.21	#6 (50232)	1.0 (3)	PS	-5.92331e-3 (0.00%)	4.62869e-1 (0.00%)
HPC2.22	#6 (50232)	1.0 (3)	NN	-5.92331e-3 (0.00%)	4.62869e-1 (0.00%)
HPC2.23	#6 (50232)	1.0 (3)	BDD	-5.92331e-3 (0.00%)	4.62869e-1 (0.00%)
HPC2.24	#6 (50232)	1.0 (3)	FETI-1	-	-
HPC2.25	#6 (50232)	1.0 (3)	FETI-DP	-5.92331e-3 (0.00%)	4.62869e-1 (0.00%)
Reference	#7 (100620)	3.0 (1)	-	-5.92358e-3	4.62892e-1
HPC2.26	#7 (100620)	1.0 (3)	PS	-5.92358e-3 (0.00%)	4.62891e-1 (0.00%)
HPC2.27	#7 (100620)	1.0 (3)	NN	-5.92358e-3 (0.00%)	4.62891e-1 (0.00%)
HPC2.28	#7 (100620)	1.0 (3)	BDD	-5.92358e-3 (0.00%)	4.62891e-1 (0.00%)
HPC2.29	#7 (100620)	1.0 (3)	FETI-1	-	-
HPC2.30	#7 (100620)	1.0 (3)	FETI-DP	-5.92358e-3 (0.00%)	4.62891e-1 (0.00%)

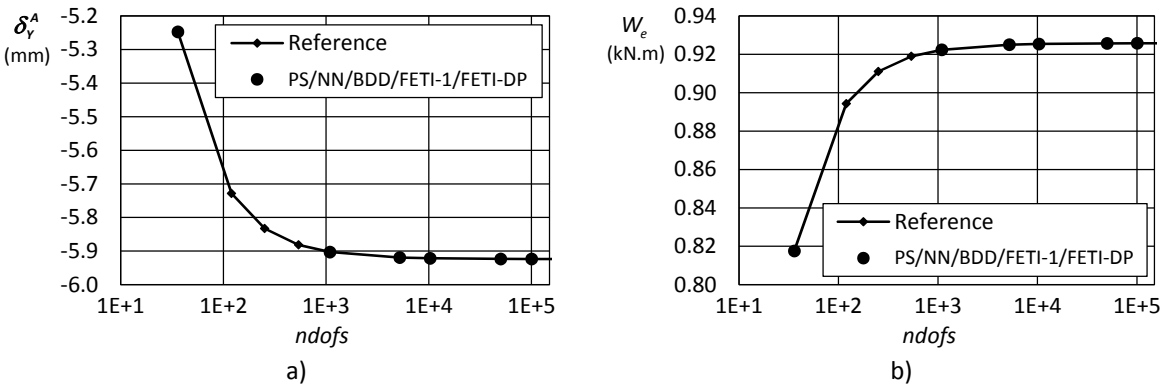

Figure V.29: Example HPC2 – Evolution of some structural response parameters for the different problem sizes considered.

As presented in Annex A, this operation requires approximately $O\left(8n^3/3\right)$ floating point operations and generally results in two full matrices and one diagonal matrix of size $n \times n$. As will be presented later in this section (Table V.15), the subdomain stiffness matrices have around 16500 and 33300 *dofs* for mesh #6 and #7, respectively. This would result in $O\left(1.19\times10^{13}\right)$ and $O\left(9.85\times10^{13}\right)$ operations and 6231 MB and 25380 MB of storage space only for the results, if the three operators are stored as full double precision matrices. Considering that each subdomain is running on a dedicated processing unit with CR of 1.6 GHz the minimum time required for this computation would be 31 min and 256 min, respectively, only for the first step of the method. Considering these figures, it was not possible and feasible to compute the SVD for these meshes with the available hardware. Nevertheless, this was not considered a key issue and the objectives for this example are not dependent on this computation.

Table V.10 and Figure V.30 present the results obtained for the condition number of the most significant structural operators. As presented in Annex A, the condition number is a singularity measure of the matrix. It also represents the sensitivity of the solution vector to variations of the *rhs* vector and is used to characterize the accuracy of the solution. Using iterative solvers, the condition number is also related to the number of iterations required to compute the solution for a given tolerance. In this work, the condition number is computed considering the Euclidean norm $\left(p=2\right)$. These values result from the ratio between the maximum and minimum singular values (see Annex A). Table V.10 also presents the information regarding the subdomains and the governing system dimension for the reduced problem.

The results show that for all DD methods the condition number presents a clear tendency to increase. The only exception is the FETI-1 method, in which the condition is small and decreases slightly. This behaviour is consistent with the expected trend. For example, the condition number is proven to be bounded by (V.102) and (V.122) when the BDD and the FETI-1 methods are used. Therefore, increasing the problem size and leaving the subdomain size unchanged, would result in an increase of the ratio H/h, and consequently, a tendency for the condition number limit to increase at a polylogarithmic rate.

It is possible to argue that the results are not comparable for different Domain Decomposition methods due to the significant differences between them, namely in terms of formulation, solving method and preconditioner. Nevertheless, the comparison between the evolutions of the condition numbers is possible, although it must be performed with caution.

Larger values for the condition number were obtained for the stiffness matrices defined for the global domain, *i.e.* without using any DD method. This gives an indication that substructuring does not automatically imply an accuracy decrease for the different problem sizes considered. The *Neumann-Neumann* method presents the highest condition numbers of all the DD methods and for all problem sizes. On the other hand, the condition number associated with the Primal Substructuring method also reaches large values and presents a higher increase rate with increasing problem sizes.

Table V.10: Example HPC2 – Results from the analyses for the influence of the problem size.

Analysis	Mesh (*ndofs*)	DD Method	Reduced Problem (RP)	*ndofs* (RP)	κ (RP)
Reference	#1 (36)	-		36	2144.9
Reference	#2 (1092)	-		1092	71870.3
Reference	#3 (5220)	-	**K**	5220	337057.5
Reference	#4 (10332)	-	Eq.: (II.111).	10332	663393.9
Reference	#6 (50232)	-		50232	3197588.0
Reference	#7 (100620)	-		100620	6394600.4
HPC2.01	#1 (36)	PS		12	266.5
HPC2.06	#2 (1092)	PS		56	1744.3
HPC2.11	#3 (5220)	PS	$\mathcal{S}$	120	3763.6
HPC2.16	#4 (10332)	PS	Eq.: (V.85).	168	5271.5
HPC2.21	#6 (50232)	PS		368	11545.9
HPC2.26	#7 (100620)	PS		520	16312.3
HPC2.02	#1 (36)	NN		12	6289.4
HPC2.07	#2 (1092)	NN		56	16668.3
HPC2.12	#3 (5220)	NN	$\mathbf{M}_{NN}^{-1}\,\mathcal{S}$	120	19728.9
HPC2.17	#4 (10332)	NN	Eqs.: (V.85), (V.88).	168	20623.0
HPC2.22	#6 (50232)	NN		368	21994.3
HPC2.27	#7 (100620)	NN		520	22384.7
HPC2.03	#1 (36)	BDD		12	6.3
HPC2.08	#2 (1092)	BDD		56	11.9
HPC2.13	#3 (5220)	BDD	$\mathbf{M}_{BDD}^{-1}\,\mathcal{S}$	120	12.7
HPC2.18	#4 (10332)	BDD	Eqs.: (V.96), (V.85).	168	13.1
HPC2.23	#6 (50232)	BDD		368	13.9
HPC2.28	#7 (100620)	BDD		520	14.2
HPC2.04	#1 (36)	FETI-1		12	738.0
HPC2.09	#2 (1092)	FETI-1		56	488.5
HPC2.14	#3 (5220)	FETI-1	$\mathbf{M}_{D}^{-1}\,\mathbf{F}$	120	461.9
HPC2.19	#4 (10332)	FETI-1	Eqs.: (V.118), (V.112).	168	456.1
HPC2.24	#6 (50232)	FETI-1		368	-
HPC2.29	#7 (100620)	FETI-1		520	-
HPC2.05	#1 (36)	FETI-DP		4	2.0
HPC2.10	#2 (1092)	FETI-DP		48	4.9
HPC2.15	#3 (5220)	FETI-DP	$\mathbf{M}_{D}^{-1}\,\mathbf{F}_{bb}^{*}$	112	6.6
HPC2.20	#4 (10332)	FETI-DP	Eqs.: (V.118), (V.148).	160	7.5
HPC2.25	#6 (50232)	FETI-DP		360	10.4
HPC2.30	#7 (100620)	FETI-DP		512	12.1

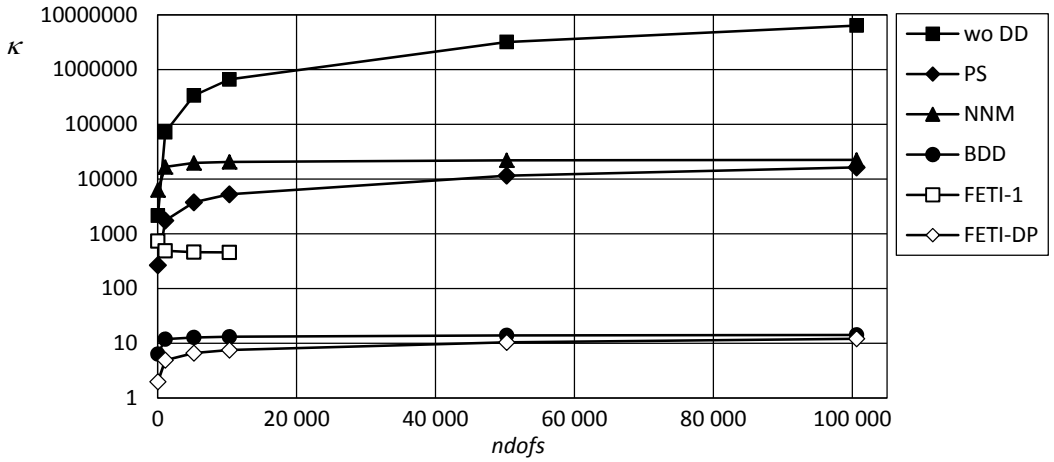

Figure V.30: Example HPC2 – Evolution of the condition number with the problem size.

From this point of view, the best results for the condition number were obtained with the preconditioned operator used for the coarse problem associated with the FETI-DP method, followed closely by the BDD method. This can be related to the fact that the FETI-DP method combines primal and dual constraints between subdomains and avoids computing the pseudoinverse and the null spaces, which are calculated using algorithms with smaller accuracy. On the other hand, although the BDD method uses the pseudoinverse and null spaces, the preconditioner directly implements a residue balancing scheme between the subdomains.

For the case of the Domain Decomposition methods that are associated with iterative solvers, the number of iterations required for convergence is presented in Table V.11 and in Figure V.31. The results include the number of iterations for all mesh densities using and not using a preconditioner. This data shows that the number of iterations required for convergence increased with the problem size for all DD methods. Higher increases occurred using the *Neumann-Neumann* method. This can be justified by the importance of the preconditioner to the convergence rate of this method, which does not have a coarse problem to propagate the residues throughout the subdomains. The BDD method also showed a large increase for the number of iterations required for convergence.

It is also possible to notice evidence that the effect of the preconditioner is more meaningful for larger problem sizes, by observing the relative increase in the number of iterations. As a conclusion, the data collected clearly confirms the importance for the convergence rate of using a preconditioner with iterative methods.

Table V.11: Example HPC2 – Influence of the preconditioners on the number of iterations required for convergence.

Analysis	Mesh (*ndofs*)	DD Met.	Preconditioner	*niter*	Preconditioner	*niter*
HPC2.02	#1 (36)	NN	Neumann-Neumann	12	No Preconditioner	12
HPC2.07	#2 (1092)	NN	Neumann-Neumann	17	No Preconditioner	39
HPC2.12	#3 (5220)	NN	Neumann-Neumann	18	No Preconditioner	58
HPC2.17	#4 (10332)	NN	Neumann-Neumann	18	No Preconditioner	70
HPC2.22	#6 (50232)	NN	Neumann-Neumann	19	No Preconditioner	109
HPC2.27	#7 (100620)	NN	Neumann-Neumann	18	No Preconditioner	128
HPC2.03	#1 (36)	BDD	Neumann-Neumann	4	No Preconditioner	7
HPC2.08	#2 (1092)	BDD	Neumann-Neumann	7	No Preconditioner	32
HPC2.13	#3 (5220)	BDD	Neumann-Neumann	8	No Preconditioner	46
HPC2.18	#4 (10332)	BDD	Neumann-Neumann	8	No Preconditioner	55
HPC2.23	#6 (50232)	BDD	Neumann-Neumann	8	No Preconditioner	86
HPC2.28	#7 (100620)	BDD	Neumann-Neumann	8	No Preconditioner	100
HPC2.04	#1 (36)	FETI-1	Dirichlet	4	No Preconditioner	5
HPC2.09	#2 (1092)	FETI-1	Dirichlet	6	No Preconditioner	15
HPC2.14	#3 (5220)	FETI-1	Dirichlet	6	No Preconditioner	22
HPC2.19	#4 (10332)	FETI-1	Dirichlet	6	No Preconditioner	24
HPC2.24	#6 (50232)	FETI-1	Dirichlet	-	No Preconditioner	-
HPC2.29	#7 (100620)	FETI-1	Dirichlet	-	No Preconditioner	-
HPC2.05	#1 (36)	FETI-DP	Dirichlet	4	No Preconditioner	4
HPC2.10	#2 (1092)	FETI-DP	Dirichlet	8	No Preconditioner	14
HPC2.15	#3 (5220)	FETI-DP	Dirichlet	8	No Preconditioner	20
HPC2.20	#4 (10332)	FETI-DP	Dirichlet	8	No Preconditioner	23
HPC2.25	#6 (50232)	FETI-DP	Dirichlet	9	No Preconditioner	31
HPC2.30	#7 (100620)	FETI-DP	Dirichlet	10	No Preconditioner	34

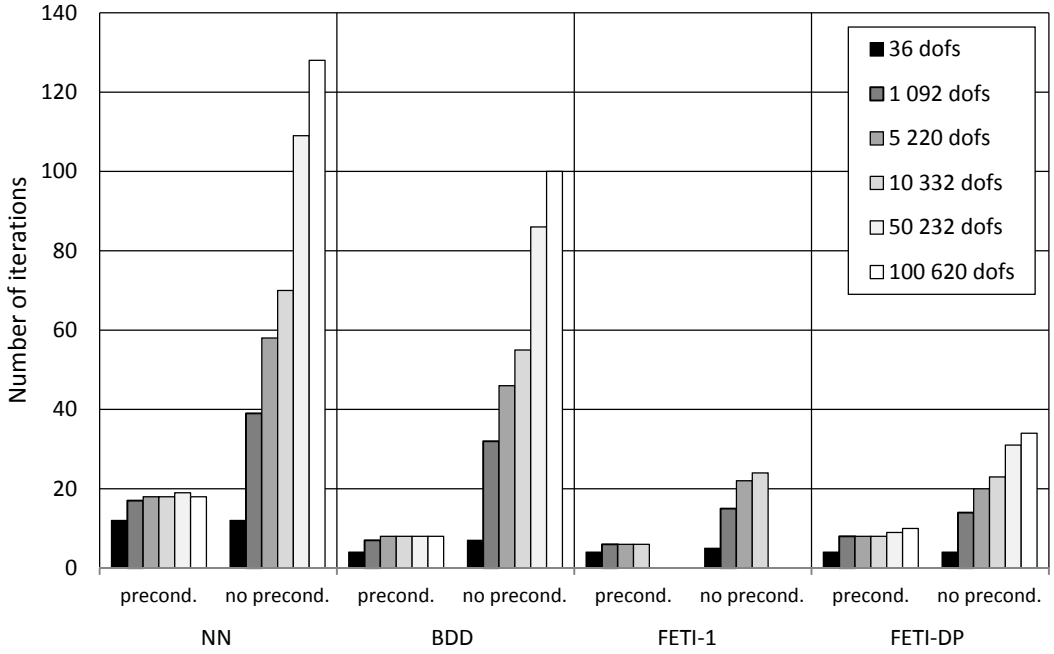

Figure V.31: Example HPC2 – Influence of the preconditioners on the number of iterations required for convergence.

This example includes a group of analyses (#31 to #50) performed to assess the effect of the number of subdomains on the accuracy and efficiency of the numeric algorithms. The same mesh density was used for these analyses (10332 *dofs*) and the number of subdomains chosen was 3, 6, 12 and 24, as presented in Figure V.32. As before, the subdomain distribution was selected in order to avoid changing the similarity of the meshes and introducing additional numerical phenomena that could influence the results (*e.g.* nodes connected to more than two subdomains). The mesh characteristics are presented in Table V.12 and the analyses included the PS, BDD, FETI-1 and FETI-DP methods. The results were compared with the data obtained using the commercial FE software *ADINA* [3]. In the analyses with the FETI-DP method, corner nodes were used to avoid having singular subdomains by constraining the *dofs* of the two nodes at the top and bottom corners of the subdomains, as represented in Figure V.32.

The results obtained are presented in Table V.13 in terms of the vertical displacement at point A and for the work done by the discrete external forces. It is possible to observe that the number of subdomains had no noteworthy influence on the numerical results of the analyses.

Table V.14 and in Figure V.33 present the condition number evolution of the reduced problem. Once again, the condition number can be used to measure the accuracy of the solution and the convergence rate when iterative methods are used to solve the governing system.

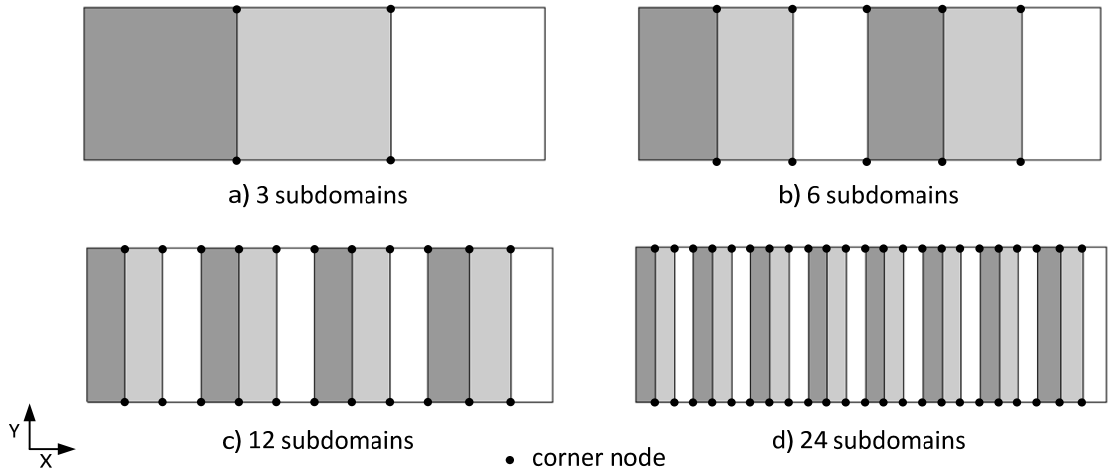

Figure V.32: Example HPC2 – Representation of the analyses used for assessing the influence of the number of subdomains.

Table V.12: Example HPC2 – Mesh characteristics of the analyses used for assessing the influence of the nº of subdomains.

Analysis	H_h (m) (*nsd*)	***ndofs***	Master ***dofs***	Subdomain interior ***dofs***
HPC2.31/35/39/43/47	1.000 (3)	10332	168	#1 & #2: 3360; #3: 3444
HPC2.32/36/40/44/48	0.500 (6)	10332	420	#1 & #5: 1680; #2 to #4: 1596; #6: 1764
HPC2.33/37/41/45/49	0.250 (12)	10332	924	#1 to #9: 756; #10 & #11: 840; #12: 924
HPC2.34/38/42/46/50	0.125 (24)	10332	1932	#1 to #21: 336; #22 & #23: 420; #24: 504

Table V.13: Example HPC2 - Results of the analyses used for assessing the influence of the number of subdomains.

Analysis	Mesh (***ndofs***)	H_h (m) (*nsd*)	DDM	$\delta_y^A\left(\boldsymbol{e}_{rel}\right)$ (m)	$W_e = -U^e\left(e_{rel}\right)$ (kN.m)
Reference	#4 (10332)	3.000 (1)	-	-5.92142e-3	4.62714e-1
HPC2.31	#4 (10332)	1.000 (3)	PS	-5.92142e-3 (0.00%)	4.62714e-1 (0.00%)
HPC2.32	#4 (10332)	0.500 (6)	PS	-5.92142e-3 (0.00%)	4.62714e-1 (0.00%)
HPC2.33	#4 (10332)	0.250 (12)	PS	-5.92142e-3 (0.00%)	4.62714e-1 (0.00%)
HPC2.34	#4 (10332)	0.125 (24)	PS	-5.92142e-3 (0.00%)	4.62714e-1 (0.00%)
HPC2.35	#4 (10332)	1.000 (3)	NN	-5.92142e-3 (0.00%)	4.62714e-1 (0.00%)
HPC2.36	#4 (10332)	0.500 (6)	NN	-5.92142e-3 (0.00%)	4.62714e-1 (0.00%)
HPC2.37	#4 (10332)	0.250 (12)	NN	-5.92142e-3 (0.00%)	4.62714e-1 (0.00%)
HPC2.38	#4 (10332)	0.125 (24)	NN	-5.92142e-3 (0.00%)	4.62714e-1 (0.00%)
HPC2.39	#4 (10332)	1.000 (3)	BDD	-5.92142e-3 (0.00%)	4.62714e-1 (0.00%)
HPC2.40	#4 (10332)	0.500 (6)	BDD	-5.92142e-3 (0.00%)	4.62714e-1 (0.00%)
HPC2.41	#4 (10332)	0.250 (12)	BDD	-5.92142e-3 (0.00%)	4.62714e-1 (0.00%)
HPC2.42	#4 (10332)	0.125 (24)	BDD	-5.92142e-3 (0.00%)	4.62714e-1 (0.00%)
HPC2.43	#4 (10332)	1.000 (3)	FETI-1	-5.92142e-3 (0.00%)	4.62714e-1 (0.00%)
HPC2.44	#4 (10332)	0.500 (6)	FETI-1	-5.92142e-3 (0.00%)	4.62714e-1 (0.00%)
HPC2.45	#4 (10332)	0.250 (12)	FETI-1	-5.92142e-3 (0.00%)	4.62714e-1 (0.00%)
HPC2.46	#4 (10332)	0.125 (24)	FETI-1	-5.92142e-3 (0.00%)	4.62714e-1 (0.00%)
HPC2.47	#4 (10332)	1.000 (3)	FETI-DP	-5.92142e-3 (0.00%)	4.62714e-1 (0.00%)
HPC2.48	#4 (10332)	0.500 (6)	FETI-DP	-5.92142e-3 (0.00%)	4.62714e-1 (0.00%)
HPC2.49	#4 (10332)	0.250 (12)	FETI-DP	-5.92142e-3 (0.00%)	4.62714e-1 (0.00%)
HPC2.50	#4 (10332)	0.125 (24)	FETI-DP	-5.92142e-3 (0.00%)	4.62714e-1 (0.00%)

Making the same reservations regarding the comparison of results from different *Domain Decomposition* techniques, it is possible establish the following conclusions. As expected, the *Neumann-Neumann* (NN) method presents the higher condition number and high increase rates when the number of subdomains are increased. This result is expected because, as mentioned in section 2.6.3, this method lacks a coarse problem to distribute the residue throughout the subdomains. The number of iterations required to achieve convergence in the PCG method (1909 out of 1932 when 24 subdomains are adopted) is a clear demonstration of the convergence difficulties and of the inefficiency of this method when a large number of subdomains is considered. The *Primal Substructuring* (PS) method also presented a high condition number, although much lower than the *Neumann-Neumann* method and with lower increase rate when the number of subdomains are increased. For this method, the number of iterations is not displayed because a direct method was used to solve the system of equations. Once again, the best performance from this point of view was achieved by the *Balancing Domain Decomposition* (BDD) and by the *Dual-Primal Finite Element Tearing and Interconnecting* (FETI-DP) methods, probably due to the same reasons presented for the analysis of the problem-size influence. The number of iterations required to achieve convergence shows the same behaviour. This number always increases with the number of subdomains and the worst performance was clearly obtained with the *Neumann-Neumann* method.

In conclusion, considering the results from the tests, it is possible to state that all *Domain Decomposition* methods were able to compute the solution of the problem without major difficulties. Nevertheless, the efficiency of the algorithm tends to decrease when the problem size and the number of subdomains increase.

Table V.14: Example HPC2 – Example HPC2 - Results from the analyses for the influence of the number of subdomains.

Analysis	H_n (m) (*nsd*)	**DDM**	**Reduced Problem (RP)**	***ndofs* (RP)**	κ **(RP)**	***niter***
HPC2.31	1.000 (3)	PS		168	5271.5	-
HPC2.32	0.500 (6)	PS	$\mathcal{S}$	420	15287.4	-
HPC2.33	0.250 (12)	PS	Eq.: (V.85).	924	35350.4	-
HPC2.34	0.125 (24)	PS		1932	76024.8	-
HPC2.35	1.000 (3)	NN		168	20623.0	18
HPC2.36	0.500 (6)	NN	$\mathbf{M}_{NN}^{-1}\,\mathcal{S}$	420	1232936.9	42
HPC2.37	0.250 (12)	NN	Eqs.: (V.85); (V.88).	924	152290443.3	191
HPC2.38	0.125 (24)	NN		1932	38757848403.2	1909
HPC2.39	1.000 (3)	BDD		168	13.1	8
HPC2.40	0.500 (6)	BDD	$\mathbf{M}_{BDD}^{-1}\,\mathcal{S}$	420	64.1	12
HPC2.41	0.250 (12)	BDD	Eqs.: (V.96), (V.85).	924	370.5	22
HPC2.42	0.125 (24)	BDD		1932	5437.0	66
HPC2.43	1.000 (3)	FETI-1		168	456.1	6
HPC2.44	0.500 (6)	FETI-1	$\mathbf{M}_{D}^{-1}\,\mathbf{F}$	420	2478.4	11
HPC2.45	0.250 (12)	FETI-1	Eqs.: (V.118), (V.112).	924	72191.4	42
HPC2.46	0.125 (24)	FETI-1		1932	4029150.1	273
HPC2.47	1.000 (3)	FETI-DP		160	7.5	8
HPC2.48	0.500 (6)	FETI-DP	$\mathbf{M}_{D}^{-1}\,\mathbf{F}_{bb}^{*}$	400	33.0	16
HPC2.49	0.250 (12)	FETI-DP	Eqs.: (V.118), (V.148).	880	924.7	53
HPC2.50	0.125 (24)	FETI-DP		1840	53903.4	347

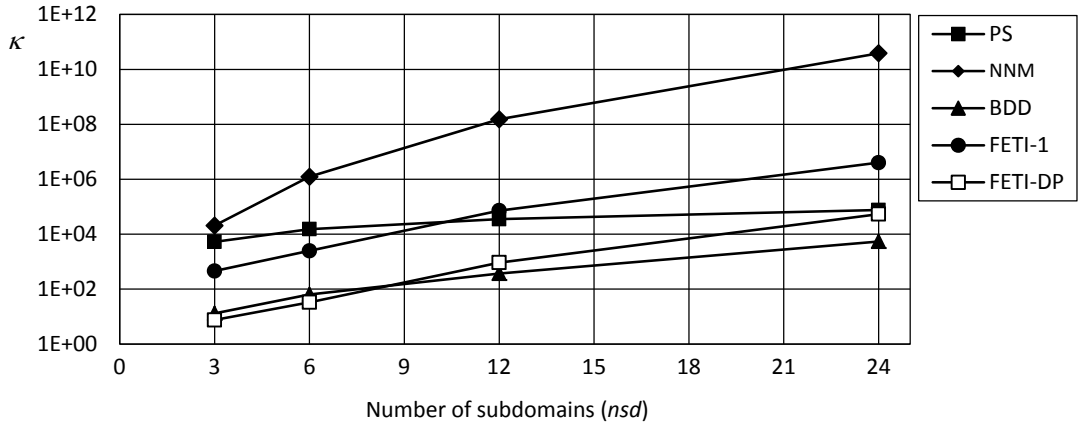

Figure V.33: Example HPC2 – Evolution of the condition number with the number of subdomains.

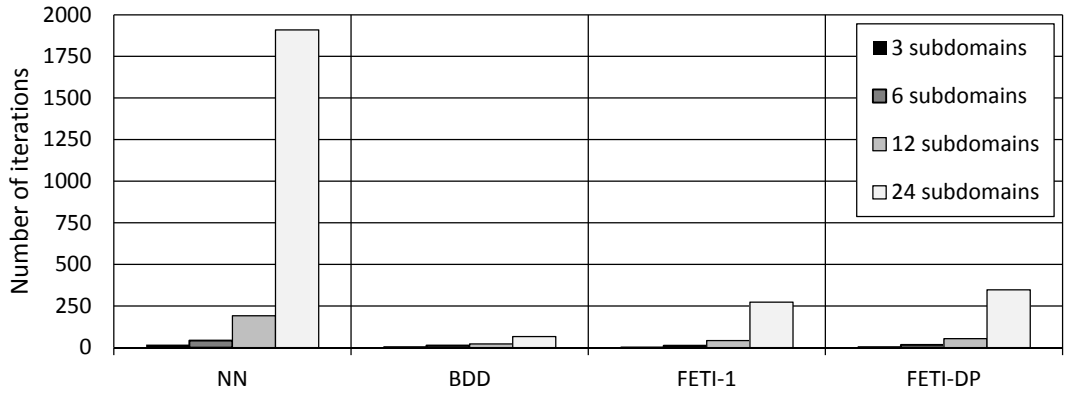

Figure V.34: Example HPC2 – Evolution of the number of iterations with the number of subdomains.

- Static Analyses: Computational performance of the PS method for different problem sizes

The natural subsequent analysis regarding the performance of the *Domain Decomposition* methods is to assess the computational performance in terms of the computing time. This represents a difficult and demanding task, because it is necessary to control some hardware and software related issues in order to obtain meaningful results.

In terms of hardware, it is necessary to have a computer using multiple processing units and to be aware of their operating characteristics, regarding processing, memory access and other aspects that could influence the performance. Regarding these issues, the validation example HPC1 gave important information regarding the working conditions of the computer used in this work (see Table V.3 and Table V.4 for more details).

In terms of software, it is required to understand some basic aspects about the *Operating System* (OS), such as how the *queue scheduler* works and possible ways to mitigate the uncertainties related to having system or secondary processes using significant computing resources, which could compromise the overall performance. Modern operating systems implement a complex scheduling

procedure that often results from a combination of different algorithms, which consider the order of arrival of the processes, the time remaining to complete each task, the statically and dynamically assigned priority, *etc*. [63, 565]. The process static priority can be used to mitigate the perturbations on the performance by other processes and achieve a more efficient, predictable and stable computing time. This property can be easily changed in *Windows* using the *task manager* tool or using shell commands in *Linux*.

Another possibility to control the process execution is to set the *processor affinity* or in other words to set the allowed or preferred processing unit, or group of processing units, that are allowed to execute the computations of the process. By default, a process can be executed in any processor available. Using this possibility could result in a more efficient system due to cache memory reuse [564] and in a more comprehensible behaviour. However, in the general case this may result in a more rigid response and lead to longer computing times. Additionally, most unnecessary processes and services were stopped to reduce the interference probability, leading to an operating level convenient for the performance analysis.

In this work, all processes related to the computation (*Matlab's Client Session*, *Matlab workers*, and the *spmd* and *mpiexec* processes) were executed with high priority levels. The processor affinity of the processes was left unchanged. Consequently, the processes can run on any of the available processing units. Furthermore, all computations were made after a warm-up computation that tried to set similar operating conditions for all the runs made. This is important because of the clock speed dynamic changes associated with Intel's *Turbo Boost* technology implemented on the CPU used (see validation example HPC1 for more details).

Also related to the software, the FE code and the implementation of the *Primal Substructuring* (PS) method were carefully written and optimized in order to produce consistent and representative results regarding the efficiency of the model. A significant effort would be required to set the other DD methods to the required level of optimization. This was the reason why only analyses using the PS method are presented. Taking into consideration that the comparison between the performances of different DD methods is not the main objective of this thesis, the performance analysis will be restricted to the PS method.

The performance analysis was made using the computation of a single time step increment, which led to only one iteration because linear materials were used. No computations associated with the pre-processing, post-processing phases or to the initialization of processing stage were included in this analysis. This choice can be considered as misleading for the overall performance. However, the main two reasons that led to this decision are easily understandable. Firstly, the final goal of this work is to compute incremental dynamic analyses, whose efficiency is strongly related to the performance of the incremental procedure. Secondly, pre-processing and processing initializations are more affected by the overheads associated with the *Matlab* computing environment. The inclusion of these phases in the overall results would produce heterogeneous results because of the distorted relative weight of the high-level data creation and management implemented in Matlab, when compared to the main core computations.

The characteristics of the analyses are presented in Table V.15. A total of 30 analyses were performed by changing the problem size from around 1000 to 100000 *dofs* and by running the following five computing cases: 1 subdomain using the sequential version of the code and 1 to 4 subdomains with the parallel version. It is important to emphasize that, even if the sequential version of the code runs completely using a single process on the *Matlab Client Session*, this version of the code is prepared to run either sequentially or in parallel. Therefore, there is some overhead regarding code restructuring and data reorganization in order to have the parallelization capacity.

Table V.15: Example HPC2 – Characteristics of the analyses made to assess the performance of the DD methods.

Analysis	Mesh (ndofs)	H_h (m) (*nsd*)	Master *dofs*	Slave *dofs*: sd#1,sd#2,...	DD	Algorithm
HPC2.51	#2 (1092)	3.00 (1)	-	1092	PS	Sequential
HPC2.52	#2 (1092)	3.00 (1)	-	1092	PS	Parallel
HPC2.53	#2 (1092)	1.50 (2)	28	532, 532	PS	Parallel
HPC2.54	#2 (1092)	1.00 (3)	56	336, 336, 364	PS	Parallel
HPC2.55	#2 (1092)	0.75 (4)	84	252, 252, 224, 280	PS	Parallel
HPC2.56	#3 (5220)	3.00 (1)	-	5220	PS	Sequential
HPC2.57	#3 (5220)	3.00 (1)	-	5220	PS	Parallel
HPC2.58	#3 (5220)	1.50 (2)	60	2580, 2580	PS	Parallel
HPC2.59	#3 (5220)	1.00 (3)	120	1680, 1680, 1740	PS	Parallel
HPC2.60	#3 (5220)	0.75 (4)	180	1260, 1260, 1200, 1320	PS	Parallel
HPC2.61	#4 (10332)	3.00 (1)	-	10332	PS	Sequential
HPC2.62	#4 (10332)	3.00 (1)	-	10332	PS	Parallel
HPC2.63	#4 (10332)	1.50 (2)	84	5124, 5124	PS	Parallel
HPC2.64	#4 (10332)	1.00 (3)	168	3360, 3360, 3444	PS	Parallel
HPC2.65	#4 (10332)	0.75 (4)	252	2520, 2520, 2436, 2604	PS	Parallel
HPC2.66	#5 (20532)	3.00 (1)	-	20532	PS	Sequential
HPC2.67	#5 (20532)	3.00 (1)	-	20532	PS	Parallel
HPC2.68	#5 (20532)	1.50 (2)	118	10148, 10226	PS	Parallel
HPC2.69	#5 (20532)	1.00 (3)	236	6726, 6726, 6844	PS	Parallel
HPC2.70	#5 (20532)	0.75 (4)	354	5074, 4956, 5074, 5074	PS	Parallel
HPC2.71	#6 (50232)	3.00 (1)	-	50232	PS	Sequential
HPC2.72	#6 (50232)	3.00 (1)	-	50232	PS	Parallel
HPC2.73	#6 (50232)	1.50 (2)	184	25024, 25024	PS	Parallel
HPC2.74	#6 (50232)	1.00 (3)	368	16560, 16560, 16744	PS	Parallel
HPC2.75	#6 (50232)	0.75 (4)	552	12328,12512,12328,12512	PS	Parallel
HPC2.76	#7 (100620)	3.00 (1)	-	100620	PS	Sequential
HPC2.77	#7 (100620)	3.00 (1)	-	100620	PS	Parallel
HPC2.78	#7 (100620)	1.50 (2)	260	50180, 50180	PS	Parallel
HPC2.79	#7 (100620)	1.00 (3)	520	33280, 33280, 33540	PS	Parallel
HPC2.80	#7 (100620)	0.75 (4)	780	24960,24960,24700,25220	PS	Parallel

Table V.16: Example HPC2 – Measured computing times for different problem sizes and levels of parallelization.

ndofs	Sequential (s)	Parallel 1 sd (s)	Parallel 2 sd (s)	Parallel 3 sd (s)	Parallel 4 sd (s)
1092	0.497	1.063	1.424	1.701	1.823
5220	3.079	4.058	3.489	3.350	3.408
10332	9.289	10.794	6.377	6.227	5.786
20532	33.649	37.293	18.410	14.796	12.366
50232	188.395	196.188	83.502	62.014	47.377
100620	693.078	712.324	288.175	197.276	144.175

The computing times obtained in the analyses are presented in Table V.16. This data results from the average of at least five valid runs. Despite the measures taken to reduce this problem, a small amount of analyses presented an elapsed time with a significant variation from the rest of the runs. These cases were easily identified due to the large variations in the computing time (*e.g.* sometimes more than 100% longer) and clearly resulted from interference of other processes or from losing priority in the scheduler. The valid runs presented an extremely low variation for each analysis type. The mean *relative standard deviation*, defined by the ratio between the standard deviation and the arithmetic mean, was 0.888% with a maximum of 2.297% for all cases, which clearly demonstrates the consistency of these measurements.

A clearer analysis of these results can be made by observing Figure V.35, which presents the same information shown in Table V.16 but in this case normalized by the elapsed time for the run with the sequential code (one subdomain). It is possible to conclude that the analyses with 1092 *dofs* were found to be insufficient to potentiate the advantages of the parallelization, or in other words, the gains from parallelizing the computations are small and insufficient to compensate for the inherent overhead (*e.g.* sending and receiving data from and to the workers). As a matter of fact, the computing time increased with the number of subdomains. This is expected because the number of *dofs* associated with the subdomains decreases with the increase in the number of subdomains (see Table V.15).

With the exception of the smaller problem size, all the other results showed a very consistent pattern. The runs with one subdomain and using the parallelized algorithm revealed a small increase in computing time (between 31.8% for 5220 *dofs* and 2.8 % for 100620 *dofs*). It should be emphasized that for the mesh with 5220 *dofs*, the parallelization already exhibited the tendency of reducing the computing time. However this effect is still small and insufficient to compensate for the

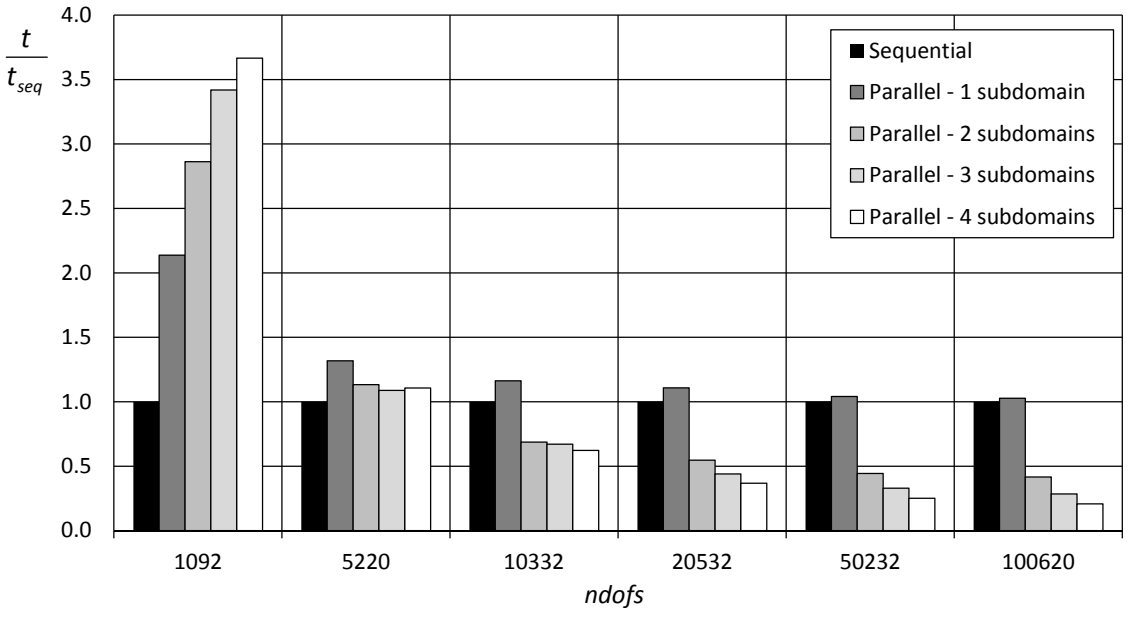

Figure V.35: Example HPC2 - Normalized measured computing times for different problem sizes and levels of parallelization.

overhead and reduce the total computing time from the sequential analysis. For the remaining cases, increasing the number of subdomains led to a gradual computing time reduction and the highest efficiency was obtained with the highest levels of parallelization tested. To assess the efficiency of the parallelization, Table V.17 and Figure V.36 present the *concurrent* speed-up and efficiency, which for this homogenous system can be computed from equations (V.3) and (V.4), respectively. These results confirms that for the meshes with 1092 and 5220 *dofs,* the parallelization does not introduce any advantage in terms of computing time and is associated with speed-up values smaller than one. For the other analyses the speed-up and the efficiency values clearly confirm the consistency of the performance gains with increasing number of subdomains, The results are close to linear scalability and even higher for the larger problem sizes (up to 120% efficiency).

At this stage, it is important to emphasize that, contrary to the situation discussed in section 2.1.10, the computations to be executed change significantly when moving from the sequential to the parallel version of the code, thus explaining the super linear speed-up results. Possible examples are all the changes reported for the structural analysis algorithm (see sections 2.6 and 4.3).

Another aspect that must be taken into consideration is the clock speed changes in the CPU installed in the computer used. This problem was addressed in section 2.1.2 and studied in the benchmark example HPC1. These tests revealed that for intensive computations associated with 1, 2, 3 and 4 subdomains, *i.e.* with active processing units, the clock speed can be characterized by the values $\{2.80;2.20;1.60;1.60\}$ GHz respectively, which leads to the following values of the correction factors $\gamma=\{1.000;0.786;0.571;0.571\}$.

Considering fully intensive computations on the active processing units may not be representative of the actual processing state and may lead to deviations with regard to the performance analysis. This is because the code is partially executed at the Matlab client session and at the worker sessions. The changes of computation profile can be easily observed by the variations of the processing unit activity levels using a monitoring tool (*e.g. Task Manager* under *Windows*), and also, by observing the fan speed changes used to cool down the processor. The impact of this issue is difficult to assess and

Table V.17: Example HPC2 – Speed-up and efficiency of the parallelized algorithm.

nsd	1092 *dofs*	5220 *dofs*	10332 *dofs*	20532 *dofs*	50232 *dofs*	100620 *dofs*
1	0.47 (47%)	0.76 (76%)	0.86 (86%)	0.90 (90%)	0.96 (96%)	0.97 (97%)
2	0.35 (17%)	0.88 (44%)	1.46 (73%)	1.83 (91%)	2.26 (113%)	2.41 (120%)
3	0.29 (10%)	0.92 (31%)	1.49 (50%)	2.27 (76%)	3.04 (101%)	3.51 (117%)
4	0.27 (7%)	0.90 (23%)	1.61 (40%)	2.72 (68%)	3.98 (99%)	4.81 (120%)

Table V.18: Example HPC2 – Corrected speed-up and efficiency of the parallelized algorithm.

nsd	1092 *dofs*	5220 *dofs*	10332 *dofs*	20532 *dofs*	50232 *dofs*	100620 *dofs*
1	0.47 (47%)	0.76 (76%)	0.86 (86%)	0.90 (90%)	0.96 (96%)	0.97 (97%)
2	0.41 (20%)	1.03 (51%)	1.70 (85%)	2.13 (107%)	2.63 (132%)	2.81 (140%)
3	0.41 (14%)	1.29 (43%)	2.09 (70%)	3.19 (106%)	4.26 (142%)	4.92 (164%)
4	0.38 (10%)	1.27 (32%)	2.25 (56%)	3.81 (95%)	5.57 (139%)	6.73 (168%)

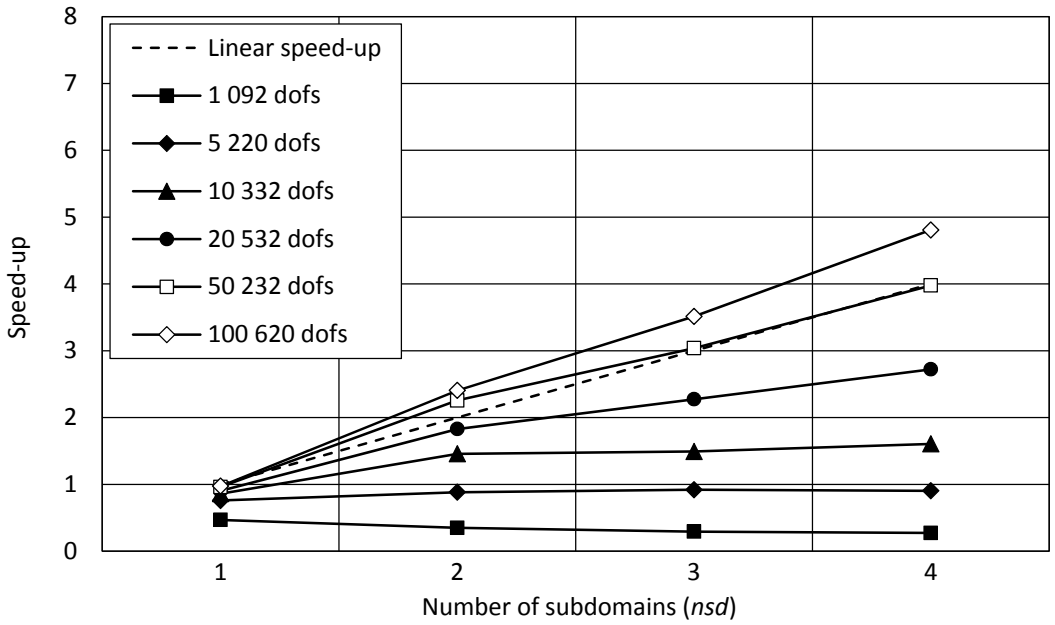

Figure V.36: Example HPC2 – Speed-up values of the parallelised incremental algorithm.

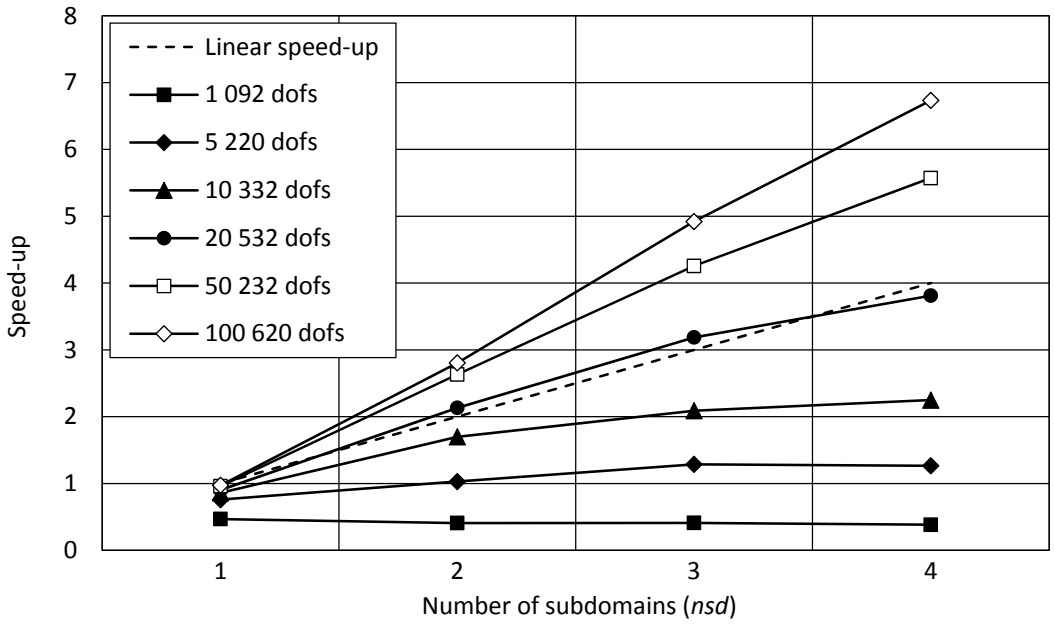

Figure V.37: Example HPC2 – Corrected speed-up values of the parallelised incremental algorithm.

reproduce with mathematical well-founded expressions. Consequently, a subjective approach was used based on monitoring the activity of the processes. It was considered that only during 2/3 of the total computing time is the computation executed at the Matlab workers, which can be associated with fully intensive computations. This hypothesis results in reducing the correction factors by using $\alpha = 2/3$ in the expression:

$$\gamma^* = 1 + \alpha\left(\gamma - 1\right), \tag{V.219}$$

resulting in the new correction factors: $\gamma^* = \{1.000; 0.857; 0.714; 0.714\}$. Table V.18 and Figure V.37 present the concurrent speed-up and efficiency values corrected by these new factors. As a result, these quantities increased when two to four subdomains were used, reaching speed-up and efficiency values of 6.73 and 168% for the largest problem size and using four subdomains. These results will be analysed after introducing the partial computing time for different code segments.

Figure V.38 presents a plot showing the measured computing times *vs.* the average number of the subdomain interior *dofs*. These two parameters should present a strong correlation as a result of the data parallelism approach used (see section 2.1.8), which results in computing times governed by the size and balance of the partitioned problems. The results displayed in Figure V.38 confirm this supposition. The regression line plotted in that figure was found by fitting a second order polynomial to the data set using a least-squares approach. It is possible to observe a relatively small dispersion between the regression line and the measured data and to conclude that the second order polynomial fits the data very well, as evidenced by the value close to unity of the R^2 value, which is a correlation parameter that measures the goodness of the fit.

Similarly to what was done previously, the measured computing time was corrected using the factors γ^*, resulting in the data displayed in Figure V.39. From the analysis of this figure, it is possible to extract the following two conclusions: Firstly, it can be seen that the overall dispersion of the computing times for similar number of *dofs* decreased. It is clear that the corrections made to the computing times lead to more consistent results. Secondly, the dispersion associated with the polynomial regression also decreased and the goodness of the fit measured by the R^2 parameter increased from 0.982 to 0.995, which can be considered as very good results.

The main reason for analysing these two parameters was to support the conclusion that the number of subdomains, and consequently the number of interior *dofs*, should not be set in such a way that the subdomains are associated with a large number of interior *dofs*, because the computing time tends to increase at a quadratic rate. On the other hand, in this example it was also clearly observed that, if this number is too small, the gains from substructuring diminish or even vanish. As a result, the discretization (problem size) and the number of subdomains must be chosen taking these two constraints into consideration. From the experience obtained in this work, it seems that good values for the number of subdomain interior *dofs* may vary between 5000 and 20000, because this way the gains from parallelizing the code are already present and the total computing times are not too large.

To improve the knowledge regarding the behaviour and the consequences for the computational performance of using substructuring, the following paragraphs address the analysis of different code segments from a typical FE algorithm. The incremental procedure was divided into the following four sections: i) *Stiffness Matrix*; ii) *Corrector*; iii) *Unbalanced Forces*; and iv) *Other*. The segment for computing the stiffness matrix includes computing the element stiffness matrices and assembling the global or subdomain stiffness matrices. The *Corrector* segment includes the procedure used to find the iterative correction of the discrete displacements in order to try reducing the unbalanced forces. Moreover, computing the unbalanced forces includes the prior computations for the element's

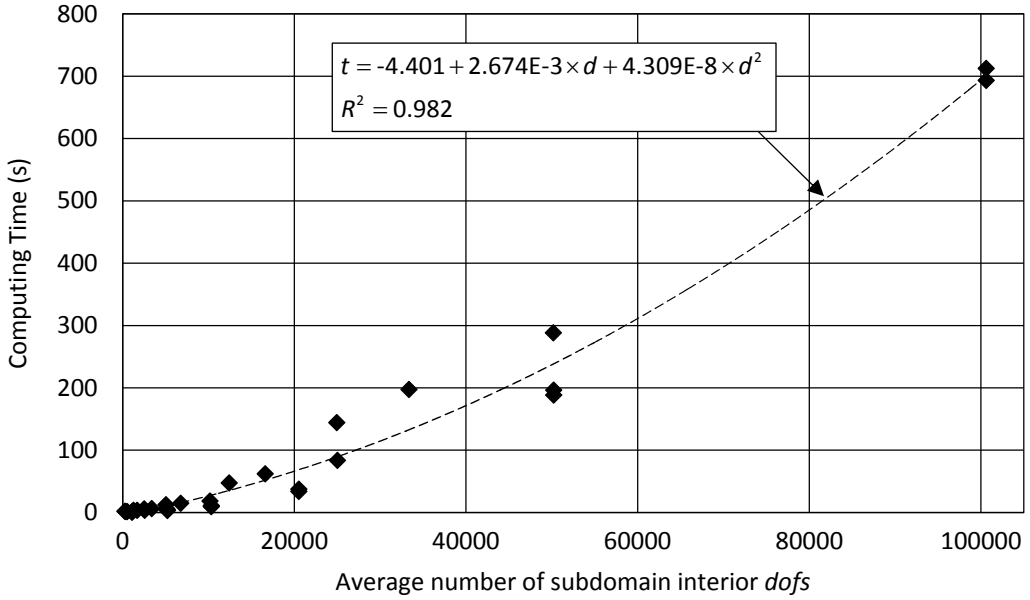

Figure V.38: Example HPC2 – Relation between the computing time and the average number of interior *dofs.*

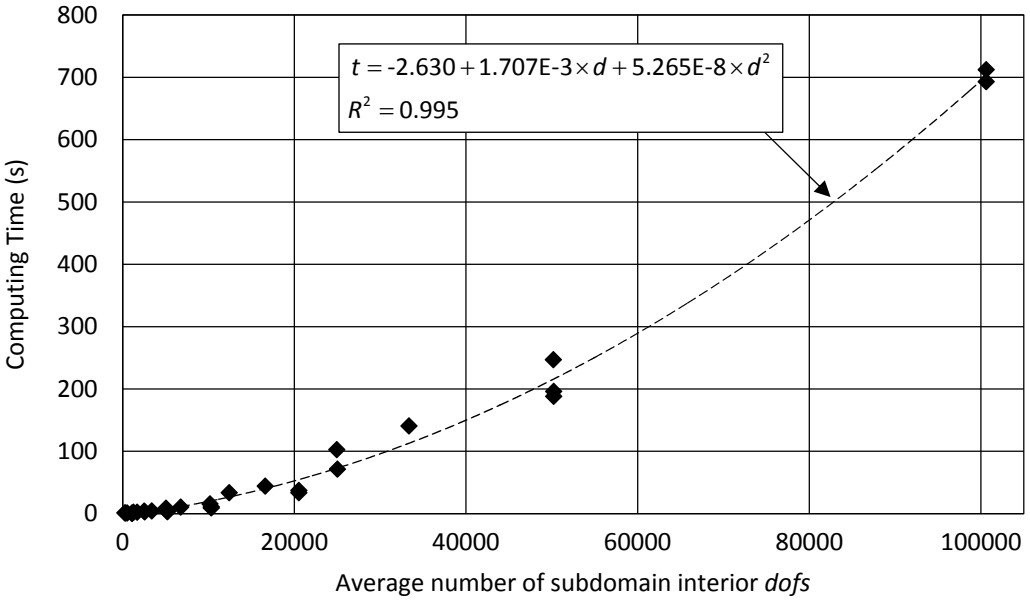

Figure V.39: Example HPC2 – Relation between the corrected computing time and the average number of interior *dofs.*

strains, state determination, stresses, and finally, the global or subdomain internal forces. The *Other* segment includes the time step initialization, computing the applied external forces, retrieving and saving variables, and the auxiliary computations associated with ending the time step.

Figure V.40 presents the percentage of computing time spent on each code segment for the different problem sizes considered. The data presented led to the following conclusions:

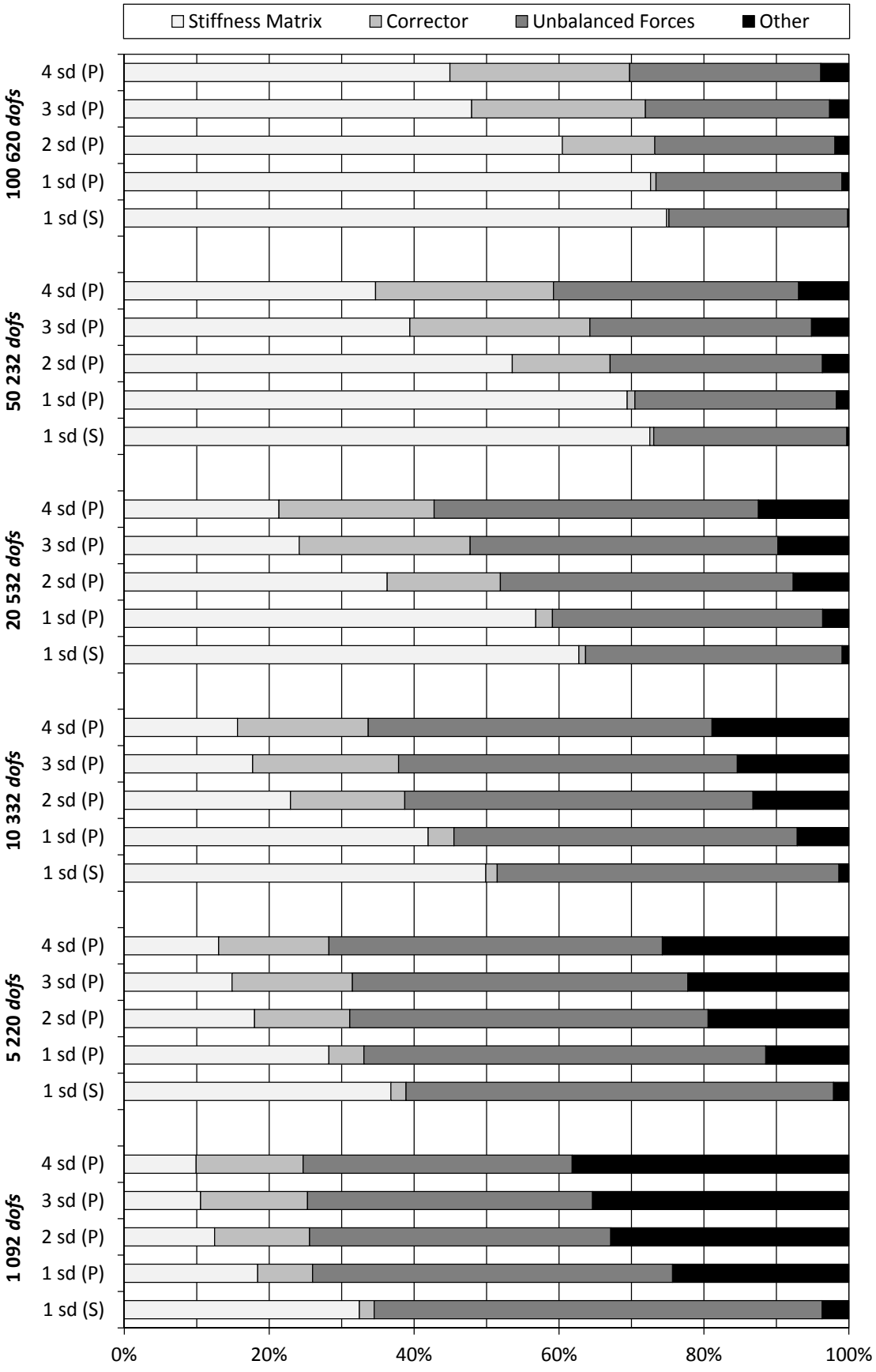

Figure V.40: Example HPC2 – Percentage of computing time for different code segments.

Firstly, the overall weight increase of the computation associated with the stiffness matrix with increasing problem sizes can be seen. On the other hand, the *other* segment reduces its percentage for larger problem sizes. This is expected because the computations included in the *other* segment are much less sensitive to the problem size. The remaining two segments roughly maintain their relative weight in the analyses.

Secondly, when comparing the analyses without substructuring (both using the sequential and the parallel codes), to the analyses with substructuring, it is easy to observe that the percentage of computing time increases greatly for the corrector segment and tends to decrease for the stiffness matrix segment. This is a fundamental aspect for the algorithm performance and deserves an in-depth analysis. The first issue to be noted is that for the substructured analysis the corrector phase is completely different and more complex. For the analyses performed with only one subdomain, the corrector segment corresponds basically to the solution of the linearized system of equations using a direct method. On the other hand, using the *Primal Substructuring* method requires the previous computation of the subdomains and of the global *Schur Complements* (V.81). Additionally, when there is only one domain, the assemblage of the operator to be used in the corrector phase is made in a single step and outside this code segment (mainly at the *stiffness matrix* segment). On the other hand, when substructuring is used, the structural operators, such as the stiffness matrix, are first assembled at the subdomain level and only in the corrector segment are joined together for computing the reduced problem. Therefore, it is possible to conclude that for multi-domain computations there is load transference to the corrector phase and that the computing times are not just a matter of parallelization efficiency, but result from using different solving schemes.

It is also possible to observe from Figure V.40 that the segment *unbalanced forces* maintains roughly its relative weight. This is related to the fact that most of the computations associated with this segment are performed at the element level and with good conditions for scalability, therefore maintaining their relative weight. Furthermore, for the parallel version of the code, the segment *Other* presents a tendency of increasing its relative weight with increasing number of subdomains. This is expected because using the parallel version of the code results in a large overhead for the tasks associated with this segment (*e.g.* retrieving the unknowns from the Matlab workers for ending the time step). Additionally, in this segment there are several tasks that are executed in the Matlab client session, therefore, without the possibility to scale with the number of subdomains (*e.g.* storing the unknowns on hard disk and ending the time step).

To confirm the observations made in the previous paragraph, Figure V.41 and Figure V.42 present the computing times for the analysis with 100620 *dofs*, obtained for the different code segments and the computing times normalized by the analysis made using the sequential version of the code. In both cases, it is confirmed that the computing time associated with the *Other* segment increases its computing time using the parallel code and stays relatively constant independently of the number of subdomains. Similarly, it is possible to confirm that the time elapsed in the *Unbalanced Forces* segment tends to scale linearly. This is quite evident in the normalized times of around $\left(1/2; 1/3; 1/4\right)$ for $\left(2; 3; 4\right)$ subdomains (see Figure V.42).

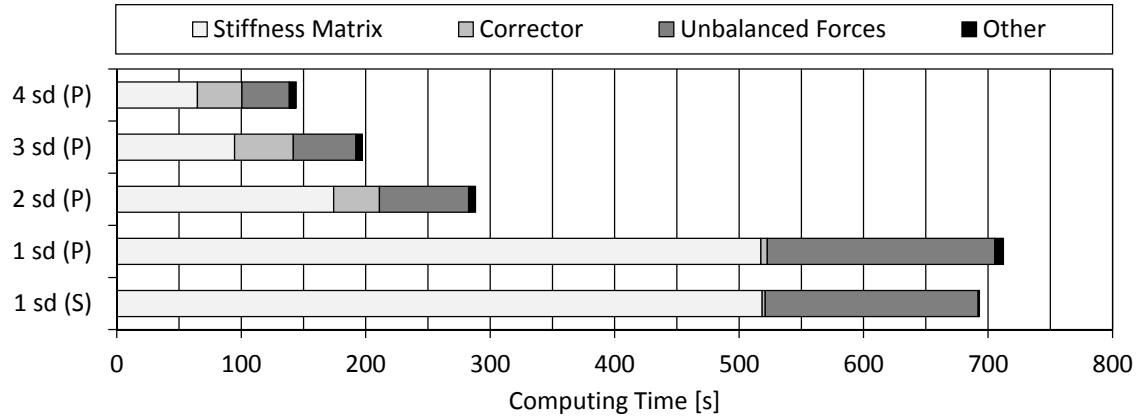

Figure V.41: Example HPC2 – Computing times of different code segments for the analysis with 100620 *dofs*.

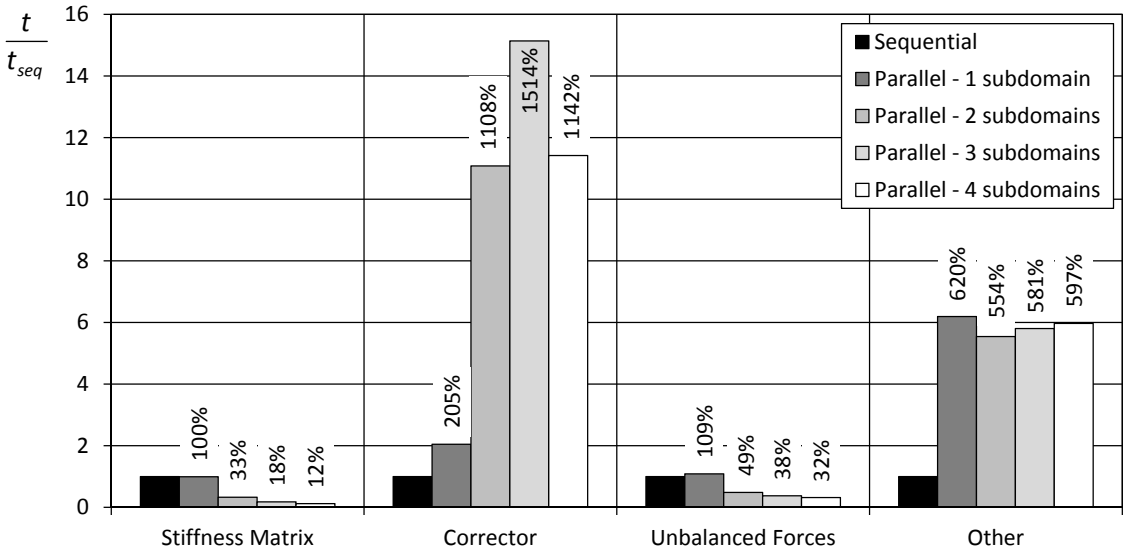

Figure V.42: Example HPC2 – Computing times normalized by the sequential computing time for the analysis with 100620 *dofs*.

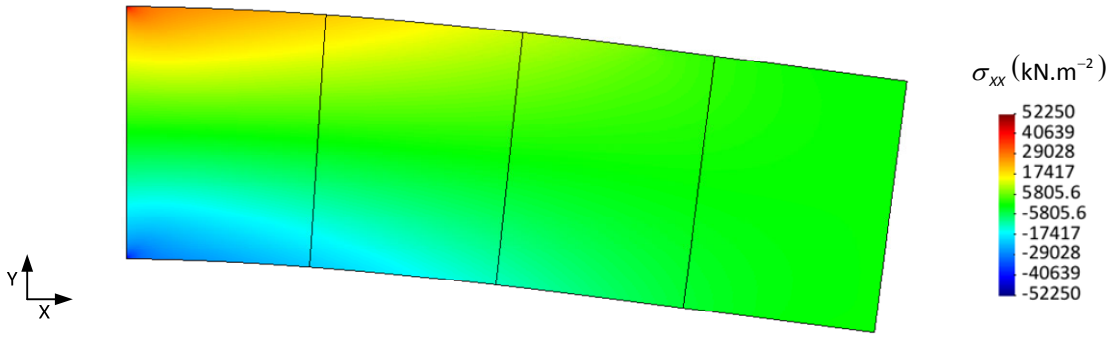

Figure V.43: Analysis HPC2.80 – Deformed mesh (magnified by 50) and stress field σ_{xx} (100620 *dofs*).

These figures also confirm the large increase in the *Corrector* segment and the large decrease in the stiffness matrix segment for the analyses with substructuring. The normalized percentage of this last segment presented in Figure V.42 clearly shows a super linear behaviour and an increase in the corrector segment of more than 10 times. The larger relative weight associated with the computation of the stiffness matrix in the incremental algorithm led to the overall super linear speed-up values measured for the larger problem sizes and for the highest levels of parallelization.

It is important to mention that these analyses were developed in a simple computer using several processing units and a *shared* memory system. As a result, the memory access is made locally and does not require external communication, which would increase the total computing time and decrease the speed-up levels measured in this work. Although, supercomputers are becoming more and more accessible to engineering, it is also true that powerful workstations are also becoming popular. Nowadays, it is possible to have workstations with 48 PUs (4 processors with 12 cores) and more than 100 GB of RAM accessed through several memory buses. This type of solution turns out to be a competitive alternative for performing structural analyses with substructuring.

Figure V.43 presents the stress field σ_{xx} on the deformed mesh for the analysis with 4 subdomains and 49923 elements (HPC2.80). In this figure it is possible to confirm that the kinematic and stress fields do not present any perturbation related to the use of substructuring.

Even though, the *Primal Substructuring* method is the only *Domain Decomposition* method assessed for the computational performance, from the experience gained for the accuracy and efficiency analyses made in this example, it is possible to stress that computing the null space and the pseudoinverse of a matrix is a demanding computational task because this requires computing full SVD decompositions, which for large matrices may become prohibitive. This is the case of the *Neumann-Neumann*, *Balancing Domain Decomposition* and FETI-1 methods. However, the latter algorithm presents a more significant disadvantage because these operations are applied to the subdomains matrices (V.108), instead of the reduced problem matrices as in the other two methods (V.88) and (V.96). This matrix size difference results in a very significant increase in the necessary computing time and memory demand to calculate the full SVD decomposition.

- Modal Analyses: Accuracy using the Guyan Reduction method

The validation example HPC2 includes an assessment for the accuracy of modal analyses using the *Guyan Reduction* (GR) method. Table V.19 lists the characteristics of the computations that differ by the nodes considered as boundary and by using a mass scaling procedure (see Figure V.44). Mass scaling was introduced in the analyses HPC2.83 and HPC2.85 to compensate for the mass not included in the model due to being associated with internal nodes. Additionally, in the analyses HPC2.84 and HPC2.85, the three nodes on the rightmost edge of the mesh were forced to be considered as boundary *dofs*, even though they do not belong to any subdomain interface (see Figure V.44). The objective is to improve the representativeness of the simulation using the GR method. Furthermore, lumped mass matrices were used in all the analyses.

Table V.19: Example HPC2 – Characteristics of the modal analyses.

Analysis	H_h [m](*nsd*)	**DD**	**Assembled Mass** (ton)	**Observations**
HPC2.81	3.00 (1)	-	0.70125	-
HPC2.82	1.00 (3)	GR	0.25500	-
HPC2.83	1.00 (3)	GR	0.70125	Mass scaled
HPC2.84	1.00 (3)	GR	0.31875	Additional boundary *dofs*
HPC2.85	1.00 (3)	GR	0.70125	Additional boundary *dofs* + mass scaled

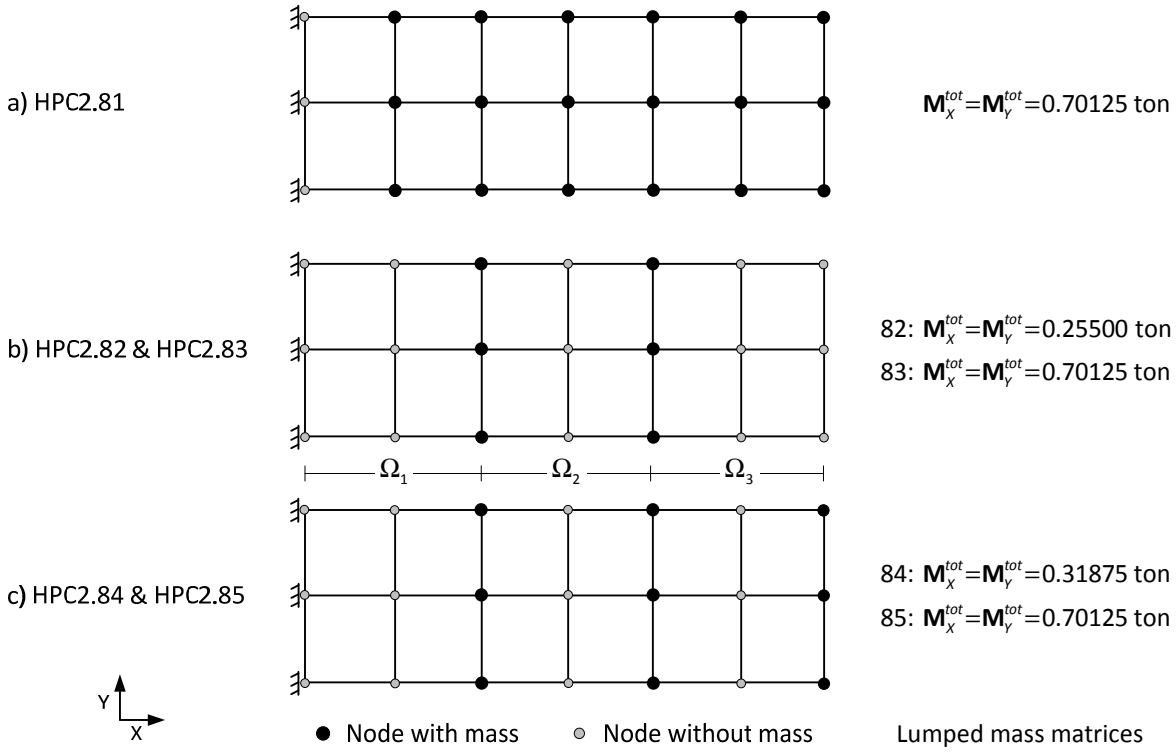

Figure V.44: Example HPC2 – Masses considered for the different analyses.

The results obtained in terms of the frequencies for the first 10 modes are presented in Table V.20 and are compared with a reference analysis performed with the FE code *ADINA* [3].

As expected, observing the results presented in Table V.20, it is possible to verify that the analysis without substructuring (HPC2.81) returned the same solution as the reference analysis, because the same formulation and the same finite elements are used. Furthermore, when the GR is used (analyses HPC2.82-85), the approximated nature associated with this methodology results in losing some accuracy for the solution. The results are worse when the total mass considered is less than that of the reference solution (HPC2.82 and HPC2.84). On the other hand, the accuracy increases when the distribution of the mass becomes closer to the reference solution (HPC2.82 *vs*. HPC2.84 and HPC2.83 *vs.* HPC2.85). Figure V.45 presents a graphical representation of the modal configuration for the first two modes for the analysis without substructuring (HPC2.81) and for the

analysis with substructuring, mass scaling and additional boundary dofs (HPC2.85). It is possible to verify that the configurations are very similar. Moreover, the relative error between the mode frequency of these two analyses was typically between 5% and 15% (see Table V.20), which is considered to be a good result.

Finally, it is possible to conclude that the substructuring method used together with the GR approach is a viable method to improve the efficiency of the modal analyses. The method will be exact if all the mass is part of the boundary *dofs* and only approximated when there is mass associated with interior *dofs*. The accuracy of the results can be improved by enforcing that the total amount of mass considered in the substructured analysis equals all the mass in the global model. Additionally, the accuracy also increases if the distribution of mass in the boundary *dofs* is as representative as possible of the distribution of mass in the global model.

Table V.20: Example HPC2 – Results of the modal analyses.

Mode #	Reference (Hz)	HPC2.81 (Hz) (e_{rel})	HPC2.82 (Hz) (e_{rel})	HPC2.83 (Hz) (e_{rel})	HPC2.84 (Hz) (e_{rel})	HPC2.85 (Hz) (e_{rel})
1	59.7	59.7 (0.0%)	122.9 (105.7%)	74.1 (24.0%)	81.8 (36.9%)	55.1 (-7.7%)
2	269.5	269.5 (0.0%)	478.8 (77.6%)	288.7 (7.1%)	352.4 (30.7%)	237.6 (-11.9%)
3	285.7	285.7 (0.0%)	515.9 (80.5%)	311.1 (8.9%)	400.7 (40.2%)	270.2 (-5.5%)
4	579.5	579.5 (0.0%)	1041.5 (79.7%)	628.0 (8.4%)	706.7 (22.0%)	476.5 (-17.8%)
5	832.9	832.9 (0.0%)	1247.8 (49.8%)	752.5 (-9.7%)	1088.0 (30.6%)	733.5 (-11.9%)
6	863.7	863.7 (0.0%)	1313.3 (52.1%)	791.9 (-8.3%)	1158.0 (34.1%)	780.7 (-9.6%)
7	1067.1	1067.1 (0.0%)	1412.8 (32.4%)	852.0 (-20.2%)	1301.5 (22.0%)	877.5 (-17.8%)
8	1118.7	1118.7 (0.0%)	1445.0 (29.2%)	871.4 (-22.1%)	1345.0 (20.2%)	906.8 (-18.9%)
9	1134.6	1134.6 (0.0%)	1450.6 (27.9%)	874.8 (-22.9%)	1399.9 (23.4%)	943.8 (-16.8%)
10	1227.5	1227.2 (0.0%)	1501.0 (22.3%)	905.1 (-26.3%)	1424.1 (16.0%)	960.1 (-21.8%)

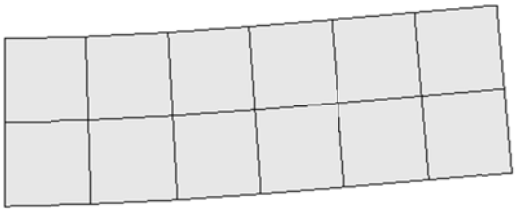

a) HPC2.81: Mode #1 (59.7 Hz)

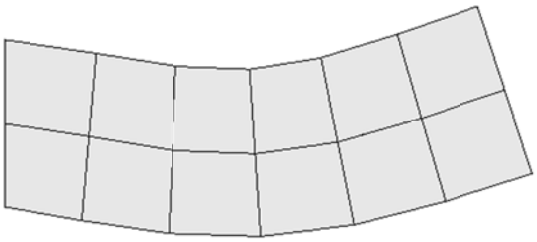

b) HPC2.81: Mode #2 (269.5 Hz)

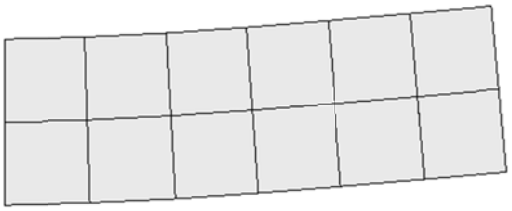

c) HPC2.85: Mode #1 (55.1 Hz)

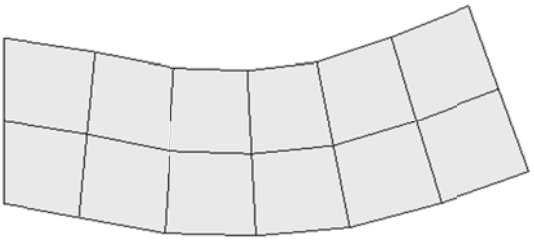

d) HPC2.85: Mode #2 (237.5 Hz)

Figure V.45: Example HPC2 – Configuration of the first two vibration modes.

5.3 Example HPC3 – Elastic cantilever column

The purpose of this example is to test the algorithm for modal and incremental dynamic analyses using substructuring and the *Hybrid Discretization* technique. To cope with this objective, the elastic cantilever column, presented in Figure V.46, was chosen. The material response is considered elastic for simplicity and four meshes were considered. The meshes #1 and #2 include 80 8-noded hexahedrons (H8) and one domain and four subdomains, respectively. Moreover, meshes #3 and #4 simulate the interior of the column span as Euler-Bernoulli beam (EBB) elements and only 40 H8 elements are used. For these cases, one domain and two subdomains were considered. Table V.21 summarizes the main characteristics of the meshes.

Global Kinematic Constraints (GKC) enforced using *Lagrange Multipliers* (LM) were adopted (see section 2.4.3) and the *Primal Substructuring* method was used as the *Domain Decomposition* method. Two types of loads were considered in the analyses. The first is the distributed force on the top surface of the column and the second is an imposed displacement at the base of the column (see Figure V.46). The mass was concentrated on the top surface of the column and a lumped mass matrix was considered. The results are compared with the data from the FE software *ADINA* [3] obtained using the Mesh #1 discretization, which was considered as the reference for the tests.

- Static Analyses

A group of static analyses were performed to assess the accuracy of the results for the different meshes considered and adopting the distributed force on the top surface of the column (Load #1).

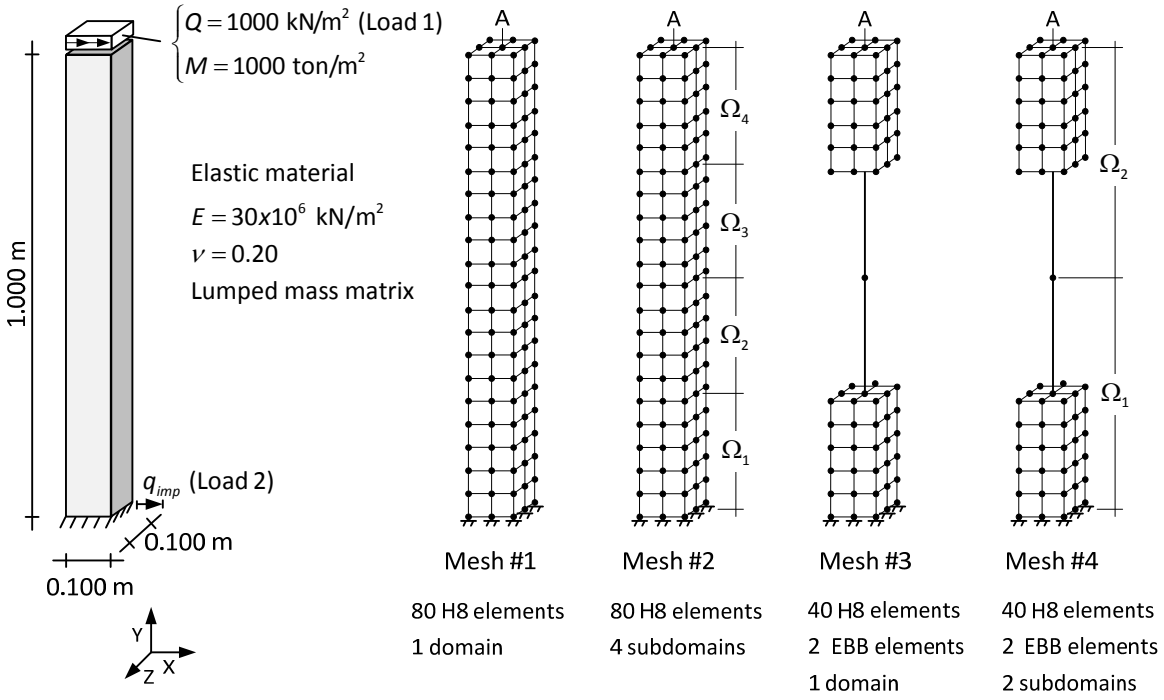

Figure V.46: Example HPC3 – Definition of the problem.

The characteristics and the selected results of the analyses are presented in Table V.22. This data shows that the results obtained in the reference analysis were recovered in the analyses HPC3.01 and HPC3.02. On the other hand, the analyses HPC3.03 and HPC3.04 returned a result in terms of the *X* displacement at node A about 4.24% above the former. This occurs because the models are different and the discretization of the column with less solid elements results in a stiffer response. Additionally, comparing the results from the analyses #1 and #2 and the results between analyses #3 and #4, it is possible to confirm that substructuring does not change the outcome of the simulations.

- Modal Analyses

Four modal analyses were performed to assess the dynamic behaviour associated with different meshes and discretization approaches. The top surface nodes were considered as boundary *dofs*, even though they do not belong to the subdomain boundaries, to avoid the approximation implicit in using the *Guyan Reduction*. In these simulations, as in the subsequent incremental dynamic analyses, lumped mass matrices were used. The characteristics of the computations are presented in Table V.23 and the first ten modal frequencies are compared in Table V.24. Similarly to the static analyses, it is possible to observe that the analyses #5 and #6 present results similar to the ones obtained with the reference model. In addition, the data using the meshes with hybrid discretization returned lower mode frequencies for the first two modes as a result of the mesh differences. From Table V.23, it is possible to observe that the other mode frequencies match the data from the reference analysis. This happens because starting from the third mode, the modes are local and mainly affect the region near the top surface, which is not influenced by the zone of the structure with a different discretization. This can be seen in Figure V.47 which represents the modal configuration for the first three modes.

Table V.21: Example HPC3 – Mesh Characteristics.

Mesh	*nnod*	*nel*	*ndofs*	*nsd*	Constraints
#1	189	80 (H8)	540	1	-
#2	189	80 (H8)	540	4	-
#3	111	40 (H8), 2 (EBB)	315	1	Beam2Solid (GKC-LM)
#4	111	40 (H8), 2 (EBB)	315	2	Beam2Solid (GKC-LM)

Table V.22: Example HPC3 – Characteristics and results of the static analyses.

Analysis	Mesh (*ndofs*)	DD Met. (nsd)	Load	$\delta_x^A\ (e_{rel})$ [m]	$W_e = -U^e\ (e_{rel})$ [kN.m]
Reference	#1 (540)	- (1)	#1	1.19281e-2	5.96401e-2
HPC3.01	#1 (540)	- (1)	#1	1.19281e-2 (0.00%)	5.96401e-2 (0.00%)
HPC3.02	#2 (540)	PS (4)	#1	1.19281e-2 (0.00%)	5.96401e-2 (0.00%)
HPC3.03	#3 (315)	- (1)	#1	1.24334e-2 (4.24%)	6.21665e-2 (4.24%)
HPC3.04	#4 (315)	PS (2)	#1	1.24334e-2 (4.24%)	6.21665e-2 (4.24%)

Table V.23: Example HPC3 – Characteristics of the modal analyses.

Analysis	Mesh (*ndofs*)	DD Met. (nsd)	Mass Assembled [ton]	Observations
HPC3.05	#1 (540)	- (1)	10.00	
HPC3.06	#2 (540)	PS (4)	10.00	Top surface *dofs* (X dir.) were set as boundary
HPC3.07	#3 (315)	- (1)	10.00	
HPC3.08	#4 (315)	PS (2)	10.00	Top surface *dofs* (X dir.) were set as boundary

Table V.24: Example HPC3 – Results of the modal analyses.

Mode #	Reference (Hz)	HPC3.05-06 (Hz) (e_{rel})	HPC3.07-08 (Hz) (e_{rel})
1	1.45726e+00	1.45726e+00 (0.00%)	1.42734e+00 (-2.05%)
2	2.03277e+01	2.03277e+01 (0.00%)	1.94712e+01 (-4.21%)
3	9.22877e+01	9.22877e+01 (0.00%)	9.22877e+01 (0.00%)
4	9.43993e+01	9.43993e+01 (0.00%)	9.43993e+01 (0.00%)
5	9.91988e+01	9.91988e+01 (0.00%)	9.91988e+01 (0.00%)
6	9.99013e+01	9.99013e+01 (0.00%)	9.99013e+01 (0.00%)
7	1.09731e+02	1.09731e+02 (0.00%)	1.09731e+02 (0.00%)
8	1.26083e+02	1.26083e+02 (0.00%)	1.26083e+02 (0.00%)
9	1.48255e+02	1.48255e+02 (0.00%)	1.48255e+02 (0.00%)

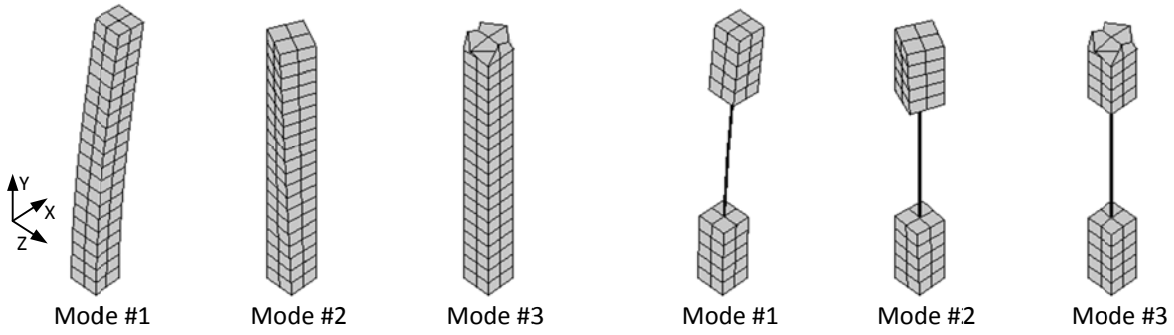

a) HPC3.05 & HPC3.06 b) HPC3.07 & HPC3.08

Figure V.47: Example HPC3 – Mode shapes

- Incremental Dynamic Analyses

One of the major goals of this example is the assessment of the response of the model for *Incremental Dynamic Analyses* (IDA). With this objective, a set of simulations was designed for the four meshes considered (see Table V.25). The *average acceleration* method was used as a time integration algorithm and proportional damping was considered by imposing 5% of damping at 1 Hz and 10 Hz. Both the distributed forces at the top of the column (Load #1) and the prescribed displacement at the base of the columns (Load #2) were considered in the analyses. Time functions were used for defining the evolution of the loads throughout the analyses. Time Function #1 is basically two inverted triangle waves and was associated with Load #1.

Table V.25: Example HPC3 – Characteristics of the incremental dynamic analyses.

Analysis	Mesh	DD Met. (nsd)	Time Integration	Damping	Loads	Time Function
HPC3.09	#1	- (1)	Newmark	Proportional		
HPC3.10	#2	PS (4)	γ=0.50;ν=0.25	α_d=5.7119E-1	#1 (Q)	#1
HPC3.11	#3	- (1)	Δt = 0.01 s	β_d=1.4468e-3		
HPC3.12	#4	PS (2)				
HPC3.13	#1	- (1)	Newmark	Proportional		
HPC3.14	#2	PS (4)	γ=0.50;ν=0.25	α_d=5.7119E-1	#2 (q_{imp})	#2
HPC3.15	#3	- (1)	Δt = 0.01 s	β_d=1.4468e-3		
HPC3.16	#4	PS (2)				

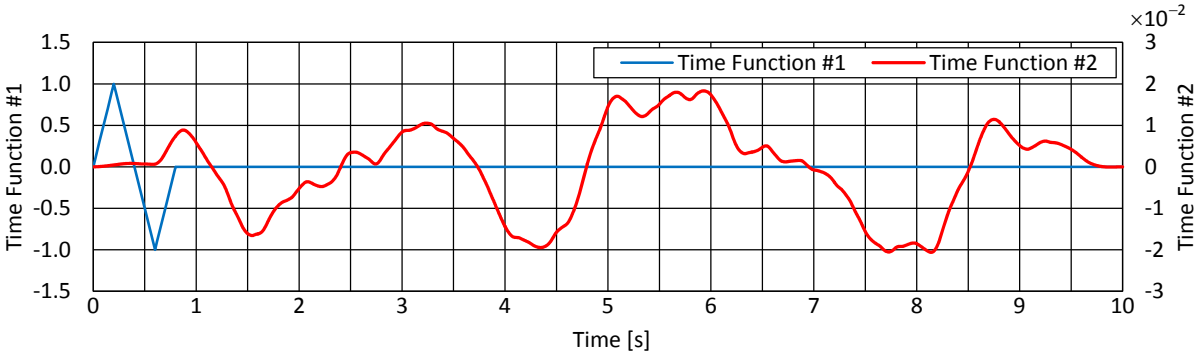

Figure V.48: Example HPC3 – Graphical representation of Time Functions #1 and #2.

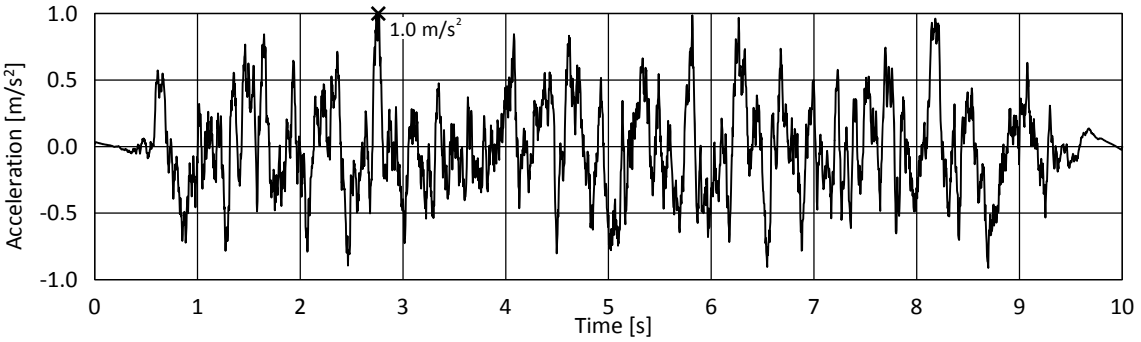

Figure V.49: Example HPC3 – Time-history generated by the double integration of Time Function #2.

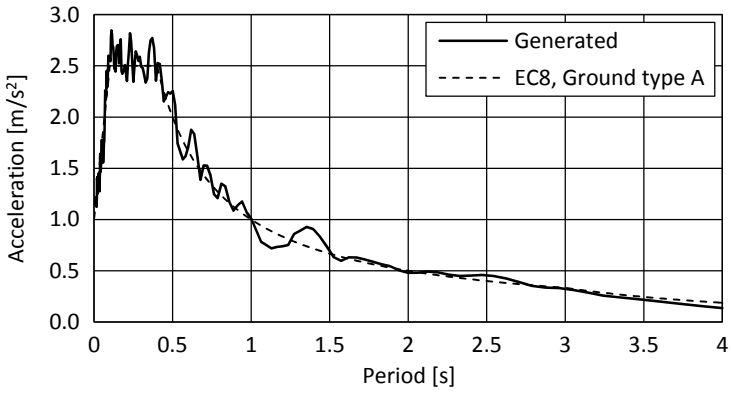

Figure V.50: Example HPC3 – Elastic response spectra computed from Time History #2 $(\xi = 5\%)$.

Furthermore, Time Function #2 will be considered as a displacement record (in metres) for the prescribed displacement at the bottom of the column. In this case, the accelerations associated with the imposed displacement may be computed by double integration of the displacement record, resulting in the time history displayed in Figure V.49, which shows that the acceleration record is normalized for a PGA of 1 m/s^2. The elastic response spectra computed using the software *LNEC-SPA* [395] is displayed in Figure V.50, revealing that this record was generated to match the design response spectra of Eurocode 8 [92] for a ground type A and 5% of damping.

The time-histories of the displacement at node A (*X* direction) are presented in Figure V.51 for the analyses #9 and #10, and in Figure V.52 for the analyses #11 and #12, together with the results obtained by the reference FE analysis. These results show that the analyses #9 and #10 recovered the reference solution, as a result of using the same mesh, element and FE formulation. On the other hand, for the analyses #11 and #12 the response shows small differences in the amplitude and a minor time offset. This results from having different structural responses that change the amplification and the main frequency of vibration.

At the end of the analysis, the response is ruled by free vibration dominated by the first mode of vibration. Comparing Figure V.51 to Figure V.52, a difference can be clearly seen in the periods in the free vibration period. The data presented in Table V.26 was obtained by analysing the last 3 seconds of the records using the software *LNEC-SPA* [395]. This tool uses the *Levenberg-Marquardt* algorithm to find the best fit through a minimization of the weighted mean square error between the data and the analytical expression for the sub-critical damped *sdof* response [116]:

$$q(t) = \rho\, e^{-\xi\,\omega t} \cos\left(\omega_d\, t - \phi\right) + q_0\,, \tag{V.220}$$

where ρ is the displacement amplitude, ξ is the damping ratio, ϕ is the phase offset, q_0 is the displacement offset, ω is the circular natural frequency, and ω_d is the circular damped frequency defined by:

$$\omega_d = \omega\sqrt{1-\xi^2}\,. \tag{V.221}$$

The results show a nearly perfect match with those obtained in the modal analyses (see Table V.24). As an additional confirmation, Figure V.53 presents the damping ratio associated with the frequencies obtained in the nonlinear fit and with the formula for proportional damping (II.114):

$$\xi_i = \frac{1}{2}\left(\frac{\alpha_d}{\omega_i} + \beta_d\,\omega_i\right),$$

which returned nearly the same values obtained in the nonlinear fit made to the response.

In conclusion, the differences in the response of the meshes with and without hybrid discretization are small, expected and related to the structural differences in both models. Regarding the analyses with the earthquake loading (Time Function #2), it is possible to observe from Figure V.54 that the results using Mesh #1 and #2 are an exact match with those obtained in the reference analysis. In addition, the results using Mesh #3 and #4 are also very consistent with the reference, although with some differences for the reasons already presented.

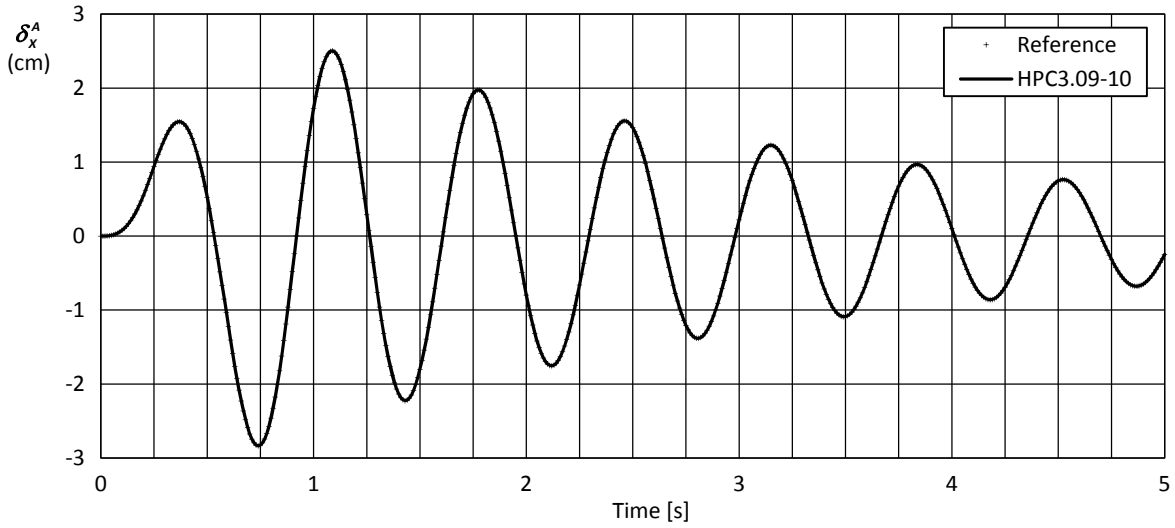

Figure V.51: Analyses HPC3.09 and HPC3.10 – Results from the incremental dynamic analyses.

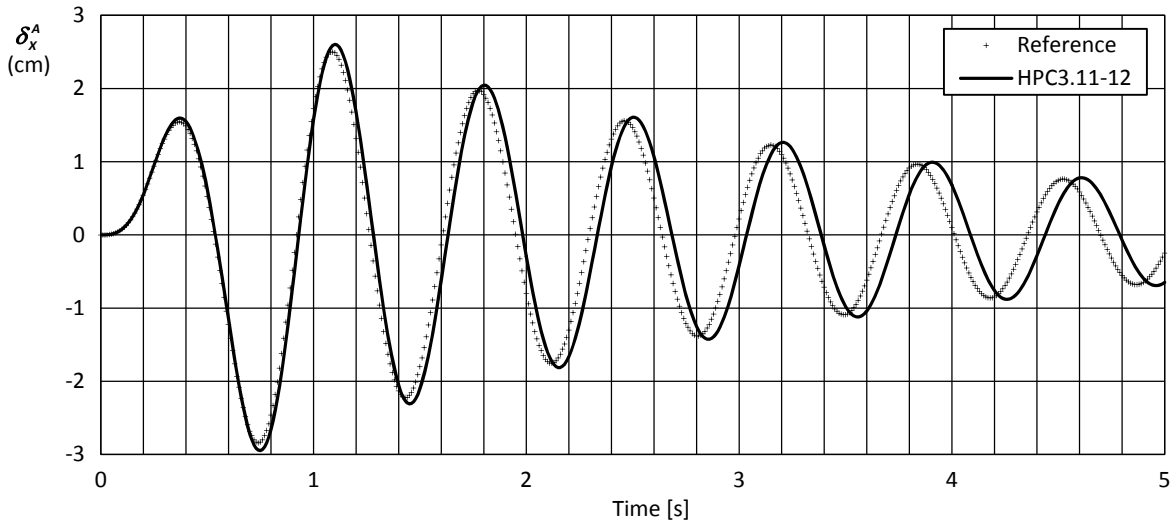

Figure V.52: Analyses HPC3.11 and HPC3.12 – Results from the incremental dynamic analyses.

Table V.26: Example HPC3 – Nonlinear fit to the free vibration part of the disp. records and comparison with previous data.

Analysis	**Modal Frequency** From Table V.24 (Hz)	**Damping Ratio** From Equation (II.114) (%)	**Natural Frequency** Nonlinear Fit (Hz) (e_{rel})	**Damping Ratio** Nonlinear Fit (%) (e_{rel})
HPC3.05-06 vs. 09-10	1.45726	3.78157	1.45727 (0.001%)	3.77846 (-0.08%)
HPC3.07-08 vs. 11-12	1.42734	3.83335	1.42743 (0.006%)	3.82824 (-0.13%)

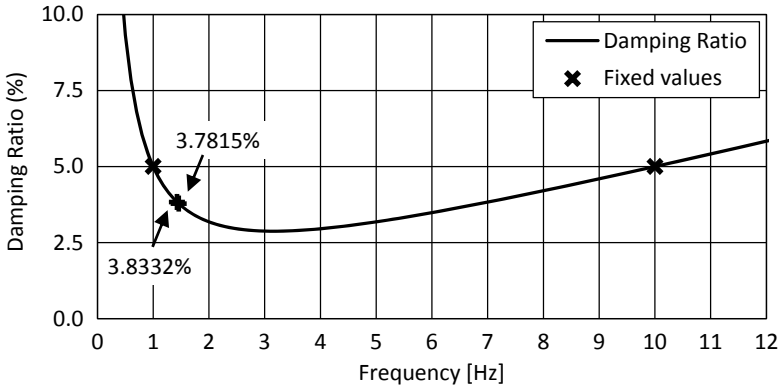

Figure V.53: Example HPC3 – Damping ratio - Proportional damping $\left(\alpha_d = 5.7119\text{E-}1;\ \beta_d = 1.4468\text{e-}3\right)$.

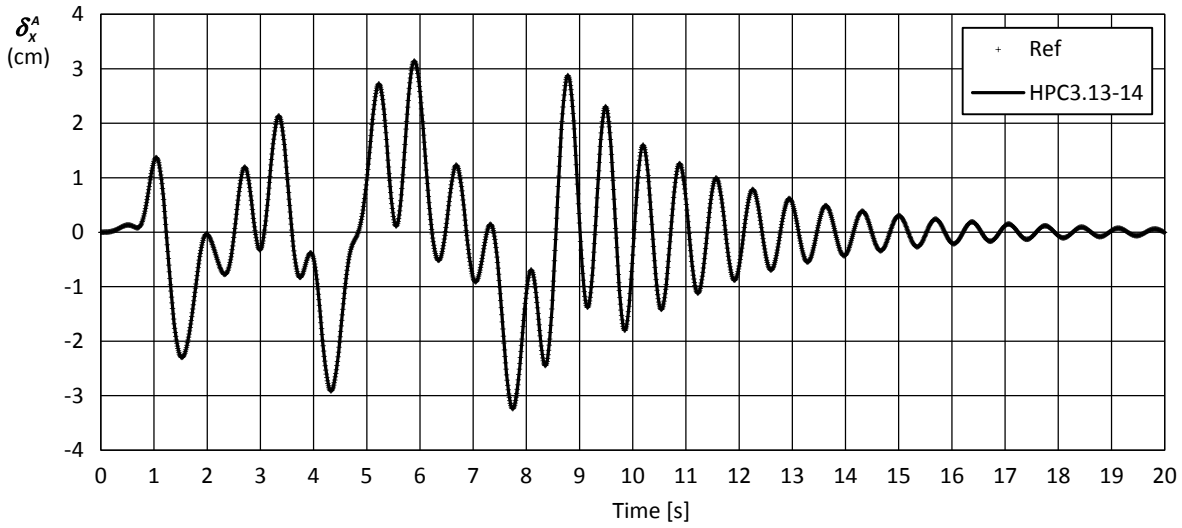

Figure V.54: Analyses HPC3.13-14 – Results from the incremental dynamic analyses.

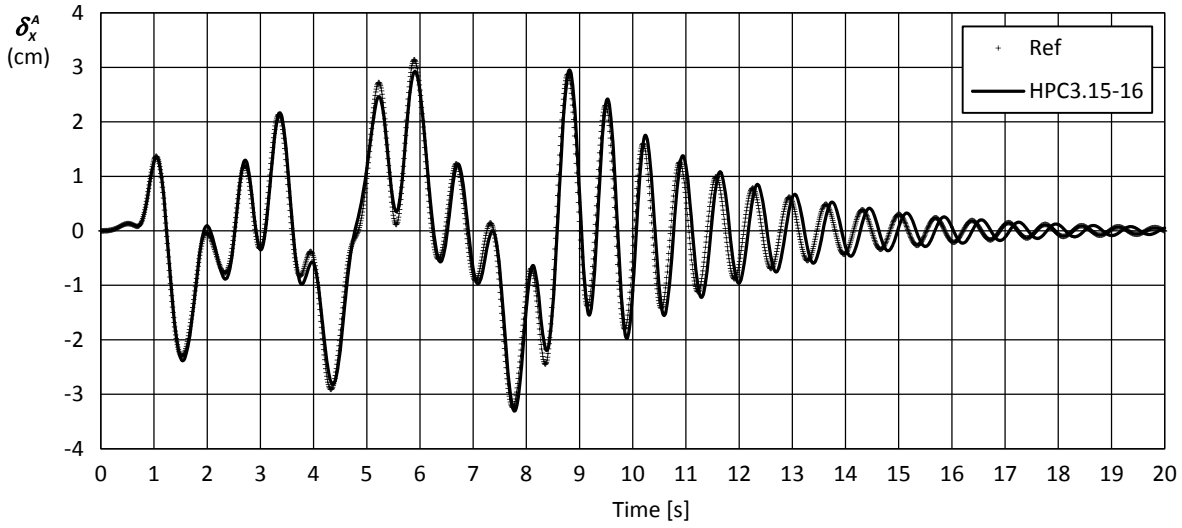

Figure V.55: Analyses HPC3.15-16 – Results from the incremental dynamic analyses.

5.4 Example HPC4 – Elastic frame

The purpose of this example is to test the accuracy and efficiency of using different methods to enforce the *Kinematic Constraints* (KC), as required for the *Hybrid Discretization* (HD) technique. Both *Global Kinematic Constraints* (GKC), enforced using *Lagrange Multipliers* (LM), and *Local Kinematic Constraints* (LKC), enforced using the *Master-Slave Elimination* (MSE) method, are tested in this example.

The problem chosen consists of a single-bay frame 5.0 m wide and 3.0 m high (see Figure V.56). The columns have a square cross-section of 25 cm and the beam has a rectangular cross-section of 25x40 cm^2. Moreover, a small foundation with 45x45 cm^2 and height 10 cm was used to simulate the connection of the columns to the foundation. The overall layout of the structure is symmetric although this property was not used to simplify the analyses. The considered loading consists of a distributed vertical load in Mesh #1 and a concentrated load in Mesh #2, as presented in Figure V.56. The origin of the coordinate system is positioned at the base of the leftmost column as indicated in Figure V.56 (smaller *X* coordinates).

Two types of meshes were used to simulate the structure. The first type (Mesh #1) considers 7124 solid elements (H8, 8-noded isoparametric hexahedrons) and the second type joins 3624 H8 elements and 6 Euler-Bernoulli beam (EBB) elements (L2, 2-noded with linear geometry). All materials were considered to be elastic linear. In addition, Mesh #2 was created by implementing the partition associated with expression (V.150) with $\lambda_h = 2.5$. Other mesh characteristics are presented in Table V.27.

All the H8 elements are cubes with length 5 cm , and consequently there is not an alignment of nodes coincident with the symmetry axis at $X = 2.500$ m . For that reason, the load was distributed

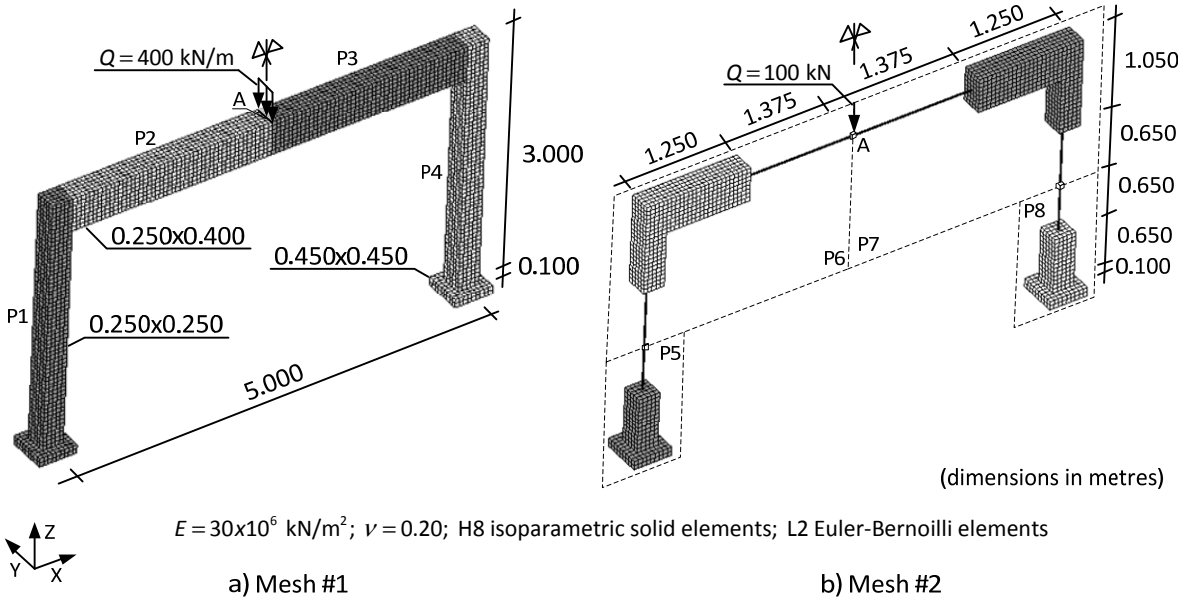

Figure V.56: Example HPC4 – Definition of the problem.

Table V.27: Example HPC4 – Mesh Characteristics.

Mesh	*nnod*	*nel*	*ndofs*
#1	9996	7124 (H8)	29388
#2	5289	3624 (H8) + 6 (L2)	15294

Table V.28: Example HPC4 – Characteristics of the subdomains for each analysis.

Analysis	Mesh (*ndofs*)	Subdomains (*nsd*)	Boundary *dofs*	Interior *dofs*: *sd#1,sd#2,...*
HPC4.01	#1 (29 388)	P1+P2+P3+P4 (1)	-	29338
HPC4.02	#1 (29 388)	P1+P2+P3+P4 (1)	-	29338
HPC4.03	#1 (29 388)	P1+P2; P3+P4 (2)	162	14694; 14532 (50%; 50%)
HPC4.04	#1 (29 388)	P1; P2; P3; P4 (4)	486	6918; 7614; 7452; 6918 (24%; 26%; 26%; 24%)
HPC4.05	#2 (15 294)	P5+P6+P7+P8 (1)	-	15294
HPC4.06	#2 (15 294)	P5+P6+P7+P8 (1)	-	15294
HPC4.07	#2 (15 294)	P5+P6; P7+P8 (2)	798	7650; 7650 (50%; 50%)
HPC4.08	#2 (15 294)	P5; P6; P7; P8 (4)	810	1896; 5346; 5346; 1896 (13%; 37%; 37%; 13%)
HPC4.09	#2 (15 294)	P5+P6+P7+P8 (1)	-	15294
HPC4.10	#2 (15 294)	P5+P6+P7+P8 (1)	-	15294
HPC4.11	#2 (15 294)	P5+P6; P7+P8 (2)	6	7644; 7644 (50%; 50%)
HPC4.12	#2 (15 294)	P5; P6; P7; P8 (4)	18	2010; 5628; 5628; 2010 (13%; 37%; 37%; 13%)

Table V.29: Example HPC4 – Characteristics of the substructured structural analysis and of the kinematic constraints.

Analysis	DDM	Algorithm	K. Constraints (*nkc*)	Reduced Problem Size
HPC4.01	-	Sequential	-	29338
HPC4.02	PS	Parallel	-	29338
HPC4.03	PS	Parallel	-	162
HPC4.04	PS	Parallel	-	486
HPC4.05	-	Sequential	Global KC-LM (756)	15294+756=16050
HPC4.06	PS	Parallel	Global KC-LM (756)	15294+756=16050
HPC4.07	PS	Parallel	Global KC-LM (756)	798+756=1554
HPC4.08	PS	Parallel	Global KC-LM (756)	810+756=1566
HPC4.09	-	Sequential	Local KC-MSE (756)	15294-756=14538
HPC4.10	PS	Parallel	Local KC-MSE (756)	15294-756=14538
HPC4.11	PS	Parallel	Local KC-MSE (756)	6
HPC4.12	PS	Parallel	Local KC-MSE (756)	18

into two alignments along the *Y* axis ($X = 2.475$ m and $X = 2.525$ m). Moreover, reference point A for Mesh #1 has coordinates $(2.525, 0.025; 3.000)$ m and for Mesh #2 $(2.500, 0.000; 2.800)$ m.

Once again, the results are compared with the FE software *ADINA* [3] using the same discretization as adopted in Mesh #1, which is considered as the reference in this example.

Three numbers of subdomains were considered in the analyses for both meshes (see Table V.28). When only one subdomain was considered, the analysis was executed with the sequential and the parallel version of the code, in order to assess the parallelization overhead (see Table V.29). Moreover, when two subdomains were adopted the subdomain boundary was positioned in the

symmetry axis, hence resulting in uniform element and *dof* divisions, apart from Mesh #1 where the elements passing through the symmetry axis were included in subdomain #1. Furthermore, when four subdomains are adopted the division was made by separating each column and respective foundation, and the interior part of the beam into two nearly identical halves (partitions P1, P2, P3 and P4 represented in Figure V.56). The same geometric division was used for Mesh #2 (partitions P5, P6, P7 and P8). This resulted in a non-uniform *dof* distribution, with both column-beam subdomains having around 2/3 of the total number of interior *dofs* and the remaining 1/3 divided in equal shares by both column bases.

The characteristics of the substructured structural analysis and of the kinematic constraints used in the analyses are also presented in Table V.29. This data shows that when more than one subdomain is considered, the *Primal Substructuring* (PS) method was adopted and that the analyses #5-#8 were made using 756 *global kinematic constraints* (GKC) and the analyses #9-#12 with 756 *local kinematic constraints* (LKC).

Table V.29 also presents the size of the governing system to be solved. For the analyses with only one subdomain, all *dofs* are considered as interior and are present in the governing system. When GKC are used, the 756 constraint equations are added to the system, because the Lagrange Multipliers method is used. Moreover, when LKC are implemented, the *dofs* associated with the 756 constraint equations are eliminated from the governing system.

For the case of more than one subdomain, the governing system to be solved is the reduced problem defined by the inter-subdomain *dofs.* When GKC are implemented, the reduced problem is also augmented with the equations associated with the constraints. On the other hand, when LKC is used the size of the reduced problem does not change because the constraints are applied for the internal *dofs* of each subdomain, which is an important difference between the two methods.

- Accuracy of the results

Table V.30 presents the results for the vertical displacement at point A and for the work done by the discrete external forces, which in this case is equal to the symmetric of the elastic strain energy. The results show that for Mesh #1 the solution matches that obtained using the FE code *ADINA* [3]. This is the expected result because the mesh, the element and the global formulations are the same. Regarding the analyses with Mesh #2, two important observations must be made concerning the data presented. Firstly, the same results were obtained for all domain partitions and methods used to enforce the kinematic constraints. Secondly, the results are very similar to the analyses without using the hybrid discretization technique $\left(e_{rel} \leq 1.20\%\right)$, both in terms of the displacements and of the work done by external forces. This result shows that the approximation level associated with using the hybrid discretization technique is small when compared to the structure modelled using only solid elements.

From these results, it is possible to confirm that substructuring does not introduces any loss of accuracy in the results. Additionally, both methodologies for imposing the kinematic constraints are equivalent in terms of the overall results.

Table V.30: Example HPC4 – Selected results from the analyses.

Analysis	$\delta_z^A\left(e_{rel}\right)$ (m)	$W_e = -U^e\left(e_{rel}\right)$ (kN.m)
Reference	-4.20086e-3	2.10112e-1
HPC4.01	-4.20086e-3 (0.00%)	2.10112e-1 (0.00%)
HPC4.02	-4.20086e-3 (0.00%)	2.10112e-1 (0.00%)
HPC4.03	-4.20086e-3 (0.00%)	2.10112e-1 (0.00%)
HPC4.04	-4.20086e-3 (0.00%)	2.10112e-1 (0.00%)
HPC4.05	-4.15165e-3 (-1.17%)	2.07583e-1 (-1.20%)
HPC4.06	-4.15165e-3 (-1.17%)	2.07583e-1 (-1.20%)
HPC4.07	-4.15165e-3 (-1.17%)	2.07583e-1 (-1.20%)
HPC4.08	-4.15165e-3 (-1.17%)	2.07583e-1 (-1.20%)
HPC4.09	-4.15165e-3 (-1.17%)	2.07583e-1 (-1.20%)
HPC4.10	-4.15165e-3 (-1.17%)	2.07583e-1 (-1.20%)
HPC4.11	-4.15165e-3 (-1.17%)	2.07583e-1 (-1.20%)
HPC4.12	-4.15165e-3 (-1.17%)	2.07583e-1 (-1.20%)

Table V.31: Example HPC4 – Measured computing times for different mesh and constraints types.

Analysis Type	Sequential (s)	Parallel 1 sd (s)	Parallel 2 sd (s)	Parallel 4 sd (s)
Mesh #1	97.060	99.580	52.016	41.640
Mesh #2-Global K. Constraints	27.753	29.052	24.722	22.021
Mesh #2-Local K. Constraints	27.626	28.410	12.769	11.581

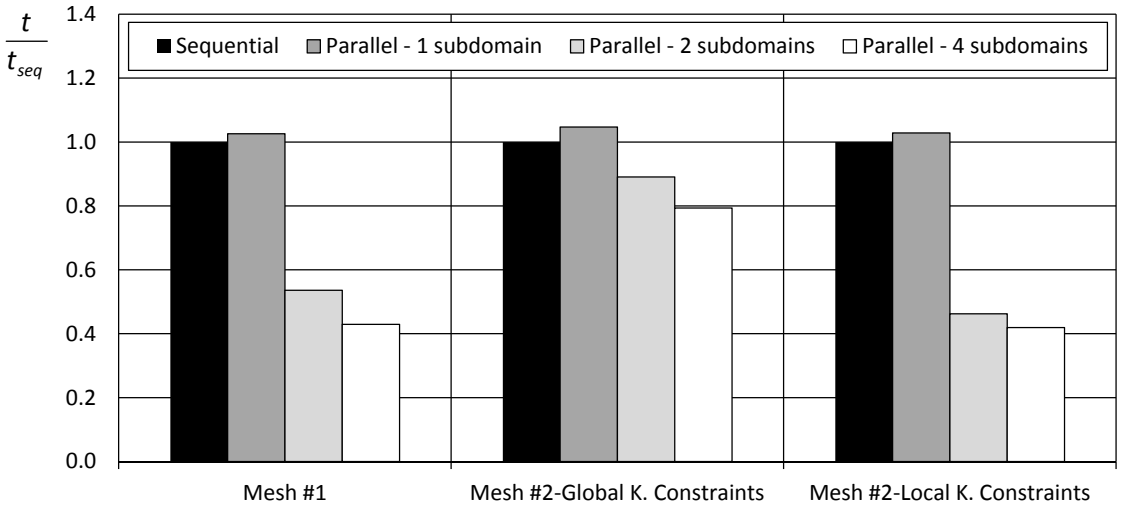

Figure V.57: Example HPC4 – Normalized measured computing times for different mesh and constraints types.

- Performance analysis

This analysis was made for assessing the efficiency of the KC-enforcing methods, when combined with substructured structural analysis (PS method). The same procedure implemented in the example HPC2 for the performance analysis was adopted (see section 5.2). The computing times of five incremental runs were measured and the average values are presented in Table V.31 for the twelve analyses made.

Figure V.57 presents the graphical representation of these results normalized by the computing times obtained with the sequential code. The analyses with one subdomain confirmed a small computing time increase for the parallelized version of the code due to the implicit overhead. Moreover, for the analysis with two and four subdomains, the computing time decreased significantly for Mesh #1 and Mesh #2 combined with LKC and this decrease was less significant for Mesh #2 and GKC.

A deeper analysis regarding the computational efficiency can be made by introducing the concept of *concurrent speed-up* and *efficiency* as described in section 2.1.10. Let us start by assessing the effect of using substructuring for each mesh and KC-enforcing method. These results are presented in Table V.32 and Table V.33 for the measured and corrected computing times, respectively. The same procedure presented and discussed in section 5.2 was adopted, *i.e.* the γ^* factors (V.219) were used to correct the measured computing times, in order to take into consideration the dynamic overclock procedure implemented in the computer's CPU (see section 5.2 for more details).

The speed-up results are presented graphically in Figure V.58 and Figure V.59. For both the measured and for the corrected speed-up values the results present the same trend. The only change is in the quantitative results for the analyses with two and four subdomains as a result of the dynamic overclock procedure. This data clearly shows that for two subdomains using Mesh #1 and Mesh #2 with LGK, the speed-up values show linear scalability with the parallelization level and even super linear scalability, *i.e.* efficiency above 100%, for the corrected computing time values. These results are consistent with the ones presented in Figure V.36 and in Figure V.37 for the Example HPC2, with the equivalent number of *dofs*.

Table V.32: Example HPC4 – Speed-up and efficiency values for the parallelized algorithm.

Analysis Type	Parallel 1 sd	Parallel 2 sd	Parallel 4 sd
Mesh #1	0.97 (97.5%)	1.86 (93.3%)	2.33 (58.3%)
Mesh #2-Global Constraints	0.96 (95.5%)	1.12 (56.1%)	1.26 (31.5%)
Mesh #2-Local Constraints	0.97 (97.2%)	2.16 (108.2%)	2.39 (59.6%)

Table V.33: Example HPC4 – Corrected speed-up and efficiency values for the parallelized algorithm.

Analysis Type	Parallel 1 sd	Parallel 2 sd	Parallel 4 sd
Mesh #1	0.97 (97.5%)	2.18 (108.9%)	3.26 (81.6%)
Mesh #2-Global Constraints	0.96 (95.5%)	1.31 (65.5%)	1.77 (44.1%)
Mesh #2-Local Constraints	0.97 (97.2%)	2.52 (126.2%)	3.34 (83.5%)

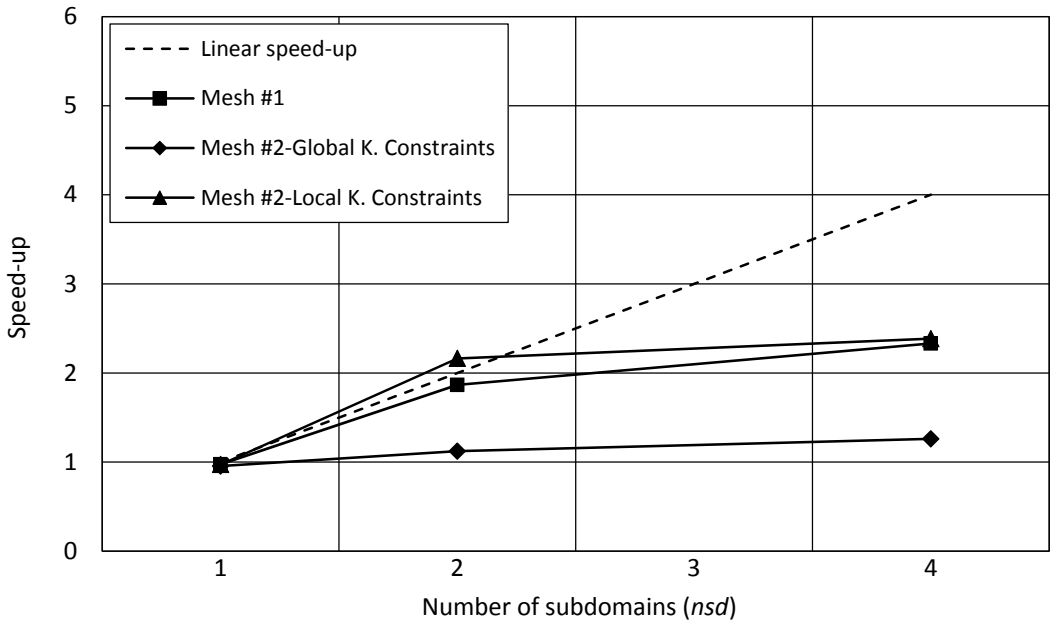

Figure V.58: Example HPC4 – Speed-up values for the parallelised algorithm.

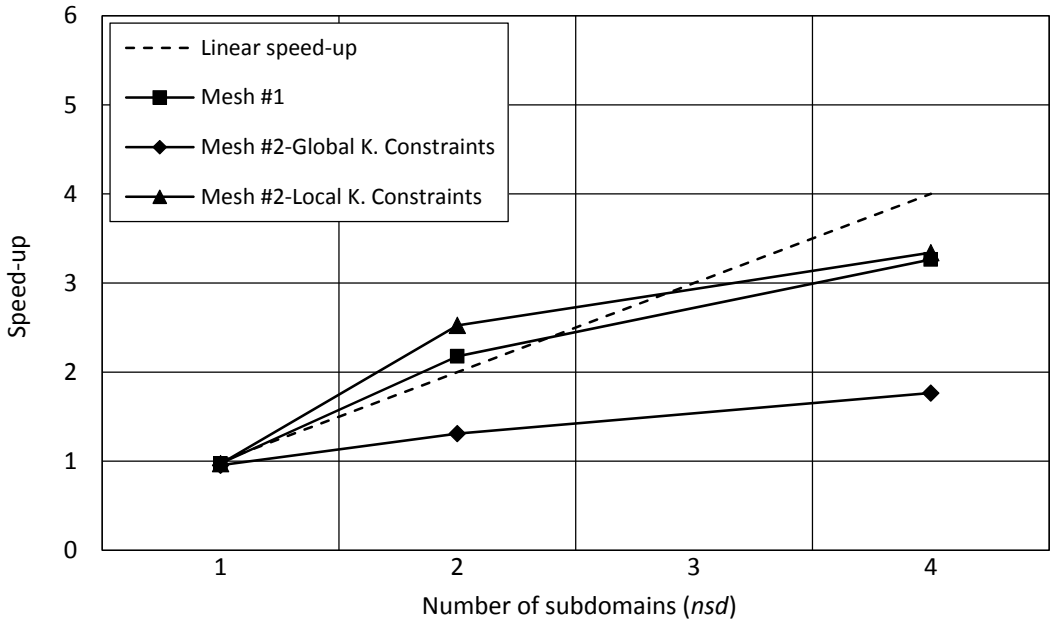

Figure V.59: Example HPC4 – Corrected speed-up values for the parallelised algorithm.

The speed-up values are significantly smaller when Mesh #2 is used with GKC. This response can be associated with two main aspects. At first, when the GKC method is implemented in the reduced problem, which is solved at the *Master Processing Unit*, it does not benefit from the parallelization, contrary to the LKC, which are enforced at the subdomain level and hence, computed in parallel. Secondly, for this case in particular, enforcing the GKC results in nearly doubling the size of the

reduced problem, which also contributes to worse results in terms of the concurrent speed-up and efficiency values. For the analyses with four subdomains, the speed-up and efficiency values are reduced bellow the linear scalability level. This behaviour is expected because of the load unbalancing associated with the mesh partition with four subdomains, as presented in Table V.28 and discussed before. This aspect results in a significant loss of efficiency because under the data parallelism approach, the light-weighted processing units must wait idle until the most loaded units finish their computations.

Another valuable source of information can be extracted from the speed-up values grouped for the different meshes and KC-enforcing methods. These results are numerically presented in Table V.34 and graphically in Figure V.60. It is worth noting that in this case there is not any difference in the speed-up values for the measured and corrected computing times because the reference value is associated with the same number of subdomains/workers, so it is also affected by the dynamic overclock procedure. The curves associated with one subdomain show higher speed-up values for Mesh #2 than for Mesh #1, as a result of decrease in *ndofs* associated with the *Hybrid Discretization* technique. Moreover, comparing the result using GKC and LKC it is possible to observe that similar

Table V.34: Example HPC4 – Corrected and measured speed-up values for the different mesh types.

Analysis Type	Mesh #1	Mesh #2-Global C.	Mesh #2-Local C.
Sequential 1 subdomain	1.00	3.50	3.51
Parallel 1 subdomain	1.00	3.43	3.51
Parallel 2 subdomains	1.00	2.10	4.07
Parallel 4 subdomains	1.00	1.89	3.60

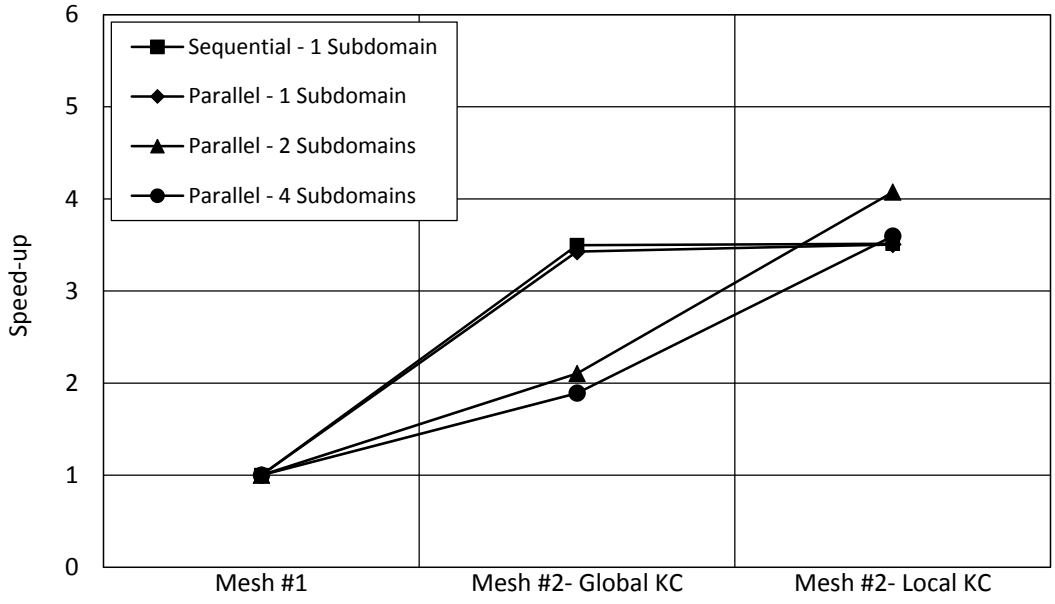

Figure V.60: Example HPC4 – Measured and corrected speed-up values for the different mesh types.

results were obtained. This is expected because for one subdomain it is not possible to gain from parallelization for the LKC and the supplementary equations added to the governing system using GKC, represent only a minor increase in the size with almost insignificant effect on the overall performance. Furthermore, the curves associated with two and four subdomains show speed-up values of about two for Mesh #2 using GKC when compared to Mesh #1. These gains in efficiency are mainly associated with the decrease in the *ndofs* using the HD technique. The speed-up values increase even further using LKC due to the extra parallelization associated with this technique.

The next step in the analysis consists of combining the effect of using substructuring and the HD technique, which led to the results presented in Table V.35 and in Figure V.61. These results were normalized by the analysis made with only one subdomain and using Mesh #1. This data shows a combined speed-up of between 4 and 6 times, when two or four subdomains are used together with the GKC. In addition, the efficiency gains are even more significant when LKC are used, reaching values between 9 and 12, which represent very significant and encouraging performance gains.

Table V.35: Example HPC4 – Speed-up combining parallelization levels and different mesh types.

Analysis Type	Measured	Corrected
Sequential 1 subdomain - Mesh #1	1.00	1.00
Parallel 2 subdomains - Mesh #2 - Global Constraints	3.93	4.58
Parallel 4 subdomains - Mesh #2 - Global Constraints	4.41	6.17
Parallel 2 subdomains - Mesh #2 - Local Constraints	7.60	8.87
Parallel 4 subdomains - Mesh #2 - Local Constraints	8.38	11.74

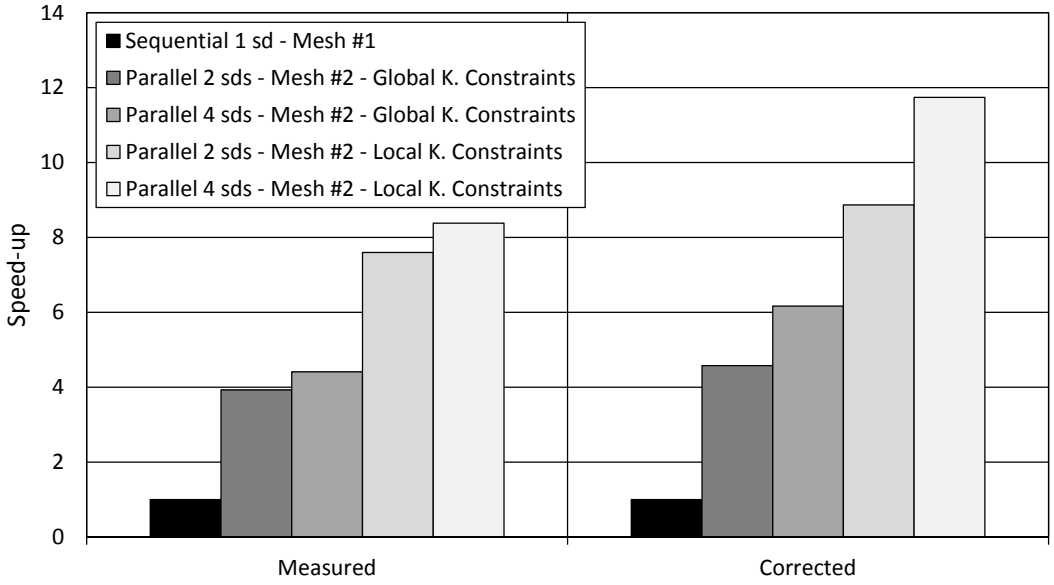

Figure V.61: Example HPC4 – Speed-up values combining parallelization levels and different mesh types.

At this point, it should be stressed that even better performance gains could have been achieved if the load balancing had been more uniform for Mesh #2 with four subdomains. Moreover, better results may also be achieved using higher level of parallelization and by adjusting the number of subdomain interior *dofs* to optimal values, *e.g.* to around 10000-20000 *dofs*, rather than 2000-5000 in this example using four subdomains.

More detailed information regarding the response of the algorithm can be extracted from the analysis of the different code segments. The incremental procedure was divided into the same four sections as in Example HPC2, namely: i) *Stiffness Matrix*; ii) *Corrector*; iii) *Unbalanced Forces*; and iv) *Other* (see section 5.2 for more details) and the relative computing times are presented in Figure V.62. Most of the observations made before can be also made for this case. For example, the *Other* segment tends to increase with parallelization for all cases and the relative size of the *Unbalanced Forces* segment stays roughly constant for the same reasons as those presented in section 5.2. In addition, the *Corrector* segment tends to increase its relative weight for the analyses with substructuring and the *Stiffness Matrix* segments presents the inverse behaviour. This can be related to the computation effort transfer between these two segments already discussed in section 5.2. The most relevant fact is that this effect is considerably less significant for the analyses associated with Mesh #2 with two and four subdomains and using LKC. The reasons for this response can be associated with two main aspects: firstly, the size of the reduced problem for the analyses with LKC is

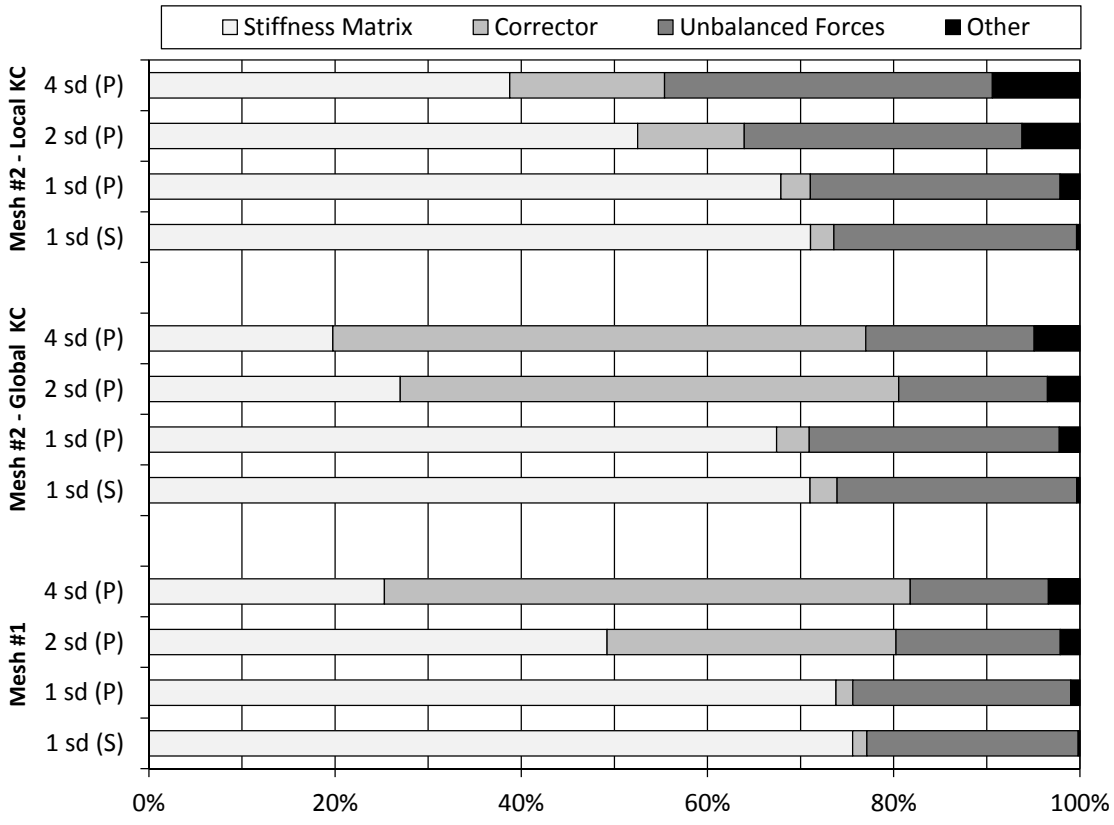

Figure V.62: Example HPC4 – Percentage of computing time for different code segments.

extremely small (*e.g.* 6 or 12 *dofs*, see Table V.29); secondly, the enforcement of the KC is made in the *Corrector* segment, but for the case of LKC, it is made in the scope of the subdomain, which has the possibility of gaining efficiency from the parallelization.

Finally, Figure V.63 presents the stress field σ_{xx} plotted on the deformed mesh for the analysis with Mesh #2, four subdomains and using LKC. In this figure is possible to confirm that the expected deformed shape and stress distribution is retrieved. It should be clearly stressed, that the loading characteristics were chosen in order to be simple and easy to compute. Consequently, the most stressed part of the structure is in the middle span of the beam, which is not compatible with the hybrid discretization adopted. Nevertheless, this example was designed for testing the efficiency of the different KC-enforcing techniques, for which these examples were found to be suitable.

It should be stressed that in the deformed configuration presented in Figure V.63 and throughout this thesis, the beam elements are drawn using a line connecting the extremity nodes, hence, the rotations in the element are not graphically represented.

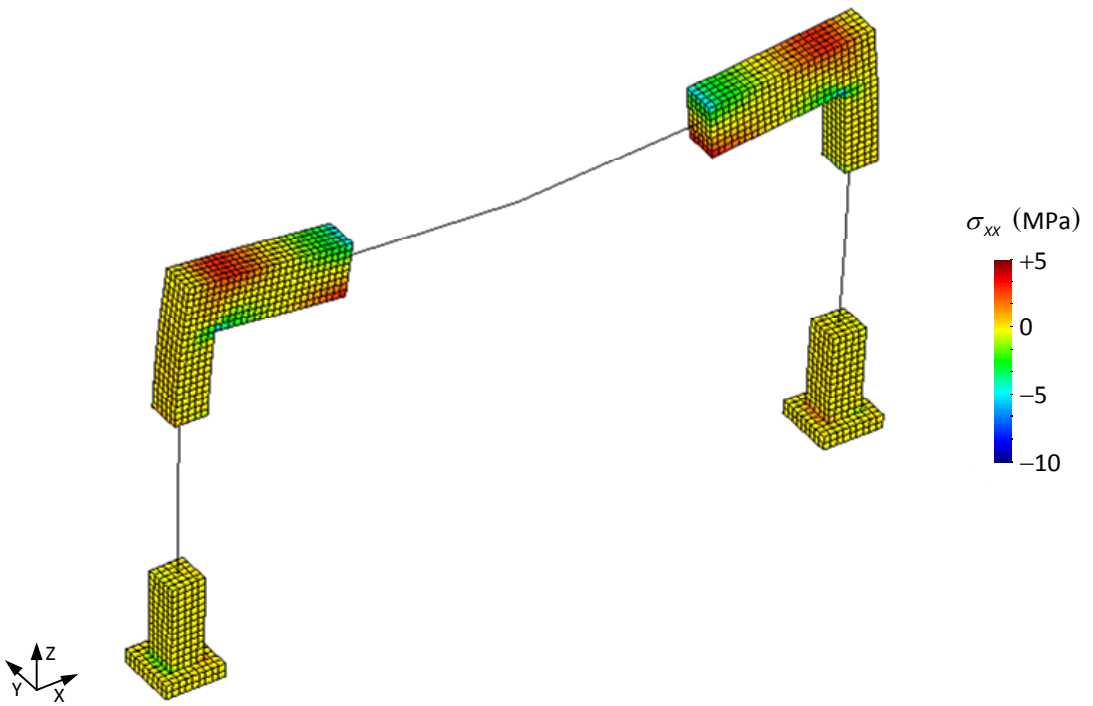

Figure V.63: Example HPC4 – Deformed mesh (magnified by 50) and stress field σ_{xx} for the analysis with Mesh #2 and LKC.

5.5 Example HPC5 – Elastic 2-storey structure

This example was created with the following two main objectives: i) to test the parallelized model in a more general and common problem for earthquake engineering with RC structures; and ii) to address some issues related to enforcing inter-subdomain relations using substructured structural analysis. To cope with these objectives, the 2-storey RC structure presented in Figure V.64-a was considered as the prototype for this example. The structure presents a single-bay in each horizontal direction, with widths of 5.00 and 4.00 m along the *X* and *Y* directions, respectively. The storeys are 3.00 m high and all the columns present a square cross-section of 25 cm, except for column C2 that has a rectangular cross-section of 25x50 cm^2. All the beams are rectangular with 25x40 cm^2 and both slabs are 20 cm thick. Figure V.64-b presents the model used in the numerical simulation.

At this point it should be clearly stressed that the discretization options adopted in this example were taken only for testing reasons, hence sometimes the most adequate modelling options are not adopted. Having this in mind, the prototype was discretized using a hybrid mesh for the first storey and a simplified mesh in the upper storey. In the first storey, $\lambda_h = 2.5$ was adopted for expression (V.150) to create the mesh partitions, except for the case of column C2 for which this criteria would lead to a small length of the simplified mesh so it was not considered.

The solid to beam transitions were enforced using the *Beam2Solid* technique presented in sections 3 and 4.4 (see Figure V.65-a). The same procedure was used to connect both storeys, as presented in Figure V.65-b. All these constraints are local for the respective subdomains, hence enforced using the *Master-Slave Elimination* method. Furthermore, a rigid diaphragm hypothesis was adopted to simulate the floor slabs, as used many times for this type of problem, by considering that the solid RC slabs present a substantial axial stiffness. Consequently, a global master node was positioned at the

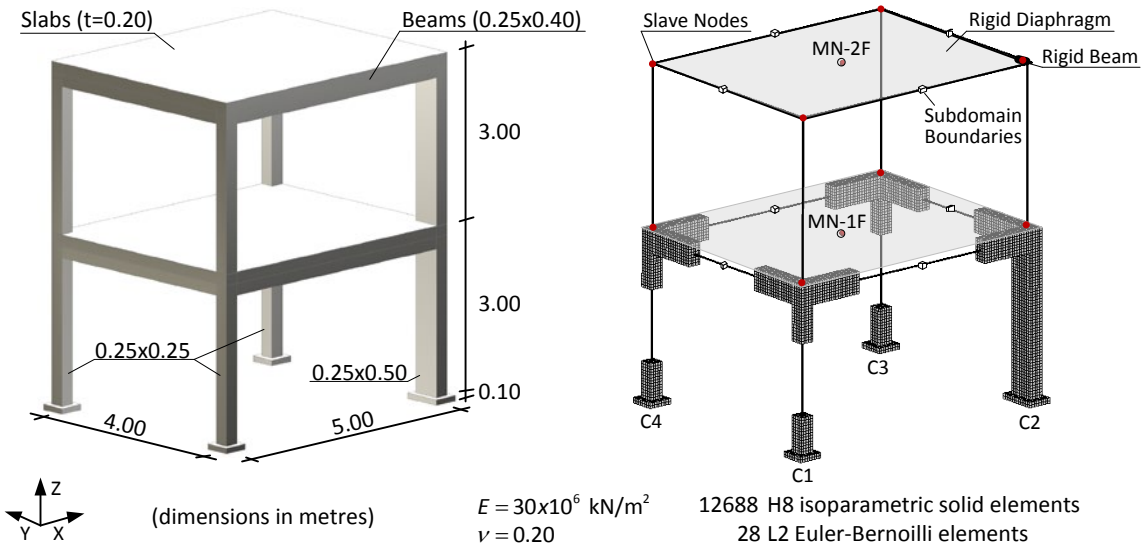

a) Prototype b) Model

Figure V.64: Example HPC5 – Definition of the problem.

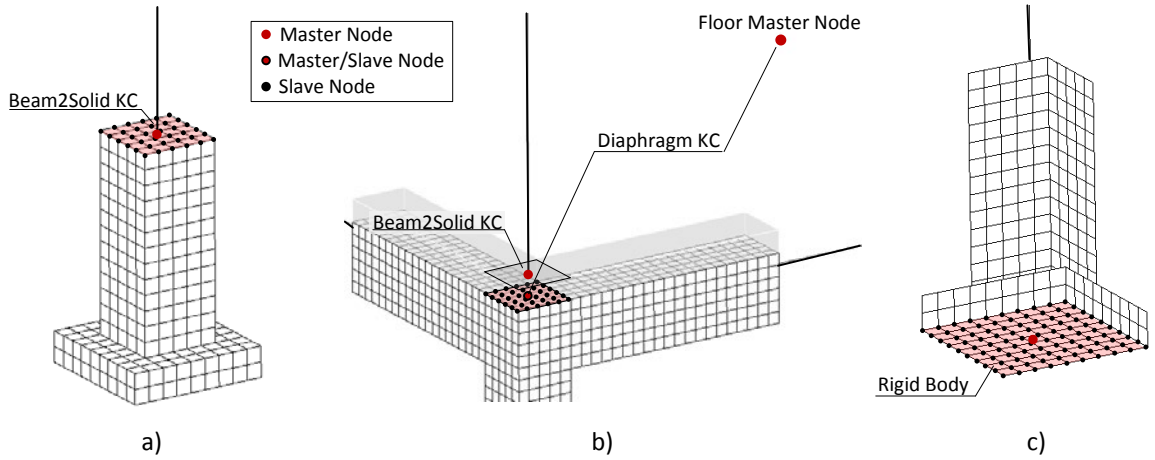

Figure V.65: Example HPC5 – Modelling techniques.

centre of mass of each slab to join the translational mass and rotational inertia associated with the slabs. The master node's *dofs* that are not associated with the diaphragm constraint were restrained $(q_Z, \theta_X, \theta_Y)$. A slave node was added to the centre of the alignment of each column, as presented in Figure V.65-b. The floor diaphragm was enforced in the reduced problem using GKC (Lagrange Multipliers). The connection to the subdomain scope is made by the slave node mentioned before, which becomes a master node for the subdomain and transmits the kinematic relations to a set of slave *dofs* in the column alignment using LKC (see in Figure V.65-b). This is an important aspect of this methodology, because it makes it possible to enforce global structural behaviour for substructured structural analyses. If the load transfer to the column is too strong using only one horizontal layer, additional slave node layers can be considered (*e.g.* within the slab thickness) and would result in a more smooth stress transfer, which can influence the response under nonlinear analyses.

Finally, a master node was added at the base of the foundation associated with each column for the analysis with earthquake loading. The objective is to avoid increasing the *ndofs* in the reduced problem because imposed displacements were enforced using Lagrange Multipliers. This master node is connected through a rigid body enforced with LKC to the slave nodes at the base of each column (see Figure V.65-c), thus increasing the *ndofs* in the reduced problem at most with 6 *dofs* for each column base and condensing the *dofs* associated with the slave nodes in each subdomain.

The main characteristics of the analyses and of the meshes adopted are presented in Table V.36 and in Table V.37. It can be seen that only a modal and an incremental dynamic analyses were computed in this example and that the meshes included 12688 8-noded hexahedrons (solid elements) and 28 2-noded Euler-Bernoulli elements. The four subdomains associated with each column were used in all analyses (see Figure V.64-a), leading to about 53000 *dofs*, 3500 LKC and 50 GKC. Some small variations in the number of *dofs* and constraints can be observed, which are associated with some differences in the models. For example, the base nodes of each column were fully restrained in the modal analyses.

Table V.36: Example HPC5 – Characteristics of the analyses.

Analysis	Type	Mass Assembled (MN-1F, MN-2F)	Local KC	Global KC
HPC5.1	Modal	$M_x = M_y = 14.272$ ton; $I_z = 48.760$ ton.m^2	2814	42
HPC5.2	Incremental Dynamic		4164	54

Table V.37: Example HPC5 – Characteristics of the subdomains for each analysis.

Analysis	Mesh (*ndofs*)	DD Met. (nsd)	Master *dofs*	Slave *dofs*: sd#1, sd#2, sd#3, sd#4
HPC5.1	#1 (52068)	PS (4)	102	10896, 19287, 10896, 10869 (21%; 37%; 21%; 21%)
HPC5.2	#2 (53430)	PS (4)	114	11196, 19728, 11196, 11196 (21%; 37%; 21%; 21%)

It is worthwhile noting that the number of subdomains adopted was set taking into consideration the number of processing units (NPU=4) in the computer used for running the example. In addition, the *ndofs* associated with column C2 led to some unbalance between the mesh partitions, because of its size and discretization characteristics

In both analyses, the mass was concentrated at the master nodes (MN) at the centre of mass of each slab. Only horizontal translational mass and vertical rotational moment of inertia were considered. The total mass associated with each floor was obtained from the RC slab dimensions (5.0x4.0x0.2 m^3) and an additional mass associated with other permanent and reduced live loads of 1 kN/m^2, distributed in the slab surface, leading to 14.272 ton of mass. The rotational moment of inertia was computed considering the slab as a thin rectangular plate:

$$I_z = \frac{M}{12}\left(a^2 + b^2\right), \tag{V.222}$$

where M is the total mass and a and b are the dimensions, which resulted in 48.760 ton.m^2.

As before, the results were compared to the ones obtained using another numerical tool, which in this case was the *SAP2000* [497] commercial FE software. A simplified mesh was adopted that resulted from using the same discretization in the first storey that is presented for the second floor in Figure V.64-b, resulting in 20 frame elements and 48 *dofs*. The base of the columns was fully restrained and a similar diaphragm KC was used to enforce the rigid slab. These results will be referred to as the *reference* values to maintain the nomenclature used before.

- Modal analysis

The results obtained from the modal analysis are presented in Table V.38 and the mode shape configuration is presented in Figure V.66. It can be observed that the numerical values are very similar and consistent in terms of the frequency values. The mode frequencies showed that the refined model used in this work resulted in about 4% higher frequencies, hence in a stiffer structure. This can be justified by having smaller spans in the elements due to considering in some cases the exact geometry of the elements, instead of using the spans between the element axes.

Table V.38: Analysis HPC5.1 – Results of the modal analysis.

Mode #	Reference (Hz)	HPC5.1 (Hz) (e_{rel})	Type
1	3.124413	3.272830 (4.75%)	Translational - 1st mode (X predominant)
2	3.610651	3.745606 (3.74%)	Translational - 1st mode (Y predominant)
3	6.831120	6.974106 (2.09%)	Torsional - 1st mode
4	9.250594	9.666098 (4.49%)	Translational - 2nd mode (X predominant)
5	10.751972	11.18772 (4.05%)	Translational - 2nd mode (Y predominant)
6	21.636088	22.36050 (3.35%)	Torsional - 2nd mode

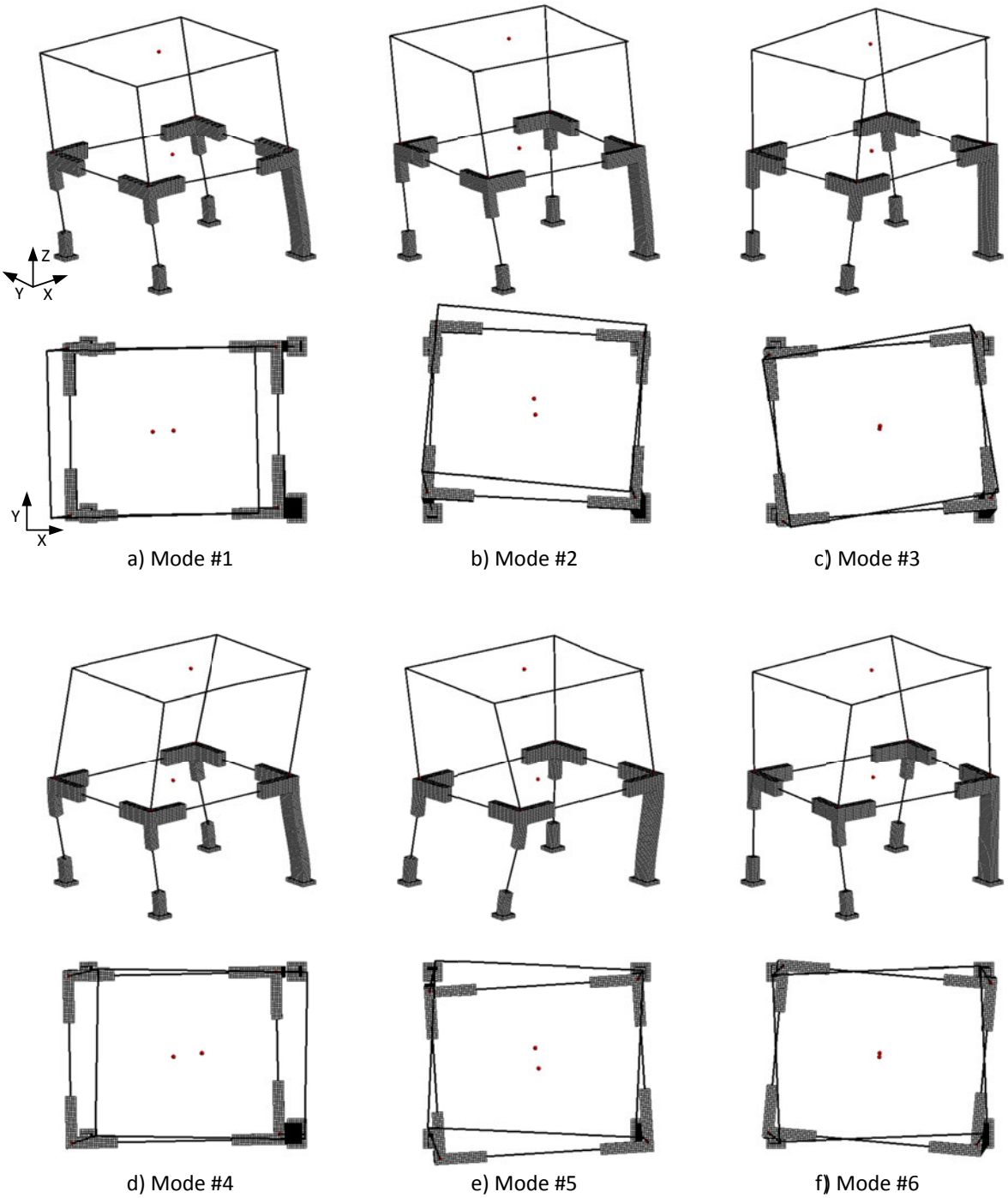

a) Mode #1 b) Mode #2 c) Mode #3

d) Mode #4 e) Mode #5 f) Mode #6

Figure V.66: Analysis HPC5.1 – Mode shape configurations.

Regarding the mode shape configurations, it can be easily observed from Figure V.66 that the first two modes are nearly pure X-Y translational modes, and only a small coupling occurs due to the asymmetry created by column C2. The third mode is torsional and the same pattern repeats for the fourth to the sixth modes. This is the expected behaviour for this mass and stiffness distribution and these results are considered to be very well correlated to the ones from the reference model.

- Incremental dynamic analysis with earthquake loading

The first step for running an *Incremental Dynamic Analysis* (IDA) was to define the earthquake loading. It was decided to use the data from acceleration records obtained from a real seismic event. The *L'Aquila-Abruzzo* earthquake was chosen that occurred in Italy on April 6th, 2009, at 03:32:39 local time. This event had magnitude 6.3 $\left(M_w\right)$ and took 308 human lives, injured more than 1500 people and damaged many constructions, including historic monuments [464]

Figure V.67 to Figure V.69 present the three components of the most intense 20 seconds of the record from station AQV (Centro Valle) and Figure V.71 presents the elastic response spectra $\left(\xi = 5\%\right)$ for these records. In addition, Figure V.70 presents the computed ground displacements that were obtained using the software *LNEC-SPA* [395], by filtering low frequencies (<0.2 Hz) and making a double frequency domain integration on the acceleration records. Considering that small residual displacements occurred at the beginning and at the end of the records, a cosine-tape window was applied to the final records in order to have a smooth beginning and ending.

The time integration was performed considering a time step increment of $\Delta t = 0.02\,\text{s}$ and the trapezoidal integration rule was adopted by setting the *α-Method* parameters to: $\alpha = 0.00$; $\gamma = 0.50$ and $\nu = 0.25$. Proportional damping was once again considered and in this case, taking into consideration the mode frequencies computed in the previous analysis, the parameters were set considering 5% of damping for the frequencies of 3.0 Hz and 10.0 Hz, leading to the coefficients $\alpha_d = 0.144997$ and $\beta_d = 1.224269\text{E-}3$.

At this stage, it is worth noting that the prototype considered in this example is already a feasible specimen to be tested in the LNEC's triaxial shaking table facility. Figure V.72 presents a schematic representation of a full scale model of the prototype. It can be observed that this model is nearly reaching the capacity of the facility in terms of the dimensions in plan (4.60x5.60 m^2) and in terms of the total mass of the model (2x14.272 ton) that must be below 40 ton. In conclusion, it is possible to say that the dimensions of the structure considered in this example are representative of the models being tested for seismic performance in modern European large-scale dynamic testing facilities.

Figure V.73 to Figure V.78 present the time histories obtained from the IDA for the displacements (*X* and *Y*) and for the rotation along the *Z*-axis, for the first and second storey master nodes, respectively. These results are directly compared with the equivalent data obtained using *SAP2000* [497]. From the observation of these plots, it is possible to conclude that the results are very similar, only with slight differences for the rotation along the vertical axis. These differences are considered small and clearly justified by the differences in the numerical models, namely in the discretization.

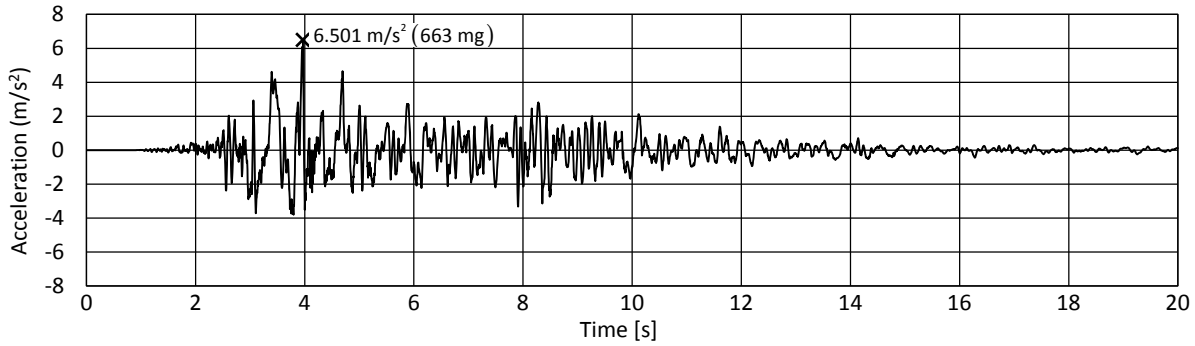

Figure V.67: Analysis HPC5.2 – L'Aquila Earthquake (2009): Ground acceleration at station AQV (Centro Valle)-Channel XTE.

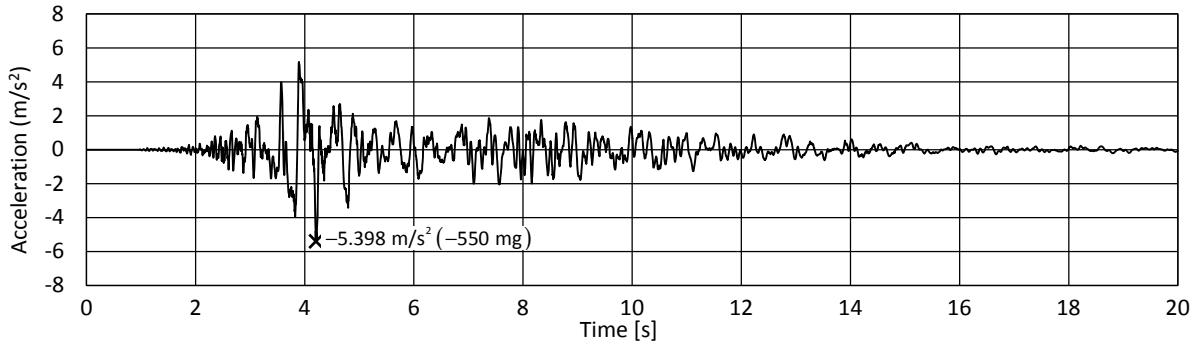

Figure V.68: Analysis HPC5.2 – L'Aquila Earthquake (2009): Ground acceleration at station AQV (Centro Valle)-Channel YLN.

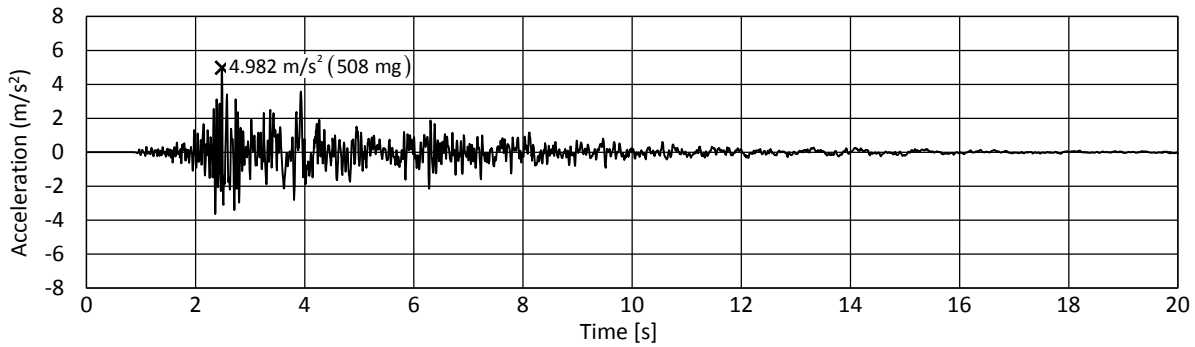

Figure V.69: Analysis HPC5.2 – L'Aquila Earthquake (2009): Ground acceleration at station AQV (Centro Valle)-Channel ZUP.

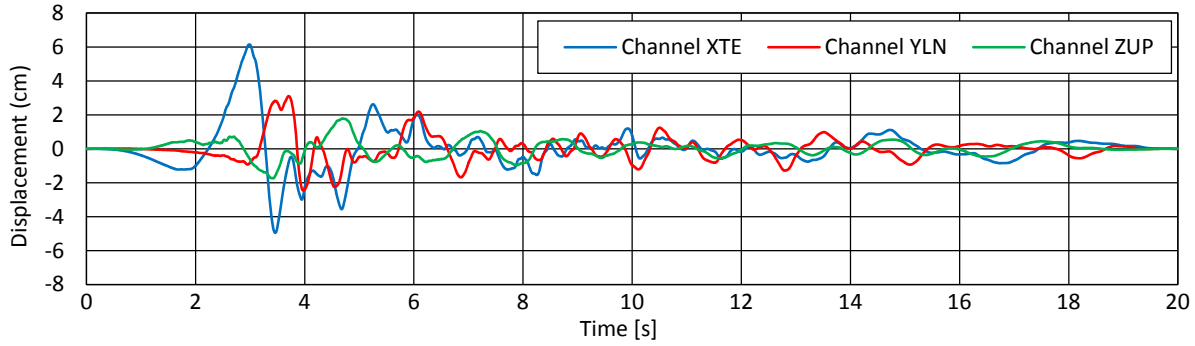

Figure V.70: Analysis HPC5.2 – L'Aquila Earthquake (2009): Computed displacements for station AQV (Centro Valle).

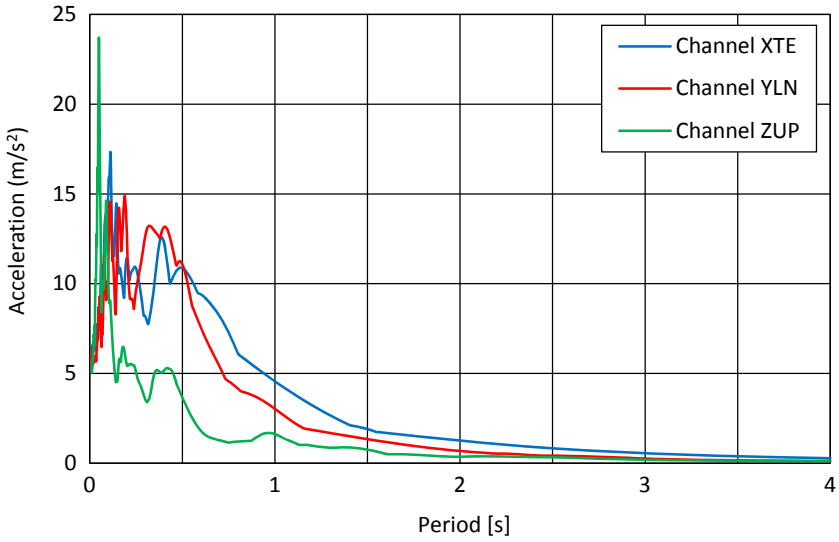

Figure V.71: Analysis HPC5.2 – L'Aquila Earthquake (2009), AQV station (Centro Valle): Elastic response spectra $(\xi = 5\%)$.

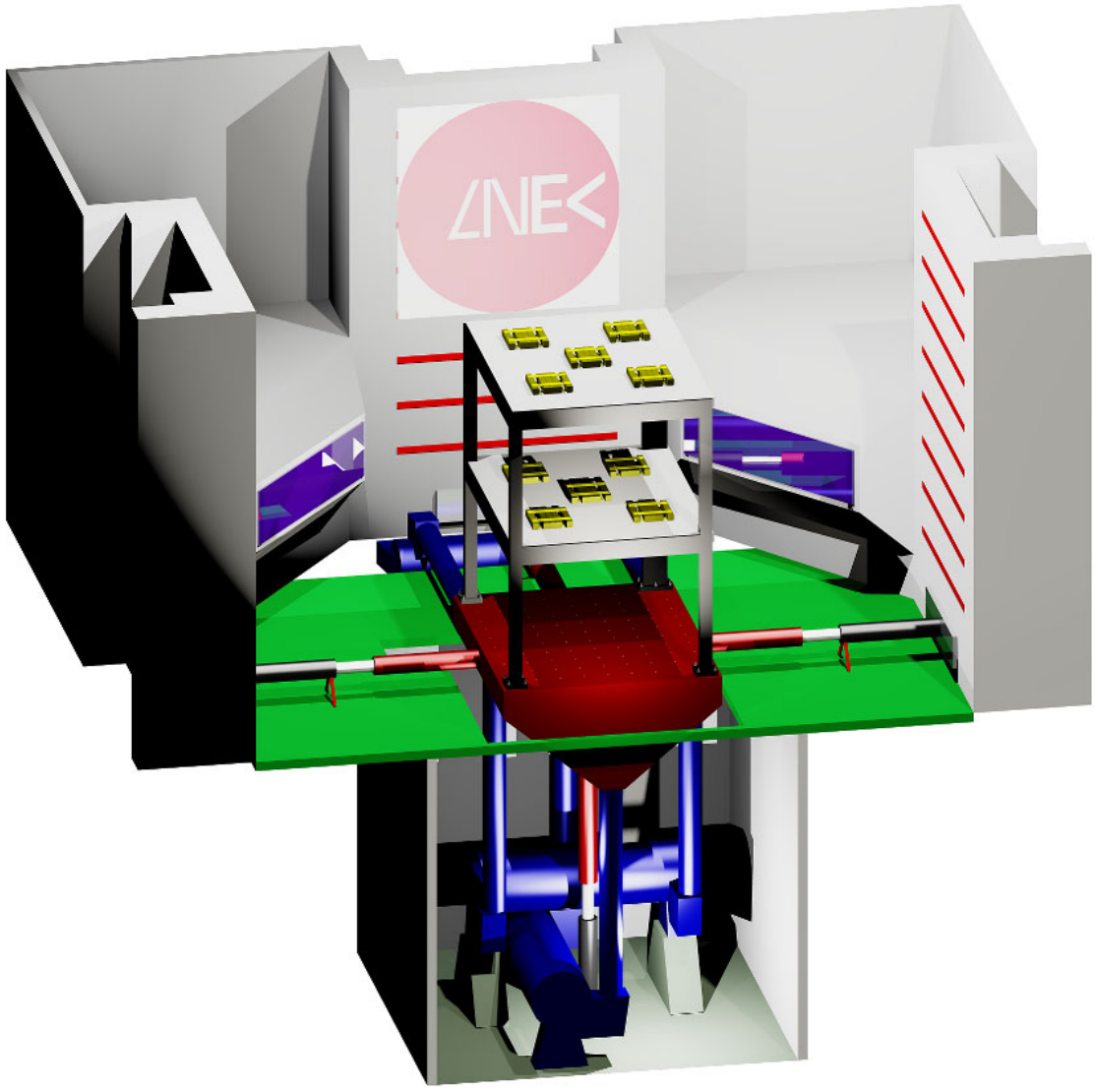

Figure V.72: Example HPC5 – 3D Representation of the prototype considered being tested at LNEC's triaxial shaking table.

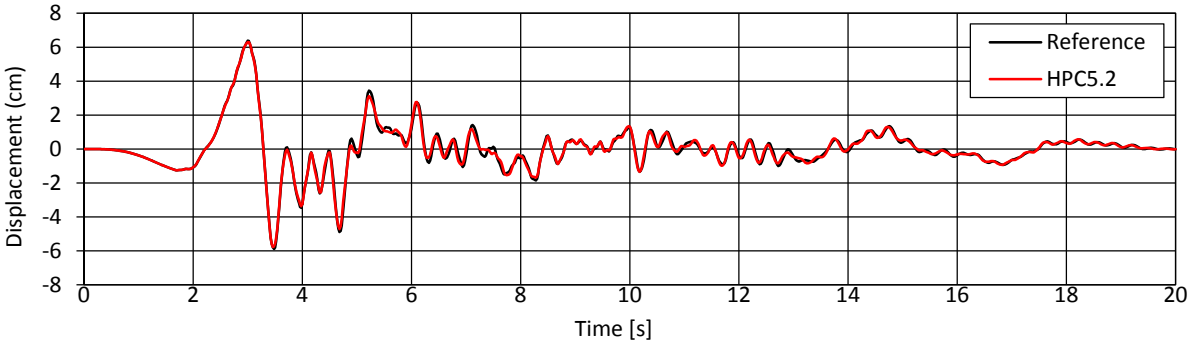

Figure V.73: Analysis HPC5.2 – Displacement at first floor master node along the x direction.

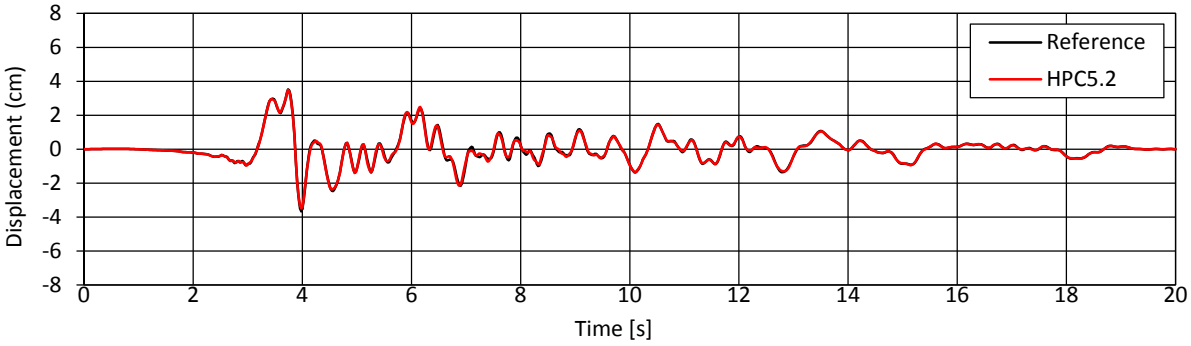

Figure V.74: Analysis HPC5.2 – Displacement at first floor master node along the y direction.

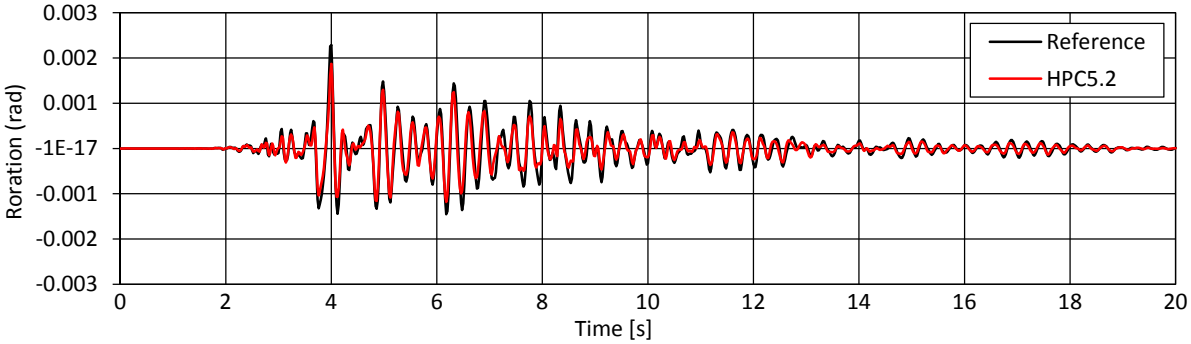

Figure V.75: Analysis HPC5.2 – Rotation at first floor master node along the z direction.

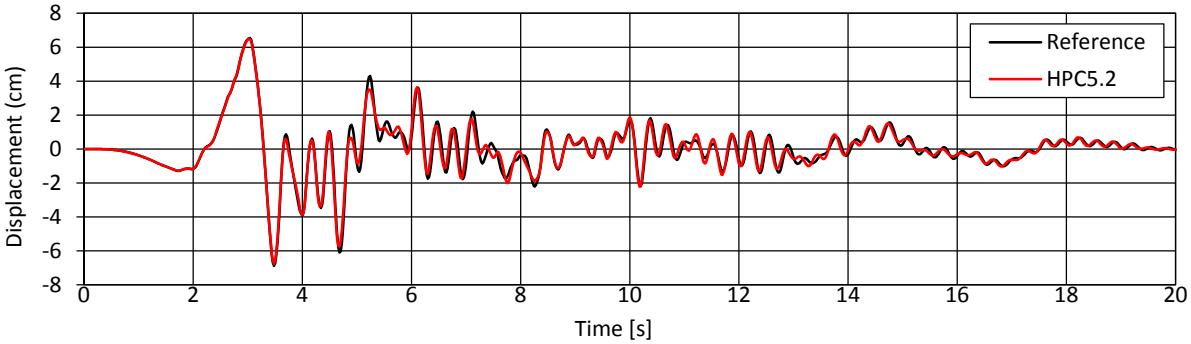

Figure V.76: Analysis HPC5.2 – Displacement at second floor master node along the x direction.

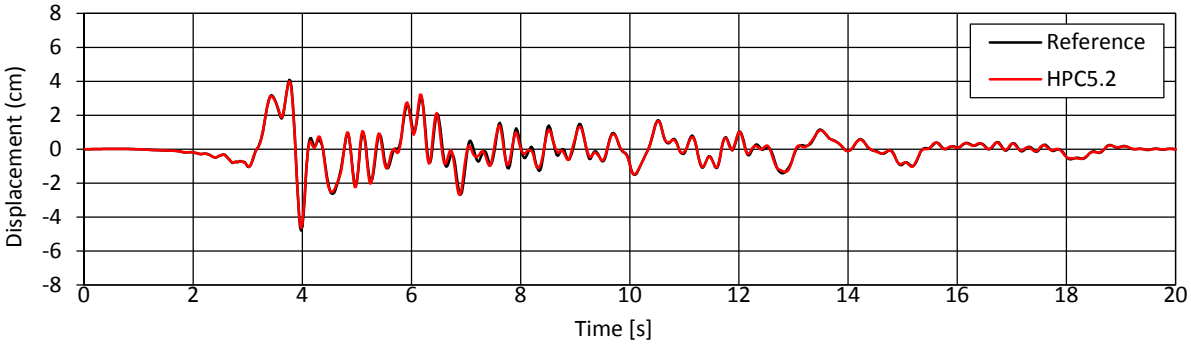

Figure V.77: Analysis HPC5.2 – Displacement at second floor master node along the y direction.

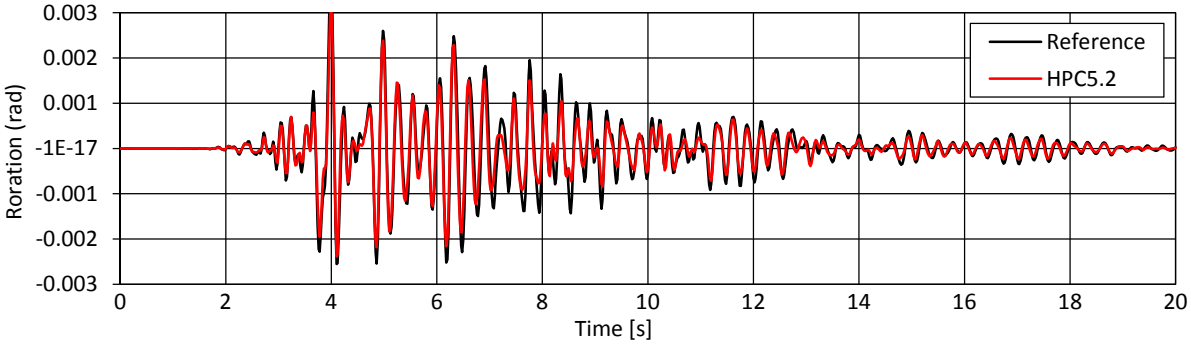

Figure V.78: Analysis HPC5.2 – Rotation at second floor master node along the z direction.

It should be stressed that although the vertical component of the earthquake was considered in the analysis, no inertia forces were mobilized because the model did not include mass along this direction.

Another common graphical representation in experimental seismic engineering studies is plotting the displacements of the slab's centre of mass along both horizontal directions (*X vs. Y*), when it can be considered as rigid in its plane. This is the case of the absolute and relative displacements presented in Figure V.79 and Figure V.80, which are associated with the master nodes from the first and second storeys, respectively. The absolute displacement curves are dominated by the ground displacements, namely the large displacement amplitudes in the time histories at around 3-4 s. On the other hand,

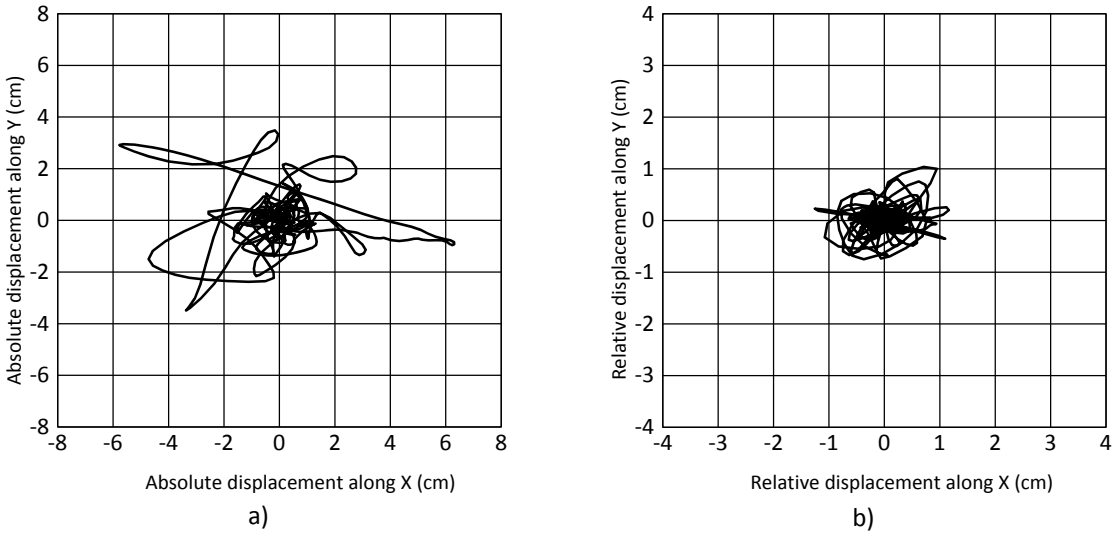

Figure V.79: Analysis HPC5.2 – *X vs. Y* displacements at the first floor master node.

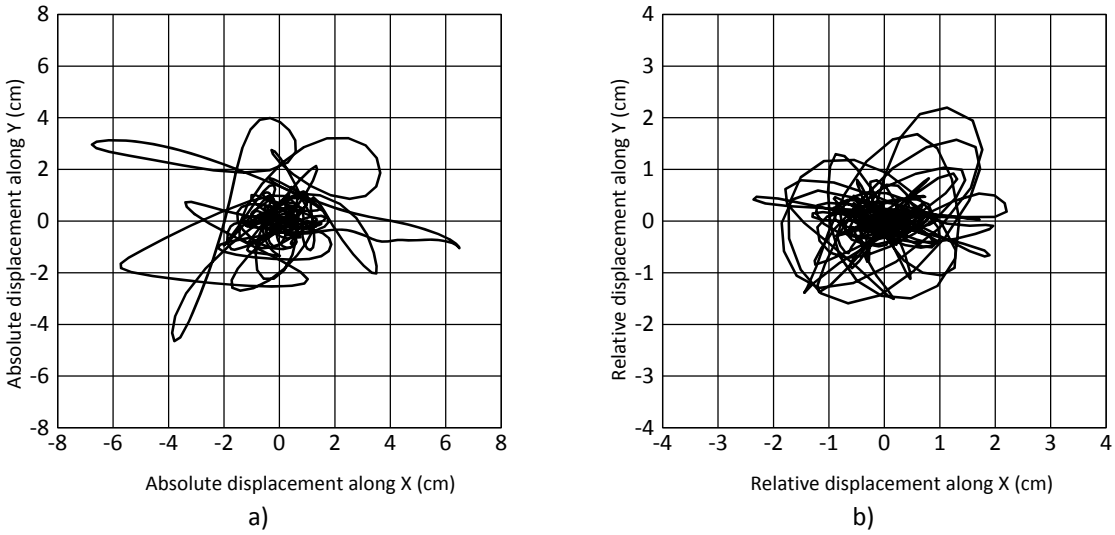

Figure V.80: Analysis HPC5.2 – *X vs. Y* displacements at the second floor master node.

the relative displacements are as expected smaller and represent a maximum inter-storey drift of around 0.45% on both storeys. The shape of these curves shows a regular pattern, defining nearly a circle, which is a consequence of the linear response of the structure and of similar earthquake intensity in both horizontal directions.

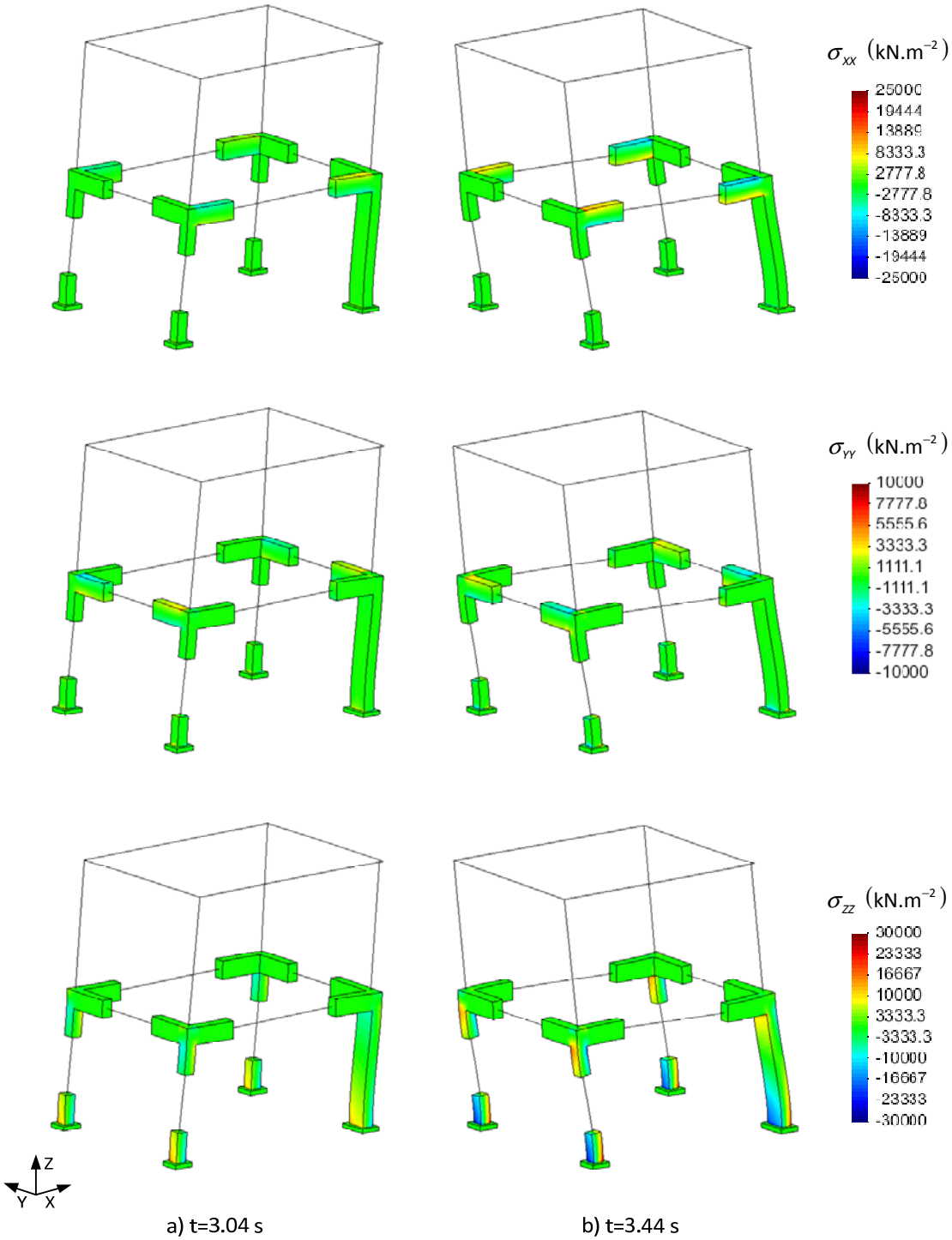

Figure V.81: Analysis HPC5.2 – Deformed mesh (magnified by 50) and stress fields σ_{XX}, σ_{YY}, σ_{ZZ} at selected time steps.

Finally, Figure V.81 presents the stress field σ_{XX}, σ_{YY}, σ_{ZZ} plotted on the deformed mesh at chosen time steps. The observation of the stresses is difficult because the stress peaks govern the colour distribution in the structure. Nevertheless, it is possible to confirm that for this type of loading, higher stresses concentrate near the edges of the elements, corroborating the underlying hypothesis for the hybrid discretization adopted.

Chapter VI

Conclusions and Future Research

1 Introduction

The work carried out in this thesis focused on the development of advanced numerical models for simulating *reinforced concrete* (RC) structures under earthquake loading. As stressed in the introductory chapter, the motivation to develop this work was to contribute with solutions that could speed up the process for having more accurate, robust and practical numerical tools to complement the experimental activity being carried out in large-scale seismic testing facilities.

The methodology adopted is based on using refined three-dimensional meshes and advanced constitutive models to perform dynamic incremental analyses. These characteristics are combined to improve the simulation capacity for complex inelastic phenomena that develop in RC structural members, *e.g.* the imperfect bond between the concrete and the reinforcements. One important drawback of this approach is related to the fact that it leads to very large problem sizes. Consequently, the computational efficiency of the proposed numerical models was improved using parallel computations and efficient analysis and discretization techniques.

This chapter includes a summary of the work done and an overall assessment of the achievements made and the difficulties experienced. Afterwards, the original contributions of this work are compiled in a list and possible topics to be addressed in future research are identified.

2 Summary and overall assessment

This work started by formulating a set of objectives and by making some choices regarding the modelling techniques. These can be recalled and summarized in the following list:

i. To use refined three-dimensional meshes, the traditional *Finite Element Method* (FEM) and a suitable *Time Integration* (TI) algorithm to perform *Nonlinear Incremental Dynamic Analyses* (NL-IDA);
ii. To combine different types of constitutive models to simulate the RC response under reversed cyclic loading. In particular, damage mechanics models for the concrete and phenomenological models for the reinforcing steel bars;
iii. To simulate the bond failure between the concrete and the reinforcing steel using a bond model suitable for general loading;
iv. To improve the computational performance of seismic analyses using high performance computations and suitable structural analysis techniques.

These can be seen as the main characteristics and research lines followed in this thesis. A summary and a global assessment of the work carried out in each of these topics are presented in the following paragraphs.

- The use of refined 3D meshes, the traditional FEM and a suitable TI algorithm for NL-IDA

The concrete was simulated with 4-noded plane elasticity elements (Q4) and 8-noded solid elements (H8). The use of 20-noded hexahedra was also tested (H20). This type of elements only includes the translational *degrees of freedom* (*dofs*). The three-dimensional analyses performed revealed that accurate results can be obtained by using cubes with 2.5 to 5.0 cm of edge length for common RC members. The reinforcing bars were modelled using truss or beam-column elements implemented in 2-noded linear geometry elements (L2). Uniform structured meshes were used, which present the advantage of being easier to create and not requiring complex mesh generators.

Using the traditional displacement-based FEM was a choice taken at an early stage of this work. As mentioned before, the reasons for selecting this option were related to the flexibility and to the advanced evolution stage reached by this formulation. In addition, most of the modelling approaches adopted in this work were already tested with the traditional FEM and with good results, *e.g.* the *continuum damage models*. From the work developed, it is possible to conclude that this formulation is adequate for the objectives of this work and that the initial expectations were fulfilled.

Furthermore, the α-Method was chosen as the TI algorithm because this formulation is unconditionally stable and second-order accurate, and consequently, it makes it possible to use relatively large time steps without compromising the accuracy or the stability. Typical values for the time step used for seismic analyses were between 0.005 s and 0.02 s. In addition, another advantage of the α-Method is the capacity for adding controlled levels of numeric dissipation to damp out high frequency spurious modes. The possibility of recovering different types of TI algorithms with simple adjustments of the parameters is also valued. In conclusion, this TI method turned out to be a good choice and led to accurate results. Nevertheless, additional testing is still required.

- To combine different types of constitutive models to simulate RC under general loading

The constitutive model adopted for the concrete is based on the *continuum damage mechanics* (CDM) approach. As presented before, this technique adopts a smeared simulation of cracking and can capture many aspects of the concrete response.

In the tests performed for this thesis, the CDM approach proved to be adequate for simulating the initial diffuse cracking but could become less realistic and inefficient for advanced inelastic states. In fact, the complexity levels of the validation examples presented in Chapter III were limited by the performance and accuracy of the CDM approach adopted for modelling the concrete.

Moreover, under reversed loading, it was possible to identify convergence difficulties for some of the most prominent models, in particular when models with two scalar damage variables were used (*e.g. Mazars' model*) and the reloading is made after severe damage in the opposite direction. In addition, the energy-based regularization does not avoid the mesh-dependence and nonlocal models increase the complexity of the model and the computational demand. Furthermore, using the secant stiffness proved to be a robust approach, but the convergence rate was very poor, leading to a large number of iterations for achieving convergence for the time steps associated with high inelasticity.

As a conclusion, it is possible to stress that concrete modelling with three-dimensional refined meshes still requires a large research effort, in order to have a practical and robust model that can produce accurate and realistic results under general loading cases.

The reinforcing steel bars were simulated using two semi-analytical models. The first model was called the *Simplified Steel* (*SSteel*) model and includes the most significant phenomena that characterize the response of the reinforcements, like the nearly elastic stiffness of the loading and unloading branches and the strain hardening. In addition, after reaching the ultimate stress a softening branch can be simulated until bar rupture. Moreover, the statistical dispersion associated with the yielding and the ultimate stress can be introduced by specifying the coefficient of variation of these parameters.

The *SSteel* model presents the advantages of having a simple formulation and an easy utilization (four essential model parameters out of seven in total), and turned out to be very efficient from the computational point of view. After comparing experimental results with the ones obtained with the *SSteel* model, it was possible to conclude that the basic characteristics of the response under general loading cases can be simulated. However, some differences were identified for the loading and unloading curvatures after reversal (*Bauschinger effect*) and for the peak stress at reversal. In conclusion, this model was considered to be adequate when the structural response is not too dependent on the individual response of the steel reinforcements, *e.g.* large structures.

A second model was proposed for the reinforcing steel bars. The so-called *Refined Steel* (*RSteel*) model tries to capture most of the phenomena identified in the state of the art, concerning the steel reinforcements response under general loading cases. This model is characterized by having a bilinear response for the first loading, which is followed by a softened branch defined by the well-known *Guiffrè-Menegotto-Pinto* equation improved by Filippou *et al.*

A new proposal is presented for the yield surface evolution that makes it possible to consider the isotropic cyclic hardening observed in the reinforcements. Moreover, a new definition was proposed for the *R* parameter evolution, which is associated with the curvature of the softened branch. The model was also enhanced by an innovative proposal for considering the effect of low-cycle fatigue, which results in a continuum and significant strength decrease that can even lead to premature failure under earthquake loading. The same approach for considering the statistical variance of the yielding and the ultimate stress adopted for the *SSteel* model was also included in this model.

The resulting formulation is completely defined by 11 parameters, which can be reduced to 7 if the low-cycle fatigue and the strength dispersion are not considered. The comparison made with experimental results showed that this model can reproduce the loading and unloading paths for multiple load-reload cycles with a very interesting accuracy. In addition, it was possible to define the tangent stiffness matrix, which presents a significant advantage with respect to the computational efficiency of the model.

The effect of the buckling of the reinforcements and the strain-rate effect were not introduced in the model because of the additional complexity associated with these effects and because the efficiency of the model would be compromised. At the end, the *RSteel* model turned out to be robust, efficient and balanced for simulating the steel reinforcements subjected to earthquake loading.

The *SSteel* and *RSteel* models for modelling the reinforcing steel bars were implemented in truss and in beam-column elements, in which the remaining deformation modes (bending, twisting and shear) were considered elastic.

- The simulation of the bond mechanism between the concrete and the reinforcing steel bars

A new interface element was proposed to simulate the bond mechanism for general loading cases. This interface element is based on the isoparametric formulation of the *zero-thickness* interface elements proposed by Beer [48]. An innovative semi-analytical nonlinear bond model was proposed in this thesis. This model is defined at the reinforcement scale and makes it possible to simulate the following characteristics of the bond mechanism:

i. the response in the perfect bond domain;
ii. the premature collapse for smooth bars;
iii. the stiffness decrease for ribbed bars until reaching the peak stress;
iv. the effect of splitting cracks on the peak stress;
v. the softening and friction branches after the peak stress under monotonic loading;
vi. the unloading and the friction branches upon load reversal;
vii. the stiffness regain on reloading;
viii. the cyclic degradation;
ix. the evolution of the slip at peak stress;
x. the evolution of the reload slip;
xi. the radial stress effect.

The large number of phenomena covered led to 22 model parameters. This number is considered

high and a drawback of the proposed model. To mitigate this problem, the bond was developed using a hierarchal approach, by defining a base model with 9 parameters and a group of 4 sub-models for the simulation of the cyclic degradation, the peak stress slip evolution, the reload slip evolution and the radial stress effect, using 2, 1, 3 and 7 additional parameters, respectively. This hierarchal approach makes it possible to use the model for reversed loading cases by defining only the 9 parameters required for the base model by setting the other parameters to default values. Each sub-model can be added only if the simulated effect is significant for the response.

As an overall assessment, it is possible to stress that the proposed solution presents a balanced and robust way to simulate the large majority of phenomena that characterize the bond mechanism. The proposed implementation in a zero-thickness interface element revealed to be a viable and reasonable way to incorporate the bond mechanism into refined three-dimensional meshes. Furthermore, the proposed solution was able to simulate the response observed in experimental tests with a very satisfactory response in terms of accuracy and robustness.

- The computational performance improvement

In this thesis, the computational performance was improved by taking advantage of concurrent computations, advanced substructuring techniques and hybrid discretizations.

The use of concurrent computations was implemented in the finite element code developed and makes it possible to take advantage of the data parallelism associated with the FEM and partitioned subdomains, *e.g.* for the element's state determination and for the computation of the structural operators.

On the other hand, substructuring techniques, *a.k.a.* Domain Decomposition (DD) methods, can also be used to enhance the gains from using concurrent computations by adapting the structural analysis algorithm. Several domain decomposition methods were tested, namely: the *Primal Substructuring* (PS) method, the *Neumann-Neumann* (NN) method, the *Balancing Domain Decomposition* (BDD) method, the *One-level Finite Element Tearing and Interconnecting* (FETI-1) method and the *Dual-Primal Finite Element Tearing and Interconnecting* (FETI-DP) method.

The combination of concurrent computations and substructuring techniques was tested with high levels of parallelization (up to 24 subdomains) and the results showed that the DD methods returned results with similar levels of accuracy. Moreover, the computational performance was measured for the PS method in terms of the concurrent speed-up and efficiency using up to 4 subdomains, due to hardware constraints. The results exposed super linear speed-up values of up to 6.7, for the largest problem sizes considered (around 100,000 *dofs*) and using 4 processing units. These results exceeded the initial expectations and were considered very promising and extremely encouraging.

The third technique used to improve the computational performance was the so-called *Hybrid Discretizations* (HD) technique. This technique combines different types of meshes and can reduce the size of the problem to be analysed enormously. As an example, in the HPC4 example presented in Chapter V, the reduction of the total number of unknowns was about 48% and it was possible to measure speed-up values of 3.5 using sequential computations and 4.1 using concurrent

computations. The gains using sequential computations resulted from the approximately quadratic increases of the number of operations required when the problem size increases linearly, *e.g.* for solving a linear system. In the second case, the performance was also enhanced by the code parallelization. Please note that the concurrent speed-up values take into consideration the number of processors. Furthermore, when combining the improvements associated with concurrent computations with the ones resulting from substructuring techniques and with hybrid discretization, it was possible to measure speed-up values of up to 11.7, even though for that case the mesh partition led to some load unbalance.

The *Hybrid Discretization* (HD) proposed also presents the following two additional benefits: firstly, it creates a natural and efficient partition between the subdomains that can be used in the substructured analysis. In addition, hybrid discretization increases the modelling flexibility by promoting the use of different element types in different parts of the structure (see Figure V.14).

Furthermore, it was necessary to test different methods to enforce *Kinematic Constraints* (KC) associated with the HD, to enforce global structural behaviour for partitioned subdomains and to impose displacements to simulate earthquake loadings. This research concluded that the best way to enforce the *Beam2Solid* KC is to use subdomain-based KC enforced by the Master-Slave Elimination method, called *Local Kinematic Constraints* (LKC) in the scope of this work. Using this technique, the model can benefit from the parallelization and scale with the number of processors. In addition, when the objective is to enforce inter-subdomain behaviour then the best solution is to use *Global Kinematic Constraints* (GKC), enforced by *Lagrange Multipliers* and using additional LKC to reduce the number of unknowns added to the coarse problem. Lagrange Multipliers were also used to impose displacements on the structure, and as before, trying to reduce the number of unknowns added to the reduced problem using LKC.

3 Original contributions

The statement that a specific feature of this work is original must be stressed with caution because it is impossible to have an absolute confidence that it was not already proposed by other authors. Taking this into consideration, the elements of the following list should be interpreted as the original contributions of this work, considering the knowledge acquired by the author during the bibliographic research undertaken:

i. The changes made in *Mazars'* model by introducing a new definition for the response under tensile loading and the introduction of probabilistic-based mechanical properties for modelling the concrete;
ii. The proposal of two new models for the axial response of the steel reinforcements. In particular, the *RSteel* model that is based on the well-known *Guiffrè-Menegotto-Pinto* equation and presents new contributions for the definition of the yield surface evolution and to the curvature-related parameter *R*. In addition, an innovative low-cycle fatigue model was proposed and a probabilistic-based definition of the yielding and of the ultimate stress was introduced;

iii. The proposed hierarchal semi-analytical bond model incorporated in a isoparametric zero-thickness interface element;
iv. The comparison of different *Domain Decomposition* methods in terms of accuracy and performance, when implemented for nonlinear incremental dynamic analyses;
v. The combination of the *Primal Substructuring method* with the use of *Global Kinematic Constraints* to enforce global structural behaviour associated with multiple subdomains. In addition, the use of master-slave equations to enforce local kinematic relations and to reduce the number of unknowns in the reduced problem;
vi. The use of the *Hybrid Discretization* proposed to reduce the problem size, to ease the domain partitioning and to promote the use of different mesh types in the same simulation.

4 Future research

There are still many limitations for the numerical modelling of structures subjected to earthquake loading, in particular for RC structures. The use of refined three-dimensional meshes to simulate the seismic response results in complex and demanding computer simulations. These simulations require having representative and efficient models for concrete, steel reinforcements and other phenomena that are considered relevant for the seismic performance, like bond failure. In addition, adopting a high performance computational implementation is required for practical and feasible simulations.

The overall performance in terms of the representativeness and computational performance is conditioned by the weakest link of this chain of components. From the work developed in this thesis, it was possible to conclude that this weakest link is the solution used to model concrete. The conclusion drawn in this work is that, even if it is possible to simulate some of the phenomena that develop in the concrete, the use of CDM seems not to be the best approach, by itself, to simulate the concrete response.

To cope with this limitation, a possible approach is to combine the CDM for the early fracture, with discrete fracture after localization into a macro-crack [130, 422, 561]. This methodology represents the best of both worlds and would allow making a unified structural analysis without the need of interrupting for remeshing, as in the traditional discrete crack approach. Moreover, the results of the CDM can be used to predict the location and the properties of the macro-cracks.

The chosen CDM should be representative of the concrete response and robust for general loading cases and the discontinuity may be introduced by using FE with *embedded cracks* by locally enriching the displacement approximation. This may be done within the scope of the extended versions of the FEM [15, 31, 133, 159, 185, 186, 244, 252, 368, 401, 402, 514, 527, 528], which are based on the *partition of unity method* [22, 187, 391, 513, 555].

Nonlinear Elastic Fracture Mechanics can be used to avoid the problem associated with unbounded stresses near the crack front for the linear approaches (see Figure III.5). One of the simplest models that can be used is the *cohesive fracture* model*,* in which the crack mobilization and propagation are governed by a finite region called the *fracture process zone* (see Figure III.4), which is controlled by

constitutive relations in terms of the crack opening/closing *vs.* the installed force. Some basic concepts of fracture mechanics can be used, like the fracture energy [253] or other techniques to predict the crack propagation [270, 287, 478]. Previous works in this field [112, 162, 368, 454, 455, 525] gave good expectations about the feasibility of this approach.

The procedure for the transition to the discrete model is not yet generally accepted, although some proposals have been made in the bibliography [130, 329, 422, 561]. In addition, the mechanical characteristics of the *fracture process zone* are still subject to some debate. For example, the authors Comi *et al*. [130-134] proposed making the transition to the discrete cohesive crack model when a critical level of damage is exceeded. This critical level depends on the local mesh size and on an analytical estimate of the localization band by means of a perturbation analysis. Moreover, the cohesive law is defined through an energy balance criterion taking into consideration the energy left to dissipate at the localization bands.

Apart from concrete modelling, there are other topics that seem relevant for future research following on from this work. It would be interesting:

i. to continue the validation of the *RSteel* model with additional experimental results, in particular, the proposed low-cycle fatigue sub-model;
ii. to include the buckling of the steel reinforcements and the strain-rate effect into the *RSteel* model;
iii. to test the possibility of using other techniques to simulate damping, like implementing hysteresis loops on the constitutive relations (see Figure II.7-c);
iv. to continue the validation of the CSI model proposed to simulate the bond mechanism with additional experimental results, in particular, when subjected to dynamic loading;
v. to incorporate the loading rate effect in the CSI model and the possibility of simulating the corrosion level directly;
vi. to implement the proposed models in a more efficient framework, like using fully compiled code, rather than using the Matlab environment;
vii. to test the parallelized model for higher parallelization levels than the 24 subdomains used in the accuracy tests and the 4 subdomains used for efficiency analysis;
viii. to test the computational behaviour of the model running in a fully distributed environment (*e.g*. cluster), rather than using local computations and shared memory systems (*e.g.* PCs and workstations), because of the differences in the communications between processing units and due to hardware scaling;
ix. to measure the efficiency gains for problem sizes where the iterative solvers are more efficient than direct solvers;
x. to test the possibility and the efficiency of using different reduced problem levels, *e.g.* a first-level reduced problem defined per building storey and a global reduced problem combining all storeys;
xi. to compare the computational efficiency of different *Domain Decomposition* methods, *e.g.* the FETI-DP method.

Annex A Mathematic Supporting Relations

1 Linear algebra

Consider the linear system of equations:

$$\mathbf{A}\mathbf{x}=\mathbf{b}, \tag{A.1}$$

if no further indication is made, $\mathbf{A}$ is a $n\times n$ real and invertible matrix and **x** and **b** are vectors defined in R^n.

1.1 Basic relations

$$\left(\mathbf{A}\mathbf{B}\right)^t=\mathbf{B}^t\mathbf{A}^t, \tag{A.2}$$

$$\left(\mathbf{A}\mathbf{B}\right)^{-1}=\mathbf{B}^{-1}\mathbf{A}^{-1}, \tag{A.3}$$

$$\left\langle \mathbf{u},\mathbf{v}\right\rangle=\mathbf{u}^t\mathbf{v}. \tag{A.4}$$

A symmetric matrix $\mathbf{A}$ is positive-definite if $\mathbf{x}^t\mathbf{A}\mathbf{x}>\mathbf{0}$, for all $\mathbf{x}\in R$, with $\mathbf{x}\neq\mathbf{0}$ and has all eigenvalues positive.

1.2 Orthogonal bases and orthogonalization

An *orthogonal basis* is a set of orthogonal vectors $\mathbf{q}_k$ that can be used to span a vector space. If these orthogonal vectors have unit length, the base is said to be *orthonormal*. For an orthonormal basis the following relations are verified:

$$\left\langle \mathbf{q}_i,\mathbf{q}_j\right\rangle=\begin{cases}1, \text{ if } i=j\\ 0, \text{ otherwise}\end{cases}. \tag{A.5}$$

If the orthogonal vectors $\mathbf{q}_k$ are grouped into the columns of the matrix **Q**, the following relations can be proved [526]:

$$\mathbf{Q}^t\mathbf{Q}=\mathbf{I}, \tag{A.6}$$

$$\mathbf{Q}^t=\mathbf{Q}^{-1} \text{ (if } \mathbf{Q} \text{ is not a square matrix, } \mathbf{Q}^t \text{ is only the left-inverse)}, \tag{A.7}$$

$$\left\|\mathbf{Q}\mathbf{x}\right\|=\left\|\mathbf{x}\right\|. \tag{A.8}$$

The Gram-Schmidt orthogonalization is a process for finding a set of orthonormal columns $\mathbf{q}_k$ of matrix **A** with independent column vectors $\mathbf{u}_k$. The procedure can be described as follows: i) Set the first vector equal to the first column of the matrix $\mathbf{q}_1=\mathbf{u}_1$; ii) For the following vectors, start with the k^{th} column of the matrix and remove all the component of the previously computed vectors, using:

$$\mathbf{q}_k = \mathbf{u}_k - \sum_{j=1}^{k-1} \frac{\langle \mathbf{u}_k, \mathbf{q}_j \rangle}{\langle \mathbf{q}_j, \mathbf{q}_j \rangle}; \tag{A.9}$$

iii) At the end, each vector **q** is divided by its norm to become orthonormal.

1.3 Permutation matrices

A *permutation matrix* $\mathbf{P}_\pi$ is a square binary matrix where each row has exactly one unitary entry and zeros elsewhere [245]. The permutation matrices can be used to interchange the rows or columns of a matrix by multiplication. These matrices are orthogonal, and according to (A.7), the following property holds [245]:

$$\mathbf{P}_\pi^{-1} = \mathbf{P}_\pi^t . \tag{A.10}$$

Consequently:

$$\mathbf{P}_\pi^{-1} \mathbf{P}_\pi = \mathbf{I} . \tag{A.11}$$

The product of permutation matrices is also a permutation matrix [245].

1.4 Projection matrices

The component of vector **b** on the column space of **A** can be computed from [526]:

$$\mathbf{p} = \mathbf{P}\mathbf{b} , \tag{A.12}$$

where **P** is a *projection matrix* that is defined by:

$$\mathbf{P} = \mathbf{A}\left(\mathbf{A}^t\mathbf{A}\right)^{-1}\mathbf{A}^t . \tag{A.13}$$

Similarly, the component of the vector **b** on the orthogonal complement of **A** can be computed using the projection matrix $(\mathbf{I}-\mathbf{P})$:

$$\mathbf{p}^* = (\mathbf{I}-\mathbf{P})\mathbf{b} . \tag{A.14}$$

The projection matrices have two basic properties [526]:

$$\mathbf{P}^2 = \mathbf{P} , \tag{A.15}$$

$$\mathbf{P}^t = \mathbf{P} . \tag{A.16}$$

Consequently, any symmetric matrix that fulfils (A.15) represents a projection [526].

1.5 Eigenvalues and eigenvectors

The definition of an eigenvector of the matrix **A** is a vector that after being multiplied by **A** results into a vector in the same direction [526]:

$$\mathbf{A}\mathbf{x} = \lambda \mathbf{x} , \tag{A.17}$$

where **x** is the eigenvector and λ is the eigenvalue.

Rewriting (A.17) as:

$$\left(\mathbf{A}-\lambda\mathbf{I}\right)\mathbf{x}=\mathbf{0}\,, \tag{A.18}$$

the term between parentheses must be singular, which leads to the characteristic equations:

$$\det\left(\mathbf{A}-\lambda\mathbf{I}\right)=\mathbf{0}\,, \tag{A.19}$$

Some of the properties of eigenvalues are the following:

$$\mathrm{tr}\left(\mathbf{A}\right)=\sum_{k=1}^{n}\lambda_k\,, \tag{A.20}$$

$$\det\left(\mathbf{A}\right)=\prod_{k=1}^{n}\lambda_k\,, \tag{A.21}$$

1.6 Singular value decomposition

The *singular value decomposition* (SVD) is a matrix factorization that results in representing the real matrix **A** in the following format [526]:

$$\mathbf{A}=\mathbf{U}\boldsymbol{\Sigma}\mathbf{V}^t\,, \tag{A.22}$$

where **U** is a $m\,x\,m$ orthogonal matrix, $\boldsymbol{\Sigma}$ is a $m\,x\,n$ diagonal matrix and **V** is a $n\,x\,n$ orthogonal matrix, defined by:

$$\begin{cases}\mathbf{U}=eigenvectors\left(\mathbf{A}\,\mathbf{A}^t\right)\\ \boldsymbol{\Sigma}=\sqrt{eig\left(\mathbf{A}\,\mathbf{A}^t\right)}=\sqrt{eig\left(\mathbf{A}^t\,\mathbf{A}\right)}\\ \mathbf{V}=eigenvectors\left(\mathbf{A}^t\mathbf{A}\right)\end{cases}. \tag{A.23}$$

Computing the full SVD is a computational intensive procedure and for the general case may require a large amount of free memory, because at least the matrices **U** and **V** will be represented by full matrices. Typically, the SVD computation is made in a two-step procedure: firstly, by reducing the matrix to bi-diagonal format and then by computing the SVD factorization of the bi-diagonal matrix. According to Trefethen *et al.* [544], the first operation is the most expensive and requires $O\left(8n^3/3\right)$ operations for the three-step bi-diagonalization of square matrices. Applications of the full SVD include computing the rank, the null space, the condition number and the pseudoinverse of a matrix.

In many situations, it is not necessary to compute the full SVD decomposition and a *reduced* or *thin* SVD is used, usually associated to iterative methods. These variations are more attractive from the computational point of view because they require much less resources.

1.7 Pseudoinverse

The *Moore–Penrose pseudoinverse* or simply *pseudoinverse* $\mathbf{A}^+$ [57, 406, 443] is a generalization of the inverse matrix of **A** that always exists, is unique and has the following properties [444]:

$$\begin{cases} \mathbf{A}\,\mathbf{A}^{+}\,\mathbf{A}=\mathbf{A} \\ \mathbf{A}^{+}\,\mathbf{A}\,\mathbf{A}^{+}=\mathbf{A}^{+} \\ \left(\mathbf{A}\,\mathbf{A}^{+}\right)^{t}=\mathbf{A}\,\mathbf{A}^{+} \\ \left(\mathbf{A}^{+}\,\mathbf{A}\right)^{t}=\mathbf{A}^{+}\mathbf{A} \end{cases}. \tag{A.24}$$

This matrix can be computed form the singular value decomposition of **A**:

$$\mathbf{A}=\mathbf{U}\boldsymbol{\Sigma}^{+}\,\mathbf{V}^{*}, \tag{A.25}$$

where $\boldsymbol{\Sigma}^{+}$ can be found by computing the reciprocal of the non-null diagonal elements of $\boldsymbol{\Sigma}$.

1.8 Vector and matrix norms

The *p-norm* of a real vector can be defined as [245, 444]:

$$\left\|\mathbf{v}\right\|_{p}=\left(\sum_{i=1}^{n}\left|v_{i}\right|^{p}\right)^{1/p}, \tag{A.26}$$

leading to:

$$\left\|\mathbf{v}\right\|_{1}=\sum_{i=1}^{n}\left|v_{i}\right|, \tag{A.27}$$

$$\left\|\mathbf{v}\right\|_{2}=\sqrt{\mathbf{v}^{t}\mathbf{v}}, \tag{A.28}$$

$$\left\|\mathbf{v}\right\|_{\infty}=\max_{i}\left|\mathbf{v}_{i}\right|. \tag{A.29}$$

Matrix norm can be seen as the extension of the vector norm into matrices. The *induced* or *operator norm,* corresponding to the *p-norm* for vectors, can be defined for real matrices by [245, 444]:

$$\left\|\mathbf{A}\right\|_{p}=\max_{\mathbf{v}\neq\mathbf{0}}\frac{\left\|\mathbf{A}\,\mathbf{v}\right\|_{p}}{\left\|\mathbf{v}\right\|_{p}},$$

leading to:

$$\left\|\mathbf{A}\right\|_{1}=\max_{j}\sum_{i=1}^{n}\left|\mathbf{A}_{ij}\right|, \tag{A.30}$$

$$\left\|\mathbf{A}\right\|_{2}=\sqrt{\max\left(eig\left(\mathbf{A}^{t}\mathbf{A}\right)\right)}, \tag{A.31}$$

$$\left\|\mathbf{A}\right\|_{\infty}=\max_{i}\sum_{j=1}^{n}\left|\mathbf{A}_{ij}\right|. \tag{A.32}$$

1.9 Condition number

The condition number of **A** is a parameter that can be used to measure how close is the matrix to be singular. It also can be used to assess the sensitivity of the solution **x** regarding changes in the vector **b**. If the condition number is small (near one) the solution is weakly affected by small changes in **b**.

On the contrary, if it is large the solution is strongly affected and nearly singular.

The condition number can be defined using matrix norms using [526]:

$$\kappa(\mathbf{A}) = \|A\|_p \left\|A^{-1}\right\|_p . \tag{A.33}$$

Usually the Euclidean norm is considered $(p=2)$. In this case, the condition number can be computed from the maximal and minimal singular values, using [444]:

$$\kappa(\mathbf{A}) = \|\mathbf{A}\|_2 \left\|\mathbf{A}^{-1}\right\|_2 = \sqrt{\max\left(eig\left(\mathbf{A}^t\mathbf{A}\right)\right)}\sqrt{\max\left(eig\left(\mathbf{A}^{-1,t}\mathbf{A}^{-1}\right)\right)} = \frac{\sigma_{\max}(\mathbf{A})}{\sigma_{\min}(\mathbf{A})}.$$

For a symmetric, positive-definite matrix, the last expression can be computed from:

$$\kappa(\mathbf{A}) = \|\mathbf{A}\|_2 \left\|\mathbf{A}^{-1}\right\|_2 = \max\left(eig(\mathbf{A})\right)\ \max\left(eig\left(\mathbf{A}^{-1}\right)\right) = \frac{\max\left(eig(\mathbf{A})\right)}{\min\left(eig(\mathbf{A})\right)}.$$

1.10 Direct solvers

- Gaussian Elimination

The *Gaussian Elimination* (GE) is a direct solving procedure composed by two steps: the forward-elimination and back-substitution of an augmented matrix. If no zeros are found in pivot positions, the computation cost is the following: $\left(2n^3+3n^2-5n\right)/6$ multiplications, $\left(2n^3+3n^2-5n\right)/6$ subtractions and $n(n+1)$ divisions, resulting in a total of $2n^3/3+2n^2+O(n)$ floating point operations [174].

- LU factorization

If **A** is a real, invertible, *n x n* matrix, is possible to perform the following decomposition [245]:

$$\mathbf{A} = \mathbf{LU}, \tag{A.34}$$

where **L** is a lower triangular matrix that holds the pivots used in the decomposition and **U** an upper triangular matrix equal to the one obtained by forward-elimination in the Gaussian elimination.

After the decomposition is complete, the vector of unknowns can be obtained by:

$$\text{Find } \mathbf{x}\text{: } \mathbf{Ly} = \mathbf{b};\ \mathbf{Ux} = \mathbf{y}. \tag{A.35}$$

The Gaussian Elimination is computationally more efficient for solving one linear system of equations because it avoids storing the lower triangular matrix **L**. However, LU factorization becomes more attractive if the linear system must be solved for multiple *rhs*, because after factorization it is only required to solve two systems, defined with triangular matrices.

The number of floating point operation is the same as in Gaussian Elimination. However, if zeros are found in pivot positions, it is necessary to perform row exchanges that can be done using permutation matrices, as follows: $\mathbf{PA} = \mathbf{LU}$. This will result in additional floating point operations.

- Cholesky factorization

If **A** is a symmetric, positive-definite $n\,x\,n$ matrix, there is a unique decomposition in the format:

$$\mathbf{A} = \mathbf{L}\mathbf{L}^t, \tag{A.36}$$

where **L** is lower triangular matrix defined by [245]:

$$\begin{cases} L_{jj} = \sqrt{A_{jj} - \sum_{k=1}^{j-1} L_{jk}^2}, \text{ for } j = 1,\ldots,n \\ L_{ij} = \left(A_{ij} - \sum_{k=1}^{j-1} L_{ik}\, L_{jk} \right) \Big/ L_{jj}, \text{ for } i > j \end{cases}. \tag{A.37}$$

After the decomposition is complete, the vector of unknowns can be obtained by:

$$\text{Find } \mathbf{x}\text{: } \mathbf{L}\,\mathbf{y} = \mathbf{b};\ \mathbf{L}^t\,\mathbf{x} = \mathbf{y}\,. \tag{A.38}$$

The computational cost is the following: $n^3/6 + O\left(n^2\right)$ additions, $n^3/6 + O\left(n^2\right)$ multiplications, $n^2/2 + O\left(n\right)$ divisions and $O\left(n\right)$ square root extractions, resulting in a total of $n^3/3 + O\left(n^2\right) + O\left(n\right)$ floating point operations, which is about half the requirements of the Gaussian Elimination for full, unsymmetrical matrices.

The Cholesky factorization is numerically more stable and efficient than the LU factorization and there are formulas for finding the entries of matrix **L** that do not require computing square roots.

- QR factorization

If **A** is a real, full column rank, $m\,x\,n$ matrix, the following decomposition is possible [245]:

$$\mathbf{A} = \mathbf{Q}\mathbf{R}, \tag{A.39}$$

where $\mathbf{Q}$ is an orthogonal matrix and $\mathbf{R}$ is an upper triangular matrix.

These matrices can be computed by several methods. One of the simplest is to use the *Gram-Schmidt* process (see section 1.2) to find **Q** and using the relation $\mathbf{R} = \mathbf{Q}^t\mathbf{A}$ to find **R**. However, the numerical stability of the *Gram-Schmidt* process is not the best and therefore other algorithms like the *Householder transformation* are commonly used. Using the *Householder transformation*, it can be proved the number of floating point operation is of the order $2n^2\left(m - n/3\right)$.

1.11 Iterative solvers

- Conjugate Gradient method

The *Conjugate Gradient* (CG) method [264] is an iterative procedure for solving linear systems, in which the coefficient matrix is symmetric and positive-definite. This method is very efficient for large and sparse systems [492].

If **A** is a $n \times n$ symmetric and positive-definite matrix. For finding better approximations for the vector of unknowns **x**, the CG method defines the residue vector **r** and a set of A-orthogonal search directions **p**, which are computed from the previous preconditioned residue **z** and an increment in

the previous search direction defined by β. It can be proved that the increment in each search directions will be exact, and consequently, the method will converge in at most in *n* iterations.

A *preconditioner matrix* **M** can be used to improve the converge rate of the iterative procedure used to find the solution. To be effective, this matrix should not be too expensive to be implemented [505]. Common preconditioners for generic linear systems are the *Jacobi preconditioner*, which uses the diagonal of **A** that can also be scaled. Another option is the *Gauss-Seidel preconditioner* that uses a triangular part of **A**. In additions, preconditioners resulting from incomplete LU or *Cholesky factorizations* are also used.

The algorithm of the *Preconditioned Conjugate Gradient* method is presented in the Algorithm A.1.

1.12 Least squares solution of an inconsistent system

The least squares solution is the one that satisfies:

$$\widehat{\mathbf{x}}:\ \min\left\|\mathbf{e}\right\|^2 = \min\left\|\mathbf{A}\mathbf{x}-\mathbf{b}\right\|^2, \tag{A.40}$$

and can be found by computing [526]:

$$\mathbf{A}^t\mathbf{A}\,\widehat{\mathbf{x}} = \mathbf{A}^t\,\mathbf{b}\,. \tag{A.41}$$

If the columns of A are linearly independent then $\mathbf{A}^t\mathbf{A}$ is a square invertible matrix and the desired solution can be found by computing:

$$\widehat{\mathbf{x}} = \left(\mathbf{A}^t\mathbf{A}\right)^{-1}\mathbf{A}^t\,\mathbf{b}\,. \tag{A.42}$$

Algorithm A.1: Preconditioned Conjugate Gradient method.

1. Compute: $\mathbf{r}^0 = \mathbf{b} - \mathbf{A}\mathbf{x}^0$;
2. Compute: $\mathbf{z}^0 = \mathbf{M}^{-1}\mathbf{r}^0$;
3. Compute: $\mathbf{p}^0 = \mathbf{z}^0$;
4. While $i \le niter_{\max}$
   - 4.1 Compute: $\alpha^i = \dfrac{\left\langle \mathbf{r}^i, \mathbf{z}^i \right\rangle}{\left\langle \mathbf{p}^i, \mathbf{A}\mathbf{p}^i \right\rangle}$;
   - 4.2 Compute: $\mathbf{x}^{i+1} = \mathbf{x}^i + \alpha^i\,\mathbf{p}^i$;
   - 4.3 Compute: $\mathbf{r}^{i+1} = \mathbf{r}^i - \alpha^i\,\mathbf{A}\mathbf{p}^i$;
   - 4.4 If $\left\langle \mathbf{r}^{i+1}, \mathbf{r}^{i+1} \right\rangle < tol$ Exit;
   - 4.5 Compute: $\mathbf{z}^{i+1} = \mathbf{M}^{-1}\mathbf{r}^{i+1}$;
   - 4.6 Compute: $\beta^i = \dfrac{\left\langle \mathbf{r}^{i+1}, \mathbf{z}^{i+1} \right\rangle}{\left\langle \mathbf{r}^i, \mathbf{z}^i \right\rangle}$;
   - 4.7 Compute: $\mathbf{p}^{i+1} = \mathbf{z}^{i+1} + \beta^i\,\mathbf{p}^i$;
   - 4.8 Increment i;

End While

Table A.1: Data from the Gauss-Legendre quadrature.

n	y	w
1	0.000000000000000	2.000000000000000
2	±0.577350269189626	1.000000000000000
3	0.000000000000000	0.888888888888889
	±0.774596669241483	0.555555555555556
4	±0.339981043584856	0.652145154862546
	±0.861136311594053	0.347854845137454

Table A.2: Data from the Gauss-Lobatto quadrature.

n	y	w
1	0.000000000000000	2.000000000000000
2	±1.000000000000000	1.000000000000000
3	0.000000000000000	1.333333333333333
	±1.000000000000000	0.333333333333333
4	±0.447213595499958	0.833333333333333
	±1.000000000000000	0.166666666666667

1.13 Numerical integration

Table A.1 and Table A.2 present the abscissas and the weights of the Gauss-Legendre and of the Gauss-Lobatto quadrature, respectively.

2 Differentiation

The Leibniz's rule for differentiation for definite integrals states that [522]:

$$\frac{d}{dx}\int_{y_0}^{y_1} f(x,y)\,dy = \int_{y_0}^{y_1} \frac{\partial}{\partial x} f(x,y)\,dy\,. \tag{A.43}$$

3 Vector calculus

The *divergence theorem*, *a.k.a. Gauss' theorem*, relates the flux of a vector field through a surface to the behaviour of the vector field inside the surface [567].

If Ω is a subset of R^n that is a compact and has piecewise smooth boundary and if $\boldsymbol{f}$ is continuously differentiable vector field defined on a neighbourhood of Ω, then:

$$\iiint \left(\nabla\cdot\mathbf{f}\right) \mathrm{d}\Omega = \iint \left(\mathbf{f}\cdot\mathbf{n}\right) \mathrm{d}\Gamma\,. \tag{A.44}$$

Annex B Elastic Constitutive Relations

1 Generalized Hooke's law

For a general material, the stress and strain second-order tensors are related by forth-order constitutive tensors:

$$\sigma_{ij} = C_{ijkl}\,\varepsilon_{kl}\,. \tag{B.1}$$

In its general form, the *stiffness* or *elasticity tensor* C_{ijkl} has 81 independent components (3^4). Considering the symmetry conditions of the stress and strain tensors $\left(\sigma_{ij}=\sigma_{ji};\ \varepsilon_{ij}=\varepsilon_{ji}\right)$, only 36 of the 81 components are independent. Furthermore, if the components of the constitutive tensor C_{ijkl} do not change for different reference coordinate systems, than the material is said to be *isotropic*:

$$C_{ijkl}\left(x_k\right) = C_{ijkl}\left(x'_k\right). \tag{B.2}$$

It can be proved that for an linear elastic and isotropic material the constitutive relation (B.1) can be written as [98]:

$$\sigma_{ij} = \lambda\,\delta_{ij}\,\varepsilon_{kk} + 2\mu\,\varepsilon_{ij}\,, \tag{B.3}$$

or in matrix format:

$$\begin{bmatrix}\sigma_{11}\\ \sigma_{22}\\ \sigma_{33}\\ \sigma_{12}\\ \sigma_{13}\\ \sigma_{23}\end{bmatrix} = \begin{bmatrix}\lambda+2\mu & \lambda & \lambda & 0 & 0 & 0\\ \lambda & \lambda+2\mu & \lambda & 0 & 0 & 0\\ \lambda & \lambda & \lambda+2\mu & 0 & 0 & 0\\ 0 & 0 & 0 & 2\mu & 0 & 0\\ 0 & 0 & 0 & 0 & 2\mu & 0\\ 0 & 0 & 0 & 0 & 0 & 2\mu\end{bmatrix}\begin{bmatrix}\varepsilon_{11}\\ \varepsilon_{22}\\ \varepsilon_{33}\\ \varepsilon_{12}\\ \varepsilon_{13}\\ \varepsilon_{23}\end{bmatrix}, \tag{B.4}$$

where λ and μ are well-known *Lamé's* constants. The constant λ does not have any direct physical meaning, however the constant μ relates the tangential stress and strain, as follows:

$$2\mu = \frac{\sigma_{12}}{\varepsilon_{12}} = \frac{\sigma_{13}}{\varepsilon_{13}} = \frac{\sigma_{23}}{\varepsilon_{23}}\,. \tag{B.5}$$

Considering that the material is subjected to a force only along direction x_1 $\left(\sigma_{22}=\sigma_{33}=\sigma_{12}=\sigma_{13}=\sigma_{23}=0\right)$, the constitutive equations can be defined in the flexibility format:

$$\varepsilon_{11} = \frac{\lambda+\mu}{\mu\left(3\lambda+2\mu\right)}\sigma_{11};\quad \varepsilon_{22}=\varepsilon_{33}=-\frac{\lambda}{2\mu\left(3\lambda+2\mu\right)}\sigma_{11};\quad \varepsilon_{12}=\varepsilon_{13}=\varepsilon_{23}=0\,, \tag{B.6}$$

which can be used to define the following variables:

$$E = \frac{\mu\left(3\lambda+2\mu\right)}{\lambda+\mu}, \tag{B.7}$$

$$\nu = \frac{\lambda}{2(\lambda+\mu)}, \tag{B.8}$$

where *E* represents the *elasticity* or *Young's modulus* and ν the *Poisson's ratio*, relating the longitudinal stress to the longitudinal and transversal strains, respectively. Inserting these variables into (B.6), the following relations are obtained:

$$\frac{\sigma_{11}}{\varepsilon_{11}} = E, \tag{B.9}$$

$$\frac{\varepsilon_{22}}{\varepsilon_{11}} = \frac{\varepsilon_{33}}{\varepsilon_{11}} = -\nu. \tag{B.10}$$

Considering a material subjected to a hydrostatic tension σ^h, the stress tensor trace becomes [98]:

$$\sigma_{kk} = 3\sigma^h. \tag{B.11}$$

In this case equation (B.3) leads to:

$$\sigma_{kk} = \lambda 3\varepsilon_{kk} + 2\mu\varepsilon_{kk} = (3\lambda + 2\mu)\varepsilon_{kk}. \tag{B.12}$$

Joining the last two equations, it is possible to obtain:

$$\varepsilon_{kk} = K\sigma^h, \tag{B.13}$$

where *K* is often-called the *compression* or *bulk modulus*, representing the relation between the volumetric stress and strain. This quantity is defined by:

$$K = \lambda + \frac{2}{3}\mu. \tag{B.14}$$

According to Fung [229], the admissible values for the Poisson's ratio of isotropic linear elastic materials are bounded between -1 and 0.5. This can be proved by the requirement of having a positive strain energy, due to thermodynamic considerations. It can be demonstrated that a sufficient condition is that the *bulk* and *shear moduli* are positive [229]:

$$\begin{cases} K = \dfrac{E}{3(1-2\nu)} > 0 \\ \mu = \dfrac{E}{2(1+\nu)} > 0 \end{cases}. \tag{B.15}$$

The bounds can be retrieved from these inequalities due to the condition $E > 0$.

The possible relations between different moduli combinations for representing linear elastic, isotropic materials can be found in the work of Chandrasekharaiah *et al.* [98] and Bower [64].

2 Special cases – Two-dimensional elasticity

- Plane strain

In this case, there will not be out-of-plane strains (direction x_3), therefore $\varepsilon_{33}=\varepsilon_{13}=\varepsilon_{23}=0$. This is a typical situation for tunnels with loads at the cross-section plane. The constitutive relation in stiffness format can be obtained by removing lines and columns from (II.28) [493]:

$$\begin{bmatrix}\sigma_{11}\\ \sigma_{22}\\ \sigma_{12}\end{bmatrix}=\frac{E}{(1+\nu)(1-2\nu)}\begin{bmatrix}1-\nu & \nu & 0\\ \nu & 1-\nu & 0\\ 0 & 0 & \frac{1-2\nu}{2}\end{bmatrix}\begin{bmatrix}\varepsilon_{11}\\ \varepsilon_{22}\\ \gamma_{12}\end{bmatrix}, \tag{B.16}$$

and the out-of-plane stress can be computed using one of the following expressions:

$$\sigma_{33}=\nu\sigma_{11}+\nu\sigma_{22}, \tag{B.17}$$

$$\sigma_{33}=\frac{E\nu(\varepsilon_{11}+\varepsilon_{22})}{(1+\nu)(1-2\nu)}. \tag{B.18}$$

Rearranging the equations for flexibility format, the following expression is obtained:

$$\begin{bmatrix}\varepsilon_{11}\\ \varepsilon_{22}\\ \gamma_{12}\end{bmatrix}=\frac{1+\nu}{E}\begin{bmatrix}1-\nu & -\nu & 0\\ -\nu & 1-\nu & 0\\ 0 & 0 & 2\end{bmatrix}\begin{bmatrix}\sigma_{11}\\ \sigma_{22}\\ \sigma_{12}\end{bmatrix}. \tag{B.19}$$

- Plane stress

In this case, there will not be out-of-plane stress (direction x_3), hence $\sigma_{33}=\sigma_{13}=\sigma_{23}=0$. This is typical of a thin plate under in-plane loading. The relation (II.28) can be simplified into [493]:

$$\begin{bmatrix}\varepsilon_{11}\\ \varepsilon_{22}\\ \gamma_{12}\end{bmatrix}=\frac{1}{E}\begin{bmatrix}1 & -\nu & 0\\ -\nu & 1 & 0\\ 0 & 0 & 2(1+\nu)\end{bmatrix}\begin{bmatrix}\sigma_{11}\\ \sigma_{22}\\ \sigma_{12}\end{bmatrix}, \tag{B.20}$$

and the out-of-plane strain can be computed using one of the following expressions:

$$\varepsilon_{33}=-\frac{\nu}{1-\nu}(\varepsilon_{11}+\varepsilon_{22}), \tag{B.21}$$

$$\varepsilon_{33}=-\frac{\nu}{E}(\sigma_{11}+\sigma_{22}). \tag{B.22}$$

Rearranging the equations for stiffness format, it is possible to obtain:

$$\begin{bmatrix}\sigma_{11}\\ \sigma_{22}\\ \sigma_{12}\end{bmatrix}=\frac{E}{1-\nu^2}\begin{bmatrix}1 & \nu & 0\\ \nu & 1 & 0\\ 0 & 0 & \frac{1-\nu}{2}\end{bmatrix}\begin{bmatrix}\varepsilon_{11}\\ \varepsilon_{22}\\ \gamma_{12}\end{bmatrix}. \tag{B.23}$$

Bibliographic References

1. ACI (1968). "Effect of Steel Strength and Reinforcement Ratio on the Mode of Failure and Strain Energy Capacity of Reinforced Concrete Beams", Journal ACI, ACI Committee 439 66(3): 165-173.
2. Addessi, D., S. Marfia, and E. Sacco (2002). "A plastic nonlocal damage model", Computer Methods in Applied Mechanics and Engineering 191(13-14): 1291-1310.
3. ADINA (2008). "ADINA - Automatic Dynamic Incremental Nonlinear Analysis", version 8.5, ADINA R & D Inc.
4. Aktan, A., B. Karlsson, and M.A. Sozen (1973). "Stress-Strain Relationships of Reinforcing Bars Subjected to Large Strain Reversals", Structural Research Series nº397. University of Illinois.
5. Al-Shemmeri, T. (2010). "Engineering Thermodynamics", Tarik Al-Shemmeri & Ventus Publishing ApS.
6. Almunia, J.A.S. (1993). "Evaluación del comportamiento funcional y de la seguridad estrutural de puentes existentes de hormingón armado y pretensado", Tesis Doctoral, Escola Tècnica Superior D'Enginyers de Camins, Canals I Ponts, Universitat Politècnica de Catalunya, Barcelona, Spain.
7. Almusallam, A.A., A.S. Al-Gahtani, A.R. Aziz, and Rasheeduzzafar (1996). "Effect of reinforcement corrosion on bond strength", Construction and Building Materials 10(2): 123-129.
8. Amdahl, G. (1967). "Validity of the Single Processor Approach to Achieving Large-Scale Computing Capabilities", AFIPS Conference Proceedings.
9. Anagnostopoulos, S.A. (1972). "Non-linear dynamic response and ductility requirements of building structures subjected to earthquakes", Research Report Nº R72-54. M.I.T. Dept. of Civil Engineering, Cambridge, Ma.
10. Anderson, E., Z. Bai, C. Bischof, J. Demmel, J. Dongarra, J.D. Croz, A. Greenbaum, S. Hammarling, A. McKenney, S. Ostrouchov, and D. Sorensen (1992). "LAPACK's user's guide", Society for Industrial and Applied Mathematics 3rd Ed.
11. Antoniou, S. and R. Pinho (2004). "Advantages and Limitations of Adaptive and Non-Adaptive Force-Based Pushover Procedures", Journal of Earthquake Engineering 8(4): 497 - 522.
12. Arantes e Oliveira, E.R. (1969). "Resistência dos Materiais - Livro 2: Elementos da Teoria da Elasticidade", AEIST, Lisboa.
13. Arêde, A. (1997). "Seismic Assessment of Reinforced Concrete Frame Structures with a New Flexibility Based Element ", Doutoramento em Engenharia Civil, Faculdade de Engenharia da Universidade do Porto, Porto.
14. Arêde, A. and A.V. Pinto (1998). "Flexibility based global element model for seismic analysis of RC frame structures", 11th European Conference on Earthquake Engineering, Balkema, Rotterdam.
15. Areias, P.M.A. and T. Belytschko (2005). "Analysis of three-dimensional crack initiation and propagation using the extended finite element method", International Journal for Numerical Methods in Engineering 63(5): 760-788.
16. Arruda, M.R.T. (2011). "Static and dynamic analysis of concrete structures using damage mechanics", Doutoramento em Engenharia Civil (under development), Universidade Técnica de Lisboa, Instituto Superior Técnico, Lisboa.
17. Asaro, R.J. and V.A. Lubarda (2006). "Mechanics of Solids and Materials", Cambridge University Press, Cambridge.

18. ATC (1996). "ATC 40: Seismic evaluation and retrofit of concrete buildings", Applied Technology Council, Redwood City, CA, USA.
19. ATC (1997). "FEMA-273: NHERP Guidelines for the Seismic Rehabilitation of Buildings", Applied Technology Council, Federal Emergency Management Agency, Redwood City, CA, USA.
20. ATC (2000). "FEMA-356: Prestandard and Commentary for the Seismic Rehabilitation of Buildings", Applied Technology Council, Federal Emergency Management Agency, Redwood City, CA, USA.
21. ATC (2005). "FEMA-440: Improvement of nonlinear static seismic analysis procedures", Applied Technology Council, Federal Emergency Management Agency, Redwood City, CA, USA.
22. Babuska, I. and J.M. Melenk (1997). "The partition of unity method", International Journal for Numerical Methods in Engineering 40(4): 727-758.
23. Bacarji, E. (2001). "Aplicação do Método dos Elementos de Contorno à Análise de Pavimentos de Edifícios", Tese apresentada para obtenção do Título de Doutor em Engenharia de Estruturas, Escola de Engenharia de São Carlos - Universidade de São Paulo, São Paulo.
24. Bairrão, R. (2008). "Shaking Table Testing", Modern Testing Techniques for Structural Systems. Edited by O. Bursi and D. Wagg. Wien, Springer.
25. Balázs, G.L. (1987). "Bond model with non-linear bond-slip law", Studi e Ricerche, Politecnico di Milano, Italy 9: 157-180.
26. Balázs, G.L. (1992). "Fatigue of bond", ACI Materials Journal 88(6): 620-630.
27. Balmer, G. (1949). "Shearing Strength of Concrete under High Triaxial Stress – Computation of Mohr's Envelope as a Curve", Report Nº SP-23. Structural Research Laboratory - U.S. Bureau of Reclamation.
28. Bamonte, P.F., D. Coronelli, and P.G. Gambarova (2002). "Size effects in high-bond bars", Bond in Concrete - Proceedings of the conference held at the Budapest University of Technology and Economics, Budapest, Hungary.
29. Bamonte, P.F. and P.G. Gambarova (2007). "High-Bond Bars in NSC and HPC: Study on Size Effect and on the Local Bond Stress-Slip Law", Journal of Structural Engineering 133(2): 225-234.
30. Banreblatt, G.I. (1959). "Equilibrium cracks formed during brittle fracture", Prikl. Mat. Mech. 26.
31. Barros, F.B., S.P.B. Proença, and C.S. Barcellos (2004). "Generalized finite element method in structural nonlinear analysis – a p-adaptive strategy", Computational Mechanics 33(2): 95-107.
32. Bathe, K.J. (1996). "Finite Element Procedures", Prentice-Hall, New Jersey.
33. Bathe, K.J. and E.L. Wilson (1973). "Solution methods for eigenvalue problems in structural mechanics", International Journal for Numerical in Engineering 6: 213-226.
34. Bažant, Z.P. (1984). "Size Effect in Blunt Fracture: Concrete, Rock, Metal", Journal of Engineering Mechanics 110(4): 518-535.
35. Bažant, Z.P. (1994). "Nonlocal Damage Theory Based on Micromechanics of Crack Interactions", Journal of Engineering Mechanics 120(3): 593-617.
36. Bažant, Z.P. and P. Bhat (1977). "Prediction of Hysteresis in Reinforced Concrete Members", Journal of Structural Engineering 103 (ST1): 151-167.
37. Bažant, Z.P. and L. Cedolin (1991). "Stability of Structures Elastic Inelastic Fracture and Damage Theories", Dover Publications, Inc., Mineola, New York, USA.
38. Bažant, Z.P. and R. Desmorat (1994). "Size Effect in Fiber or Bar Pullout with Interface Softening Slip", Journal of Engineering Mechanics 120(9): 1945-1962.
39. Bažant, Z.P. and L. Feng-Bao (1988). "Nonlocal Smeared Cracking Model for Concrete Fracture", Journal of Structural Engineering 114(11): 2493-2510.

40. Bažant, Z.P. and M. Jirásek (1994). "Damage nonlocality due to microcrack interactions: statistical determination of crack influence function ", Fracture and Damage in Quasi-Brittle Structures. Edited by Z.P. Bažant, Z. Bittnar, M. Jirásek, and J. Mazars. London, UK, E & FN SPON,: 3–17.
41. Bažant, Z.P. and M. Jirásek (2002). "Nonlocal integral formulations of plasticity and damage: survey of progress", ASCE Journal of Engineering Mechanics(128): 1119-1149.
42. Bažant, Z.P. and M.T. Kazemi (1990). "Determination of fracture energy, process zone length and brittleness number from size effect, with application to rock and concrete", International Journal of Fracture 44(2): 111-131.
43. Bažant, Z.P., Z. Li, and M. Thoma (1995). "Identification of Stress-Slip Law for Bar or Fiber Pullout by Size Effect Tests", Journal of Engineering Mechanics 121(5): 620-625.
44. Bažant, Z.P. and B.H. Oh (1983). "Crack band theory for fracture of concrete", Materials and Structures(16): 155-177.
45. Bažant, Z.P. and G. Pijaudier-Cabot (1988). "Nonlocal Continuum Damage, Localization Instability and Convergence", Journal of Applied Mechanics 55(2): 287-293.
46. Bažant, Z.P. and G. Pijaudier-Cabot (1989). "Measurement of Characteristic Length of Nonlocal Continuum", Journal of Engineering Mechanics 115(4): 755-767.
47. Bažant, Z.P. and J. Planas (1998). "Fracture and size effect in concrete and other quasi-brittle materials". Edited by CRC Press. USA.
48. Beer, G. (1985). "An isoparametric joint/interface element for finite element analysis", International Journal for Numerical Methods in Engineering 21(4): 585-600.
49. Belytschko, T. and R. Mullen (1976). "Mesh partitions of explicit—implicit time integrators", Formulations and Computational Algorithms in Finite Element Analysis. Edited by K.J. Bathe, J.T. Oden, and W. Wunderlich. Cambridge, MA, MIT Press: 673–690.
50. Bento, R. (1996). "Avaliação do Comportamento Sísmico de Estruturas Porticadas de Betão Armado – Uma Abordagem Baseada em Índices de Danos", Doutoramento em Engenharia Civil, Instituto Superior Técnico, Universidade Técnica de Lisboa, Lisboa.
51. Bento, R., C. Bhatt, and R. Pinho (2010). "Using nonlinear static procedures for seismic assessment of the 3D irregular SPEAR building", Earthquakes and Structures 1(2).
52. Bertero, V. (1997). "V. V. Bertero's Introduction to Earthquake Engineering ", Retrieved 2005/05/06, from http://nisee.berkeley.edu/bertero/.
53. Bertero, V.V. and C.A. Felippa (1964). "Discussion of "Ductility of Concrete" by H.E.H. Roy and M.A. Sozen", Proceedings of the International Symposium on Flexural Mechanics of Reinforced Concrete, Miami, USA.
54. Bertero, V.V. and E.P. Popov (1975). "Hysteretic behavior of ductile moment-resisting reinforced concrete frame components", Report No. UCB/EERC-75/16. Earthquake Engineering Research Center, University of California, Berkeley, USA.
55. Bhatt, C. and R. Bento (2010). "Extension of the CSM-FEMA440 to plan-asymmetric real building structures", Earthquake Engineering & Structural Dynamics Published online in Wiley Online Library (wileyonlinelibrary.com).
56. Bischoff, P. and S. Perry (1991). "Compressive behaviour of concrete at high strain rates", Materials and Structures 24(6): 425-450.
57. Bjerhammar, A. (1951). "Application of calculus of matrices to method of least squares; with special references to geodetic calculations". Trans. Roy. Inst. Tech. Stockholm.
58. Bocca, P., A. Carpinteri, and S. Valente (1991). "Mixed mode fracture of concrete", International Journal of Solids and Structures 27(9): 1139-1153.

59. Bonelli, A. and O.S. Bursi (2004). "Generalized-alpha methods for seismic structural testing", Earthquake Engineering & Structural Dynamics 33(10): 1067-1102.

60. Bonelli, A., O.S. Bursi, L. He, G. Magonette, and P. Pegon (2008). "Convergence analysis of a parallel interfield method for heterogeneous simulations with dynamic substructuring", International Journal for Numerical Methods in Engineering 75(7): 800-825.

61. Borino, G., P. Fuschi, and C. Polizzotto (1999). "A Thermodynamic Approach to Nonlocal Plasticity and Related Variational Principles", Journal of Applied Mechanics 66(4): 952-963.

62. Bousias, S.N., T.B. Panagiotakos, and M.N. Fardis (2002). "Modelling of RC members under cyclic biaxial flexure and axial force", Journal of Earthquake Engineering 6(2): 213-238.

63. Bovet, D.P. and M. Cesati (2005). "Understanding the Linux Kernel", O'Reilly, 3rd Ed.

64. Bower, A.F. (2010). "Applied Mechanics of Solids", CRC Press, Taylor & Francis Group, USA.

65. Brancalconi, F., V. Ciampi, and R. Di Antonio (1983). "Rate-Type Models for Non Linear Hysteretic Structural Behavior", EUROMECI Colloquium, Palermo, Italy.

66. Brenner, S.C. and L.Y. Sung (2007). "BDDC and FETI-DP without matrices or vectors", Computer Methods in Applied Mechanics and Engineering 196(8): 1429-1435.

67. Bresler, B. and K.S. Pister (1958). "Strength of Concrete Under Combined Stresses", Journal ACI 55(3): 321-345.

68. Briseghella, L. and R. Gori (1982). "La Risposta Sperimentale Monotonica e Ciclica di Acciai da Cemento Armato", Istituto di Scienza delle Costruzioni, Facoltà di Ingegneria, Università di Padova, Padova, Italy.

69. Briseghella, L. and R. Gori (1984). "Aggregate Interlock Cyclic Response of R.C. Critical Section", 8th World Conference on Earthquake Engineering, San Francisco, California.

70. Brookshire, D.S., S.E. Chang, H. Cochrane, R.A. Olson, A. Rose, and J. Steenson (1997). "Direct and Indirect Economic Losses from Earthquake Damage", Earthquake Spectra 13(4): 683-701.

71. Brown, J. (1996). "Fatigue Characteristics of Reinforcing Bars Under Simulated Seismic Loading", M.Sc. Thesis, Department of Civil and Environmental Engineering, University of Central Florida, Orlando, USA.

72. Brown, J. and S.K. Kunnath (2000). "Low cycle fatigue behavior of longitudinal reinforcement in reinforced concrete bridge columns", NCEER Technical Report 00-0007. Multidisciplinary Center For Earthquake Engineering Research, University at Buffalo, State University of New York, Buffalo, USA.

73. Burns, N.H. and C.P. Seiss (1962). "Load-Deformation Characteristics of Beam-Column Connections in Reinforced Concrete", Civil Engineering Studies, Structural Research Series No. 234. University of Illinois.

74. Callister, W.D. (2007). "Materials Science and Engineering", John Wiley & Sons, Inc., 7th Ed.

75. Camacho, G.T. and M. Ortiz (1996). "Computational modelling of impact damage in brittle materials", International Journal of Solids and Structures 33(20-22): 2899-2938.

76. Carneiro, F.L.L.B. and A. Barcellos (1953). "Concrete tensile strength", Bull. No. 13 - Int. Assoc. of Testing and Research Laboratories for Materials and Structures.

77. Carol, I. and E.E. Alonso (1983). "A new joint element for the analysis of fractured rock", 5th Int. Congr. Rock Mech. Melbourne, Australia. Vol. F: 147-151.

78. Carpinteri, A. (1980). "Static and energetic fracture parameters for rocks and concretes", Report Istituto di Scienza delle Costruzioni-Ingegneria. University of Bologna, Italy.

79. Carpinteri, A. (1986). "Mechanical damage and crack growth in concrete: plastic collapse to brittle fracture", Martinus Nijhoff Publishers, 1st Ed.

80. Carpinteri, A. and B. Chiaia (1996). "Size effects on concrete fracture energy: dimensional transition from order to disorder", Materials and Structures 29(5): 259-266.

81. Carvalho, E.C. (1998). "Seismic testing of structures", 11th European Conference on Earthquake Engineering, Rotterdam, Netherlands.

82. Casarotti, C. and R. Pinho (2007). "An adaptive capacity spectrum method for assessment of bridges subjected to earthquake action", Bulletin of Earthquake Engineering 5(3): 377-390.

83. Castellani, A., F. Scirocco, and G. Boffi (1993). "Reinforced Concrete Columns Under Cyclic Axial Compressive Forces", ASCE Journal of Structural Engineering 119(11): 3426-3433.

84. Castro, L.M.S.S. (1996). "Wavelets e Séries de Walsh em Elementos Finitos", Doutoramento em Engenharia Civil, Universidade Técnica de Lisboa, Instituto Superior Técnico, Lisboa.

85. CEB (1980). "Manuel de Sécurité", Bulletin d'Information Nº 128. Comité Euro-International du Béton.

86. CEB (1983). "Response of R.C. critical regions under large amplitude reversed actions", Bulletin d'Information Nº161. Comité Euro-International du Béton, Paris.

87. CEB (1991). "Behavior and analysis of reinforced concrete structures under alternate actions inducing inelastic response. Volume 1: General Models", Bulletin d'Information Nº210, Comité Euro-International du Béton, London.

88. CEB (1996). "RC elements under cyclic loading", Bulletin d'Information Nº230. T. Telford. Comité Euro-International du Béton, London.

89. CEB (1996). "RC frames under earthquake loading", Bulletin d'Information Nº230, T. Telford, Comité Euro-International du Béton, London.

90. Çelebi, M. and J. Penzien (1973). "Experimental investigation into the seismic behavior of critical regions of reinforced concrete components as influenced by moment and shear", Report No. UCB/EERC-73/04. Earthquake Engineering Research Center, University of California, Berkeley, USA.

91. CEN (2001). "Eurocode 2: Design of concrete structures. Part 1: General rules and rules for buildings", 2nd draft, Comité Européen de Normalisation, Brussels.

92. CEN (2003). "Eurocode 8: Design of structures for earthquake resistance. Part 1: General rules, seismic actions and rules for buildings", Draft No 6, Stage 49, Comité Européen de Normalisation, Brussels.

93. CEN (2003). "Eurocode 8: Design of structures for earthquake resistance. Part 2: Bridges", Draft No 3, Stage 32, Comité Européen de Normalisation, Brussels.

94. Ceriolo and Tommaso (1998). "Fracture Mechanics of Brittle Materials - A Historical Point of View", 2nd Int. PhD Symposium in Civil Engineering, Budapest.

95. Cervera, M., J. Oliver, and R. Faria (1995). "Seismic evaluation of concrete dams via continuum damage models", Earthquake Engineering & Structural Dynamics 24(9): 1225-1245.

96. Chaboche, J.L. (1978). "Description thermodynamique et phénoménologique de la viscoplasticité cyclique avec endommagement", Ph.D. Thesis, Université Paris, Paris.

97. Chandra, R., R. Menon, L. Dagum, D. Kohr, D. Maydan, and J. McDonald (2000). "Parallel Programming in OpenMP", Morgan Kaufmann.

98. Chandrasekharaiah, D.S. and L. Debnath (1994). "Continuum Mechanics", Academic Press Limited, San Diego.

99. Chang, K.C. and G.C. Lee (1987). "Strain Rate Effect on Structural Steel Under Cyclic Loading", Journal of Engineering Mechanics 113 (9): 1292-1301.

100. Chappuis, P. (1987). "Modélisation Non-Linéaire du Comportement du Béton sous des Sollicitations Dynamiques", Thèse Nº 155, ETH, Swiss Federal Institute of Technolog, Zurich.

101. Chen, K. (2005). "Matrix Preconditioning Techniques and Applications", Cambridge University Press, Cambridge.

102. Chen, W. (1982). "Plasticity in Reinforced Concrete", McGraw-Hill, New York.

103. Chen, W. (1994). "Constitutive Equations for Engineering Materials, Volume 2: Plasticity and Modeling", Elsevier.
104. Chintanapakdee, C. and A.K. Chopra (2003). "Evaluation of modal pushover analysis using generic frames", Earthquake Engineering & Structural Dynamics 32(3): 417-442.
105. Chopra, A.K. (1995). "Dynamic of Structures: Theory and Applications to Earthquake Engineering", Prentice-Hall, Inc., New Jersey.
106. Chopra, A.K. and R.K. Goel (2002). "A modal pushover analysis procedure for estimating seismic demands for buildings", Earthquake Engineering & Structural Dynamics 31(3): 561-582.
107. Chopra, A.K. and R.K. Goel (2004). "A modal pushover analysis procedure to estimate seismic demands for unsymmetric-plan buildings", Earthquake Engineering & Structural Dynamics 33(8): 903-927.
108. Chopra, A.K. and R.K. Goel (2006). "Evaluation of the modal pushover analysis procedure for unsymmetric-plan buildings", 1st European Conference on Earthquake Engineering and Seismology, 3-8 September, Geneva.
109. Chopra, A.K., R.K. Goel, and C. Chintanapakdee (2003). "Statistics of Single-Degree-of-Freedom Estimate of Displacement for Pushover Analysis of Buildings", Journal of Structural Engineering 129(4): 459-469.
110. Ciampi, V. and L. Carlesimo (1986). "A Nonlinear Beam clement for Seismic Analysis of Structures", 8th European Conference on Earthquake Engineering, Lisbon, Portugal.
111. Ciampi, V., R. Eligehausen, V.V. Bertero, and E.P. Popov (1981). "Analytical model for deformed-bar bond under generalized excitations", Trans. IABSE Colloquium on Advanced Mechanics of Reinforced Concrete, Delft.
112. Cirak, F., M. Ortiz, and A. Pandolfi (2005). "A cohesive approach to thin-shell fracture and fragmentation", Computer Methods in Applied Mechanics and Engineering 194(21-24): 2604-2618.
113. Clément, J.L. (1987). "Interface acier-béton et comportement des structures en béton armé: caractérisation - modélisation", Thèse de l'Université Paris VI, Paris.
114. Clough, R.W., K. Benuska, and W. R. (1965). "Inelastic Earthquake Response of Tall Buildings", 3rd World Conference on Earthquake Engineering, New Zealand.
115. Clough, R.W. and S.B. Johnston (1966). "Effect of stiffness degradation on earthquake ductility requirements", Japan Earthquake Engineering Symposium, Tokyo.
116. Clough, R.W. and J. Penzien (1995). "Dynamics of Structures", McGraw-Hill, Inc., 3rd Ed., Singapura.
117. Coelho, E. (1992). "Comportamento Sísmico de Estruturas em Pórtico de Betão Armado", Doutoramento em Engenharia Civil, Instituto Superior Técnico, Universidade Técnica de Lisboa, Lisboa.
118. Coelho, E., A. Campos Costa, P. Candeias, M.J. Falcão Silva, and L.A.M. Mendes (2005). "Shake table tests of a 3-storey irregular RC structure designed for gravity loads", SPEAR International Workshop, JRC 4-5 April, Ispra, Italy.
119. Coffin, L.F.J. (1954). "A study of the effects of cyclic thermal stresses on a ductile metal", Trans. American Society of Mechanical Engineers 76: 931-950.
120. Coleman, B. and M. Gurtin (1967). "Thermodynamics with internal state variables", J. Chem. Phys. 47: 597–613.
121. Coleman, J. and E. Spacone (2001). "Localization issues in force-based frame elements", Journal Structural Engineering 127(11): 1257–1265.

122. Combescure, D. (2000). "Etude d'une structure portique de 4 etages en beton arme ayant de mauvaises dispositions constructives (portique Ispra). Influence des remplissages en maçonnerie sur le comportement sismique". Direction des Reacteurs Nucleaires.
123. Combescure, D. (2006). "Eléments de dynamique des structures Illustrations à l'aide de CAST3M". Commissariat a l'Energie Atomique, Saclay, France.
124. Combescure, D. and P. Pegon (1994). "Alpha-operator splitting time integration technique for pseudodynamic testing: error propagation analysis", Special Publication No. I.96.34, EC, JRC, Ispra, Italy.
125. Combescure, D. and P. Pegon (1996). "Introduction of Two New Global Models in CASTEM 2000 for Seismic Analysis of Civil Engineering Structures", Special Publication Nr.I.96.34. Structural Mechanics Unit, Institute for Systems Informatics and Safety, JRC, Ispra, Italy.
126. Combescure, D. and P. Pegon (1997). "[alpha]-Operator splitting time integration technique for pseudodynamic testing error propagation analysis", Soil Dynamics and Earthquake Engineering 16(7-8): 427-443.
127. Comi, C. (1999). "Computational modeling of gradient-enhanced damage in quasi-brittle materials", Mechanics of Cohesive-frictional Materials(4): 17-36.
128. Comi, C. (2001). "A Non-local Model With Tension and Compression Damage Mechanisms", Eur. J. Mech. A/Solids 20: 1-22.
129. Comi, C. and L. Driemeier (1998). "On gradient regularization for numerical analysis in the presence of damage", John Wiley & Sons, Chichester.
130. Comi, C., S. Mariani, and U. Perego (2002). "From localized damage to discrete cohesive crack propagation in nonlocal continua", 5th World Congress on Computational Mechanics, Vienna.
131. Comi, C., S. Mariani, and U. Perego (2002). "On the transition from continuum nonlocal damage to quasi-brittle discrete crack models", 3rd Joint Conference of Italian Group of Computational Mechanics and Ibero-Latin American Association of Computational Methods in Engineering. Italy.
132. Comi, C., S. Mariani, and U. Perego (2004). "An extended finite element strategy for the analysis of crack growth in damaging concrete structures", European Congress on Computational Methods in Applied Sciences and Engineering - ECCOMAS 2004. Jyvaskyla, Finland.
133. Comi, C., S. Mariani, and U. Perego (2005). "Cohesive crack propagation in damaging concrete structures discretized by extended finite elements", 11th International Congress on Fracture, Torino, Italy.
134. Comi, C., S. Mariani, and U. Perego (2007). "An extended FE strategy for transition from continuum damage to mode I cohesive crack propagation", International Journal for Numerical and Analytical Methods in Geomechanics 31(2): 213-238.
135. Comi, C. and U. Perego (1996). "A Generalized Variable Formulation for Gradient Dependent Softening Plasticity", International Journal for Numerical Methods in Engineering 39(21): 3731-3755.
136. Comi, C. and U. Perego (2000). "A bi-dissipative damage model for concrete with applications to dam engineering", ECCOMAS 2000, Barcelona, Spain
137. Comi, C. and U. Perego (2001). "Fracture Energy Based Bi-dissipative Damage Model for Concrete", International Journal of Solids and Structures 38: 6427-6454.
138. Comi, C. and U. Perego (2001). "Nonlocal aspects of nonlocal damage analyses of concrete structures", European Journal of Finite Elements 10: 227-242.
139. Comi, C. and U. Perego (2001). "Symmetric and non-symmetric non-local damage formulations: an assessment of merits", European Conference on Computational Mechanics - ECCM 2001, Cracow.

140. Comi, C. and U. Perego (2004). "Criteria for Mesh Refinement in Non-local Damage Finite Element Analyses", European Journal of Mechanics A/Solids 23: 615–632.
141. Cook, R.D., D.S. Malkus, and M.E. Plesha (1989). "Concepts and Applications of Finite Element Analysis", John Wiley & Sons, Inc., 3rd Ed., New York.
142. Cordebois, J.P. and F. Sidoroff (1982). "Anisotropic damage in elasticity and plasticity", Journal de Mécanique théorique et appliquée 2: 45-60.
143. Corley, W. (1966). "Rotational Capacity of Reinforced Concrete Beams", Journal of Structural Division 97 (ST5).
144. Coronelli, D., P.G. Gambarova, and P. Ravazzani (2001). "Size effect in steel-concrete bond: test results and modelling for smooth bars", Fracture Mechanics of Concrete Structures. Edited by R. de Borst: 669-676.
145. Costa, A.G. and A. Campos Costa (1987). "Modelo Histerético das Relações Forças-Deslocamentos Adequado à Análise Sísmica de Estruturas", Relatório LNEC, Lisboa.
146. Coulomb, C.A. (1873). "Sur une application des regles de maximis et minimis a quelques problèmes de statique relatifs a l'architecture", Acad. R. Sci. Mem. Math. Phys. par divers svants 7: 343-382.
147. Courant, R. (1943). "Variational Methods for the Solution of Problems of Equilibrium and Vibration", Bulletin of the American Mathematical Society(49): 1-23.
148. Coutinho, S. and A. Gonçalves (1994). "Fabrico e propriedades do betão", Vol. III - 2ª Edição. Edições LNEC. Laboratório Nacional de Engenharia Civil, Lisboa.
149. Cowell, W.L. (1965). "Dynamic Tests of Concrete Reinforcing Steels", US Naval Civil Engineering Laboratory - AD 622554 - Report R394, Port Huenembe, CA, USA.
150. Cox, J.V. and L.R. Herrmann (1998). "Development of a plasticity bond model for steel reinforcement", Mechanics of Cohesive-frictional Materials 3(2): 155-180.
151. Cox, J.V. and L.R. Herrmann (1999). "Validation of a plasticity bond model for steel reinforcement", Mechanics of Cohesive-frictional Materials 4(4): 361-389.
152. Crisfield, M.A. (1981). "A fast incremental/iterative solution procedure that handles 'snap-through'", Computers & Structures(13): 55-62.
153. Crisfield, M.A. (1983). "An arc-length method including line searches and accelerations", Int. J. Num. Meth. Engng.(19): 1269-1289.
154. Crisfield, M.A. (1991). "Non-Linear Finite Element Analysis of Solids and Structures - Volume 1: Essentials", John Wiley & Sons Ltd, New York.
155. Crisfield, M.A. (1997). "Non-Linear Finite Element Analysis of Solids and Structures - Volume 2: Advanced Topics", John Wiley & Sons Ltd, New York.
156. Cros, J.M. (2003). "A preconditioner for the Schur complement domain decomposition method", 14th International Conference on Domain Decomposition Methods, Cocoyoc, Mexico
157. D'Ambrisi, A. and F.C. Filippou (1999). "Modeling of Cyclic Shear Behavior in RC Members", Journal of Structural Engineering 125(10): 1143-1150.
158. Daoud, A. (2003). "Etude expérimental de la liaison entre l'acier et le béton autoplaçant - contribution à la modélisation numérique de l'interface", These de Doctorat, Institut National des Sciences Appliquées (INSA), Toulouse, France.
159. Daux, C., N. Moës, J. Dolbow, N. Sukumar, and T. Belytschko (2000). "Arbitrary branched and intersecting cracks with the extended finite element method", International Journal for Numerical Methods in Engineering 48(12): 1741-1760.
160. Davis, R.O. and A.P.S. Selvadurai (2002). "Plasticity and Geomechanics", Cambridge University Press, Cambridge, UK.

161. Davison, L. and A.L. Stevens (1973). "Thermomechanical constitution of spalling elastic bodies", Journal of Applied Physics 44(2): 668-674.

162. de Borst, R., M.A. Gutiérrez, G.N. Wells, J.J.C. Remmers, and H. Askes (2004). "Cohesive-zone models, higher-order continuum theories and reliability methods for computational failure analysis", International Journal for Numerical Methods in Engineering 60(1): 289-315.

163. Denarié, E., V.E. Saouma, A. Iocco, and D. Varelas (2001). "Concrete Fracture Process Zone Characterization with Fiber Optics", Journal of Engineering Mechanics 127(5): 494-503.

164. Desai, C.S., M.M. Zaman, J.G. Lightner, and H.J. Siriwardane (1984). "Thin-layer element for interfaces and joints", International Journal for Numerical and Analytical Methods in Geomechanics 8(1): 19-43.

165. Désir, J.M., M.R.B. Romdhane, F.J. Ulm, and E.M.R. Fairbairn (1999). "Steel-concrete interface: revisiting constitutive and numerical modeling", Computers & Structures 71(5): 489-503.

166. Desmorat, R. (2006). "Damage and Fatigue - Continuum damage mechanics modeling for fatigue of materials and structures", REGC – 10/2006. Geomechanics in energy production: 849-877.

167. Dhondt, G. (2004). "The Finite Element Method for Three-dimensional Thermomechanical Applications", John Wiley & Sons Ltd, West Sussex, England.

168. di Prisco, M., L. Ferrara, F. Meftah, J. Pamin, R. de Borst, J. Mazars, and J.M. Reynouard (2000). "Mixed mode fracture in plain and reinforced concrete: some results on benchmark tests", International Journal of Fracture 103(2): 127-148.

169. Dohrmann, C.R. (2003). "A Preconditioner for Substructuring Based on Constrained Energy Minimization", SIAM Journal on Scientific Computing 25(1): 246-258.

170. Dolenc, M. (2009). "A Vision of a Computing Environment for the Web 2.0 Era", Glasgow, UK.

171. Doltsinis, I. (2000). "Elements of Plasticity - Theory and Computation", WIT Press.

172. Dominguez, N. (2005). "Etude de la Liaison Acier-Béton: De la modélisation du Phénomène à la Formulation d'un Elément fini enrichi "Béton Armé"", Thèse de Doctorat, Laboratoire de Mécanique et Technologie, L'Ecole Normale Supérieure de Cachan, Cachan, France.

173. Dongarra, J. (2006). "Trends in High-Performance Computing", Handbook of Nature-Inspired and Innovative Computing, Springer: 511-520.

174. Dongarra, J.J., P. Luszczek, and A. Petitet (2003). "The LINPACK Benchmark: past, present and future", Concurrency and Computation: Practice and Experience 15(9): 803-820.

175. Dostál, Z. (2009). "Optimal Quadratic Programming Algorithms With Applications to Variational Inequalities", Springer Verlag.

176. Dostál, Z., F.A.M. Gomes Neto, and S.A. Santos (2000). "Duality-based domain decomposition with natural coarse-space for variational inequalities", Journal of Computational and Applied Mathematics 126(1-2): 397-415.

177. Dostál, Z., F.A.M. Gomes Neto, and S.A. Santos (2000). "Solution of contact problems by FETI domain decomposition with natural coarse space projection", Computer Methods in Applied Mechanics and Engineering 190: 1611-1627.

178. Dostál, Z., D. Horák, R. Kucera, V. Vondrák, J. Haslinger, J. Dobiás, and S. Pták (2005). "FETI based algorithms for contact problems: scalability, large displacements and 3D Coulomb friction", Computer Methods in Applied Mechanics and Engineering 194(2-5): 395-409.

179. Dragon, A., D. Halm, and T. Désoyer (2000). "Anisotropic damage in quasi-brittle solids: modelling, computational issues and applications", Computer Methods in Applied Mechanics and Engineering 183(3-4): 331-352.

180. Driemeier, L. (1999). "Contribuição ao Estudo da Localização de Deformações com Modelos Constitutivos de Dano e Plasticidade", PhD Thesis, Escola de Engenharia de São Carlos - Universidade de São Paulo, São Paulo.
181. Driemeier, L., S.P. Baroncini Proença, and M. Alves (2005). "A contribution to the numerical nonlinear analysis of three-dimensional truss systems considering large strains, damage and plasticity", Communications in Nonlinear Science and Numerical Simulation 10(5): 515-535.
182. Driemeier, L., C. Comi, and S.P.B. Proença (2005). "On nonlocal regularization in one dimensional finite strain elasticity and plasticity", Computational Mechanics 36(1): 34-44.
183. Drucker, D.C. (1951). "A more fundamental approach to plastic stress–strain relations", 1st US National Congress of Applied Mechanics, ASME, New York.
184. Drucker, D.C. and W. Prager (1952). "Soil mechanics and plastic analysis of limit design", Quarterly of Applied Mathematics 10: 157–165.
185. Duarte, C.A., I. Babuska, and J.T. Oden (2000). "Generalized finite element methods for three-dimensional structural mechanics problems", Computers & Structures 77(2): 215-232.
186. Duarte, C.A., O.N. Hamzeh, T.J. Liszka, and W.W. Tworzydlo (2001). "A generalized finite element method for the simulation of three-dimensional dynamic crack propagation", Computer Methods in Applied Mechanics and Engineering 190(15-17): 2227-2262.
187. Duarte, C.A. and J.T. Oden (1995). "A Meshless Method to Solve Boundary-Value Problems", TICAM-Technical Report 95-05. University of Texas, Austin.
188. Duff, I.S. (1989). "Direct solvers", Computer Physics Reports 11(1-6): 21-50.
189. Duff, I.S., A.M. Erisman, and J.K. Reid (1986). "Direct Methods for Sparse Matrices", Oxford Science Publications, Oxford.
190. Dugdale, D.S. (1960). "Yielding of Steel Sheets Containing Slits", Journal of Mechanics and Physics of Solids 8: 100-104.
191. Dureisseix, D. and P. Ladevèze (1998). "A 2-level and Mixed Domain Decomposition Approach for Structural Analysis", Contemporary Mathematics: 238-245.
192. Dureisseix, D., P. Ladevèze, and B.A. Schrefler (2003). "A LATIN computational strategy for multiphysics problems: application to poroelasticity", International Journal for Numerical Methods in Engineering 56(10): 1489-1510.
193. Eligehausen, R., V. Bertero, and E. Popov (1983). "Local bond stress-slip relationships of deformed bars under generalized excitations", Report nº UCB/EERC-83/23. Earthquake Engineering Research Center, University of California, Berkeley, USA.
194. Elnashai, A.S. (2002). "Do We Really Need Inelastic Dynamic Analysis?", Journal of Earthquake Engineering 6(Special Issue 1): 123-130.
195. Engelen, R.A.B., M.G.D. Geers, and F.P.T. Baaijens (2003). "Nonlocal implicit gradient-enhanced elasto-plasticity for the modelling of softening behaviour", International Journal of Plasticity 19(4): 403-433.
196. Fajfar, P. (2000). "A Nonlinear Analysis Method for Performance Based Seismic Design", Earthquake Spectra 16(3): 573-592.
197. Fajfar, P. (2002). "Structural analysis in earthquake engineering - A breakthrough of simplified non-linear methods", 12th European Conference on Earthquake Engineering, London.
198. Fajfar, P. and M. Fischinger (1987). "Non-Linear Seismic Analysis of R/C buildings", European Earthquake Engineering 1: 31-43.
199. Fajfar, P. and M. Fischinger (1988). "N2 - A method for non-linear seismic analysis of regular buildings", 9th World Conference on Earthquake Engineering, Tokyo, Kyoto.
200. Fajfar, P. and P. Gaspersic (1996). "The N2 Method for the Seismic Damage Analysis of RC Buildings", Earthquake Engineering & Structural Dynamics 25(1): 31-46.

201. Fajfar, P., P. Gaspersic, and D. Drobnic (1997). "A simplified nonlinear method for seismic damage analysis of structures", International Workshop Seismic design methodologies for the next generation of codes, Slovenia, Rotterdam, Balkema, 24-27 June.

202. Fajfar, P., D. Marusic, and I. Perus (1999). "The N2 Method for Asymmetric Buildings", 1st European Conference on Earthquake Engineering and Seismology, Geneva, Switzerland.

203. Fajfar, P., D. Marušić, and I. Peruš (2005). "Torsional effects in the pushover-based seismic analysis of buildings", Journal of Earthquake Engineering 9(6): 831-854.

204. Farhat, C., P.S. Chen, and J. Mandel (1995). "A Scalable Lagrange Multiplier Based Domain Decomposition Method for Time-Dependent Problems", International Journal for Numerical Methods in Engineering 38(22): 3831-3853.

205. Farhat, C., P.S. Chen, J. Mandel, and F.X. Roux (1998). "The Two-Level FETI Method - Part II: Extension to Shell Problems, Parallel Implementation and Performance Results", Computer Methods in Applied Mechanics and Engineering 155: 153-180.

206. Farhat, C., M. Lesoinne, P. LeTallec, K. Pierson, and D. Rixen (2001). "FETI-DP: a dual-primal unified FETI method - part I: A faster alternative to the two-level FETI method", International Journal for Numerical Methods in Engineering 50(7): 1523-1544.

207. Farhat, C., M. Lesoinne, and K. Pierson (2000). "A scalable dual-primal domain decomposition method", Numerical Linear Algebra with Applications 7(7-8): 687-714.

208. Farhat, C., J. Li, and P. Avery (2005). "A FETI-DP method for the parallel iterative solution of indefinite and complex-valued solid and shell vibration problems", International Journal for Numerical Methods in Engineering 63(3): 398-427.

209. Farhat, C. and J. Mandel (1998). "The Two-level FETI Method for static and dynamic plate problems - Part I: An optimal iterative solver for biharmonic systems", Computer Methods in Applied Mechanics and Engineering 155: 129-152.

210. Farhat, C. and F.X. Roux (1991). "A Method of Finite Element Tearing and Interconnecting and its Parallel Solution Algorithm", International Journal for Numerical Methods in Engineering 32: 1205-1227.

211. Faria, R. (1994). "Avaliação do Comportamento Sísmico de Barragens de Betão Através de um Modelo de Dano Contínuo", Doutoramento em Engenharia Civil, Faculdade de Engenharia da Universidade do Porto, Porto.

212. Faria, R., J. Oliver, and M. Cervera (1998). "A Strain-based Plastic Viscous-Damage Model for Massive Concrete Structures", Int. J. Solids Structures 35(14): 1533-1558.

213. Faria, R., J. Oliver, and M. Cervera (2004). "Modeling Material Failure in Concrete Structures under Cyclic Actions", Journal of Structural Engineering-ASCE 130(12): 1997-2005.

214. FIB (2000). "Bond of reinforcement in concrete", State-of-art report - Bulletin 10. International Federation for Structural Concrete (FIB), Lausanne, Switzerland.

215. FIB (2003). "Displacement-based seismic design of reinforced concrete buildings", State-of-art report - Bulletin 25. International Federation for Structural Concrete (FIB), Lausanne, Switzerland.

216. Filippou, F.C. and A. Issa (1988). "Nonlinear Analysis of Reinforced Concrete Frames under Cyclic Load Reversals", Report No. UCB/EERC–88/12. Earthquake Engineering Research Center, University of California, Berkeley, USA.

217. Filippou, F.C., E. Popov, and V. Bertero (1983). "Effects of Bond Deterioration on Hysteretic Behavior of Reinforced Concrete Joints", Report nº UCB/EERC-83/19. Earthquake Engineering Research Center, University of California, Berkeley, USA.

218. Filippou, F.C., E.P. Popov, and V.V. Bertero (1983). "Modeling of R/C Joints under Cyclic Excitations", Journal of Structural Engineering 109(11): 2666-2684.

219. Fleury, F. (1996). "Prédiction du comportement des structures en béton arme sous sollicitations sismiques: Proposition d'un modelé global de nœud d'ossature intégrant le comportement de la liaison acier/béton", Ph.D. Thesis, Université Blaise-Pascal-Clermont II, Lyon.
220. Flynn, M. (1972). "Some Computer Organizations and Their Effectiveness", IEEE Transactions on Computing 21(9): 948-960.
221. Foster, I., J. Geisler, W. Gropp, N. Karonis, E. Lusk, G. Thiruvathukal, and S. Tuecke (1998). "Wide-area implementation of the Message Passing Interface", Parallel Computing 24(12-13): 1735-1749.
222. Foster, I. and C. Kesselman (2003). "The Grid: Blueprint for a New Computing Infrastructure", Morgan Kaufmann.
223. Fox, G.C., M.A. Johnson, G.A. Lyzenga, S.W. Otto, J.K. Salmon, and D.W. Walker (1988). "Solving Problems on Concurrent Processors ", Volume 1, Prentice Hall, Englewood Cliffs, New Jersey, USA.
224. Fragakis, Y. and M. Papadrakakis (2003). "The mosaic of high performance domain Decomposition Methods for Structural Mechanics: Formulation, interrelation and numerical efficiency of primal and dual methods", Computer Methods in Applied Mechanics and Engineering 192(35-36): 3799-3830.
225. Fragakis, Y. and M. Papadrakakis (2004). "The mosaic of high-performance domain decomposition methods for structural mechanics-Part II: Formulation enhancements, multiple right-hand sides and implicit dynamics", Computer Methods in Applied Mechanics and Engineering 193(42-44): 4611-4662.
226. Freeman, S.A. (1978). "Prediction of response of concrete buildings to severe earthquake motion", Proceedings of Douglas McHenry International Symposium on Concrete Structures, Detroit.
227. Frémond, M. (2006). "The Clausius-Duhem Inequality, an Interesting and Productive Inequality", Nonsmooth Mechanics and Analysis, Advances in Mechanics and Mathematics. Edited by P. Alart, O. Maisonneuve, and R.T. Rockafellar, Springer. 12(107-118.
228. Frémond, M. and B. Nedjar (1996). "Damage, gradient of damage and principal of virtual power", International Journal of Solids and Structures(33): 1083-1103.
229. Fung, Y.C. (1965). "Foundations of Solid Mechanics", Prentice-Hall, Inc., New Jersey.
230. Gambarova, P. and G. Rosati (1996). "Bond and splitting in reinforced concrete: test results on bar pull-out", Materials and Structures 29(5): 267-276.
231. Gambarova, P.G. and G.P. Rosati (1997). "Bond and splitting in bar pull-out: Behavioural laws and concrete cover role", Magazine of Concrete Research 49(179): 99-110.
232. Garusi, E. and A. Tralli (2002). "A hybrid stress - assumed transition element for solid-to-beam and plate-to-beam connections", Computers & Structures 80: 105-115.
233. Gastebled, O.J. and I.M. May (2000). "Numerical simulation of pulled specimens", ACI Structural Journal 97(2): 308-315.
234. Gdoutos, E.E. (2005). "Fracture Mechanics - An Introduction", Springer, 2nd Ed.
235. Geist, A., A. Beguelin, J. Dongarra, W. Jiang, R. Manchek, and V. Sunderam (1994). "PVM: Parallel Virtual Machine: A Users' Guide and Tutorial for Network Parallel Computing", MIT Press, Massachusetts.
236. Gerstle, K. (1973). "Behaviour of Concrete under Biaxial Stresses", J. Eng. Mech. Div. ASCE 99(EM4).
237. Ghaboussi, J., E.L. Wilson, and J. Isenberg (1973). "Finite element for rock joints and interfaces", Journal of the Soil Mechanics and Foundations Division, ASCE, 99(SM10): 833-48.

238. Ghandehari, M., S. Krishnaswamy, and S. Shah (2000). "Bond-Induced Longitudinal Fracture in Reinforced Concrete", Journal of Applied Mechanics 67(4): 740-748.

239. Giberson, M. (1967). "The Response of Nonlinear Multi-story Structures Subjected to Earthquake Excitation", PhD Thesis, California Institute of Technology, Pasadena, CA, USA.

240. GiD (2011). "GiD - The personal pre and postprocessor", version 10.1.8d x64, CIMNE, Barcelona.

241. Giuffrè, A. and P. Pinto (1970). "Il Comportamento del Cemento Armato per Sollecitazioni Cicliche di Forte Intensità", Giornale del Genio Civile.

242. Giuriani, E. (1982). "On the effective axial stiffness of a bar in cracked concrete", Applied Science Publishers.

243. Gmur, T.C. and R.H. Kauten (1993). "3D solid to beam transition elements for structural dynamics analysis", International Journal for Numerical Methods in Engineering 36: 1429-1444.

244. Góis, W. and S.P.B. Proença (2005). "Generalized Finite Element Method in mixed variational formulation: a study of convergence and solvability", ECCOMAS Thematic Conference on Meshless Methods - Meshless 2005, Lisbon.

245. Golub, G.H. and C.F.V. Loan (1996). "Matrix Computations", The Johns Hopkins University Press, 3rd Ed., Baltimore, USA.

246. Gomes, A. (1992). "Comportamento e Reforço de Elementos de Betão Armado Sujeitos a Acções Cíclicas", Doutoramento em Engenharia Civil, Instituto Superior Técnico, Universidade Técnica de Lisboa, Lisboa.

247. Gomes, A. and J. Appleton (1997). "NonLinear Cyclic Stress Strain Relation of Reinforced Bars Including Buckling", Engineering Structures 19(10): 822-826.

248. Goodman, R.E., R.L. Taylor, and T.L. Brekke (1968). "A model for the mechanics of jointed rock", Journal of the Soil Mechanics and Foundations Division ASCE 94(SM3): 637-659.

249. Gopalaratnam, V.S. and S.P. Shah (1985). "Softening Response of Plain Concrete in Direct Tension", ACI Materials Journal 82(3): 310-323.

250. Gosselet, P. and C. Rey (2006). "Non-overlapping domain decomposition methods in structural mechanics", Archives of Computational Methods in Engineering 13(4): 515-572.

251. Goto, Y. (1971). "Cracks formed in concrete around tension bars", ACI Journal 68(4): 244-251.

252. Gravouil, A., N. Moës, and T. Belytschko (2002). "Non-planar 3D crack growth by the extended finite element and level sets - Part II: Level set update", International Journal for Numerical Methods in Engineering 53(11): 2569-2586.

253. Griffith, A.A. (1921). "The Phenomena of Rupture and Flow in Solids", Philosophical Transactions of the Royal Society of London 221: 163–198.

254. Guedes, J. (1997). "Seismic Behavior of Reinforced Concrete Bridges Modelling - Numerical Analysis and Experimental Assessment", Doutoramento em Engenharia Civil, Faculdade de Engenharia da Universidade do Porto, Porto.

255. Gupta, A. and V. Kumar (1990). "On the scalability of FFT on parallel computers", Frontiers 90 Conference on Massively Parallel Computation, IEEE Computer Society Press.

256. Guyan, R.J. (1965). "Reduction of Stiffness and Mass Matrices", American Institute of Aeronautics and Astronautics (AIAA) Journal 3(2): 380-380.

257. Han, W. and B.D. Reddy (1999). "Plasticity - Mathematical Theory and Numerical Analysis", Springer Verlag, New York.

258. Hansen, J. and J. Brinch (1965). "Some stress-strain relationships for soils", 6th Int. Conf. Soil Mechanics, Montreal, Canada.

259. Hanson, J. (2007). "Cornell University/NSF Project", from http://simscience.org/.

260. Hassanzadeh, M. (1991). "Behaviour of fracture process zones in concrete influenced by simultaneously applied normal and shear displacements", Ph.D. Thesis, Division of Building Materials - Lund Institute of Technology, Lund, Sweden.

261. Hawkins, N.M., I.J. Lin, and F.L. Jeang (1982). "Local bond strength of concrete for cyclic reversed actions", Bond in Concrete, London.

262. Hellesland, J. and A. Scordelis (1981). "Analysis of RC Bridge Columns Under Imposed Deformations", IABSE Colloquium, Delft, Netherlands.

263. Henriques, A.A.R. (1998). "Aplicação de Novos Conceitos de Segurança no Dimensionamento do Betão Estrutural", Doutoramento em Engenharia Civil, Faculdade de Engenharia da Universidade do Porto, Porto, Portugal.

264. Hestenes, M.R. and E. Stiefel (1952). "Methods of conjugate gradients for solving linear systems", Journal of Research of the National Bureau of Standards 49(6).

265. Hilber, H.M. (1976). "Analysis and design of numerical integration methods in structural dynamics", UCB/EERC-76/29, Earthquake Engineering Research Center. Earthquake Engineering Research Center, University of California, Berkeley, USA.

266. Hilber, H.M. and T.J.R. Hughes (1978). "Collocation, Dissipation and Overshoot for Time Integration Shemes in Structural Dynamics", Earthquake Engineering & Structural Dynamics 6: 99-117.

267. Hilber, H.M., T.J.R. Hughes, and R.L. Taylor (1977). "Improved Numerical Dissipation for Time Integration Algorithms in Structural Dynamics", Earthquake Engineering and Structural Dynamics 5(3): 283-292.

268. Hillerborg, A. (1984). "Additional concrete fracture energy tests performed by 6 laboratories according to a draft RILEM recommendation". Div of Building Materials LTH, Lund university, Lund, Sweden.

269. Hillerborg, A. (1985). "The theoretical basis of a method to determine the fracture energy Gf of concrete", Materials and Structures 18(4): 291-296.

270. Hillerborg, A., M. Modéer, and P.E. Petersson (1976). "Analysis of crack formation and crack growth in concrete by means of fracture mechanics and finite elements", Cement and Concrete Research 6(6): 773-781.

271. Hilsdorf, H.K. and W. Brameshuber (1991). "Code-type formulation of fracture mechanics concepts for concrete", International Journal of Fracture 51(1): 61-72.

272. Hilsdorf, K. and H. Rusch (1969). "Behaviour of Concrete under Biaxial Stresses", J. Am. Concr. Inst. 66(8): 656-666.

273. Hinton, E., T. Rock, and O.C. Zienkiewicz (1976). "A note on mass lumping and related processes in the finite element method", Earthquake Engineering & Structural Dynamics 4(3): 245-249.

274. Hjorth, O. (1976). "Ein Beitrag zur Frage der Festigkeiten und des Verbundverhaltens von Stahl und Beton bei hohen Beanspruchungsgeschwindigkeiten", PhD Thesis, Techn. Univ. of Brunswick, Brunswick.

275. Hopkinson, B. (1914). "A Method of Measuring the Pressure Produced in the Detonation of High Explosives or by the Impact of Bullets", Philosophical Transactions of the Royal Society of London. Series A, Containing Papers of a Mathematical or Physical Character 213(ArticleType: research-article / Full publication date: 1914 / Copyright © 1914 The Royal Society): 437-456.

276. Houbolt, J.C. (1950). "A Recurrence Matrix Solution for the Dynamic Response of Elastic Aircraft", J. Aeronaut. Sci. 17: 540-550.

277. Hu, X. and F. Wittmann (1992). "Fracture energy and fracture process zone", Materials and Structures 25(6): 319-326.

278. Hughes, B.P. and G.P. Chapman (1966). "The Complete Stress-Strain Curve for Concrete in Direct Tension", RILEM Bull. 30.

279. Hughes, T.J.R. (1987). "The finite element method - Linear static and dynamic finite element analysis", Prentice-Hall, Inc., New Jersey.

280. Hughes, T.J.R. and W.K. Liu (1978). "Implicit-Explicit Finite Elements in Transient Analysis: Implementation and Numerical Examples", Journal of Applied Mechanics 45(2): 375-378.

281. Hughes, T.J.R., W.K. Liu, and A. Brooks (1979). "Finite element analysis of incompressible viscous flows by the penalty function formulation", Journal of Computational Physics 30(1): 1-60.

282. Hughes, T.J.R., K.S. Pister, and R.L. Taylor (1979). "Implicit-explicit finite elements in nonlinear transient analysis", Computer Methods in Applied Mechanics and Engineering 17-18(Part 1): 159-182.

283. Ibijola, E.A. (2002). "On some fundamental concepts of Continuum Damage Mechanics", Computer Methods in Applied Mechanics and Engineering 191(13-14): 1505-1520.

284. Intel Corporation (2008). "White Paper - Intel Turbo Boost Technology in Intel Core Microarchitecture (Nehalem) Based Processors", Doc: 320354-001.

285. Intel Corporation (2009). "Datasheet - Intel Core i7-900 Mobile Processor Extreme Edition Series, Intel Core i7-800 and i7-700 Mobile Processor Series - Volume 1", Doc: 320765-001.

286. Intel Corporation (2009). "Datasheet - Intel Core i7-900 Mobile Processor Extreme Edition Series, Intel Core i7-800 and i7-700 Mobile Processor Series - Volume 2", Doc: 320766-002.

287. Irwin, G. (1957). "Analysis of stresses and strains near the end of a crack traversing a plate", Journal of Applied Mechanics 24: 361–364.

288. Irwin, G.R. (1958). "Fracture - Encyclopaedia of physics, Vol VI", Springer, Berlin, Germany.

289. JCI (2003). "Method of test for fracture energy of concrete by use of notched beam", Japan Concrete Institute Standard. JCI-S-001-2003.

290. Jefferson, A.D. (2002). "Constitutive modelling of aggregate interlock in concrete", International Journal for Numerical and Analytical Methods in Geomechanics 26(5): 515-535.

291. Jirásek, M. (1998). "Nonlocal models for damage and fracture: comparison of approaches", International Journal of Solids and Structures(35): 4133-4145.

292. Jirásek, M. (1999). "Computational aspects of non-local models", ECCM '99 - European Conference on Computational Mechanics, München, Germany.

293. Jirásek, M. (2001). "Modelling of localized damage and fracture in quasi- brittle materials", Continuous and discontinuous modelling of cohesive frictional materials - Lecture Notes in Physics 568. P.A. Vermeer and et al., Springer, Berlin: 17–29.

294. Jirásek, M. (2002). "Objective modeling of strain localization", Revue Française de Génie Civil 6(6): 1119-1132.

295. Jirásek, M. and B. Patzák (2002). "Consistent tangent stiffness for nonlocal damage models", Computers & Structures 80: 1279-1293.

296. Jirásek, M., S. Rolshoven, and P. Grassl (2004). "Size effect on fracture energy induced by non-locality", International Journal for Numerical and Analytical Methods in Geomechanics 28(7-8): 653-670.

297. Ju, J.W. (1989). "On energy-based coupled elastoplastic damage theories: constitutive modelling and computational aspects", Int. Journal of Solids and Structures 25: 803-833.

298. Kaba, S.A. and S.A. Mahin (1984). "Refined modelling of reinforced concrete columns for seismic analysis", Report No. UCB/EERC-84/03. Earthquake Engineering Research Center, University of California, Berkeley, USA.

299. Kachanov, L.M. (1958). "Time of the Rupture Process Under Creep Conditions", Izvestija Akademii Nauk SSSR-Otdelenie Techniceskich Nauk 8: 26–31.
300. Kachanov, L.M. (1986). "Introduction to continuum damage mechanics", Martinus Nijhoff Publishers, Dordrecht, The Netherlands.
301. Kachanov, L.M. (2004). "Fundamentals of the Theory of Plasticity", Dover Publications, Inc.
302. Kalkan, E. and S.K. Kunnath (2006). "Adaptive Modal Combination Procedure for Nonlinear Static Analysis of Building Structures", Journal of Structural Engineering 132(11): 1721-1731.
303. Karsan, P. and J.O. Jirsa (1969). "Behaviour of Concrete under Compressive Stress-Strain Loading", Journal Structural Division ASCE 95(ST12): 2543-2563.
304. Kent, D.C. and R. Park (1973). "Cyclic Load Behaviour of Reinforcing Steel", Strain 9(3): 98-103.
305. Klawonn, A. and O. Rheinbach (2010). "Highly scalable parallel domain decomposition methods with an application to biomechanics", ZAMM - Journal of Applied Mathematics and Mechanics / Zeitschrift für Angewandte Mathematik und Mechanik 90(1): 5-32.
306. Klawonn, A. and O. Widlund (2001). "FETI and Neumann-Neumann iterative substructuring methods: Connections and new results", Communications on Pure and Applied Mathematics 54(1): 57-90.
307. Koh, S.K. and R.I. Stephens (1991). "Mean Stress Effects on Low Cycle Fatigue for a High Strength Steel", Fatigue & Fracture of Engineering Materials & Structures 14(4): 413-428.
308. Kormeling, H.A. and H.W. Reinhardt (1987). "Strain rate effects on steel fibre concrete in uniaxial tension", Int. Journal of Cement Composites and Lightweight Concrete 9(4): 197-204.
309. Krajcinovic, D. (1996). "Damage Mechanics", North-Holland, Elsevier Science B.V., Amsterdam.
310. Krajcinovic, D. and G.U. Fonseka (1981). "The continuous damage theory of brittle materials", Journal of Applied Mechanics 48: 809–824.
311. Krawinkler, H. and G.D.P.K. Seneviratna (1998). "Pros and cons of a pushover analysis of seismic performance evaluation", Engineering Structures 20(4-6): 452-464.
312. Kreslin, M. and P. Fajfar (2010). "Seismic evaluation of an existing complex RC building", Bulletin of Earthquake Engineering 8(2): 363-385.
313. Kreslin, M. and P. Fajfar (2011). "The extended N2 method taking into account higher mode effects in elevation", Earthquake Engineering & Structural Dynamics Published online in Wiley Online Library (wileyonlinelibrary.com).
314. Kupfer, H., K. Hilsdorf, and H. Rüsch (1969). "Behavior of Concrete Under Biaxial Stress", Journal ACI 66(8).
315. L'Hermite, S. (1973). "Influence de la dimension absolue sur la résistance de fléxion", Annales de l'ITBTP. 309-310: 39-41.
316. La Borderie, C. (1991). "Phénomènes Unilatéraux Dans un Matériau Endommageable: Modélisation et Application à l'Analyse de Structures en Béton", PhD Thesis, ENS Cachan, Cachan, France.
317. La Borderie, C. and G. Pijaudier-Cabot (1987). "Etude expérimentale du comportement des matériaux renforcés", Rapport LMT Cachan; Contrat I70/1F 3146 - Electricité de France, Cachan, France.
318. Ladevèze, P. (1999). "Nonlinear Computational Structural Mechanics - New Approaches and Non-Incremental Methods of Calculation", Springer-Verlag., Berlin, Germany.
319. Ladevèze, P., O. Loiseau, and D. Dureisseix (2001). "A micro–macro and parallel computational strategy for highly heterogeneous structures", International Journal for Numerical Methods in Engineering 52(1-2): 121-138.

320. Ladevèze, P., D. Néron, and P. Gosselet (2007). "On a mixed and multiscale domain decomposition method", Computer Methods in Applied Mechanics and Engineering 196(8): 1526-1540.
321. Ladevèze, P. and A. Nouy (2003). "On a multiscale computational strategy with time and space homogenization for structural mechanics", Computer Methods in Applied Mechanics and Engineering 192(28-30): 3061-3087.
322. Ladevèze, P., J.C. Passieux, and D. Néron (2010). "The LATIN multiscale computational method and the Proper Generalized Decomposition", Computer Methods in Applied Mechanics and Engineering 199(21-22): 1287-1296.
323. Le Bellégo, C., J. François Dubé, G. Pijaudier-Cabot, and B. Gérard (2003). "Calibration of nonlocal damage model from size effect tests", European Journal of Mechanics - A/Solids 22(1): 33-46.
324. Le Tallec, P. (1994). "Domain decomposition methods in computational mechanics", Computational Mechanics Advances, North-Holland. 1(2): 121-220.
325. Le Tallec, P., J. Mandel, and M. Vidrascu (1993). "Balancing domain decomposition for plates", 7th International Conference on Domain Decomposition Methods, Pennsylvania, USA.
326. Le Tallec, P., J. Mandel, and M. Vidrascu (1998). "A Neumann-Neumann domain decomposition algorithm for solving plate and shell problems", SIAM Journal on Numerical Analysis 35(2): 836-867.
327. Lee, J. and G.L. Fenves (1998). "A plastic-damage concrete model for earthquake analysis of dams", Earthquake Engineering & Structural Dynamics 27(9): 937-956.
328. Lemaitre, J. (1984). "How to use damage mechanics", Nuclear Eng. and Design 80: 233-245.
329. Lemaitre, J. (1996). "A Course on Damage Mechanics", Springer, 2nd Ed., Berlin.
330. Lemaitre, J. and J.L. Chaboche (1985). "Mécanique des Matériaux Solides", Dunod, Paris.
331. Lemaitre, J. and J.L. Chaboche (1990). "Mechanics of solids materials", Cambridge University Press, Cambridge.
332. Lemaitre, J. and R. Desmorat (2005). "Engineering Damage Mechanics - Ductile, Creep, Fatigue and Brittle Failures", Springer, Berlin.
333. Leslie, P.D. (1974). "Ductility of Reinforced Concrete Bridge Piers", Master of Engineering Report. University of Canterbury, Christchurch, New Zealand.
334. Levenberg, K. (1944). "A method for the solution of certain problems in least squares", Quarterly of Applied Mathematics 2: 164-168.
335. Levy, M. (1871). "Extrait du mémoire sur les équations générales des mouvements intérieures des corps solides ductiles au delà des limites où l'élasticité pourrait les ramener à leur premier état.", J Math Pures Appl 16(369-372).
336. Li, J., X. Gao, and P. Zhang (2007). "Experimental investigation on the bond of reinforcing bars in high performance concrete under cyclic loading", Materials and Structures 40(10): 1027-1044.
337. Li, J. and O.B. Widlund (2006). "FETI-DP, BDDC, and block Cholesky methods", International Journal for Numerical Methods in Engineering 66(2): 250-271.
338. Lim, Song, and Seog (2001). "Formulation method for solid-to-beam transition finite elements", KSME International Journal 15(11): 1499-1506.
339. Lin, Z. and L. Wood (2003). "Concrete Uniaxial Tensile Strength and Cylinder Splitting Test", Journal of Structural Engineering 129(5): 692-699.
340. Liu, G.R. and S.S. Quek (2003). "The finite element method - A practical course", Butterworth-Heinemann.

341. LNEC (1998). "Varões de aço A400 NR para armaduras de betão armado - Características, ensaios e marcação", Especificação LNEC. Lisboa, LNEC. E449-1995.

342. Lowes, L.N. (1999). "Finite element modeling of reinforced concrete beam-column bridge connections", PhD Thesis, University of California, Berkeley.

343. Lu, M., Y.W. Mai, and L. Ye (2001). "Crack-tip field for fast fracture of an elastic-plastic-viscoplastic material coupled with quasi-brittle damage. Part 2. Small damage regime", International Journal of Solids and Structures 38(50-51): 9403-9420.

344. Lubliner, J. (2006). "Plasticity Theory", Pearson Education, Inc.

345. Lubliner, J., J. Oliver, S. Oller, and E. Oñate (1989). "A plastic-damage model for concrete", International Journal of Solids and Structures 25(3): 299-326.

346. Lutz, L.A. and P. Gergely (1967). "Mechanics of bond and slip of deformed bars in concrete", ACI Structural Journal 64(11): 711-721.

347. Lutz, L.A., P. Gergely, and G. Winter (1966). "The mechanics of bond and slip of deformed reinforcing bars in concrete", Structural Engineering Report No. 324, August. Cornell University.

348. Ma, S.M., V.V. Bertero, and E.P. Popov (1976). "Experimental and Analytical Studies on the Hysteretic Behaviour of Reinforced Concrete Rectangular and T-Beams", Report Nº EERC 76-2. Earthquake Engineering Research Center, University of California, Berkeley, USA.

349. Mahasuverachai, M. and G.H. Powell (1982). "Inelastic analysis of piping and tubular structures", Report nº UCB/EERC-82/27. Earthquake Engineering Research Center, University of California, Berkeley, USA.

350. Mahin, S.A., V.V. Bertero, M.B. Atalay, and D. Rea (1972). "Rate of Loading Effects on Uncracked and Repaired Reinforced Concrete Members", Report No. UCB/EERC-72/09. Earthquake Engineering Research Center, University of California, Berkeley, USA.

351. Maker, B.N. and T.A. Laursen (1994). "A finite element formulation for rod/continuum interactions: The one-dimensional slideline", International Journal for Numerical Methods in Engineering 37(1): 1-18.

352. Malvar, L.J. (1991). "Bond of reinforcement under controlled confinement", NCEL Technical Note N-1833. Naval Civil Engineering Laboratory, Port Hueneme.

353. Malvar, L.J. (1992). "Bond of reinforcement under controlled confinement", ACI Materials Journal 89(6): 593-601.

354. Malvar, L.J. and J.E. Crawford (1998). "Dynamic Increase Factors for Steel Reinforcing Bars", 28th DDESB Seminar, Karagozian & Case.

355. Mandel, J. (1993). "Balancing Domain Decomposition", Communications in Numerical Methods in Engineering 9(3): 233-241.

356. Mandel, J. and M. Brezina (1996). "Balancing domain decomposition for problems with large jumps in coefficients", Mathematics of Computations 65(216): 1387-1401.

357. Mandel, J. and C.R. Dohrmann (2003). "Convergence of a balancing domain decomposition by constraints and energy minimization", Numerical Linear Algebra with Applications 10(7): 639-659.

358. Mandel, J., C.R. Dohrmann, and R. Tezaur (2005). "An algebraic theory for primal and dual substructuring methods by constraints", Applied Numerical Mathematics 54(2): 167-193.

359. Mandel, J., B. Sousedík, and C. Dohrmann (2008). "Multispace and multilevel BDDC", Computing 83(2): 55-85.

360. Mandel, J. and R. Tezaur (1996). "Convergence of a substructuring method with Lagrange multipliers", Numerische Mathematik 73(4): 473-487.

361. Mandel, J. and R. Tezaur (2001). "On the convergence of a dual-primal substructuring method", Numerische Mathematik 88(3): 543-558.

362. Mander, J., M. Priestley, and R. Park (1984). "Seismic Design of Bridge Piers", Research Report 84-2. University of Canterbury, Christchurch, New Zealand.

363. Mander, J.B. (1983). "Seismic Design of Bridge Piers", PhD Thesis, Civil Engineering, University of Canterbury, Christchurch, New Zealand.

364. Mander, J.B., F.D. Panthaki, and A. Kasalanati (1994). "Low-Cycle Fatigue Behavior of Reinforcing Steel", Journal of Materials in Civil Engineering 6(4): 453-468.

365. Manjoine, M.J. (1944). "Influence of Rate of Strain and Temperature on Yield Stresses of Mild Steel", Journal of Applied Mechanics 11: 211-218.

366. Manson, S.S. (1953). "Behavior of materials under conditions of thermal stress", Heat Transfer Symp., University of Michigan Engineering Research Institute, Ann Arbor, Mich. 9-75.

367. Mari, A. and A. Scordelis (1984). "Nonlinear Geometric Material and Time Dependent Analysis of Three Dimensional Reinforced and Prestressed Concrete Frames", SESM Report 82-12. Department of Civil Engineering, University of California, Berkeley, CA, USA.

368. Mariani, S. and U. Perego (2003). "Extended finite element method for quasi-brittle fracture", International Journal for Numerical Methods in Engineering 58(1): 103-126.

369. Marquardt, D. (1963). "An algorithm for least-squares estimation of nonlinear parameters", SIAM Journal on Applied Mathematics 11: 431-441.

370. Martín, F., A. Benavent-Climent, and R. Gallego (2008). "A scheme for imposing constraints and improving conditioning of structural stiffness matrices", Int. J. Numer. Meth. Biomed. Engng 26: 1117-1124.

371. Martin, H. (1973). "On the interrelation among surface roughness, bond and bar stiffness in the reinforcement subject to short-term loading", Deutscher Ausschuss Stahlbeton 228: 1-50.

372. Martin, J. (2006). "Materials for Engineering", CRC Press, 3rd Ed.

373. Martino, A., R. Landolfo, and F. Mazzolani (1990). "The use of the Ramberg-Osgood law for materials of round-house type", Materials and Structures 23(1): 59-67.

374. Mathew, T.P.A. (2008). "Domain Decomposition Methods for the Numerical Solution of Partial Differential Equations", Springer Berlin Heidelberg, Berlin.

375. Mathew, T.P.A. (2008). "Schur Complement and Iterative Substructuring Algorithms", Domain Decomposition Methods for the Numerical Solution of Partial Differential Equations. Berlin Springer Heidelberg. 61(107-230).

376. MathWorks Inc. (2010). "MATLAB - The Language of Technical Computing", Version 7.11 R2010b 64-bit (win64), MathWorks Inc.

377. MathWorks Inc. (2010). "MATLAB Distributed Computing Server - System Administrator's Guide", Version 5.0 (R2010b), MathWorks Inc.

378. MathWorks Inc. (2010). "MATLAB Parallel Computing Toolbox - User's Guide", Version 5.0 (R2010a), MathWorks Inc.

379. Mattock, A. (1967). "Discussion of "Rotational Capacity of Reinforced Concrete Beams" by W. Corley", Journal of Structural Division 93 (ST2).

380. Mau, S.T. and M. El-Mabsout (1989). "Inelastic Buckling of Reinforcing Bars", Journal of Engineering Mechanics 115(1): 1-17.

381. Mazars, J. (1984). "Application de la mécanique de l'endommagement au comportement non linéaire et à la rupture du béton de structure", PhD Thesis, Université Paris VI, Paris.

382. Mazars, J. (1986). "A description of micro- and macroscale damage of concrete structures", Engineering Fracture Mechanics 25(5-6): 729-737.

383. Mazars, J. (1991). "Damage models for concrete and their usefulness for seismic loadings", Experimental and Numerical Methods in Earthquake Engineering. Edited by J. Donea and P.M. Jones, Kluwer Academic Publishers.

384. Mazars, J., L. Davenne, P. Kotronis, F. Ragueneau, and G. Casaux (2002). "A 3D fiber beam element analysis for RC structural walls", 12th European Conference on Earthquake Engineering, London, UK.

385. Mazars, J., P. Kotronis, F. Ragueneau, and G. Casaux (2006). "Using multifiber beams to account for shear and torsion: Applications to concrete structural elements", Computer Methods in Applied Mechanics and Engineering 195(52): 7264-7281.

386. Mazars, J. and G. Pijaudier-Cabot (1996). "From damage to fracture mechanics and conversely: A combined approach", International Journal of Solids and Structures 33(20-22): 3327-3342.

387. Mazars, J., G. Pijaudier-Cabot, and C. Saouridis (1991). "Size effect and continuous damage in cementitious materials", International Journal of Fracture 51(2): 159-173.

388. Mazars, J., F. Ragueneau, and G. Pijaudier-Cabot (2002). "Continuum damage modelling for concrete structures in dynamic situations", Continuum Damage Mechanics of Materials and Structures. Edited by O. Allix and F. Hild: 259-294.

389. Mazars, J. and D. Walter (1980). "Endommagement mécanique du béton", In Délégation Générale à la Recherche Scientifique et Technique, France. 78.7.2697 to 78.7.2698.

390. MC90 (1991). "Model Code 90", CEB-FIB, Thomas Telford.

391. Melenk, J.M. and I. Babuska (1996). "The partition of unity finite element method: Basic theory and applications", Computer Methods in Applied Mechanics and Engineering 139(1-4): 289-314.

392. Mendes, L., E. Coelho, and A. Campos Costa (2006). "Seismic Tests of a RC Precast Building System", 1st European Conference on Earthquake Engineering and Seismology, 3-8 September, Geneva, Switzerland.

393. Mendes, L., E. Coelho, and A.C. Costa (2006). "Shaking Table Tests of a Reinforced Concrete Precast Building System", Relatório nº97/2006 - NESDE. Laboratório Nacional de Engenharia Civil, Lisboa.

394. Mendes, L., E. Coelho, and A.C. Costa (2007). "Cyclic Tests of Joints from a Reinforced Concrete Precast Building System", Relatório nº30/2007 - NESDE. Laboratório Nacional de Engenharia Civil, Lisboa.

395. Mendes, L. and A.C. Costa (2007). "LNEC-SPA, Signal Processing and Analysis Tools for Civil Engineers – Version 1.0 - Build 12", Report nº29/2007-NESDE. Laboratório Nacional de Engenharia Civil, Lisboa.

396. Menegotto, M. and P.E. Pinto (1973). "Method of Analysis for Cyclically Loaded R. C. Plane Frames Including Changes in Geometry and Non-Elastic Behavior of Elements Under Combined Normal Force and Bending", IABSE Symposium on Resistance and Ultimate Deformability of Structures Acted on by Well Defined Repeated Loads, LNEC, Lisboa.

397. Miramontes, D., O. Merabet, and J.M. Reynouard (1996). "Beam global model for the seismic analysis of RC frames", Earthquake Engineering & Structural Dynamics 25(7): 671-688.

398. Miranda, E. and V.V. Bertero (1994). "Evaluation of Strength Reduction Factors for Earthquake-Resistant Design", Earthquake Spectra 10(2): 357-379.

399. Mirza, S.A. and J.G. MacGregor (1979). "Variability of Mechanical Properties of Reinforcing Bars", ASCE Journal of the Structural Division 105(ST5): 921-937.

400. Mirza, S.M. and J. Houde (1979). "Study of bond stress-slip relationships in reinforced concrete", ACI Journal Proceedings 76(1): 19-46.

401. Moës, N., J. Dolbow, and T. Belytschko (1999). "A finite element method for crack growth without remeshing", International Journal for Numerical Methods in Engineering 46(1): 131-150.
402. Moës, N., A. Gravouil, and T. Belytschko (2002). "Non-planar 3D crack growth by the extended finite element and level sets - Part I: Mechanical model", International Journal for Numerical Methods in Engineering 53(11): 2549-2568.
403. Monteiro, V. and E.C. Carvalho (1985). "Comportamento de Elementos de Betão Armado Sujeitos a Acções Repetidas e Alternadas ", Curso sobre Estruturas de Betão Armado sujeitas à Acção dos Sismos. Laboratório Nacional de Engenharia Civil, Lisboa.
404. Monti, G., F.C. Filippou, and E. Spacone (1997). "Analysis of hysteretic behavior of anchored reinforcing bars", ACI Structural Journal 94(3): 248-261.
405. Monti, G. and C. Nuti (1992). "Nonlinear Cyclic Behavior of Reinforcing Bars Including Buckling", Journal of Structural Engineering 118(12): 3268-3284.
406. Moore, E.H. (1920). "On the reciprocal of the general algebraic matrix", Bulletin of the American Mathematical Society 26: 394–395.
407. Moran, M.J. and H.N. Shapiro (2006). "Fundamentals of Engineering Thermodynamics", John Wiley & Sons, Inc., 5th Ed., West Sussex, UK.
408. Morita, S. and T. Kaku (1973). "Local bond stress-slip relationship under repeated loading", IABSE Symposium: Resistance and Ultimate Deformability of Structures Acted on Well Defined Repeated Loads, LNEC, Lisbon, Portugal.
409. Mühlhaus, H.B. and E.C. Alfantis (1991). "A variational principle for gradient plasticity", International Journal of Solids and Structures 28(7): 845-857.
410. Murakami, S. and N. Ohno (1981). "A continuum theory of creep and creep damage", Creep in Structures. Edited by A.R.S. Ponter and D.R. Hayhurst, Springer Verlag.
411. Nakashima, M., T. Akazawa, and O. Sakaguchi (1993). "Integration method capable of controlling experimental error growth in substructure pseudodynamic test", Journal of Structural Construction Engineering (AIJ) 454: 61– 71.
412. Nakashima, M., T. Kaminosomo, M. Ishida, and K. Ando (1990). "Integration techniques for substructuring pseudodynamic test", 4th U.S. National Conference on Earthquake Engineering (Volume 2), Palm Springs, CA, USA.
413. Néron, D., P. Ladevèze, and B.A. Schrefler (2006). "A time-space framework suitable for the LATIN computational strategy for multiphysics problems", III European Conference on Computational Mechanics. Edited by C.A. Motasoares, J.A.C. Martins, H.C. Rodrigues, J.A.C. Ambrósio, C.A.B. Pina, C.M. Motasoares, E.B.R. Pereira, and J. Folgado, Springer Netherlands: 357-357.
414. Neto, P., J. Alfaiate, J.R. Almeida, and E.B. Pires (2004). "The influence of mode II fracture on concrete strengthened with CFRP", Computers & Structures 82: 1495-1502.
415. Newmark, N.M. (1959). "A Method of Computation for Structural Dynamics", Journal of the Engineering Mechanics Division - ASCE EM3: 67-94.
416. Nguyen, D.T. (2006). "Finite element methods - Parallel-sparse statics and eigen-solutions", Springer Science, Inc.
417. Nicholson, D.W. (2003). "Finite Element Analysis - Thermomechanics of Solids", CRC Press LLC.
418. Nilson, A. (1968). "Nonlinear analysis of reinforced concrete by the finite element method", ACI Journal 65(9): 757-766.
419. Oliveira, C.S. (2008). "Efeitos naturais, impacte e mitigação", Sismos e Edifícios. Edited by M. Lopes. Amadora, Portugal, Edições Orion.

420. Oliver, J. (1989). "A consistent characteristic length for smeared cracking models", International Journal for Numerical Methods in Engineering 28(2): 461-474.

421. Oliver, J., M. Cervera, S. Oller, and J. Lubliner (1990). "Isotropic Damage Models and Smeared Crack Analysis of Concrete", Journal of Eng. Materials and Techn. 105: 99-105.

422. Oliver, J., A.E. Huespe, M.D.G. Pulido, and E. Chaves (2002). "From continuum mechanics to fracture mechanics: the strong discontinuity approach", Engineering Fracture Mechanics 69(2): 113-136.

423. Ortiz, M. (1985). "A constitutive theory for the inelastic behaviour of concrete", Mechanics of Materials 4: 67-93.

424. Otani, S. (1980). "Nonlinear dynamic analysis of reinforced concrete building structures", Canadian Journal of Civil Engineering 7(2): 333-344.

425. Ouglova, A. (2004). "Etude de l'effet de la corrosion sur le comportement des structures", Thèse de Doctorat, ENS Cachan, Cachan, France.

426. Ouglova, A., Y. Berthaud, F. Foct, M. François, F. Ragueneau, and I. Petre-Lazar (2008). "The influence of corrosion on bond properties between concrete and reinforcement in concrete structures", Materials and Structures 41(5): 969-980.

427. Owen, D.R.J. and E. Hinton (1980). "Finite Elements in Plasticity - Theory and Practice", Pineridge Press Limited, Swansea, U.K.

428. Pamin, J. (1994). "Gradient-dependent plasticity in numerical simulation of localization phenomena", PhD Thesis, Delft Technical University, Delft.

429. Panthaki, F.D. (1992). "Low cycle fatigue behavior of high strength and ordinary reinforcing steels", Master Science, State University of New York at Buffalo, Buffalo, USA.

430. Park, K.C. (1975). "Evaluating Time Integration Methods for Nonlinear Dynamic Analysis", Finite Element Analysis of Transient Nonlinear Behaviour AMD-Vol.14, ASME, New York.

431. Park, R., D.C. Kent, and R.A. Sampson (1972). "Reinforced Concrete Members with Cyclic Loading", Journal of the Structural Division, ASCE 98(ST7): 1341-1360.

432. Park, R. and T. Paulay (1975). "Reinforced Concrete Structures", John Wiley & Sons, Inc., 1st Ed., New York.

433. Park, Y.J., A.H.S. Ang, and Y.K. Wen (1984). "Seismic damage analysis and damage-limiting design of RC buildings". University of Illinois, Urbana, USA.

434. Park, Y.J., A.H.S. Ang, and Y.K. Wen (1987). "Damage-limiting aseismic design of buildings", Earthquake Spectra 3(1): 1-26.

435. Paulay, T. and M.J.N. Priestley (1992). "Seismic design of reinforced concrete and masonry buildings", Wiley, New York.

436. Peerlings, R.H.J. (1999). "Enhanced damage modelling for fracture and fatigue", PhD Thesis, Delft Technical University, Delft.

437. Peerlings, R.H.J., R. De Borst, W.A.M. Brekelmans, and J.H.P. De Vree (1996). "Gradient enhanced damage for quasi-brittle materials", International Journal for Numerical Methods in Engineering 39(19): 3391-3403.

438. Peerlings, R.H.J., R. de Borst, W.A.M. Brekelmans, J.H.P. de Vree, and I. Spee (1996). "Some observations on localization in non-local and gradient damage models", European Journal of Mechanics A/Solids 15(6): 937-953.

439. Peerlings, R.H.J., R. de Borst, W.A.M. Brekelmans, and M.G.D. Geers (1998). "Gradient-enhanced damage modelling of concrete fracture", Mechanics of Cohesive-frictional Materials 3(4): 323-342.

440. Peerlings, R.H.J., M.G.D. Geers, R. de Borst, and W.A.M. Brekelmans (2001). "A critical comparison of nonlocal and gradient-enhanced softening continua", International Journal of Solids and Structures 38(44-45): 7723-7746.

441. Pegon, P. (2001). "Alternative characterization of time integration schemes", Computer Methods in Applied Mechanics and Engineering 190(20-21): 2707-2727.

442. Pegon, P. (2008). "Continuous PsD Testing With Substructuring", Modern Testing Techniques for Structural Systems. Edited by O. Bursi and D. Wagg. Wien, Springer.

443. Penrose, R. (1955). "A generalized inverse for matrices", Proceedings of the Cambridge Philosophical Society 51: 406–413.

444. Petersen, K.B. and M.S. Pedersen (2008). "The Matrix Cookbook", Technical University of Denmark, Version 2008-11-10.

445. Petersson, P.-E. (1981). "Crack Growth and Formation of Fracture Zones in Plain Concrete and Similar materials", PhD Thesis, Div of Building Materials LTH, Lund university, Lund, Sweden.

446. Petyt, M. (1990). "Petyt, M., Introduction to Finite Element Vibration Analysis", Cambridge University Press, Cambridge, UK.

447. Pijaudier-Cabot, G. (2000). "Continuum damage modelling", Numéro spécial de la Revue Française de Génie Civil, Ecole d'été ALERT, Constitutive Modelling of Geomaterials, Cambou and Di Prisco ed. 4(5): 33-57.

448. Pijaudier-Cabot, G. and Z.P. Bažant (1987). "Nonlocal Damage Theory", Journal of Engineering Mechanics 113(10): 1512-1533.

449. Pinho, R., R. Bento, and C. Bhatt (2008). "Assessing the 3D Irregular SPEAR building with nonlinear static procedures", 14th World Conference on Earthquake Engineering, October 12-17, Beijing, China.

450. Pinto, A.V. (1998). "Earthquake Performance of Structures - Behavioural, Safety and Economical Aspects", PhD, Instituto Superior Técnico - Universidade Técnica de Lisboa, Lisboa.

451. Pipa, M. (1993). "Ductilidade de Elementos de Betão Armado Sujeitos a Acções Cíclicas - Influência das Características Mecânicas das Armaduras", Doutoramento em Engenharia Civil, Instituto Superior Técnico, Universidade Técnica de Lisboa, Lisboa.

452. Pippard, A.B. (1966). "Elements of Classical Thermodynamics", University Press, Cambridge, UK.

453. Pituba, J., S. Proença, and M. Álvares (1999). "Estudo do desempenho de modelos de dano para estruturas reticuladas em concreto armado", Computational Methods in Engineering '99, São Paulo, Brazil.

454. Planas, J. and M. Elices (1992). "Asymptotic analysis of a cohesive crack: 1. Theoretical background", International Journal of Fracture 55(2): 153-177.

455. Planas, J. and M. Elices (1993). "Asymptotic analysis of a cohesive crack: 2. Influence of the softening curve", International Journal of Fracture 64(3): 221-237.

456. Plesha, M.E. and T. Belytschko (1985). "A constitutive operator splitting method for nonlinear transient analysis", Computers & Structures 20(4): 767-777.

457. Pochanart, S. and T. Harmon (1989). "Bond-slip model for generalized excitation including fatigue", ACI Materials Journal 86(5): 465-476.

458. Prager, W. (1949). "Recent developments in the mathematical theory of plasticity", J. Appl. Phys. 20: 235-241.

459. Prandtl, L.T. (1924). "Spannungsverteilung in plastischen Korpern", Proc. 1st Intern. Congr. Mechanics, Delft.

460. Priestley, M.J.N. and R. Park (1987). "Strength and Ductility of Concrete Bridge Colums Under Seismic Loading", ACI Structural Journal 84(S8).

461. Proença, S.P.B. (2008). "Introdução às Mecânicas do Dano e Fratura", Escola de Engenharia de São Carlos, Universidade de São Paulo, São Paulo.

462. Proença, S.P.B. and A.R. Balbo (2004). "On a regular convex solver potential for an elastic-damage constitutive model: a theoretical analysis", International Journal of Solids and Structures 41(7): 1975-1989.

463. Proença, S.P.B. and J.J.C. Pituba (2003). "A damage constitutive model accounting for induced anisotropy and bimodular elastic response", Latin American Journal of Solids and Structures 1(1): 101-117.

464. Protezione Civile. (2011). "Terremoto in Abruzzo - 2009", Retrieved 2011-02-02, from http://www.protezionecivile.it/jcms/it/emergenza_abruzzo.wp.

465. Przemieniecki, J.S. (1963). "Matrix structural analysis of substructures", Am. Inst. Aero. 1: 138-147.

466. Rabotnov, Y.N. (1968). "Creep Rupture", 12th International Congress of Applied Mechanics, Stanford.

467. Ragueneau, F., N. Dominguez, and A. Ibrahimbegovic (2006). "Thermodynamic-based interface model for cohesive brittle materials: Application to bond slip in RC structures", Computer Methods in Applied Mechanics and Engineering 195(52): 7249-7263.

468. Ramberg, W. and W. Osgood (1943). "Description of Stress-Strain Curves by Three Parameters", Technical notes. National Advisory Committee for Aeronautics, Washington.

469. Ramtani, S. (1990). "Contribution à la modélisation du comportement multiaxial du béton endommagé avec description du caractère unilatéral", PhD Thèse, Université de Paris VI, Paris.

470. Ramtani, S., Y. Berthaud, and J. Mazars (1992). "Orthotropic behavior of concrete with directional aspects: modelling and experiments", Nuclear Engineering and Design 133(1): 97-111.

471. REBAP (1983). "Regulamento de Estruturas de Betão de Armado e Pré-Esforçado", Decreto-Lei nº 349-C/83 de 30 de Julho, Imprensa Nacional Casa da Moeda. Lisboa.

472. Reddy, J.N. (1993). "An Introduction to The Finite Element Method", McGraw-Hill Inc., 2nd Ed., New York.

473. Rehm, G. (1957). "The fundamental law of bond", Proceedings of the Symposium on Bond and Crack Formation in Reinforced Concrete, Stockholm, Sweden, Tekniska Hogskolans Rotaprinttrynchkeri.

474. Rehm, G. (1961). "The basic principle of bond between steel and concrete", Deutscher Ausschuss fur Stahlbeton, no. 138 (C & CA Library Translation no. 134, 1968), Wilhelm Ernest and Sohn, Berlin.

475. Reinhardt, H.W., H.A.W. Cornelissen, and D.A. Hordijk (1986). "Tensile Tests and Failure Analysis of Concrete", Journal of Structural Engineering 112(11): 2462-2477.

476. Reinhardt, H.W. and X. Shilang (2000). "A practical testing approach to determinate mode II fracture energy for concrete", International Journal of Fracture 105: 107-125.

477. Reynolds, O. (1885). "On the dilatancy of media composed of rigid particles in contact", Phil. Mag. 5th Ser. 20: 469.

478. Rice, J.R. (1968). "A path independent integral and the approximate analysis of strain concentration by notches and cracks", Journal of Applied Mechanics 35: 379-386.

479. Richard, B., F. Ragueneau, C. Cremona, L. Adelaide, and J.L. Tailhan (2010). "A three-dimensional steel/concrete interface model including corrosion effects", Engineering Fracture Mechanics 77(6): 951-973.

480. Richart, F., A. Brandtzaeg, and R. Brown (1928). "A study of the failure of concrete under combined compressive stress", Bulletin nº 185. University of Illinois Engineering Experimental Station, Chicago.

481. Riks, E. (1972). "The application of Newton's method to the problem of elastic stability", J. Appl. Mech. 39: 1060-1066.

482. Riks, E. (1979). "An incremental approach to the solution of snapping and buckling problems", Int. J. Solids & Structs. 15: 529-551.

483. RILEM (1985). "Determination of the fracture energy of mortar and concrete by means of three-point bend tests on notched beams", Materials and Structures 18(4): 287-290.

484. Roeck, Y.-H.D. and P. LeTallec (1990). "Analysis and Test of a Local Domain Decomposition Preconditioner", 4th International Conference on Domain Decomposition Methods, Moscow, Russia.

485. Romdhane, M.R.B. and F.J. Ulm (2002). "Computational mechanics of the steel–concrete interface", International Journal for Numerical and Analytical Methods in Geomechanics 26(2): 99-120.

486. Roux, F. (1997). "Parallel implementation of direct solution strategies for the coarse grid solvers in 2-level FETI method", Technical Report, ONERA, Paris, France.

487. Roylance, D. (2001). "Introduction to Fracture Mechanics", Department of Materials Science and Engineering. Massachusetts Institute of Technology, Cambridge, MA, USA.

488. RSA (1983). "Regulamento de Segurança e Acções para Estruturas de Edifícios e Pontes", Decreto-Lei nº 235/83 de 31 de Maio, Imprensa Nacional Casa da Moeda. Lisboa.

489. RSCCS (1958). "Regulamento de Segurança das Construções contra os Sismos", Imprensa Nacional, Decreto nº 41658 de 31 de Maio. Lisboa.

490. Russo, G. and F. Romano (1992). "Cracking Response of RC Members Subjected to Uniaxial Tension", Journal of Structural Engineering 118(5): 1172-1190.

491. Russo, G., G. Zingone, and F. Romano (1990). "Analytical Solution for Bond-Slip of Reinforcing Bars in R.C. Joints", Journal of Structural Engineering 116(2): 336-355.

492. Saad, Y. (2000). "Iterative Methods for Sparse Linear Systems", with corrections - January 3rd, 2nd Ed.

493. Sadd, M.H. (2005). "Elasticity - Theory, Applications and Numerics", Elsevier Inc., USA.

494. Saiidi, M. and M.A. Sozen (1979). "Simple and complex models for nonlinear seismic response of reinforced concrete structures ", UILU-ENG-79-2013, 1979-08, University of Illinois at Urbana-Champaign.

495. Saiidi, M. and M.A. Sozen (1981). "Simple Nonlinear Seismic Analysis of R/C Structures", ASCE, Journal of the Structural Division 107(ST5): 937-52.

496. Saouma, V.E. (2000). "Lecture Notes in Fracture Mechanics", CVEN-6831. University of Colorado - Dept. of Civil Environmental and Architectural Engineering, Boulder, USA.

497. SAP2000 (2009). "SAP2000 - Structural Analysis Program", version Advanced 14.0.0, Computers & Structures Inc.

498. SCEDC. (2011). "Southern California Earthquake Data Center", Retrieved 2011-07-16, from http://www.data.scec.org/chrono_index/slide_ncsun1.html.

499. Scott, M.H. and G.L. Fenves (2006). "Plastic Hinge Integration Methods for Force-Based Beam--Column Elements", Journal of Structural Engineering 132(2): 244-252.

500. Seabold, J. (1970). "Dynamic Shear Strength of Reinforced Concrete Beams - Part III", Technical Report R695. Naval Civil Engineering Laboratory, Port Hueneme, CA, USA.

501. SEAOC (1995). "Performance based seismic engineering of buildings, Part 2: Conceptual framework - Vision 2000 Committee". Structural Engineers Association of California, Sacramento, California.

502. Sener, S., Z.P. Bažant, and E. Becq-Giraudon (1999). "Size Effect on Failure of Bond Splices of Steel Bars in Concrete Beams", Journal of Structural Engineering 125(6): 653-660.

503. Sharma, G. and J. Martin (2009). "MATLAB: A Language for Parallel Computing", Int. J. Parallel Prog(37): 3-36.

504. Sharma, K.G. and C.S. Desai (1992). "Analysis and Implementation of Thin-Layer Element for Interfaces and Joints", Journal of Engineering Mechanics 118(12): 2442-2462.

505. Shewchuk, J.R. (1994). "An Introduction to the Conjugate Gradient Method without the Agonizing Pain". School of Computer Science, Carnegie Mellon University, Pittsburgh, USA.

506. Shima, H., L. Chou, and H. Okamura (1987). "Bond characteristics in post-yield range on deformed bars", Concrete Library of JSCE 10: 113-124.

507. Shima, H., L. Chou, and H. Okamura (1987). "Micro and macro models for bond behavior in reinforced concrete", Journal of the Faculty of Engineering 39(2): 133-194.

508. Silva, C.M. (2006). "Modelos de Dano em Elementos Finitos Híbridos e Mistos", Doutoramento em Engenharia Civil, Universidade Técnica de Lisboa, Instituto Superior Técnico, Lisboa.

509. Silva, C.M. and L.M.S.S. Castro (2003). "Aplicação de modelos HM à análise fisicamente não linear de pórticos de betão armado", VII Congresso de Mecânica Aplicada e Computacional, Évora, Portugal.

510. Silva, C.M. and L.M.S.S. Castro (2005). "Hybrid-mixed stress model for the nonlinear analysis of concrete structures", Computers & Structures 83(28-30): 2381-2394.

511. Silva, C.M. and L.M.S.S. Castro (2007). "Hybrid-displacement (Trefftz) formulation for softening materials", Computers & Structures 85(17-18): 1331-1342.

512. Simone, A. (2003). "Continuous-discontinuous modelling of failure", Ph.D Thesis, Delft Technical University, Delft.

513. Simone, A. (2004). "Partition of unity-based discontinuous elements for interface phenomena: computational issues", Communications in Numerical Methods in Engineering 20(6): 465-478.

514. Simone, A., C.A. Duarte, and E. Van der Giessen (2006). "A Generalized Finite Element Method for polycrystals with discontinuous grain boundaries", International Journal for Numerical Methods in Engineering 67(8): 1122-1145.

515. Sinha, B., K. Gerstle, and L. Tulin (1964). "Stress and Strain Relationships for Concrete under Cyclic Loading", Journal ACI 61(2).

516. Smith, K.N., P. Watson, and T.H. Topper (1970). "A stress strain function for the fatigue of metals", J. Materials 5(767-776).

517. Solomos, G. and M. Berra (2005). "Compressive Behaviour of Plain Concrete at Higher Strain-Rates", Journal of the Mechanical Behavior of Materials 16(1-2): 113-121.

518. Somayaji, S. and S.P. Shah (1981). "Bond stress versus slip relationship and cracking response of tension members", ACI Journal 78(3): 217-225.

519. Sonntag, R.E., C. Borgnakke, and G.J. Van Wylen (2003). "Fundamentals of Thermodynamics", John Wiley & Sons, Inc., 6th Ed.

520. Sousa, M.L. (2006). "Risco Sísmico em Portugal Continental", Doutoramento em Engenharia do Território, Universidade Técnica de Lisboa - Instituto Superior Técnico, Lisboa.

521. Spacone, E., V. Ciampi, and F.C. Filippou (1992). "A beam element for seismic damage analysis", Report No. UCB/EERC-92/07. Earthquake Engineering Research Center, University of California, Berkeley, USA.

522. Spiegel, M.R. and L. Abellanas (1990). "Fórmulas e Tabelas de Matemática Aplicada", McGraw-Hill.

523. Spiliopoulos, K.V. and G.C. Lykidis (2006). "An efficient three-dimensional solid finite element dynamic analysis of RC structures", Earthquake Engineering & Structural Dynamics 35: 137-157.

524. Stanton, J.F. and H.D. McNiven (1979). "The development of a mathematical model to predict the flexural response of reinforced concrete beams to cyclic loads, using system identification", Report No. UCB/EERC-79/02. Earthquake Engineering Research Center, University of California, Berkeley, USA.

525. Stolarska, M., D.L. Chopp, N. Moës, and T. Belytschko (2001). "Modelling crack growth by level sets in the extended finite element method", International Journal for Numerical Methods in Engineering 51(8): 943-960.

526. Strang, G. (1988). "Linear Algebra and Its Applications", Brooks/Cole - Thomson Learning, 3rd Ed.

527. Strouboulis, T., I. Babuska, and K. Copps (2000). "The design and analysis of the Generalized Finite Element Method", Computer Methods in Applied Mechanics and Engineering 181(1-3): 43-69.

528. Strouboulis, T., K. Copps, and I. Babuscaronka (2000). "The generalized finite element method: an example of its implementation and illustration of its performance", International Journal for Numerical Methods in Engineering 47(8): 1401-1417.

529. Stutzman, P. (2007). "The concrete microscopy library", from http://cee.uiuc.edu/research/dlange/concretemicroscopy/index.html.

530. Suaris, W. and S.P. Shah (1983). "Properties of Concrete Subjected to Impact", Journal of Structural Engineering 109: 1727-1741.

531. Suaris, W. and S.P. Shah (1984). "Rate-Sensitive Damage Theory for Brittle Solids", Journal of Engineering Mechanics 110(6): 985-997.

532. Suaris, W. and S.P. Shah (1985). "Constitutive Model for Dynamic Loading of Concrete", Journal of Structural Engineering 111(3): 563-576.

533. Suidan, M.T. and R.A. Eubanks (1973). "Cumulative Fatigue Damage in Seismic Structures", Journal of the Structural Division - ASCE 99(ST5): 923-941.

534. Takayanagi, T. and W.C. Schnobrich (1979). "Non-linear analysis of coupled wall systems", Earthquake Engineering & Structural Dynamics 7(1): 1-22.

535. Takeda, T., M.A. Sozen, and M.N. Nilsen (1970). "Reinforced Concrete Response to Stimulated Earthquakes", Journal of Structural Engineering 96(12).

536. Tassios, T.P. (1979). "Properties of bond between concrete and steel under load cycles idealizing seismic actions", CEB - Bulletin d'Information Nº131, Vol. 1, Rome.

537. Taucer, F.F., E. Spacone, and F.C. Filippou (1991). "A fiber beam-column element for seismic response analysis of reinforced concrete structures", Report No. UCB/EERC-91/17. Earthquake Engineering Research Center, University of California, Berkeley, USA.

538. Tepfers, R. (1979). "Cracking of concrete cover along anchored deformed reinforcing bars", Magazine of Concrete Research 31(106): 3-12.

539. Timoshenko, S.P. and J.N. Goodier (1982). "Theory of Elasticity", McGraw-Hill, 3rd Ed., Singapore.

540. Top500. (2011). "Interconnect Family share for 11/2010", Retrieved 2011-01-15, from http://www.top500.org/charts/list/36/connfam.

541. Topping, B.H.V. (2009). "High Performance Computations for Engineering: Introduction", Lecture notes on the "High Performance Computations for Engineering, Ph.D. Course, Pécs, Hungary.

542. Toselli, A. and O. Widlund (2005). "Domain Decomposition Methods - Algorithms and Theory", Springer, New York.

543. Totman, C.A. and J.P. Dempsey (2003). "Design of Concrete Fracture Experiments", Proceedings of the 2003 American Society for Engineering Education Annual Conference & Exposition.

544. Trefethen, L.N. and I. David Bau (1997). "Numerical Linear Algebra", Society for Industrial and Applied Mathematics, Philadelphia.

545. Tresca, H. (1864). "Sur l'écoulement des Corps solides soumis à des fortes pressions", C R Acad Sci Paris 59: 754–756.

546. Trunk, B. and F.H. Wittmann (1998). "Experimental investigation into the size dependence of fracture mechanics parameters", Fracture mechanics of concrete structures - 3rd Int. Conf. of Fracture Mechanics of Concrete Structures, Aedificatio Publ.

547. Türk, K., A. Benli, and Y. Calayir (2008). "Bond strength of tension lap-splices in full scale self-compacting concrete beams", Turkish J. Eng. Env. Sci. 32(6): 377-386.

548. Türk, K., S. Caliskan, and M.S. Yildirim (2005). "Influence of loading conditions and reinforcement size on the concrete/reinforcement bond strength", Structural Engineering and Mechanics 19(3): 337-346.

549. Turner, M.J., R.W. Clough, H.C. Martin, and L.J. Topp (1956). "Stiffness and Deflection Analysis of Complex Structures", Journal of Aeronautical Science 23: 805-823.

550. USGS. (2011). "Earthquakes with 50000 or more Deaths - Most Destructive Known Earthquakes on Record in the World", Retrieved 2011-03-03, from http://earthquake.usgs.gov/earthquakes/world/most_destructive.php.

551. Vakulenko, A.A. and M.L. Kachanov (1971). "Continuum theory of medium with cracks", Mekhanika Tverdogo Tela 4: 159–166.

552. van Doormaal, J., C.A.M., J. Weerheijm, and L. Sluys, J. (1994). "Experimental and numerical determination of the dynamic fracture energy of concrete", J. Phys. IV France 04(C8): C8-501-C8-506.

553. Vaz, C.T. (1992). "Comportamento Sísmico de Pontes com Pilares de Betão Armado", Doutoramento em Engenharia Civil, Faculdade de Engenharia da Universidade do Porto, Porto.

554. Venant, J.B.d.S. (1871). "Mémoire sur l'établissement des équations différentielles des mouvements intérieurs opérés dans les corps solides ductiles", J. Math. Pures et Appl. 16: 308-316.

555. Ventura, G. (2006). "On the elimination of quadrature subcells for discontinuous functions in the eXtended Finite-Element Method", International Journal for Numerical Methods in Engineering 66(5): 761-795.

556. Vermeer, P.A. and R. de Borst (1984). "Non-associated plasticity for soils, concrete and rock", Heron, TU Delft 29(3).

557. Vidic, T., P. Fajfar, and M. Fischinger (1994). "Consistent inelastic design spectra: Strength and displacement", Earthquake Engineering & Structural Dynamics 23(5): 507-521.

558. Viwathanatepa, S., E. Popov, and V. Bertero (1979). "Effects of generalized loadings on bond of reinforcing bars embedded in confined concrete blocks", Report UCB-EERC-79/22. Earthquake Engineering Research Center, University of California, Berkeley, USA.

559. Von Mises, R. (1913). "Mechanik der festen Koerper in Plastisch deformabelm Zustand", Geottinger Nachr. Math. Phys.: 582-592.

560. Vos, E. and H. Reinhardt (1982). "Influence of loading rate on bond behaviour of reinforcing steel and prestressing strands", Materials and Structures 15(1): 3-10.

561. Wells, G.N., L.J. Sluys, and R. de Borst (2002). "Simulating the propagation of displacement discontinuities in a regularized strain-softening medium", International Journal for Numerical Methods in Engineering 53(5): 1235-1256.

562. Wempner, G.A. (1971). "Discrete approximations related to nonlinear theories of solids", Int. J. Solids & Structs.(7): 1581-1599.

563. Wikipedia. (2007). "Concrete", Retrieved 2007-10-19, from http://en.wikipedia.org/wiki/Concrete.

564. Wikipedia. (2010). "Processor affinity", Retrieved 2010-12-23, from http://en.wikipedia.org/w/index.php?oldid=392954891.

565. Wikipedia. (2010). "Scheduling (computing)", Retrieved 2010-12-27, from http://en.wikipedia.org/wiki/Scheduling_%28computing%29#Operating_system_scheduler_implementations.

566. Wikipedia. (2010). "Speedup", Retrieved 2011-01-07, from http://en.wikipedia.org/w/index.php?oldid=404095630.

567. Wikipedia. (2011). "Divergence theorem", Retrieved 2011-07-14, from http://en.wikipedia.org/wiki/Divergence_theorem.

568. Wikipedia. (2011). "Flynn's taxonomy", Retrieved 2011-01-15, from http://en.wikipedia.org/wiki/Flynn%27s_taxonomy.

569. Wikipedia. (2011). "Moore's law", Retrieved 2011-01-12, from http://en.wikipedia.org/wiki/Moore%27s_law.

570. Wikipedia. (2011). "Ramberg–Osgood relationship", Retrieved 2011-04-11, from http://en.wikipedia.org/wiki/Ramberg%E2%80%93Osgood_relationship.

571. Wikipedia. (2011). "Thermodynamic free energy", Retrieved 2011-07-12, from http://en.wikipedia.org/wiki/Thermodynamic_free_energy.

572. Wikipedia. (2011). "Thermodynamics", Retrieved 2011-03-12, from http://en.wikipedia.org/wiki/Classical_thermodynamics.

573. Wikipedia. (2011). "Thesis", Retrieved 2011-03-02, from http://en.wikipedia.org/wiki/Thesis.

574. Wilson (2002). "3D static and dynamic analysis of structures", Computers and Structures, Inc., 3rd Ed., Berkeley, California, USA.

575. Wilson, E.L. (1968). "A Computer Program for the Dynamic Stress Analysis of Underground Structures", SESM Report No. 69-1. Division of Structural Engineering and Structural Mechanics - University of California, Berkeley.

576. Wilson, E.L., A. Der Kiureghian, and E.P. Bayo (1981). "A replacement for the SRSS method in seismic analysis", Earthquake Engineering & Structural Dynamics 9(2): 187-192.

577. Wischers, G. (1978). "Application of Effects of Compressive Loads on Concrete". Betontech. Ber. Nº 2-3, Düsseldorf.

578. Wittmann, F.H. (2002). "Crack formation and fracture energy of normal and high strength concrete", Crack formation & fracture energy of concrete 27(Part 4): 413–423.

579. Wood, D.S. (1956). "Rapid Loading Tests on Three Grades of Reinforcing Steel", Contract Report R-56-5 under Contract N0y-90922. Naval Civil Engineering Laboratory, Port Hueneme, CA, USA.

580. Wu, H.C. (2005). "Continuum Mechanics and Plasticity", Chapman & Hall/CRC Press.

581. Xu, X.P. and A. Needleman (1994). "Numerical simulations of fast crack growth in brittle solids", Journal of the Mechanics and Physics of Solids 42(9): 1397-1434.

582. Yankelevsky, D.Z. and H.W. Reinhardt (1989). "Uniaxial Behavior of Concrete in Cyclic Tension", Journal of Structural Engineering 115(1): 166-182.

583. Yazdani, S. and H.L. Schreyer (1990). "Combined Plasticity and Damage Mechanics Model for Plain Concrete", Journal of Engineering Mechanics 116(7): 1435-1451.

584. Yu, M.H. (2006). "Generalized Plasticity", Springer-Verlag, Berlin.

585. Ziegler, H. (1977). "An Introduction to Thermomechanics", North-Holland.

586. Zienkiewicz, O.C., B. Best, C. Dullage, and K. Stagg (1970). "Analysis of nonlinear problems in rock mechanics with particular reference to jointed rock systems", 2nd International Congress on Rock Mechanics. Belgrade.

587. Zienkiewicz, O.C. and R.L. Taylor (1989). "The Finite Element Method - Volume 1 - Basic Formulation and Linear Problems", McGraw-Hill, 4th Ed., London.

588. Zienkiewicz, O.C. and R.L. Taylor (2000). "The Finite Element Method - Volume 1 - The Basis", Butterworth-Heinemann, 5th Ed., Oxford.

589. Ziyaeifar and Noguchi (2000). "A refined model for beam elements and beam column joints", Computers and Structures 76: 551-564.

ERRATA

For the PhD Thesis of Luís André Marcos Mendes

REFINED THREE-DIMENSIONAL SEISMIC ANALYSIS
OF REINFORCED CONCRETE STRUCTURES
(as of January 6, 2012)

Page	Where	Reads	Should read
14	Equation (II.11)	$\sigma_{ij}\, n_i = t_{\gamma i}$, on Γ_σ	$\sigma_{ij}\, n_i = t_{\gamma j}$, on Γ_σ
87	Equation (III.37)	$\frac{(1-\nu^2)\, K_{\mathrm{I}}^2}{E}$, plane stress	$\frac{(1-\nu^2)\, K_{\mathrm{I}}^2}{E}$, plane strain
176	3rd par.; 1st line	Accordingly, the results obtained by Mander *et al.* [72] …	Accordingly, the results obtained by Mander *et al.* [364] …
177	Figure III.83-Caption	… Mander *et al.* [72].	… Mander *et al.* [364].
181	Table III.18	e_f	ε_f
181	Figure III.86-b	leftmost branch is labelled "4"	"3"
240	Figure IV.3	bond stress (τ_s)	bond stress (τ_b)
280	Figure IV.31-b	arrow is off place	should be placed on the second leftmost unloading branch, labelled "1"
283	3rd par.; 3rd line	… for very large values of γ_b, thus …	… for very large values of s^*, thus …
283	4th par.; 4th line	… and γ_n that can be used …	… and ii) γ_n that can be used …
286	Figure IV.39-Caption	Sub-model for the peak stress slip …	Sub-model for the reload slip …
288	Equation (IV.21)	$\mathbf{v}_3 = \mathbf{v}_1 \times \mathbf{v}_2$	$\mathbf{v}_3 = \mathbf{v}_2 \times \mathbf{v}_1$
288	Equation (IV.22)	$\mathbf{n} = \mathbf{v}_3 \times \mathbf{v}_1$	$\mathbf{n} = \mathbf{v}_3 \times \mathbf{v}_2$
289	Equation (IV.29)	$s_{adh}(\eta) = s_{adh}(\eta_0)\, \eta$	$s_{pb}(\eta) = s_{pb}(\eta_0)\, \eta$
288	Reference to Equation (II.11)	$\sigma_{ij}\, n_i = t_i$	$\sigma_{ij}\, n_i = t_j$
297	(IV.57)	$\mathbf{B}^t(y_1,y_2,y_3)_{gp}\, \mathbf{k}^*_{gp}\, \mathbf{B}(y_1,y_2,y_3)_{gp} \det\mathbf{J}(y_1,y_2,y_3)$	$\mathbf{B}^t(y_1)_{gp}\, \mathbf{k}^*_{gp}\, \mathbf{B}(y_1)_{gp} \det\mathbf{J}(y_1)$
298	(IV.59)	$\mathbf{B}^t(y_1,y_2,y_3)_{gp} \left(\frac{\partial\boldsymbol{\sigma}}{\partial\mathbf{q}^{rel}}\right)_{gp} \mathbf{B}(y_1,y_2,y_3)_{gp} \det\mathbf{J}(y_1,y_2,y_3)_{gp}$	$\mathbf{B}^t(y_1)_{gp} \left(\frac{\partial\boldsymbol{\sigma}}{\partial\mathbf{q}^{rel}}\right)_{gp} \mathbf{B}(y_1)_{gp} \det\mathbf{J}(y_1)_{gp}$
384	Equation (V.155)	$\delta\mathbf{q}_i^{sd} = \mathbf{K}_{ii}^{sd,-1}\left(-\mathbf{g}_{,i}^{sd} - \mathbf{K}_{ib}^{sd}\, \delta\mathbf{q}_{ib}^{sd}\right)$	$\delta\mathbf{q}_i^{sd} = \mathbf{K}_{ii}^{sd,-1}\left(-\mathbf{g}_{i}^{sd} - \mathbf{K}_{ib}^{sd}\, \delta\mathbf{q}_{b}^{sd}\right)$
395	Equation (V.202)	$\delta\mathbf{q}_i^{sd} = \mathbf{K}_{ii}^{sd,-1}\left(-\mathbf{g}_{,i}^{sd} - \mathbf{K}_{ib}^{sd}\, \delta\mathbf{q}_{b}^{sd}\right)$	$\delta\mathbf{q}_i^{sd} = \mathbf{K}_{ii}^{sd,-1}\left(-\mathbf{g}_{i}^{sd} - \mathbf{K}_{ib}^{sd}\, \delta\mathbf{q}_{b}^{sd}\right)$
432	3rd line	…may be computed by double integration …	…may be computed by double differentiation …
461	1st line	To mitigate this problem, the bond …	To mitigate this problem, the bond model…